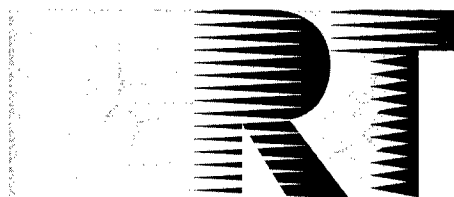


NORTH ATLANTIC TREATY ORGANIZATION



RESEARCH AND TECHNOLOGY ORGANIZATION

BP 25, 7 RUE ANCELLE, F-92201 NEUILLY-SUR-SEINE CEDEX, FRANCE

RTO MEETING PROCEEDINGS 5

Missile Aerodynamics

(Aérodynamique des Missiles)

Papers presented and discussions recorded at the Applied Vehicle Technology Panel Symposium held in Sorrento, Italy, 11-14 May 1998.



DISTRIBUTION STATEMENT A:
Approved for Public Release -
Distribution Unlimited

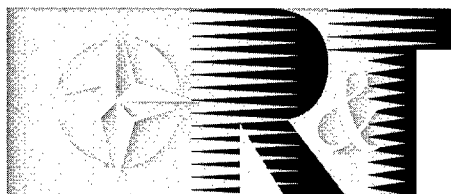
19990126 013

THIS QUALITY DOCUMENT

Published November 1998

Distribution and Availability on Back Cover

NORTH ATLANTIC TREATY ORGANIZATION



RESEARCH AND TECHNOLOGY ORGANIZATION

BP 25, 7 RUE ANCELLE, F-92201 NEUILLY-SUR-SEINE CEDEX, FRANCE

RTO MEETING PROCEEDINGS 5

Missile Aerodynamics

(Aérodynamique des Missiles)

Paper presented and discussions recorded at the Applied Vehicle Technology Panel Symposium held in Sorrento, Italy, 11-14 May 1998.



AQF99-04-0705

The Research and Technology Organization (RTO) of NATO

RTO is the single focus in NATO for Defence Research and Technology activities. Its mission is to conduct and promote cooperative research and information exchange. The objective is to support the development and effective use of national defence research and technology and to meet the military needs of the Alliance, to maintain a technological lead, and to provide advice to NATO and national decision makers. The RTO performs its mission with the support of an extensive network of national experts. It also ensures effective coordination with other NATO bodies involved in R&T activities.

RTO reports both to the Military Committee of NATO and to the Conference of National Armament Directors. It comprises a Research and Technology Board (RTB) as the highest level of national representation and the Research and Technology Agency (RTA), a dedicated staff with its headquarters in Neuilly, near Paris, France. In order to facilitate contacts with the military users and other NATO activities, a small part of the RTA staff is located in NATO Headquarters in Brussels. The Brussels staff also coordinates RTO's cooperation with nations in Middle and Eastern Europe, to which RTO attaches particular importance especially as working together in the field of research is one of the more promising areas of initial cooperation.

The total spectrum of R&T activities is covered by 6 Panels, dealing with:

- SAS Studies, Analysis and Simulation
- SCI Systems Concepts and Integration
- SET Sensors and Electronics Technology
- IST Information Systems Technology
- AVT Applied Vehicle Technology
- HFM Human Factors and Medicine

These Panels are made up of national representatives as well as generally recognised 'world class' scientists. The Panels also provide a communication link to military users and other NATO bodies. RTO's scientific and technological work is carried out by Technical Teams, created for specific activities and with a specific duration. Such Technical Teams can organise workshops, symposia, field trials, lecture series and training courses. An important function of these Technical Teams is to ensure the continuity of the expert networks.

RTO builds upon earlier cooperation in defence research and technology as set-up under the Advisory Group for Aerospace Research and Development (AGARD) and the Defence Research Group (DRG). AGARD and the DRG share common roots in that they were both established at the initiative of Dr Theodore von Kármán, a leading aerospace scientist, who early on recognised the importance of scientific support for the Allied Armed Forces. RTO is capitalising on these common roots in order to provide the Alliance and the NATO nations with a strong scientific and technological basis that will guarantee a solid base for the future.

The content of this publication has been reproduced
directly from material supplied by RTO or the authors.



Printed on recycled paper

Published November 1998

Copyright © RTO/NATO 1998
All Rights Reserved

ISBN 92-837-0002-3



*Printed by Canada Communication Group Inc.
(A St. Joseph Corporation Company)
45 Sacré-Cœur Blvd., Hull (Québec), Canada K1A 0S7*

Missile Aerodynamics

(RTO MP-5)

Executive Summary

This symposium was dedicated to the memory of Dr. Jack Nielsen, who was one of the fathers of missile aerodynamics.

The end of the Cold War has brought us lower production rates of missiles, and therefore, less money for new developments. New types of international conflicts demand new kinds of missiles and a higher flexibility to react to different scenarios. The new missiles have to be of higher modularity and the complete defense system that includes the missile has to be easily transportable. In addition, the design process has to become faster and cheaper. In the future, there will probably be fewer basic missile types but with a higher modularity and closer international standardization. All these trends will, of course, influence the aerodynamic design. One can expect that it will become more complex and that interdisciplinary activities will be of higher importance.

This was the third NATO Symposium on Missile Aerodynamics. At the first Symposium in 1982, the major subjects were vortex shedding, aerodynamic aspects of stealth configurations, and rolling missiles. The use of Computational Fluid Dynamics (CFD) codes was thought to be too costly for practical use. At the second Symposium in 1990, unsteady phenomena played a major role, the problems of stealth design were highlighted, and Panel Methods were the standard prediction code. CFD codes were still quoted as too costly, but promising. In the last 8 years, there has been a lot of progress in experimental techniques and in prediction codes. It is now standard to apply CFD methods to standard problems. Thus, numerical tools have experienced major progress during each of the intermediate periods. However, CFD methods still need better standards and insights into turbulence modeling and faster grid generation.

Aérodynamique des Missiles

(RTO-MP-5)

Synthèse

Ce symposium a été dédié à la mémoire du Dr Jack Nielsen, l'un des fondateurs de l'aérodynamique des missiles.

Avec la fin de la guerre froide la production des missiles a baissé, avec pour conséquence une diminution des budgets de développement. Les nouveaux types de conflits internationaux requièrent de nouveaux types de missiles, associés à une plus grande souplesse face aux différents scénarios qui se présentent. Les nouveaux missiles devront être plus modulaires et facilement transportables par les systèmes complets de défense qu'ils équipent. En outre, il faudra réduire les délais et les coûts de conception. Il est vraisemblable qu'à l'avenir il y aura moins de types de missiles, mais plus de modularité et une plus grande standardisation internationale. Naturellement, toutes ces tendances auront un impact sur la conception aérodynamique. Selon toute probabilité elle deviendra plus complexe avec plus d'importance accordée aux activités interdisciplinaires.

Il s'agit du troisième symposium OTAN sur l'aérodynamique des missiles. Les principaux sujets examinés lors du premier symposium organisé en 1982 étaient l'échappement tourbillonnaire, les aspects aérodynamiques des configurations de furtivité et le roulis des missiles. A cette époque, les codes de calcul CFD étaient considérés comme trop coûteux pour permettre une utilisation pratique. Lors du deuxième symposium en 1990, les phénomènes instationnaires ont joué un rôle important, ainsi que les problèmes de furtivité. Les méthodes de discrétisation avaient été adoptées comme norme pour les codes de prévision, mais les codes de calcul CFD étaient encore considérés comme trop coûteux, quoique prometteurs. Les huit dernières années ont vu des progrès considérables dans le domaine des techniques expérimentales et les codes de prévision. Il est désormais courant d'appliquer les méthodes CFD aux problèmes classiques et des avancées considérables ont été réalisées pendant chacune des périodes intermédiaires. Néanmoins, il ya lieu d'améliorer les normes en matière de méthodes CFD, de mieux comprendre la modélisation des tourbillons et d'écourter les délais de génération des maillages.

Contents

	Page
Executive Summary	iii
Synthèse	iv
Recent Publications of the Former Fluid Dynamics Panel of AGARD	viii
Applied Vehicle Technology Panel Programme Committee	x
	Reference
Technical Evaluation Report by P. Hennig	T
KEYNOTE SESSION	
Contributions to Missile Aerodynamics	1
A Tribute to Dr. Jack N. Nielsen by M.F.E. Dillenius and M.R. Mendenhall	
Future Missile System Trends (U.S.) and their Impact on Aerodynamic Technology by W.C. McCorkle Jr.	2
SESSION 1: AERODYNAMIC DESIGN	
Considérations sur l'Aérodynamique pour le Pilotage et le Guidage des Engins Tactiques by J.-P. Harcaut, E. Larcher, J.-P. Bonnet and S. Dupont	3
Missile Fin Planform Optimization for Improved Performance by D.J. Lesieutre, M.F.E. Dillenius and T.O. Lesieutre	4
Aeroelastic/Aeroservoelastic Tailoring for Hinge Moment Minimization of Missile Fins by P.C. Chen, D. Sarhaddi, D.D. Liu, M. Ratwani and T. Minahen	5
SESSION 2: UNCONVENTIONAL CONFIGURATIONS	
Conformal Lifting and Control Surfaces for Weapon Stowability by L.B. Simpson, F.A. Davis, B.G. Kruggel and E. McLaughlin	6
Aerodynamics of Wrap Around Fins using Experimental and Computational Techniques by C. Berner, G. Abate and A. Dupuis	7
Aerodynamics of Wrap-Around Fins at High Supersonic Speeds by C.P. Tilmann, T.C. McIntyre, R.D.W. Bowersox and T.A. Buter	8
Lattice Controls: A Comparison with Conventional, Planar Fins by G.M. Simpson and A.J. Sadler	9

Experimental Investigations of Grid Fin Aerodynamics: A Synopsis of Nine Wind Tunnel and Three Flight Tests	10
by W.D. Washington and M.S. Miller	
Aerodynamic Prediction Methodology for Grid Fins	11
by R.W. Kretzschmar and J.E. Burkhalter	
Computation of Flows Past Grid Fin Missiles	12
by M. Khalid, Y. Sun and H. Xu	
Experiments and Analyses of an Aerospike Flow Environment for Protecting Infrared Missile Dome	13
by E.J. Boudreaux, V.S. Krishnamurty, A.M. Mitchell and W. Shyy	
Hypersonic Shroud Discard at High Dynamic Pressure	14
by T. Cain and A. Redman	

SESSION 3: JET EFFECTS

The Near Interaction of Lateral Control Jets and Hypervelocity Cross Flow	15
by K.W. Naumann, H. Ende, A. George and G. Mathieu	
Interactions Aérodynamiques sur un Intercepteur Hypersonique Piloté par Jets Transversaux	16
by M. Leplat, P. Champigny, G. Girard, J.V. Hachemin and N. Delattre	
Navier Stokes Simulation Around a High Velocity Missile with Cross-Flow Jet	17
by St.M. Hitzel, P. Hennig and H. Esch	
Etudes Fondamentales sur les Aspects Aérodynamiques et Thermiques des Ecoulements à l'Arrière-corps des Missiles	18
by P. Serval, Ph. Reijasse, R. Benay and B. Corbel	

SESSION 4: FLOW PHYSICS AND TURBULENCE MODELLING

Couche limite autour d'un fuselage de missile en incidence en écoulement supersonique Etude expérimentale et calculs Navier Stokes	19
by P. d'Espiney, P. Champigny, D. Baudin and J.A. Pilon	
Algebraic Turbulence Modelling for Vortical Flows around Slender Bodies	20
by N. Qin and C. Jayatunga	
Filtering Algebraic Turbulence Models for Supersonic High-Incidence Missile Flows	21
by M. Amato and G. Iaccarino	
Simulation of Laminar and Turbulent Flow over an Ogive Cylinder	22
by E. van der Weide and H. Deconinck	
Turbulence Modelling for Supersonic Missile Aerodynamics: From Mixing-Length to Reynolds-Stress Models	23
by F. Thivet, H. Deniau, J.-M. Moschetta and J.-V. Hachemin	
Simulation of Viscous and High Temperature Gas Effects on Standard Shapes in Hypersonic Flow	24
by J.-M. Charbonnier, W. Dieudonné, S. Paris, J. Muylaert and L. Walpot	

A Review of Some Recent New and Improved Semi-Empirical Aeroprediction Methods	25
by F.G. Moore, R.M. McInville and T.C. Hymer	

SESSION 5: PREDICTION METHODOLOGY

Le code de prévision aérodynamique de l'ONERA: "MISSILE"	26
by P. Denis	
3D Euler and Thin Layer Navier Stokes Solutions for Missiles at Supersonic Speeds and High Angles of Attack	27
by E. Oktay, N. Alemdaroğlu, E. Tarhan, P. Champigny and P. d'Espiney	
Computational Investigations of Subsonic High Angle of Attack Missile Flows	28
by I.H. Tuncer, M.F. Platzer and R.D. VanDyken	
Prediction of Pitch-Damping for Symmetric Missiles	29
by P. Weinacht	
Computational Fluid Dynamics Modeling of Multibody Missile Aerodynamic Interference	30
by J. Sahu, H.L. Edge, K.R. Heavey and E.N. Ferry	
Advances in Missile Aeropropulsive Flowfield Simulation	31
by S.M. Dash and B.J. Walker	
Industrial Use of CFD for Missile Studies: New Trends at Matra BAe Dynamics France	32
by M. Brédif, F. Chapin, C. Borel and P. Simon	
Role of CFD in Missile Aerodynamic Design: A Review of Recent Efforts at Raytheon	33
by B. Srivastava, J. Furtek, A. Shelton and R. Paduano	
Missile Aerodynamic Testing at the Arnold Engineering Development Center (AEDC)	34
by E.J. Marquart, W.R. Lawrence and F.C. Lawrence	

SESSION 6: SPECIAL PROBLEMS

An Experimental and Numerical Study of a Supersonic Spinning Missile	35
by S.T. McIlwain, P.C.G. Mallon, R.J. Fleming and G. McConnell	
Air Intake Studies: Experimental Measurements and Computational Modelling	36
by P.E.H. Abrahamsen, B.A. Pettersson Reif, L. Sætran and J.B. Fossdal	
Optimal Missile Inlet Design by means of Automated Numerical Optimization	37
by M. Blaize, D. Knight, K. Rasheed and Y. Kergaravat	
Couplet Aerokinetic Heating of Missile Structures at High Velocities	38
by S.R. Körber	
Aero-optic and Aerothermal Performance of Externally Cooled Infrared Window at Hypersonic Flight Conditions	39
by G.W. Sutton and J.E. Pond	
Time-Averaged and Unsteady Loads on a Missile at Launch from an Internal Weapons Bay	40
by J.A. Ross and J. Odedra	
Paper 41 withdrawn	
General Discussion	GD

Recent Publications of the Former Fluid Dynamics Panel of AGARD

AGARDOGRAPHS (AG)

Turbulent Boundary Layers in Subsonic and Supersonic Flow

AGARD AG-335, July 1996

Computational Aerodynamics Based on the Euler Equations

AGARD AG-325, September 1994

Scale Effects on Aircraft and Weapon Aerodynamics

AGARD AG-323 (E), July 1994

Design and Testing of High-Performance Parachutes

AGARD AG-319, November 1991

Experimental Techniques in the Field of Low Density Aerodynamics

AGARD AG-318 (E), April 1991

Techniques Expérimentales Liées à l'Aérodynamique à Basse Densité

AGARD AG-318 (FR), April 1990

A Survey of Measurements and Measuring Techniques in Rapidly Distorted Compressible Turbulent Boundary Layers

AGARD AG-315, May 1989

REPORTS (R)

Turbulence in Compressible Flows

AGARD R-819, Special Course Notes, June 1997

Advances in Cryogenic Wind Tunnel Technology

AGARD R-812, Special Course Notes, January 1997

Aerothermodynamics and Propulsion Integration for Hypersonic Vehicles

AGARD R-813, Special Course Notes, October 1996

Parallel Computing in CFD

AGARD R-807, Special Course Notes, October 1995

Optimum Design Methods for Aerodynamics

AGARD R-803, Special Course Notes, November 1994

Missile Aerodynamics

AGARD R-804, Special Course Notes, May 1994

Progress in Transition Modelling

AGARD R-793, Special Course Notes, April 1994

Shock-Wave/Boundary-Layer Interactions in Supersonic and Hypersonic Flows

AGARD R-792, Special Course Notes, August 1993

Unstructured Grid Methods for Advection Dominated Flows

AGARD R-787, Special Course Notes, May 1992

Skin Friction Drag Reduction

AGARD R-786, Special Course Notes, March 1992

Engineering Methods in Aerodynamic Analysis and Design of Aircraft

AGARD R-783, Special Course Notes, January 1992

ADVISORY REPORTS (AR)

A Selection of Test Cases for the Validation of Large-Eddy Simulations of Turbulent Flows

AGARD AR-345, April 1998

Ice Accretion Simulation

AGARD AR-344, Report of WG-20, December 1997

Sonic Nozzles for Mass Flow Measurement and Reference Nozzles for Thrust Verification

AGARD AR-321, Report of WG-19, June 1997

Cooperative Programme on Dynamic Wind Tunnel Experiments for Manoeuvring Aircraft

AGARD AR-305, Report of WG-16, October 1996

Hypersonic Experimental and Computational Capability, Improvement and Validation

AGARD AR-319, Vol. I, Report of WG-18, May 1996

Aerodynamics of 3-D Aircraft Afterbodies

AGARD AR-318, Report of WG-17, September 1995

A Selection of Experimental Test Cases for the Validation of CFD Codes

AGARD AR-303, Vols. I and II, Report of WG-14, August 1994

Quality Assessment for Wind Tunnel Testing

AGARD AR-304, Report of WG-15, July 1994

Air Intakes of High Speed Vehicles

AGARD AR-270, Report of WG-13, September 1991

Appraisal of the Suitability of Turbulence Models in Flow Calculations

AGARD AR-291, Technical Status Review, July 1991

Rotary-Balance Testing for Aircraft Dynamics

AGARD AR-265, Report of WG11, December 1990

Calculation of 3D Separated Turbulent Flows in Boundary Layer Limit

AGARD AR-255, Report of WG10, May 1990

CONFERENCE PROCEEDINGS (CP)

Advanced Aerodynamic Measurement Technology

AGARD CP-601, May 1998

Aerodynamics of Wind Tunnel Circuits and Their Components

AGARD CP-585, June 1997

The Characterization & Modification of Wakes from Lifting Vehicles in Fluids

AGARD CP-584, November 1996

Progress and Challenges in CFD Methods and Algorithms

AGARD CP-578, April 1996

Aerodynamics of Store Integration and Separation

AGARD CP-570, February 1996

Aerodynamics and Aeroacoustics of Rotorcraft

AGARD CP-552, August 1995

Application of Direct and Large Eddy Simulation to Transition and Turbulence

AGARD CP-551, December 1994

Wall Interference, Support Interference, and Flow Field Measurements

AGARD CP-535, July 1994

Computational and Experimental Assessment of Jets in Cross Flow

AGARD CP-534, November 1993

High-Lift System Aerodynamics

AGARD CP-515, September 1993

Theoretical and Experimental Methods in Hypersonic Flows

AGARD CP-514, April 1993

Aerodynamic Engine/Airframe Integration for High Performance Aircraft and Missiles

AGARD CP-498, September 1992

Effects of Adverse Weather on Aerodynamics

AGARD CP-496, December 1991

Manoeuvring Aerodynamics

AGARD CP-497, November 1991

Vortex Flow Aerodynamics

AGARD CP-494, July 1991

Missile Aerodynamics

AGARD CP-493, October 1990

Aerodynamics of Combat Aircraft Controls and of Ground Effects

AGARD CP-465, April 1990

Computational Methods for Aerodynamic Design (Inverse) and Optimization

AGARD CP-463, March 1990

Applications of Mesh Generation to Complex 3-D Configurations

AGARD CP-464, March 1990

Fluid Dynamics of Three-Dimensional Turbulent Shear Flows and Transition

AGARD CP-438, April 1989

Applied Vehicle Technology Panel

(Former Fluid Dynamics Panel)

CHAIRMAN: (Pro Tem)
Mr. Louis J. WILLIAMS
Director, Alliance Development
National Aeronautics & Space Administration, RL
WASHINGTON, DC 20546

PROGRAMME COMMITTEE

Prof. Dr. Roland DECUYPERE
Ecole Royale Militaire
Avenue de la Renaissance 30
B-1000 Brussels

Mr. Jean M. MUYLAERT
ESTEC
Aerothermodynamic Section
Postbus 299
2200 AG Noordwijk

Dr. Louis CHAN
High Speed Aerodyn.Lab. - U66
Institute for Aerospace Research
National Research Council Canada
Montreal Road
Ottawa, Ontario K1A 0R6

Mr. Robert LACAU (Chairman)
Aerospatiale Missiles (E/ECN)
Centre des Gatines
91370 Verrières le Buisson Cedex

Dipl. Ing. Peter W. SACHER
Daimler Benz Aerospace
LMLE 3
Postfach 801160
D-81663 MUCHEM

Major H. SMYRLIS
HAF Research and Technology Center
(KETA) Terpsithea Post Office
Glyfada
16501 ATHENS

Prof. Giuseppe P. Russo
Universita di Napoli
Dept di Scienza e Ingegneria dello
Spazio "Luigi G. Napolitano"
Piazza V. Tecchio 80
80125 NAPOLI

Prof. Carmine GOLIA
CIRA
Via Maiorise
81043 CAPUA (CE)

IR Bram ELSENAAR
National Aerospace Laboratory NLR
Anthony Fokkerweg 2
1059 CM AMSTERDAM

Mr. Oyvind GRANDUM
Division for Weapons and Materiel
Norwegian Defence Research Establ.
P.O. Box 25
N-2007 Kjeller

Dr. Luis P. RUIZ CALAVERA
INTA-Dpto Dinamica de Fluidos
Div. de Aerodinamica y Vuelo
Carretera Torrejon Ajalvir, Km 4.5
28850 Torrejon de Ardoz (Madrid)

Prof. Dr. Col. Mehmet AKCAY
Armament & Defence Research
Dept of Turkish General Staff
06100 Ankara

Mr. P.G.C. HERRING
British Aerospace plc
Sowerby Research Centre
FPC 267
P.O. Box 5 - Filton
Bristol BS12 7QW

Mr. David SELEGAN
AFRL/XPA
4375 Chidlaw Road, Suite 6
WRIGHT-PATTERSON AFB
OH 45433-5006

PANEL EXECUTIVE

Mr. J.K. MOLLOY

Mail from Europe:
RTA/OTAN
BP 25
7, Rue Ancelle
F-92201 Neuilly-sur-Seine Cedex
France

Mail from USA and Canada:
RTA/NATO
Unit PSC 116
APO AE 09777

Tel: 33 (1) 55 61 22 75
Fax: 33 (1) 55 61 22 98

Technical Evaluation Report

P. Hennig

Daimler-Benz Aerospace

LFK - Lenkflugkörpersysteme GmbH

Abteilung, FTE12, Postfach 80 11 49

D-81663 München, Germany

Introduction

The following remarks are intended to give a general idea of the major subjects discussed during the Sorrento Symposium and of the trends in future missile aerodynamics that we can recognize at present.

The Sorrento meeting was the third symposium dedicated to „Missile Aerodynamics“. The first one took place 1982 in Trondheim. In the technical evaluation and in the general discussion of this symposium the major subjects were vortex shedding, aerodynamic aspects of stealth configurations and rolling missiles. Prediction codes were the major tools in the studies presented and they also were the main objects for code development. Panel methods were quoted to be „promising“ for the future, and the CFD codes were thought to be „too costly for practical use“. In the next meeting, 1990 in Friedrichshafen, unsteady phenomena played a major role in the presentations and also, again, stealth design problems. In addition to the usual points of interest, as separated flow and the progress in experimental techniques and prediction codes, the panel methods were a „standard“ tool already at that time. The CFD codes, predominantly represented by Euler simulations, were quoted as „still too costly but promising“. Now, after another eight years, the Sorrento Symposium showed a lot of applications for unconventional components and for high speed flow and, as usual, the high angle-of-attack problems. There is still a lot of progress in experimental techniques and in prediction codes. For all institutions it is standard now to apply CFD methods, among others, to standard problems or to execute validation tests. Comparing the résumé of these three symposia one can see that the time of eight years between them marks relevant changes in scientific focuses within missile aerodynamics. Especially the numerical tools have experienced major progress during each of the intermediate periods.

Status and Deficits in Missile Aerodynamics (according to the presentations)

To judge the status of the discipline from the presentations one has to bear in mind the meaning of such a presentation. It usually doesn't show a real standard „state of the art“ but, to be honest, problem solutions for which the speaker is proud of, because he has solved them for the first time with a - in relation to his possibilities - high effort. Therefore, we certainly may assume that the studies presented in such a con-

ference give a more or less true picture of what are the most progressive solutions and research themes in the field of aerodynamics as applied to missiles.

The status of the different design tools is of major interest for the expert involved in projects. Experimental techniques are continuously developed, mainly in pure research studies or for applications other than missiles. Missile studies often can use them only after they have become standard due to their high costs. High speed measurements of 2-D and 3-D distributions of aerodynamic parameters are the most important innovation for future project work. Special techniques are needed for rotating missiles and for the realistic simulation of separation problems of different kind. The transformation of experimental data to free-flight parameters is a major problem that has to be solved by good prediction methods. These methods are still the major tools for the project aerodynamicist and will be so for the next future. They reach from pure empirical methods using large data bases to different kinds of semi-empirical approaches. Usually they set up a physical model for a class of problems, find analytical solutions and adapt certain physical parameters to empirical data. Nowadays, panel methods are often integrated into this procedure and even higher CFD codes may be used in the future for the solution of certain details. The prediction codes mainly aim to be very efficient in time and costs. This might become less important in the future, because of the still increasing computer power, but it will be still valid when aerodynamic simulations are integrated into programs of other disciplines.

The fact that so many CFD results have been shown in the presentations leads to the conclusion that CFD applications are presently the major problem for research aerodynamicists in industry. This means that, on one hand, CFD is not yet really a standard tool in project design but is, on the other hand, widely in use to study special aspects of standard problems. The major difficulties for industrial CFD application are the missing standardization of the codes, the still rather high effort in grid generation for complex geometries, and the reliability of the results for problems with new parameters. Above all, the selection of the optimal turbulence model for each simulation is by far not solved. The problem of handling the large amount of data and of their physical interpretation will arise even more urgently than now when CFD simulations become really standard in the design process. Modern experimental 2-D and 3-D techniques lead to a similar need for the data handling.

The presentations in Sorrento showed a clear tendency to missiles with higher velocity. High supersonic or hypersonic speeds were major project areas, although many of the examples shown originated from conventional supersonic tests. This is possibly due to the fact that hypersonic tests are difficult and expensive and that only a few standard test cases exist for this regime. But the impression caused by the dominating high velocity presentations must be corrected. Also for the other flow regimes not all the problems have been solved. The transonic regime still seems to show the most complex flow phenomena. New approaches are needed in order to simulate them properly for new types of missiles with unconventional shape. Boundary-layer flow, separation and vortical flow are a constant research subject for missiles at high angles of attack, even if not referred to explicitly within the titles of the presentations. In addition to these characteristic flow phenomena for missiles, afterbody and jet flow are of major interest, including their interaction with different objects.

The different problems connected to specific flight conditions can be condensed to the description of unsteady and interference effects of several kinds. Recent applications include for example missiles spinning at high frequency, fast manoeuvres, store separation and separation of submunitions or missile components like sabots or shrouds.

One of the major subjects of the symposium were the unconventional components, especially those for control purposes. Due to the high velocity and the high manoeuvrability of many recently projected missiles new control methods for the hypersonic regime are of very high technological interest. Lateral thrust devices and grid or lattice fins are possible solutions for some of the problems. Hinge moments and the design of actuators are of specific interest for these new control fins, but also aspects of structural mechanics, aerothermodynamics and materials have to be considered. The flow phenomena for both control components are very complex. It seems that we still lack a thorough understanding of the physics. A consistent physical model for the interdependence of the many parameters involved is the precondition for the development of fast design codes needed urgently to meet the already existing project requirements.

Other modern components of high interest include IR seekers and light-weight radomes for high velocities and intakes for airbreathing missiles. A problem that will become more urgent in future is the integration of components like intakes into an optimized shape for high subsonic or supersonic speeds. The store carriage and release from an internal weapons bay and the increasing range of new missiles will increase the need for optimally integrated missile shapes.

In the Sorrento symposium the tendency to multidisciplinary design and simulation was observable already. Aerodynamic aspects of aerothermodynamics, aeroelastics, aeroacoustics, guidance and control, and of design optimization procedures were presented. A coupled simulation of flight mechanics and aerodynamics is of high importance for cases like high precision store release. A full simulation of the missile performance is also needed for critical manoeuvres during the launch phase and in the endgame, especially if hit-to-kill is desired. The simulation of signatures (for example IR signatures of missile bodies and of jets) and the transmission of a laser beam through jet and afterbody flow has to include aerodynamics, too.

Considering these aspects of missile aerodynamics derived from the presentations one can see that further progress is taking place in spite of the heavy difficulties in budgets and manpower. These fast advances are necessary, since the present problems arising in project design and are much ahead of the capabilities of our standard tools and our physical knowledge.

General Deficits in Missile Aerodynamics

The following section shall refer more general observations. Many publications on missile aerodynamics in the literature and during conferences cover rather special details in geometry, flow conditions and problems with numerical tools. This is due to the close connection between these scientific studies and project needs. This close coupling, on the other hand, often leads to shortcomings in general scientific insight. With our lower budgets of today we cannot afford a lot of very specific studies any more. One of the methods to increase the efficiency of a study is to develop a better understanding of the physics of the problem. This will help in many other cases, while a study of even a large set of special parameter combinations supplies us only with a few points in a multidimensional parameter space. This is in particular valid for unconventional geometries and flow conditions. Therefore, we have to ask each aerodynamicist to study the general physical meaning of his problem and to set up his experimental and numerical tests in a way that not only his project needs are met but that also as much progress as possible is made in understanding the physics.

To many people some deep gap seems to exist between traditional design methods and CFD, and the characteristics of the different approaches are often discussed rather emotionally. This distinction is not justified. Considering the state-of-the-art in this area, CFD tools are still „semi-empirical“ in many aspects.

Mainly the turbulence modelling, but also the grid generation (type and size) and sometimes the solvers have to be „validated“ and adapted to the different types of configurations and flow conditions before they can be applied to new project problems. This means that most of the present CFD studies are preparing future applications instead of using a standard tool. The major difference between CFD and semi-empirical methods is the difference in the fundamental approach. In pure CFD we make basic approximations in the flow physics (for example continuum flow, parabolization and others) and we then set up its mathematical formulation. The problems that appear during applications are mainly of mathematical nature and they are solved by adapting numerical parameters until the results are satisfactory. In semi-empirical methods we model the flow physics of a special problem and formulate it, mostly in analytical form. Differences between predictions and experimental or free-flight results are handled by adapting the physical parameters. In this way the influence of an adaptation on the physics is more direct and clear. The CFD methods seem to be far away from understanding what it really means when a numerical parameter is changed. To become a standard tool in the design process this question has to be solved in a reasonable way. We must know which numerical parameters and which mathematical models have to be used for which problem area.

What will or should the near future bring to the experimental, semi-empirical and CFD methods in aerodynamics?

As mentioned, CFD methods need better standards and insights into turbulence modelling. They also need faster standard grid generations. Increasing routine in applications and a further standardization of codes together with still decreasing computer costs and better performance will help to form it into a tool for design purposes. The large number of output data produced for 3D meshes and for unsteady time steps has to be handled in a more efficient way. Fast post-processing and careful data reduction are urgently needed.

This latter problem also applies to the modern experimental techniques with high space and time resolution. Similar tools as for CFD are necessary and, therefore, a co-ordinated development would be efficient. Detailed experimental data still will be needed for the validation of semi-empirical and CFD methods, while visualization helps in the development of physical models and in the interpretation of the results. To increase the efficiency of experiments - which are the most expensive tool - new methods of constructing and manufacturing the windtunnel models have to be found and introduced. Not all parameters can be adapted to project conditions during

windtunnel tests, especially for high speed flow. Free-flight experiments are therefore a necessary additional test method. A reliable acquisition of aerodynamic data is here the basic problem that is by far not solved yet.

In the past, project aerodynamicists used semi-empirical methods because they were fast and cheap. With increasing computer power this advantage has decreased considerably, although CFD methods still need a lot more time in preparation and postprocessing. More important is now the fact that semi-empirical methods allow the adaptation of experimental results to project conditions and of CFD results to experiments. Since semi-empirical methods use problem-adapted and evident physical models, they can validate the trends of the other methods. With increasing efficiency of the CFD codes they can be integrated into semi-empirical methods to solve special parts of the problem. Panel methods are used already in a similar way. Multi-disciplinary design will become more important in future. To integrate the aerodynamic simulation into the codes of other disciplines is a challenge for both sides. Here, the higher speed of the semi-empirical codes will probably be the deciding factor for their application.

For efficient design all methods have to be used equally. Therefore, a separation of the users into different project units is not optimal, although there might be specialists for the development of methods. To meet the present project needs all methods have to become much faster and cheaper in design applications. The direct and the multi-disciplinary optimization of components and of the complete airframe will increase in importance. A permanent problem of the aerodynamicist is the transfer of the data to the final users in the design process. This means not only the pure data handling but also the understanding of the meaning and of the problems of the aerodynamic solution. The funding of aerodynamic research depends heavily on the customer's understanding of its necessity. This understanding has to be imparted in a better way.

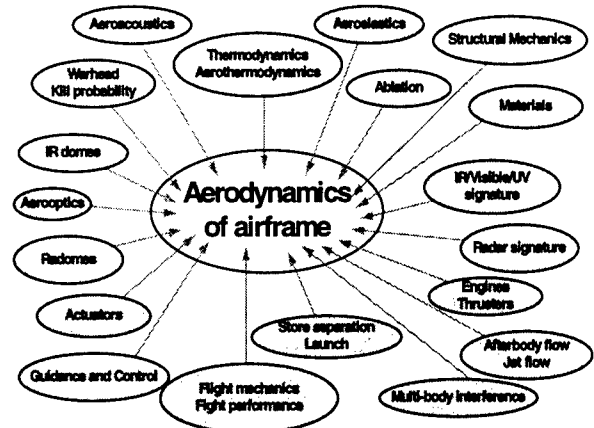
Future Trends in Missile Aerodynamics

The external influences on missile aerodynamics have been discussed quite often and shall be mentioned here only very shortly. The end of the Cold War has brought us a lower production rate of missiles and, therefore, less money for new developments. New constellations and new types of international conflicts demand new kinds of missiles and a higher flexibility to react to different scenarios. The new missiles, therefore, have to be of higher modularity and the complete defence system that includes the missile has to be easily transportable. The increasing industriali-

zation of the defence industry has pushed the profit instead of the quality to the dominating criterion in missile design. In consequence, the design process continuously has to become faster and cheaper. We have to expect international fusion of companies and institutes to increase the profit by using synergy effects. This and the general trend to globalization arises the problem of efficient work sharing, co-operation and integration of many partners while basic national competence usually shall be kept. Due to increasing licence productions in customer countries and to the lower production costs in many non-NATO countries it is to be expected that only work packages of high complexity in design and production will stay in the industrially advanced nations.

The recent trends in missile projects have changed in the last years according to the above political boundary conditions. For out-of-area missions long range missiles, fire and forget and cruise missiles, many of them with submunitions, are of increasing interest. Secondly, self-defence scenarios (against TBM, missiles, cruise missiles, radar, terrain-following aircraft) are considered more often now. The design velocity of the missiles increases, sometimes up to hypersonic values. The subsonic and transonic regime is valid mainly for drones and dispensers. Major aspects in the design process are high precision guidance including hit-to-kill capability and „surgical“ characteristics to keep collateral damage low. This leads to very high manoeuvrability at high speeds and gives rise to rather precise simulations of the end-game, of the store separation - especially from manoeuvring airplanes and helicopters - and of the separation of components and submunition. The electronic components represented by highly intelligent control and modern seekers now dominate the missile design. The missile systems have to meet the new strategic needs. This means high flexibility of the system for different geographical and political scenarios, good transportability, low volume and low weight. In future, we will probably have fewer basic missile types, but with a higher modularity and closer international standardization. The longer life-cycles of the missile systems will lead to higher effort in combat enhancement. More concepts for advanced systems will be developed without realization or with prototype and technology tests only.

All these trends will, of course, influence more or less the aerodynamic design process. One can expect that it will become more complex and that interdisciplinary activities will be of higher importance. The following diagram shows the presently closest connections between aerodynamics and other disciplines.



Consequences for Future RTO Activities

As discussed before, the three symposia on 'Missile Aerodynamics' in Trondheim, Friedrichshafen and Sorrento mark big steps in aerodynamic knowledge and application. A higher frequency of meetings is, therefore, desirable to follow new trends more closely. According to the general conditions for future aerodynamics and according to the subjects of the new RTO-AVT panel such meetings should include multi-disciplinary aspects in addition to aerodynamics. They should bring the different specialists together to initiate interdisciplinary discussions and better understanding.

One of the major problems discussed in Sorrento was the standardization of the turbulence models used in CFD codes. To implement them into the everyday design process, existing turbulence models have to be characterized in their validity for the specific needs of different missile types and typical flow conditions. A working group is suggested for this purpose.

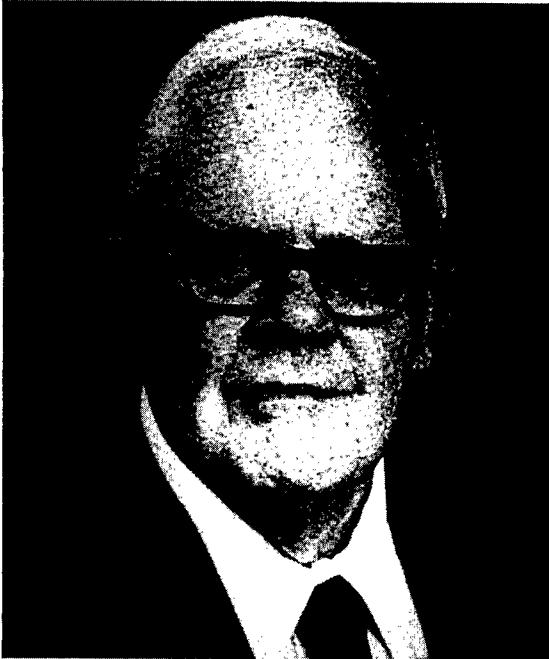
Hypersonic and high supersonic missiles often operate at the limits of the present technology. Multi-disciplinary problems as aerothermodynamics, materials, new control methods, seekers and others are arising very often. A meeting of specialists for the different disciplines in this field is recommended.

The other major missile type of future projects is represented by long range dispensers with air-breathing engine and at transonic speed. Again, multi-disciplinary aspects (signature, store separation, release of submunition, intakes) are relevant. Another meeting on this subject is suggested.

CONTRIBUTIONS TO MISSILE AERODYNAMICS A TRIBUTE TO DR. JACK N. NIELSEN

Marnix F. E. Dillenius and Michael R. Mendenhall

Nielsen Engineering & Research, Inc.
526 Clyde Ave
Mountain View, CA 94043-2212 USA



SUMMARY

This symposium is dedicated to the memory of Dr. Jack N. Nielsen, known all over the world as "the father of missile aerodynamics" and acknowledged as an authority on supersonic aerodynamics. He had 49 years experience in research and development in the fields of theoretical and applied fluid mechanics; his findings were published in more than 200 technical documents. A list of Dr. Nielsen's papers and documents is included in the reference section of this paper. This paper provides an overview of his life, major accomplishments, and research activities. Short descriptions are presented of Dr. Nielsen's major contributions to missile aerodynamics including analysis of wing-body interference, nonlinear flow phenomena, and store separation modeling.

1. INTRODUCTION

In this section, some of the vital statistics of Dr. Nielsen are detailed. Milestones in his educational background are listed.

1.1 Vital Statistics

Jack Norman Nielsen was born on November 21, 1918, in Caernarvon, Wales, Great Britain. His father was a Danish merchant marine ship captain. He had one brother. The family emigrated to the United States, and he became a U.S. citizen at age 12. He grew up in Marin County (north of San Francisco, CA). After he finished undergraduate university, he worked for the National Advisory Committee for Aeronautics (NACA) at the Langley Aeronautical Laboratory from 1941 to 1944. He served in the U.S. Army Engineers from 1944 to 1946.

While on duty in Germany, Jack Nielsen married his wife Gisela in 1945. The Nielsen's had one daughter Dagmar, later married to Dr. Leon Glover, and three grandchildren. On November 1, 1990, he passed away peacefully in his sleep of a heart attack at age 71, in Monterey, CA, after having spent his last day building a brick walkway, one of his favorite pastimes.

1.2 Education

After middle school in Marin County, Jack Nielsen went to the University of California, Berkeley, and in 1941 obtained the Bachelor of Science Degree (with Honors) in Mechanical Engineering. In 1949, he obtained his Master of Science Degree in Mechanical Engineering from the California Institute of Technology. In 1951, Jack Nielsen earned his Doctor

Copyright 1998 by Nielsen Engineering & Research (NEAR). Published with permission of the authors.

of Philosophy in Aeronautics (Magna Cum Laude) from the California Institute of Technology. His thesis addressed wing-body interference using specially developed mathematical functions.

2. OVERVIEW OF ACCOMPLISHMENTS

This section highlights Dr. Nielsen's accomplishments during his career and service including affiliations, awards, and distinctions bestowed on him. For the sake of completeness, the references at the end of this paper include most of Dr. Nielsen's publications. This collection demonstrates the versatility of his scientific endeavors. This versatility has its basis in Dr. Nielsen's practical experience and in his analytical pursuits.

2.1 Scientific Career

2.1.1 NACA Period

After obtaining his B.S. degree, Jack Nielsen worked as a mechanical engineer at the NACA Langley Aeronautical Laboratory, VA, from 1941-1944. He worked on problems/projects in aerodynamics, engine cooling, and compressibility effects. The first six papers in the references cover this period. After his discharge from the U.S. Army in 1946, he joined the NACA Ames Aeronautical Laboratory, Moffett Field, CA, to work in the 3-foot supersonic tunnel. He undertook extensive research in supersonic aerodynamics including interference between aerodynamic components, becoming a nationally recognized authority in that area. References 7-33 cover this work. One of Dr. Nielsen's earlier (1957) major contributions to missile aerodynamics was the seminal work reported by him and collaborators in Reference 29 ("Lift and Center of Pressure of Wing-Body-Tail Combinations at Subsonic, Transonic, and Supersonic Speeds", NACA R 1307.)

During this time, Jack Nielsen commenced work on his well-known book "Missile Aerodynamics", first published in 1960 (Ref. 40).

2.1.2 Commercial Period

In 1958, Dr. Jack Nielsen co-founded Vidya, Inc., (later a division of Itek Corporation, Palo Alto, CA) to engage in fluid mechanics and thermodynamic research. His position in Vidya was Director of Research, and his activities included research on

aerodynamic and thermodynamic problems in aerial photography for the U.S. Corps of Engineers and others. He also conducted analytical and experimental investigations on rocket stabilization, satellite attitude stabilization, three-dimensional orbits of earth satellites including controlled reentry, and flexible rotor systems. Other studies were concerned with aerodynamics of sails and parawings, laminar boundary layers at hypersonic speeds, communication problems of antimissile missiles, subsonic separated flows over delta wings, optical errors in stellar navigation systems, and flow separation issues associated with submarine hulls. Descriptions of these studies are available in References 34-80.

In 1966, Dr. Nielsen founded Nielsen Engineering & Research, Inc., (NEAR). This company was located originally in Palo Alto, then moved to Mountain View, CA. Much like Dr. Nielsen's first company Vidya, NEAR was positioned to engage in research and development in fluid mechanics, thermodynamics, and physics essentially under contract to various U.S. government agencies. At NEAR, in addition to management, Dr. Nielsen's activities included research with staff members in the areas of parawings, ducted propellers, laminar boundary layer separation, vortex shedding from bodies, wake turbulence, parawings, sail rotors, submarine hydrodynamics, and dispersions in estuaries. Starting in 1969, Dr. Nielsen and coworkers developed analytical methods for prediction of separation trajectory characteristics of external stores, analysis of airplane and missile aerodynamic characteristics at high angles of attack, flow separation effects on aerodynamic control characteristics, turbulent boundary-layer separation, and more. The technical documents in References 81-201 cover this work.

2.1.3 NASA Period

In 1983, Dr. Nielsen resigned from NEAR and became the Chief Scientist of NASA/Ames Research Center, Moffett Field, CA, until his retirement in June, 1990. During that time he conducted research on circulation control airfoils (Refs. 202, 209), and examined arrays for minimum wave drag of multiple bodies (Ref. 203). Dr. Nielsen wrote survey papers on supersonic wing-body interference (Ref. 206), published definitive articles on the equivalent-angle of attack concept (Refs. 194, 204, 208), and co-edited the AIAA volume entitled "Tactical Missile Aerodynamics" (Ref. 207). In 1988, Dr. Nielsen

presented a paper on the present status and future of missile aerodynamics (Ref. 211).

2.2 Affiliations

During his service and career, Dr. Jack Nielsen was elected Fellow (the highest level of membership) of the American Institute of Aeronautics and Astronautics. He also received the rank of Fellow of the Royal Aeronautical Society in the U.K. From 1966 until 1969, Dr. Nielsen was a Director of the American Astronautical Society.

2.3 Awards, Distinctions, Appointments

Among the many awards, distinctions, and appointments bestowed on Dr. Nielsen, the following are most significant.

Dr. Nielsen played a key role in consolidating the Institute of Aerospace Sciences and the American Rocket Society into the American Institute of Aeronautics and Astronautics (AIAA). He served as the first chairman of the San Francisco section. He also served as a member of the Fluid Dynamics and the Atmospheric Flight Mechanics Technical Committees of the AIAA, and was the General Chairman of the Fifth AIAA Aerospace Sciences Meeting held in 1967.

In recognition of his status as the leading authority on missile aerodynamics in the U.S., Dr. Nielsen was elected in 1979 by the AIAA to present the Distinguished Wright Brothers Lectureship in Aeronautics entitled, "Missile Aerodynamics - Past, Present, Future" (Ref. 170). He was also on the AIAA Technical Committee on Missile Systems

In 1986, Dr. Nielsen was elected a Member of the National Academy of Engineering with the following citation, "For his pioneering contributions to missile aerodynamics, and for contributions to the interference effects among aerodynamic components in supersonic flight". This membership is considered the highest professional distinction that an engineer can receive.

Dr. Nielsen was a member of the Navy Aeroballistic Advisory Committee on Missile Stability and Performance as well as a member of the NASA Research and Technology Advisory Council, Committee on Aerodynamics and Configurations.

3. MAJOR CONTRIBUTIONS TO MISSILE AERODYNAMICS

3.1 Missile Aerodynamics Book

Dr. Nielsen's book, "Missile Aerodynamics", (Ref. 40) copyrighted in 1960, was and is still known as "the bible of missile aerodynamics". Some time ago, unauthorized translated versions were found. An approved reprint, with corrections, was issued in 1988 by NEAR. The information in this significant reference book provides insight and background for aerodynamicists, especially useful today in the computerized world of computational fluid dynamics. Dr. Nielsen compiled his knowledge and the knowledge of his professional colleagues into a body of aerodynamic information of great utility which includes a summary of basic theories for calculating pressure distributions, forces, and moments.

Dr. Nielsen was co-editor of Volume 104 in the AIAA series Progress in Aeronautics and Astronautics, copyrighted in 1986, entitled "Tactical Missile Aerodynamics" (Ref. 207). This comprehensive work includes chapters containing technology originated and/or motivated by him; for example, the equivalent-angle-of-attack concept, vortex cloud model, and paneling methods with vorticity effects.

3.2 Highlights of Technical/Analytical Contributions

Dr. Jack Nielsen's accomplishments in the fields of theoretical fluid mechanics, applied aerodynamics, including missile aerodynamics, and related fields are many. This is clearly visible in Dr. Nielsen's publications listed in the Reference section.

Dr. Nielsen's evolutionary approach to the analysis of missile (and other flight vehicle) configuration aerodynamics using decomposition, and what later became known as component build-up, and the equivalent-angle-of-attack techniques is described in a following section. His analysis and modeling of body-shed vorticity is also described. This work was performed independently and merged later with the component build-up approach for missile aerodynamics analysis. Today, the component build-up and interference factor technique is embodied in several engineering-level missile aerodynamics prediction codes in the U.S. and abroad (for example, the NEAR M3HAX, the U.S. Air Force Missile DATCOM, and the U.S. Navy AP95/98 codes). In addition, Dr. Nielsen's major contributions

to the analytical prediction of store separation characteristics are highlighted.

3.2.1 *Early Account of Wing-Body Interference*

In his thesis (1951, Ref. 13), Jack Nielsen presented an analytical method for solving supersonic wing-body problems. At that time, closed form solutions were not possible for such combinations. Nielsen decomposed the wing-body problem into simpler problems (see Figure 1). This figure shows how the complicated wing-body problem was decomposed into a body-alone problem designated 1b, plus two wing-body problems of the same type with the body at zero angle of attack and wings of the same planform but differing in twist, problems designated 1a and 1c. Nielsen's thesis considered the solution of problems 1a and 1c. It was assumed that the boundary conditions can be specified on a plane for the wing and on a cylinder for the body, and that the wing leading edge is supersonic; effects of the wing tips were not considered. Nielsen then decomposed the problem 1a (or 1c) further as shown in Figure 2. Here Φ_w is the perturbation potential of the wing alone, and Φ is the interference potential. Nielsen assumed that the normal velocity against the body induced by the wing can be expanded in a cosine Fourier series of even multiples of the polar angle Θ . As a result, the solution involved a wing-alone plus a number of Fourier series solutions for the normal velocity induced at the body surface by the wing alone. Each component is solved using Laplace transform theory, and the method is then shown to be equivalent to a distributed solution method like that of Karman and Moore for bodies of revolution at supersonic speeds. In his development, Nielsen "invented" two sets of universal functions to obtain strength distributions of fundamental solutions along the body axis, and to determine directly the pressures acting on the body.

Apart from the mathematical elegance (and complexity) of Nielsen's method, he laid out the beginnings of the component build-up approach by his definition of interference, using the example of two bodies: "the difference between the joint pressure fields and the sum of the body-alone pressure fields is known as the interference pressure field". For a wing-body combination, the sum of the wing-alone, body-alone, and interference pressure field will be unique in so far as the external flow past the wing-body combination is unique. Therefore, one must define the wing-alone in the manner best suited to the problem at hand.

Nielsen made the point that aircraft designers had been cognizant of the important effects of interference among the various parts of an airplane. For low speed flight where the governing equation is the Laplace equation, no solutions for a three-dimensional wing-body combination had yet been found. Interference effects were evaluated by wind-tunnel tests. In many instances, the wings were sufficiently large so that no important effects of interference were encountered, and if there were adverse effects, they could be alleviated by suitable fairing of the wing-body juncture. However, for supersonic aircraft, the wings tended to be of low aspect ratio for which interference effects can be very important. The properties of the governing differential equations were such that some hope of obtaining mathematical solutions exists.

In his conclusions, Nielsen mentioned that a very urgent need existed for a simple approximate method for estimating pressures acting on wing-body combinations in the region where slender-body theory was known to be inapplicable. It should be noted here that slender-body theory was being developed by various aerodynamicists (for example, John Spreiter) in that period. Also, panel method approaches had not yet been invented mostly because "automatic calculation machines" or computers were not yet ready to invert large matrices.

3.2.2 *First Practical Aerodynamic Prediction Method for Wing-Body-Tail Combinations*

In Reference 29 (1957), Dr. Nielsen and collaborators presented a practical method for calculating lift and center-of-pressure characteristics of circular-cylindrical bodies in combination with triangular, rectangular, or trapezoidal wings or tails through the subsonic, transonic, and supersonic speed ranges. The method was restricted to small angles of attack and small angles in wing or tail incidence. Angle of roll or bank was limited to zero. This method was the first of its kind which could be applied to wing-body and wing-body-tail combinations.

In this work, the wing-body or tail-body interference was obtained by a new development using certain factors (later known as lift carry-over or interference factors) that are the ratios of the lift on the components in combination to the lift of the wing alone. These ratios were obtained from slender body

theory which was developed to a high level by Spreiter and others in the mid 1950's. Morikawa first developed the lift interference method adopted by Nielsen and coworkers. Details of this early work is discussed in Reference 29. Nielsen and his coworkers knew that for wing-body combinations which were not slender, lift-curve slopes were overestimated by slender-body theory. However, in many cases the ratio of the lift of the wing-body combination to that of the wing alone can be accurately predicted by slender body theory.

The lift breakdown is indicated in Figure 3 for the case of a wing-body-tail combination. The overall lift is given by the sum of the seven principal components indicated in the figure. Definitions of the various lift ratio factors are shown in Figure 4. The solution of the problem requires a determination of these ratios. The lift on any component can then be estimated from the wing-alone slope. The "best" value of the wing-alone slope should be used (Nielsen and colleagues recommended De Young and Harper, three-dimensional linear theory, or experimental data in Ref. 29). In general, the ratio factors and centers-of-pressure locations were determined using slender-body theory.

Wing-tail interference was treated by assuming one completely rolled-up vortex per wing panel and evaluating the tail load by strip theory. The paths of the vortices are either obtained from charts based on vapor screen data, or they were assumed to lie along the freestream direction. Tables and charts for the interference factors and other quantities necessary to obtain lift and center-of-pressure positions are provided in Reference 29. This reference even contains a sample calculation sheet to guide the user through the procedure. All that is required is a slide rule, sharp eyes, and perseverance to extract and combine properly data from the charts and tables! A clever approach that would work today.

A very valuable summary of sources for experimental data was also supplied. Some of these data were taken and analyzed by Dr. Nielsen earlier during his research activities in the 3-ft supersonic wind-tunnel at the NACA Ames Aeronautical Laboratory. Dr. Nielsen's access to this supersonic wind tunnel was a key to the development of this approach because it allowed him to create the experimental database required to verify the method.

Some examples of comparisons between prediction and experimental data are shown in Figure 5, taken from Reference 29, for two different wing-body-tail configurations. The upper part of the figure shows an airplane type configuration and data for Mach 0.2. The lower part shows an "unusual" missile type shape with data for Mach 1.62. Predicted results for lift and center-of-pressure location with and without wing-tail (vortical) interference are compared with experimental data. Note that the angle-of-attack range can be considered low by today's standards. Regardless, these 1957 predictions are considered in good agreement with experiment for both configurations and Mach numbers. The importance of including wing-tail vortical interference is clear especially for center-of-pressure and thus pitching moment.

The conclusions made by Nielsen et al in Reference 29 state that overall lift-curve slopes for most combinations were predicted to within 10 percent through the speed range. However, in the transonic range nonlinear effects could reduce the accuracy. Wing-tail interference could change overall lift by 35 to 40 percent. Center-of-pressure positions were predicted to within 0.02 of body length. Transonic effects could degrade the accuracy. Wing-tail vortical interference could change the center-of-pressure position by as much as 20 percent of body length.

Nielsen and colleagues also mentioned that limitations in the method included the lack of models for body vorticity, more than one vortex per wing panel, and that viscous crossflow theory should be added in order to make the method valid at higher angles of attack. Furthermore, effects of inverse taper, swept-forward wings, wing panels with twist and camber, or large gaps between wing or tail and the body would violate assumptions inherent to the method of Reference 29.

3.2.3 Equivalent Angle-of-Attack Approach

During the sixties and seventies, estimating fin (or wing) forces and moments in the presence of a body and other fins with sufficient accuracy to predict lateral (in addition to longitudinal) and control characteristics up to high angles of attack was rarely attempted without using previously developed data bases. An exception to this state of affairs was the development of panel method-based missile aerodynamics prediction codes which included modeling of vortical and other nonlinear effects (Refs. 139, 162). The development of these codes was

strongly encouraged and guided by Dr. Nielsen during the cited time period. One of his motivations was to employ the panel method-based missile aerodynamics prediction codes (applicable to banked cruciform wing-body-cruciform tail combinations) to test and check the next development in experimental data-based codes using the equivalent-angle-of-attack concept pioneered by Dr. Nielsen. A comprehensive description is given in References 194, 204, 208.

With the advent of new systematic data bases and the continued development of vortex tracking methods, the possibility of the task listed above was made considerably easier. However, some means were still necessary for properly accounting for effects not in the data bases, e.g., different fin span-to-body diameter ratios, different vortical flow fields, and nonlinear body flow effects associated with high Mach numbers. The method developed by Dr. Nielsen and coworkers for this purpose depended on the innovative equivalent-angle-of-attack concept.

Dr. Nielsen started with his concept of "modified" slender body theory explored in the classic report NACA R 1307 (Ref. 29); this concept is reflected in the factor K_C shown in Figure 4. In Reference 194, the modified slender body theory was applied to the normal force coefficient acting on the equally deflected horizontal fins of a missile in the "plus" attitude. The formulation is shown in Figure 6. The basic result, marked Equation 3 in that figure, was that the normal force acting on the horizontal fins of a fin-body combination could be related to the normal force acting on a wing alone (formed by joining the fins at their root chords) by using the equivalent-angle-of-attack α_{eq} . This important finding is illustrated in Figure 7 for a moderate and a low aspect ratio fin mounted on a body for Mach numbers 0.8 and 1.3. Experimental data of the normal force coefficients correlate well for different fin deflections. Wing-alone data are also shown for comparison for the subsonic Mach number. Note that the basic expression marked Equation 3 in Figure 6 provides the opportunity to account for different fin span-to-body diameter ratios, fin deflections, and vortical flowfields through the factors K_w , k_w , and $(\Delta\alpha)_v$. However, in order to handle cruciform fin missiles in a banked attitude and for very high angles of attack, a more general formula was needed. The derivation is detailed in References 194, 204, 208. The basic approach taken was to consider the actual flowfield seen by the fin including vortical and other

nonlinearities. Elements of slender body theory were still included, particularly to account for angle of roll and for fin-on-fin interference. In addition, it was observed by Dr. Nielsen and coworkers that center-of-pressure locations on the fin could also be related to the equivalent-angle-of-attack and thus to fin normal force for cases without fin deflection as a minimum.

It is clear that Dr. Nielsen's equivalent-angle-of-attack approach is very powerful in its application to the experimental database and/or semiempirical missile aerodynamics prediction methods. As a result, his concept is in use in several semiempirical missile aerodynamics prediction programs, including the codes used routinely at NEAR.

3.2.4 Body and Fin Vorticity Modeling

Early in the development of missile aerodynamics, Dr. Nielsen and his colleagues recognized that fin and body vortices were an essential part of any theory which was to have any success in the prediction of missile aerodynamics. In NACA R 1307 (Ref. 29) the effects of wing vorticity were included through the use of empirical information and observations. The details of the vorticity strength and position were described in tables developed from experiments. Nielsen and Kaattari (Ref. 28) discussed methods for calculating lateral stability derivatives including effects of body and fin vorticity. The key to this effort was to obtain the correct vortex strength and position with respect to the tail surfaces of the missile. Dr. Nielsen recognized the need for including body vorticity in a wide range of applications as can be seen in some of the early work in submarine hydrodynamics described in References 64, 65, and 191. The simplified vortex model used in Reference 29 is shown in Figure 8(a).

Details of the early knowledge of the effects of body vortices on missile aerodynamics at high angles of attack are found in Chapter 4 of "Missile Aerodynamics" (Ref. 40). Here, the early information on the location of separation on slender bodies, the strength of the vortices, and the vertical and lateral positions are developed from experimental measurements. In addition, the slender-body tracking procedure for predicting the motion of vortices past circular and noncircular bodies is described.

At NEAR and at other organizations, the importance of the body vorticity in the prediction of high angle-of-attack aerodynamic characteristics was recognized, and there was a long term effort directed at this technology under the guidance and supervision of Dr. Nielsen. NEAR, under contracts to NASA and the U.S. Navy, developed a distributed vortex or vortex cloud approach to predicting the body separation vorticity. A sketch of the vortex cloud model is shown in Figure 8 (b).

The slender body tracking procedure played an important role in the development of the vortex cloud methodology. Much of this work was accomplished by the second author; however, a number of similar approaches were under development around the world at the same time. The approach at NEAR was to develop the body vortex predictive technology in parallel with the other developments in the prediction of missile aerodynamics. As the body vortex technology matured, it was included in the missile aerodynamics prediction methods, including those based on the equivalent-angle-of-attack approach and the panel methods. In the early days, this analytical information was treated like experimental data; however, with advances in the theory and computer resources, the body vortex models became an integral part of the missile aerodynamics methods. The codes containing this technology are still in use as engineering prediction methods for high angle of attack flight conditions.

3.2.5 Store Separation Methodology

Up to the middle sixties, methods to perform theoretical analyses of store separation were not available in the public domain. Instead, store certification (safe separation) relied on flight tests often accompanied by disastrous results.

In the late sixties, Dr. Nielsen set out to develop an analytical method (then called a rational method) to predict the trajectory characteristics of stores launched from subsonic aircraft. The initial effort was limited to three degrees of freedom for store motion, but it was later extended to full six degrees of freedom. Using an inertial set of axes, Dr. Nielsen wrote the equations of motion applicable to the three-dimensional (finite size) store accounting for center-of-gravity offset. A vortex-lattice panel method and distributions of sources/sinks and doublets were employed to model the components of

the parent aircraft for lift and thickness effects. Noncircular fuselage cross sections were handled by an application of a composite solution which included polar harmonics. Modified slender body theory was applied to estimate the aerodynamic forces and moments acting on the finned store in nonuniform flow. Dr. Nielsen made clever use of reverse flow theorems with aspect ratio correction for the fin section (empennage). Fin-on-body and fin-on-fin interference were included. Again, the wing-alone lift curve slopes were the basis of the analysis. In addition, when the angle of attack seen by the store was sufficiently high, the normal force acting on the store was based on crossflow drag considerations. Details of these classic approaches are available in References 124, 128, 140.

Early on, Dr. Nielsen realized that computer running time could be enormous for store separation prediction. Therefore, he decided on several schemes which would speed up the trajectory calculation. One was to simplify the mutual interference between the aircraft and store by including the store volume effects in the boundary condition applied to the wing and pylon of the parent aircraft. This simplification was arrived at after performing an iterative calculative analysis to determine the "build-up" of mutual interference. For the cases considered at the time, most of the mutual interference was accounted for during the first iteration which included the store volume effects. In this way, the parent aircraft needed to be solved only once at the start of the trajectory calculation. Another time-saving scheme was to employ the simplest possible parent aircraft flow modeling scheme; for example, for cases with circular cross section fuselages, fast running centerline singularity distributions were employed.

Another of Dr. Nielsen's clever ideas was to insist on a wind-tunnel test program to be conducted concurrently with the theoretical development. These systematic tests were performed during the late sixties and early seventies. The tests involved measurements of velocity components, load distribution, and captive store separation measurements. Later, similar tests were conducted for supersonic conditions. A valuable database was generated using generic models shown in Figure 9. Among other things, the tests helped decide when to employ the crossflow considerations. The duct could be removed to form a circular cross section fuselage. The store could be a body alone, or it could have rectangular tail fins.

A sample comparison between predicted trajectory characteristics and captive store test results is shown in Figure 10. The store was released with 10 ft/sec downward ejection velocity from under the pylon located at one-third wing semispan. In this sample, the fuselage was circular in cross section. The store had a cruciform tail fin set. In Figure 10, the translational characteristics of the store center of gravity are shown in the left portion, the angular attitude angles are on the right. It is worth noting here that captive store tests include a change in attitude angle of the store to account for damping due to translation. This causes the store to be in a slightly different position when aerodynamic calculations are updated during the trajectory. In addition, rotational damping is not measured by the captive store method in the wind tunnel and thus not included in the off-line 6-degrees of motion integration scheme. To show an indication of the difference, Dr. Nielsen insisted on being able to calculate the trajectory characteristics with and without rotational effects in all three angular motions. The damping effects are (fortunately) negligible except in the pitching oscillation as shown in the figure. When comparing present day CFD-based calculations to captive store data, these considerations should be taken into account.

4. PERSONAL REMARKS BY PEERS AND AUTHORS

4.1 Dean R. Chapman

Dr. Chapman was a former colleague of Dr. Nielsen at NASA/Ames Research Center in the period during which much of the work described above was taking place. The following excerpt is taken from the "National Academy of Engineering Tributes", Vol. 6, 1993, written after Dr. Nielsen's death.

"Dr. Jack N. Nielsen was a man very tolerant of those whose life styles and beliefs were far from his own. He was always sympathetic to people less fortunate than most, and invariably exhibited professional integrity without facade or pretense. Very direct and forthright in his demeanor, Dr. Jack N. Nielsen would state clearly if something appeared good, and would not hesitate to exclaim even more clearly, sometimes in deep stentorian voice, if it did not".

4.2 Barry Haines

Mr. Haines, Chairman of the Aerodynamics Group Committee of the Royal Aeronautical Society, wrote the following obituary for publication in "Aerospace".

"Dr. Nielsen played an active part in many international conferences, and in 1989 he readily accepted an invitation to speak and act as a session chairman at the R.Ae.S Conference on Store Carriage, Integration and Release held at Bath in April 1990. Later in the same month, it was hoped that he would act as the Technical Evaluator for an AGARD International Conference on Missile Aerodynamics in Germany. He was very disappointed when he had to withdraw from both of these conferences owing to ill health. It is sad to think that we will never again hear his pungent comments in discussions on aerodynamic issues. These comments were always to the point; they always revealed his clear thinking. He never shirked the need to criticize when he felt criticism was merited but, on the other hand, he was unstinted in his praise for promising young members of the research fraternity. His advice, enthusiasm, and encouragement will be sorely missed".

4.3 M. F. E. Dillenius

The lead author was hired by Dr. Jack Nielsen in 1969 to work on applications of panel methods. One of Dr. Nielsen's favorite sayings was to exclaim how easy it was for young engineers to perform aerodynamic wing-body (including interference) calculations using panel methods in contrast to the complex approach he had developed in his thesis. As time went on, Dr. Nielsen would amaze the lead author on many occasions with his ability to use an alternate analytic means to check on a result obtained from a panel method calculation. This was usually done on the back of an envelope or on a soiled napkin in ink. Dr. Nielsen simultaneously was a father figure, mentor, and teacher, who if necessary would not hesitate to provide constructive criticism. The lead author will remember Dr. Jack N. Nielsen with awe and affection.

4.4 M. R. Mendenhall

I had the good fortune to begin my professional career at Vidya where I only saw Dr. Nielsen "from afar" as was befitting a junior engineer. At NEAR, beginning in 1966, I worked for seventeen years very closely with him on a day-to-day basis. I will never forget the

technical meetings in a small conference room or office with Dr. Nielsen and his ever-present cigar. I remember him in many ways; as a thorough researcher and teacher, as a patient mentor, and most importantly as a friend. I will never forget his sense of ethics, his professional integrity, his dedication to technical excellence, his willingness to give credit when due and to share blame even when he was not responsible, and his overwhelming desire to do a good job and give the customer what he paid for. He taught me to sell research, how to do research, and to be critical of my own work. He also had an intuitive feel for aerodynamics and fluid mechanics that most of us will never understand. In the early days of computers and the development of computational aerodynamics, he made a comment we should all remember, "We must have a healthy scepticism for CFD results!"

I will remember his prodigious appetite for knowledge, good food, good wine, and good times. All of us have our favorite anecdotes about Jack Nielsen, but the one that comes up in many conversations, even this long after his death, is the time in his office when in the middle of a technical discussion he set his wastebasket on fire with a misdirected cigar ash, and then got his foot stuck in the basket trying to stamp out the flames.

Those of us in the missile aerodynamics community who were fortunate enough to work with him miss seeing him in his familiar seat in the front row of technical sessions. He was our conscience, keeping us technically honest at the risk of being the recipient of one of his direct questions. If he left us a legacy, it was to never lose sight of the flow physics in our desire to predict the aerodynamics of missiles. If we never forget this, he will have done his job.

5. CONCLUDING REMARKS

Dr. Jack N. Nielsen was a pioneering developer of theoretical methods (in many cases quite sophisticated and mathematically elegant) for analyzing the aerodynamic characteristics including interference effects of flight vehicles. He was and still is internationally renowned in aerospace engineering, especially for his highly original contributions to missile aerodynamics. His methods are very useful today in missile aerodynamics prediction and other codes, as well as for testing and checking CFD-based results.

Individuals of Dr. Nielsen's character, integrity, and professional capability are not common. He not only loved his work but also had a zest for life. He loved to share his enthusiasm about his findings with colleagues and employees usually over a hearty repast and plentiful libations. Dr. Nielsen was also very proud of his personal library containing early editions of famous literary works. His figure was bigger than life.

Even though Dr. Nielsen passed away eight years ago, he is still missed by his family, friends, professional colleagues, and employees of the companies he founded.

6. ACKNOWLEDGMENTS

Many sources of information were used in the preparation of this paper on Dr. Jack N. Nielsen. The authors would like to thank Dr. Charles A. Smith, Deputy Chief of Aeronautical Information Technology, NASA/Ames Research Center, Moffett Field, CA, for releasing the official obituary and other information about Dr. Nielsen. The authors would also like to thank Dr. Michael J. Hensch, Lockheed Engineering Services, Hampton, VA, for his suggestions concerning Dr. Nielsen's major contributions to the analysis of missile aerodynamics. Both Dr. Smith and Dr. Hensch were employees of Dr. Nielsen at NEAR.

7. REFERENCES

1. Nielsen, J. N., "Effect of turbulence on air-flow measurements behind orifice plates", NACA ARR 3G30, 1943.
2. Nielsen, J. N. and Schumacher, L. E., "Analysis of the high-altitude cooling of the Ranger SGV-770 D-4 engine in the Bell XP-77 airplane", NACA CMR 20, 1943.
3. Rupert, K. F., Corson, B. W., Jr., and Nielsen, J. N., "The advantages of uniform fuel distribution for air-cooled engines from considerations of cooling requirements and fuel economy", NACA CB 3L07, 1943.
4. Nielsen, J. N., "High-altitude cooling, III - Radiators", NACA ARR L4I11b, 1944.
5. Nielsen, J. N., "Compressibility effects on heat transfer and pressure drop in smooth cylindrical tubes", NACA ARR L4C16, 1944.
6. Nielsen, J. N. and Sweberg, H. H., "Note on the compressibility effects on downwash at the tail at subcritical speeds", NACA CB L5C09, 1945.

7. Nielsen, J. N., "Effect of aspect ratio and taper on the pressure drop at supersonic speeds of unswept wings at zero lift", NACA TN 1487, 1947.
8. Vincenti, W. G., Nielsen, J. N., and Matteson, F. H., "Investigation of wing characteristics at a Mach number of 1.53, I - Triangular wings of aspect ratio 2", NACA RM A7I10, 1947.
9. Nielsen, J. A., Matteson, F. H., and Vincenti, W. G., "Investigation of wing characteristics at a Mach number of 1.53, III - Unswept wings of differing aspect ratio and taper ratio", NACA RM A8E06, 1948.
10. Nielsen, J. N. and Perkins, E. W., "Charts for the conical part of the downwash field of swept wings at supersonic speeds", NACA TN 1780, 1948.
11. Nielsen, J. N. and Matteson, F. H., "Calculative method for estimating the interference pressure field at zero lift on a symmetrical swept-back wing mounted on a circular cylindrical body", NACA RM A9E19, 1949.
12. Nielsen, J. N., Katzen, E. D., and Tang, K. K., "Lift and pitching-moment interference between a pointed cylindrical body and triangular wings of various aspect ratios at Mach numbers of 1.50 and 2.02", NACA RM A50F06, 1950; NACA TN 3795, 1956.
13. Nielsen, J. N., "Supersonic wing-body interference", Pasadena, CA, California Institute of Technology, Doctoral thesis, 1951.
14. Nielsen, J. N. and Grigsby, C. E., "Lift and moment interference of wings and bodies, Part I - Lift and moment interference at zero angle of bank; Part II - Division of lift and moment between wing and body at zero angle of bank and some results for cruciform configurations", Presented at NACA Conference on Aerodynamic Design Problems of Supersonic Guided Missiles, Moffett Field, CA/2-3 October 1951.
15. Nielsen, J. N. and Kaattari, G. E., "Method for estimating lift interference of wing-body combinations at supersonic speeds", NACA RM A51J04, 1951.
16. Kaattari, G. E., Nielsen, J. N., and Pitts, W. C., "Method for estimating pitching-moment interference of wing-body combinations at supersonic speeds", NACA RM A52B06, 1951.
17. Nielsen, J. N. and Pitts, W. C., "Wing-body interference at supersonic speeds with an application to combinations with rectangular wings", NACA TN 2677, 1952.
18. Nielsen, J. N., Kaattari, G. E., and Drake, W. C., "Comparison between prediction and experiment for all-movable wing and body combinations at supersonic speeds - Lift, pitching moment, and hinge moments", NACA RM A52D29, 1952.
19. Nielsen, J. N., Kaattari, G. E., and Anastasio, R. F., "A method for calculating the lift and center of pressure of wing-body-tail combinations at subsonic, transonic, and supersonic speeds", NACA RM A53G08, 1953.
20. Nielsen, J. N. and Pitts, W. C., "The effects of angle of attack and wing incidence on the loading of a rectangular wing and body combination at supersonic speeds", Presented at NACA Conference on Aircraft Loads, Flutter, and Structures/2-4 Mar 1953.
21. Pitts, W. C., Nielsen, J. N., and Gionfriddo, M. P., "Comparison between theory and experiment for interference pressure field between wing and body at supersonic speeds", NACA TN 3128, 1954.
22. Nielsen, J. N., "Aerodynamics of airfoils and bodies in combination at supersonic speeds", NACA RN 338, 1954, Paper 16.
23. Kaattari, G. E., Hill, W. A., Jr., and Nielsen, J. N., "Controls for supersonic missiles", NACA RM A55D12, 1955.
24. Nielsen, J. N., "Quasi-cylindrical theory of wing-body interference at supersonic speeds and comparison with experiment", NACA R 1252, 1955.
25. Nielsen, J. N., Spahr, J. R., and Centolanzi, F., "Aerodynamics of bodies, wings, and wing-body combinations at high angle of attack at supersonic speeds", NACA RM A55L13c, 1956.
26. Nielsen, J. N. and Van Dyke, M. D., "Application of the generalized W-functions to problems in fluid dynamics", Presented at IX International Congress of Applied Mechanics, Brussels/September 1956.
27. Nielsen, J. N. and Pitts, W. C., "General theory of wave-drag reduction for combinations employing quasi-cylindrical bodies with an application to swept-wing and body combinations", NACA TN 3722, 1956.
28. Nielsen, J. N. and Kaattari, G. E., "The effects of vortex and shock-expansion fields on pitch and yaw instabilities of supersonic airplanes", Presented at the Institute of Aeronautical Sciences National Summer Meeting/17-20 June 1957.
29. Pitts, W. C., Nielsen, J. N., and Kaattari, G. E., "Lift and center of pressure of wing-body-tail combinations at subsonic, transonic, and supersonic speeds", NACA R 1307, 1957.
30. Nielsen, J. N., "Tables of characteristic functions for solving boundary-value problems of the wave equation with application to supersonic interference", NACA TN 3873, 1957.
31. Nielsen, J. N., "The effects of body vortices and the wing shock-expansion field on the pitch-up characteristics of supersonic airplanes", NACA RM A57L23, 1958.
32. Pitts, W. C. and Nielsen, J. N., "A body modification to reduce drag due to wedge angle of wing with unswept trailing edge", NACA TN 4277, 1958.
33. Nielsen, J. N., Goodwin, F. K., and Mersman, W. A., "Three-dimensional orbits of Earth satellites, including effects of earth oblateness and atmospheric rotation", NACA TN 4363, NASA Memo 12-4-58A, 1958.

34. Nielsen, J. N. and Rubesin, M. W., "Comparison of reentry vehicles for manned space flight", Vidya 2, 1958.
35. Nielsen, J. N., "Three-dimensional satellite orbits with emphasis on reentry dynamics and oblateness effects", Vidya 3, 1958.
36. Nielsen, J. N., Rubesin, M. W., and Goodwin, F. K., "Study of flow separation in supersonic flight with application to flared bodies", Vidya 10, 1959.
37. Nielsen, J. N., Goodwin, F. K., Ragent, B., and Sacks, A. H., "Effects of supersonic and hypersonic aircraft speed upon aerial photography", First interim technical report, Vidya 12, 1959.
38. Nielsen, J. N., Sacks, A. H., Goodwin, F. K., and Rubesin, M. W., "Effects of supersonic and hypersonic aircraft speed upon aerial photography", Second interim technical report, Vidya 14, 1959.
39. Nielsen, J. N., Sacks, A. H., Goodwin, F. K., and Rubesin, M. W., "Effects of supersonic and hypersonic aircraft speed upon aerial photography", Final technical report, Vidya 17, 1960.
40. Nielsen, J. N., "Missile aerodynamics", New York, McGraw-Hill, 1960; Reprint, Mountain View, CA, Nielsen Engineering & Research, 1988.
41. Goodwin, F. K. and Sacks, A. H., "Effect of supersonic speed on aerial photography taken from two specific army drones", Vidya 22, 1960.
42. Nielsen, J. N., Sacks, A. H., Goodwin, F. K., and Burnell, J. A., "Effects of supersonic and hypersonic aircraft speed upon aerial photography", First interim report, Phase II, Vidya 24, 1960.
43. Nielsen, J. N., Sacks, A. H., Goodwin, F. K., and Burnell, J. A., "Effects of supersonic and hypersonic aircraft speed upon aerial photography", Second interim report, Phase II, Vidya 28, 1960.
44. Nielsen, J. N. et al, "Missile optical window study", Vidya 35, Vol 1, Vol 2, 1961.
45. Nielsen, J. N. and Goodwin, F. K., "Stability and control of inflated winged vehicles in reentry flight", Vidya 36, 1961.
46. Nielsen, J. N., Goodwin, F. K., Sacks, A. H., and Burnell, J. A., "Effects of supersonic and hypersonic aircraft speed upon aerial photography", Final Report, Phase II, Vidya 37, 1961.
47. Sacks, A. H. and Nielsen, J. N., "An analytical study of the low-speed aerodynamics of straight and swept wings with flow separation", Vidya 38, 1961.
48. Goodwin, F. K. and Nielsen, J. N., "Boundary-layer effects on aerial photography at supersonic speeds with emphasis on thick turbulent boundary layers", Vidya 43, 1961.
49. Nielsen, J. N., "Design plan for development and construction of flexirotor recovery system", Phase I, Vidya 49, 1961.
50. Nielsen, J. N. and Goodwin, F. K., "Environmental effects of supersonic and hypersonic speeds on aerial photography", Photogrammetric Engineering, 27, 3, June 1961, pp 427-435.
51. Nielsen, J. N., Burnell, J. A., and Sacks, A. H., "Investigation of flexible rotor systems - Results of Phases I and II", ASD TR 61 660, 1961.
52. Nielsen, J. N. and Hanson, C. W., "Investigation of the dynamic stability of parachute-rotor combinations (Project SAND)", Vidya 58, 1962.
53. Nielsen, J. N. and Goodwin, F. K., "Investigation of hypersonic flow separation and its effect on aerodynamic control characteristics", Vidya 63, 1962.
54. Nielsen, J. N. and Burnell, J. A., "Wind-tunnel tests of model flexirotor recovery system; Design and construction of drop-test model", Vidya 70, 1962.
55. Nielsen, J. N. et al, "Missile optical window study II", Vidya 77, 1962.
56. Abbott, D. E., Holt, M., and Nielsen, J. N., "Investigation of hypersonic flow separation and its effects on aerodynamic control characteristics", ASD TDR 62 963, Vidya 81, 1962.
57. Nielsen, J. N. and Burnell, J. A., "Flexible-rotor design", Presented at Retardation and Recovery Symposium, Wright-Patterson Air Force Base, OH/13-14 November 1962, Vidya Paper 6.
58. Nielsen, J. N., Kriebel, A. R., and Goodwin, F. K., "Theoretical aerodynamics of flexible wings at low speeds - I - One-lobed parawings", Vidya 84, 1962.
59. Nielsen, J. N., "Preliminary study of influence of isotropic atmospheric turbulence on photographic resolution", Vidya 320 TN 1, 1962.
60. Nielsen, J. N. et al, "Electromagnetic communication to a hypersonic missile undergoing extensive ablation", Vidya 87, 1963.
61. Sacks, A. H., Nielsen, J. N., and Goodwin, F. K., "A theory for the low speed aerodynamics of straight and swept wings with flow separation", Vidya 91, 1963.
62. Kriebel, A. R., Sacks, A. H., and Nielsen, J. N., "Theoretical investigation of dynamic stability derivatives of ducted propellers", Vidya 63 95, 1963.
63. Abbott, D. E., Holt, M., and Nielsen, J. N., "Studies of separated laminar boundary layers at hypersonic speed with some low Reynolds number data", AIAA 63 0172, 1963.
64. Spangler, S. B., Sacks, A. H., and Nielsen, J. N., "The effect of flow separation from the hull on the stability of a high-speed submarine, Part I - Theory", Vidya 107, 1963.
65. Spangler, S. B., Sacks, A. H., and Nielsen, J. N., "The effect of flow separation from the hull on the stability of a high-speed submarine, Part II - Comparisons with data for a specific submarine configuration", VIDYA 107 Pt.2, 1963.

66. Nielsen, J. N., Hanson, C. W., and Spangler, S. B., "Study of photographic resolution in the X-15 flight environment", *Vidya* 108, 1963.
67. Nielsen, J. N., "Theory of flexible aerodynamic surfaces", *J. of Appl. Mech.*, 30, Series E, 3, September 1963, pp 435-42.
68. Nielsen, J. N., Barakat, R., Goodwin, F. K., and Rudin, M., "Theoretical aerodynamics of flexible wings at low speeds, II - Two-lobed parawings", *Vidya* 133, 1964.
69. Kriebel, A. R. and Nielsen, J. N., "Theoretical aerodynamics of flexible wings at low speeds, III - Approximate results for wings of large aspect ratio", *Vidya* 146, 1964.
70. Nielsen, J. N., "Aerodynamics systems", in "Systems engineering handbook", edited by R. E. Machol, New York, McGraw-Hill, 1965, Chapter 18.
71. Nielsen, J. N., Kriebel, A. R., and Goodwin, F. K., "Theoretical aerodynamics of one-lobed flexible parawings at low speeds", *J. Aircraft*, 2, 2, March-April 1965, pp 127-135.
72. Nielsen, J. N., Lynes, L. L., Goodwin, F. K., and Holt, M., "Calculation of laminar separation with free interaction by the method of integral relations", *AIAA* 65 0050, 1965.
73. Burnell, J. A. and Nielsen, J. N., "Theoretical aerodynamics of flexible wings at low speeds, IV - Experimental program and comparison with theory", *Vidya* 172, 1965.
74. Nielsen, J. N., Lynes, L. L., and Goodwin, F. K., "Calculation of laminar separation with free interaction by the method of integral relations, Part I - Two-dimensional supersonic adiabatic flow", *Vidya* 185, 1965.
75. Goodwin, F. K., Lynes, L. L., and Nielsen, J. N., "Computer program for the calculation of laminar separation with free interaction for two-dimensional supersonic adiabatic flow", *Vidya* 194, 1965.
76. Nielsen, J. N. and Burnell, J. A., "Theoretical aerodynamics of flexible wings at low speeds, V - Engineering method for estimating parawing performance", *Vidya* 209, 1965.
77. Goodwin, F. K., Lynes, L. L., and Nielsen, J. N., "Computer program for the calculation of laminar separation with free interaction for two-dimensional and axisymmetric supersonic adiabatic and nonadiabatic flow", *Vidya* 210, 1965.
78. Nielsen, J. N., Lynes, L. L., and Goodwin, F. K., "Calculation of laminar separation with free interaction by the method of integral relations, Part II - Two-dimensional supersonic nonadiabatic flow and axisymmetric supersonic adiabatic and nonadiabatic flows", *AFFDL TR* 65 107, Part II, 1966.
79. Nielsen, J. N., Lynes, L. L., and Goodwin, F. K., "Theory of laminar separated flows on flared surfaces including supersonic flow with heating and cooling", in "Separated flows", *AGARD CP* 4, 1966, Paper 34.
80. Nielsen, J. N., Lynes, L. L., and Goodwin, F. K., "The theoretical characteristics of one-lobed parawings in combined pitch and sideslip", *Vidya* 220, 1966.
81. Spangler, S. B., Mendenhall, M. R., and Nielsen, J. N., "A method for estimating the aerodynamic characteristics of two-lobed conical parawings up to the critical speed", *NEAR TR* 1, 1967.
82. Goodwin, F. K., Nielsen, J. N., and Lynes, L. L., "Calculation of laminar boundary layer-shock wave interaction on cooled walls by the method of integral relations", *NASA CR* 73461, 1967.
83. Mendenhall, M. R., Spangler, S. B., and Nielsen, J. N., "Investigation of methods for predicting the aerodynamic characteristics of two-lobed parawings", *NASA CR* 1166, 1968.
84. Mendenhall, M. R., Spangler, S. B., and Nielsen, J. N., "Review of methods for predicting the aerodynamic characteristics of parawings", *J. Aircraft*, 5, 6, November-December 1968.
85. Goodwin, F. K., Nielsen, J. N., and Lynes, L. L., "Recent applications of the method of integral relations to laminar boundary-layer problems", *AIAA* 68 0738, 1968.
86. Kuhn, G. D., Lynes, L. L., and Nielsen, J. N., "Computer program for turbulent boundary layers on nonadiabatic two-dimensional or axisymmetric bodies with prescribed pressure distributions", *NASA CR* 182463, 1968.
87. Mendenhall, M. R., Goodwin, F. K., and Nielsen, J. N., "Preliminary investigation of a separated laminar boundary layer in a two-dimensional cavity", *NASA CR* 73267, 1968.
88. Nielsen, J. N. and Kuhn, G. D., "Recent applications of the method of integral relations to turbulent boundary layers with heat transfer and pressure gradients", in *NASA SP* 216, pp 389-410, 1968.
89. Lynes, L. L., Nielsen, J. N., and Kuhn, G. D., "Calculation of compressible turbulent boundary layers with pressure gradients and heat transfer", *NASA CR* 1303, 1969.
90. Lynes, L. L., Nielsen, J. N., and Goodwin, F. K., "Inhibition of flow separation at high speed, Vol 1 - Supersonic turbulent boundary layers", *AFFDL TR* 68 119, Vol 1, 1969.
91. Goodwin, F. K., Nielsen, J. N., and Lynes, L. L., "Inhibition of flow separation at high speed, Vol 2 - Calculation of nonadiabatic laminar boundary layers", *AFFDL TR* 68 119 Vol 2, 1969.
92. Nielsen, J. N., Lynes, L. L., and Goodwin, F. K., "Inhibition of flow separation at high speed, Vol 3 - Experimental results for laminar boundary layers", *AFFDL TR* 68 119 Vol 3, 1969.
93. Nielsen, J. N., "Review of applications of the method of integral relations to boundary-layer problems", Presented at Symposium on Boundary-Layer Separation and Reattachment, Marietta, GA/20-21 February 1969.

94. Kuhn, G. D., Spangler, S. B., and Nielsen, J. N., "Theoretical study of vortex shedding from bodies of revolution undergoing coning motion", NASA CR 1448, 1969.
95. Nielsen, J. N., Goodwin, F. K., and Mansfield, J. A., "A calculative method for predicting store separation trajectories at speeds up to the critical speed", in *Proceedings of the 1969 Aircraft/Stores Compatibility Symposium*, 4, pp 4-1 through 4-25, 1969.
96. Goodwin, F. K. and Nielsen, J. N., "A calculative method for predicting store separation trajectories at speeds up to the critical speed", Phase I, Interim report, NEAR TR 19, 1969.
97. Kuhn, G. D., Goodwin, F. K., and Nielsen, J. N., "Prediction of supersonic laminar flow separation by the method of integral relations with free interaction", AFFDL TR 69 87, 1970.
98. Nielsen, J. N., Spangler, S. B., Stahara, S. S., and Lee, A. L., "An exploratory aerodynamic and structural investigation of all-flexible parawings", NASA CR 167, 1970.
99. Nielsen, J. N., Goodwin, F. K., and Dillenius, M. F. E., "A calculative method for predicting store separation trajectories at speeds up to the critical speed", Phase II, Interim report, NEAR TR 22, 1970.
100. Nielsen, J. N., Goodwin, F. K., and Dillenius, M. F. E., "A calculative method for predicting store separation trajectories at speeds up to the critical speed", in AGARD CP 71, 1970, Paper 26.
101. Nielsen, J. N. and Schwind, R. G., "Decay of a vortex pair behind an aircraft", Presented at Symposium on Aircraft Wake Turbulence, Seattle, WA/1-3 September 1970.
102. Spangler, S. B. and Nielsen, J. N., "Theoretical investigation of the aerodynamic characteristics of all-flexible parawings", AIAA 70 1188, 1970.
103. Nielsen, J. N. and Schwind, R. G., "Decay of a vortex pair behind an aircraft", in *Aircraft Wake Turbulence and its Detection*, New York, Plenum Press, 1971, pp 413-54.
104. Kuhn, G. D., Spangler, S. B., and Nielsen, J. N., "Theoretical analysis of vortex shedding from bodies of revolution in coning motion", AIAA Journal, 9, 5, 1971, pp 784-790.
105. Nielsen, J. N., Goodwin, F. K., and Kuhn, G. D., "Review of the method of integral relations applied to viscous interaction problems including separation", in NASA CR 117051, 1971, pp 31-82.
106. Goodwin, F. K., Nielsen, J. N., and Dillenius, M. F. E., "A method for predicting three-degree-of-freedom store separation trajectories at speeds up to the critical speed", AFFDL TR 71 81, 1971.
107. Nielsen, J. N. and Mendenhall, M. R., "Feasibility study of a TDV delivery concept", NEAR TR 31, 1971.
108. Spangler, S. B., Schwind, R. G., Nielsen, J. N., and Stahara, S. S., "Theoretical and experimental investigation of sail rotors for a high altitude platform", NEAR TR 32, 1971.
109. Kuhn, G. D. and Nielsen, J. N., "An analytical method for calculating turbulent separated flows due to adverse pressure gradients", NEAR TR 34, 1971.
110. Goodwin, F. K., Dillenius, M. F. E., and Nielsen, J. N., "Method of predicting loading and trajectories of single or TER or MER mounted stores on swept-wing aircraft", in *Aircraft/stores compatibility symposium proceedings*, 2, AFFDL TR 72 67, 1972, pp 231-306.
111. Kuhn, G. D. and Nielsen, J. N., "Analytical studies of aircraft trailing vortices", AIAA 72 0042, AFOSR TR 72 0771, 1972.
112. Spangler, S. B. and Nielsen, J. N., "Theoretical and experimental investigation of sail rotors", AIAA 72 0066, 1972.
113. Goodwin, F. K., Dillenius, M. F. E., and Nielsen, J. N., "Prediction of six-degree-of-freedom store separation trajectories at speeds up to the critical speed, Vol. I - Theoretical methods and comparisons with experiment", AFFDL TR 72 83, 1972.
114. Nielsen, J. N. and Kuhn, G. D., "Application of boundary-layer theory to dispersion in nonstratified two-dimensional estuaries", NEAR TR 45, 1972.
115. Spangler, S. B., Dillenius, M. F. E., Schwind, R. G., and Nielsen, J. N., "Assessment of a wake vortex flight test program", NASA CR 114736, 1973.
116. Nielsen, J. N. and Kuhn, G. D., "Application of boundary layer theory to dispersion of pollutants in two-dimensional estuaries", AIAA 73 0136, 1973.
117. Nielsen, J. N., Stahara, S. S., and Woolley, J. P., "A study of ingestion and dispersion of engine exhaust products in trailing vortex systems", NASA CR 114721, 1973.
118. Kuhn, G. D. and Nielsen, J. N., "Prediction of turbulent separated boundary layers", AIAA Journal, 12, 7, 1974, pp. 881-882, AIAA 73 0663, 1973.
119. Hemsch, M. J. and Nielsen, J. N., "A study of induced rolling moments for cruciform-winged missiles, Task I - Panel-panel interference", NEAR TR 56, 1973.
120. Dillenius, M. F. E., Goodwin, F. K., Nielsen, J. N., and Dyer, C. L., "Extensions to the method for prediction of six-degree-of-freedom store separation trajectories at speeds up to the critical speed, including interactive graphics applications and bodies of arbitrary cross section", Presented at Symposium on 2nd JTCG/ALNNO Aircraft/Store Compatibility, Sacramento, CA/18-20 Sept 1973, JTCG/ALNNO WP-12-2, 2, pp 135-206.
121. Kuhn, G. D. and Nielsen, J. N., "Studies of an integral method for calculating time-dependent turbulent boundary layers", NEAR TR 57, 1973.

122. Spangler, S. B., Hemsch, M. J., and Nielsen, J. N., "A study of induced rolling moments for cruciform-winged missiles, Task III - Canard-tail interference", NEAR TR 59, 1973.
123. Nielsen, J. N., Spangler, S. B., and Hemsch, M. J., "A study of induced rolling moments for cruciform-winged missiles", NEAR TR 61, 1973.
124. Dillenius, M. F. E., Goodwin, F. K., and Nielsen, J. N., "Extension of the method for predicting six-degree-of-freedom store separation trajectories at speeds up to the critical speed to include a fuselage with noncircular cross section, Vol. I - Theoretical methods and comparisons with experiment", AFFDL TR 74 130, 1974.
125. Nielsen, J. N., Stahara, S. S., and Woolley, J. P., "Ingestion and dispersion of engine exhaust products by trailing vortices for supersonic flight in the stratosphere", AIAA 74 0042, 1974.
126. Kuhn, G. D. and Nielsen, J. N., "Application of boundary-layer theory to dispersion in well-mixed estuaries", NEAR TR 63, W74-12858, 1974.
127. Nielsen, J. N., "Preliminary study of induced rolling moments for SAM-D missile", NEAR TR 64, 1974.
128. Dillenius, M. F. E., Goodwin, F. K., and Nielsen, J. N., "An analytical method valid up to the critical speed for predicting store separation characteristics from modern aircraft", AIAA 74 0775, 1974.
129. Hemsch, M. J. and Nielsen, J. N., "Test report for canard missile tests in Ames 6- by 6-foot supersonic wind tunnel, NEAR TR 72, 1974.
130. Dillenius, M. F. E. and Nielsen, J. N., "Supersonic lifting-surface computer program for cruciform wing-body combinations in combined pitch and sideslip", NEAR TR 74, 1974.
131. Nielsen, J. N., Hemsch, M. J., and Dillenius, M. F. E., "The induced rolling moments of cruciform wing-body combinations as influenced by panel-panel interference", NEAR TR 75, 1974.
132. Spangler, S. B., Goodwin, F. K., and Nielsen, J. N., "Analytical investigation of hinge moments on missile trailing-edge control surfaces", NEAR TR 76, 1974.
133. Mendenhall, M. R., and Nielsen, J. N., "Effect of symmetrical vortex shedding on the longitudinal aerodynamic characteristics of wing-body-tail combinations", NASA TR 2473, 1975.
134. Nielsen, J. N., Hemsch, M. J., and Dillenius, M. F. E., "Further studies of the induced rolling moments of canard-cruciform missiles as influenced by canard and body vortices", NEAR TR 79, 1975.
135. Kuhn, G. D. and Nielsen, J. N., "Prediction of turbulent separated flow at subsonic and transonic speeds including unsteady effects", in AGARD CP 168, 1975, Paper No. 26.
136. Hemsch, M. J., Nielsen, J. N., and Dillenius, M. F. E., "Method for calculating induced rolling moments for cruciform canard missiles at angles of attack up to 20 degrees", NWC TP 5761, 1975.
137. Spangler, S. B. and Nielsen, J. N., "Exploratory study of aerodynamic loads on a fighter-bomber at spin entry", NEAR TR 87, 1975.
138. Dillenius, M. F. E., Nielsen, J. N., and Hemsch, M. J., "Supersonic lifting-surface program for cruciform missiles with applications to induced roll", Presented at 10th Navy Symposium on Aeroballistics, Fredericksburg, VA/15-17 July 1975.
139. Dillenius, M. F. E. and Nielsen, J. N., "Prediction of aerodynamics of missiles at high angles of attack in supersonic flow", NEAR TR 99, 1975.
140. Dillenius, M. F. E., Goodwin, F. K., and Nielsen, J. N., "Analytical prediction of store separation characteristics from subsonic aircraft", J. Aircraft, 12, 10, October, 1975, pp 812-818.
141. Fidler, J. E., Schwind, R. G., and Nielsen, J. N., "An investigation of slender-body wake vortices", NEAR TR 108, 1976.
142. Nielsen, J. N., "Recent developments in aerophysics", Presented at Navy Tactical Missile Systems Colloquium, Naval Postgraduate School, Monterey, CA/25-30 April 1976.
143. Nielsen, J. N., "Predictions of forces and moments on external stores at transonic speeds", NEAR Paper 41, 1976.
144. Mendenhall, M. R., Spangler, S. B., Nielsen, J. N., and Goodwin, F. K., "Calculation of the longitudinal aerodynamic characteristics of wing-flap configurations with externally blown flaps", NASA CR 2705, 1976.
145. Dillenius, M. F. E., Goodwin, F. K., and Nielsen, J. N., "Prediction of supersonic store separation characteristics, Vol. I - Theoretical methods and comparisons with experiment", AFFDL TR 76 41 VOL 1, 1976.
146. Nielsen, J. N., McIntosh, S. C., Jr., Mendenhall, M. R., and Goodwin, F. K., "Determination of the aerodynamic characteristics of the heavy lifter", NEAR TR 113, 1976.
147. Nielsen, J. N., McMillan, O. J., McIntosh, S. C., Jr., and Spangler, S. B., "Aerodynamic characteristics of heavy lifter as measured at low speed", NASA CR 151919, 1976.
148. Nielsen, J. N., McMillan, O. J., McIntosh, S. C., and Spangler, S. B., "Feasibility study of modern airships (phase II), Vol. 1 - Heavy lift airship vehicle - Book III - Aerodynamic characteristics of heavy lift airship as measured at low speed", NASA CR 151919, 1976.
149. Nielsen, J. N., "Assessment of flight versus wind tunnel data of Rockwell/USAF GBU-15 cruciform wing weapon", NEAR TR 121, 1976.
150. Hemsch, M. J., Smith, C. A., Nielsen, J. N., and Perkins, S. C., Jr., "Calculation of component forces and moments of arbitrarily banked cruciform missiles with control deflections", ONR CR215 226 3, 1976.

151. McMillan, O. J., Schwind, R. G., Nielsen, J. N., and Dillenius, M. F. E., "Rolling moments in a trailing vortex flow field", NASA CR 151961, 1977.
152. Nielsen, J. N., Hemsch, M. J., and Smith, C. A., "A preliminary method for calculating the aerodynamic characteristics of cruciform missiles to high angles of attack including effects of roll angle and control deflections", ONR CR215 226 4F, 1977.
153. Fidler, J. E., Schwind, R. G., and Nielsen, J. N., "An investigation of slender body wake vortices", AIAA 77 0007, 1977.
154. Hemsch, M. J., Nielsen, J. N., Smith, C. A., and Perkins, S. C., Jr., "Component aerodynamic characteristics of banked cruciform missiles with arbitrary control deflections", AIAA 77 1153, 1977.
155. Fidler, J. E., Schwind, R. G., and Nielsen, J. N., "An investigation of slender body vortices", AIAA Journal, 15, 12, 1977, pp 1736-1741.
156. Smith, C. A., Nielsen, J. N., Dillenius, M. F. E., and Mendenhall, M. R., "A preliminary method for calculating the aerodynamic characteristics of missiles having elliptic bodies, monoplane wing, and interdigitated tails: Computer program user's manual", NEAR TR 170, 1977.
157. McMillan, O. J., Schwind, R. G., Nielsen, J. N., and Dillenius, M. F. E., "Rolling moments in a trailing vortex flow field", J. Aircraft, 15, 5, 1978, pp 280-286.
158. Nielsen, J. N. and Mendenhall, M. R., "Symmetric and asymmetric vortices from inclined bodies of revolution - Theory and experiment", Archiwum Mechaniki Stosowanej, 30, 4-5, 1978, pp 531-551.
159. Nielsen, J. N., "Nonlinearities in missile aerodynamics", AIAA 78 0020, 1978.
160. Nielsen, J. N., "Preliminary method for predicting aerodynamic characteristics of cruciform missiles to high angles of attack", Presented at 11th U.S. Navy Symposium on Aeroballistics, Philadelphia, PA/22-24 August 1978.
161. Smith, C. A., Nielsen, J. N., and Hemsch, M. J., "Prediction of aerodynamic characteristics of cruciform missiles to high angles of attack", AIAA 79 0024, 1979.
162. Dillenius, M. F. E. and Nielsen, J. N., "Computer programs for calculating pressure distributions including vortex effects on supersonic monoplane or cruciform wing-body-tail combinations with round or elliptical bodies", NASA CR 3122, 1979.
163. Nielsen, J. N., "Some stability and control nonlinearities of cruciform missiles at high angles of attack", in "Missile system flight mechanics", AGARD CP 270, May 1979, Paper 43.
164. Smith, C. A. and Nielsen, J. N., "Nonlinear aerodynamics of all-movable controls", in "Aerodynamic characteristics of controls", AGARD CP 262, 1979, Paper 25.
165. Crisalli, A. J., Stahara, S. S., Nielsen, J. N., and Spreiter, J. R., "The development of rapid predictive methods for three-dimensional transonic flowfields about fighter bomber aircraft", AFOSR TR 79 1281, 1979.
166. Klopfer, G. H. and Nielsen, J. N., "Basic studies of wing-body interference including vortex effects at high angles of attack and supersonic speeds", ONR CR 215 263 1, 1979.
167. Mendenhall, M. R., Fidler, J. E., and Nielsen, J. N., "A preliminary investigation of the hydrodynamic characteristics of a submersible vehicle", NEAR TR 207, 1979.
168. Smith, C. A. and Nielsen, J. N., "Prediction of aerodynamic characteristics of cruciform missiles to high angles of attack utilizing a distributed vortex wake", NEAR TR 208, 1979.
169. Klopfer, G. H. and Nielsen, J. N., "Euler solutions for wing and wing-body combination at supersonic speeds with leading edge separation", AIAA 80 0126, 1980.
170. Nielsen, J. N., "Missile aerodynamics - Past, present, future", J. Spacecraft and Rockets, 17, 3, May-June 1980, pp. 165-176.
171. Goodwin, F. K. and Nielsen, J. N., "Experimental and theoretical study of flow fields and store forces in close proximity to a triple ejection rack at transonic speeds", NWC TP 6210, 1980.
172. Klopfer, G. H. and Nielsen, J. N., "Basic studies of body vortices at high angles of attack and supersonic speeds", NEAR TR 226, 1980.
173. Canning, T. N. and Nielsen, J. N., "The influence of sting and strut supports on the aerodynamic loads on an ogive cylinder at high angles of attack at transonic speeds", AFATL TR 80 118, 1980.
174. Nielsen, J. N., Briggs, M. M., and Hemsch, M. J., "An R&D program to improve the aerodynamic performance of Army tactical missiles", NEAR TR 234, 1980.
175. Canning, T. N. and Nielsen, J. N., "Experimental study of the influence of supports on the aerodynamic loads on an ogive cylinder at high angles of attack", AIAA 81 0007, 1981.
176. Klopfer, G. H. and Nielsen, J. N., "Euler solutions of the body vortices of tangent ogive cylinders at high angles of attack and supersonic speeds", AIAA 81 0361, 1981.
177. Hemsch, M. J. and Nielsen, J. N., "Status report on triservice data base extension of PROGRAM MISSILE", Presented at 12th Navy Aeroballistics Symposium, David W. Taylor Naval Ship R&D Center, Bethesda, MD/12-14 May 1981.
178. Goodwin, F. K. and Nielsen, J. N., "Study of flow fields and store forces in close proximity to a triple ejection rack at transonic speeds", Presented at 12th Navy Aeroballistics Symposium, David W. Taylor Ship R&D Center, Bethesda, MD/12-14 May 1981.

179. Nielsen, J. N., "Missile aerodynamics - Dim past and indefinite future", Presented at 12th Navy Aeroballistics Symposium, David W. Taylor Naval Ship R&D Center, Bethesda, MD/12-14 May 1981.
180. Hemsch, M. J. and Nielsen, J. N., "Triservice program for extending missile aerodynamic data base and prediction program using rational modeling", NEAR TR 249, 1981.
181. Nielsen, J. N., Goodwin, F. K., and Smith, C. A., "Methods for predicting tail control effects on conical afterbodies of submersibles", NCSC TM 347 82, 1982.
182. Nielsen, J. N., Kuhn, G. D. and Klopfer, G. H., "Euler solutions of supersonic wing-body interference at high incidence including vortex effects", NEAR TR 263, 1982.
183. Nielsen, J. N. and Goodwin, F. K., "Preliminary method for estimating hinge moments of all-movable controls", NEAR TR 268, 1982.
184. Canning T. N. and Nielsen, J. N., "Influence of support systems on the aerodynamics of an inclined ogive cylinder", J. Spacecraft and Rockets, 19, 3, May-June 1982, pp 205-210.
185. Hemsch, M. J. and Nielsen, J. N., "The equivalent angle-of-attack method for estimating the nonlinear aerodynamic characteristics of missile wings and control surfaces," AIAA 82 1338, 1982.
186. Nielsen, J. N., "Missile aerodynamics - Introduction, review, and historical perspective", Presented at AIAA Professional Study Seminar Series "Missile Aerodynamics", San Diego, CA/12-13 August 1982.
187. Hemsch, M. J. and Nielsen, J. N., "Triservice program for extending missile aerodynamic data base and prediction program using rational modeling", NEAR TR 282, 1982.
188. Nielsen, J. N., "Nonlinear flow phenomena at high angles of attack and recent advances in their prediction", in "AGARD Conference on Missile Aerodynamics", AGARD CP 336, September 1982, Paper 11.
189. Klopfer, G. H. and Nielsen, J. N., "Computational fluid dynamic applications to missile aerodynamics", in "AGARD Conference on Missile Aerodynamics", AGARD CP 336, September 1982, Paper 3.
190. Briggs, M. M., Reed, R. E., and Nielsen, J. N., "Wing-alone aerodynamic characteristics to high angles of attack at subsonic and transonic speeds", ARO-16030.1-EG, 1982.
191. Mendenhall, M. R., Perkins, S. C., Jr., Spangler, S. B., and Nielsen, J. N., "Hydrodynamic analysis of submersible vehicles undergoing large unsteady maneuvers, Vol. 1 - Theory", NEAR TR 288, 1982.
192. Goodwin, F. K. and Nielsen, J. N., "Determination of optimum fin planform and airfoil section for minimizing fin hinge moment", NEAR TR 286, 1982.
193. Nielsen, J. N., "Aerodynamic characteristics of missile controls", in "AGARD Special Course on Aerodynamic Characteristics of Controls", AGARD R 711, March 1983, Paper 10.
194. Hemsch, M. J. and Nielsen, J. N., "Equivalent angle-of-attack method for estimating nonlinear aerodynamics of missile fins", J. Spacecraft and Rockets, 20, 4, 1983, pp 356-362.
195. Klopfer, G. H., Kuhn, G. D., and Nielsen, J. N., "Euler solutions of supersonic wing-body interference at high incidence including vortex effects", AIAA 83 0460, 1983.
196. Nielsen, J. N., "Problems associated with the aerodynamic design of missile shapes", Presented at 2nd Symposium on Numerical and Physical Aspects of Aerodynamic Flows, 2nd, California State University, Long Beach, CA/17-20 January 1983.
197. Hemsch, M. J. and Nielsen, J. N., "Aerodynamic characteristics of missile control fins in nonlinear flow fields", AIAA 83 2083, 1983.
198. Hemsch, M. J. and Nielsen, J. N., "Triservice program for extending missile aerodynamic data base and prediction program using rational modeling", NEAR TR 305, 1983.
199. Nielsen, J. N. and Kuhn, G. D., "Studies of vorticity effects by the Euler equations with emphasis on supersonic flow fields", NEAR TR 310, 1983.
200. Nielsen, J. N., Goodwin, F. K., Dillenius, M. F. E., and Hemsch, M. J., "Prediction of cruciform all-movable control characteristics at transonic speeds", AIAA 84 0312, 1984.
201. Nielsen, J. N., Goodwin, F. K., and Dillenius, M. F. E., "Prediction of cruciform all-moveable control characteristics at transonic speeds", NEAR TR 321, 1984.
202. Wood, N. and Nielsen, J., "Circulation control airfoils past, present, future", AIAA 85 0204, 1985.
203. Nielsen, J. N., "Arrays for minimum wave drag of bodies of revolution", AIAA 85 0449, 1985.
204. Hemsch, M. J. and Nielsen, J. N., "Extension of equivalent angle-of-attack method for nonlinear flowfields", In J. Spacecraft and Rockets, 22, 3, 1985, pp 304-308.
205. Nielsen, J. N., "Arrays of bodies of revolution for minimum wave drag", J. Aircraft, 22, 10, October 1985, pp 901-901.
206. Nielsen, J. N., "Supersonic wing-body interference at high angles of attack with emphasis on low aspect ratios", AIAA 86 0568, 1986.
207. Hemsch, M. J., editor, and Nielsen, J. N., editor, "Tactical missile aerodynamics", New York, AIAA, 1986.
208. Nielsen, J. N. and Hemsch, M. J., "The equivalent angle-of-attack concept for engineering analysis", Chapter XI in "Tactical Missile Aerodynamics", New York, AIAA, 1986.

The wing alone is defined as the exposed half-wings joined together. The lift of the wing alone by the factor K_C which is to be determined.

$$L_C = K_C L_W$$

The factor K_C is decomposed into three factors $K_{B(W)}$, $K_{W(B)}$, and K_N which represent the ratios of the body lift, wing lift, and nose lift of the combination to that of the wing alone.

$$K_C = K_{B(W)} + K_{W(B)} + K_N$$

$$K_{B(W)} = \frac{L_{B(W)}}{L_W} = \frac{(C_{L_\alpha})_{B(W)}}{(C_{L_\alpha})_W} \quad \delta = 0$$

$$K_{W(B)} = \frac{L_{W(B)}}{L_W} = \frac{(C_{L_\alpha})_{W(B)}}{(C_{L_\alpha})_W} \quad \delta = 0$$

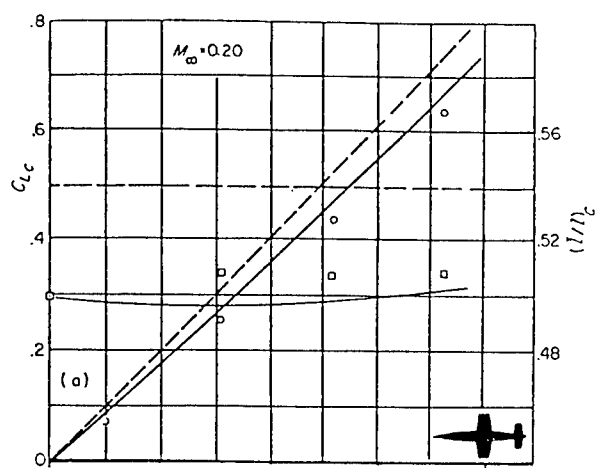
$$K_N = \frac{L_N}{L_W} = \frac{(C_{L_\alpha})_N}{(C_{L_\alpha})_W}$$

The factors $K_{B(W)}$ and $K_{W(B)}$ are defined for the case in which the angle of attack of the combination is varying but the wing-(or tail) incidence angle is zero. For the case in which the incidence angle is varying but the angle of attack of the body is zero, two analogous factors are defined.

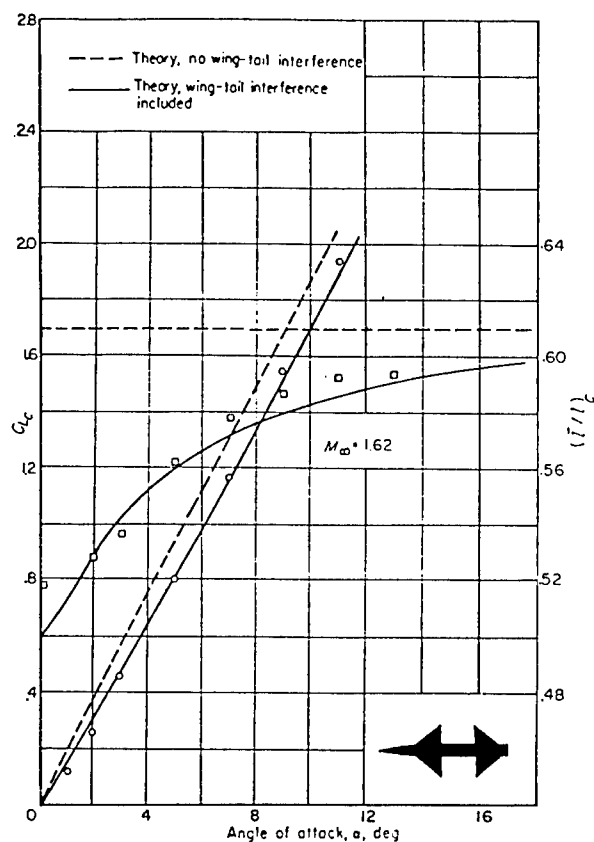
$$k_{B(W)} = \frac{L_{B(W)}}{L_W} = \frac{(C_{L_\delta})_{B(W)}}{(C_{L_\alpha})_W} \quad \alpha = 0$$

$$k_{W(B)} = \frac{L_{W(B)}}{L_W} = \frac{(C_{L_\delta})_{W(B)}}{(C_{L_\alpha})_W} \quad \alpha = 0$$

Figure 4. Definition of lift ratio factors



(a) Subsonic



(b) Supersonic

Figure 5. Lift and center-of-pressure characteristics of wing-body-tail combinations

$$C_{N_{F(B)}} = [K_w \alpha_c + k_w \delta + (\Delta\alpha)_v] (C_{N_\alpha})_w \quad (1)$$

where $C_{N_{F(B)}}$ is the normal-force coefficient acting on the fins in the presence of the body, K_w the Beskin upwash factor, k_w a factor which accounts for the nonperfect reflection plane at the fin root, $(\Delta\alpha)_v$ an average angle-of-attack induced on the fins by vortices, and $(C_{N_\alpha})_w$ the slope at zero angle-of-attack of the normal-force coefficient curve of the wing alone. The quantity $(\Delta\alpha)_v$ is found by estimating vortex positions and strengths and determining the average angle-of-attack induced by them and their images inside the body on the fins.

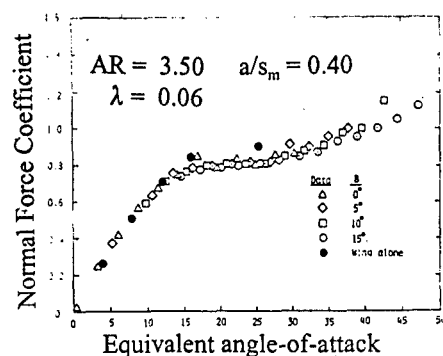
Equation (1) is limited to small angles. It can, however, be extended to higher angles by defining the equivalent angle-of-attack, α_{eq} , such that

$$\alpha_{eq} = K_w \alpha_c + k_w \delta + (\Delta\alpha)_v \quad (2)$$

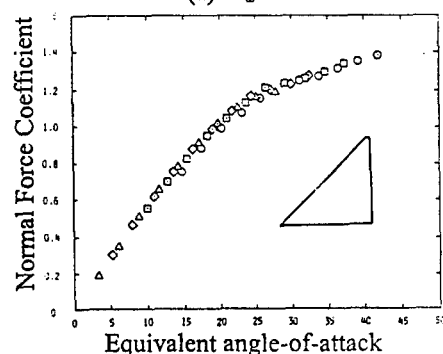
and rewriting Eqn. (1) as

$$C_{N_{F(B)}} = C_{N_w}(\alpha_{eq}) \quad (3)$$

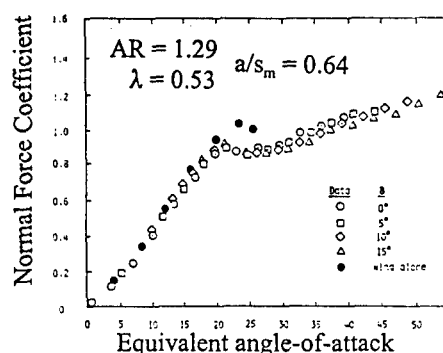
Figure 6. Basic definition of α_{eq}



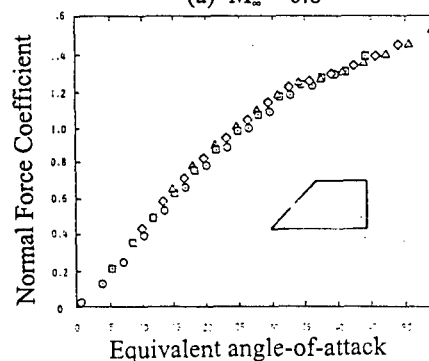
(a) $M_\infty = 0.8$



(b) $M_\infty = 1.3$



(a) $M_\infty = 0.8$



(b) $M_\infty = 1.3$

(b) Low aspect ratio fin on a body

Figure 7. Correlation of normal-force coefficient with equivalent-angle-of-attack

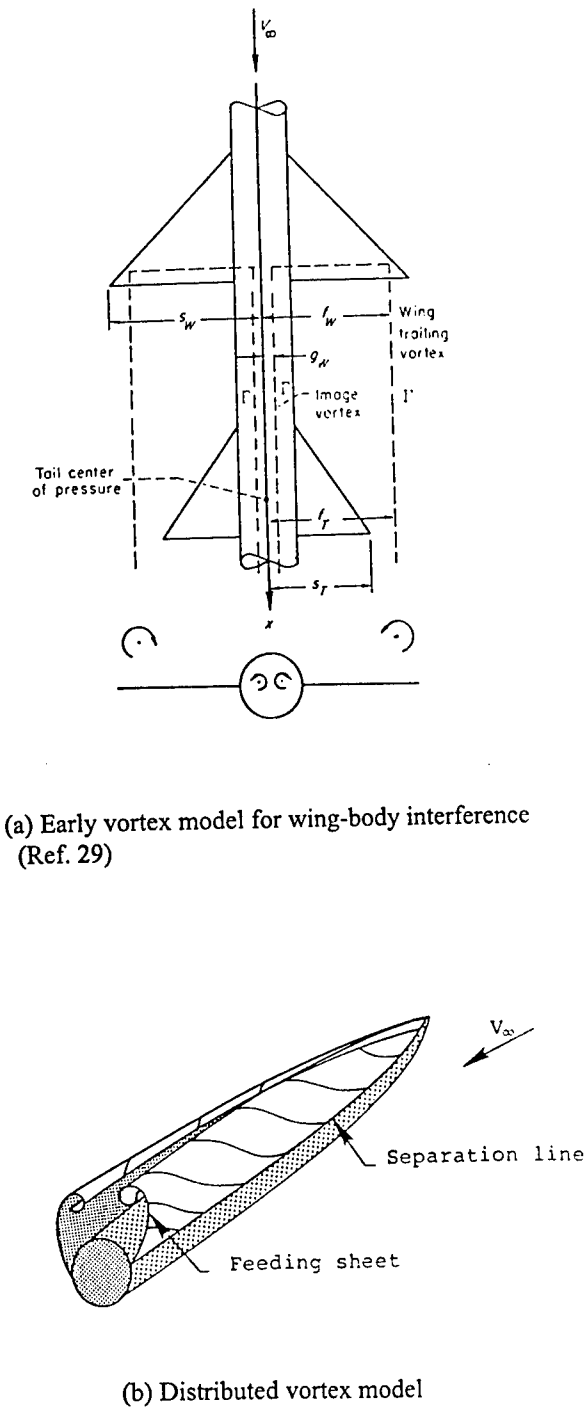


Figure 8. Evolution of theoretical vortex models

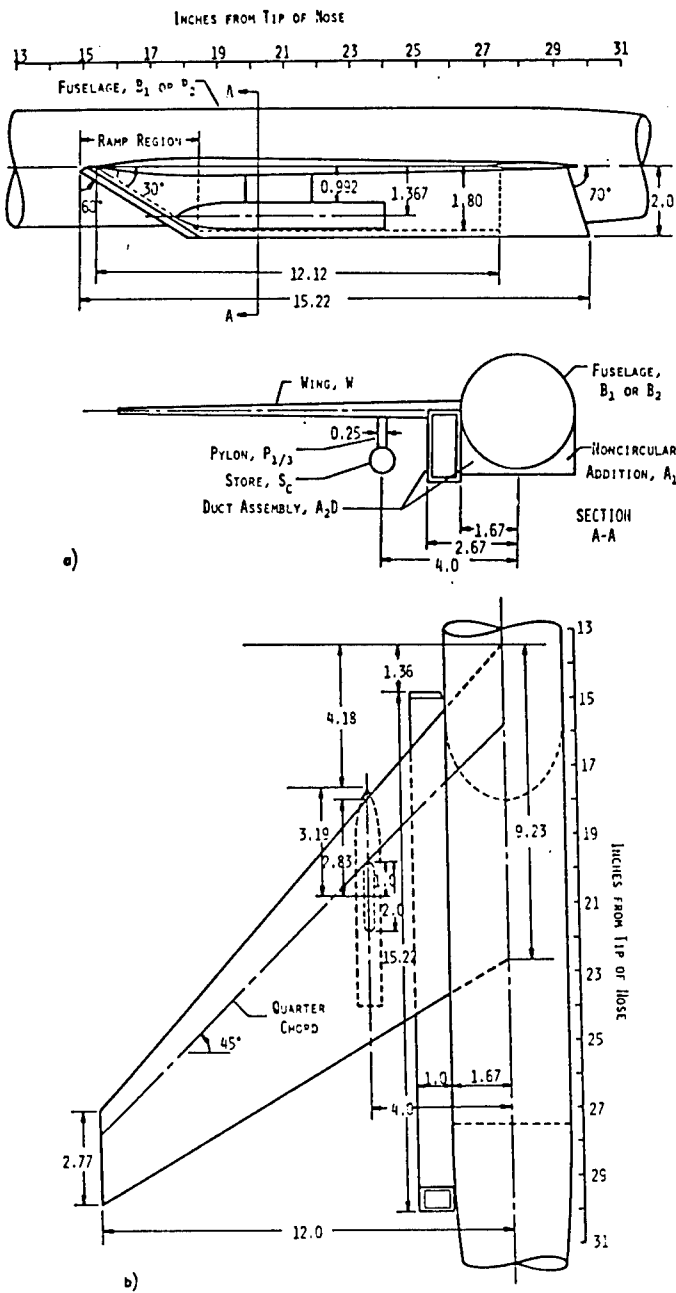


Figure 9. Wind-tunnel model a) Wing and duct attached to circular fuselage, b) Top view of wing and duct attached to circular fuselage

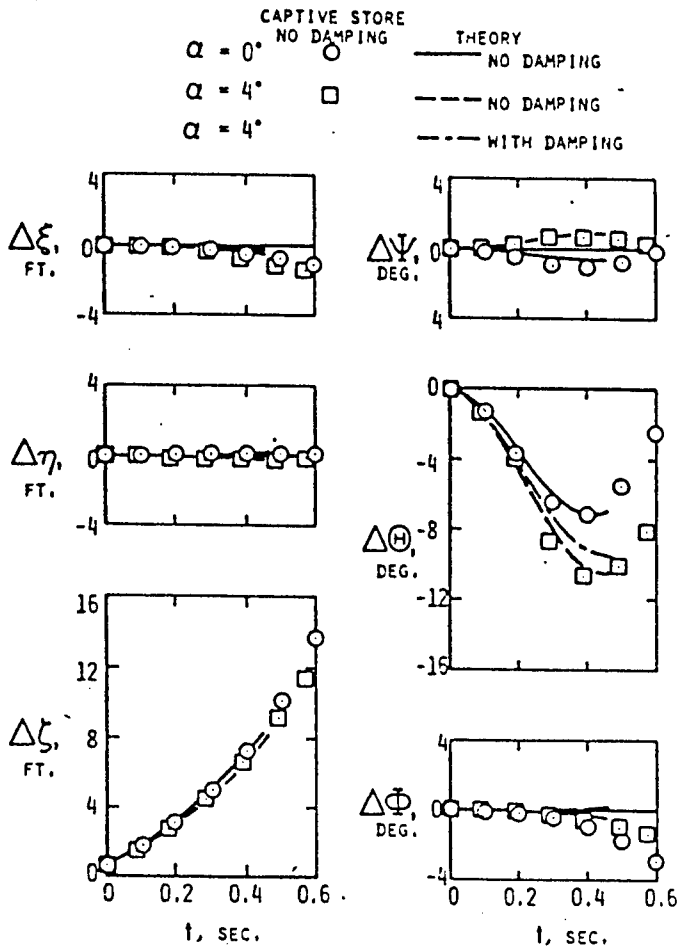


Figure 10. Comparison between calculated trajectories and captive-store trajectories of store with empennage; $M_\infty = 0.4$

FUTURE MISSILE SYSTEM TRENDS (U. S.) AND THEIR IMPACT ON AERODYNAMIC TECHNOLOGY

William C. McCorkle, Jr.
Executive Director, Missile Research, Development, and Engineering Center (MRDEC)
US Army Aviation & Missile Command (AMCOM)
Redstone Arsenal, AL 35898-5252, USA

SUMMARY

This paper presents a prognosis of missile design trends within the United States for the next decade. The views are those as perceived by the author and do not constitute an official position of the Department of Defense or any of its branches of service. It is based primarily on open literature briefings and Internet information combined with the experiences of the author acquired in rocket and missile design over the past forty years (at the US Army Aviation and Missile Command and its predecessor organizations). Expected trends in missile design and their resulting airframe requirements are interpreted in terms of advancements in aerodynamic technology, which greatly enhance the probabilities of successfully meeting overall system performance goals.

1.0 INTRODUCTION.

World events over the past decade and the perceived future threats to our forces and national interests will cause dramatic changes in the posture of U.S. Armed Forces. Any attempt to forecast future missile design trends or aerodynamic technology advancements must be preceded by a careful examination of national goals and policies. These goals are summarized in Figure 1.

- Maintain near-perfect, real time knowledge of the enemy posture and communicate information to all friendly forces in near real-time.
- Engage regional forces promptly in decisive combat, on a global basis.
- Employ a range of capabilities more suitable to actions that achieve military objectives with minimum casualties and collateral damage.
- Control the use of space.
- Counter threat of weapons of mass destruction to the CONUS and deployed forces.

Figure 1. Goals for Future Warfighting Capabilities.

1.1 Vectors Shaping the Force. There are many controlling factors, referred to as the external environment or vectors, which govern overall response to these goals and ultimately shape the force structure and capabilities. The major factors are illustrated in Figure 2. Let us examine some of the major vectors for all services but particularly for the U.S. Army.

CONUS Based Forces. Having a CONUS based force requires a capability to rapidly deploy large numbers of personnel and materiel to any threat area in the world. Missile systems must become smaller and lighter while maintaining their capability of defeating assigned targets. Wherever possible, they must serve multiple roles to minimize the logistics of supplying and supporting many different weapon systems.

- Mainly CONUS Based U.S. Forces
 - Emphasis on Force Projection- Premium on Deployability
 - Logistics-Challenged Legacy Army
- Future Victories Must Cost Fewer Lives
 - Very High Favorable Loss Exchange Ratios
 - Maximum Avoidance of "Close Combat" Shoot Outs
- Information Technology Revolution
 - Win the Information War
 - Provide Real-time Battlefield Information
- Worldwide High Threat Proliferation
 - Strong Active Market for World-class Weapons
 - Increasingly Sophisticated Terrorist Activities
- Affordability
 - Shrinking military budget

Figure 2. Vectors Shaping the Force.

Recent technology advances and expected gains in capabilities suggest that smaller, lighter and more effective missiles will be achievable within the next decade. These advances are occurring across the board in all missile technology areas. The challenge to missile system developers is the integration of these technologies in a manner which provides a CONUS based Force with weapon systems and materiel enabling their rapid deployment worldwide and provides a capability to initially contain and quickly achieve decisive victory against well-equipped hostile forces.

Lower Casualties and Collateral Damage. The desire in any military action is to achieve its mission rapidly and decisively with minimum casualties and collateral damage. Minimum casualties become a necessity when the adversary has numerically larger forces. Missiles for the next decade will be able to defeat targets at longer ranges with pinpoint accuracy. With these missiles and expected real-time battlefield information, close combat engagements can be minimized.

Real-time Battlefield Information. Advances in sensor suites and digital communication promise the availability of real-time, secure battlefield information gathering and dissemination to all units. Knowing the location and movements of enemy forces is vital to controlling the battlefield scenario.

Worldwide Threat. There has been a worldwide proliferation of high quality weapon systems since the end of the cold war. A significant number of third world countries now have or will have sophisticated land, sea and air weapons to support military operations. This situation influences the need for a rapid deployment capability to any worldwide location.

Affordability. The current trend of a reduced defense budget places greater attention on affordability of weapon systems. Improvements in current missiles and future developments must address not only increased effectiveness but also means of reducing training cost to maintain proficiency; reduced cost and elapsed time for fabrication; lower maintenance costs through critical monitoring of wear, stress and fatigue, and extending operational life of weapon components.

1.2 Achieving Goals. The stated warfighting goals can be achieved within the identified constraints only by effecting a change in the approach to weapon system research and development. Efforts in all related technologies must be focused toward these goals. Evolving new technology capabilities must be carefully evaluated in regards to their significance for performance enhancements of

current missile systems as well as their benefits when integrated into a completely new system. Critical evaluation through appropriate analysis and testing must precede modifications to current missile systems or before initiating new development programs.

Aerodynamics is one of the disciplines that can make significant contributions to the stated goals. We will briefly review a cross-section of national missile incentives and development programs where aerodynamic technology improvements are expected to have an important impact.

2.0 EVOLVING MISSILE SYSTEM CONCEPTS AND DEVELOPMENT PROGRAMS.

Missile concepts and development systems reviewed herein are limited primarily to those that experience most of their flight within the sensible atmosphere. Those addressed represent a cross-section of airframe types and flight performance characteristics that are of interest to the aerodynamics community. Effort was made to include missile systems from all the U.S. Armed Services; however, the Army missile systems are emphasized because of their familiarity. Additionally, a number of the advanced missile concepts are of interest to more than one service and in some cases are being pursued jointly. There is no particular order to their presentation except their grouping according to the primary service interest.

2.1 U. S. Air Force Systems. The Wright Laboratory conventional armament technology plan focuses on five "Integrating Concepts" missiles as shown in Figure 3. These missile concepts provide vehicles for assessing improvements in overall performance and lethality resulting from sensor, control and ordnance technology advances.

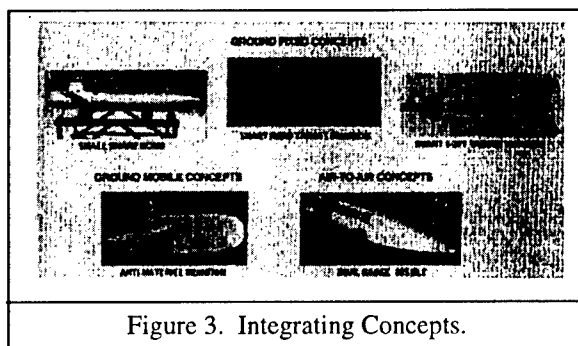


Figure 3. Integrating Concepts.

Three of the five concepts focus on improving the delivery accuracy and effectiveness of ordnance of smart munitions used to attack fixed ground targets. The major aerodynamic considerations for these type weapons are lower drag to increase range and

control effectiveness. The remaining two concepts introduce greater aerodynamic challenges.

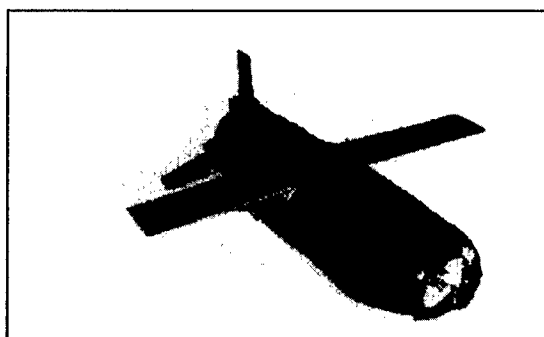


Figure 4. LOCAAS.

LOCAAS (Low Cost Autonomous Attack Submunition). The anti-materiel munition concept focuses on the defeat of ground mobile targets. It is a small, low cost sub-munition with the capability of searching a broad target area, detect and classify a variety of ground mobile and fixed targets. A typical configuration is shown in Figure 4. LOCAAS concepts are being pursued also by the U. S. Army as potential payloads for MLRS and ATACMS. A high lift-to-drag ratio airframe is desired to broaden the search and attack footprint.

The remaining integrating concept addresses improvements in air-to-air missile capabilities. With the development of wide field of regard seekers and small reaction control devices it becomes feasible to greatly improve the engagement envelope of air launched missiles such as the AIM-120 Advanced Medium Range Air-to-Air Missile.

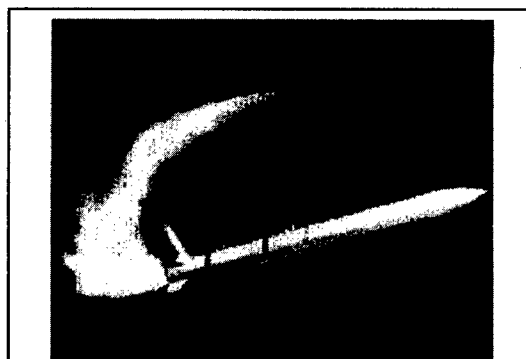


Figure 5. Dual Range Missile.

Utilizing a wide view, off-boresight seeker and attitude control reaction jets allow the missile to turn quickly after launch reaching angles-of attack over 90 degrees and directing the propulsive thrust immediately toward the target. It is clear that such a flight profile results in highly challenging

aerodynamic flow fields that must be characterized accurately for a successful missile design. This concept has broad interest within all of the Services. Figure 5 depicts an artist sketch of a dual range missile configuration.

2.2 U.S. Navy Systems. The U.S. Naval Air Warfare Center is embarking on a long-term program to explore, demonstrate and develop a family of hypersonic air breathing cruise missiles that would replace the current family of land and ship attack missiles. This common family of strike weapons would have the capability to attack and destroy time critical mobile targets at long standoff ranges. The High Speed Strike System (HiSSS) and Hypersonic Strike Initiative (HyStrike) are both components of this program. Figure 6 illustrates a possible scenario for achieving the neckdown process to arrive at a common family of weapons.

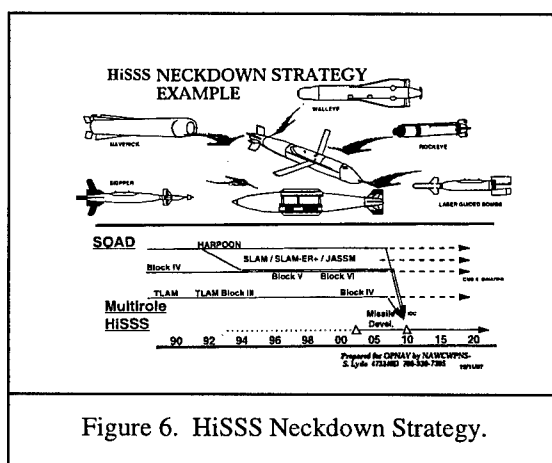
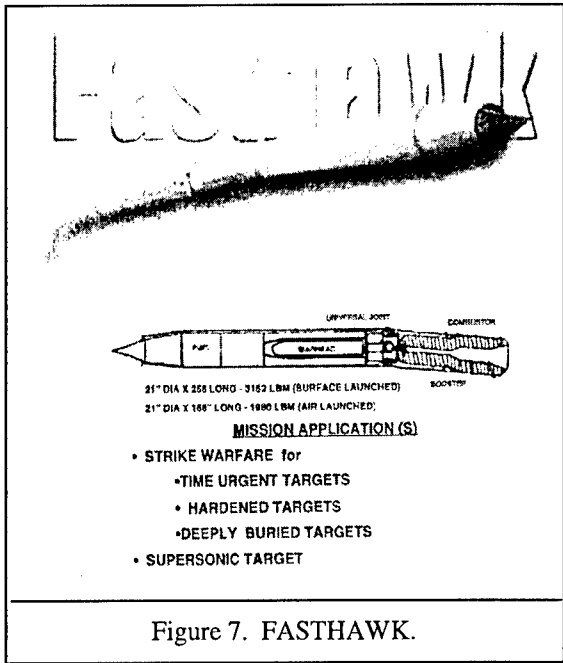


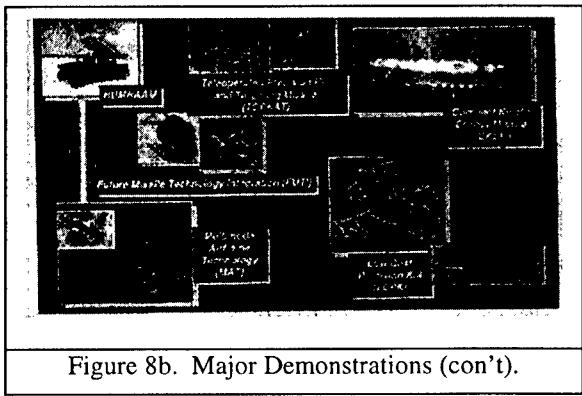
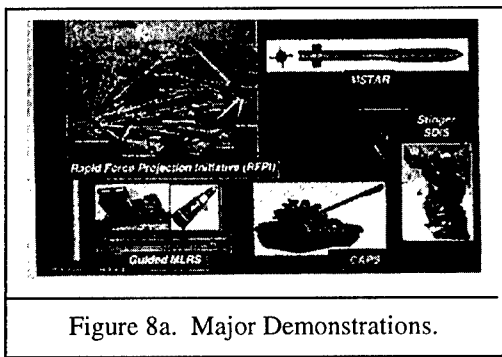
Figure 6. HiSSS Neckdown Strategy.

Projected flight profiles extend to a range of 600 nautical miles at average Mach numbers from 3.5 to 7. This flight environment surely challenges the aerodynamic community to provide low drag adaptive airframes, efficient inlet designs, high control response and solutions to the severe aerodynamic heating conditions. Real gas effects become of greater concern at hypersonic speeds in addition to conditions where mixed flow from control jets and the exhaust plume strongly interact with free stream flow.

The U.S. Navy is pursuing a related Advanced Technology Demonstration (ATD) Program leading to the Low Cost Missile System (LCMS) called FASTHAWK. This high-speed cruise missile has similar flight performance as the HiSSS program. The LCMS concept airframe comprises a fixed geometry annular nose inlet, a solid fuel booster/ramjet engine, and an aft located finless bending body for flight control. Geometry and performance goals are depicted in Figure 7.



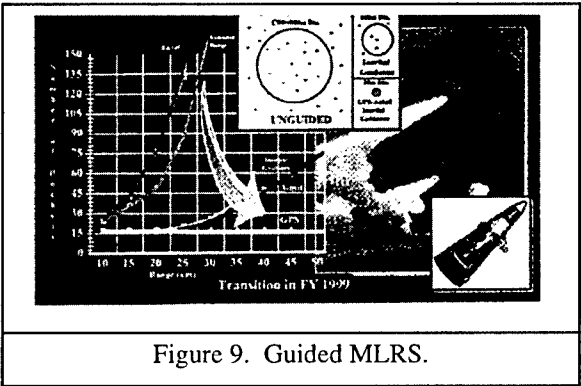
2.3 U. S. Army Programs-Tactical Systems. Missile system programs for the U. S. Army are centered principally at the Aviation and Missile Command (AMCOM) and its Missile Research, Development and Engineering Center (MRDEC) which carries out the related research and development activities. MRDEC is pursuing advanced technology and missile demonstration programs to support product improvements of current missile systems and future missile concepts. These programs are depicted in the following graphics (Figures 8a and 8b):



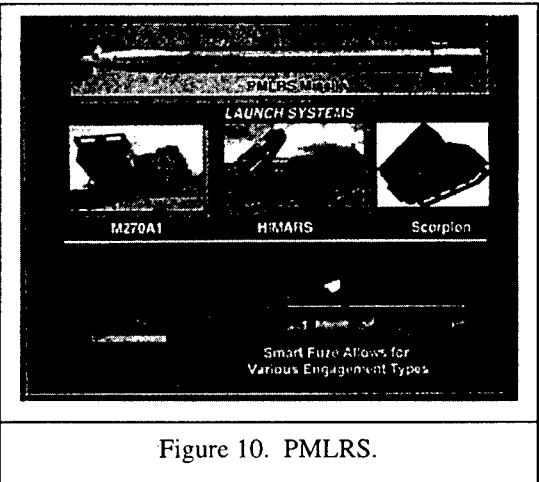
These missile technology demonstration programs focus planned improvements in current missile systems and expected trends for future missile designs during the next decade. Brief overviews are presented for the programs most influenced by advancements in missile aerodynamics.

Multiple Launch Rocket System (MLRS). MLRS is the mainstay fire support rocket system for the U.S. and a number of NATO armed forces. There is strong impetus to maintain its effectiveness and viability well into the next decade. MRDEC is pursuing at least three missile related technology demonstration programs that support MLRS capability enhancement.

Point-hit MLRS (PMLRS). Increasing delivery accuracy will have a major impact on the number of rounds required to defeat targets at the upper end of MLRS range capability. This has a profound impact on the logistics required to initiate and sustain a military action as illustrated in Figure 9:



The technology demonstration program will establish the accuracy improvements that are obtainable by adding a low cost guidance and control package. Guidance information is acquired from a combined inertial and GPS package and planar canard surfaces are used to correct the missile flight trajectory. All additional components are location in the forward section of the nose. The resulting airframe configuration and other planned improvements are shown in Figure 10:



Aerodynamic considerations are related to defining a canard design that maintains adequate control over a broad Mach number region without a significant increase in drag.

MLRS Smart Tactical Rocket (MSTAR). This technology demonstration program addresses the problems of packaging and axial dispensing smart munitions from MLRS. BAT and SADARM are the smart munitions of interest.

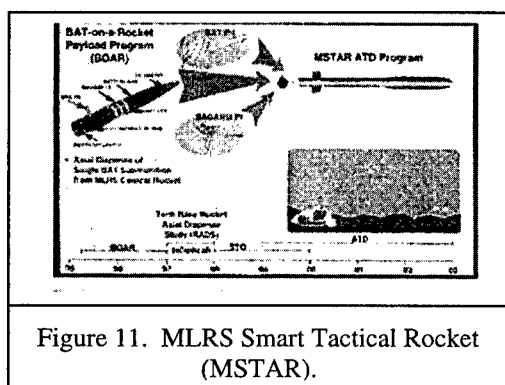


Figure 11. MLRS Smart Tactical Rocket (MSTAR).

Bat-on-a-Rocket (BOAR). The BOAR Program recently demonstrated the viability of axial dispense. A dummy BAT munition was successfully dispensed from an MLRS nose section after it was separated from the boost motor. The separating nose section was stabilized at a small angle-of-attack by cruciform grid fins, which deployed during separation, enhancing a clean axial dispense. A more detailed understanding of aerodynamic flow fields and resultant forces on the dispensed airframe would enhance successful design of missile dispensing systems.

High Quantities Anti-materiel Sub-munitions (HI-QUAMS). The goal of this advanced technology program is to demonstrate a small sub-munition, which employs an advanced miniaturized seeker to detect, classify and identify threat signatures. The sub-munition will be powered to extend both range and the area search and attack footprint. A typical packaging arrangement is shown in Figure 12 for an MLRS payload. It is noteworthy that a non-circular airframe with tri-form control surfaces is needed to achieve high packaging density.

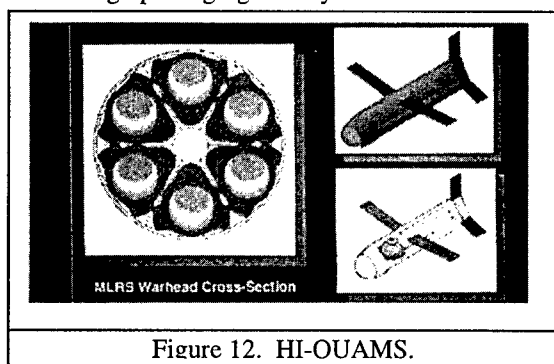


Figure 12. HI-OUAMS.

2.75 Guided Rocket Program. Advanced technology and flight demonstration programs are underway to greatly improve the delivery accuracy of the helicopter launched 2.75-inch rocket, HYDRA-70. One milli-radian delivery accuracy is expected by adding a low cost guidance and control package. The components of a technology demonstration program are shown in Figure 13. Both reaction jet and aerodynamic control systems are being considered, but canard controls are the current choice. An airframe with a free rolling tail assembly is being considered to mitigate the usual unfavorable flow field interference effects of canards on downstream stabilizing surfaces.

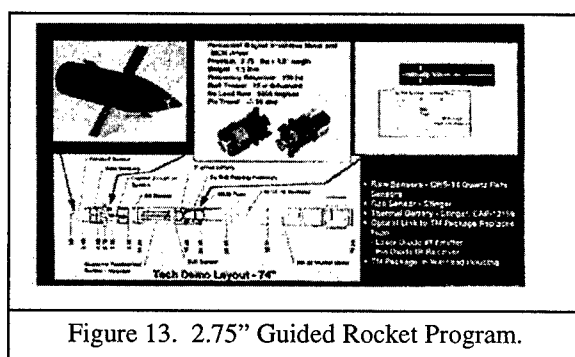


Figure 13. 2.75" Guided Rocket Program.

Compact Kinetic Energy Missile (CKEM) Technology Program. The current LOSAT missile is an effective anti-armor weapon system. However, future anti-armor weapons must be lighter and deliver sufficient kinetic energy to the target to defeat advanced and active threat armors. The Missile RDEC CKEM Technology program focuses on efforts to develop and demonstrate advanced technology necessary for the next generation hypervelocity anti-tank weapon system. The U. S. Army has identified the need for a hypervelocity kinetic energy missile, which is smaller, lighter, faster, maneuverable, and provides overwhelming lethality against armored ground targets. The approach of the CKEM Technology program is to develop and demonstrate "leap ahead" technology at the component level within a missile testbed configuration, which can easily be transitioned into a "leap ahead" weapon system. The technical challenges are derived from the anticipated operational requirements and capabilities of hypervelocity missiles. Successful achievement of the operational requirements for future hypervelocity missiles requires advancements in the state-of-the-art of several missile component technologies, as well as understanding the interactions of the various technologies for developing and demonstrating an advanced state-of-the-art hypervelocity missile system. The overall System perspective is a major effort of the CKEM Technology program, since advancements in one technological area stress the overall system and create requirements for advancements in other

component technology areas. A CKEM layout concept is shown in Figure 14. Many of the technology challenges for CKEM and similar type hypervelocity missiles are discussed in more detail in Section 3.0.

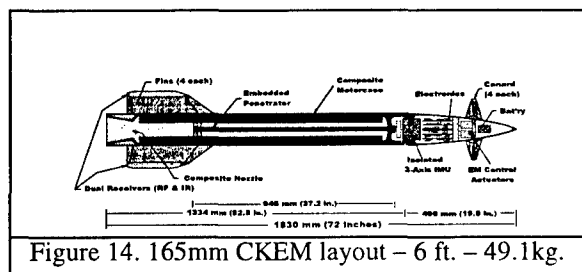


Figure 14. 165mm CKEM layout - 6 ft. - 49.1kg.

Control authority of the LOSAT missile during flight is achieved through the use of attitude control reaction jets. The Missile RDEC Advanced Kinetic Energy Missile (ADKEM) Hypervelocity Missile Component technology program, which was the predecessor to the CKEM program, uses control actuation system (CAS) tail fins embedded in the booster motors exhaust flow field to provide control during boost. Once the boost phase is complete (approximately 0.5 sec), the boost motors are discarded and the same CAS all movable tail fins provide control of the coast phase K.E. kill centerbody to target impact. CKEM will use canard controls to reduce weight and provide a better off-axis engagement capability. The CKEM concept utilizes an Annular motor configuration with the K.E. kill mechanism embedded in the motor to help reduce length, mass, and overall missile size. Weight, length, and kinetic energy goals challenge the aerodynamics designer to develop an airframe that has very low drag, while providing adequate control authority and response for both low and high-speed maneuvers.

Ducted Rocket Engine (DRE) Technology. The DRE technology demonstration program is a joint effort with Japan to explore the performance characteristics of a ducted rocket engine that utilizes minimum smoke, insensitive munitions type propellants. This program is investigating the total propulsion system including booster, low profile inlets, gas generators, control valves and the integration of these components into a demonstration vehicle. This technology has direct application to extending range of artillery missiles such as MLRS and ATACMS without significant increases in size or weight of the airframe while maintaining compatibility with existing launcher and support equipment.

Multimode Airframe Technology-LONGFOG. MRDEC is developing and demonstrating tele-operated missile systems which provide many of the capabilities the Army has stated it needs,

including flexible mission planning, improved Identification Friend or Foe, minimum collateral damage and precision hit. The Multi-mode Airframe Technology program is the latest in-house technical demonstration of these capabilities in a missile capable of extended ranges, out to 100 km. The airframe has unique features for a tactical missile, which were designed to make the missile as mission flexible as possible. The missile is launched using only the thrust provided by the turbojet engine that provides approximately 1-g of vertical acceleration. Control of the missile during this soft launch is possible because the control fins are embedded in the exhaust of the turbojet providing the equivalent aerodynamic control achieved at 100 m/s. The airframe is designed to fly-out at high speed without the drag of the wings, which can be kept stored in the fuselage. The missile slows to less than 100 m/s to allow the man-in-the-loop gunner to search for targets. Lift is maintained by deploying the wings in a bi-plane configuration with flaps deployed on the top wing. In the target attach phase, equal maneuverability in both pitch and yaw is achieved by transitioning the wing to an "X" cruciform. The missile can reaccelerate at a level flight 2.25-g to regain the high speed required to attack air vehicles. A sketch of the airframe in flight is shown in Figure 15.

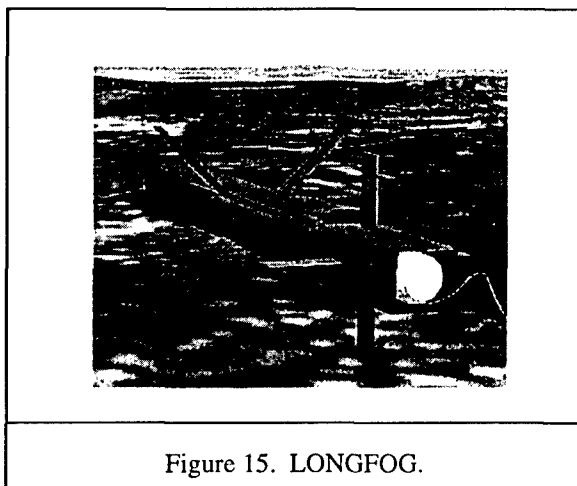


Figure 15. LONGFOG.

The LONGFOG airframe is representative of the trend in many emerging missiles, which utilize an adaptive airframe to optimize flight performance during a broad range of trajectory conditions.

2.4 U.S. Programs - Air and Missile Defense Systems. The major U. S. air and missile defense programs are directed by the Ballistic Missile Defense Organization (BMDO). BMDO's mission addresses three broad areas; Theater Missile Defense, National Missile Defense, and the Supporting Technology Program. Its immediate and highest priority efforts are directed toward theater missile defense. The four core programs are

PATRIOT Advanced Capability-3 (PAC-3), Navy Area TBMD, Theater High Altitude Area Defense (THAAD), and Navy Theater Wide systems.

Patriot Advanced Capability (PAC-3). The fielded Patriot air defense system is presently undergoing significant improvements to enhance its theater ballistic missile defense capabilities. These improvements are directed toward making the Patriot more capable in defending troops and fixed assets from short and medium range ballistic missiles, cruise missiles, and all air breathing threats. One major upgrade is the PAC-3 missile, a smaller, lighter and more capable interceptor, which employs both aerodynamic surfaces and attitude control motors for control. The attitude control motors provide rapid missile response characteristics that are needed during the end game engagement for a hit-to-kill intercept. The general airframe configuration of the PAC-3 missile is shown in Figure 16.

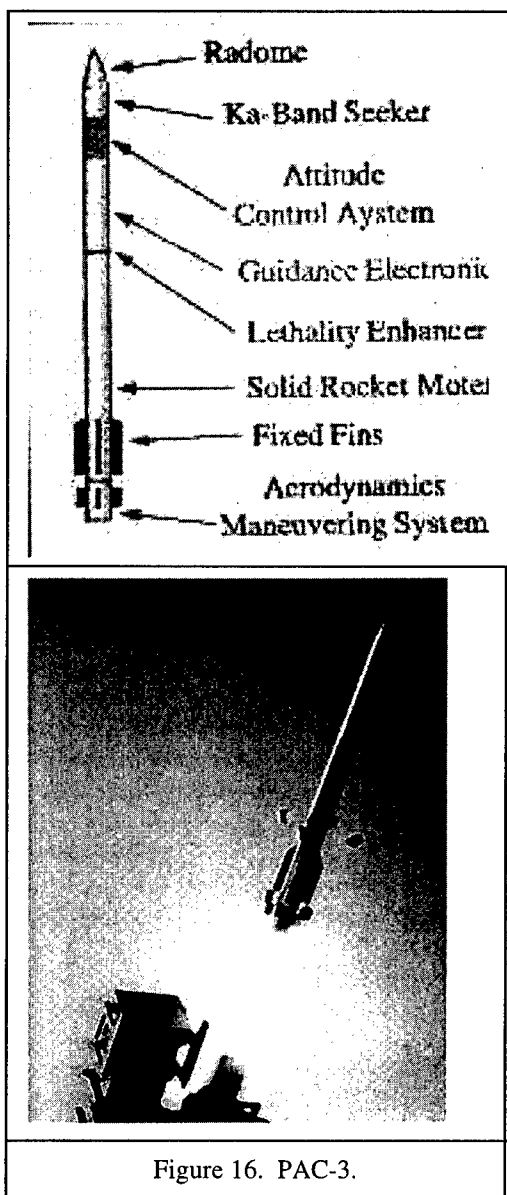


Figure 16. PAC-3.

Theater High Altitude Area Defense (THAAD) System. THAAD is being developed as the high endo-atmospheric and exo-atmospheric interceptor for theater missile defense. The missile comprises a Propulsion System and a Kill Vehicle. The propulsion system is made up of a single stage solid propellant booster, a Thrust Vector Control (TVC) system, and deployable aerodynamic flares. The booster delivers the Kill Vehicle to the speed and altitude required to intercept an incoming threat. The TVC system steers the missile during the boost phase of the flight. The booster's aerodynamic flares deploy shortly after launch to provide proper aerodynamic stability during flight. The booster and kill vehicle interstage houses ordnance components that enable separation. The Kill Vehicle, which actually intercepts the incoming TBM, is a technically sophisticated device that can search for and lock onto a target, and then accurately intercept and destroy that target using only the kinetic energy of high speed impact. The Kill Vehicle consists of a conical nose attached to a midbody structure. A two piece shroud covers the forebody during endo-atmospheric flight to reduce aerodynamic drag and to protect the seeker window from aerodynamic heating. Some of the key features of the Kill Vehicle are the infrared seeker with an uncooled sapphire window that provides guidance information and a Divert and Attitude Control System (DACS) that provides precise terminal control. Figure 17 illustrates the THAAD missile in flight.

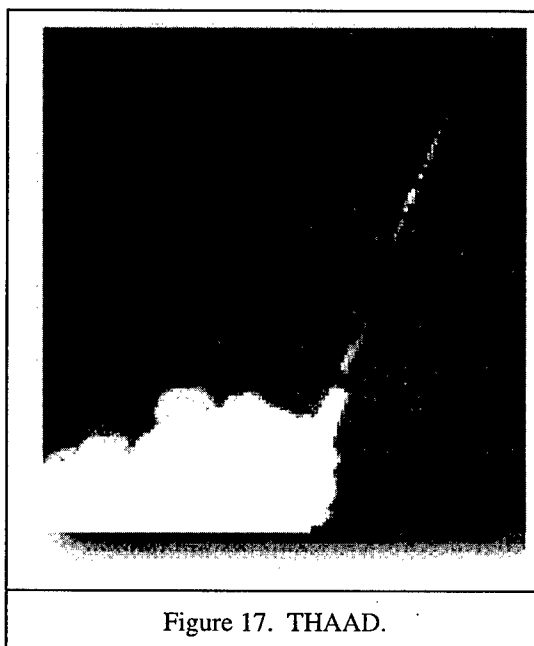


Figure 17. THAAD.

2.5 Atmospheric Interceptor Technology (AIT). AIT is currently BMDO's only broadbased atmospheric technology program supporting advanced TMD. The objectives of the AIT program are to develop, integrate and demonstrate advanced lightweight technologies for hypersonic hit-to-kill intercepts of threat missiles within the atmosphere.

AIT has a variety of multi-service applications or risk reduction opportunities, including THAAD, Patriot, UAV-based Boost Phase Intercept, CorpsSAM/MEADS for cruise missile (CM) defense and Navy Upper/Lower Tier. The technology also provides a hedge against future threats (e.g., maneuvering, stealth, etc.) and naturally occurring threat characteristics (e.g., SCUD break-up).

The Atmospheric Interceptor Technology (AIT) Program supports all three BMDO priorities by developing the technology to enable an effective and affordable capability to intercept targets within the atmosphere (less than 100 km altitude) along with a residual capability for intercepts outside the atmosphere. Many tactical ballistic missile trajectories are entirely within the earth's atmosphere and all longer range ballistic missiles operate in the atmosphere during the ascent and decent phases of their trajectory. Therefore atmospheric systems and technology play an important role for all missile defense applications.

High velocity atmospheric intercepts are essential to maintain sufficient battlespace, lethality and coverage/footprint performance. Hit-to-kill with aimpoint selection will enable high lethality with a low weight interceptor. However, such conditions provide severe aerodynamic, aerothermal, and structural requirements. AIT is providing significant technology advancements in the window/forebody (small cooled aperture), strapdown seeker, solid propulsion control systems and vehicle integration. Testing to date has shown the feasibility of small and lightweight cooled aperture/forebody and greatly advances the state of the art of lightweight hit-to-kill interceptors. Lower weight and smaller size will enable affordable block upgrades of existing systems.

Therefore atmospheric systems and technology play an important role for all missile defense applications. The AIT program is addressing several areas of concern regarding aerodynamics; the window design for an optical seeker, solid propellant divert and attitude control system and development of an aerodynamic ground test facility (AOEC) that duplicates the true flight velocities and atmospheric conditions.

Divert and Attitude Control System-(DACS). An atmospheric high velocity interceptor encounters a broad range of control force and response requirements that must be met to achieve the desired hit-to-kill intercept. Controllable reaction jet systems are the most promising means of meeting these requirements. AIT is developing solid propellant divert and attitude control systems that contribute significantly to lightweight, small

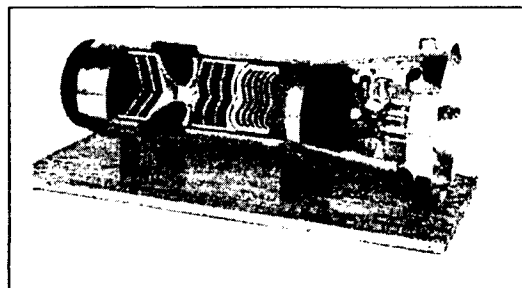


Figure 18. Solid Divert and Attitude Control System (DACS).

size and safety goals of the integrated interceptor airframe. The DACS (Figure 18) designs use an insensitive munitions type propellant configured in multiple grains with individual igniters. The aero-optic effects are minimized by selecting a propellant with low H_2O content in the plume exhaust and reduced start shock transients on seeker and electronic components. A successful design must utilize extensive flow analyses including the significant flow interaction that exists between the external flow and the DACS exhaust plume.

Cooled Window/Forebody. Interceptors operating at hypersonic speeds within the atmosphere encounter severe aerodynamic heating conditions particularly in the nose region where the seeker and its optical window are usually located. Ablative heat protection is not acceptable because of their distortion effects on seeker accuracy. AIT has pursued both internally and externally cooled window designs that have been demonstrated successfully in ground tests. The window design program has made extensive use of computational fluid dynamic (CFD) analyses, which include real gas effects and tests in the Aero-Optic Evaluation Center (AOEC). Figure 19 shows the cooled window / forebody as tested in the AOEC facility.

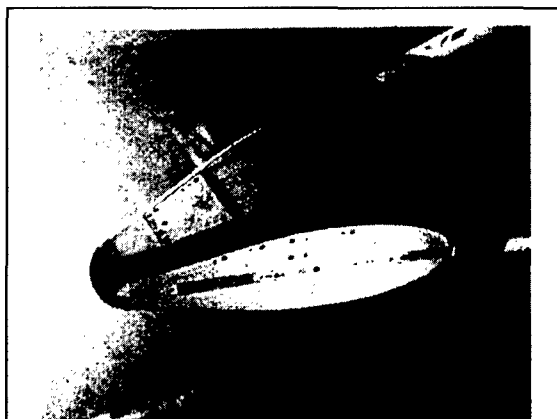


Figure 19. AIT Full-scale Forebody in AOEC/LENS Tests.

Aero-Optic Evaluation Center (AOEC). The AIT program has developed and is maintaining a test

facility for testing all of the critical components of advanced hypersonic interceptors at real flight conditions. AOEC (Figure 20) augments the type and range of tests that can be conducted in the LENS (Large Energy National Shock) tunnel and utilizes most of the LENS hardware. This facility is being used to validate designs and performance of the AIT seekers, optical windows, DACS, and full-scale airframes. AOEC can simulate accurately flight Mach numbers to 18 and altitudes to 80 km.

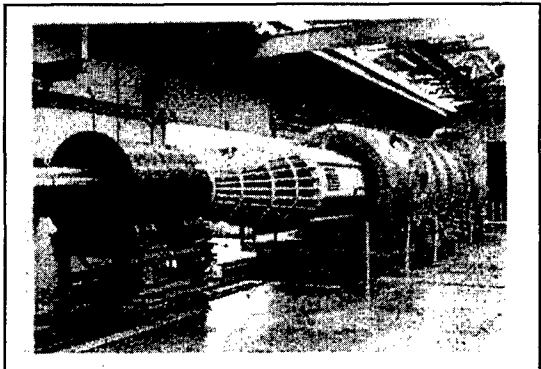


Figure 20. LENS/AOEC Facility.

3.0 A Case Study of Hypervelocity Missile System Design and Development.

The goals and factors influencing future U.S. Armed Forces, as discussed in the introduction, stress the need for rapidly deployable CONUS based forces to engage regional threats promptly in decisive combat on a global basis. Size and weight are paramount factors for weapon systems supporting this future force structure. Hypervelocity kinetic energy (KE) missiles offer a highly viable means of maintaining weapon effectiveness at substantially lower weight and reduced length while achieving significantly greater effective range than KE tank gun projectiles. These characteristics are particularly important for missiles fired from both armored vehicles and air vehicles (helicopters). The systems technology requirements and developments to achieve the required reductions in weight and size are discussed in this case study. This discussion focuses on a potential future lightweight armored vehicle (15 to 20 tons) weapon system that utilizes a hypervelocity kinetic energy missile system as opposed to a gun launched KE projectile for its primary kill mechanism. The primary purpose of this discussion is to emphasize the need for well planned and executed system development efforts which start with coordinated technology advancements in all supporting disciplines, aerodynamics being one of the major technologies.

The technology challenges addressed in this case study have evolved from the LOSAT, ADKEM, and now the CKEM hypervelocity missile programs. The major operational requirements associated with CKEM for the development of the next hypervelocity missile include a significant decrease in the total flight time, a peak velocity or more than MACH 6.5, a lethal range of 200-5000 meters, a low signature high performance propulsion, a significant improvement in launch platform survivability, and a LOSAT equivalent lethality with a reduced mass/size missile. The desire to develop a hypervelocity kinetic missile that is less than 1.8 meters long, 130-150 mm in diameter, and less than 50 kg. at takeoff, with the above operational capabilities provides a significant increase in vehicle stowed kills, but significantly complicates the system integration. The challenges associated with accomplishing the desired operational capabilities require technological advancements in several critical areas to include: 1) more efficient propulsion; 2) missile lethality enhancements; and 3) miniaturization of guidance & control component technology.

Many advanced technology developments were conducted under the Missile RDEC ADKEM Hypervelocity Missile Component technology program to validate operational capabilities of future hypervelocity missiles. The miniature component technology developments in the ADKEM program identified the capability to conduct a simple state-of-the-art operational hypervelocity missile system demonstration. Additionally, ADKEM identified the various types of System complications associated with combining and implementing new technology. ADKEM is boosted to its maximum velocity by a four motor cluster that separates from the centerbody after booster burnout (Figure 21).



Figure 21. ADKEM.

The overall ADKEM missile envelope and separation challenges have driven the design to the smaller and more efficiently packaged CKEM configuration. Unfortunately, many of the

advantages of hypervelocity and high performance propulsion significantly increase the magnitude of problems analogous with the missile aerodynamics, control authority, aeroelasticity, drag, aerothermal heating, and high velocity missile accuracy.

3.1 Background. The Line-of-Sight Anti-Tank (LOSAT) Advanced Development demonstrated a substantial decrease in the flight time, and a significant increase in lethality (single shot kill probability) as compared to KE tank gun projectiles and currently fielded antitank missiles which destroy targets with chemical energy, shaped charge warheads. The decrease in flight time improves greatly the missile and launch platform survivability. Lethality increases and reduced flight time enhance the combat loss exchange ratio and increases the number of stowed kills per sortie or combat vehicle munitions load.

The LOSAT missile delivers almost an order of magnitude more total kinetic energy to the tank target than gun fired kinetic energy penetrators resulting in catastrophic structural kills. Such assured lethality is of great interest to the U.S. Army Infantry and Armor Schools, which are responsible for materiel requirements.

LOSAT's major drawback is its weight and length which makes it difficult to stow a large number of missiles within the armored vehicle. The goal of a future hypervelocity weapon is to achieve a missile with about one-half the weight and 0.7 the length of LOSAT while delivering essentially the same penetrator kinetic energy on target. Achieving this goal requires a well integrated system approach which assures the proper focus and complementary efforts from all the supporting technological areas. Coordinated advances are needed in the disciplines of warheads, propulsion, structures, guidance, controls, autopilot, instruments, simulation and aerodynamics. The challenges for each discipline are addressed briefly, herein.

3.2 Penetrator Lethality. The primary lethality challenge is to demonstrate the perforation of advanced tank armor, such as composite steel/ceramic armor covered with increasingly sophisticated explosive and non-explosive reactive armor, by kinetic energy penetrators in the weight class (3 - 5 kilograms) commonly delivered by gun launched munitions. An additional challenge is to establish or prove the lethality of a range of reasonable size Kinetic Energy Penetrators (4.0 to 9.1 kilograms) traveling at 1500 - 2500 meters per second. Warhead technologists are confident that ample latitude exists to develop an effective warhead/penetrator in the range of 3 - 5 kilograms when the impact velocity is greater than 2000 meters per second. The trade between penetrator

weight and impact velocity has a profound effect on the total missile weight as these are the primary variables influencing the design of the propulsion sub-system.

3.3 Propulsion. Solution of several propulsion technical challenges are crucial to the development of future operational hypervelocity missiles which would represent significant advances over the current state-of-the-art. Although the coupling between the guidance system wavelength and propellant smoke characteristics is discussed later in the guidance section of this paper, it suffices to say that the use of line-of-sight optical guidance techniques, used in current short range antitank missiles and fire control, requires the use of minimum smoke propellants. Crew and vehicle survivability drive a desire for non-detonable propellants (defined simply for the purposes of this paper a 0 card gap propellant) which should enable missile systems to have significantly improved results in insensitive munitions test requirements. Small takeoff weights and volume drive the need for high specific impulse and energy density, while maximizing the propellant weight fraction (PWF), by use of high strength to density ratio composite motor cases. Very short burn times and high mass flow rates are required in order to compete with the minimum range of tank launched kinetic energy penetrators and to decrease velocity loss due to drag. Hypervelocity missile solid rocket propulsion research and development has focused on simultaneously achieving four goals which are widely perceived to be mutually conflicting. The four goals are:

- 1) high specific impulse (>250)
- 2) very high burn rate propellants (~75mm/second)
- 3) non-detonable propellants
- 4) minimum smoke propellants

3.4 Structures. The challenge to provide increased kinetic energy lethality against advanced tank armors, at minimum and extended ranges, requires a high performance propulsion unit and a control system capable of surviving the hypervelocity boost and coast phases. Filament wound carbon reinforced composite motor cases using high strength to density ratio fibers and high performance propellant technology provide the baseline for achieving the desired MACH 6 velocity with a burn time of 0.35 seconds. Remarkable advances have been made in the use of carbon reinforced materials in filament wound or braided motor cases. Propellant Weight Fractions (PWF) in excess of 80 percent have been demonstrated in a motor which provides 12,500 pounds of thrust for 0.4 seconds. Even greater PWF designs appear to be feasible for these high pressure rocket motors. A major

challenge is to increase the maximum temperature of the cured resin materials from the neighborhood of 375 degree Fahrenheit to the neighborhood of that of steel (~750 degrees Fahrenheit). Success would significantly reduce the amount of thermal protection material required for the centerbody case.

The composite motor PWF is enhanced by using lightweight composite nozzles and/or nozzle inserts.

Development of composite nozzle materials capable of surviving the severe heating environment generated by the large mass fluxes of high performance rocket motors is required to achieve high PWF motors. Since concepts for propulsion include clustered motors and an annular motor configuration, the nozzle throat areas must maintain a uniform cross section to minimize thrust misalignment. This requires that nozzle(s) materials erode consistently or, the problem can be minimized if the materials do not erode. However, a majority of lightweight, low cost composite materials will experience some degree of erosion or ablation. The challenge is to minimize the erosion and establish repeatable performance.

The challenge of developing lightweight control fins focuses on development of metal matrix, refractory, or composite materials. One approach for boost phase control is to use small lightweight thrust vectoring control fins in the boost motor plume/exhaust, while the coast phase uses the same fins with aerodynamic control. The control fins must be lightweight, withstand initial shock at booster ignition, and survive the high temperature and high velocity environment for the 0.35 second boost phase environment, as well as the duration of up to 10 kilometer range flight. Minimum fin material ablation and erosion is essential to maintain fin stability for adequate control throughout the boost to coast phase. The weight of less than 450 grams (total) for the control fins is required to minimize the system weight and to maintain a favorable center of gravity for aerodynamic stability, both during boost and coast after the booster is expended or has been discarded. Mass loss and shape change must be minimized, as in the challenge for developing the composite nozzles.

3.5 Thermal Protection Materials. Experience has shown that silica-phenolic is a reasonable material to consider for the total range of hypervelocity missile conditions. Other materials (ex. rubber-modified-silica-phenolic) may perform better thermally over a portion of the flights or for only a portion of the configuration, but it will require a more detailed investigation (along with more

specific trajectories and design configurations). Protecting a missile traveling at velocities up to 3000 meters per second is definitely feasible, but major issues are the weight and drag penalties associated with the protection material.

3.6 Guidance and Control. The demonstrated guidance method, used in hypervelocity missiles which attack surface targets, has been "modified automatic command to line of sight (ACLOS)" using optical guidance methods in both the short and long infrared wavelengths. This is the desired operational capability so that the operator is not required to acquire or track the target, and so that multiple missiles can be launched simultaneously, or nearly simultaneously, against an array of targets. Command guidance concepts are negatively impacted by higher velocities for hypervelocity missiles in that the higher velocity requirements, for the same burnout range of the booster motor, will produce a greater volume of smoke from the rocket motor propellant. This will aggravate two problems, target/missile tracking, and communication with the missile. The higher velocities will also cause a higher thermal signature to be generated as the missile heats the surrounding air. For differential guidance, the addition of this heated air to the motor plume will increase the error in the estimation of the missile position relative to the target. The target signature in the tracking device, usually a Forward Looking Infrared (FLIR) sensor, could also be obscured in this plume. Both effects cause the missile accuracy to be degraded, and lower lethality for the system would be predicted. For beamrider concepts which depend on accurate target tracking by the FLIR, an obscured target means a guidance failure. The accuracy and ability to cost effectively field an optical CLOS system for hypersonic missiles has been proven (ADATS/LOS-F-H). The ADATS/LOS-F-H missile system required a minimum smoke motor which uses a detonable propellant. The LOSAT advanced development program demonstrated the accuracy of long wavelength optical CLOS guidance concept when combined with a minimum smoke motor which contains a detonable propellant.

3.7 Control Actuator Systems. The higher velocities of hypervelocity missiles increase the required bandwidth and control force for control mechanisms. Since aerodynamic force is abundantly available at hypervelocity missile velocities at low altitudes, the control issue is centered at low velocities while the missile is accelerating. As with the terminal homing sensors aperture situation, the control systems must be extremely small to achieve low drag configurations of tactical hypervelocity missiles. Designers are driven to maximize the control force per pound and per cubic inch of volume. To date, this has led to

the choice of discrete thrusters as the control mechanism in several hypervelocity missile programs. Discrete thrusters limit the maneuver capability of the missile since only a finite number of control commands can be given. The use of discrete thrusters to intercept targets that are rapidly maneuvering, such as high-speed aircraft, is likely to be unsatisfactory as compared to the performance available from continuous aerodynamic control. Continuous control actuators suffer from a lack of bandwidth and control force per pound/unit of volume of actuator when compared to discrete thrusters, however. Continuous control via fluidic systems has not been actively pursued and may prove to be a viable hybrid control system. The control actuator technical challenge is to provide continuous control actuation systems that possess equal, or better, bandwidth/phase characteristics and packaging efficiency as compared to current discrete thruster systems.

3.8 Auto-pilot/Navigation Law Design and Implementation. Small, tactical hypervelocity missiles have used CLOS guidance systems which do not use an onboard missile auto-pilot. These systems tend to suffer degraded accuracy when engaging short range targets (<500 - 800 meters). They suffer also from a lack of flexibility regarding the relationship of the missile trajectory relative to the line-of-sight to the target. Adding an auto-pilot and the necessary instruments (angular rate and/or acceleration) is a potential means to improve the short range accuracy as well as to meet the requirement to deliver the missile on target with an angle of attack of less than 1 degree. The small angle of attack limitation is needed if the target is a tank and the lethal mechanism is a long rod kinetic energy penetrator.

A major technical challenge for auto-pilot design is the development of suitable algorithms and integration of electronic instruments, digital hardware and software to execute the algorithms at a rate compatible with the bandwidth and packaging requirements of the missile.

3.9 Aerodynamics and Aeroelasticity.

Computation Fluid Dynamics. Many improvements have been made in predictive CFD codes, but the uncertainty associated with the estimates requires that significant wind tunnel experimental programs be undertaken to determine aerodynamic characteristics prior to missile flight. The uncertainty also leads to a selection of airframe shapes that are considered to be low risk because the airframe is similar to what has been done in the past. The desire to guide during boost adds the uncertainty of how the motor plume interacts with

the airframe aerodynamics. The interaction of either aerodynamic control surfaces, discrete thrusters, fluidic control mechanisms with the airframe aerodynamics is a high risk in all hypervelocity missile programs.

The first technical challenge is to provide better predictive CFD codes which can be used to lower the cost of hypervelocity missile programs by directly decreasing the need for extensive wind tunnel tests. Also risks are reduced that are associated with the interaction of control mechanisms with the free-stream or motor exhaust gases in thrust vector controlled missiles. The next technical challenge is to provide estimates of the radiation attenuation and scattering of the CLOS guidance beam by the motor plume aerodynamic wake. The third challenge is to provide codes which accurately estimate the complex flow fields which exist during booster separation

Booster Separation. The capability to cleanly separate the boosters from tactical hypervelocity missiles has yet to be demonstrated and is therefore a major technical risk. Strap-on boosters are routinely separated in space launch applications such as the Space Shuttle or satellite launch vehicles such as Delta. The lack of a CFD estimate of the aerodynamic behavior of either the multiple strap-on booster concept or the single annular motor, either still burning or expended, is a significant disadvantage since separation alternatives are based solely upon intuition and prior experience. Techniques discussed to date include passive fly away since the drag is higher on the boosters, a clam shell configuration where the boosters essentially peel away from the center body, a small amount of propulsion on the center body to forcibly separate the bodies, and explosive devices to strip the boosters from the center body.

Aerodynamic Stability. Current aerodynamic design tools do not adequately predict rocket motor plume effects on airframe stability and control. Also, the thrusters disturb the aerodynamic flow around the front of the missile and add to uncertainties in the predicted aerodynamic characteristics. Conducting meaningful wind tunnel tests which simulate the aerodynamic effects of hot plumes is not feasible either for cost or technical considerations. The technical challenge is either to develop a relatively low cost, hot plume wind tunnel capability or to estimate the effects with confidence via CFD.

3.10 System Simulation. Comprehensive digital and hardware in the loop simulations of hypervelocity missile systems are required. The demands for fidelity of these simulations continue to increase as demands for reduced product development time and cost escalate. Fidelity is

limited by the state of scientific and engineering knowledge and the capability of modern computer/simulation tool hardware and software. The technical challenges facing the CFD analysis of hypervelocity missiles is a subset of this technical area.

The nature of hypervelocity missile flight demands that digital simulations include the actual software used in any component in order to study the detailed timing interactions present at the system level. The same timing interactions drive the use of detailed component simulations for all missile flight components such as the control actuation system and inertial measurement unit. Often this forces component designers to use high order differential and integral equations to model the physical behavior of these components. The validation of these models is critical. The technical challenges for digital simulations of hypervelocity missiles is the rapid development of mathematical models and conversion of these models into software that accurately models the performance of the system components and the interaction of the components. The interaction is particularly critical and the "goodness" of the model depends on the accuracy of event timing.

Hardware-in-the-Loop (HWIL) simulations and hybrid HWIL and digital simulations are required to reduce the risk of failure in flight tests. The major technical challenge is to provide rate tables and control software that replicates the expected flight environment. This generally requires a real time control and data gathering. The major technical challenges are the development of very high angular rate tables, accurate target and clutter signature simulation in both digital and HWIL simulations, and real time simulation control, data acquisition and near real time automated data review and reduction.

3.11 Summary. The technical issues and challenges discussed in this case study are difficult to solve and are on the cutting edge of missile technology. The solution of these technical challenges should be accomplished in a missile system context. This should be done even if the entire missile system will never be flown and will only be used to investigate the interaction of the components in a virtual prototype. The tradeoff between hypervelocity missile component performance and missile system performance and cost requirements is perhaps the greatest technical challenge of all. The pursuit of component performance, without the focus of system constraints, can be very unproductive.

4.0 FUTURE MISSILES AERODYNAMIC CHALLENGES.

The future missile systems reviewed herein reveal a broad range of airframe configurations and flight environmental conditions that challenge the aerodynamics community. Although the generic nature of the problems are not new, their solutions stretch the current analytical and testing capabilities of the aerodynamic community. Evidence of the long standing nature of these issues is given by the 1979 AIAA Wright Brothers Lectureship in Aeronautics titled "Missile Aerodynamics-Past, Present , Future" presented by Dr. Jack Nielsen , which addressed a number of these problems. Before proceeding further it is appropriate to recall a statement by Dr. Nielsen in his 1979 lecture.

"Let us turn now to the prediction of future developments in missile aerodynamics. This is a task which is simultaneously appealing and daunting; the former, because one is not constrained by facts, and the latter because of the ever present danger of misprognostication with its subsequent effects upon future reader of this paper. Indeed, with future developments in energy and laser weapons, these readers may be few and confined to archivists of technology".

This author has similar concerns, however, I do not believe that laser and other high energy weapons will displace completely missiles in the near future and that there will be a continuing need in the future for significant advancements in aerodynamic analysis tools and testing facilities. With these thoughts in mind, let us project some of the anticipated aerodynamic technology advancements needed to meet the performance goals of certain classes of future missile systems.

Improved Lift-to-Drag Ratio and Low Trim Drag Airframes. Higher lift-to-drag ratio performance can lead to significant reductions in size and weight for missiles such as LONGFOG, the powered submunition, LOCAAS, extended range ATACMS and the Navy's hypersonic airbreathing HiSSS. Fuel weight required to sustain velocity during the long post-boost flight is directly related to the drag at trim flight conditions. Also, high lift-to-drag ratio is important for missiles that must perform target search after launch. The fact that most missiles are launched from confined areas such as canisters or tubes limit the size and shape of lifting surfaces that are required for highly efficient aerodynamics characteristics such as that achievable by aircraft. The aerodynamics community must become even more multi-disciplinary in their analysis and design efforts to apply the characteristics of adaptive structures, Micro-Electro-Mechanical Systems

(MEMS), and related evolving technologies to improving missile aerodynamic performance.

High Angle-of-Attack Aerodynamics. High angle of attack (high alpha) aerodynamics for missiles has been a concern since the inception of guided missiles and continues to be a paramount design problem as the range of angle-of attack and angular rates continue to grow. Missile concepts, typified by the air-to-air Dual Range Missile, the hypervelocity anti-armor CKEM and vertical launched all aspect air defense missiles (MEADS), may encounter angles-of-attack in the vicinity of 90 degrees and angular rates exceeding 10 radians per second shortly after launch to increase their off axis target engagement zone. Maneuvers of this magnitude are becoming more feasible with the development of small, efficient attitude (reaction jet) control systems. The problems are compounded when the airframe has wings an/or tail fins and additional aerodynamic controls (typical PAC-3 airframe). Contemporary aerodynamic design tools are of little help in accurately predicting aerodynamics characteristics at this range of angles-of-attack even at subsonic speeds and employing computational fluid dynamic (CFD) codes. One encounters all of the difficult and poorly understood flow phenomena including boundary layer transition, separated flows, vortex shedding and highly transient flow conditions. Wind tunnel tests can provide insight into the associated design problems, but great care and attention must be given to the facility characteristics, test article support mechanism and measurement systems. Successful development of missiles which encounter very high angles-of-attack and rapid angular rates requires continued efforts to improve both aerodynamic analytical tools and testing techniques.

Emerging CFD codes show promise of eventually handling these conditions and should be encouraged and supported. High strength structural materials offer the possibility of reducing the size of model support systems thereby minimizing interference effects in conducting high alpha wind tunnel tests. Recent advances in highly miniaturized instrumentation gives hope that detailed surface and flow field measurements can be conducted with minimum intrusion of the basic flow field.

Canard Control Aerodynamics. The use of canard controls appears to have its greatest utility for adding guidance and control to existing bombs, rockets and sub-munitions. Future concepts and systems that favor canard controls are the small, low cost guided air-to-surface missile, guided MLRS, the hypervelocity anti-armor missile (CKEM) and the 2.75" Guided Rocket programs. The significant aerodynamic concerns are the

continuing difficulty in assessing the canard vortex and wake interference effects on downstream missile components such as stabilizing tail fins. This interaction is exacerbated if the canards are mounted on the nose section where the local diameter is less than the maximum. Proper application of emerging CFD techniques are expected to predict these interactions at moderate angles-of-attack and control deflections and at speeds below hypersonic. Advancements in methodology are needed for expanded performance boundaries.

Adaptive Airframes. Missiles, which have multiple mission functions, such as LONGFOG and LOCAAS, gain significant performance advantages from an adaptive airframe, which alters its configuration to meet the specific requirements of each flight phase. A number of future missile concepts utilize a flight profile that includes a target search and identification mode.

Airframe shape changes are normally made to maximize flight performance. Currently, this involves deploying planar wings to increase lift for lower speed flight. Also grid fins/wings are commanding considerable attention because of their high lift with a constrained span, simplicity of deployment, and their ease of folding into the basic airframe. Future systems demanding smaller and lighter characteristics will require more innovative approaches that can develop high lift at lower drag through creation of dynamic flow fields by adaptive compliant structures.

High Supersonic Sub-munitions Dispense/Stage Separation. Future missile systems are increasingly dependent on the dispersal of smart munitions for precision target accuracy. These higher performance systems will necessarily be more interested in higher speed sub-munitions dispensing than is currently being developed. It is vital to dispense these sub-munitions in a manner that assures their survival and successful operation in attacking their targets. Both axial and lateral dispensing approaches are of interest; since both have their merits depending on specific system requirements and the flow environment at the time of dispense. Dispensing at higher supersonic speeds will amplify the importance of understanding the aerodynamic interaction between individual sub-munitions as well as the interaction between sub-munitions and the carrier missile. The transient interaction forces and moments will become critical to safe and accurate dispense operation. Similar interactive flow fields and induced aerodynamic forces occur during separation of missile stages. Improved analytical tools and test facilities addressing the multi-body interaction flow fields

should suffice for the proper design of both dispensing and separation systems.

A CFD design tool is currently being developed to determine these interactive flow field and resulting aerodynamic forces. This methodology has a flow field grid(s) that moves with the missile carrier/sub-missile. It contains also a parallel architecture to follow multiple sub-munitions. The solution algorithm is time accurate and utilizes advanced turbulence models to account for viscous effects.

Interaction of Multiple Flow Fields. The trend toward hypervelocity and higher maneuverability missiles expands the potential use of divert and attitude control systems (DACS) in the future. The strong interaction of the DACS reaction plume with the external flow about the airframe requires a much better understanding of this area to design and incorporate properly DAC systems. To this end, the U.S. Army has instituted a major technology program to design, analyze and test solid propellant DACS for future hypersonic interceptors. The technology challenges in this area include:

- Occurrence and level of afterburning in the vicinity of the control jet
- Effects of afterburning in the control jet on the separated flow region
- Extent of the separated flow region around the control jet
- Aero-optic effects of the control jet and interaction flow field
- Two phase flow effects

Major advancements in this technology area require substantial advances in CFD code capability as well as the continuing development of a test facility such as the LENS/AOEC that can test full-scale hardware and duplicate the flight environment of full-scale interceptors.

Aerodynamic Prediction Tools for Preliminary Design. Greater emphasis on packaging density, stealth and aerodynamic efficiency requirements will lead to a departure from the contemporary trend of axi-symmetric missile airframes. Also, a growing number of hypersonic missile concepts impose the need to have preliminary design aerodynamic prediction tools that include prediction capability for non-circular body shapes, Mach numbers to 15, a broader range of airbreathing inlets and initial consideration of aerodynamic heating effects. Prediction codes such as the Air Force's Missile Datcom and the Navy's aeroprediction code AP-97, can serve as starting points for upgrading.

5.0 CONCLUSIONS.

The rapidly emerging technology gains in all missile related areas offer the opportunity to significantly improve performance of existing missile systems. Concurrently, the technology gains are being integrated into demonstration programs that will help validate the great expectations of the new missile concepts. This paper describes briefly a number of these programs being pursued in the United States.

ACKNOWLEDGEMENTS

The author wishes to acknowledge the invaluable efforts of the following principle contributors to this paper: Raymond A. Deep, George A. Snyder, and Mark Miller.

Considérations sur l'aérodynamique pour le pilotage et le guidage des engins tactiques

Jean-Philippe Harcaut, Eric Larcher, Jean-Paul Bonnet, Stéphane Dupont

AEROSPATIALE MISSILES

B.P. 84

2, rue Béranger

92323 CHATILLON CEDEX

1. SOMMAIRE

Cet article passe en revue les relations qui existent entre le pilotage-guidage et l'aérodynamique externe d'une cellule, depuis la phase de conception préliminaire jusqu'à la réalisation de la simulation de vol.

Les différents points abordés sont les suivants :

- définition d'une configuration aérodynamique,
- modèle aérodynamique de simulation numérique,
- facteurs aérodynamiques prépondérants pour le pilotage et le guidage.

2. DÉFINITION D'UNE CONFIGURATION AÉRODYNAMIQUE

La configuration aérodynamique d'un engin tactique est définie pour répondre à une spécification militaire (contraintes d'empont, cibles...).

La charge militaire et la classe de distance de passage recherchée se déduisent de l'analyse des caractéristiques des types de cibles pris en compte par le système considéré.

Un missile guidé est un système asservi à plusieurs niveaux. La capacité d'atteindre le but dépend d'une part des senseurs mesurant les paramètres relatifs à la cible, et d'autre part des lois de guidage-pilotage. La détermination des forces et couples qu'il faut exercer sur l'engin s'en déduit, ce qui permet de définir les besoins en propulsion et les caractéristiques aérodynamiques.

La définition d'une formule aérodynamique pour un engin tactique est donc un processus itératif complexe faisant intervenir différentes techniques de base : les structures, la propulsion, l'aérodynamique, le pilotage-guidage, les charges militaires.

Trois exemples présentés ci-après illustrent le fait que les contraintes "système" sont déterminantes dans le choix d'une formule aérodynamique.

D'autres exemples seraient à citer : hypervélocité pour antichar-antihélicoptère (contrainte de temps de réaction, portée), formule canard pour un armement air-sol modulaire bas coût (contraintes d'intégration)...

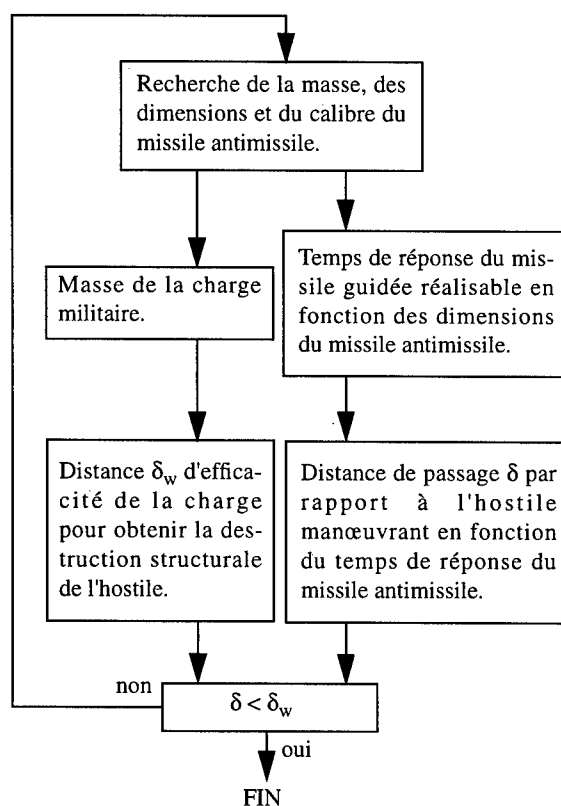
2.1. Exemple 1 : missile Sol-Air ASTER (antimissile)

- Nécessité de réduire le temps de réponse des missiles défenseurs

L'étude de conception du missile intercepteur capable d'obtenir la destruction structurale d'hostiles très performants (évoluant à une vitesse élevée et capables d'effectuer des manœuvres à fort facteur de charge) en environnement brouillé et attaques saturan-

tes consiste à mettre en œuvre la démarche présentée sur la figure suivante.

figure 1 : démarche de conception missile



- Limites du pilotage aérodynamique classique

Compte tenu des performances des assaillants prévisibles pour les décennies à venir, la démarche de conception itérative qui vient d'être décrite fait apparaître qu'il n'existe pas de solution cohérente de missile sol-air à pilotage purement aérodynamique permettant de répondre au problème posé.

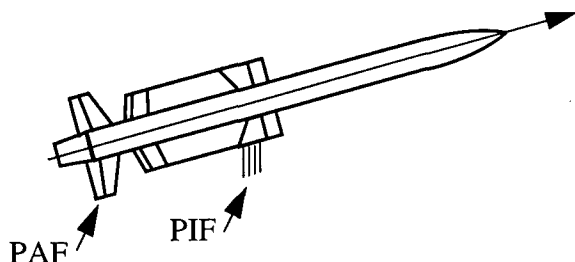
Un pilotage aérodynamique apparaît limité d'une part en temps de réponse, et d'autre part en capacité de manœuvrabilité à haute altitude. La limitation du temps de réponse est liée au temps nécessaire pour générer du facteur de charge par l'intermédiaire de gouvernes aérodynamiques : le braquage des gouvernes doit en effet d'abord créer un couple imprimant un mouvement angulaire à l'engin, qui engendre la prise d'incidence fournissant la portance aérodynamique permettant enfin de réaliser la manœuvre. La limitation en capacité de manœuvre à haute altitude est elle due à la faible pression dynamique.

- Solution du pilotage mixte PIF-PAF

Un pilotage propulsif en force permet de ne plus subir ces deux limitations : rapidité d'exécution et capacité de manœuvre à haute altitude sont en effet caractéristiques d'un tel dispositif de pilotage. Mais par contre, un pilotage propulsif ne peut être envisagé seul pour des durées de vol importantes compte tenu de contraintes d'encombrement.

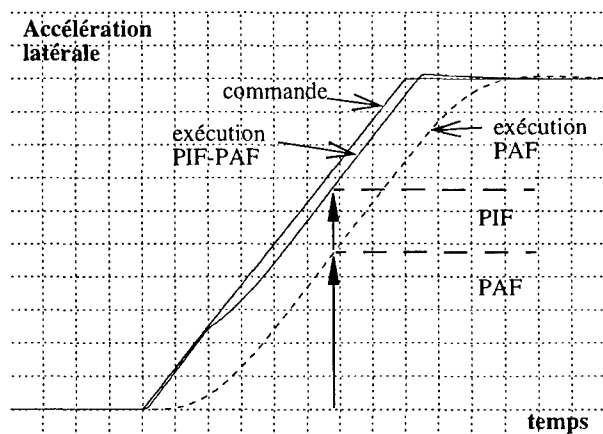
La solution retenue, présentée figure 2, est celle du pilotage mixte PIF-PAF en fin de vol (PIF, pilotage en force, associé au PAF, pilotage aérodynamique fort). Elle permet de profiter au mieux des propriétés de chacun des deux modes de pilotage.

figure 2 : pilotage mixte PIF-PAF



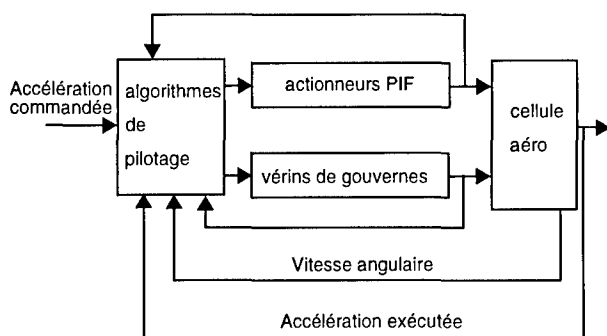
Pour illustrer l'avantage de retenir une telle solution, la figure 3 fournit une courbe correspondant à un exemple de réponse à une commande d'accélération pour un pilotage mixte PIF-PAF : le retard d'exécution de la commande du pilotage aérodynamique est compensé par le PIF.

figure 3 : réponse du pilotage mixte PIF-PAF à une commande d'accélération latérale



L'autopilote mixte mis en œuvre correspond alors à un asservissement à plusieurs actionneurs, schématisé par la figure 4 ci-après.

figure 4 : schéma de principe de l'autopilote PIF-PAF



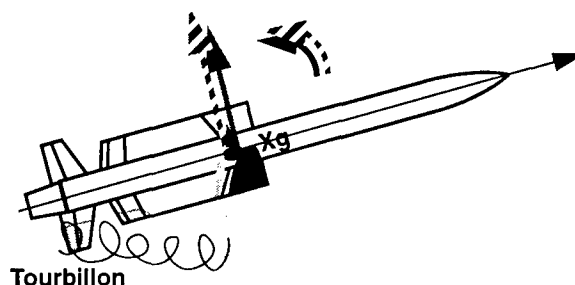
La cellule et la disposition des tuyères PIF sont optimisées afin d'assurer :

- un rendement en force,

$$K = \frac{\text{Force propulsive} + \text{Force d'interaction}}{\text{Force propulsive}}$$
 voisin de un, voire supérieur à un,
- des couples d'interactions transverses et de roulis compatibles avec une pilotabilité suffisante du missile.

L'effet du jet sur l'aérodynamique du missile est schématisé sur la figure 5 dans le cas où le rendement en force est supérieur à un. Y figurent les zones où l'influence aérodynamique du jet est porteuse et celles où l'influence est déportuse.

figure 5 : effet du jet sur l'aérodynamique de la cellule



Tourbillon

- zone où l'influence aérodynamique du jet est porteuse
- zone où l'influence aérodynamique du jet est déportuse
- effort ou couple propulsif
- effort ou couple total
- effort ou couple aérodynamique induit par l'effet du jet

2.2. Exemple 2 : missiles de croisière

Dans le cas d'un missile de croisière, l'analyse du besoin en pénétration fait ressortir deux types de solution.

2.2.1. Missile subsonique furtif EPF

Pour assurer la pénétration, on cherche ici à ramener la Surface Equivalente Radar (SER) et la Signature InfraRouge (SIR) à un niveau suffisamment faible pour que le missile ne soit pas détecté, ou en tout cas trop tard pour pouvoir être engagé par les défenses sol-air.

Les contraintes opérationnelles imposées à un tel missile sont alors

- une très faible SER/SIR,
- une précision « chirurgicale »,
- une portée de plusieurs centaines de kilomètres.

La conjugaison des contraintes de portée et de SIR oriente le choix de la propulsion vers une solution à base de turboréacteur ; la forme de l'entrée d'air est optimisée pour ne pas pénaliser la SER du missile.

Par ailleurs, la « furtivisation » de la cellule conduit

- d'une part à réduire la dimension des surfaces portantes, donc à une cellule instable,
- d'autre part, à privilégier des formes de type « lenticulaire », très dissymétriques et présentant ainsi de forts niveaux de roulis induit (cf. § 4.2.3).

- Limite des lois classiques de pilotage

Les niveaux de roulis induit rencontrés s'avèrent incompatibles des structures classiques de pilotage (cf. § 4.2.2), le couplage induit conduisant à une déstabilisation de l'autopilote.

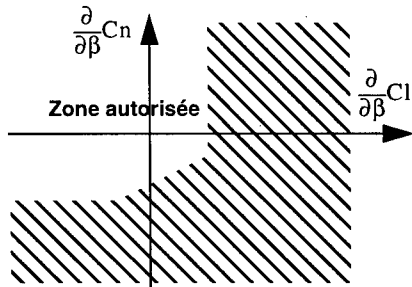
Pour s'affranchir de ce phénomène, des lois de pilotage dites «multivariables» ont été mises au point (cf. § 4.4), qui permettent la prise en compte explicite du roulis induit lors de la conception de l'autopilote.

Ceci permet de déterminer un pilotage «optimal», qui minimise l'impact du roulis induit sur les performances de la cellule pilotée.

- Domaine aérodynamique pilotable

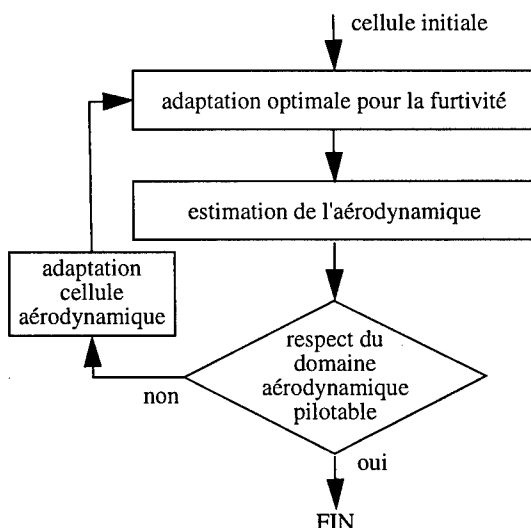
Afin de faire converger la boucle de conception système, on commence par définir le «domaine aérodynamique pilotable». Il s'agit ici de définir les limites acceptables en terme d'instabilité et de roulis induit, qui garantissent que l'on saura piloter la cellule. Pour un missile piloté type avion, on aboutit à une spécification aérodynamique du type de celle de la figure 6, ci-dessous.

figure 6 : spécification pour une cellule pilotée type avion



La boucle de conception système est alors celle présentée ci-après, figure 7.

figure 7 : boucle de conception système



2.2.2. Missile supersonique ANF

La pénétration est ici obtenue par la combinaison

- d'une vitesse élevée, minimisant le nombre d'engagements possibles par les défenses sol-air,
- de la capacité à réaliser des manœuvres alternées à fort facteur de charge, générant des distances de passage importantes vis-à-vis des missiles antiaériens adverses.

Les contraintes opérationnelles sont donc :

- un nombre de Mach élevé en vol (Mach supérieur à deux),
- une portée de plusieurs centaines de kilomètres,
- un facteur de charge transversal élevé,
- un vol en sea-skimming.

La conjugaison des contraintes de portée et de Mach imposent le choix d'un statoréacteur.

La cellule est optimisée pour réduire les couplages de type roulis induit, afin de pouvoir combiner les manœuvres de pénétration et le vol en sea-skimming.

Le choix aérodynamique le plus simple est alors une cellule cruciforme. Une cellule plus complexe, à deux plans de symétrie, est cependant possible si l'on utilise un pilote multivariable, celui-ci permettant de minimiser la perte d'altitude lors de la phase de pénétration.

2.3. Exemple 3 : missile antichar ERYX

Le besoin d'efficacité face au char moderne fait apparaître la nécessité :

- d'emporter une charge militaire importante,
- de tirer en espace confiné pour se protéger,
- de disposer d'une manœuvrabilité suffisante pour suivre des cibles défilant rapidement.

Ces contraintes impliquent de disposer dès le début du vol d'un facteur de charge transversal important (masse de charge élevée, fort défilement des cibles), tout en acceptant un départ à basse vitesse (tir en confinement). Ceci oriente donc naturellement vers un concept piloté en force.

D'autre part, la recherche d'une conception «bas coût», donc de formules aérodynamiques et propulsives simples, conduit à adopter une distribution spatiale du facteur de charge en autorotation, à l'aide d'intercepteurs de jet bi-statiques disposés dans un seul plan.

3. MODÈLE AÉRODYNAMIQUE DE SIMULATION NUMÉRIQUE

Le modèle aérodynamique de simulation numérique est un modèle fin qui doit rendre compte de différents phénomènes, caractéristiques du comportement de la cellule étudiée.

3.1. Coefficients aérodynamiques

Le modèle aérodynamique est l'outil (code numérique) qui calcule les coefficients aérodynamiques, puis les forces et moments aérodynamiques, pour tous les points du domaine de vol.

Les efforts aérodynamiques sont fonction du nombre de Mach M , de l'altitude H , du centrage, de l'incidence totale α_T et du roulis aérodynamique ϕ_A (ou des angles d'incidence α et de dérapage β), du vecteur rotation instantanée (dont les composantes sont notées p , q , r en axes liés), des braquages de gouvernes équivalents en roulis, tangage et lacet ξ , η et ζ , et de la présence ou non de jets latéraux.

Le modèle est bâti à partir de calculs et d'essais en soufflerie ; il est recalé par les essais en vol.

Il comprend le modèle nominal de la cellule et les dispersions pouvant être attendues et devant être prises en compte. Ces dispersions peuvent être modélisées par exemple par une loi gaussienne ou par une loi de dispersion uniforme sur un intervalle donné. Des tirages aléatoires sont alors effectués avant chaque simulation afin de prendre en compte cette méconnaissance sur la valeur numérique des coefficients aérodynamiques.

Le modèle aérodynamique est utilisé pour les études de pilotage proprement dites, pour le choix et le dimensionnement des équipements, pour la simulation de développement et de performances du système d'arme.

3.2. Phases de séparation

Les phases de séparation induisent des phénomènes aérodynamiques spécifiques qu'il est nécessaire de modéliser, par exemple dans le cas d'un largage sous avion (aérodynamique du missile tenant compte des interactions avec l'avion).

3.3. Déformations

Différents types de problèmes peuvent nécessiter un modèle de répartition des efforts aérodynamiques.

- *déformations statiques* : pour des structures légères et à fort allongement L/D , le missile souple se déforme sous fort facteur de charge et les coefficients aérodynamiques peuvent être modifiés (perte de stabilité...),

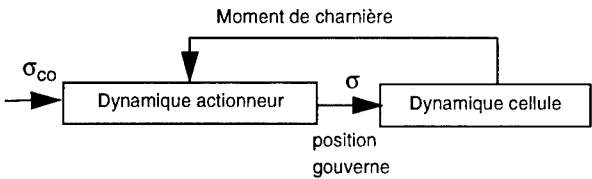
- *déformations dynamiques* : l'aéroélasticité concerne le couplage avec les modes de structure vus par les gyromètres et accéléromètres. Des traitements dans l'autopilote peuvent être nécessaires (filtrages adaptés...).

Dans le cas particulier d'un engin à deux étages, considéré comme constitué de deux parties rigides, avec une liaison souple, la mécanique du vol et l'aérodynamique peuvent être à représenter sur chacune des deux parties, notamment pour une première approche du composite souple et pour l'étude de la séparation des étages.

3.4. Efforts sur les gouvernes

Les moments de charnière sont dimensionnants pour la classe de vérin. Il faut en effet prendre en compte le niveau des couples à contrer, et leur gradient par rapport au braquage. Ceci est dimensionnant vis-à-vis de la puissance à fournir et de la bande passante du vérin. Le choix de l'axe de rotation de la gouverne doit être particulièrement optimisé.

figure 8 : moment de charnière



Les efforts d'encastrement doivent également être pris en compte lors du dimensionnement global des vérins et des gouvernes.

Notons que les moments de charnière sont particulièrement difficiles à prédire et ne sont généralement bien connus qu'après passage en soufflerie.

4. FACTEURS AÉRODYNAMIQUES PRÉPONDÉRANTS POUR LE GUIDAGE ET LE PILOTAGE

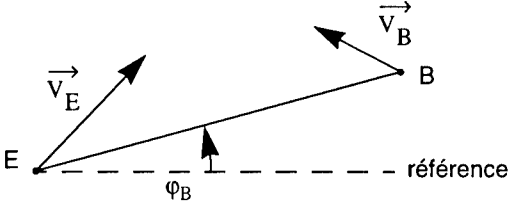
4.1. Besoins du guidage

4.1.1. La fonction guidage

Le guidage de la cellule consiste à maîtriser l'évolution de la trajectoire de l'engin. La loi de guidage permet de s'adapter aux caractéristiques cinématiques du but et ainsi de commander la

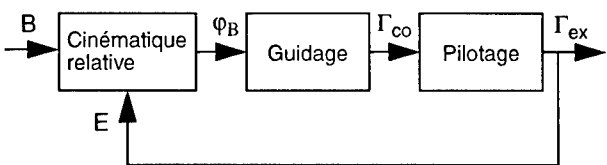
cinématique relative entre l'engin et le but en faisant tourner le vecteur vitesse de l'engin (cf. figure 9).

figure 9 : cinématique relative engin-but



Les ordres qui proviennent du guidage sont ensuite réalisés par le pilotage de la cellule qui a pour fonction de générer les accélérations transverses commandées tout en maîtrisant le comportement dynamique de la cellule autour de son centre de gravité.

figure 10 : boucle de guidage



Les performances de la loi de guidage dépendent en grande partie, de façon directe ou indirecte, des caractéristiques aérodynamiques de la cellule comme cela est rappelé dans le tableau suivant, figure 11.

figure 11 : besoins du guidage

Contraintes	Facteurs prépondérants
portée / vitesse	CX, CN
manœuvrabilité	CN, {Cm_alpha, Cm_eta} roulis induit configuration BTT/STT* pilotage en couple/en force
stabilité et temps de réponse	linéarité, marge statique Cm_eta, Cm_alpha, CN configuration BTT/STT pilotage en couple/en force
furtivité	forme
découplage ligne de visée	CN_alpha pilotage en couple/en force
rigidité	aéroélasticité
équipements	moments de charnière couples

* BTT : bank to turn ; STT : skid to turn.

4.1.2. Portée-vitesse

Les paramètres de portée, vitesse moyenne, vitesse finale, sont optimisés vis-à-vis du domaine d'action, du temps de réaction du système et de la létalité. Les facteurs primordiaux sont la motorisation (propulseur à poudre, turboréacteur, statoréacteur), la traînée de forme et la traînée induite (due à l'incidence totale nécessaire pour équilibrer la pesanteur ou pour réaliser le facteur de charge).

4.1.3. Manœuvrabilité

Le besoin en manœuvrabilité est multiple : mettre en forme la trajectoire, rattraper des dépointages, contrer la manœuvre du but et traiter les bruits de guidage.

Dans le cas d'un pilotage en couple, pour parvenir à développer un fort facteur de charge, il faut pouvoir équilibrer une incidence élevée (ce qui nécessite un faible rappel aérodynamique Cm_α , et une forte efficacité de gouverne aérodynamique ou propulsive Cm_η) et à incidence donnée, avoir une portance élevée (fort gradient de portance par rapport à l'incidence CN_α).

Outre l'autorité des gouvernes et les limitations dues aux saturations, la recherche des incidences élevées est limitée par les problèmes de pilotabilité de la cellule (effet des non linéarités et des couplages, et notamment du roulis induit).

Par ailleurs, rappelons également qu'un pilotage en force propulsif restera manœuvrant à haute altitude malgré la chute de la pression dynamique.

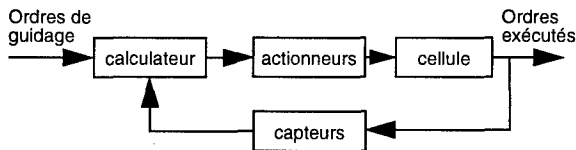
4.1.4. Temps de réponse

Le comportement naturel de la cellule pour réaliser les manœuvres de guidage peut dans certains cas être satisfaisant sans asservissement spécifique : c'est le cas pour des systèmes dont les domaines de fonctionnement sont limités et pour lesquels le bas coût est primordial (exemple : certains antichars téléguidés en alignement).

Dans les autres cas, un autopilote est défini pour exécuter les ordres de guidage avec une réponse rapide, bien amortie, et ceci dans un large domaine de fonctionnement, tout en réduisant les effets des perturbations.

Ceci conduit à la conception d'une chaîne de pilotage dont un schéma fonctionnel est présenté ci-dessous figure 12.

figure 12 : schéma fonctionnel d'une chaîne de pilotage



Dans le cas notamment où il y a un autoguidage terminal, la constante de temps de guidage est un paramètre primordial. Celle-ci se compose essentiellement de la somme de la constante de temps de la cellule pilotée et de celle nécessaire pour l'élaboration des informations relatives engin-but.

La mise en œuvre de lois de guidage optimales peut permettre de pallier en partie ce temps de réponse en le prenant en compte de façon explicite dans les équations du modèle de synthèse de la loi de guidage, mais les performances effectivement obtenues sont alors très sensibles à la détermination du temps restant avant l'interception. Elles sont donc beaucoup plus difficiles à mettre en œuvre en environnement brouillé.

Compte tenu de ces difficultés de mise en œuvre, il est clair que la meilleure façon de réduire la constante de temps de guidage, tout en étant robuste vis-à-vis des incertitudes, reste la minimisation de la constante de temps de la cellule pilotée.

L'autopilote est adapté à l'aérodynamique pour obtenir une cellule pilotée optimale compte tenu des dispersions attendues et des imperfections des équipements de pilotage. Les paramètres aérodynamiques influents (linéarité, efficacité, stabilité, portance...) seront précisés ci-après.

Notons que la configuration de pilotage est dimensionnante vis-à-vis du temps de réponse. Une configuration BTT peut être favorable par exemple pour diminuer la traînée ou pour faciliter l'intégration sous avion ; elle peut être également nécessaire pour limiter le dérapage (par exemple vis-à-vis du fonctionnement d'un statoréacteur) ; mais elle est défavorable vis-à-vis du temps de réponse effectif de pilotage : il faut incliner l'engin en roulis avant de pouvoir réaliser la manœuvre.

Notons également que le pilotage en force est aussi par nature plus rapide que le pilotage en couple. Il permet en effet de générer directement l'accélération transversale demandée par l'élaborateur d'ordres de guidage, sans avoir à attendre la prise d'incidence.

De plus à haute altitude, le pilotage en couple sera encore ralenti par l'accroissement de la constante de temps de mise en virage induite par la chute de la pression dynamique. L'effet est encore aggravé si les gouvernes sont purement aérodynamiques (i.e. ne sont pas des gouvernes de jets), l'efficacité chutant avec l'altitude. Dans ce dernier cas, pour maintenir un certain niveau de performances, les gains de pilotage seront plus forts : les vérins de gouvernes devront alors être capables de générer des vitesses de braquage élevées.

4.2. Missiles conventionnels

4.2.1. Modèle aérodynamique pour la synthèse des lois de guidage-pilotage

La mise au point de la chaîne de guidage-pilotage utilise en fait deux modèles aérodynamiques du missile :

- un modèle fin, élaboré à partir d'essais en soufflerie, et recalé par les essais en vol, qui correspond au modèle aérodynamique de simulation numérique présenté précédemment,
- un modèle simplifié, défini «grossièrement» en phase d'avant-projet, puis déduit du modèle précédent dès que celui-ci est disponible.

La simplicité du second modèle (principalement sa linéarité) permet d'utiliser les méthodes des asservissements linéaires. On peut alors établir des allocations de performances et régler les lois de guidage et de pilotage (on règle alors plus particulièrement la stabilité de la boucle de guidage-pilotage et ses performances dynamiques).

Le modèle aérodynamique de simulation numérique est ensuite utilisé pour valider les travaux effectués à partir du modèle simplifié. Il permet de prendre en compte a posteriori les non linéarités du système pendant la phase de validation.

Le passage du modèle fin au modèle simplifié comporte de façon générale certaines difficultés :

- choix de points de linéarisation,
- linéarisation avec l'évaluation quantitative de tous les termes et la simplification de tous les termes négligeables (linéarisation plus difficile sur les missiles à jets latéraux, couplage entre la commande et l'incidence...).

4.2.2. Chaîne de tangage découplée

Les équations simplifiées régissant le mouvement d'une chaîne de tangage découplée sont les suivantes.

$$\begin{cases} I_Y \dot{q} = M(\alpha, \eta) + M_q q \\ -m \ddot{Z} = F(\alpha, \eta) \\ \dot{\alpha} = \frac{\ddot{Z}}{V} + q \end{cases}$$

Les équations de la dynamique des petits mouvement autour d'un point d'équilibre (α_0, η_0) , vérifiant, en négligeant q_0 ,

$$M(\alpha_0, \eta_0) = 0$$

$$F(\alpha_0, \eta_0) = m\Gamma_0$$

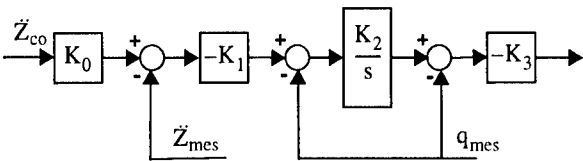
sont obtenues par un développement limité au premier ordre de l'expression du moment et de la force aérodynamiques fonctions de l'angle d'incidence et du braquage équivalent en tangage :

$$M(\alpha, \eta) = M(\alpha_0, \eta_0) + M_\alpha(\alpha_0, \eta_0)\Delta\alpha + M_\eta(\alpha_0, \eta_0)\Delta\eta$$

$$F(\alpha, \eta) = F(\alpha_0, \eta_0) + F_\alpha(\alpha_0, \eta_0)\Delta\alpha + F_\eta(\alpha_0, \eta_0)\Delta\eta$$

L'autopilote correspond alors à la mise en œuvre d'une loi permettant de braquer la gouverne en fonction des retours gyrométriques et accélérométriques mesurés par les capteurs. Un exemple d'autopilote est présenté ci-dessous figure 13.

figure 13 : exemple de chaîne de tangage d'un autopilote



Les retours ainsi constitués modifient alors les retours naturels en q et α de la cellule afin d'obtenir une fonction de transfert pilotée adéquate entre l'accélération transverse commandée et l'accélération effectivement exécutée. Les gains de pilotage (K_1, K_2, K_3) sont adaptés aux gradients aérodynamiques naturels, les valeurs fondamentales étant l'efficacité de gouverne Cm_η qui agit directement sous forme de coefficient multiplicateur sur les retours, le rappel aérodynamique Cm_α définissant la pulsation à piloter, le gradient de portance CN_α reliant l'incidence à l'accélération. Pour un pilotage en couple, CN_η doit être négligeable, la situation étant inverse pour un pilotage en force.

L'autopilote doit être robuste aux variations aérodynamiques, mais un domaine de dispersions trop vaste peut, soit rendre la cellule impilotable, soit nécessiter de dégrader de façon intolérable les performances de l'autopilote. Notons qu'un comportement linéaire de l'aérodynamique de la cellule est également un facteur favorable. La cellule doit être réglée pour trouver des compromis vis-à-vis de la manœuvrabilité et de la stabilité dans l'enveloppe du domaine de vol.

En tout état de cause, l'autopilote doit être réglé en connaissant la plage de variations des coefficients aérodynamiques pour chaque point du domaine de vol. Ceci est d'autant plus indispensable lorsque le comportement naturel de la cellule peut devenir instable : les gains adaptés pour de tels points de vol sont alors moins adaptés à des points de vol stables.

De façon qualitative, des gains de pilotage grands désensibilisent l'autopilote à la connaissance du rappel aérodynamique, mais on est limité par la bande passante des équipements qui empêche d'aller chercher une bande passante de pilotage trop grande. Notons que classiquement, c'est la bande passante de l'actionneur (vérin de gouverne) qui limite la bande passante de pilotage, la bande passante de l'actionneur pouvant elle même dépendre des efforts aérodynamiques.

Par ailleurs, les effets aéroélastiques et les filtrages associés qu'il est nécessaire de mettre en œuvre peuvent agir eux aussi directement sur la pilotabilité de l'engin.

Une conception intégrée, c'est-à-dire une optimisation simultanée et globale de la cellule et de son autopilote, est généralement nécessaire pour obtenir les performances recherchées. Notons que d'autres contraintes imposées pourront limiter les degrés de liberté : par exemple une certaine stabilité de la cellule pourra être exigée si celle-ci doit être larguée d'avion avec des contraintes spécifiques de sécurité.

4.2.3. Roulis induit

Le terme de roulis induit $L(\alpha_T, \phi_A)$ couple l'équation de moment du roulis avec les mouvements de la cellule en tangage et lacet.

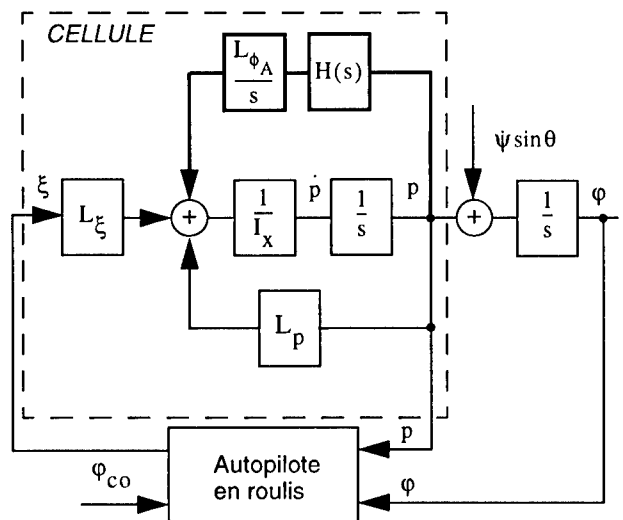
$$I_X \dot{p} = L_\xi \xi + L_p p + L(\alpha_T, \phi_A)$$

Pour les petits mouvements autour d'une position d'équilibre, le roulis induit se linéarise sous la forme :

$$dL = \frac{\partial L}{\partial \alpha_T} d\alpha_T + \frac{\partial L}{\partial \phi_A} d\phi_A$$

Les variations $d\alpha_T$ et $d\phi_A$ se déduisent du transfert du pilote automatique. On obtient alors le schéma aux petits mouvements présenté figure 14.

figure 14 : effet du roulis induit



Selon les valeurs atteintes par le gradient $\frac{\partial L}{\partial \phi_A}$, notée L_{ϕ_A} , l'asservissement peut devenir instable.

Le coefficient de roulis induit $L(\alpha_T, \phi_A)$ croît exponentiellement avec l'incidence de sorte que ce phénomène peut limiter les incidences pilotables, soit que l'autorité de gouverne équivalente en roulis ξ devienne insuffisante pour contrer le couple de roulis induit, soit que le couplage induit entre voies de pilotage déstabilise l'autopilote.

Le roulis induit par la prise d'incidence est donc un phénomène directement dimensionnant vis-à-vis des performances atteignables.

4.2.4. Découplage de la ligne de visée des mouvements missile.

La prise d'assiette pour réaliser un facteur de charge est défavorable à la stabilité de l'autoguidage. Les imperfections des équipements créent alors des rebouclages comme l'illustrent les exemples suivants.

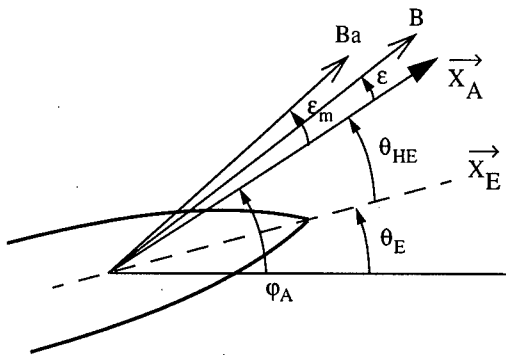
Pour un pilotage aérodynamique, des constantes de temps de mise en virage fortes sont davantage critiques vis-à-vis de ces rebouclages (surtout en altitude ou à bas Mach) : des forts gra-

dients de portance par rapport à l'incidence CN_α sont donc à favoriser. Un pilotage en force par contre est bénéfique.

Exemple 1 : aberrations de radôme

Dans le cas de l'utilisation d'un autodirecteur électromagnétique, le signal à mesurer est dévié en fonction du débattement de la ligne de visée dans le radôme, comme cela est précisé figure 15.

figure 15 : aberrations de radôme



$$\epsilon_m = \epsilon + \Delta\epsilon$$

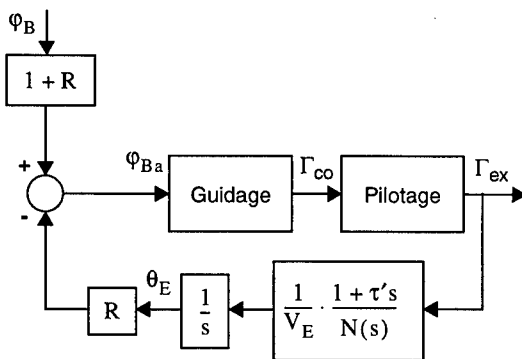
$$\Delta\epsilon = R \cdot \theta_{HE} = R \cdot [\varphi_A - \theta_E]$$

$$\varphi_{Ba} = \varphi_B + R \cdot [\varphi_A - \theta_E]$$

R : pente d'aberration de radôme linéarisée

Ceci induit un couplage entre le pilotage et le guidage, comme l'explique le schéma de la figure 16, mélangeant les mouvements d'assiette aux accélérations commandées au travers de la constante de temps de mise en virage τ' . Un tel effet peut dégrader les performances, voire déstabiliser un autoguidage.

figure 16 : effet des aberrations de radôme via la constante de temps de mise en virage



Pour les missiles les plus performants, l'aberration de radôme est compensée numériquement par ordinateur à l'aide de tables de mesures mémorisées. Même dans ce cas, le couplage reste cependant à minimiser vis-à-vis des aberrations résiduelles.

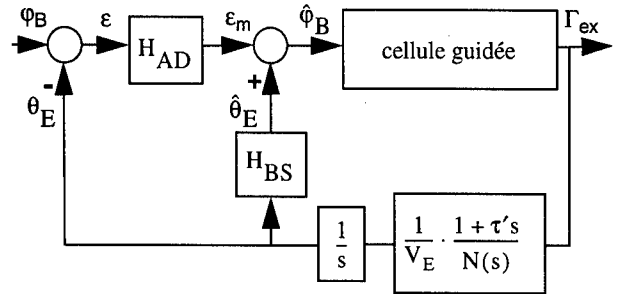
L'effet n'est pas similaire pour les différents types de pilotage. Il est naturellement minimisé pour un pilotage en force. Pour un pilotage en couple, le gradient de portance CN_α est à maximiser.

Notons par ailleurs que vis-à-vis des aberrations de radôme, un compromis entre la traînée et l'aberration de radôme est à rechercher, les aberrations étant plus fortes pour des radômes effilés.

Exemple 2 : autodirecteur fixe

Le même type de couplage existe aussi dans le cas d'un autodirecteur lié à l'engin : le schéma suivant montre que dans la reconstruction de la ligne de visée, une dynamique différentielle mal compensée entre l'autodirecteur (H_{AD}) et le bloc senseur inertielle (H_{BS}) introduit des rebouclages de guidage via le mouvement d'attitude de l'engin.

figure 17 : autodirecteur fixe



Notons également que dans le cas de l'utilisation d'un autodirecteur strapdown, minimiser l'incidence (fort CN_α , pilotage en force) est également essentiel pour conserver la cible dans le champ de mesure du senseur lors des prises de facteur de charge.

4.3. Missiles conventionnels tournants

4.3.1. Nécessité d'une modélisation du vecteur en repère non tournant

La synthèse du guidage-pilotage d'un engin tournant s'appuie sur une modélisation du vecteur dans un repère «engin non tournant».

En effet, les boucles de guidage-pilotage ont pour mission de contrer au mieux des perturbations qui s'expriment naturellement dans un repère non tournant (pesanteur, vent, défilement des cibles) en respectant des consignes de guidage qui s'expriment également dans un repère non tournant (écartométries). Une synthèse linéaire de ces boucles de guidage-pilotage nécessite donc l'élaboration d'un modèle du vecteur dans un repère non tournant.

Le repère «engin non tournant» est déduit du repère engin par une rotation de $-\varphi$ (démodulation par rapport au roulis).

Notons qu'une synthèse en repère tournant serait non linéaire (cosinus et sinus) ou aurait des entrées/sorties modulées, avec des critères de réglage difficiles...

4.3.2. Ecriture d'un modèle aérodynamique en repère non tournant

- Approche théorique

L'analyse du passage repère engin (tournant) / repère non tournant permet de comprendre ce que deviennent les efforts aérodynamiques et notamment les dissymétries de révolution.

On part donc des efforts aérodynamiques exprimés en repère engin (tournant) : $Cm_\alpha \alpha$ en tangage et $Cn_\beta \beta$ en lacet (on s'appuie ici sur le moment de rappel, mais pour les autres efforts aérodynamiques, le raisonnement est identique). α et β correspondent à l'incidence et au dérapage du repère engin (tournant) par rapport au vecteur vitesse aérodynamique.

Les termes sont multipliés ensuite par $\cos \varphi$ et $\sin \varphi$ pour le passage en repère non tournant.

On introduit alors la notion de roulis aérodynamique ϕ_{ANT} du repère non tournant, avec les relations suivantes :

$$\alpha = \alpha_T \cos(\varphi - \phi_{ANT})$$

$$\beta = \alpha_T \sin(\varphi - \phi_{ANT})$$

où α_T est l'incidence totale.

On introduit également les notions d'incidence α_{NT} et β_{NT} du repère non tournant :

$$\alpha_{NT} = \alpha_T \cos \phi_{ANT}$$

$$\beta_{NT} = \alpha_T \sin \phi_{ANT}$$

Les termes aérodynamiques deviennent alors :

$$\frac{(Cm_\alpha - Cn_\beta)\alpha_{NT}}{2} + \text{un terme d'harmonique 2 d'amplitude } \frac{(Cm_\alpha + Cn_\beta)}{2}$$

et

$$\frac{(Cm_\alpha - Cn_\beta)\beta_{NT}}{2} + \text{un terme d'harmonique 2 d'amplitude } \frac{(Cm_\alpha + Cn_\beta)}{2}$$

On constate alors que les dissymétries aérodynamiques sont «gommées», mais au prix d'efforts parasites d'harmonique deux à moyenne nulle sur un tour.

- Construction pratique du modèle

Les essais en soufflerie sont réalisés soit de façon «classique», avec une vitesse de rotation en roulis nulle, et un balayage en incidence et en roulis aérodynamique, soit en autorotation. Dans les deux cas, les efforts sont exprimés en repère engin (tournant) et décomposés en harmoniques. Cette décomposition en harmoniques permet de construire rapidement un modèle en repère non tournant : l'harmonique un en repère engin correspond au terme constant en repère non tournant (on peut faire apparaître si nécessaire les termes de couplage, efforts en dehors du plan d'incidence).

La linéarisation (en incidence principalement) du modèle de synthèse obtenu s'effectue ensuite, après ce «changement de repère».

4.4. Missiles non conventionnels

L'utilisation de techniques de commande multivariable permet de réaliser la synthèse globale des chaînes de pilotage en roulis, tangage et lacet, sans faire d'hypothèse de découplage entre les différentes chaînes. La connaissance des termes de couplages aérodynamiques permet alors d'affiner une telle démarche puisqu'il est possible de les faire intervenir dans un modèle de synthèse multivariable.

Pour des missiles dont l'aérodynamique est fortement non linéaire (missiles hypervéloces, missiles furtifs...) et notamment à haute incidence, on peut même envisager de mettre en œuvre une loi de commande non linéaire pour piloter le missile en profitant au mieux de la connaissance disponible a priori sur le comportement du missile.

L'apport d'une loi de pilotage non linéaire repose en grande partie sur la validité des caractéristiques non linéaires du modèle considéré pour la synthèse de la loi de commande. Comme les principales incertitudes sur les non linéarités du modèle proviennent de l'expression des coefficients aérodynamiques, une détermination précise de ces coefficients permet de profiter au mieux de ce type de loi de commande. On peut alors en effet envisager de compenser de façon explicite certaines non linéarités, au lieu de se contenter des modèles de synthèse linéaires obtenus par différentiation du modèle non linéaire autour des points de fonctionnement considérés.

Bien entendu, de telles techniques non linéaires peuvent également être retenues pour des missiles dits conventionnels afin d'augmenter le domaine de pilotabilité. Ceci est d'autant plus vrai dans le cas des engins hypervéloces pour lesquels les problèmes aérodynamiques sont exacerbés.

Ainsi, les performances de plus en plus accrues demandées aux engins nécessitent une connaissance et une utilisation plus fines des modèles aérodynamiques.

5. CONCLUSION

Les éléments précédents montrent qu'une analyse système est déterminante pour le choix de la configuration aérodynamique et que la connaissance du modèle aérodynamique est fondamentale pour l'optimisation des performances du système. Une concertation étroite entre les différents métiers de concepteurs de missile est nécessaire.

photo 1 : autopilote PIF-PAF d'ASTER en fonctionnement

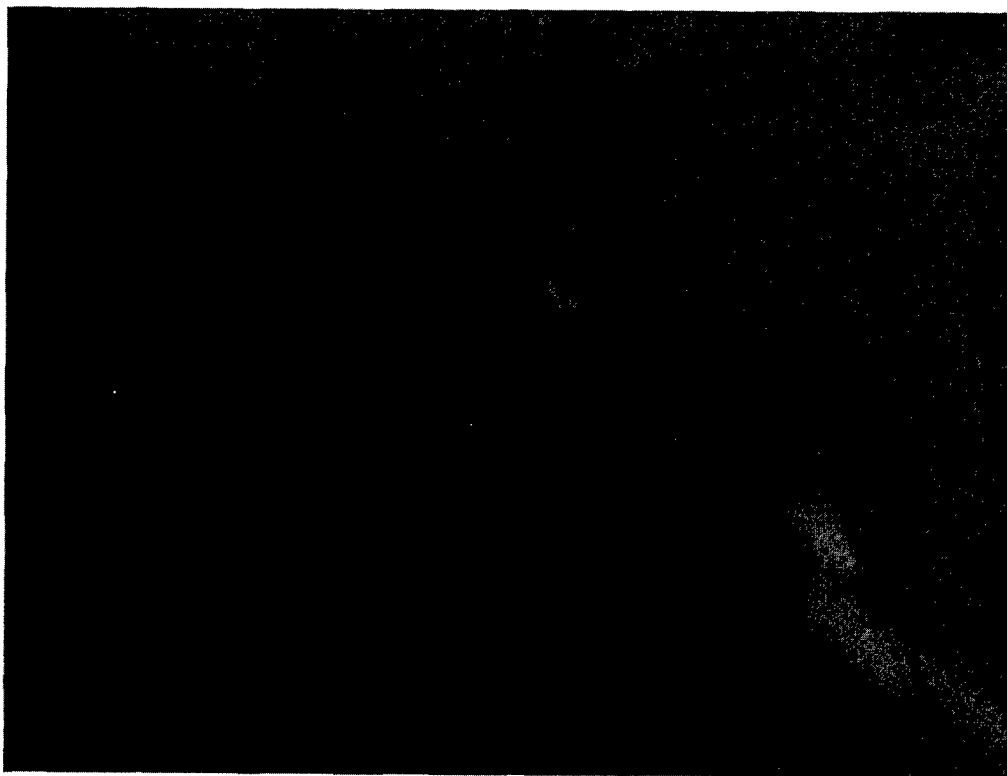


PHOTO DGA-CEL

photo 2 : ASTER 15 - montage photographique montrant la trajectoire d'un tir à courte distance

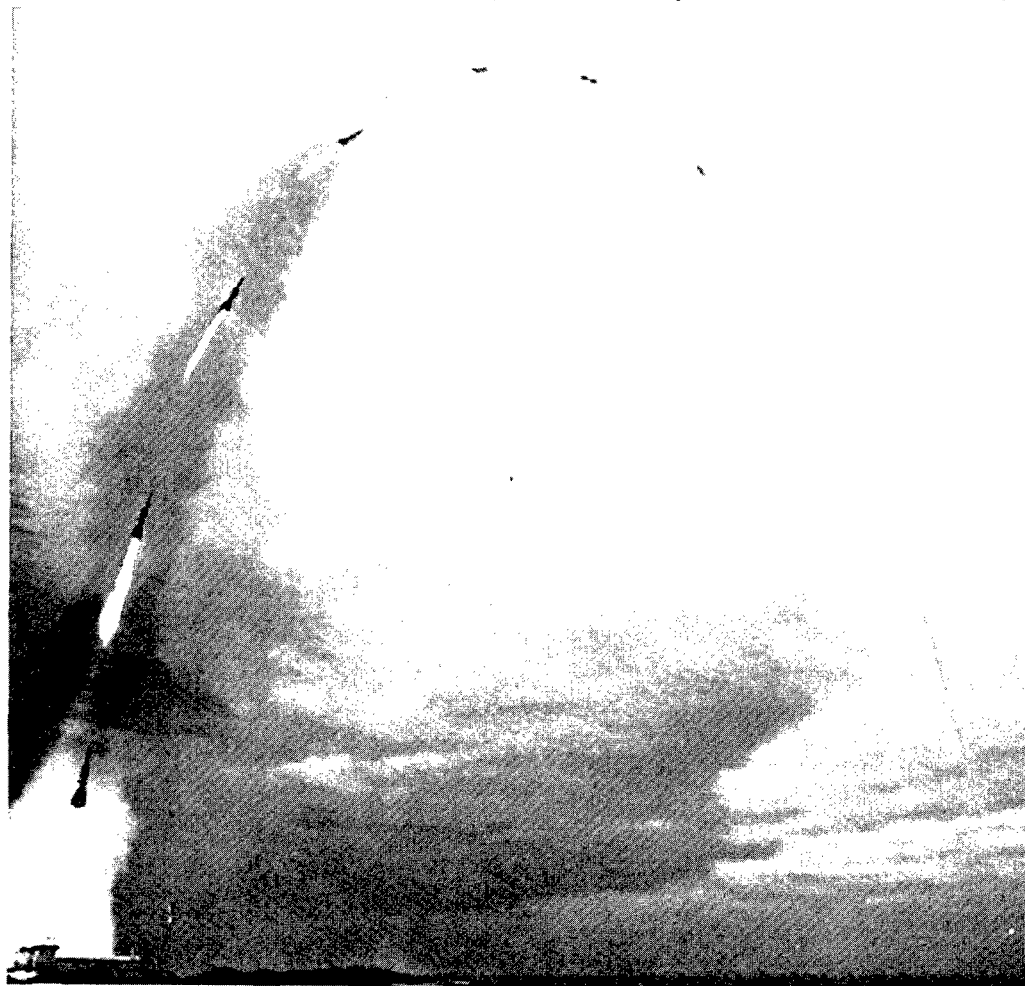


PHOTO DGA-CEL / AEROSPATIALE

photo 3 : missile antinavire supersonique ANF

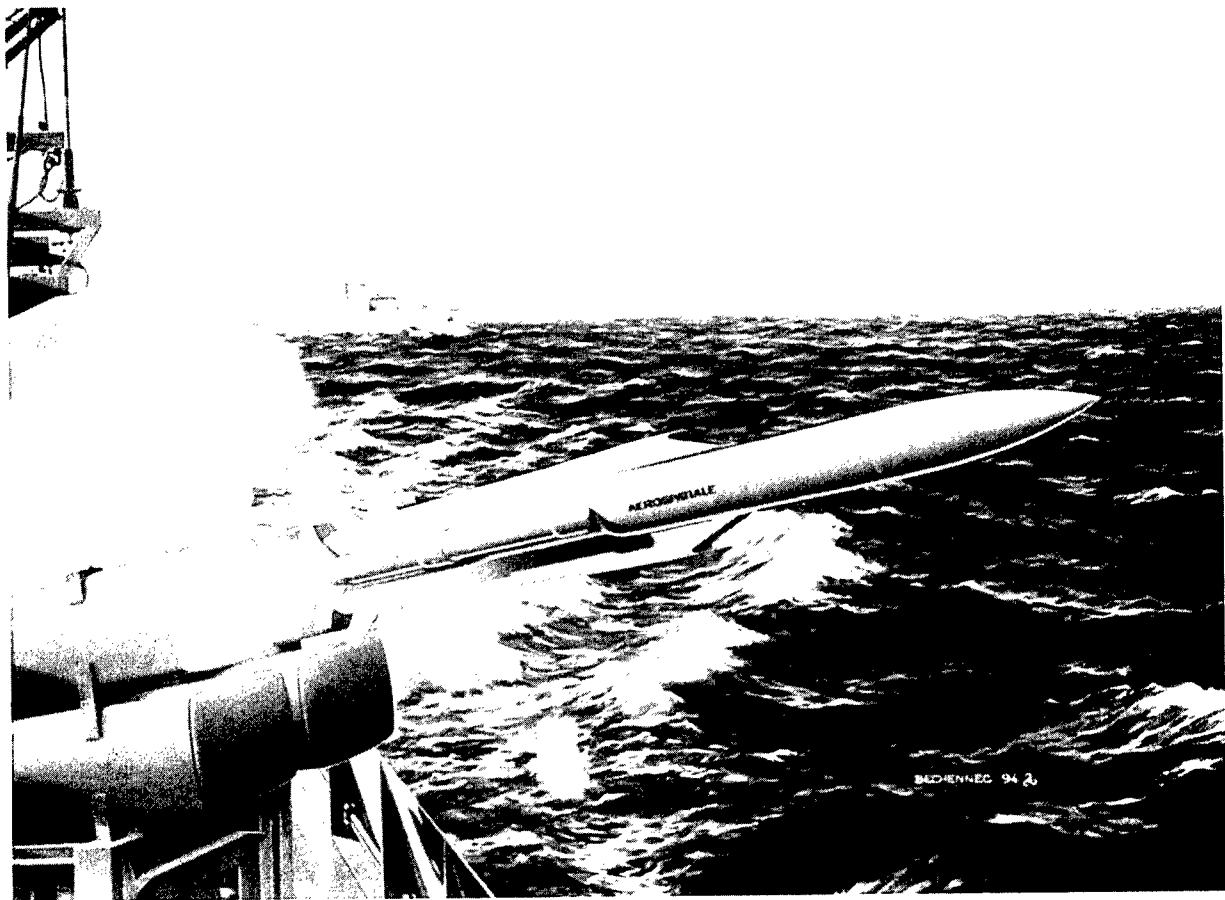


Illustration Daniel BECHENNEC

photo 4 : tir ERYX de nuit



PHOTO AEROSPATIALE

MISSILE FIN PLANFORM OPTIMIZATION FOR IMPROVED PERFORMANCE

Daniel J. Lesieutre, Marnix F. E. Dillenius, Teresa O. Lesieutre

Nielsen Engineering & Research, Inc.

526 Clyde Avenue

Mountain View, California 94043-2212 USA

1. SUMMARY

The aim of the research described herein was to develop and verify a fast running optimization-based aerodynamic/structural design tool for missile fin and configuration shape optimization. The developed software was used to design several missile fin planforms which were tested in the wind tunnel. Specifically, this paper addresses fin planform optimization for minimizing fin hinge moments, as well as aeroelastic design (flexible fin structures) for hinge moment control. The method is also capable of shape optimization of fin-body combinations with geometric constraints. The inclusion of aerodynamic performance, geometric constraints, and structural constraints within the optimization software facilitates multidisciplinary analysis and design. The results of design studies and wind tunnel tests are described.

2. LIST OF SYMBOLS

AR	fin aspect ratio of two fins joined at root chord,
C_{NF}	fin normal-force coefficient, normal force/ $q_\infty S_{ref}$
C_{NFS}	fin normal-force coefficient based on fin area, normal force/ $q_\infty S_{fin}$
c_R	root chord
c_T	tip chord
f	design objective
g	equality constraint
h	inequality constraint
IP	index of performance (cost function)
M_∞	Mach number
q_∞	freestream dynamic pressure
S_{fin}	exposed planform area of one fin
S_{ref}	reference area, body cross-sectional area
s	exposed fin span
t	fin thickness
x_{CP}/c_R	fin axial center of pressure, measured from root chord leading edge, normalized by root chord
x_{HL}	fin hinge line location aft of fin leading edge
y_{CP}/s	fin spanwise center of pressure, measured from root chord, normalized by exposed fin span
α	body angle of attack, degrees
δ	fin deflection angle, degrees
ϕ_f	fin polar angle location, 0° = horizontal, 90° = windward meridian, -90° = leeward meridian
λ	fin taper ratio, c_T/c_R

3. BACKGROUND

This paper describes recent research performed by Nielsen Engineering & Research^{1,2,3} aimed at developing practical methods for missile control fin design and for missile configuration shape optimization. Some background information is presented which describes the importance and difficulties of predicting and designing efficient control fins. This is followed by a description of the technical approach and design code developed. Results from the design code and wind tunnel tests are presented.

Missile control fins have been, and are arguably still, the most efficient means of controlling a tactical missile and guiding it to a target. They can efficiently generate the required maneuvering force either by a direct action near the center of gravity, as in a mid-wing control missile, or through rotation of the missile to higher α , as in canard or tail control missiles. Affecting all of these aerodynamically controlled configurations are the sizing and power requirements of the control surface actuators. Other means of control, such as thrust vector control and control jets are also important to high performance missiles. Thrust vector control can improve both the initial engagement of a threat, including engagement of a rear target, and the end game maneuvering (if thrust is still available). Control jets, depending on placement, can be utilized to translate or rotate a missile. Both thrust vectoring and control jets provide fast response and also provide control at high altitudes where aerodynamic control becomes ineffective. Lacau⁴ details the advantages and disadvantages of different missile control configurations.

The primary effects of control fins on missile system design are the available maneuvering force and the time response associated with maneuvering. In terms of subsystem design, the control fins determine the actuator sizing. The actuators influence the missile weight directly through their size and power requirements. Briggs⁵ describes the performance parameters which affect control fin actuator design and size. These include frequency-response bandwidth, stall torque, rated torque, and fin deflection rate at rated torque. The stall torque is the maximum expected "worst case" applied torque felt by the actuator and is composed of the sum (multiplied by a factor of safety) of the aerodynamic hinge moment and the frictional bearing torque associated with the fin root

Copyright 1998 by Nielsen Engineering & Research (NEAR). Published with permission of the authors.

bending moment. Rated torque is the maximum expected applied torque (friction + aerodynamic) over a nominal flight envelope. Fin deflection rate capability must permit three axis missile control up to the structural load limit or maximum value of total normal force acting on the missile. Rated torque multiplied by deflection rate determines the power requirements of the actuator. Actuator mass is determined primarily by the power requirements and can account for 10% of the missile mass. Reductions in hinge moments can significantly reduce this mass fraction.

Current and future air-to-air missiles are being designed for internal carriage. Internal carriage sets limits on fin span due to stowage requirements. This results in fins with reduced aspect ratios. Hinge-moment coefficients typically increase for lower aspect ratio fins due to larger variations in the axial center-of-pressure travel with both load and Mach number. The reduced span results in lower bending moments thus making the frictional bearing torques small compared to the aerodynamic hinge moments.

Historically, hinge moments have always been considered in missile designs. This has been accomplished through the choice of the most beneficial location of the hinge line over the expected flight envelope. Nielsen⁶ states that, *"It is often contended that calculations of hinge moments are not reliable because of frequent nonlinear variation of hinge-moment coefficient with control deflection and angle of attack"* (1960). This is especially true for small values of hinge moment (desired). However, Nielsen notes that, when hinge moments are small, nonlinearities are not so important. Lacau⁴ mentions, *"Theoretical estimate of these moments is not yet possible because the control forces center of pressure cannot be calculated with the needed accuracy. Therefore, control forces and hinge moments are obtained from wind tunnel tests"* (1988). Some examples of fins developed under considerable effort by manufacturers to minimize center-of-pressure travel are reproduced from Lacau⁴ in Figure 1.

Not much has fundamentally changed since 1960 or 1988 in regards to the prediction or estimation of hinge moments. They are highly nonlinear with respect to M_∞ , α , ϕ , and δ , and are difficult to predict with computational methods which lack experimental empiricism. Lesieutre and Dillenius⁷ documented and correlated the axial and spanwise fin center of pressure for fins in the Triservice experimental data base.⁸ C_{NFS} , x_{CP}/c_R and y_{CP}/s are nonlinear with the flow conditions and deflection angles. It was shown⁷ that x_{CP}/c_R and y_{CP}/s correlate with C_{NFS} for undeflected fins in the absence of strong vortical effects. Figure 2 depicts the experimental x_{CP}/c_R versus C_{NFS} for Triservice FIN52 ($AR = 2$, $\lambda = 1/2$) for $M_\infty = 3.0$. There are 990 data points plotted corresponding to 11 angles of attack from 0° to 45° , 10

windward side roll angles, ϕ_r , from 0° to 90° , and 9 deflection angles from -40° to $+40^\circ$. Data for $\delta = 0^\circ$ are shown as solid circles and correlate fairly well with C_{NFS} . There is considerable variation of x_{CP}/c_R with deflection angle: up to 14% of c_R . When lower Mach numbers are considered, this variation is even greater since the center of pressure is further forward. Much of the deflected x_{CP}/c_R variation is associated with nonlinear effects due to the fin-body gap which are extremely difficult to predict. Results for Triservice FIN42 ($AR=1$, $\lambda=1/2$) are shown in Figure 3. Compared to FIN52, Figure 2, this lower aspect ratio fin shows more variation of x_{CP}/c_R with C_{NFS} for both zero and nonzero deflections. With deflection, the fin-body gap is physically larger for FIN42 than for FIN52 due to different root chord lengths. Aerodynamic nonlinearities such as those depicted present a strong challenge to designers of highly maneuverable missiles which operate from subsonic to hypersonic speeds.

The approach described herein^{1,2,3} to design control fins with improved performance is a practical one which utilizes numerical optimization and nonlinear aerodynamic prediction methods. The primary goal was to design fins with improved performance over that of the initial or baseline fin. Therefore, it is not strictly necessary that the aerodynamic prediction accurately model all the nonlinearities present. However, it must estimate the relative performance of fins adequately. Promising designs were analyzed with CFD for verification prior to wind tunnel testing.

4. TECHNICAL APPROACH

A numerical optimization shell has been coupled with subsonic and supersonic fast running panel method-based missile aerodynamic prediction programs which include nonlinear high angle of attack vortical effects, and a structural finite element code.^{1,2} Program OPTMIS^{1,2} for missiles with arbitrary cross section bodies and up to two fin sections was developed under a U.S. Air Force Small Business Innovative Research (SBIR) contract. A U.S. Navy SBIR effort investigated the extension to and design of flexible composite fin structures which aeroelastically minimize hinge moments.³ A description of the methodology employed follows.

4.1 Summary of Methodologies Employed

The optimization algorithm implemented in the OPTMIS² design software is a direct search algorithm, Powell's Conjugate Directions Method.^{1,9,10} The Nielsen Engineering & Research (NEAR) subsonic and supersonic panel method-based aerodynamic prediction modules, SUBDL¹¹ and SUPDL,^{12,13} are employed as the aerodynamic prediction modules within the design code. The VTXCHN¹⁴ methodology is used to model circular and noncircular body shapes within the SUBDL and

SUPDL modules. The structural constraints are included through the CNEVAL-FEMODS^{1,3} module which employs automatic gridding and structural finite elements to compute displacements, stresses, fin weight, and natural mode frequencies.

For aeroelastic design studies, subiterations between the aerodynamic and structural analysis module CNEVAL-FEMODS^{1,3} are performed to ensure a consistent load distribution and deformed fin shape. Initially, fin displacements are calculated with the flat-fin (rigid) load distribution. The fin displacements are used to define a new fin shape for the aerodynamic load calculation, and the aerodynamic loads are recalculated. Fin displacements are determined with the updated loads, and this iterative process is continued until the changes in displacements are less than a user-specified tolerance.

4.2 Optimization Problem Formulation

The *OPTMIS*² design software minimizes an Index of Performance (cost function) which includes objectives, equality constraints, and inequality constraints. This formulation is an extension of the Sequential Unconstrained Minimization Technique (SUMT) of Fiacco and McCormick.¹⁵ The SUMT formulation was enhanced so that multiple objective functions and multiple design point studies could be included. The following SUMT Index of Performance is employed:

$$IP(\mathbf{x}, \mathbf{w}) = \sum_m [\sum_i f_i(\mathbf{x}, m) / w_i] + \sum_j [h_j^2(\mathbf{x}) / w_j] + \sum_k [w_k / g_k(\mathbf{x})] \quad (1)$$

where the indices m , i , j , and k represent sums on the number of flow conditions, objectives, equality constraints, and inequality constraints, respectively. The constraint weights, w_j and w_k , are monotonically decreased during the optimization procedure. The inequality constraints $g_k(\mathbf{x})$ add a large positive value to the IP if $g_k(\mathbf{x})$ approaches zero. If there are no inequality constraints, the minimization problem being solved is an unconstrained minimization of $f(\mathbf{x})$ when w_j is large. As w_j decreases toward zero, the equality constraints become important. This representation of the Index of Performance is very versatile and allows single and multiple point designs to be investigated.

In *OPTMIS*,² the index of performance formulation given by Eqn. (1) is further divided into three terms governing design objectives and constraints applicable to the fin, body, and overall configuration. The complete form of the IP is given by:

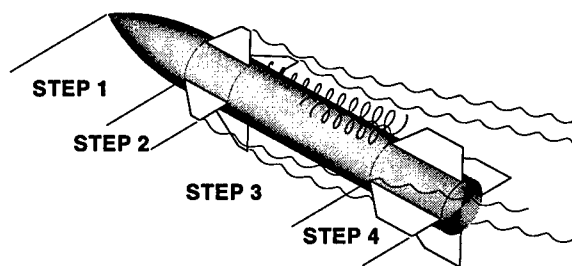
$$IP(\mathbf{x}, \mathbf{w}) = IP_{\text{overall}}(\mathbf{x}, \mathbf{w}_o) + IP_{\text{body}}(\mathbf{x}, \mathbf{w}_b) + IP_{\text{fin}_n}(\mathbf{x}, \mathbf{w}_{f_n}) \quad (2)$$

where IP_{overall} , IP_{body} , and IP_{fin} each have the form of Eqn. (1) and correspond to overall, body, and fin objectives and constraints, respectively. IP_{fin} includes objectives and constraints for up to two fin sections. Typically, objectives are formulated with respect to aerodynamic performance variables, and constraints with respect to geometric variables.

Program *OPTMIS*² has two methods for handling the inequality constraints specified. The first is in the manner specified in Eqn. (1), through a penalty within the IP. The second is as a side constraint. If an initial feasible design is specified, then the optimization procedure will not allow a design change in a direction where an inequality constraint is violated. This is the manner in which all structural constraints computed by the CNEVAL-FEMODS^{1,3} module are handled.

4.3 Aerodynamic Modeling

This section gives a brief summary of the body and fin aerodynamic modeling methodologies used in the *OPTMIS* code. The NEAR nonlinear panel method-based missile aerodynamic prediction programs SUBDL¹¹ and SUPDL^{12,13} which include models of body and fin shed vorticity at high angles of attack, as well as nonlinear shock expansion and Newtonian analyses, were chosen as appropriate aerodynamic codes for inclusion in the aerodynamic optimization tool. General descriptions of programs SUPDL and SUBDL follow. The original SUBDL and SUPDL codes modeled axisymmetric bodies. The VTXCHN code¹⁴ has replaced the body model within SUBDL and SUPDL and can model circular and noncircular cross section bodies including those with chines. The aerodynamic calculation proceeds stepwise as follows: 1) VTXCHN computes the forebody loads including vortex shedding and tracking, 2) fin section loads are calculated including the effects of forebody vorticity, 3) vorticity shed from the forebody and the fin set is tracked aft including additional vortices shed from the afterbody, and 4) if a second fin set is present, steps 2 and 3 are repeated. This procedure is depicted below.



4.3.1 VTXCHN Body Modeling Methodology

The aerodynamic analysis of a body by VTXCHN,¹⁴ including effects of vortex shedding, comprises conformal mapping, elements of linear and slender body theory, and

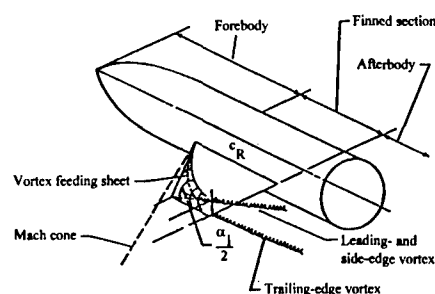
nonlinear vortical modeling. The analysis proceeds from the nose to the base. Noncircular cross sections are transformed to corresponding circles in the mapped plane. As a result, an axisymmetric body is created in the mapped space. If the actual body is axisymmetric, this step is omitted. The axisymmetric body is modeled by three-dimensional sources/sinks for linear volume effects and by two-dimensional doublets for linear upwash/sidewash effects. For subsonic flow three-dimensional point sources/sinks are used, and for supersonic flow three-dimensional line sources/sinks are used. At a cross section near the nose, velocity components are computed at points on the transformed body and transformed back to the physical plane. The circumferential pressure distribution is determined in the physical plane using the compressible Bernoulli equation. For smooth cross sectional contours, the code makes use of the Stratford separation criterion applied to the pressure distribution to determine the separation points. If the cross section has sharp corners or chine edges, vortices are positioned slightly off the body close to the corner or chine points in the crossflow plane. The locations of the shed vortices are transformed to the mapped plane. The strengths of the shed vortices are related to the imposition of a stagnation condition at the contour corner or chine points in the mapped plane. The vortices are then tracked aft to the next cross section in the mapped plane. The procedure for the first cross section is repeated. The pressure distribution calculated at the second cross section in the physical plane includes nonlinear effects of the vortices shed from the first cross section. The resulting pressure distribution is integrated to obtain the aerodynamic forces and moments. Along the body, the vortical wake is represented by a cloud of point vortices with known strengths and positions.

4.3.2 Supersonic Aerodynamic Prediction Method

SUPDL^{12,13} is a panel method-based program which together with the VTXCHN¹⁴ body module can analyze an arbitrary cross section body with a maximum of two fin sections in supersonic flow. Fins may have arbitrary planform, be located off the major planes, and be attached at arbitrary angles to the body surface. The fins are modeled by supersonic panels laid out in the chordal planes of the fins. In addition, a set of panels is laid out in a shell around the body over the length of the fin root chord to account for lift carry-over. The panel method is based on the Woodward constant pressure panel solution¹⁶ for modeling lift. In SUPDL this panel is designated the constant u-velocity panel because the pressure on the panel is computed using the compressible Bernoulli velocity/pressure relationship. Each panel has a control point at which the flow tangency condition is applied. On the fin, the flow tangency boundary condition includes mutual interaction with all other constant u-velocity panels

in the fin section, contributions from free stream due to angle of attack, body-induced effects (upwash), and vortical wakes from upstream fins and body flow separation. The constant u-velocity panels on the interference shell only experience the mutual interaction with the constant u-velocity panels on the fins and fin thickness effects. Effects of fin thickness can be included by thickness panels in the chordal plane of the fin. The strengths of the thickness panels are directly related to the local thickness slopes. The strengths of all of the constant u-velocity panels in a fin section are obtained from a solution of a set of simultaneous equations.

Fins can develop nonlinear leading- and side-edge separation vorticity as the angle of attack is increased. If the side edge is long (similar in length to the root chord, for example), vorticity can be generated at angles of attack as low as 5° . Along the leading edge, vorticity can be generated at supersonic speeds provided the leading edge lies aft of the Mach cone emanating from the root leading edge (a subsonic leading edge). If this is the case, the leading-edge vortex joins the side-edge vortex. The combined vortex gains strength and rises above the fin as shown in the sketch which follows. This sketch shows how SUPDL models the path of the combined leading- and side-edge vortex by locating it above the fin plane at an angle equal to one-half of the local angle of attack (as seen by the fin).



The vortical phenomena along the leading- and side-edges are accompanied by an augmentation to normal force which is nonlinear with angle of attack seen by the fin. This nonlinearity is modeled by calculating the suction distribution along the leading and side edges. In accordance with an extension¹⁷ of the Polhamus suction analogy,¹⁸ the suction is converted to normal force in proportion to vortex lift factors. The result is a distribution of nonlinear, additional normal force along the leading and the side edge.

Another nonlinear effect is related to nonlinear compressibility. For M_∞ in excess of approximately 2.5, the fin leading edge shock may lie close to the surfaces (usually the lower surface) of the fin. This situation can

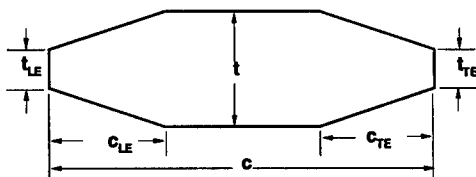
also occur at low supersonic Mach numbers if the angle of attack is high. In either case, the fin loading prediction based on the constant u-velocity panel method and the Bernoulli velocity/pressure relationship is no longer adequate. As an option, the pressures acting along chordwise strips can be calculated with nonlinear shock expansion or Newtonian theories. A unique feature is the option to include strip-on-strip interference based on the linear constant u-velocity panel solution to correct the flow angle used in either the shock expansion or Newtonian pressure calculation methods. Details can be found in References 17 and 19.

4.3.3 Subsonic Aerodynamic Prediction Method

Program SUBDL¹¹ is a panel method-based program which together with the VTXCHN¹⁴ body module can analyze an arbitrary cross section body with a maximum of two fin sections in subsonic flow. The addressable geometries are the same as those described for SUPDL previously. The lifting surfaces and the portions of the body spanned by the lifting surfaces are modeled with planar horseshoe vortex panels. The strengths of the lifting surface singularities are obtained from a set of linear simultaneous equations based on satisfying the flow tangency condition at a set of discrete aerodynamic control points. The horseshoe vortices on the interference shell around the body are used only to model the carryover forces between the body and fins (the body volume and angle-of-attack effects are obtained from the three-dimensional sources and doublets and conformal mapping procedure in the VTXCHN module). The nonlinear vorticity effects associated with fin edges described above for SUPDL are also modeled in SUBDL.

4.4 Fin Structural Modeling

For fin structural modeling, five parameters for the root and five parameters for the tip define the thickness distributions. The parameters for any intermediate section are defined by linear interpolation. The generic section is a symmetric truncated double wedge with finite thicknesses at the leading and trailing edges and is illustrated in the sketch below.



The fin can be cantilevered at the root, or supported on a shaft to represent an all-movable control surface.

The fin is modeled with constant-thickness, triangular nonconforming bending elements,²⁰ with modifications to allow for anisotropy.²¹ The meshed fin is divided into

quadrilateral patches. In the simplest model, each patch is represented by two bending elements. However, since nonconforming elements do not reproduce the proper symmetry properties for a rectangular or a square planform, there is an option to model each patch with two pairs of elements which eliminates any asymmetries. For all-movable fins, the control shaft is modeled with a beam in bending and a rod in torsion. No transverse shear effects are included, and both elements are uniform. These elements are also described in detail in Reference 22. There are three degrees of freedom per structural node: two rotations in the plane of the fin, plus a transverse displacement. For dynamic problems, consistent inertia elements from Reference 22 are used.

Structural Constraint Evaluation. There are two options for displacement constraints. In the first option, up to 10 upper bounds and their associated node numbers can be specified. Displacement ratios (actual/allowable) are calculated at the specified nodes; if any ratio is greater than unity, the number of violated displacement constraints is incremented, and the node number and displacement ratio are recorded. In the second option, only a single upper bound for the maximum absolute value of any displacement is specified. If this bound is exceeded, then the number of violated displacement constraints is set to unity, and the node number and displacement ratio are recorded. For the stress constraint, the maximum value of the von Mises bending stress is found. If this value exceeds the allowable, the constraint-violation flag is set to unity and the associated node number and stress ratio are recorded. Up to five lower-bound frequency constraints can be imposed by specifying the lower bounds and their mode numbers. A frequency constraint is considered violated when the frequency for any specified mode becomes less than its bound. The number of violated constraints and the corresponding mode numbers and frequency ratios are recorded. For the weight constraint, the weight of the initial design is saved. The weight of each subsequent design is ratioed to this initial weight.

5. RESULTS

This section describes results including fin planform design studies, wind tunnel tests, verification of aerodynamic performance prediction, and aeroelastic fin design. Additional design studies are described in References 1, 2, and 3.

5.1 Fin Planform Optimization Design Studies

Descriptions of two fin planform optimization designs which were tested in the Lockheed-Martin High Speed Wind Tunnel in Dallas, TX, are given below. For the fin designs tested in the wind tunnel, four (4) small span fins, FIN1 - FIN4, with exposed span of 0.72 diameters, and two (2) large span fins, FIN5 and FIN6, with exposed

span of 1.4 diameters were tested. FIN1 was the small span trapezoidal reference fin used to start the design optimization for FIN2, FIN3, and FIN4. FIN6 was the large span trapezoidal reference fin used to start the design optimization for FIN5. The design studies for FIN3 and FIN5 are described in this paper. Further details can be found in Reference 1.

FIN3 and FIN5 were designed using *OPTMIS*² to minimize the fin axial center-of-pressure travel from subsonic to supersonic flow. The fin normal force based on fin area was to be maintained. To achieve this objective, the ratio $|x_{CP2} - x_{CP1}|/|C_{NF2} - C_{NF1}|$ was minimized. The subscript "2" refers to the supersonic design flow condition, and the subscript "1" refers to the subsonic design flow condition. This design objective also tends to give a flat x_{CP} response with increasing fin normal force. The design flow conditions were: $(M_\infty, \alpha) = (0.5, 2^\circ), (2.0, 15^\circ)$. For the reference fins, the low M_∞ number, low α design condition gave a center of pressure forward on the fin, whereas the supersonic Mach number, high angle-of-attack condition gave an aft center-of-pressure location. The design objective was to minimize this center-of-pressure travel. The design variables were third-order Chebyshev polynomials describing the leading- and trailing-edge shapes. The resulting geometries of FIN3 and FIN5 are shown in Figures 4 and 10, respectively.

5.2 Wind Tunnel Test Description

The fin planforms described above were tested in the Lockheed-Martin High Speed Wind Tunnel in Dallas, TX, during the period March 3 - 8, 1997. Existing test hardware consisting of a body with fin strain-gage balances was utilized. The model consisted of a two-caliber tangent ogive nose and a cylindrical body 5.2 calibers long. A pair of fin balances were positioned 3.4 diameters aft of the nose tip. Figures 4, 6, and 10 depict the fins described herein. All tests were conducted with identical fins on the left and right balances to insure symmetry. The three-component outputs for the fins, (1) normal force, (2) root-bending moment, and (3) hinge moment, were the only model data collected. The internal structure of the body permitted mounting the fins at deflection angles from -20° to $+20^\circ$ at 5° intervals. The fin force, C_{NF} , and moment data, C_{HM} and C_{BM} , were reduced to provide fin axial and spanwise center-of-pressure locations, x_{CP}/c_R and y_{CP}/s , respectively. The tests included Mach numbers of 0.5, 1.5, 2.0, and 3.0. The angle of attack range was -12° to 22° , and fin deflection angles of 0° and 20° were tested.

5.3 Prediction Verification for Reference FIN1

The predicted and measured aerodynamic performance of the small span reference fin FIN1 is shown in Figures 4 and 5. The variation of fin normal force C_{NFS} and fin

axial center of pressure x_{CP}/c_R with α are shown for $M_\infty = 0.5$ and 2.0 and for $\delta = 0^\circ$ and 20° . Experimental data are shown as open symbols. Predicted results from *OPTMIS*² are shown as solid symbols with solid lines, and results from the NASA OVERFLOW Navier-Stokes solver²² (zero deflection only) are shown as solid symbols with dashed lines.

The comparison of the measured and predicted C_{NFS} for $\delta = 0^\circ$ are in good agreement for both Mach numbers. *OPTMIS* slightly overpredicts C_{NFS} at $M_\infty = 2.0$ and $\alpha = 20^\circ$. OVERFLOW slightly underpredicts C_{NFS} at $M_\infty = 0.5$ and $\alpha = 20^\circ$. The axial center-of-pressure location is also predicted well for the $\delta = 0^\circ$ conditions. All design studies have been performed at $\delta = 0^\circ$. The predicted aerodynamic results for $\delta = 20^\circ$ are not in as good an agreement with the experiment. For $M_\infty = 0.5$, the *OPTMIS* results for C_{NFS} agree fairly well at low angles of attack but do not have the correct stall behavior as angle of attack increases. The predicted axial center of pressure is forward of the experimental result for angles of attack above 10° . This is most likely due to inadequate modeling in *OPTMIS* of the gap between the deflected fin and the body which changes the fin loads near the root chord leading or trailing edge. The subsonic prediction module, SUBDL, currently models the effects of deflection through the boundary conditions and not through geometric deflection of the fin. This accounts for both the overprediction of normal force and the forward location of the center of pressure. The deflected results for the supersonic Mach number, $M_\infty = 2.0$, show the opposite trend. The normal force is underpredicted in this case. The supersonic prediction module, SUPDL, does model deflection effects through geometric deflection of the fin. However, the nonlinear flow field (local Mach number and local dynamic pressure variations) present behind the nose bow shock can be important when the fin is close to the nose. For this forward fin position, the flow field can vary significantly circumferentially around the body. For large deflections this places the leading and trailing edges in different local flow fields. The local flow fields behind the bow shocks close to the body surface can only be predicted well by Euler or Navier-Stokes flow solvers. The panel method-based programs are not capable of predicting these local flow conditions. However, corrections based on CFD calculations could be included. In spite of the above, the axial center of pressure is predicted well by *OPTMIS*.

5.4 Prediction Verification for Optimized FIN3

The predicted and measured performance of FIN3 is shown in Figures 6 and 7. C_{NFS} and x_{CP}/c_R are shown for $M_\infty = 0.5$ and 2.0 and $\delta = 0$ and 20° as a function of α . The results for FIN3 are similar to FIN1. The comparisons of the measured and predicted C_{NFS} for $\delta = 0^\circ$ are in good agreement for both Mach numbers.

However, *OPTMIS* slightly overpredicts the normal force at $\alpha = 20^\circ$. *OVERFLOW* results are shown for $M_\infty = 2.0$ and match the normal force well. The axial center-of-pressure location is also predicted well for the $\delta = 0^\circ$ conditions, within 2% of c_R . The predicted results for $\delta = 20^\circ$ are similar to those of FIN1 in terms of C_{NFS} . The predictions for axial center of pressure do not agree with experiment for $\delta = 20^\circ$. The reasons for the lack of agreement given above for FIN1 apply here also.

5.5 Comparison of FIN1 and FIN3

A detailed comparison of experimental x_{CP}/c_R data for reference FIN1 and optimized FIN3, along with predicted results, are shown in Figure 8 for the design Mach numbers 0.5 and 2.0. Again, the design objective for FIN3 was to minimize axial center-of-pressure travel from subsonic to supersonic speeds. Measured and predicted results for FIN3 (optimized) and FIN1 (reference) are shown for $\delta = 0^\circ$. The axial center of pressure is plotted as a function of C_{NF} (based on base diameter). Predicted results are shown from the *OPTMIS*² code and the *OVERFLOW*²² code. The experimental data, the results from the *OPTMIS* code, and the CFD results indicate that the optimized FIN3 has less center-of-pressure travel from subsonic to supersonic speeds and that the optimized fin has a flatter axial center-of-pressure variation with increasing C_{NF} as compared to the reference fin. For $C_{NF} = 0.3$ FIN3 has 50% less center-of-pressure travel than FIN1. There is, in general, good agreement between the predictions and the experiment. FIN3 produces less normal force than FIN1 for the same angle of attack, due to the smaller fin area. However, the normal force can be increased by a higher angle of attack or fin deflection without adversely affecting center-of-pressure travel.

Figure 9 compares the FIN1 and FIN3 axial center-of-pressure location for all four test Mach numbers and for $\delta = 0^\circ$ and 20° . The vertical axis (x_{CP}/c_R) for both graphs in Figure 6 spans 0.32. For supersonic Mach numbers (1.5, 2.0, and 3.0), FIN3 shows only slight variations of x_{CP}/c_R with either α or δ compared to the reference FIN1.

5.6 Results for Optimized FIN5 and Reference FIN6

The predicted and measured performance of the large span fins FIN5 and FIN6 is shown in Figure 10. C_{NFS} and x_{CP}/c_R are shown for $M_\infty = 0.5$ and 2.0 for $\delta = 0^\circ$ as a function of angle of attack. The comparisons of the measured and predicted C_{NFS} for $\delta = 0^\circ$ are in good agreement for both Mach numbers. *OPTMIS* does not predict the stall characteristics for the $M_\infty = 0.5$ flow condition. The axial center-of-pressure location is predicted slightly aft of the experimental value for moderate angles of attack (unstalled), within 5% of c_R .

FIN5 was designed to have a reduced center-of-pressure travel from subsonic to supersonic speeds. The design flow conditions were: $(M_\infty, \alpha) = (0.5, 2^\circ)$ and $(2.0, 15^\circ)$. Both fins have similar normal force characteristics. The optimized fin FIN5 delays stall and reaches a higher peak normal force than the reference fin at subsonic speeds. The axial center-of-pressure results for $M_\infty = 0.5$ and 2.0 indicate that FIN5 has reduced center-of-pressure travel from subsonic to supersonic speed up to the onset of stall of the reference fin FIN6.

5.7 Aeroelastic Fin Design

Aeroelastic design studies have been performed to improve missile fin performance through beneficial passive deformations of the fin structure under aerodynamic load. A description of the design and testing of an aeroelastic fin structure¹³ used to demonstrate the potential of chordwise flexibility to control center-of-pressure location is described. This is followed by a recent study³ aimed at using aeroelastically tailored composite fins.

In the earlier study,¹³ an aeroelastic tailoring procedure was developed based on the SUPDL^{12,13} code and a structural finite element code FEMOD.¹³ The design procedure was successfully applied to a grooved aluminum lifting surface resulting in grooves in essentially the spanwise direction. The grooved aluminum trapezoidal fin is shown in Figure 11(a). C_{NFS} and x_{CP}/c_R are shown in Figure 11(b) and 11(c), respectively, for the flexible and rigid fins as a function of α for $M_\infty = 1.5, 2.5$, and 3.5. Predictions are designated TAILOR in Figure 11. The design objective was to shift x_{CP}/c_R forward to the maximum possible extent by varying the direction of the grooves. The design calculations indicated that x_{CP}/c_R could be shifted forward, without appreciable change in C_{NFS} , with grooves in a near spanwise direction. The experimental data shown in Figure 11 confirm this result.

The objective of the recent study³ was to minimize the fin axial center-of-pressure travel over a Mach number range of 1.2 to 2.5 for $\alpha = 5^\circ$. The planform shape was fixed and the fin was undeflected. The design variables governing the fin structure are the fin thickness parameters at the fin root and the fin tip, and the principal stiffness axis orientation, β , of the composite fin lay-ups. A single orientation can be chosen, or the fin can be modeled as composed of up to three different layup orientation regions: the leading edge area of the fin, the middle portion of the fin, and the trailing edge region. The configuration modeled and the design variables governing the aeroelastic design are shown in Figure 12. Details of the structural modeling of the composite layup and structural properties can be found in Reference 3. Structural displacement and stress constraints ensure that realistic fin structures are considered during the optimization process.

To start the optimization, a constant thickness fin was specified. The thickness distribution of the optimized fin is depicted in Figure 13. The principal structural axes for this fin are $\beta_{LE} = 2.7^\circ$ for $x/c_R \leq \frac{1}{3}$ and $\beta_{TE} = -48.3^\circ$ for $x/c_R \geq \frac{1}{3}$. The deformation of the fin midplanes at $M_\infty = 1.2$ and 2.5 are shown in Figure 14. A large deformation of the fin at the root chord leading edge is indicated. The normal force and axial center-of-pressure performance of the fin are shown in Table 1 and Figure 15. Figure 15 indicates that the optimized flexible fin maintains the normal force of the rigid fin. The space marching NEARZEUS²³ results shown in Figure 15 extends the normal force prediction to high Mach numbers. The reduced center-of-pressure travel is indicated in Figure 15 for the aeroelastic fin. NEARZEUS²³ predicts a similar forward shift of the center of pressure for the flexible fin.

Table 1.- Rigid and Optimized Flexible Performance

	M_∞	α	C_{NFS}	x_{cp}/c_R	$\Delta x_{cp}/c_R$
Rigid					
OPTMIS	1.2	5°	0.208	0.36	13.8%
OPTMIS	2.5	5°	0.168	0.5	
Opt.					
OPTMIS	1.2	5°	0.214	0.34	6.10%
OPTMIS	2.5	5°	0.168	0.4	
Optimized fin $\Delta x_{cp}/c_R$ reduced 56% vs. Rigid					

The optimized fin has nearly the same normal force characteristics of the rigid fin but the center-of-pressure travel over the Mach number range is reduced 56%.

6. CONCLUSIONS

An optimization-based design tool for missile fin and configurations design and analysis has been developed. The design capabilities of the method for fin planform optimization have been verified with CFD calculations and with a wind tunnel test. Significant improvements to center-of-pressure travel, and hence hinge moments, can be obtained through planform optimization. Initial studies of aeroelastic fin structures indicate that significant improvements to fin performance can be obtained through the use of flexible structures. The speed and multidisciplinary capabilities of the method make it an excellent tool for preliminary design. Both conventional circular body and unconventional noncircular body configurations can be designed and analyzed.

7. ACKNOWLEDGEMENTS

The authors would like to thank Dr. Andy Sullivan and Mr. Fred Davis of the Air Force Research Labs, Flight Vehicle Branch WL/MNAV, at Eglin AFB for their support of this work under Air Force Contract F08630-94-C-0054, also, Dr. Craig Porter from NAWCWPNS, China Lake for sponsoring the aeroelastic fin design effort under Navy Contract N68936-97-C-0152. Dr. Samuel McIntosh, McIntosh Structural Dynamics, Palo Alto, CA, was responsible for the structural modeling described.

8. REFERENCES

1. Lesieutre, D.J., Dillenius, M.F.E., and Lesieutre, T.O., "Optimal Aerodynamic Design of Advanced Missile Configurations With Geometric and Structural Constraints", NEAR TR 520, September 1997.
2. Lesieutre, D.J., Dillenius, M.F.E., and Lesieutre, T.O., "Planform/Configuration Optimization Program OPTMIS For Arbitrary Cross Section Configurations With Up To Two Fin Sets - Software User's Manual - Software Programmer's Manual", NEAR TR 519, October 1997.
3. Lesieutre, D.J., Dillenius, M.F.E., Love, J.F., and Perkins, S.C., Jr., "Control of Hinge Moment by Tailoring Fin Structure And Planform", NEAR TR 530, December 1997.
4. Lacau, R.G., "A Survey of Missile Aerodynamics", in Proceedings, NEAR Conference on Missile Aerodynamics, October 1988.
5. Briggs, M.M., "Systematic Tactical Missile Design", in Tactical Missile Aerodynamics: General Topics, 141, 3, Progress in Astronautics and Aeronautics, AIAA, 1991.
6. Nielsen, J.N., "Missile Aerodynamics", New York, McGraw-Hill, 1960; Reprint, Mountain View, CA, Nielsen Engineering & Research, 1988.
7. Lesieutre, D.J. and Dillenius, M.F.E., "Chordwise and Spanwise Centers of Pressure of Missile Control Fins", AGARD CP 493, April 1990, Paper 30.
8. Allen, J.M., Shaw, D.S., and Sawyer, W.C., "Remote Control Missile Model Test", AGARD CP 451, May 1988, Paper 17.
9. Powell, M.J.D., "An Efficient Method for Finding the Minimum of a Function of Several Variables Without Calculating Derivatives", Computation Journal, 7, 1964, pp 155-162.
10. Sargent, R.W.H., "Minimization without Constraints", in "Optimization and Design", Avriel, M., Rijckaert, M.J., and Wilde, D.J., (Eds.), Englewood Cliffs, New Jersey, Prentice-Hall, 1973.

11. Lesieutre, D.J., Dillenius, M.F.E., and Whittaker, C.H., "Program SUBSAL and Modified Subsonic Store Separation Program for Calculating NASTRAN Forces Acting on Missiles Attached to Subsonic Aircraft", NAWCWPNS TM 7319, May 1992.
12. Dillenius, M.F.E., Perkins, S.C., Jr., and Lesieutre, D.J., "Modified NWCDM--NSTRN and Supersonic Store Separation Programs for Calculating NASTRAN Forces Acting on Missiles Attached to Supersonic Aircraft", Naval Air Warfare Center Report NWC TP6834, September 1987.
13. Dillenius, M.F.E., Canning, T.N., Lesieutre, T.O., and McIntosh, S.C., "Aeroelastic Tailoring Procedure to Optimize Missile Fin Center of Pressure Location", AIAA Paper 92-0080, January 1992.
14. Hegedus, M.C. and Dillenius, M.F.E., "VTXCHN: Prediction Method For Subsonic Aerodynamics and Vortex Formation on Smooth and Chined Forebodies at High Alpha", AIAA Paper 97-0041, January 1997.
15. Fiacco, A.V. and McCormick, G.P., "Nonlinear Programming", New York, John Wiley & Sons, Inc., 1968.
16. Carmichael, R.L. and Woodward, F.A., "An Integrated Approach to the Analysis and Design of Wings and Wing-Body Combinations in Supersonic Flow", NASA TN D-3685, October 1966.
17. Dillenius, M.F.E., "Program LRCDM2, Improved Aerodynamic Prediction Program for Supersonic Canard-Tail Missiles With Axisymmetric Bodies", NASA CR 3883, April 1985.
18. Polhamus, E.C., "Prediction of Vortex-Lift Characteristics Based on a Leading-Edge Suction Analogy", J.Aircraft, 8, April 1971, pp 193-199.
19. Dillenius, M.F.E. and Perkins, S.C., Jr., "Computer Program AMICDM, Aerodynamic Prediction Program for Supersonic Army Type Missile Configurations with Axisymmetric Bodies", U.S. Army Missile Command Technical Report RD-CR-84-15, June 1984.
20. Przemieniecki, J.S., "Theory of Matrix Structural Analysis", New York, McGraw-Hill, 1968.
21. McIntosh, S.C., "Optimization and Tailoring of Lifting Surfaces with Displacement, Frequency, and Flutter Performance Requirements", NWC TP 6648, April 1987.
22. Buning, P.G., Chan, W.M., et al., "OVERFLOW User's Manual - Version 1.6be" unpublished NASA document, February 1996.
23. Perkins, S.C., Jr., Wardlaw, A.W., Jr., Priolo, F., and Baltakis, F., "NEARZEUS User's Manual, Vol. I: Operational Instructions, Vol. II: Sample Cases, Vol. III: Boundary Layer Code ZEUSBL", NEAR TR 459, May 1994.

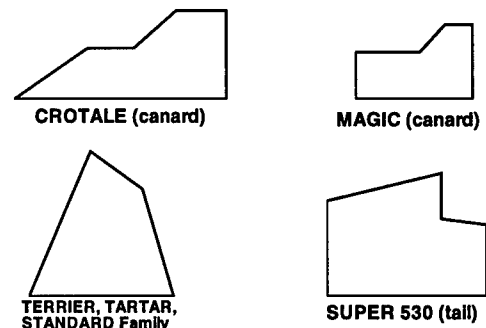


Figure 1.- Control surfaces with limited center-of-pressure shifts.⁴

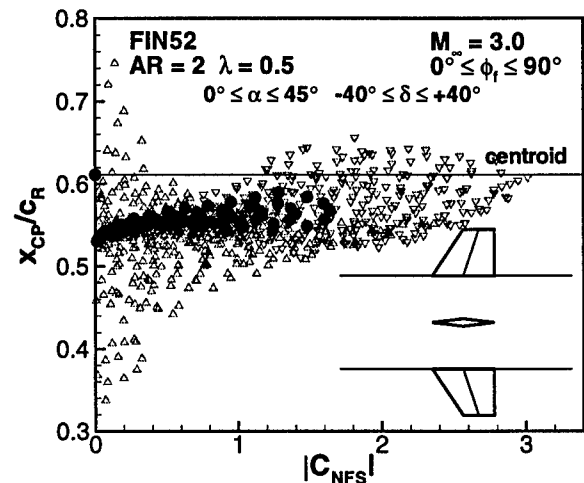


Figure 3.- Triservice FIN42, x_{CP}/c_R as function of C_{NFS} at $M_\infty = 3.0$ for $0^\circ \leq \alpha \leq 45^\circ$, $0^\circ \leq \phi_f \leq 90^\circ$ and $-40^\circ \leq \delta \leq +40^\circ$ (solid symbols are $\delta = 0^\circ$).

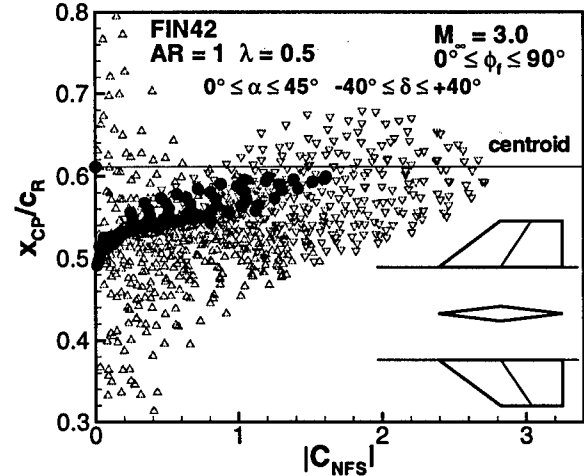


Figure 3.- Triservice FIN42, x_{CP}/c_R as function of C_{NFS} at $M_\infty = 3.0$ for $0^\circ \leq \alpha \leq 45^\circ$, $0^\circ \leq \phi_f \leq 90^\circ$ and $-40^\circ \leq \delta \leq +40^\circ$ (solid symbols are $\delta = 0^\circ$).

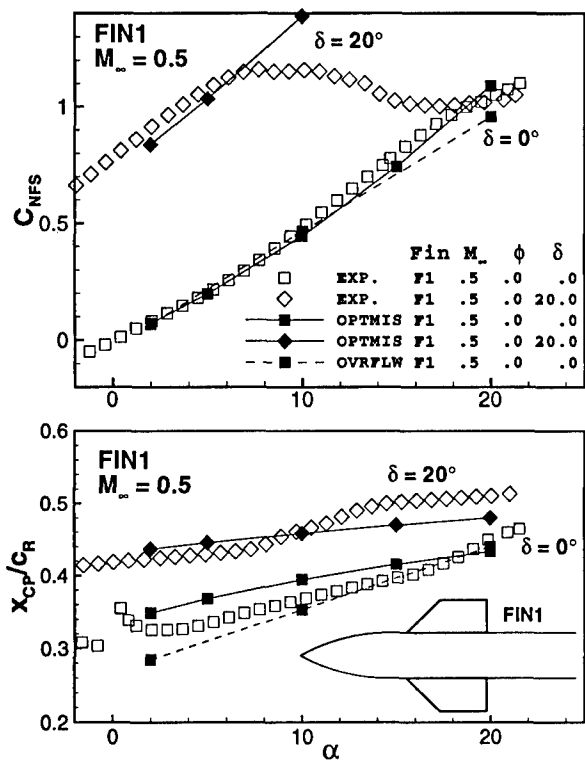


Figure 4.- Comparison of measured and predicted C_{NFS} and x_{CP}/c_R for FIN1 at $M_\infty = 0.5$.

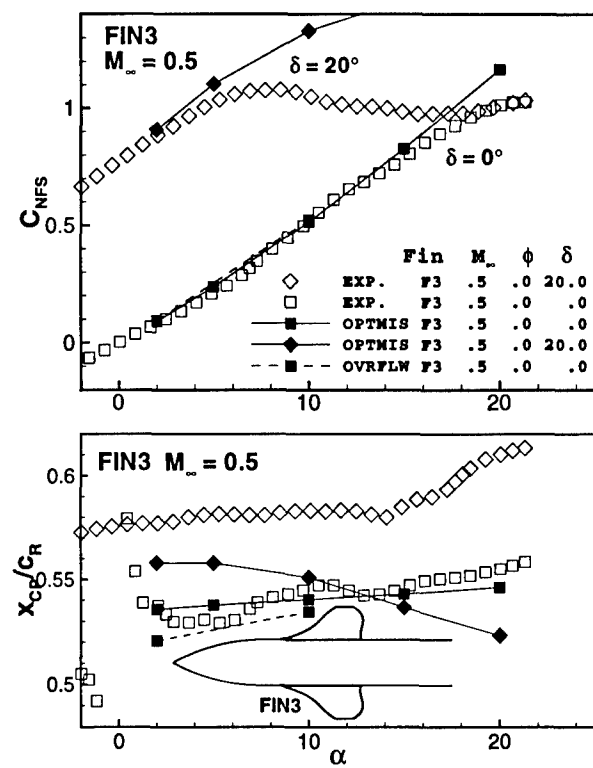


Figure 6.- Comparison of measured and predicted C_{NFS} and x_{CP}/c_R for FIN3 at $M_\infty = 0.5$.

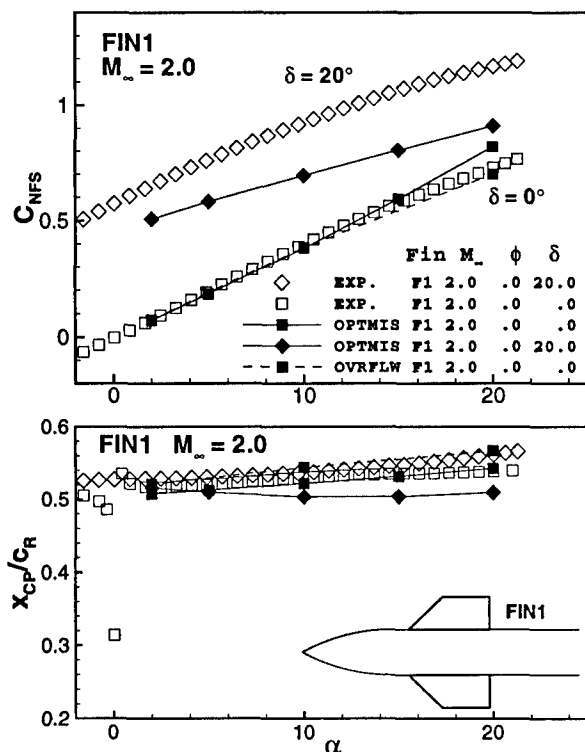


Figure 5.- Comparison of measured and predicted C_{NFS} and x_{CP}/c_R for FIN1 at $M_\infty = 2.0$.

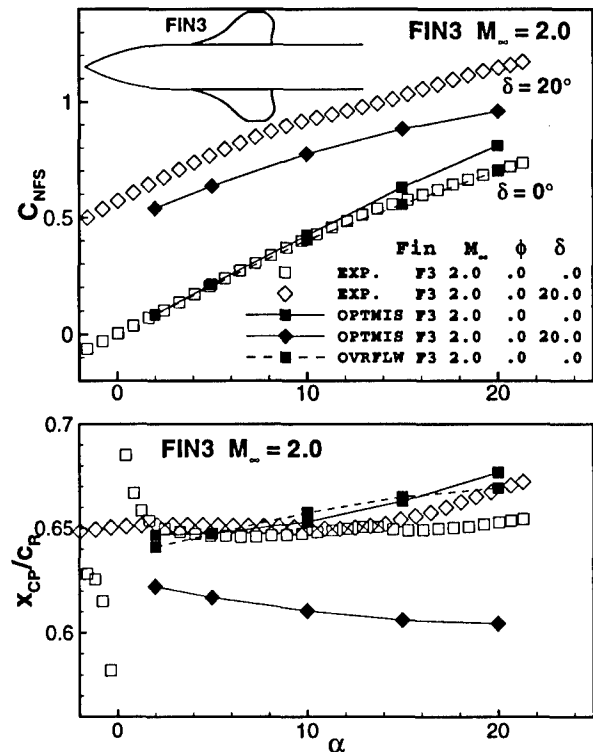
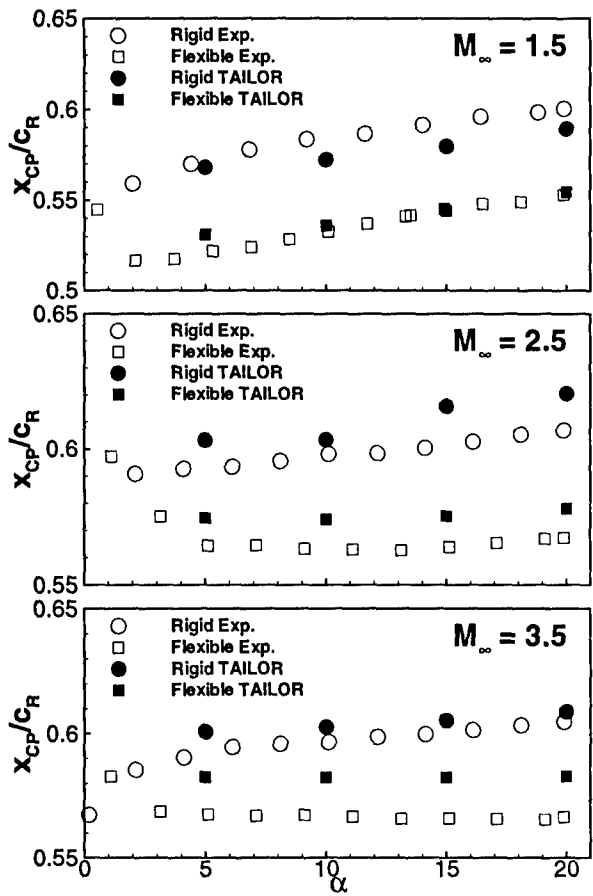


Figure 7.- Comparison of measured and predicted C_{NFS} and x_{CP}/c_R for FIN3 at $M_\infty = 2.0$.



(c) Variation of x_{CP}/c_R with angle of attack.
Figure 11.- Concluded.

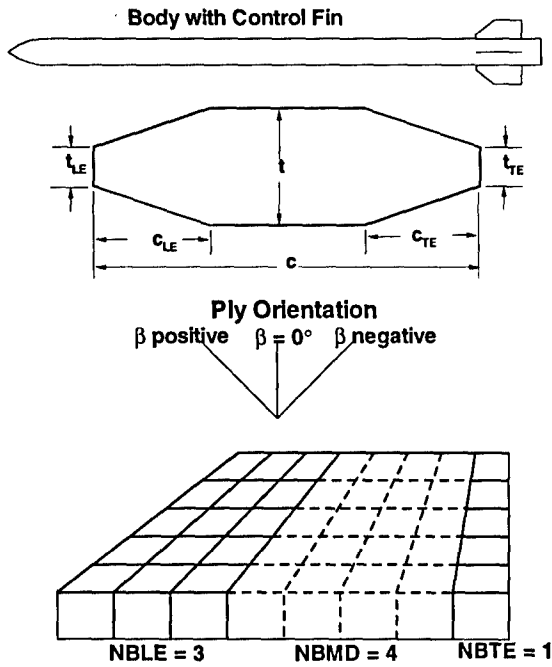


Figure 12.- Configuration and design variables used for the aeroelastic fin design study.

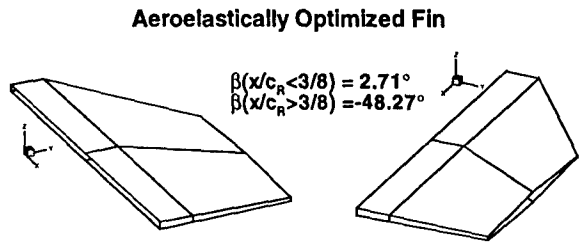


Figure 13.- Optimized aeroelastic fin thickness.

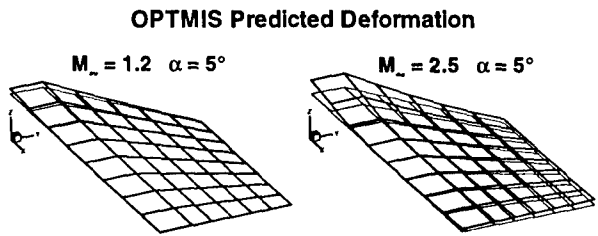


Figure 14.- Predicted aeroelastic deformations.

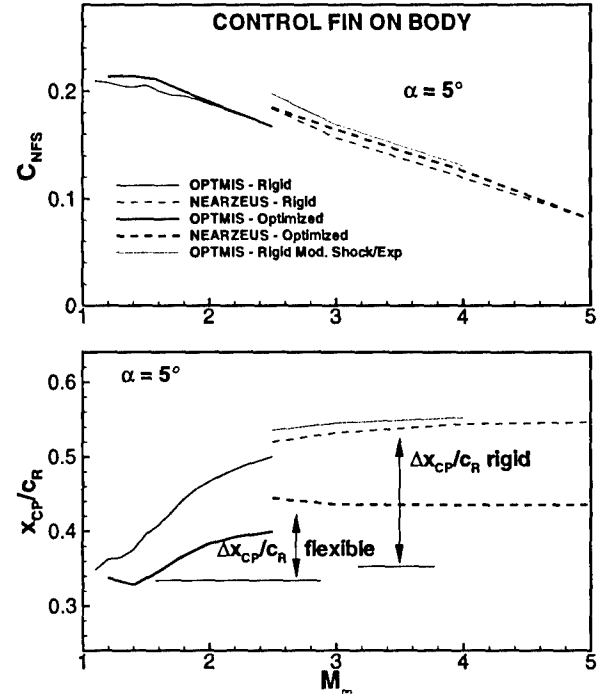


Figure 15.- Comparison of rigid and flexible fin performance.

Aeroelastic/Aeroservoelastic Tailoring for Hinge Moment Minimization of Missile Fins

P.C. Chen, D. Sarhaddi, D.D. Liu
ZONA Technology, Inc.
7430 E. Stetson Drive, Ste. 205
Scottsdale, Arizona 85251, USA

M. Ratwani
R-Tec Inc., Rolling Hill Estate, California 90274, USA

T. Minahen
Raytheon, Tucson, Arizona 85734, USA

Abstract

This paper reports our recent development of a new missile-fin design methodology. In particular, we present the results of a feasibility study on the minimization of the hinge moment of a generic tactical missile (GTM) fin by passive profile means. The final goal is aimed at achieving a significant reduction in the feasible minimum hinge moment so that a sizable payoff in cost and performance of the whole missile system can be achieved. With the selection of a generic missile fin, a global design methodology involving three design loops has been successfully developed. Aeroelastic tailoring of a composite missile fin has been thoroughly conducted by extensively applying ASTROS optimization in an inner design loop. ASTROS* is an enhanced version of a MDO software ASTROS (Automated STRuctural Optimization System) with the ZAERO module, a unified unsteady/steady aerodynamic module covering subsonic to hypersonic Mach numbers. With an optimal forward shift of the hingeline, the present aeroelastic tailored design has achieved over 25% improvement in the hinge moment reduction, while satisfying all constraints imposed by the critical flight conditions. The optimized ply thickness distribution shows promising producibility for composite fin manufacturing, and an affordable manufacturing cost can be achieved.*

INTRODUCTION

Current tactical missiles are required to achieve high maneuverability, agility and extended range under a wide scope of critical flight conditions. Major design goals amount to the minimization of the control fin hinge moment while maintaining the aerodynamic normal force under high-g maneuvering. Meanwhile, the affordability in manufacturing cost for the control-fin is another important design concern. A question of feasibility arises as to whether both technical and cost requirements can be met with today's technology.

An innovative research work has recently attempted to study this feasibility to some extent, but no definite methodology was offered to reach the design goal (Ref 1). With the advent of existing technologies in composite structures and in multidisciplinary design and optimization (MDO), the missile control-fin problem is subject to a renewed investigation. The feasibility question is to be answered by an entirely different and new approach with a proven engineering tool.

Our approach is to apply aeroelastic tailoring to a composite fin structure by passive profile control means. Aeroelastic tailoring technology is not new for the wing design of advanced aircraft (e.g. X-29, HiMAT). But such a technology might not have been applied to the missile fin design. Aeroelastic tailoring usually provides desirable stiffness to a composite structure that allows ample design freedom. Thus the resulting flexibility under airload is expected to shift the aerodynamic center in a controllable manner in favor of a reduction in the fin hinge moment. A feasible minimum hinge moment is defined as the minimum required actuator torque to overcome the largest hinge moments among all critical flight conditions considered. However, the crux of the matter lies in how to achieve a significant reduction in the feasible minimum hinge moment so that a sizable payoff in cost and performance

of the total missile system can be ascertained. Recent research suggests that active profile control by means of adaptive structure could be a promising alternative. But this approach might complicate the final trade-off with additional considerations in power required, control system complexity and composite/piezo structure manufacturing.

To achieve a significant reduction of the fin hinge moment by either passive or active means is formally an optimization problem. An optimal solution can only be found in a multi-dimensional design space by a MDO software system. The final structural design must satisfy all physical design requirements in strength, flutter, maneuverability and control system response. Meanwhile this design must also meet the requirement of producibility and affordability. Together these requirements call for (1) selection of composite materials sustaining high temperature; (2) innovative structural design concept for low cost manufacturing; and (3) a proven engineering design software which includes all disciplines that impact the structural design. A design strategy for the controlled fin is formulated in which an outer loop governs the parametric study in terms of fin planform and profile selection and a middle loop for optimal hingeline position. In the inner loop lies the core optimizer ASTROS*, whose design variables are the ply thicknesses. ASTROS* is an enhanced version of ASTROS (Automated STRuctural Optimization System, Ref 2), an acclaimed MDO software developed under the Air Force sponsorship. Under contractual support by Wright Lab (AF/STTR Phase I/II), ZONA Technology has further enhanced the software system through the integration of the ZAERO (ZONA Aerodynamics) module and the ASE (Aeroservoelastic) module into the ASTROS* software (Refs 3, 4, 5). With this ideally suitable proven tool at hand, we are therefore in a unique position to perform the fin design project.

Under the Navy/NAWC contractual support, the ZONA team has achieved the primary objective in that a new fin-design methodology involving three design loops has been developed and applied to demonstrate the feasibility of missile-fin hinge moment minimization by passive profile means. Aeroelastic tailoring of a polyimide composite GTM fin has been successfully conducted by extensively applying ASTROS* in the inner design loop. With the optimal forward shift of the hingeline, ZONA has thus far obtained over 25% improvement in hinge moment reduction for the GTM fin. A trade-off design point is selected where optimized ply thickness distribution obtained show promising features for composite manufacturing. It is estimated that an affordable manufacturing cost for the composite GTM fin can be achieved.

OVERALL DESIGN STRATEGY

It is important to clarify the role of the fin hinge moment and its possible minimization in an optimization cycle of ASTROS. For a fixed fin geometry, the fin hinge moment is a function of the aerodynamic normal force and aerodynamic distributed load, where the former is a performance constraint and the latter is a function of flight conditions, such as Mach number, AOA, etc. In principle, for a given set of critical flight conditions, the minimum hinge moment is dependent upon planform shape, hinge line position and stiffness distribution of the fin. To identify the true minimum fin hinge moment requires that ASTROS be recast into a multi-level optimization formulation. This would amount to a major modification of the existing ASTROS methodology, a formidable task that is outside the scope of the present work. However, by adopting the existing ASTROS methodology, it is possible to formulate a global design-loop strategy to search for a feasible minimum hinge moment for all given critical flight conditions. This strategy is shown in Fig 1 and can be described as follows.

A global design loop can be established where the outer loop is a parametric study of planform and profile shapes and the middle loop is the search for a hingeline position which yields the minimum hinge moment. The inner optimization loop is essentially the ASTROS* software for the application to the fin structural design by means of aeroelastic tailoring. The implementation of the global design-loop procedure can be demonstrated with an optimization-cycle example. With a baseline GTM fin configuration provided (outer loop input fixed), we will select a set of candidate hingeline positions in the middle loop. For a given hingeline position, ASTROS* optimization will satisfy all design constraints including those imposed by all the critical flight conditions. In the end, it results in a optimized design solution, including composite ply thicknesses with set orientations and a minimized structural weight (the objective function).

ZAERO AND ASTROS: ASTROS*

ASTROS provides a unique automated capability to tailor composite materials for requisite strength and stiffness for minimum structural weight. For structural analysis, ASTROS has both statics and normal modes capabilities, and is based on the NASTRAN style input format for its finite element methodology. For optimization, ASTROS adopts Vanderplatts method of feasible directions (Ref 6). Other analysis modules in ASTROS include the sensitivity analysis, aeroelastic analysis, control response, and aerodynamic modules.

ZONA AERodynamic (ZAERO) Module

Under contracts with Wright Laboratory, ZONA has further developed ASTROS* by the integration of a unified steady/unsteady, wing-body aerodynamic module for all Mach numbers (the ZAERO Module) and an aeroservoelastic Module (ASE Module) into the system (Ref 3). Thus ASTROS* is named after the integration of ASTROS with the ZAERO module and ASTROServo is named after the integration of ASTROS* with the ASE module. Because of the stringent requirements of the present design problem, ASTROS* is proposed as a viable engineering tool in searching for a feasible solution to maximize the hinge moment reduction. In fact, ASTROS* forms the base of our hinge moment minimization strategy.

The ZAERO module consists of four major steady/unsteady aerodynamics codes that jointly cover the complete domain of all Mach number ranges, namely ZONA6, ZONA7, ZTAIC and ZONA7U (Refs 7,8/9,10,11/12, respectively). As can be seen in Fig 1, the aerodynamic modules currently integrated into MSC/NASTRAN and ASTROS only have the purely subsonic and supersonic capabilities for lifting surface types of configurations. By contrast, the ZAERO module serves as a unified aerodynamic tool which is capable of generating steady/unsteady aerodynamic data of wing-body configurations throughout the complete Mach number ranges by means of a unified AIC (Aerodynamic Influence Coefficient) approach, called UAIC^{5,11,13,14,15}.

For a description of each code contained in the ZAERO module, one is referred to Figs 2,3,4, 5, 6 and 7.

Fig 2 presents the integrated ASTROS/ZAERO (or ASTROS*) program architecture. The aerodynamic geometric parameters for the ZAERO module are computed by a unified Aerodynamic Geometry Module (AGM) (see Fig 7).

The ZAERO computation is triggered by a new bulk data entry MKAEROZ which defines the flight conditions and reduced frequencies as well as the mean flow conditions. The ZAERO module computes the UAIC matrices, gust force vectors, control surface aerodynamic force vectors and steady aerodynamic force vectors of trim parameters. Database entities generated by AGM, 3-D spline and ZAERO modules are computed once and for all in the ASTROS preface phase and will not be recomputed in the analysis/optimization loop.

The ASE Module in ASTROS* will facilitate the inclusion of multi-input, multi-output (MIMO) control system effects on the dynamic stability and response in the ASTROS capability in multidisciplinary analysis and design/optimization.

For the functionality, other features and general flow chart of the ASE module in ASTROServo, one is referred to Refs 13,14,15.

ASTROS* OPTIMIZATION FOR FIN DESIGN

To achieve an aeroelastically tailored composite fin with feasible minimum hinge moment, it is required to formulate this engineering problem in terms of an ASTROS* optimization paradigm. In so doing, the

objective function, design variables and constraints of ASTROS* need to be defined according to their corresponding physical parameters in the present problem.

Objective Function

The structure weight is always a primary design objective of flight vehicles. Here, the fin structure weight is selected as the objective function to be minimized. This minimal structure weight has a direct impact on the cost of manufacturing the fin.

Design Variables

Shape type design variables (DESVARs) are utilized for the skins. Shape linking enables polynomial thickness distributions over a group of elements. Constant, linear spanwise, linear chordwise, quadratic chordwise and quadratic spanwise ASTROS SHAPE's will be computed for the upper and lower fin skin element groups. DESVARs are assigned for each of the four ply orientations, with separate sets for the upper and lower skins. Interpretation of results generally suggests adding design variables to capture beneficial effects. The design authority provided by the DESVARs must encompass some combination of design variables capable of achieving the objective. Novel or unexpected solutions are what design optimization can uncover as a fundamental part of the process. If the only results that emerge are the conventional ones, then no breakthroughs would be likely. Creative selection of additional DESVARs is crucial to the solution.

Constraints

Notched strain allowables for the fin skin material and actuator torque limits as well as flutter at selected critical flight conditions are the primary quantities constraining the design optimization. Secondary constraints for minimum gage are also included.

TRIM Condition in ASTROS for Maneuverability Constraints

In order to satisfy the performance/maneuverability constraint, the aerodynamic normal force and trim condition requirement must be met. As a prerequisite measure, ASTROS always ensures self-trim of a vehicle at any given flight condition before its execution of a design/analysis procedure.

Generally, a trim analysis is performed by solving the following static aeroelastic equation

$$([K] - [AIC])\{u\} + [M]\{\ddot{u}\} = [P]\{\delta\} \quad (1)$$

where $[K]$ and $[M]$ are the stiffness and mass matrices, respectively

$\{u\}$ is the structural displacement

$[P]$ is the unit aerodynamic loads matrix

$[AIC]$ is the static aerodynamic influence

coefficient matrix provided by ZAERO

and $\{\delta\}$ is a solution vector of trim parameter. It can be an angle of attack, control surface deflection angle, yaw angle, roll rate, pitch rate, or yaw rate.

For given prescribed flight conditions (e.g. given normal and pitch accelerations) Eq (1) is solved for the trim parameters δ and the structural displacements u . The latter solution then yields the structural response in terms of stress, strain and integrated loads (hinge moments). Note that the above ASTROS formulation is most general, in that Eq (1) solves the trim vector for a flexible body with motion in six degrees of freedom. The formulation by Schindel and Lam (Ref 16) is a special case of the above which only solves for the longitudinal trim of a rigid body.

All above constraints will be imposed simultaneously in a single ASTROS optimization cycle; therefore, if a optimal solution is found, the resultant designed structure will meet all practical design requirements at all critical flight conditions.

ASTROS* MODELING AND CRITICAL FLIGHT CONDITIONS

An ASTROS structural model and a ZAERO steady/unsteady aerodynamic model of a right half of the Generic Tactical Missile was constructed with emphasis placed on the aft fin (Fig 9a and Fig 9b). The finite element model was developed with an intent for design optimization of a feasible minimum hinge moment while satisfying all design constraints.

Structural Model

The fin construction has a finer mesh than the rest of the missile with enough detail to capture the design intent and accurately address aeroelasticity, but small enough to facilitate quick changes as the design evolved (Fig 10). The geometry of the fin has faceted surfaces following the specification of the GTM design. Each facet was then meshed with QUAD4's and blended with the neighboring facets with TRIA3's as necessary. Modeling of the fin substructure has the root rib/spar/spindle built up from QUAD4 plates and the honeycomb core with IHEX1 bricks filled in one deep between the facesheet elements.

For clarification of the functionality of the actuator model in terms of the FEM model fin substructure, a finite element substructural model and its corresponding mechanical model are presented in Figs 11 and 12, respectively.

In Fig 11, a connection rod (CONROD) connected to the top of the spindle at the root rib provides actuator torque tracking and control (Actuator (A)). A "Boot Strap" CONROD connected at the centerline of the spindle at the root rib reacts the applied load from the actuator resulting in pure torque within the aft fin assembly (Boot Strap (B)). The Bearing (BG) is a single GRID point that is attached to a corner point of four CQUAD4 plate elements located within the missile body wall. Since the CQUAD4 elements possess no stiffness in the in-plane rotational direction, the GRID is free to rotate about the basic system y-axis.

Fig 12 shows the equivalent mechanical model to the finite element model. The Boot Strap (B) connects the Spindle (S) to a constrained support within the missile body. Actuator (A) is connected from the constrained support to the Spindle Arm (SA) (exaggerated moment arm). Both the Actuator (A) and Boot Strap (B) are pinned at free-joint ends (i.e. free rotating connections) thus restricting the member forces to tension and compression. The spindle exits the missile wall through the Bearing (BG).

Scenario Cases: Six Trim Flight Conditions

Two scenario cases to be used in the ASTROS* optimization were chosen to represent the critical flight conditions that could generate the largest hinge moments (i.e. critical hinge moments). These critical flight conditions serve ASTROS* as additional constraints to the other ordinary constraints. Thus, a typical case for fin design utilizing ASTROS* optimization case is properly formulated. Fig 13 presents the scenario cases in consideration. Scenario A is an abrupt pull-up maneuver where the pitch acceleration \dot{q} is constant. The fin provides a download to achieve the imposed \dot{q} . The missile flight is at 1-g loading. Scenario B is a sustained turn at 25-g loading where the pitch rate q is held constant. This maneuver occurs at a high angle-of-attack (AOA) in a sustained turn to maintain the 25-g loading. The force balance for this scenario is given by

$$F_{\alpha} - F_{\delta} - F_g = 0 \quad (2)$$

where

F_{α} = force on the missile due to flight path AOA

F_{δ} = force on the missile fin

F_g = force due to centrifugal acceleration

Three Mach numbers were considered for both scenario cases giving a total of six trim flight conditions used in the ASTROS* optimization procedure (Table 1). Trim flight conditions for the supersonic Mach number cases (at Mach 3.0 and 4.0) employed dynamic pressures at 30,000 feet altitude. The subsonic trim flight conditions (at Mach 0.8) employed dynamic pressures at sea level. The angle-of-attack (ALPHA) and fin deflection (ELEV1) are considered as trim variables and are a part of the computed solution in the ASTROS* aeroelastic trim analysis.

The critical flight conditions for flutter constraints were defined at four Mach numbers ($M=0.8, 0.9, 1.2$ and 2.0) and at sea level. The first ten structural modes are used in the flutter analysis.

ASTROS* OPTIMIZATION

Fig 14 shows a resulting deformed missile fin under a given airload as designed by the present aeroelastic-tailoring procedure provided by ASTROS*. The dashed-line fin represents an aeroelastically-tailored (AET) GTM fin at no airload condition (wind-off), whereas the solid-lined fin represents an AET/GTM fin at a given airload (wind-on). Maximum hinge moment reduction is achieved by means of the present AET design procedure in combination with a proper forward shift of the hingeline (spindle) position. In fact, to achieve a properly shifted hingeline position is primarily the objective of the middle design loop layer (i.e. Hingeline Position Loop) of the global-design-loop strategy (see Fig 1).

Aeroelastic Tailoring

Aeroelastic tailoring can only be achieved through the use of anisotropic materials, such as composites. For

the present case, the ASTROS* optimization tends to result in a fin design with higher stiffness along the fin spanwise direction (to suppress spanwise bending deformation and the bending moment induced stresses) and with lower stiffness along the chordwise direction (to encourage chordwise bending and alter the local angle of attack thus moving the aerodynamic center).

To conveniently assess the reduction in hinge moment by the AET procedure requires the introduction of a baseline configuration. Here the baseline configuration (or baseline) is a rigid metallic GTM fin configuration with hingeline located at the midchord. Therefore, **the critical hinge moment** (i.e. the largest hinge moment resulting from all critical flight conditions) for this configuration should occur at subsonic speeds where the aerodynamic center (A.C.) is located around quarter chord. An AET fin is an AET/GTM fin with exact exterior dimensions of the baseline configuration. Since the AET procedure can only move the A.C. forward at any airspeed, an AET fin at subsonic speeds with hingeline located at midchord will result in a larger hinge moment than that of a baseline configuration. In this case, one would resort to moving the hingeline position forward in order to achieve a substantial hinge moment reduction at subsonic speed. The increase of hinge moment at supersonic speed due to the forward shift of hingeline position can be suppressed by the AET procedure. An optimized hingeline position can be determined by the combined procedures of the inner and the middle design loop procedures. The hinge moment reduction from the baseline hinge moment at this optimized hingeline position should be a maximum one (called **the maximum hinge moment reduction**). And this location should lie somewhere between the subsonic A.C. location (near quarter chord) and the supersonic A.C. location (near midchord)[†]. This hingeline position relative to the midchord is defined here as h_0 . The effect of h_0 on the critical hinge moment is described next.

Impact of Hinge Line Positions (h_0)

As an example to demonstrate the impact of hingeline position according to ASTROS*, Fig 15 shows the resulting A.C. locations of both the rigid and tailored fins due to two selected Mach numbers ($M=0.8$ and 3.0) at abrupt pull-up maneuvers with the hingeline placed at the baseline position $h_0=0"$ and at a forward position $h_0=1.45"$.

The resulting hinge moments of Fig 15 can be measured directly by their moment arms (indicated by ΔL). Simple measurements quickly reveal the data (as shown in Table 2).

A more comprehensive study consisting of six critical flight conditions of Scenarios A and B at three Mach numbers ($M=0.9, 3.0$ and 4.0) can be found in Ref 17. For the six critical flight conditions considered, the $h_0=1.45"$ case by the ASTROS*/AET procedure ends up with a considerable increase of hinge moment at $M=4.0$ due to an excessive forward shift in the hingeline position. ASTROS* results show that the AET procedure would have to largely reduce the stiffness at the aft fin portion, in order to sufficiently reduce the hinge moment at $M=4.0$. Such a low stiffness structure would fail if the fin were under the airloads due to the six critical flight condition cases, i.e. its stress level exceeds the strength requirement of the composite material properties.

[†] Note that no effort is made to distinguish the difference between C.P. and A.C. in the present context. However, knowingly $x_{C.P.} = C_M/C_L$, whereas $x_{A.C.} = C_{M\alpha}/C_{L\alpha}$

The middle design loop selects the cases of $h_0=0"$ and $h_0=1.45"$. By the inner design loop procedure, the optimized solution for the former case yields a nearly rigid fin structure almost waiving the AET procedure, whereas that of the latter case yields a low-stiffness structure, through an excessive AET procedure. It appears that these two cases result in two extreme stiffness designs of the fin. This observation then prompts the selection of a mid-point hingeline position (i.e. $h_0=0.725"$) as a potential compromised candidate to achieve the maximum hinge moment reduction.

Search for Feasible Minimum Hinge Moment

For a given hingeline position, the inner design loop procedure is executed for the feasible minimum hinge moment search. A hinge moment reduction is imposed as a constraint in a ASTROS* optimization computation, (via the design stress constraint DCONVMM). According to the search procedure described previously, this moment reduction is sequentially increased until a final design point is reached, where ASTROS* yields the ultimate solution before ceasing to satisfy all design constraints. This ultimate ASTROS* solution is the feasible minimum hinge moment. In other words, the largest hinge moment reduction achievable resulting from the last ASTROS* solution is defined as the "feasible minimum hinge moment." Its corresponding hinge moment value and percentage reduction is shown in Table 3 and in Fig 16, respectively. Here, the hinge moment reduction is defined as the tailored solution normalized by the rigid solution. It is seen that a 25% hinge moment reduction is achieved at a forward hingeline position of $h_0=0.725"$.

Iterative History of Hinge Moment

Fig 17 presents the hinge moments of the six flight conditions over design iteration steps for the case of $h_0=0.725"$, where case (f) is found to be the most critical.

As can be seen in Fig 17f, the optimized solution converges and the procedure terminates at the 19th iteration. By a converged solution, it is meant that ASTROS* has resulted in an optimized solution which has achieved at best a critical hinge moment reduction while satisfying all constraints.

A Trade-Off Design

ASTROS* also provides the optimized weight at each iteration. Fig 18 presents the resulting weight solutions together with the optimized hinge moment history (Fig 17f). It is seen that the minimum fin weight does not coincide with the critical hinge moment.

The 10th iteration appears to be a plausible design point solution for the current configuration yielding the best combination of minimum weight and hinge moment. This design point is selected because further reduction in hinge moment from the 10th to 19th iterations (less than 1%) does not justify a drastic increase (over 30%) in the fin weight.

A Flutter-Free Design

The 10th iteration flutter results for the first four modes at sea level density are computed by ZAERO in ASTROS* (see Ref 18). All damping curves are observed to be stable for all Mach numbers considered

showing that there is no flutter problem for the present GTM fin design.

Ply Thickness and Drop-Off

Finally, the ply thickness distributions for the 10th iteration along with the total thickness (i.e. sum of individual ply thicknesses) are presented in Fig 19. The same ply thickness distributions with a superimposed grid used to generate the structural drawings are presented in Ref 18. The total maximum thickness is 0.1076" near the hingeline position and drops off smoothly from the root to the tip with a minimum thickness of 0.0135"; therefore, it is believed that the designed ply thicknesses are reasonable and producible.

CONCLUSIONS

A new fin-design/analysis methodology involving three design loops has been developed and applied to demonstrate the feasibility of missile-fin hinge moment minimization by passive profile means. Aeroelastic tailoring of a polyimide composite fin for a Generic Tactical Missile (GTM) has been successfully conducted by extensively applying ASTROS* in the inner design loop. With the optimal forward shift of the hingeline, we have thus far obtained over 25% improvement in hinge moment reduction for the GTM fin. A trade-off design point is selected where optimized ply thickness distribution obtained show promising features for composite manufacturing. Our cost analysis shows that such a fin design is producible and affordable.

ASTROS* has achieved a new fin design solution while satisfying all realistic constraints for structural integrity. But much work remains to be done for further development of a comprehensive design tool for the next generation missiles and missile fins. This prompts the further enhancement of the capability of the present fin design/analysis methodology in the following areas:

- inclusion of the design loop with planform and profile optimization
- aerothermoelasticity/aerothermoservoelasticity accounting for high temperature effect due to hypersonic aerodynamic-heating
- hypersonic steady/unsteady aerodynamics for missile bodies in ZAERO

Other pending tasks include:

- add in a CFD-validation procedure in the design/analysis loop.
- wind tunnel and/or flight testing of the present composite fin design for result validation
- study on the impact of the hinge moment reduction on the actuator size and power requirement
- studies of cost/performance benefit in terms of total missile system.

ACKNOWLEDGMENT

The present work is supported in part by a Navy (NAWC/WPNS) SBIR Phase I contract. We thank Dr. Craig Porter and Dr. Frank MacDonald of NAWC/Navy for advice and valuable discussion of this project. In particular, Dr. Porter's initiation of the passive control concept leading to the present design is much appreciated. Our discussion with Dr. Frank Moore of NSWC/Navy and his providing ZONA with the AP-95 code is gratefully acknowledged.

References

1. Dillenius, M., Canning, T., McIntosh, S., and Lesieutre, T., "Aeroelastic Tailoring Procedure to Optimize Missile Fin Center of Pressure Location," paper AIAA 92-0080 presented at the 30th Aerospace Sciences Meeting & Exhibit, Reno, NV, Jan 6-9, 1992.
2. Johnson, E.H. and Venkayya, V.B., "Automated Structural Optimization System (ASTROS), Theoretical Manual," AFWAL-TR-88-3028, Vol. 1, December 1988.
3. Chen, P.C., Liu, D.D., Sarhaddi, D., Striz, A.G., Neill, D.J., and Karpel, M., "Enhancement of the Aeroservoelastic Capability in ASTROS," STTR Phase I Final Report, WL-TR-96-3119, Sept. 1996.
4. Chen, P.C., Sarhaddi, D., Liu, D.D., Karpel, M., "A Unified Aerodynamic-Influence-Coefficient Approach for Aeroelastic/Aeroservoelastic and MDO Applications," AIAA 97-1181, AIAA/ASME/ASCE/AHS 38th Structures, Structural Dynamics and Materials Conference, Kissimmee, FL, April 7-10, 1997.
5. Chen, P.C., Sarhaddi, D. and Liu, D.D., "A Unified Unsteady Aerodynamic Module for Aeroelastic and MDO Application," AGARD Structures and Material Panel (SMP)-Workshop 2 "Numerical Unsteady Aerodynamics and Aeroelastic Simulation," Alborg, Denmark, Oct. 13-17, 1997.
6. Vanderplatts, G., "MICRO-DOT User's Manual Version 1.0," Engineering Design Optimization Inc., Santa Barbara, CA, 1985.
7. Chen, P.C., Lee, H.W. and Liu, D.D., "Unsteady Subsonic Aerodynamics for Bodies and Wings with External Stores Including Wake Effect," *Journal of Aircraft*, Vol. 30, No. 5, Sept.-Oct. 1993, pp. 618-628.
8. Chen, P.C. and Liu, D.D., "Unsteady Supersonic Computations of Arbitrary Wing-Body Configurations Including External Stores," *Journal of Aircraft*, Vol. 22, No. 2, pp. 108-116.
9. Chen, P.C. and Liu, D.D., "A Harmonic Gradient Method for Unsteady Supersonic Flow Calculations," *Journal of Aircraft*, Vol. 22, No. 5, May 1985, pp. 371-379.
10. Chen, P.C., Sarhaddi, D. and Liu, D.D., "Transonic AIC Approach for Aeroelastic and MDO Applications," presented at the Euromech Colloquium 349 at DLR, Göttingen, Germany, Sept. 16-18, 1996.
11. Liu, D.D., Chen, P.C., Yao, Z.X. and Sarhaddi, D., "Recent Advances in Lifting Surface Methods," *The Aeronautical Journal*, Royal Aeronautical Society, Vol. 100, No. 998, Oct. 1996, pp. 327-339.
12. Liu, D.D., Yao, Z.X., Sarhaddi, D. and Chavez, F., "From Piston Theory to a Unified Hypersonic-Supersonic Lifting Surface Method," ICAS Paper 94-2.8.4, 1994, *Journal of Aircraft*, Vol. 34, No. 3, May-June 1997.
13. Chen, P.C., Liu, D.D., Sarhaddi, D., Striz, A.G., Neill, D.J. and Karpel, M., "Enhancement of the Aeroservoelastic Capability in ASTROS," STTR Phase I Final Report, WL-TR-96-3119, Sept 1996.
14. Chen, P.C., Sarhaddi, D., Liu, D.D. and Karpel, M., "A Unified AIC Approach for Aeroelastic/Aeroservoelastic and MDO Applications," AIAA Paper No. 97-1181CP.
15. Chen, P.C., Sarhaddi, D., Liu, D.D., Karpel, M., Striz, A.G. and Jung, S.Y., "A Unified Unsteady Aerodynamic Module for Aeroelastic, Aeroservoelastic and MDO Applications," International Forum on Aeroelasticity and Structural Dynamics, Rome, Italy, June 1997.
16. Schindel, L.H. and Lam, L., "Payoffs of Improved Missile Control Effectiveness," AIAA-95-1898-CP, 1995.
17. Chen, P.C., Sarhaddi, D., Liu, D.D., Ratwani, M., Minahan, T., "Aeroelastic/Aeroservoelastic Tailoring for Hinge Moment Minimization of Missile Fins," SBIR Phase I Final Report (N68936-97-C-0151), Dec. 1998.

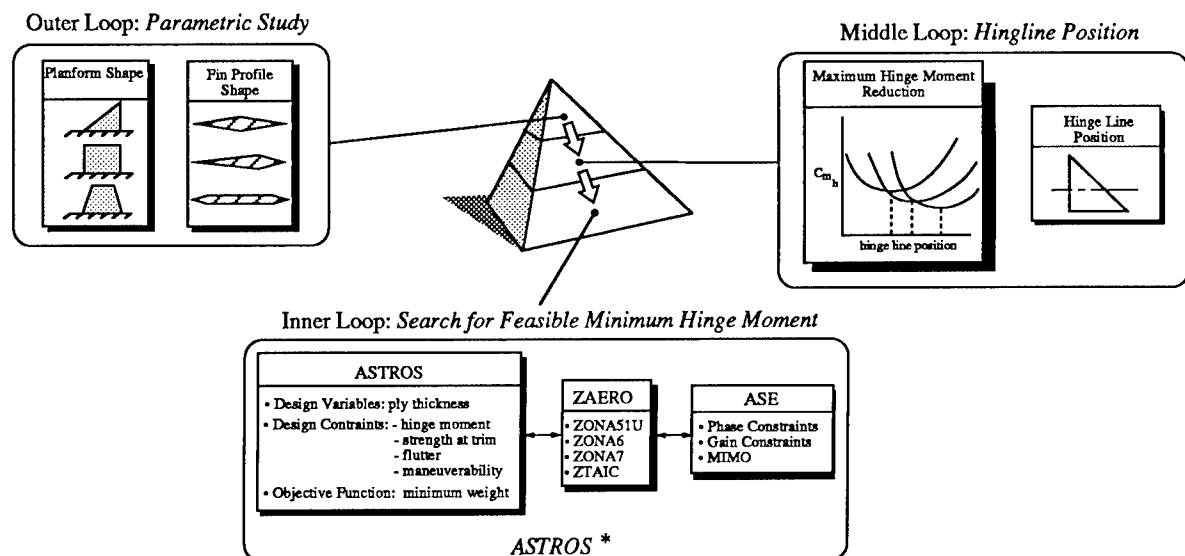
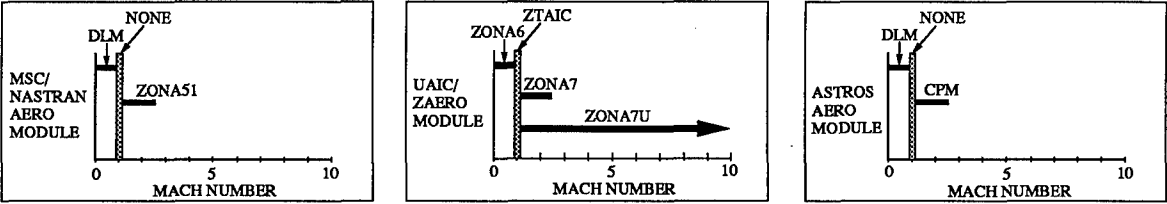


Figure 1. Global Design Loop Strategy.



(a)

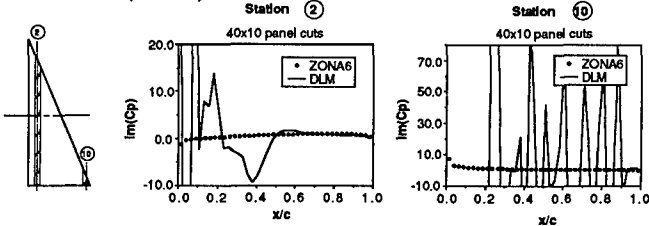
ZAERO Module:	ZONA Unsteady/Steady Aerodynamic Codes						
	ZONA51	ZONA51U	ZONA7	ZONA7U	ZONA6	ZTAIC	ZTAIC6
• Lifting Surfaces (L.S.)	•	•	•	•	•	•	•
• Thickness Effect		•		•		•	•
• L.S. + Body = Whole Aircraft			•	•	•		•
• Subsonic Aerodynamics					•	•	•
• Transonic Aerodynamics						•	•
• Supersonic Aerodynamics	•	•	•	•			
• Hypersonic Aerodynamics		•		•			
Descriptions	Fig 6	Fig 6	Fig 5	Fig 6	Fig 3	Fig 4	---

(b)

Figure 2. ZAERO Codes in ASTROS, (a) Mach Number Ranges, and (b) Capability.

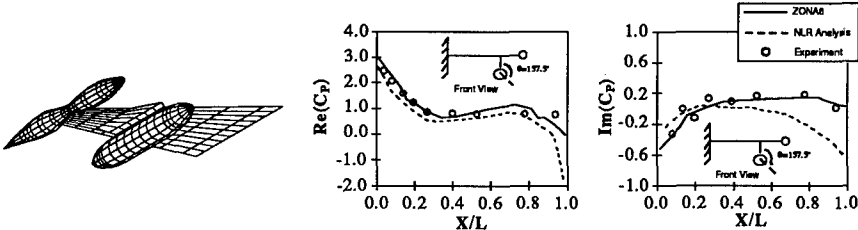
• High-order panel formulation for lifting surfaces.

Delta Wing example demonstrating the robustness of ZONA6 while the lower order Doublet Lattice Method (DLM) breaks down.



Out-of-phase pressures on two spanwise stations. 70° Delta Wing at $M=0.8$, $k=0.5$, pitch axis= $0.5c_R$

• Unsteady body panels for arbitrary fuselage and stores.



Unsteady pressures along store of NLR wing-tiptank-pylon-store configuration at $M=0.45$, $k=0.3055$, pitch axis = $0.15c_R$

Figure 3. ZONA6: Subsonic Steady/unsteady Aerodynamics for Arbitrary Wing-Body Configurations with External Stores Including Body Wake Effects.

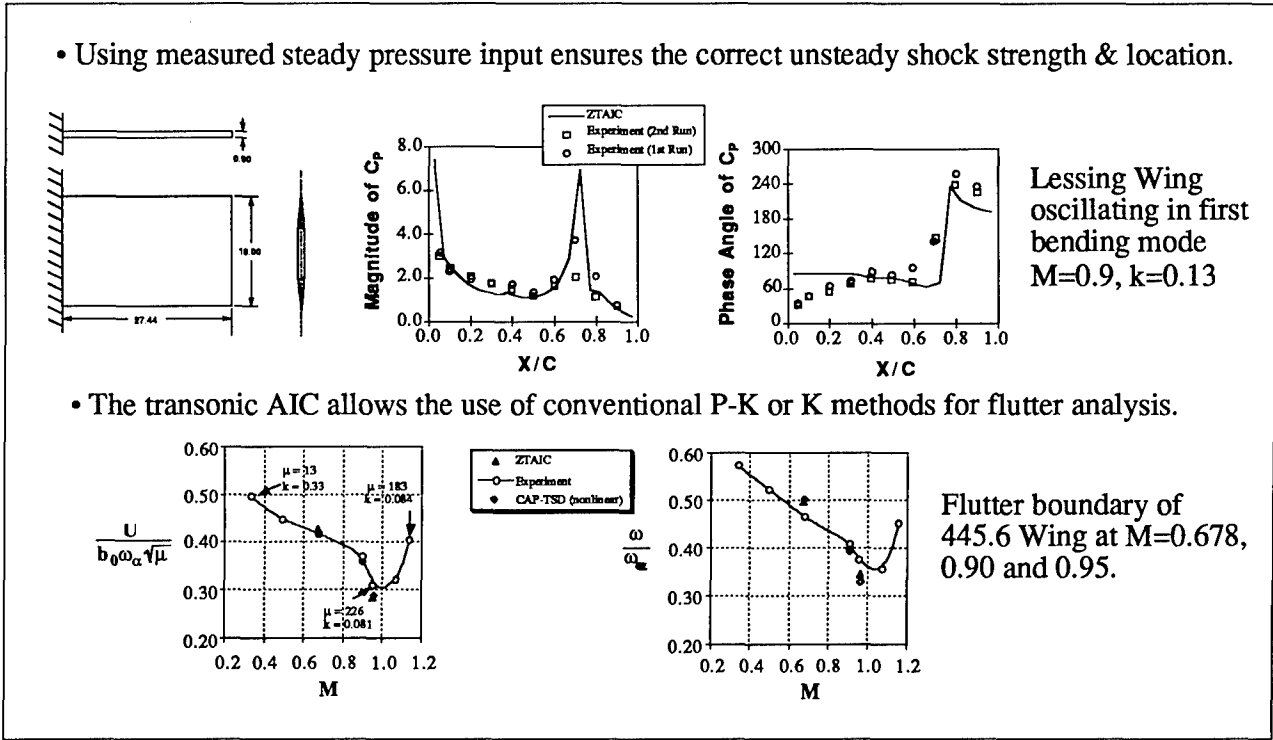


Figure 4. ZTAIC: Unsteady Transonic AIC Method Using Externally-Provided Steady Pressure.

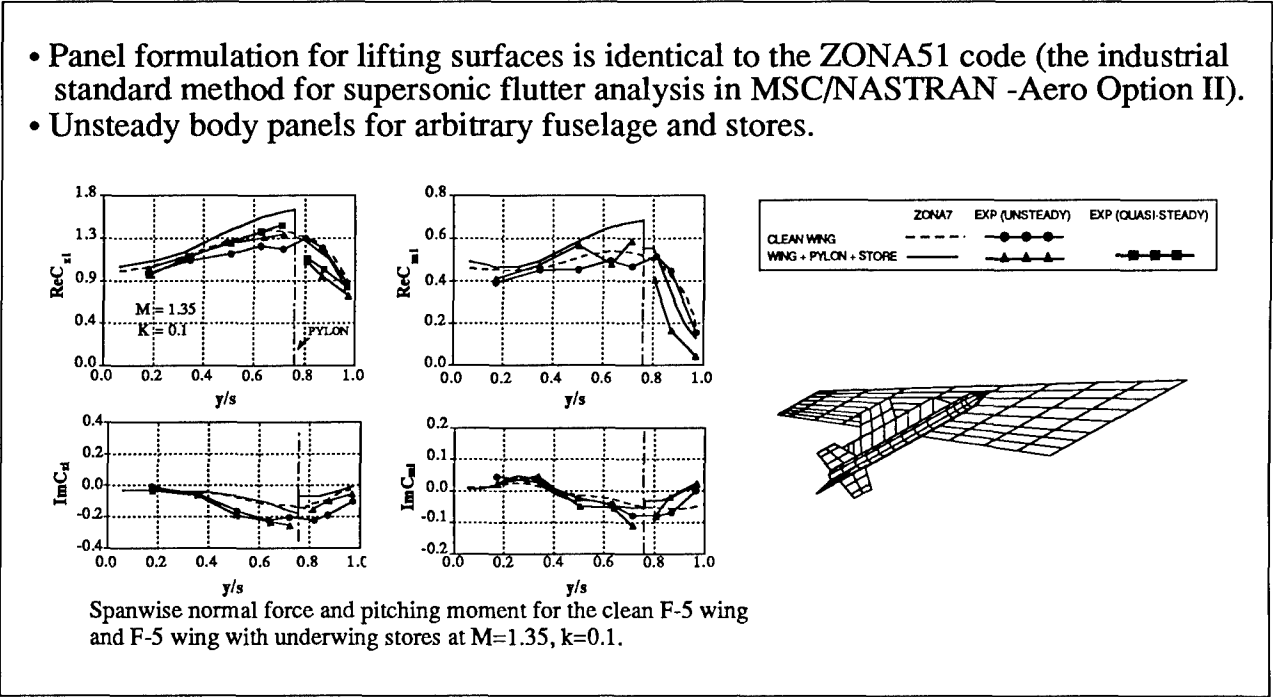
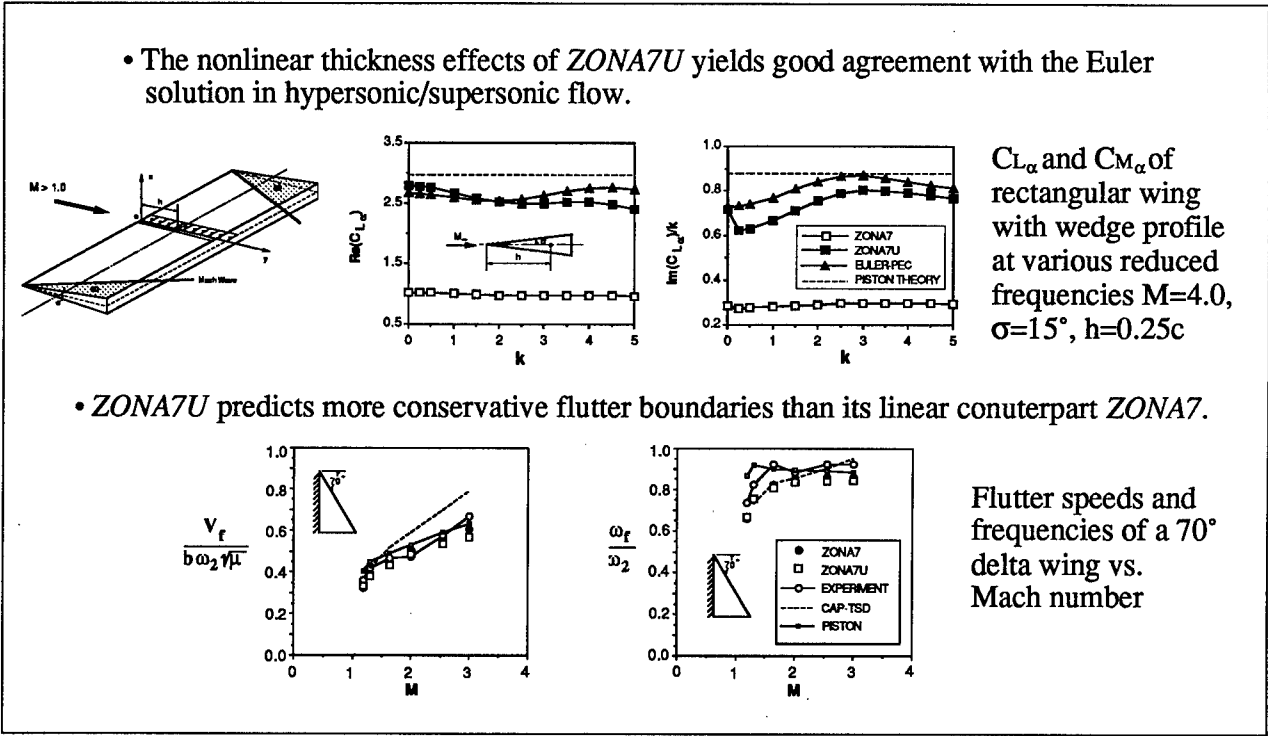


Figure 5. ZONA7: Supersonic Steady/Unsteady Aerodynamics for Arbitrary Wing-Body Configurations with External Stores.



- Database entities generated by *AGM*, *3-D Spline* and *ZAERO* Modules are computed during the *ASTROS* preface phase and are not recomputed in the analysis/optimization loop.

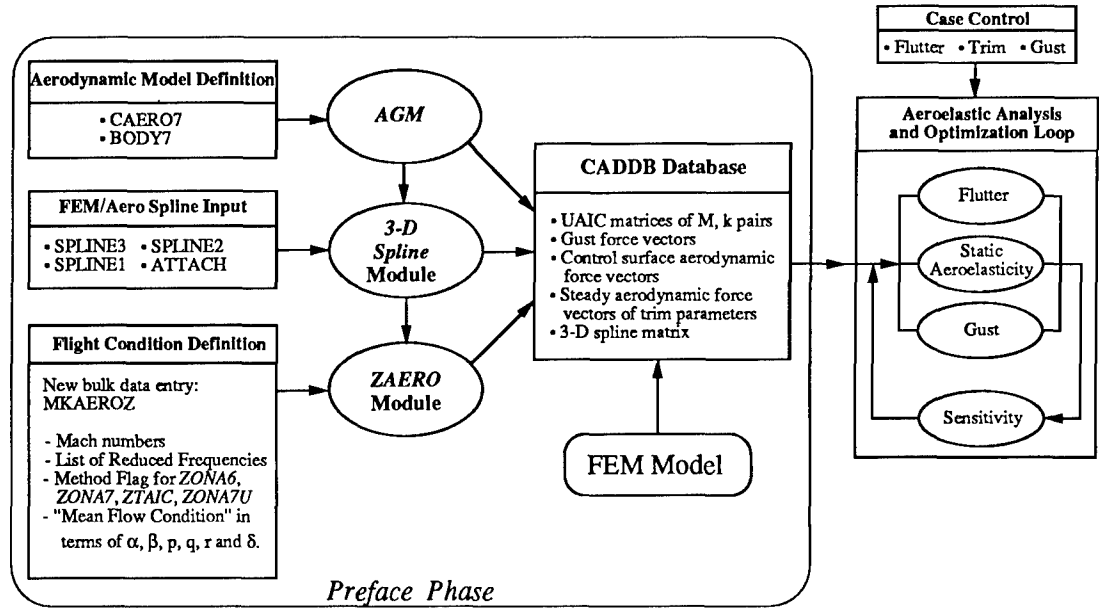


Figure 8. ASTROS/ZAERO Program Architecture.

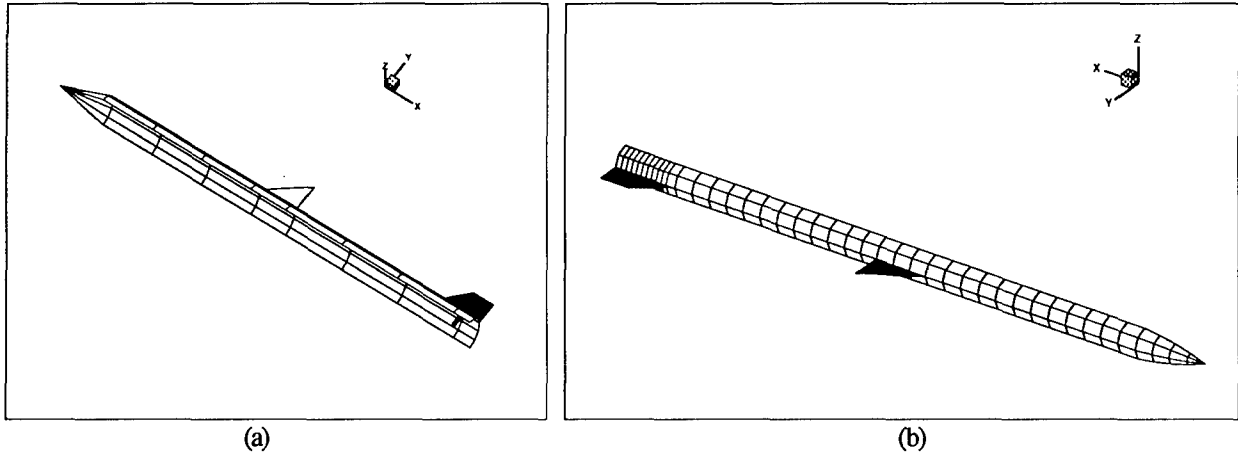


Figure 9. Right Half GTM: (a) Structural Model, (b) ZAERO Steady/Unsteady Aerodynamic Model.

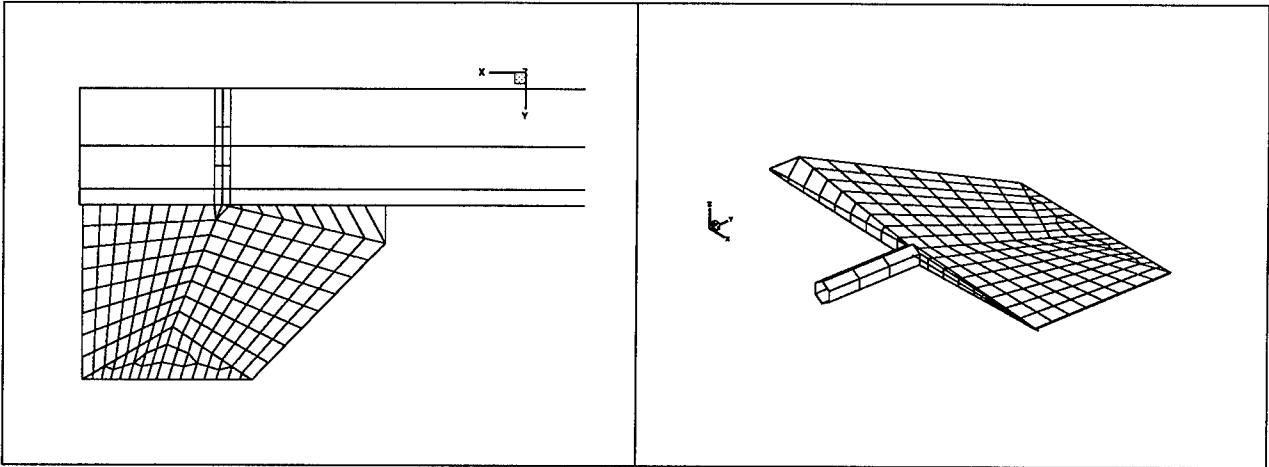


Figure 10. Views of Aft Fin Structural Model.

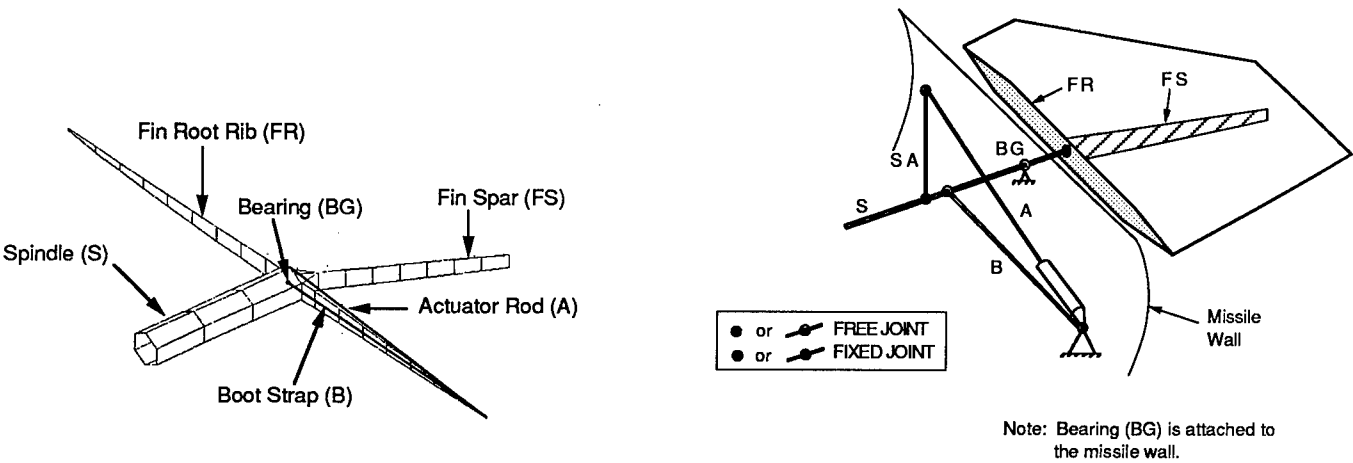


Figure 11. Fin/Actuator Model: Finite Element Model.

Figure 12. Fin/Actuator Model: Mechanical Model.

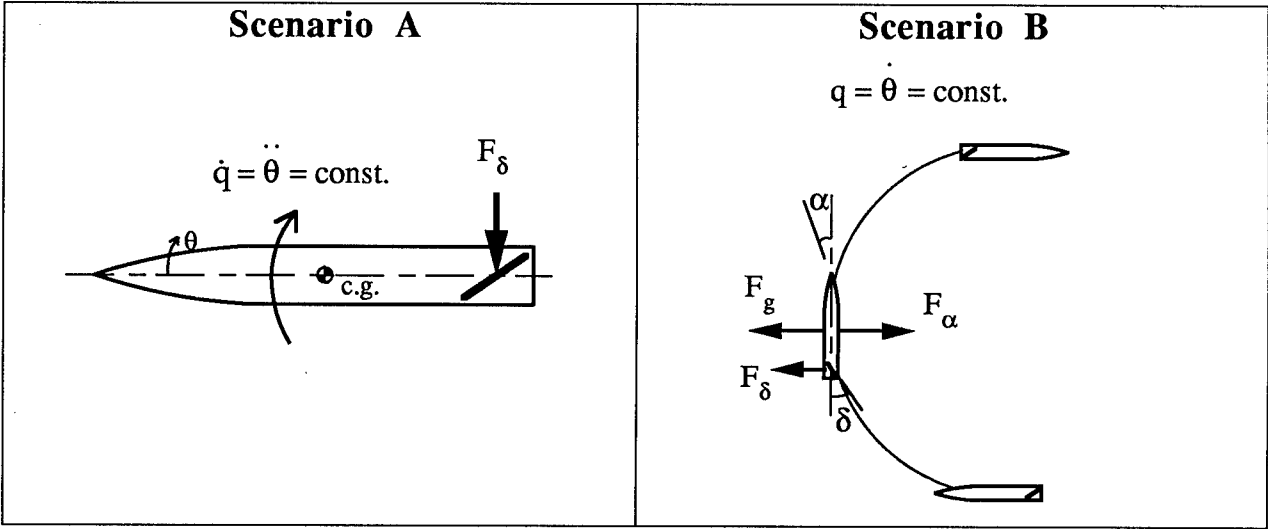


Figure 13. Two Critical Flight Condition Scenarios for GTM.

Table 1. ASTROS* Trim Flight Conditions Used in Optimization Procedure.

	Abrupt Pull-Up Maneuver			Steady Pull-Up (25-g) Maneuver		
Mach No.	4.0	3.0	0.8	4.0	3.0	0.8
Dynamic Pressure (psi)	48.568 (@30KFT)	27.32 (@30 KFT)	6.566 (@ 0 KFT)	48.568 (@30KFT)	27.32 (@30 KFT)	6.566 (@ 0 KFT)
True Velocity (in/s)	47,728	35,796	10,713	47,728	35,796	10,713
Trim Parameters						
Vertical Acceleration (Load Factor) (in/s ²)	-470	-470	-892	9,650	9,650	9,650
Pitch Acceleration (QACCEL) (r/s ²)	46.7	46.7	88.8	0.0	0.0	0.0
Thickness and Camber (THKCAM)	0.0	0.0	0.0	0.0	0.0	0.0
Angle of Attack (ALPHA)	FREE	FREE	FREE	FREE	FREE	FREE
Fin Deflection (ELEV1)	FREE	FREE	FREE	FREE	FREE	FREE

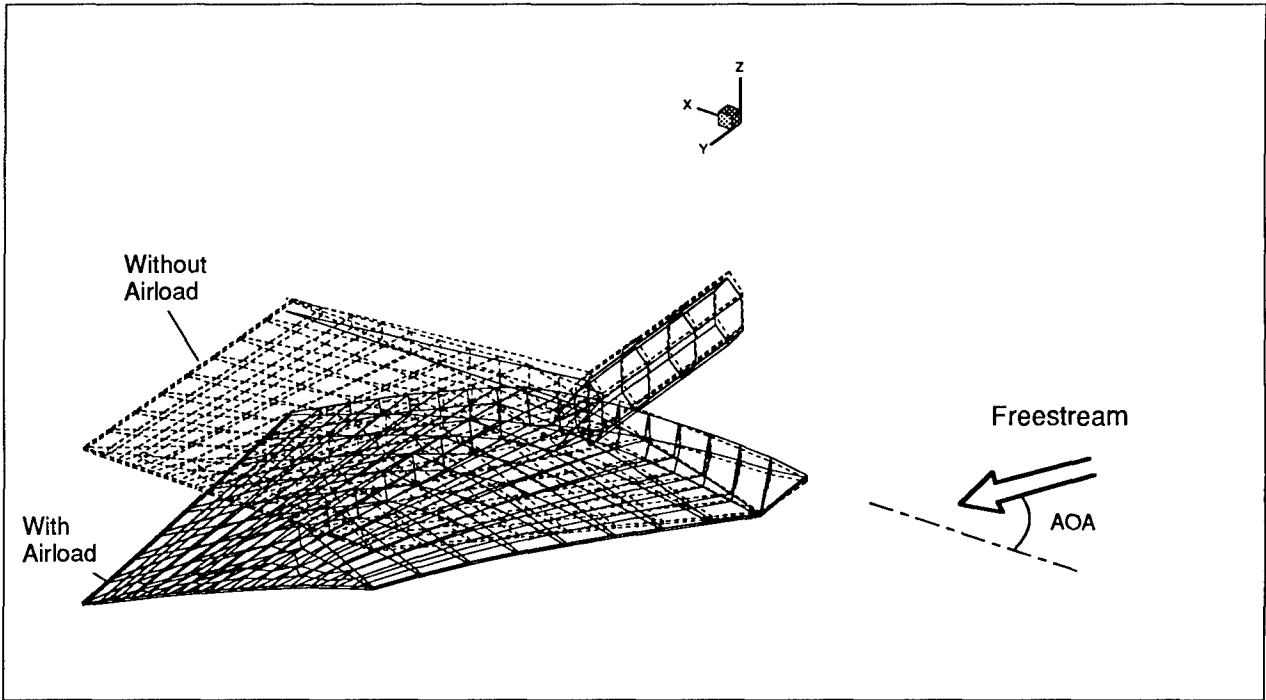


Figure 14. Typical Deformation of an AET Missile Fin Under Given Airload.

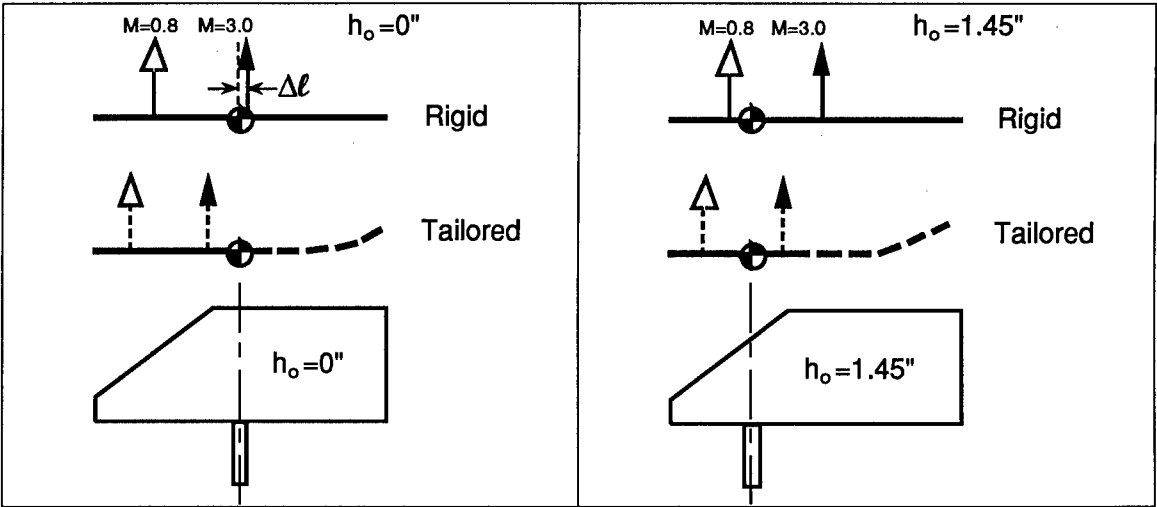


Figure 15. Impact of forward Hingeline Position Showing Hinge-Moment Reductions.

Table 2. Moment Arms At Two Hingeline Positions (all in inches).

Baseline ($h_o=0''$)			Forward ($h_o=1.45''$)		
	M = 0.8	M = 3.0		M = 0.8	M = 3.0
$\Delta \ell_{\text{Rigid}}$	2.38	-0.1	$\Delta \ell_{\text{Rigid}}$	0.94	-1.66
$\Delta \ell_{\text{Tailored}}$	2.52	0.4	$\Delta \ell_{\text{Tailored}}$	1.15	-0.93

Table 3. ASTROS* Feasible Hinge Moment Values for Four Hingeline Positions.

Hinge Line Position (h_o)	Hinge Moment (in-lbf)
0.0"	1,142
0.725"	-829
1.088"	981
1.45"	1,317

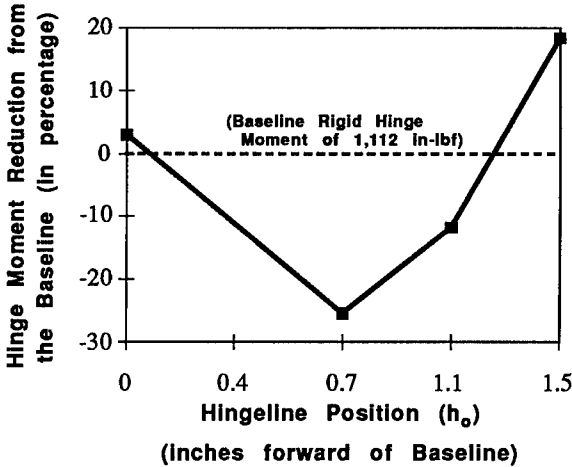


Figure 16. Identification of Maximum Hinge Moment Reduction.

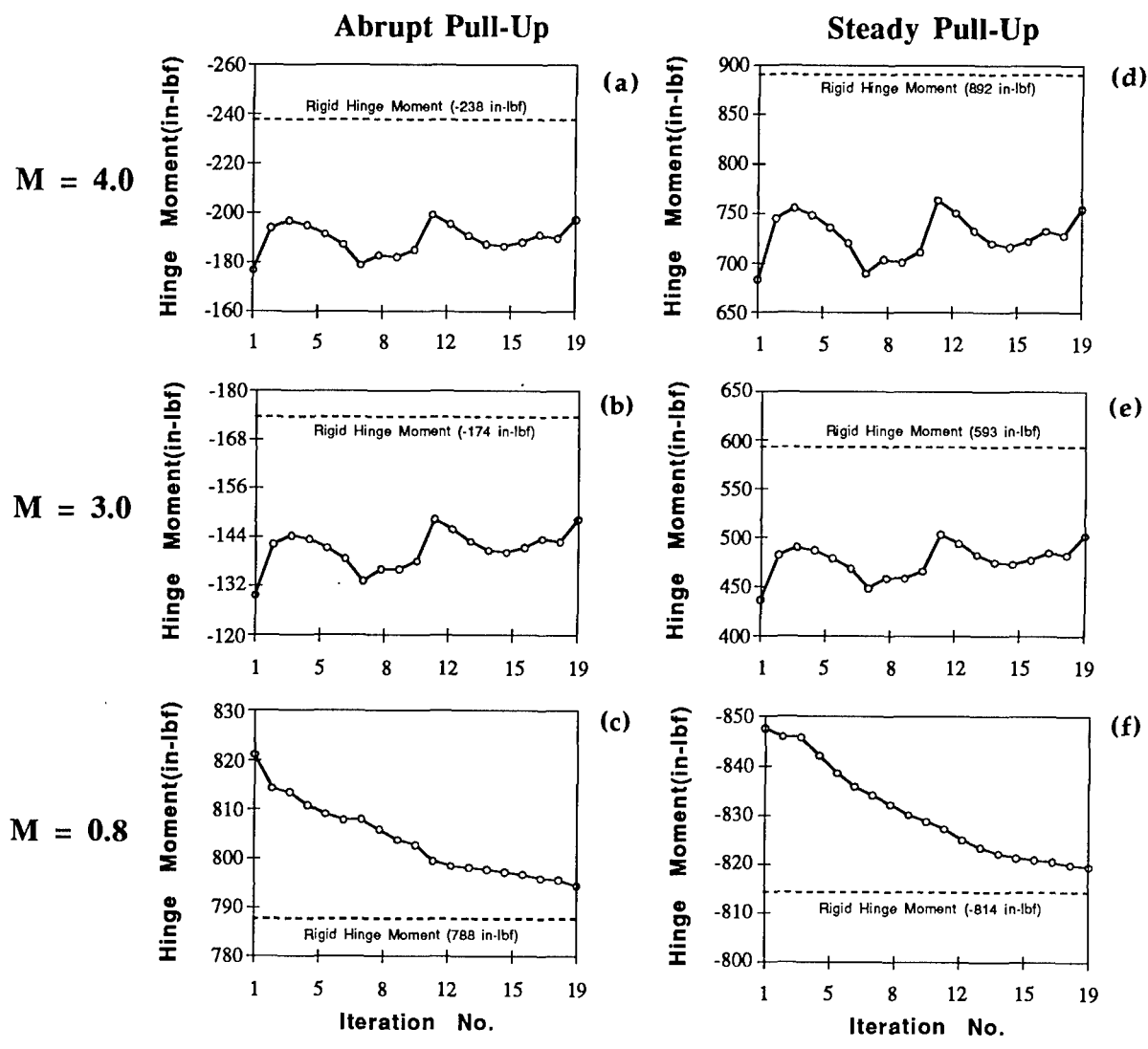


Figure 17. Iterative History of Hinge Moment ($h_o=0.725''$).

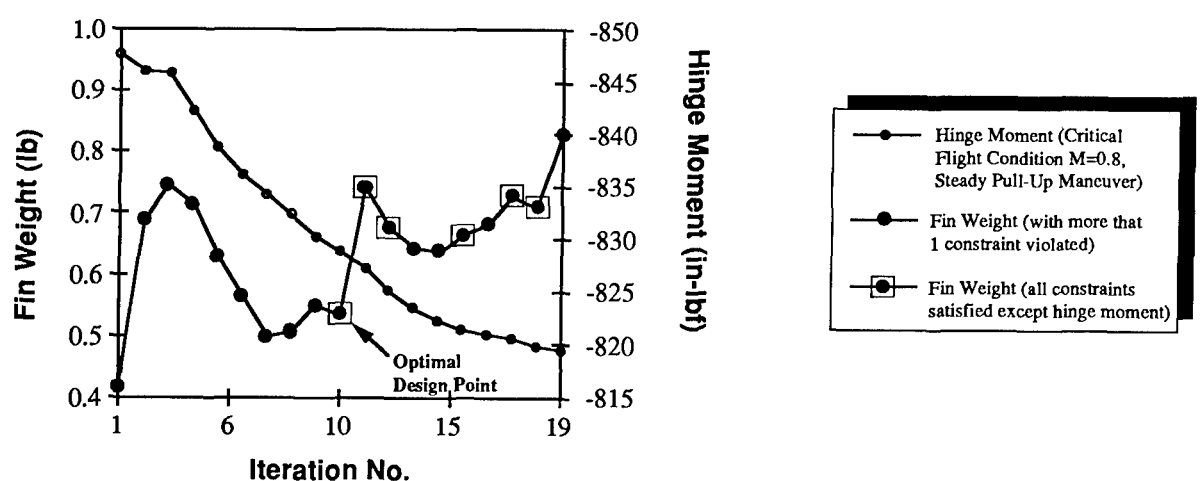


Figure 18. Trade-Off Study for Fin Weight versus Critical Hinge Moment ($h_o=0.725''$).

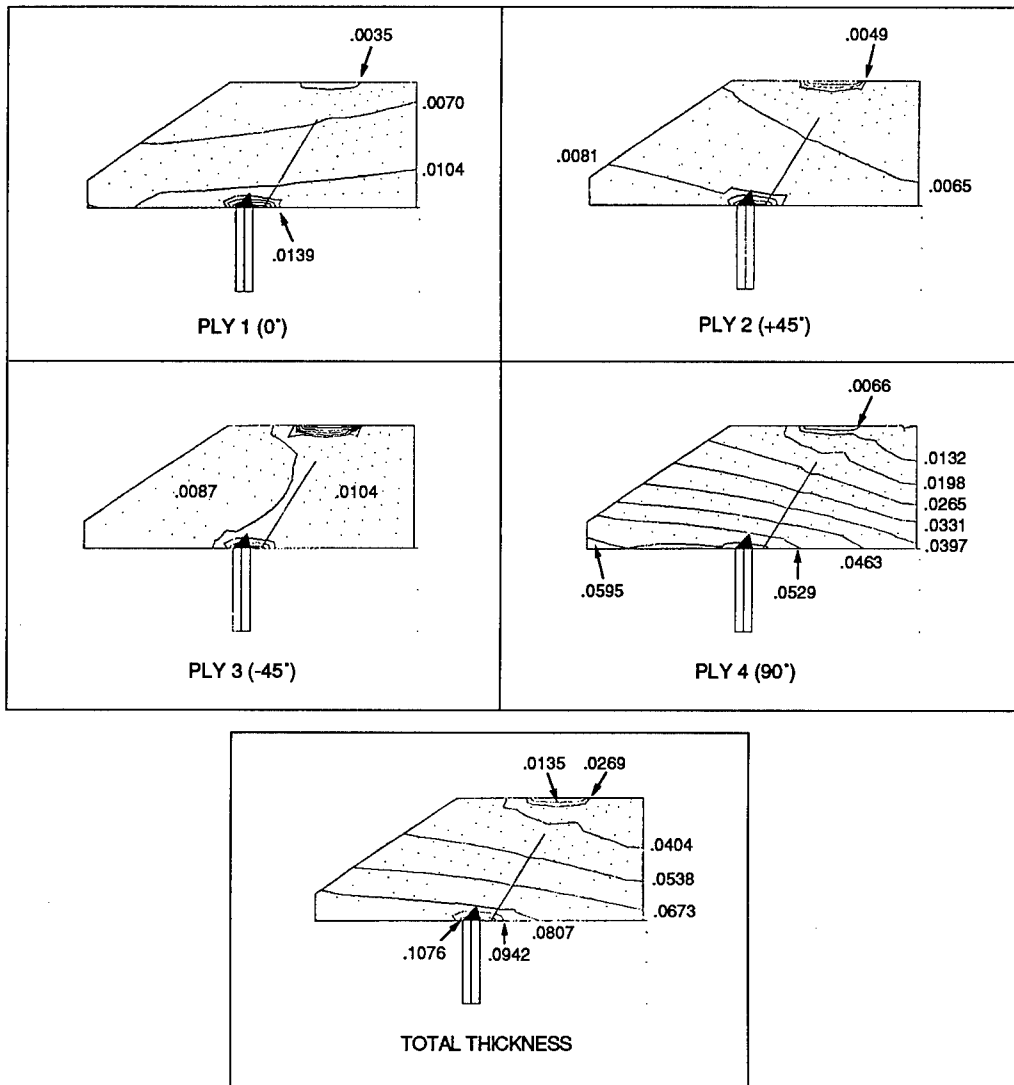


Figure 19. Composite Ply Thickness Distribution of GTM Missile Fin ($h_o=0.725$ ").

CONFORMAL LIFTING AND CONTROL SURFACES FOR WEAPON STOWABILITY

Dr. L. Bruce Simpson
Mr. Frederick A. Davis
Lt. Benjamin G. Kruggel
Air Force Research Laboratory
Munitions Directorate
101 West Eglin Boulevard
Eglin Air Force Base, Florida 32542
United States of America

Mr. Ed McLaughlin
Coleman Research Corporation
7675 Municipal Drive
Orlando, Florida 32819
United States of America

SUMMARY

The aerodynamic characteristics of a conformal ring-wing and wrap-around fin system were studied experimentally. The ring-wing and wrap-around fins were mounted on a body of revolution consisting of a 1.66 caliber tangent ogive nose with an 8.5 caliber afterbody. The aerodynamic performance of the system was studied at Mach 0.5 and 0.9 in a trisonic blow-down wind tunnel. Angle of attack sweeps from -10 to +20 degrees were made for yaw angles of 0, ± 5 , and ± 12 degrees. While the conformal ring-wing and wrap-around fin system has excellent performance in storage for internal bays and tube launched dispensers, the aerodynamic results show that the lifting potential of the ring-wing was not as good as initially predicted. Asymmetric aerodynamics and cross-coupling effects were larger than normal due to the tunneling effect the ring-wing had on the airflow impinging the leeward tail surfaces.

LIST OF SYMBOLS

α , alpha	Angle of attack
β , beta	Yaw angle
δ , delta	Tail deflection angle
C_N	Normal force
C_l	Rolling Moment
C_n	Yawing Moment
L/D	Lift to drag ratio
K	Equation-defined ratio
C_p	Center of pressure
CG	Center of gravity
M	Mach number
In ²	Square inches
Psf	Pounds per square foot
°	Degrees

B	Body alone
BTX	Body and X-tail
BW1TX	Body, swept ring-wing, and X-tail
BW2ATX	Body, unswept ring-wing in aft position, and X-tail
BW2FTX	Body, unswept ring-wing in fore position, and X-tail

1. INTRODUCTION

Studies of warfare have shown that the victor must be capable of delivering more weapons to more targets in the shortest amount of time. To apply this premise to future battles involving air-delivered munitions, aircraft must be able to deliver many weapons and strike multiple targets in a single sortie.

What this means for weapon development is increased aircraft loadout and extended weapon footprint. There are many other factors that influence weapon effectiveness, such as accuracy and warhead lethality. However, a weapon that can be stored in a compact size, while extending its range beyond a ballistic trajectory, will have the greatest impact in future conflicts.

2. MISSION FLEXIBILITY

Loadout. There are two reasons why a weapon should be stored in the smallest size possible. First, smaller weapons allow greater loadout on current external carriages. Putting more weapons on an aircraft provides the capability to strike more targets per aircraft sortie.

Second, future generations of fighter aircraft are being designed with internal bays for weapon storage. This allows new aircraft to maintain stealth while carrying a full array of weapons. Since size and space are limited,

smaller weapons will again provide greater loadout and striking power.

Extended Range. Increasing the weapon footprint also serves a two-fold purpose. Releasing munitions far from their intended target allows the warfighter to stay out of potential high threat areas. The weapon can then guide itself to the target, keeping the warfighter out of harm's way. Future applications of this principle could even lead to launching small, stealthy weapons beyond the range of enemy detection, thus striking without any warning.

The second benefit of extended range weapons is increased strike potential. Weapons with large standoff ranges allow the warfighter to fly to a release point, launch several independently targetable weapons, and strike multiple targets miles apart. This off-boresight delivery capability is a vast improvement over ballistic trajectories, which require the pilot to be guiding toward a single target prior to weapon release.

Extended range can be achieved by two means: lifting surfaces (i.e. wings) or propulsion devices (i.e. rockets). While propulsion devices provide large standoff ranges, and even generate kinetic energy that can be used against certain targets, the size, weight, cost, and complexity of the system often decreases the performance of the munition.

On the other hand, lifting surfaces provide extended range with little detriment to the overall weapon. They are simple, effective, and relatively cheap.

3. PREVIOUS STUDIES

Lifting Surfaces. Because of their relative simplicity and low cost, lifting surfaces have been studied for years in range extension applications.

The U.S. Army studied a curved wing system in 1983. This system had wing surfaces that folded about the missile body similar to wrap-around fins. Wind tunnel tests showed that the curved wings produced an inherent rolling moment, even at zero angle of attack. The wings also imparted a rotational effect on the flow behind the wings. When this swirling flow impacted the tail surfaces, it created an additional rolling moment. The static aerodynamic forces were nominally affected by the wing curvature, but the wing-tail interference created a significant change from typical planar wing-tail interference.¹

In 1986, the Arnold Engineering Development Center (AEDC) experimentally investigated several different types of lifting surfaces on behalf of the Air Force Research Laboratory Munitions Directorate (AFRL/MN). Lifting surfaces investigated included planar wings, full and half ring-wings, box wings, and

strakes. Figures 1 and 2 show two of the wind tunnel models. All of the lifting surfaces had the same chord length and were tested under the same flight conditions.

The box wing and strake configurations both produced less lift and pitching moment than the planar wings. The box wing also produced more drag. The full and half ring-wings were aerodynamically similar to the planar wing configuration. At moderate angles of attack (below $\alpha=12^\circ$) the curved wings produced slightly more lift than the planar wings. At higher angles of attack, the planar wings performed better. The full ring-wing developed less pitching moment than the planar wings and became neutrally stable or slightly unstable at high angles of attack.²

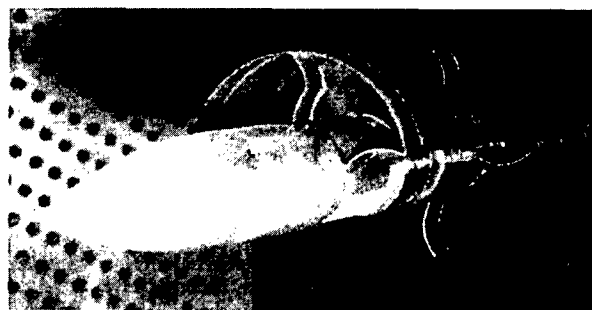


Figure 1. Half Ring-Wing Model for 1986 AEDC Wind Tunnel Tests.

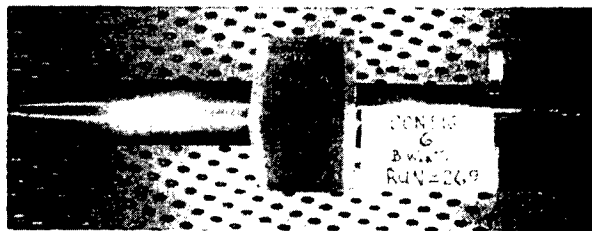


Figure 2. Box-Wing Model for 1986 AEDC Wind Tunnel Tests.

Control Surfaces. Conventional control surfaces have primarily been cruciform tails, which provide stability, well understood aerodynamics, and effective weapon control. However, cruciform fins do not fold efficiently into a compact size without taking away internal storage.

Various control surfaces have been studied to decrease storage size. Studies have been done on offset fins, grid fins, and wrap-around fins.

Wrap-Around Fins. Wrap-around fins (Figure 3) have the greatest potential for stowability. When folded, the fins match the curvature of the munition body, thereby only increasing the overall dimensions of the weapon by the fin thickness. However, wrap-around fins reverse the rolling motion of the munition when transitioning through Mach 1 and again at high supersonic speeds.³

They also exhibit significant pitch-yaw coupling and generate side forces and moments at angles of attack due to the asymmetry of the fins.⁴

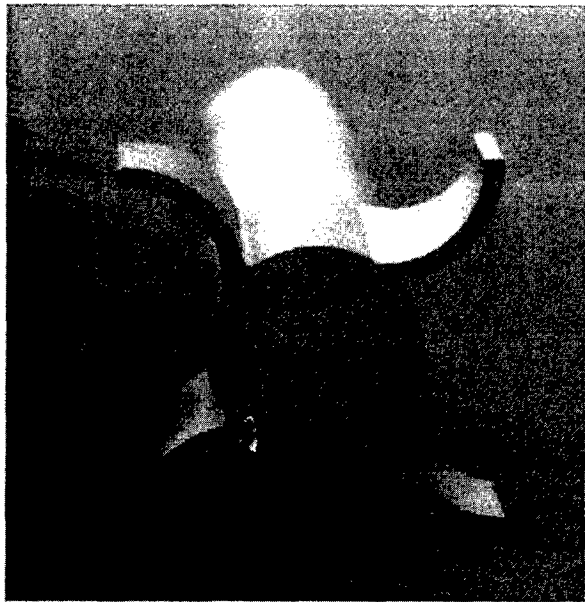


Figure 3. Wrap-Around Fins.

Offset Fins. Another solution to storing fins is to deploy them at an angle less than perpendicular (90°). Offset fins (Figure 4) can exhibit similar characteristics to wrap-around fins, depending on the offset angle. The closer the fin offset gets to 0° , the closer the fins act like a wrap-around fin. Above 60° , the fins generally act like cruciform fins. Below 45° , the offset fins begin to exhibit wrap-around fin characteristics. To minimize the adverse aerodynamic affects, the offset angle must be close to 90° , which decreases the storage capability.⁵

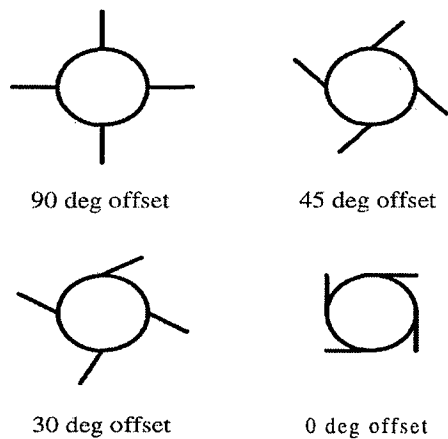


Figure 4. Offset Fins.

Grid Fins. The unconventional design of the grid fin (Figure 5) allows it to be stored compactly by folding up against the missile body. It also provides unique

aerodynamic characteristics that can be advantageous over other fin designs. The grid fin allows a large amount of lifting surface to be housed along the body of the weapon without causing large increases in overall diameter. Near zero hinge moments and small center of pressure variations are generated by the small chord length, thereby reducing the size of the control actuator. However, there is a significant drag penalty of about 3 or 4 times that of conventional fins. There is also a problem with flow choking through the grid fin cells when flying through the transonic region. This requires a system tradeoff between the optimal aerodynamic performance and the simplest control system.⁶

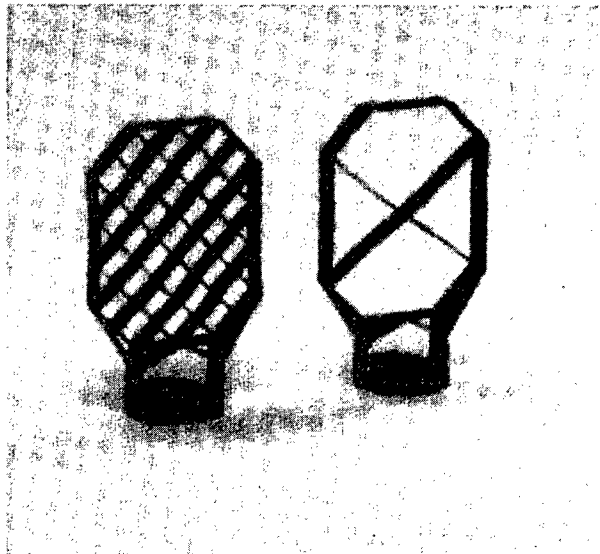


Figure 5. Grid Fins.

4. SYSTEM SELECTION

After evaluating all of the previous work in compressible wing and fin technology, AFRL/MN decided to investigate the aerodynamic characteristics of a cost effective weapon with maximum storage capability and extended range.

The system that was chosen had a diameter of 3.5 inches and a length of 8.5 calibers, with a 1.66 caliber tangent ogive nose, ring-wing and wrap-around fins (Figure 6). The bulbous section aft of the ring-wing was necessary to accommodate commercial off the shelf fin actuators.

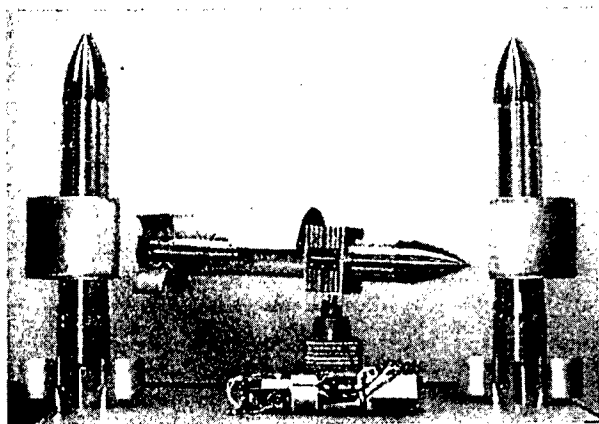


Figure 6. Ring-Wing and Wrap-Around Fin System

5. SYSTEM EFFECTIVENESS

This project investigated the aerodynamics of a conformal ring-wing and wrap-around fin system and its potential use on a flight vehicle. It did not study the storage methods, release mechanisms or deployment devices needed to field an operational system. However, these problems have been investigated before, and those results were applied to this system.

Wind tunnel tests were performed at the Lockheed Martin Vought Systems High Speed Wind Tunnel, Grand Prairie, Texas. This wind tunnel is a trisonic blow-down type with a test section of 4x4 feet. Tests were primarily conducted at $M=0.5$ with a dynamic pressure of 450 psf. A few tests were conducted at $M=0.9$ and a dynamic pressure of 968.5 psf. The tests were conducted at a constant β of 0, ± 5 , and ± 12 degrees with α sweeps between -10 and $+20$ degrees.

Two different ring-wing designs were tested. The first was based on previous studies and had a 45 degree sweep to the leading edge. Its chord length was 7.0 inches. It had a projected span of 9.75 inches, and a projected wing area of 68.27 in². The second design had the same chord, projected span, and projected wing area as the first ring-wing but no leading edge sweep. It was tested in two different locations: one to put the center of pressure at the same location as the swept ring-wing and the other to put the wing mounts in the same location.

Two tail configurations were also tested. Both used wrap-around fins, but one had the tails arranged in the + configuration, while the other had the tails in an X arrangement. These two configurations were tested to determine the best stability and control characteristics of the wrap-around fins with a ring-wing.

Aerodynamics. There were several performance goals going into the wind tunnel. These goals were based on previous tests and aerodynamic predictions. They were:

1. Have a maximum L/D of 4.0 to 5.0 so that it has a long glide range capability.
2. Be at least 2.00 inches (0.571 caliber) stable throughout its flight envelope.
3. Trim to at least 15 degrees and up to 20 degrees α with no more than ± 20 degrees δ .
4. Provide maximum lift at 10 degrees α .

Based upon initial tradeoff wind tunnel studies, the unswept ring-wing in the aft location with the tail fins in the X configuration was chosen for more in-depth tests. The X tail arrangement allowed the missile to be trimmed to an α greater than 20 degrees with no more than 20 degrees of δ . The aft location of the unswept ring-wing moved the C_p to its furthest aft location, providing more stability throughout the projected flight envelope of the missile. The swept wing had a larger C_N at all $+\alpha$, but its static margin did not meet the stability requirements for the predicted flight envelope.

Figure 7 shows C_N for the component build up during the wind tunnel tests. The aerodynamic performance of the unswept ring-wing and X tail configuration was not as good as the predicted goals going into the wind tunnel. C_N values shown are untrimmed. To trim out the pitch, yaw, and roll moments requires tail deflections, which reduces C_N even more than shown. At 10 degrees α , the trimmed C_N was 2.4, which is significantly less than the desired value of 4.0. To achieve 4.0, the vehicle must be at 18 degrees α . Figure 8 shows the L/D performance for the unswept ring-wing in the aft location. The maximum L/D for trimmed conditions at 10 degrees α is 3.7, which is again less than the desired value. The transonic drag rise did not occur until about $M=0.87$, which is comparable to conventional missile designs.

The stability of the vehicle also did not achieve its design goals. At subsonic speeds ($M=0.5$) the static margin is 3.2 inches stable. However, at transonic speeds ($M=0.9$), the static margin is reduced 0.378 calibers, and is only 1.88 inches stable. This is less than the minimum required static margin of 2.00 inches.

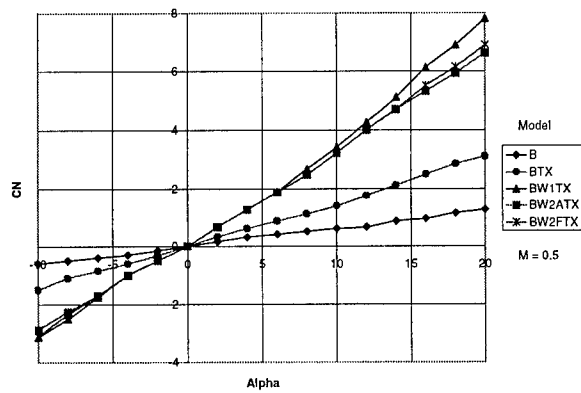


Figure 7. Normal Force Coefficient for Component Build-up.

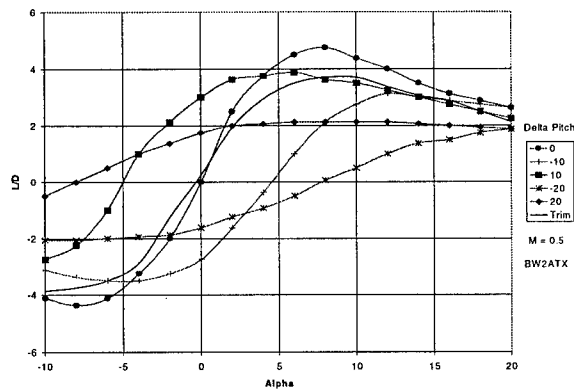


Figure 8. Lift to Drag Ratio for Unswept Ring-Wing in Aft Location.

Control. There were severe cross-coupling effects and non-linearities in the aerodynamics that called into question the ability to control a ring-wing lifting surface with wrap-around fins. For large δ and/or large α and/or β , the cross-coupling terms are large. This is especially true of the roll induced by yaw deflections and the yaw induced by roll deflections.

Conventional aerodynamic cross coupling is due to the reduction of tail effectiveness of the leeward tail surfaces due to body shielding. For these cases, a positive yaw deflection would induce a negative C_l as the positive roll due to the two deflected leeward fins is less than the negative roll due to the two deflected windward fins. The data in Figures 9-10 show that the opposite occurs. In Figure 9, K is the ratio of C_l induced by yaw deflections to C_l due to pure roll deflections. Figure 10 is the ratio of C_n induced by roll deflections to C_n due to pure yaw deflections. In equation form, this becomes:

$$K_{Fig9} = \frac{\Delta C_l \delta_{yaw}}{\Delta C_l \delta_{roll}} \quad \text{or} \quad K_{Fig10} = \frac{\Delta C_n \delta_{roll}}{\Delta C_n \delta_{yaw}}$$

The induced roll due to yaw for a positive yaw deflection produces a positive C_l . This infers that the two leeward fins are more effective than the two windward fins - which is opposite of what happens for conventional wing and tail surfaces. Based upon the signs of the cross-coupling terms, and determining which fins are more effective during given combined deflections, it seems that the ring-wing channels and straightens the flow on the leeward side of the body such that much of the effect of angle of attack and of yaw are removed from the flow that strikes the leeward tail surfaces. In a sense, the ring-wing is tunneling the flow and re-energizing it on the leeward side of the missile (Figure 11).

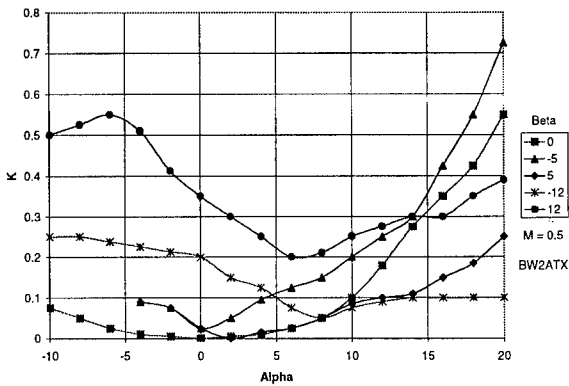


Figure 9. Roll due to Yaw Cross Coupling.

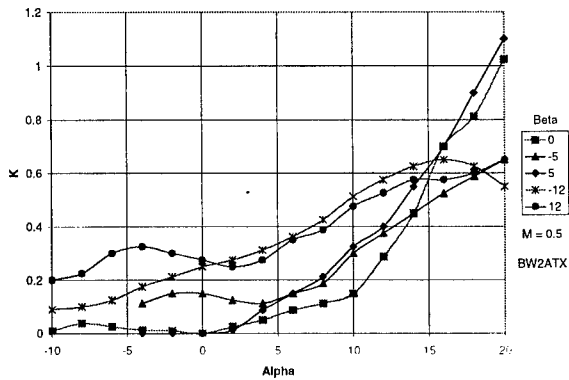


Figure 10. Yaw due to Roll Cross Coupling.

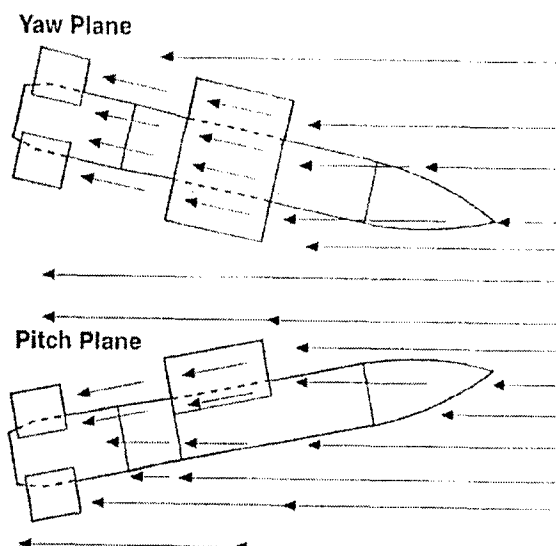


Figure 11. Ring-Wing Tunneling Effects.

The non-linearity in the aerodynamics is partially due to the wrap-around fins. With wrap-around fins, there is no plane of symmetry to the flight vehicle. Thus, deflecting the tail -10 degrees does not produce the same result as deflecting the tail +10 degrees. This asymmetry is especially noticeable at large α or β . Figures 12-13 show the asymmetries due to ± 10 degrees roll and ± 10 degrees yaw deflections. In these figures, K is the ratio of C_L or C_n due to negative roll or yaw deflections to C_L or C_n due to positive deflections. In equation form this is:

$$K_{\text{Fig12}} = \frac{\Delta C_L [-\delta_{\text{roll}}]}{\Delta C_L [+ \delta_{\text{roll}}]} \quad \text{or} \quad K_{\text{Fig13}} = \frac{\Delta C_n [-\delta_{\text{yaw}}]}{\Delta C_n [+ \delta_{\text{yaw}}]}$$

If the effects were small, K would be 1.0 or nearly 1.0. Because of the non-linearities in tail effectiveness and because of possible tail stalling at large α plus δ combinations, the effects are large, sometimes being more than ± 50 percent.

The aerodynamic asymmetry of the wrap-around fins is compounded by the unequal interference due to the wake and vortices from the ring-wing and its supports impinging on the tail surfaces. This limits the effectiveness of the tail surfaces, especially during combined deflections (deflecting the tail to produce yaw and/or pitch and/or roll) and at large α or β .

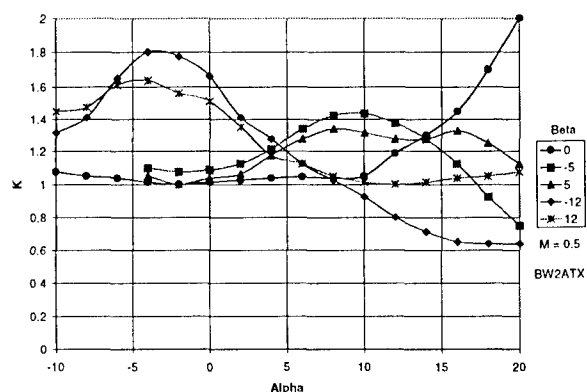


Figure 12. Aerodynamic Asymmetries due to Roll Deflections.

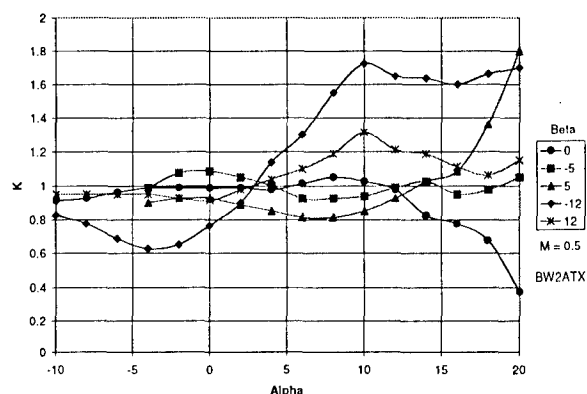


Figure 13. Aerodynamic Asymmetries due to Yaw Deflections.

Storage. Storage capability is primarily measured by a weapon's box size. The box size of this munition without the ring-wing and wrap-around fins is 20.25 in². This is measured at the maximum cylindrical diameter of the weapon, which is located at the bulbous section aft of the ring-wing. With the ring-wing and wrap-around fins in the stowed position, the box size of the vehicle increases to 22.5625 in², a change of only 10.25%.

This increase comes solely from the thickness of the wrap-around fins. The ring-wing collapses into a box size of 20.75 in². Since it is located along the main body, the bulbous tail and wrap-around fins hide its effects.

The ring-wing does not conform exactly to the missile body when collapsed like the wrap-around fins. This is due to the wing supports. In the stowed position, the wing supports create a 0.2 inch gap between the ring-wing and the missile body. However, as mentioned before, the bulbous tail section hides this effect. It can be alleviated by creating a recess in the body for the wing supports to collapse into, allowing the ring-wing

to conform exactly to the missile body. This may cause aerodynamic problems and needs to be investigated further.

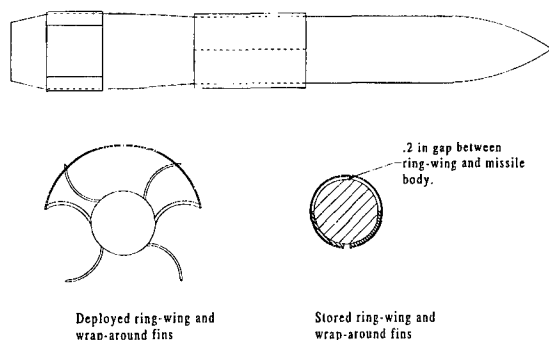


Figure 14. Stored Ring-Wing and Wrap-Around Fin System.

Deployment. Deploying the ring-wing and wrap-around fins in an operational environment was not studied in this project. However, previous studies have shown that the ring-wing can use the natural spring forces and aerodynamics to erect the lifting surface. Prior to launch, some sort of holding device, such as a steel band, would be needed to keep the ring-wing in its stored position. After launch, the band could be stripped away, allowing the internal stored energy of the ring-wing to deploy itself.⁷ The wrap-around fins require a spring device or other actuator for deployment.

During conventional bomb rack/bay deployments, the erection of the ring-wing and wrap-around fins could be initialized by the launch. The nature of the ring-wing and wrap-around fins suits them for tube-launched dispensers, especially rear-ejection devices. During a rear-ejection, the wrap-around fins would be erected first, providing stability to the weapon. After it has completely cleared the dispenser, the ring-wing could deploy.

6. CONCLUSIONS

Modern warfare requires more efficient strike potential for each aircraft sortie. This can be done by increasing the aircraft loadout and extending the weapon footprint. In order to maximize the storage capabilities of current external weapon carriages and future internal bays, weapon systems will need to have conformal lifting and control surfaces.

Previous studies have investigated conformal lifting surfaces (ring-wings, box wings, and folding planar wings) and control surfaces (wrap-around fins, grid fins, and offset fins) separately. These wind tunnel tests showed the effects of a ring-wing lifting device and

wrap-around control fins together. The aerodynamic performance of this system is not as good as initially indicated in previous experiments. The degraded performance is mainly due to three factors. First, the ring-wing lifting surface does not produce a normal force comparable to conventional lifting surfaces. Second, wrap-around fins inherently produce asymmetric aerodynamics during tail deflections. This can cause control problems if the asymmetries are not properly characterized. Finally, and possibly most importantly, non-linear aerodynamics and severe cross-coupling occur during pitch, roll, and/or yaw maneuvers. This is due to the tunneling effects the ring-wing has on the leeward wrap-around fins.

7. REFERENCES

1. Washington, W.D., "Experimental Investigation of Rolling Moment for a Body-Wing-Tail Missile Configuration with Wrap Around Wings and Straight Tails at Supersonic Speeds," AIAA 83-2081, August 1983.
2. Young, Jr., R.P., "Aerodynamic Characteristics of Several Wrap-Around Wing/Tail Missile Configurations Suitable for Compressed Carriage," AEDC-TR-87-4, February 1987.
3. Vitale, L.R.E., Abate, G., Winchenbach, G.L., and Riner, W., "Aerodynamic Test and Analysis of a Missile Configuration with Curved Fins," AIAA 92-4495, 1992.
4. Tilmann, C.P., Huffman, R.E. Jr., Buter, T. A., and Bowersox, R.D.W., "Characterization of the Flow Structure in the Vicinity of a Wrap-Around Fin at Supersonic Speeds," AIAA 96-0190, January 1996.
5. Mikhail, A.G., "Roll Damping for Finned Projectiles Including: Wraparound, Offset, and Arbitrary Number of Fins," AIAA 93-3460, August 1993.
6. Washington, W.D., and Miller, M.S., "Grid Fins - A New Concept for Missile Stability and Control," AIAA 93-0035, January 1993.
7. August, H.A., Osborn, R., and Pinney, M., "Ring Wing Missile for Compressed Carriage on an Aircraft," AIAA 93-3656, January 1993.

AERODYNAMICS OF WRAP AROUND FINS USING EXPERIMENTAL AND COMPUTATIONAL TECHNIQUES

by

Claude Berner*, Gregg Abate*, and Alain Dupuis**
French-German Research Institute of Saint-Louis (ISL)
5, rue du Général-Casagnau, B.P. 34
68301 Saint Louis Cedex, France

Abstract

This paper presents carefully made experiments in wind tunnel and aeroballistic range facilities as well as results of numerical simulations for wrap around fin (WAF) configurations. The experimental program consisted of flow visualization, static pressure, force, and flow velocity measurements made in wind tunnels and of free flight tests made in an instrumented aeroballistic range facility. Flow field predictions were carried out using a fully implicit, combined finite volume/flux elements 3D Navier-Stokes employing a standard k-ε model with wall functions. Experimental and CFD results were obtained, depending on the measurements, for nominal Mach numbers in the subsonic, transonic, and supersonic regime and for angles of attack ranging between -15 and 15 degrees and for roll angle positions of 0 and 45 degrees. Results obtained numerically were compared with the free flight and wind tunnel tests. Comparisons of the different aerodynamic coefficients show favorable agreement.

Introduction

The wrap around fin (WAF) offers excellent packaging of control surfaces on missile/projectile configurations for tube-launched applications. However, WAFs have unique aerodynamics associated with them that are not completely understood and have been the study of numerous research efforts of the past number of years.

This paper will detail the results of a WAF configuration that has been studied in two different wind tunnels, launched in a free-flight ballistics range and been studied via computational fluid dynamics (CFD). The underlying goal is a better understanding of the flow physics that make WAF missile configurations aerodynamically challenging.

Nomenclature

l	projectile length
d	projectile diameter
M	Mach number
CA	Axial Force Coefficient
CA0	Zero Yaw Axial Force Coefficient
CDf	Forebody Drag Coefficient
CN	Normal Force Coefficient
CNα	Normal Force Coefficient Slope
Cm	Pitching Moment Coefficient
Cmα	Pitching Moment Coefficient Slope
Cn, Cnsm	Side Moment Coefficient
Cnα	Side Moment Coefficient Slope
Cl	Roll Moment Coefficient
Clp	Roll Damping Moment Coefficient

Cl ₀	Roll Moment Coefficient at α=0°
α	Angle of Attack
φ	Roll Angle Orientation

Background

Missile configurations, which employ wrap around fins, have been studied extensively over the years. Such configurations offer excellent packaging advantages for tube-launched and dispenser launched applications. Aerodynamically, such configurations can present problems in the form of roll reversal through Mach 1, roll moments at 0° angle-of-attack, and the generation of a side force/moment when at angle-of-attack. Although such configurations have been tested extensively through the years, results have merely shown cause-and-effect relations for various WAF components (i.e. fin opening angle, leading/trailing edge geometry, fin attachment method, fin planform, etc.) and offered little towards the complete understanding of the aerodynamic cause of such anomalies.

Dahlke of the US Army Missile Command (MICOM) has published numerous reports on the subject of wrap around fins^{1, 2, 3}. Studies of WAF configurations date back to the mid 1950's where much of the same phenomena discussed above was first noticed. Dahlke's re-

* ISL, French-German Research Institute, Saint-Louis, France

+ Air Force Research Laboratory, Aeroballistics Section, Eglin AFB, FL

** Defense Research Establishment, Valcartier, Quebec, Canada

ports^{2, 3} document wind tunnel tests in which parametric studies of WAF configurations were tested at Mach numbers ranging from 0.3 to 3.0. Here again, specific cause-and-effect relations were established for various parameters but no specific aerodynamic cause was determined for the WAF flow phenomena.

The Navy became interested in wrap around fin configurations and investigated unique methods of aerodynamic control. One of these methods involved the use of fin slots to help alleviate known aerodynamic problems. Daniels in the early 1970's investigated fin slots to help alleviate spin-yaw lock-in which can lead to catastrophic failure^{4, 5}. Such slots were effective and, in 1975, Daniels and Hardy of the Naval Surface Weapons Center (NSWC) conducted wind tunnel tests to investigate fin slots and fences on WAF configurations⁶. They were successful in roll-stabilizing missiles in incompressible flow regimes and recommended further tests at higher speeds.

These free-flight tests clearly showed the dynamic effect of the aerodynamic anomalies associated with WAF configurations. Free-flight motion patterns, as shown in Figure 1, are noticeably affected. Figure 1 shows the motion of the center of gravity (CG) of the model as viewed from behind as it flies downrange (the circles represent discrete data points and the lines represent the fit motion profile). Figure 1a represents a dynamically stable missile configuration with straight fins. Note the elliptic pattern of motion and that the magnitude damps as the model traverses the range. Figures 1b-1d show the motion of a WAF missile. What stands out immediately is the circular motion pattern. This is due to the presence of a small side force generated when the model is at angle of attack. The small side force leads to a side moment, which, if of sufficient magnitude, can cause catastrophic failure. Figure 1b illustrates a motion where the side moment is damped, Figure 1c illustrates a motion where the side moment is neutral, and Figure 1d illustrates a motion where the side moment is undamped.

Another aspect of WAF aerodynamic anomalies that is dramatically shown in aeroballistic tests⁷ is the roll moment dependence with Mach number. Previous wind tunnel tests document the fact that the curved fin has some non-zero lift force at 0° angle of attack, that the magnitude is dependent on Mach number, and that the direction of this lift force changes direction through Mach 1. The consequences of these phenomena for a WAF missile in free flight are clearly seen in Figure 2. Here we see the roll vs. down range distance (the slope being the roll rate) for a typical WAF missile. For the subsonic tests, the WAF model rolls in a "positive" direction and for supersonic tests, the models roll in the "negative" direction. Of great concern are those shots whose flight Mach number is close

to Mach 1. Here we see roll reversals of the models as their flight Mach number crosses from supersonic to subsonic. This phenomena is of great concern to designers of missiles in order to avoid spin-yaw lock-in; especially for those designs where the missile is designed to fly great distances and whose Mach number will change significantly during flight.

Configurations

The configuration investigated in this study is a variant of the USAF Basic Research Model. The model is 6 calibers long with a 2.5 caliber tangent-ogive. The fins are rectangular in shape with a chord length of 0.64 calibers. The fin span is derived from the wrap around fin geometry and is 0.707 calibers per fin or 2.414 calibers tip-to-tip. Each fins leading edge and tip are beveled at 45 degrees. The fin's thickness to chord ratio (t/c) is 16.3%. This thickness, larger than usual wrap-around fin configurations, was necessary because test models were instrumented with pressure taps on the fin surface, on the body in the fin region, and on the base. Figure 3 depicts the model geometry.

An additional fin set model was constructed which employed fin slots. Fin slots, investigated in previous free-flight tests⁸ as a possible means of reducing or eliminating the side force while at angle of attack, were also investigated for these tests as well.

Experimental Technique

Experimental facilities

The experimental data gathered for this investigation were collected at three facilities: the ISL wind tunnel, the DREV wind tunnel, and the AFRL Aeroballistics free flight range (ARF). The following describes these facilities in detail:

DREV Indraft Wind Tunnel - The wind tunnel experiments were conducted in the DREV trisonic 60 cm x 60 cm wind tunnel⁹. It is an indraft type drawing air into an evacuated tank with a running time of about 14 seconds. Supersonic flow is achieved by the use of interchangeable nozzle blocks. Transonic flow is obtained by the use of a perforated chamber with boundary layer control through suction. Subsonic flow is obtained with one nozzle block with a downstream choked valve. Standard instrumentation (pitot tubes, wall pressure taps and temperature probes) located in the plenum chamber and in the test section were used to monitor the tunnel free stream conditions. Forces and moments are measured with 12.7 mm and 19.05 mm six component strain gauge balances.

ISL Wind Tunnel - The wind tunnel that was used at the French-German Research Institute of Saint-Louis (ISL) is a blow down type facility capable of Mach numbers from, 1.7 to 4.38 and has a test section of 20cm x 20cm. The run time for this wind tunnel is approximately 50 seconds with a 20-minute recharge time. Pitot tubes and temperature probes mounted in the settling chamber allow for the determination of the freestream conditions. The facility has two sting support systems to hold the models. One is a lateral strut that holds the model from the rear. The other sting is an upstream sting, which is supported in the settling chamber of the tunnel and extends through the nozzle throat into the measurement section. Such a sting is ideal for base flow measurements.

AFRL ARF - The ARF¹⁰ is an enclosed concrete structure used to examine the exterior ballistics of various munitions while in unrestrained flight. The ARF is 207 meters long and has a 13.4 square meter cross-section for the first 69 meters and opens up to 23.8 square meters for the remaining length. There are 50 orthogonal shadowgraph stations used to record the spatial position and angular orientation of the model at each station in time as it traverses the range. The position, orientation, and time data are then used to reconstruct the experimental trajectory. A six-degree-of-freedom analysis technique is applied to the data to determine the aerodynamics of the model.

Test Procedures and Techniques

DREV - The wind tunnel models tested at DREV were supplied by ISL and had a diameter of 20 mm. The models tested had a length to diameter (l/d) ratio of 6 and 8. Both fin configurations, solid and slotted, were tested. The 12.7 mm Able balance was utilized for these experiments. For each run, the analog output signals and the pressure transducers were digitized and then fed into a HP-375 micro-computer for storage and analysis. Separate tare runs were

conducted before each run to obtain the correction of the balance outputs for the model weight. The aerodynamic coefficients were obtained by best-fit polynomials through the measured experimental data.

The wind tunnel aerodynamic results presented (CA0, CN, Cm, C, and Cn) were obtained from a combination of model sweeps between -10° and +10° incidence at roll orientations of 0° and +45°. A positive roll orientation is clockwise when viewed from the rear. The tests were conducted at one supersonic Mach number of 1.5 and at nominal subsonic Mach numbers of 0.92, 0.8, 0.7, 0.6 and 0.5. The slopes of the normal force and the pitching moment coefficients were obtained from the best fit line through the experimental data between -5° and +5°. The axial force at zero angle of attack, CA0, values are uncorrected for base effects, i.e. it is the value as measured by the balance. The roll moment, Cl, provided is the one measured at zero angle of attack. The side moment coefficient slope, Cnα, was obtained with the best fit line through the data between -10° and +10°. The scatter in the measured values for this coefficient was extremely high. In some cases and where warranted, multiple runs were conducted at each Mach number.

Because the DREV facility is an indraft tunnel, the Reynolds number drops to very low values at high Mach numbers. The Reynolds number based on the length of the projectile for these tests are given in Table 1 below and are compared with those of the ISL wind tunnel, the free-flight ones and the ones used for the CFD analysis.

ISL - Experiments were divided into two test categories: the characterization of the flow around the body and the characterization of the afterbody flow. Results include flow visualization, static wall pressure, force, and velocity measurements. Instrumentation of this wind tunnel includes a pressure measurement system, balances for the determi-

Table 1. REYNOLDS NUMBER COMPARISON (based on projectile length l=114 mm)

Wind Tunnel DREV		Wind Tunnel ISL		Free Flight Eglin AFB		CFD	
Mach	Re	Mach	Re	Mach	Re	Mach	Re
0.5	1.14 x 10 ⁶	---	---	0.5	1.29 x 10 ⁶	0.5	1.29 x 10 ⁶
0.6	1.28 x 10 ⁶	---	---	0.6	1.55 x 10 ⁶	0.65	1.68 x 10 ⁶
0.7	1.44 x 10 ⁶	---	---	0.7	1.81 x 10 ⁶	0.7	1.81 x 10 ⁶
0.8	1.55 x 10 ⁶	---	---	0.8	2.07 x 10 ⁶	0.8	2.08 x 10 ⁶
0.92	1.67 x 10 ⁶	---	---	0.92	2.38 x 10 ⁶	0.9	2.33 x 10 ⁶
1.5	1.70 x 10 ⁶	---	---	1.5	3.88 x 10 ⁶	1.4	4.74 x 10 ⁶
---	---	1.7	4.96 x 10 ⁶	1.7	4.39 x 10 ⁶	1.7	5.40 x 10 ⁶
---	---	2.06	4.67 x 10 ⁶	2.06	5.32 x 10 ⁶	2.0	6.01 x 10 ⁶
---	---	2.44	3.53 x 10 ⁶	2.44	6.31 x 10 ⁶	2.44	6.56 x 10 ⁶
---	---	3.0	3.76 x 10 ⁶	3.0	7.75 x 10 ⁶	3.0	7.15 x 10 ⁶

nation of the forces and moments as well as a two-component Laser Doppler Velocimeter (LDV) for the determination of the flow velocities. Flow visualization techniques in the form of oil flow patterns or by optical methods such as direct shadowgraphs or Schlieren photographs are also available.

Flow visualization, pressure and velocity measurements were obtained for a nominal Mach number of 2.06 while force measurements were obtained for Mach numbers ranging between 1.7 and 3.0. The models were tested between -12° and $+6^\circ$ angle of attack. In addition, the models tested at angle of attack were configured in both the "+" configuration (i.e. fins horizontal and vertical) and in the "x" configuration (fins at 45° to horizontal and vertical). Models mounted on the upstream sting were only tested at 0° angle of attack. Pressures, forces and moments were obtained using the same test procedures as for the DREV wind tunnel. Details regarding the data acquisition, data reduction procedure as well as results of flow visualization, pressure and velocity data are given in Ref. 11.

AFRL - Extraction of the aerodynamic coefficients and derivatives is the primary goal in analyzing the trajectories measured in the ARF. After the models were flown through the instrumented range, the time-position history and mass properties were used in conjunction with the ARFDAS (Aeroballistic Research Facility Data Analysis System)¹² to determine the aerodynamic coefficients and stability derivatives. This system utilizes a linear theory reduction routine to get preliminary results, which are subsequently passed to a six degree of freedom (6DOF) numerical integration routine. The 6DOF program uses the Maximum Likelihood technique¹³ to match the theoretical equations of motion to the experimentally measured trajectory. ARFDAS then uses the same routine to simultaneously analyze multiple flights for a much better determination of Mach number and angle of attack dependency in the measured trajectory data. Once the aerodynamic coefficients and derivatives have been extracted from the experimentally measured trajectories, ARFDAS summarizes the results for use in reports.

Computational Fluid Dynamic (CFD) Approach

Code

CFD was carried out to calculate the aerodynamic coefficients, especially the drag, the lift, the pitching moment, and the roll moment coefficients. Numerical simulation of the flow field was conducted by means of the 3D Navier-Stokes code "TASCflow"*. This code is based on a fully implicit, collocated, combined finite volume/flux

element approach¹⁴ with a flux -element based discretization of geometry that can utilize various numerical upwind schemes to ensure the global conservation of mass, continuity, momentum, and energy. The term flux element is only used to distinguish the approach from classical finite element methods. The different upwind schemes range from low accuracy but robust Upwind Difference Schemes (UDS), to high accuracy Mass Weighted Skew (MWS), and Linear Profile Skew (LPS) schemes. A Physical Advection Correction (PAC) term is also used to improve the accuracy of these upstream differencing schemes. The code implements a general non-orthogonal, structured, boundary-fitted grid. Turbulence effects can be modeled using either a standard k- ϵ model or a two-layer model with wall functions and with special treatment for compressibility effects (i.e. compressible wall functions, compressible Reynolds stress model, and compressible turbulent kinetic energy production model). For the present calculation, only the k- ϵ model was used because the number of grid points inside the boundary layer can be kept small. Further details regarding the code capabilities are reported in Ref.15.

Computational Domain and Boundary Conditions

Because of calculations at angle of attack and of the asymmetry of the geometry of the curved fins, a complete four-fin domain was required. The computational grid, designed for viscous computations, was generated algebraically for only a 90° arc of the projectile and the end attaching feature was then used four times to complete the full geometry as shown in Figure 4. Fins were defined by a block-off technique. As usual for viscous flow calculations, grid points were clustered close to the projectile body surface. Grid embedding was necessary for the subsonic and low supersonic predictions in the fin regions, especially for the slotted fins. Figure 4b shows an expanded view of the computational grid in the region of the slotted fin configuration. The resulting grids contained four attached domains for a total number of 463,000 nodes for $M < 1.4$ and a total of 150,000 nodes for $M > 1.4$.

The projectile surface was specified as a solid turbulent adiabatic wall with zero velocity component normal to the wall and a tangent velocity calculated by the mass flow through a region defined by a log-law function. With this approach the number of grid points inside the boundary layer is small. For the supersonic regime, the inlet and outlet conditions were specified as a uniform supersonic flow and a supersonic outlet, respectively. For the subsonic regime, the inlet conditions were specified by the velocity components and the outlet conditions were set by a constant static pressure over the outlet region. For the calculations at Mach numbers < 1.5 , the computational grid was enlarged. Symmetry boundary conditions were used for the axis (zero area) and for the far field.

*TASCflow™ is a trademark of ASC Ltd.

For the zero angle of attack simulation, the solutions were marched from either wind tunnel or sea level, free-flight conditions everywhere until the final converged solutions were obtained. These solutions were then used as an initial guess to start the next angle of attack calculation. The turbulent kinetic energy was obtained for a turbulent intensity of 1.5%, with a characteristic eddy length scale of 1.0×10^{-4} . For the present computations, the residual at each location was reduced by at least three orders of magnitude. Investigations have shown that for the studied cases, larger reductions have little influence on the final solutions. Flow solutions were calculated for Mach numbers ranging between 0.5 and 3.0 and for angles of attack up to 8 degrees.

Results and Discussions

DREV Wind Tunnel Results

The results of the aerodynamic coefficients obtained in the DREV wind tunnel are given in Table 2 for the solid fin data and in Table 3 for the slotted fin data.

ISL Wind Tunnel Results

The results of the aerodynamic coefficients obtained in the ISL wind tunnel are summarized in Table 4 for the solid fin data and in Table 5 for the slotted fin data.

AFRL ARF Results

The results of the aeroballistic tests conducted at the ARF are presented in Table 6. Note that the ARF tests were for the solid fin configuration only.

CFD Results

For the reference configurations and in all cases, computations give a faithful representation of the flow field whose main features are remarkably well predicted if compared with the flow visualization shown in Figures 5a and 5b. They figures represent photo-montages of oil flow visualization associated to shadowgraph pictures, respectively for the solid fin and the slotted fin configurations.

Figures 6a and 7a show surface pressure distributions for the solid fins on the concave and convex sides for an incidence of 0° at $M=0.8$ and 2.0 , respectively. Surface pressure distributions at angles of attack are shown for the same Mach numbers in Figures 6b and 7b. Examples of the computed pressure field between the fins for axial locations of 5%, 50%, and 100% of the fin length are presented for the same conditions in Figures 8, and 9. They give a good indication of the overall flow structure generated by

wrap-around fin configurations. From these figures one can clearly see that for all cases a difference in the chordwise pressure exists between the concave and the convex side of the fin. In the subsonic regime, a region of high pressure takes place on the convex side of the fin whereas a region of low pressure exists on the concave side of the fin. In the case of a supersonic flow, the phenomenon is reversed. Maximum pressure occurs on both fin sides at about half-span and half-chord (50% of fin length). This pressure difference gives rise to a rolling moment at $\alpha=0^\circ$ and also indicates that the direction of the rolling moment changes direction. Figure 8 and 10 indicate a roll direction towards the fin's center of curvature whereas Figure 9 and 11 indicate a roll reversal. This enhances the analysis made from the static wall pressure measurements carried out in the wind tunnel¹¹. Figures 7a and 7b also show the asymmetric flow separation ahead of the leading edge of the fins due to the strong bow shocks generated by the leading edge of the fins. One also can note the development of a region of high pressure close to the concave side of the fin that is due to the interaction between the bow shocks emanating from the fin leading edges. This complex three-dimensional flow pattern is qualitatively in very good agreement with the results of oil flow visualization¹¹, shown in Figure 5a, and with the analysis of computational results made in the vicinity of a single wrap around fin^{16, 17}. Figures 10 and 11 show the angle of attack effects on the pressure distributions between the fins for an axial location of 50% of the fin length for angles of attack ranging between 2° and 9° at $M=0.8$ and 2.0 , respectively. Again, one can note that there is a roll reversal between the subsonic and the supersonic regime due to the pressure difference between the concave and convex side of the fins. One can also note that a high pressure difference, especially obvious in the subsonic regime, is generated with increasing α . These asymmetric pressure distributions between the fins do not only induce a roll moment but also a side moment. Previous results¹⁸ suspected that a variation of about 20% of the side moment can be observed for wrap-around fin configuration under angle of attack.

Figures 6c and 7c show surface pressure distributions for the slotted fins on the concave and convex sides for an incidence of 0° at $M=0.8$ and 2.0 , respectively. Computed pressure contours between the fins for axial locations of 5%, 50%, and 100% of the fin length are presented for the same conditions in Figures 12 and 13. For the slotted configuration, the flow pattern is not significantly different between the two configurations except in the vicinity of the fins. Also for this configuration, the flow pattern is qualitatively in very good agreement with the results of oil flow visualization¹¹, shown in Figure 5b. Due to the flow existing in the slots, the pressure difference between the concave and convex side of the fin is smaller than for the solid fin configuration. Therefore, the magni-

tude of the roll moment coefficient as well as for the side moment coefficient is decreased. Figures 14 and 15 present the angle of attack effects on the pressure distributions between the fins for an axial location of 50% of the fin length for angles of attack of 6 and 5° at $M=0.8$ and 2.0, respectively. For the supersonic regime, the flow pattern is again not significantly different between the two studied configurations except in the vicinity of the fins. For the subsonic regime, flow pattern is also quite similar but slots generate a smaller pressure difference between the upper and lower surfaces of the fins. This difference provides smaller roll and side moments if compared with the solid fin configuration.

In order to understand the fin thickness effects, CFD predictions were carried out for two solid fin configurations with fin thickness of 2mm and 1mm. Simulations were performed at Mach numbers of 0.8 and 2.06 and for angles of attack ranging between 0 and 8°. Figures 16a and 17a show the surface pressure distributions for the solid 2mm thick fins on the concave and convex sides for an incidence of 0° at $M=0.8$ and 2.0, respectively. Figures 16b and 17b show the same results obtained for the 1mm thick fin configuration. Computed pressure contours between the fins for an axial location of 50% of the fin length are presented in Figures 18 and 19 for the same conditions as Figures 16 and 17. For both subsonic and supersonic regimes, the overall flow structure on the projectile and between the fins remains similar to the 4mm thick case. However, the dramatic difference between the 4mm and 1mm thick fins is the decrease of the pressure ratio between the concave and the convex side of the fins. This means that decreasing fin thickness will reduce the drag coefficient as well as the roll and side moment coefficients.

Forces and moments acting on the body were calculated by integration of the pressure and viscous force components. CFD results were confirmed by comparison with aerodynamic coefficients obtained experimentally. Results of the aerodynamic coefficients obtained for the different CFD predictions are presented for the 4mm thick fins in Table 7 for the solid fin data and Table 8 for the slotted fin data. Table 9 and 10 present the aerodynamic coefficients obtained for the solid fin data, respectively for the 2mm thick fin and the 1mm thick fin.

Zero Yaw Axial Force Coefficient

The wind tunnel axial force coefficient vs. angle of attack is provided in Figures 20a and 20b for the solid and slotted fin configurations, respectively. Figure 20c presents the zero yaw axial force coefficient CA_0 vs. Mach number. For the numerical predictions, only the forebody drag, C_{Df} , is represented. In case of thick fins, base drag cannot be estimated empirically from experimental results because

its value becomes very high and can even represent up to 50% of the total drag at transonic or moderately high Mach numbers. To determine the base drag in this range of flow regime, additional CFD base flow predictions are in progress.

The main trend as well as the magnitude of CA_0 is in excellent agreement between the experimental results. The zero yaw axial force plot shows little difference between the solid and the slotted fin configurations. However, a slight overall increase in drag was observed for the slotted fins at supersonic Mach numbers. This slight increase is due to the presence of a small recirculating region generated by the slots.

Normal force coefficient

The wind tunnel normal force coefficient vs. angle of attack is provided in Figures 21a and 21b for the solid and slotted fin configurations, respectively. The supersonic data for the solid fin configuration is basically linear over the tested angles of attack range. At the subsonic velocities, there is an abrupt change in the slopes of the CN data at approximately +5° and -5° and it is also symmetrical. The CN data is quite linear between these two angles of attack. This abrupt change in slope (closer to zero) indicates that the fin is losing effectiveness and is partially stalling. There are slight variations in the slopes between -5° and +5° as the Mach number changes.

The slotted fin normal coefficient (Fig 21b) shows two distinct patterns. A change in slope between the subsonic and supersonic data is quite evident with less slope for the subsonic data indicating less lift. There are also no sudden changes in the slope vs. angle of attack as was noticed in the solid fin results. When compared with the solid fin data, the supersonic CN slope for the slotted fin is less and it is even lesser for the subsonic data.

The normal force coefficient slope (CN_α) for both the solid and slotted models are compared vs. Mach number for all the tests and numerical simulations that were conducted in Figure 21c. The slotted fins CN_α is less than the solid ones by approximately 20% supersonically and by approximately a factor of two subsonically. The effectiveness of the slotted fins subsonically is greatly reduced due to the decreased fin surface area and its effectiveness approaches the solid fins as the Mach number increases supersonically. The wind tunnel data for the solid fin model is higher than the free-flight data by about 16% at Mach 1.5. The CFD predictions for the solid fins agree quite well with the wind tunnel data for both subsonic and supersonic flow regimes. For the slotted configurations,

agreement is also very good, except for $M=0.5$ where CFD over predicts $CN\alpha$ by more than 30%.

Static Pitch moment coefficient

The static pitch moment coefficient versus angle of attack from the wind tunnel tests for all the tested Mach numbers are compared in Figures 22a and 22b for the solid and slotted finned projectiles, respectively. The reference location is about the base of the projectile. The C_m results are linear over the tested angle of attack range for both fin types. There are two distinct patterns for both models. The supersonic and subsonic data are grouped together at two definite slope patterns. It should also be noticed that there is no abrupt change in the slope of the C_m data with angle of attack for the solid fin projectile as was seen in the CN results. This implies that there was a sudden shift in the center of pressure to compensate for the abrupt change of CN at approximately -5° and $+5^\circ$ angle of attack for C_m to be linear with angle of attack from -10° to $+10^\circ$. Comparing the solid and slotted fin data between angles of attack of -5° to $+5^\circ$, it is quite evident that the slotted fin slopes are less than the solid ones.

This is easier to discern when the pitch moment coefficient slope ($C_m\alpha$) from all the tests and the computations are compared versus Mach number in Figure 22c. The $C_m\alpha$ in Figure 22c were transferred to center of gravity of the free flight tested projectile, which is located at 2.89 caliber from the base of the projectile. From the wind tunnel data, at supersonic velocities, the slotted fin $C_m\alpha$ is less than the solid one by approximately 40% while subsonically it is less by a factor of 4.5. The wind tunnel $C_m\alpha$ data agrees extremely well with the free flight reduced results supersonically. The computational predictions for $C_m\alpha$ are 30% higher than the wind tunnel results at the high Mach numbers and approximately 40% higher at about Mach 1.5. Since the CFD normal force coefficient slope agreed quite well with the wind tunnel data at the high Mach numbers, this seems to indicate that the computational procedure has difficulty in predicting the location of the center of pressure. Subsonically the overall trend of the CFD predictions for the solid fin show good agreement but are under predicting the wind tunnel data by about 25%. Concerning the slotted configuration, the same remarks can be made as for $CN\alpha$.

Center of Pressure

The center of pressures (about the base of the projectile) from the experimental tests and computational procedure are compared versus Mach number in Figure 23. The location of the center of gravity (2.89 cal from the base) is shown as a solid thick line. Supersonically and

from the wind tunnel results, the center of pressures of the slotted fin projectile is a shifted forward 0.3 caliber of the solid fin projectile and by approximately 1.0 caliber subsonically. The wind tunnel data and CFD predictions for the center of pressure location agree quite well with the free-flight data at about Mach 1.7 and over predict by approximately 0.4 cal at Mach 1.5, even though the wind tunnel and CFD agree quite well at this Mach number. The CFD estimates under predict the wind tunnel data by approximately 0.4 cal at the higher Mach numbers.

Subsonically and from the wind tunnel data, the center of pressure of the slotted fin projectile is forward of the solid one by roughly 0.8 caliber.

For both configurations, CFD data are in quite good agreement with the experimental data for supersonic Mach numbers but showed some discrepancies for $M < 0.8$.

Side Moment Coefficient

The side force coefficient is positive to the right when looking at the projectile from the top and with the nose located at the front.

The wind tunnel side moment coefficient (about the center of gravity of the projectile) is shown versus angle of attack for various Mach numbers in Figures 24a and 24b for the solid and slotted finned projectiles, respectively. There is some scatter in the data that is more pronounced subsonically. The supersonic data for C_n had less scatter in the results and it was basically linear over the tested angle of attack range. Even though multiple tests were conducted at the same Mach number, only one per Mach number is shown in the graphs. As the Mach number decreases for the solid fin projectile, the slopes tend to decrease. The slopes of C_n seem less pronounced for the slotted fin projectile.

To be able to compare with the free-flight data which reduces for the slope of the side moment coefficient about the cg ($C_n\alpha$); a best fit line was fitted through the wind tunnel experimental data over the whole angle of attack range (for DREV this was between -10° to $+10^\circ$). The results are given in Table 2 and 4 and Table 3 and 5 for the solid and slotted finned projectiles, respectively. To provide an indication of the scatter in the results, the data was grouped depending on the level of the correlation coefficient, r , which represents the "goodness of the fit". The data was categorized in three groupings as indicated in the Tables. The data in the c grouping ($M=0.92$ for the solid fins) indicates very large scatter in the results and should probably not be considered.

The side moment coefficient slope ($Cn\alpha$) for both the solid and slotted models are compared vs. Mach number for the experimental tests that were conducted in Figure 24c. By comparison with the solid fin configuration, the inclusion of slots provides supersonically a reduction in side moment by about an average value of 38%. The wind tunnel data for the solid fin configuration shows the same trend but is higher than the free flight by about 30%. For subsonic Mach numbers, this difference is much higher and represents an average value of 58%. With increasing Mach number, $Cn\alpha$ is decreasing for the solid fin whereas $Cn\alpha$ remains almost constant for the slotted fin.

No comparison was made with the CFD data. Indeed, results obtained during this investigation for the side moment coefficient showed grid size dependencies. Therefore additional simulations need to be conducted for better accuracy of the side moment coefficient predictions.

Roll Moment Coefficient

The roll moment is positive clockwise when viewing the projectile from the rear.

The wind tunnel roll moment coefficient vs. angle of attack for the solid and slotted fin configurations are compared in Figures 25a and 25b, respectively, for various Mach numbers. Even though multiple tests were conducted at the same Mach number, only one per Mach number is shown in the graphs. There is some large scatter in the wind tunnel results at the subsonic velocities.

For the solid fin configuration and at the supersonic Mach numbers (Figure 25a), the shape of the Cl vs. angle of attack is of a parabolic nature with Cl increasing negatively as the angle of attack increases. Cl at zero angle of attack is negative indicating counterclockwise moment acting on the projectile. At the subsonic Mach numbers, the Cl vs. angle of attack for the solid fin is of an "M" profile, i.e., the profile is of a parabolic nature at the higher angles of attack as at the supersonic velocities, but between $-5^\circ < \alpha < +5^\circ$ the Cl data dips negatively to reach a local minimum at $\alpha=0$. To confirm if this was repeatable, multiple wind tunnel tests were conducted at Mach 0.5 and this is shown in Figure 25c. The data is repeatable and consistent for the four tests at Mach 0.5. Two more wind tunnel tests were made at Mach 0.5 and at a fixed angle of attack of 0.16 , and the average Cl obtained from these two runs was -0.0245 , which is consistent with the continuous sweep runs. The reasons for this change in Cl subsonically between $-5^\circ < \alpha < +5^\circ$ are unknown at the present time. There may be a Reynolds number effect but without further testing in a different facility it may be difficult to resolve the issue. CFD calculations at various Reynolds number might be useful in understanding this phenomena. It should

be noted that without this drop between $-5^\circ < \alpha < +5^\circ$, there would have been a roll reversal subsonically, that is Cl positive at $\alpha=0$. The data scatter at Mach 0.92 was very high.

The slotted fin Cl has a similar supersonic profile of the solid fin results except that now the subsonic Cl data is of a "W" profile. Again the reasons for this are unknown and the same comments as the in the previous paragraph hold. All of the Cl data for the slotted finned data has shifted upwards positively compared to the solid fin results. At the high Mach numbers ($M>1.5$) Cl_0 is negative for both the solid and slotted fin projectiles indicating a counterclockwise motion. At Mach 1.5 the solid fin has a negative Cl_0 while the slotted fin one is positive indicating a roll reversal for the slotted fin projectile compared with solid one. All the subsonic Cl_0 data for the solid fin is negative while it positive for the slotted fin data.

To be able to compare Cl_0 with the free-flight results and the computational predictions versus Mach number, the wind tunnel for Cl_0 was taken at $\alpha = 0.0$. This data is provided in Table 1 and 2 for the DREV wind tunnel data and in Table 4 and 5 for the ISL data. Due to the large scatter in the DREV wind tunnel data in some cases the data was classified as provided in the tables. All the DREV wind tunnel data for Cl at Mach 0.92 had too much scatter to resolve a Cl_0 and there was large scatter in some of the other results as indicated in the tables.

Figure 25d shows the variation of rolling moment coefficient as a function of Mach number for experimental data and computations. One can clearly see that there exists a roll moment that varies with the Mach number. Direction of this rolling moment changes close to Mach 1. This behavior is in complete agreement with previous CFD predictions and experimental data¹⁷. Comparison with results of Euler computations¹⁸ obtained for very thin fins shows that the present results are in good agreement with the overall trend but are under- or over-predicted in magnitude. This indicates that fin thickness contributes significantly to the roll moment generation at 0° angle of attack. Computations and wind tunnel results compare quite well for supersonic Mach numbers but compare poorly at subsonic Mach numbers. Indeed, the value of the experimental roll moment coefficient is about zero around $M=1.0$ but remains negative for $M<1.0$ whereas the predicted roll moment is positive and increases greatly in magnitude.

Free flight roll moment coefficients that are only available for $M>1.4$ present a variation of more than 50% relative to the wind tunnel and CFD results. However, they agree well with some previous Euler predictions carried out for wrap around fin configurations with solid thin fins.

There is a discrepancy that is not completely understood at this time.

Fin thickness effects on the aerodynamic coefficients are presented in Figures 26a to 26d. Figure 26a shows the forebody drag coefficient C_{Df} vs. Mach number. As expected from the pressure distributions on the body and between the fins, one can note that for the supersonic regime C_{Df} is decreased by a factor 1.5 and 3 with decreasing fin thickness, respectively for 2mm and 1mm. For the subsonic regime, C_{Df} remains identical for a 2mm thick fin whereas C_{Df} is reduced by 50% for the 1mm thick fin. The normal force coefficient derivative $C_{N\alpha}$ and the pitching moment coefficient derivative $C_{m\alpha}$ vs. Mach number are shown in Figures 26b and 26c, respectively. $C_{N\alpha}$ and $C_{m\alpha}$ are slightly smaller for subsonic Mach numbers but remained constant for supersonic Mach numbers. The fin thickness effects on the roll moment coefficient $C_{l\alpha}$ is shown in Figure 26d. For both flow regimes, one can clearly see that fin thickness contributes significantly to the roll moment generation at 0° angle of attack. Indeed, $C_{l\alpha}$ becomes smaller when decreasing fin thickness, especially for $M > 1.0$. For the thin fins (1mm), predicted results are in the order of magnitude with those obtained by Euler computations¹⁸.

Conclusions

A detailed investigation including experiments and theoretical predictions for wrap around fin projectile configurations was conducted for nominal Mach numbers ranging between 0.5 and 3.0, for angles of attack ranging between -15 and 15 degrees, and for fin roll orientations of 0° and 45° . Solid fin and slotted fin configurations were studied. Fin thickness effects on the aerodynamic coefficients were also earned out numerically. Experiments were conducted at the Aeroballistic Research Facility at Eglin AFB, FL, and at the ISL, France, and DREV, Canada, wind tunnels. In order to take in account viscous effects, predictions were carried out on four-finned configurations using a 3D Navier-Stokes code.

The experimental and computational results described in this paper are but a small part of the complete data set. By comparison between the different results, one can note that viscous calculations can capture the flow physics of these complicated flowfields and provide insight to fin/fin and fin/body interactions. Aerodynamic coefficients were calculated from the flowfield solutions and compared with the experimental data. Supersonically, an overall good agreement was obtained for the aerodynamic coefficients. Subsonically, a good agreement was observed as far as concerning the trends but there are still some differences in magnitude for some of the coefficients. Fin

thickness effects showed that thin fins reduce drag and also decrease the roll moment coefficient.

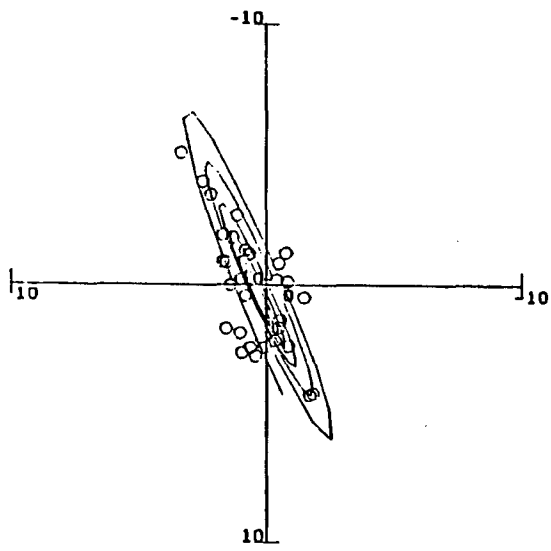
Future Work

In order to complete the database, further investigations will include wind tunnel force measurements in the transonic range ($0.95 < M < 1.2$). Subsonic and transonic free flight tests will also be conducted for comparison with the results obtained in the wind tunnels and from the CFD data predictions. Grid size dependencies on the side moment coefficient will also be studied in more details, especially in the subsonic flow regime. Model length, fin attachment geometry, fin curvature effects will also be investigated numerically. A complete data package for all conditions (i.e. angle of attack, roll orientation,...) including experiments and predictions is planned^{19,20}.

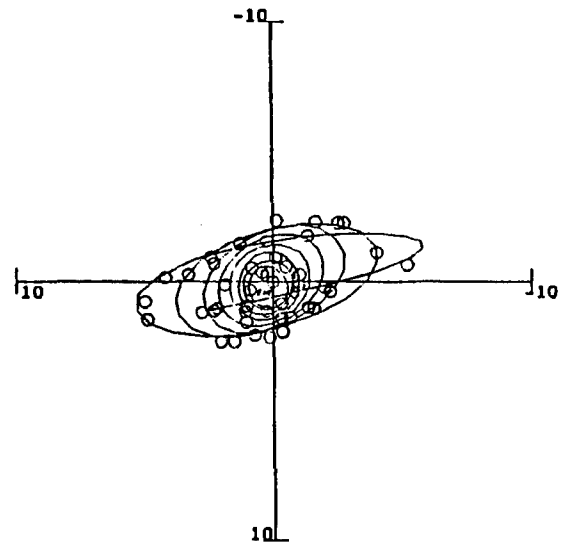
References

1. Dahlke, C. W., "Experimental Investigation of Several Wraparound Fins on Bodies of Revolution from Mach 0.3 to 1.3," Data Report, US Army Missile Command, Redstone Arsenal, AL, September 1971, Report No. RD-TM-71-12.
2. Dahlke, C. W., "The Aerodynamic Characteristics of Wrap-Around Fins at Mach Numbers of 0.3 to 3.0," Technical Report, US Army Missile Command, Redstone Arsenal, AL, October 1976, Report No. RD-77-4.
3. Dahlke, C. W., "A Summary of Aerodynamic Characteristics for Wrap Around Fins from Mach 0.3 to 3.0," Technical Report, US Army Missile Command, Redstone Arsenal, AL, March 1977, Report No. RD-77-5.
4. Daniels, P., "The Effect of Fin Slots and Fin Tabs on the Dynamic Stability Characteristics of the Navy Low Drag Bomb," Technical Report, US Naval Weapons Laboratory, Dahlgren, VA, May, 1970, Report No. TR-2403.
5. Daniels, P., "Effect of Fin Slots on the Static and Dynamic Stability Characteristics of the Finned Bodies," Technical Report, US Naval Weapons Laboratory, Dahlgren, VA, June, 1971, Report No. TR-2582.
6. Daniels, P. and Hardy, S. R., "Roll-Rate Stabilization of a Missile Configuration with Wrap Around Fins in Incompressible Flow," Technical Report, Naval Surface Weapons Center, Dahlgren, VA, December 1975, Report No. TR-3346.
7. Kim, Y. H., Winchenbach, G. L., "Roll Motion of a Wraparound Fin Configuration at Subsonic and Transonic Mach Numbers," AIAA Paper 85-1977, August 1985.

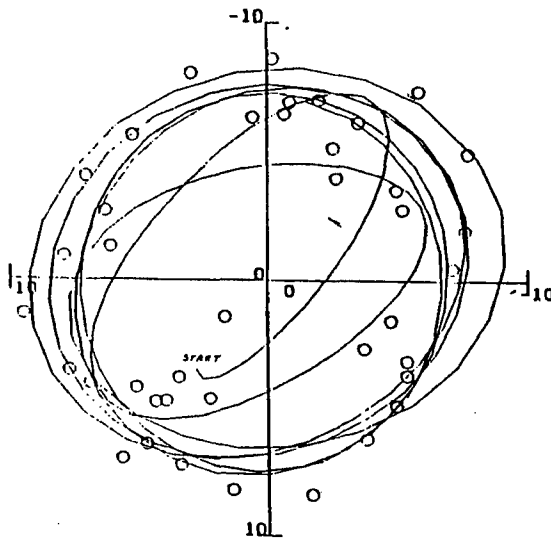
9. Abate, G. L., Winchenbach, G.L., "Aerodynamics of Missiles with Slotted Fin Configurations", AIAA Paper 91-0676, January 1991.
9. Dilworth, Secord, Meagher and Associates Ltd., "Commissioning Report of the DREV 2 ft Indraft Tunnel", Report No. 695/912, March 1977
10. Kittyle, R. L., Packard, J. D., Winchenbach, G. L., "Description and Capabilities of the Aeroballistic Research Facility," Air Force Armament Laboratory Technical Report, AFATL-87-08, May 1987
11. Abate, G. L., Berner, C., "Wind Tunnel Measurements of Wrap Around Fins at Mach 2.06", AIAA Paper 94-3499, August 1994
12. Fischer, M. A., Hathaway, W.H., " Aeroballistic Research Facility Data Analysis System," Air Force Armament Laboratory Technical Report, AFATL-88-48, September 1988
13. Hathaway, W., "Free Flight Data Analysis Using Maximum Likelihood Technique," Paper 545, Presented at the 28th meeting of the Aeroballistic Range association, September 1977.
14. Raw, M., Galpin, P. F., Hutchinson, B. R., "A Co-Located Finite Volume Method for Solving the Navier-Stokes Equations for Incompressible and Compressible Flows in Turbomachinery: Results and Applications", Canadian Aeronautics and Space Journal, Vol. 35, No.4, 1989.
15. ASC Advanced Scientific Computing Limited, "TASCflow - Version 2.4: Theory and User Documentation", Waterloo, Ontario, Canada, March 1995.
16. Tilmann, C. P., Buter, T. A., Bowersox, R. D. W., "Characterization of the Flow near a Wrap-Around Fin at Mach 2.8", AIAA Paper 97-0522, Reno, NV, January 1997.
17. Edge, H.L., "Computation of the Roll Moment for a Projectile with Wrap-Around Fins", Journal of Spacecraft and Rockets, Vol.31, No.4, July-August 1994.
18. Abate, G. L., Cook, T., "Analysis of Missile Configurations with Wrap around Fins using Computational Fluid Dynamics", AIAA Paper 93-3631, Monterey, CA, August 1993.
19. Abate, G. L., Berner, C., Dupuis, A., "Aerodynamics of Wrap Around Fins. Part 1: Free Flight and Wind Tunnel Results", To be published in 1998.
20. Berner, C., "Aerodynamics of Wrap Around Fins. Part 1: CFD Results", To be published in 1998.



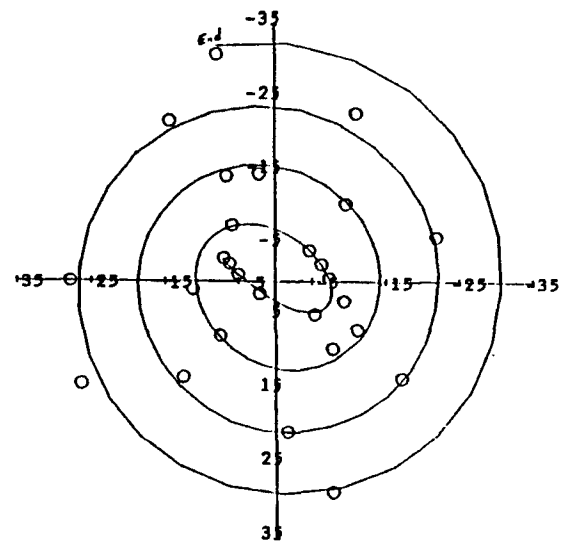
a) Straight Fin Missile Motion



b) WAF missile with damped side moment



c) WAF missile with neutral damped side moment



d) WAF missile with undamped side moment

Fig.1 Wrap Around Fin Motion Patterns

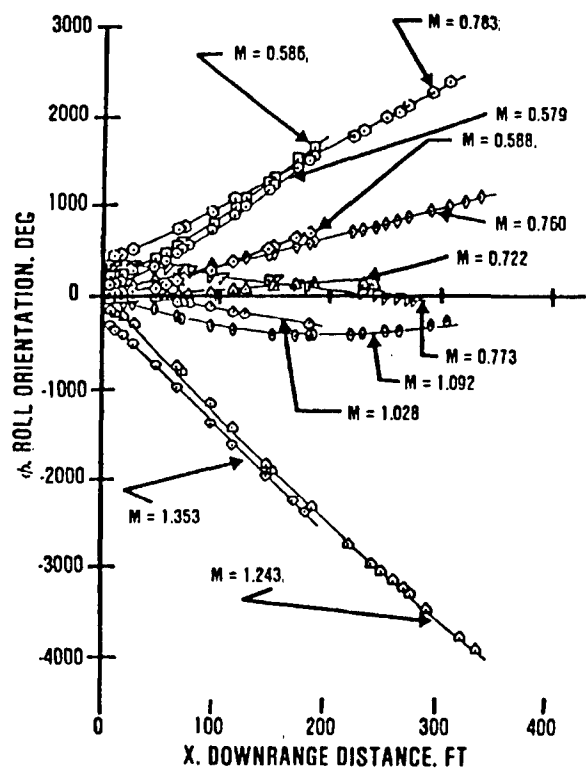


Fig.2 Roll vs. Downrange Distance for Wrap Around Fin Configurations

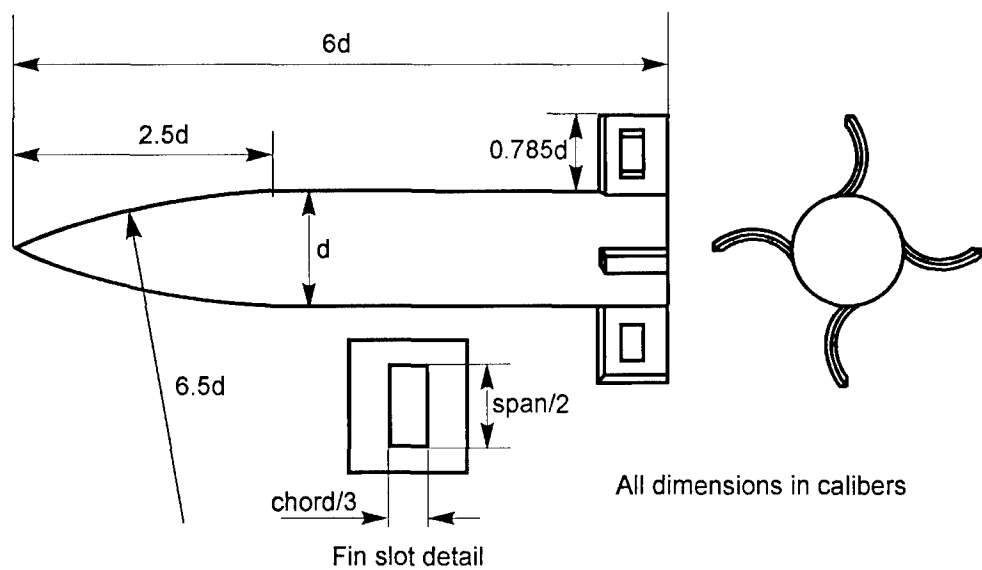


Fig.3 Configuration Geometry (*not all models had "slots")

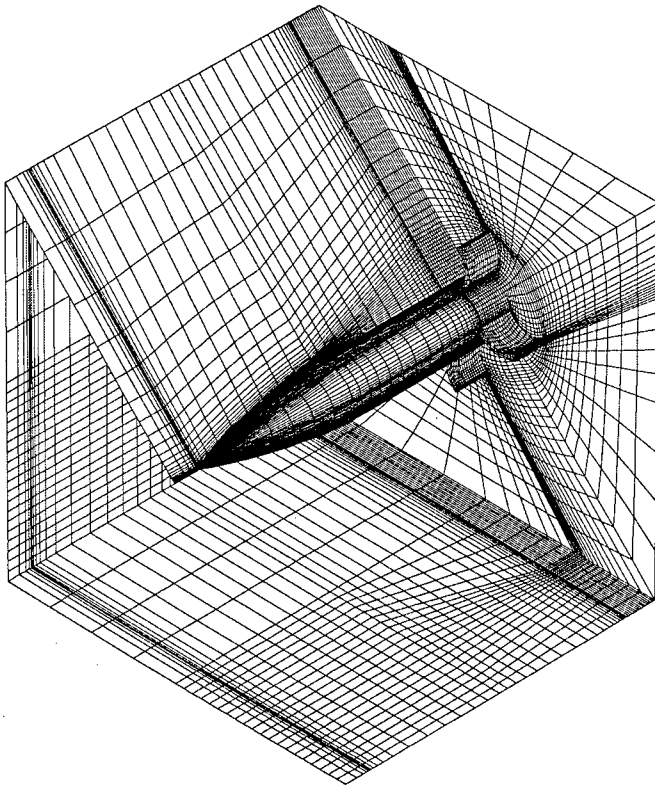


Fig.4a Overall Computational Grid for solid fin

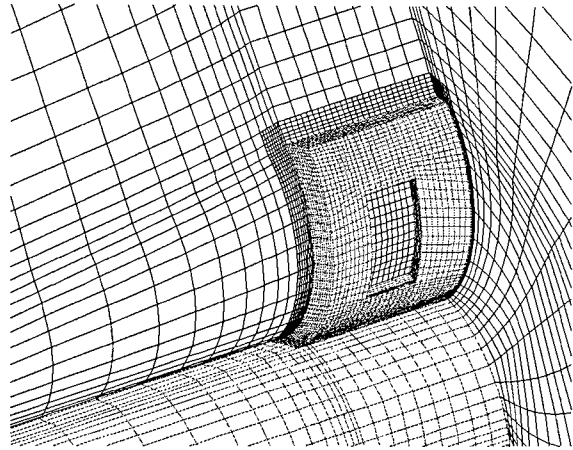


Fig.4b Expanded view of slotted fin region

Table 2. DREV Wind Tunnel Results, Solid Fins, $l/d = 6$, $\phi = 0^\circ$

Mach Number	$C_{N\alpha}$ (/rad)	$C_{m\alpha}^{base}$ (/rad)	C_{x0}	x_{cp} (cal from base)	$C_{m\alpha}^{cg}$ (/rad)	$C_{n\alpha}^{cg}$ (/rad)	C_l
1.461	7.89	12.58	1.079	-1.59	-10.23	-	-0.0283
1.489	7.87	13.24	1.098	-1.68	-9.49	-1.140 ^a	-0.0302
1.489	7.85	13.17	1.097	-1.68	-9.53	-	-0.0339
0.920	8.61	11.88	0.808	-1.38	-13.00	-0.557* ^c	TMS
0.920	8.56	11.87	0.809	-1.39	-12.86	-0.401 ^c	TMS
0.789	6.60	10.85	0.566	-1.64	-8.22	-1.047 ^b	-0.0323 - LS
0.789	6.60	10.60	0.570	-1.61	-8.48	-1.144 ^b	-0.0312 - LS
0.693	7.29	11.24	0.527	-1.54	-9.84	-1.255 ^a	-0.0311 - LS
0.695	7.83	11.90	0.520	-1.52	-10.73	-1.169 ^a	-0.0341 - LS
0.598	8.22	12.21	0.494	-1.49	-11.54	-1.261 ^b	-0.0302
0.598	7.94	11.70	0.493	-1.47	-11.26	-1.246 ^b	-0.0319
0.499	8.32	11.93	0.481	-1.43	-12.11	-1.357 ^b	-0.0290
0.499	8.03	11.72	0.483	-1.46	-11.48	-1.443 ^b	-0.0309
0.499	8.34	11.94	0.490	-1.43	-12.16	-1.483 ^b	-0.0298
0.499	8.46	12.18	0.476	-1.44	-12.27	-1.437 ^b	-0.0304

Goodness of fit

a) $R > 0.9$

b) $0.8 < R < 0.9$

c) $R < 0.8$

TMS - Too Much Scatter

LS - Large Scatter

Table 3. DREV Wind Tunnel Results, Slotted Fins, l/d = 6, phi = 0.0

Mach Number	$C_{N\alpha}$ (/rad)	$C_{m\alpha}^{base}$ (/rad)	C_{X0}	X_{cp} (cal from base)	$C_{m\alpha}^{cg}$ (/rad)	$C_{n\alpha}^{cg}$ (/rad)	C_l
1.489	6.43	12.66	1.107	-1.97	-5.92	-0.590 ^a	0.0119
0.920	4.51	10.02	0.845	-2.22	-3.01	-0.561 ^b	TMS
0.694	4.29	9.76	0.536	-2.27	-2.64	-0.526 ^c	0.0234 - LS
0.500	4.34	9.98	0.509	-2.30	-2.57	-0.505 ^c	0.0200 - LS
Goodness of fit							
a) $R > 0.9$				TMS - Too Much Scatter			
b) $0.8 < R < 0.9$				LS - Large Scatter			
c) $R < 0.8$							

Table 4. ISL Wind Tunnel Results, Solid Fins, l/d = 6, phi = 0.0

Mach Number	$C_{N\alpha}$ (/rad)	$C_{m\alpha}^{base}$ (/rad)	C_{X0}	X_{cp} (cal from base)	$C_{m\alpha}^{cg}$ (/rad)	$C_{n\alpha}^{cg}$ (/rad)	C_l
3.00	5.904	13.734	0.787	-2.33	-3.30	-0.495	-0.0552
2.44	6.531	14.468	0.908	-2.22	-4.41	-0.583	-0.0686
2.06	6.753	13.978	0.996	-2.07	-5.54	-0.527	-0.0746
1.70	7.429	13.644	1.072	-1.94	-7.83	-0.933	-0.0573

Table 5. ISL Wind Tunnel Results, Slotted Fins, l/d = 6, phi = 0.0

Mach Number	$C_{N\alpha}$ (/rad)	$C_{m\alpha}^{base}$ (/rad)	C_{X0}	X_{cp} (cal from base)	$C_{m\alpha}^{cg}$ (/rad)	$C_{n\alpha}^{cg}$ (/rad)	C_l
3.00	5.406	13.766	0.802	-2.55	-1.86	-0.384	-0.0176
2.44	5.823	14.522	0.919	-2.49	-2.31	-0.369	-0.0289
2.06	5.971	13.923	0.996	-2.33	-3.33	-0.504	-0.0699
1.70	6.411	13.403	1.066	-2.09	-5.13	-0.931	-0.0170

Table 6. Air Force Research Laboratory ARF Data

Shot Number	Mach Number	c.g. (% body length)	C_{x0}	$C_{N\alpha}$	$C_{m\alpha}$	C_{lp}	C_{nsm}
9	1.287	51.73	1.066	7.55	-12.696	-4.170	-.67
4	1.447	51.70	1.069	6.50	-11.415	-3.843	-.57
11	1.540	51.66	1.026	6.50	-10.430	-3.590	-.62
6	1.731	51.56	1.011	6.16	-7.600	-3.470	-.44
7	1.900	51.57	1.004	6.11	-6.383	-2.738	-.22
11 & 4	1.494	-	1.029	6.41	-10.88	-3.84	-.63
6 & 7	1.816	-	1.006	6.58	-7.180	-3.47	-.37

Table 7. CFD, Solid Fins (4mm thick fin), $l/d = 6$, $\phi = 0.0$

Mach Number	α (°)	$C_{N\alpha}$ (/rad)	$C_{m\alpha}^{base}$ (/rad)	C_{DF}	X_{cp} (cal from base)	$C_{m\alpha}^{cg}$ (/rad)	C_l
3.00	0	---	---	0.501	---	---	-0.069
3.00	3	6.24	12.53	0.505	-2.01	-5.50	-0.073
2.44	0	---	---	0.538	---	---	-0.086
2.44	3	6.54	12.70	0.542	-1.94	-6.21	-0.090
2.06	0	---	---	0.561	---	---	-0.104
2.06	2	6.72	12.64	0.560	-1.88	-6.79	-0.110
2.06	5	6.93	12.97	0.552	-1.87	-7.05	-0.109
2.06	8	7.22	13.47	0.540	-1.86	-7.40	-0.107
1.70	0	---	---	0.573	---	---	-0.087
1.70	3	7.84	12.84	0.549	-1.64	-9.82	-0.093
1.40	0	---	---	0.542	---	---	-0.046
1.40	3	11.50	18.60	0.554	-1.61	-14.63	-0.054
0.97	0	---	---	0.720	---	---	-6.4 ^E -3
0.97	3	6.48	15.08	0.583	-2.33	-9.65	-5.3 ^E -3
0.90	0	---	---	0.711	---	---	0.017
0.90	3	5.82	12.73	0.541	-2.09	-8.10	1.03 ^E -2
0.85	3	6.02	9.28	0.337	-1.54	-8.11	0.018
0.80	0	---	---	0.330	---	---	0.045
0.80	3	6.08	10.11	0.401	-1.66	-7.46	0.081
0.80	6	5.9	10.76	0.391	-1.82	-6.29	0.095
0.80	9	5.22	11.03	0.369	-1.92	-5.59	0.080
0.70	3	6.61	8.29	0.378	-1.73	-6.62	0.149
0.65	0	---	---	0.280	---	---	0.068
0.65	3	7.41	13.24	0.235	-1.79	-8.18	0.041
0.50	0	---	---	0.254	---	---	0.113
0.50	3	8.23	14.85	0.192	-1.81	-8.91	0.106

Table 8. CFD, Slotted Fins (4mm thick fin), $l/d = 6$, $\phi = 0.0$

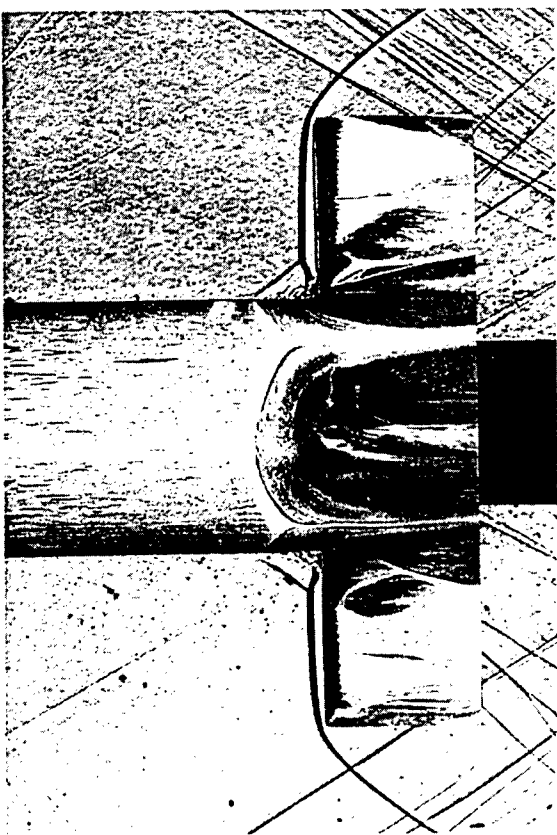
Mach Number	α (°)	$C_{N\alpha}$ (/rad)	$C_{m\alpha}^{base}$ (/rad)	C_{DF}	X_{cp} (cal from base)	$C_{m\alpha}^{cg}$ (/rad)	C_l
3.00	0	---	---	0.536	---	---	-0.056
3.00	3	5.65	12.36	0.539	-2.19	-3.98	-0.058
2.43	0	---	---	0.577	---	---	-0.072
2.43	3	5.83	12.49	0.580	-2.14	-4.36	-0.074
2.06	0	---	---	0.601	---	---	-0.088
2.06	3	6.06	12.49	0.603	-2.06	-5.02	-0.089
2.06	5	6.21	12.75	0.605	-2.05	-5.20	-0.090
2.06	8	6.46	13.25	0.608	-2.05	-5.42	-0.082
1.70	0	---	---	0.600	---	---	-0.071
1.40	0	---	---	0.598	---	---	-0.068
0.80	0	---	---	0.364	---	---	0.018
0.80	3	4.24	10.92	0.324	-2.58	-1.32	0.016
0.80	6	4.43	10.98	0.345	-2.48	-1.81	0.013
0.80	9	4.64	11.18	0.350	-2.41	-2.22	0.015
0.65	3	4.94	11.25	0.272	-2.27	-3.03	0.029
0.50	3	6.41	13.08	0.260	-2.04	-5.44	0.055

Table 9. CFD, Solid Fins (2mm thick fin), l/d = 6, phi = 0.0

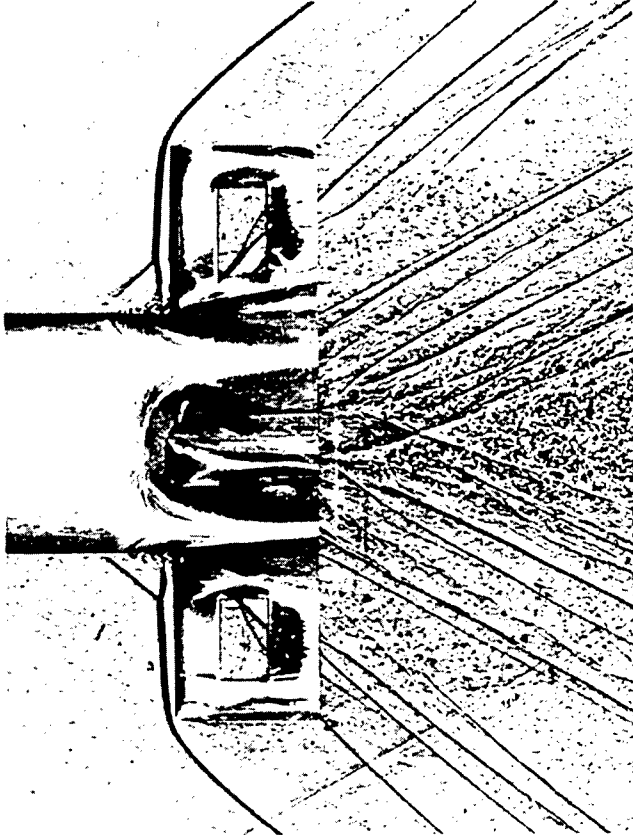
Mach Number	α (°)	$C_{N\alpha}$ (/rad)	$C_{m\alpha}^{base}$ (/rad)	C_{DF}	x_{cp} (cal from base)	$C_{m\alpha}^{cg}$ (/rad)	C_l
2.06	0	---	---	0.321	---	---	-0.074
2.06	2	6.88	12.60	0.320	-1.83	-7.29	-0.076
2.06	5	7.02	12.91	0.318	-1.84	-7.37	-0.081
2.06	8	7.26	13.42	0.316	-1.85	-7.56	-0.090
0.80	0	---	---	0.290	---	---	0.045
0.80	3	5.11	11.40	0.199	-2.23	-3.38	0.034

Table 10. CFD, Solid Fins (1mm thick fin), l/d = 6, phi = 0.0

Mach Number	α (°)	$C_{N\alpha}$ (/rad)	$C_{m\alpha}^{base}$ (/rad)	C_{DF}	x_{cp} (cal from base)	$C_{m\alpha}^{cg}$ (/rad)	C_l
2.06	0	---	---	0.194	---	---	-0.024
2.06	2	6.77	12.46	0.193	-1.87	-7.09	-0.028
0.80	0	---	---	0.132	---	---	0.0129
0.80	3	4.89	11.40	0.130	-2.33	-2.74	0.0124



a) solid fin



b) slotted fin

Fig.5 Shadowgraph and Oil Flow Visualization at Mach=2.06 and $\alpha=0^\circ$

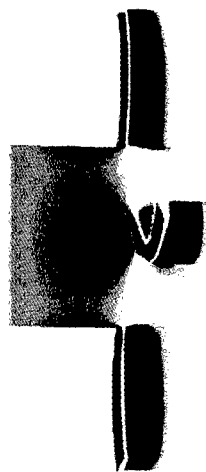


Fig.6a CFD Surface Pressure Distributions
(solid fin; $M=0.8$, $\alpha=0^\circ$)

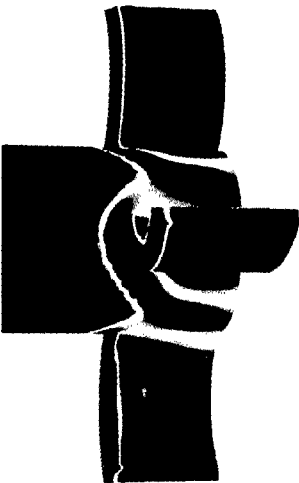


Fig.7a CFD Surface Pressure Distributions
(solid fin; $M=2.0$, $\alpha=0^\circ$)

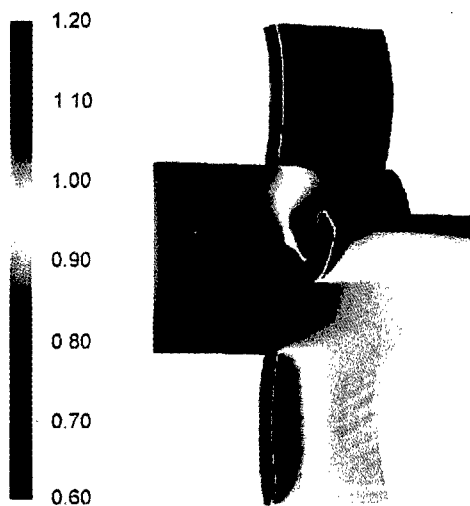


Fig.6b CFD Surface Pressure Distributions
(solid fin; $M=0.8$, $\alpha=9^\circ$)

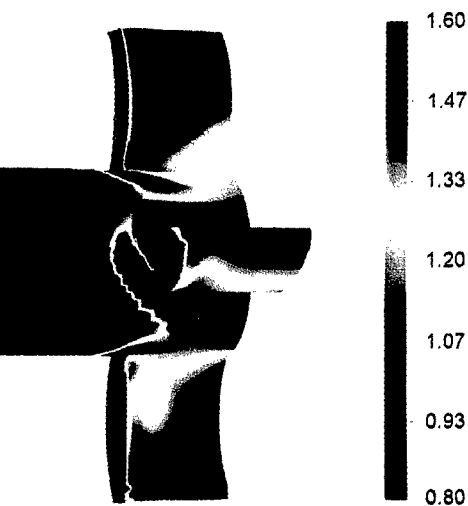


Fig.7b CFD Surface Pressure Distributions
(solid fin; $M=2.0$, $\alpha=8^\circ$)

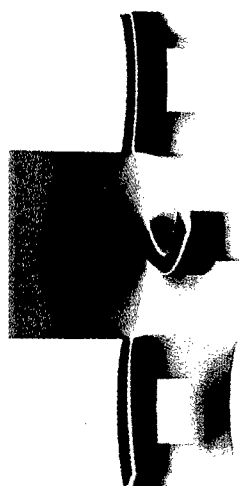


Fig.6c CFD Surface Pressure Distributions
(slotted fin; $M=0.8$, $\alpha=0^\circ$)

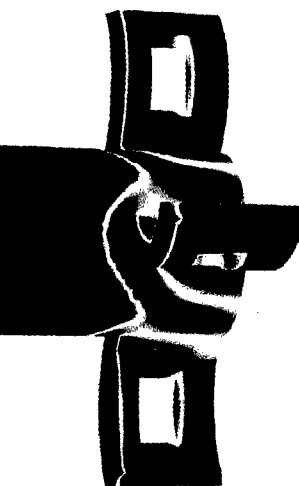
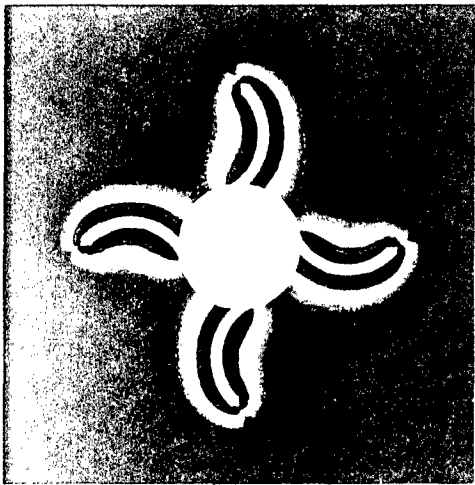
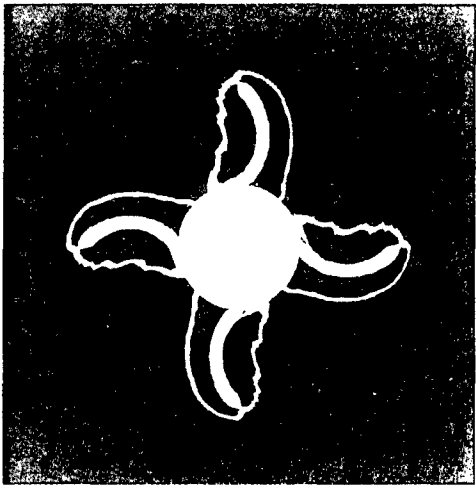


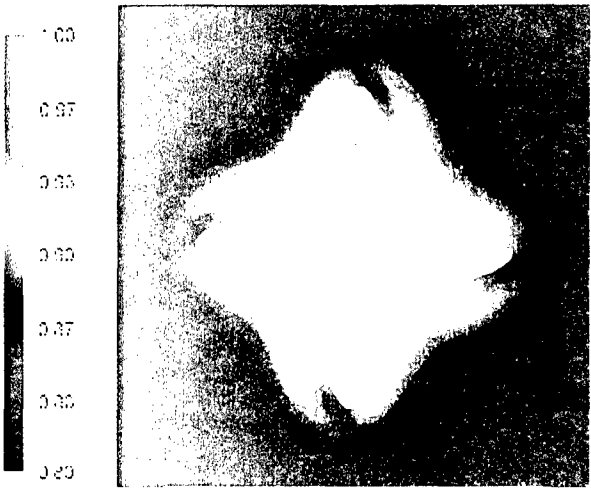
Fig.7c CFD Surface Pressure Distributions
(slotted fin; $M=2.0$, $\alpha=0^\circ$)



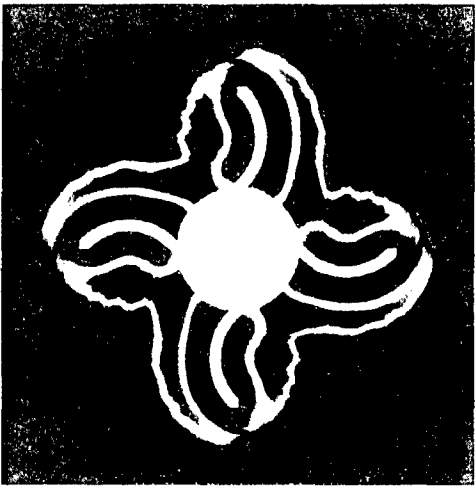
a) 5% fin length



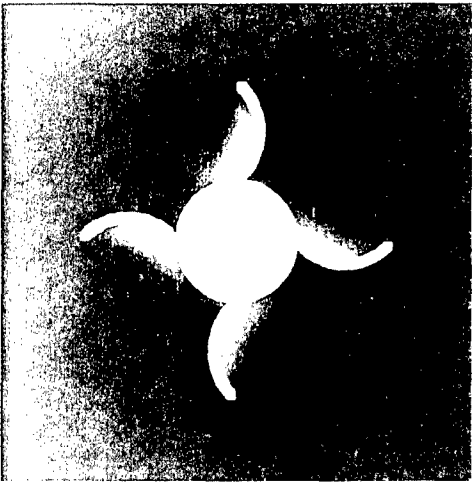
a) 5% fin length



b) 50% fin length



b) 50% fin length



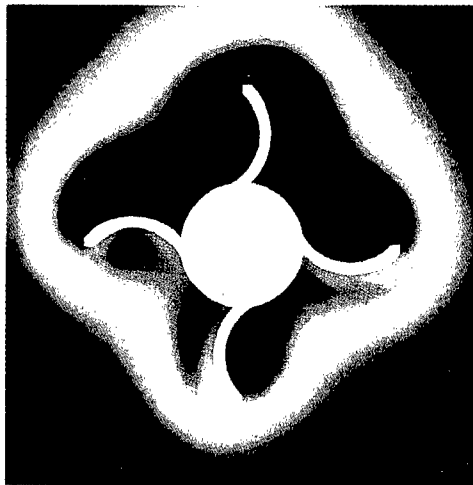
c) 100% fin length



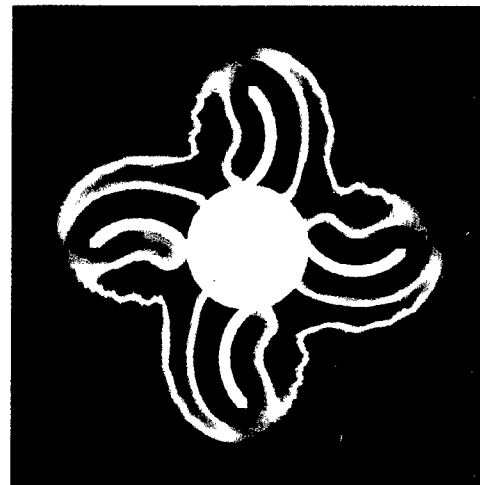
c) 100% fin length

Fig.8 CFD Pressure Contours
(4mm thick solid fin; $M=0.8$, $\alpha=0^\circ$)

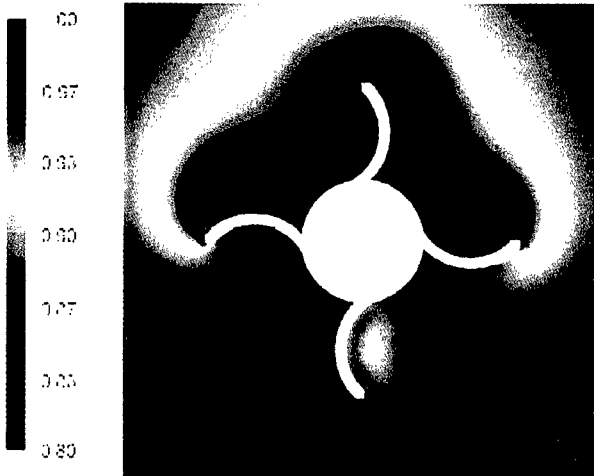
Fig.9 CFD Pressure Contours
(4mm thick solid fin; $M=2.0$, $\alpha=0^\circ$)



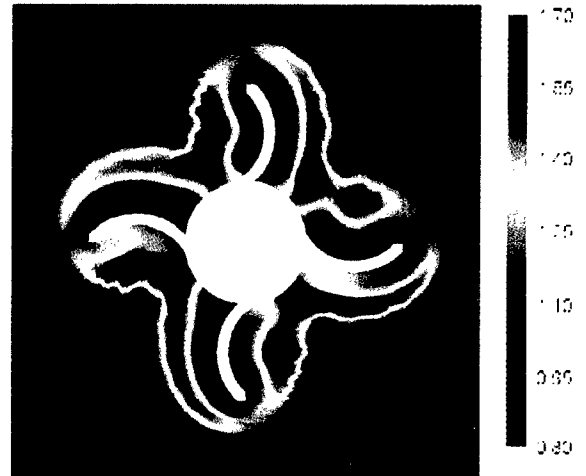
a) $\alpha=3$ degrees



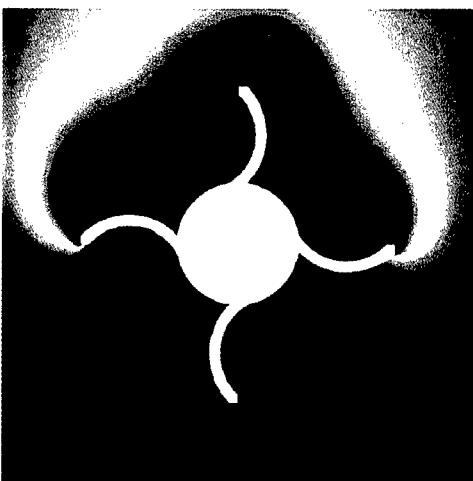
a) $\alpha=2$ degrees



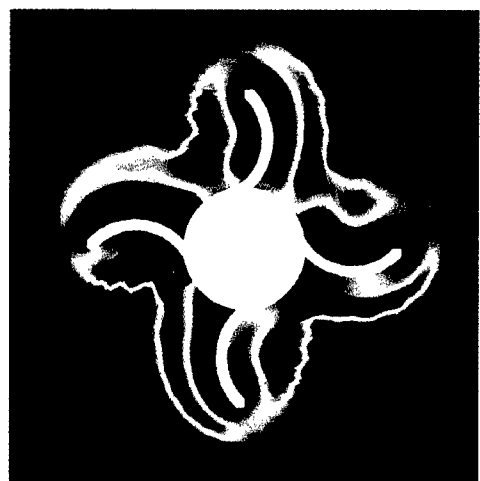
b) $\alpha=6$ degrees



b) $\alpha=5$ degrees



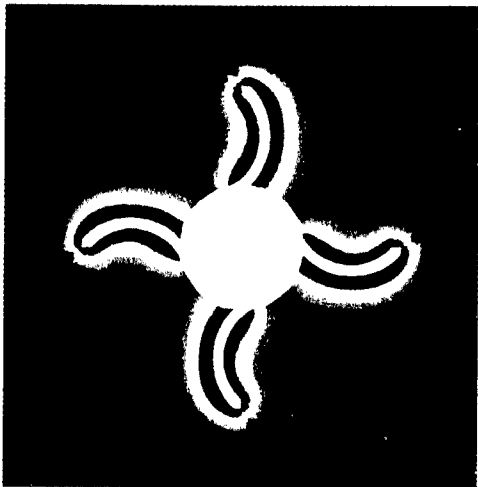
c) $\alpha=9$ degrees



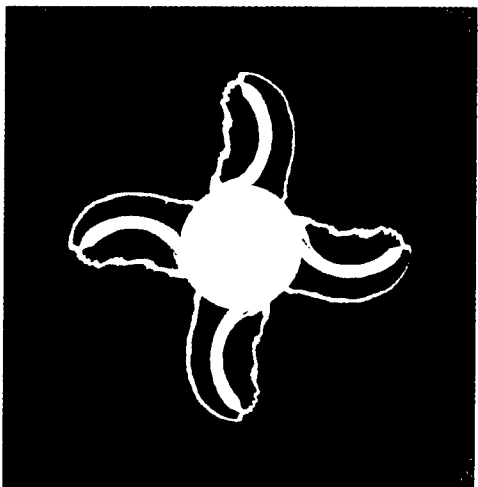
c) $\alpha=8$ degrees

Fig.10 CFD Pressure Contours at 50% of fin length
(4mm thick solid fin; $M=0.8$)

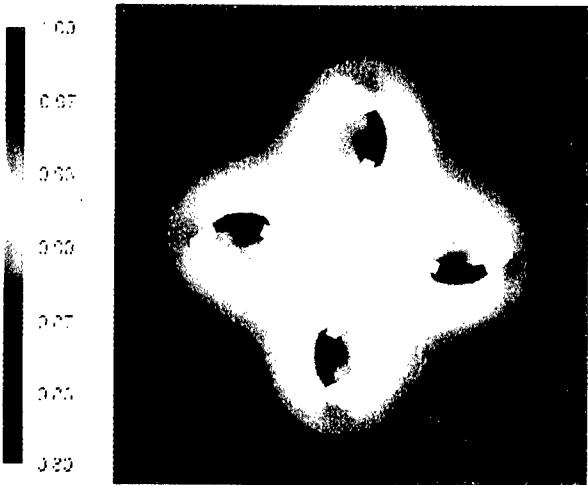
Fig.11 CFD Pressure Contours at 50% of fin length
(4mm thick solid fin; $M=2.0$)



a) 5% fin length



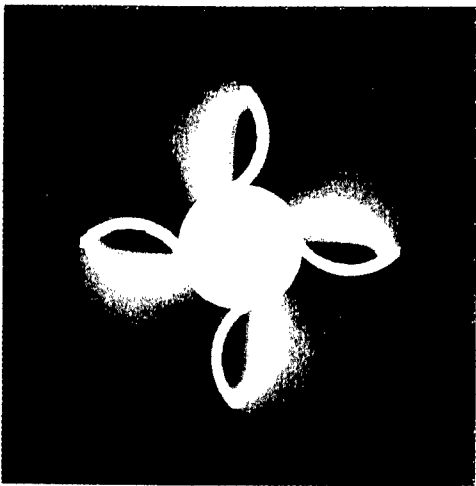
a) 5% fin length



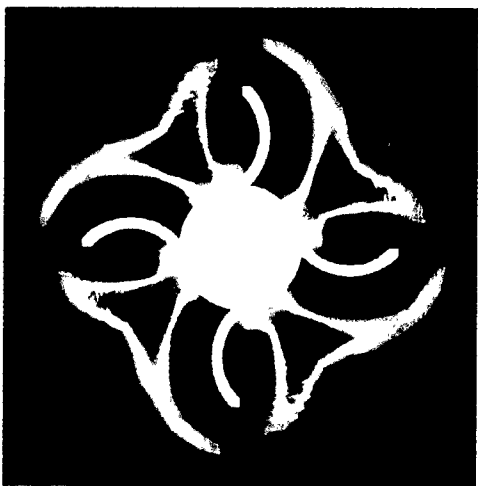
b) 50% fin length



b) 50% fin length



c) 100% fin length



c) 100% fin length

Fig.12 CFD Pressure Contours
(4mm thick slotted fin; $M=0.8$, $\alpha=0^\circ$)

Fig.13 CFD Pressure Contours
(4mm thick slotted fin; $M=2.0$, $\alpha=0^\circ$)

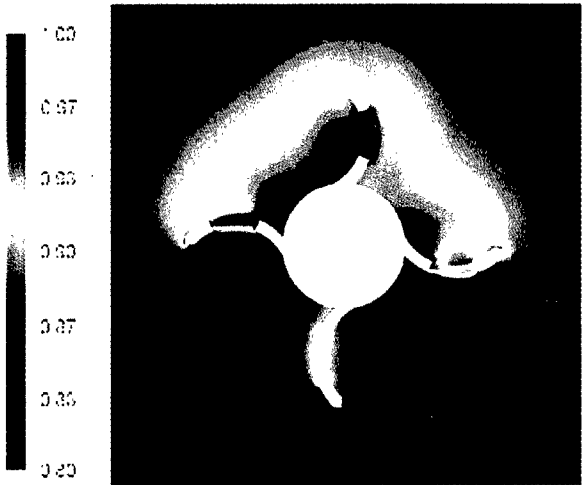


Fig.14 CFD Pressure Contours at 50% of fin length
(4mm thick slotted fin; $M=0.8$, $\alpha=6$ degrees)

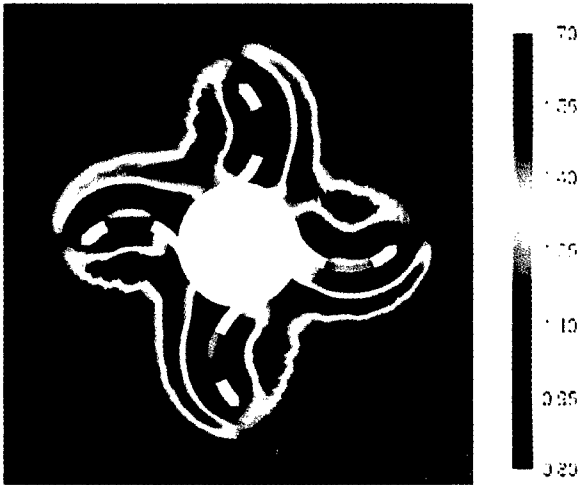


Fig.15 CFD Pressure Contours at 50% of fin length
(4mm thick slotted fin; $M=2.0$, $\alpha=5$ degrees)

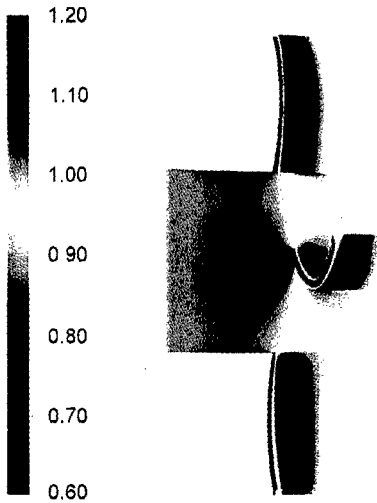


Fig.16a CFD Surface Pressure Distributions
(2mm thick solid fin; $M=0.8$, $\alpha=0^\circ$)

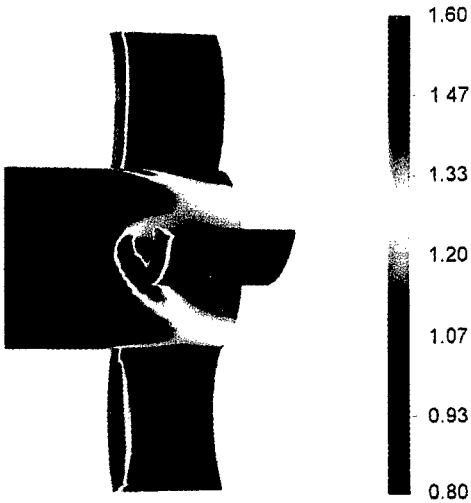


Fig.17a CFD Pressure Surface Distributions
(2mm thick solid fin; $M=2.0$, $\alpha=0^\circ$)

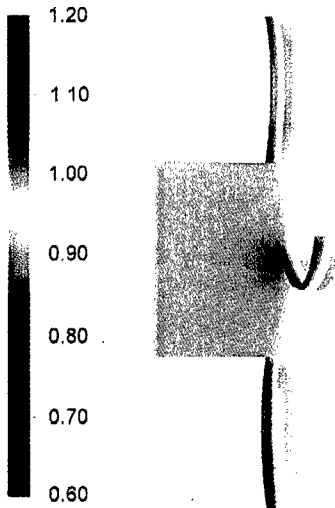


Fig.16b CFD Surface Pressure Distributions
(1mm thick solid fin; $M=0.8$, $\alpha=0^\circ$)

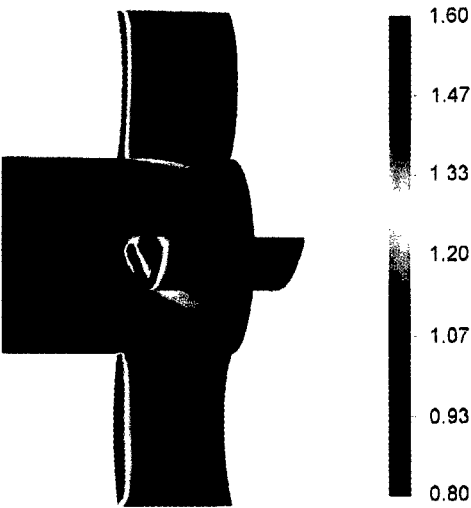


Fig.17b CFD Pressure Surface Distributions
(1mm thick solid fin; $M=2.0$, $\alpha=0^\circ$)

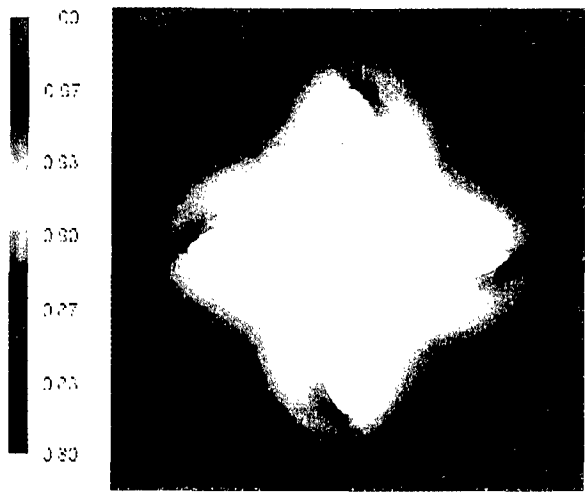


Fig.18a CFD Pressure Contours at 50% of fin length
(2mm thick slotted fin; $M=0.8$, $\alpha=0^\circ$)

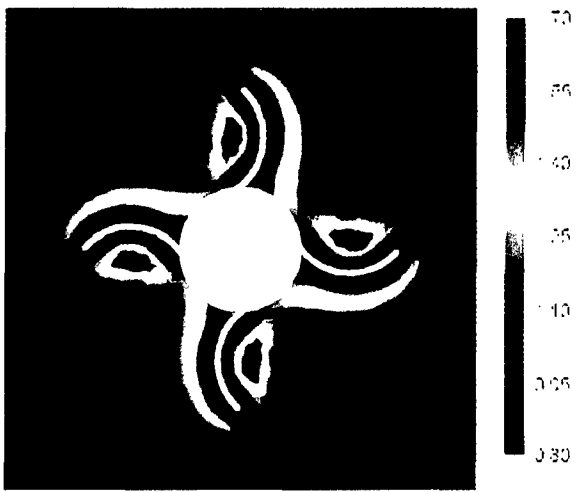


Fig.19a CFD Pressure Contours at 50% of fin length
(2mm thick slotted fin; $M=2.0$, $\alpha=0^\circ$)

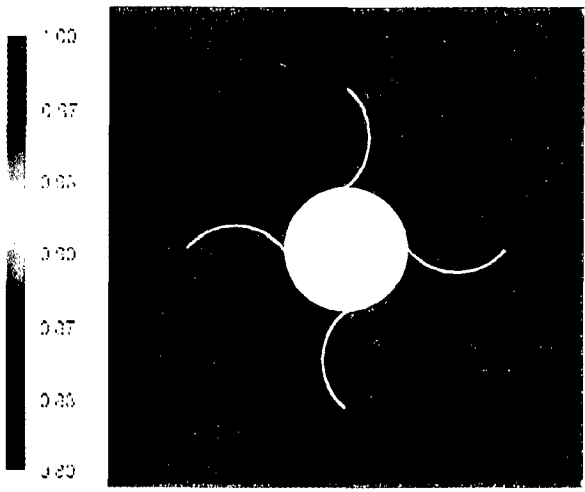


Fig.18b CFD Pressure Contours at 50% of fin length
(1mm thick slotted fin; $M=0.8$, $\alpha=0^\circ$)

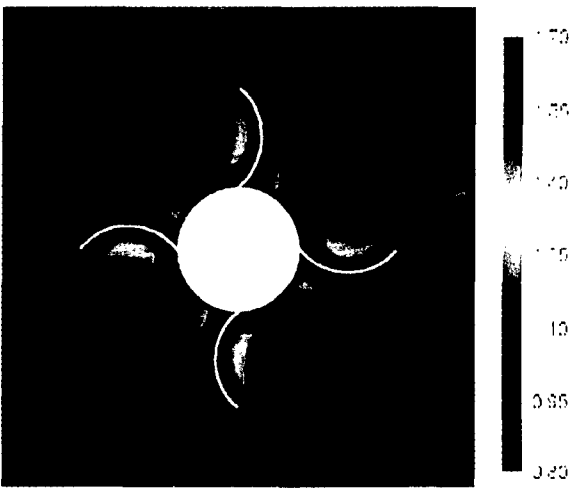


Fig.19b CFD Pressure Contours at 50% of fin length
(1mm thick slotted fin; $M=2.0$, $\alpha=0^\circ$)

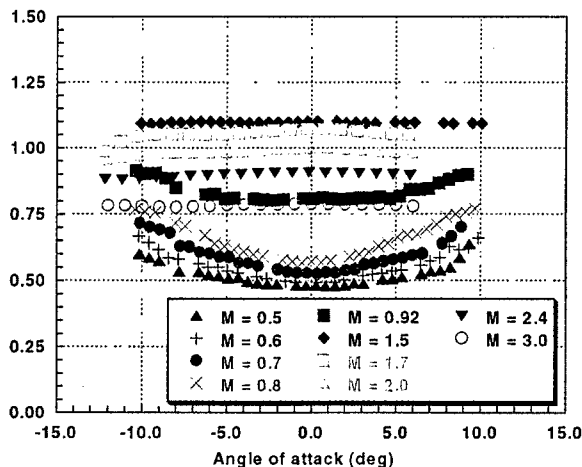


Fig.20a CA vs. α (solid fin; $l/d=6$; $\varphi=0^\circ$)

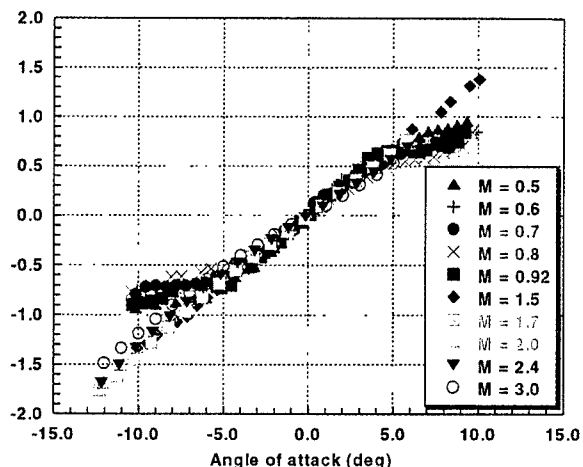


Fig.21a CN vs. α (solid fin; $l/d=6$; $\varphi=0^\circ$)

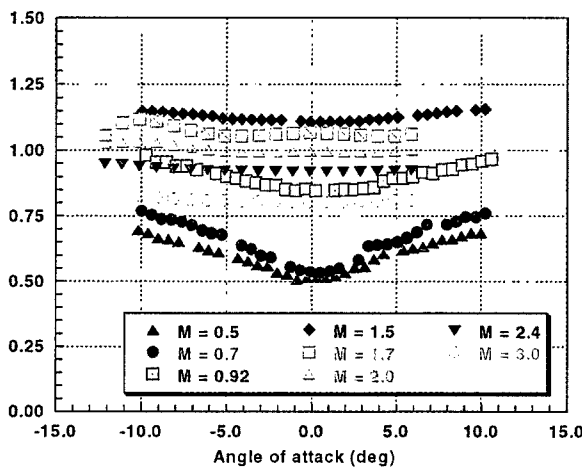


Fig.20b CA vs. α (slotted fin; $l/d=6$; $\varphi=0^\circ$)

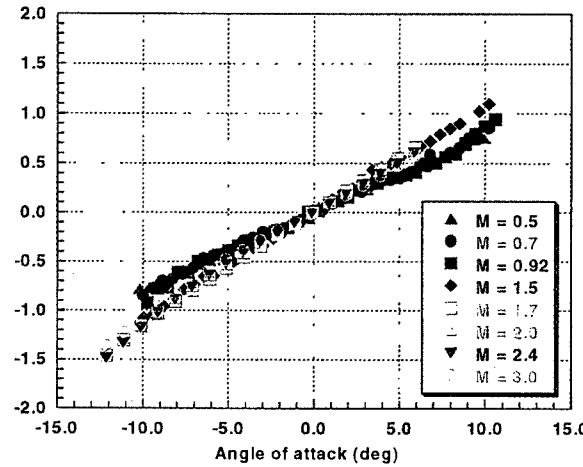


Fig.21b CN vs. α (slotted fin; $l/d=6$; $\varphi=0^\circ$)

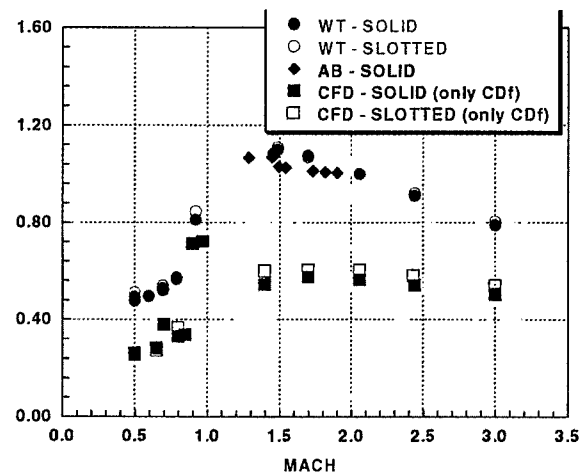


Fig.20c Zero Axial Force Coefficient Derivative

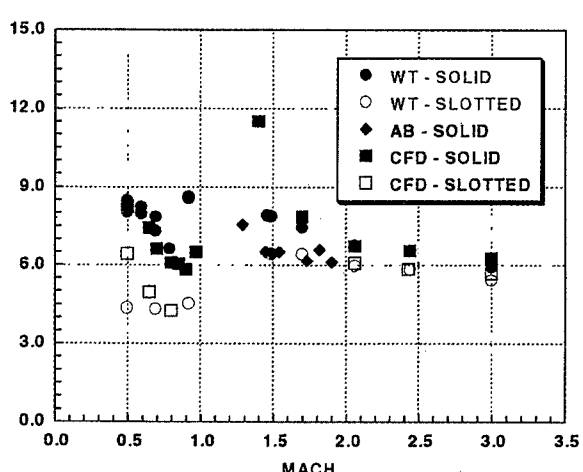


Fig.21c Normal Force Coefficient Derivative

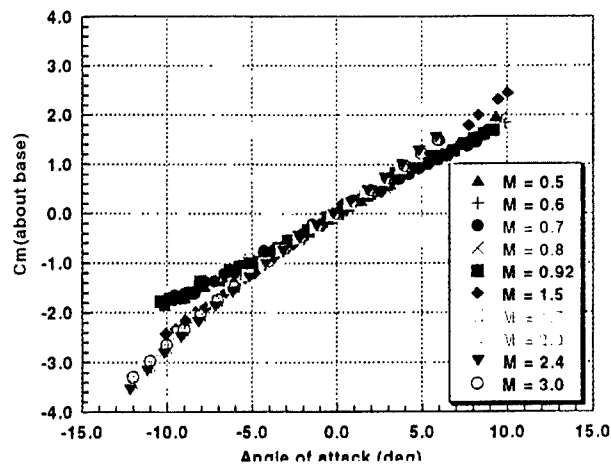


Fig.22a Cm vs. α (solid fin; $l/d=6$; $\phi=0^\circ$)

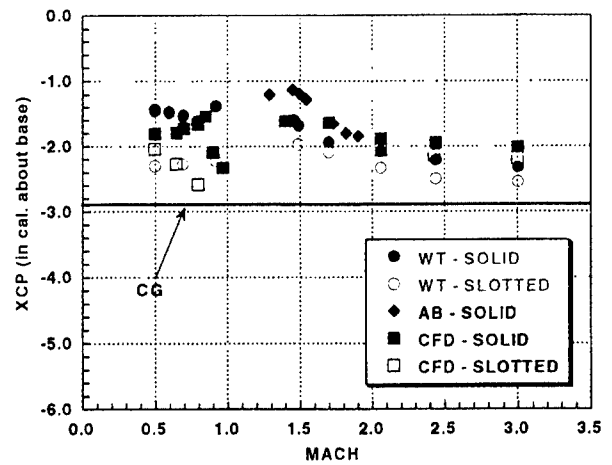


Fig.23 Center of pressure location

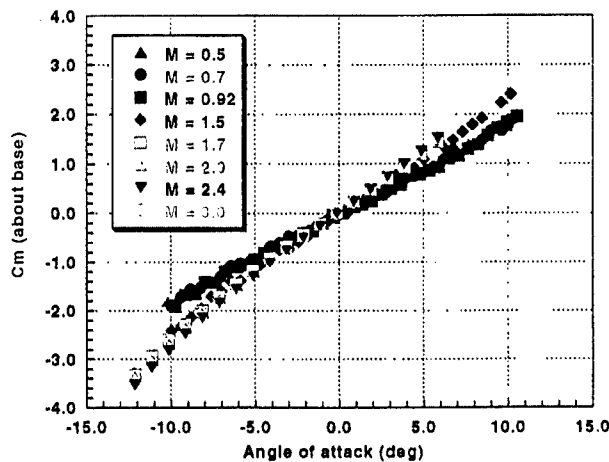


Fig.22b Cm vs. α (slotted fin; $l/d=6$; $\phi=0^\circ$)

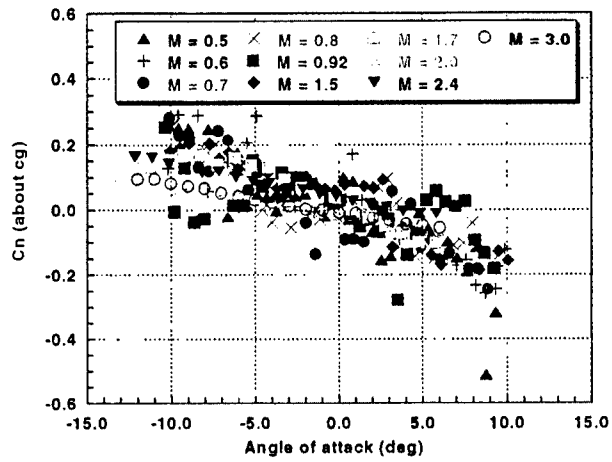


Fig.24a Cn vs. α (solid fin; $l/d=6$; $\phi=0^\circ$)

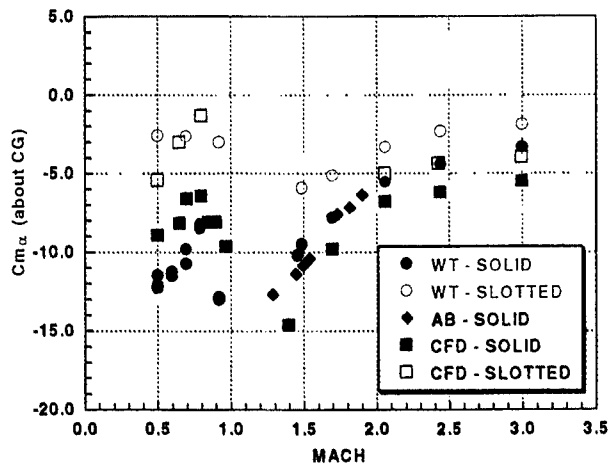


Fig.22c. Pitching Moment Coefficient Derivative

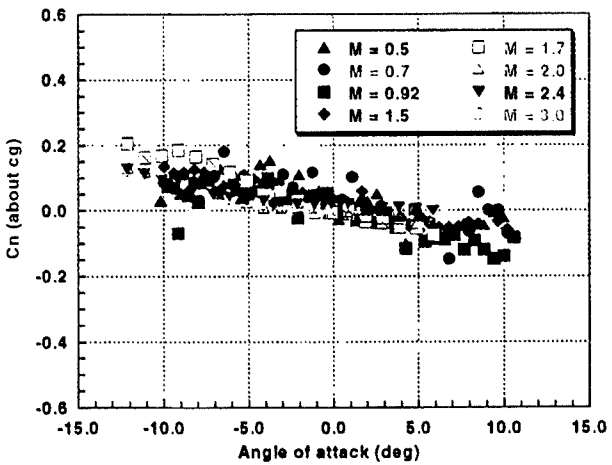


Fig.24b Cn vs. α (slotted fin; $l/d=6$; $\phi=0^\circ$)

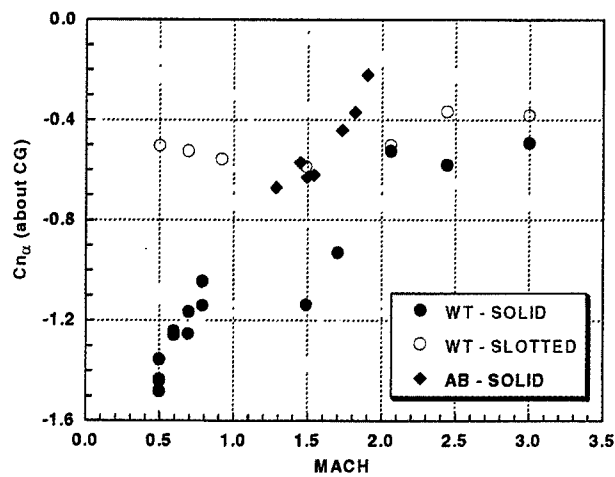


Fig.24c Cn_{α}/cg vs. Mach number

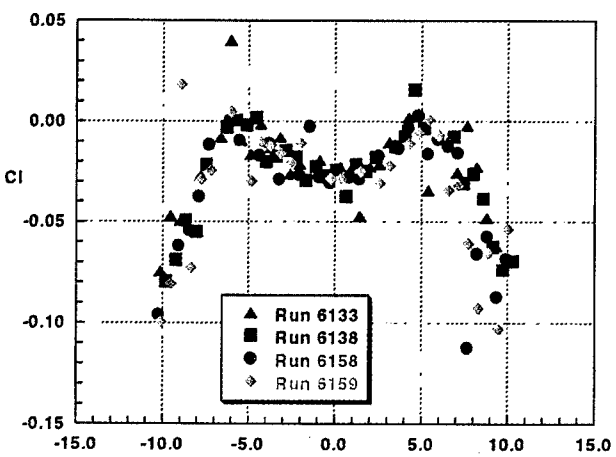


Fig.25c Cl vs. α (solid fin; $l/d=6$; $\phi=0^\circ$; $M=0.5$)

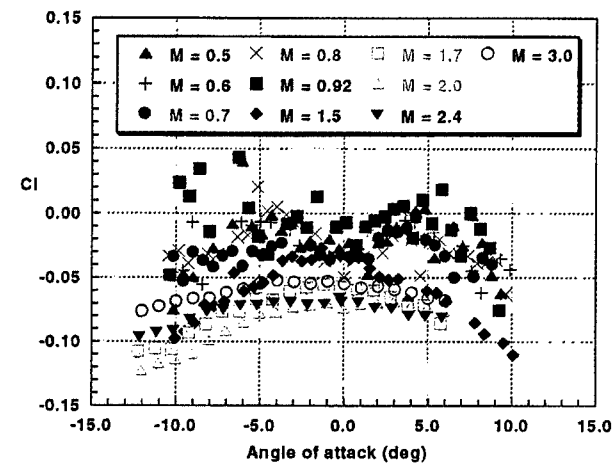


Fig.25a Cl vs. α (solid fin; $l/d=6$; $\phi=0^\circ$)

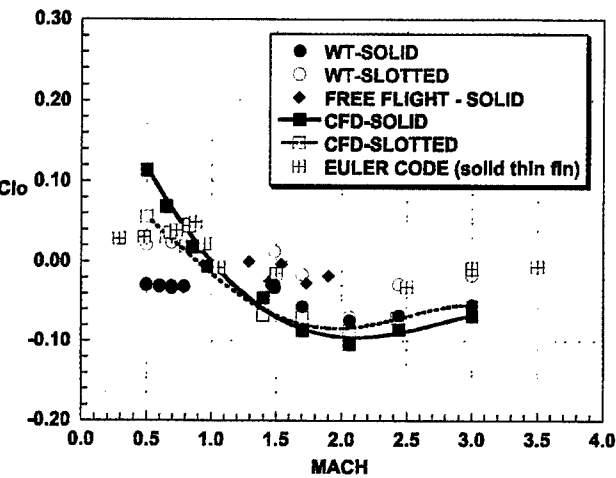


Fig.25d Roll Moment Coefficient vs. Mach

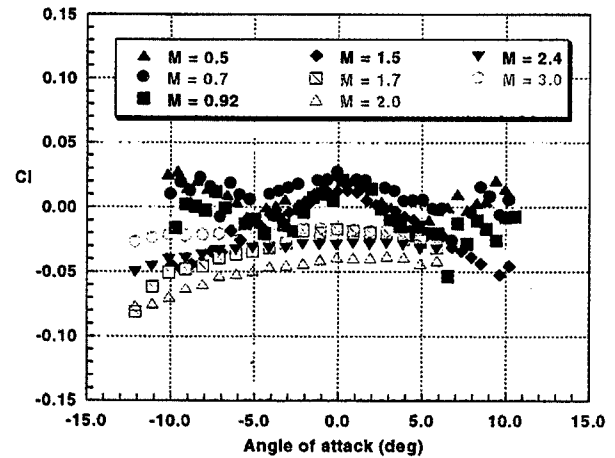


Fig.25b Cl vs. α (slotted fin; $l/d=6$; $\phi=0^\circ$)

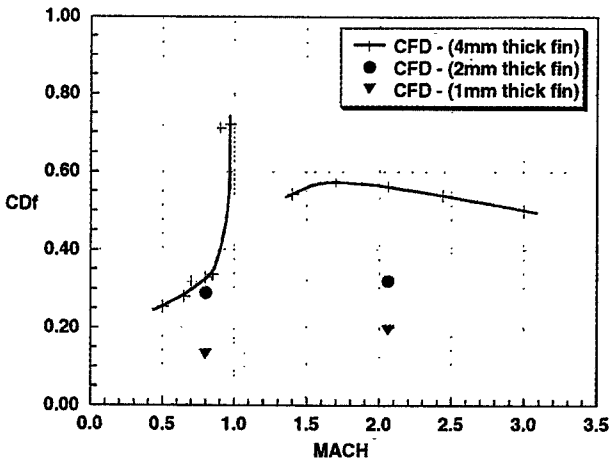


Fig.26a Fin Thickness Effects on CA_0 (solid fin; $l/d=6$; $\phi=0^\circ$)

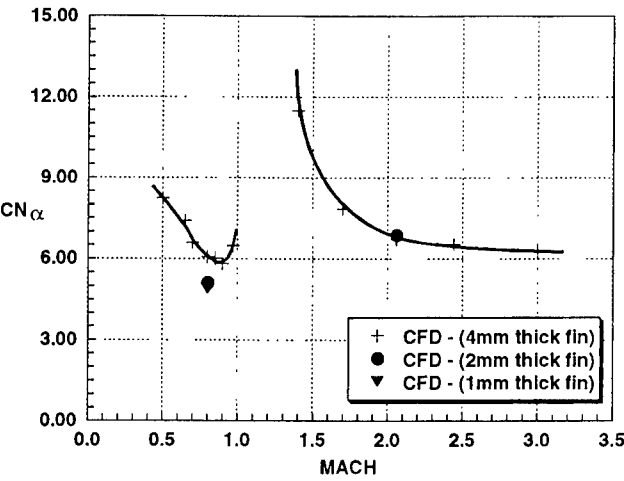


Fig.26b Fin Thickness Effects on CN_{α} (solid fin;

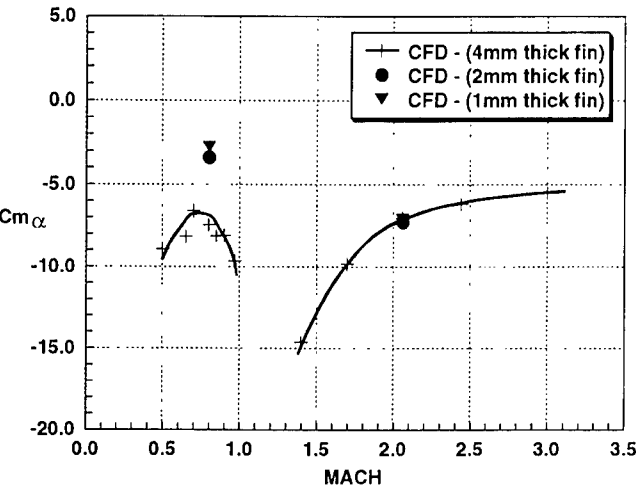


Fig.26c Fin Thickness Effects on Cm_{α} (solid fin;

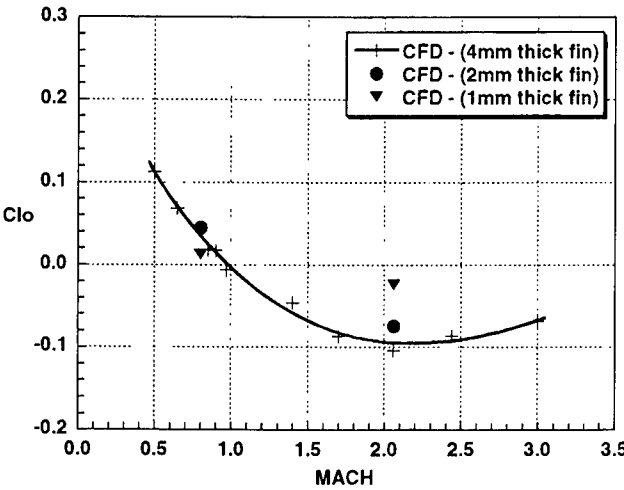


Fig.26d Fin Thickness Effects on C_{lo} (solid fin; $l/d=6$)

Aerodynamics Of Wrap-Around Fins At High Supersonic Speeds

Carl P. Tilmann

Air Vehicles Directorate, Air Force Research Laboratory
2645 Fifth Street, Suite 7, Wright-Patterson AFB, Ohio 45433-7913

Thomas C. McIntyre

SMC/CLNP, 160 Skyret Street, Suite 1215
Los Angeles AFB, El Segundo, CA 90245-4683, USA

Rodney D.W. Bowersox

Department of Aerospace Engineering and Mechanics, University of Alabama
Box 870280, Tuscaloosa, Alabama 35487-0280

Thomas A. Buter

Air Force Test Pilot School
220 S. Wolfe Ave., Edwards AFB, California 93524-6485

SUMMARY

Wrap-around fins (WAFs) have been investigated experimentally and numerically at supersonic speeds with the objective of understanding the flowfield in the vicinity of the fin, and its influences on rolling behavior. Experimental techniques used include conventional pressure surveys, cross-wire hot-film anemometry, schlieren and shadowgraph imaging, pressure-sensitive paint, and surface oil-flow visualizations.

First, a wall-mounted semi-cylindrical model fitted with a single wrap-around fin was investigated both numerically and experimentally, with the objective of characterizing the mean and turbulent flowfield in the vicinity of the fin. These investigations were conducted at Mach numbers of 2.8 and 4.9, and chord Reynolds numbers 0.37 and 1.52 million, respectively. Results were used to determine the nature of the flowfield, and to quantify the effects of fin curvature on the character of the flow near WAFs. Numerical techniques ranged from inviscid Euler methods to solving the full Navier-Stokes equations with an algebraic eddy viscosity model. Correlation with experimental data suggests that the latter method captured the essential features of this complicated flowfield.

Second, experiments were conducted on multiple-finned WAF configurations to investigate the effects of Mach number on rolling moment. Photo-luminescent pressure-sensitive paint techniques were used to obtain surface pressures that were integrated to estimate rolling moments. The Mach numbers ranged from 2.14 to 3.83. Two curved geometry fins were tested; one solid and the other slotted.

Results indicate that the flow structure near the WAF is qualitatively invariant over the conditions tested. However, the strength and location of salient features in the flowfield which act on the fin can be significantly influenced by Mach number. The flowfield is characterized by very strong and complicated inviscid-viscous interactions, which have a large impact on the aerodynamic loading of the fins. In particular, a vortex is generated in the fin/body juncture region on the convex side of the fin. This vortex, not predicted by inviscid methods, can greatly influence the pressure loading on the fin near the root. Changes in this vortex structure may contribute to the rolling moment reversal observed at high supersonic speeds in recent flight test experiments.

LIST OF SYMBOLS

c = chord length of the fin
 d = diameter of missile body
 Cm_x = rolling moment coefficient for 4 fins, $8M/\rho U^2 \pi D^3$
 l = reference length
 M = Mach number
 P = static pressure
 P_{i2} = pitot pressure
 r = model fin radius of curvature = $d/2$

Re_c = chord Reynolds number, $\rho_\infty u_\infty c / \mu_\infty$
 T = temperature (K)
 u, v, w = mean Cartesian velocity components
 x, y, z = Cartesian coordinates
 Y = distance from body surface y direction
 y^+ = inner turbulent coordinate $y u_\tau / \nu$; $u_\tau^2 = \tau_w / \rho_w$
 δ = boundary layer thickness (where $M=0.95M_c$)
 δ_0 = reference boundary layer thickness, 6.1 mm
 δ_∞ = reference boundary layer thickness, 10.2 mm
 ν = molecular kinematic viscosity, μ/ρ
 ρ = density
 θ = horizontal flow angularity, $\tan^{-1}(v/u)$
 ϕ = azimuthal flow angularity, $\tan^{-1}(w/u)$
 $(\cdot)'$ = Reynolds fluctuating component of variable
Subscripts
 t = total condition
 w = wall condition
 ∞ = free stream condition

1. INTRODUCTION

1.1 Wrap-Around Fins

The term "wrap-around fin" (WAF) usually refers to a projectile stabilizing or control surface, which has the same curvature as the missile body, and can be wrapped around the projectile until deployment (Fig.1). Since stealth capability has become a design parameter for many aircraft, WAFs have become even more attractive for their reduced cross-section and stowability. Wrap-around fins can also simplify the design of airframes that integrate the weapon in partial or full concealment, avoiding complications associated with fin-fuselage contact.

While WAFs enable many design possibilities, several stability anomalies are inherent for missiles employing them. The most recognized of which are roll reversal near sonic speeds, and pitch-yaw-roll coupling (at all speeds) due to the asymmetric fin geometry. Although WAFs have been used by designers for several years on low-speed tube launched missiles and dispenser-launched sub-munitions, extending the flight envelope toward high supersonic speeds had posed new challenges. Of primary concern is the rolling moment reversal which has been observed

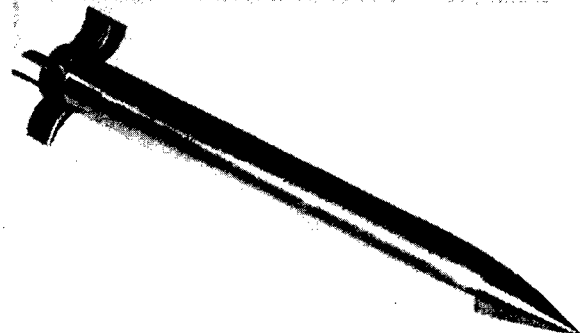


Fig.1: Generic WAF missile configuration

during aeroballistic range tests over a small range of supersonic speeds ($M=4.5-4.7$).^{1,2} This can quickly lead to unstable coning motions due to the WAF's inherent pitch-yaw coupling. To date, this phenomenon has not been simulated with computational methods, and its primary sources have not been positively identified. It has been proposed that this loss of static stability may be related to the complex shock structure in the fin region.² Cross-flow induced by missile pitch and spinning may also be a contributing factor. Interaction with the missile bow shock is also plausible at high pitch angles.

The majority of previous WAF experiments have focused on ascertaining stability characteristics via sub-scale flight tests, most of which emphasized the subsonic and transonic flight regimes. While these experiments have identified the unusual stability characteristics of WAFs, they have not inspired an understanding of the flowfield. Limited surface pressure measurements, planar LDV data, and excellent surface oil-flow visualizations have also been previously obtained on a low-supersonic WAF configuration.³ However, these methods do not alone provide detailed flowfield description.

A limited number of numerical simulations have also been performed on wrap-around finned missiles. These studies have primarily been focused on characterizing the fin shock structures, and the interactions between fins. This has typically been done using inviscid CFD methods on configurations with fins of little or no thickness^{2,4}, or with viscous methods on low aspect ratio fins (where fin interaction is significant) having blunt leading edges⁵.

1.2 Overview of Present Research

The present paper is intended to provide an overview of our research on WAF aerodynamics, and to document the more significant findings of the studies. The bulk of this research was performed at the Air Force Institute of Technology (AFIT), and was sponsored by the Air Force Research Laboratory's Munitions Directorate (AFRL/MN).

The primary goal of the research reported here has been to characterize the flow structure near WAFs at supersonic conditions. This has involved a series of investigations on static single and multiple fin configurations using several analytical techniques, and has resulted in a basic understanding of the mean and turbulent flowfield characteristics for supersonic non-spinning WAFs. Such an understanding is critical to further development of such configurations, given the dependence of stability characteristics on Mach number.

A second objective was to contribute a complete set of mean flow and turbulence data over a three-dimensional fin juncture geometry characterized by a shock/boundary layer interaction and significant streamline curvature effects for numerical turbulence model validation. Prior to this study, no detailed flowfield measurements (mean flow or turbulence) existed for WAF missile configurations.

As a first step toward understanding the flow structure near WAFs, a simple model consisting of a single wrap-around fin mounted on a partial fuselage (Fig.2) was investigated.^{6,7,8,9,10,11} This simplified model allowed experimental data to be obtained at much higher spatial resolution than would have been possible

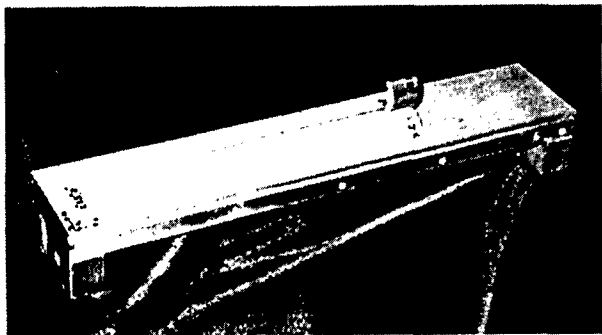


Fig.2: Single wrap-around fin model.

on a full-body four-finned configuration scaled to fit in the available tunnel space. Also, the single-WAF static model isolates the effects of fin curvature from the effects of upstream cross-flow and interaction of the multiple fin shocks.

Measured flowfield data were obtained in the AFIT Mach 3 and Mach 5 wind tunnels on the single-fin model (Fig.2). The flow around this test article was surveyed at several stations along its length, concentrating on the region near the fin. Detailed mean flow measurements were obtained using conventional cone-static and pitot pressure probes, as well as hot-film cross-wire probes. The experiments focused on examining the shock/boundary layer interaction at the juncture of the fin and the fuselage, and determining its effect on the fuselage boundary layer characteristics. The flow data measured with the hot-film probes were also used to estimate turbulence quantities. Shadowgraph and schlieren photographs were also obtained for flow visualization. The surface flow has also been analyzed using pressure sensitive paint and oil flow techniques. In the Mach 5 tunnel, mean flow (pressure) measurements, as well as shadowgraph and schlieren photography were obtained.

Although these experimental investigations provided significant amounts of mean flow and turbulence data not previously available, the subsequent application of computational fluid dynamics has provided a much more complete understanding of the flowfield. The numerical results were obtained by solving the Reynolds-averaged Navier-Stokes (RANS) equations, with an algebraic turbulence model, over the single-WAF model geometry at test conditions.^{8,10} Solutions were obtained with a widely used commercial simulation package (GASP¹²), and the numerical results were compared to the experimental results. Taken in concert, the experimental and numerical information has been examined with a view toward characterizing the net effect of the complex flowfield in the vicinity of the WAF on aerodynamic loading.

Experiments were then conducted on WAF missile configurations having multiple fins in a variable Mach number wind tunnel.^{13,14} The primary purpose of this study was to investigate the effects of Mach number on rolling moment. The viscous surface flow in the fin region was also examined. Two

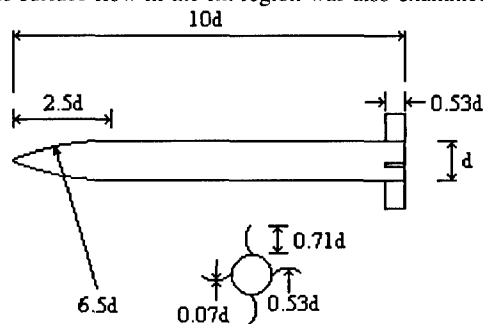


Fig.3: Solid fin model.

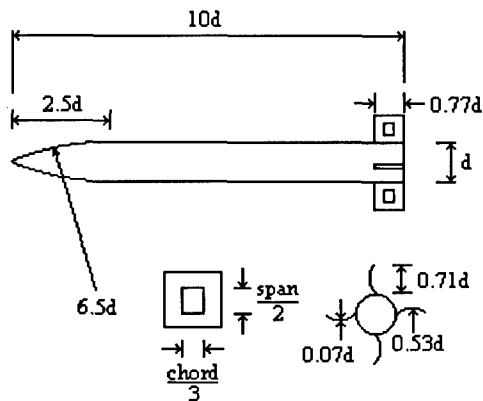


Fig.4: Slotted Fin Model.

four-fin models were tested. One model had a solid fin (Figs.1&3), and the other had a slotted fin (Fig.4). The purpose of the slot was to provide pressure relief, thereby reducing the Mach number dependence of the rolling moment. Photoluminescent pressure-sensitive paint techniques were used to obtain surface pressures which were integrated to estimate rolling moments. Surface oil flow visualizations and schlieren photography were used to analyze the surface flow structure and shock structure, respectively. In addition to the Mach number parametric investigation in the variable Mach wind tunnel, the single-fin configuration was re-examined in the AFIT Mach 3 wind tunnel using the same apparatus, and comparisons were made to the numerical predictions.¹⁴

2. EXPERIMENTAL FACILITIES

2.1 WAF Models

The single-fin WAF model (Fig.2) was comprised of a cylinder of the fin radius, $r=1.59\text{cm}$, blended to a removable test section wall, and had a maximum height of $0.5r$. It was designed to represent a single fin of a typical WAF configuration, and sized to maximize data resolution while avoiding tunnel blockage. The fin had the same proportions as aeroballistic models tested at the Air Force Research Laboratory Munitions Directorate^{1,2}, with a thickness of $0.2r$, a span of $\sqrt{2}r$, and a chord length of $c=1.28r$. The leading edge and tip of the fin were beveled at 45° (90° included angle). The cylinder was $5.12r$ in length and the single fin was placed at the downstream base. Upstream, the cylinder was blended smoothly to the tunnel wall over a region $5r$ long with a polynomial chosen to ensure second order continuity in the streamwise direction.

The two four fin models used for testing are shown in Fig.3 and Fig.4 where the projectile diameter, $d=1.91\text{cm}$, was used to scale the major physical features of the models. The slotted fin model had 28.6% more surface area than the solid fin model, when viewed from the side. These are actually flight test models that have been tested in the Aeroballistic Range Facility at the Air Force Research Laboratory's Munitions Directorate^{1,2}, and were adapted for sting-mounting in the wind tunnel.

2.2 Mach 3 Wind Tunnel

The first experiments took place in this intermittent pressure-vacuum wind tunnel. At a location just downstream of the test section entrance (8.4 chord lengths ahead of the fin leading edge) the freestream Mach number was determined to be 2.8 ($U_\infty=601\text{m/s}$), with a measurement uncertainty of 2.8%. The boundary layer at this location was fully turbulent with a measured thickness of 5.3mm at the centerline, defined by the distance from the surface where $M=0.95M_\infty$. The settling chamber total pressure and temperature were $2.14\pm0.02\text{atm}$ and $294\pm2\text{K}$ respectively, yielding a freestream unit Reynolds number of $Re/l=18\times10^6\text{m}^{-1}$ ($Re_c=0.37\times10^6$).

2.3 Mach 5 Wind Tunnel

Experimental results were also obtained in the AFIT Mach 5 wind tunnel. This blow-down wind tunnel has a heated air supply and has been operated over a range of unit Reynolds numbers ($Re/l\approx32-75\times10^6\text{m}^{-1}$). Although the tunnel is capable of producing much longer run-times, the current experiments only required total run-times of 10–15 seconds. More detailed information on this facility is available in Reference 8.

2.4 Variable-Mach Wind Tunnel

A variable Mach supersonic blow-down wind tunnel was used for testing the missile models shown in Figs.3&4. This Aerolab, Inc. brand wind tunnel provided a uniform Mach number across the test-section to within 1–2% at each test condition. The test section static pressure and total pressure were recorded during each run, and the total temperature was constant at 295K for all runs. The test section area ($15.24\times15.24\text{cm}$) limited the lower Mach number. For Mach numbers less than 2.14, the missile nose shock reflections off the tunnel walls intersected with the tail of the missile. The nominal flow conditions for each test condition are summarized in Table 1.

3. EXPERIMENTAL TECHNIQUES

3.1 Field Pressure Surveys

Pitot probes and cone-static probes (10° and 20°) were used to measure pressures throughout the flowfield in the test section. Through the manipulation of results from conical and normal shock relations, the pressure data obtained from these probes can be used to calculate the local Mach number. Curve fits of the form $M=f(\xi)$, where ξ is the ratio of the pressures sensed by the cone static and pitot probes, were generated to simplify data reduction.⁹ The usual gasdynamic relations for a calorically perfect gas, with an assumption of constant total temperature, were used to calculate the density and the velocity magnitude.

3.2 Hot Film Surveys

Two TSI brand hot-film cross-wire probes were used to survey the flow near the single-fin model in the Mach 3 tunnel. Both probes were two-component cross-wire hot-film probes, each with two thin films of platinum 1mm long and $51\mu\text{m}$ in diameter. One probe had the films oriented in the vertical ($u-v$) plane, angled at $\pm45^\circ$ to the horizon; the other probe had its films oriented in the horizontal ($u-w$) plane and similarly angled. The transverse separation between the two films was 1mm . Since the traverse was moving very slowly (about 0.2mm/s) relative to the flow, pressure and hot-film measurements were taken while the probes were in motion. The hot-film probes were connected to a TSI brand Intelligent Flow Analyzer¹⁵ which sampled data at 16.7kHz . Although the probe volume was relatively large, the Reynolds shear stresses measured with these cross-wires have been shown to compare very well to laser Doppler velocimetry measurements, obtained in a much smaller probe volume.¹⁶

One of the key features of cross-wire anemometry is how the Reynolds turbulent shear stress can be estimated as the negative of the directly measured mass-flux correlation term combined with the density fluctuation. Neglecting third order terms allows the Reynolds shear stress to be written as¹⁷

$$\tau_{ij}^T = -\frac{(\rho u_i)'(\rho u_j)'}{\bar{\rho}} + \overline{\rho u_i' u_j'} \left(\frac{\rho'}{\bar{\rho}} \right)^2 \quad (i \neq j) \quad (1)$$

where the second term is usually much smaller than the first term for small flow angles. This was confirmed for the present experiments by estimating the second term assuming small pressure fluctuations.⁸ The second term was always at least an order of magnitude smaller than the first term. Since the total temperature fluctuations in the boundary layers were below 2.0% ²¹, and the films were operated at high overheat ratios (i.e. $R_{\text{film}}/R_{\text{ref}} \geq 2.0$), a single overheat data reduction method was used¹⁸

Table 1: Nominal Test Conditions

Mach Number	P_{t1} (atm)	$Re_c (\times 10^6)$
2.15 ^b	2.8	0.33
2.15 ^b	6.1	0.72
2.15 ^b	7.0	0.83
2.41 ^b	3.9	0.40
2.41 ^b	7.1	0.74
2.41 ^b	8.6	0.90
2.80 ^a	2.1	0.37
2.86 ^b	5.8	0.48
2.86 ^b	8.2	0.68
2.86 ^b	9.8	0.81
3.25 ^b	8.9	0.60
3.25 ^b	10.4	0.70
3.50 ^b	8.7	0.52
3.50 ^b	10.0	0.60
3.50 ^b	11.3	0.68
3.83 ^c	11.5	0.58
3.83 ^c	12.1	0.61
4.87 ^a	32.0	1.52

^a Single-fin experiments

^b Solid and slotted multiple-fin models

^c Solid multiple-fin model only

3.3 Pressure-Sensitive Paint

Pressure-sensitive paint (PSP) was used to analyze fin pressures. This non-intrusive method provided continuous pressure data on the missile body and fins. Since the fins are the source of rolling moment due to pressure forces, the pressure measurements were concentrated in the fin region.

Measurements are based on the phenomenon of photoluminescence. A probe molecule absorbs a photon of specific energy, exciting it to a higher state. The molecule then returns to the ground state by emitting a photon of lower energy. However, if an oxygen molecule is present, the excess energy of the probe molecule will be transmitted to the oxygen during a collisional deactivation. The oxygen-quenching phenomenon can be modeled with the Stern-Volmer relationship:

$$\frac{I_0}{I} = 1 + K_q P_{O_2} \quad (2)$$

where I is the luminescence, I_0 is the luminescence in the absence of oxygen, K_q is the Stern-Volmer constant, and P_{O_2} is the partial pressure of oxygen. Variations in temperature affect I_0 and K_q , causing temperature sensitivities. In the present study, short test times (<30sec) and 30-minute tunnel reservoir recharge periods resulted in the missile surface remaining at room temperature (295 K).

The Stern-Volmer equation was applied by taking images at a reference pressure condition (ambient pressure) and at the test condition. The ambient pressure intensity, I_{ref} , was then divided by the test intensity, I . The ratio of intensities was calibrated at room temperature. The correlation coefficient for the resulting calibration was 0.999.

The pressure-sensitive material applied to the WAF missiles was developed at the Air Force Arnold Engineering Development Center (AEDC)¹⁹. The probe molecule consisted of platinum octaethylporphyrin (PtOEP), diluted in toluene and sprayed over a white Krylon titanium dioxide primer layer of paint. This primer removed intensity variations caused by the mixed metallic construction of the missile fins and body. The maximum excitation wavelengths of the PtOEP paint were at 380 and 540nm, with emissions at 650nm. A scientific grade Pixel Vision charge-coupled device (CCD) camera recorded photographs, using a 516x516-pixel resolution and a 50mm lens. The paint was excited with a Spectra-Physics Millennia continuous wave laser at 532nm. The 0.6 Watt laser light was diffused by a plate of packed, ground glass and shined on the test subject. A red filter was placed over the camera lens to ensure that only paint emissions would be captured on the CCD. Ten "air-off" images were taken and averaged to remove systematic ambient nonuniformities.

3.4 Surface Oil Flow Visualizations

To obtain surface streamlines, a fluorescent powdered yellow die was diluted into 200cS silicon oil. During the tunnel run, the die was illuminated with two 115 V Black-Ray B-100A ultraviolet lamps. Images were acquired with a Kodak DCS 420 color digital camera (ISO setting of 200, shutter speed of 1/30th of a second).

3.5 Schlieren and Shadowgraph Visualizations

In the Mach 3 and Mach 5 tunnels, a Xenon brand 10 nanosecond spark light source was used to create schlieren and shadowgraph images of the flowfields, which were recorded on Polaroid film.

In the variable-Mach wind tunnel, schlieren photography was used to characterize the shock structures. Long duration (time averaged) and short duration spark (600 μ s) horizontal knife-edge schlieren photographs were acquired. The Kodak DCS 420 digital camera was used to acquire the schlieren images (again with an ISO setting of 200, and a shutter speed of 1/30th of a second).

3.6 Experimental Uncertainty

To quantify the uncertainty associated with the flowfield measurements, the Euclidean (L_2) norm was utilized to assess the cumulative effects of error sources. Approximate error

bounds on the reduced data were then calculated by propagating the measurement errors through the data reduction process, where the equations were linearized. The uncertainty of each experimental result is indicated on all presented data accounting for probe location, measurement, digitization, and propagation errors associated with the data reduction. Details regarding the uncertainty analysis are contained in Reference 8.

Taking into account transducer uncertainties, the free stream flow condition uncertainties for the PSP measurements (in the variable Mach wind tunnel) were estimated as $\pm 0.3\%$, 2.5% , and 2.0% for the Mach number, dynamic pressure and Reynolds number, respectively. The calibration curve used for PSP measurements resulted in an uncertainty of ± 2.068 kPa which, coupled with the transducer calibration uncertainties, produced P/P_t uncertainties of ± 0.009 . The pressure data were used to determine rolling-moments which, coupled with the pixel resolution, resulted in a rolling-moment uncertainty of ± 0.0053 N-m for the solid fin and ± 0.0064 N-m for the slotted fin. This error contribution, along with wind tunnel errors, resulted in an average rolling-moment coefficient error of ± 0.0066 for the solid fin and ± 0.0077 for the slotted fin.

In addition to the inherent random uncertainties of the PSP measurement techniques, two other sources of bias error influenced the rolling-moment data. First, the leading edge data of the missile fins were neglected in the rolling moment calculations. These high stagnation pressures were outside of the calibration range of the PtOEP paint. Thus, only pressure data on the sides and tips were used to compute a rolling-moment. In order to quantify the error involved in this negligence, images of numerical solution at Mach 2.8 were processed with the same software used for the experimental data. Neglecting the leading edge contribution to the rolling-moment under-predicted the rolling-moment coefficient by nominally 2%. Second, the effects of shear stress on the rolling-moment were also neglected. The CFD pressure images were again processed using the entire fin. Neglecting the shear stress forces resulted in rolling-moment coefficients that were overestimated by nominally 5%. Hence, a net 3% over prediction bias is expected.

4. NUMERICAL TECHNIQUES

The flowfield over single-fin WAF geometry (Fig.2) has been numerically simulated using computational methods of varying complexity. All solutions to the governing equations were obtained using the General Aerodynamic Simulation Program (GASP)¹², a fully conservative shock capturing code that has been widely used by the CFD community for the analysis of supersonic and hypersonic flows.

As a means of establishing the most suitable locations for experimental measurements, pilot numerical simulations were first conducted by solving the Euler equations upstream and in the vicinity of the WAF^{6,8}. These simulations were performed on grids representing the single-WAF model as installed in the wind tunnel test sections, and used data that was previously obtained in empty test sections for the upstream boundary condition (Table 2). The details of these inviscid computations have been discussed in References 6&8.

Viscous numerical solutions on the single fin geometry were also obtained at measured test conditions ($M=2.8,4,9$). The details of these computations, including convergence issues and computational requirements, have been documented in References 8,10,&11. Here, we present a brief overview of the

Table 2: Freestream conditions for pilot Euler calculations.

Condition	Value	Value
M	2.9	5.0
P_t	2.0 atm	20.4 atm
P	0.0633 atm	0.03858 atm
T_t	294 K	375 K
T	109.6 K	62.5 K
U	607 m/s	792 m/s
ρ	0.2039 kg / m ³	0.2179 kg / m ³

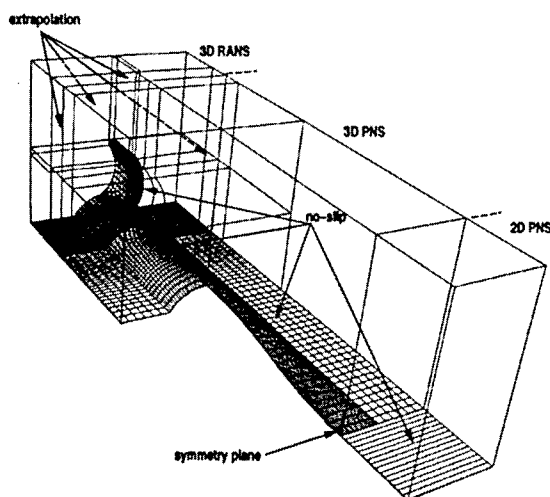


Fig.5: Grid boundaries and zonal structure for viscous simulations.

strategy used to solve the Reynolds-averaged Navier-Stokes (RANS) equations with the algebraic turbulence model of Baldwin and Lomax²⁰ (using GASP¹²). The same computational grid and solution strategy were used to obtain both viscous solutions.

4.1 Grid Definition & Computational Domain

The entire computational mesh consisted of 12 computational zones, (the edges of which are shown in Fig.5) connected by 21 zonal boundaries and was comprised of 8.2×10^6 cells. The flow variable values were passed through the zonal boundaries via five-point overlaps. To resolve the features of the flowfield in the vicinity of the fin and to provide the resolution required by the turbulence model, the grid was clustered near the fin and cylinder surfaces. At a location $0.4c$ upstream of the fin leading edge the fuselage grid spacing corresponded to a y^+ value of roughly 0.15, and more than half of the points were in the boundary layer.

On the model surfaces, shown as a mesh in Fig.5, a no-slip condition on the velocity, and vanishing normal pressure gradient were enforced. The wall temperature was 294K for the Mach 2.8 simulation. For the Mach 4.9 case, computations using relatively hot (340K) and adiabatic walls indicated that the thermal boundary condition at the wall had a negligible influence on the solution.^{8,11} The results presented here were obtained with a 294K isothermal boundary condition, and are indistinguishable from those obtained using the other thermal boundary conditions.

Based on the results of the early experiments and inviscid numerical investigation^{6,8}, it was known that the side and opposing tunnel walls had a minimal influence on the flowfield near the fin. Thus, although the size of the computational domain represents the Mach 3 test section, flow variables were extrapolated from the interior at these boundaries, affording great computational savings. It also allowed use of the same grid for the Mach 4.9 simulation, even though the test section was larger. The flow conditions were also extrapolated at the downstream plane.

4.2 Solution Strategy

Since flow disturbances do not propagate upstream in a fully supersonic flow, and since experimental results indicated that the blended body produced no separated flow regions, the flowfield was simulated by solving the parabolized Navier-Stokes (PNS) equations from the upstream boundary to a location $0.5c$ ahead of the fin. This location was deemed sufficiently far upstream of the fin interaction region based on previously conducted visualization experiments at Mach 2.8.^{6,7,9} To allow for the specification of a two-dimensional upstream boundary condition derived from pitot pressure data, the PNS equations were solved on a two-dimensional grid for a short

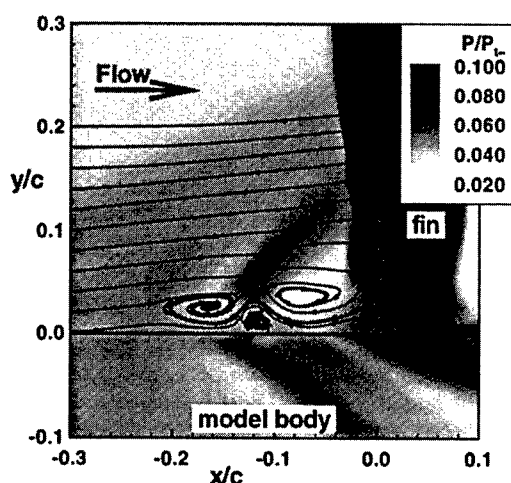


Fig.6: Computed vortical structure ahead of the fin $M=2.8$.

distance ($0.8r$) ahead of the model body blending region. Owing to probe volume effects, experimental data could not be obtained sufficiently close to the wall to include the laminar sublayer. However, the two-dimensional PNS region allowed the boundary layer to develop into a fully turbulent profile upstream of the three-dimensional blended body region. The two-dimensionality of the flows in the AFIT Mach 3 and Mach 5 wind tunnels has been documented.^{8,21}

Starting at the leading edge of the blended body, the two-factor approximately-factored equations were space marched in the streamwise direction employing 3rd-order upwind biasing and relaxation. In the cross-flow plane, 2nd-order up-winding with Roe's flux difference splitting was used. The symmetry of the model body was exploited by solving half of the blended body region and employing an x - y symmetry condition at the $z=0$ plane. In the vicinity of the fin ($x \geq -0.5c$) the RANS equations were solved to 3rd-order spatial accuracy using Jacobi inner iterations¹². The inviscid fluxes were split by the method of van Leer²², and the min-mod limiter²³ was used. This region was comprised of 8 computational zones, containing a total of 4.2×10^6 cells.

4.3 Convergence Issues

In brief, a three-grid sequencing method was used which not only accelerated solution convergence, but also afforded an expedient means to evaluate grid consistency.^{8,10,11} Temporally converged solutions were obtained on all three grids, each grid having 8 times the number of cells than the next coarser grid. Although it would not accelerate convergence in the upstream region evaluated by space-marching (PNS), grid sequencing was also employed here to evaluate grid consistency. Comparison of the solutions at the exit of this region indicated^{8,10} that the boundary layer predicted on the 'medium' grid was unchanged by further grid refinement.

Close examination of the vortical structures ahead of the fin leading edge ($-0.5 \leq x/c \leq 0$) has revealed a predicted vortical structures (Fig.6) ahead of the fin leading edge (under the λ -shock) of increasing complexity and detail with each grid refinement. It is important to note that this region is the most difficult area of the flowfield to resolve, since the flow character is changing drastically over short distances. Due to the fact that these particular vortical structures are swept away from the fin, minimizing the effects of their inner composition on the fin loading, it is probably not necessary to resolve this region of the flow precisely.⁸ In the present case, while the predicted flowfield ahead of the fin is slightly altered by the last grid refinement, the flowfield behind the interaction region and the pressures on the fin surface were essentially unchanged. Predicted rolling moment coefficients for the two finest meshes agreed within 0.2% and 1.4%, for the Mach 2.8^{8,10} and 4.9¹¹ simulations, respectively, indicating that grid convergence was achieved in the region of interest.

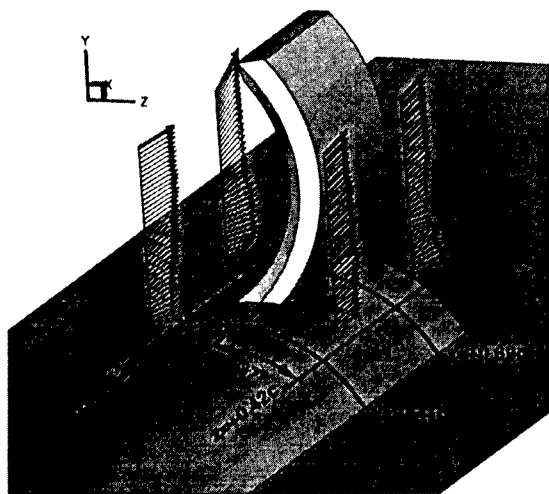


Fig. 7: Probe locations for Mach 2.8 Single Fin Experiment.

Temporal convergence was demonstrated at each sequence by recording the solution on lines corresponding to experimental surveys. When the solution ceased changing with further integration, Euclidean norm of the residual vector was typically reduced by three to four orders of magnitude.

4.4 Computational Requirements

As expected, the computational requirements for the RANS calculations (fin region), both in terms of memory and CPU, increase by approximately a factor of eight with each grid refinement. For the finest grid (4.17×10^6 cells), GASP required 113×10^6 Words of memory and 134 seconds per iteration on a Cray C916 (with Baldwin-Lomax turbulence model). Details of the computational requirements for all of the calculations are provided in References 8,10,&11.

5. WAF FLOWFIELD AT MACH 2.8

In the data presentation, the probe position (x,y,z) is nondimensionalized by the fin chord, $c=20.3\text{mm}$, where the coordinate origin is located at the intersection of the body surface centerline and leading edge of the fin. Negative x values are upstream of the leading edge, and negative z values are to the concave side of the fin. Boundary layer data is presented as a function of the distance, from the model body, Y . This relative position from the body is normalized by a reference boundary layer thickness, $\delta_0=6.1\text{mm}$, which was measured on the model centerline $0.41c$ ahead of the leading edge of the fin, and defined by the distance from the surface where $M=0.95\% M_\infty$.

The flow over the single WAF geometry has been experimentally explored^{6,7,8,9} by extensively probing the flowfield near the model. As part of this investigation, the fuselage boundary layer was surveyed at four locations on the ceiling mounted model as shown in Fig. 7. These locations were chosen to represent the *upstream* and *downstream* regions on either side of the fin, since two of the stations set the reference for the flow upstream of the fin bow shock (at $x=-0.41c$) and the other two stations were positioned downstream of the shock (at $x=+0.69c$). At each of these axial locations, the flow was surveyed with the pressure probes on the concave (Cc) side, and convex (Cv) side of the fin (at $z=\pm 0.47c$). The hot-film surveys were conducted at these same axial locations and at very near transverse locations; $z=-0.52c$ on concave (Cc) side, and $z=+0.42c$ on the convex (Cv) side. Note that the transverse locations of the hot-film surveys had been previously reported⁹ as identical to the locations of the pressure probe surveys. Based upon extensive comparison with the present numerical results and a subsequent uncertainty analysis of the experiment⁸, it is now believed that these locations are slightly different (by approximately one hot-film probe width). Results from the companion numerical study are compared with the experimental data at the survey locations, and the combined numerical and experimental data are examined for the purpose of characterizing the flowfield.

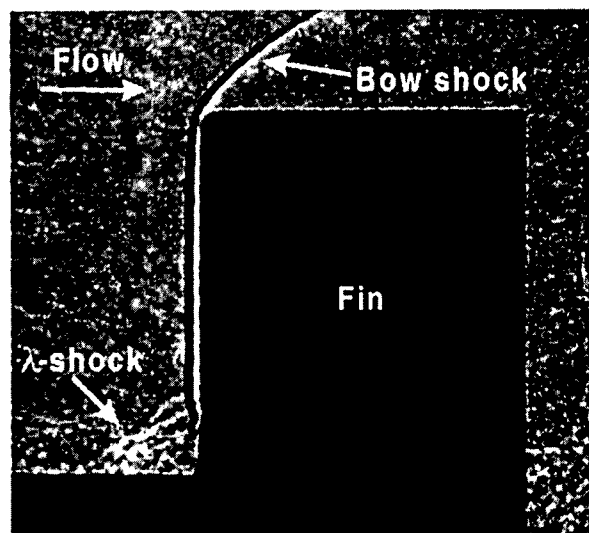


Fig. 8: Shadowgraph of the λ -shock region.

5.1 Flow Ahead of the Fin

To get an initial understanding of the flowfield ahead of the fin, shadowgraph images were obtained with the model in the test section (Fig. 8).⁶ The bow shock remains detached over the full span of the fin, and the shock-boundary layer interaction produces the same type of λ -shock that has been typically observed in front of blunt fins and cylinders mounted on flat plates. Configurations possessing blunt leading edges have a stagnation point on the leading edge which corresponds to the end of a 'parting line' in the flow, indicating the furthest location from the body at which particles become entrained into the vortical flow ahead of the leading edge. The present test article has a sharp leading edge, making it difficult to identify any stagnation point in the CFD solutions. However, particle traces of the viscous CFD solution (Fig. 6) indicates that the distance from the body at which streamlines diverge as they encounter the fin leading edge is at $y=0.19c$. This agrees quite well with the λ -shock height indicated by photography of $y=0.20c$.^{6,8,9}

At the upstream measurement location, which is ahead of the bow shock, both computed and experimental pitot pressures and mass-flux profiles (see Figs. 9&10) correspond to those of a largely "undisturbed" boundary layer. While it appears that the numerical solution predicts a thinner boundary layer than measured experimentally, the agreement is good in the outer region. The calculations also suggest a high degree of flow symmetry in the outer flow at the upstream measurement locations, while the degree of measured asymmetry was within the experimental uncertainty. At these upstream locations, the numerical results indicate that the flow in the boundary layer is moving slightly away from the centerline (Figs. 9d&10d). The flow very near the body is being swept away from the centerline at a very high angle, indicating this part of the boundary layer feels the presence of the fin.

5.2 Effect of Fin Curvature on the Mean Flowfield

While 2-D photography indicates flow features similar to those seen on straight fins, conventional pressure probes, hot-film anemometry, and CFD have all demonstrated that the flow near the fin is highly asymmetric. This asymmetry can be clearly seen in the computed and measured pitot pressures at the $x=0.69c$ plane (Fig. 11). On the concave side of the fin, a high pressure region is produced between the fin and its center of curvature where pitot pressure (and mass-flux levels) are greatly increased over the free-stream value. This produces large region of relatively high surface pressures near the half-span of the fin that contributes to a negative rolling moment. Here, rolling moment will be defined in the vehicle stability sense, thus a negative value indicates a moment acting in the direction of negative curvature. In contrast, the outer flow on the convex side of the fin exhibits a structure reminiscent of conical flow, with the pressure gradient in the direction normal to the fin

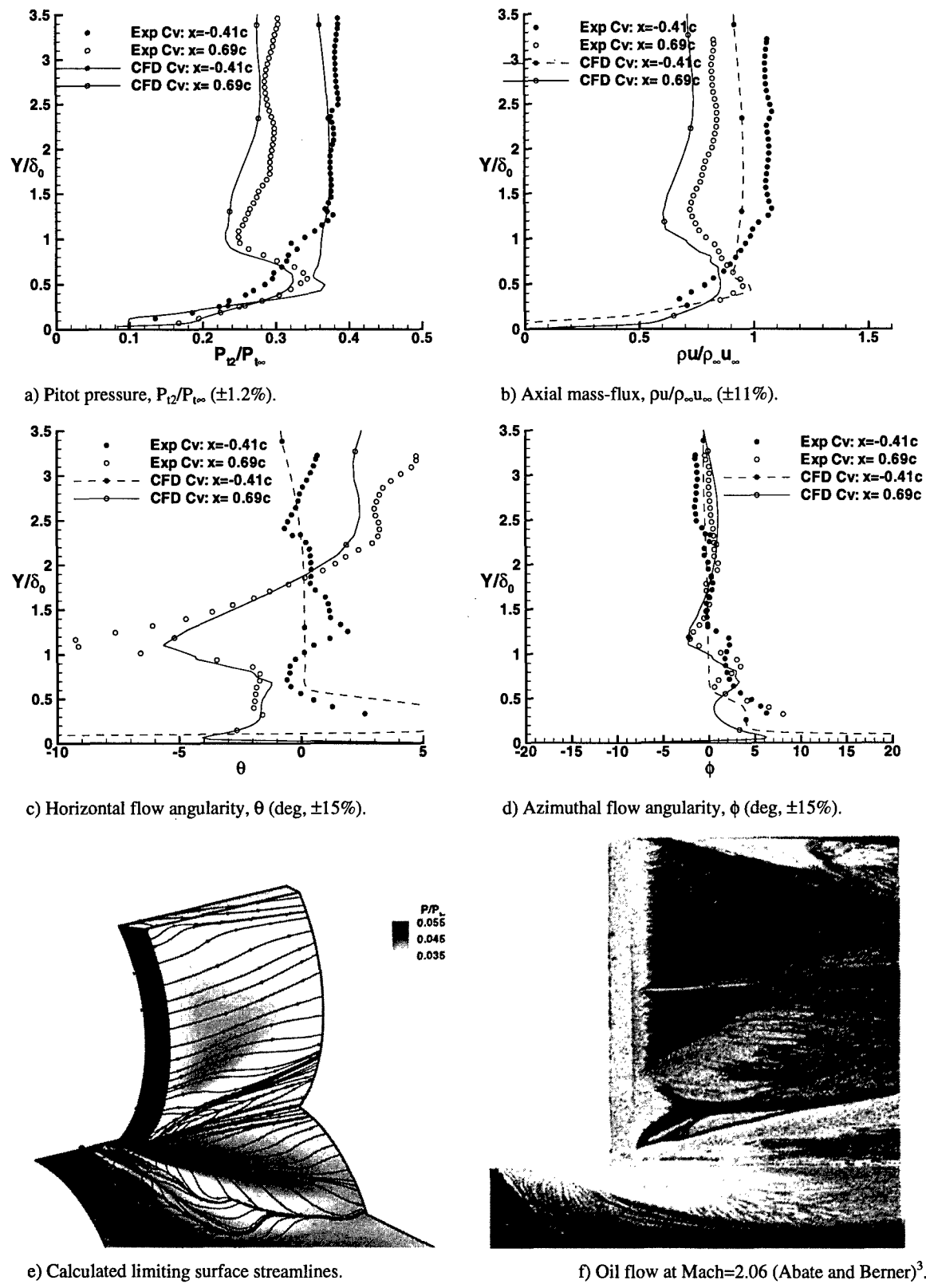


Fig.9: Numerical and experimental flow variables; convex side of fin.

chiefly independent of span-wise location. Agreement between the inviscid numerical results and experiment suggests that the position and strength of the bow shock is, not surprisingly, dominated by inviscid characteristics of the flow except in the immediate vicinity of the fin/body juncture where the fuselage boundary layer becomes important.

5.2.1 Flow on the Convex Side of the Fin
As the flow nears the fin on the convex side, the outer flow ($Y/\delta_0 > 1.5$) passes through a strong shock (Fig.12). This shock induces a strong compression and deceleration. As the fluid passes the fin it is expanded through a large region of favorable pressure gradient between the shock and the downstream measurement location (seen in Fig.12) due primarily to the convex fin curvature.

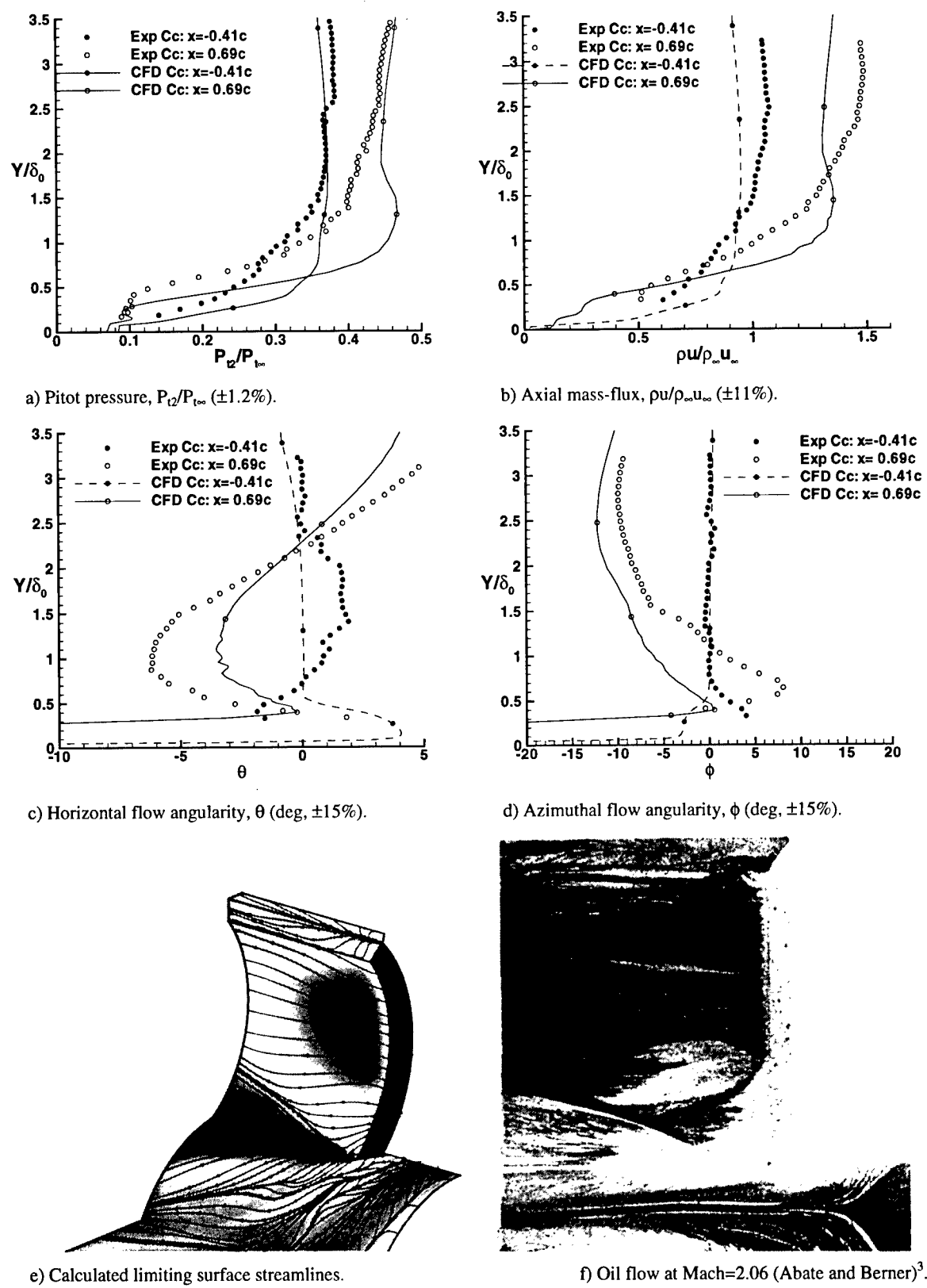
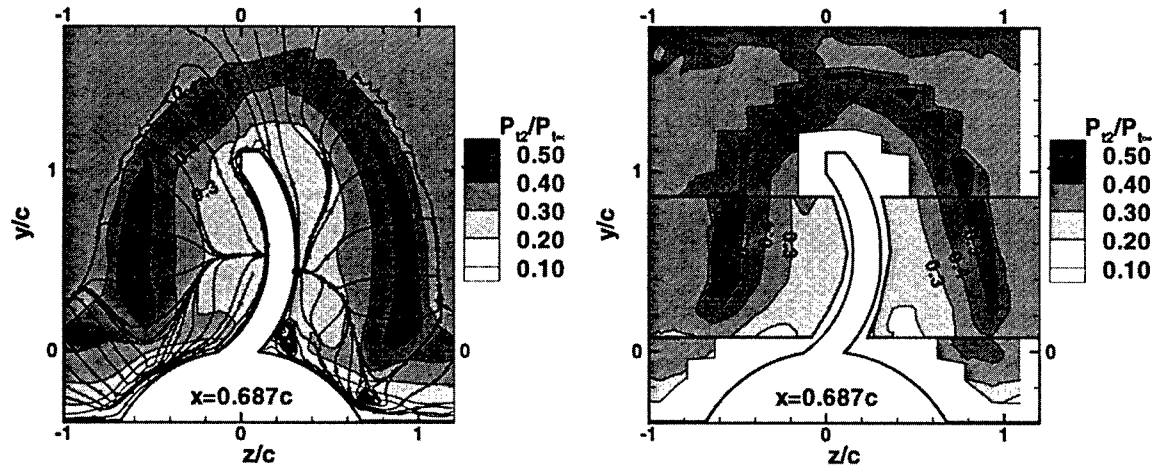


Fig.10: Numerical and experimental flow variables; concave side of fin.

At the downstream survey location, the pitot pressure and mass-flux in the outer flow has been decreased on the convex side relative to the upstream reference plane. At this measurement station the outer flow is directed away from the body, but only mildly away from the fin. These effects were captured by both inviscid⁶ and viscous numerical methods, and are seen in the experimental data (Figs.9a&b).

Profiles of pressure and momentum in the boundary layer at this location are characterized by a large inflection (Figs.9a&b). The flow near $Y/\delta_0 \approx 1.1$ has passed over the horseshoe vortex system produced by the shock/boundary-layer interaction ahead of the fin (see Fig.12). In this process, the flow greatly expands while only slightly accelerating; the net result is a decrease in the mass-flux. Flow in this region is directed strongly toward the body as indicated by the inflection in the horizontal flow angularity (Fig.9c). Agreement with experimental data is



a) Numerical pitot pressure and streamlines
b) Experimental pitot pressure ($\pm 1.2\%$)
Fig.11: Flow at $x=0.69c$ measurement plane given by numerical simulation and experiment.

considered excellent, although the flow turning angle is slightly under-predicted. Examination of the numerical results has revealed that this turning effect is due to a vortex embedded in the fin/fuselage juncture which entrains fluid, pulling it toward the body (seen in Fig.11a). This vortex also contributes to the pitot pressure inflections seen both numerically and experimentally (Fig.9a). At roughly the same location, an inflection in the azimuthal flow angularity (ϕ) is observed (Fig.9d). The agreement between the numerical and experimental ϕ profiles is considered excellent, and well within the uncertainty of the measurements.^{8,9} The predicted profiles for ϕ in this region were found to be influenced significantly by small errors in probe location in the z direction. Also, the flattening of the θ profile in the experimental data over the range $0.3 < Y/\delta_0 < 0.8$ is closely duplicated. It is notable that the juncture vortex and its effects are viscous phenomena and thus have not been captured by inviscid methods.⁶

Slightly closer to the body ($0.3 < Y/\delta_0 < 1.0$), the flow experiences a compression from above while it is at the same time aligned with the x -axis near the body. The net effect is a sharp increase in axial mass-flux. Below $Y/\delta_0 \approx 0.3$, the body forces a decrease in mass-flux and pitot pressure. The flow is directed downward and away from the fin over a very small region ($Y/\delta_0 < 0.2$), following the contour of the body. The numerical results and oil flow patterns at Mach 2.06³ (discussed below) suggest that the azimuthal flow angularity, ϕ , at this location tends toward zero at the wall.

Given its proximity to the fin, and hence its effects on the aerodynamic loading, more discussion on the 'juncture' vortex is warranted. The juncture vortex (Fig.13) originates near the leading edge of the fin/body juncture and remains tucked into the fin/body junction, growing in strength and size as it progresses along the fin. The size and orientation of this vortex is clearly evident in limiting surface streamlines calculated from the numerical solution (Fig.9e) and in the surface oil flow patterns obtained by Abate and Berner³ at Mach 2.06 (Fig.9f). Surface streamlines starting at the leading edge travel downward along the beveled edge and join with streamlines flowing up from the root to form an accumulation of oil film (or convergence of streamlines) on the surface. This convergence line marks the separation line formed by the juncture vortex, and moves away from the juncture as it travels toward the trailing edge. The complicated flow structure observed in the oil flow patterns closely resembles that predicted by the numerical solution, suggesting that the flow structure near the juncture changes little within this Mach number range. On the body, a weak attachment line (surface streamline divergence) moving outward from the leading edge is clearly evident in both the numerical solution (Fig.9e) and the oil flow (Fig.9f).

Evidence of such a vortex has also been observed in oil flow patterns on straight blunt fins mounted on flat plates.^{24,25} Such vortices have been observed to change rotational direction on straight fins depending on incidence angle.²⁵ The present viscous numerical results indicate that the rotation of the juncture vortex is of the same sense as that seen on the compression side of a straight fin at incidence. Thus, with respect to the juncture vortex, fin curvature and attachment angle can induce similar effects to those produced by cross-flow.

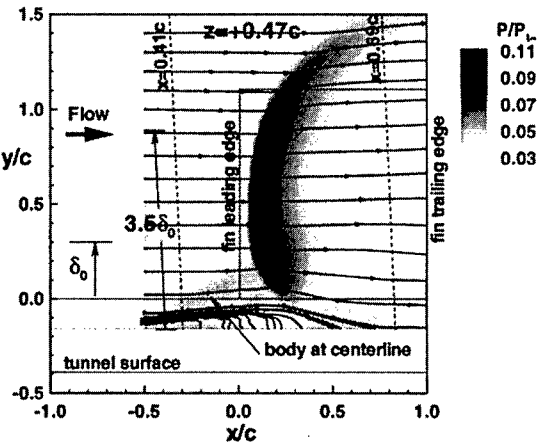


Fig.12: Convex measurement plane ($z=+0.47c$) pressure levels and mass-flux streamlines ($\rho u, \rho v$) given by numerical simulation. Outline of fin is overlaid. Dashed lines represent survey locations.

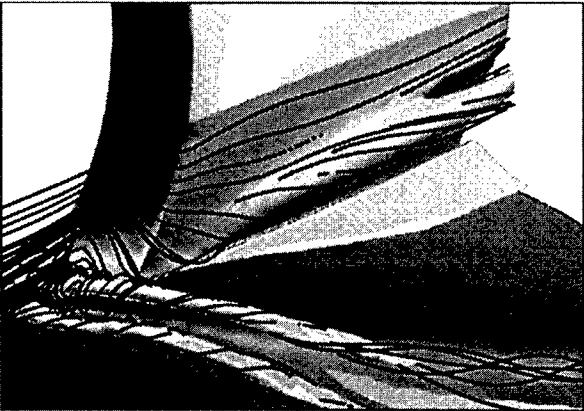


Fig.13: Stagnation pressure iso-surfaces and streamlines in vortex juncture region on convex side of the fin.

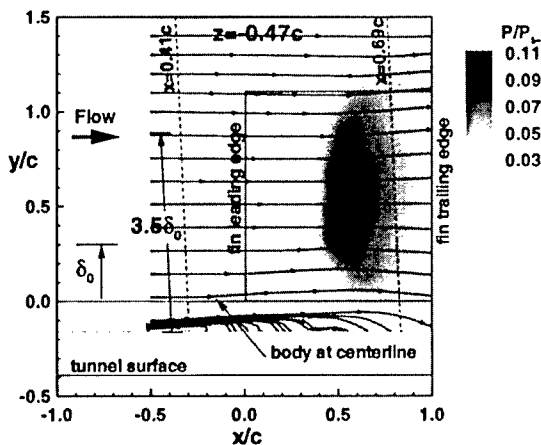


Fig.14: Concave measurement plane ($z=-0.47c$) pressure contours and mass-flux streamlines ($\rho u, \rho v$) given by numerical simulation. Outline of fin is overlaid. Dashed lines represent survey locations.

5.2.2 Flow on the Concave side of the Fin

In contrast to the flow on the convex side of the fin, the flow on the concave side passes through a somewhat weaker shock (Fig.14). Thus, the flow undergoes a much more modest deceleration. Also, the post-shock expansion is partially offset by the compressive effects of fin curvature. The net effect is a dramatic increase in the mass-flux (up to 30%) at the downstream measurement location as compared to the upstream location. This increase is observed in both the numerical and experimental data. The overprediction of the pitot pressure in the outer boundary layer on this side of the fin is probably the result of the lack of pressure gradient effects in the algebraic turbulence model. As will be shown in Section 5.3, the turbulence levels on this side of the fin are highly attenuated, leading to significant turbulent shear stresses.

On this side of the fin, the outer flow is strongly directed away from the fin (Fig.10d) at flow angles, ϕ , up to 10° at the mid-span ($Y/\delta_0 \approx 2.5$). Here, numerical and experimental results indicate that $\theta \approx 0^\circ$, meaning that the flow is directed toward the center of fin curvature (Figs.10c&11a).

Approaching the body, the fluid momentum decreases (Figs.10a&b). Over a small region inside the boundary layer ($0.5 < Y/\delta_0 < 1.0$), the numerical solution suggests that there is a large inflection in the azimuthal angularity (Fig.10d) where the flow is almost aligned with the vertical plane ($\phi \approx 0^\circ$). This inflection is more pronounced in the experiment data, but occurs at the same location. This effect is likely to be a combination of the flow wrapping around the fin and an expansion which reflects off of the bow shock as a compression. The inviscid numerical results^{6,7,9} only faintly hinted at this trend. Over this same range, the experimental data (Fig.10c) suggests that the magnitude of the horizontal flow angularity is greatly reduced

(i.e. $\theta \rightarrow 0$ at $Y/\delta_0 \approx 0.3$). This trend was also captured to some extent in the numerical solution.

Closer to the body ($Y/\delta_0 < 0.5$) there is a small region in which measured and computed pitot pressures do not change. The numerical results suggest that the flow is moving downward and away from the fin ($\theta \approx -30^\circ, \phi \approx -39^\circ$), leading to the flattening of pitot pressure. Cross-wire volume effects precluded detailed experimental examination of this region.^{7,9}

On this side of the fin, surface streamlines starting at the leading edge also travel downward along the beveled edge and join with streamlines flowing up from the root. However the streamline convergence is 'incomplete' from below, and no juncture vortex is indicated. As on the convex side, the similarities between the predicted surface streamlines and the observed oil flow patterns of Abate and Berner at Mach 2.06³ suggest that the flow structure near the juncture on this side of the fin changes little within this Mach number range. The downstream measurement station on this side of the fin is located just behind a separation line on the body, which is seen in the computational results and oil flow pattern. Presumably due to the oblique attachment angle ($\approx 135^\circ$) and perhaps the adverse pressure gradient, no juncture vortex was observed on the concave side of the fin in either the numerical or experimental studies, nor is one indicated by the oil flow visualizations³ at Mach 2.06 (Figs.10e&f).

In comparing the numerical results to the oil flow patterns of Abate and Berner³, it is notable that the latter was obtained on a four-finned missile. Thus the similarity between fin surface streamline patterns suggests that the single-fin model produces the relevant flow features present on configurations with multiple wrap-around fins.

5.3 Effect of Fin Curvature on Turbulence

Turbulence quantities were extracted from the cross-wire data taken at the locations discussed in the previous section. Although the downstream probe location on the concave side of the fin is in a region of mild favorable pressure gradient, it is still close to the bow shock. Examination of the turbulence intensity in this region indicates that the shock induces an increase in the axial and transverse turbulence intensities (Fig.15), which is consistent with the destabilizing effects of adverse pressure gradients on turbulent boundary layers.²⁶

On the convex side, the turbulence intensities at the same streamwise location are far lower, since the flow has experienced a favorable pressure gradient over an extended streamwise distance (Fig.12). Expansions have been reported to stabilize, or reduce the turbulence levels.²⁶ Also contributing to this dramatic recovery is the rapid flow acceleration induced by the convex curvature of the fin. Both of the secondary mass-flux turbulence intensities experience a sharp rise near $Y/\delta_0 = 1.1$, but not so the axial component. The rise in cross-flow turbulence intensity occurs at the same location where the mean flow is being turned sharply toward the body by the juncture vortex, producing similar discontinuities in the mean flow angularity (notably θ).

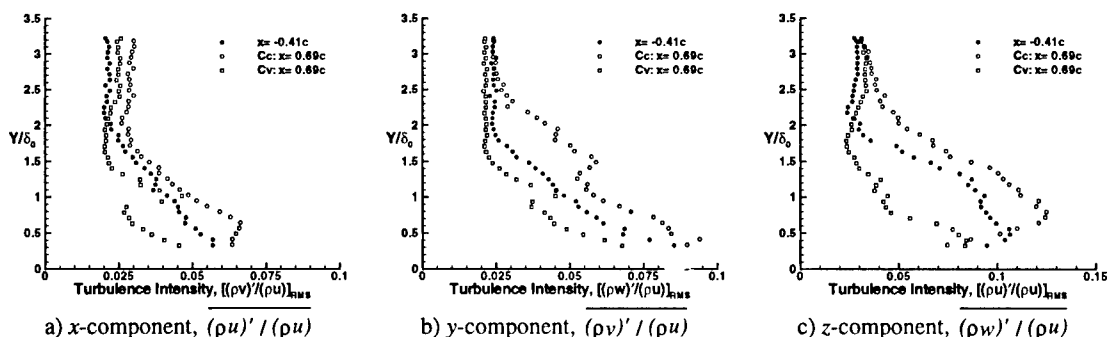


Fig.15: Turbulence intensity profiles ($\pm 11\%$).

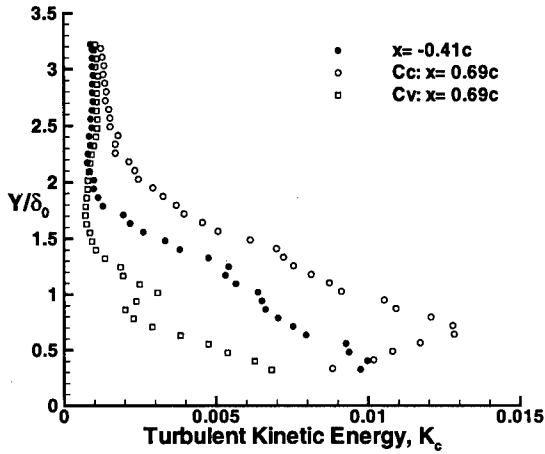
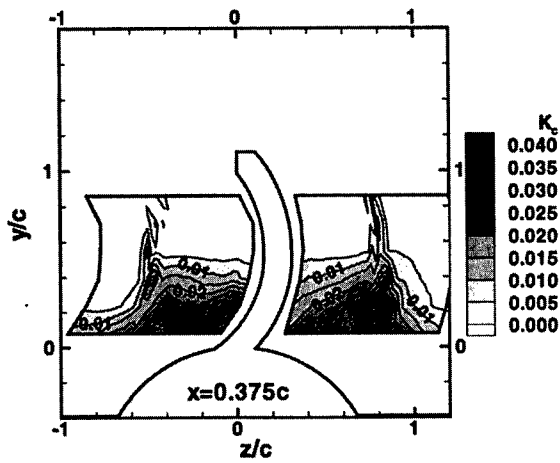


Fig.16: TKE, K_c (Eqn. 3, $\pm 16\%$).

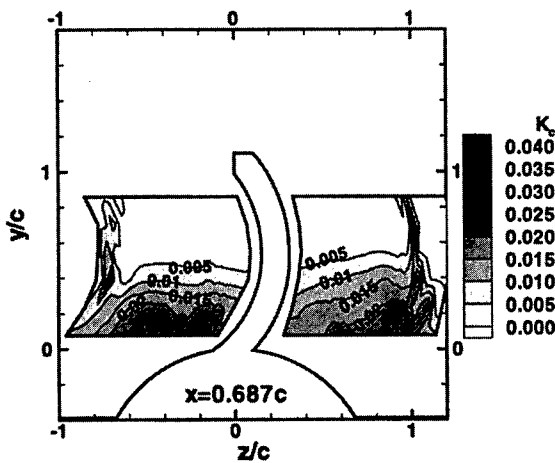
The net effects of the bow shock and fin curvature are illustrated in Figs.16&17 via the nondimensional turbulent kinetic energy (TKE), K_c , defined by

$$K_c = \frac{1}{2} \left\{ \left[\frac{(\rho u)'}{\rho u} \right]^2 + \left[\frac{(\rho v)'}{\rho u} \right]^2 + \left[\frac{(\rho w)'}{\rho u} \right]^2 \right\} \quad (3)$$

The TKE is significantly elevated on the concave side of the fin and reduced on the convex side relative to values upstream of the shock (Fig.16).



a) $x = 0.37c$



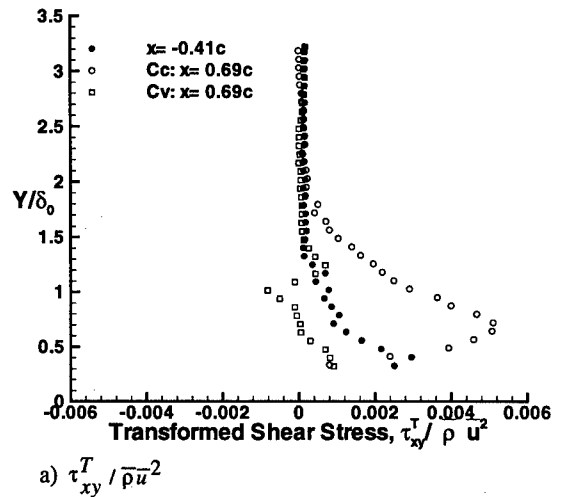
b) $x = 0.69c$

Fig.17: TKE, K_c (Eq. 3, $\pm 16\%$).

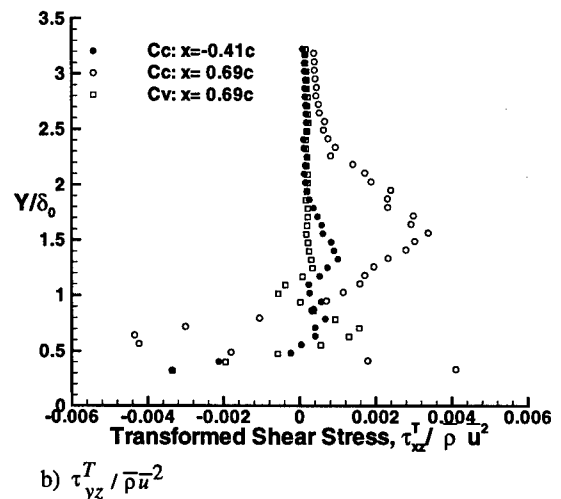
The nondimensional TKE at two streamwise stations is shown in Fig.17; one at the same location as the boundary layer measurements ($x=+0.69c$), and one further upstream at $x=+0.38c$. These surveys, which included the upper portion of the boundary layer, indicate that TKE levels on the convex side are markedly greater than those on the concave side at both stations. Also, TKE is dissipating in the axial direction on both sides of the fin, as the flow passes through regions of favorable pressure gradient. Thus, as the flow continues to recover, the TKE levels on the concave side of the fin are likely to continue decreasing in the downstream direction, possibly to the levels seen on the convex side.

The boundary layer stabilizing and destabilizing effects on either side of the fin are also apparent in the Reynolds shear stress estimates measured with the cross-wire (Fig.18). Upstream of the fin, the shear stress profile corresponds to that of an undisturbed boundary layer, with levels comparable to those upstream of the model. This indicates that the effects of the compression caused by the blended region of the model have been damped to levels comparable to an equilibrium turbulent boundary layer. Note that the second term of the total turbulent shear stress in Eq.1 has been determined to be at least an order of magnitude smaller than the first term for all surveyed regions.

On the convex side of the fin, a reduction of turbulent shear stress with downstream position is indicative of the strong stabilizing effect of favorable pressure gradient. Indeed, as observed by other researchers investigating correlations between streamline distortion and turbulence²⁷, the expansion associated with a favorable pressure gradient can result in reduced (or even negative) turbulent shear stress. Conversely, the turbulent shear stress on the concave side is increased by roughly 100-200%,



a) $\tau_{xy}^T / \bar{\rho} u^2$



b) $\tau_{yz}^T / \bar{\rho} u^2$

Fig.18: Measured turbulent shear stresses, (Eq. 1, $\pm 21\%$).

commensurate with the previously noted increases in turbulence intensity and turbulent kinetic energy. This pattern is consistent with other measurements obtained in regions of large compression.²⁷ Note too that the boundary layer thickness has dramatically increased (by about 60–70%) on the concave side, while it was reduced slightly on the convex side. The large increase in turbulent shear stress on the concave side of the fin may be the primary reason that measured pitot pressure and mass flux levels were less than those predicted by the numerical simulation in the outer boundary layer (Figs.10a&b), since the turbulence model used was not designed to simulate the effects of pressure gradient on turbulence.

Before to this study, no detailed mean flow or turbulence measurements existed for WAF missile configurations. The present experiments have produced a significant amount of turbulence data on this shock/boundary layer interaction flowfield. It is expected that these turbulence data will be useful for validation of turbulence closure models intended to predict flows having large pressure gradients.

6. WAF FLOWFIELD AT MACH 4.9

In experiments aimed at determining the structure of the mean flowfield at a high-speed condition, the single-WAF model was also investigated (experimentally and numerically) at Mach 4.9 and a unit Reynolds number of $Re/l=75\times10^6m^{-1}$ ($Re_c\approx1.52\times10^6$). In the experiment, the mean flow around the ceiling-mounted WAF configuration was surveyed using pitot and cone-static probes and was visualized using shadowgraph and schlieren photography in the AFIT Mach 5 wind tunnel. Fuselage boundary layer surveys were again obtained upstream and downstream of the bow shock.

In the viscous numerical simulation, the Navier-Stokes equations were solved using the same computational grid and numerical strategy used for the Mach 2.8 simulation. The algebraic turbulence model of Baldwin and Lomax²⁰ was again employed. Experimental pressure data were used to define the upstream boundary condition for this calculation. The resulting numerical solution is compared with the experimental data and the combined sets of information are examined to characterize the flowfield.

The experimental and numerical results suggest that the flow near the fin is highly asymmetric as it was at Mach 2.8. In fact, most of the qualitative discussion on the flowfield structure at Mach 2.8 applies at Mach 4.9 as well.

6.1 Shadowgraph and Schlieren Photography

Shadowgraphs and schlieren images of the fin region (Figs.19& 20) again indicate that fin shock remained detached over the full span of the fin as it did at Mach 2.8, although stand-off distance was reduced. The same principal features observed at

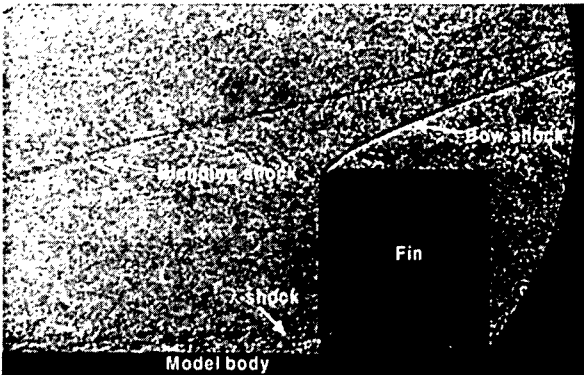


Fig.19: Shadowgraph of fin region (M=4.9).

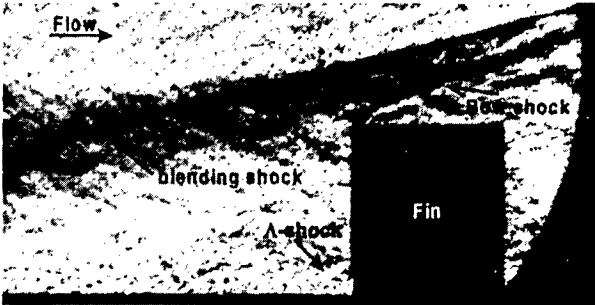
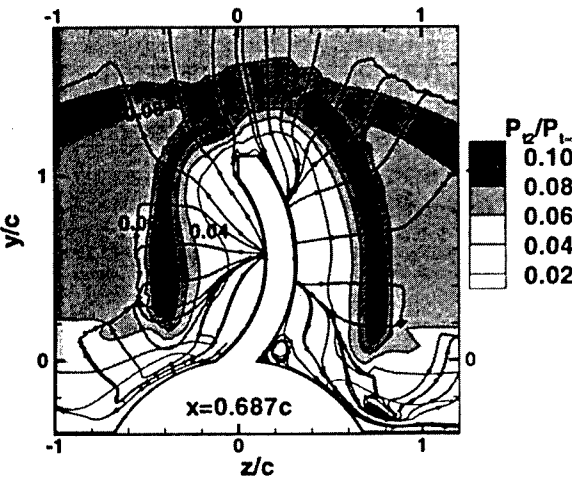


Fig.20: Schlieren photograph (M=4.9).

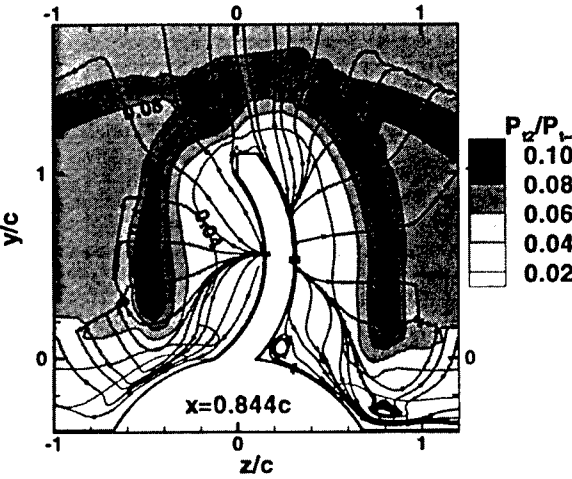
the lower Mach number were again visible, including the shock caused by the blended forebody and the bow shock, both of which were more highly swept than at Mach 2.8. The λ -shock was also distinct, though somewhat unsteady, and positioned slightly closer to the body and at a shallower angle than observed in the Mach 2.8 experiment (*cf* Figs.8&19). This trend was also captured in the viscous numerical solutions. As expected, the fin's domain of influence in the outer flow was reduced from that at Mach 2.8 (Fig.21).

6.2 Effect of Fin Curvature on the Mean Flowfield

The fuselage boundary layer flow was explored near the fin on the ceiling mounted model, as it was in the Mach 3 tunnel. Placement of the measurement stations for the experiment was again guided by preliminary inviscid computations^{8,11} and by experience gained from the experiment in the Mach 3 tunnel. The probe locations were the same in the span-wise direction ($z=\pm0.47c$) as they were in the Mach 2.8 experiment, and the stations that set the reference for the flow were again placed just upstream of the flow interaction at $x=-0.41c$. However, the probes were positioned further aft at the downstream locations ($x=+0.84c$) so as to remain well behind the bow shock.



a) $x=0.69c$ (M=2.8 measurement plane, *cf* Fig.11a).



b) $x=0.84c$ (M=4.9 measurement plane).

Fig.21: Computed pitot pressure and secondary streamlines

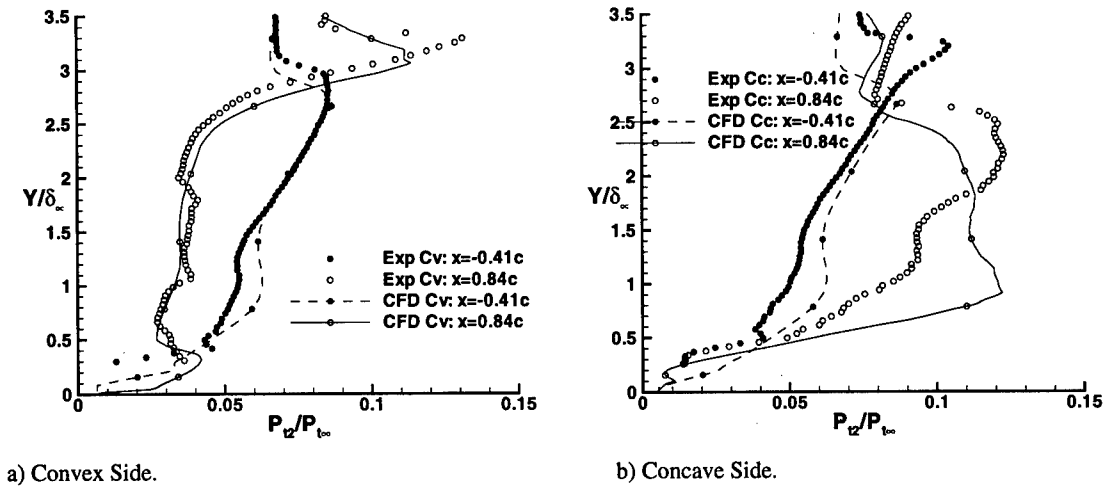


Fig.22: Experimental and numerical pitot pressure.

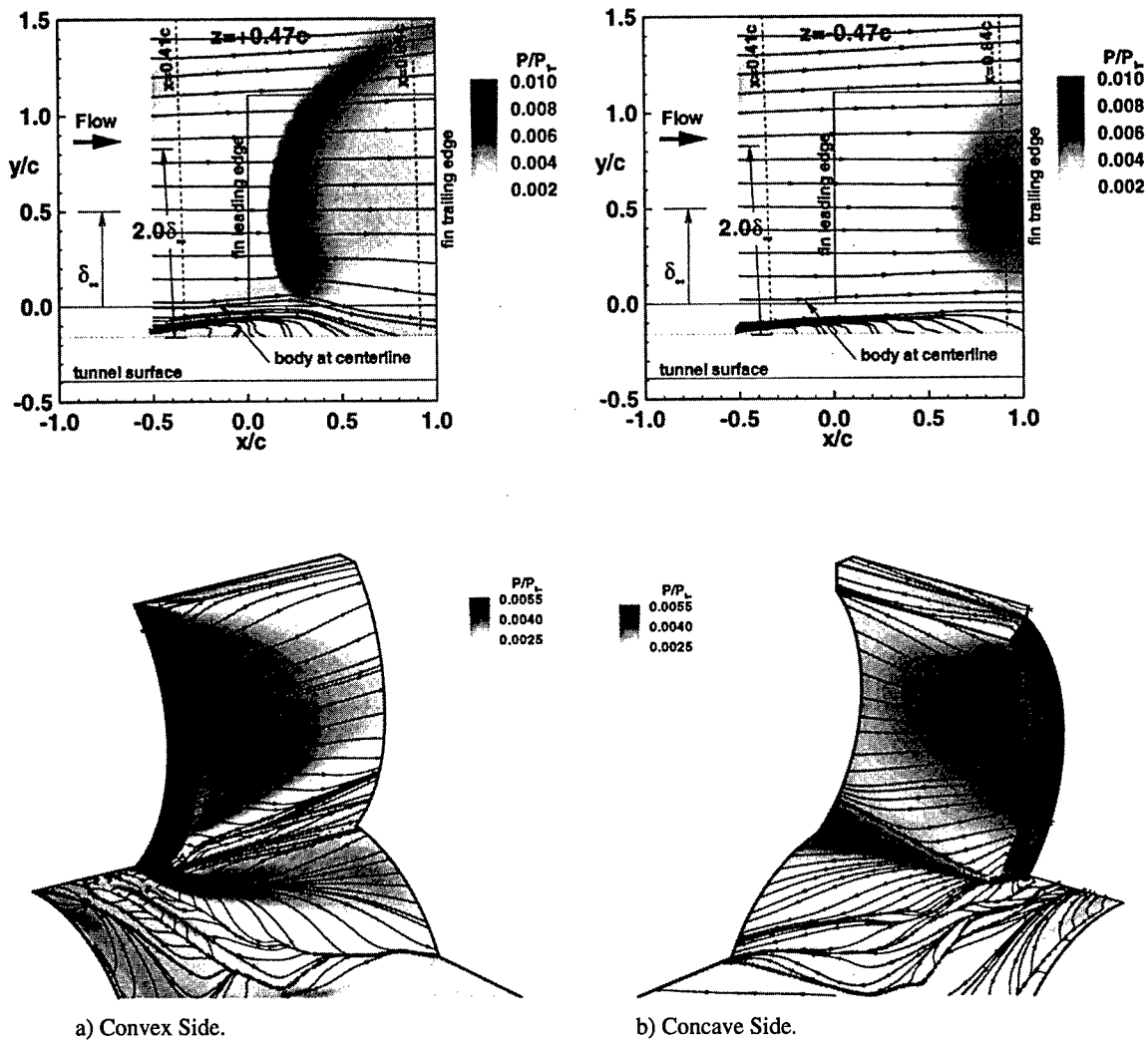


Fig.24: Computed limiting surface streamlines at M=4.9.

In the presentation of the results, the probe position (x,y,z) is nondimensionalized by the fin chord as it was for the Mach 2.8 results. Boundary layer data are presented as a function of the distance from the model body, Y . This relative position from the body is normalized by a reference boundary layer thickness, $\delta_{\infty}=10.2\text{mm}$, which was measured on the tunnel centerline $0.8r$ ahead of the blended body. Note that this is larger than the dimension ($\delta_0=6.2\text{mm}$) by which the Mach 2.8 results were normalized. The locations at which the numerical solution is

compared to experimental results are canted to mimic the flexing experienced by the probes ($\approx 1.1^\circ$).

The measured flow asymmetry at the upstream measurement plane was minimal (Fig.22), and well within the experimental uncertainty⁸ (especially considering that the data were acquired on different days). At this upstream location, there is a much larger pressure gradient in the direction away from the body than was observed at Mach 2.8 due to the relative proximity of the blending shock.

6.2.1 Flow on the Convex Side of the Fin

As seen at Mach 2.8, the flow on the convex side of the fin passes through a strong shock (Fig.23a), and then expands through a large region of favorable pressure gradient between the shock and the downstream measurement location due to the convex fin curvature. Relative to its upstream value, the pitot pressure in the outer flow at the downstream measurement station has been decreased by about 40% (Fig.22a). Agreement between experimental and computed pitot pressures is considered excellent on this side of the fin.

The calculated pitot pressure profile features a large inflection in the inner region (Fig.22a). This inflection is more difficult to identify in the experimental results than it was at Mach 2.8. While the larger volume of the pitot probe used at Mach 5 precluded a definitive assessment of this feature, it appears that the inflection may be closer to the body and not as large as that predicted by the numerical simulation. The computed pressure peak is at the approximately the same physical distance from the fuselage at both Mach numbers ($0.3\delta_\infty \approx 0.5\delta_0$). Recall from the Mach 2.8 discussion that this inflection in pitot pressure was associated with the existence of vortex embedded in the fin/fuselage juncture. This vortex is also present in the solution at Mach 4.9 (Fig. 21), and is probably present in the experimental flowfield, although the pressure data do not provide conclusive evidence.

The predicted rotational direction of the juncture vortex at Mach 4.9 is the same as it was at Mach 2.8, but the predicted location is slightly closer to the fuselage (cf Figs.11a&21a). The size and orientation of this vortex is also indicated by the calculated limiting surface streamlines (Fig.24a). While the structure of the surface streamlines on the fin are very similar to those calculated at Mach 2.8, the separation line formed by the juncture vortex is slightly closer to the body. Also, the weak attachment line on the body moving outward from the leading edge is slightly closer to the fin than predicted at Mach 2.8.

6.2.2 Flow on the Concave Side of the Fin

As was the case at Mach 2.8, the outer flow ($Y/\delta_\infty > 1.0$) on the concave-side measurement plane passes through a somewhat weaker shock than on the convex side (Fig.23b). Again, the post-shock expansion is partially offset by the compressive effects of fin curvature. It should also be noted that the survey location is very close to the shock to the fin shock. The net effect is a very large increase in the pitot pressure (up to 90%) and momentum by the time the flow reaches the downstream measurement location. This increase is observed in both the numerical and experimental data (Fig.22b), and is even more dramatic than at Mach 2.8. The overprediction of the pitot pressure in the outer boundary layer on this side of the fin is probably again the result of the lack of pressure gradient effects in the algebraic turbulence model. Close to the body ($Y/\delta_\infty < 0.4$) there is a small region over which measured and numerical pitot pressures do not change. The viscous simulations suggest that the flow in this region is moving down and away from the fin at angles comparable to those predicted at Mach 2.8, leading again to a 'flattening' of pitot pressure. The downstream measurement station on this side of the fin is again located just behind a separation line on the body which is predicted to be at approximately the same location as it was at Mach 2.8 (cf Figs.24b&10e). The calculated secondary flow structure is also very similar to that predicted at Mach 2.8 (cf Figs.21a&11a). The outer flow is strongly directed away from the fin toward the center of fin curvature at the mid-span, and there is no evidence of a juncture vortex in the experimental or numerical results on this side of the fin.

7. EFFECTS OF MACH NUMBER

7.1 Surface Oil-flow Visualization

The primary objective of the surface flow experiments was to examine the effects of Mach number on flow structure. Fig.25 shows surface oil-flow visualizations for the solid- and slotted-fin missiles for $M=2.15$, 2.86, and 3.83. The top and bottom fins are showing their concave and convex sides, respectively. Qualitatively, the surface streaklines on the fin are very similar

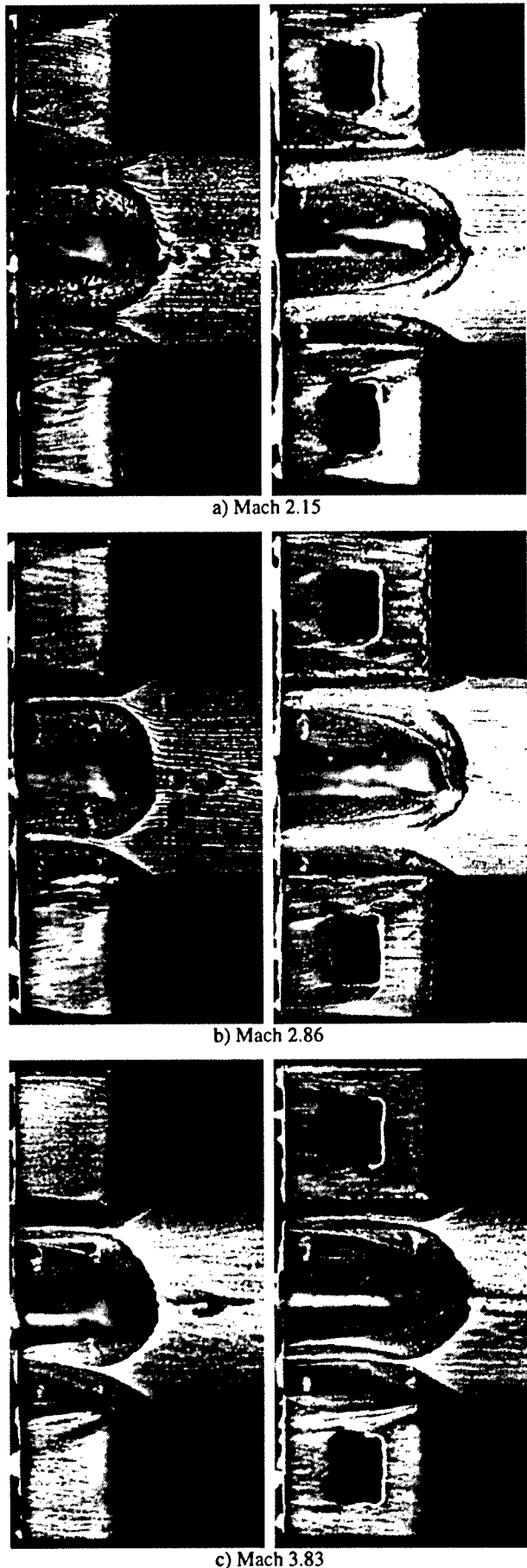


Fig.25: Solid- and slotted fin surface oil-flow visualizations

to those of the single-fin numerical solutions. However, the surface streaklines on the body are affected by the multiple fin shock interactions, and did not compare well. Examination of these images reveal the Mach number dependence on the salient flow features described previously.

Concentrating first on the surface phenomena on the convex side of the solid-fin (bottom fin in Fig.25), the flow near the fin root is characterized by a vortex embedded in the juncture of the fin and fuselage. The relatively large accumulation of oil that began near the fin leading edge root region and progressed downstream at an angle relative to the fuselage provides an indication of the size and shape of the vortex. The size of the dark regions above and below the vortex, which indicate streamline divergence toward the vortex, also provides an indication of the vortex strength (i.e., the strength of the entrainment process). While the vortex is confined to a much smaller region as Mach number is increased, the strength of the vortex appears to increase. At $M=3.83$, a large portion of the flow, as indicated by the strong divergence of streaklines (dark region just outward of the juncture vortex), over the fin has been entrained into the vortex.

The surface oil-flow visualizations also highlight the flow pattern near the outer tip of the fin. The dark wedge structure oil pattern, which emanated from the leading edge tip region, provided evidence for a slight leakage or separation from the fin, which, like the juncture vortex, was more prominent at the low Mach number. The flow over the central region of the fin was relatively orderly for the higher Mach number experiments (≥ 2.41). For the $M=2.15$ case, a large disturbance emanates from the leading edge root and proceeding to the trailing edge mid-fin-height. It is thought that this feature created a region of relatively low pressure, and thus, had a strong impact on the rolling-moment.

On the concave side of the fin (top fin in Fig.25), the juncture region is characterized by a separation, indicated by the wedge-like region near the root that is void of oil. As the Mach number was increased, the size of the separation region decreased dramatically. The oil patterns near the tip suggest that the flow diverged slightly out toward the fin bevel. As on the convex side, the flow over a large region of the fin (away from the root separation) was reasonably well ordered.

The surface oil-flow visualizations also highlight the fuselage flow. Progressing in the flow direction (right-to-left), the asymmetric separation line at the foot of the λ -shock is the first surface disturbance. As the Mach number was increased the shock structure became more oblique. The next line of separation indicates the location of the fin-fuselage horseshoe vortex system, which is also highly asymmetric. As the Mach number was increased from 2.15 to 3.83, the horseshoe vortex moved closer to the fin on its concave side, but remained fixed on the convex. This was not the case in the single-fin numerical solutions, perhaps due to the lack of fin interaction.

The slotted-fin surface oil-flow visualizations indicate that the presence of the slot dramatically changed the fin surface flowfield. Concentrating on the convex side of the fin (bottom fin in Fig.25) at Mach 2.15, the juncture vortex described above was present upstream of the slot. However, the vortex encounters the slot region of the fin, and its strength is reduced aft of the slot. This slot interaction effect was observed to diminish with increasing Mach since the vortex region becomes smaller and more oblique as the Mach number is increased. Furthermore, the slot appears to have eliminated the tip leakage separation near the fin tips.

The slots also had a significant impact on the fuselage flow patterns. First, at $M=2.15$, the extent of the fin shock influence was greatly reduced, indicating that the slot reduced the apparent blockage of the fin. This translates into potential wave drag reduction. This effect was so strong that a relatively large region of undisturbed flow existed between the shock structures generated by adjacent fins. This was not the case for any of the solid-fin experiments. Interestingly, as the Mach number was increased past 2.86, the shock structure upstream of the fin became more symmetrical and somewhat independent of Mach number. As the Mach number was increased, the adjacent fin generated shock structure interactions became more severe and the undisturbed region diminished in size, until no longer present at $M=3.83$.

7.2 Aerodynamic Loading on the Fin

The diverse flow topologies on either side of the WAF produce a dramatically different load distributions on the opposing fin surfaces. While inviscid calculations have captured many of the essential flow features, the flow near the fin/fuselage juncture is dominated by viscous effects and can provide a significant aerodynamic load.

7.2.1 Fin Surface Pressures

To highlight the viscous effects on the fin loading, the fin surface pressures and streaklines predicted by the pilot inviscid simulations⁶ of the single-fin model in the Mach 3 tunnel are shown in Fig.26. On the concave side of the fin, the fin curvature creates a large region of relatively high surface pressures near the half-span of the fin which contributes to the negative rolling moment typically experienced in supersonic flight. These inviscid calculations also predicted a region of high pressure near the fin root on the convex side, where pressure levels were near the magnitudes predicted on the concave side. We initially attributed this compression to the fin being canted in the convex direction ($\approx 45^\circ$) at its base. However, the viscous numerical results and pressure sensitive paint experiments have shown that this high pressure region is actually displaced away from the juncture, and significantly weakened by the juncture vortex (Figs.9e&10e). The root region is characterized instead by low pressures induced by the juncture vortex.

In simulations of the single-fin model in the Mach 5 tunnel, the same salient flow features predicted in the $M=2.8$ simulations were observed. Qualitatively similar surface pressure patterns

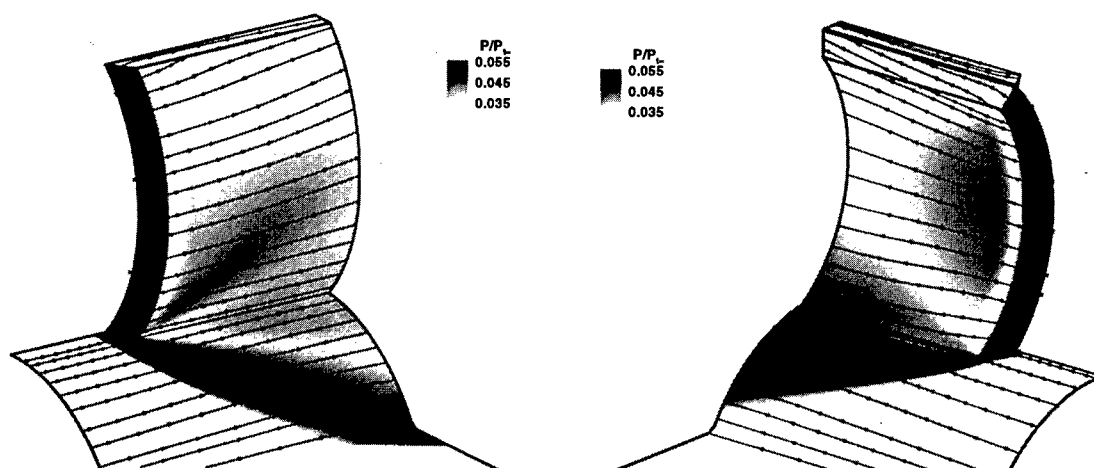


Fig.26: Computed inviscid surface pressures ($M=2.9$).

were observed, and viscous effects had similar influences on the solution.¹¹ Pressure sensitive paint images at the test conditions indicated in Table 1 were also examined. These images revealed very similar fin surface pressure patterns to those predicted in the viscous simulations, which appeared to be influenced in the same manner by Mach number.^{13,14}

7.2.2 Fin Rolling Moment

It has been previously shown⁴ using Euler methods that the rolling moment is a function of both the fin curvature and fin attachment angle. However, it is now clear that the effect of fin attachment angle is not fully captured by an inviscid analysis. For the single-fin geometry, the viscous CFD ($M=2.8$) predicted 10% greater rolling moment than the preliminary Euler analysis^{6,8} ($M=2.9$). While both viscous and inviscid methods predicted a decrease in rolling moment with increasing Mach number (confirming the test range trend described by Abate¹), the viscous simulations predict a much stronger trend (40% less rolling moment at $M=4.9$).

To obtain a more continuous inviscid baseline to which the results of the viscous simulations could be compared, the Euler equations were solved over the single wrap-around fin geometry at several other supersonic Mach numbers ($2.5 \leq M \leq 5.0$). For these simulations, the effect of the blending region from the flat tunnel wall to the semi-cylindrical body was neglected by imposing the freestream boundary condition shortly upstream of the fin. The computational grid was identical to the 8-zones surrounding the fin in the pilot inviscid study at Mach 2.8^{7,9}, and the same numerical methods were used. The computed rolling moment decreased with increasing Mach number in a manner consistent with previous inviscid calculations of WAFs⁴, and are shown (solid line) with the computed rolling moments from the two viscous simulations in Fig.27.

The PSP images at each Mach number were processed to estimate rolling moments. In order to avoid cooling effects on the PtOEP paint, the first three photographs at each flow condition were used. During this 12-sec. period, the total pressure varied, resulting in the Reynolds number variations in Table 1. The changes in Reynolds number significantly influenced the predicted loadings, as has been observed in data obtained at McDonnell Douglas, AEDC, NASA Langley, and NASA's Jet Propulsion Laboratory.⁵ While the Reynolds number variations did produce increased scatter of the data, all of the data suggested a strong reduction in the rolling-moment coefficient with increased Mach number (Fig.27). To reduce the apparent experimental scatter due to Reynolds number variations, the data shown corresponds to the experiments with a Reynolds numbers of nominally 0.6×10^6 , and a dynamic pressure of 100kPa ($\pm 10\%$). However, for the Mach 2.15 and 2.41 cases, the plotted data correspond to Reynolds numbers of 0.33×10^6 and 0.40×10^6 , respectively. The values were averaged for the Mach numbers with more than one data point in this range. The expected uncertainties have been described in the Experimental Uncertainty section.

Considering the relatively large uncertainty associated with the

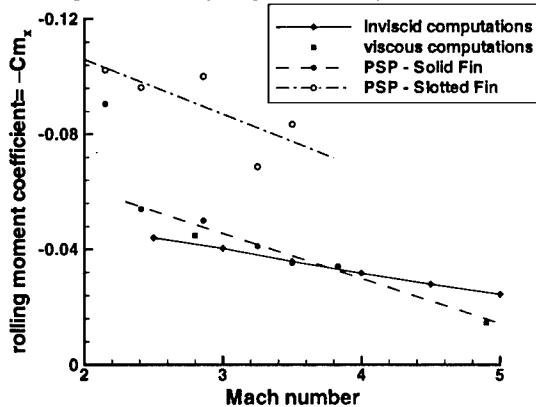


Fig.27: Computed rolling moments (for four fins).

experimental data and the slightly different fin models, the agreement between the CFD predictions and experimental data is considered to be excellent. The dashed line indicates a linear curve fit for $2.41 \leq M \leq 3.83$, and is extrapolated to $M=5$. As indicated, the CFD prediction at $M=4.9$ follows this extrapolation. The $M=2.15$ data point did not follow this trend. The large flow disturbance across the fin described in Surface Oil-flow Visualization Section is probably the cause for this discrepancy. Limited PSP experiments were also performed at $M=2.28$, and the corresponding rolling-moment was similarly well above the linear trend. If the linear trend were to persist to higher Mach numbers, then the rolling-moment would reach zero at $M=5.92$.

The rolling moment coefficients derived from PSP data for the slotted-fin configuration are also shown in Fig.27. The scatter associated with the slotted-fin was higher because of the increased uncertainty associated with locating the slot in the data reduction procedure. This effect, coupled with the aforementioned Reynolds number variations obscured the Mach number trends. In general, the rolling moment coefficients were roughly twice those of the solid-fin values (although the fin area was only 28.6% greater). However, these data also suggest a decrease in rolling moment coefficient with increasing Mach number.

8. CONCLUSIONS

The structure of the flowfield wrap-around fins has been investigated at high speeds using both experimental and numerical methods. A single-finned model was first extensively tested at a Mach number of 2.8. In this experiment, the flow around the test article was surveyed at several stations along its length, concentrating on the region near the fin. The result was a mapping of the pressure, velocity, and turbulent properties near the fin. The mean flow near the model was then investigated at a Mach number of 4.9. Taken together, these experimental studies comprise a set of mean flow and turbulence data not previously available for curved fins.

Companion numerical studies were also performed wherein the Reynolds averaged Navier-Stokes equations were solved with the algebraic turbulence model of Baldwin and Lomax²⁰ in the vicinity of the single-WAF model. The excellent agreement with experimental data suggests that the calculations have captured the relevant flow physics involved in this complicated flowfield. It is notable that the oil flow patterns to which these results compared so favorably was obtained on four-finned missiles. Thus the resemblance of computed and observed surface streamline patterns on the fin suggests that the simplified single-fin model, captures the relevant flow features in the fin region for a non-spinning missile with multiple wrap-around fins. Taken in concert, the experimental and numerical results have been interpreted to characterize the flowfield in the vicinity of a wrap-around fin.

One of the more significant findings of the study is that both inviscid and viscous properties play significant roles in determining the structure of the flowfield near WAFs. The outer flowfield exhibits asymmetries caused by the effects of pressure gradient, streamline curvature, and differing shock/expansion structures – while viscous phenomena induce asymmetries near the fuselage. Regarding the latter, the Navier-Stokes simulations predicted a vortex in the fin/body juncture on the convex side of the fin. The existence of this viscous-induced vortical structure was corroborated by hot-film anemometry, surface flow visualizations, and pressure sensitive paint. This vortex, not present on the concave side presumably due to the oblique fin attachment angle, increases the pressure loading near the fin root. The net result is a pressure differential across the fin which alters the rolling moment. It is known that the structure and strength of such juncture vortices can be changed by any of several factors, including the incidence angle of the fin. Such a change could greatly influence the rolling moment, possibly to the point of a reversal. Inviscid numerical simulations cannot produce this vortex and thus may not be expected to reasonably predict the stability behavior of missiles

having WAFs. That said, many aspects of the flowfield were accurately captured by solving the Euler equations. The bow shock created by the wrap-around fin is an inviscid phenomenon. Except in the immediate vicinity of the fin/body intersection where the bow shock interacts with the missile body boundary layer, the fin pressures are dominated by inviscid effects. This has been demonstrated through the excellent agreement between measured quantities and those predicted by inviscid (and viscous) numerical methods in the outer region of the flow. The shock remains detached over the full span of the fin for $2.15 \leq M \leq 4.9$, and its interaction with the fuselage boundary layer creates the same type of λ -shock associated with blunt fins in supersonic flowfields.

The reduction of data from the pitot, cone-static and hot-film probes at Mach 2.8 also produced a significant amount of turbulence data. These data yielded some interesting insights. As expected, the bow shock causes a dramatic increase in turbulent kinetic energy and Reynolds shear stress on both sides of the fin. The flow experiences an expansion as it passes the fin which reduces the turbulence intensity. However, for a fixed streamwise location, the reduction is far greater on the convex side of the fin, where the flow experiences a stronger favorable pressure gradient over a longer distance. This results in lower turbulence intensities, producing lower, though still significant, shear stresses. It is notable that the turbulence model used was not designed to account for the effects of pressure gradient and streamline curvature. This may be largely responsible for the over-prediction of momentum levels in the outer boundary layer on the concave side of the fin in the present numerical simulations. It is expected that these turbulence data will be useful for validation of turbulence closure models intended to predict flows having large pressure gradients.

At Mach 4.9, both the numerical and experimental results qualitatively resemble those obtained at Mach 2.8. Examination of the computed surface streamline patterns suggests that the flow structure near the fin is qualitatively invariant over this range of Mach number. However, the juncture vortex on the convex side of the fin is observed to shift slightly toward the body with increasing Mach number, causing a dramatic reduction in computed rolling moment compared to that predicted by inviscid theory. The high pressure region at the base of the fin on the concave side is also reduced in size and magnitude in a manner consistent with a rolling moment reduction or reversal. While none of the computations predicted a rolling moment reversal at either of the Mach numbers investigated, the results suggest that Mach number has a much stronger influence on rolling moment than inviscid simulations would imply, and underscore the significant influence that viscous effects can have on the rolling moment produced by curved fins.

The complex viscous flowfield features in the vicinity of the fin for two WAF missiles were also characterized as a function of Mach number using pressure-sensitive-paint, surface oil-flow visualizations, and schlieren photography. In these experiments, the Mach number was again found to have a profound impact on both the viscous phenomena and fin loading. The rolling-moment rapidly decreased (almost discontinuously) by a factor of nearly 2 between the Mach numbers of 2.28 and 2.41. For $M \geq 2.41$ and above, the rolling-moment decreased almost linearly with increasing Mach number and agreed well with numerical results.

Adding a slot to the fin for pressure relief was found to dramatically reduce the strength of the shock structure produced by the fin at the lower Mach numbers. This finding could translate into reduced wave drag. While the slotted fin also displayed a decreasing rolling-moment trend with Mach number, it also produced rolling moment magnitudes almost double those of the solid-fin, with only 28.6% more wetted surface area.

ACKNOWLEDGMENTS

The authors would like to acknowledge Mr. Gregg Abate of the Air Force Research Laboratory's Munitions Directorate for providing funding for much of this work.

REFERENCES

- Abate, G.L., "Aerodynamic Research of Wrap Around Fin Missile Configurations and Alternative Wrap Around Fin Designs", WL-TR-94-7015, February 1994.
- Vitale, R.E., Abate, G.L., Winchenbach, G.L., & Riner, W., "Aerodynamic Test and Analysis of a Missile Configuration with Curved Fins", AIAA Paper 92-4495, August 1992.
- Abate, G.L., & Berner, C., "Wind Tunnel Measurements Wrap-Around Fins at Mach 2.06", AIAA Paper 94-3499, August 1994.
- Abate, G.L., & Cook, T., "Analysis of Missile Configurations with Wrap-Around Fins using Computational Fluid Dynamics", AIAA Paper 93-3631, August 1993.
- Edge, H.L., "Computation of the Roll Moment for a Projectile with Wrap-Around Fins", *Journal of Spacecraft and Rockets*, 31(4), pp 615-620, July-August 1994.
- Tilman, C.P., Huffman, R.E., Jr., Buter, T.A., & Bowersox, R.D.W., "Characterization of the Flow Structure in the Vicinity of a Wrap-around Fin at Supersonic Speeds", AIAA Paper 96-0190, Jan 1996.
- Huffman, R.E., Jr., Tilman, C.P., Buter, T.A., & Bowersox, R.D.W., "Experimental Flow Structure Investigation of a Wrap-around Fin at Mach 2.9", AIAA Paper 96-2450, June 1996.
- Tilman, C.P., "Numerical and Experimental Investigation of the Flowfield Near a Wrap-Around Fin", AFIT/DS/ENY/97-1, PhD thesis. School of Engineering, Air Force Institute of Technology (AU), Wright-Patterson AFB OH, March 1997.
- Tilman, C.P., Huffman, R.E., Jr., Buter, T.A., & Bowersox, R.D.W., "Experimental Investigation of the Flow Structure Near a Single Wrap-around Fin", *Journal of Spacecraft and Rockets*, 34(6), pp 729-736, November-December 1997.
- Tilman, C.P., Buter, T.A., & Bowersox, R.D.W., "Characterization of the Flowfield Near a Wrap-around Fin at Mach 2.8", AIAA Paper 97-0522, January 1997.
- Tilman, C.P., & Bowersox, R.D.W., "Characterization of the Flowfield Near a Wrap-around Fin at Mach 4.9", AIAA Paper 98-0684, January 1998.
- "The General Aerodynamic Simulation Program, Version 3 Users Manual," Aerosoft Inc., Blacksburg, Virginia, 1996.
- McIntyre, T.C., "Flow Field and Loading Analysis On A Wrap-Around Fin Missile," Master's Thesis, Air Force Institute of Technology, AFIT/GAE/ENY/97D-04, December 1997.
- McIntyre, T.C., Bowersox, R.D.W., & Goss, L.P., "Pressure Sensitive Paint Measurements on a Wrap Around Fin Missile at Supersonic Velocities," 17th International Congress on the Instrumentation of Aerospace Facilities (ICIASF), Monterey, CA, October 1997.
- "IFA 100 System: Instruction Manual," TSI Inc., St. Paul, MN, 1987.
- Bowersox, R.D.W., "Combined Laser Doppler Velocimetry and Cross-Wire Anemometry Analysis for Supersonic Turbulent Flow," *AIAA Journal*, 34(11), pp 2269-2275, November 1995.
- Bowersox, R.D.W., and Schetz, J.A., "Compressible Turbulence Measurements in a High-Speed High Reynolds Number Mixing Layer," *AIAA Journal*, 32(4), pp 758-764, April 1994.
- Bowersox, R.D.W., "Thermal Anemometry, from Handbook of Fluid Dynamics and Fluid Machinery," John Wiley & Sons., Chap. 15.4.2, pp 965-983, 1995.
- Sellers, M.E., "A Comparison of an AEDC and a Russian Developed Pressure Sensitive Paint in the AEDC Propulsion Wind Tunnel 16T," Technical Report AEDC-TR-95-18, December 1995.
- Baldwin, B.S. and Lomax, H., "Thin Layer Approximation and Algebraic Model for Separated Turbulent Flow," AIAA Paper 78-0257, January 1978.
- Miller, R., Dotter, J., Bowersox, R.D.W., and Buter, T.A., "Compressible Turbulence Measurements in Supersonic Boundary Layers With Favorable and Adverse Pressure Gradients," *Transactions of the ASME, Journal of Fluids Engineering*, pp 193-200, August 1995.
- van Leer, B., "Flux-Vector Splitting for the Euler Equations," *Lecture Notes in Physics*, Vol. 170, 1980.
- Hirsch, C., "Numerical Computation of Internal and External Flows, Volumes 1 and 2," John Wiley and Sons, New York, 1992.
- Dolling, D.S., & Bogdonoff, S.M., "Blunt Fin-Induced Shock Wave Turbulent Boundary Layer Interaction," *AIAA Journal*, 20(12), December 1982, pp 1674-1680.
- Fomison, N.R., & Stollery, J.L., "The Effects of Sweep and Bluntness on a Glancing Shock Wave Turbulent Boundary Layer Interaction," *AGARD Conference Proceedings 428*, NATO, pp 8:1-8:18, 1987.
- Spina, E., Smits, J., & Robinson, K., "The Physics of Supersonic Turbulent Boundary Layers," *Annual Review of Fluid Mechanics*, Vol. 26, pp 287-319, 1994.
- Bowersox, R.D.W., & Buter, T.A., "Mass-Weighted Turbulence Measurements in a Mach 2.9 Boundary Layer Including Mild Pressure Gradients," *AIAA Journal*, 34(12), pp2479-2483, Dec 1996.

LATTICE CONTROLS: A COMPARISON WITH CONVENTIONAL, PLANAR FINS

G. M. Simpson

A. J. Sadler

High Speed and Weapon Aerodynamics Department,
DERA Bedford,
Clapham, MK41 6AE, UK.

1. SUMMARY

This analysis of the DERA lattice controls data has centred on a comparison between the lattice controls and conventional, planar controls which were the subject of previous research. All types of control surface studied were mounted as tail controls. The comparisons were justified on the basis of equal longitudinal stability imparted to the body at zero incidence. The vertical lattice controls of a cruciform set were found to impart a significant proportion of the static stability, but to contribute nothing to the control effectiveness. Other characteristics of lattice controls are small hinge moments with low centre of pressure variation with Mach number and incidence, increased yaw stability at incidence, reduced effect of vortex interaction and, at lower supersonic speeds, lower configuration drag at high angle of attack than equivalent conventional configurations. However, the particular lattice control designs studied here were found to exhibit reduced control effectiveness at high combined incidence and deflection.

2. LIST OF SYMBOLS

C_D	drag coefficient (coef.)
C_l	rolling moment coef. (resolved axis, main balance)
C_{IP}	fin rolling moment coef.
C_m	pitching moment coef. (resolved axis, main balance)
C_{m_α}	pitching moment coef. slope w.r.t. incidence
C_{mP}	fin hinge moment coef.
C_n	yawing moment coef. (resolved axis, main balance)
C_{nB}	yawing moment coef. (body axis, main balance)
C_x	axial force coef. (resolved axis, main balance)
C_y	side force coef. (resolved axis, main balance)
C_{yP}	fin side force coef.
C_z	normal force coef. (resolved axis, main balance)
C_{zP}	fin normal force coef.
D	body diameter (3.7 inches)
k_η	control effectiveness
M	Mach number
α	angle of attack (tangent definition)
β	angle of yaw (sine definition)
δ	control deflection
η	elevator deflection
λ	roll orientation of model
σ	incidence of model
Δ	used as a prefix to indicate incremental data i.e. (body+fans) - (body alone)

3. INTRODUCTION

A lattice control, or grid fin, is an unconventional lifting and control surface that consists of an outer frame supporting an inner grid of intersecting vanes of small chord. A typical lattice control design is characterized by a number of geometrical parameters including span, height, chord, distance between vanes, vane/frame thickness, and cross-sectional shape of the members. The effect of each of these parameters on lattice control performance is not fully understood at this

stage. Schematic representations of two designs of lattice control are shown in figure 1.

Although there is evidence¹ that the lattice control concept has been around for some time, their use as missile stability and control surfaces is a fairly recent innovation. Lattice controls are employed on the AA-12 medium range air-to-air missile, understood to be equivalent to the US AMRAAM. Grid fins are also used on various ballistic missiles of the former Soviet Union and have even been used as emergency drag brakes on the Soyuz TM-22 spacecraft. Thus grid fins have found a number of applications within the sphere of missile aerodynamics. It is the purpose of this paper to explore the aerodynamic characteristics of these devices in order to understand how configurations may benefit from their use. Specifically, the research has been directed at discovering what advantages lattice controls may confer to tail controlled air-to-air missile configurations. This has been achieved by comparing the lattice controls with conventional, planar controls.

During the experimental phase of this research two designs of lattice control were mounted on an existing missile research model and tested in both the DERA (Defence Evaluation and Research Agency) 8ft×8ft wind tunnel, at Mach numbers from 0.7 to 2.4, and the 3ft×4ft facility at Mach numbers from 2.5 to 4.5. Conventional controls had been investigated previously at DERA Bedford, using the same body, and the current investigation capitalized on the availability of the conventional data, covering an identical range of Mach numbers.

3. EXPERIMENTAL DETAILS

Control surfaces that have been investigated are shown schematically in figure 1. They consist of two lattice control designs, L1 and L2, and two conventional controls with square (C2) and delta (C1) planforms. An alternative lattice control (L3) was identical to L2 except for the increased thickness of the inboard webs.

Two types of body were used. For the Mach number range 0.7 to 2.4 (Reynolds number 2×10^6 /ft) the controls were mounted on a 11.5D cylindrical body with a slightly blunted 1.5D tangent-ogive nose (denoted B1C). For the Mach number range 2.5 to 4.5 (Reynolds number 4×10^6 /ft) the controls were mounted on a 10D cylindrical body with a sharp 3D tangent-ogive nose (denoted B1A). In both cases the control hinge lines were located 1.5D from the base of the body. A selection of these configurations is shown in figure 2.

Overall forces and moment were measured using a six component strain gauge balance, hereafter referred to as the main balance. Individual fin forces and moments were measured on two of the four fins using four component panel balances.

4. BASIS OF COMPARISON

Both sets lattice controls were designed to impart identical levels of longitudinal static stability to the baseline body at

Mach 3.5. Static stability was considered a sensible criterion on which to base the comparison of control performance as the effect of a cruciform set of fins on the complete configuration is taken into account. Static stability is also an important design parameter, especially for highly agile missiles. A plot of pitching moment slope (Cm_α) at zero incidence against Mach number for the four types of control is shown in figure 3. The moment reference point (MRP) for this plot was taken as the nose tip. Lattice controls L1 and L2 clearly provide very similar levels of static stability at Mach 3.5 and across the high Mach number range, fulfilling the design criterion.

The square planform, planar control (C2) imparts similar levels of static stability to the baseline body across the high Mach number range as controls L1 and L2. The delta planform control (C1), which has half the planform area as C2, imparts considerably less stability. Thus, in the following analysis a direct comparison can be made between the lattice controls, L1 and L2/L3, and the square planform, planar fin (C2). Comparisons with data for control C1 are only of a qualitative nature.

5. STATIC STABILITY

Longitudinal

Returning to figure 3, it can be seen that for Mach numbers above approximately 2 the change in longitudinal stability with Mach number for the lattice controls is little different than for the conventional controls. However, the lattice control suffers a loss in stability at Mach 1.45 indicating that transonic effects are considerably more severe than for the conventional controls. Calculations indicate that the individual lattice cells choke above approximately Mach 0.8 and this explains their poor performance in the transonic regime.

The data for Mach 0.7 also appears to indicate that at subsonic speeds lattice controls may have improved stability performance in comparison with the planar controls.

An important difference between lattice controls and conventional controls is the ability of the lattice controls to generate significant transverse, or side, force. Consequently, at low incidences in particular, the vertical fins of a cruciform set contribute a significant proportion of the stability. It is possible to quantify this effect by calculating the incremental pitching moment slope due to each fin and comparing the values with the overall stability. Other aspects of lattice side force are discussed later.

The incremental pitching moment slope is the change in pitching moment due to the addition of a set of controls to a body, i.e.

$$\Delta Cm = (Cm)_{\text{body+fins}} - (Cm)_{\text{body}}$$

It is possible to estimate the contribution to this of each individual fin by multiplying the fin force (from panel balance data and resolved normal to the missile axis) by the non-dimensional moment arm of 11.5.

Figure 4 shows the individual fin force resolved normal to the body axis for configuration B1AL1, and clearly shows the lifting effectiveness of the controls at each orientation around the body. The horizontal fins produce the greatest force as they have a larger effective lifting area, the offset between the two horizontal fins is probably due to small fin misalignment. The leeside fin is the least effective at high angles of attack but at small incidences generates equal force to the windward fin. The non-linear nature of the leeside fin side force would be difficult to model using a semi-empirical code.

Figure 5 plots incremental pitching moment calculated from main balance data, and estimated from panel balance data, against incidence for B1AL1 at Mach 3.5. Clearly the vertical fins (2&4) generate a significant proportion of the pitching moment. The gradient, at zero incidence, of the estimated incremental pitching moment curves indicate the level of stability due to the fins. Using this it has been shown² that the level of longitudinal static stability due to the vertical fins is approximately 30% across the Mach number range.

Note also that the difference between the calculated and estimated values of ΔCm gives an indication of the level of fin-body interference, which can be seen to be small at this Mach number, but increasing with incidence. At transonic speeds it is considerable².

Lateral

In the past, the maximum normal acceleration, or LATAX, achieved by missile configurations employing conventional controls has been limited by the loss of controlled flight at high incidences. An increase in the LATAX capability, and hence agility, could therefore be achieved if it were possible to attain improved lateral (yaw) stability at high incidences.

Yaw stability is here defined as,

$$\frac{\partial CnB}{\partial \beta}$$

where CnB is the yawing moment coefficient in body axis and β is the angle of yaw. Figure 6 plots the variation of incremental yaw stability with incidence at Mach 3.5 for the various controls under consideration. Across the incidence range L1 and L2 provide a greater amount of yaw stability than the conventional control C2. This extra stability is attributable to the side force generated by the two horizontal fins.

All four fins lose yaw stability effectiveness in the region of 16° incidence and, in each case, this is due to the interaction of the leeside fin with the body vortices. The loss in yaw stability is significantly attenuated for the lattice controls. Later it is shown that other effects of the interaction with the body vortices are reduced for the lattice controls. The effect of this negative interaction is further reduced for the lattice control configurations because the leeside fin contributes proportionally less to the overall yaw stability than the leeside fin in a conventional configuration. It is also interesting to note that at $\sigma = 0^\circ$ L1 imparts approximately 10% greater yaw stability than fin C2, and at $\sigma = 24^\circ$ L1 imparts approximately 24% more stability. This would suggest that at high incidences lattice controls could provide significantly more yaw stability than conventional fins, although at present no high incidence data exists in order to confirm this trend.

Figure 7 shows the effect, at Mach 3.5, of deflecting the horizontal (elevator) fins by $\eta = 20^\circ$ on the yaw stability. No deflected fin data was available for C2 at this Mach number and it is assumed that the results for C1 are representative of conventional fins. It can be seen that the effect on L1 is small, the largest reduction in stability occurring at $\sigma = 24^\circ$. However, the conventional fin C1 suffers a large reduction in stability across the incidence range.

Figure 8 shows the effect of Mach number on lattice control incremental yaw stability. At low incidences the lattice control would provide considerably more yaw stability effectiveness at Mach 1.45 as expected; for $\sigma = 0^\circ$ the variation of yaw stability with Mach number is identical to the trend shown in figure 3 for longitudinal stability. However, at Mach 1.45 yaw stability

continuously reduces with incidences up to $\sigma = 22^\circ$, and it is not clear whether this is recovered at higher incidences.

Finally, the variation of incremental yaw stability with orientation is shown in figure 9. Data for both the L1 and C2 controls orientated in the '+' and 'x' positions are compared. This plot shows that both types of control have similar properties.

6. CONTROL EFFECTIVENESS

Pitch control effectiveness is a measure of the ability of the controls to produce change in the overall configuration pitching moment, and is conveniently defined as,

$$k_\eta = \frac{\partial Cm}{\partial \eta}$$

For the evaluation of control effectiveness the MRP was taken to be 6.5D aft of the nose, i.e. mid-body, so that the results of the analysis would be readily applicable to typical missile systems.

Main balance pitching moment data for each control are plotted against elevator deflection for Mach numbers of 1.45, 1.8 and 3.5 in figures 10 to 12 respectively. Comparisons at three incidences are included in each figure. As only five fin deflections were tested it is difficult to accurately calculate k_η (the slope of the curves). However, the overall trend can be judged.

In general, a combination of high incidence and large control deflection reduces the effectiveness of the lattice controls. Figures 10 and 11, for example, indicate that, at Mach 1.45 and 1.8, the change in pitching moment between $\eta = 10^\circ$ and $\eta = 20^\circ$ at an incidence of 20° is nearly zero for the lattice controls. This shows that the lattice controls have lost effectiveness. Neither C1 or C2 lose effectiveness in the incidence and deflection range investigated.

At Mach 1.45 and Mach 1.8 fin C2 is the most effective of the controls. At Mach 1.45 L3 and C1 are equally effective at 0° incidence; interestingly, at this Mach number they both impart similar levels of static stability.

As no deflected fin data is available at Mach 3.5 data for fin C2, only L1, L2 and C1 are plotted in figure 12. Both lattice designs have equal effectiveness at low incidence, but for positive fin deflections of $\sigma = 20^\circ$, L1 appears to be more effective. It is clear that the lattice controls operate more efficiently at high Mach numbers as they remain effective over the whole incidence range investigated. At Mach 3.5 the delta control C1 is less effective than the lattice controls at low incidences, however, at very high combined incidence and deflection C1 becomes more effective.

It is important to understand the difference between the control effectiveness of the lattice controls and the conventional control C2. For the conventional configuration orientated in the '+' position, the horizontal fins contribute all of the longitudinal stability and are responsible for all of the control effectiveness. For a lattice control configuration, the horizontal fins contribute only 70% of the longitudinal stability and 100% of the control effectiveness. Thus, for a given longitudinal stability the lattice configuration will be less effective. It is obviously possible to increase the control effectiveness of the lattice controls by using larger fins. Additionally, when a missile is in a state of positive incidence and fin deflection the vertical fins will tend to reduce the pitching moment increment, although the magnitude of this effect will vary considerably with incidence.

An alternative method for investigating control effectiveness would be to compare values of control effectiveness normalized by the effectiveness at zero incidence and deflection, i.e. compare values of $k_\eta/k_{\eta(\eta=0^\circ, \sigma=0^\circ)}$. However, this would need data for a large number of fin deflections in order to calculate accurately.

7. PANEL LOADS

Normal force characteristics

Comparisons of lattice and conventional fin normal force, for an individual control at $\lambda = 0^\circ$, are plotted in figures 13 to 15 where the comparisons are made for deflections (δ) of 0° , 10° and 20° respectively. As expected from the control effectiveness investigation C2 generates the largest normal force of all the fins. At Mach 1.45 L3 and C1 generate almost the same normal force; for $\delta = 0^\circ$ L3 generates slightly more normal force but for $\delta = 20^\circ$ this margin is lost. At this Mach number the lattice cells are choked, reducing lifting effectiveness. At other Mach numbers the lattice controls produce significantly more normal force than C1.

In figure 13f it can be seen that at Mach 3.5 and with no control deflection L1 and L2 produce almost identical normal force across the incidence range shown. However, with higher fin deflection L1 and L2 begin to display different characteristics. This is particularly so at Mach 3.5, figure 15d, where above 5° incidence and with a fin deflection of $\delta = 20^\circ$ L1 generates more normal force than L2.

In figures 15c and 15d the normal force curves display anomalous regions above approximately 10° incidence. A similar feature is displayed by all three fin types at similar incidences. It is not clear what this effect may be but it can be observed that the existence of the effect is not dependent on the fin geometry (but it is more noticeable on the lattice controls). Also the effect appears not to occur at Mach 4.5.

To illustrate how normal force varies with roll position figure 16 plots normal force coefficient against roll angle in the range $0^\circ < \lambda < 180^\circ$. In this range of λ the fin is in the leeward flowfield, dominated by the body vortices. It is immediately obvious that, in contrast to the conventional control, the lattice control shows no sign of control reversal. In this roll range both types of control interact with the body vortices that emanate from the nose of the missile. For the planar fins the interaction is adverse and the aerodynamic force on the control changes sign; the lattice controls, however, merely suffer a slight drop in normal force and no sign reversal occurs. This property could be a significant advantage over the use of planar fins, reducing demands on the autopilot. Lattice controls exhibit this property because, in general, the flow conditions experienced by the control will vary significantly across its span and height. This is illustrated in figure 17 where the outline of lattice L1 has been superimposed upon experimentally obtained pitot pressure contours in the flowfield around body B1A at Mach 3.5 and $\sigma = 14^\circ$. In the vortex dominated flowfield the local effective angle of attack will vary significantly over the lattice control, indeed it is possible for some parts of the control to experience a negative angle of attack while other parts experience an effective positive angle of attack. The adverse effect of the body vortices is in this way reduced. At other incidences² the vortices have minimal effect on either L1 or L2.

Side force characteristics

The unique ability of the lattice controls to generate side force has received little attention in the literature. It has been shown in figure 5 how this increases the stability of the configuration, but contributes little to the control effectiveness. Here the variation of fin side force with roll position is investigated.

Side force data, from the starboard panel at $\lambda = 0^\circ$, is plotted against roll angle in figure 18. Data for fin deflections of $\delta = 0^\circ, 10^\circ$ and 20° are shown. Side force data for the planar controls are not shown as it is of course negligible. Three features are obvious from figure 18: a side force is generated at $\lambda = 0^\circ$; side force does not vary with fin deflection except in the region $-180^\circ < \lambda < -100^\circ$; and most significantly there is a large drop in the side force in the region of $\lambda = -90^\circ$.

The finite side force generated at $\lambda = 0^\circ$ is due to the variation of upwash along the span of the lattice control. The distinctive drop in side force in the region of $\lambda = -90^\circ$ is due to the downwash from the two body vortices giving the lattice control a net negative incidence.

Hinge moment characteristics

The variation of hinge moment with incidence for the L3 control across the Mach number range is shown in figure 19. The origin of the offset at $\sigma = 0^\circ$ is not clear, but is approximately constant for all Mach numbers, and the overall magnitude of the moments are very small indeed. As Mach number increases the slope of the curves decrease and it is clear from the small gradient of the curve for Mach 2.4 that the XCP has moved almost to the hingeline. This is consistent with predictions from linear aerodynamic, where for a flat plate the XCP is located at 25% chord at subsonic speeds and at 50% chord at supersonic speeds. The XCP would be located a little less than 50% chord due to loss of lift on the rear portion of each element of the lattice caused by shock interference. Because of the small chord of the lattice controls the absolute magnitude of the shift in centre of pressure is small.

Figure 20 compares the hinge moments of the lattice and conventional fins at Mach 0.7. It is clear that the lattice control has the lowest hinge moment, and, in comparison with the planar fins, has minimal variation across the incidence range. However, a comparison of the hinge moments at Mach 2.4, shown in figure 21, indicate that at high supersonic speeds the small delta control has minimal hinge moment. This is because the choice of hingeline was chosen to coincide with the XCP at high Mach numbers. Thus, although it is possible to design conventional fins with low hinge moments, it is only possible to do so at particular Mach numbers; consequently the XCP variation with Mach number is an important parameter.

The variation of centre of pressure location with Mach number for various incidences is shown in figure 22. It is clear that the lattice controls display the smallest variation of XCP with Mach number and incidence.

8. DRAG CHARACTERISTICS

The high drag of lattice type controls has been the principal concern over their use. The individual fin axial force can be as much as 3 or 4 times higher than a planar fin with comparable lifting ability³. However, Miller and Washington⁴ have shown that by suitable adjustment of web thickness and frame cross-section shape the drag can be tailored considerably with minimal impact on other aerodynamic properties.

The variation of incremental axial force coefficient (ΔC_x) with Mach number at zero incidence is shown in figure 23. The data shown includes the total axial force on all four fins. At both subsonic and supersonic speeds the lattice controls exhibit much greater drag than the conventional controls. At Mach 4.5, for example, L2 has an axial force 3 times greater than C2. In the supersonic regime lattice axial force coefficient is almost constant with Mach number in contrast with the significant drop off for the conventional controls. The fact that L1 exhibits greater drag than L2 even though they have similar lifting capability confirms that it is possible to tailor drag by varying the lattice geometry without reducing control effectiveness. The difference in drag is due to the extra wave drag generated by the larger cross-sectional area of L1. The variation of axial force with incidence is moderate for the lattice controls and for most mach numbers is not significantly different from the conventional controls².

Plots of incremental drag force, rather than axial force, indicate an interesting feature of lattice controls. Incremental drag force is plotted against incidence for the L3 and C2 controls at Mach 1.8 in figure 24. Above 12° incidence the lattice configuration drag is less than that of the planar control. This feature also occurs at other Mach numbers, although the incidence at which this happens increases with Mach number². This effect is partly due to the lower normal force generated by the lattice controls, and also that the difference in axial force between the two types of control is lower for lower Mach numbers.

9. CONCLUSIONS

The aerodynamic characteristics of the lattice controls have been compared with those of conventional, planar controls and the relative advantages and disadvantages judged. The basis of comparison between the configurations was chosen to be equal longitudinal static stability.

Lattice controls offer the following advantages; improved yaw stability at incidences up to 24° (due to the ability of the lattice controls to generate side force), small hinge moments with minimal variation of centre of pressure with Mach number and incidence, and the attenuated effect of body vortex interference, improving roll control and autopilot demands. The available data also indicate that lattice controls may offer improved yaw stability at high incidence, which may increase the LATAX capability through increased controllability at these incidences.

Lattice controls suffer the following disadvantages; large axial force, which can be as high as 3 or 4 times that of a conventional fin, poorer control effectiveness for a given static stability than a conventional square planform fin, and a decrease in lattice control effectiveness in the transonic region (due to the individual cells choking). However, lattice axial force can be tailored by correct shaping of the frame and web cross-sections, and by careful design of the lattice geometry. In the transonic region lattice control axial force may not be significantly higher than that of conventional fins.

At some Mach numbers lattice control drag, rather than axial force, was found to be less than conventional fin drag at high incidences. This would be advantageous for an agile missile which may maintain high incidence, or high control deflection, for large parts of the flight duration.

When the lattice controls are orientated in a cruciform '+' arrangement, the vertical fins contribute approximately 30% of the static longitudinal stability. Consequently, if the lattice controls are designed to impart a given longitudinal static

stability, as assumed in this paper, then the overall size of the lattice fins can be reduced to account for the extra contribution of the vertical fins. However, the control effectiveness would be reduced because of the smaller size of the fins and because the vertical fins do not contribute to the control effectiveness. This explains the poorer control effectiveness performance of the lattice controls in relation to the conventional, square planform control. The control effectiveness can be increased by increasing the size of the controls, but only if the extra stability, and drag, is not problematic.

The high incidence behaviour of the lattice control designs considered here was not as good as originally expected. However, the fact that the two lattice designs tested displayed slightly different characteristics at high incidence shows that, to a certain extent, the normal force characteristics of lattice controls can be tailored by correct geometric design. However, the relationship between the geometrical factors and normal force generation is not fully understood at this stage.

10. REFERENCES

- 1. Belotserkovskiy, S. M., et al, "Wings with internal framework", Machine Translation, FTD-ID(RS)-1289-86, Foreign Technology Division, February 1987.
- 2. Simpson, G.M., Unpublished DERA Material.
- 3. Washington, W. D., Miller, M. S., "Grid fins - a new concept for missile stability and control", AIAA 93-0035, January 1993.
- 4. Miller, M. S., Washington, W. D., "An experimental investigation of grid fin drag reduction techniques", AIAA 94-1914-CP.

© British Crown Copyright 1998 /DERA

Published with the permission of the Controller of Her Britannic Majesty's Stationery Office

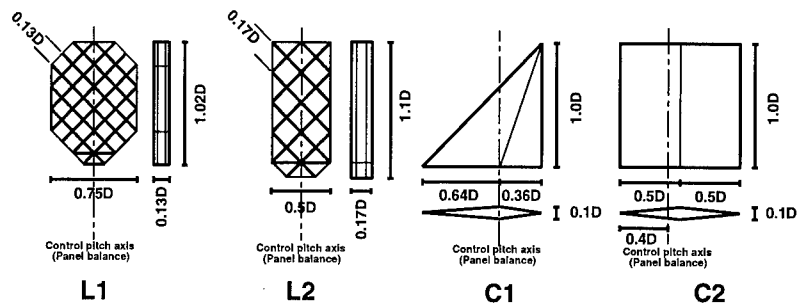


Figure 1; The controls tested (D=3.7'').

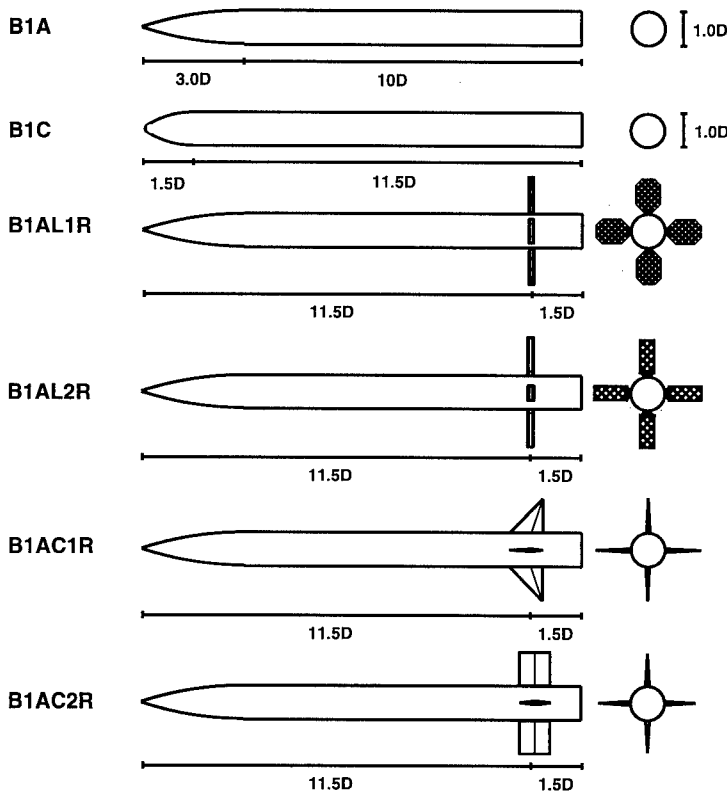


Figure 2; Various configurations tested (D=3.7'').

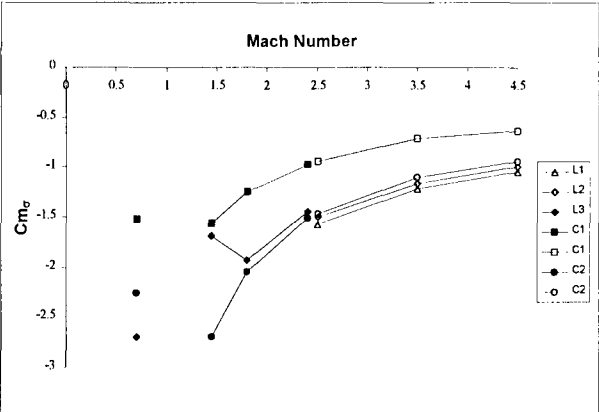


Figure 3; Longitudinal static stability at zero incidence. ('+' configuration.)

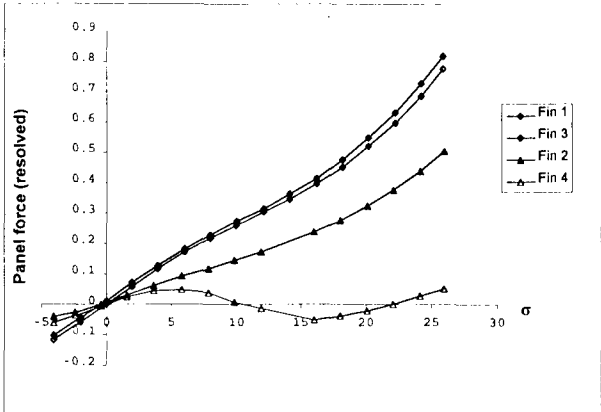


Figure 4; Panel force normal to body centreline for B1AL1R M=3.5.

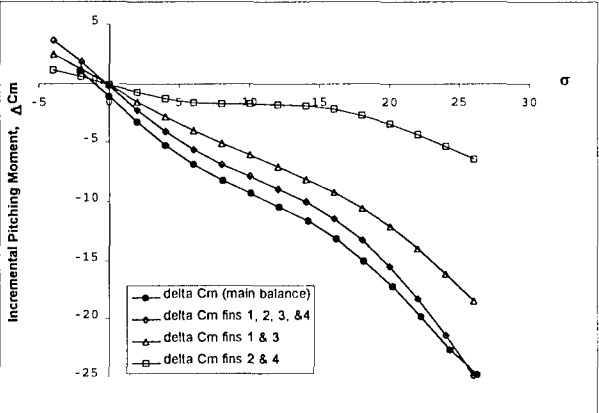


Figure 5; Incremental pitching moment B1AL1R M=3.5.

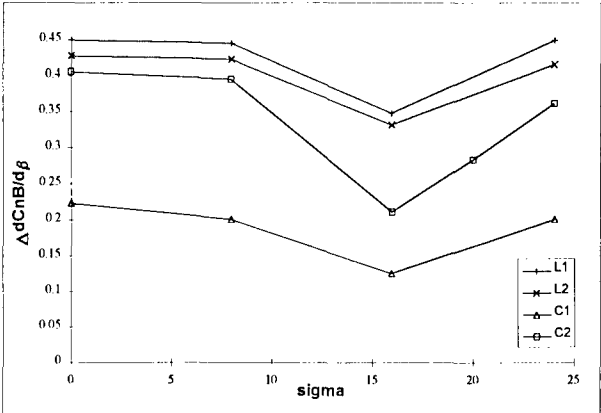


Figure 6; Incremental yaw stability M=3.5.

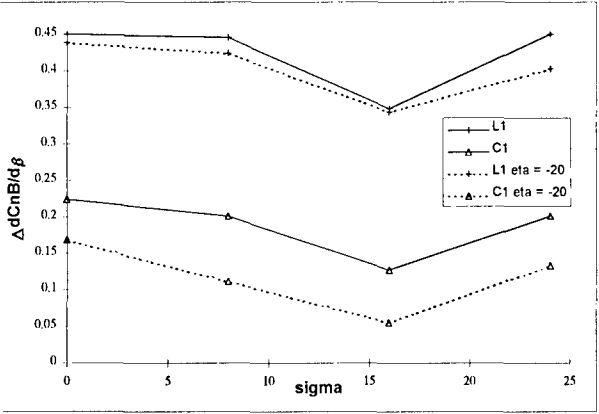


Figure 7; Incremental yaw stability M=3.5, comparison with fin deflected.

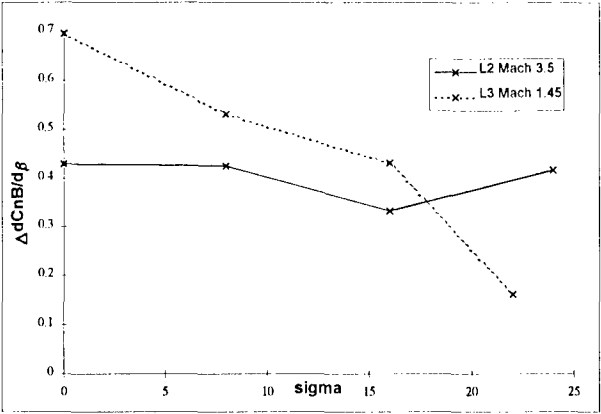


Figure 8; Incremental yaw stability M=3.5, variation with Mach number.

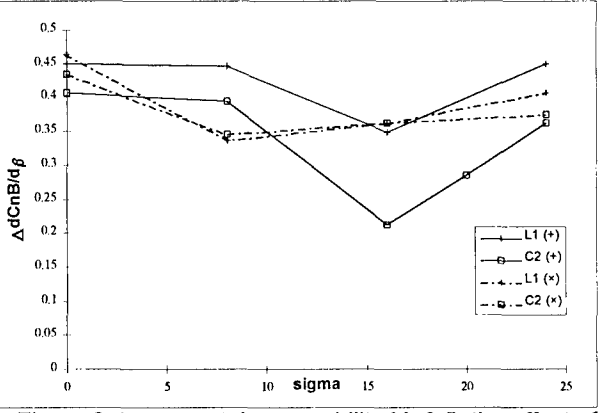
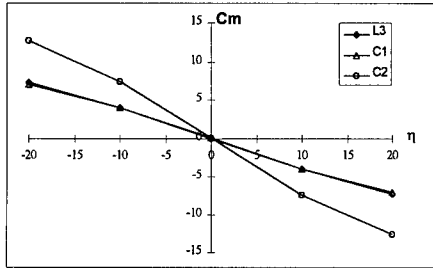
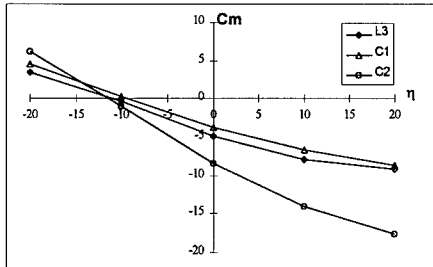


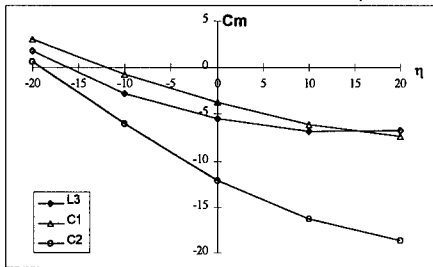
Figure 9; Incremental yaw stability M=3.5, the effect of orientation.



10a., $\sigma=0^\circ$

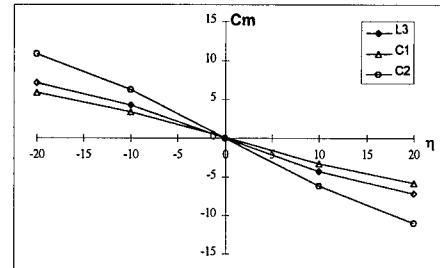


10b., $\sigma=10^\circ$

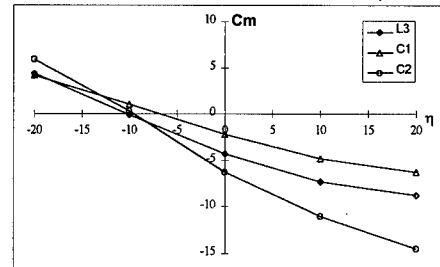


10c., $\sigma=20^\circ$

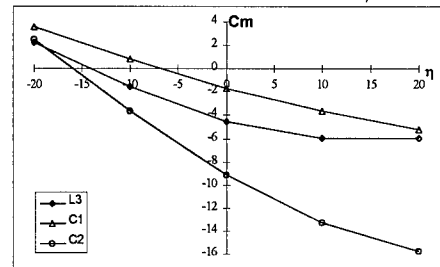
Figure 10; Control effectiveness (C_m - η curves). $M=1.45$.



11a., $\sigma=0^\circ$

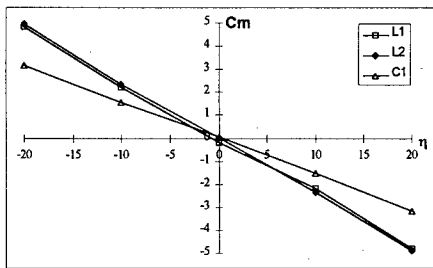


11b., $\sigma=10^\circ$

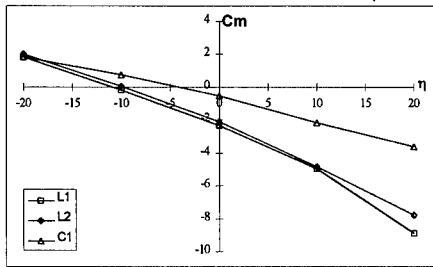


11c., $\sigma=20^\circ$

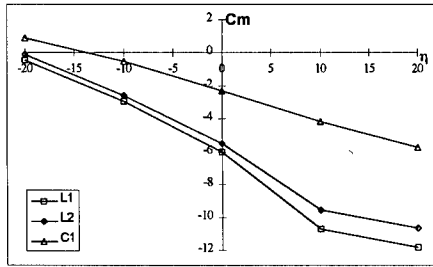
Figure 11; Control effectiveness (C_m - η curves). $M=1.8$.



12a., $\sigma=0^\circ$

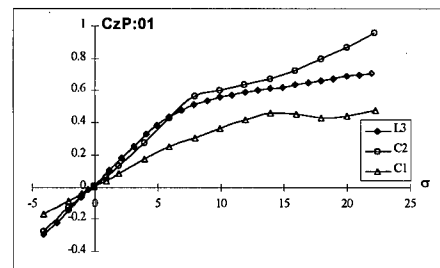


12b., $\sigma=10^\circ$

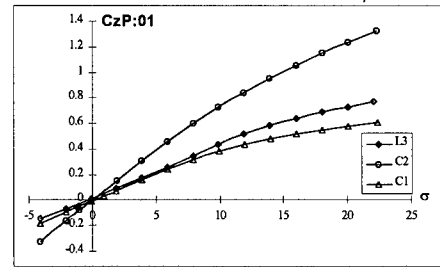


12c., $\sigma=20^\circ$

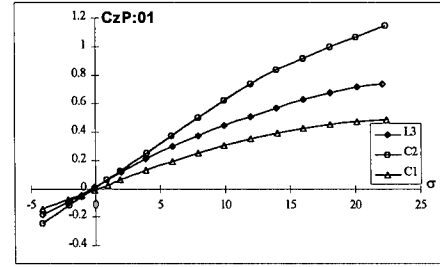
Figure 12; Control effectiveness (C_m - η curves). $M=3.5$.



13a., $M=0.7$

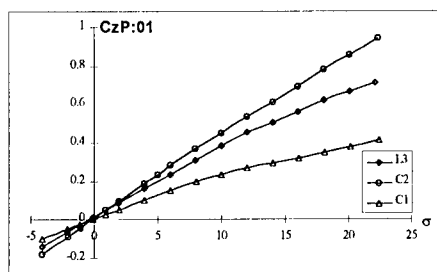
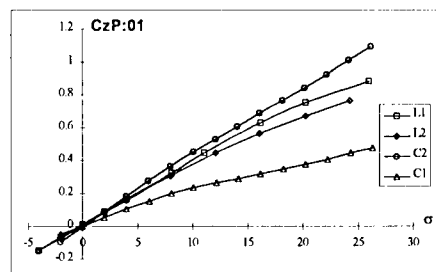
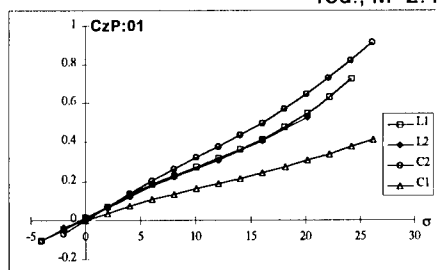
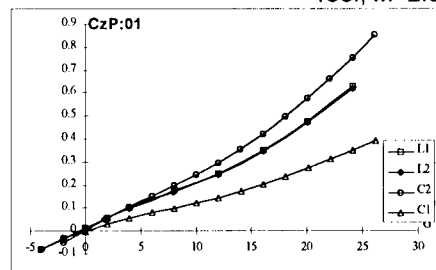
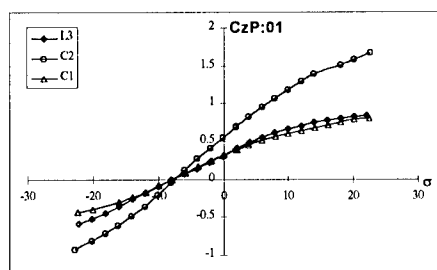
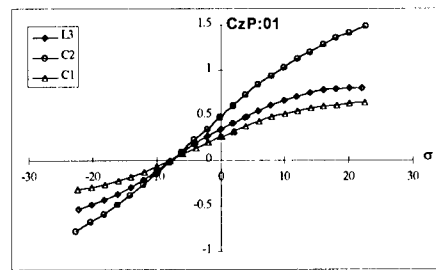
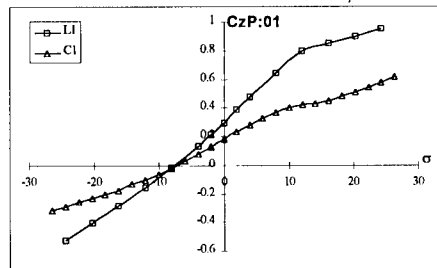
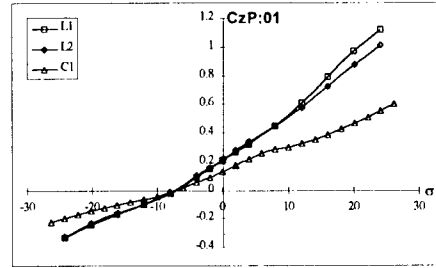
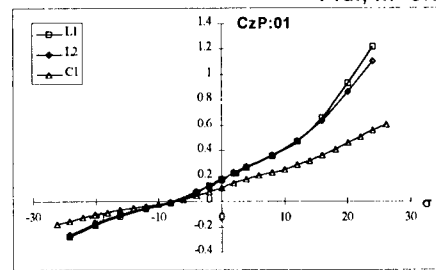


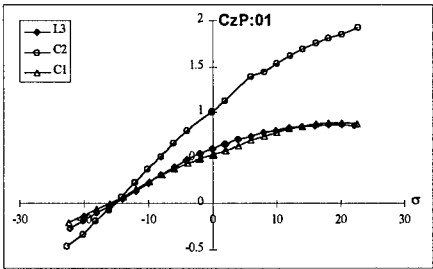
13b., $M=1.45$



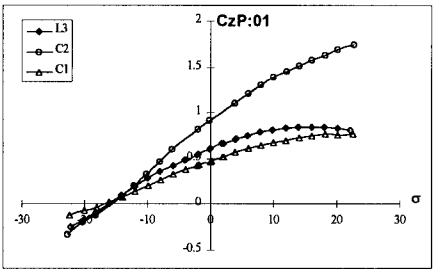
13c., $M=1.8$

Figure 13., Fin normal force, $\delta=0^\circ$.

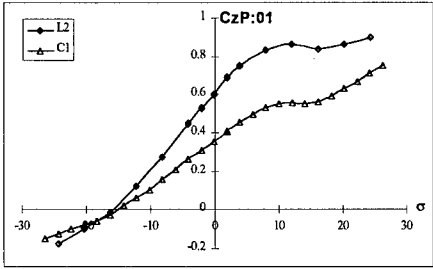
13d., $M=2.4$ 13e., $M=2.5$ 13f., $M=3.5$ 13g., $M=4.5$ Figure 13; ., Fin normal force, $\delta=0^\circ$.
(Concluded)14a., $M=1.45$ 14b., $M=1.8$ 14c., $M=2.5$ 14d., $M=3.5$ Figure 14; Fin normal force, $\delta=10^\circ$.14e., $M=4.5$



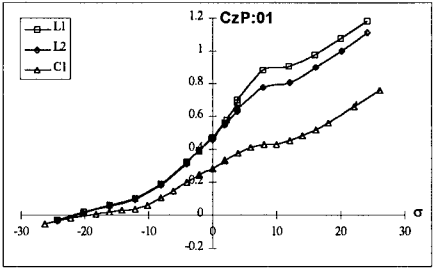
15a., M=1.45



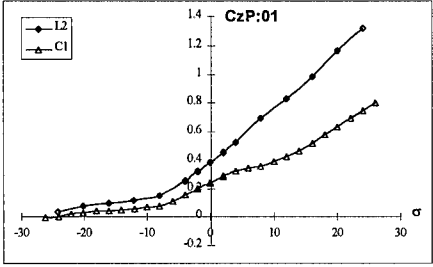
15b., M=1.8



15c., M=2.5



15d., M=3.5



15e., M=4.5

Figure 15; Fin normal force, $\delta=20^\circ$.

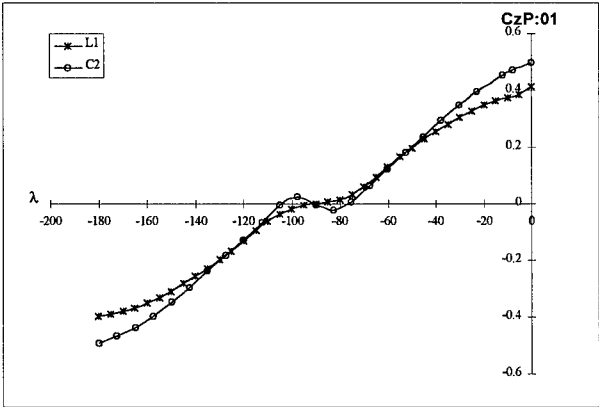


Figure 16; Variation of normal force with roll.
(M=3.5 $\sigma=16^\circ$)

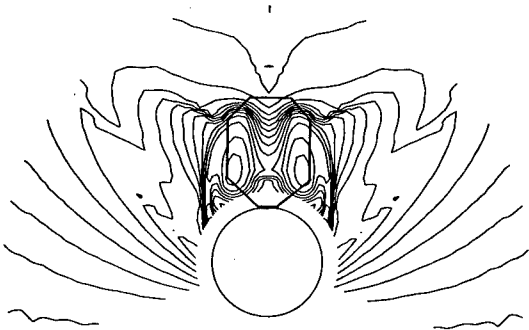


Figure 17; Pitot pressure contours:
B1A M=3.5 $\sigma=14^\circ$ at 11.5D aft of nose.

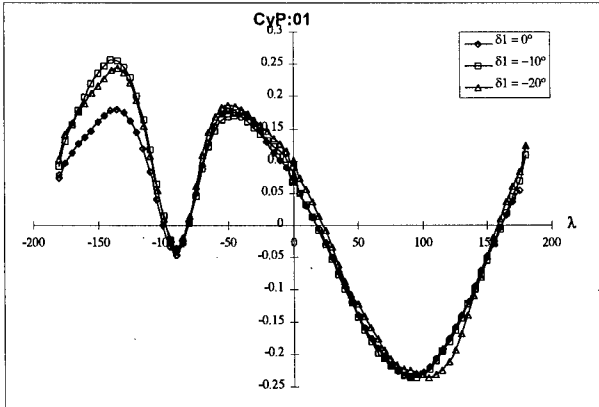


Figure 18; Variation of side force with roll.
(M=3.5 $\sigma=16^\circ$)

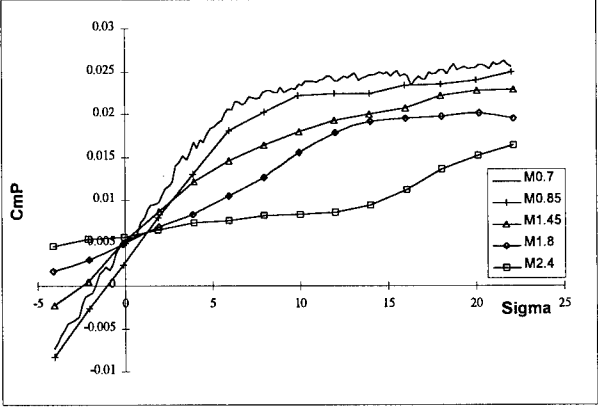


Figure 19; Lattice control hinge moment variation with
Mach number.

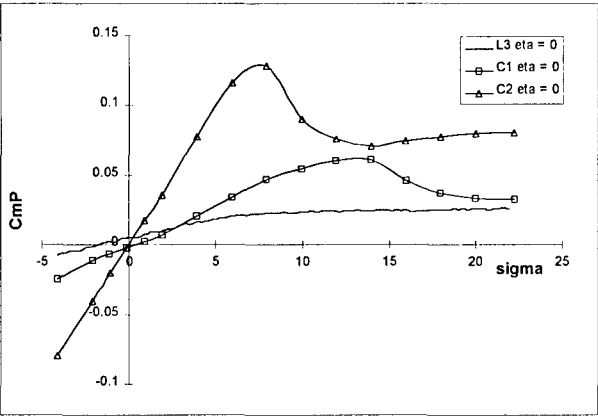


Figure 20; Hinge moment comparison, $M=0.7$.

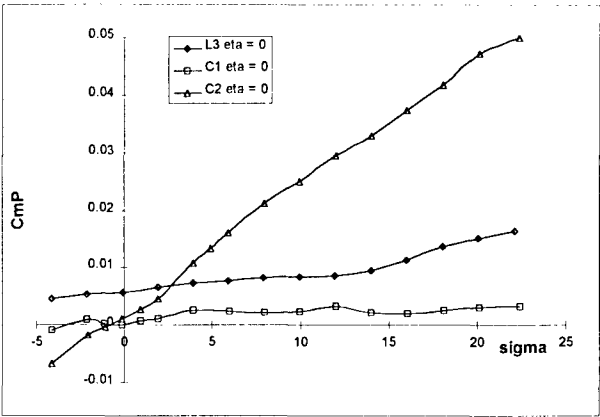


Figure 21; Hinge moment comparison, $M=2.4$.

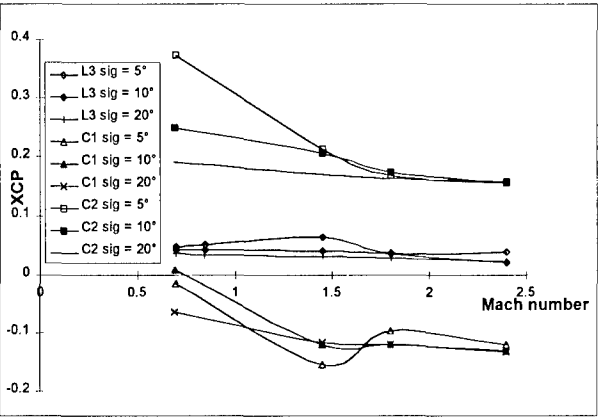


Figure 22; Fin XCP variation with Mach number. (Calibres form hinge line.)

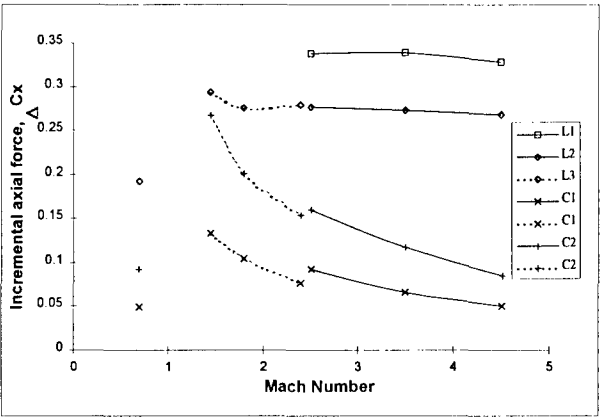


Figure 23; Incremental axial force ($\sigma=0^\circ$).

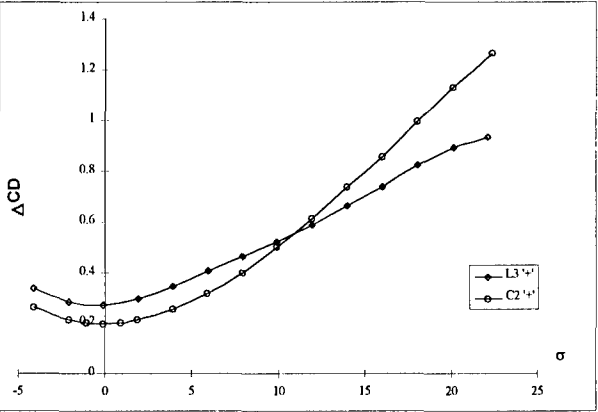


Figure 24; Incremental drag force vs. incidence at $M=1.8$.

EXPERIMENTAL INVESTIGATIONS OF GRID FIN AERODYNAMICS: A SYNOPSIS OF NINE WIND TUNNEL AND THREE FLIGHT TESTS

Wm. David Washington
U.S. Army Aviation and Missile Command
Attn: AMSAM-RD-SS-AT
Redstone Arsenal, Alabama 35898-5000, USA

Mark S. Miller
Dynetics, Inc., P.O. Box 5500
Huntsville, Alabama 35814-5500, USA

SUMMARY

Wind tunnel and flight tests have been conducted to investigate the aerodynamic characteristics of grid fins and to demonstrate their utility in actual flight hardware and ballistic flight performance. Nine wind tunnel tests have been conducted on 26 different grid fin configurations. Test parameters have included Mach numbers ranging from 0.35 to 3.5 with nominal angles of attack up to 17 degrees. Investigative issues have included: basic aerodynamic coefficients, grid fin curvature for efficient packaging, drag reduction techniques, transonic choke regions, geometric variables (span, chord, height, cell spacing and web thickness), fin sweep back effects, and grid fin/planar fin comparisons.

Two flight tests, with rockets launched out of a circular launch tube, successfully demonstrated the capability to package and stow grid fins within a circular rocket body shape, deploy grid fins during flight, despin, and stabilize the warhead section after stage separation until completion of the mission. An additional air drop flight test was conducted to demonstrate the flight worthiness of a rocket payload section during aft dispense of multiple submunitions.

1. INTRODUCTION

The Research Development and Engineering Center of the U. S. Army Aviation and Missile Command, Huntsville, Alabama has investigated the aerodynamics of grid fins since 1985. A total of nine wind tunnel tests have been conducted in order to gain greater insight into the aerodynamic characteristics of grid fins for Mach numbers ranging from 0.3 to 3.5. Table 1 summarizes the objectives of each test. As indicated in Table 1, six wind tunnel tests were dedicated to understanding the unique aerodynamic characteristics of grid fins.

An additional two tests were focused on evaluating specific point designs as part of the Bat-On-A-Rocket (BOAR) missile technology demonstration program.

The grid fin is a unique device that can be used as either an aerodynamic stabilizer or a control surface. Its unique design and aerodynamic characteristics separate it from conventional planar fins. Planar fins can generally be described with information about the root chord, tip chord, span and thickness. Grid fins, however, possess an extra dimension. Grid fins require five geometric parameters to describe their geometry (span, chord, height, cell spacing and element thickness). An attempt has been made through a series of tests to understand the importance of each of these parameters. A description of test articles and a synopsis of findings are presented in this extended abstract.

2. TEST ARTICLE DESCRIPTION

A total of 26 separate grid fin designs have been evaluated to identify critical design parameters. Table 2 provides a listing and configuration code for each of the designs tested; an accompanying photograph of these designs is presented in Figure 1. Many of the designs listed in Table 2 have been tested while mounted on a 10.4 caliber body of revolution with a three caliber tangent ogive nose section, followed by a 7.4 caliber cylindrical section. (See Figure 2). The 5-inch diameter body was mounted on a six component main balance for all tests. Four fin balances were attached to the aft section, 1.2 calibers forward of the model base. Both five-component (measuring all components except fin drag) and six-component fin balances have been utilized. Test conditions generally ranged from Mach 0.5 to 2.5, with a limited amount of data taken at Mach 3.5. Additional

subsonic data have also been obtained on grid fins mounted on a splitter plate to measure isolated six-component fin data. Unless otherwise noted, all grid fin aerodynamic coefficients presented are based on fin balance measurements (obtained in the presence of a body) with a consistent reference area of 19.635 in² (body cross sectional area).

3. SYNOPSIS OF TEST RESULTS

3.1 High Angle of Attack Characteristics

One of the advantages of grid fins is their capability to produce effective aerodynamic control forces at high angles of attack over wide Mach number ranges. Unlike conventional planar fins, grid fins do not experience classical "stall" at higher angles of attack. This characteristic leads to more effective stability and control characteristics at intermediate and large angles of attack. Figure 3 presents splitter plate (fin alone) data obtained on two grid fin designs at Mach 0.35. Maximum normal force occurs at approximately a 40 degree angle of attack. There is no characteristic stall break which is typical of planar fins at moderate angles of attack.

Figure 4 presents grid fin control characteristics (fin balance data obtained in the presence of a body) at subsonic, low supersonic and high supersonic speeds. Note the almost linear characteristic with angle of attack for supersonic Mach numbers. This characteristic indicates that grid fins are very effective control devices for missiles at supersonic speeds. A comparison with planar fins (Section 3.8) shows grid fins to be more effective than planar fins at supersonic speeds.

3.2 Hinge Moment / Packaging Advantages

Two other advantages of grid fins relative to planar fins are: small hinge moments and excellent packaging characteristics. Figure 5 presents hinge moment coefficients as a function of angle of attack for flat, concave and convex grid fins tested at subsonic, transonic and supersonic Mach numbers. Curved grid fins were fabricated with a radius of curvature equal to the 2.5-inch radius of the cylindrical section of the wind tunnel model shown in Figure 2. The projected planform of each grid fin was exactly the same. Results indicate that hinge moments are very small. The small hinge moments generated by grid fins are very attractive for missile applications. Smaller actuators are less expensive and require less control power and internal volume.

Additional findings are that curved grid fins (both concave and convex) and flat grid fins produce essentially the same aerodynamic forces. Variations in normal force due to curvature are barely distinguishable. These results give greater flexibility for packaging in practical missile design. Curved grid fins can be easily stowed within the moldline of a missile body by folding forward or backward and then deployed after launch or staging for multi-stage missiles. This concept was demonstrated in flight tests discussed later in the paper.

3.3 Drag Reduction Techniques

One of the most serious concerns related to the utilization of grid fins is the likelihood of increased drag over an equivalent planar fin. Six grid fins were designed and tested to examine the drag characteristics of grid fins and evaluate various techniques for reducing drag levels. One of the easiest approaches for reducing drag levels is to alter the cross section shape of the outer frame design. Figure 6 illustrates the different frame cross sections tested. Geometric parameters were frame shape, web thickness and frame thickness. Note that the grid fin planform shape was unchanged for these models. Results from the test are shown in Figure 7 for Mach numbers of 0.7 and 2.5. At least a 25% reduction in fin drag is realized by altering the shape of the grid fin frame.

3.4 Transonic Aerodynamics

Figure 8 presents a plot of grid fin normal force coefficient slope versus Mach number. Unlike conventional planar fins which experience maximum normal force coefficient values at transonic Mach numbers, grid fins experience what is commonly referred to as a "transonic bucket". To understand this phenomenon, one must look at a grid fin as a collection of individual cells acting as separate inlets.

Referring to Figure 9, the reduction in the inlet cross-sectional area, created by the presence of the cell walls and the boundary layer buildup on the walls, causes the flow passing through the cell to accelerate to sonic conditions (i.e., the flow becomes choked) at freestream Mach numbers less than 1.0. As the flow increases beyond Mach 1.0, a detached normal shock forms in front of the cell. The cell remains choked until the normal shock is "swallowed". It is the flow spillage from the choked flow that causes the reduction in normal force. At higher Mach numbers, a leading edge

shock passes through the cell undisturbed and the grid fin exhibits normal force characteristics similar to conventional planar fins.

3.5 Design Parameter Variation

One of the six research wind tunnel tests examined the influence of grid fin geometric parameters for Mach numbers ranging from 0.7 to 2.5. Five grid fins were tested to evaluate the effects of span, chord and cell spacing (see Figure 10). Sample results are shown in Figure 11. The general trends for subsonic and supersonic speeds are as expected. The more dense cell spacing and the greater span produce higher fin normal force. However, at transonic speeds, span seems to be the discriminate, which most likely confirms the hypothesis that the grid fins experience a choked condition.

A point about linear aerodynamic scaling of grid fins can be illustrated with this data. If one calculates the total area of all lifting surfaces of each grid fin tested (within the set of five shown in Figure 10), and then references the normal force coefficients to the projected lifting area for each fin, then one will find that the normal force coefficient does not scale linearly with the projected lifting area. Keep in mind that the grid fins tested (Figure 10) are not a linear scale of one another, but are totally independent. Therefore, one should not expect to demonstrate a linear scaling law with this data. A set of three linearly scaled grid fins have been fabricated and are planned for future wind tunnel testing.

3.6 Grid Fin Center of Pressure

The spanwise and chordwise centers of pressure for grid fins are comparable to planar fins. Figure 12 presents center of pressure data, at zero angle of attack, for Mach numbers ranging 0.5 to 3.5. (Note that the center of pressure measurements are based on fin balance data with the grid fins in the presence of a body.) The chordwise center of pressure for grid fins is very similar to that for planar fins, generally varying between the 25% and 50% of the chord length. For the more practical grid fin design (G1), the chordwise center of pressure variation is relatively constant at approximately 30% of the chord. This result indicates a very small hinge moment for grid fin controls, which is supported by test data. The spanwise center of pressure is approximately at the 40% to 45% of span, which is essentially the same as planar fins.

3.7 Sweep Effects

One of the more curious characteristics of grid fins is the correlation of fin normal force and axial force with fin sweep angle (forward or aft). The definition of grid fin sweep angle is shown in Figure 13. A wind tunnel test was conducted to examine the effect of sweeping the grid fins forward and backward. Results from the test indicated that sweeping a fin forward or backward gives essentially the same result. A correlation of fin normal force (from fin balance data) with sweep angle is shown in Figure 14 for Mach numbers 0.5, 1.1 and 2.5. Note that fin curvature effects are small.

A correlation of fin axial force (from main balance data) is shown in Figure 15. For sweep angles of ± 30 degrees, the axial force is amplified by a factor of 2 to 3, while the fin normal force is essentially unchanged. This result indicates that grid fins could be swept forward or backward to increase fin axial force, while maintaining fin normal force. The utility of the sweep parameter might be in using the grid fins as drag brakes while maintaining stability.

3.8 Grid Fins Versus Planar Fins

One of the most asked questions about grid fins is: "How do grid fins compare to planar fins?". A qualitative assessment of that question is shown in Figures 16 and 17. Figure 16 presents a grid fin and a planar fin that have essentially the same fin normal force at subsonic speeds and low supersonic speeds. Both fins were wind tunnel tested on an ogive cylinder body of revolution at Mach numbers 0.8, 1.8 and 2.5. The reference area for both fins is the cylinder cross sectional area. The data indicates that the grid fin produces the same normal force as the planar fin at low speeds, and approximately 50% more normal force at Mach 2.5. At the higher supersonic speeds, the grid fin normal force tends to be more linear with angle of attack than the planar fin. This characteristic has been observed in other grid fin test data at Mach numbers up to 3.5.

A qualitative assessment of axial force for two grid fins is shown in Figure 17. The frame leading and trailing edges of the grid fins are blunt. Previous test and analysis have shown that grid fin axial force can be reduced by at least 25% by simply shaping the cross section frame or reducing the web thickness. This axial force comparison is somewhat misleading, however. In general, grid

fin axial force will be higher than the comparative planar fin axial force at subsonic speeds, whereas at high supersonic speeds, the comparative grid fin will be smaller, producing less axial force for the comparative normal force. Consequently, the supersonic axial force of a grid fin might be very comparable to the axial force of a planar fin which generates an equivalent amount of normal force. Further test and analysis is required to better answer this question.

4. FLIGHT TEST PROGRAM

Grid fins were first flown in the United States on rocket flight and air drop flight tests conducted in 1996. These flight tests were a culmination of an 18-month technical demonstration program involving alternate submunition dispense technology. This program, known as Bat-On-A-Rocket (BOAR), was conducted by the Army Aviation and Missile Command, Missile Research Development and Engineering Center during 1995 and 1996. Photographs of the rocket and air drop flight test hardware are presented in Figures 18 and 19, respectively.

Figure 20 presents an illustration of the rocket flight test scenario. The forward section (warhead) of the rocket was equipped with grid fins which were stowed by folding forward into a cavity within the cylindrical boundary of the rocket body. The warhead section was attached to a tactical rocket booster and launched from a tactical launcher with cylindrical launch tubes. During the flight, the warhead was separated from the booster (near apogee), the grid fins were deployed, and the warhead section continued on the trajectory. Curved grid fins were used in this application because of their excellent packaging characteristics. Grid fins were folded forward into cavities and shielded with cover plates. Grid fin deployment occurred after booster separation in order to stabilize and despin the warhead.

The center of pressure of the warhead section with grid fins was measured in wind tunnel tests of the model shown in Figure 21. Empirical prediction methods were used to design the grid fins and to predict flight characteristics. Comparisons between original design predictions and measured center of pressures are shown in Figure 22. These results indicate that the center of pressure of a rocket, or missile, with grid fins can be accurately estimated with engineering level aerodynamic prediction methods.

In the rocket flight test, the rocket was forced to spin in flight (about 6-8 rps) to minimize flight perturbations. After stage separation, the warhead section was required to de-spin immediately. The de-spin characteristics (roll damping) of grid fins were unknown at that time, since no grid fin roll damping data were available. Consequently, a roll damping wind tunnel test was conducted to measure the roll damping characteristics of the grid fins which were specifically designed for the rocket flight test.

Figure 23 presents a comparison between original predicted and measured roll damping coefficient data. The prediction data is based on classical aerodynamic prediction methods. Although refinements using test results would lead to improvements in prediction method accuracy, the results indicate that grid fins have very effective roll damping characteristics and that the prediction of grid fin roll damping is clearly within the realm of classical aerodynamic analysis methods.

As mentioned earlier, an airdrop test of a simulated rocket warhead section was also conducted. Release conditions corresponded to Mach 0.9 at an altitude of 40,000 feet. The flight hardware shown in Figure 19 flew a ballistic trajectory and successfully dispensed two submunitions at designated altitudes.

5. CONCLUSIONS

Based on a series of nine wind tunnel tests of grid fins, two flight tests of rockets stabilized with grid fins, and one air drop flight test stabilized with grid fins, certain conclusions can be stated. It is clear that grid fins offer some definite advantage over conventional planar fins. These advantages include:

- Excellent supersonic control characteristics.
- Compact storage, relatively easy to deploy.
- Excellent high angle of attack characteristics.
- Small center of pressure variations over wide Mach number ranges.
- Ability to tailor drag using frame shaping.
- Ability to alter lift and drag using fin sweep.
- High strength-to-weight ratios.
- Small hinge moments minimize actuator requirements.

The aerodynamic characteristics of grid fins, coupled with their excellent storage characteristics, make them particularly attractive devices for canister launched missiles, ship launched missiles, multi-stage missiles, artillery launched munitions, missiles designed for deployment from internal weapon bays, compressed carriage weapons and dispensed submunitions. Some of the more notable unknowns concerning grid fins include: minimum drag levels, radar cross section and mass production manufacturing techniques.

Table 1. Grid Fin Wind Tunnel Test Summary

Test Date	Test Facility	Test Objective
AUG 1985	Vought HSWT (Grand Prairie, TX)	Exploratory investigation of flat grid fins
FEB 1989	Vought HSWT (Grand Prairie, TX)	Exploratory investigation of curved grid fins and sweep effects
OCT 1993	NTS 4 × 4 TWT (Saugus, CA)	Investigation of grid fin design as control surface for TACAWS
NOV 1993	NTS 4 × 4 TWT (Saugus, CA)	Investigation of grid fin drag reduction techniques
SEP 1994	NTS 4 × 4 TWT (Saugus, CA)	Investigation of new grid fin designs (parametric variation)
OCT 1995	NTS 4 × 4 TWT (Saugus, CA)	BOAR warhead vehicle application BOAR airdrop vehicle application
OCT 1995	Loral Vought Systems HSWT (Grand Prairie, TX)	Roll damping investigation of BOAR and other grid fin designs
NOV 1996	USAF SARL (WPAFB, OH)	Subsonic splitter plate test for 2-D aerodynamics of grid fin designs
MAY 1997	USAF SARL (WPAFB, OH)	Subsonic investigation of grid fin aerodynamics in presence of body

Table 2. Grid Fin Configuration Summary

Configuration Code	Fin Description	Wind Tunnel Test
G1	Flat Grid Fin - dense webbing	Vought 1985
G2	Flat Grid Fin - sparse webbing	
G3	Fin G1 with revised attachment structure	Vought 1989
G4	Fin G1 with convex curvature	
G5	Fin G1 with concave curvature	
G6	Baseline fin with no frame shaping	NTS 1993 USAF SARL 1996 USAF SARL 1997
G7	Baseline with modified double wedge frame	
G8	Baseline with modified single wedge frame	
G9	Baseline with half diamond frame	
G10	Fin G7 with thicker web	
G11	Baseline with thin modified double wedge frame	NTS 1994 NTS 1995 Loral Vought 1995 USAF SARL 1996 USAF SARL 1997
G12	Fin G6 with modifications	
G13	Fin G12 with longer span	
G14	Fin G12 with denser webbing	
G15	Fin G13 with sparser webbing	
G16	Fin G13 with increased web depth	NTS 1995 Loral Vought 1995 USAF SARL 1996 USAF SARL 1997
G17	MLRS BOAR flight hardware - 50.35% scale	
G18	Fin G17 with longer span	
G19	MLRS BOAR flight hardware - 24.77% scale	Not Tested
G20	TACAWS Grid Fin Design	NTS 1993 USAF SARL 1996 USAF SARL 1997
G21	Non-orthogonal design with dense webbing	USAF SARL 1996
G22	Non-orthogonal design with less dense webbing	USAF SARL 1997
G23	Research fin, curved with long span	USAF SARL 1996
G24	Research fin, curved with short span	
G25	Fin G6 with attach structure on side of frame	USAF SARL 1996
G26	Fin G13 with attach structure on side of frame	

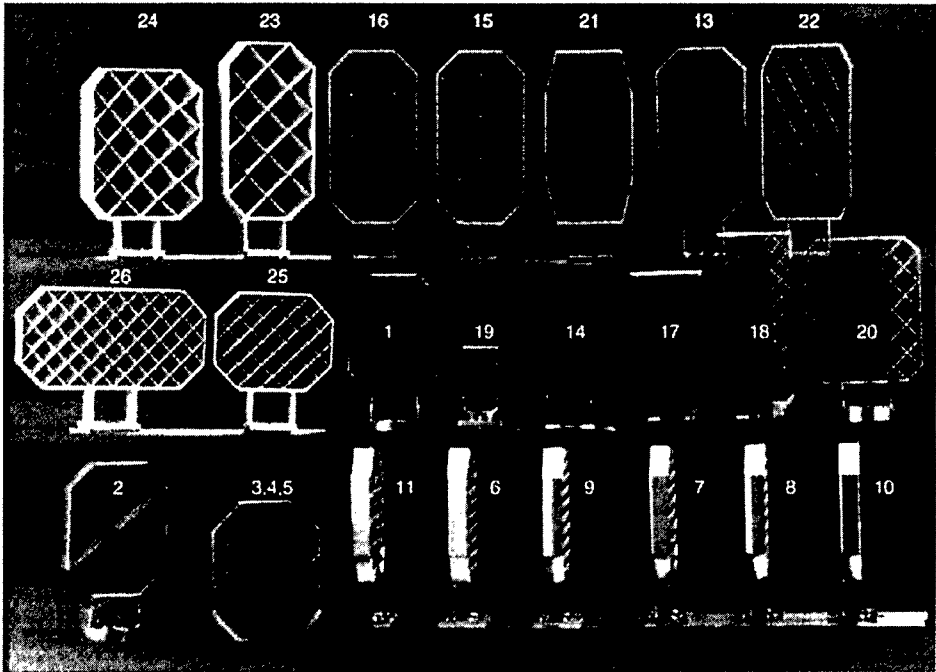


Figure 1. Photograph of Grid Fin Designs

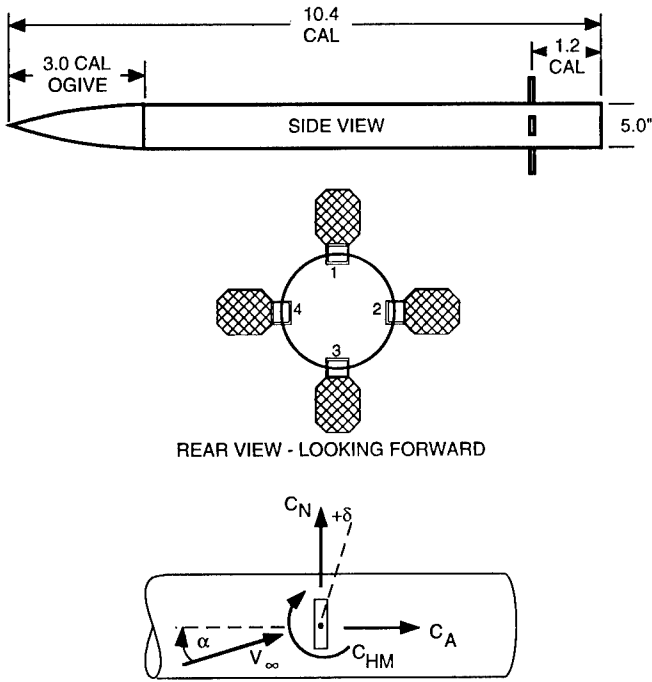


Figure 2. Model and Sign Conventions

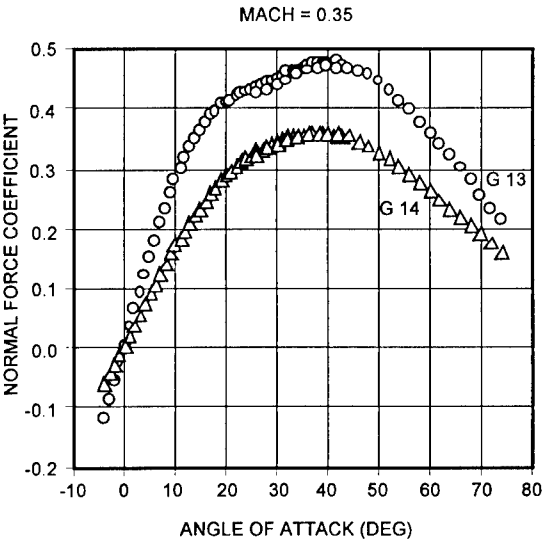


Figure 3. High Angle of Attack Characteristics

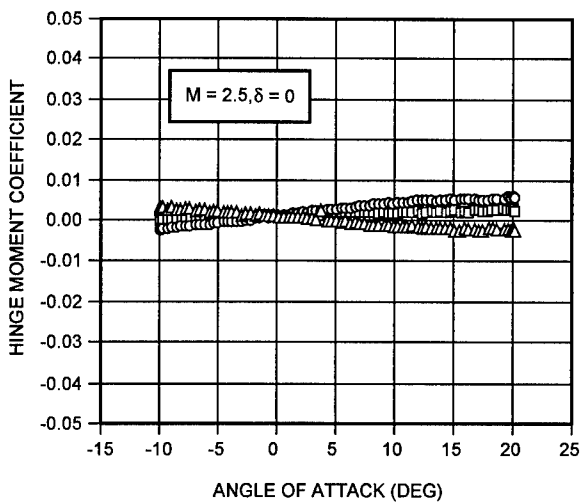
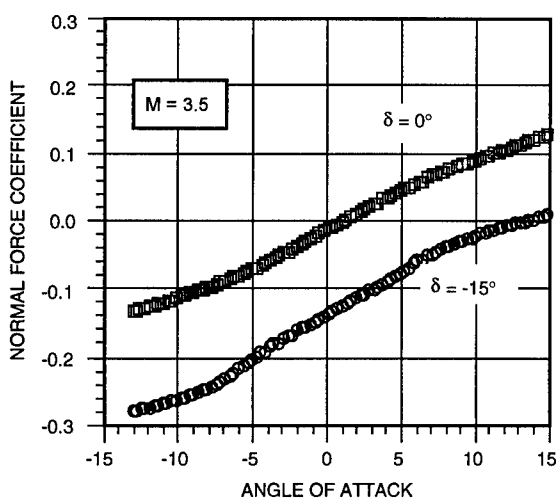
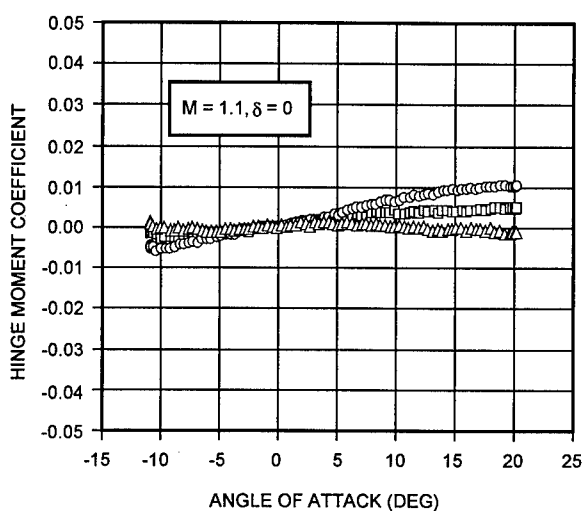
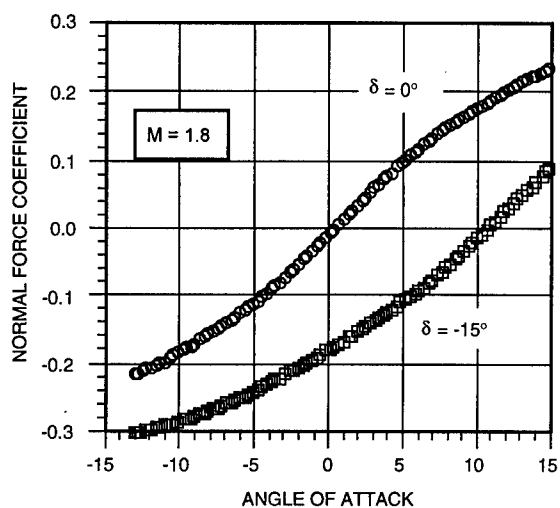
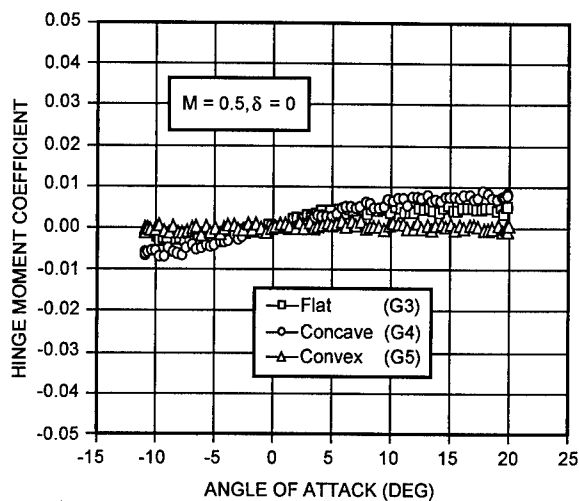
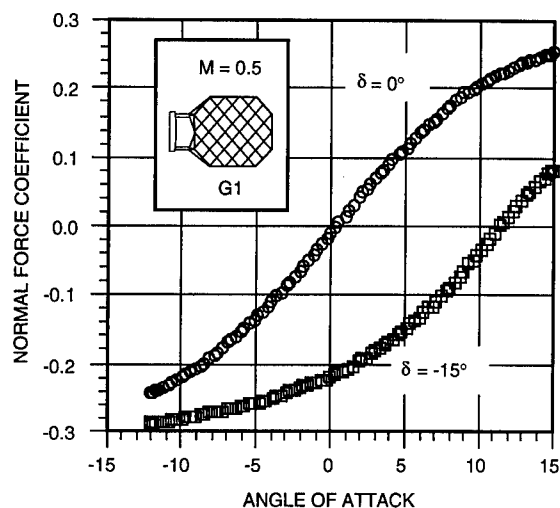


Figure 4. Normal Force Control Characteristics

Figure 5. Curvature Effects on Hinge Moments

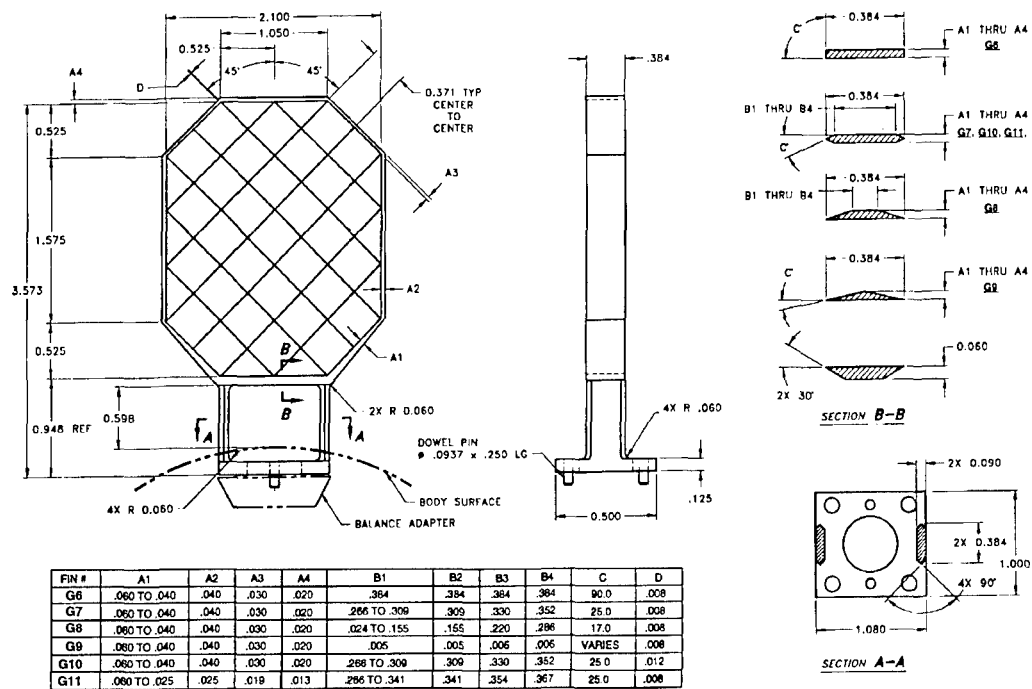


Figure 6. Grid Fin Designs Used for Drag Evaluation Test

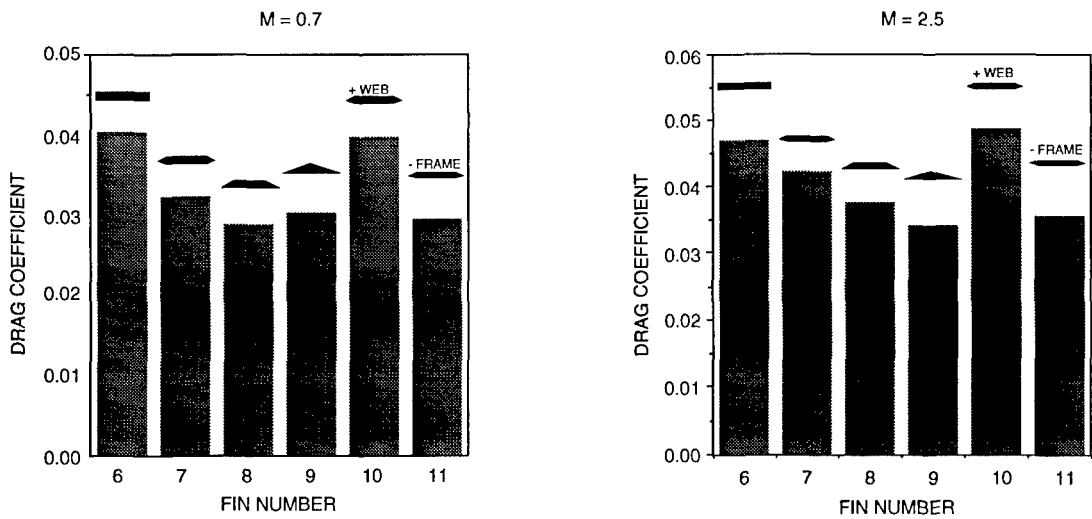


Figure 7. Drag Evaluation Test Results

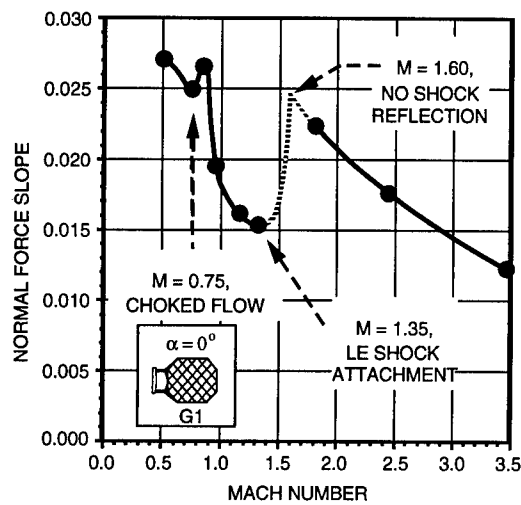


Figure 8. Normal Force Slope Variation

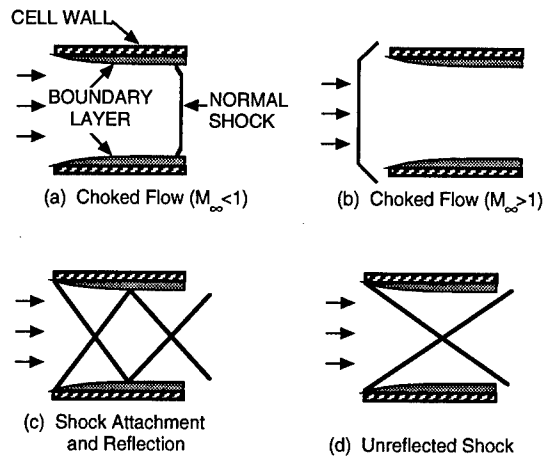


Figure 9. Grid Fin Flow Regimes

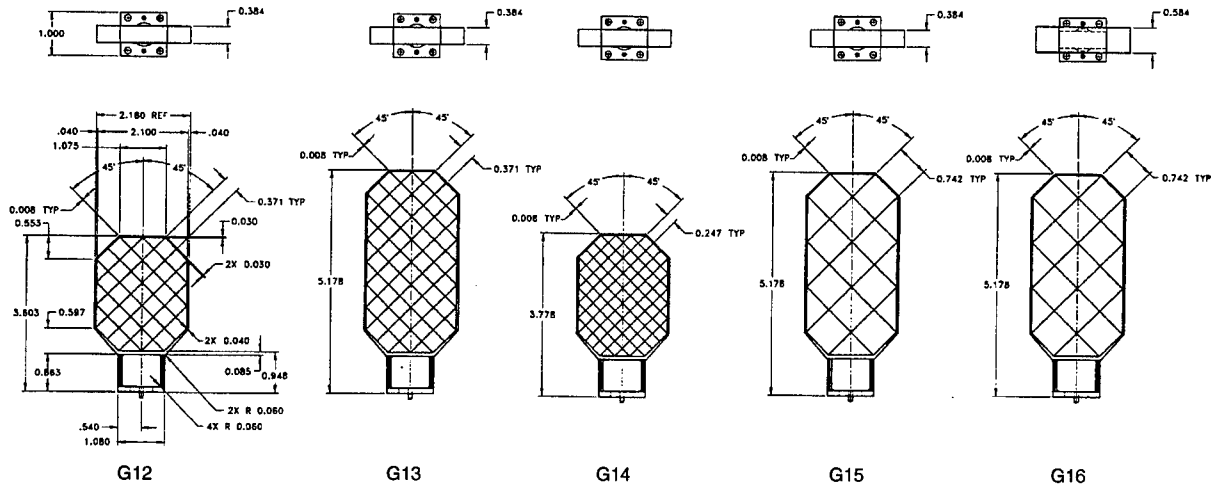


Figure 10. Grid Fins Used for Parametric Design Evaluation Testing

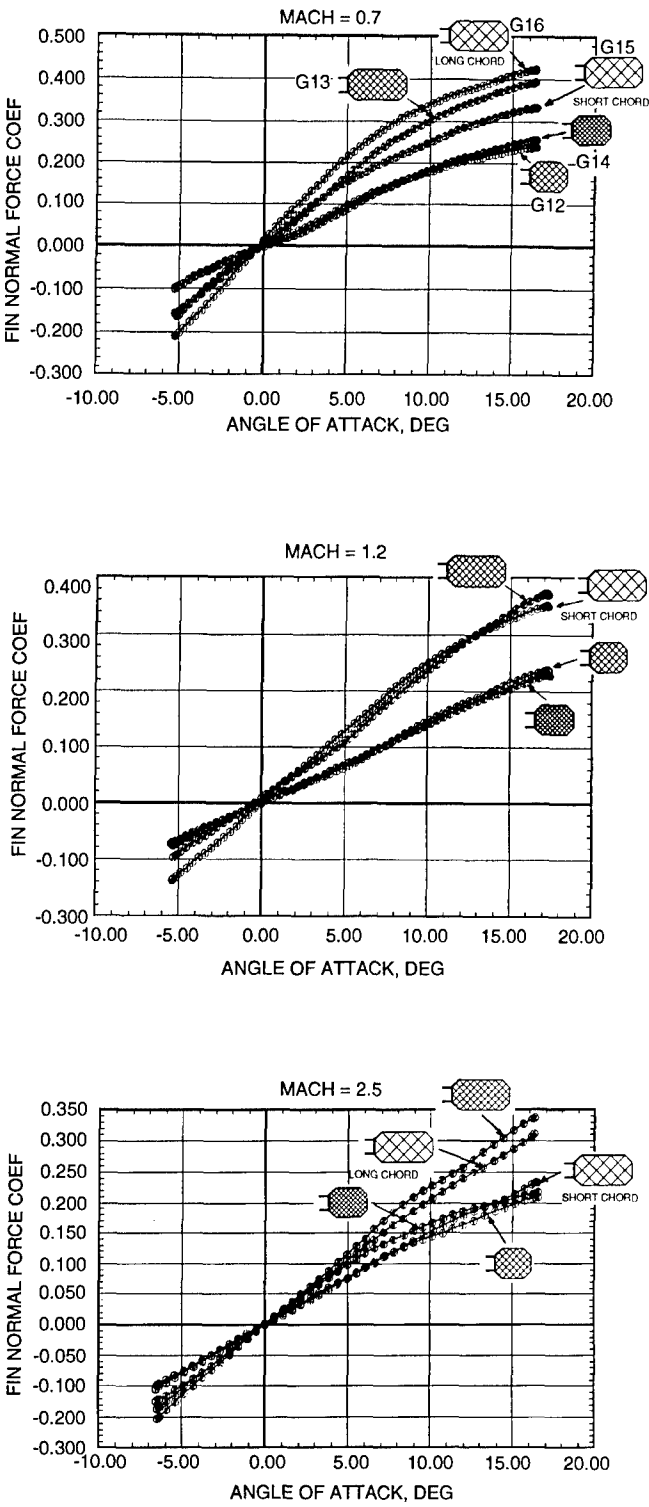


Figure 11. Parametric Design Test Results

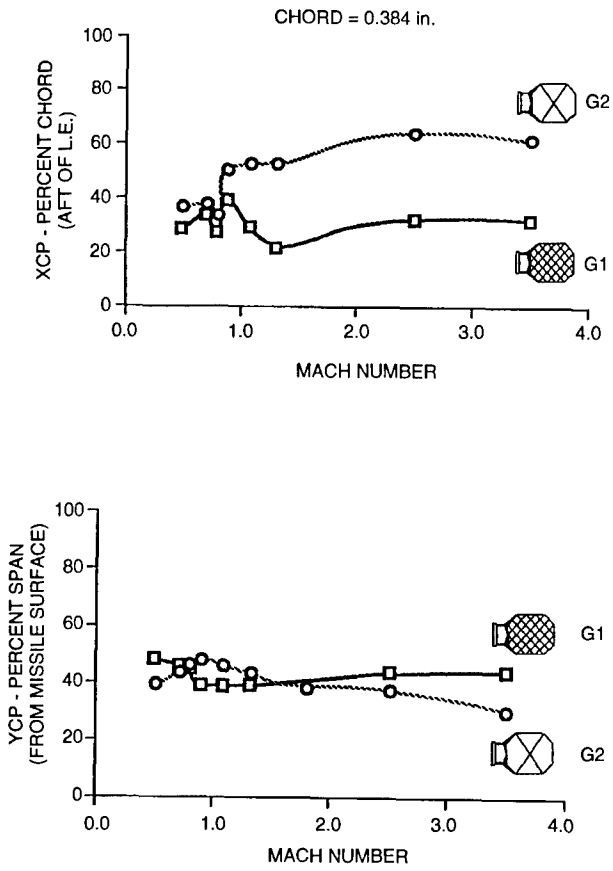


Figure 12. Grid Fin Center of Pressure Variations

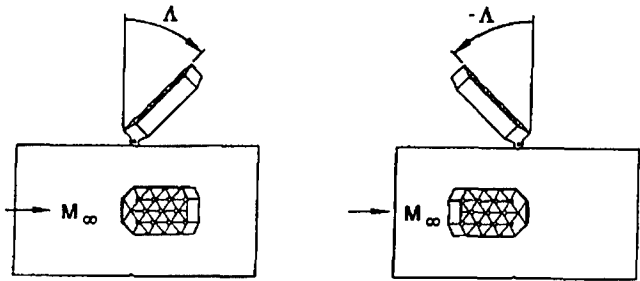


Figure 13. Sweep Sign Conventions

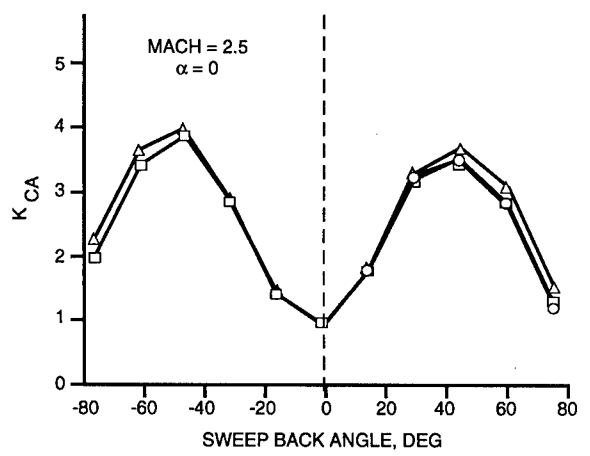
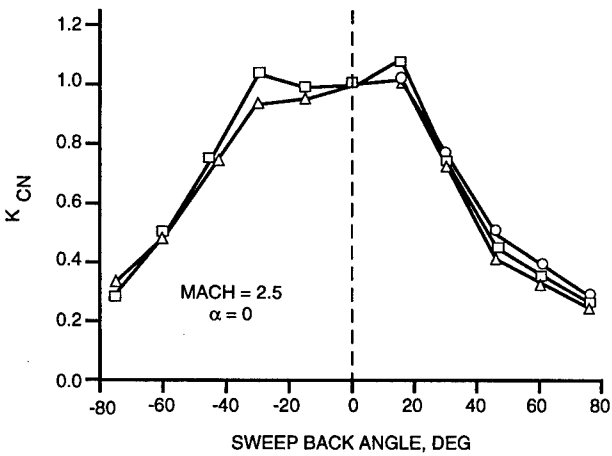
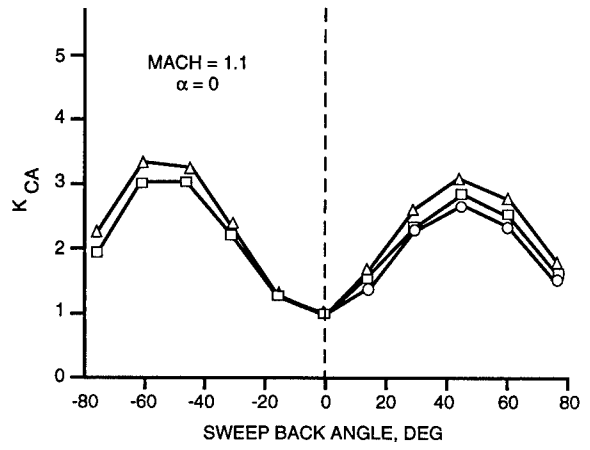
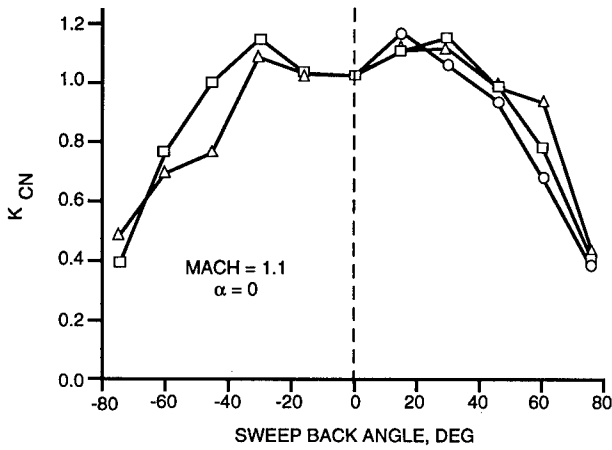
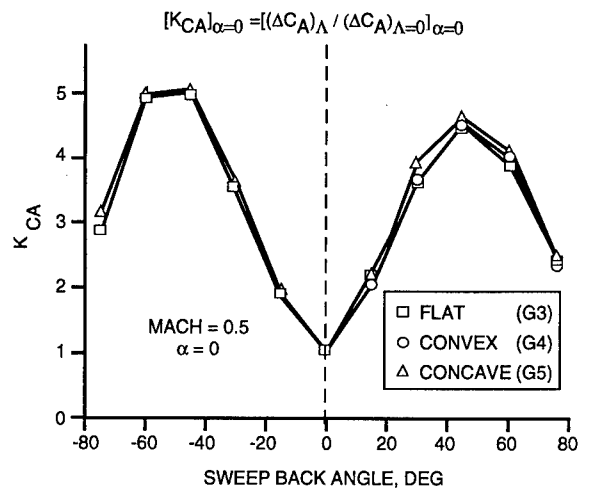
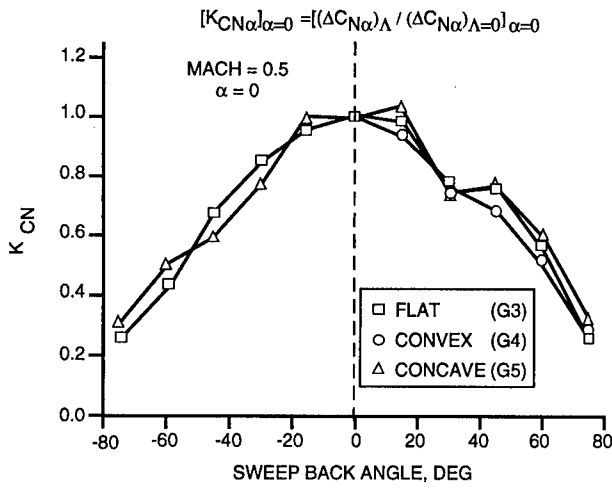
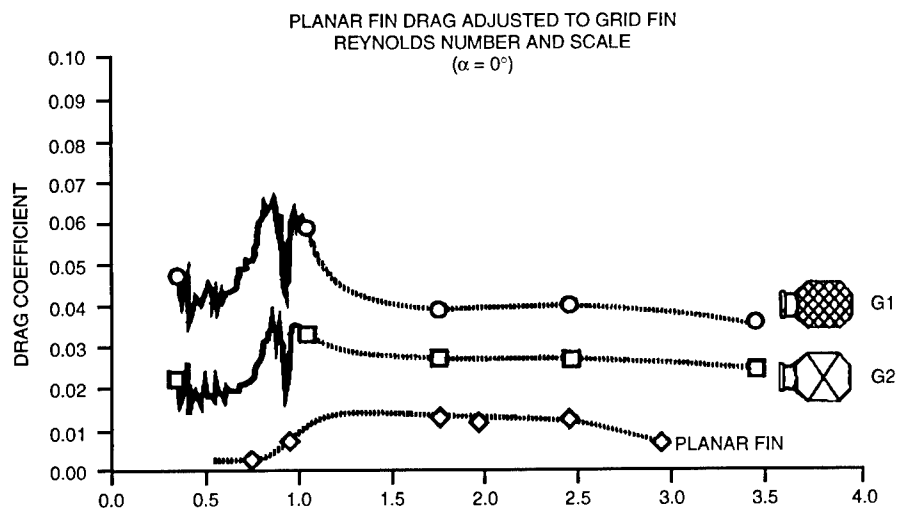
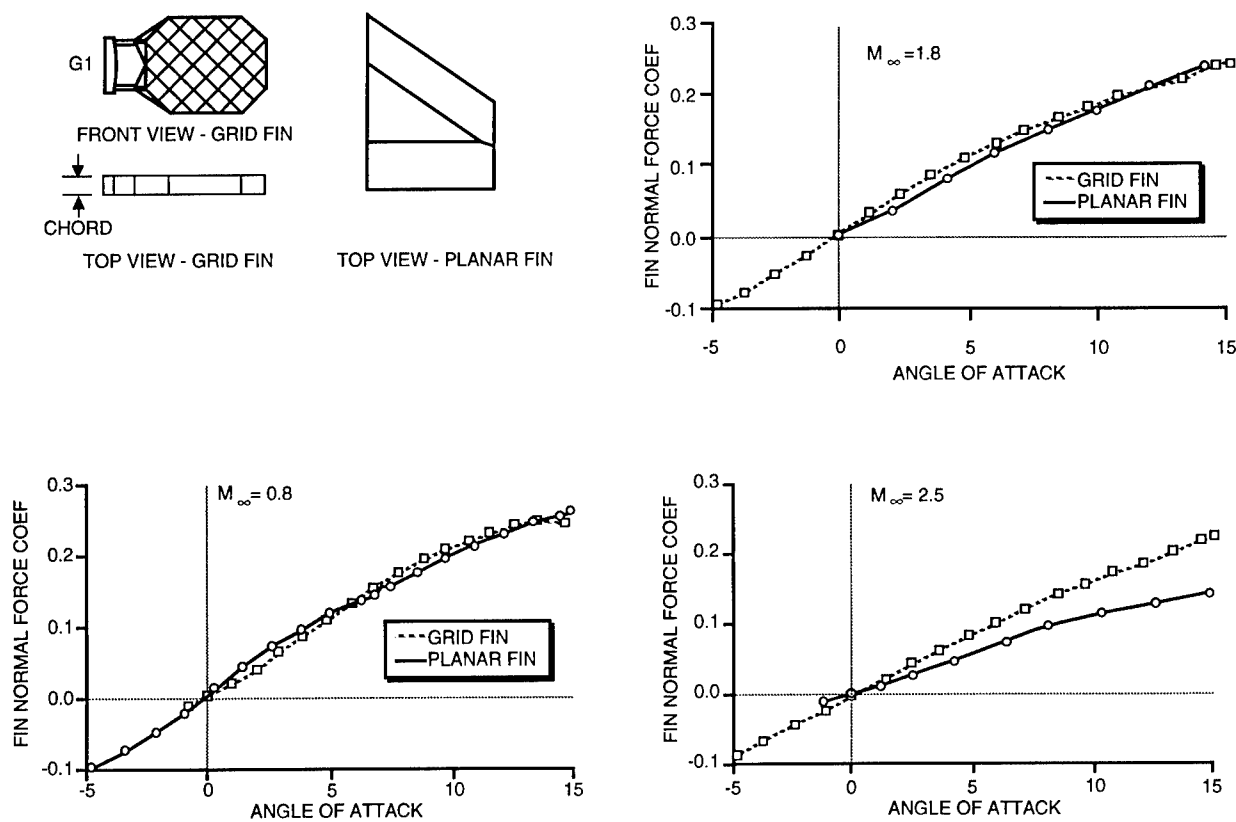


Figure 14. Sweep Effects on Normal Force

Figure 15. Sweep Effects on Axial Force



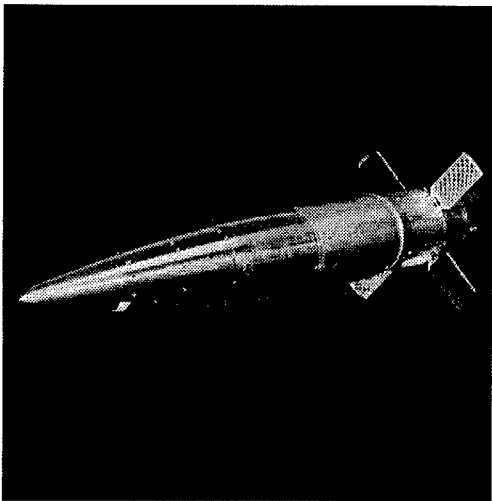


Figure 18. BOAR Rocket Warhead Flight Hardware

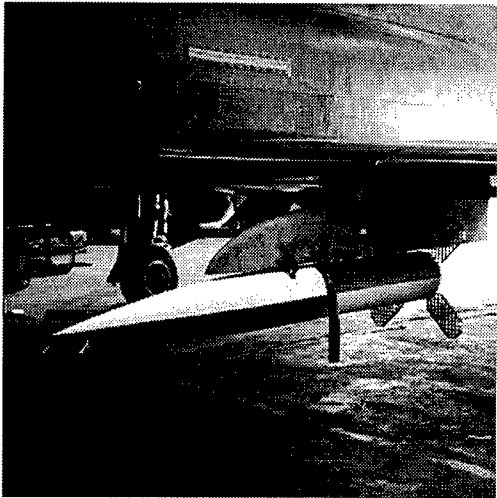


Figure 19. BOAR Airdrop Flight Hardware

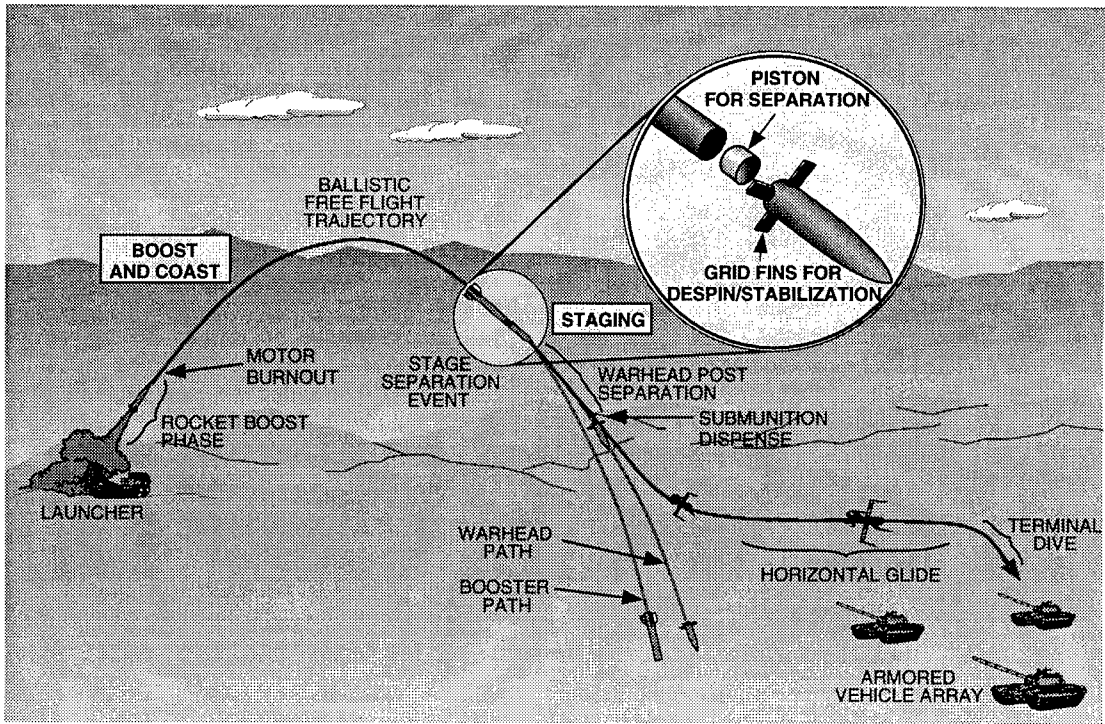


Figure 20. Bat-On-A-Rocket (BOAR) Flight Scenario

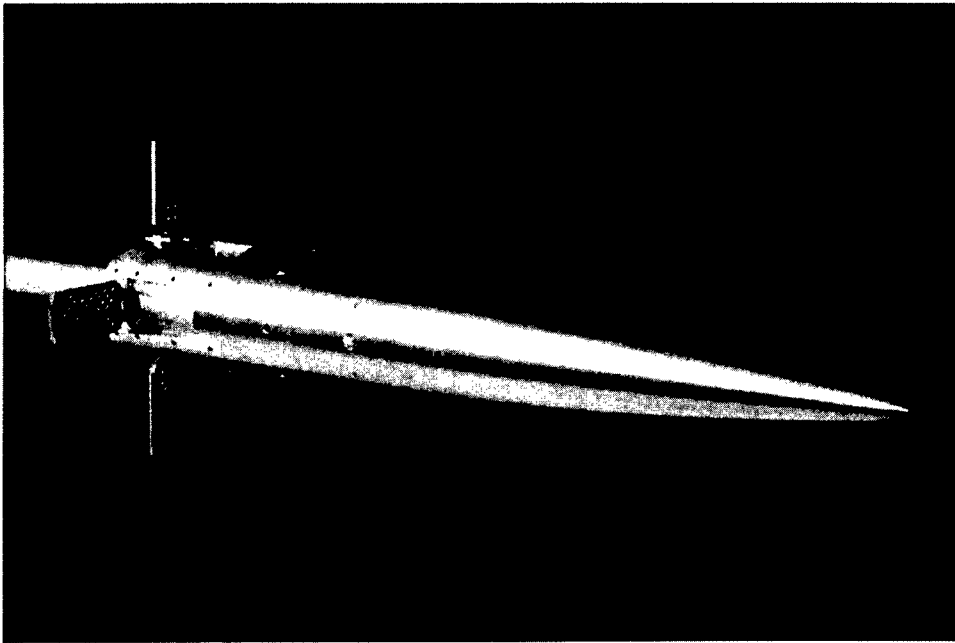


Figure 21. BOAR Warhead Section Wind Tunnel Model

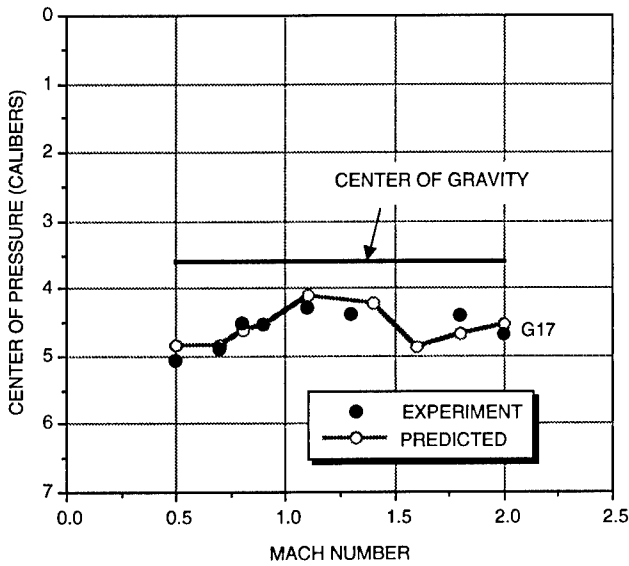


Figure 22. Warhead Center of Pressure Comparisons

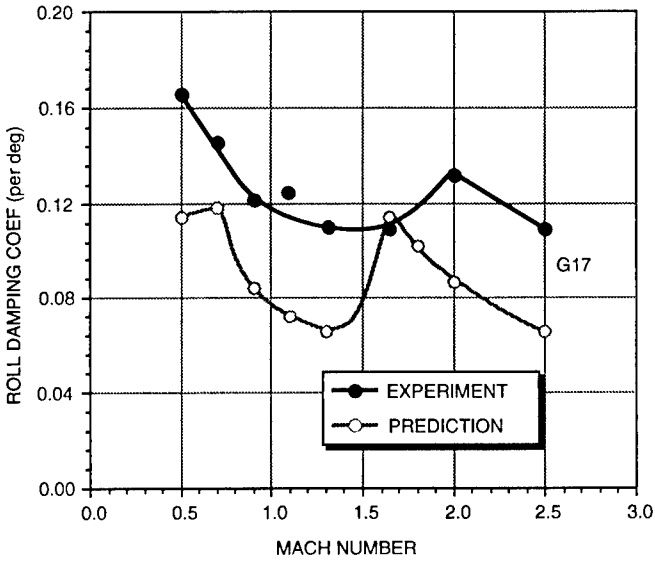


Figure 23. Warhead Roll Damping Comparisons

Aerodynamic Prediction Methodology for Grid Fins

Richard W. Kretzschmar

Missile Research Development and Engineering Center
U.S. Army Aviation and Missile Command
Attn: AMSAM-RD-SS-AT
Redstone Arsenal, AL 35898-5000, USA

Dr. John E. Burkhalter

Department of Aerospace Engineering
Auburn University, AL 36849, USA

SUMMARY

Formulation and validation of a theoretical methodology to predict the aerodynamic forces and moments associated with missile configurations utilizing grid fins in subsonic, transonic and supersonic Mach regimes is discussed in detail. Comparisons with experimental data collected on a variety of grid fin configurations are presented to provide an indication of the methodology accuracy. Conclusions regarding the accuracy and limitations of the prediction methodology are drawn from these comparisons.

1.0 LIST OF SYMBOLS

A	Subelement Area
B_2	Fin Span from Body Centerline
B_f	Fin Span
C	Fin Chord Length
$C_{\hat{F}}$	Element Force Coefficient
$C_{\hat{N}}$	Element Normal Force Coefficient
$C_{\hat{Y}}$	Element Side Force Coefficient
$C_{\hat{A}}$	Element Axial Force Coefficient
H	Fin Height
H_b	Height of Fin Support Structure
i_{base}	Number of Cells in Fin Base Corner
i_{tip}	Number of Cells in Fin Tip Corner
M	Mach Number
n_{dy}	Number of Cells in Horizontal Direction
n_{dz}	Number of Cells in Vertical Direction
\bar{n}	Component of Unit Normal Vector
S	Element Slant Length
S_{ref}	Reference Area
\bar{u}	Component of Velocity
y_{fs}	Span of Fin Support Structure
X_h	Longitudinal Position of Fin Hinge Line
α	Angle of Attack
β	Compressibility Factor
δ	Fin Deflection Angle
Γ	Vortex Strength
ϕ	Fin Azimuthal Orientation Angle
θ	Azimuthal Angle from Horizontal Y axis

2.0 INTRODUCTION

The Missile Research Development and Engineering Center of the U.S. Army Aviation and Missile Command has developed a prediction methodology to accurately predict the aerodynamic forces and moments associated with missile configurations utilizing grid fins as lift and control surfaces.

Flow field analyses conducted by Russian researchers have provided a basic understanding of and highlighted the substantial differences in flow field characteristics, particularly the shock structure, resulting from the presence of grid fins in various Mach regimes.¹ These differences required separate development of theoretical formulations for the subsonic, transonic and supersonic Mach regimes.

Independent of the Mach regime, the unique grid fin geometry requires prediction techniques which address multiple lifting surfaces oriented at angles other than the traditional "wing" plane. Existing theoretical techniques, such as vortex lattice theory for subsonic applications and Ekvard's theory for supersonic applications, lend themselves to this type of analysis and were therefore applied directly or in slightly modified form to the grid fin problem.

Due to the linear nature of the selected theoretical formulations, their application was limited to missile orientations at which nonlinear aerodynamic characteristics are minimal i.e. small angles of attack. Investigation of experimental data has indicated linear aerodynamic characteristics are maintained up to approximately 7.0 deg. for most grid fin configurations. To extend the applicable range of these theories, a series of empirical equations were developed to correlate the prediction results for both subsonic and supersonic cases with experimental data collected in a series of wind tunnel tests. Limited validation of the theoretical formulations has been accomplished through comparisons with experimental data.

3.0 GRID FIN GEOMETRIC DEFINITION

Theoretical formulations developed in this analysis are quite robust and apply to nearly all grid fin shapes of practical interest. However, some geometric restrictions are necessary to limit the programming complexity related to the application of these theories. Currently, application is limited to grid fin configurations which are symmetric about the "Y" axis and have a hinge line which is coincident with a radial vector from the body centerline outward. Additionally, the geometry of each fin within a fin set must be identical.

Due to the complexity of the grid fin geometry, numerous geometric parameters are required for accurate definition. In addition to the obvious parameters such as fin span, height, chord length and longitudinal position on the missile body, parameters to define the span and height of the support structure, the number of cells in the vertical and horizontal directions and the number of cells in the inboard and outboard corners are also required. An illustration of these parameters is provided in Figure 1.

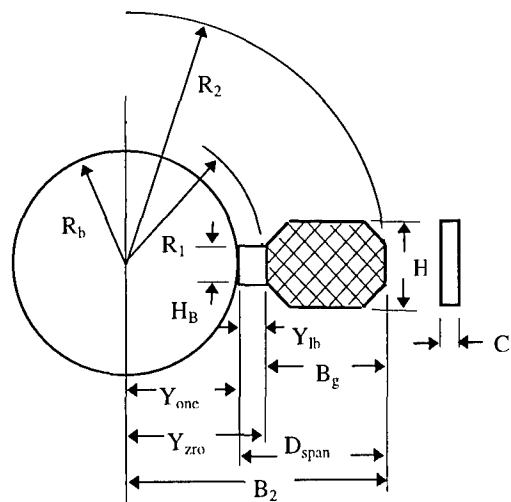


Figure 1. Geometric Parameters Used to Define Grid Fin Geometry

Two angles, the azimuthal and deflection angle must be specified to define the orientation of each individual fin relative to the missile body. Fin azimuthal position is defined in the Y-Z plane and is positive counterclockwise from the Y axis. Fin deflection angle is defined such that a positive fin deflection results in a counterclockwise roll of the missile and is referenced about the fin hinge line. Sign convention for each of these angles is illustrated in Figure 2.

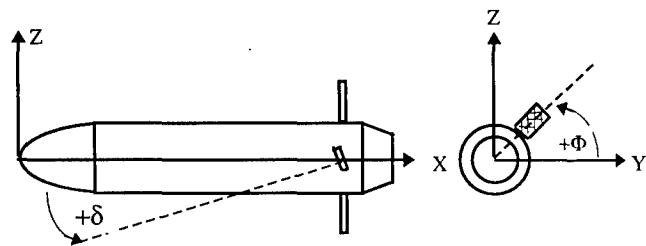


Figure 2. Orientation Angle Sign Convention.

4.0 THEORETICAL FORMULATION

Selection of the proper theoretical formulation is governed by the freestream Mach number being considered. Analysis of existing wind tunnel data has provided a general understanding of the flow field surrounding a generic grid fin design.^{2,3} Table 1 provides a descriptive summary of the assumed flow structure and specifies the applicable theoretical formulation.

Table 1. Summary of Assumed Flowfield Structure.

Mach Number	Formulation	Assumed Flow Structure
$M < 0.8$	Subsonic	Local Flow structure completely subsonic. Compressible subsonic formulation is required.
$0.8 < M < 1.0$	Transonic	Flow through Grid Structure is Typically Choked Requiring Application of Coefficient Correction Factors.
$1.0 < M < 1.4$	Transonic	Bow shock in front of grid fin. Flow is subsonic behind the bow shock and a compressible subsonic solution is required.
$1.4 < M < 1.9$	Supersonic	Grid fin swallows shock. Each element acts as a thin wing with an attached leading shock which impinges on adjacent fin elements producing a reflected shock dominated flow region.
$1.9 < M < 3.5$	Supersonic	Leading edge shock on each fin element does not impinge on adjacent elements and internal flow is primarily supersonic with minimal reflected shock effects
$M > 3.5$	Supersonic	Strong leading edge shock transitioning to hypersonic flow.

4.1 Subsonic Formulation

The theoretical formulation developed for the subsonic Mach regime utilizes a vortex lattice solution to calculate the loading on each individual element in the lattice.⁴ Body upwash and wing-body carryover terms resulting from interaction between the missile components are also accounted for using theoretical techniques.

Fin geometry is modeled by replacing the grid fin with a vortex lattice structure. This lattice consists of a series of horseshoe vortices and associated control points and normal vectors affixed to each individual panel element. Defining the vortex lattice structure is a multi-stepped process outlined in detail in Reference 4 and summarized here for clarity. The process begins by defining the intersection points between the panels making up the grid fin structure. When these points are connected and given a chord depth, the three dimensional aspects of the grid fin are established. If one considers a single element of a grid fin located arbitrarily in the freestream, the element would appear as a flat plate as illustrated in Figure 3.

A horseshoe vortex is affixed to each panel and is defined using 10 node points. Node points 1 and 6, located at the panel quarter chord and node points 2 and 7, located at the trailing edge of the panel define the bound portion of the vortex. The remaining 6 nodes define the vortex trailing legs and are positioned to trail off in the direction of the freestream. A control point and unit normal vector are positioned at the midspan and three quarter chord of each panel, respectively.

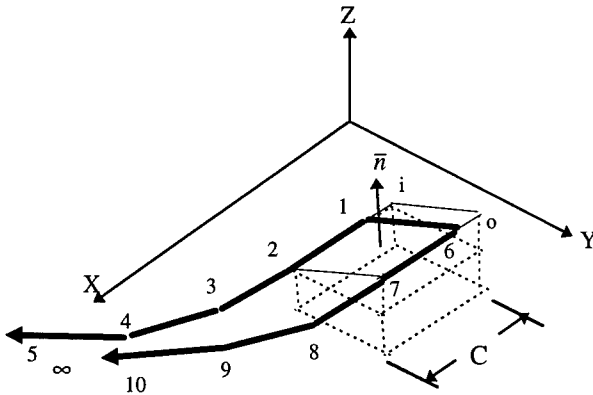


Figure 3. Schematic of an Individual Grid Fin Element and Associated Vortex Lattice Structure.

To determine the loading on each grid fin, the strengths of each vortex must first be determined. This is accomplished by applying boundary conditions requiring the flow to be tangent to each panel at the control point. The velocity vector at a control point is composed of three components, the freestream velocity, the crossflow velocity or body upwash component, and the induced velocity from each vortex filament in the flowfield. Determination of the cross flow velocity magnitude is accomplished using a potential flow solution for an infinite doublet in a freestream. An illustration of the flow field generated by a doublet in a freestream is provided in Figure 4.

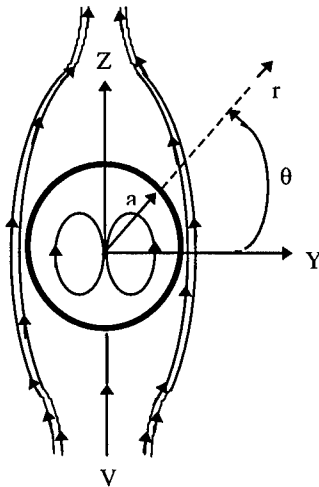


Figure 4. Flowfield Resulting from a Freestream Doublet Combination.

General expressions for the velocity components in Cartesian coordinates resulting from the potential flow solution of an infinite doublet are,

$$u_y = -\sin \alpha \sin 2\theta \left(\frac{r_b^2}{|r|^2} \right)$$

$$u_z = \sin \alpha \left[1 + (1 - 2 \sin^2 \theta) \left(\frac{r_b^2}{|r|^2} \right) \right]$$

The compressible form of the Biot-Savart integral is used to determine the velocity induced by a vortex filament segment at a control point and may be written as,

$$\bar{v}_r = -\frac{\Gamma \beta^2}{4\pi} \int \frac{\bar{r} x d\bar{l}}{|r_\beta|^3}$$

where β is the compressibility factor,

$$\beta = \sqrt{1 - M^2}$$

The velocity vector at the control point can be determined by summing the contributions of the freestream doublet combination and the velocities induced by the vortex filaments.

$$\bar{v}_i = \bar{v}_r + u_x \hat{i} + u_y \hat{j} + u_z \hat{k}$$

The dot product of the velocity vector and the panel unit normal yields the component of velocity normal to the panel surface. For the flow tangency boundary condition to be satisfied, this normal velocity must be zero. Application of this condition yields an equation which when reorganized isolates the unknown vortex strengths and is conducive to solution using numerical methods

$$\bar{v}_r \cdot \bar{n} = \left[\left(-\frac{\beta^2}{4\pi} \int \frac{\bar{r} x d\bar{l}}{|r_\beta|^3} \right)_x \cdot n_x + \left(-\frac{\beta^2}{4\pi} \int \frac{\bar{r} x d\bar{l}}{|r_\beta|^3} \right)_y \cdot n_y + \left(-\frac{\beta^2}{4\pi} \int \frac{\bar{r} x d\bar{l}}{|r_\beta|^3} \right)_z \cdot n_z \right] \cdot \Gamma = B$$

Application of the above equation to all vortices in the flowfield yields an expression which is best expressed in matrix format.

$$[\Gamma] = [A]^{-1} \cdot [B]$$

In the above expression, the "A" matrix is the inverse of the bracketed term above, the "B" matrix represents the known velocities induced at the control point by the freestream doublet combination, and the "Γ" term is the matrix of unknown vortex strengths.

Vortex strengths are determined simultaneously using an iterative procedure to avoid problems in inverting the often large "A" matrix. The solution process for a missile with 4 fins is as follows; First, vortex strengths of fin #1 are found as if no other fins were present. Second, the vortex strengths of fin #2 are determined as if only fin #1 and #2 exist and the strengths of the vortices on fin #1 are known. This process continues for the remaining fins, each time including the known vortex strengths of the previous grid fins. When the vortex strengths of fin #4 have been found, the entire process is repeated for several iterations until the updated vortex strengths are no longer significantly different from the values calculated in the previous iteration. In this manner, inversion of large matrices is avoided. From past experience, only a few iterations are necessary to obtain a converged solution.

Aerodynamic loads on the grid fin can be computed directly from the calculated vortex strengths by considering the loading on each individual panel separately. Application of

This semiempirical formulation utilizes the initial lift curve slopes from vortex lattice theory and attempts to incorporate the influence of the most prominent geometric parameters effecting the grid fin aerodynamic characteristics, the ratio of fin span to height (b_g/h) and the ratio of fin chord length to height (C_h/h). A complete summary of the nonlinear formulation development can be found in reference 5.

4.2 Transonic Aerodynamics

Unlike conventional planar fins which experience maximum normal force coefficient values at transonic Mach numbers, a grid fin experiences what is commonly referred to as the "transonic bucket". To understand this phenomenon, one must look at a grid fin as a collection of individual cells acting as separate inlets.⁹

Reduction in the inlet cross-sectional area caused by the presence of the cell walls and the boundary layer buildup on these walls causes the flow passing through the cell to accelerate to sonic conditions (i.e., become choked) at freestream Mach numbers less than 1.0. As the flow increases past Mach 1.0, a detached normal shock forms in front of the cell. The cell remains choked until the normal shock is swallowed. It is the flow spillage caused by the choked flow that causes the reduction in normal force. An illustration of this transonic bucket is presented in Figure 6.⁹

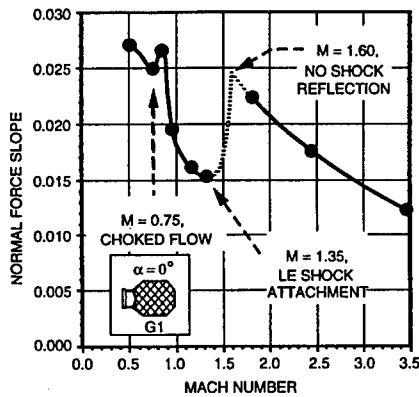


Figure 6. Reduction of Grid Fin Normal Force in Transonic regime.

To accommodate the transonic flow characteristics at Mach numbers less than 1.0, a theoretical formulation was developed to determine whether choked conditions exist for the particular subsonic Mach number / grid fin combination being investigated. In addressing this phenomenon, a laminar boundary layer and isentropic conditions are assumed within the cell structure. Blasius' theorem is utilized to calculate the displacement thickness associated with the local Reynolds number and chord length.

$$\delta_{th} = \frac{1.7208 * C}{\sqrt{Re_c}}$$

By assuming this displacement thickness is present on all fin elements, the corresponding reduction in fin capture area can be determined.

$$A_{\delta_{th}} = 2 * \delta_{th} + thk * ttle$$

Where "ttle" is the total length of the grid fin elements in the plane perpendicular to the freestream. By subtracting this area from the total capture area of the fin, the exit area A_{ex} is determined.

For a given freestream Mach number, there exists a minimum exit area known as the throat area (A^*) at which sonic flow will occur. The ratio between this area and the flow capture area is determined using the isentropic relationship.

$$A^* = \frac{A_{cap} * M}{\left[\frac{2 \left(1 + \frac{\gamma-1}{2} M^2 \right)}{\gamma+1} \right]^{\frac{1}{2} \left(\frac{\gamma+1}{\gamma-1} \right)}}$$

If the calculated exit area A_{ex} is less than A^* the flow is considered choked and a correction factor is determined by calculating the reduction in mass flow rate between the choked and unchoked conditions. The correction factor is determined using the following equation.

$$CF = \frac{A_{ex} * \sqrt{\gamma P_o \rho_o \left(\frac{2}{\gamma+1} \right)^{\left(\frac{\gamma+1}{\gamma-1} \right)}}}{A_{cap} \rho_{\infty} V_{\infty}}$$

By utilizing this correction factor as a multiplier to reduce the calculated fin forces and moments, the loss of fin effectiveness due to the reduction in mass flow through the grid fin is quantified.

For transonic Mach numbers above Mach 1.0, it is assumed a normal shock exists in front of the entire grid fin surface. After passing through the normal shock wave, the flowfield experienced by the grid fin is again subsonic. Mach number and dynamic pressure behind the shock are calculated using historical normal shock relations and are then applied in the subsonic prediction formulation. Equations relating static pressure and Mach number in front of and behind a normal shock are presented below.

$$\frac{p_2}{p_1} = \frac{2\gamma M_1^2 - (\gamma - 1)}{\gamma + 1}$$

$$M_2^2 = \frac{(\gamma - 1) M_1^2 + 2}{2\gamma M_1^2 - (\gamma - 1)}$$

An illustration of the transonic flowfield structure surrounding a typical grid fin is provided in Figure 7.⁹

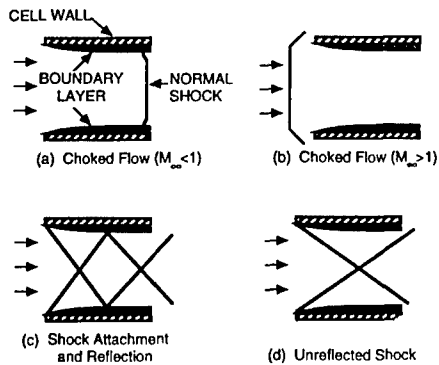


Figure 7. Flowfield Structure Around a Grid Fin at Transonic Conditions.

4.3 Supersonic Aerodynamics

Prediction formulation developed for supersonic flow is similar to the subsonic formulation in that an existing linear aerodynamic technique is applied to the problem by considering the grid fin on a panel by panel basis. In this case, a modified form of Evvard's theory was utilized in the linear aerodynamic range. Modifications to the basic theory were necessary to account for the endplate effects resulting from the grid structure when addressing the individual panel elements. In its original form, Evvard's theory does not properly address this condition.

The original form of Evvard's theory provides generalized formulas for ΔC_p distributions for the case of a swept wing planform with a supersonic leading edge. Figure 7 illustrates the various supersonic regions associated with a typical planar wing. Figures 8 and 9 indicate the regions associated with a grid fin element taking into account the endplate effects for cases in which the Mach lines emanating from the intersection points do not intersect one another and do intersect one another, respectively. As indicated, for a grid fin element, pressure calculations for regions 1, 2 and perhaps 4 are of practical interest.

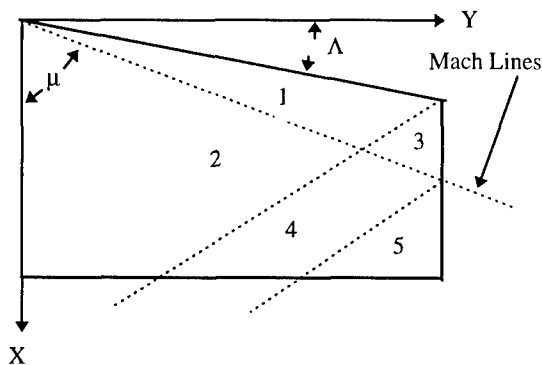


Figure 7. Regions of Influence on a Planar Wing in Supersonic Flow.

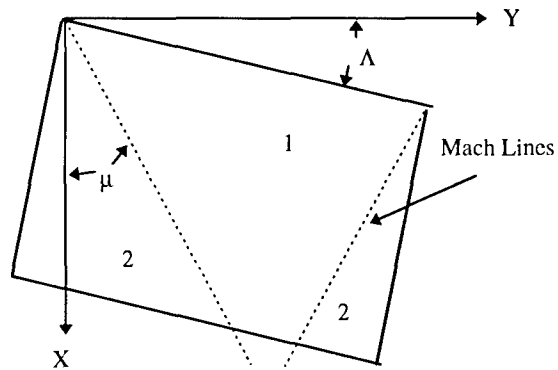


Figure 8. Regions of Influence on a Grid Fin Element in Supersonic Flow, Without Mach Line Interaction.

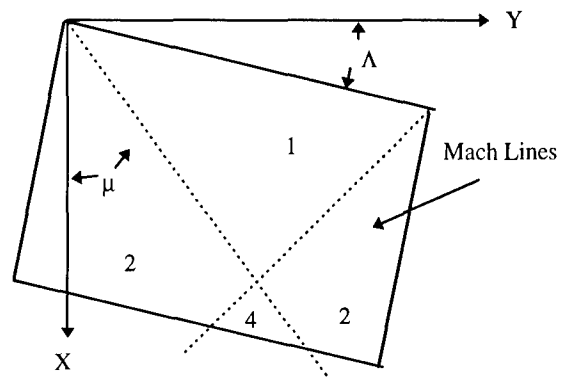


Figure 9. Regions of Influence on a Grid Fin Element in Supersonic Flow, with Mach Line Interaction

Equations which determine the differential pressure loading in regions 1, region 2 and region 4 were developed by Evvard and are presented below.

Region 1:
$$\Delta C_p = \frac{4\alpha}{\sqrt{M^2 - 1 - \tan^2 \lambda}}$$

Region 2:

$$\Delta C_p = \frac{4\alpha}{\pi \sqrt{B^2 - \tan^2 \lambda}} \left[\cos^{-1} \left(\frac{x \tan \lambda - B^2 y}{B(x + y \tan \lambda)} \right) + \cos^{-1} \left(\frac{x \tan \lambda - B^2 y}{B(x - y \tan \lambda)} \right) \right]$$

Region 4:

$$\Delta C_p = \left[\Delta C_p \right]_{reg2} - \frac{4\alpha}{\pi \sqrt{B^2 - \tan^2 \lambda}} \left[-\cos^{-1} \left(\frac{x_a + y_a (2B + \tan \lambda)}{(x_a + y_a \tan \lambda)} \right) \right]$$

To compute the loading on each element, the element is subdivided into a series of small rectangles. On each of these subelements, a ΔC_p value, determined using the appropriate equations for the particular region in which the subelement resides, is applied to the subelement area A . Equations for the various forces are presented below.

$$\Delta C_N = \frac{\Delta C_p AU_{NZ}}{S_{ref}}$$

$$\Delta C_A = \frac{\Delta C_p AU_{NX}}{S_{ref}}$$

$$\Delta C_Y = \frac{\Delta C_p AU_{NY}}{S_{ref}}$$

Incremental moment coefficients are determined as follows,

$$\Delta C_{hm} = -\Delta C_N \frac{x_{dis}}{L_{ref}} + \Delta C_A \frac{z_{dis}}{L_{ref}}$$

$$\Delta C_{bm} = -\Delta C_N \frac{y_{dis}}{L_{ref}} + \Delta C_Y \frac{z_{dis}}{L_{ref}}$$

$$\Delta C_{ym} = -\Delta C_Y \frac{x_{dis}}{L_{ref}} + \Delta C_A \frac{y_{dis}}{L_{ref}}$$

Force and moment coefficients for the entire fin are determined by summing the force contributions from the individual subelements.

Fin-body carryover effects are accounted for through application of the same imaging scheme described in the subsonic formulation summarized in section 5.1. Similarly, in determining the total fin axial force, the component contribution summation described for the subsonic theoretical formulation in section 5.1 is also included in the supersonic theoretical formulation.

Nonlinear Aerodynamic Formulation

As in the subsonic case, observations of available experimental data indicate significant nonlinear aerodynamic characteristics in the supersonic Mach regime at angles of attack above approximately 7.0 deg. In this regime, the nonlinearities are attributed to the complex shock structure associated with the grid fin configurations. These nonlinearities again preclude the sole use of a purely linear theory such as Evvard's solution in predicting the aerodynamic characteristics of grid fins. However, similar to the subsonic formulation, Evvard's theory is used to determine the initial lift curve slopes of the grid fin configurations, forming a basis for the nonlinear theory.

Unlike the subsonic formulation, only minimal experimental data were available with which to develop the supersonic nonlinear formulation. In this case, the parametric equation which seems to fit the prediction of grid fin normal force may be written as

$$C_N = \left. \frac{C_{N\delta} \delta}{1 + \frac{\delta}{\delta_{max}}} \right|_{\alpha=0} + \left. \frac{C_{N\alpha} \alpha}{1 + \frac{\alpha}{\alpha_{max}}} \right|_{\delta=0} * \left(1 - \left. \frac{C_{N\delta} \delta}{1 + \left(\frac{\delta}{\delta_{max}} \right)^2} \right|_{\alpha=0} \right)$$

This equation has the required linear limit as either α or δ approach zero and reaches a maximum value at α_{max} or at δ_{max} . A complete summary of the development of this formulation can be found in reference 11.

5.0 COMPARISONS WITH EXPERIMENTAL RESULTS

Results from the theoretical formulations have been compared with wind tunnel test data for various fin alone configurations to illustrate the accuracy and identify the limitations of the prediction techniques. The primary concentration in this validation effort has been determining the accuracy of the theoretical formulations in predicting the normal force and axial force of various grid fin configurations in the horizontal position at fin deflection angles of zero deg. This concentration is necessary to limit the scope of the paper and is justified in that accurate grid fin force prediction is the basis for all other aerodynamic characteristic estimation. Additionally, although the nonlinear formulations include the fin deflection parameter " δ ", due to the lack of sufficient wind tunnel test data, no effort was made to validate the contribution of this parameter to the overall aerodynamic characteristics of the grid fin configurations.

Wind Tunnel Model Configurations

A schematic of the grid fin Missile body combination with an arbitrary set of fins is provided in Figure 10. As indicated, the test article consisted of a 5.0 in. body of revolution 52. in. in length, with a three caliber tangent ogive nose. Four grid fins were mounted in the cruciform orientation with grid fins 2 and 4 in the horizontal and grid fins 1 and 3 in the vertical positions.

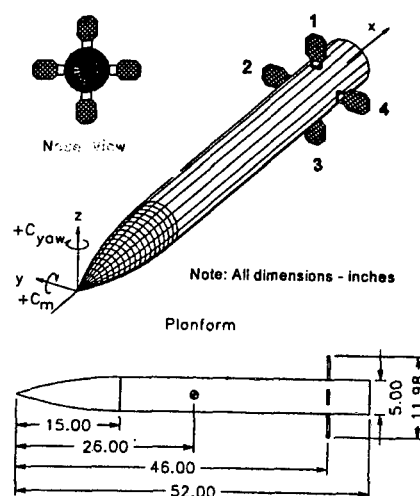


Figure 10. Grid Fin Missile Configuration.

Grid fin configurations utilized in this comparison represent a parametric set of configurations which address the majority of geometric parameters effecting their aerodynamic characteristics. Geometric parameters addressed include, fin span, cell density and fin chord length. Variation of these specific parameters are made on a fin by fin basis while holding the remaining geometric parameters constant. The effect of fin span variations are addressed by fins “G12” and “G13”. Cell density variations are addressed using fins “G12” and “G14” as well as fins “G13” and “G15”. Fin chord variation effects are investigated using fins “G15” and “G16”. Regardless of fin geometry, the fin base structure is consistent for all configurations tested. Illustrations of the various grid fin configurations are provided along with their designations in Figure 11.

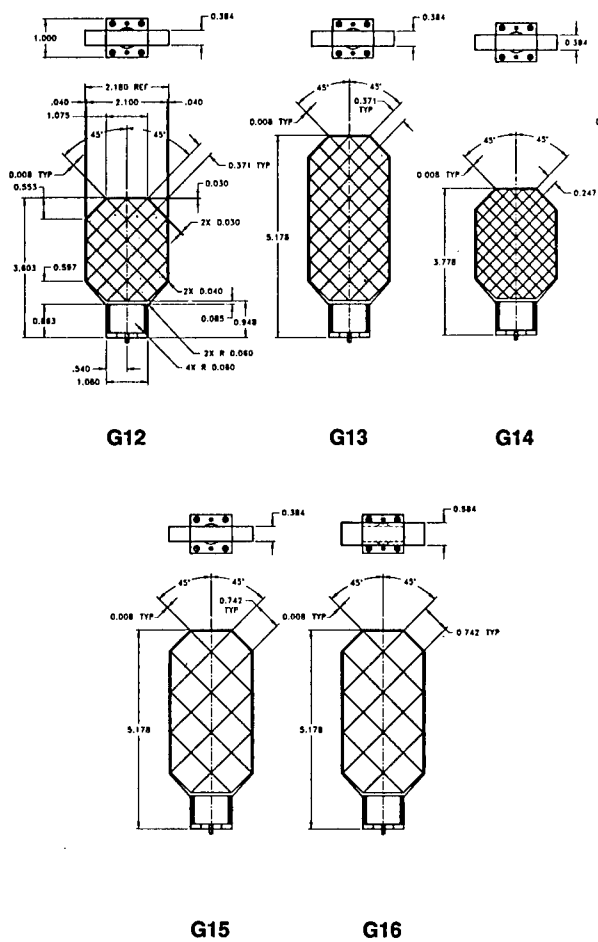


Figure 11. Grid Fin Configurations Used in Validation Process.

Experimental Accuracy

Experimental data presented in this report was collected using a 6-component fin balance mounted inside the wind tunnel body. Quoted accuracy for the fin balances is 1.5% of the rated loads, which results in an accuracy of ± 2 lb. for normal force. Repeatability proved much better, quoted to be within 0.1% of the rated loads. In all experimental test data, the reference length and area are the missile base diameter (5.0 in.) and base area (19.63 in²), respectively.

Analysis

Figures 12 through 14 illustrate the comparison between wind tunnel data and theoretical computations of normal force and axial force coefficient for a single “G13” fin at Mach 0.25, Mach 0.5 and Mach 0.7, respectively. As indicated, the theoretical computations provide an excellent approximation of the initial normal force curve slope at all three subsonic Mach numbers. As a result, the agreement between the theoretical and experimental data is excellent through the linear aerodynamic range to approximately 7 deg. angle of attack. At higher angles of attack, the semiempirical formulation used to predict the nonlinear portions of the curve correctly approximates the curve trend, but significantly underpredicts the normal force coefficient magnitude. Axial force coefficient is slightly overpredicted at Mach 0.25 at small angles of attack. However, at Mach 0.5 and 0.7, CA is accurately predicted throughout the angle of attack range.

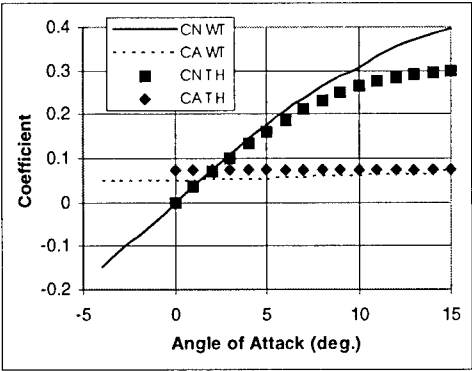


Figure 12. CN and CA Comparison for Fin G13 at Mach 0.25.

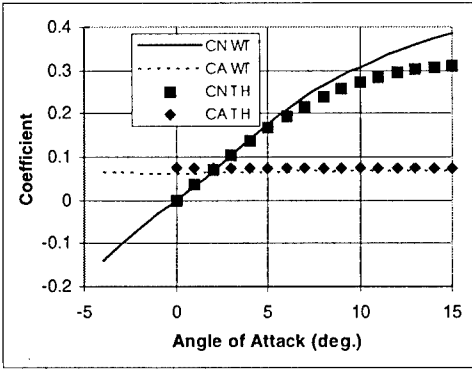


Figure 13. CN and CA Comparison for Fin G13 at Mach 0.5.

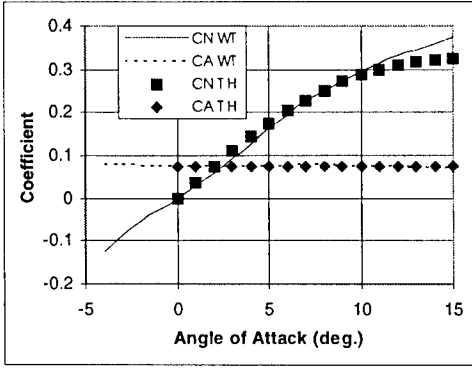


Figure 14. CN and CA Comparison for Fin G13 at Mach 0.7

Significant improvement in the normal force coefficient prediction is evident at both Mach 0.5 and 0.7 as illustrated in Figures 15 and 16, respectively. As indicated, the initial coefficient slope is accurately predicted and the nonlinear aspect of the curves are captured throughout the angle of attack ranges. Axial force coefficient is also predicted accurately for this configuration although a slight overprediction is evident for this coefficient at Mach 0.7.

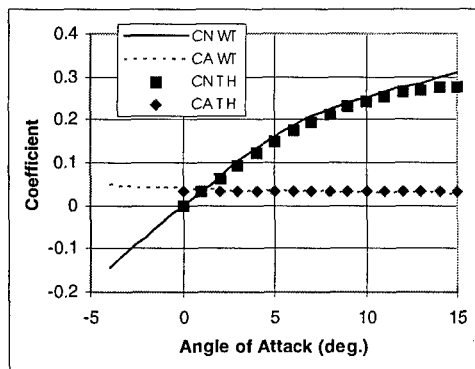


Figure 15. CN and CA Comparisons for Fin G15 at Mach 0.5.

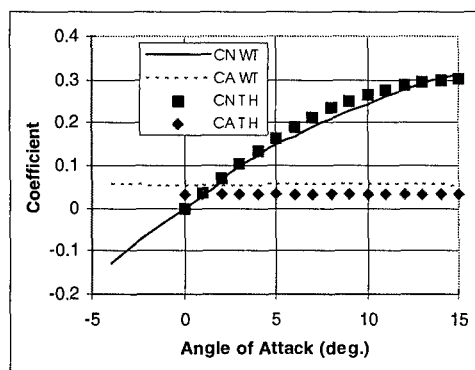


Figure 16. CN and CA Comparisons for Fin G15 at Mach 0.7.

A slight shortcoming in the theoretical formulations prediction accuracy is exhibited in Figures 17 and 18, which illustrate the CN and CA comparisons for fin G16 at Mach 0.5 and 0.7, respectively. As indicated in Figure 11, the geometric difference between fin G16 and G15 is the 0.2 in. increase in fin chord length for G16. This additional lifting area provides a significant increase in normal force coefficient magnitude for G16. Although the initial normal force coefficient slope is accurately predicted at both Mach numbers, the nonlinear aspects of the curves are underpredicted for this fin configuration. This indicates the nonlinear formulation utilized in predicting normal force coefficient does not accurately model the effects of chord length increase on a fin. Axial force prediction results are very similar to those for G15. At Mach 0.5, the CA prediction is accurate throughout the angle of attack range, while at Mach 0.7, the coefficient is underpredicted.

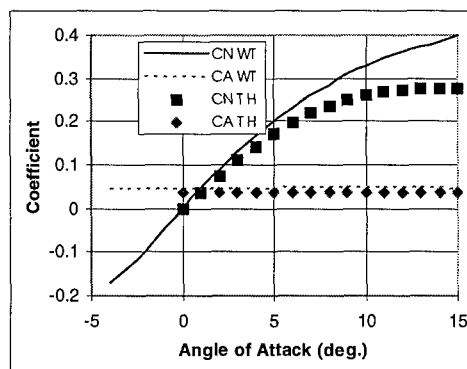


Figure 17. CN and CA Comparisons for Fin G16 at Mach 0.5.

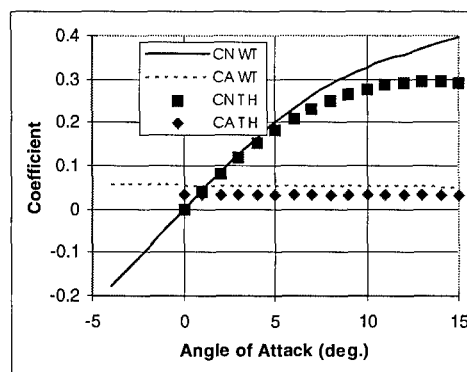


Figure 18. CN and CA Comparisons for Fin G16 at Mach 0.7.

Excellent prediction results were obtained for fin G12 at Mach 0.7. As indicated in Figure 19, both linear and nonlinear aspects of the normal force coefficient curve and the magnitude of the axial force coefficient were accurately predicted throughout the angle of attack range.

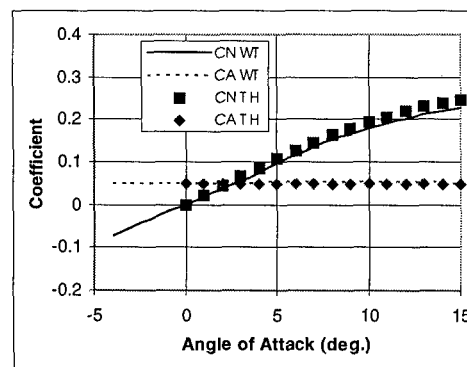


Figure 19. CN and CA Comparisons for Fin G12 at Mach 0.7.

Theoretical formulations developed for supersonic Mach numbers also provided reasonably accurate prediction results. Figures 20 through 23 illustrate the CN and CA comparisons for various grid fins in the horizontal position at Mach 2.5. As with the subsonic experimental data, these data were taken directly from the fin balance and therefore include the effects of body upwash.

As indicated in the various illustrations, grid fin configurations exhibit much more linear aerodynamic behavior in the supersonic Mach regime. As a result, inaccuracies in normal force coefficient prediction due to the

nonlinear semiempirical formulation are not nearly as significant as in the subsonic case. In all cases, the initial normal force coefficient slope is slightly overpredicted. However, discrepancies between the theoretical and experimental curves are less than 15% throughout the angle of attack range.

Axial force prediction using the supersonic formulations were consistently accurate for all grid fin configurations investigated, although the slight drop off in axial force magnitude with increasing angle of attack was not captured. This result occurs because the fin axial force was assumed independent of angle of attack in development of the formulation.

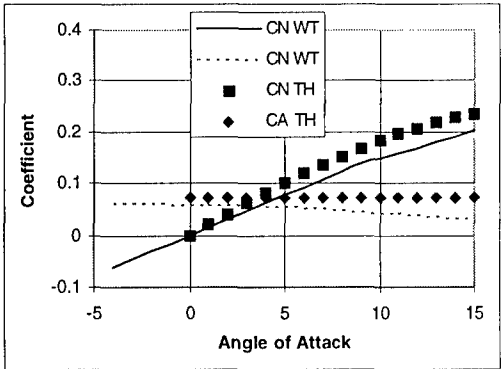


Figure 20. CN and CA comparisons for G12 at Mach 2.5.

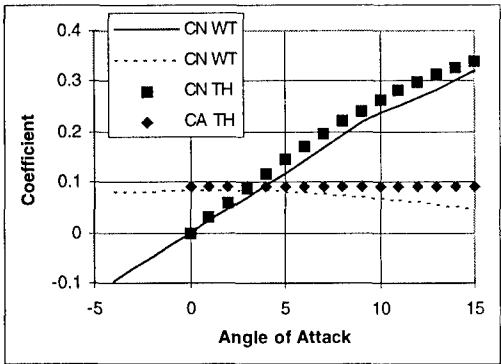


Figure 21. CN and CA comparisons for G13 at Mach 2.5.

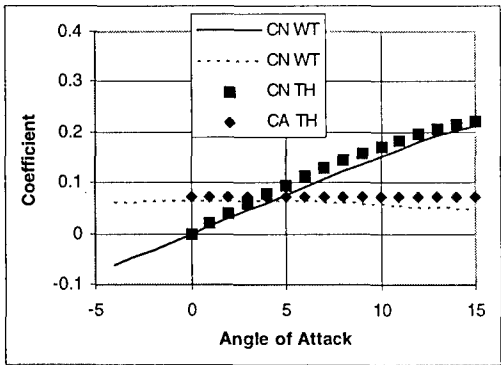


Figure 22. CN and CA comparisons for G15 at Mach 2.5.

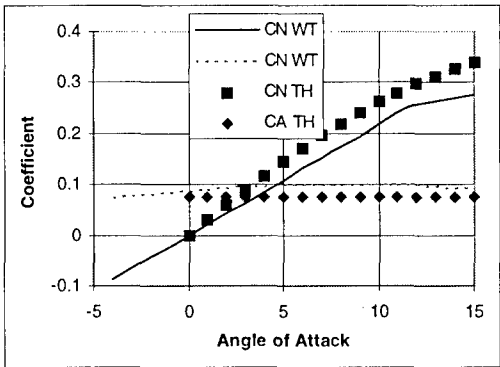


Figure 23. CN and CA comparisons for G16 at Mach 2.5.

Experimental data for fin orientations other than cruciform are somewhat limited, however, data were obtained for fin G13 in the "X" orientation at Mach 0.7 and 2.5. Prediction results for these fin orientations were very similar to those already presented. Figure 24 illustrates fin CN and CA coefficients for fin G13 rolled 45 deg. from the horizontal position. Similar to the cruciform orientation results, the linear aerodynamic portion of the curve is correctly predicted and nonlinear aspects of the curve are significantly underpredicted. Axial force coefficient is again predicted accurately throughout the angle of attack range.

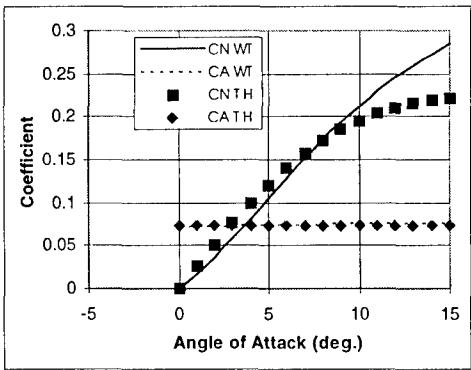


Figure 24. CN and CA comparisons for G13 at a 45 deg. Roll Angle at Mach 0.7.

Theoretical approximations at Mach 2.5 for fin G13 at a 45 deg. roll angle are presented with appropriate experimental data in Figure 25. As indicated, the normal force coefficient is accurately predicted throughout the angle of attack range, while the axial force is again overpredicted.

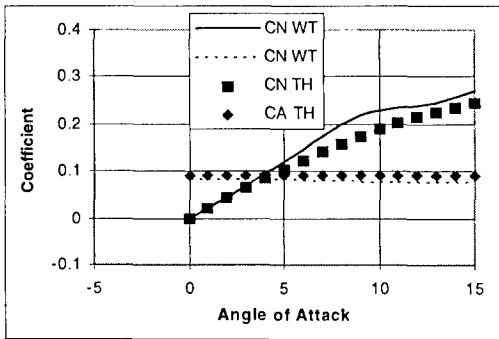


Figure 25. CN and CA comparisons for G13 at a 45 deg. Roll Angle at Mach 2.5.

6.0 CONCLUSIONS

1) The theoretical formulations developed for predicting the aerodynamic characteristics of grid fins in subsonic flow appear adequate for preliminary design purposes. Vortex lattice theory provides an adequate estimation of grid fin normal and axial force in the linear aerodynamic range provided body upwash terms are included. Empirical formulations developed to extend aerodynamic prediction capability to higher angles of attack provide good agreement with experimental data for a wide variety of grid fin configurations.

2) Theoretical formulations developed for application in the supersonic Mach regime are also adequate for preliminary grid fin design purposes. Application of a slightly modified version of Evvard's theory provides adequate estimations of grid fin lift curve slopes in the linear aerodynamic range. Empirical formulations developed to extend prediction capability to higher angles of attack provide good agreement with available experimental data.

3) Flowfield structure within the grid fin cells is not well understood in the transonic Mach regime, complicating the development of adequate prediction theories. However, initial theory development for transonic Mach numbers both above and below Mach 1.0 are promising.

4) Available experimental data have not been collected with theoretical development as a primary concern. As a result, separate validation of the various components effecting the force and moment characteristics of grid fins such as body upwash and fin carryover are not yet possible. Additionally, the influence of grid fin roll orientation on the force and moment characteristics is not well understood. Future experimental analysis and theoretical development which address these components separately should provide a more accurate means of predicting grid fin aerodynamic characteristics.

7.0 REFERENCES

1. Belotserkovsky, S. M., Odnovol, L.A., et.al, "Wings With Internal Framework", Machine Translation, FTD-ID(RS)T-1289-86, Foreign Technology Division, Feb. 1987.
2. Washington, W. D. and Booth, P. F., "Post Test Report for a Grid Fin Technology Wind Tunnel Test," Technical Report -RD-SS-89-6, US Army Missile Command, Redstone Arsenal, AL, July 1989.
3. Washington, W. D. and Miller, M. S., "Grid Fins - A New Concept for Missile Stability and Control," AIAA 93-0035, January 1993.
4. Burkhalter, J.E., Frank, Harris M., "Grid Fin Aerodynamics for Missile Applications in Subsonic Flow," Journal of Spacecraft and Rockets, Vol. 33, No. 1, Jan-Feb 1996.
5. Burkhalter, J.E., "Validation of Aerodynamic Prediction Methods for Grid Fins in Subsonic Flow," Contractor Final Report, Auburn University, U.S. Army Missile Command Contract No. DAAL03-91-C-0034, Jan., 1997.
6. Roskam, J., Methods for Estimating Drag Polars for Subsonic Airplanes, Published by the Author, 519 Boulder, Lawrence, Kansas, 1971.
7. Washington, W.D. and Booth, P. F., "Wind Tunnel Data Analysis for a Curved Grid Fin Concept," TTCP Technical Panel W-2, Internal Rept., Eglin AFB, FL, May 1990.
8. Miller, M.S., "An Experimental Investigation of Grid Fin Drag Reduction Techniques" AIAA 94-1914, June 1994.
9. Washington, W. D., Miller, M. S., "Experimental Investigation of Grid Fin Aerodynamics: A Synopsis of Nine Wind Tunnel and Three Flight Tests", AGARD Applied Vehicle Technology Panel Symposium and Meeting on Missile Aerodynamics, Paper 10, May 1998.
10. Burkhalter, J.E., "Characterization of Grid Fin Aerodynamics for Subsonic Flow," Final report, Cotntract No. DAAL03-91-C-0034, TCN Number:95-197, Scientific Services Program, AMSMI-RD-SS-AT, Redstone Arsenal, AL, Sept. 1995.
11. Burkhalter, J. E., "Grid Fins in Supersonic Flow," Contractor Final Report, Contract No. DAAH01-92-D-R002, DO Number NRC 0211, AMSMI-RD-SS-AT, Redstone Arsenal, AL, Sept. 1994.

Computation of Flows Past Grid Fin Missiles

M. Khalid, Y. Sun, and H. Xu.

Institute for Aerospace Research, National Research Council,
Ottawa, K1A 0R6, Ontario, Canada

Mahmood.Khalid@nrc.ca

Summary

The paper contains a CFD study of flows past missiles and isolated stores equipped with different types of control surface devices or other attachment equipment used for carriage purposes. Traditionally, missile designers have relied on planar surface control mechanisms, both as wings and/or fins for providing the necessary aerodynamic adjustment for in-flight guidance. It has been found, however, that grid fin type control surfaces may be more advantageous in terms of generating relatively higher normal force coefficients (C_N) and smaller hinge moments. The drag from these grid fin control surface devices tends to be somewhat higher. This feature is not always altogether undesirable, particularly when the intent is to decelerate a missile released from a fast moving aircraft.

Introduction

Grid fins are a paneled frame work of flow channels rather like honey bee structures, which are installed normally on missile aft surfaces to function like control fins. The inner density and shape of flow-through channels may be designed to tailor a certain lift and drag requirement. In order to minimize drag, the wetted area in the axial sense is rather short and stubby in the radial direction, which provides attractive hinge moment features. The lifting capabilities of grid panels make them ideal for enhanced lift and pitching moment characteristics. The fact that they can be deployed in an all rotating sense (synchronous or counter rotating), provides for a trim incidence setting of the grid fin with respect to the mean missile angle of attack. This provides fine tuning in roll, and also permits additional control for the pitching moment adjustments without imposing intolerable hinge moments experienced on conventional fins. They can also be made to move about their hinge axis to allow a forward and backward sweep angle setting. All these attributes make grid fins good candidates as in-flight control devices worthy of both CFD and experimental investigation.

The first research work on grid fins, as control surface devices for missiles, was carried out by Belotserkovskiy and Odnovol et al [1]. Earlier theoretical work relied mainly on empirical formulae produced by curve fitting experimental data and using charts and tables produced from various wind tunnel measurements.

In terms of subsonic flow modeling for grid fins, vortex lattice method [2] has been used previously, which enabled some basis of comparison with measurements. Strictly speaking, these subsonic studies were valid at low angles of attack, but failed to represent the flow meaningfully at angles of attack beyond 5 to 8 degrees. For supersonic flow, the researchers have relied on either the Evvard's theory as described in [3], which is applicable to thin wings (3D flow), or the shock expansion / Prandtl Meyer theory [4] which is only valid for 2-D regions of the flow with no accountability for the end effects.

The complexity of the flow through grid fins, especially at higher angles of attack, where even the flow on a simple missile without any control devices becomes challenging, warrants that computational methods be considered as realistic options for solving the complete flow field.

Unfortunately, in the past little effort has been made in applying CFD to grid fin problems. Except for the work reported by the present authors in [5] and [6], there have been no CFD studies of grid fin missiles. The theoretical work mentioned earlier introduced empirical adjustments to account for the higher angles of attack restrictions or the end plate effects in the case of the 2-D shock expansion theory. Equally, there is no evidence of any accounting for the viscous or the blockage effects from a boundary layer, which may develop within the channels. A meaningful CFD investigation would attempt to address some of these critical issues.

The present investigation contains an Euler study of grid fin missiles, with flow through channels ranging from a coarse configuration of 9 panels to a dense configuration containing 38 panels facing the flow. The Euler option was mainly dictated by the limitations of computational resources, however, it would not be too difficult to convert the present grids for an equivalent viscous investigation.

As there is little flow field information available on grid fin missiles in literature, it was considered appropriate to compare some of the present CFD flow predictions on simpler missile shapes against available data. The simple ogive-cylinder [7] was one of the shapes selected for this preliminary exercise. Similarly, where detailed flow field information on more complex missile shapes was not available, integrated Euler loads on a plane fin missile and a DREV Mk-82 store with control fins and attachment lugs, were compared with measurements to judge the suitability of Euler predictions. Where possible the aerodynamic performance of the grid fin missile was also compared directly against a corresponding conventional fin missile.

Grids

The grid for the simple ogive-cylinder was produced using an algebraic algorithm. The resulting (60X60X60) mesh was used for both Euler and Navier Stokes computations in the present study and is shown in Figure 1. This one block mesh has one degenerate surface at its cylindrical axis, which communicates with the far field cylindrical surface, while the upstream surface talks to the downstream mesh at the trailing edge of the missile. Free stream conditions were imposed at the upstream and at the radial far field boundary, which enclosed the two symmetry planes of the cylindrical grid. The plane containing the base of the missile contained the extrapolation boundary condition.

For structured multi-block meshing of various configurations, ICEM CFD grid generation package was used. The DDN and MULCAD facilities, which are special routines in the grid generator for treating the geometry and the mesh details respectively, were extensively used during grid generation. The CFD Mulcad module is then used in conjunction with Padamm mesher, which employs both the transfinite interpolation and Hermite transfinite interpolation schemes. The resulting mesh is mapped onto the geometry using patch surface association facility.

The block structure arrangement in the near field for the Mk-82 store without any lugs is shown in Figure 2. The topology for this configuration is relatively simple. In all, the complete mesh required 8 separate domains to produce the mesh. As observed in Figure 2, next to the inner domain, an exterior larger domain (not shown) is placed, which envelopes the complete flow field stretching out to the far field in the radial direction. In axial directions, this exterior domain extends for about 4 missile lengths ahead of the nose in the upstream direction containing the free stream boundary condition. For the downstream flow field, an extrapolation boundary condition is imposed at about 3 missile lengths aft of the base. In the azimuthal direction, the computational domain is closed with two planes on which the symmetric boundary conditions are prescribed. In the radial direction, far field free stream boundary condition is imposed on the plane joining the two symmetry planes at a radius of about 10 missile diameters. Separate domains have also been installed in between the fins and the inner cylindrical surface of the store. A close up of the topology and the associated mesh in regions between the fins is shown in Figure 3 and Figure 4 for the + and x configurations of the store, respectively.

For all the surfaces (cylindrical body and plane fin surfaces) of the inner domains, a fine block mesh was installed next to the surface. The mesh points in this domain could, in later adjustments, be used for fine tuning the mesh density normal to the surface. In fact, wall distances for a few Navier Stokes computations of this lugs-off missile, were suitably adjusted for viscous resolutions.

A similar strategy to the one described above, was used for constructing the mesh for the plane fin missile used for performance comparison against the grid fin missile. The grid for this missile is shown in Figure 5.

The mesh generation for the Mk-82 with lugs was more complicated and needed a total of some 19 domains for the complete mesh. It required a number of separate domains for regions in between, ahead of and on top of the lugs. The mesh [See Ref. 8 for details] for Mk-82 with lugs is shown in Figure 6.

For the grid fin missile, the grid topology consists of a main cylindrical domain, which wraps around the main body of the missile and

extends to the far field in the radial direction. In the axial direction, this cylindrical domain stretches from far upstream towards the base of the missile. The blocks for each panel are appropriately housed within this main cylindrical domain. The meshes for each channel consist of regular six face block meshes as shown in Figure 7. The mesh blocks for individual channel also stretched from the far upstream towards the downstream in parallel with the main block. The grid fin panel surfaces are appropriately selected from mesh block interfaces. Since the present study did not involve any yaw displacement ($\Psi=0$) of the model, only a symmetric plane model was meshed. As shown in Figure 7, all of the half-model missile configurations required meshing of at least 2 complete grid fin systems. The most complicated mesh for missile with grid fin surfaces contained 97 blocks (38 panel per grid fin) with some 1.5 million grid points for the complete mesh. Beyond the grid fin wall geometry, the mesh expands gradually in the radial direction towards the far field. This type of individual block topology is particularly well suited for the situation when one grid fin may be deployed at an α setting different from its pairing counterpart or when the grid fins are swept backwards or forwards from their normal setting. The last feature was utilized when studying grid fin missile performance with grid fin deflected through a sweep angle of 20 degrees.

Analytical Methods

In order to provide some background to the earlier theoretical work, it would be appropriate to provide an outline (for details see appropriate references) of the analytic methods that have been used in the past for investigating the grid fin missile performance. As mentioned earlier, vortex lattice methods were first used for evaluating the aerodynamic coefficients in the subsonic flow regimes.

The vortex lattice approach is based on the Biot-Savart equation for the field velocity V :

$$\bar{V}(x, y, z) = -\frac{\Gamma\beta^2}{4\pi} \int \frac{\bar{r} \times d\bar{l}}{|\bar{R}_\beta|^3}$$

Where Γ is the filament strength, and r is the vector from a field point (x, y, z) to a differential length of the vortex filament. β is the compressibility factor $\sqrt{1-M^2}$ and R_β is the elliptic radius. Ref [2] carries detailed description on how various vortex filaments may

be distributed on the fin panels. Essentially the procedure is based on placing bound vortices on each side (element) of the four-sided parallelogram, which constitutes a given panel. The element in turn is divided into a rectangular array of sub elements each containing a lattice network of bound vortices. For the fine grid fin configuration studied in the present investigation, the number of elements required to model the fin as well as the support brackets would be close to 90. Again it was learnt in earlier studies that the theory was basically applicable to flows with angle of attack up to about 5 to 8 degrees, beyond which point empirical corrections based on wind tunnel measurements were necessary to extend its range to higher angles of attack.

The analytic supersonic flow modeling of grid fin geometry is based on the work reported in reference [3]. The theory is applicable to thin wings and is used to calculate the change in pressure coefficient (ΔC_p) across a flat plate at angle of attack. Based on the shock expansion techniques the pressure perturbation equation is given by:

$$\Delta C_p = \frac{\Delta p}{1/2\rho V^2} = \frac{2\rho V\phi_x}{1/2\rho V^2} = \frac{4}{V}\phi_x$$

The pressure perturbation is represented by Δp and ρ refers to the fluid density. The potential function ϕ satisfies the linearized partial difference equation of the flow, which is solved using various boundary conditions associated with the panel. As explained in [9] the evaluation of the pressure coefficient is not a straightforward process, because the shock pattern resulting from different regions of the panel at some α and supporting end plates is quite complex. The aerodynamic loads are evaluated by suitable integration of the pressure loads. It must again be recognized that above supersonic theory cannot adequately account for high angle of attack end plate or viscous effects. As for the subsonic vortex lattice theory, the supersonic theory too has been adjusted empirically to provide reasonable agreement with measurement at angles of attack as high as 12 degrees.

Numerical Method

The present computations were performed using NPARC code, where the implicit pentadiagonal form of the approximate factorization scheme due to Beam and Warming [10] is used for solving the Euler/Navier-Stokes equations. The multi-step Runge-Kutta scheme due to Jameson, et al. [11] based on the cell-vertex control volume, is also available. Second and fourth order artificial dissipation are used in both schemes, and the corresponding dissipation coefficients are set at 0.25 and 0.64 for fast convergence. There are a number of options available within NPARC for selecting the type of implementation strategy used for the second and fourth order dissipation coefficients. These include: the Jameson-style artificial viscosity model, the cell Reynolds number monitoring scheme or the one based on directional coordinates due to Siclari et al [12].

In the present study, the NPARC version supplied in 1996 by the NASA LeRC/AEDC Alliance [13] was used for both Euler and Navier-Stokes computations. Among other updates furnished in this version are the relaxation of the overlap condition for abutting meshes in a multi-block problem, and a provision for the time accurate solution. While the NPARC code already has provision for a number of algebraic (Baldwin-Lomax), one equation turbulence model (Baldwin-Barth) and two equation models ($k - \epsilon$, $k - \omega$), another turbulence model by Spalart-Allmaras has been added to the existing turbulence model library. Various details regarding theoretical background and other capabilities of NPARC can be found in the reference by Cooper and Sirbaugh [14].

In the present study, owing to computational resource limitations, most of the grid fin solutions were obtained using the Euler option in NPARC. For the simpler missile cases such as the ogive-cylinder and Mk-82 lugs-off missile some Navier Stokes computations were carried out using the Baldwin-Lomax turbulence model. Once appropriate computational power is in place, other higher order turbulence models will be studied for more challenging grid-fin configurations. The implementation of the boundary conditions in the NPARC restart file is produced using the interface facility provided by ICM CFD grid generation package.

Results and Discussion

As there are no flow field measurements available for the grid fin, the simple missile shown in Figure 1 was selected for this portion of the validation exercise.

Figure 8 shows the flow field pressure contours for the DREV missile at $M = 3.5$, $\alpha = 8^\circ$ at a Reynolds number of 1.123×10^6 when normalized with respect to the missile diameter. As expected the flow shows a region of high pressure field between the shock and the nose at the most windward generator. The opposite side of the ogive nose shows the typical expansion flow region. More explicit surface pressure coefficient comparisons at a number of stations along the length of the missile, from both Euler and Navier Stokes computations are shown in Figures 9 to 11. The quality of agreement between the Navier Stokes computations based on Baldwin-Lomax turbulent model closure, and the experimental data speaks for itself. The Euler results seem to be satisfactory for forward regions of the missile, but beyond an axial station of about $x/D \approx 3.0$, the discrepancy between measurements and Euler results becomes more noticeable.

This behaviour, as observed from the pitot pressure traces in Figure 12 must result from increasing separated flow in the aft regions of the missile. The pitot pressure traces shown in Figure 12 were also compared more explicitly against the measurements [7]. Figure 13 shows that the computed pitot traces at station $x/D = 11.5$, matched very well against the experimentally obtained pitot traces.

To assess the quality of the integrated data on a relatively more sophisticated missile shape, the drag coefficients as obtained from present Euler computations on Mk-82 missile with attachment lugs and fins were plotted against the measured data in Figure 14. For this particular case, an empirical skin friction component based on ogive-cylinder and flat plate estimates as described in [15], were also appropriately added to the Euler results. For the simple lugs-off Mk-82 case, results from two complete Navier Stokes computations are also shown. Owing to security restrictions, only two experimental data points obtained from a Canadian facility [16] are shown. The data obtained from another foreign source were removed. A comparison of the complete data (not shown here) shows a

satisfactory comparison between the present Euler+skin friction results and the measurements.

In the absence of any flow field data, the Mach number contours past a 38 panel fine grid fin system is shown in Figure 15 without any formal comparison of results with any surface measurements. The flow displays a rather complex system of shock patterns from various edges and corners of the channels.

Figure 16, however, shows a more meaningful comparison of the normal force coefficient data from Euler computations on a coarse and a fine grid fin against measurements from [17]. In order to compare the performance of grid fin against a more conventional type fin, computed and measured data for a corresponding planar missile are also shown. The free stream Mach number for these computations, was set at $M = 2.5$ and the angle of attack α ranged from 0 to about 15 degrees. It is confirmed that grid fins of appropriate grid channel density can provide higher lifts than the corresponding planar fins. It was also noted that comparison between Euler and measured data for the grid fins was much better than the comparison for the plane fins. This is attributed to the fact that axial geometry of panels on the grid fins is much shorter and stubbier than the larger surfaces of the plane fins. The flow on grid fins does not really get a chance to impart its more elaborate viscous effects. Without having to put up with strong viscous implications, that would be present on a larger plane fin, the Euler computations perform better on the grid fins. For thicker grid panels under strong shock conditions the agreement would deteriorate. Thus, in most weak shock cases a simple Euler or a laminar flow calculation would provide a good estimate of the aerodynamic loads.

Computations on grid fin missiles were also carried with the grid-fin deployed at a sweep back of 20 degrees. As mentioned earlier, the existing mesh for the normal grid fin configuration was suitably adjusted by realigning certain blocks within the same mesh. Present computations at $M = 2.5$ and $\alpha = 0$ with the grid fin sweep angle at 20 degrees gave a C_N value of about 0.09 as compared to a value of about 0.1 from experiment [18]. Mach number contours for this case with the grid fin deployed at a sweep back angle of $\psi = 20$ degrees is shown in Figure 17.

Conclusion

It was observed that CFD provides a reliable means of studying flows past missiles equipped with different types of control surfaces or other attachment equipment installed for carriage purposes.

It was also verified that appropriately designed grid fin surfaces can provide higher normal loads in comparisons to missiles with planar control surfaces. The hinge moments from the grid-fin missile owing to a smaller moment arm are expected to be lower than those obtained from planar fin missile.

It is recommended that flow field measurements such as:

- the pressure measurements on the surface,
- pitot pressure measurements at appropriate locations of the missile near the grid fin region,
- flow visualization aft of the grid fin region,

as well as additional balance load measurement under different grid fin deployments (twist and yaw) be carried out for a more complete verification of the advantages of this control surface technology.

References

1. Belotserkovskiy, S. M., Odnovol, L. A., et al, 'Wings With Internal Framework,' Machine Translation FTD-ID(RS)T-1289, Foreign Technology Division, Feb. 87.
2. Burkhalter, J. E., et al, 'Nonlinear Aerodynamic Analysis of Grid Fin Configuration,' Journal of Aircraft, Vol. 32, No. 3, May-June 1995.
3. Harmon, S. M., and Jeffreys, I., 'Theoretical Lift and damping in Roll of thin Wings with Arbitrary Sweep and Taper at Supersonic Speeds- Supersonic Leading and Trailing Edges,' NACA TN 2114, 1950.
4. Kueth, A. M., and Chow, C. Y., Foundations of Aerodynamics, John Wiley and Sons, New York, Fourth Edition, 1986, pp 222-236.
5. Sun, Y. and Khalid, M. 'Prediction of Supersonic Flow around Grid Fin Missile Using NPARC', The Fifth Annual Conference of the Computational Fluid Dynamics Society of Canada, CFD 97 May 25-27, 1997.
6. Sun, Y. and Khalid, M. 'A CFD investigation of Grid Fin Missiles', AIAA 98-3568, 34th, AIAA/ASME/SAER/ASEE Joint propulsion Conference & Exhibits, July 13-15, 1998 / Cleveland, OH.

7. Sturek, W. B., et al 'The application of CFD to the Prediction of Missile Body Vortices', AIAA 97-0637, 35th. Aerospace Sciences Meeting & Exhibits, January 6-10, 1997/Reno, NV.
8. Xu, H. Y., Khalid, M. and Sun, Y., 'A CFD study of Mk-82 Store with Attachment Lugs,' CFD 98, The Sixth Annual Conference of the CFD Society of Canada, June 1998.
9. Burkhalter, J., 'Grid Fins for Missile Application in Supersonic Flow,' AIAA 96-0194, 34th. Aerospace Sciences Meeting & Exhibits, January 15-18, 1996/Reno, NV.
10. Beam, R. and Warming, R. F., 'An implicit Finite Difference Algorithm for Hyperbolic Systems in Conservation Law Form.' Journal of Computational Physics, Vol. 22, No. 1, September 1976, pp. 87-110.
11. Jameson, A., Schmidt, W., and Turkel, E., 'Numerical Solutions of the Euler Equations by Finite Volume Methods Using Runge-Kutta Time-Stepping schemes.' AIAA Paper No. 81-1259, AIAA 14th. Fluid and Plasma Dynamics Conference, Palo Alto, California, 1981.
12. Siclari, M. J., Delguidice, P., Jameson, A. 'A Multigrid Finite Volume Method for Solving the Euler and Navier-Stokes Equations for High Speed Flows.' AIAA paper No. 89-0283, AIAA 27th. Aerospace Sciences Meeting, Reno, Nevada, January 1989.
13. NPARC User's Guide', NASA LeRC/AEDC Alliance, Version 3.0, Sept., 1996. Washington,
14. Cooper, G. K., and Sirbaugh, J. R. PARC Code: Theory and Usage. AEDC-TR-89-15, Sverdrup Technology, Inc.
15. Special Course on Missile Aerodynamics, AGARD Report 804, June 1994.
16. Lesage, F., Private Communication (DREV).
17. Washington, W. D., and Miller, M. S., 'Grid Fins- A New Concept for Missiles Stability and Control,' .'' AIAA paper No. 93-0035, AIAA 31st. Aerospace Sciences Meeting, Reno, Nevada, January 11-14, 1993.
18. Washington, D. Wm. And Miller, Mark S., 'Curvature and Leading Edge Sweep Back Effects on Grid Fin Aerodynamic Characteristics,' AIAA 93-3480-CP

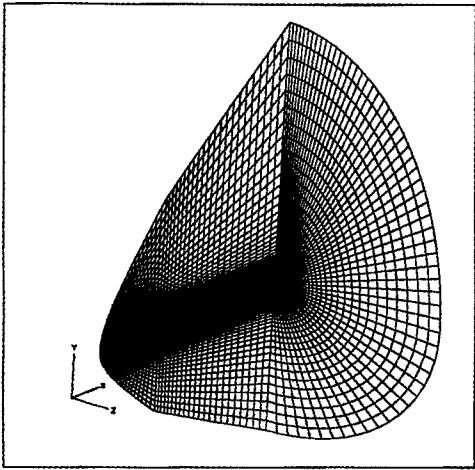


Figure 1: Mesh around simple ogive-cylinder missile

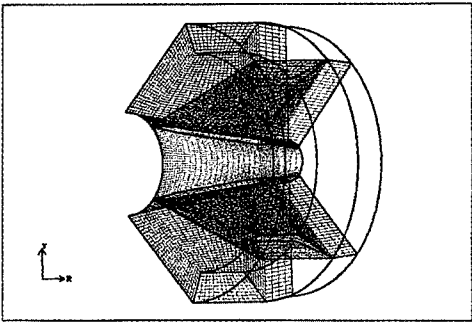


Figure 4: Topology and grid arrangement near the fins for x configuration

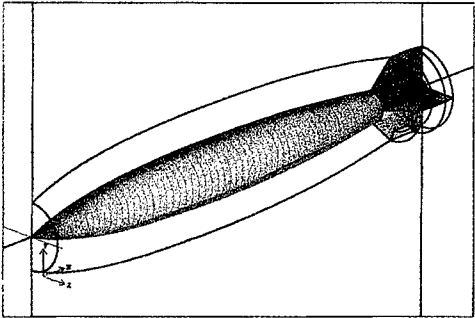


Figure 2: Mesh and domain topology in the near field of Mk-82 store

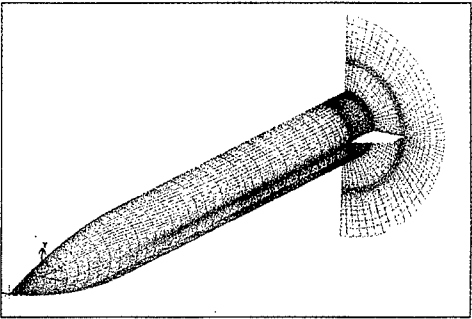


Figure 5: Surface grid of plane missile

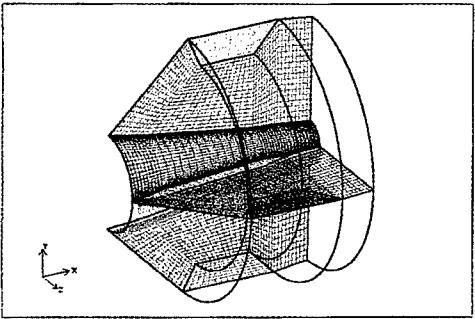


Figure 3: Topology and grid arrangement near the fins for + configuration

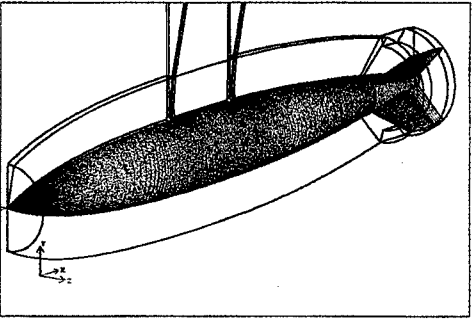


Figure 6: Mesh and domain topology around Mk-82 store fins at x configuration

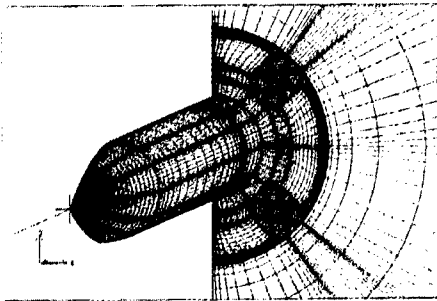


Figure 7: Structured grid for a Grid Fin Missile

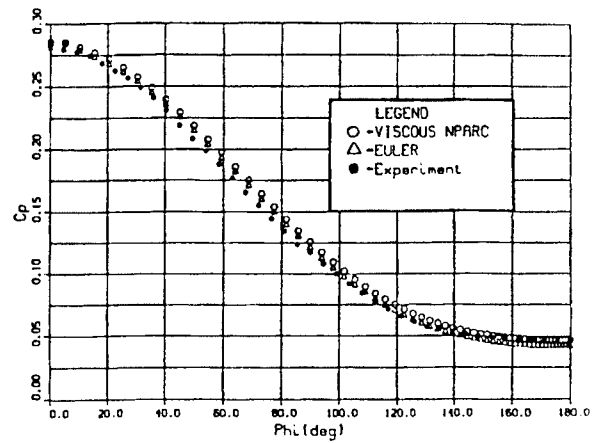


Figure 9: C_p distribution at $x/D=0.8$, $M=3.5$, $\alpha=8$, $R/D=1.123 \times 10^6$



Figure 8: Pressure distribution of ogive-cylinder missile from N-S computation at $M=3.5$, $\alpha=8.0$ deg, $R/D=1.123 \times 10^6$

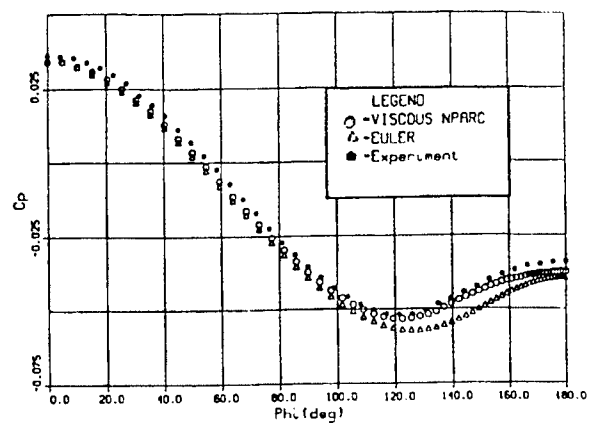


Figure 10: C_p distribution at $x/D=3.5$, $M=3.5$, $\alpha=8$, $R/D=1.123 \times 10^6$

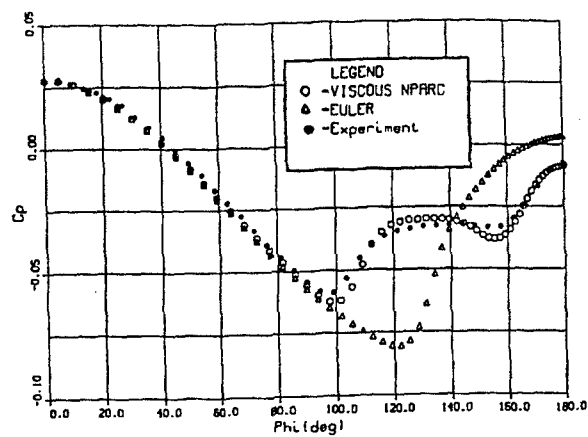


Figure 11: C_p distribution at $x/D=6.5$, $M=3.5$, $\alpha=8$, $R/D=1.123 \times 10^6$

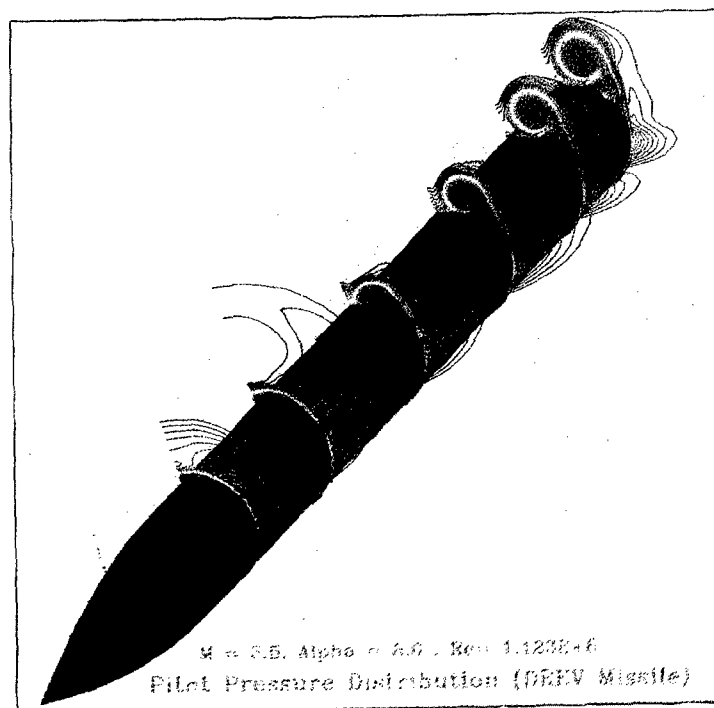


Figure 12: Pitot pressure distribution of ogive-cylinder missile at $M=3.5$, $\alpha=8.0$ deg, $R/D=1.123 \times 10^6$

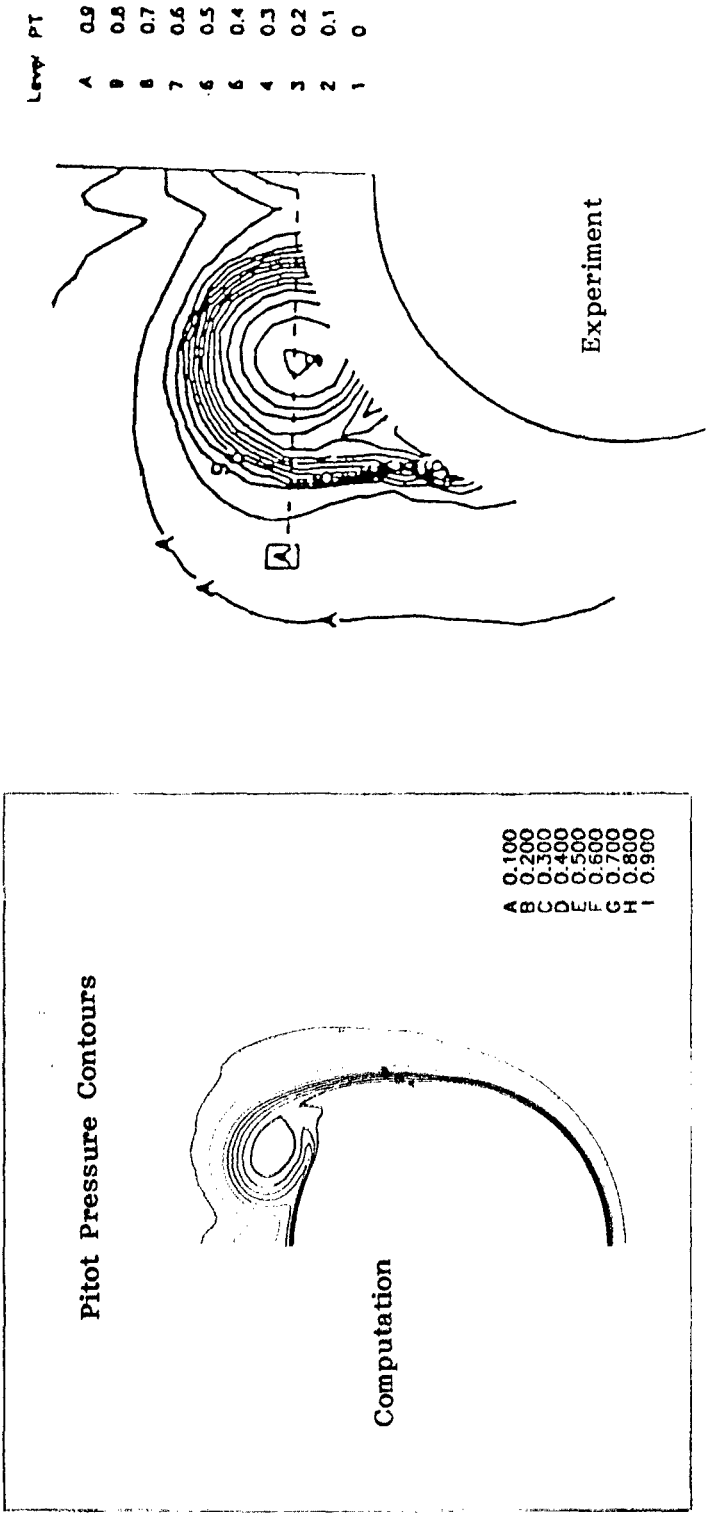


Figure 13: Comparison of pressure distribution between computation and experiment at station $x/D=11.5$, $M=3.5$, $\alpha=8.0$ deg, $R/D=1.123\times 10^6$

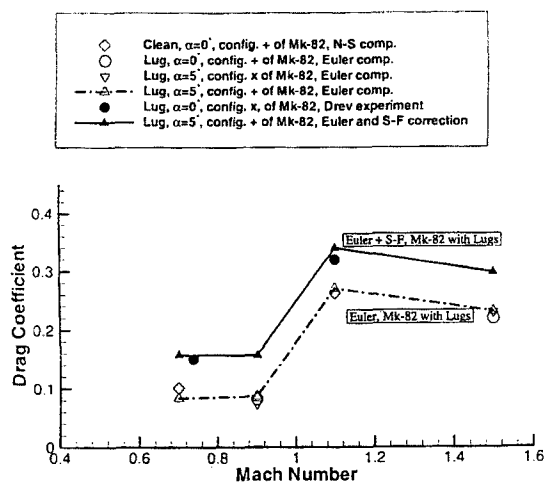


Figure 14: Drag coefficient versus Mach number for Mk-82 store

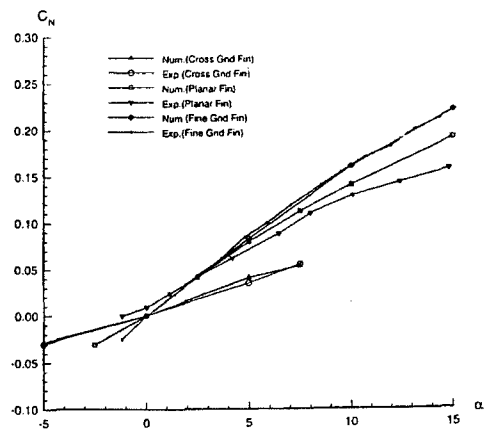


Figure 16: Normal force coefficient C_N versus angle of attack

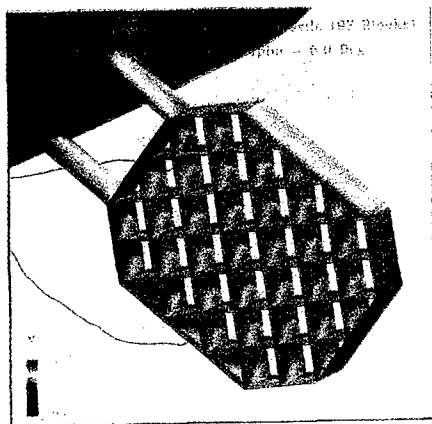


Figure 15: Mach number distribution of Grid Fin Missile at $M=2.51$, $\alpha=5^\circ$ deg

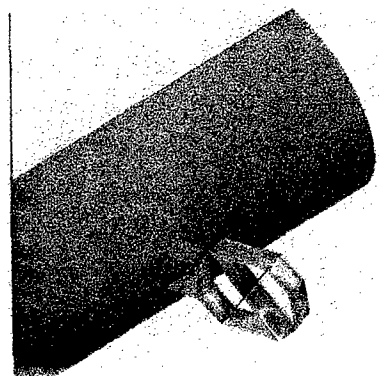


Figure 17: Mach number distribution of Grid Fin Missile at $M=2.51$, $\alpha=2.5^\circ$ deg. Grid Fin Sweep Angle $\psi=20^\circ$ deg

Experiments and Analyses of an Aerospike Flow Environment for Protecting Infrared Missile Dome

E. J. Boudreaux¹, V. S. Krishnamurty^{2,3}, A. M. Mitchell¹ and W. Shyy²

¹United States Air Force Research Laboratory
Munitions Directorate
Eglin Air Force Base, Florida 32542 U.S.A.

²University of Florida
Department of Aerospace Engineering, Mechanics & Engineering Science
Gainesville, Florida 32611 U.S.A.

³Kohler Co., Kohler, Wisconsin 58044 U.S.A.

SUMMARY

In the late 1980s, Air Force Research Laboratory began research in the use of aerospike technology to reduce the heating rate on an infrared dome for a high speed, extended range tactical missile. Results from wind tunnel tests, simulations and analyses provided a database for modelling the flow field created by an aerospike. The effects of turbulence on the performance of the aerospike arrangements were analyzed in the k- ϵ based modelling framework with emphasis on the influence of factors such as streamline curvature and shock discontinuities.

1. INTRODUCTION

In the late 1980s and early 1990s the Air Force Research Laboratory Munitions Directorate began investigating dual band imaging infrared (IR) and radio frequency (RF) terminal sensors and domes for an advanced tactical high speed, long range air-to-air missile (Refs. 1, 2, 3, 4 and 5). A dual band terminal sensor and dome suite integrated in a long range, high speed tactical missile can provide a unique capability at launch and in the terminal phase of the missile trajectory against enemy counter measures. A tactical missile operating in this scenario requires a unique sensor and dome configuration that must satisfy several technological challenges. These challenges include electromagnetic compatibility of the sensors, sensor and dome survival in a high speed, long range flight environment, and configuration compatibility among the sensors, domes and the missile to minimize drag effects which reduce missile flyout distances.

An example of one of the technological challenges for this type of tactical mission is the performance of the sensor suite in this harsh flight environment. Unique architectural, physical and electromagnetic features of a dual band sensor suite are required to satisfy these environmental requirements. Several dual band

sensor and dome designs are possible solutions for this tactical air-to-air scenario. However, many designs become too expensive to be serious candidates for reasonable-to-low-cost tactical missiles. Unique design features, including separate apertures and sensors and exotic dome materials, such as diamond, that will allow dual band sensors to operate and survive in a harsh tactical flight environment, are too expensive. Robust design features, such as large apertures, add significantly to the cost of the missile and to this particular tactical mission.

One of the key objectives of the program was to identify a dual band sensor and dome suite that could be a low-cost concept. The next objective is to maximize the electromagnetic transmissions of both energy sources to the sensors. Third, the design of a dome which houses a dual band sensor must ensure adequate performance of both bands. Similarly, designs which accommodate two domes, each housing a sensor of a distinct band, must be such that each dome-sensor configuration performs adequately. Furthermore, the dual band design has to operate in a high speed long range flight environment where severe penalties from drag and aero-heating effects will be detrimental to the performance of the mission.

This paper discusses the concept, modeling and computational analyses of a dual band dome configuration, and an aerospike with a common aperture dome concept. Experimental test results of the concept are discussed (Ref. 6). This concept was considered the most effective configuration that was studied for this unique tactical air-to-air mission. An aerospike configuration will allow a dual band terminal sensor and dome to operate and to survive the severe drag and aero-heating penalties encountered in a long range, high speed air-to-air scenario.

TIME (SEC)	0.00	4.00	6.00	8.00	10.00 - 20.00
ALTITUDE (METERS) (Medium) (High)	3000 30,000	3000 30,000	3000 30,000	3000 30,000	3,000 30,000
MACH NUMBER (Medium) (High)	0.8 0.8	2.08 2.08	2.72 3.92	3.38 4.96	4.00 6.00
MAX SURFACE PRESSURE (KPA)	34.8 0.69	381.6 11.7	627.4 22.8	972.2 36.5	1,503 53.8
MAX DRIVING TEMPERATURE (C)	56 7	269 379	440 701	647 1094	888 1554
MAX HEAT TRANSFER COEFFICIENT (W/M ² K)	590.5 59.1	1,976 282.2	2,771 306.6	3,770 416.8	4,622 547.9

TABLE 1
AERODYNAMIC AND THERMAL LOAD SUMMARY

The effects of compressibility on the evolution of a turbulent shear layer has been extensively studied and reviewed (Ref. 8). Direct Numerical Simulation (DNS) studies (Refs. 9 and 10) indicate that the effect of compressibility on both decaying compressible turbulence and homogeneous shear turbulence is a dissipative one. The modifications for the extra dissipation due to dilatational effects and the pressure dilatation correlation have been successful in predicting the reduction in growth rate and reduction in magnitudes of turbulence correlation coefficients of free shear layers (Ref. 11). But these modifications have been shown to aggravate the deficiencies of the eddy viscosity models in predicting the growth of turbulent wall shear layers (Refs. 12 and 13).

Based on an examination of the equations that describe the evolution of a compressible turbulent flow field, modifications have been proposed for the turbulent mass flux (and hence the enthalpic production) and the baroclinic effect (Ref. 14).

2. TACTICAL REQUIREMENTS

Future air-to-air missiles with a dual band sensor suite and a long range propulsion system will provide a significant increase in capability as an anti-air weapon. Long range performance can be achieved with improved tactical missile propulsion technology such as pulse propulsion, ramjets and integral rocket ramjets. Solutions which combine these two mission

capabilities of dual band sensors and better propulsion will be influenced by the design and shape of the tactical vehicle. Of particular importance is the physical configuration of the terminal sensor and dome suite that will operate in this flight environment.

A proposed performance profile for the next generation air-to-air missile is shown in Fig. 1. The improved flight performance for the next generation missile should have high velocities (Mach 4-6) which can provide much longer trajectories and flight times than current air-to-air missiles. These improvements must occur at both medium and high altitudes to yield an effective air-to-air weapon. These trajectories will significantly increase the severity of the aero-heating requirements imposed on a dual band sensor and dome.

Thermal and pressure effects from aero-heating are major concerns in the design of a dual band sensor and dome suite operating in a high speed tactical environment. This flight scenario imposes several major concerns in the design of a terminal seeker. These concerns include the thermal response of the dome material; the thermal and pressure forces and the thermal shock impinging on the dome material; and the cooling mechanism, forced or natural that may be required to allow the sensors and domes to perform electrically. The interactions between the atmospheric and electrical performance of the sensors and domes are very complex. It is further

complicated with thermal and pressure conditions that vary within these proposed flight profiles. For example, previous studies have found that even though the heat transfer coefficient on the dome was a strong function of dome geometry and angle of attack, the adiabatic wall temperature of the dome is also strongly influenced by the velocity and altitude of the missile. Hence, the different thermal and pressure environments from these flight profiles severely complicates the design and modelling of the electromagnetic capabilities of the sensor and dome. Several additional observations can be made of the trajectory profiles of Fig. 1. For these time and velocity profiles the high altitude trajectory at 30 Km/s with a Mach 6 peak velocity generates the maximum driving temperature and higher temperature in an uncooled dome. However, the conditions at the medium altitude of 3 Km/s with a Mach 4 peak velocity are the most severe with respect to thermal shock and cooling requirements. The reason is the long dwell time at the maximum velocity. Also, much larger surface pressures and heat transfer coefficients can occur in the medium altitude missile trajectory than in a high altitude missile trajectory.

Table 1 shows some predictive temperature distributions at medium and high altitudes. The

maximum driving temperature of 888 °C (1630 °F) for the medium altitude profile is 649 °C (1200 °F) cooler than the maximum driving temperature for the high altitude profile. The heat transfer coefficient is much higher at the medium altitude than at the higher altitude. Analysis of the heating profiles indicates that at the initial 10 seconds time-of-flight the maximum temperature gradient occurs through the thickness and across the outside surface of the infrared dome. The maximum temperature of the infrared dome occurs at 20 seconds time-of-flight.

3. AEROSPIKE SEEKER CONCEPT

Several types of sensors could be candidates for this type of air-to-air mission. Table 2 provides a list of sensor spectra that could be considered as viable candidates for an advanced air-to-air seeker. Given preferred spectral bands and a database of target types, a designer will be able to select aperture sizes, sensors and dome materials to satisfy the requirements of the mission. For example, future missile seeker systems may require both infrared bands, 3-5 and 8-12 micrometers. Since these spectral bands have unique attributes for searching and tracking air targets, sensors in both IR bands could enhance the midcourse and terminal guidance

IR	RF	ENVIRONMENT
3 -5 and/or 8 - 12 μm MTF Not to be degraded by more than 10 % due to Ice, Rain and High Temperature 0.25 mrad Resolution Greater than 90 % transmission at wavebands of interest	Primary Frequencies 2 - 18 GHz Passive 8 -12 GHz Active Additional Frequencies 33 GHz / 94 GHz Max. BSE - 0.5Deg Max. BSES - 0.1 Deg/Deg Uncompressed Sidelobe Levels 1st Sidelobe Increase NGT 1 dB Due To Dome System Gain With Dome 24 dB at X - Band Signal Attenuation 1 dB Due to Dome	Rain and Ice Erosion Solar Irradiance

TABLE 2
ELECTROMAGNETIC GOALS

of the missile. Similarly, enhanced performance in search and track could also be obtained with both a passive and an active RF system. A combination of RF and IR bands provides an effective long term counter measure capability. Unfortunately, the implementation of a dual band system with aperture size(s) large enough to be effective is one of the most challenging objectives of this concept. It is particularly challenging if a lock-on-before-launch mode of the terminal seeker is a requirement. The problem is how to configure the aperture sizes and sensors at the front of the missile to achieve the best performance from both sensors. References 3 and 7 provide more information on the attributes of combining sensor alternatives.

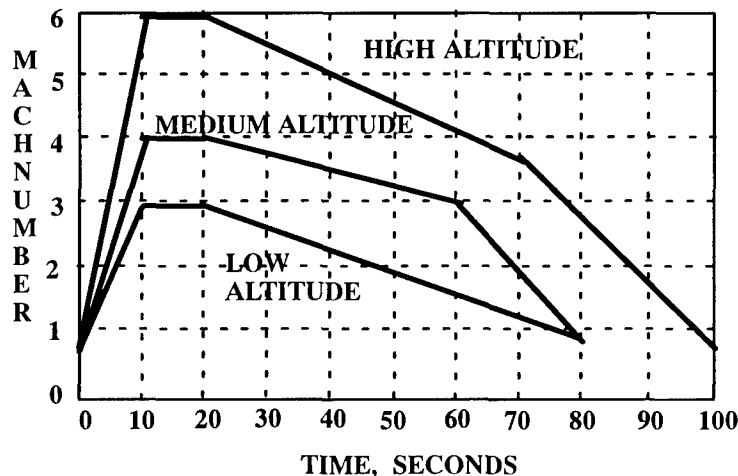
Previous studies have shown that a common aperture with both an RF and IR sensor and an infrared sensor and dome with a conformal radio frequency antenna are two of the more promising sensor and dome designs to meet the requirements of a dual band system. A common aperture dome concept is deemed the more feasible and less costly of the two concepts for near term applications. This particular concept allows the maximum electromagnetic energy from both sensors to be transmitted using a common hemispherical dome. In this seeker design the front configuration of the missile is greatly simplified for a high speed, long range missile trajectory.

Soft infrared materials such as magnesium fluoride have electromagnetic properties to perform in a role as a conventional IR dome as well as RF dome. This infrared material can fulfill a dual band sensor and dome requirement if it is properly protected from the

flight environment. However, very few dual band dome materials can survive these supersonic flight environments without adequate thermal protection. These soft infrared materials begin to lose their electromagnetic performance as soon as the flight thermal environment deteriorates the dome material. At these velocities the dome material is subjected to large aerodynamic heating rates and large surface pressure forces from the bow shock waves. The aero-thermal environment impinging on the surface of the dome is severe enough to even cause catastrophic structural failure of the infrared material early in the flight. The excessive heating on the dome will also impose severe wavefront distortion at the infrared transmittance band. The tracking capability of the seeker will be seriously degraded when wavefront distortion becomes too large for corrections.

One effective means of mitigating the severity of the harsh flight environment involves configuring the dual band sensor and dome with an aerospike. An aerospike, also called probe, located in front of the dome provides thermal and over-pressure protection to the soft material dome. For example, an aerospike can generate a shock wave at supersonic conditions that protects the dome material from over-heating. Fig. 2 illustrates the aerodynamic flow concept that is created from the aerospike under supersonic conditions. An analysis of the aerodynamic flow around the aerospike under test conditions will be presented in a later section of this paper.

The optimal length of an aerospike to provide this favorable aerodynamic flow environment is one of



High Altitude Profile
Altitude: 98,425 ft (30 KM)
Peak Velocity: Mach 6
Peak Vel. Duration: 10 sec
Average Velocity: Mach 4

Altitude: 9843 ft (3 KM)
Peak Velocity: Mach 4
Peak Vel. Duration: 10 sec
Average Velocity: Mach 3

Low Altitude Profile
Altitude: 3,281 ft (1 KM)
Peak Velocity: Mach 3
Peak Vel. Duration: 10 sec
Average Velocity: Mach 2

FIGURE 1
FLIGHT PROFILES OF AIR-TO-AIR MISSILES

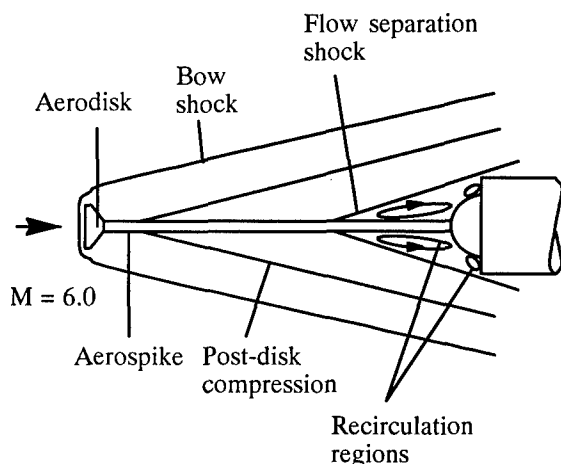


FIGURE 2
AEROSPIKE FLOWFIELD

the key design features to generating the protective shock wave. The optimal length of the spike varies with the Mach number and altitude. The configuration at the tip of the aerospike such as a large cap or hollow tube is also another enhancing feature that will expand the effectiveness of the shock wave. Both of these features can be related to the missile body as well as the shock wave over the seeker dome. For example, studies have shown that the length-to-missile-diameter ratio of a capped aerospike is about unity with the diameter of the circular cap about 12 to 14 per cent of the missile body diameter. Other studies of the concept indicate that a cap at the tip of the aerospike can establish the separation point of the boundary layer of the shock wave. All of these design features can optimize a favorable flow effect and in turn lower the drag and heating on the dome surface. Fig. 3 shows one of the types of aerospike tips. Another type will be a hollow tube at the tip called an aeroscoop. Both tip concepts have demonstrated similar results in the wind tunnel tests. The operating principle of the aeroscoop is that high speed ram air is created during the flight. The ram air enters the scoop and is bled off through several orifices positioned along the scoop. The bled air from the orifices pushes the shock wave away from the scoop spreading the shock wave further out from the dome. Hence the dome and the dual band sensor has a larger umbrella of thermal protection from the expanded shock wave induced by the bled air.

4. FLUID FLOW MODELLING AND COMPUTATIONAL TECHNIQUES

To gain necessary insight into optical transmittance behavior, detailed turbulence modeling and analysis

of the flow and thermal fields is required. To meet this need, we have developed modeling and computational capabilities for turbulent flows with substantial compressibility effects.

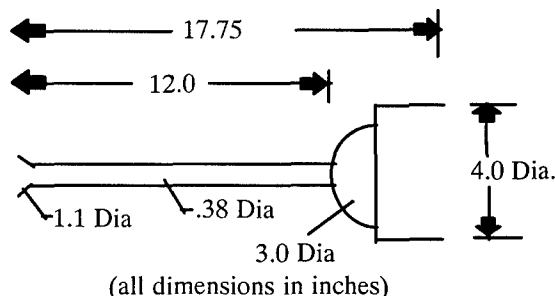


FIGURE 3
AEROSPIKE MODEL GEOMETRY

4.1. Modelling of Compressibility Effects

In the equations governing the compressible turbulent flow field, terms can be identified which are of relevance and different from those of incompressible flows (see Ref. 8). From the governing equations given in Refs. 8, 19 and 25, the terms that are unique to compressible turbulent flows (and not accounted for in "incompressible" models) are $\overline{\sigma_{ij}''}$, $\overline{p' \frac{\partial u_i''}{\partial x_i}}$ and $\overline{u_i'' \frac{\partial p}{\partial x_i}}$, in addition to the dilatational effects on the rate of dissipation of the turbulent kinetic energy (TKE). $\overline{\sigma_{ij}''}$ is purely a result of Favre averaging and at low Mach numbers it does not represent compressibility effects. Therefore, in order to close the system of equations we need to suitably account for $\overline{p' \frac{\partial u_i''}{\partial x_i}}$ and $\overline{u_i'' \frac{\partial p}{\partial x_i}}$. We will refer, henceforth, to the first term as the pressure dilatation term and the second term as the enthalpic production term. A detailed description of the modifications that have been proposed to model the extra dissipation due to dilatational effects is presented in Ref. 8. Here we will briefly present the form of the modifications that have been used in the comparative study presented in this article.

From a direct numerical simulation (DNS) analysis of compressible flows (Refs. 9 and 10), it was concluded that the effect of compressibility on the turbulence structure was a dissipative one. Compressibility introduces an extra amount of dissipation (of the turbulent fluctuations) due to the non-divergent nature of the velocity fluctuations, as can be seen by

examining the definition of the rate of dissipation of TKE (Refs. 9 and 10).

Through some mathematical manipulations the dissipation rate (of TKE) in compressible turbulent flows can be written as a sum of a "solenoidal" dissipation rate (the first term on the right hand side of Eqn. 1) and a "dilatational dissipation" rate. Thus,

$$\rho\epsilon = \rho(\epsilon_s + \epsilon_d) \quad (1)$$

where

$$\rho\epsilon_s = \mu \left(\overline{\omega_p'' \omega_p''} \right) ; \quad \rho\epsilon_d = \frac{4}{3} \mu \overline{d''^2} \quad (2)$$

where ω_p'' is the fluctuation in vorticity and $d'' = \frac{\partial u_k''}{\partial x_k}$ is the divergence of the fluctuating velocity field.

The solenoidal dissipation rate can be thought of as the dissipation due to the regular process of cascading of energy to the smaller scales and in the absence of dilatational effects it can be considered to be equivalent to the "incompressible" dissipation rate. The dilatational dissipation (also referred to as compressible dissipation) is due to the non-divergent nature of the velocity fluctuations.

The pressure dilatation $\overline{p'd''}$ where $d'' = \frac{\partial u_k''}{\partial x_k}$, appears explicitly in the governing equations (see Refs. 8, 19) in the case of compressible turbulent flows due to the non-divergent fluctuating velocity field. The pressure dilatation refers to the work done due to simultaneous fluctuations in the volume of the fluid cell corresponding to the fluctuations in pressure. It can be either positive or negative and where negative represents an extra dissipation.

Based on an analysis of the evolution of the fluctuations on an acoustic time scale Sarkar et al. (Ref. 10) proposed a model for the dilatational dissipation rate which is given as

$$\epsilon_d = \alpha_1 \epsilon_s M_t^2 \quad (3)$$

where α_1 is an arbitrary constant of $O(1)$. The constant α_1 is determined from an analysis of the predictions made of decaying compressible turbulence.

Borrowing ideas from the modelling of the pressure-strain correlations in incompressible turbulent flows Sarkar (Ref. 17) modelled the pressure dilatation term as

$$\overline{p'd''} = -\alpha_3 P_k M_t^2 + \alpha_4 \rho \epsilon_s M_t^2 \quad (4)$$

where $\alpha_3 = 0.4$, $\alpha_4 = 0.2$ and $M_t = \frac{\sqrt{2k}}{a}$. In addition α_1 in Eqn. 3 is set equal to 0.5. The constants are obtained from a curve fit of the model with DNS simulations.

We will refer to the modifications proposed by El Baz and Launder (Ref. 18) as the E & L modification through the remainder of this article. To account for the extra dissipation due to compressibility effects, El Baz and Launder (Ref. 18) chose to modify the constant $C_{\epsilon 2}$ to match the observed decay rate of compressible isotropic turbulence. Therefore, $C_{\epsilon 2}$ is modified as

$$C_{\epsilon 2}' = \frac{C_{\epsilon 2}}{1 + 3.2 M_t^2} \quad \text{where } M_t = \frac{\sqrt{k}}{a} \quad (5)$$

with $C_{\epsilon 2}'$ used instead of $C_{\epsilon 2}$ in the modelled form of the transport equation for ϵ .

The modification for the pressure dilatation term is obtained from a contraction of the model for the rapid part of the pressure-strain correlation and is given as

$$\overline{p' \frac{\partial u_i''}{\partial x_i}} = F \left[\frac{8}{3} \rho k \frac{\partial U_k}{\partial x_k} - P_k \right] \quad (6)$$

where F is the constant which is considered to be an intrinsic function of compressibility. The function F is assumed to be a function of the turbulent Mach number, that is

$$F = \beta M_t^2 ; \quad \text{where } M_t = \frac{\sqrt{k}}{a} \quad (7)$$

where β is a constant, prescribed to be 1.5

The Present model

The modifications proposed by Krishnamurty and Shyy (Ref. 14) will be referred to as the K & S modification. The methodology predominantly used in computing compressible flow fields is to use Favre averages for velocity components and temperature and Reynolds average for pressure and density. The stress tensor and the heat flux vector are computed using Reynolds averages. The implicit assumption here is that the turbulence is homogeneous and therefore the turbulent mass flux and the fluctuating stress tensor are negligible which could be erroneous in the case of high supersonic and hypersonic flow fields (Ref. 22). In order to accurately model the exact form of the governing equations (except for the dissipation rate transport equation) account must be made of the turbulent mass flux term.

The turbulent mass flux is modelled as a function of the gradients in temperature and Reynolds stress (Ref. 14) and is expressed as

$$\overline{u_j'''} = C_1 \left\{ \left(\frac{\mu_i C_p}{Pr_i} \right) \left(\frac{\gamma - 1}{\bar{\rho} a^2} \right) \frac{\partial \tilde{T}}{\partial x_j} + \left[\frac{(\gamma - 1)}{\bar{\rho} a^2} \tilde{U}_i \overline{\rho u_i'' u_j''} \right] \right\} \quad (8)$$

where C_1 is an arbitrary constant and C_p is the specific heat at constant pressure and

$$C_1 = \frac{2M_t}{1 - M_t} \text{ where } M_t = \frac{\sqrt{2k}}{a} \quad (9)$$

It should be noted that the above modification has been derived based on a constant enthalpy assumption (as a starting point). The mean velocity is defined with respect to a reference solid body, which in this case is the projectile.

The modelling of the transport equation for ϵ_s usually follows the incompressible form and ignores the effect of the baroclinic torque. ϵ_s is usually defined as the correlation between the vorticity fluctuations, that is, $\epsilon_s = \overline{v \omega_i'' \omega_i''}$ where v is the kinematic viscosity. The assumption made in the proposal for the algebraic

modification for the dilatational dissipation is that the solenoidal dissipation rate is relatively unaffected in the case of compressible flows.

The exact form of the governing equation for the solenoidal dissipation rate, ϵ_s is given in Ref. 8, 19. ϵ in the equations that follow is used to denote the solenoidal dissipation rate ϵ_s .

B_ϵ represents the baroclinic term and arises due to differences in direction between the gradients of pressure and density, i.e., the term arising due to $\left[\vec{\nabla} \left(\frac{1}{\rho} \right) \times (\vec{\nabla} p) \right]$. In the case of the mean flow, the baroclinic term represents a production of vorticity due to the interaction of the pressure and density gradients. Based on an order of magnitude analysis (Ref. 14) the effect of the baroclinic torque is modelled as $-C_{\epsilon 1} \frac{\epsilon}{k} \overline{u_i''} \frac{\partial P}{\partial x_i}$. The turbulent mass flux terms appear in the transport equations for both k and ϵ and can be thought of as an account for both the mean and fluctuating components of the baroclinic effect. Therefore, the modelled form of the transport equations for k and ϵ are given below, with the constants given in Refs. 8 and 19.

$$\frac{\partial}{\partial t}(\rho k) + \frac{\partial}{\partial x_j}(\rho U_j k) = P_k - \rho \epsilon + \frac{\partial}{\partial x_j} \left[\left(\mu + \frac{\mu_t}{\sigma_k} \right) \frac{\partial k}{\partial x_j} \right] - \overline{u_i''} \frac{\partial P}{\partial x_i} + \overline{p' \frac{\partial u_i''}{\partial x_i}} \quad (10)$$

$$\frac{\partial}{\partial t}(\rho \epsilon) + \frac{\partial}{\partial x_j}(\rho U_j \epsilon) = C_{\epsilon 1} \frac{\epsilon}{k} \left(P_k - \overline{u_i''} \frac{\partial P}{\partial x_i} \right) - C_{\epsilon 2} \rho \frac{\epsilon^2}{k} + \frac{\partial}{\partial x_j} \left[\left(\mu + \frac{\mu_t}{\sigma_\epsilon} \right) \frac{\partial \epsilon}{\partial x_j} \right] \quad (11)$$

4.2 Modelling of Non-Equilibrium Effects

One of the issues of concern (even for incompressible flows) in using the k - ϵ model is that the rate of production of TKE tends to be over-predicted and there is a lag in the response of the dissipation rate to variations in the mean strain rate. To allow ϵ to respond faster to the variations in the mean strain rate Chen and Kim (Ref. 15) proposed an algebraic modification to the constant $C_{\epsilon 1}$ in the ϵ -equation which is given as $\left(1.15 + 0.25 \frac{P_k}{\epsilon} \right)$. It works to enhance the development of ϵ when the mean strain is strong (or large production rate) and to reduce it

when the mean strain is weak (or small production rate).

Shyy et al. (Ref. 19) proposed a modification to alter the constant $C_{\epsilon 2}$ in the ϵ equation to $\left(1.45 + 0.45 \frac{P_k}{\epsilon} \right)$, to be used in conjunction with $C_{\epsilon 1}$ because of observations of the computations made of flow past a backward facing step and the hill flow inside a channel. The $C_{\epsilon 1}$ modification reportedly over-predicts the length of the recirculating flow due to increased levels of the "production of dissipation" term. Further tests (Ref. 23) conducted using this modification seemed to indicate an improvement in

the predictions made, over the non-equilibrium modification for $C_{\epsilon 1}$. The standard model in its unmodified form indicates that there is an equilibrium between the production and dissipation of TKE. The $C_{\epsilon 2}$ modification has the effect of an added time scale which may be thought of as representing the relaxation time required for any imbalance between production and dissipation rates of TKE to return to an equilibrium situation. Previous studies (Ref. 24) on homogeneous shear flows have shown that there is definitely a need for a "relaxation-time-scale" based modification. However, the modification in this form will tend to over-predict the rate of decay of TKE in the case of decaying isotropic turbulence.

5. AEROSPIKE MODELS AND TESTING

In the early 1990s the Air Force Munitions Directorate expanded its study of this concept with wind tunnel tests with scaled models. The first series of wind tunnel tests was conducted in a 6-inch supersonic wind tunnel facility at California State Polytechnic University, Pomona, California. A second series of wind tunnel tests was conducted at the United States Air Force Arnold Test Center in Tullahoma, Tennessee. Both series of tests were conducted in wind tunnels with untreated atmospheric air. A third series of wind tunnel tests was conducted at the National Aeronautics Space Administration (NASA) Langley Research Center, Hampton, Virginia. In these last wind tunnel tests, models were instrumented with high temperature sensors (Ref. 6). These wind tunnel tests were conducted in a 20-inch Mach 6 tunnel at a stagnation pressure of 475 pounds per square inch absolute (psia), a stagnation temperature of 875 degree Rankine ($^{\circ}R$) at a free stream Reynolds number of 8.0×10^6 per foot. A detailed analysis of these test results will be presented later in this paper.

The models used in the wind tunnel tests at the NASA Langley Research Center were instrumented with both high temperature and pressure sensors. The scaled models were designed by four engineering design teams. The teams include the Munitions Directorate (sensors and vehicle designers), NASA (wind tunnel designers), Micro Craft Corporation (fabricators of the models) and Medterm Corporation (model sensor and installers). The instrumentation on the scaled models was designed to achieve a maximum amount of collected data across the face of the hemispherical dome and on the external wall of the seeker. Fig. 5 illustrates the instrumented configurations of the wind tunnel model.

6. COMPUTATIONAL STUDY OF WIND TUNNEL TEST CONDITIONS

Computations of the wind tunnel test data have been performed using a cell-centered, finite volume second-order upwind scheme with a multi-stage Runge-Kutta time stepping scheme (Ref. 25). We will refer to the projectile forebody problem as the spike-off case and the problem with the spike and aerodisk assembly as the spike-on case. Unless specified otherwise all spatial locations presented in this section are in inches. From prior experimental results (Ref. 20) we know that the inflow conditions are such that the flow field can be expected to be turbulent.

6.1 Dome without Spike

A sketch of the computational domain (for the spike-off case) is shown in Fig. 4. The coordinate

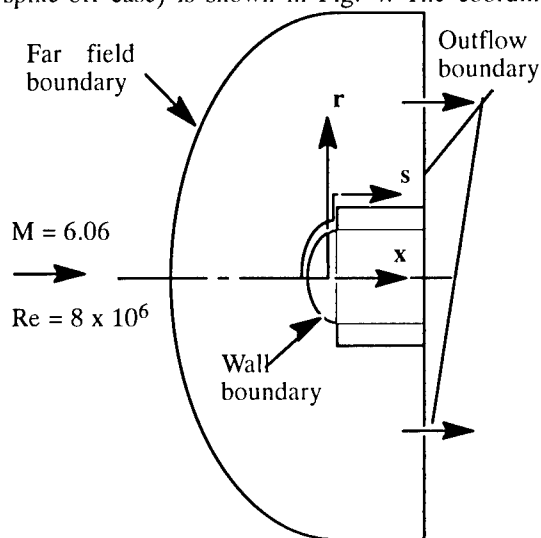


FIGURE 4.
SKETCH OF COMPUTATIONAL DOMAIN
WITH INFLOW CONDITIONS

system is set up such that the dome of the hemisphere is at $x = -1.5$ inches (the radius of the hemisphere). The outer boundary of the computational domain extends out to 6.0 inches from the cylinder surface. The boundary conditions at the far field were fixed at the experimental inflow conditions. A freestream turbulence intensity of 0.3% was used to prescribe the turbulent kinetic energy and the dissipation rate, ϵ , in the freestream. This value is consistent with intensities of turbulence observed in most supersonic wind tunnels. At the outflow boundary a simple extrapolation procedure was used because the flow is supersonic at this boundary. At the wall boundary, the

compressible form of the wall function technique (Ref. 25) has been used.

Computations made with the unmodified form of the k - ϵ model will be denoted as $Sk\epsilon$. The computations made using the modification to the constant $C_{\epsilon 1}$ in conjunction with the modification for the extra dissipation due to compressibility (Eqn. 3) will be referred to as $E_k\epsilon 1$. The computations made using the $C_{\epsilon 1}$ modification and the $C_{\epsilon 2}$ modification (Ref. 19) and the compressibility modification (Eqn. 3) are referred to as $E_k\epsilon 2$.

Fig. 6 shows a comparison between the computed values of TKE along the stagnation line. The unmodified model predicts a much higher value of TKE compared to the modified models, $E_k\epsilon 1$ and $E_k\epsilon 2$. Also, the modification has been observed to substantially improve the predictions made of low speed, recirculating flows²³. The rate of production and rate of dissipation show a similar trend as far as the peak levels in P_k and ϵ are concerned. However, the level of production and dissipation predicted by the unmodified model is much larger than that predicted by the modified models and the predictions made by the modified models ($E_k\epsilon 1$ and $E_k\epsilon 2$) are virtually identical. Let us consider the predictions made by the unmodified model at a given instant in time. The rate of production is about three times the rate of dissipation and so results in a substantial increase in the rate of "production of dissipation" term in the ϵ equation (using the $C_{\epsilon 1}$ modification).

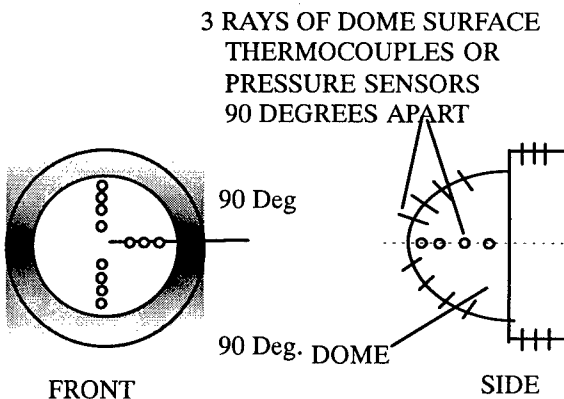


FIGURE 5

INSTRUMENTED TEMPERATURE OR
PRESSURE DOME MODEL WITHOUT
AEROSPIKE

The result is an increase in the predicted value of dissipation rate and when this magnitude of dissipation rate is added to the k equation it results in a decrease in the predicted value of k and the eddy viscosity. The reduction in eddy viscosity leads, in turn, to a reduction in viscous stresses and thereby a reduction in the production rate. As the flow evolves it results in substantially reduced values of TKE, ϵ and P_k .

Fig. 7 shows a plot of the pressure distribution on the surface of the dome and a comparison of the predicted values with experimental data. The predictions made by the various models are very similar, which could be expected, because there is an equilibrium between the production and dissipation in the log-layer of the boundary layer on the surface of the projectile. The compressibility modification does not play a major role because the flow is almost subsonic downstream of the shock. A possible difference between the predictions made by the models could be expected in the region where the boundary layer separates. But the differences seen in the predictions made are minimal.

In the figure, a region of discrepancy between the experimental measurements and the computational predictions has been highlighted. The jump in pressure is because of the separation of the boundary layer on the dome surface. To accommodate this separation the flow goes through a weak compression wave. The shadowgraphs and Schlieren pictures of the flow field clearly indicate this weak compression wave. But the pressure taps on the dome of the hemispherical surface fail to pick up this jump. Other computational studies, provided by L. D. Huebner, have also confirmed the jump in pressure.

Fig. 8 presents a comparative plot of the predicted values of rate of production and dissipation of TKE along the stagnation line. The modifications due to El Baz and Launder (Ref. 18) are denoted as "E & L". The term "K & S" has been used to denote the computations made using the modifications proposed by Krishnamurty and Shyy (Ref. 14). It should be noted that the K & S modifications are used in conjunction with the modification for compressible dissipation rate (Eqn. 3). The values predicted by the K & S modifications and that predicted by the Sarkar et al. (Ref. 10) and Sarkar (Ref. 17) models are virtually identical. To understand the reason for this let us consider the production of turbulent kinetic energy (TKE)

Production of TKE

$$= - \overline{\rho u_i'' u_j''} \frac{\partial U_i}{\partial x_j} - \overline{u_i''} \frac{\partial P}{\partial x_i} \quad (12)$$

where the first term on the right hand side is termed the kinetic part and the second term the enthalpic part. The kinetic part can be further split up into a

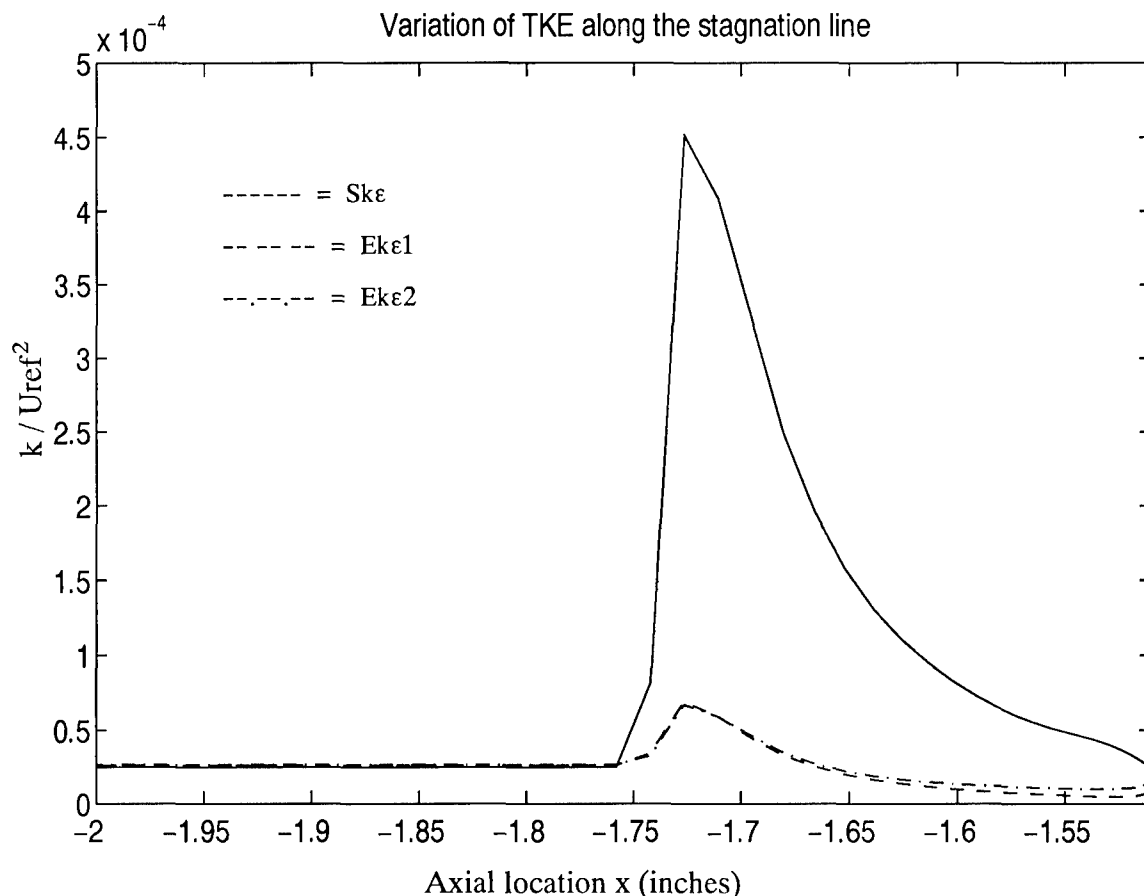


FIGURE 6.
COMPUTED VARIATION OF TKE FOR THE SPIKE-OFF CASE.

dilatational part and an iso-volumetric part with the dilatational part reflecting the effect of bulk dilatation on the rate of production of TKE.

Dilatational Part:

$$P_{kd} = \left(\frac{1}{3} \overline{\rho u_k'' u_k''} \right) \frac{1}{\bar{\rho}} \frac{D\rho}{Dt} \quad (13)$$

Iso-volumetric Part

$$P_{kiv} = \left[\left(\overline{\rho u_i'' u_j''} - \frac{1}{3} \overline{\rho u_k'' u_k''} \delta_{ij} \right) \times \left(S_{ij} - \frac{1}{3} U_{k,k} \delta_{ij} \right) \right] \quad (14)$$

$$\text{Enthalpic part: } - \overline{u_i''} \frac{\partial P}{\partial x_i} \quad (15)$$

A plot of the enthalpic production rate compared with the dilatational component of the production rate and the iso-volumetric part of the production rate is shown

in Fig. 9. The figure shows that the enthalpic production rate as predicted by the current modification is not of the same order of magnitude as the other two parts of the production which explains the minor impact of the current modifications on the mean flow solution.

There is no appreciable difference seen in the predictions, made of the surface pressure distribution, by the various models that address the effect of compressibility on the turbulent flowfield.

6.2. Dome with Spike

Fig. 10 shows representative contour plots of the radial gradient in density and this is compared with the experimental Schlieren photographs. The inflow Mach number and Reynolds numbers are respectively, 6.06 and 8.0×10^6 . The Reynolds number is based on the projectile diameter. The features of the flow field are clearly seen. The top half

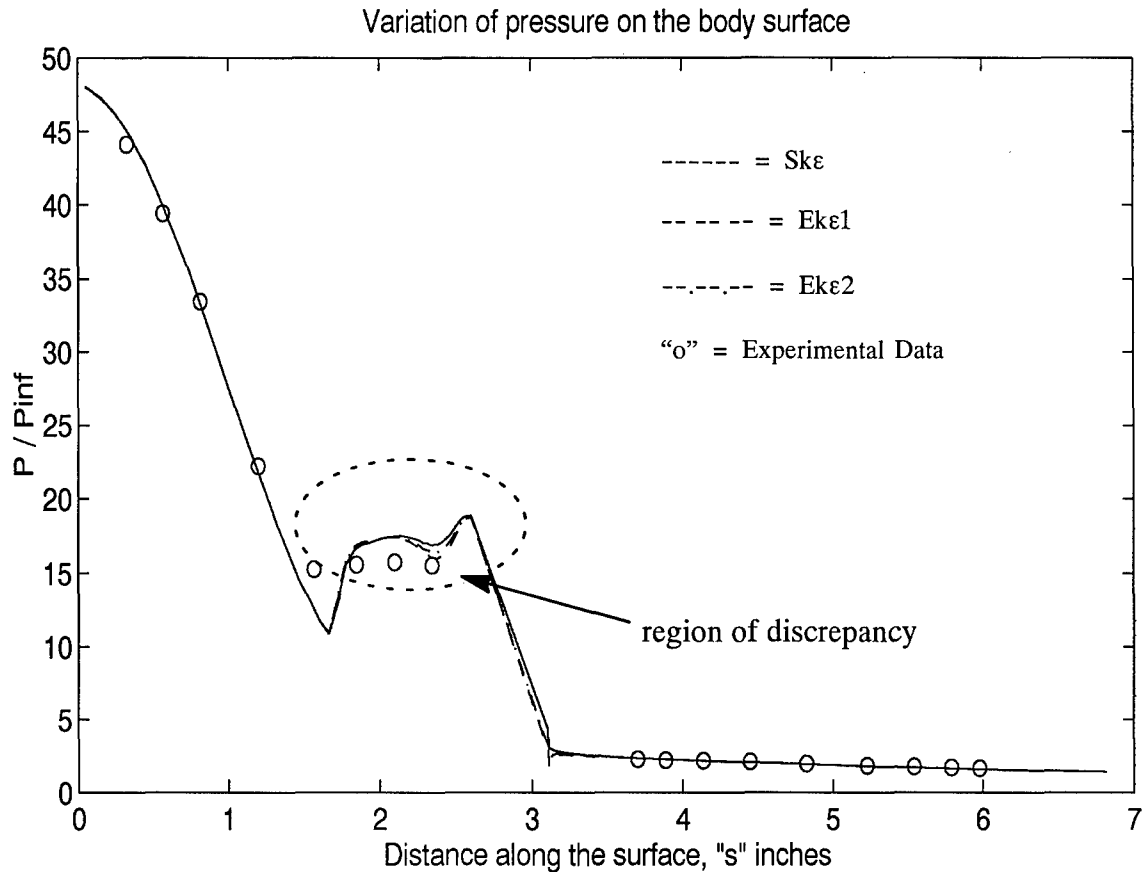


FIGURE 7.

COMPARISON OF COMPUTED AND EXPERIMENTAL PRESSURE DATA ON DOME SURFACE

is the Schlieren from the experimental measurements (Ref. 6). The lower half has been computed using the K & S model. As the flow behind the bow shock expands around the aerodisk a weak compression is formed at its base. The wake flow caused by the aerodisk and the nearly stagnant flow near the dome creates the conically shaped recirculation region. The region is separated from the inviscid flow by a flow separation shock. It is expected that this shock will isolate the recirculation region thereby enabling the reduction of pressure and heating rates on the dome surface. Additional pockets of recirculation region are created at the shoulder region between the hemispherical dome and the cylindrical body of a larger diameter.

Fig. 11 presents a comparison between the pressure distributions on the dome surface, with and without the spike and aerodisk combination. The results presented here are those obtained with the K & S modifications. It is quite clear from this plot that the spike-disk combination helps in reducing the pressure

on the projectile surface. The decrease in pressure is almost ten times the value obtained in the spike-off case. The distribution of temperature on the surface of the projectile, with and without the spike, is shown in Fig. 12. Even though there is substantial reduction in pressure, the use of the aerospike does not change the temperature level in the dome region substantially. Relative to the bow shock of the spike-off case, the oblique shocks of the spike-on case do not affect the thermal profile as much. However, the temperature on the dome of the projectile remains fairly constant in the spike-on case, which is desirable. It should be noted that the current computations were restricted to an angle of attack of zero degrees.

From previous computational studies (Ref. 14) it was learnt that the $Ek\epsilon_2$ model resulted in an "optimum" prediction. The predictions in the afterbody case gave reasonable predictions of both the mean flow quantities as well as the turbulence quantities, such as the turbulent kinetic energy and the Reynolds shear stress. With this in mind, we decided to compare the

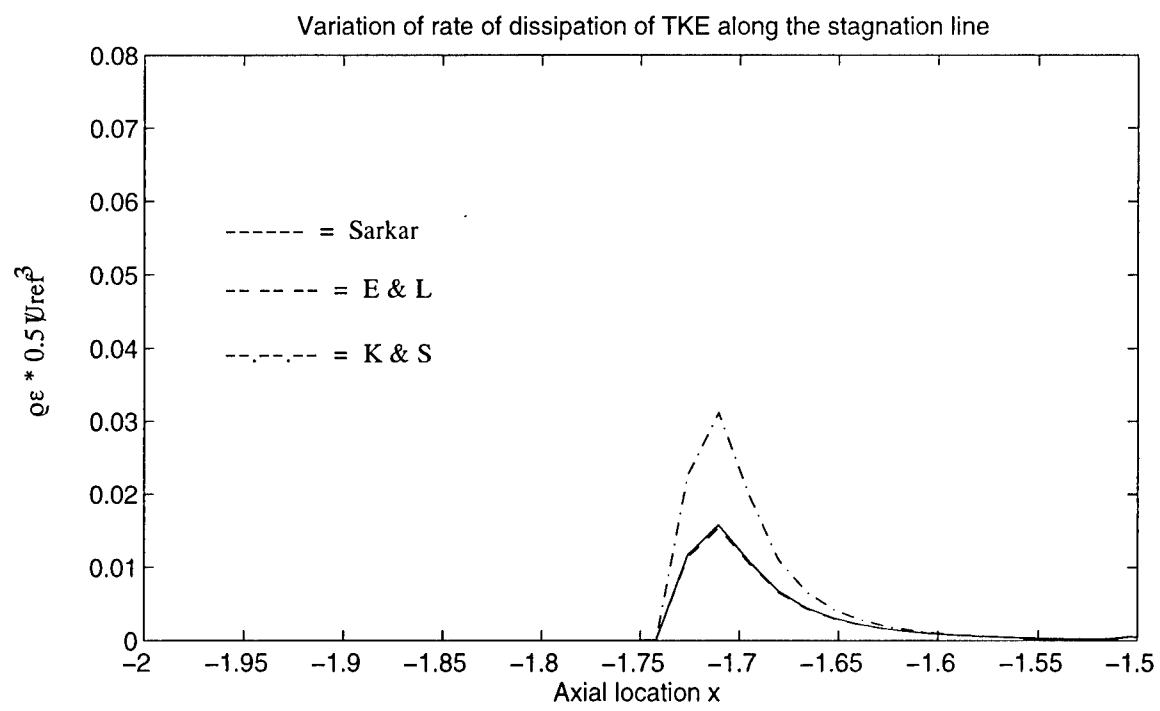
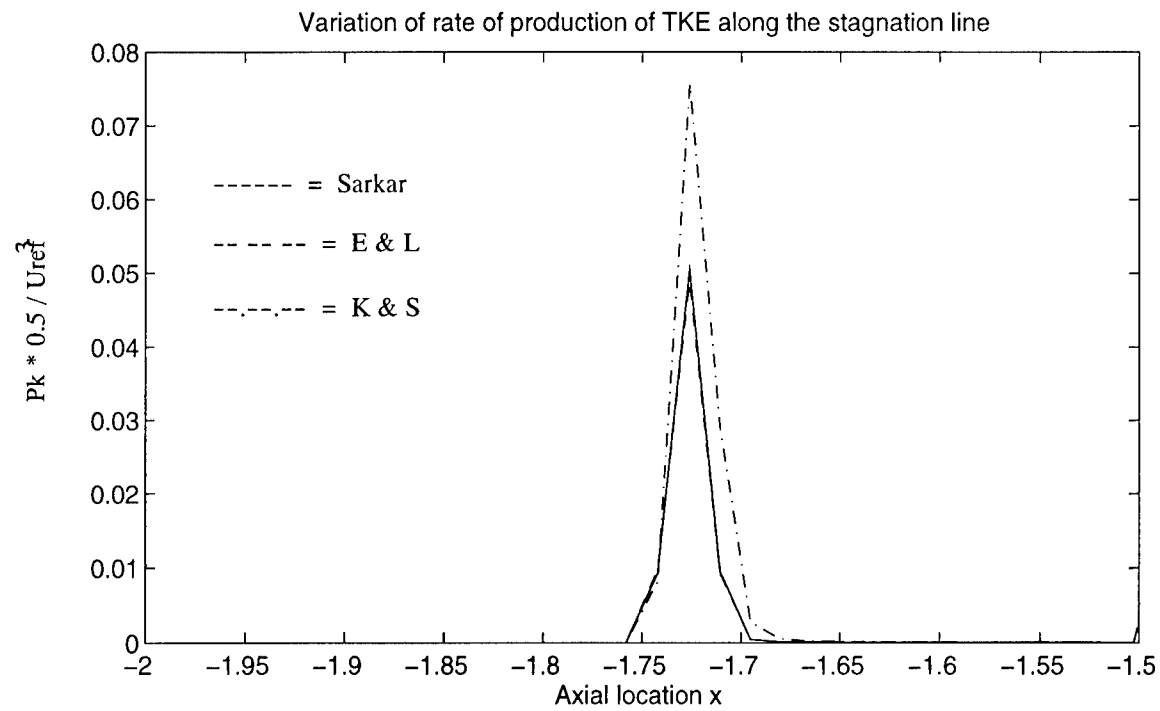


FIGURE 8.
VARIATION OF RATE OF PRODUCTION AND DISSIPATION ALONG THE STAGNATION LINE.

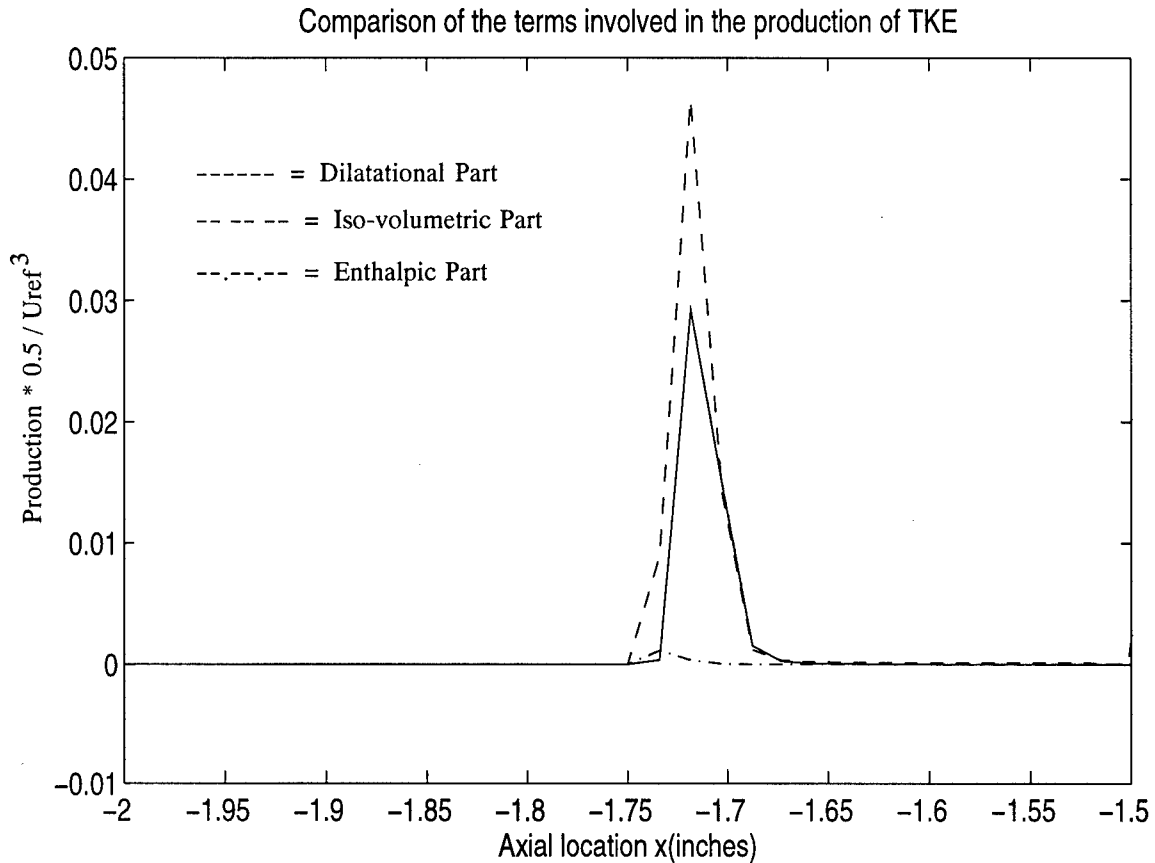


FIGURE 9.
VARIATION OF THE PARTS OF PRODUCTION OF TKE, ALONG THE STAGNATION LINE.

Eke2 model against the predictions made by the unmodified model.

Fig. 13 presents a comparison between the predictions made of the pressure distribution on the surface of the projectile. There is a distinct difference between the predictions made by the eddy-viscosity models and the experimental data, which could be expected, because the variations in pressure on the surface are dictated largely by the mechanism at play in the recirculating region. The pressure distributions on the dome surface show distinct differences between the two models with the unmodified model predicting a much higher value of pressure on the surface of the projectile and the extended model predicting a lower value of pressure. Profile comparisons of the components of velocity and the turbulent kinetic energy were compared (Ref. 25) and are not presented here for the sake of brevity and the fact that only

qualitative information can be derived from these plots due to the lack of experimental measurements of these variables.

Fig. 14 shows a comparison between the predictions made of the pressure distribution along the surface of the projectile. The K & S modifications offer a slight improvement over the other two modifications with the possible implication that the K & S modifications are a step in the right direction. It is noted that the E & L modification predicts the lowest level of TKE in the flow field. The K & S modifications predict an increased level of TKE which is again very similar to our observations for the afterbody flowfield (Ref. 14). The reduced level of TKE predicted by the modifications due to E & L modifications is largely due to the increased dissipation rates predicted by that model. A lateral shift in the location of peak values is

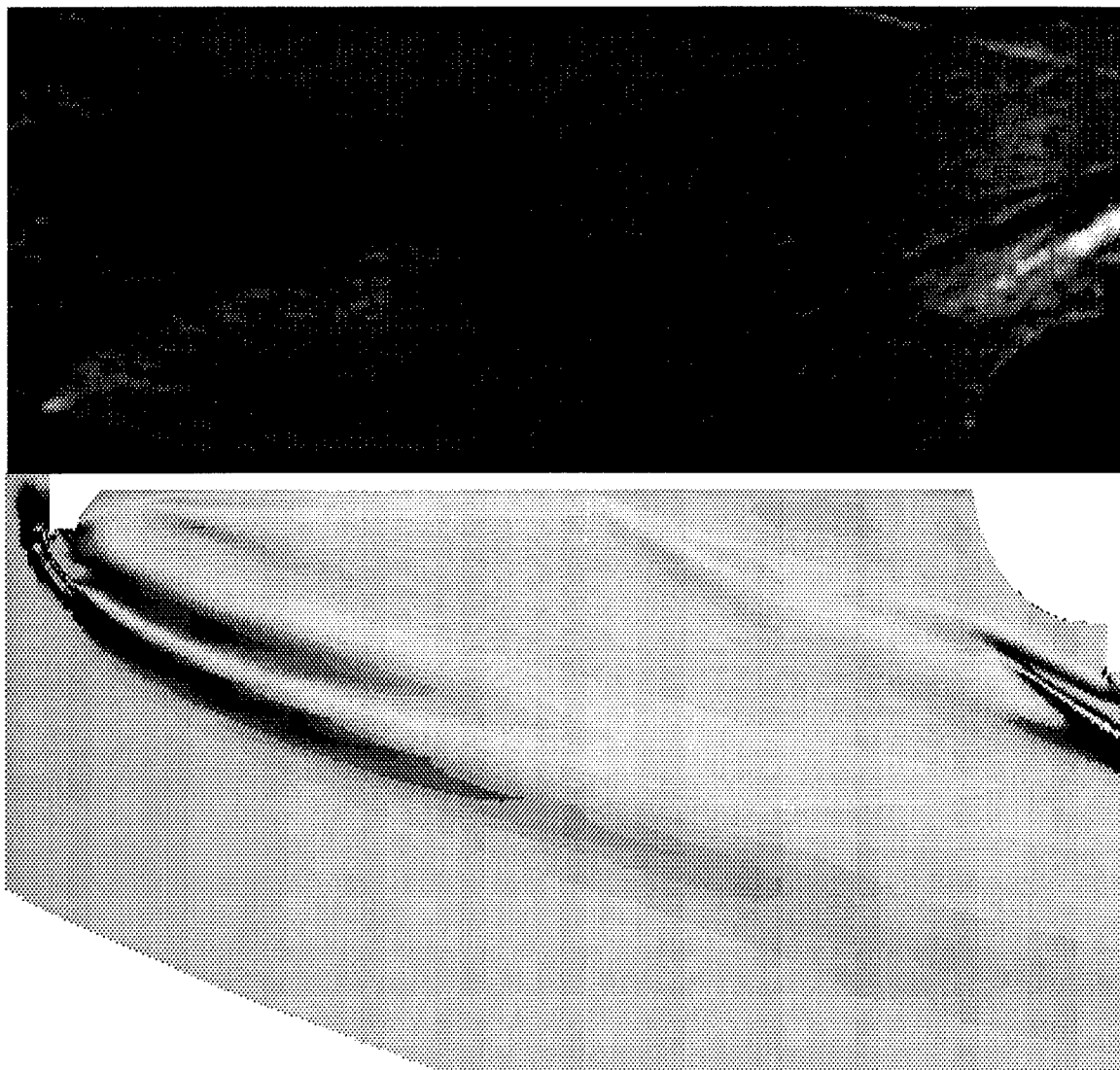


FIGURE 10.

COMPARISON OF EXPERIMENTAL SCHLIEREN WITH COMPUTED VALUE OF DENSITY GRADIENT IN THE RADIAL DIRECTION. COMPUTED USING THE K & S MODEL.

observed in the computations made using the E & L model.

7. SUMMARY

Improved computational and modeling approaches have been proposed to address the issue of non-equilibrium between the rate of production and dissipation, and the effect of compressibility. The standard model predicts higher rates of production of

TKE, across the shock wave, in comparison with the non-equilibrium models. The use of the spike-aerodisk assembly, in front of the projectile, does reduce the pressure at the projectile surface (by almost a factor of 10). The temperature distributions on the projectile surface do not display such a dramatic reduction. However, there is a significant rise in temperature at the separation-shock location (on the surface of the spike). For the spike-on case, the Ek ϵ^2 model (combination of the modifications for

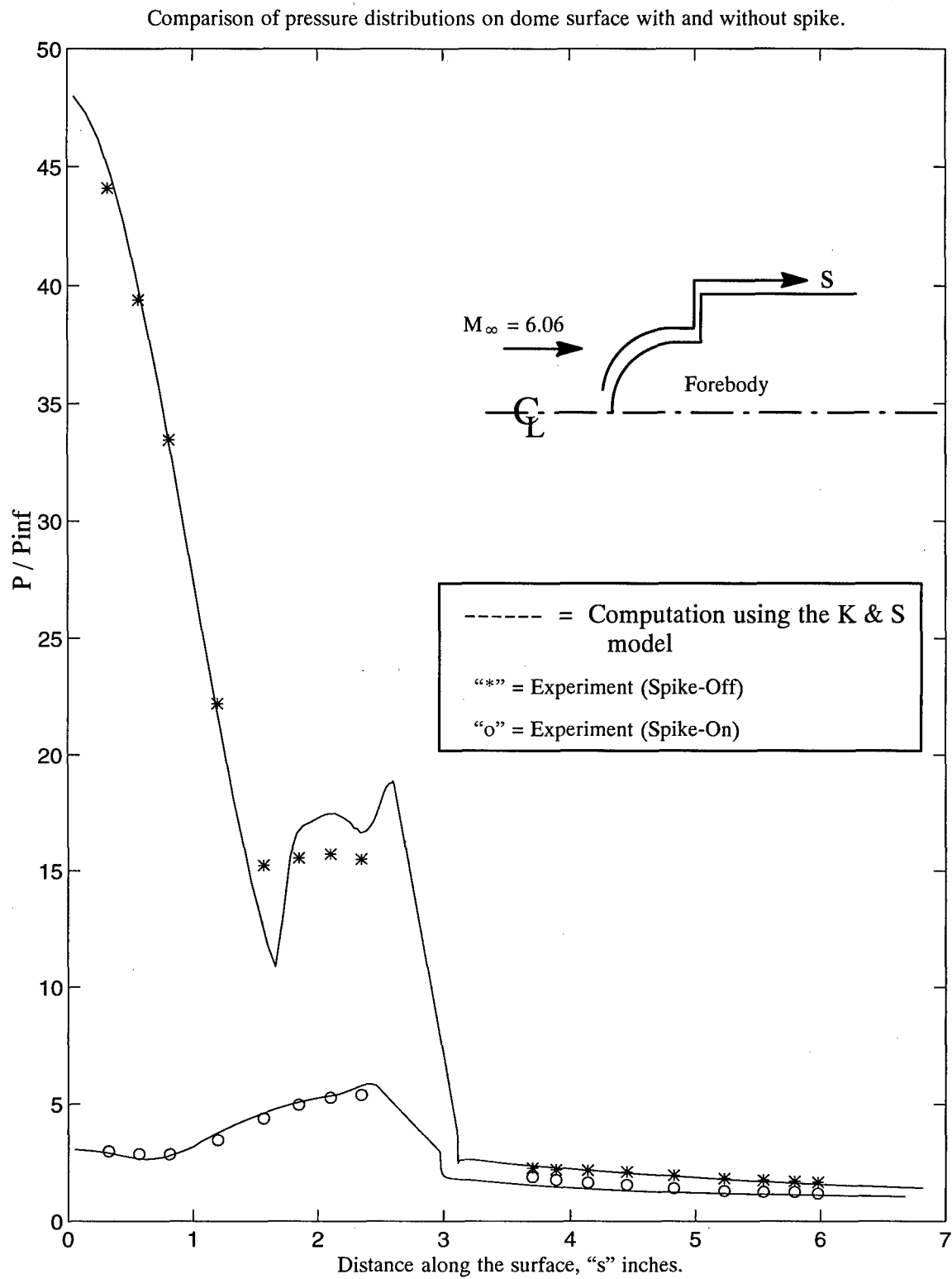


FIGURE 11.
COMPARISON OF THE PRESSURE DISTRIBUTIONS ON THE PROJECTILE SURFACE

Comparison of spike-off Vs. spike-on surface temperature distributions.

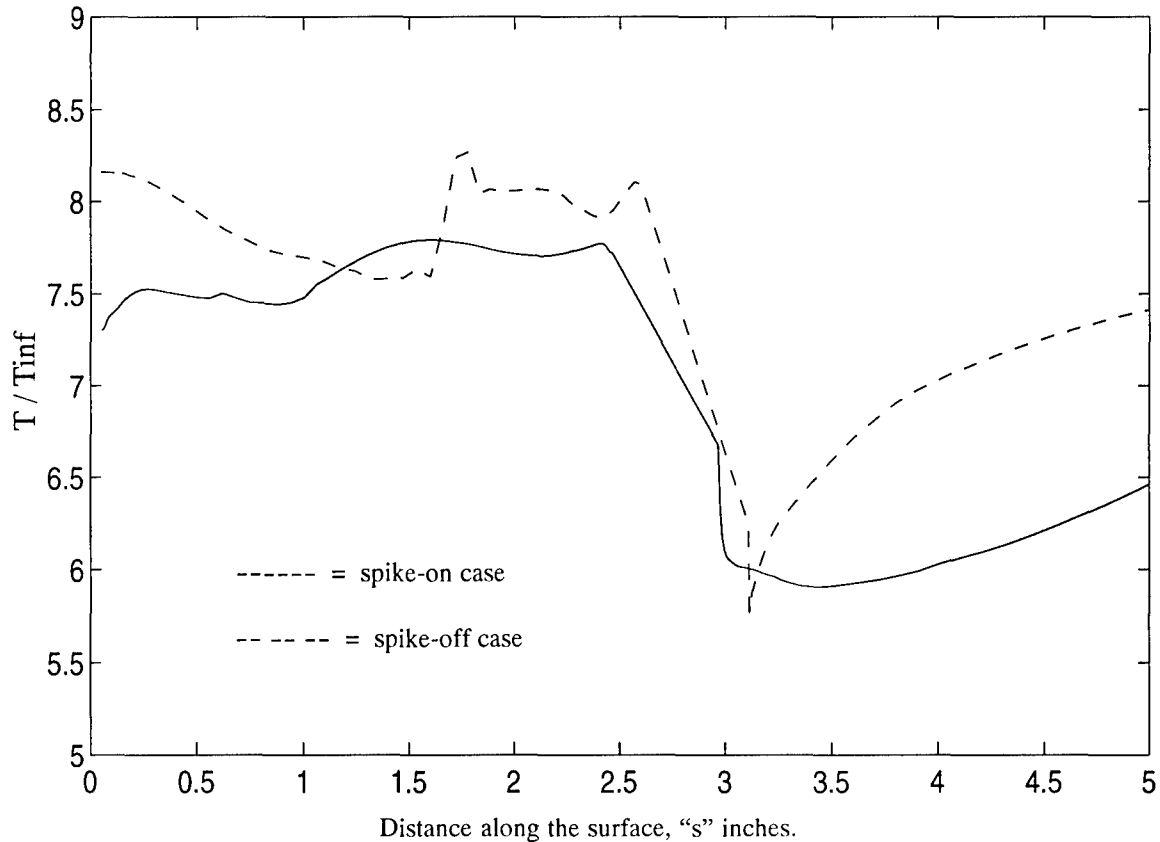


FIGURE 12.

COMPARISON OF THE TEMPERATURE DISTRIBUTIONS ON THE PROJECTILE SURFACE, WITH AND WITHOUT THE SPIKE. COMPUTED WITH THE "K & S" MODEL

$C_{\epsilon 1}$, $C_{\epsilon 2}$ and compressible dissipation ϵ_d) predicts a longer recirculating region. The present model predicts a pressure distribution that is closer to the experimental data. The capabilities presented in this paper highlight that by accounting for the added complexities in turbulence nonequilibrium and transport, caused by the high speed environment, we can now characterize the the compressible turbulent flows surrounding an aerospike in front of a dome. Key features such as flow recirculation and pressure and temperature nonuniformities can be assessed in detail with the aid of computational simulation.

8. REFERENCES

1. Lee, C., McDonnell, R., Purington, D., Trotta, P., Vamiokeren, B. and Yoesting, O., "IR/RF Dome Technology," WL/MN-TR-91-47, Volumes I and II, April 1992.
2. Boland, P., Chazin, S., Couture, M., Fassett, M., Kantelis, J., Waugh, J., C., Ward, C., Willingham, C. and Wirth, S., "IR/RF Dome Technology," WL/MN-TR-91-50, January 1992.
3. Winderman, J., Drake, P., Ginsberg, N., Kuffer, F., Nakum, R., Robins, B. and White, J., "IR/RF Dome Technology Report," WL/MN-TR-91-46, November 1992.
4. Rowe, W., Blume, A. and Boudreaux, E., "Dual-Mode Dome Requirements for Future Air-to-Air Missile," in 3rd DoD Electromagnetic Windows Symposium, Redstone Arsenal AL, 14-16 November 1989.
5. Boudreaux, E., "IR/RF Dome Technology for Missiles," in AIAA Missile Sciences Conference, Naval Postgraduate School, Monterey, CA, 22-24 February 1993.
6. Huebner, L., Mitchell, A. and Boudreaux, E., "Experimental Results on the Feasibility of an

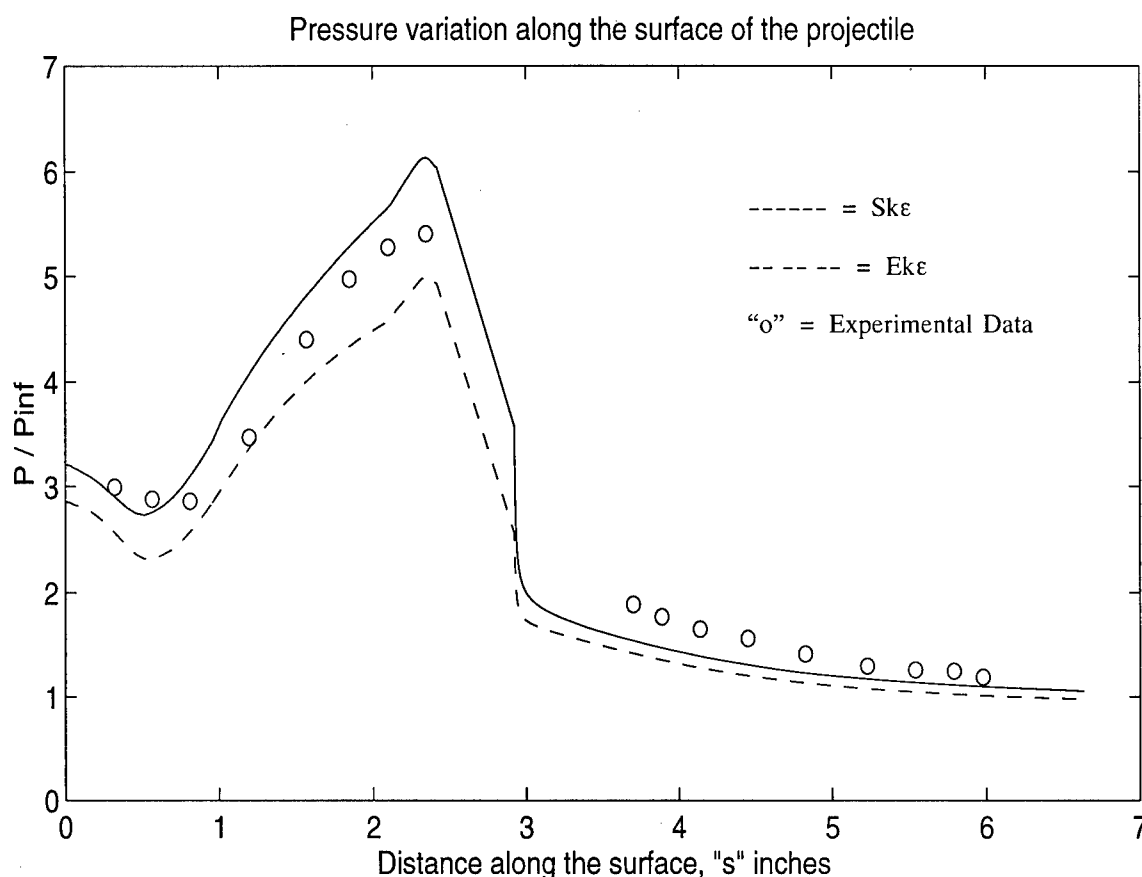


FIGURE 13.
PRESSURE DISTRIBUTION ALONG THE SURFACE OF THE PROJECTILE.

- Aerospike for Hypersonic Missiles," AIAA 95-0737, 33rd Aerospace Sciences Meeting and Exhibit, Reno, NV, 9-12 January 1995.
7. Fleeman, E., "Sensor Alternatives for Future Unmanned Tactical Aircraft," NATO AGARD 8th Symposium on Unmanned Tactical Aircraft, Athens GR, 7-9 October 1997.
 8. Shyy, W. and Krishnamurty, V. S., "Compressibility effects in modelling complex turbulent flows," *Progress in Aerospace Sciences*, Vol. 33, 1997, pp.587-645.
 9. Zeman, O., "Dilatation dissipation : The concept and application in modelling compressible mixing layers," *Physics of Fluids A*, Vol. 2 (2), February, 1990, pp. 178-188.
 10. Sarkar, S., Erlebacher, G., Hussaini, M. Y. and Kreiss, H. O., "The analysis and modelling of dilatational terms in compressible turbulence," *Journal of Fluid Mechanics*, Vol. 227, 1991, pp. 473-493.
 11. Sarkar, S. and Lakshmanan, B., "Application of a Reynolds-stress turbulence model to the compressible shear layer," *AIAA Journal*, Vol. 29, No. 5, 1991, pp. 743-749.
 12. Wilcox, D. C., *Turbulence Modelling for CFD*, DCW Industries, Inc., La Canada, CA., 1992, pp. 183-189.
 13. Huang, P. G., Bradshaw, P. and Coakley, T. J., "Turbulence models for compressible boundary layers," *AIAA Journal*, Vol. 32, No. 4, 1994, pp. 735-740.
 14. Krishnamurty, V. S. and Shyy, W., "Study of the k- ϵ Based Modelling of Compressible Turbulent Flows," *Physics of Fluids*, Vol. 9 (9), September, 1997, pp. 2769-2788.
 15. Chen, Y. S. and Kim, S. W., "Computation of turbulent flows using an extended k- ϵ turbulence closure model," October, 1987, NASA CR 179204.
 16. Thakur, S. S., Wright, J. F., Shyy, W., Liu, J., Ouyang, H. and Vu, T., "Development of

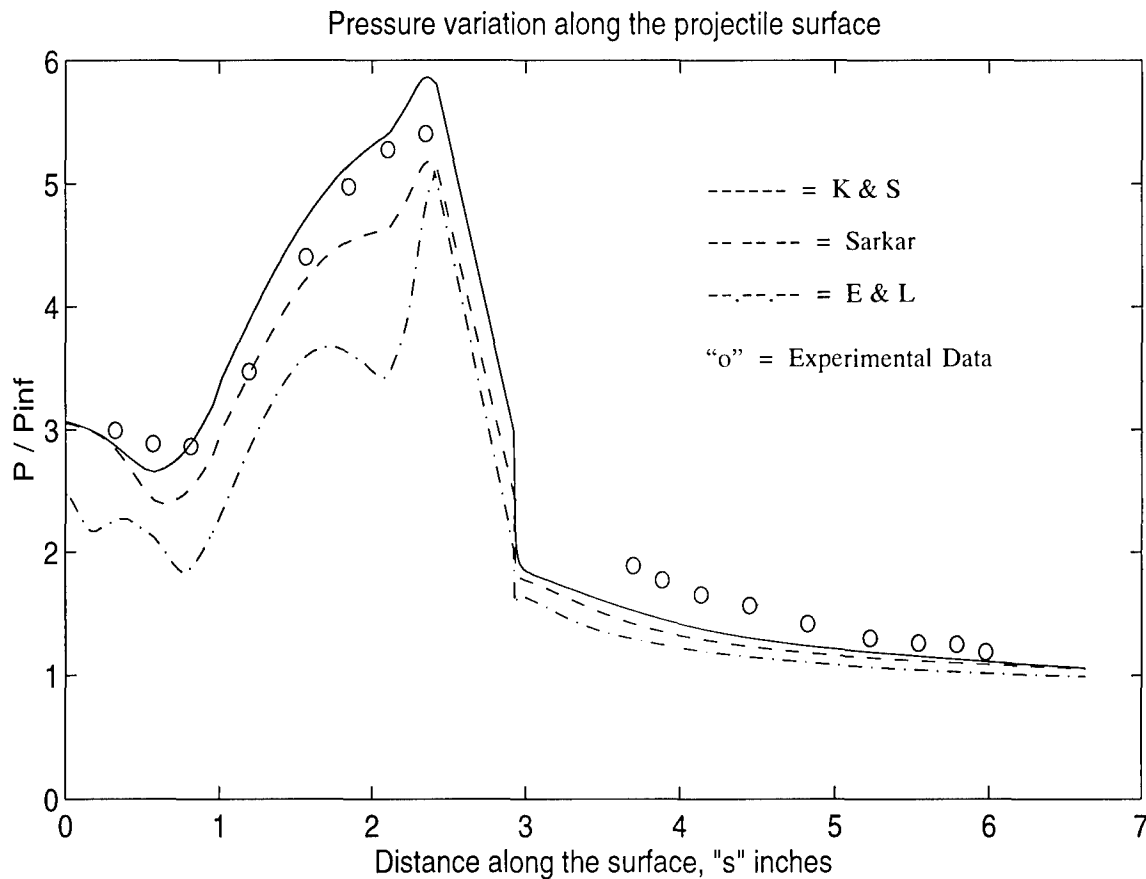


FIGURE 14.
COMPARISON OF THE COMPRESSIBILITY MODIFICATIONS

- pressure-based composite multigrid methods for complex fluid flows," *Progress in Aerospace Sciences*, Vol. 32, No. 4, 1996, pp. 313-375.
17. Sarkar, S., "The pressure dilatation correlation in compressible flows," *Physics of Fluids A*, Vol. 4 (12), December, 1992, pp. 2674-2682.
 18. El Baz, A. M., and Launder, B. E., "Second-moment modelling of compressible mixing layers," *Engineering Turbulence Modelling and Experiments*, edited by Rodi, W. and Martelli, F., Elsevier Science Publishers B. V., Florence, Italy, 1993, pp. 63-72.
 19. Shyy, W., Thakur, S.S., Ouyang, H., Liu, J. and Blosch, E.L., *Computational Techniques for Complex Transport Phenomena*, Cambridge University Press, New York, 1997, pp. 175-187.
 20. Crawford, D. H., "Investigation of the flow over a spiked-nose hemisphere cylinder at a Mach number of 6.8," *NASA TN D-118*, December, 1959.
 21. Schlichting, H., 1968, *Boundary Layer Theory*, McGraw-Hill, Inc.
 22. Ristorcelli, J. R., "A representation for the turbulent mass flux contribution to Reynolds stress and two-equation closures for compressible turbulence," *NASA CR 191569*, November, 1993.
 23. Vu, T. C., Boyer, B. and Shyy, W., "Draft Tube Loss Prediction by Viscous Flow Analysis - The Quest For Accuracy," *Proceedings of the 1996 Hydro Power Conference*, Beijing, PRC.
 24. Bernard, P. S. and Speziale, C. G., "Bounded energy states in homogeneous turbulent shear flow -- An alternative view," *Journal of Fluids Engineering*, Vol. 114, pp. 29-39, 1992.
 25. Krishnamurty, V. S., "Effect of Compressibility On The Turbulence Structure and Its Modelling," Ph. D. Dissertation, University of Florida, Department of Aerospace Engineering, Mechanics and Engineering Science, Gainesville, 1996.

Hypersonic shroud discard at high dynamic pressure

T. Cain and A. Redman
WX9 Aerophysics
Y13 Building
DERA-Farnborough
GU14 0LX

1. SUMMARY

The paper describes analytical techniques for predicting shroud trajectory and experimental techniques for a dynamic study of the initial stages of shroud separation. Dimensional analysis of hypersonic shroud discard at high dynamic pressure is presented. A key feature of the process is the high accelerations due to the high aerodynamic force to weight ratio of practical shrouds. Since Froude number is not critical the experimenter can arrange the discard time to suit his facility. Methods of mass producing small scale model shrouds as well as controlling their release from the core vehicle are described.

2. INTRODUCTION

The intercept of a Ballistic Missile at low altitude may require the kill vehicle to discard a protective shroud at high Mach number and high dynamic pressure. During the discard there is potential to upset the core vehicle either by direct impact with shroud segments or by abnormal aerodynamic loads created through interaction of the shroud and vehicle flowfields. The thin skin construction of probable shrouds results in a large ratio of aerodynamic force to weight and therefore the shroud rapidly accelerates near the vehicle and can achieve extreme attitudes while still in close proximity.

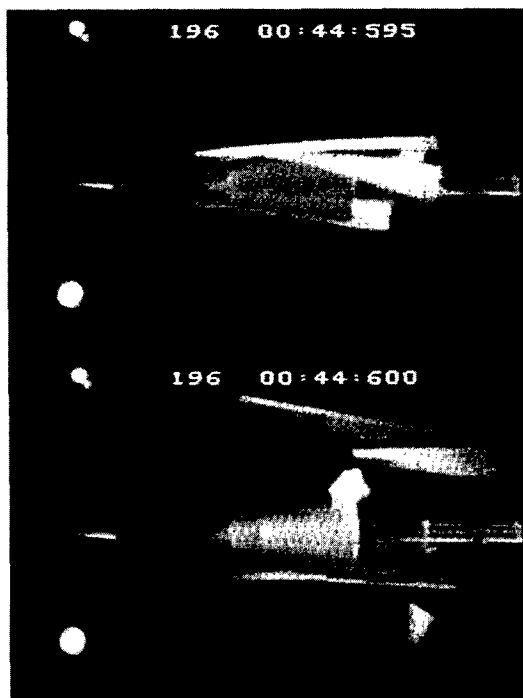


Figure 1 High speed video (200fps) sequence of conical shroud/shroud collision at Mach 5.

The unique features of this aerodynamic problem stem from the high shroud acceleration. The designer is forced to

© British Crown Copyright 1998/DERA. Published with the permission of the Controller of Her Majesty's Stationary Office.

consider solutions in which the shroud is unstable such that it rapidly obtains pitch attitudes which peel it away from the vehicle. Allowing the shroud to drift away, as is more common in weapons release, would leave the highly manoeuvrable shroud within striking distance of its host (figure 1).

The complicated three dimensional flowfield that develops between the lifting shroud and core vehicle varies rapidly during opening. To compute the flowfield at even one instance would be a challenge. Once the concave shroud segment has left the vehicle, the unconventional body still creates a complicated flowfield and it would take considerable time to compute enough information for a shroud trajectory calculation. In this paper we develop Newtonian analysis for the flight of thin rolling shell segments and outline the design of dynamic wind tunnel experiments for investigation of the release. Dimensional analysis of the problem is presented that demonstrates that, with certain constraints, there is a reasonable degree of flexibility in the timescale of the discard and small scale model tests can provide good representation of discard in flight. Methods of mass producing the disposable model shrouds and controlling the release are also described.

3. DIMENSIONAL ANALYSIS

3.1 Full Similarity

Consider a shroud segment that has position defined by co-ordinates with an origin on the core vehicle. The co-ordinates for the segment are included in the vector \tilde{x} along with the co-ordinates of all other shroud petals. Similarly the angles defining the attitude of all parts are included in the vector $\tilde{\theta}$. Thus \tilde{x} , $\tilde{\theta}$ and time, t , are sufficient to describe the trajectory of all the shroud components relative to the vehicle. The air stream is defined by the velocity V and the gas properties ρ_∞ , T , R and γ which are density, temperature, gas constant and ratio of specific heats, respectively. Therefore for a given vehicle of length L , and mass m , the problem is defined by,

$$f(\rho_\infty, V, T, R, \gamma, \mu, L, m, \tilde{x}, \tilde{\theta}, t, g, F) = 0$$

The last parameter is the force applied by the actuators and it may depend on \tilde{x} , $\tilde{\theta}$ and t . A model of the vehicle can be any length L but it must be geometrically similar and for this dynamic problem the centre of gravity location and radii of gyration must all scale with L .

Taking ρ_∞ , V , L , T as the independent variables for mass, time, length and temperature respectively and combining with the remaining seven dimensional parameters,

$$f\left(M, Re, \gamma, \frac{\rho_\infty L^3}{m}, \frac{\tilde{x}}{L}, \frac{\tilde{\theta}}{L}, \frac{Vt}{L}, \frac{Lg}{V^2}, \frac{F}{qL^2}\right) = 0$$

To test the complete full scale system in a wind tunnel the tunnel freestream density must correspond to that in flight (fourth term). Since the velocity in cold hypersonic tunnels will generally be less than in flight this results in lower q and therefore the actuator force must be reduced accordingly (last term). The other consequence of a lower wind tunnel velocity is that the time scale is increased and the discard takes place more slowly. Provided that the acceleration is always large compared to g the trajectory will be identical to that in flight. If gravity could not be neglected then for equivalent Froude number (V/\sqrt{Lg}) a full scale wind tunnel test requires an air velocity equal to that in flight. Since the discard will not generally take place with the missile horizontal it is practically impossible to simulate the general case in a wind tunnel. Fortunately high accelerations are a key feature of hypersonic shroud discard and therefore it is not necessary to account for gravity since it will result in a negligibly small trajectory perturbation.

In addition to scaling the magnitude of the actuator force with q it is also necessary to ensure that the actuator speed is adjusted proportionally to the L/V time scale.

Note that exact similarity can also be achieved with small scale tests in cold hypersonic tunnels. The fourth parameter results in the greatest restriction since it implies that the effective shroud density must scale with the air density. The discard time will be shorter for small models but this is partly compensated by the lower wind velocities. The greatest problem with short discard times is likely to be associated with instrument response times, particularly if measurement of forces on the core vehicle is required.

3.2 Similarity approximations

In addition to Froude number it might also be reasonable to relax the Reynolds number equivalence since the aerodynamic forces will have a weak dependence on Reynolds number. Although hypersonic the problem is likely to remain Mach number dependent largely through its influence on shock layer thickness and therefore on the interference between the various bodies.

Further simplification can be made if the flowfield can be regarded as steady. In that case, the aerodynamic force calculation can be separated from the dynamics of the motion and, neglecting gravity, the problem is defined by,

$$f\left(M, Re, \gamma, \frac{\tilde{x}}{L}, \theta, q, L, m, t, F\right) = 0$$

The first seven parameters define the aerodynamic force. The shroud mass along with the co-ordinates and time define the shroud motion in response to the aerodynamic and actuator forces. Taking q, L, m as the independent variables for time, length and mass respectively and combining with the remaining two dimensional parameters,

$$f\left(M, Re, \gamma, \frac{\tilde{x}}{L}, \theta, t, \sqrt{\frac{qL}{m}}, \frac{F_i}{qL^2}\right) = 0$$

Note that in this case there is no longer a direct restriction on shroud/air density ratio. This gives the experimenter the opportunity to choose air density to match Reynolds number and then scale actuator force proportionally to q . Alternatively if Reynolds number has no significant effect then densities and model lengths can be chosen to produce an appropriate discard time scale. This is particularly useful in short duration test facilities such as gun tunnels.

The time scale is now given by $\sqrt{m/(qL)}$ and the speed of the actuator must be adjusted accordingly.

4. NEWTONIAN ANALYSIS

4.1 Shroud design and co-ordinate system

The experiment depicted in figure 1 involved conical shrouds that were a close fit to the conical core vehicle. The shrouds were allowed to slide backwards and in so doing lifted from the surface and were carried away in the Mach 5 wind.

Calculation of the aerodynamic forces on the conical petals is simplified by choosing appropriate co-ordinates. The petal can always be considered as part of a complete cone and the axis of this cone and the direction of the free stream velocity define the Pitching plane. In this way, regardless of the petals attitude to the air stream, the problem reduces to that of a cone at incidence. The only significant difference is associated with the integration limits.

4.2 The Geometry of a cone at incidence

The Newtonian calculation is largely an exercise in geometry and examples for general bodies of revolution can be found in text books such as the one by Truitt [1]. The details are presented here for two reasons. Firstly, the calculation for a cone can be done in a very direct fashion and secondly the direct approach makes it possible to demonstrate how the inner shroud surface can be treated with only a minor modification to the external result.

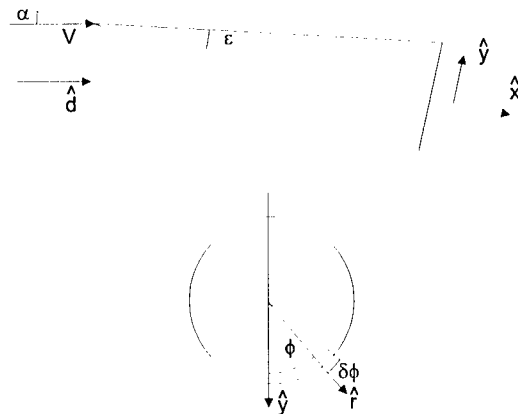


Figure 2 Cone fixed co-ordinate system

Figure 2 shows a cone of half angle ϵ at an incidence α . Consider the slice of cone area δA bounded by the surface rays $\phi + \delta\phi$. That is,

$$\delta \tilde{A} = \frac{R^2 \delta\phi}{2 \sin \epsilon} \hat{n}$$

$\delta \tilde{A}$ can be resolved into components parallel to the axis and parallel to the radius, that is,

$$\delta \tilde{A} = |\delta A| \cos \epsilon \hat{r} + |\delta A| \sin \epsilon \hat{x}$$

The component of area normal to the axis and in the pitching plane (defined by the axis and the free stream velocity vector) is,

$$\delta \tilde{A} \cdot \hat{y} = \delta \tilde{A} \cdot \hat{r} \cos \phi = |\delta \tilde{A}| \cos \varepsilon \cos \phi$$

Consider the area that the slice presents to the flow,

$$\begin{aligned} \delta \tilde{A} \cdot \hat{d} &= \delta \tilde{A} \cdot \hat{y} \sin \alpha + \delta \tilde{A} \cdot \hat{x} \cos \alpha \\ &= |\delta \tilde{A}| (\cos \varepsilon \cos \phi \sin \alpha + \sin \varepsilon \cos \alpha) \\ &= f_d |\delta \tilde{A}| \end{aligned}$$

The mass flow to the slice is therefore,

$$\delta \dot{m} = \rho V \delta \tilde{A} \cdot \hat{d} = \rho V f_d \delta A$$

The mass flow is positive provided $f_d > 0$ and therefore,

$$\phi_{\max} = \cos^{-1}(-\tan \varepsilon \cot \alpha)$$

normally represents an upper limit to the integration for $\alpha > \varepsilon$. However since the inner skin of the shroud may be exposed to the flow in this circumstance, the limit becomes a boundary between the inner and outer flows. The actual limits for the internal flow may fall within the ϕ_{\max} boundaries if the shroud edges shield the region in the cross flow plane.

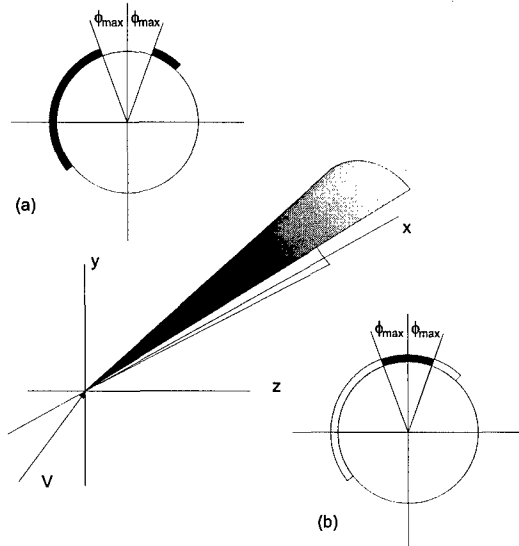


Figure 3 Integration limits for (a) external and (b) internal flow.

4.3 Force coefficients

The force on each slice is simply,

$$\delta \vec{F} = \delta \dot{m} \vec{V} \cdot \hat{n} = \delta \dot{m} V f_d \hat{n}$$

Therefore the force coefficients based on the full cone base area can be obtained by summing integrals of the form,

$$\begin{aligned} C_x &= \int_{\phi_1}^{\phi_2} \frac{f_d^2}{\pi} d\phi \\ C_y &= \int_{\phi_1}^{\phi_2} \frac{f_d^2 \cos \phi}{\pi \tan \varepsilon} d\phi \end{aligned}$$

$$C_z = \int_{\phi_1}^{\phi_2} \frac{f_d^2 \sin \phi}{\pi \tan \varepsilon} d\phi$$

$$C_{M_x} = -\frac{2}{3\pi} \int_{\phi_1}^{\phi_2} \sin \phi \cos \phi f_d^2 d\phi$$

$$C_{M_y} = -\frac{2}{3} \frac{C_z}{\cos^2 \varepsilon}$$

$$C_{M_z} = -\frac{2}{3} \frac{C_y}{\cos^2 \varepsilon}$$

The integrals have standard analytical solutions. The integration limits are determined as described in the preceding section and drawn schematically in figure 3.

5. TRAJECTORY CALCULATION

The aerodynamic forces and moments are known at the tip of the shroud petal and are translated to the centre of gravity to find the moment \tilde{M}_{CG} . The angular motion with respect to the laboratory co-ordinate system, $\tilde{\omega}$, is obtained by solution of the first order differential equation;

$$[I] \dot{\tilde{\omega}} - \tilde{M}_{CG} + \tilde{\omega} \times [I] \tilde{\omega} = 0$$

where $[I]$ is the inertia matrix defined about the centre of gravity [2]. The third term is the cause of the effects commonly associated with gyroscopes [2]. This equation is solved simultaneously with the second order differential equations for the linear motion using a library Runge-Kutta routine.

6. EXPERIMENTS

6.1 Outline

The experiments were conducted in a Mach 5 Ludweig tube and a Mach 10 gun tunnel. Both facilities are short duration with periods of steady flow of 70ms and 20ms respectively.

The concept investigated in the Ludweig tube experiments relied on passive shroud separation. It is necessary to correctly match Reynolds number in order to simulate the skin friction which is responsible for the initial rearward movement of the shroud petals. The Mach number / Reynolds number combination effectively set the dynamic pressure and therefore the model-shroud density is the only parameter with which to control the discard time. The air/shroud density ratio has to be considerably lower than would be of interest for flight, in order to extend the discard time to 20ms. Therefore it is not possible to correctly duplicate unsteady flow (section 3.1) but it is possible to simulate quasi-steady flight (section 3.2).

The vehicle investigated in the Gun tunnel experiments uses an actuator for opening the shroud petals. The actuator is simulated by fine wires that span the test section flow and attach to an external spring. The spring force is chosen to match the actuator/aerodynamic force ratio (section 3.1). The dynamic pressure is obtained by matching Reynolds number at a particular altitude but in general a mismatch in Reynolds number is tolerated as this is essentially an inviscid discard process. In this way a variety of altitudes can be simulated by simply varying the actuator spring constant.

6.2 Model manufacture

The Ludweig tube conical model shrouds were cast MCP-70 Alloy (Wood's Alloy). MCP-70 melts at 70°C and has a

density of 9.67 g.cm^{-3} [3]. Liquid metal at about 90°C was poured into a conical vase section (female) of a stainless steel mould. The mould was preheated by soaking in a tub of near boiling water. The conical section (male) of the mould was inserted into the vase displacing the molten MCP-70 except for that in the 1mm gap between male (cone) and female (vase) parts.

The mould was quenched in a cold water bath before separating the mould parts and removing the shroud from the male part. A light coating of WD40 oil followed by a wipe with a dry rag prior to casting prevented sticking of the shroud to the conical mould. If the oil was not all but removed, the surface finish of the mould was dimpled and pitted. If no oil was applied it was very difficult to separate the mould without damage to the shroud. The shroud was cut lengthways into two or three petals before removing from the male mould.

The shrouds for the gun tunnel experiments are considerably more complex than the generic cone model tested in the Ludweig tube. For Dynamic Similarity, the shrouds also had to be much lighter and plastic was an ideal material. Stereo lithography¹ was used to reproduce the shrouds with their internal structure. Additional recesses were incorporated for insertion of copper weights to correct moments of inertia. The cost of the Stereo Lithography is dominated by the required Computer Aided Design work and this meant it was relatively economic to mass produce the complicated disposable shrouds.

6.3 Shroud release

Shroud petals are kept in place in both experiments by light plastic ties. A single strand of resistance wire (approx. 4Ω) is looped around each of the plastic ties (in turn) and then its ends are connected to a 100V, 10mF capacitor set. A thyristor is used to switch the current and cut the ties once steady flow is established in the tunnel.

7. CONCLUSIONS

Dimensional analysis and practical experience have shown that it is possible to simulate hypersonic shroud discard with small scale models in a short duration facility.

A passive shroud discard mechanism that relied on skin friction to initiate the separation resulted in erratic shroud trajectories some of which resulted in shroud/shroud collisions and shroud/host collisions. A system that positively sets the initial conditions for the shroud motion should prove more effective.

8. REFERENCES

1. Truitt R.W., "Hypersonic Aerodynamics", Ronald Press Company, NY, 1959.
2. Meriam, J.L. and Kraige, L.G., "Engineering Mechanics Vol. 2 Dynamics", 3rd edition, John Wiley and Sons, 1993, pg559.
3. Mining and Chemical Products Ltd, "MCP-70 Alloy", Technical Information leaflet No. 5, Whitchurch, UK, 1995

¹ A manufacturing process in which epoxy resin is photo hardened in typically $12\mu\text{m}$ layers. Three dimensional shapes with included cavities can be built up this way.

The Near Interaction of Lateral Control Jets and Hypervelocity Cross Flow

K.W. Naumann, H. Ende, A. George, G. Mathieu
 French-German Research Institute of Saint-Louis ISL
 5, rue du Général-Cassagnou, F-68301 Saint-Louis, France
 Postfach 1260, D-79574 Weil am Rhein, Deutschland

SUMMARY

Experiments on the interaction of gaseous jets blowing laterally into hypervelocity cross-flow are carried out using physical and optical measuring methods in ISL shock tunnel "B". Different models producing 1 to 3 perpendicularly oriented jets of different gases, gas mixtures, and solid propellant are used. The force effect acting on the model is measured directly using the ISL millisecond aerodynamic force measurement technique. A specially trimmed free-flying model gives sufficient measuring time to allow measurements also on instationary effects during the starting phase of the test flow. The result is that the force effect acting on the model shows reproducible non-stationary behaviour. The visualisation of the jet/cross-flow interaction flowfield is carried out by differential interferometry and illumination by a laser light sheet of particles seeded into the jet flow. The pictures show that single jets in all cases are deflected supersonically by an oblique shock. The space between this internal jet shock and the jet bow shock is filled with large vortices. A detailed quantitative quasistationary description of the flowfield derived from the experiments explains the action and the cause of the essential effects.

LIST OF SYMBOLS

a	acceleration
$C_{i,z}$	jet interaction coefficient in Z-direction
D	diameter of a body
$D_{j,e,con}$	orifice diameter of a conical nozzle
D_j	nozzle throat diameter
$F_{i,z}$	jet interaction force in Z-direction
$F_{j,z}$	jet thrust in Z-direction
f_c	cut-off frequency of low-pass filter
K	parameter of proportionality
Ma	Mach number
$Ma_{j,e}$	Mach number at the jet exit
p	pressure
p_{pit}	Pitot pressure
$p_{0,j}$	jet plenum pressure
p_∞	static pressure of ambient flow
S_j	spacing of the side-jets
t	time
T	temperature
v	velocity
X, Y, Z	model coordinates
x, y, z	test chamber coordinates
ε	angular acceleration of the model
ω	angular velocity of the model
φ	angle of attitude of the model
τ	time measured from test flow onset

Indices

i	interaction
---	-------------

j	jet
t	total
∞	ambient flow conditions
0	stagnation or plenum conditions

Abbreviations

CJ	conical side-jet
DI	differential interferometry
LLS	laser-light-sheet
NI	near interaction flowfield
PR	pressure ratio = $p_{pit}/p_{0,j}$
SJ	sonic side jet

INTRODUCTION

The use of laterally blowing thrusters for the control of hypervelocity projectiles and missiles is under study for different reasons:

- At velocities of more than about 1500 m/s aerodynamic heating is so intense that the durability of a structure depends strongly on its size and thickness. Hence exposed and thin structures thus as wings, flaps, rudders, and actuating devices are particularly affected and should be reduced or omitted as far as possible.
- The efficiency of side-jet control increases with the Mach number of flight, if it exceeds, say 3, and if the shape of the vehicle and the location of the thrusters are appropriately matched.
- Side-jets are well suited for rapid-reaction control, for example, terminal manoeuvring. In addition they are as well effective in the very early launch phase; but this is not a subject of this paper.

Figure 1 shows a simplified sketch of the interaction flowfield and gives the designations of the primary phenomena. In general the side-jets are designed to produce as much thrust as possible, and their plumes are therefore underexpanded with respect to the static ambient pressure. In the case of expansion into hypervelocity cross-flow the collision of jet and cross-flow creates a high-pressure zone at the front side of the jet plume, and a low-pressure zone in the wake. The jet gets deflected, thereby acting on the cross-flow like an obstacle, producing a bow shock and a front separation zone. Underneath the bow shock and this front separation zone the pressure acting on the surface is higher than the ambient static pressure, in the wake it is less. With increasing Mach numbers, both effects become more intensive; but while the wake pressure could drop to utmost zero, the pressure rise due to the windward phenomena depends roughly on Ma^2 .

The first aim of the studies carried out in the ISL shock tunnel was to measure the "efficiency" of the interaction

between laterally blowing gaseous jets and hypervelocity cross-flow. Efficiency in this sense means the component in jet thrust direction of that force increment which is produced by the interaction of the jet and the cross-flow and acts on the surface of the vehicle (see for example Reference 1). Dependent on the location of the jet on the projectile, the shape of the projectile's surface, the inclination of the jet orifice, and a number of other parameters (see Ref. 2), the resultant interaction force acts in direction of the jet thrust, or adverse. The principal parameter of our studies is the influence of the jet gas species, because the numerous reported experiments in wind tunnels had generally to be carried out with pure gases instead of corroding combustion products. Hence the question is whether these results give a realistic representation of the true case. The other aim of our investigation is the description of the flowfield in order to give data which can be used to validate the codes needed to predict the control performance of vehicles.

With these experiments, flowfield visualization by differential interferometry was used routinely with no anticipation of novel findings, because the phenomenology of the interaction flowfield had been widely investigated (see Ref. 2 and the literature cited therein). The impetus to carry out more detailed experiments on the topology of the flowfield came from the fact that at exposure times of about $0.5 \mu\text{s}$ the jet bow shock wave is bulged, indicating the existence of unsteady phenomena.

EXPERIMENTAL SETUP AND TECHNIQUES

Shock Tunnel

All of our experiments are carried out in the ISL shock tunnel "B" (see Fig. 2). Its special capability is to duplicate hypervelocity flow conditions in the lower atmosphere, down to main sea level. For the experiments reported here it is run with parameters duplicating the conditions at a pressure altitude of 500 HPa. Table 1 gives the flow data of the shock tunnel configurations of the different test series.

Aerodynamic Force Measurement Technique

The interaction force is measured directly using generic models, which are set into the test flow. Because the testing time of our shock tunnel is just some milliseconds, a special method was developed, which is described in detail in References 3 and 4. The method is based on direct measurement of model acceleration by a set of small accelerometers. A special mechanical mounting support sets the model free for the time of test flow and fixes it again before it is accelerated too much by the driver gas, which passes the test chamber after the test gas. The parallel time-dependent measurement of the histories of model acceleration, pitot pressure, and side-jet stagnation pressure allows to use a straightforward data evaluation procedure. It compensates to some extent flow variations, if the flow is quasistationary, and allows to determine, whether the flow is quasistationary at any time. Moreover, it is insensitive against disturbances from the starting process of side jets and test flow around complex models.

Models

Different models are used, which produce either "hot" jets of gunpowder charges (Refs. 4, 5), or "cold" jets using internally stored pure gases. References 6 and 7 present the first tests with nitrogen and helium. Subsequently the number of gas species was extended to argon, hydrogen, and mixtures

of 75%He/25%Ar (He75/Ar25) and 50%H₂/50%N₂ (H₂50/N₂50).

All models (see for example Fig. 3) have a flat main wing with supersonic leading edges. This is the surface over which the jet/cross-flow interaction takes place. The body underneath this main wing carries the installations for the side-jets, i. e. charges, valves, reservoir, etc., and accelerometers and pressure transducers. For the side jets, 1 to 3 conical nozzles, oriented perpendicularly to the direction of the ambient flow, or a sonic orifice are mounted flush into the flat surface. The lateral positions of the twin jets are $Y = -20; +20$ mm, for triple jets $Y = -20; 0; +20$ mm. Figure 4 shows a sketch of the internal design of model #3, for "cold" gases, and Table 2 gives the data for all models and jets mentioned in this paper.

Model #5, the latest version, is an evolution of model #3. It is especially adapted to the "reflected-mode" operation of our shock tunnel, which offers a prolonged testing time of about 5 ms. During earlier test series it turned out (Ref. 7) that the models hit the stop before the testing time was over. With an additional trim wing below the nose model #5 is trimmed so that the pitch angle ϕ_y remains small for that time, if the jets are active. Figure 5 shows the histories of X -, Z -, and pitch acceleration, velocity, and displacement or angle, respectively, of a run without side-jets blowing, Fig. 6 of a test with 1 conical jet (CJ) of He75/Ar25. If not indicated otherwise, f_c is 3000 Hz. The figures show that the model can be trimmed exactly only for one condition; in our case it is that with active side-jets. The gain in usable measuring time (see Fig. 6) has to be paid for by a slightly prolonged phase of almost 1 millisecond of disturbed flow around the complex forebody, and slight oscillations of a_z (see Fig. 5A). Whether the model flies free or not can be seen best by the velocity histories, which are integrated directly from the acceleration histories. The displacement histories show that the model travels about 20 mm in streamwise direction during the testing time. A look to the pitch motion in Figs. 5 and 6 shows that an active side-jet changes its direction. Figure 6C shows that the Z -displacement is kept at about zero by a pitch-down-angle of about 21 mrad.

Figure 7 shows a differential interferogram of model #5 in established flow. In order to shield the jet interaction zone against disturbances, which originate at the trim wing addition, the main wing of model #5 has to be extended. This extension into the circumferential shear layer of the test flow does not affect the jet interaction force measurements. Nevertheless, it creates phase objects in the differential interferograms, which are indicated in Fig. 7. These phase objects represent the more-and-more steepening shock which originates at the leading edge of the outer parts of the main wing. They are equally present in all other differential interferometry pictures of model #5, and we have to keep in mind that they are not at all a part of the effects under study.

Flow Visualisation Techniques

Our standard technique for flow visualisation is differential interferometry (DI). Figure 7 shows an example, and Reference 8 and the literature cited therein give detailed information. Two perpendicularly polarised light beams pass the flow field, there separated by a certain distance from each other. When they are brought together by an analysing optical component, the different optical lengths of the two light paths produce interference patterns. These can be fringes, or

changes in light intensity if the fringe space is chosen to be infinite. In this case the pictures look like schlieren pictures. The fringe shift is proportional to the difference of the density integral along the optical path. The exposure time of the DI pictures shown here is about 0.5 microseconds.

It is the nature of those integrating methods that they cannot give information on details in 3-dimensional flowfields. Visible are all phenomena which are oriented collinearly with the light beams, boundaries of spacial phenomena, and very strong local phase objects. In general limited quantitative data can be extracted from those pictures, if 3-dimensional effects are studied.

In order to obtain more detailed information about the procedure of jet deflection, we carried out laser-light-sheet (LLS) visualisation experiments. The jet flow is seeded with titanium dioxide particles, which are illuminated by a laser light sheet of 0.3 mm thickness. It is oriented parallel to the flow direction, and perpendicular to the optical axis of the test chamber. Figure 8 shows a principle sketch of the optical arrangement. The LLS position is varied from $0 \leq y \leq 20$ mm. The exposure time, i. e. the pulse duration of the illuminating ND-YAG laser, is 20 nanoseconds. This means that phase objects, travelling with 1000 m/s, displace just 20 micrometers during exposure time.

JET INTERACTION FORCE

The first experiments on "hot" jets (see Refs. 1 and 4) showed that under the condition of hypervelocity ambient flow, and a flat surface, the interaction force produced by a conical nozzle roughly equals the jet thrust. The time needed to establish quasistationary interaction conditions, i. e. constant aerodynamic coefficients, was about 1 millisecond. The first experiments on "cold" jets with model #3 gave some indication that the nature of the thruster gas has some influence on the time needed to establish quasistationary conditions (see Ref. 6). For CJs of nitrogen the then usable testing time of about 2 milliseconds was not sufficient to observe quasistationary conditions, while for sonic jets of helium and nitrogen, and conical jets of helium the settling time was less than 1 millisecond. One purpose of the experiments with model #5 is to get more information on the time-dependency of jet interaction force.

Evaluation of the Jet Interaction Coefficient

The evaluation of the jet interaction effect yields time-dependent data, because it is just ordinary arithmetics using measured histories. Obeying Newton's first law, for quasistationary conditions, i. e. the aerodynamic coefficients are constant over time, all force components of the jet interaction coefficient $C_{i,z}$ can be expressed as model accelerations using the formula

$$C_{i,z}(t) = [F_{i,z}(t) + F_{j,z}(t)] / F_{j,z}(t) = [a_{i,z}(t) + a_{j,z}(t)] / a_{j,z}(t) \quad (1)$$

The measured total acceleration is composed as

$$a_{i,z}(t) = a_{\infty,z}(t) + a_{j,z}(t) + a_{i,z}(t) \quad (2)$$

with the acceleration due to the ambient flow alone

$$a_{\infty,z}(t) = K_{\infty,z} \times p_{\text{pit}}(t) \quad (3)$$

and the acceleration due to jet thrust

$$a_{j,z}(t) = K_{j,z} \times p_{0,j}(t) \quad (4)$$

Putting this into (1) yields

$$C_{i,z}(t) = [a_{i,z}(t) - K_{\infty,z} \times p_{\text{pit}}(t) - K_{j,z} \times p_{0,j}(t)] / a_{j,z}(t) + 1 \quad (5)$$

In contrast to the experiments with models #1 to #4, the model #5 showed systematic variations of lift- and pitch coefficients. These systematic oscillations of the model which occur during the starting process of the test flow as a result of the complex shape can be partially eliminated by calculation of a time-dependent coefficient; in this case: $K_{\infty,z}(t)$, using measured histories to yield

$$K_{\infty,z}(t) = a_{\infty,z}(t) / p_{\text{pit}}(t) \quad (6)$$

and consequently

$$C_{i,z}(t) = [a_{i,z}(t) - K_{\infty,z}(t) \times p_{\text{pit}}(t) - K_{j,z} \times p_{0,j}(t)] / K_{j,z} \times p_{0,j}(t) + 1 \quad (7)$$

Figure 9 gives $K_{\infty,z}(t)$ from 8 different tests. Because the model hits the stop at about $\tau = 3$ milliseconds, if the jets are not blowing, the history of $K_{\infty,z}(t)$ in Fig. 9 is time-dependent only for the time of free-flight of all tests, i. e. $0 < \tau < 3$ ms. For $\tau > 3$ ms $K_{\infty,z}$ is set constant using the mean value of $K_{\infty,z}(\tau > 3 \text{ ms}) = -52.96 \text{ g/MPa}$.

It turns out that the results in $C_{i,z}(t)$ differ just little, if $K_{\infty,z}(t)$ is used instead of the constant $K_{\infty,z} = -52.96 \text{ g/MPa}$. Nevertheless, all data shown are calculated using $K_{\infty,z}(t)$.

Results on Jet Interaction Coefficient

The histories of $C_{i,z}(t)$ shown in the following figures are evaluated as follows (for details see References 3 and 4):

- The data are recorded with a sampling frequency of 1 MHz. No filter in the measuring cascade is used.
- Unless indicated differently, the cut-off-frequency of the numerical low-pass filtering procedure is 2 KHz.
- The filtering procedure can be limited to selected parts of a history.
- For the time before the onset of jet flow, $C_{i,z}(t)$ is set to be zero, for the time between jet flow onset and τ it is set to be 1.
- For the time after the testing time, $C_{i,z}(t)$ is usually set to be zero, because after the impact of the model at the stop the histories become unrealistic and oscillate heavily.

Figure 10 shows $C_{i,z}(t)$ for 1 CJ of N_2 , and Fig. 11 $C_{i,z}(t)$ for 1 CJ of H_2 50/ N_2 50 and H_2 . The experiments with N_2 differ from all others, because there the jet starts after the start of the test flow. This means that the jet plume has to be established when an ambient atmosphere is present. The erratic accelerations during the first milliseconds are caused by the reservoir opening device and are shown here to give an idea about the time needed to establish regular measuring conditions. When these disturbances are over, the $C_{i,z}$ history shows regular and repeatable oscillations with a mean value of $C_{i,z} = 2$. For the experiments of Fig. 11, where the jets start first, we can see that during the first two milliseconds of test flow $C_{i,z}(t)$ is about 1, i. e. $F_{i,z}(t)$ is about zero. From $\tau \approx 2$ ms on $C_{i,z}(t)$ rises to a value of about 2 and starts to oscillate. Notice that the oscillations of both tests in Fig. 11 are

reproducible, even with respect to the phase. Figure 12 shows that for $\tau = 2$ to 3.5 ms the histories of $C_{i,z}(t)$ for CJs of H_2 , H_250/N_250 , and N_2 coincide astonishingly well, despite the different timing of the side-jet.

The $C_{i,z}(t)$ of experiments with monatomic gases are shown by the following figures. Fig. 13 shows $C_{i,z}(t)$ of two experiments with CJs of Ar. Both histories coincide very well, and show basically the same behaviour as the $C_{i,z}(t)$ of the diatomic gases: for the period till $\tau \leq 2$ ms, $C_{i,z}(t)$ is somewhat higher than for diatomic gases; no strong oscillations are visible, and the mean value drops slightly towards a value of about 1. Beginning with $\tau \approx 2$ ms, $C_{i,z}(t)$ rises to a mean value of two and starts to oscillate. Figure 14 compares $C_{i,z}(t)$ of pure Ar with that of $He75/Ar25$ and shows that there is no significant difference.

Figure 15A shows that there is no significant difference between CJs of monatomic and diatomic gases as well. The averaged $C_{i,z}(t)$ of all experiments with CJ is given by Fig. 15B.

The $C_{i,z}(t)$ with sonic jets (SJ) and monatomic gases is shown by Fig. 16A; mind the different graduation. The overall level of the $C_{i,z}(t)$ -values is higher, because for the same mass flux $F_{j,z}(t)$ is less than half of that of CJs, as can be seen from Tab. 2. If jets of the same mass flux produce an interaction force which equals the thrust of a CJ, $C_{i,z}(t)$ of a CJ is 2, but for the SJ it is 3.3 for diatomic gases. If the overall force, $F_{i,z}(t) + F_{j,z}(t)$ should be the same, $C_{i,z}(t)$ of the SJ had to be 4.6. With this in mind, we can see a similar behaviour as with the CJs before, with well reproducible histories. $C_{i,z}(t)$ decreases slightly till $\tau = 2$ ms, and begins then to oscillate around a value of 4 to 5. Figure 16B shows that the same holds for SJ of diatomic gases; neither the qualitative behaviour of the $C_{i,z}(t)$ -histories nor the absolute values differ significantly. Figure 17 shows the averaged $C_{i,z}(t)$ of all experiments with SJ.

The $C_{i,z}(t)$ of 3 CJs of diatomic gases is shown in Fig. 18. The $C_{i,z}(t)$ -histories of Fig. 18A differ from those of single CJs in two respects: The disturbances created by the starting of the jet flow are minimal, and the lighter gas, H_2 , shows stronger oscillations of $C_{i,z}(t)$ than the mixture of H_250/N_250 , at about the same mean value. The fact that the $C_{i,z}(t)$ of 3 CJs is about the same as that of single CJs indicates that in these cases the 3 CJs act independently and do not produce a coherent and extended front separation zone. This can also be taken from the DI-pictures below, and is caused from the rapid decrease of jet plenum pressure as a consequence of the very high mass flux. Particularly the hydrogen jets have almost not sufficient pressure to form a plume. Figure 18B gives the averaged $C_{i,z}(t)$ of 3 CJ.

The experiments with model #5 show that for the conditions under investigation the development of $C_{i,z}(t)$ has two phases: For $0 < \tau < 2$ ms the $C_{i,z}(t)$ -histories show small oscillations and decrease slowly towards a value of about 1. For $\tau > 2$ ms the $C_{i,z}(t)$ oscillates heavy at a frequency between 500 and 1000 Hz. For CJs the mean $C_{i,z}(\tau > 2\text{ms})$ is about 2, independent of jet gas species or molecular weight. For SJs jets the mean $C_{i,z}(\tau > 2\text{ms})$ is about 4, also independent of the jet gas.

An explanation of the behaviour of the $C_{i,z}(t)$ -histories during $0 < \tau < 4$ ms has to be incomplete, because we have

no means to take a sufficient number of pictures during this time. Hence, for the moment, we just can try to examine some possible causes of errors:

- The model itself oscillates as a consequence of its complex shape with multiple shock/shock interactions. This possible cause is partially eliminated for $0 < \tau < 3\text{ms}$ by the use of $K_{\tau,z}(t)$. Moreover, since the model oscillates equally from the beginning, $C_{i,z}(t)$ is comparatively quiet for $0 < \tau < 2$ ms. The first oscillation of $C_{i,z}(t)$ takes place before the constant part of $K_{\tau,z}(t)$.
- Oscillations of the jet flow could be a possible reason. Earlier experiments with an instrumented nozzle showed that the jet flow establishes very rapidly (see Ref. 6). Some of the jet plenum pressure histories show mild oscillations, but these smooth down during the first 3 milliseconds, and they have a frequency of about 2 kHz. Nevertheless, experiments are planned in order to quantify the possible influence on $C_{i,z}(t)$ -oscillation.

If just the mean value of $C_{i,z}$ is regarded, the oscillations are not so crucial, because these are of a harmonic nature, which allows averaging with good accuracy. Another information which can be drawn from these experiments is that $F_{i,z}(t)$ is almost immediately effective, if the jet blows into a yet established hypervelocity cross-flow. Even impulse thrusters with blowing times of little more than 1 ms produce an interaction force.

The comparison of the results presented here with those obtained earlier using model #3 (see Ref. 7) shows for single CJs a good agreement with respect to the mean value of $C_{i,z} \approx 2$. The fact that for nitrogen $C_{i,z}$ does not attain an quasistationary value within 2 ms is confirmed. The different behaviour of $C_{i,z}$ during $0 < \tau < 2\text{ms}$ has at least partially to be attributed to the different model shapes, which produce different transient phenomena during the period of test flow onset. Perhaps the change from a closed to an open test section has an influence on the model motion during this period as well. Remarkable is the good reproducibility of even the unsteady parts of the history of model motion.

For the SJs, the results obtained with model #3 for $0 < \tau < 2\text{ms}$ are confirmed insofar as $C_{i,z} \approx 2$ for this period. Nevertheless, because model #3 hit the stop at about $\tau = 2\text{ms}$, the higher values of $C_{i,z} > 4$ could not be measured under these conditions. Here the experiments with the more stably flying model #5 gave new insights on the mean $C_{i,z}$ and on the transient behaviour during the period of test flow onset.

JET INTERACTION FLOWFIELD

The experiments on jet interaction force have to be carried out using comparatively large nozzles, because the thrust level needed is very high. The large nozzles limit the range of our considerations to the near interaction (NI) flowfield, because height and width of our test chamber are just $16 \times D_{j,e,con.}$ and the length of the test section is just a little bit longer. The benefit of these conditions is a very good resolution of the immediate vicinity of the nozzle opening.

Unless otherwise indicated, all of the quantitative data mentioned in this chapter are instantaneous values, taken from the measured histories at the time of exposure.

Results from Laser-Light-Sheet Visualisation

As mentioned above, the idea to make LLS-visualisation of particles, which are seeded into the jet flow, came from the observation, that the jet bow shock contour is not smooth, but shows bulges. The results have in brief been published in Ref. 9, but for convenience they are presented here as well. Figure 19 shows pictures of 1 to 3 CJs with the LLS in the symmetry plane and at different distances aside. These jets are "hot" jets driven by gun-powder charges, which allow to have a high pressure ratio $PR = p_{\text{jet}}/p_{0,j}$ even with 3 jets. The free-jet boundaries are clearly visible, and the change of the intensity of the scattered light yields information on the shape and the position of the internal jet shocks.

It can be seen immediately that the deflection of the free jet is a highly turbulent process. In all cases the jet flow behind the internal jet shock is dominated by vortical structures. No particles can be seen in the front separation zone, or in the wake immediately behind the jets. This shows that no jet flow is entrained into both structures.

Figure 19A1 shows the particle distribution in the symmetry plane of a single CJ. Notice that effectively all of the jet flow is deflected by an oblique shock wave. Calculations below will show, that the deflection process is entirely supersonic. Since this picture is taken of a "hot" jet, the deflected jet flow has a higher velocity than the ambient flow immediately behind the bow wave, and entrains the latter. This is also indicated by the direction, into which the vortices develop. While the origin of the vortices is immediately above the frontside of the internal jet shock, this shock itself appears to be straight and not much affected by the vortices.

Figures 19A2 to 19A5 show the particle distribution outside of the jet symmetry plane for the case of 2 jets at $y = 15; 10; 5; \text{ and } 0 \text{ mm}$. At $y = 15 \text{ mm}$ (19A2) the LLS-plane cuts the jet opening a little bit. In this case the seeding is not very homogeneous. Nevertheless, we can see that the internal jet shock has about the same inclination and distance from the model surface as in the jet symmetry plane, 19A1. Behind this shock strong vortices are visible. Just besides the jet opening, at $y = 10 \text{ mm}$ (19A3), we again see the internal jet shock, at about the same position, and the intense vortices. The picture at $y = 5 \text{ mm}$, 19A4, shows not much change. At $y = 0 \text{ mm}$ (19A5), corresponding to the model symmetry plane $Y = 0 \text{ mm}$, the particle density is strongly reduced. Some vortical structures can be seen, but we certainly are near the boundary of the mixing zone. All pictures do not show particles in the front separation zone, and only few of them in the wake. These pictures, in coincidence with earlier results of force measurements, show that with the jet spacing given, and for a PR of 30 to 40, these conical jets expand almost independently. Hence picture 19A1 of the symmetry plane of a single CJ represents well the conditions of the symmetry plane of a jet in twin configuration, with a spacing of $S_j = 3.2 D_{j,e,con} = 10 D_j^*$.

The case with 3 CJs is shown in pictures 19B1 to 19B5, at the same respective y -coordinates. 19B1 shows the symmetry plane of an outer jet, 19B5 this of the central jet. For the symmetry plane of the outer jet the picture looks very much like that of a single jet. As the LLS-planes approach the centre, the inclination angle of the internal jet shock wave decreases, and the distance of its origin to the model surface increases. For the central jet the internal jet shock wave is almost perpendicular to the jet axis. In the jet deflection zone

behind the internal jet shock wave strong vortices are generally present. The only picture which does not cut a nozzle opening is 19B3 at $y = 10 \text{ mm}$. The position and shape of internal jet shock wave and vortices show that in this case the two adjacent jet plumes converge. As for all cases before, no particles can be seen in the front separation zone and in the wake.

The luminous areas, which can be seen in pictures 19A3,4,5,B1,2,3 represent no phenomena of the jet interaction flowfield that could be seen in the DI-pictures below. Since the jets had to be started before the test flow onset, this phenomenon may be caused for example by the deposition of particles at the window of the closed test chamber, being used with these experiments.

Figure 20 compares LLS-pictures of a single CJ and SJ, at about the same PR. The CJ shows the same phenomena described above. The SJ has, of course, a more expanding plume, because of the much higher Prandtl-Meyer-deflection capability of the sonic flow. The internal jet shock wave is more curved, compared to the CJ, because of the source flow characteristics of the plume. With respect to the streamline direction, all of the shock wave is oblique. In the jet deflection zone behind the internal jet shock wave the vortices are larger than those of the CJ. While just in front of the SJ some particles can be seen in the region in front of the jet plume, no particles enter the wake, despite of the very high theoretical Prandtl-Meyer deflection capability of the sonic flow.

Results from Differential Interferometry Visualisation

As mentioned before, DI-visualisation in general gives only limited information on 3-dimensional phenomena. But, in some experiments with "cold" jets of internally stored gases, we have the unanticipated advantage to get simultaneous information on wave phenomena and jet topology. The reason for this is a positive Joule-Thompson effect, which occurs at the internal expansion of some reservoir gas species after the seal is opened. Reference 7 gives a detailed description of this process. For pure nitrogen, for example, the resultant jet plenum temperature is 183 K. In the course of the expansion, the flow cools further down, and condensates partially. The particles can be seen in DI-pictures, for example Fig. 21, as shadows. Of course the information is not so exact as that obtained from LLS-visualisation, because the condensed particles are not stable, and will at last evaporate. Moreover, the shadows represent an integrated effect along the line of sight. The results presented below show that condensation takes place as well with argon, and gas mixtures containing nitrogen and argon.

Figure 21 shows DI-pictures of jets of pure nitrogen and helium from experiments with model #3. These results also have been published in brief earlier, in Ref. 9, but are included for convenience. Picture 21A shows a SJ of nitrogen. It can immediately be seen that the vortices of the jet deflection zone fill all of the space between the internal jet shock and the jet bow shock. Moreover, it is evident that the bulges of the jet bow wave result directly from these vortices, and occur at the positions where the vortices interact with the jet bow wave. A jet boundary in the sense of a limiting streamline cannot be evaluated. In contrast, there exists a broad mixing zone: While the vortices carry jet gas out till to the jet bow wave, ambient gas is entrained deep into the mixing zone as well. As the condensed particles move

downstream, the shadows fade out. This can be due to perpetual dilution during the mixing process, and to evaporation of the particles. While no information on the wake flow can be drawn from this picture, we see that the origin of the internal jet shock is coupled to the edge of the front separation bubble.

Picture 21B shows the NI of a sonic helium jet. Because He has no positive Joule-Thompson effect, we can see little more than the heavily bulging jet bow wave and the front separation zone with its conical shock.

Pictures 21C,D show the interaction of single CJs of nitrogen and helium at similar PRs. In picture 21C of the nitrogen jet we can see the vortices and the internal jet shock wave. Structure and size of the vortices differ not much from those observed by LLS-visualisation (Fig. 19A1). Again we can see that the jet bow wave shows bulges at those locations, where the vortices interact with the jet bow wave. Again the jet boundary cannot be defined clearly, because there is a broad vortical mixing zone. The DI-picture of the helium jet interaction shows similar phase objects, but yields much less information.

The DI-pictures of multiple nitrogen jets, 21E,F show the same phenomena. Because 2 and 3 jet plumes lay behind each other, the individual vortices cannot be seen as well as for the single jet. In both cases the bulges of the jet bow wave are caused by an interaction of the wave with vortices. Pictures 21A,C,E,F show that the origin of the internal jet shock is related to the edge of the front separation bubble.

Figure 22 shows DI-pictures of single "cold" CJs taken with model #5. Remember that the shock-like phase object, which crosses the picture of the interaction flowfield at a steep angle, must not be related to jet interaction, as is shown above in Fig. 7. The Pitot probe is placed over the model wing, because the flow below is too much disturbed by the trim wing. The Pitot probe is set aside as far as possible in order not to be affected by the jet interaction. On some of the pictures can be seen a blunt pressure probe, which is inclined relative to the test flow direction, and placed into the interaction flow field. The purpose is to get some idea about the order of magnitude of the pressure fluctuations there, and to evaluate whether pressure measurements in this region make sense. We have not yet evaluated the data at this time.

Picture 22A shows the interaction of a single CJ of nitrogen, as it is known from Fig. 21, in order to facilitate the comparison. The phenomena are identical with those described with picture 21C. Pictures 22B,C show the interaction of single CJs of H_2 and H_250/N_250 , respectively. Picture 22B is a rare exception, because here the internal jet shock wave is clearly visible, probably as a result of the very low density of hydrogen. Vortical structures cannot be seen because of the absence of condensation. For the H_250/N_250 mixture, condensation is present again, and we find the same phenomena as for N_2 -jets. A special phenomenon is the bulged internal jet shock wave. With some imagination we can see a similar shape in picture 22A as well.

Pictures 22D and E show single CJs of Ar. The condensation is so strong that details between jet opening and internal jet shock wave are not visible. Again we see the vortices between the internal jet shock wave and the jet bow wave. The many particles in the expanding and deflecting jet, and

the complete absence of particles in the wake zone indicate that the jet flow does not tend to reattach at the model wall near the NI flowfield. The NI of a CJ of $He75/Ar25$ in picture 22F shows no condensation effects due to the large fraction of He. With the knowledge about the topology of the interaction flowfield we can identify the internal jet shock wave. Details on mixing are not visible.

Figure 23 shows the interaction of single SJs of model #5. The interaction flowfield of a pure sonic hydrogen jet shows the heavily bulging jet bow wave, and even some shadows which indicate vortical structures. Because of the very great difference in density of the H_2 and the ambient flow, these shadows may also be caused by heavy density gradients in the flowfield. Anyhow, the NI flowfield shows the same phenomena as that of N_2 or H_250/N_250 in picture 23B. In the latter the condensing N_2 gives a good impression on the extent to which the vortices of the mixing zone interact with the jet bow wave. The SJ of Ar in 23C allows not only to identify individual vortices, but gives an indication of their spacing. The SJ of $He75/Ar25$ in 23D gives no information on internal structures.

Figure 24 shows the interaction of triple CJs of model #5 for diatomic gases. The hydrogen jets of picture 24A have a very low PR, because H_2 leaves the reservoir most rapidly. Hence the internal jet shocks lay immediately outside of the jet exit. Notice the very small front separation zone, compared to that of Fig. 21F. This supports the interpretation of the interaction force measurements above. The PR of the jets is so small that they interact mainly individually with the oncoming flow; their plumes do not converge. Because the internal jet shock is located so near to the jet opening, the separation bubble is extraordinary small, what explains the small $C_{i,z}(t)$ of this arrangement. The triple CJs of H_250/N_250 show a greater distance between jet opening and internal jet shock, due to the higher PR. The front separation zone is a little bit larger, but still not larger than those of the single CJs of Fig. 22, indicating again, in coincidence with the $C_{i,z}(t)$ -results, rather isolated action of the individual jets. The successive orientation of the jets along the line of sight again prevents the identification of isolated vortices.

Description of the Jet Interaction Flowfield

Using the results of both interaction force measurements, pressure measurements, and flow visualisation, the general description of the jet interaction flowfield is as drawn in Fig. 25 for a single CJ of "hot" gas. $Ma_{j,e}$ is 3.8, and the static pressure is about double of the static pressure of the ambient flow. The jet expands further to higher mach numbers and penetrates the cross-flow. At the forward jet boundary the jet interacts with the cross-flow, but because of the boundary layer, which develops along the wing surface, the static pressure of the separation bubble is limited to that pressure, which exists underneath the conical separation shock, in this case: $3.41p_\infty$. The flow in the separation bubble is reversed near the wall, and runs in main flow direction in the upper parts of the separation bubble. If the sonic streamline of the flow in this separation bubble is stagnated, the pressure can rise to about $6.3p_\infty$. This is not enough to force more than some marginal compression onto the front boundary of the jet plume, and it runs about straight outward till the edge of the separation bubble. There the stagnation pressure of the cross-flow rises drastically, because of the double compression due to the conical separation shock and a subsequent normal shock at the jet boundary. The stagnation

of the flow, which has passed the separation shock creates a local pressure maximum of, in this case, $55\text{--}60p_\infty$. Above this zone, where the cross-flow just passes the bow wave, the pressure is less, below $28p_\infty$. The decisive point of the flowfield therefore is "a" in Fig. 25.

The location of the "triple point a" (TPa), i. e. its distance from the nozzle opening, can be calculated as follows:

- Because of the self-similarity of the separation of hypervelocity boundary layers at blunt obstacles (see for example Ref. 2 and the literature cited therein), the deflection angle at the separation stream line is about 13 deg., which allows to calculate the angle of the conical shock from Ma_∞ .
- From this data and those of the ambient flow the stagnation pressure in TPa can be calculated.
- The jet plume expands till TPa. There the pressure of the jet immediately after the jet bow wave has to be in equilibrium with the stagnation pressure of the cross-flow. The angle between the leading jet streamline and the internal jet shock is that, which produces the optimum combination of deflection angle and pressure rise: The shock angle of maximum deflection, with a Mach number of the deflected stream line near unity. Using the given streamline direction, expansion conditions, and static pressure behind the internal jet shock, the distance of TPa from the jet opening can be calculated, as has been done for the conditions of Fig. 25.

The shocked jet flow at TPa is that of the maximum pressure and of $Ma = 1$, i. e. that of the highest stream density. It expands, maintaining roughly its flow direction after deflection, and mixing with the cross-flow. The jet streamlines further downstream need not to be compressed so much; the Mach number behind the internal jet shock is supersonic for the succeeding streamlines.

The stagnated cross-flow is subsonic in TPa. Accordingly it can expand in any direction. One effect of this expansion is that this flow acts on the separation bubble as well. The widely observed pressure peak in the immediate vicinity of the jet opening (see Ref. 2), and the coincident attachment of the separated flow there may be forced by the shocked cross-flow expanding out of TPa.

The formation of the vortices between the internal jet shock and the jet bow shock starts directly at TPa. The flow visualisation results give some indication that the position of TPa oscillates around a mean value. This would be no surprise, because most blunt hypervelocity interactions tend to oscillate. With the data available it cannot be evaluated whether this oscillation triggers the vortex formation, or depends on it, or whether both effects depend on each other reciprocally. Additional experiments are needed to get detailed information on vortex generation, and motion.

REFERENCES

1. Naumann, K. W., Ende, H., Mathieu, G., George, A., „Experiments on Interaction Force of Jets in Hypervelocity Cross-Flow in a Shock Tunnel“, AGARD-CP-534, Nov. 1993, Paper 21.

A look to the leeward side of the jet in Fig. 25 explains readily the absence of particles in the jet wake: The pressure drop over the leeward Prandtl-Meyer expansion is so strong that effectively no jet gas enters the wake. Because the gas of the front separation zone is subsonic, it can easily pass by the jet plume and enter the wake. The flow visualisation results of Fig. 19 show that this is the case even with 3 jets at $S_j = 1.6 D_{j,e,con} = 5D_j^*$. The narrow gaps between the jets obviously are sufficient to let enough gas pass from the front separation zone into the wake. As a matter of fact, the jet plume between the jet opening and the internal jet shock functions very similar to a solid body whose shape equals an inverted truncated cone.

CONCLUSION

The experiments show that model #5 successfully allowed to extend the time of free-flight from 2 to 4 ms, and sometimes even longer. Using this extended measuring time and the ISL millisecond aerodynamic force measuring technique allows to study also transient aspects of model motion, whether these are caused by jet or test flow onset, or by oscillations of the jet interaction. The good reproducibility of most of the instantaneous phenomena shows that they are systematical ones.

The $C_{iz}(t)$ measurements show that the influence of the jet gas is marginal for the range of variations studied. Neither the molecular weight (2 – 40 kg/kmole), nor gas species (monatomic, diatomic, combustion products), nor special effects (condensation, soot particles), nor jet plenum temperature have a significant influence on the mean value of C_{iz} of "established" flow. The same holds roughly for the oscillation of the $C_{iz}(t)$ histories. While the starting phase of the $C_{iz}(t)$ history takes about 2 ms if the jet starts before the test flow, the interaction force is almost immediately active if the test flow is established first.

The flow visualisation experiments of very good resolution in time and space allow a detailed quantitative quasistationary description of the essential phenomena of the interaction flowfield. This is ready to be used for the validation of CFD-codes, or engineering purposes. In all cases jets of single nozzles are deflected supersonically.

Between the internal jet shock and the jet bow shock, vortices extend from one shock to the other. Where these vortices interact with the jet bow shock, they bulge the contour of the latter. In the space between both shocks there occurs strong mixing. A jet flow boundary cannot be defined clearly in this region.

Future investigations are under way to get some more insight on the creation of these vortices, and to find out in which way the vortices and oscillations of shock waves and separation zones interact.

2. Naumann, K. W. & Srulijes, J., „Die Steuerung mittels seitlich austretender Strahlen. Literaturübersicht.“ ISL R 117/85, in German and French, 1985.
3. Naumann, K. W., Ende, H., Mathieu, G. „Technique for Aerodynamic Force Measurement within Milliseconds in Shock Tunnel“, J. Shock Waves, 1, 3, 1991, pp. 223-332.
4. Naumann, K. W., Ende, H., Mathieu, G., George, A., „Millisecond Aerodynamic Force Measurement with

Side-Jet Model in the ISL Shock Tunnel“, AIAA-J., 31 ,6, June 1993, pp. 1068-1074.

5. Naumann K. W., Ende, H., Mathieu, G., George, A. “Shock Tunnel Experiments and Approximative Methods on Hypervelocity Side-Jet Control Effectiveness”, AIAA 93-1929, ISL PU 320/93, 1993

6. Naumann K. W., Ende, H., Mathieu, G., George, A. „Millisecond Aerodynamic Force Measurement using a Free-Flying Side-Jet Model with Built-in Gas Reservoir“, in “Shock Waves, Proc.20th Int. Symp. on Shock Waves”, B. Sturtevant et al. (Eds.), World Scientific, 1995, Vol. 1, pp. 311-316.

7. Naumann K. W., Ende, H., Mathieu, G., George, A. “Shock Tunnel Experiments on Lateral Jet Interaction.

Methods and Results“, AIAA 96-2690, ISL PU 332/96, 1996.

8. Smeets. G., “Interferometry“, ISL CO 214/90, 1990.

9. Naumann K. W., Ende, H., Mathieu, G., George, A. „Shock-Tunnel Studies on Lateral Jets/Hypervelocity Cross-Flow Interaction“, to be published in “Shock Waves, Proc.21st Int. Symp. on Shock Waves“, Great Keppel Australia, 1997; ISL PU 349/97.

Acknowledgement
This study is supported by the German ministry of defense by the contract No. T/R 760/Y 0001/R 1701

Test flow	Reflected mode Model 3, 5	Direct Mode Model 2
Mach number	4,56	5,13
Stagnation pressure (MPa)	1,31	1,15
Static pressure (kPa)	48,11	33,4
Flow velocity (m/s)	1480	1860
Density (kg/m³)	0,640	0,358
Temperature (K)	253	315
Cross-section area (cm)	20x20	20x20
Duration of test flow (ms)	5	1,5
Test flow gas	N ₂	N ₂

Table 1. Typical test flow parameters.

Models	#3	#5	#2
Mass (kg)	3,12	3,72	3,45
Plenum pressure (MPa)	80	80	<100
Span (cm)	20	26	19
Gas species	N ₂ , He	N ₂ , H ₂ , He, Ar	Comb.
Nozzles		CJ	SJ
Throat diameter (mm)		4,05	3,90
Exit diameter (mm)		12, 5	3,90
Half-angle (deg)		27	
Mach number, "hot" gas		3,8	1
Mach number, diatomic gas		3,9	1
Mach number, monatomic gas		5,0	1

Table 2. Data of models and nozzles.

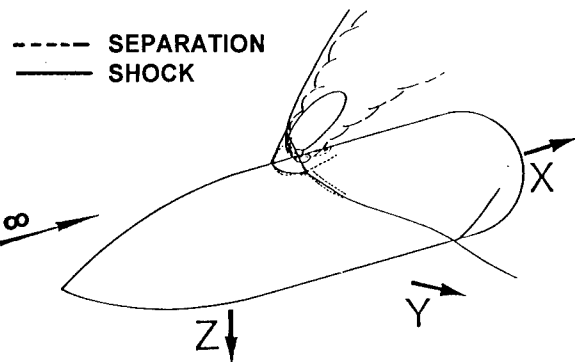


Figure 1. Principle sketch of the jet/cross-flow interaction.

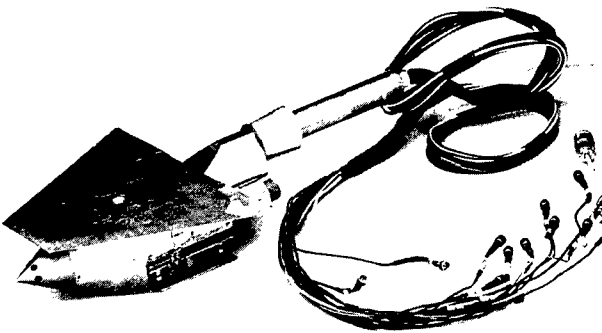
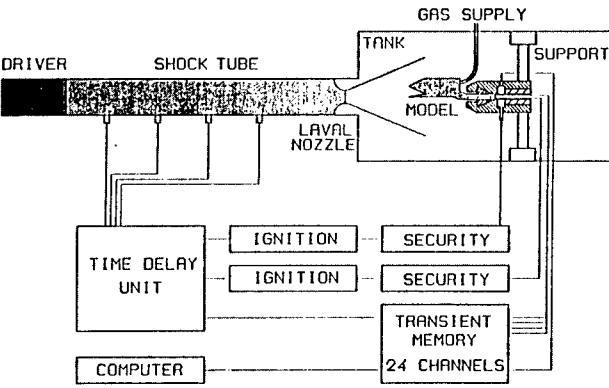


Figure 3. Model #3 fully equipped, with 1 conical jet.

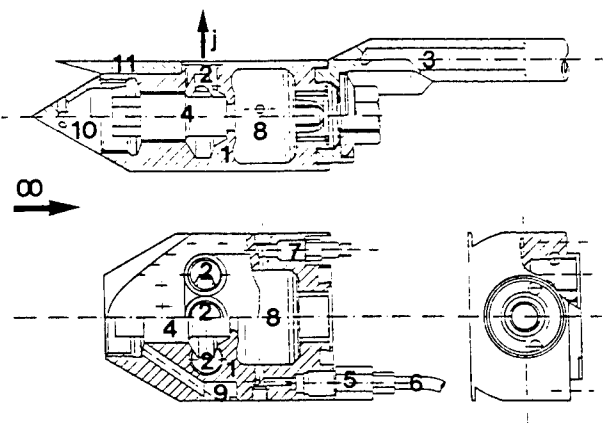


Figure 4. Drawing of model #3: 1) body, 2) side-jet locations, 3) stem, 4) reservoir opening device, 5) non-return valve, 6) flexible high-pressure tube, 7) pressure transducer, 8) gas reservoir, 9) location for X-accelerometer, 10) cap, 11) flat wing.

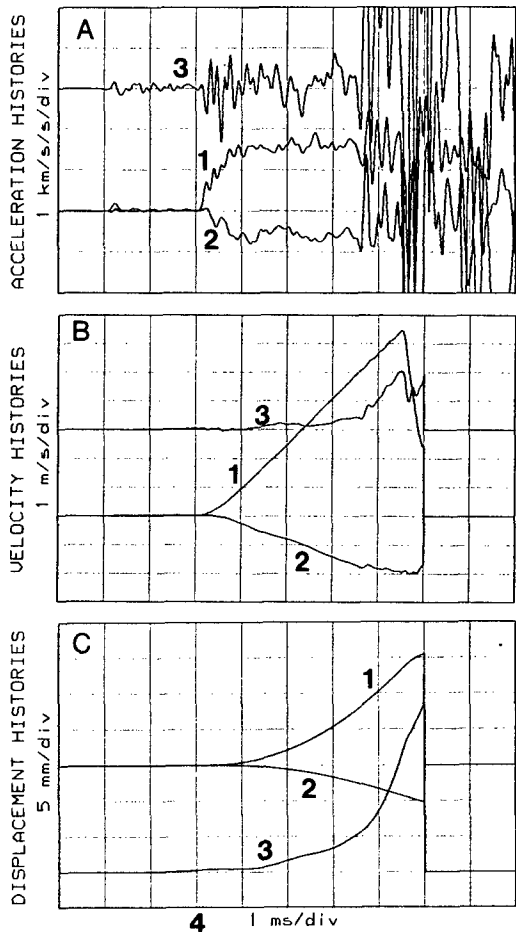


Figure 5. Histories of motion of model #5 without side-jets blowing: A) accelerations, B) velocities, C) displacement; 1) X-direction, 2) Z-direction, 3) pitch (dimensions: 10krad/s²/div, 10rad/s/div, 5 mrad/div), 4) $\tau = 0$.

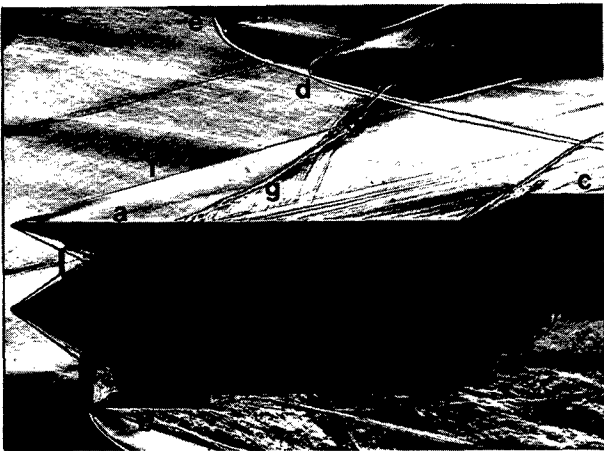


Figure 7. DI-picture of model #5 without side-jets blowing: a) surface of flat wing, b) trim wing, c) stem, d) Pitot probe, e) additional pressure probe, retracted, f) leading edge shock of the flat wing, g) steepening leading edge shock of model wing parts in the test flow boundary layer.

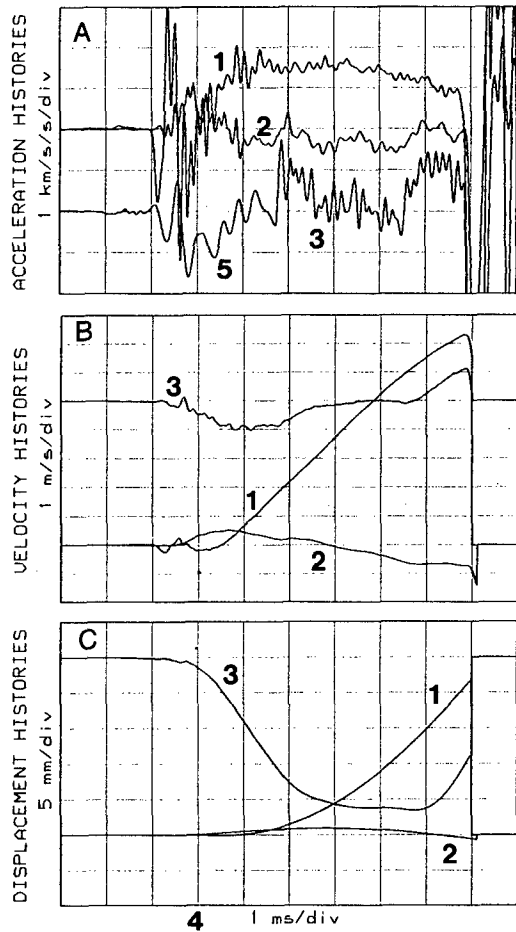


Figure 6. Histories of motion of model #5 with 1 CJ of He75/Ar25: A) accelerations, B) velocities, C) displacement; 1) X-direction, 2) Z-direction, 3) pitch (dimensions: 10krad/s²/div, 10rad/s/div, 5 mrad/div), 4) $\tau = 0$, 5) $f_c = 1500\text{Hz}$.

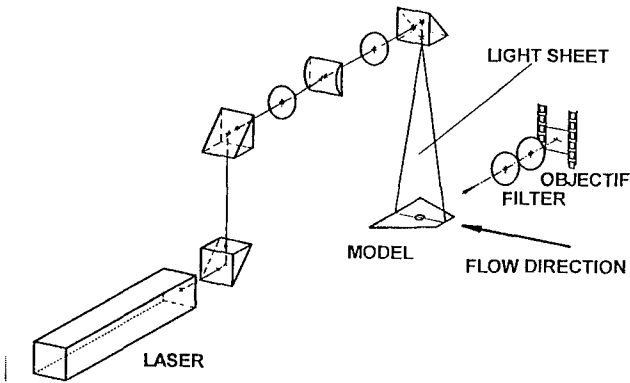


Figure 8. Principle sketch of the LLS-visualisation setup.

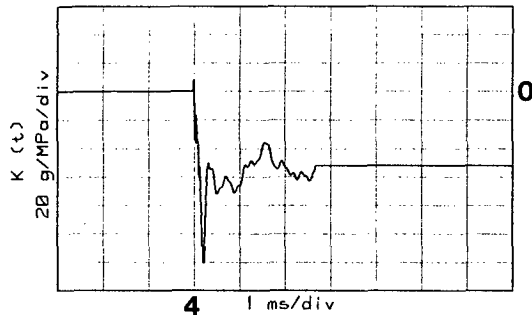
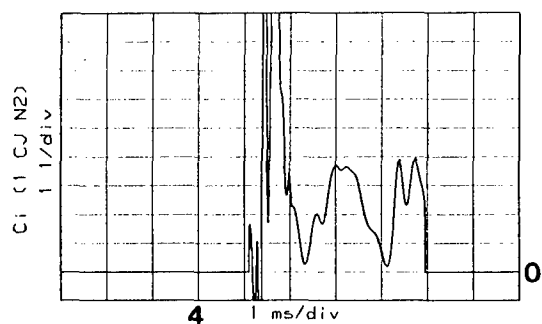
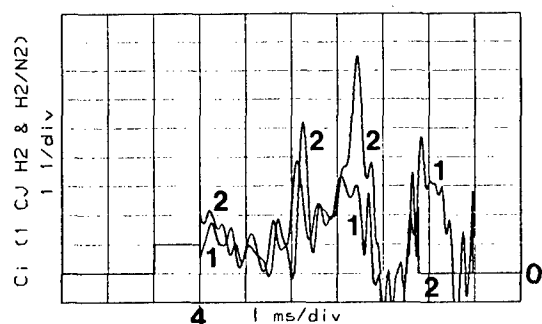
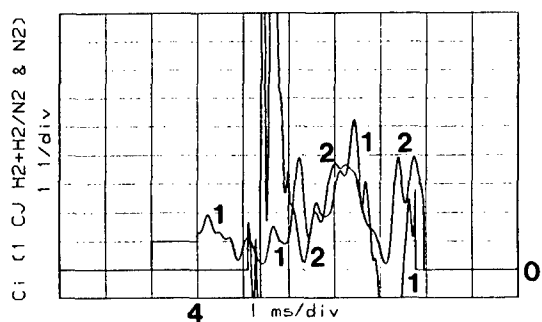
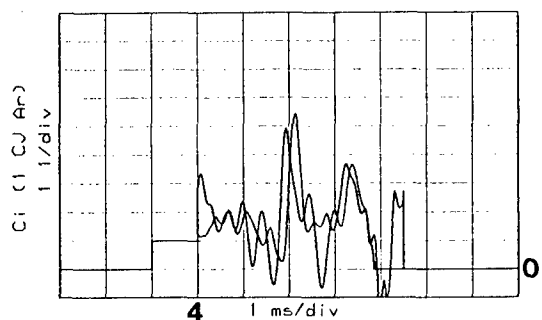
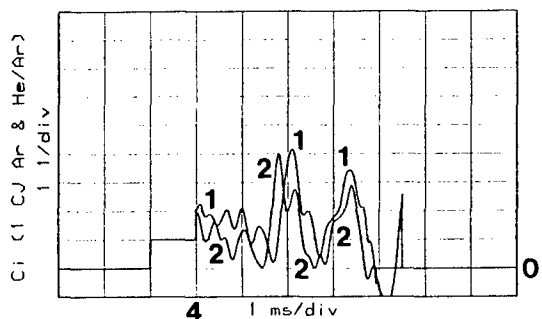
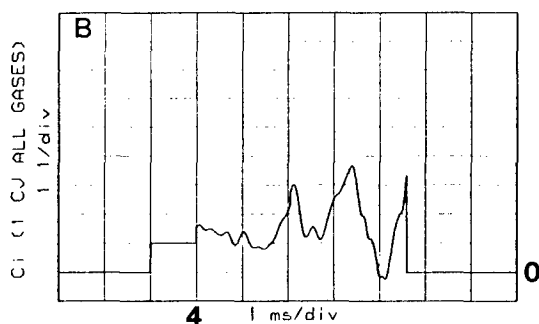
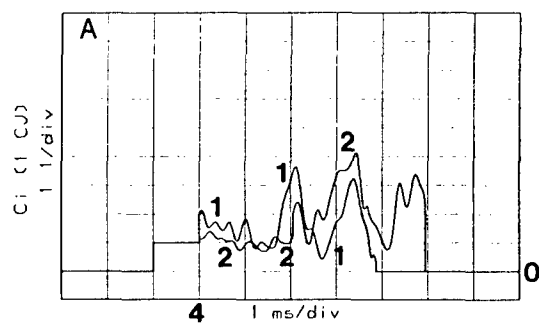
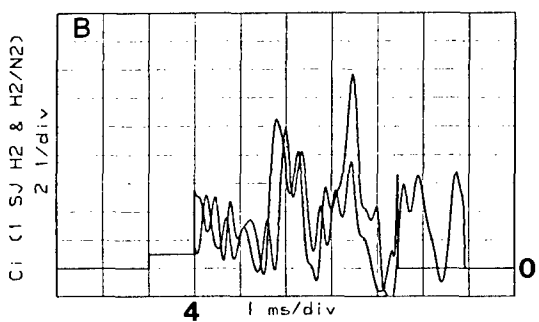
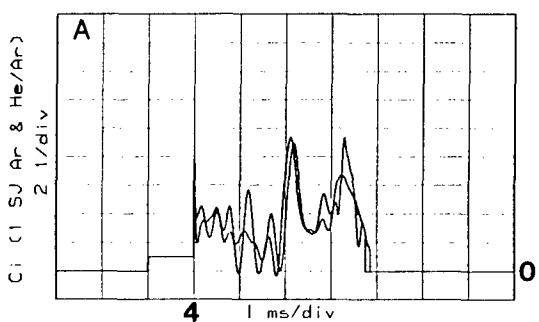
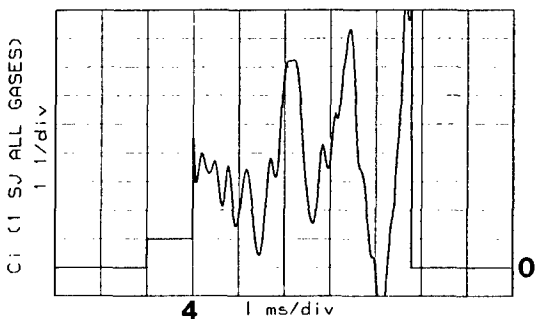


Figure 9. The proportionality parameter $K_{\infty,z}(t)$. Constant value: $K_{\infty,z}(t) = -52.96\text{ g/MPa}$, 4) $\tau = 0$.

Figure 10. $C_{iz}(t)$ for 1 CJ of of N_2 , 4) $\tau = 0$.Figure 11. $C_{iz}(t)$ for 1 CJ of 1) H_250/N_250 and 2) H_2 , 4) $\tau = 0$.Figure 12. Comparison of $C_{iz}(t)$ of diatomic gases: 1) H_250/N_250+H_2 , 2) N_2 , 4) $\tau = 0$.Figure 13. $C_{iz}(t)$ of two experiments with CJs of Ar, 4) $\tau = 0$.Figure 14. Comparison of $C_{iz}(t)$ of 1) Ar and 2) He75/Ar25, 4) $\tau = 0$.Figure 15. A) Comparison of $C_{iz}(t)$ of 1) monatomic and 2) diatomic gases, B) average with 1 CJ, 4) $\tau = 0$.Figure 16. $C_{iz}(t)$ of A) monatomic, B) diatomic gases with 1 SJ, 4) $\tau = 0$.Figure 17. $C_{iz}(t)$ of all gases with 1 SJ, 4) $\tau = 0$.

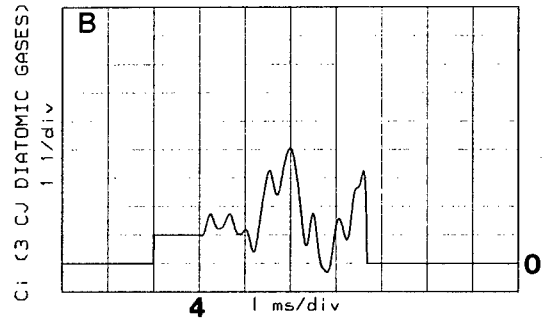
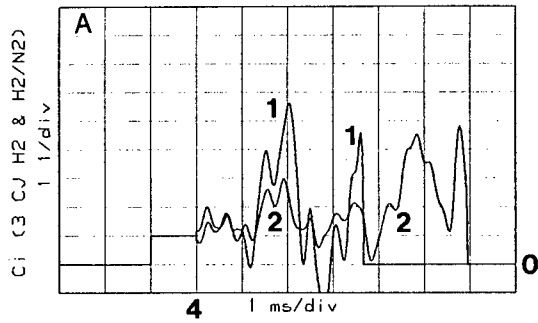
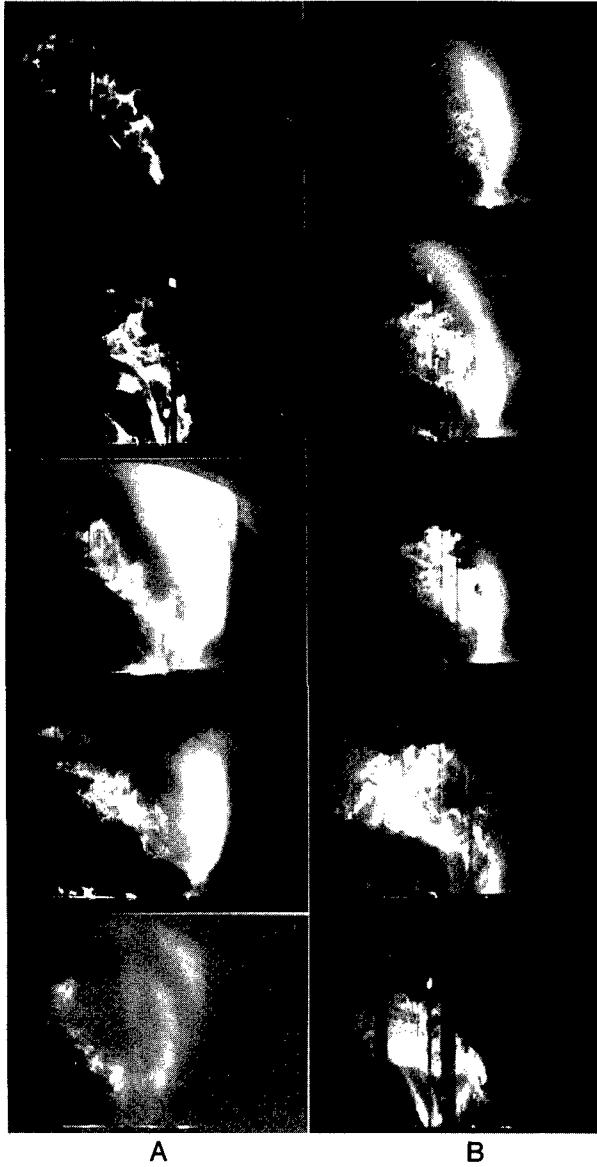


Figure 18. $C_{iz}(t)$ of 3 CJs, A) 1) H_2 , 2) $N_2 H_{250}/N_{250}$, B) all diatomic gases, 4) $\tau = 0$.



A1: 1 Jet; $y = 0$ mm; $PR = 33.75$
A2: 2 Jets; $y = 15$ mm; $PR = 31.38$
A3: 2 Jets; $y = 10$ mm; $PR = 38.37$
A4: 2 Jets; $y = 5$ mm; $PR = 36.47$
A5: 2 Jets; $y = 0$ mm; $PR = 36.89$
B1: 3 Jets; $y = 20$ mm; $PR = 27.88$
B2: 3 Jets; $y = 15$ mm; $PR = 31.66$
B3: 3 Jets; $y = 10$ mm; $PR = 35.39$
B4: 3 Jets; $y = 5$ mm; $PR = 30.82$
B5: 3 Jets; $y = 0$ mm; $PR = 33.25$

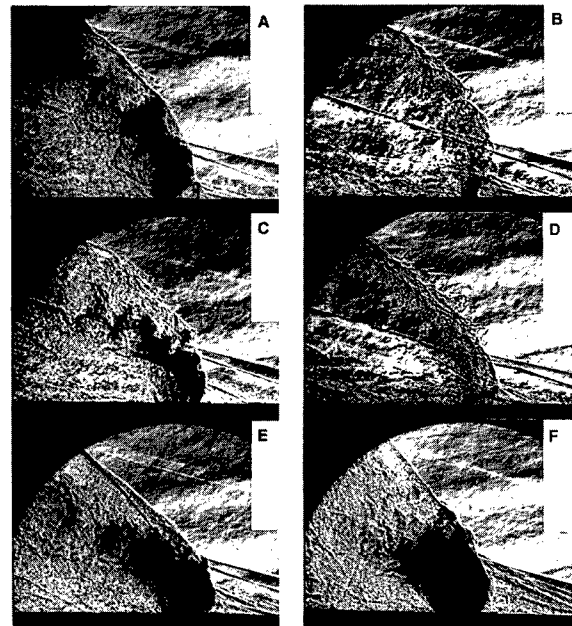
Figure 19. LLS-pictures of the NI flowfield of conical jets of "hot" gas taken at different y -planes; $Ma_\infty = 5.1$, from right to left.



A: conical jet; $PR = 41.46$

B: sonic jet; $PR = 39.32$

Figure 20. LLS-pictures of the NI flowfield of single jets of "hot" gas taken at $y = 0$ mm; $Ma_\infty = 5.1$, from right to left.



A: 1 SJ, N_2 , $PR = 15.44$

B: 1 SJ, He, $PR = 21.01$

C: 1 CJ, N_2 , $PR = 15.40$

D: 1 CJ, He, $PR = 15.62$

E: 2 CJs, N_2 , $PR = 11.30$

F: 3 CJs, N_2 , $PR = 9.29$

Figure 21. DI-pictures of the NI flowfield of jets of pure "cold" gases; $Ma_\infty = 4.5$, from right to left.

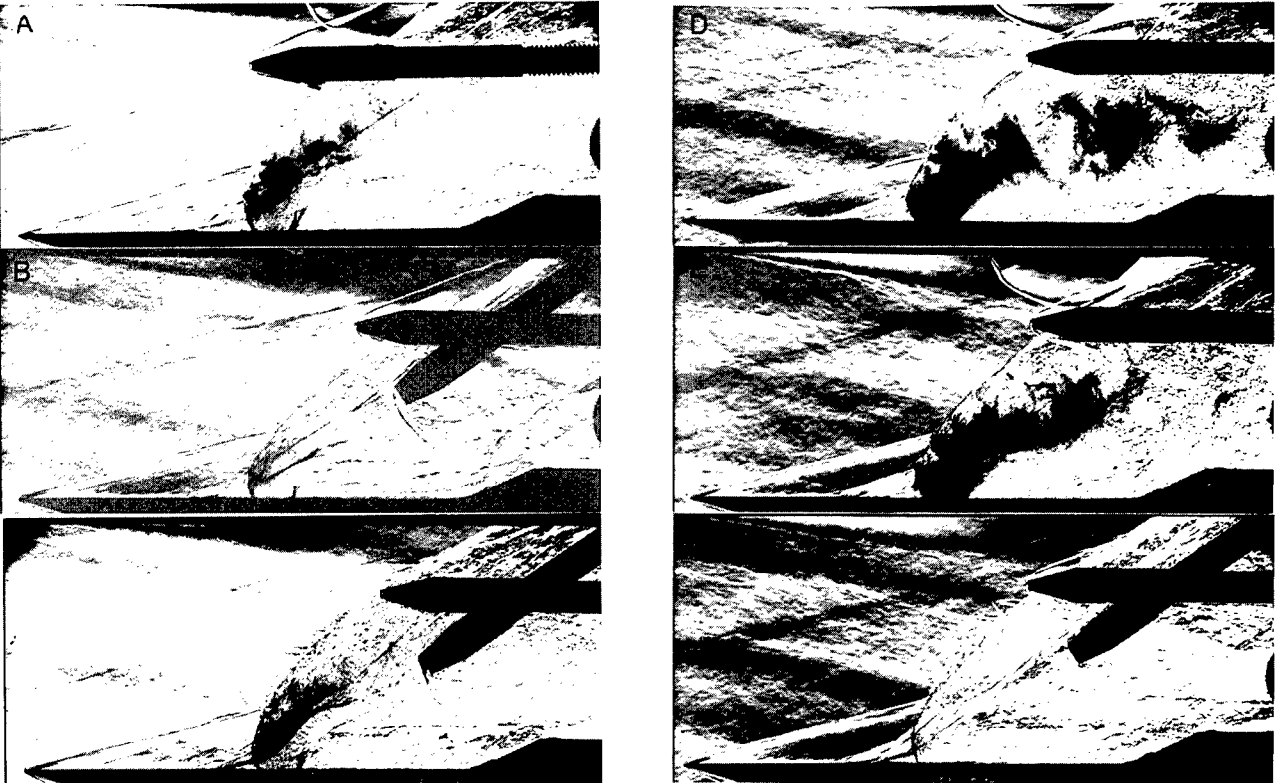


Figure 22. DI-pictures of the NI flowfield of model #5 with 1CJ of pure "cold" gas. $Ma_\infty = 4.5$, from left to right: A) N_2 , B) H_2 , C) H_250/N_250 , D & E) Ar , F) $He75/Ar25$.

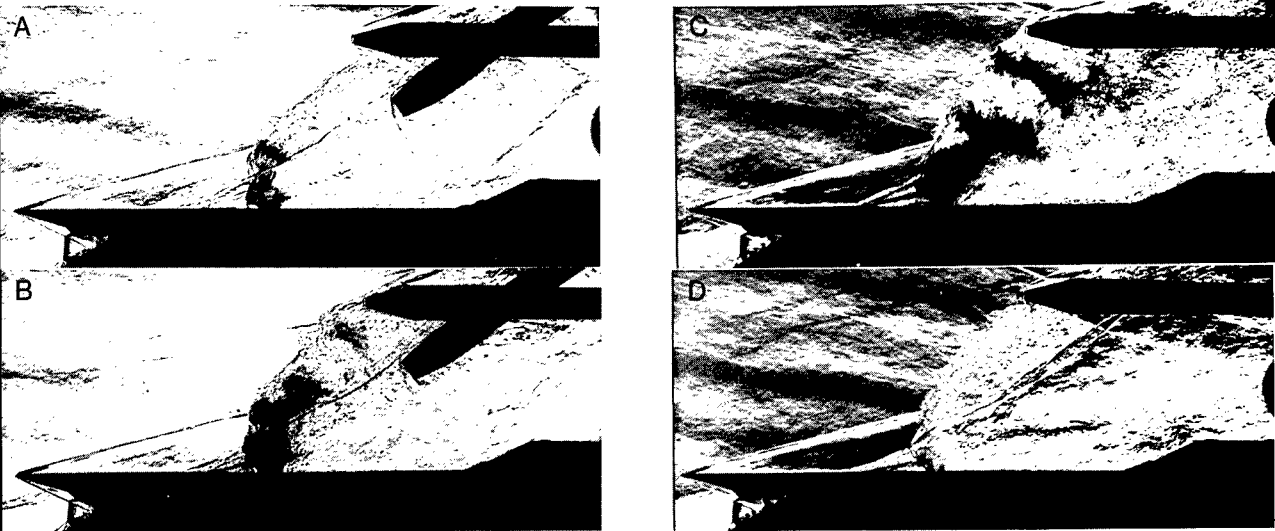


Figure 23. DI-pictures of the NI flowfield of model #5 with 1SJ of pure "cold" gas. $Ma_\infty = 4.5$, from left to right: A) H_2 , B) H_250/N_250 , C) Ar , D) $He75/Ar25$.

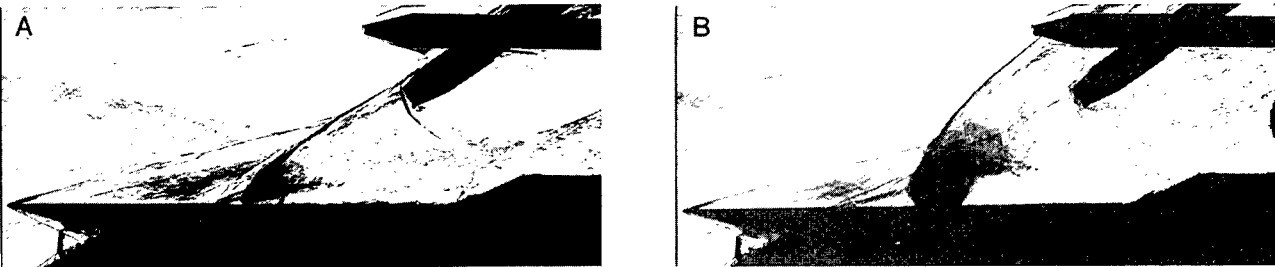


Figure 24. DI-pictures of the NI flowfield of model #5 with 3 CJs of pure "cold" gas. $Ma_\infty = 4.5$, from left to right: A) H_2 , B) H_250/N_250 .

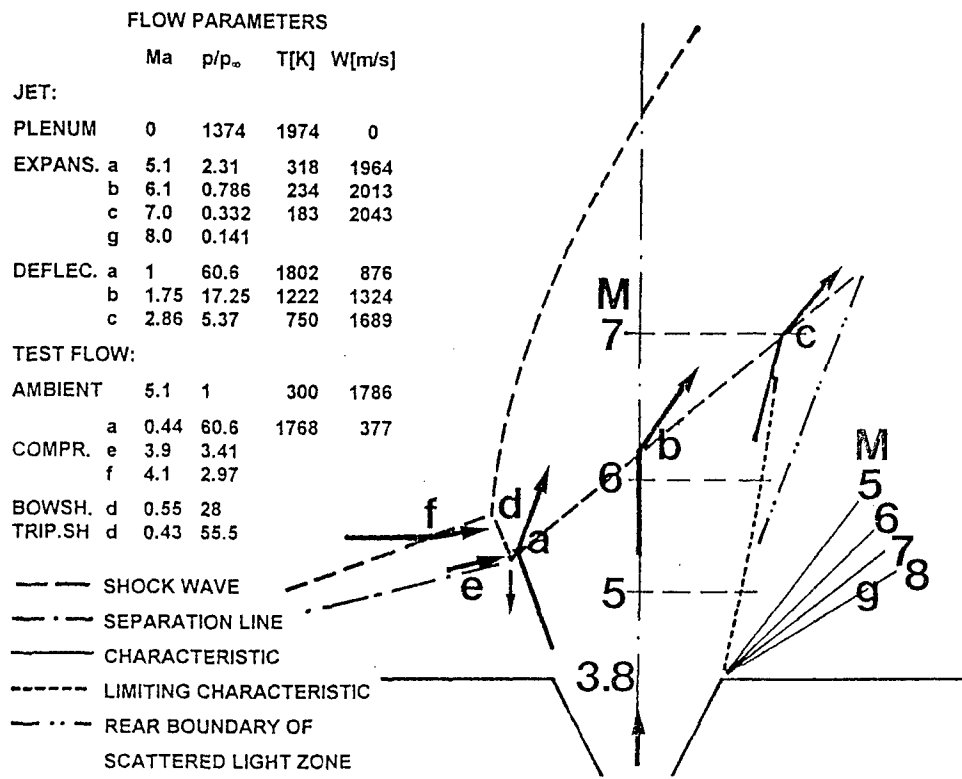


Figure 25. Parameters of the NI flowfield of 1 CJ of “hot” gas, a) triple point “a”, b) internal jet shock, c) intersection of rear limiting characteristic and internal jet shock, d) triple point “d”, e) boundary streamline of front separation bubble, f) conical separation shock, g) characteristics of leeward Prandtl-Meyer expansion, simplified calculation using 2-d equations.

Interactions Aérodynamiques sur un Intercepteur Hypersonique

Piloté par Jets Transversaux.

M. Leplat, P. Champigny

ONERA - B.P. 72 - 92322 Châtillon Cedex - France

G. Girard, J.V. Hachemin,

AEROSPATIALE Missiles - 2 Rue Béranger - B.P. 84 - 92323 Châtillon Cedex - France

N. Delattre

AEROSPATIALE Espace & Défense - B.P. 2 - 78133 Les Mureaux Cedex - France

1. SOMMAIRE

Cette communication présente les travaux expérimentaux et numériques effectués par AEROSPATIALE et l'ONERA sur une configuration schématique d'intercepteur en présence d'un jet transversal central.

Les essais dans la soufflerie S3MA de l'ONERA ont consisté en des relevés de pression pariétale sur tout le corps, la pesée des efforts et moments induits par la présence du jet ainsi que des visualisations par strioscopie. Les effets des variations des conditions de jet, de l'état de la couche limite et de l'incidence du missile ont été étudiés pour des écoulements supersoniques allant jusqu'à $M_0 = 5,5$.

Par ailleurs, des calculs Navier-Stokes ont été effectués par les deux partenaires au moyen du code FLU3M, pour des écoulements laminares et turbulents.

La confrontation des résultats numériques avec l'expérience montre une bonne reproduction de l'ensemble des phénomènes d'interaction jet transversal - écoulement externe avec en particulier une bonne prise en compte des effets visqueux prépondérants pour ce type de configuration.

2. INTRODUCTION

Pour les futurs missiles d'interception endo et exo-atmosphériques, les jets transversaux constituent le meilleur moyen de génération de forces pour le guidage et le contrôle d'attitude.

L'utilisation de tuyères placées au voisinage du centre de gravité du véhicule (DIVERT) à des altitudes où le pilotage aérodynamique est inopérant constitue un moyen de pilotage simple et performant, présentant notamment un très faible temps de réponse en manœuvre.

La mise au point d'un tel système est cependant rendue délicate du fait des interactions aérodynamiques créées

par la confluence de deux écoulements ; celles-ci sont tributaires de la géométrie et des caractéristiques de l'écoulement externe et du jet. Les forces latérales générées peuvent ainsi être très différentes (plus grandes ou plus petites) de la poussée intrinsèque du jet de pilotage.

Par ailleurs les forces d'interaction créent un couple perturbateur qui doit être contré par un système de jets secondaires (ACS) placé à l'arrière du véhicule.

L'objet de ce papier est de présenter certains travaux effectués par l'ONERA et AEROSPATIALE dans les domaines expérimental et numérique sur le thème des jets transversaux pour une configuration schématique d'intercepteur.

3. APPLICATIONS

Des missiles ayant des missions fort différentes [1] peuvent avoir recours à ce type de pilotage comme le montrent les exemples de la figure 1.

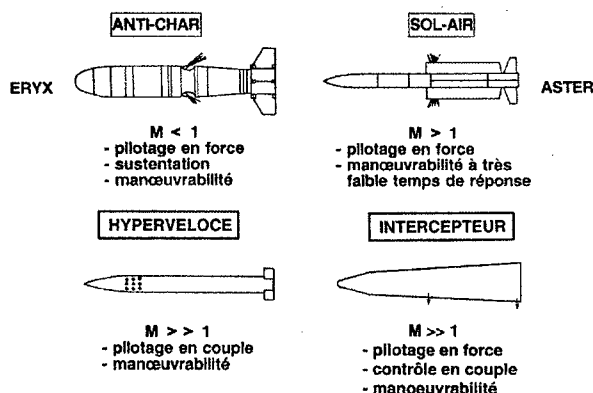


Figure 1 : Concepts pilotés par jet

Ainsi, dans le cas des antichars, comme pour le missile ERYX d'AEROSPATIALE, les jets assurent un pilotage en force au voisinage du centre de gravité ainsi que la sustentation du missile.

Pour le missile sol-air supersonique ASTER (antimissile), piloté en force, c'est un très faible temps

de réponse en manœuvre qui est recherché et dans le cas des missiles "hypervéloces" une forte manœuvrabilité est obtenue par un pilotage en couple.

Dans le cas d'un intercepteur évoluant à haute altitude et pour lequel un pilotage aérodynamique classique est inopérant, le pilotage en force sera associé à un contrôle en couple. Pour ces missiles, dépourvus de voilure, les interactions aérodynamiques en force ont a priori des valeurs modérées par rapport à la poussée de la tuyère ; toutefois pour dimensionner ces systèmes de pilotage et de contrôle, une bonne connaissance des interactions est nécessaire et ce sur un très large domaine de vol en nombre de Mach et en altitude. De plus, selon la valeur du nombre de Reynolds, les effets de jet peuvent différer fortement selon l'état de la couche limite.

4. ASPECTS PHENOMENOLOGIQUES

L'éjection d'un gaz dans un écoulement transversal conduit à un ensemble d'interactions pouvant être scindées en deux classes: les interactions proches et les interactions lointaines.

Les premières sont créées par l'effet d'obstacle du jet, qui conduit en écoulement supersonique à la formation d'un choc et à un décollement de la couche limite, comme le montre la visualisation par strioscopie de la figure 2.

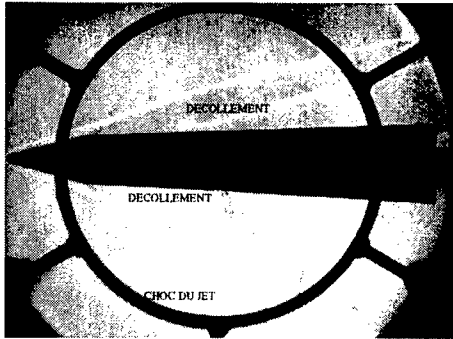


Figure 2 : Strioscopie en turbulent, $M_0=5.5$ $P_j/P_0=15000$

Le jet induit alors une forte modification de la pression sur le fuselage autour de la tuyère, avec des zones de surpression en amont et de dépression en aval (fig.3), ce qui conduit ici à un moment d'interaction cabreur.

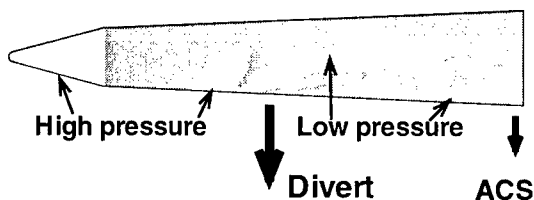


Figure 3 : Répartition de pression pariétale type

Au delà, les interactions lointaines proviennent du caractère fortement tourbillonnaire de l'écoulement en aval de la tuyère. Elles dépendent de la position relative

du sillage et du missile, c'est-à-dire du rapport des quantités de mouvement relatives du jet et de l'écoulement externe, ainsi que de l'incidence.

Dans le cas où des surfaces portantes sont présentes en aval de la tuyère, les vitesses induites par le sillage du jet affectent alors leur efficacité.

5. ETUDE EXPERIMENTALE EN SOUFFLERIE

Le thème des interactions de jet sur missile a fait l'objet, depuis le début des années 80, de nombreuses études expérimentales dans les souffleries de l'ONERA [2] , notamment pour AEROSPATIALE, dans les domaines de Mach subsonique et supersonique.

Les essais relatifs au concept d'intercepteur hypersonique réalisés dans la soufflerie S3MA en 1997 ont permis, dans un premier temps, de couvrir le domaine de Mach $2 \leq M_0 \leq 5.5$. Ils ont consisté en des pesées globales de la peau du missile (hors jet), des mesures de pression pariétale et des visualisations par strioscopie pour différentes conditions d'incidence et de pression d'alimentation de la tuyère, ceci pour des régimes d'écoulements externes laminaires et turbulents.

La maquette, de type bi-conique, présentée dans la veine d'essai figure 4, comporte une tuyère orientée normalement au fuselage et située à mi-longueur à l'intrados.

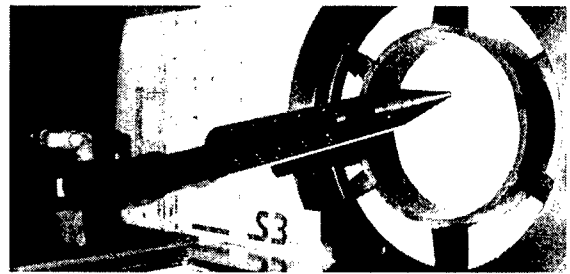


Figure 4 : Maquette dans la soufflerie S3MA de l'ONERA

Les interactions aérodynamiques, en force et moment, du jet avec l'écoulement externe sont obtenues en ne pesant que la peau du missile, ce qui permet de s'affranchir d'une connaissance très précise de la poussée de la tuyère.

Le schéma représentatif de la maquette utilisée, figure 5, montre l'alimentation de la tuyère en air et le principe de pesée de la maquette au moyen d'une balance excentrée.

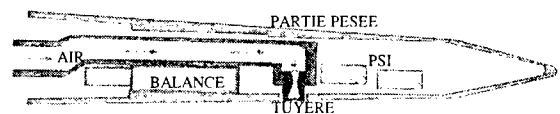


Figure 5 : Schéma du montage

Les visualisations par strioscopie des figures 6 et 7, ont été réalisées aux nombres de Mach de 2 et 5,5 pour des rapports de la pression génératrice du jet P_j à la pression

externe amont P_0 de 500 et 4200 correspondant à des rapports de quantité de mouvement voisins. Elles montrent que dans ce cas, le choc détaché et le décollement de la couche limite devant le jet sont pratiquement conservés. Il est à noter que ce décollement, bien visible à l'extrados, s'étend tout autour du fuselage.

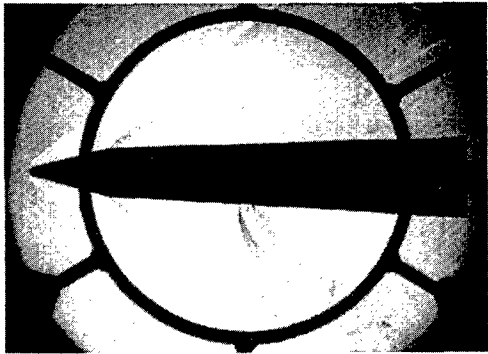


Figure 6 : Strioscopie en turbulent, $M_0=2$ $P_{ij}/P_0=500$

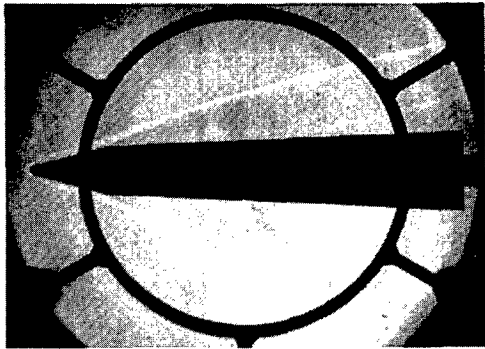


Figure 7 : Strioscopie en turbulent, $M_0=5.5$ $P_{ij}/P_0=4200$

Les photos présentées à $M_0 = 5.5$ et 10 degrés d'incidence montrent l'influence du régime de l'écoulement, laminaire (fig. 8) ou turbulent (fig. 9).

On constate que les zones de décollement en amont du jet diffèrent fortement d'un régime à l'autre, avec une avancée du décollement en laminaire.

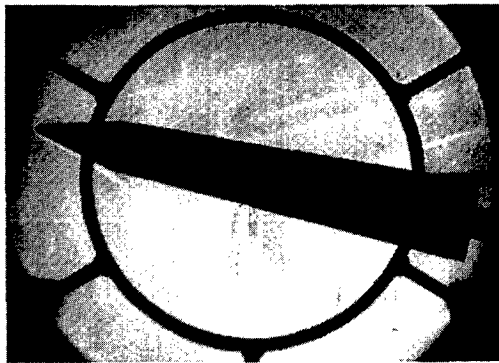


Figure 8 : Strioscopie en turbulent, $M_0=5.5$ $\alpha=10^\circ$ $P_{ij}/P_0=15000$

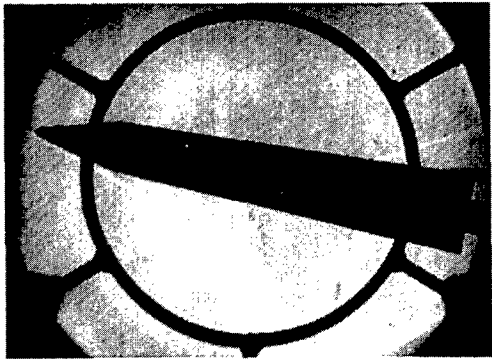


Figure 9 : Strioscopie en laminaire, $M_0=5.5$ $\alpha=10^\circ$ $P_{ij}/P_0=15000$

Par ailleurs, on constate, lorsque la pression relative du jet augmente, de $P_{ij}/P_0=4200$ (fig.7) à $P_{ij}/P_0=15000$ (fig. 2), une avancée du décollement avec un redressement des chocs devant le jet.

La sensibilité des interactions au régime de l'écoulement externe est quantifiée figure 10, où sont portées les valeurs du coefficient de pression K_p dans le plan de symétrie en écoulements laminaire et turbulent, pour un nombre de Mach de 5,5 et un rapport de pressions P_{ij}/P_0 de 15000.

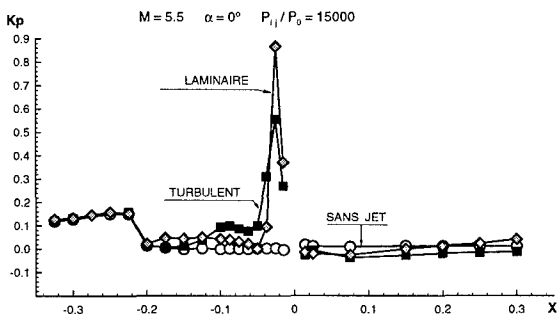


Figure 10 : Répartitions de pression pariétale - Effet du régime de l'écoulement

Il apparaît que le niveau maximum de pression juste devant la tuyère est obtenu en écoulement laminaire. En amont, on remarquera le double pic caractéristique du cas turbulent (correspondant à un choc en lambda), et en laminaire on note une plus grande avancée du décollement, mais avec un niveau de surpression moins élevé. A l'aval immédiat de la tuyère, les niveaux dépressionnaires sont moins sensibles au régime de l'écoulement.

L'influence de la valeur de la pression d'alimentation de la tuyère sur les répartitions de K_p est présentée figures 11 et 12 toujours à Mach 5,5.

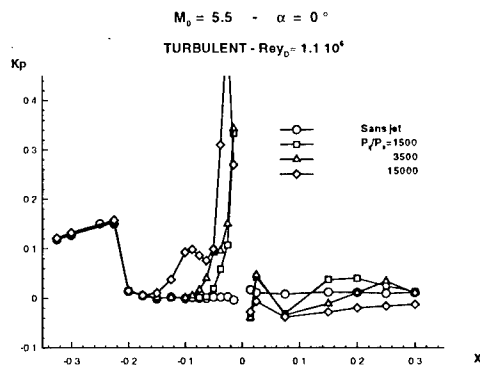


Figure 11 : Répartitions de pression pariétale - Effet du taux de détente en écoulement turbulent

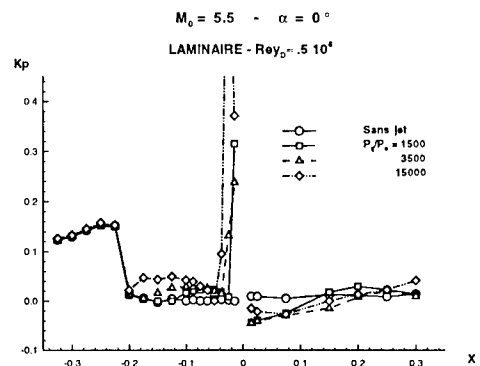


Figure 12 : Répartitions de pression pariétale - Effet du taux de détente en écoulement laminaire

On constate, sans surprise, une amplification des phénomènes dus au jet quand la pression d'alimentation augmente, que ce soit en écoulement turbulent ou laminaire, avec une augmentation du niveau des pics de pression et une avancée du décollement.

Enfin, figure 13, l'augmentation du nombre de Mach externe conduit, à taux de détente (altitude) constant, à une diminution des effets du jet sur la pression pariétale.

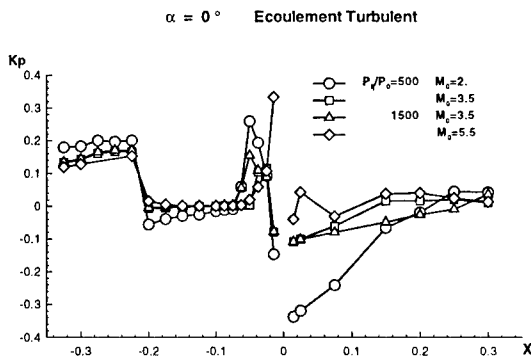


Figure 13 : Répartitions de pression pariétale - Effet du nombre de Mach externe

Des exemples de résultats globaux sont présentés figures 14 et 15 sous la forme d'évolutions des coefficients de force normale CN et de moment de tangage CM (rapporté à l'axe tuyère) en fonction du taux de détente du jet à incidence nulle.

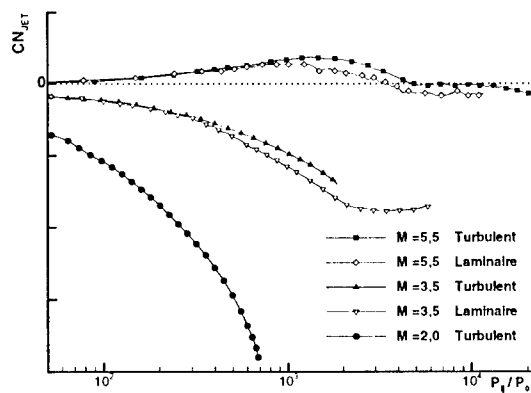


Figure 14 : Coefficient de force normale CN dû au jet - Effets du taux de détente et du nombre de Mach

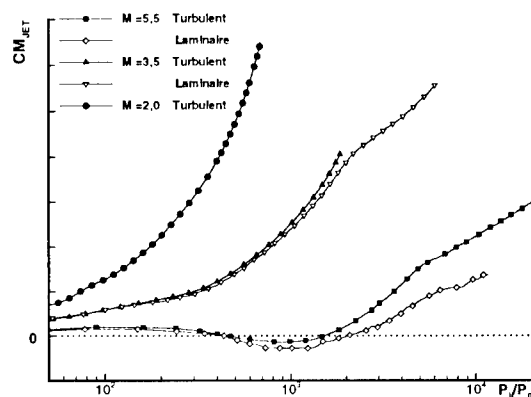


Figure 15 : Coefficient de moment de tangage CM dû au jet - Effets du taux de détente et du nombre de Mach

On constate, aux nombres de Mach de 2 et 3,5, que les interactions en force sont négatives, c'est-à-dire défavorablement opposées à la poussée de la tuyère disposée à l'intrados du fuselage. Le moment de tangage induit par la présence du jet est cabreur.

Pour le nombre de Mach de 5,5 et hormis pour les très forts taux de détente, une contribution positive du jet est obtenue en force, favorable à la manœuvre commandée ; le moment CM_{JET} reste voisin de zéro jusqu'à des taux de détente modérés puis, comme précédemment devient cabreur.

En termes d'efforts et de moments globaux, les effets de régime d'écoulement sont modérés ; on constate ici pour Mach 3,5 et 5,5 des interactions en force plus favorables en écoulement turbulent ainsi que des moments légèrement plus forts .

6. ETUDES NUMERIQUES

Depuis une dizaine d'années [3,4], de nombreuses études numériques ont été menées par AEROSPATIALE et l'ONERA sur le thème du pilotage par jet transverse. Elles ont montré par exemple la

bonne aptitude des calculs Euler à quantifier les phénomènes d'interaction dus principalement au sillage du jet pour des configurations avec voilures ; par contre, dans le cas de l'intercepteur, les phénomènes d'interaction proche, à la paroi, sont prépondérants, et une prise en compte des effets visqueux au moyen de calculs Navier - Stokes est nécessaire [5].

Les calculs présentés ont été effectués conjointement par les deux partenaires au moyen du code FLU3M [6] développé par l'ONERA .

FLU3M est un code multidomaine, utilisant des maillages structurés, qui résout les équations d'Euler et de Navier-Stokes à partir d'une formulation pseudo-stationnaire sous forme conservative, ceci en bi et tridimensionnel.

Le schéma numérique employé est du type volumes finis à variation totale décroissante (TVD).

La discrétisation en espace est faite au moyen d'un schéma explicite décentré du deuxième ordre, de type MUSCL , pour les termes non visqueux, avec les limiteurs de pente minmod ou Van Albada. En ce qui concerne les termes visqueux (discrétisés dans les trois directions) le schéma utilisé est de type centré.

Dans la phase explicite, le calcul du flux numérique utilise, au choix, différents solveurs approchés, ici celui de Roe associé à la correction entropique de Harten pour les chocs.

L'accélération de la convergence est réalisée par un schéma implicite avec un pas de temps local variable, et la résolution du système linéaire est faite par une méthode de direction alternée ADI.

Les variables sont calculées au centre des mailles (cell-center) en gaz parfait monoespèce.

Les calculs ont traité des cas d'écoulements tridimensionnels laminares, avec une viscosité laminaire de Sutherland, et turbulents en utilisant pour ces derniers cas le modèle de turbulence K- ϵ de Jones-Launder avec correction de bas Reynolds.

Les maillages de calcul utilisés, dont un exemple est présenté figure 16, sont multidomaines et comportent environ six cents mille points ; des maillages dégradés de 150000 points ont également été utilisés.

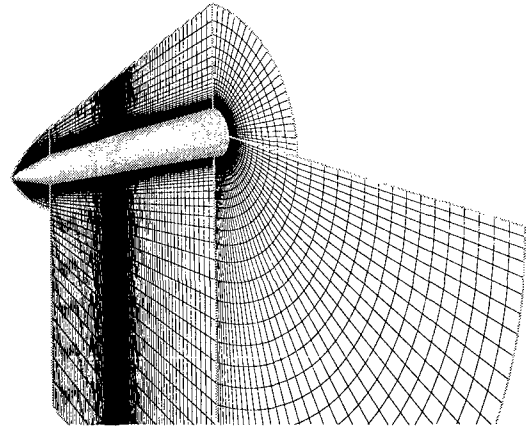
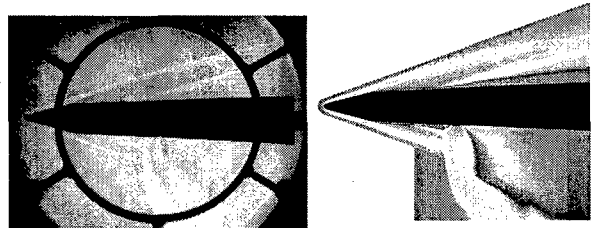


Figure 16 : Exemple de maillage pour calcul Navier - Stokes

Les plans de maillage sont particulièrement resserrés au voisinage de la tuyère ainsi qu'au nez. Les conditions du jet en sortie de tuyère sont, soit calculées, soit imposées sur les mailles correspondant à la section de sortie de la tuyère.

La figure 17 compare un exemple de résultat de calcul où sont représentées les plages iso masse volumique avec une visualisation strioscopique d'essai. Il s'agit d'un écoulement turbulent, choisi comme cas de référence, à un nombre de Mach $M_0=5,5$, une incidence de missile nulle et un taux de détente du jet P_j/P_0 égal à 15000.



Essai : Strioscopie $M_0=5,5$ $\alpha=0^\circ$ Calcul : Masse Volumique

Figure 17 : Comparaison calcul - essai

On constate que l'éclatement et le sillage du jet sont bien retrouvés par le calcul, de même que les chocs d'ogive et de jet.

Le décollement de la couche limite et le choc associé, que l'on peut distinguer ici dans le plan de symétrie du côté de la tuyère, mais également du côté opposé, sont bien restitués par le calcul.

L'étude numérique offre également un apport pour la compréhension des phénomènes d'interaction, notamment par la visualisation des lignes de frottement pariétal, comme le montre l'exemple de la figure 18 relatif au même cas d'écoulement.

Les lignes de frottement font apparaître le décollement de la couche limite très en amont du jet et son extension tout autour du fuselage, phénomène qui est amplifié en écoulement laminaire. Ensuite se forme, à partir de l'amont immédiat de la tuyère, une succession de lignes

d'attachement et de séparation jusque sous le sillage du jet.

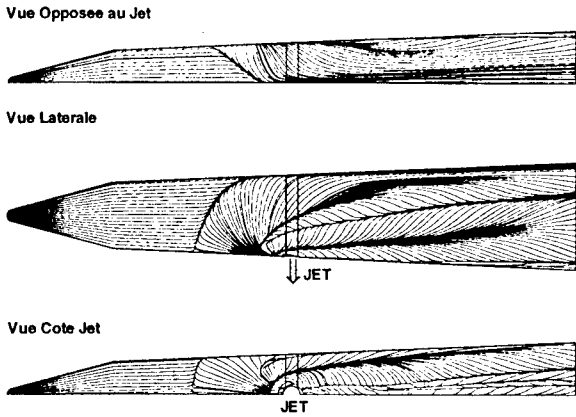


Figure 18 : Lignes de frottement

Le tracé des lignes de courant dans le plan de symétrie, figure 19, met en évidence la trajectoire du jet depuis la sortie de la tuyère, son contournement par l'écoulement principal, ainsi que la déviation de l'écoulement dans le plan opposé à la tuyère du fait du décollement de la couche limite.

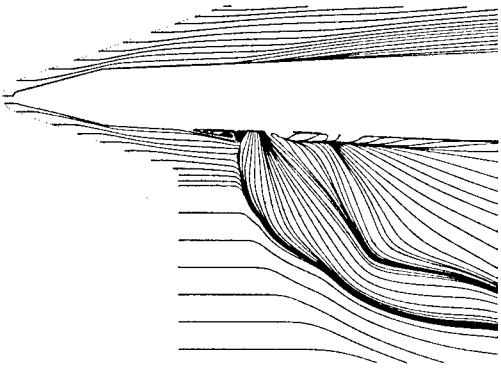


Figure 19 : Lignes de courant dans le plan de symétrie

Une analyse plus fine au voisinage de la tuyère, figure 20, montre un important écoulement de retour au pied du jet avec formation de deux tourbillons en fer à cheval entre lesquels apparaît une ligne d'attachement.

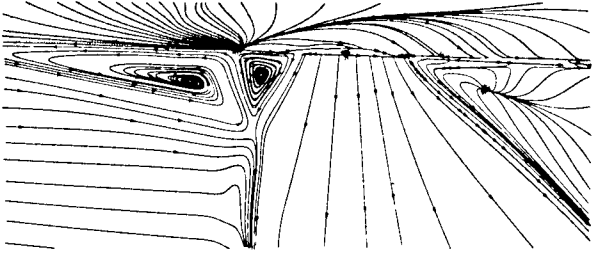


Figure 20 : Lignes de courant dans le plan de symétrie et frottement pariétal

Les comparaisons quantitatives des résultats de calcul et d'essai présentées ici concernent essentiellement les répartitions longitudinales de la pression pariétale le long de différentes génératrices situées sur tout le pourtour du missile.

Les figures 21 et 22 comparent, pour le cas d'un écoulement turbulent à $M_0 = 5.5$, incidence nulle et $P_j/P_0 = 15000$, les résultats des mesures en soufflerie et de deux calculs effectués par les deux partenaires. Le modèle de turbulence à deux équations de transport K-ε est utilisé dans les deux cas mais avec, notamment, des maillages, traitements de la tuyère, et initialisations différents.

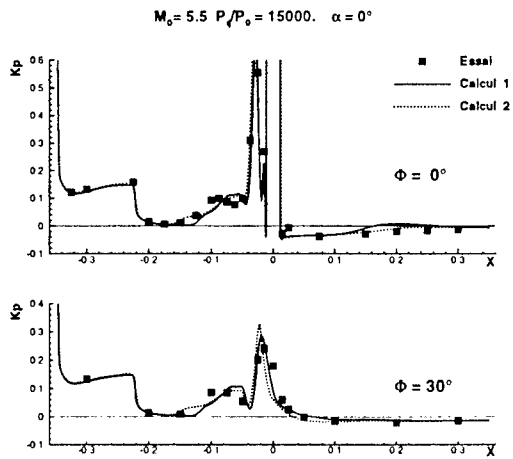


Figure 21 : Répartitions de pression pariétale en turbulent - Comparaisons calcul - essai .

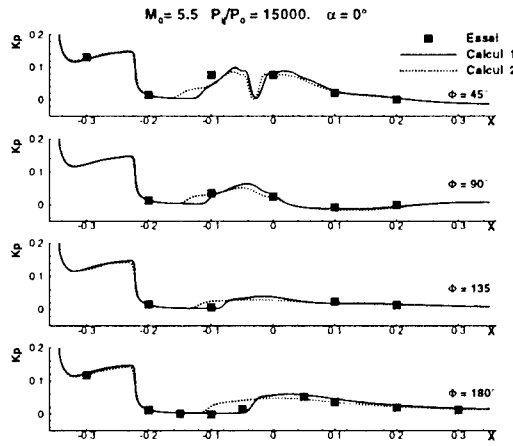


Figure 22 : Répartitions de pression pariétale en turbulent - Comparaisons calcul - essai .

Les calculs restituent bien les niveaux de pression sur l'ogive et le restent en amont de la perturbation. L'effet du jet est également globalement bien prédit et ceci sur tout le pourtour du missile tant en allure qu'en niveaux de pression. Les pics de pression dans les zones les plus perturbées, situées devant la tuyère ($\phi = 0$ et 30° , fig.21) sont bien retrouvés, avec toutefois pour les calculs une position moins avancée du premier pic. Le calcul 2 anticipe légèrement le décollement de la couche limite sur l'ensemble des génératrices ; par contre le calcul 1 est moins précis pour ce qui est des niveaux de pression dans le plan de symétrie ($\phi=0^\circ$) en aval de la tuyère. Un cas d'écoulement laminaire est présenté figure 23 pour les mêmes conditions de Mach, pression de jet et incidence.

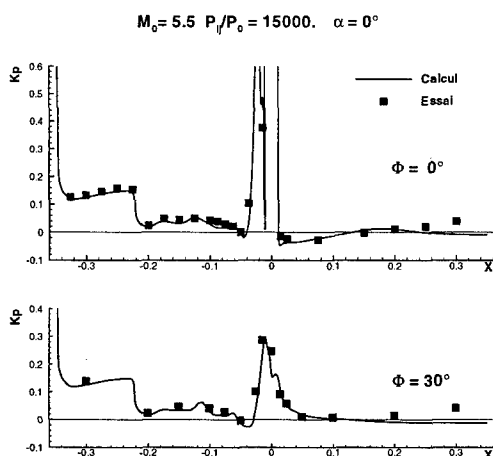


Figure 23 : Répartitions de pression pariétale en laminaire- Comparaisons calcul - essai

La comparaison des répartitions de K_p le long des génératrices $\phi = 0$ et 30° , est également assez satisfaisante. L'unique pic de pression, au lieu de deux pour l'écoulement de référence turbulent, est bien retrouvé ; il en est de même pour le plateau en surpression qui caractérise le décollement de la couche limite et qui prend naissance dès la fin de l'ogive. En revanche, les surpressions sous le sillage du jet obtenues en essai ne sont pas retrouvées.

Enfin, deux comparaisons calcul - essai sont présentées figure 24, pour la génératrice $\phi = 0^\circ$ du plan de symétrie. Elles mettent en évidence les effets de l'incidence du missile sur les répartitions de pression en présence du jet. Les conditions du cas de référence turbulent à incidence nulle, dont les résultats sont présentés figure 21, sont conservées mais pour des incidences de -10 et $+10^\circ$.

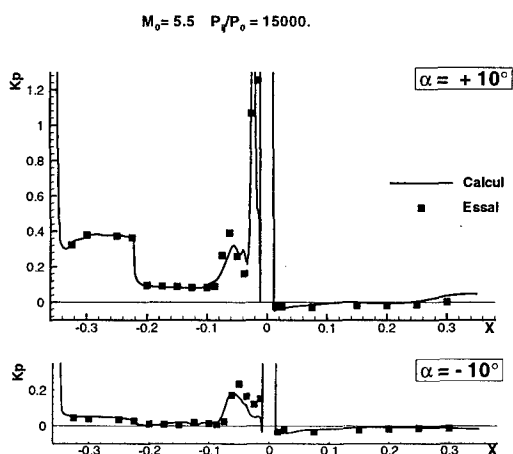


Figure 24 : Répartitions de pression pariétale en turbulent - Comparaisons calcul - essai en incidence

Les résultats d'essai montrent tout d'abord un étagement attendu, avec l'incidence, des niveaux de pression dans les régions amont non perturbées. La tuyère étant située à l'intrados, les surpressions qui apparaissent en amont du jet croissent avec la valeur de α (en particulier le niveau des pics de pression) ; ceci provient de l'augmentation de l'inclinaison relative des

deux écoulements. En aval de la tuyère, l'effet de l'incidence est par contre peu marqué.

Enfin, une quantification plus globale de ces phénomènes d'interaction entre le jet et l'écoulement externe est donnée figures 25 et 26 où sont présentées les évolutions des coefficients de force normale et de moment de tangage en fonction de l'incidence pour des écoulements turbulents à $M_0 = 5,5$ avec $(P_i/P_0 = 15000)$ et sans jet.

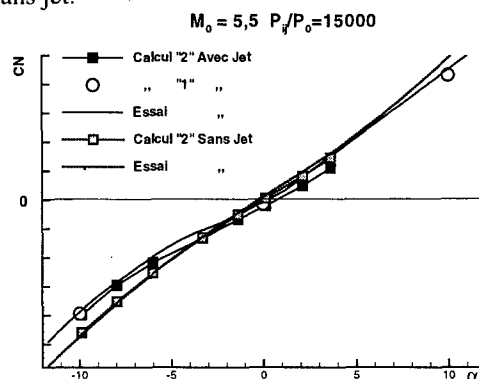


Figure 25 : Coefficient de force normale en incidence - Comparaison calcul - essai

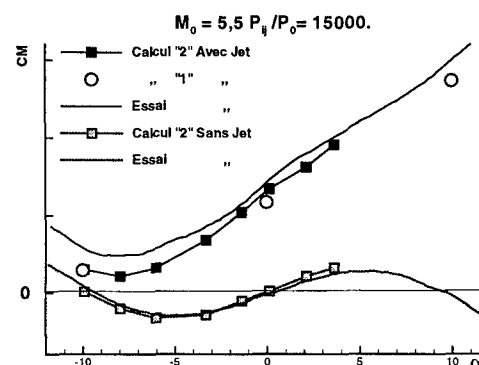


Figure 26 : Coefficient de moment de tangage en incidence - Comparaison calcul - essai

La plupart des calculs (''2'') ont été réalisés avec un maillage dégradé d'environ 150000 points, ils restituent toutefois correctement les effets des interactions globales.

Pour ces conditions de jet et de Mach, les écarts entre les évolutions avec et sans jet font apparaître, en terme de force, une contribution positive, dans le sens de la manœuvre, des interactions jet - écoulement externe pour les seules incidences négatives. En revanche, le moment induit par le jet reste cabreur quelle que soit l'attitude de l'intercepteur.

7. CONCLUSIONS

En conclusion, l'étude expérimentale réalisée en haut supersonique a mis en évidence des comportements différents du champ aérodynamique en présence d'un jet transversal selon que l'écoulement est laminaire ou turbulent. Ces phénomènes conduisent toutefois à des forces et moments d'interaction assez proches, mais plus favorables en turbulent.

Par ailleurs, pour un taux de détente (altitude) donné, les effets de l'interaction du jet avec l'écoulement extérieur diminuent lorsque le nombre de Mach augmente, que ce soit en termes de force ou de moment.

Les prolongements de l'étude expérimentale prévus dès cette année, concernent une extension jusqu'à $M_0 = 10$ du domaine de Mach étudié, ainsi que l'étude des interactions de jets pour un fonctionnement simultané de la tuyère de pilotage centrale principale et d'une tuyère de contrôle d'attitude située à l'arrière.

Le calcul, au moyen du code FLU3M, de ces écoulements tridimensionnels complexes par résolution des équations de Navier-Stokes a donné des résultats satisfaisants que ce soit en écoulement laminaire ou turbulent avec le modèle K- ϵ . Les répartitions de pression pariétale ainsi que les efforts et moments globaux mesurés en soufflerie sont assez bien retrouvés.

Les simulations numériques peuvent donc être utilisées pour analyser finement la structure de l'écoulement, en particulier pour préciser la topologie du décollement ainsi que le contournement du jet.

Par contre, les temps et coûts de calcul restent élevés et ne permettent pas actuellement une approche industrielle de ces phénomènes d'interaction jet transversal - écoulement externe.

REFERENCES

1. P. Champigny, R.G. Lacau, "Lateral Jet Control For Tactical Missile", AGARD-FDP-VKI Special Course, June 1994
2. M. Leplat, P. Champigny, M. Robert, "Interactions Aérodynamiques de Jets Transversaux sur Missiles", AGARD-CP-431, May 1987.
3. M. Dormieux, C. Mahé, "Calculs Tridimensionnels de l'Interaction d'un Jet Latéral avec un Ecoulement Supersonique Externe", AGARD-CP-437, 1988.
4. M. Dormieux, R. Marsaa-Pocy, "Numerical Assessment of Aerodynamic Interactions on Missiles with Transverse Jets Control", AGARD-CP-534, 1993.
5. N. Delattre, "Simulation Numérique d'Interactions de Jet", AAAF- 34^{ème} Colloque d'Aérodynamique Appliquée, Mars 1998.
6. L. Cambier, D. Darracq, M. Gazaix, Ph. Guillen, Ch. Jouet, L. Le Toullec, "Améliorations Récentes du Code de Calcul d'Ecoulements Compressibles FLU3M", AGARD-CP-578, April 1996.

Navier Stokes Simulation Around a High Velocity Missile with Cross-Flow Jet

St. M. Hitzel, Daimler-Benz Aerospace, Abteilung, FTE12
Postfach 80 11 49, D-81663 München, Germany
P. Hennig; DASA Lenkflugkörpersysteme GmbH, Ottobrunn;
H. Esch; DLR, Hauptabteilung Windkanäle, Köln-Porz

List of Symbols

C_p	pressure coefficient
$C_{p_{jet}}$	pressure coefficient of jet
	interference $C_{p_{diff}} = C_{p_{jet on}} - C_{p_{jet off}}$
D	diameter of cylindrical body section
M	Mach number
p_t	total pressure of wind tunnel flow
p_{jet}	total pressure of jet
p_∞	static pressure of wind tunnel flow
Re_D	Reynolds number referred to D
TR	with boundary layer tripping
T_t	total temperature of wind tunnel flow
x	distance from nose of body
α	angle of incidence of model
φ	polar angle

Introduction

The conventional control of missiles consists in responding to lateral acceleration command and in controlling some deflectable control surfaces that create moments in that way. These moments introduce the angular movements of the missile resulting in a change of incidence which in turn creates an aerodynamic lift force ensuring the desired manoeuvre.

This classical method of control has two disadvantages:

- The number of different intermediate technical steps, the aerodynamic reactions, the damping moments and the moments of inertia cause a time delay between steering command and the response of the missile. This applies to any method of moment control, whether by aerodynamic means or by jet control.
- Since the aerodynamic control devices act proportional to the dynamic pressure, they will show low effectiveness at low speed and at high altitudes.

The use of a lateral propulsive unit close to a missile's center of gravity removes some of these disadvantages and allows

- a considerable reduction of the time to response and results in a reduced passing distance off targets for which short reaction times are required.
- effective manoeuvres of missiles at very low speed and high altitude.

Two types of lateral jet control systems are used currently. One consists of a set of small, fixed, multiple, side thrusters that are arranged close to the center of gravity. The axis of each thruster can be inclined to allow its longitudinal component to support speed. The side force normal to the missile axis is used as the control force. Since the number of those thrusters is limited, this type of control is applied when the time of flight and the demands of manoeuvrability are low. Another possibility is a continuous gas generator. This device is linked to nozzles via jet interceptors or gas distributors. Two nozzles are required for an auto-rotating missile, three or four for a stabilized missile. Other systems such as liquid fuel support also are considered in current design studies. Since they can be multiple ignited they are more fuel efficient.

The aerodynamic effects of all those systems are similar. Basically they show the same flow structure of typical cross-flow injections into dominating main flows, the application of which can be found in many other areas.

The injection of a lateral jet into a high speed external flow causes local and downstream interactions. The cross-flow jet into a high supersonic flow around a high speed missile as presented here shows a spoiler effect close to the jet. Together with a supersonic shock upstream of the jet a boundary layer separation is formed in a high pressure ahead of the jet. The downstream side of the jet is dominated by a low pressure region. This pressure distribution may cause a small force or moments opposite to the direction of the intended thrust force. Thus, suitable jet-positions and jet characteristics have to be found to reduce this problem. Downstream interactions are caused by a 'horse-shoe' vortex system whose origins spring from the boundary separation just ahead of the jet, behind the pre-jet shock-system as well as from a vortex system being formed out of a 'dead-water' region behind the nozzle and the interaction of the jet itself. The flow structure induced by these vortex-systems may affect other downstream lifting or control surfaces. Designs of a missile with lateral thrust controls thus have to consider

- an interaction force that can affect the efficiency of the cross-flow thrust.
- possible unfavourable moments in pitch and roll that impair the missile's controllability.

Preparational Studies of Free-Flight Tests

A hypersonic missile technology project up to Mach 6 is being conducted in Germany. Side thrusters showed prove of concept in free-flight HFK-L1 (1995) and defined manoeuvres have been executed in HFK-L2 (1997) successfully. Figure 1 depicts the HFK-L2 technology test vehicle considering IR seekers, side thrusters and materials. Figure 2 shows the very similar HFK-L1 about 1 second after launch at the maximum speed of Mach 5.5. Figure 3 shows the side thruster component.

Semi-empirical methods were used for initial design, while those data were checked by 6-component wind-tunnel measurements. Since exact flight conditions are hard to be realized experimentally, a combination of both experimental wind tunnel investigations and numerical simulations in preliminary studies - subject of this paper - have paved the way to the successful scaling of wind tunnel results and real flight. The results of the numerical studies provide insight into the flow phenomena, while the experimental results provide data of the missiles integral aerodynamic behaviour.

Navier-Stokes-Simulation

Modern numerical methods for the solution of the full Navier-Stokes equations provide very efficient supplements to broaden one's knowledge on very complex flow structures and phenomena. They allow a simulation and investigation of undisturbed flow structures and put aside the wind tunnel scaling problems. Together with unlimited geometric modeling capabilities they help to reduce expensive wind-tunnel model construction. Clever teaming of Computational- and Experimental Fluid Dynamics (CFD and EFD) provide superior turn-around and better knowledge of the flow problems. This paper describes part of a numerical investigation into the very complex flow-phenomena around the cross-flow jet controlled high-velocity missile HFK.

Missile Geometry and Flow Cases

A typical HFK-missile configuration was selected. The missile is 3000 mm long and sports a conical nose-cone of 900 mm length. It's tail flare measures 600 mm, while the cylindrical part's diameter is 224 mm and the very end is 360 mm in diameter.

The cross-flow nozzle has a diameter of 29 mm. The nozzle's plenum pressure was 10.8 bar, massflux 1.674 kg/sec and 35.9 bar, massflux 3.340 kg/sec, respectively. In both cases the jet's Mach-number was 2.0. The pressure ratio at the nozzle's exit is 0.1278, the temperature ratio was close to 0.555.

The flow cases considered were Mach 5.3 and 6.0 at a Reynoldsnumber of 10^7 . The angle-of-attack was 0.0 degrees. The short time-schedule did not allow for other incidences.

Mesh-Generation

The geometry of the HFK was defined in a CATIA CAD environment. Here also the blockstructure of the contour conforms finite volume mesh was provided (figure 4). Its basic C-O-structure was adapted to the bow shock geometries expected for free stream Mach-numbers in-between 5.0 and 6.0. A nose-cone angle of 7.15° causes a shock angle of approximately 13.0° . To allow for angle-of-attack simulations the domains outer boundary was selected at 20.0 degrees. The total computational mesh uses 917.504 volumes with 224 in lengthwise direction, 64 volumes normal to the surface and 64 cells in circumferential direction. To allow for a proper treatment of turbulence $Y^+ = 1$ on the wetted surface was guaranteed everywhere. Special care was used for the resolution of the shock positions and the nozzle area. The nose of the missile - although almost pointed - was modeled as very small but round blunt sphere to avoid computational singularities.

Approximately two working days were sufficient for the complete block-structured geometry in a CAD-environment. Two additional days were used for the generation by the Dogrid-System [Ref. 1] of a satisfying computational mesh. Less than one day was necessary to prepare the first calculations. Given a more complex geometry (e.g. plus wings and controls) would add to this time. More recent commercial mesh-generators are in the same ballpark.

Navier-Stokes Solutions

The Navier-Stokes solver used here is the Dornier-Code Ikarus [Ref. 2]. The turbulent flow can be simulated by algebraic models [Ref. 2] or two-equation models [Ref. 3]. This well-known method solves the fluid equations in a cell-centered finite volume procedure and uses a Runge-Kutta type multi-time stepping approach. To accelerate the convergence to steady state local time stepping, implicit residual-smoothing, multi-grid and multi-level strategies are employed.

The turbulence-modeling is based on the Reynolds-averaged Navier-Stokes equations. Their unknown terms are determined according to Boussinesq's assumption of apparent turbulent viscosities. Here a K- ω model was applied. Its formulation not only regards the local development of vorticity but also the transport of the turbulent kinetic energy and it's dissipation.

Satisfying results shown here needed 1000 iterations for the finest mesh-level. The coarsest level required 400 - 600 iterations. The post-processing was executed by MIT's VISUAL3 plot-software.

Discussion of Results

Figure 5 shows close-ups of the flow in the vicinity of the cross-flow jet nozzle. The left side photograph depicts a Schlieren-picture from the DLR-wind-tunnel investigations. The others show Navier-Stokes simulations at Mach = 5.3 and Mach = 6.0 at different plenum pressures. At the time the N-S-calculations were performed no

experimental data were available, however the comparison of the flow structures reveals the same result qualitatively. In front of the jet the front shock being followed by a separation zone is visible, while the jet interaction with the missile's bow shock also can be seen in the Mach = 6.0 case. More details of the latter case are shown in figure 6. The flow approaches from the right side. The nozzle is situated on the cylindrical part of the missile body, close to its junction with the conical nose-section. Immediately in front of the jet affects the separation zone mentioned before, which results in a complicated horse-shoe vortex system causing multiple counter-rotating secondary vortices. This whole region is embedded in the oblique shock system in front of the jet. Behind the jet a complex region of separated flow has developed. The inset shows the pressure coefficient C_p in the plane of symmetry in front and behind the nozzle. The C_p -distribution begins - on the left side - with the constant pressure on the conical nose. At the discontinuous junction towards the cylindrical body a pressure-drop is caused by the expanding flow, while the first bump in this low pressure region marks the front shock mentioned. The second much smaller bump is due to the flow separation within the shock system. Naturally the following jet is clearly dominating the local flow by the huge pressure rise and the very low pressure region just behind it. Figure 7 gives an idea of the complete flow structure. The vortex systems may sport some interaction on downstream parts of the missile. Pressure losses and effects of induced velocity can result in pressure distributions that may affect the balance of the missile and/or influence control systems.

Wind tunnel tests

During the design phase a 22%-model of HFK-missile had been tested in H2K-wind tunnel of DLR. Force measurements were made at Mach number 5.3 in order to determine the effect of a side jet on normal force and pitching moment. There were some drawbacks connected with these tests: Reynolds number was by far lower than at free flight at sea level, cold air was used for jet simulation, temperatures were low, and in the wind tunnel only stationary conditions had been simulated. Consequently, the question arose how to treat the wind tunnel results. For future tests, it was felt necessary to develop a method with the object to relate wind tunnel data to free flight conditions, in addition to a Navier-Stokes simulation, by which flow phenomena resulting from cross flow jets could be better understood. To provide necessary experimental data of jet interference effects DLR started a test campaign.

A simple generic configuration had been chosen which includes elements of a high speed missile body: conical nose, cylindrical section, and flare. It resembles HFK-missile in general, but differs in some details. The model (Figure 8) has a sonic nozzle with a diameter of 1/10 of the model diameter, the axis normal to the body axis, located 1.5 diameter behind model shoulder. The nozzle is fed by dry cold air. Pressure taps are arranged in four cross sections and in three longitudinal sections. A body

diameter of $D = 40$ mm has been chosen. It allows the model to fit into the $M = 2.8$ nozzle of VMK wind tunnel. For the first phase of the test program investigations of the influence of Reynolds number have been planned. Tests have been foreseen at two Mach numbers: one supersonic ($M = 2.8$) and one hypersonic ($M = 6.0$). They were performed in the three blow down wind tunnels TMK, VMK, and H2K of DLR Köln.

The test program included angles of incidence between 10° and 15° and jet pressure ratios ranging from $p_{ij} / p_\infty = 1$ to 300. These values could not be reached at all free stream conditions due to limitations in tunnel size and pressure range.

At $M = 2.8$ pressures were recorded at every two degrees of incidence. The data were interpolated by an Akima curve fitting and recalculated for round values of angle of incidence. In Figure 9 the distribution of the pressure coefficient C_p in the longitudinal section $\varphi = 180^\circ$ is plotted versus the axial distance

x / D ($M=2.8$; $Re_D = 1.9 \cdot 10^6$; $p_{ij} / p_\infty = 300$) for the complete angle of incidence range. In the following figure only the jet interference will be shown, that is the difference $C_{p_{diff}} = C_{p_{jet on}} - C_{p_{jet off}}$ (Figure 10).

Pressure measurements at Mach number $M = 2.8$

At $M = 2.8$ tests have been performed in TMK [4] and VMK wind tunnels. In VMK sea level conditions can be reached ($p_i = 2800$ kPa, $T_i = 740$ K). Without heating wind tunnel flow Reynolds number is increased by a factor of four to a value $Re_D = 11 \cdot 10^6$. This corresponds to sea level conditions for a missile body with a diameter of 160 mm. At standard operating conditions of both wind tunnels boundary layer at the position of the side jet nozzle was always turbulent. By operating the ejector of TMK, Reynolds number was reduced to $Re_D = 0.5 \cdot 10^6$. It was only at that Reynolds number that a distinct Reynolds number effect upstream of the side jet was observed.

To show the influences of the main parameters for this configuration few plots are presented. From Figure 10 one can see that - except for the direct neighbourhood of the nozzle - the angle of incidence in the range $-10^\circ \leq \alpha \leq 15^\circ$ has roughly the same effect on jet interference as on the uninfluenced flow at the conical nose. The influence increases when the flare is reached. The separation zone of the side jet broadens with angle of incidence as the local pressure decreases. By this the jet pressure ratio based on local flow conditions increases (Figure 11). For the same reason the pressure rise in the plane of the lateral jet ($\varphi = 180^\circ$) decreases with increasing angle of incidence as the separation angle remains constant in supersonic flow but the local pressure level has decreased with higher angles of incidence. At $\alpha = 15^\circ$ pressure distribution shows some changes compared to lower angles - compare curves for $\alpha = 10^\circ$ and 15° in figures 11 and 12. This is caused by a change in flow separation of the body. At $\alpha = 15^\circ$ a pair of separated body vortices has formed leading to a distinctive

separation line on both sides of the body. Now the nozzle exit lies within a region where the oncoming flow is no longer attached but already separated. In figure 13 only a very short part of the primary separation line is visible before it is diluted by the side jet. During the transition stage, when the separation lines start to form (here at about 12°), asymmetric patterns of side jet induced separation region can be observed for high jet pressure ratios.

For otherwise identical conditions jet pressure ratio defines the penetration height of the jet and by this the separation length upstream of the nozzle. As the separation angle in supersonic flow is constant, pressure in the separation region is almost independent of jet pressure ratio except for the direct neighbourhood of the jet (Figure 14). Pressure just downstream of the side jet is more or less independent of jet pressure ratio, but the distance at which the pressure level of the configuration without side jet is reached depends strongly on jet pressure ratio.

An influence of Reynolds number on side jet effects was observed in the separation region upstream of the nozzle (Figure 15). For $Re_D = 0.5 \cdot 10^6$ separation started further upstream than for the other Reynolds numbers. This was true for negative incidences up to $\alpha = 0^\circ$. Downstream of the lateral jet no pronounced Reynolds number influence was observed except for an incidence of $\alpha = 10^\circ$. An explanation was not found, yet.

Pasting a roughness band to the body nose, the Reynolds number effect upstream of the side jet disappeared (Figure 16).

Pressure measurements at Mach number $M = 6.0$

Tests at Mach number $M = 6.0$ took place in the hypersonic wind tunnel H2K of DLR Köln. The bulk of the measurements was made at relatively small angles of incidence: $\alpha = -5^\circ, 0^\circ, 5^\circ$. Reynolds number in this wind tunnel is not high, ranging from $2 \cdot 10^6$ to $20 \cdot 10^6$ per meter at $M = 6.0$. Consequently, natural transition occurred far downstream of the nozzle when jet was off. During the present test campaign Reynolds number was varied in three steps: $Re_D = 0.1 \cdot 10^6, 0.4 \cdot 10^6$ and $0.8 \cdot 10^6$. At $Re_D = 0.4 \cdot 10^6$ boundary layer has been tripped by applying a spiked collar 50 mm behind the nose.

With rising Mach number suction areas play a decreasing role for forces and moments of flight vehicles. Comparison between results at $M = 2.8$ and $M = 6.0$ shows that due to the low pressures at small flow angles jet interference downstream of the nozzle that are detrimental to the thrust amplification factor have diminished at the hypersonic Mach number. On the cylindrical body section, at zero angle of incidence, C_p is about zero and the difference to vacuum is only $\Delta C_p \approx 0.04$ (Figure 17). But at the flare and for negative angles of incidence pressure in the longitudinal section $\varphi = 180^\circ$ increases and by this the jet interference effect, too. This leads to the well-known fact, that the amplification factor of side jet force

in general increases with supersonic Mach number and that the amplification factor increases with positive angle of incidence (see for instance [5]) when the nozzle is at the lee side of the body. Figure 18 demonstrates for the configuration tested how strongly the flare in combination with negative angles of incidence contributes to an interference force that acts in opposite direction to the thrust of the side jet.

As expected, separation due to the side jet moves upstream with angle of incidence (Figure 18) and with jet pressure ratio (Figure 19). Compared to the supersonic Mach number $M = 2.8$ (Figure 14) influence of jet pressure ratio on the pressure on the cylinder downstream of the nozzle is very small. On the flare a distinct effect is felt only for negative angles of incidence ($\alpha \leq 0^\circ$).

Reynolds number variation from $Re_D = 0.1 \cdot 10^6$ to $Re_D = 0.8 \cdot 10^6$ changed the pressure in the separation region ahead of the nozzle (Figure 20).

A massive tripping device was applied (16 spikes, $\varnothing 1$ mm, length 1.5 mm) to induce turbulent flow at the model shoulder. It had an influence on pressure distribution even without side jet. Jet interference was effected similarly as at $M = 2.8$: separation ahead of the side jet started further downstream when the tripping device was attached to the conical nose (Figure 21).

Summary / Conclusion

The cross-flow jet technology for the control of high speed missiles was investigated by free-flight tests, Navier-Stokes simulations and experimental wind-tunnel research. While the cross-flow technology shows promising benefits for the demands of high manoeuvrability a proper design needs detailed knowledge both of the integral effect on the missile behaviour and the corresponding details of the flow.

Navier-Stokes simulations were used to support wind-tunnel work for the understanding of complex flow structures. A finite volume method was employed to simulate high velocity flow in a contour conforming block-structured mesh. The turn-around time of the mesh and the numerical solver employed was less than one week. Given latest equipment this time could have been reduced further. A qualitative comparison with wind-tunnel visualizations and pressure measurements shows good agreement.

It was found necessary to develop a method by which wind tunnel results of jet interference effects can be converted to free flight conditions. DLR started a test campaign to provide experimental data as basis for a computer program. First results include Reynolds number effects in the range $0.5 \cdot 10^6 \leq Re_D \leq 11 \cdot 10^6$ for $M = 2.8$ and $0.1 \cdot 10^6 \leq Re_D \leq 0.8 \cdot 10^6$ for $M = 6.0$. It is planned to investigate the influences of other parameters that cannot be simulated correctly in standard wind tunnel tests, for example non-stationary conditions, different gases, high temperatures.

Currently more detailed experimental investigations are underway at the DLR, while supporting CFD calculations including high angle-of-attack settings can be executed using the very same computational mesh, funding provided.

A close schedule of CFD simulation and EFD experiment provide superior turn-around and better knowledge of the flow-problems. Detailed CFD-results can provide the undisturbed flow simulation and thus the missing link in between mass-data of integral forces and moments produced by the EFD wind-tunnel and the free-flight test.

References

1. Seibert, W.;
A Graphic Interactive Program-System to Generate Blockstructured Volume Grids for Fluid Flow Analysis. Functional Description, DOGRID Version 5. Do-Report-No: BF 8/90B 1990
2. Magagnato, F.;
IKARUS C: A Flow Solver for Simulation of Three-Dimensional, Turbulent Flow Fields Around Cars, Do-Report-No: BF 4/91B Sept. 1992
3. Speziale, C.G., Abid, R., Anderson, E.C.;
A Critical Evaluation of Two-Equation Models for Near Wall Turbulence, ICASE Report No. 90-46 1990
4. Esch, H.;
Druckverteilungsmessungen an einem Flugkörperrumpf im Überschall - Meßdaten. DLR Internal Report, 1997.
5. Brandeis, J.; Gill, J.;
Experimental Investigation of Side-Jet Steering for Supersonic and Hypersonic Missiles. Journal of Spacecraft and Rockets, Vol. 33, No. 3, May-June 1996.

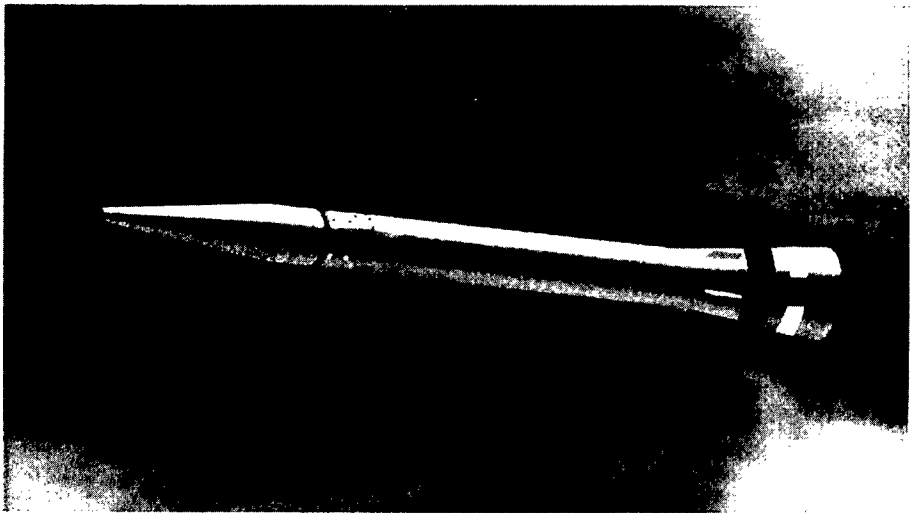


Figure 1: Technology carrier HFK-L2 with test components for IR seekers, side thrusters, and materials.

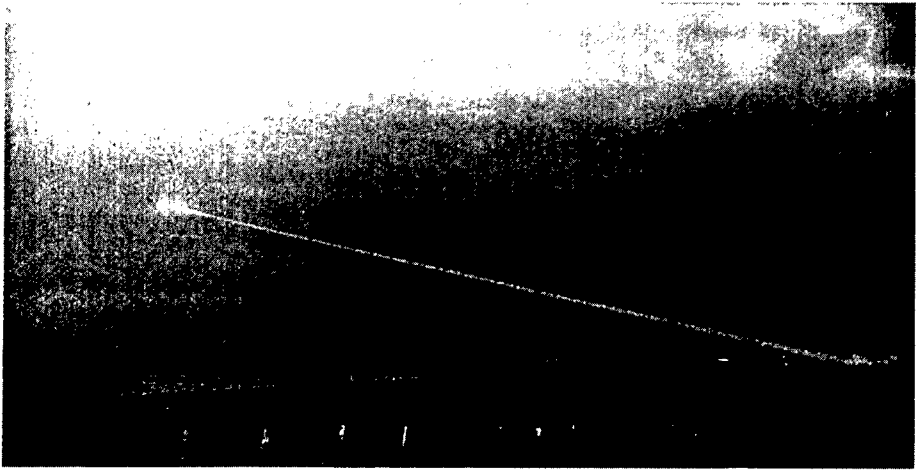


Figure 2: Hypersonic missile HFK-L1 during flight test 1995 at maximum speed.

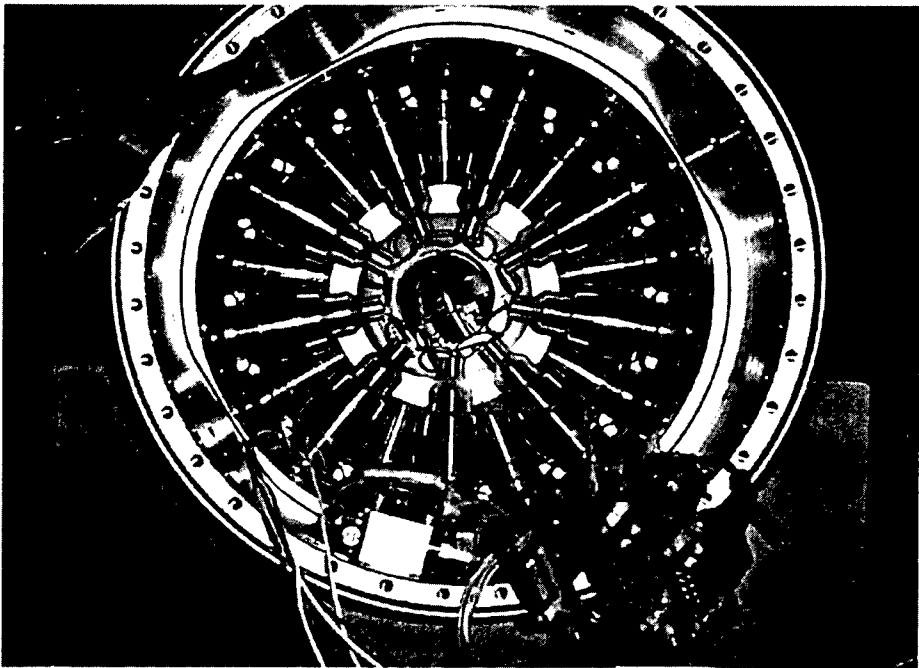


Figure 3: Side thruster component of HFK-L2.

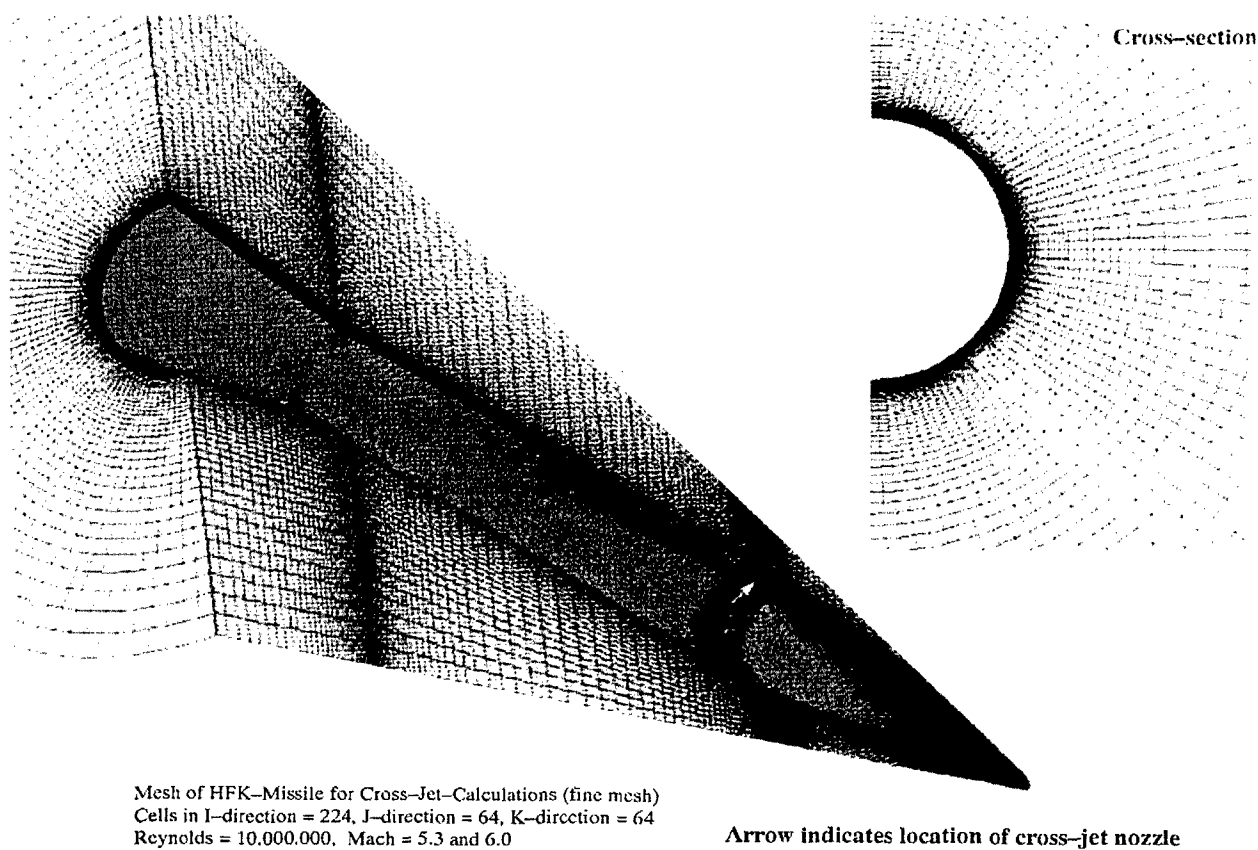
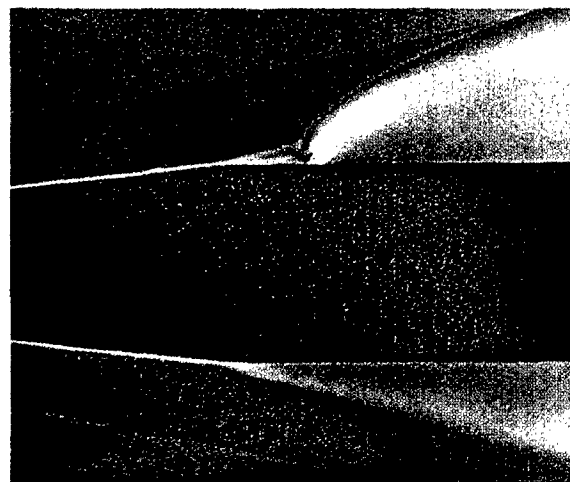
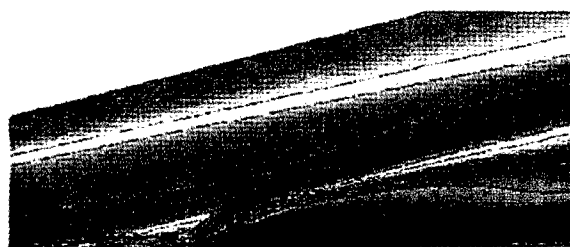


Figure 4: Fine mesh for Navier-Stokes calculation.

Qualitative comparison of windtunnel and Navier-Stokes-Simulations



Schlierenpicture of HFK-missile
with crossflow jet at Mach = 5.3,
DLR windtunnel measurements



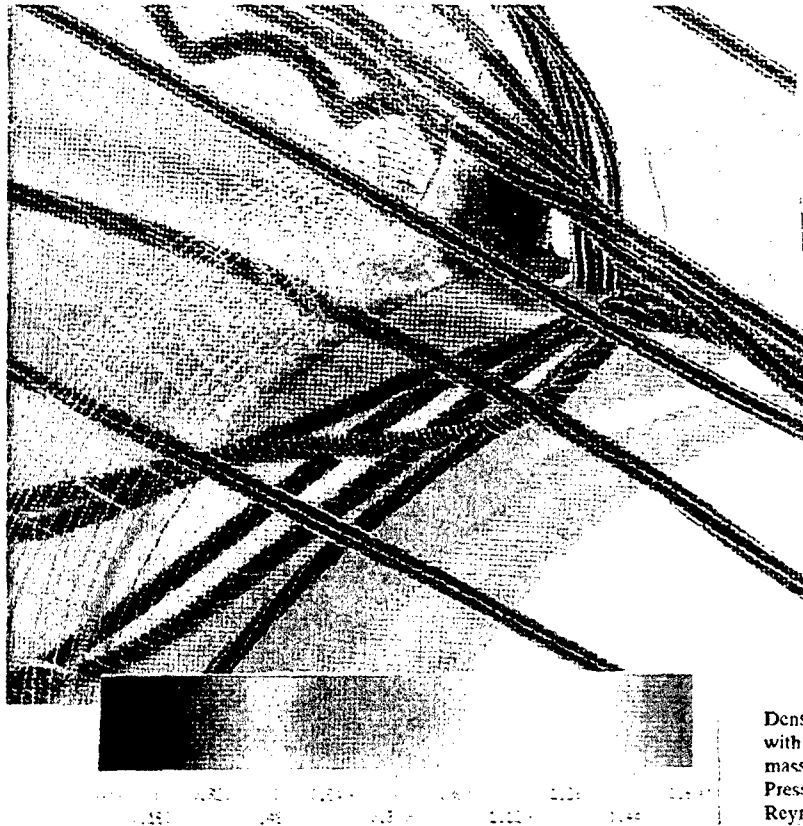
Density around HFK-Missile
with cross-jet

Jet-data: mass-flow = 1.674 kg/sec, Mach at nozzle exit = 2.0
Pressure at nozzle exit = 1.38 bar, Plenum pressure = 10.8 bar
Free-flow data: Reynolds = 10,000,000, $\alpha = 0.0$ deg, Mach = 5.3



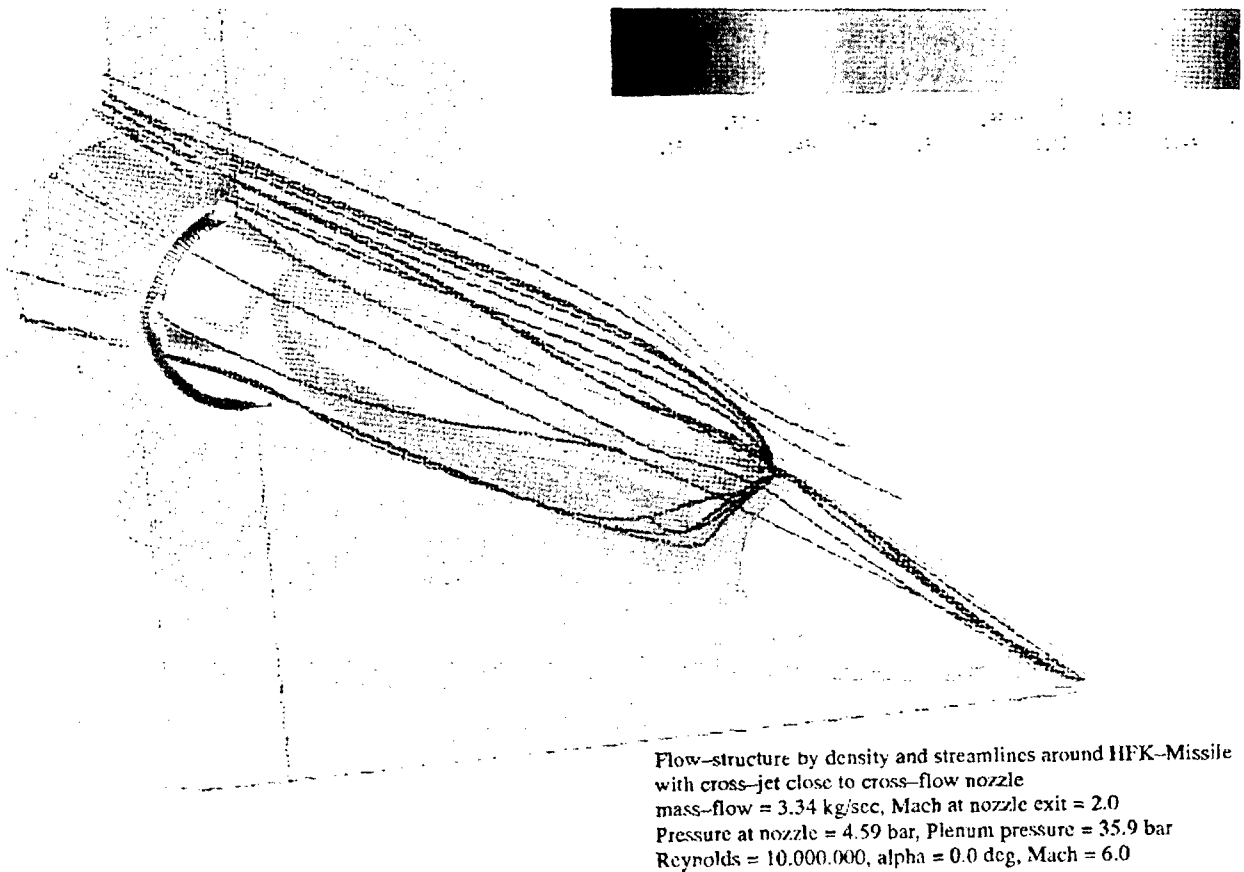
Pressure coefficient and streamlines around HFK-Missile
with cross-jet (fine mesh)
mass-flow = 3.34 kg/sec, Mach at nozzle exit = 2.0
Pressure at nozzle = 4.59 bar, Plenum pressure = 35.9 bar
Reynolds = 10,000,000, $\alpha = 0.0$ deg, Mach = 6.0

Figure 5: Schlieren picture and density contours at Mach=5.3, pressure contours at Mach=6.



Density and streamlines around HFK-Missile
with cross-jet (medium mesh)
mass-flow = 3.34 kg/sec, Mach at nozzle exit = 2.0
Pressure at nozzle = 4.59 bar, Plenum pressure = 35.9 bar
Reynolds = 10.000.000, $\alpha = 0.0$ deg, Mach = 6.0

Figure 6: Density contours and streamlines in the cross-flow area at Mach=6.



Flow-structure by density and streamlines around HFK-Missile
with cross-jet close to cross-flow nozzle
mass-flow = 3.34 kg/sec, Mach at nozzle exit = 2.0
Pressure at nozzle = 4.59 bar, Plenum pressure = 35.9 bar
Reynolds = 10.000.000, $\alpha = 0.0$ deg, Mach = 6.0

Figure 7: Density contours and streamlines at Mach=6; interaction of lateral jet flowfield with body flow and flare shock.

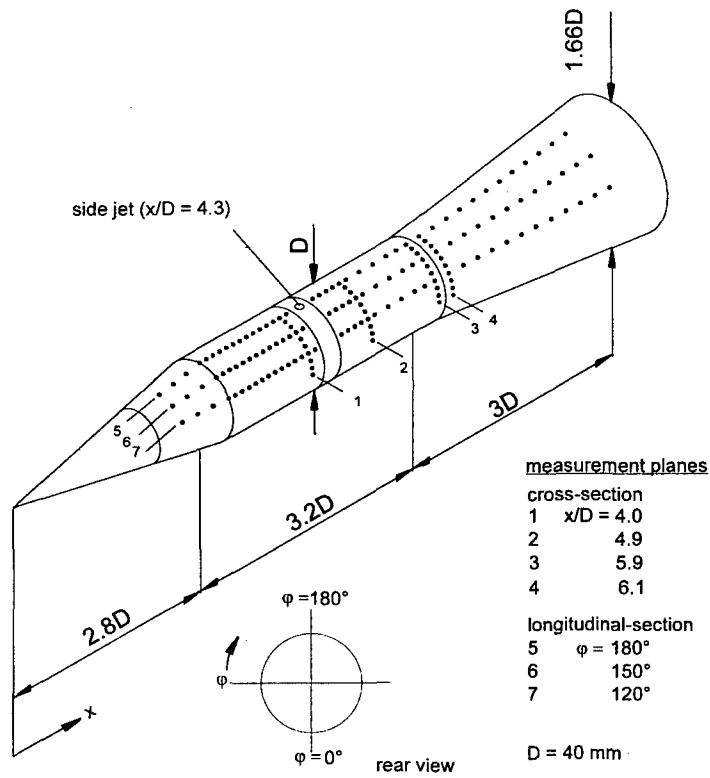
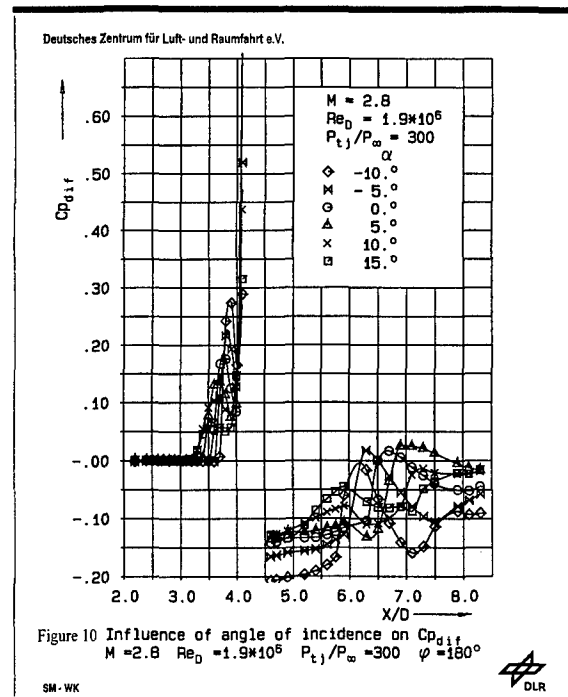
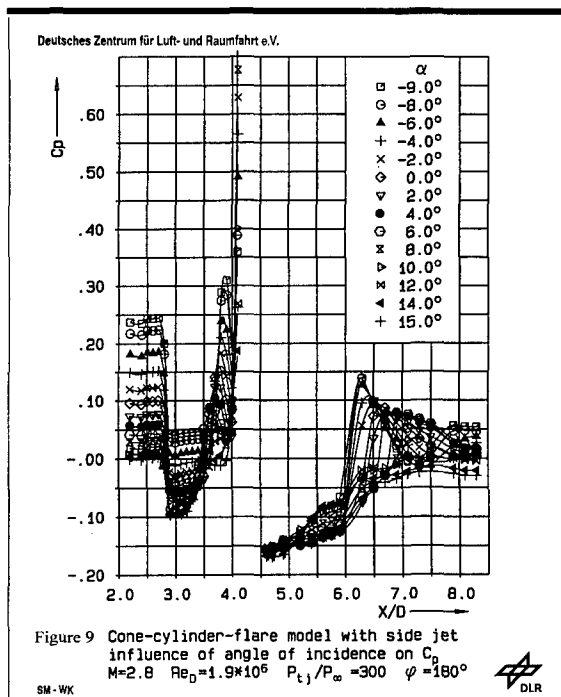


Figure 8 Cone-cylinder-flare high speed missile body with side jet for pressure distribution measurements in DLR wind tunnels



Deutsches Zentrum für Luft- und Raumfahrt e.V.

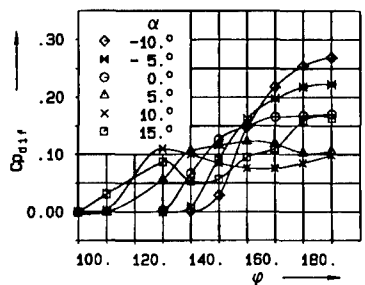


Figure 11 Variation of separation region due to side jet with angle of incidence. cross section 0.3 D upstream of nozzle $M=2.8$ $Re_D=1.9 \cdot 10^5$ $P_{tj}/P_\infty=100$

SM-WK



Deutsches Zentrum für Luft- und Raumfahrt e.V.

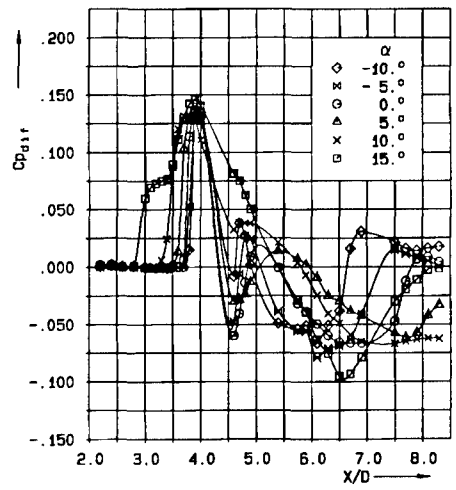


Figure 12 Influence of angle of incidence on pressure in longitudinal section $\phi=120^\circ$ $M=2.8$ $Re_D=1.9 \cdot 10^5$ $P_{tj}/P_\infty=300$

SM-WK

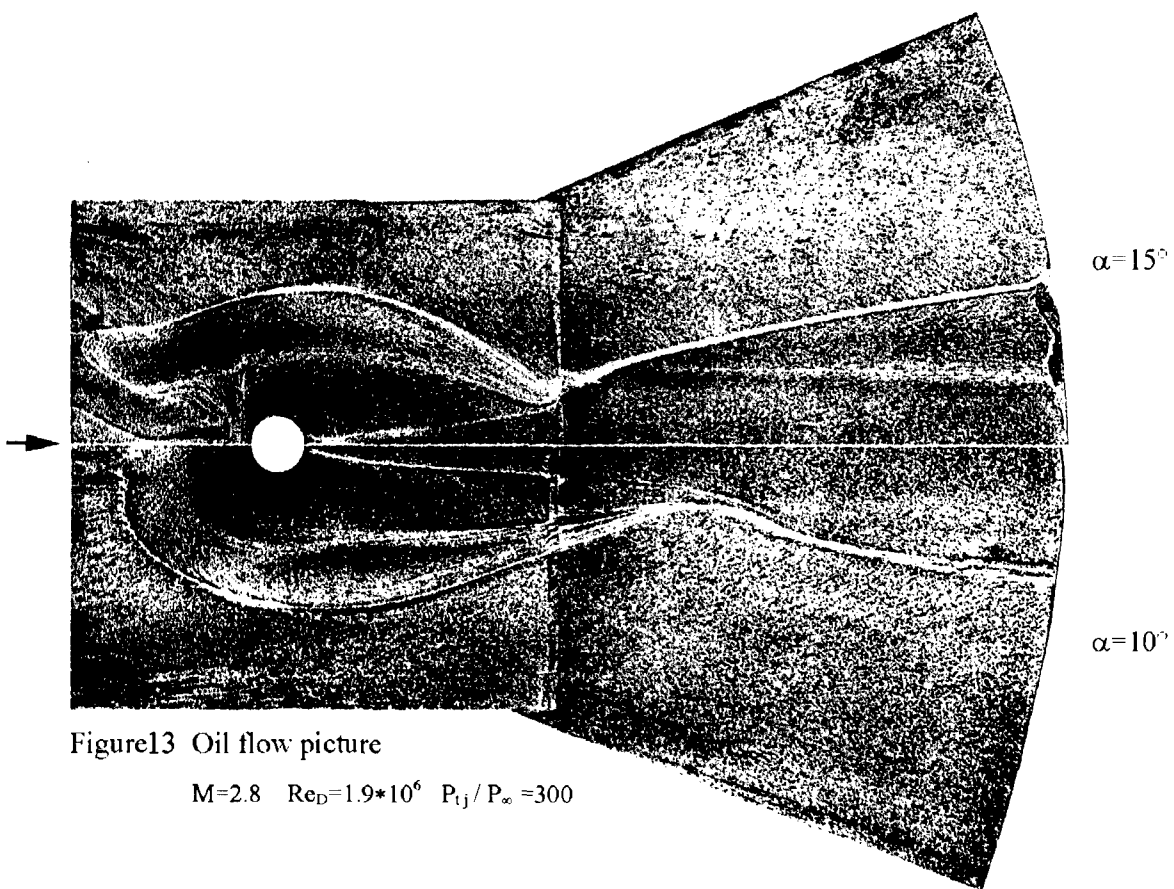
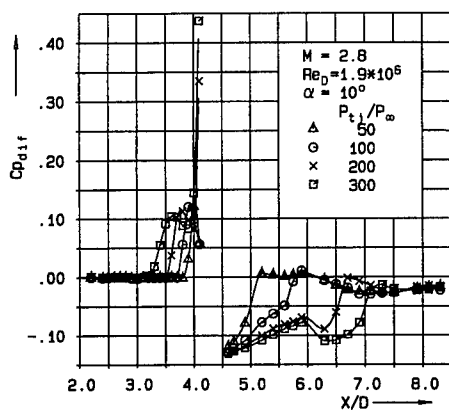


Figure 13 Oil flow picture

$M=2.8$ $Re_D=1.9 \cdot 10^5$ $P_{tj}/P_\infty=300$

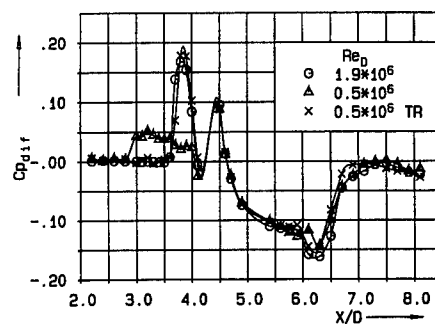
Deutsches Zentrum für Luft- und Raumfahrt e.V.

Figure 14 Influence of jet pressure ratio on pressure distribution of lee-side ($\varphi = 180^\circ$)

SM-WK



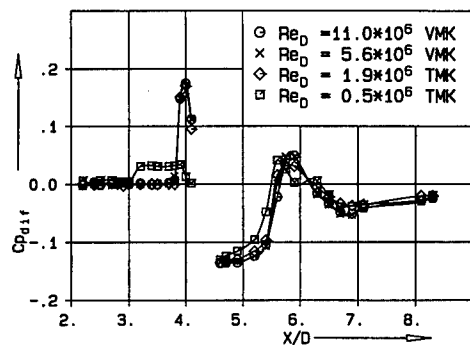
Deutsches Zentrum für Luft- und Raumfahrt e.V.

Figure 16 Influence of b.l.-tripping (TR)
 $M = 2.8$; $\alpha = 0^\circ$; $P_{tj}/P_\infty = 300$; $\varphi = 150^\circ$

SM-WK



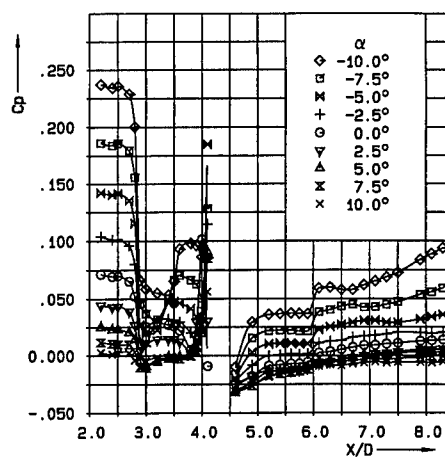
Deutsches Zentrum für Luft- und Raumfahrt e.V.

Figure 15 Pressure measurements in DLR wind tunnels
TMK and VMK at different Reynolds numbers
 $M = 2.8$ $\alpha = 0^\circ$ $P_{tj}/P_\infty = 100$ $\varphi = 180^\circ$

SM-WK



Deutsches Zentrum für Luft- und Raumfahrt e.V.

Figure 17 Influence of angle of incidence on
pressure distribution C_p $\varphi = 180^\circ$
 $M = 6.0$; $Re_D = 0.4 * 10^6$; $P_{tj}/P_\infty = 200$

SM-WK



Deutsches Zentrum für Luft- und Raumfahrt e.V.

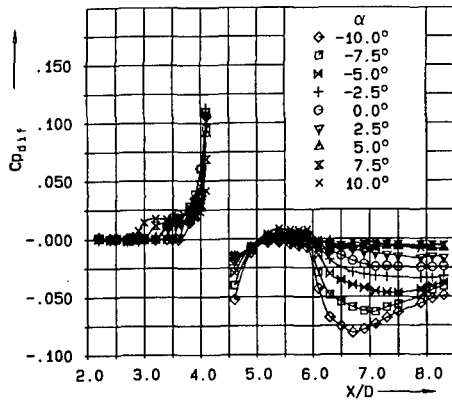


Figure 18 Influence of angle of incidence on jet interference $C_{p_{d1r}}$, with b. l. tripping
 $M = 6.0$; $Re_D = 0.4 \times 10^6$ TR; $P_{t1}/P_\infty = 200$

SM - WK



Deutsches Zentrum für Luft- und Raumfahrt e.V.

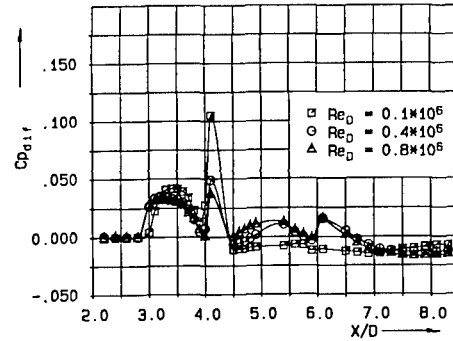


Figure 20 Influence of Reynolds number on side jet interference
 $M = 6.0$; $P_{t1}/P_\infty = 200$; $\alpha = 0^\circ$; $\varphi = 150^\circ$

SM - WK



Deutsches Zentrum für Luft- und Raumfahrt e.V.

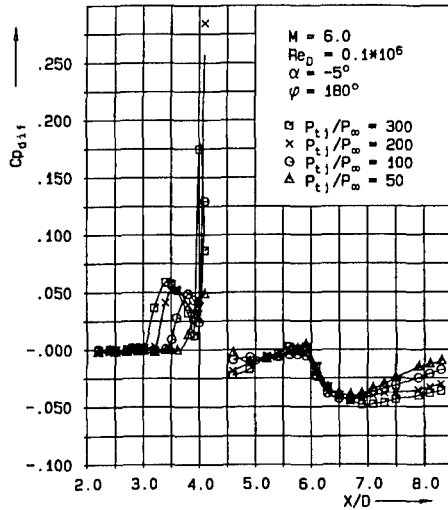


Figure 19 Influence of jet pressure ratio on pressure distribution on windward side ($\varphi = 180^\circ$)

SM - WK



Deutsches Zentrum für Luft- und Raumfahrt e.V.

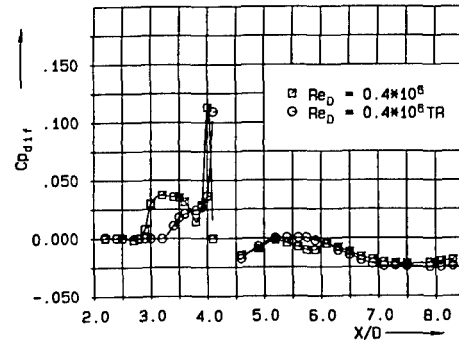


Figure 21 Influence of b. l. tripping (TR) on pressure distribution $C_{p_{d1r}}$
 $M = 6.0$; $Re_D = 0.4 \times 10^6$; $P_{t1}/P_\infty = 200$; $\alpha = 0^\circ$; $\varphi = 180^\circ$

SM - WK



Etudes Fondamentales sur les Aspects Aérodynamiques et Thermiques des Écoulements à l'Arrière-corps des Missiles

P.Servel , Ph.Reijasse , R.Benay , B.Corbel

Département d'Aérodynamique Fondamentale et Expérimentale
Office National d'Etudes et de Recherches Aérospatiales (ONERA)
8, rue des vertugadins - 92190 Meudon - France

1 – Sommaire.

Les écoulements à l'arrière-corps d'engins tels que les missiles jouent un rôle primordial sur leur traînée de "culot" et donc sur leur bilan de poussée. De plus, ils ont une influence évidente sur les charges aérothermiques qui s'exercent sur cette partie arrière soumise aux fortes températures du jet propulsif sortant de la tuyère, jet composé des gaz chauds issus de la chambre de combustion. L'exigence de performances de plus en plus pointues pour les nouveaux missiles se traduit par la nécessité de disposer de méthodes de prévision fine des écoulements et de mieux comprendre les phénomènes physiques qui s'y produisent. Pour cela, des travaux fondamentaux sur le thème des écoulements d'arrière-corps propulsés ont été effectués à l'ONERA, tant dans le domaine numérique où un code Navier-Stokes (le code NASCA) a été développé spécialement dans ce but, que dans le domaine expérimental où des expériences bien instrumentées ont été réalisées afin d'avoir une description assez détaillée de ces écoulements et de constituer des banques de données documentées pour valider les codes numériques. Cet article décrit cinq configurations axisymétriques types d'écoulements de culot, présentant mesures expérimentales et résultats de calcul pour différentes géométries d'arrière-corps et plusieurs sortes de jets propulsifs (air froid, air chaud et espèces gazeuses chaudes issues de la combustion d'un perpergol).

2 – Introduction.

Les arrière-corps des missiles sont le siège de phénomènes aérothermochimiques complexes, dus à la confluence de l'écoulement externe et du jet propulsif composé par des gaz à haute température issus de la chambre de combustion. Ces deux écoulements confluent délimitent une zone de recirculation où s'effectue un mélange entre les divers gaz issus des écoulements incidents. L'état aérodynamique de cette portion de l'écoulement, dite "eau morte" par le fait qu'elle est en contact direct avec le culot, détermine la pression sur l'arrière-corps et donc la traînée de l'engin. Toute instabilité ou extension de cette poche de fluide pratiquement inerte et à haute température peut

avoir des effets dommageables sur la structure ou rendre partiellement inefficaces des gouvernes situées près du culot. De plus, la température des gaz de l'eau morte influence directement les transferts de chaleur au culot, c'est-à-dire la charge thermique à laquelle le fond du missile est soumis. Les aspects thermiques des écoulements de culot constituent un facteur clé, notamment pour la résistance de la structure. Ces transferts sont considérablement accrus quand les gaz propulsifs, encore réducteurs, s'enflamment par mélange avec l'oxygène de l'air extérieur au sein de l'eau morte. Enfin, ces gaz à forte température enveloppent l'arrière du missile et rendent celui-ci vulnérable face à la détection infrarouge.

Au cours des 20 dernières années, les concepteurs de missiles ou de lanceurs ont vu se développer deux exigences majeures pour la phase de projet. La première de celles-ci, due au progrès des simulations expérimentales et numériques, est la précision. Les performances aérodynamiques de plus en plus pointues demandées aux engins se traduisent en effet par la nécessité de disposer de méthodes de prévision donnant une connaissance très détaillée des phénomènes. La seconde de ces exigences, issue quant à elle de pressions économiques externes, telles que la concurrence ou les réductions budgétaires, conduit à choisir les méthodes en fonction de critères de rapidité et de moindre coût. Dans cette optique, les méthodes de simulation numérique ont très vite fait l'objet d'une attention toute particulière. Toutefois, l'approche du problème sous cet angle comporte encore un important aspect expérimental, car la mise au point d'une méthode de calcul susceptible de généralisations ultérieures nécessite sa validation pour un certain nombre de cas fondamentaux, bien choisis et bien définis. La préparation de ces cas expérimentaux fondamentaux, la réalisation d'expériences à coût modeste dans des installations de dimensions réduites, la conception en parallèle de méthodes de calcul et leur validation sur les banques de données issues des expériences, constituent ainsi la méthodologie essentielle pour aboutir aux buts que l'on a évoqués plus haut.

Dans cet esprit, les travaux fondamentaux sur le thème des arrière-corps de missiles effectués à l'ONERA, dont quelques exemples constituent le sujet de cette communication, s'articulent sur deux axes principaux :

- Un axe expérimental, dont le but est la réalisation d'expériences bien instrumentées donnant une description détaillée des écoulements permettant leur analyse physique. De plus, les banques de données bien documentées ainsi obtenues constituent des cas de référence pour la validation des codes numériques.
- Un axe théorique, consistant en la modélisation des phénomènes et leur prédiction par le calcul. Cet axe a d'abord été concrétisé par l'élaboration de codes "multicomposant" [1], lesquels utilisent des hypothèses simplificatrices permettant d'évaluer rapidement les grandeurs aérothermiques globales essentielles qui régissent l'écoulement de culot, puis par la conception d'un code Navier-Stokes axisymétrique évolutif, le code NASCA [2].

Enfin, il faut préciser que tous les résultats présentés ci-dessous, expérimentaux comme numériques, sont obtenus dans des configurations axisymétriques.

3 – Arrière-corps droit propulsé par une tuyère affleurante.

La première étude que nous mentionnons était destinée, pour sa partie expérimentale, à fournir une banque de données détaillée sur les champs de vitesses et les distributions de tenseurs de Reynolds dans la zone de culot et de sillage naissant d'un arrière-corps schématisé propulsé par un jet secondaire froid [3]. Cette banque de données a ensuite été utilisée pour valider les codes alors disponibles [2,4] et nous illustrerons ces travaux par quelques exemples de résultats fournis par le code NASCA. Le nombre de Mach de l'écoulement externe est de 4,18 (la température génératrice est de 300 K et la pression génératrice de 10^5 Pa), celui du jet propulsif de 3,45 (la température génératrice est aussi de 300 K et la pression génératrice de $4,23 \cdot 10^5$ Pa). Le maillage, très raffiné, choisi pour cette configuration de validation est de 201 points en x et de 145 points en y. Sa définition résulte d'une analyse poussée de la convergence spatiale de la solution. Les calculs convergent pour cette configuration en 8000 itérations avec des temps de calcul de 8000 s dans le cas où le modèle de turbulence utilisé est le modèle à 2 équations de

transport [k-ε] de Chien (4000 itérations et 3000 s avec le modèle algébrique de Baldwin et Lomax).

La strioscopie continue de la figure 1 permet une description des écoulements externe et propulsif, en régime de confluence en aval de l'arrière-corps. On y distingue la couche limite qui se développe sur la partie cylindrique de l'arrière-corps. A l'arête du culot, l'écoulement externe décolle après avoir traversé un éventail de détentés centrées, ce qui indique une pression de culot inférieure à la pression statique externe non perturbée. De même, le jet propulsif débouchant de la tuyère décolle de la lèvre de la tuyère après avoir subi une forte détente; on parle alors d'un jet sous-détendu. Les frontières décollées des deux écoulements entrant en confluence délimitent une zone de fluide décollé torique au contact de la paroi du culot. La confluence des écoulements s'accompagne de leurs déviations mutuelles, d'où la présence d'un choc de confluence externe et d'un choc "en tonneau" pour le jet. Dans cette configuration de sous-détente, à cause du fort épanouissement du jet, la zone de réflexion du choc en tonneau sur l'axe sort du champ exploré par la strioscopie. A l'aval de la zone de confluence, la couche de mélange et le jet se transforment peu à peu en un sillage.

L'un des points les plus importants de la simulation est la prédiction de la pression de culot (fig.2). Les courbes de pression pariétale calculée par le code NASCA font apparaître une différence notable entre les niveaux de pression prédits par les deux modèles. Après une réinterprétation des résultats expérimentaux et malgré leur dispersion, ceux-ci sont approchés d'une manière satisfaisante.

L'écoulement de couche limite sur le fuselage est calculé sur une longueur de 81 mm, en partant d'un sondage expérimental, qui a été effectué à l'aide d'une sonde Pitot et a permis une approche de la paroi impossible avec la vélocimétrie laser, ce qui autorise une très bonne reproduction des couches limites par les modèles. Tous les autres sondages ont été effectués à l'aide de la vélocimétrie laser et montrent, sur les parties effectivement sondées, un bon accord calcul expérience pour les vitesses axiales, comme par exemple à 4 mm en aval du culot (fig.3). En allant plus avant dans la zone d'interaction entre le jet et l'écoulement externe (fig.4), l'accord reste satisfaisant avec toutefois un avantage pour le modèle [k-ε] en ce qui concerne les tensions de cisaillement (fig.5). Dans cette zone plus en aval ($x = 40$ mm), une plus grande étendue des résultats de mesures fait apparaître un accord relativement correct avec les prédictions du modèle [k-ε], une dispersion des valeurs expérimentales non négligeable étant visible sur la figure au voisinage de $y = 10$ mm et $y = 30$ mm.

4 - Arrière-corps propulsé avec tuyère émergente.

Nous continuons les validations du code en écoulement froid sur une configuration d'arrière-corps stylisé avec tuyère émergente [5]. La partie externe est cylindrique de diamètre $D_e = 54$ mm. La tuyère, qui a un diamètre en sortie $D_j = 28,5$ mm, émerge du culot sur une distance $L = 13,8$ mm. La tuyère produit un écoulement supersonique uniforme de nombre de Mach égal à 3,495 dans sa section de sortie (température génératrice de 275 K et pression génératrice de $19,5 \cdot 10^5$ Pa). Cette configuration est particulièrement intéressante pour valider un code de calcul car elle donne lieu à la formation d'une zone décollée étendue. Le nombre de Mach de l'écoulement externe est de 3,019 (température génératrice de 275 K et pression génératrice de 10^5 Pa). Le modèle de turbulence utilisé ici est le modèle algébrique de Baldwin-Lomax. Le maillage comprend 194 points en x et 134 points en y, les resserrements locaux ayant pour but de prendre en compte les diverses parois de la zone de culot.

Ce type d'écoulement comportant un système complexe de chocs se prête traditionnellement bien à une première comparaison qualitative entre les strioscopies et les isochores calculées qui doivent en principe reproduire le motif observé sur la strioscopie. Cette comparaison est faite sur la figure 6 et un examen attentif des positions des chocs, en particulier du choc "en tonneau", montre qu'à ce niveau, la structure reproduite par le calcul est très satisfaisante. La courbure du choc supérieur engendré par le recollement de l'écoulement externe à l'extrémité de la zone de recirculation au culot CD (fig.7) est due à la traversée du rhombe de Mach de la soufflerie ; au-delà de ce rhombe, l'écoulement n'est plus uniforme et le choc se courbe. Le calcul ne tient compte évidemment que d'un écoulement externe uniforme à l'infini et ne représente pas cet effet.

Les distributions de pressions fournies par l'expérience sont, d'une part, les pressions au culot CD mesurées à l'aide de prises pariétales, et d'autre part, des profils de pression d'arrêt mesurés avec une sonde de type Pitot dans l'écoulement. La comparaison de la pression de culot calculée avec celle mesurée dans les expériences est représentée sur la figure 7 avec une échelle très dilatée dans le but de bien évaluer la précision du calcul. La dispersion expérimentale observée est due à de légères fluctuations du taux de détente entre les expériences, consécutives à des variations de la pression génératrice du jet de l'ordre de 2 % au maximum (deux mesures

mentionnées à la même ordonnée y ont en effet été effectuées au cours de deux rafales différentes). Le taux de détente retenu pour le calcul, soit $p_{ij}/p_{ie} = 19,5$, est un taux moyen entre ceux obtenus au cours de ces diverses expérimentations. Il apparaît ainsi que le calcul se situe bien dans la plage des valeurs expérimentales et recoupe celles-ci avec un écart de l'ordre de 5 %.

La comparaison du calcul avec les sondages effectués dans le proche sillage de l'arrière-corps confirme la bonne reproduction de la structure de l'écoulement déjà observée sur les isochores. Illustrons ce fait par l'exemple d'un profil de pression d'arrêt situé en $x = 33$ mm (fig.8), l'origine de l'axe longitudinal Ox étant placée dans le plan de sortie de la tuyère. La zone à haute pression du jet propulsif devient à cette distance un pic sur l'axe de symétrie de l'écoulement. Le choc en tonneau apparaît clairement juste au-dessus de l'ordonnée $y = 20$ mm et le "décrochage" des valeurs expérimentales à partir de $y = 95$ mm est dû au fait que, la limite du rhombe de Mach de la tuyère générant l'écoulement externe étant atteinte, l'écoulement fourni par la soufflerie n'est plus à partir de ce point l'écoulement infini amont donné comme condition limite du calcul.

5 - Arrière-corps propulsé muni d'un rétreint.

Dans cette configuration avec rétreint [6,7], le nombre de Mach de l'écoulement externe est de 1,94 (température génératrice de 298 K et pression génératrice de $0,975 \cdot 10^5$ Pa). Le nombre de Mach du jet propulsif est de 1,75 (température génératrice d'environ 298 K et pression génératrice de $7,75 \cdot 10^5$ Pa). Une strioscopie "éclair" (fig.9) donne les aspects généraux des écoulements autour de l'arrière-corps de la maquette. Cette visualisation montre clairement le phénomène d'éclatement du jet propulsif qui provoque le décollement de l'écoulement externe sur le rétreint. L'écoulement externe non perturbé traverse d'abord un éventail de détentés centrées à l'arête du rétreint. La couche limite externe continue de se développer sur la première partie du rétreint avant d'aborder la zone d'interaction. Puis, vers le milieu du rétreint, un premier choc prend naissance et interagit avec la couche limite, la faisant décoller de la paroi. Ce choc d'interaction - ou choc de décollement - rejoint le choc de confluence externe dû à la déviation mutuelle des écoulements. Le décollement précoce de la couche limite en amont de l'arête du culot anticipe le processus de confluence avec le jet propulsif fortement sous-détendu, pareillement au phénomène de décollement intervenant sur des rampes ou des gouvernes trop braquées. Le jet à pression dynamique élevée constitue un obstacle de

nature fluide et joue le rôle d'une rampe de compression vis-à-vis de l'écoulement externe, l'angle de cette rampe "fluide" étant directement corrélé au taux de détente du jet. En sortie de tuyère, le jet est accéléré lorsqu'il traverse le faisceau de détonations centrées sur la lèvre de la tuyère. Immédiatement en aval du plan de sortie, la couche cisailée du jet est très fine en raison de l'influence de la détente, puis elle s'épaissit rapidement lorsqu'elle atteint la région de confluence où règne un gradient de pression adverse. Le choc en tonneau du jet, résultant d'un processus de focalisation des lignes de Mach, suit tout d'abord la couche cisailée, puis est légèrement dévié dans la région de confluence, et enfin se referme sur lui-même en direction de l'axe de symétrie. La réflexion du choc en tonneau sur l'axe est singulière, engendrant un disque de Mach délimité par deux points triples. Partant de chaque point triple, un sillage délimite une région supersonique, située derrière le choc réfléchi, et une région subsonique à l'aval du disque de Mach.

La figure 10 montre le champ des iso-nombres de Mach, déduit de mesures par vélocimétrie laser. On retrouve les principaux phénomènes déjà décrits par la striescopie éclair, tels que la couche limite externe et sa détente sur le rétreint, les chocs de décollement et de confluence, la détente du jet, le sillage et la poche subsonique en aval du disque de Mach engendré par la réflexion singulière du choc en tonneau. On distingue également la zone à basse vitesse sur le rétreint correspondant à la région décollée.

Sur la figure 11 sont comparées les évolutions des pressions pariétales mesurées et calculées à l'aide des modèles [k-ε] et Baldwin-Lomax sur la partie arrière du fuselage, en amont du culot. Les prises de pressions pariétales ont été disposées suivant quatre lignes méridiennes, intersections de la maquette avec les quatre plans méridiens dont l'angle azimutal est indiqué sur la figure 11, le plan vertical étant pris comme origine des angles ϕ . On note une prédiction correcte, notamment par le modèle [k-ε], des niveaux de pression avant rétreint ainsi que de la variation brutale de celle-ci au niveau de la première cassure de pente et de la légère détente qui suit. La divergence entre calcul et mesure commence vers le milieu de cette détente où les deux modèles trouvent une recompression très modérée préalable au décollement proprement dit. Le point de décollement prédit par le calcul, qui se situe approximativement au pied de la zone à fort gradient de pression finale, est décalé par les deux modèles vers l'aval par rapport au point expérimental. Ces points de décollement se situent respectivement en $x/D = -0,35$ et $-0,3$ pour les modèles de Baldwin-Lomax et [k-ε] et le point

expérimental est aux environs de $x/D = -0,45$. Les deux modèles étalent ainsi la compression en anticipant celle-ci vers l'amont et en retardant le point de décollement vers l'aval, ce qui est le signe dans les deux cas d'une viscosité turbulente trop importante au niveau du décollement. Cette observation commence à nous éclairer sur une des causes de difficulté pour les modèles à reproduire une zone de recirculation débordant vers l'amont sur le rétreint. Il s'agit en fait du problème de la prédiction du décollement libre. Les deux modèles retrouvent finalement le bon niveau de pression sur l'arête du culot. Pour ce décollement de faible épaisseur, le modèle algébrique de Baldwin-Lomax est plus proche de la réalité que le modèle [k-ε] de Chien.

Les profils de la figure 12 se situent à l'aval du culot, traversant la zone précédant la confluence des écoulements externe et interne à une distance de 0,065 fois le maître couple D en aval du culot. On note une reproduction correcte par le calcul des points de mesure retenus comme totalement fiables. La figure 13, où est représenté le profil des vitesses radiales à la même abscisse, confirme les variations drastiques subies par le champ de vitesses, traduisant la traversée alternative de chocs et de détonations rapides. A ce niveau, où la confluence entre les deux écoulements n'est pas encore réalisée, on assiste à la préadaptation du jet à l'écoulement externe via les zones de recirculation. Les modèles prédisent ainsi d'une manière satisfaisante les phénomènes de recirculation à ce niveau.

6 – Arrière-corps propulsé par un jet chaud.

Nous abordons à présent l'étude des aspects thermiques des écoulements de culot de missiles. Dans le passé, de nombreux essais ont été exécutés sur des maquettes d'arrière-corps dont le jet propulsif était à température ambiante. Ces essais entraient dans le cadre des travaux relatifs à la détermination des données aérodynamiques minimales pour la qualification d'écoulements de culot (il s'agissait essentiellement de mesures de pression pariétale ou de détermination des traînées globales). C'est pourquoi, les codes de calcul existants étaient généralement validés pour ces conditions de "jet froid". En revanche, les essais simulant les conditions de propulsion réelles sont beaucoup plus rares et les mesures thermiques, ou calorimétriques, souvent peu précises et difficilement exploitables. Il apparut donc la nécessité de pouvoir disposer de données expérimentales fiables et précises relatives aux effets thermiques sur l'écoulement de culot des missiles. Une première série de travaux effectués à l'ONERA au début des années 90 consista en

l'étude et la réalisation d'un dispositif expérimental devant servir pour le moyen terme à fournir des données expérimentales sur les effets thermiques au culot de missiles simplifiés [8].

Le dispositif alors réalisé est constitué d'une tuyère de révolution à corps central produisant un écoulement supersonique uniforme de nombre de Mach égal à 3,02 dans une section de sortie de diamètre 260 mm (la température génératrice est de 275 K et la pression génératrice de 10^5 Pa). La maquette d'arrière-corps est fixée à l'extrémité du corps central cylindrique de diamètre égal à 54 mm. Cette maquette est équipée d'une tuyère supersonique alimentée par l'intermédiaire du corps central en air comprimé chauffé dans le foyer d'un brûleur air-hydrogène. Ce montage permet d'obtenir un fonctionnement relativement long de l'injection de gaz chaud : il est ainsi possible d'atteindre le régime établi pour des sondes de température implantées au culot. Le temps de l'essai est limité par la durée de la rafale (une dizaine de secondes) et non par la durée du fonctionnement de l'alimentation en gaz chaud. Ceci permet d'éviter l'inconvénient des essais avec impulseurs à poudre pour lesquels une sonde de température n'a pas toujours le temps d'atteindre sa température d'équilibre pendant le temps de fonctionnement de l'impulseur (en général de l'ordre de la seconde).

Le montage fut implanté dans une soufflerie à rafales de l'ONERA à Meudon. La combustion d'hydrogène utilisée permet en principe d'atteindre des températures génératrices du jet voisines de 2500 K. Pour des raisons de coût, nous avons utilisé des matériaux dont la tenue thermique n'était garantie que jusqu'à 1300 K. Cette température imposée comme température maximale nominale du brûleur est toutefois suffisante pour obtenir des effets thermiques significatifs. Des mesures de pression de culot et de température d'eau morte ont été effectuées sur ce dispositif expérimental. En ce qui concerne la simulation numérique, le calcul avec le code NASCA (muni dans ce cas du seul modèle de Baldwin-Lomax) a été effectué dans le cas de cette configuration de "jet chaud" pour deux valeurs (6,4 et 19,4) du taux de détente du jet chaud (température génératrice égale à 1030 K). Deux types de conditions aux limites ont été imposées, suivant que l'on considère que la paroi a atteint l'équilibre thermique avec l'écoulement qui lui est proche (condition athermane) ou que celle-ci reste tout au long de la rafale à sa température initiale de 300 K. On peut constater une différence assez faible entre les deux types de conditions aux limites (fig.14). La pression est reproduite en moyenne avec une erreur non négligeable, mais inférieure à 15 %, et qui semble diminuer un peu

lorsqu'on augmente le taux de détente. Le fait moins satisfaisant est que le désaccord calcul-expérience est de signe contraire dans les deux cas testés. La variation de la pression de culot avec le taux de détente est donc sous estimée.

L'accord entre la température mesurée et la température calculée est plus satisfaisant que l'accord sur les pressions, comme le montre la figure 15, et il apparaît ici d'une manière plus nette que la condition de température de paroi initiale donnée semble induire une évolution de la température calculée plus proche de l'expérience. Cette condition aux limites sur les parois n'est, de toute manière, pas connue exactement et pourrait faire l'objet d'autres travaux.

7 - Calculs prospectifs d'écoulements d'arrière-corps avec gaz propulsif réaliste.

Comme on l'a montré dans les paragraphes précédents, les buts initialement fixés à la version primitive du code NASCA traitant d'écoulements monoespèce ont été atteints progressivement. Lors des dernières études, et en parallèle avec l'extension des codes "multicomposant" à des écoulements multiespèce puis chimiquement réactifs, a été réalisée l'extension de l'applicabilité de NASCA à des écoulements multiespèce réalistes. Le fait de travailler avec des écoulements composés de gaz de combustion réalistes revêt, comme on va le montrer, une grande importance, notamment pour la prévision du champ thermique. Cette importance apparaît, par exemple, lorsqu'il s'agit de prévoir la signature infrarouge d'un jet, la simulation numérique du champ thermique avec des écoulements composés uniquement d'air conduisant à des résultats erronés. La configuration que l'on a choisie pour illustrer cette extension du code est celle du paragraphe 3, c'est-à-dire même géométrie, mêmes nombres de Mach, mêmes pressions génératrices et même température génératrice externe; seule la température génératrice du jet change, passant de 300 K à 3000 K.

Nous avons pris comme composition des gaz issus de la tuyère les espèces issues de la combustion d'un propergol. Le code NASCA a été étendu de manière à prendre en compte un écoulement composé de 7 espèces gazeuses diffusant séparément. La formulation adoptée détermine ce mélange en chaque point du maillage et calcule, pour la température locale, toutes les grandeurs thermodynamiques utiles du gaz. Elle est basée sur l'évaluation d'un équivalent local du rapport γ des chaleurs massiques et permet d'obtenir, par une formulation totalement implicite, le transport de la quantité de mouvement, de l'énergie et des

fractions massiques des espèces formées. Des hypothèses physiques simples ont permis de définir un concept de diffusion turbulente du type "Loi de Fick". Le code NASCA est ainsi devenu un code aérothermique permettant le calcul d'écoulements décollés composés d'un mélange gazeux d'un nombre d'espèces pouvant être important, hors réactions chimiques (diffusion pure). Les calculs dont nous exposerons ici les résultats utilisent les modèles de turbulence de Baldwin-Lomax et [k-ε].

Par rapport à la configuration "jet froid" du paragraphe 3, ces calculs mettent en évidence les effets thermiques et les effets dus à la nature du gaz propulsif. Tout d'abord, en ce qui concerne la pression de culot (fig.16), on constate que lorsque la température d'arrêt du jet propulsif passe de 300 K (dans le cas de la configuration de référence du § 3) à 3 000 K, la pression du culot augmente de plus de 30 %. Lorsque l'on utilise le modèle [k-ε], on observe un effet modéré de la nature du gaz propulsif, moindre que celui prédit par le modèle de Baldwin-Lomax. Dans le cas de l'évaluation de la température au culot (fig.17) la conclusion inverse peut être faite. Nous voyons d'ores et déjà apparaître une importante disparité entre les modèles de turbulence en matière de prévision des effets thermiques et des effets liés à la nature des espèces issues de la combustion d'un propergol.

L'effet le plus intéressant de la composition chimique du jet propulsif se situe au niveau de la prédiction du champ de température dans le jet, puisqu'il conditionne la signature infrarouge de celui-ci (fig.18). On observe que l'état thermique de "l'enveloppe" du sillage, constituée essentiellement par la couche de mélange et la région à l'aval du disque de Mach (ici très peu marqué), dépend significativement de la nature du gaz propulsif. Dans une grande partie de cette enveloppe, le mélange réel avec des gaz issus de la combustion d'un propergol induit une température supérieure d'environ 150 K à celle qui est trouvée dans le cas de l'air pur lorsque l'on emploie le modèle de Baldwin-Lomax, cette différence est plutôt de l'ordre de 100 K si l'on utilise le modèle [k-ε] (fig.19). D'une manière générale, le modèle de Baldwin-Lomax prédit des niveaux de température supérieurs à ceux fournis par le modèle [k-ε], cette tendance s'amplifiant un peu avec un jet composé des espèces de combustion. Par contre, les deux modèles s'accordent sur une augmentation de température de l'ordre de 150 K dans la zone située à l'aval du disque de Mach lorsque le jet est composé des espèces de combustion prises en compte ici. La différence globale en niveau observée peut trouver un embryon d'explication dans le fait que, dans la zone de recirculation et la couche de mélange, le modèle de Baldwin-Lomax diffuse d'avantage les

espèces du jet que le modèle [k-ε], ce qui est visible sur la figure 20.

8 - Conclusion

Les recherches sur les arrière-corps dont nous venons de décrire quelques aspects saillants ont été guidées par une stratégie bien définie appliquée avec constance sur une longue période, à savoir :

- 1 - Elaborer des moyens théoriques plus perfectionnés basés sur la résolution des équations de Navier-Stokes afin de procéder à des recherches de modélisation avancée.
- 2 - Réaliser des expériences bien instrumentées afin de constituer en parallèle des banques de données suffisamment documentées permettant la validation de ces modèles sur des configurations de référence.

La plupart des objectifs visés ont été atteints à ce jour. Cependant, la conception des arrière-corps pose encore de nombreux problèmes qui sont loin d'être résolus, tant les phénomènes mis en jeu sont complexes. On peut prédire, avec un bon degré de confiance, que les arrière-corps vont demeurer au cours des années à venir une des préoccupations essentielles des concepteurs d'avion, de missiles, de lanceurs spatiaux, de projectiles. Dès à présent les thèmes de recherche suivants se dégagent :

- 1 - Modélisation plus réaliste des processus aérothermochimiques liés à la propulsion, avec notamment la prise en compte des réactions chimiques comme cela a pu être réalisé avec les méthodes "multicomposant".
- 2 - Prise en compte des interactions jet propulsif-écoulement externe, notamment dans les cas fortement hors adaptation.
- 3 - Fonctionnement des tuyères en régime de sur-détente avec décollement (aspects stationnaires, instationnaires, charges latérales, performances,...).
- 4 - Examen approfondi des fluctuations pouvant affecter les écoulements de culot et être à l'origine de phénomènes de type "buffeting".
- 5 - Evaluation des procédés passif et/ou actif visant à contrôler les écoulements de culot en vue de réduire la traînée, diminuer les flux, supprimer les phénomènes instationnaires.
- 6 - Etude de nouveaux types de tuyère à corps central (aérospike).

- 7 - Examen des configurations fortement tridimensionnelles (arrière-corps d'avion bituyère, lanceurs multi-moteurs) en vue d'élucider la topologie des écoulements entourant l'arrière-corps.

La liste ci-dessus n'est certainement pas exhaustive. Les travaux récents du Working Group 17 de l'AGARD sur les arrière-corps des avions de combat (Aerodynamics of 3-D Aircraft Afterbodies) [9] ont confirmé l'importance de ces questions, tant sur le plan de l'expérimentation que sur celui de la modélisation.

Compte tenu de la variété et de la complexité des problèmes rencontrés, une action efficace dans ce domaine devra regrouper des spécialistes de plusieurs disciplines : aérodynamiciens, chimistes, spécialistes des structures (effets aéroélastiques liés aux instationnarités)...

9 - Références.

- [1] Reijasse Ph., Benay R., Delery J. et Lacau R.G.
Missile and projectile base-flow prediction by multi-component methods.
AIAA Atmospheric Flight Mechanics Conference, Minneapolis, August 15-17, 1988.
- [2] Benay R. et Servel P.
Applications d'un code Navier-Stokes au calcul d'écoulements d'arrière-corps de missiles ou d'avions.
La Recherche Aérospatiale, 1995, n° 6, pp. 405-426
- [3] Reijasse Ph.
Modélisation de l'écoulement supersonique autour de l'arrière-corps du lanceur ARIANE-5 : expériences de validation de code sur des configurations d'arrière-corps axisymétriques.
ONERA, RF n° 17/4361 AY (avril 1992).
- [4] Charmant S. et Cambier L.
Calculs d'écoulements compressibles turbulents autour d'arrière-corps avec tuyère.
30^{ème} Colloque d'Aérodynamique Appliquée de l'AAAF, Nantes, France, 25-27 octobre 1993.
- [5] Benay R. et Servel P.
Etude théorique de l'influence de l'état thermique de la paroi sur l'écoulement au culot d'un missile.
ONERA, RF n° 30/4361 AY (octobre 1994).
- [6] Benay R., Corbel B., Reijasse Ph. et

Servel P.
Etude expérimentale et numérique d'un arrière-corps muni d'un rétreint avec jet propulsif fortement éclaté.
ONERA, RTS n° 37/4361 AY (janvier 1997)

- [7] Reijasse Ph. et Corbel B.
Décollement de l'écoulement externe induit par l'éclatement du jet propulsif sur un rétreint d'arrière-corps de missile.
34^{ème} Colloque d'Aérodynamique Appliquée de l'AAAF, Marseille, France, 23-25 mars 1998.
- [8] Reijasse Ph.
Effets thermiques au culot des missiles en vol supersonique. Exploitation des essais dans la soufflerie R2Ch (1992).
ONERA, RF n° 20/4361 AY (décembre 1992).
- [9] AGARD Working Group 17
Aerodynamics of 3-D Aircraft Afterbodies.
AGARD-AR-318 (september 1995).

10 - Remerciements.

La très grande majorité des travaux sur les arrière-corps présentés ici a été effectuée avec le support financier de la Délégation Générale à l'Armement du Ministère de la Défense.

11 - Figures.

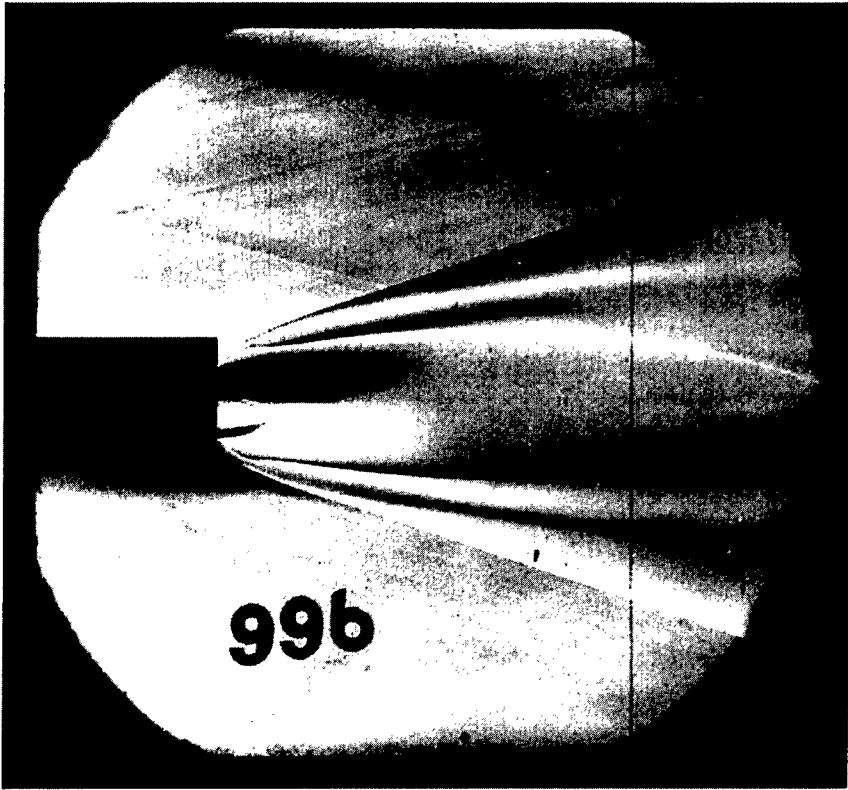


Figure 1 - Arrière-corps droit propulsé par une tuyère affleurante : visualisation strioscopique de l'écoulement.

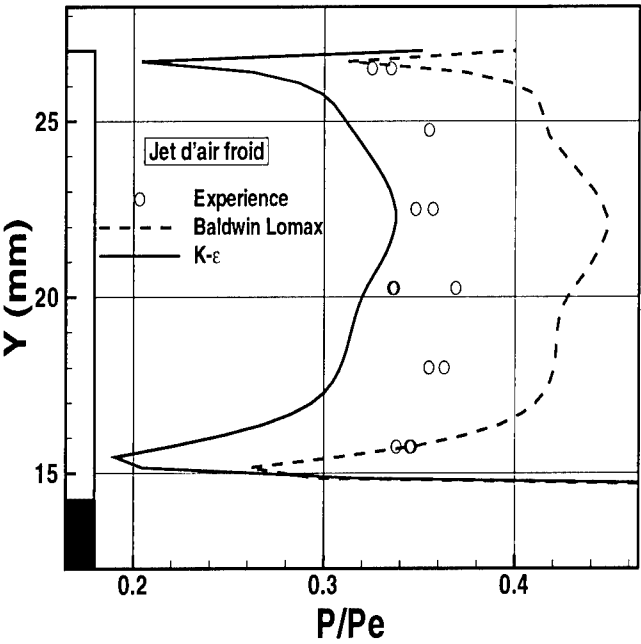


Figure 2 - Arrière-corps droit propulsé par une tuyère affleurante : profils de pression pariétale au culot.

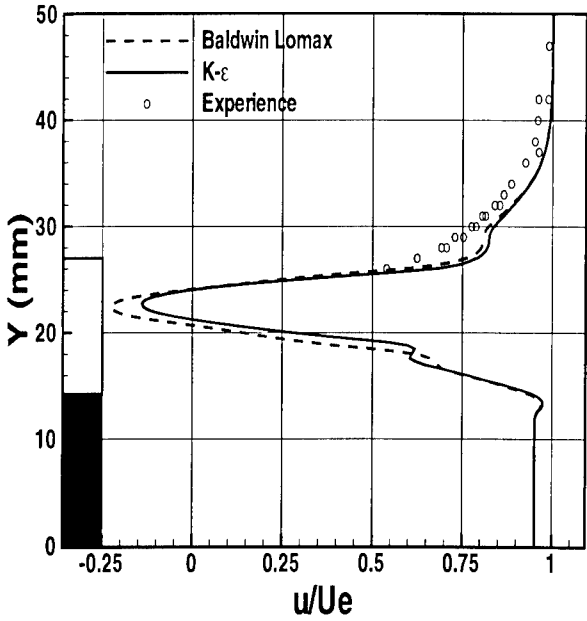


Figure 3 - Arrière-corps droit propulsé par une tuyère affleurante : profils de vitesse axiale en $x = 4$. mm .

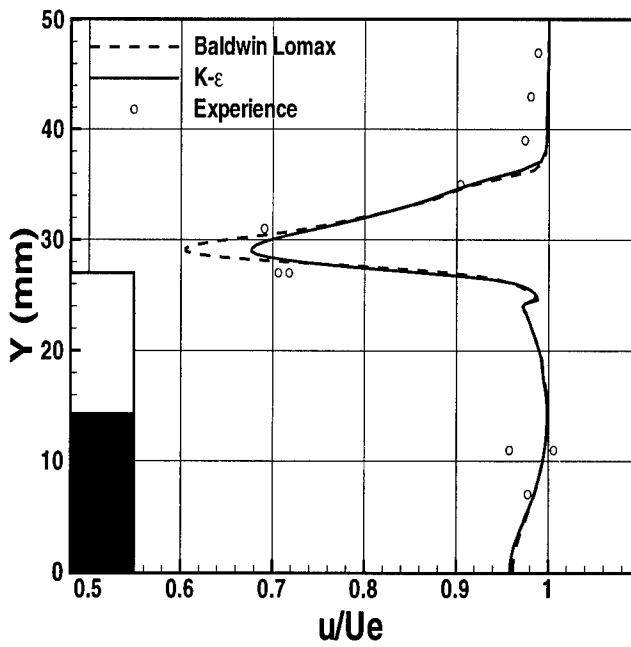


Figure 4 - Arrière-corps droit propulsé par une tuyère affleurante : profils de vitesse axiale en $x = 40$. mm .

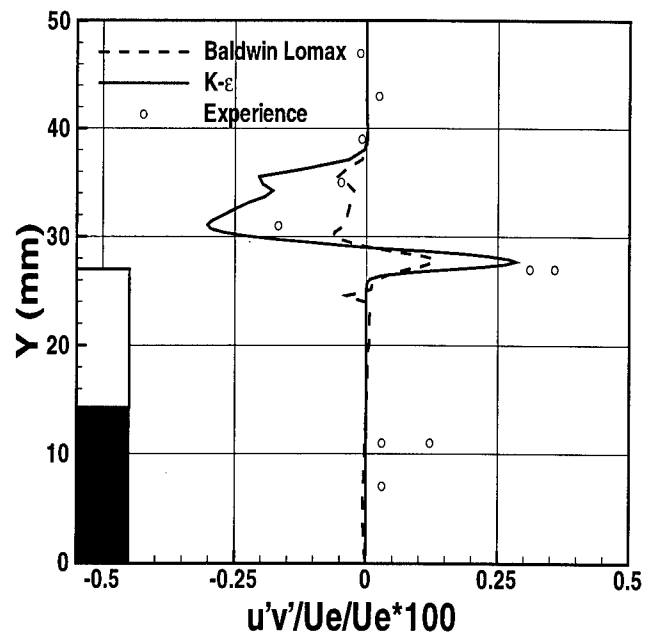


Figure 5 - Arrière-corps droit propulsé par une tuyère affleurante : profils de tensions de cisaillement en $x = 40$. mm .

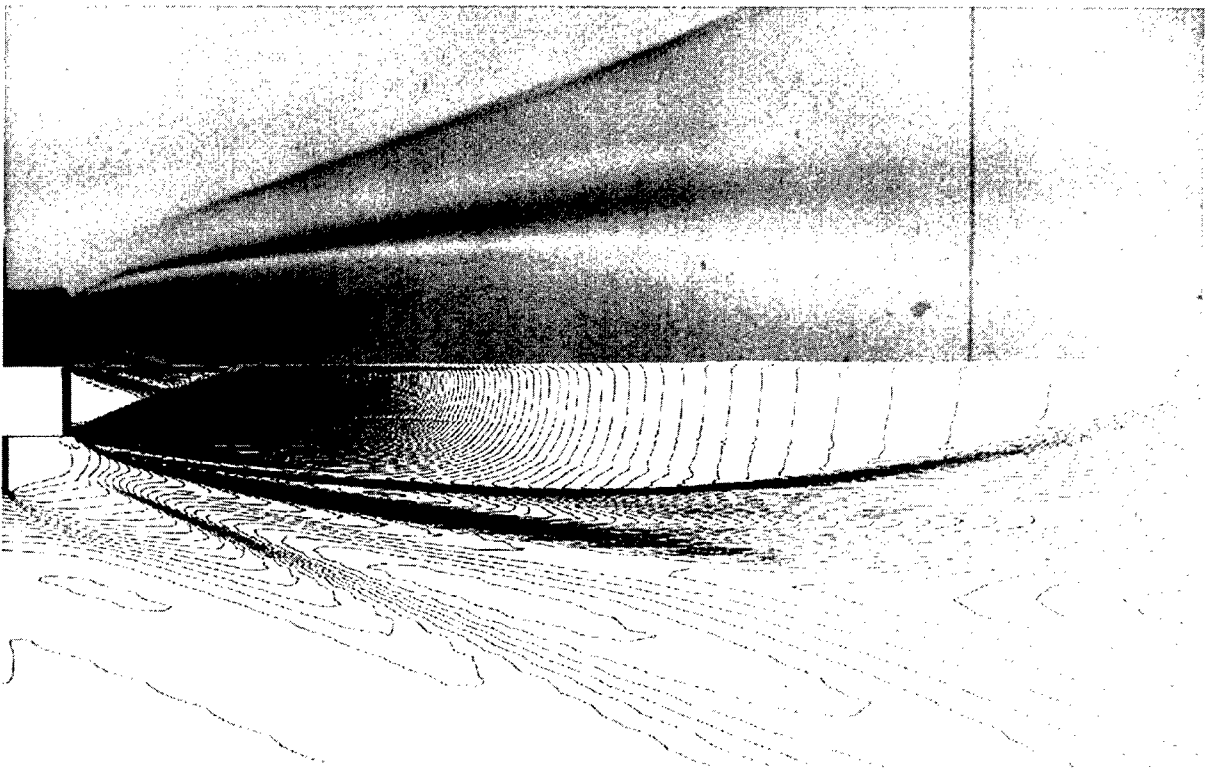


Figure 6 - Arrière-corps propulsé avec tuyère émergente : comparaison entre les lignes isochores calculées et la visualisation strioscopique expérimentale.

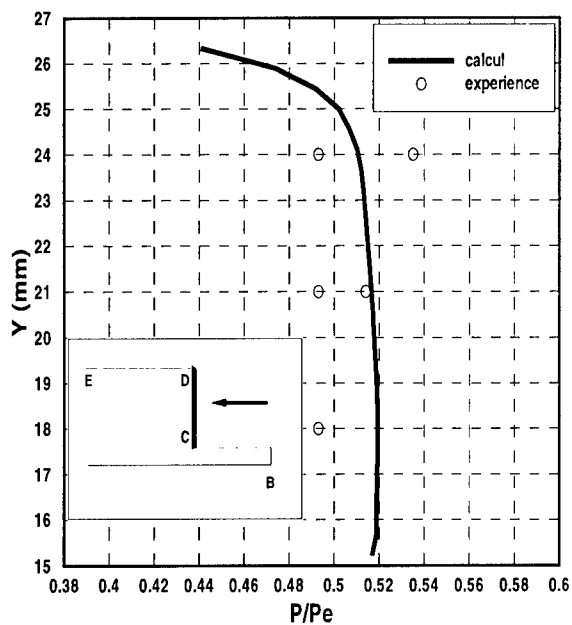


Figure 7 - Arrière-corps propulsé avec tuyère émergente : pression pariétale au culot.

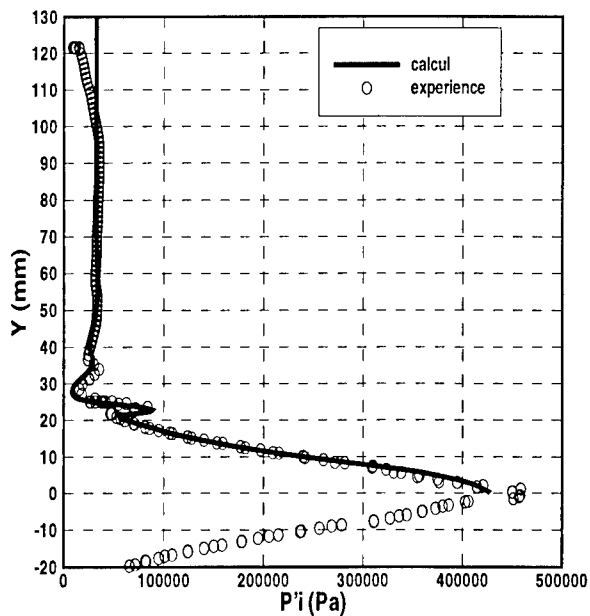


Figure 8 - Arrière-corps propulsé avec tuyère émergente : profils de pression d'arrêt en $x = 33$ mm.

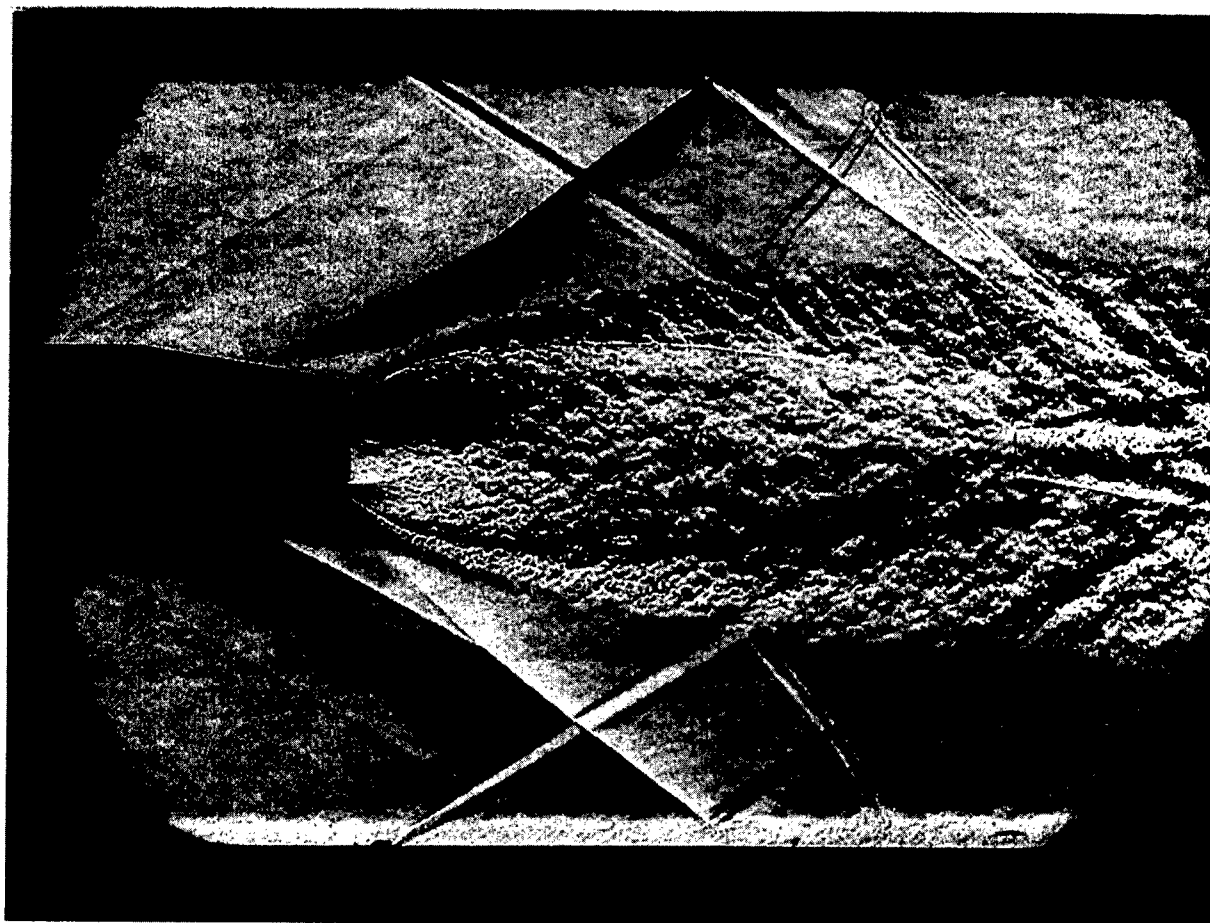


Figure 9 - Arrière-corps propulsé muni d'un rétreint : visualisation strioscopique "éclair" de l'écoulement.

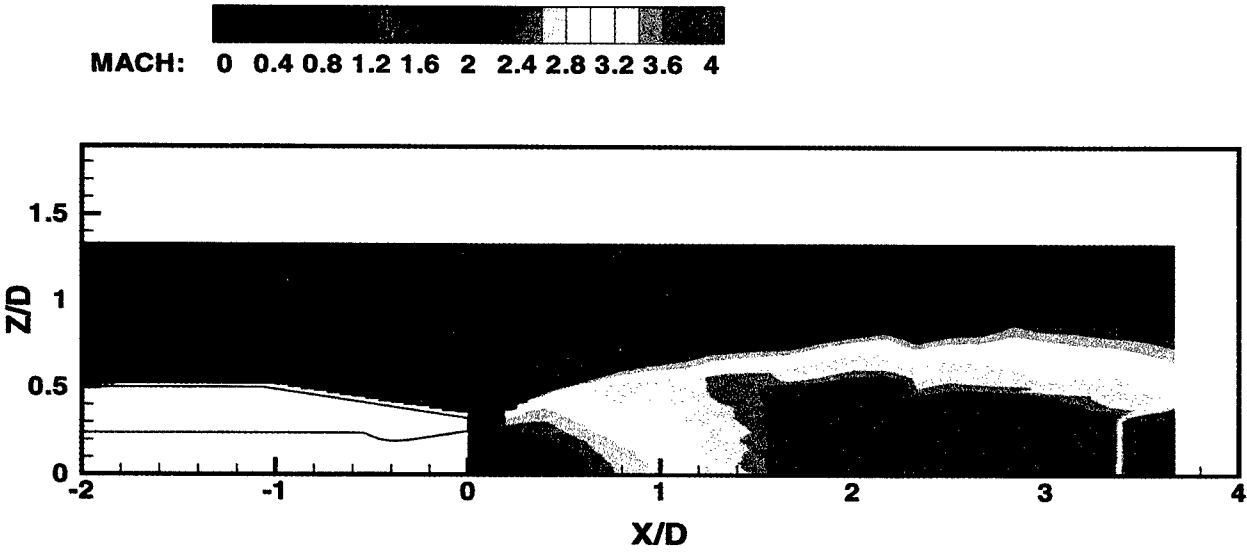


Figure 10 - Arrière-corps propulsé muni d'un rétreint : iso-nombres de Mach expérimentaux.

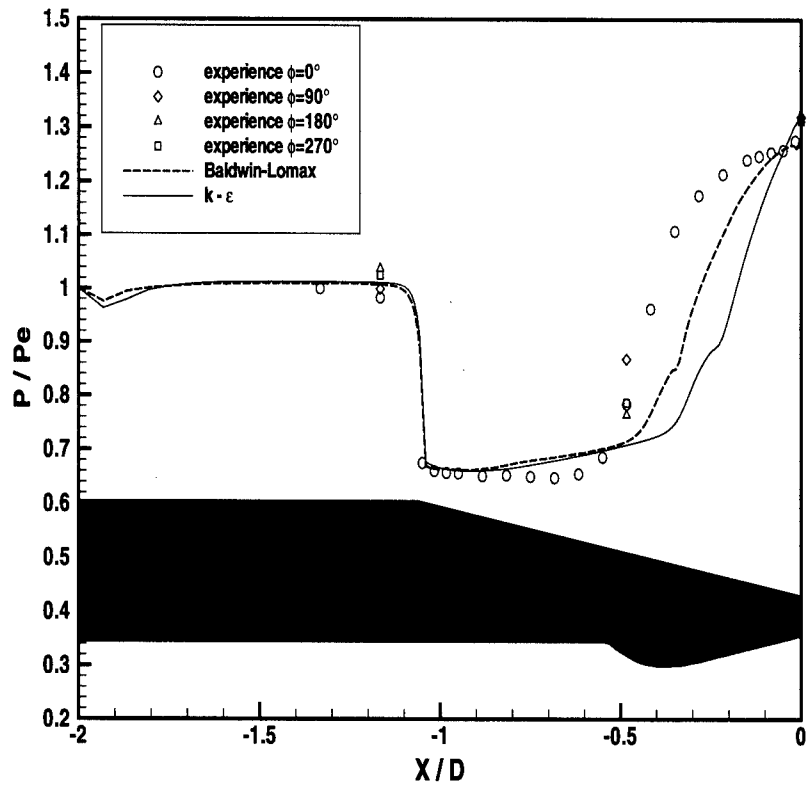


Figure 11 - Arrière-corps propulsé muni d'un rétreint : répartition de pression pariétale le long du fuselage.

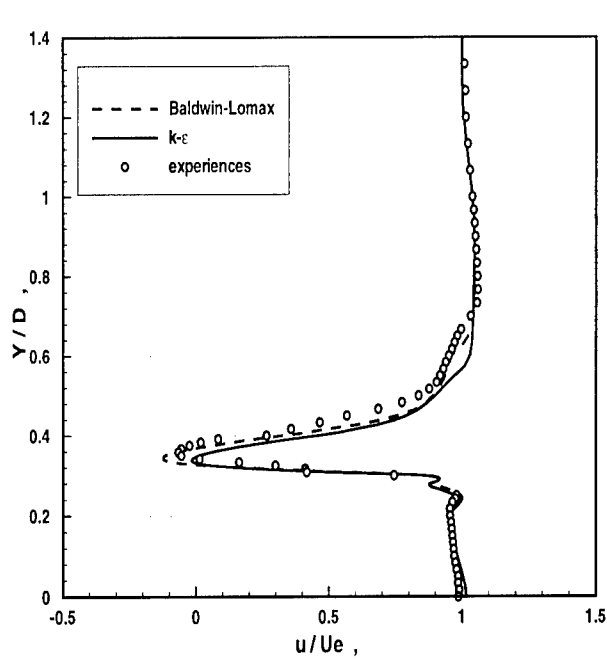


Figure 12 - Arrière-corps propulsé muni d'un rétreint : profils de vitesse axiale en $x/D = 0.065$.

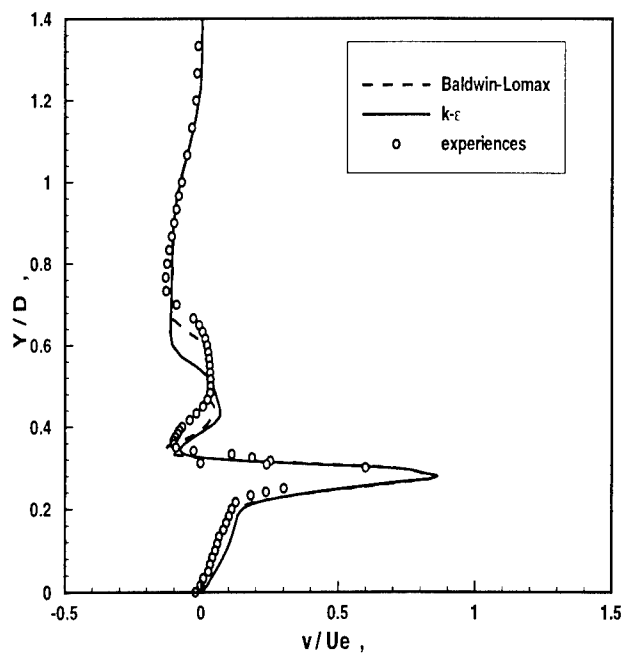


Figure 13 - Arrière-corps propulsé muni d'un rétreint : profils de vitesse radiale en $x/D = 0.065$.

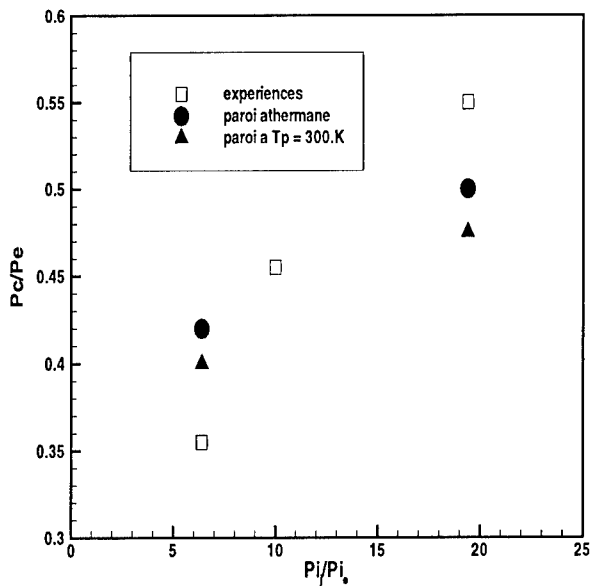


Figure 14 - Arrière-corps propulsé par un jet chaud : pression de culot en fonction du taux de détente.

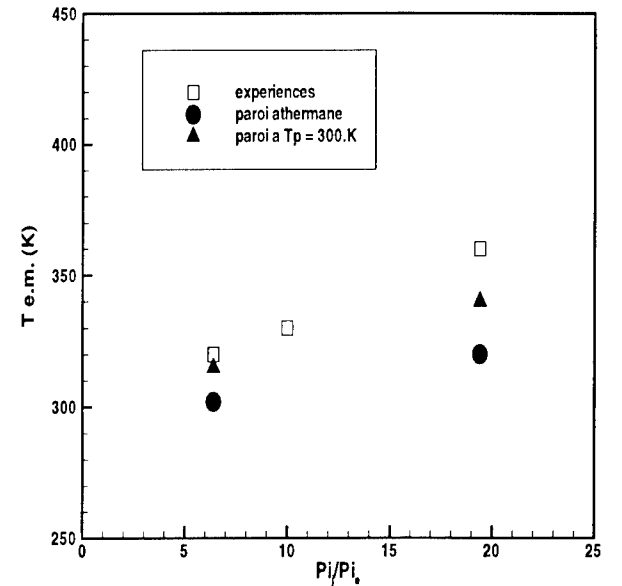


Figure 15 - Arrière-corps propulsé par un jet chaud : température d'eau morte en fonction du taux de détente.

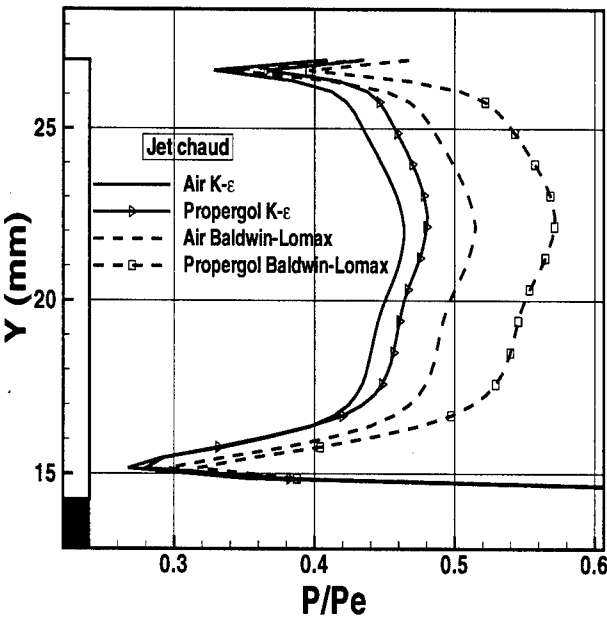


Figure 16 - Arrière-corps propulsé avec gaz propulsif réaliste : profils de pression pariétale au culot.

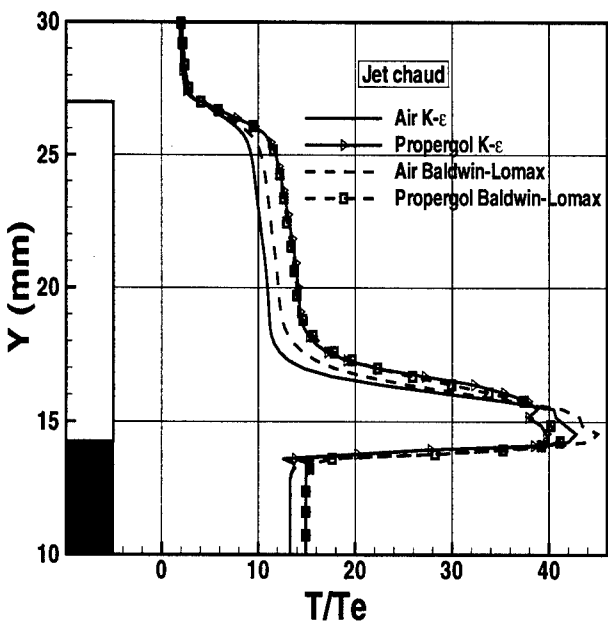


Figure 17 - Arrière-corps propulsé avec gaz propulsif réaliste : profils de température au culot.

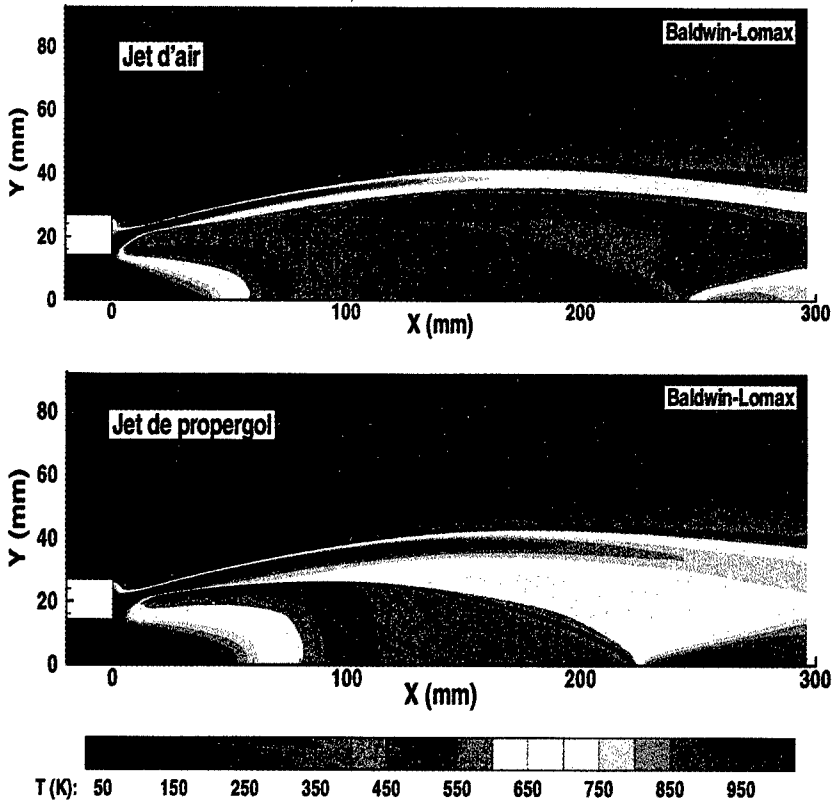


Figure 18 - Arrière-corps propulsé avec gaz propulsif réaliste : isothermes calculées avec le modèle algébrique de Baldwin et Lomax.

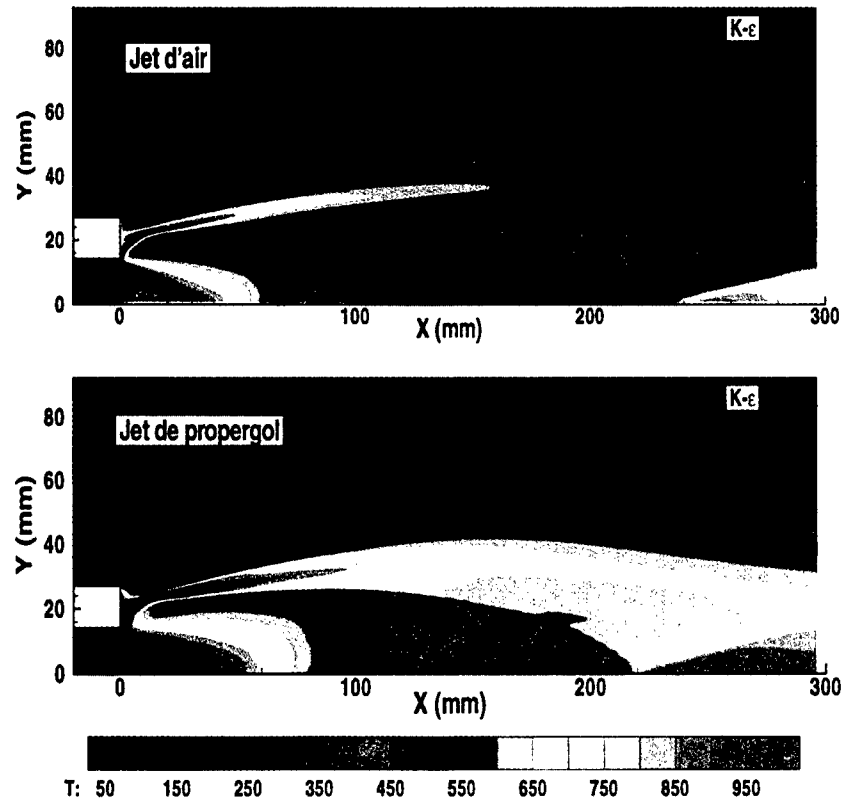


Figure 19 - Arrière-corps propulsé avec gaz propulsif réaliste : isothermes calculées avec le modèle [k-ε] de Chien

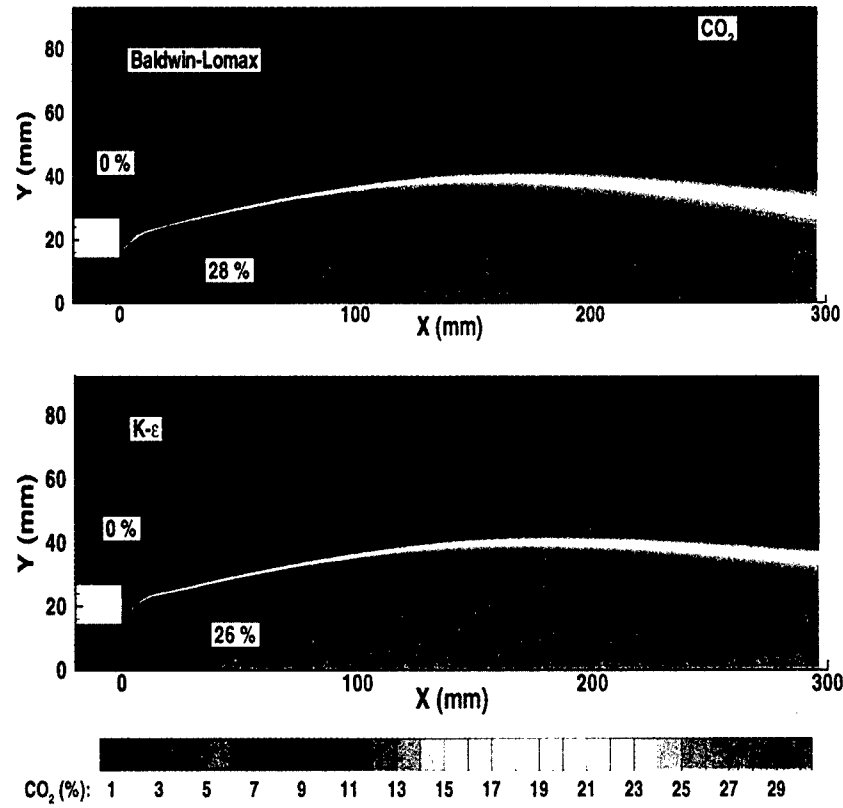


Figure 20 - Arrière-corps propulsé avec gaz propulsif réaliste : iso-pourcentages massiques en CO₂ calculées.

Couche limite autour d'un fuselage de missile en incidence en écoulement supersonique Etude expérimentale et calculs Navier Stokes

P. d'Espiney, P. Champigny, D. Baudin, J.A. Pilon

Département d'Aérodynamique Appliquée

ONERA

BP 72 - 92322 Châtillon Cedex - France

RESUME

Des mesures aérodynamiques détaillées (valeur et angle du frottement pariétal, profils de couche limite,...) ont été effectuées récemment dans les souffleries S2MA et S3MA de l'ONERA sur un fuselage ogive-cylindre à Mach 2 à 0° et 10° d'incidence. Le régime de l'écoulement est turbulent (la transition de la couche limite est déclenchée au voisinage de la pointe du fuselage) et le nombre de Reynolds basé sur le diamètre est de $1.2 \cdot 10^6$.

Des calculs Navier Stokes en écoulement turbulent ont été réalisés avec le code FLU3M développé par l'ONERA, avec utilisation des modèles de turbulence de Baldwin-Lomax et k- ϵ (formulation bas Reynolds de Jones-Launder).

Les comparaisons calcul - expérience montrent globalement un bon accord, bien que des écarts subsistent, dus principalement à une trop forte viscosité au sein des tourbillons. Ceci conduit en particulier à la formation tardive de tourbillons secondaires.

1 - INTRODUCTION

La prédiction de l'écoulement tourbillonnaire sur des fuselages de missiles est très importante pour optimiser leurs performances aérodynamiques. Pour ces types de corps, généralement élancés, les structures tourbillonnaires se développent même aux faibles incidences. De façon générale [1 et 2] on peut distinguer cinq cas :

- les incidences très faibles ($\alpha < 5^\circ$) où l'écoulement n'est pas décollé;
- les incidences modérées ($\alpha < 10^\circ$) où les structures tourbillonnaires sont alimentées par le décollement de la couche limite sur une surface lisse, phénomène exclusivement visqueux. Dans ce cas, ces structures peuvent dépendre fortement du régime de l'écoulement (laminaire ou turbulent) en modifiant la position des lignes de décollement et, en conséquence, les caractéristiques aérodynamiques (portance). Ceci a par exemple été mis en évidence, dans le cas d'un nombre de Reynolds peu élevé ($Re_D = 0.16 \cdot 10^6$), par les expériences effectuées à la soufflerie S5CH et par les calculs Naviers-Stokes correspondants [3 et 4] ;

- les incidences intermédiaires ($10^\circ < \alpha < 20^\circ$) pour lesquelles un système tourbillonnaire peut être généré par des chocs transversaux [5] si l'écoulement amont est suffisamment supersonique ; la non prise en compte du régime de l'écoulement (laminaire ou turbulent) ou de la viscosité a peu d'effet sur les caractéristiques du missile (portance et centre de poussée) ; ceci a été mis en évidence lors des calculs Euler et Navier-Stokes effectués à $M = 2$ et $\alpha = 20^\circ$ [4] ;
- les fortes incidences ($25^\circ < \alpha < 60^\circ$) qui peuvent conduire à une dissymétrisation de l'écoulement tourbillonnaire [6] ;
- les incidences extrêmes ($\alpha > 60^\circ$) pour lesquelles on ne peut plus parler d'écoulement tourbillonnaire mais plutôt de sillage de fuselage.

2 - EXPERIENCE

Les résultats expérimentaux proviennent d'un ensemble d'essais effectués entre 1993 et 1995 dans les souffleries S2MA et S3MA de l'ONERA, avec deux tailles de maquette ($D=60$ et 80 mm). Ces essais ont permis de mesurer le champ de l'écoulement pour plusieurs sections, les pressions pariétales, les efforts globaux (avec une balance), et le vecteur frottement. Des visualisations pariétales à l'aide de bouillie ont également été effectuées.

Les conditions communes à ces essais sont : $Mach = 2$, $\alpha = 0^\circ$ et 10° , $Re_D = 1.2 \cdot 10^6$ et une température génératrice T_i de 300K. La transition de la couche limite est déclenchée à $X/D = 0.12$ du nez du fuselage.

Les sondages de l'écoulement ont été effectués à la soufflerie S2MA (Fig.1) pour plusieurs sections ($X/D = 3 ; 5 ; 7 ; 9 ; 12$), sur une maquette de 80mm de diamètre. La grille de mesure est assez dense et comprend 73 points dans la direction circonférentielle (soit $\Delta\phi = 2.5^\circ$), obtenus par rotation de la maquette, et environ 75 points dans la direction radiale. Dans cette direction un explorateur muni de deux sondes a été utilisé. La première sonde clinométrique est plate, d'épaisseur 0.25 mm (Fig. 2), et comporte trois trous; elle permet du fait de sa faible épaisseur de faire des

mesures près de la paroi, dans la couche limite (champ de mesure $r/D = 0.5$ à 0.75). Elle fournit à partir de la mesure des trois pressions, la direction de la vitesse locale (incidence locale $\alpha_i = \text{Arctan} (V_o / V_x)$), ainsi que le nombre de Mach et la pression d'arrêt isentropique P_i . Une deuxième sonde clinométrique permet quant à elle, la détermination des deux angles de la vitesse (incidence locale α_i et dérapage locale β_i) mais seulement à partir d'une certaine distance de la paroi du fuselage ($r/D = 0.6$ à 0.85). La matrice d'étalonnage de ces sondes est établie, au préalable, à partir de mesures effectuées en champ uniforme.

Les mesures de la pression pariétale à S3MA ont été également effectuées tous les 2.5° , par rotation de la maquette. Les 32 prises de pression (dont 13 sur l'ogive) sont réparties selon une génératrice du fuselage entre $X/D = 0$ et 12. Ces mesures ont été réalisées à la fois dans les souffleries S2MA et S3MA.

Les mesures d'efforts ont été réalisées à l'aide d'une balance dard sur une maquette ($D=60\text{mm}$) composée de 4 tronçons démontables, ce qui nous a permis d'accéder aux coefficients globaux pour des longueurs de fuselage de $X/D = 5, 7, 9$ et 12. Par ailleurs les valeurs de la traînée de frottement ont pu être déterminées par différence entre les efforts globaux mesurés et les efforts de pression obtenus par intégration des pressions.

Les mesures locales du vecteur frottement ont été faites avec des jauges à fils chauds collées sur la paroi du fuselage au niveau des sections $X/D = 3, 5, 7, 9$ et 12. Ces jauges, dites « Mc Croskey », sont visualisées sur la figure 2. Elles sont de type bidirectionnel, et sont constituées de deux fils chauds disposés perpendiculairement. Le principe de fonctionnement est détaillé dans [7]. L'étalonnage de ces jauges (en direction et intensité) est particulièrement délicat du fait qu'il ne peut se faire qu'installées sur la maquette. En fait, on n'obtient essentiellement que la direction du vecteur frottement, et la valeur du frottement rapportée à une grandeur de référence qui correspond ici à celle obtenue à incidence nulle $C_f / C_f(\alpha=0^\circ)$. A cette incidence, le coefficient de frottement est supposé connu, et est déterminé au moyen d'un code de couche limite. Un bon recoupement est observé entre les directions du vecteur frottement mesurées et les visualisations à la bouillie.

Description de l'écoulement pour $\alpha = 10^\circ$

Expérimentalement, la topologie de l'écoulement décollé est obtenue par analyse conjointe du champ des pressions d'arrêt (fig.3), des incidences locales (ou plutôt par les pseudo lignes de courant reconstruites), figure 4, et par les visualisations effectuées à la bouillie (qualitativement assez ressemblantes aux lignes de frottement obtenues par les calculs et présentées par la suite). Le système tourbillonnaire qui se développe à

l'extrados du fuselage a une structure tout à fait classique : un tourbillon principal associé à un tourbillon secondaire contrarotatif de faible intensité, parfaitement identifié par exemple dans la section $X/D=7$ (fig.4). A ces tourbillons sont associées une ligne de décollement principal (S1) et une ligne de décollement secondaire (S2) (fig. 25). L'identification des lignes de décollement (origine et position), lieu de convergence des lignes de frottement pariétal, est une tâche délicate surtout en ce qui concerne la ligne de décollement principal (S1). En effet, celle-ci n'est pas un lieu où il y a un changement net de la direction des lignes de frottement, et on y observe plutôt une concentration de ces lignes. Ceci rend, en particulier, la détermination du point de départ du décollement principal assez imprécise. On peut décomposer schématiquement l'écoulement en trois zones :

- la zone 1 ($0 < X/D < 5$) où l'écoulement n'est pas vraiment décollé ; à l'extrados du fuselage on constate éventuellement la présence d'un écoulement rotationnel de vitesse à composante axiale non nulle ($X/D=5$), mais qui reste immergé dans l'écoulement fortement rotationnel de la couche limite ;
- la zone 2 ($5 < X/D < 7$) : c'est la zone dite à formation d'écoulement tourbillonnaire définie par le détachement d'une fraction de l'écoulement rotationnel en dehors de celui de la couche limite ; c'est aussi la zone la plus "problématique" pour les calculs Navier Stokes turbulent (lenteur de convergence, effets visibles des niveaux de la viscosité turbulente) ;
- la zone 3 ($X/D > 7$) : c'est la zone où l'écoulement tourbillonnaire est nettement formé et à la paroi on distingue clairement les deux lignes de décollement.

3 - PRESENTATION DU CODE

Le code multidomaine FLU3M, développé à l'ONERA [8], part d'une formulation pseudo-instationnaire sous forme conservative des équations d'Euler ou de Navier-Stokes. La méthode utilisée est de type volumes finis, avec schéma décentré (approche MUSCL) pour les termes non visqueux. Un limiteur de pente est introduit pour assurer la propriété TVD (Total Variation Diminishing) du schéma. La discrétisation des termes visqueux (schéma centré) est effectuée dans les trois directions de l'espace (« Full Navier Stokes »). Les choix retenus pour les calculs présentés ici sont :

- calculs axisymétrique et 3D
- variables calculées aux noeuds des mailles
- flux de ROE (avec correction entropique d'HARTEN égal à 10^{-4})
- limiteur Van-Albada sur les pentes des variables primitives
- viscosité laminaire de SUTHERLAND
- conductivités thermiques obtenues en supposant $Pr_{lam} = 0.72$ et $Pr_{turb} = 0.9$

- accélération de la convergence :
 - * pas de temps local
 - * implication de type ADI
- Modèles de turbulence :
 - * Baldwin-Lomax de base [9] (avec modification de Degani et Schiff [10])
 - * K-ε (formulation bas-reynolds de Jones-Launder) [11 à 13].

Utilisation du modèle BALDWIN-LOMAX

On rappelle que, pour les écoulements tourbillonnaires 3D, la principale difficulté rencontrée avec ce modèle à deux couches (interne et externe), est de déterminer l'échelle de longueur Y_{max} reliée au maximum de la fonction F pour l'évaluation de la viscosité turbulente. Bien que cette fonction ne s'annule pas dans le cas des décollements de type 3D ouvert (valeur du frottement pariétal non nulle sur ces lignes), elle peut avoir plusieurs maxima qui dépendent de la complexité de l'écoulement tourbillonnaire. Le problème du choix du « bon maximum » se pose près des lignes de décollement et de recollement, en particulier lorsque la couche limite et les nappes de décollement se confondent. Compte tenu de l'incidence modérée de l'écoulement, ce problème est d'autant plus délicat car il est difficile de distinguer la couche limite de l'écoulement tourbillonnaire lors de son détachement. Cette difficulté a été décrite dans la littérature et on peut trouver plusieurs remèdes. Certains auteurs préconisent de limiter la zone de recherche des maxima de la fonction F au voisinage de la paroi ; par exemple en se fixant une valeur maximale pour Y^+ , ou l'indice de maillage, ou encore par une distance à la paroi. Nous avons adopté ici la modification de Degani et Schiff à savoir :

- le premier « bon » maximum de la fonction $F(y)$ (toujours positive), est retenu lorsqu'en partant de la paroi ($F(y) = 0$) la valeur de la fonction $F(y)$ chute d'au moins 10%, par rapport à la valeur du maximum local considéré ;
- pour chaque ligne radiale du maillage, une distance « cutt off » est spécifiée en fonction du Y_{max} de la ligne radiale précédente :
- $Y_{cuttoff}(\phi) = c * Y_{max}(\phi - \Delta\phi)$;
- si aucun maximum n'a été trouvé pour $y < Y_{cuttoff}$, les valeurs de Y_{max} et F_{max} sont celles de la ligne précédente.

Initialisation du calcul K-ε

L'initialisation des valeurs de K et epsilon ont été faites à partir d'un calcul Baldwin-Lomax non convergé (1000 itérations). L'hypothèse de BRADSHAW (production d'énergie cinétique de turbulence = dissipation) permet de déterminer K et epsilon à partir de la viscosité turbulente et des profils de vitesse.

5 - DEROULEMENT DES CALCULS

Les calculs Navier Stokes ont été effectués avec une paroi supposée adiabatique ; la transition au voisinage du nez du fuselage est déclenchée par la mise en application brutale du modèle de turbulence. Plusieurs maillages distincts ont été étudiés. Ils diffèrent essentiellement par le nombre de points dans la direction circonférentielle (43 à 73 points). Les résultats étant pratiquement indépendants de la densité du maillage, celui retenu ici (Fig.5) se compose, pour la demi configuration, de :

- * 73 points dans la direction circonférentielle (ϕ) ;
- * 85 points dans la direction radiale (r) ;
- * 61 points dans la direction axiale points.

La taille de la première maille, constante selon x , est de $2.5 \cdot 10^{-6} D$, et conduit dans le cas $\alpha = 0^\circ$ à un $Y^+ < 0.5$ sur presque toute la longueur du fuselage, sauf au voisinage du nez, où il atteint la valeur de 1. Une trentaine de points est ainsi répartie dans la couche limite. A $\alpha = 0^\circ$, le calcul est effectué en axisymétrie sur un plan constitué de 85×61 points. Les résidus moyens décroissent de 5 ordres de grandeur en 9000 itérations faites en implicite à $CFL = 2$.

A 10° d'incidence le calcul Baldwin-Lomax a été mené jusqu'à 5000 itérations mais les résidus moyens sont bloqués dès 2500. A partir de 1500 itérations il a fallu réduire, d'une part le CFL de 5 à 2, et également la valeur de la constante c du cuttoff du modèle de Degani et Schiff ($c = 1.5$ à 1.1). A noter que celle-ci n'étant pas normalisée, sa valeur dépend de la densité du maillage utilisé dans la direction circonférentielle. La convergence des coefficients globaux est présentée figure 6. Le coefficient de traînée de frottement converge assez vite ; en revanche, l'évolution du coefficient de force normale CN n'est pas complètement stabilisée en raison de sa grande dépendance à la position du tourbillon principal et à celle de la ligne de décollement principale. Celle-ci se déplace vers l'extrados au cours des itérations (5° lors du passage de 1500 à 5000 itérations) et s'accompagne par ailleurs de la destruction d'une grande partie de la ligne secondaire de décollement.

La convergence du calcul K-ε est meilleure, aussi bien au niveau des résidus (chute de 4 ordres de grandeur en 7400 itérations) que des efforts globaux.

6 - COMPARAISONS CALCUL/EXPERIENCE

Alpha = 0° (Baldwin-Lomax)

Le coefficient de pression pariétal calculé est en bon accord avec celui mesuré (fig.7). Il est à noter que dans le cas d'un écoulement non décollé, ce coefficient est pratiquement insensible à la prise en compte de la

viscosité et au modèle de turbulence, comme cela a été constaté avec des calculs Euler et K- ϵ effectués par ailleurs sur un autre maillage.

Les grandeurs intégrales de la couche limite expérimentale (fig.8) sont déterminées en faisant une hypothèse classique sur l'évolution de la température dans la couche limite en fonction du Mach (loi de Crocco et paroi adiabatique). L'écart entre le calcul et l'expérience, de l'ordre de 10% sur l'épaisseur de la couche limite (δ), est sans importance, étant donné le caractère conventionnel de cette grandeur. L'indépendance de l'épaisseur de déplacement (δ_1) et du facteur de forme compressible (H) au choix du mode de détermination de δ rend ces comparaisons d'autant plus significatives et satisfaisantes. On remarquera que H est de l'ordre de 3 en fin de fuselage, valeur égale à celle de la couche limite turbulente développée sur une plaque plane soumise à un écoulement à Mach 2. Les profils de vitesse (Mach local) obtenus dans 3 sections particulières (fig.9) sont en assez bon accord avec l'expérience. Il en est de même pour le coefficient de force axiale (fig.10), et des contributions respectives de la pression et du frottement.

Alpha = 10° (Baldwin-Lomax et K- ϵ)

L'évolution circonférentielle du coefficient de pression pariétale est présentée sur les figures 11 à 13 pour trois sections caractéristiques ($X/D=5, 7$ et 9). Les résultats des calculs BL et K- ϵ sont très voisins. Par rapport à l'expérience, les écarts sont localisés principalement à l'extrados du fuselage et ils sont liés à l'écoulement tourbillonnaire. Expérimentalement, l'évolution des pressions permet de deviner dès la section $X/D = 5$ l'existence du tourbillon principal naissant (fig.11), et bien détaché de la paroi pour la section $X/D = 7$ (fig.12). En effet celui-ci produit sous lui une accélération de l'écoulement, traduite par un pic de dépression ($\phi \approx 155^\circ$), nettement plus important que celui calculé. En arrière, pour la section $X/D = 9$ (fig.13), les différences entre les calculs et l'expérience s'estompent, et vont de pair avec la réduction de ce pic, liée à l'éloignement du tourbillon principale de la paroi du fuselage.

La valeur absolue du coefficient de frottement est présentée pour ces trois sections sur les figures 14 à 16. A l'intrados du fuselage, l'évolution circonférentielle de ce coefficient d'après l'expérience est sensiblement analogue à celle donnée par les calculs. En niveau, les écarts sont relativement importants (de l'ordre de 15% pour la section $X/D=5$), mais il ne faut pas perdre de vue la difficulté à mesurer ce coefficient. Du côté de l'extrados, il est intéressant d'identifier les extremums présents; les valeurs minimales locales du frottement sont obtenues au voisinage des lignes de décollement; la coïncidence n'existe théoriquement que s'il y a symétrie des lignes de frottement aboutissant de part et d'autre de

cette ligne. Ainsi on observe des décalages non négligeables (de l'ordre de 8° pour l'expérience) entre la position angulaire de ces minima et celle des lignes de séparation correspondantes relevées à la bouillie. A noter que seul le calcul Baldwin-Lomax détecte un décollement secondaire à $X/D=9$ (présence de 2 minima). Plus distinctif est le maximum de frottement expérimental, situé près du plan de symétrie vertical ($\phi \approx 155^\circ$) pour les sections $X/D = 7$ et 9 , et qui est absent pour les calculs; il correspond au pic de dépression locale signalée dans le paragraphe précédent.

Les évolutions de la direction du frottement pariétal $\alpha_w = \text{Arctan} (C_{f_\phi} / C_{f_x})$, sont présentées sur les figures 17 à 19. Rappelons que $\alpha_w > 0$ correspond à un écoulement se dirigeant vers l'extrados. Une façon très grossière d'identifier les lignes caractéristiques peut se faire, en observant le changement du signe de α_w pour ϕ croissant : le passage d'une valeur positive à négative correspond à une ligne de décollement (S1 ou S2) et vice-versa pour une ligne de recollement (R1). Ceci n'est cependant rigoureusement exact que si ces lignes sont parallèles à l'axe du fuselage, c'est à dire si l'écoulement est indépendant de la station axiale ($X/D > 9$ dans le cas présent). L'analyse de l'incidence locale α_w confirme les observations faites précédemment : différences sensibles entre les calculs BL et K- ϵ pour $X/D \geq 7$ et une moins forte déviation de l'écoulement en dessous du tourbillon principal ($\phi \approx 155^\circ$) d'après les calculs.

Le coefficient de force axiale (fig. 20 et 21), local ou cumulé, est très bien estimé par les calculs (pression et frottement) bien que des écarts sensibles sur la valeur locale du coefficient de traînée de frottement (fig.20) soient notés. Cette différence peut s'expliquer par l'origine des valeurs expérimentales : la valeur locale du coefficient de traînée de frottement est obtenue par intégration des valeurs du C_f mesurées par les jauges, alors que la traînée globale est mesurée directement par la balance.

La répartition de force normale sur le fuselage, obtenue par intégration des pressions, est présentée figure 22. Elle a permis, d'une part de mettre en évidence rapidement la zone du fuselage concernée par la portance tourbillonnaire, en comparant notamment des calculs Euler et Navier Stokes, et d'autre part elle a permis de montrer qu'au cours de la convergence le niveau de viscosité turbulente obtenue avec le modèle BL augmentait, d'où un écoulement tourbillonnaire à l'extrados de plus en plus diffus et une portance tourbillonnaire de plus en plus faible. Les deux calculs donnent des résultats très voisins avec une portance tourbillonnaire sous-estimée. Le coefficient de force normale du fuselage complet (fig.23) est ainsi trop

faible d'environ 10% et la position du centre de poussée est située légèrement trop en avant (fig.24).

Les cartes des lignes de frottement calculées sont présentées sous forme développée sur la figure 25. La ligne de séparation principale (S1) est bien estimée par les deux calculs Baldwin-Lomax et K-ε. La ligne de séparation secondaire (S2), bien visible sur les visualisations à la bouillie, démarre au niveau de la section $X/D=7$ et traduit l'existence d'un tourbillon secondaire contrarotatif, bien établi. Celui-ci apparaît beaucoup plus tard pour les deux calculs en raison d'un excès de viscosité turbulente à l'extrados.

Les cartes d'iso-pression d'arrêt présentées figures 26 et 27 pour les trois sections $X/D=5/7/9$ confirment les résultats précédemment décrits, à savoir une trop grande diffusion au niveau de l'écoulement tourbillonnaire, celui-ci étant alors moins développé que dans l'expérience (fig.3).

Les figures 29 à 35 présentent, pour la section $X/D=7$, les profils de mach et d'incidence locale le long de quatre lignes radiales situées au voisinage de la zone tourbillonnaire (fig.28). Ces profils sont très voisins pour les deux calculs Baldwin-Lomax et K-ε et restituent bien la faible épaisseur de la couche limite dans le plan de symétrie vertical (fig.35) qui est écrasée par le tourbillon principal. Au cœur de celui-ci ($\phi \approx 150^\circ$), le ralentissement de l'écoulement est bien représenté par les calculs (fig.33), mais comme attendu, ils sous-estiment l'amplitude du cisaillement local sous le tourbillon principal (fig.34) et au pied de la nappe de décollement (fig.32).

7 - CONCLUSION

Une importante base de données expérimentales relative à l'écoulement tourbillonnaire qui s'établit autour d'un fuselage en écoulement supersonique a été créée. Elle comprend des mesures de pression pariétale, d'efforts, des sondages dans le champ, et une caractérisation de la couche limite (profils, frottement).

Cette base de données a été utilisée pour valider des calculs Navier Stokes turbulent effectués avec le code FLU3M.

Globalement, une bonne description de l'écoulement est obtenue par les calculs, ainsi qu'une bonne prévision des efforts locaux et globaux.

Cependant, il s'avère, que les deux modèles de turbulence utilisés (Baldwin-Lomax et K-ε) conduisent à un excès de viscosité dans la région de l'écoulement tourbillonnaire, d'où des tourbillons moins bien formés et une sous-estimation de la portance tourbillonnaire.

REFERENCES

[1] - J.DELERY : Physique des écoulements tourbillonnaires ; AGARD-CP-494 sur l'aérodynamique

des écoulements tourbillonnaires, Scheveningen, Pays-Bas, 1-4 Oct. 1990.

[2] P.CHAMPIGNY : High Angle of Attack Aerodynamics. AGARD-R-804, June 1994 .

[3] D.PAGAN, P. MOLTON : Basic Experiment on a Supersonic Vortex Flow around a Missile Body ; AIAA 29th Aerospace Science Meeting (Janvier 1991), ONERA TP 1991-13.

[4] M.BORREL, P.d'ESPINEY et C.JOUET Supersonic Vortical Flows Around an Ogive-Cylinder: Laminar and Turbulent Computations ; ECCOMAS-First European Computational Fluid Dynamics Conference (Sept. 1992).

[5] T.HSIEH, A.B. WARDLAW, Jr and T.J. BIRCH Vortical Flows about a Long Ogive-Cylinder at $M=3.5$ and $\alpha=18^\circ$; AIAA Paper-91-1808 - June-1991.

[6] D. DEGANI, Y. LEVY : Asymmetric turbulent vortical flows over slender bodies ; AIAA-91-3296.

[7] R. HOUEVILLE, J.C. JUILLEN et J. COUSTEIX Mesures du frottement pariétal par jauges à élément chaud en écoulement tridimensionnel. La Recherche Aérospatiale n° 1984-1.

[8] L. CAMBIER, D. DARRACQ, M. GAZAIX, Ph. GUILLEN, Ch. JOUET, L. LE TOULLEC Améliorations Récentes du Code de Calcul d'Écoulements compressibles FLU3M ; AGARD-CP-578, April 1996.

[9] B.S.BALDWIN, H.LOMAX : Thin Layer Approximation and Algebraic Model for Separated Turbulent Flows ; AIAA 78-257, Jan.1978.

[10] D.DEGANI, L.B.SCHIFF: Computation of Supersonic Viscous Flows Around Pointed Bodies at Large Incidence ; AIAA 83-0034, Janv.1983.

[11] W.P. JONES, B.E. LAUNDER : The Prediction of Low-Reynolds-Number Phenomena with a two-Equation Model of Turbulence ; International Journal of Heat Mass Transfert, vol.43, p.357-372,1981.

[12] C. JOUET and P.d'ESPINEY 3D laminar and 2D computations with Navier-Stokes solver FLU3M ; Conf. on Numerical Methods in Laminar and Turbulent Flow - University of Swansea (U.K.), July 18-23,1993

[13] GLEIZE V ; JOUET C. : Introduction de modèles de turbulence dans les codes «Navier-Stokes» Applications à des écoulements bidimensionnels. 30ème Colloque d'aérodynamique appliquée. NANTES - octobre 1993 - ONERA-TP 1994-21.

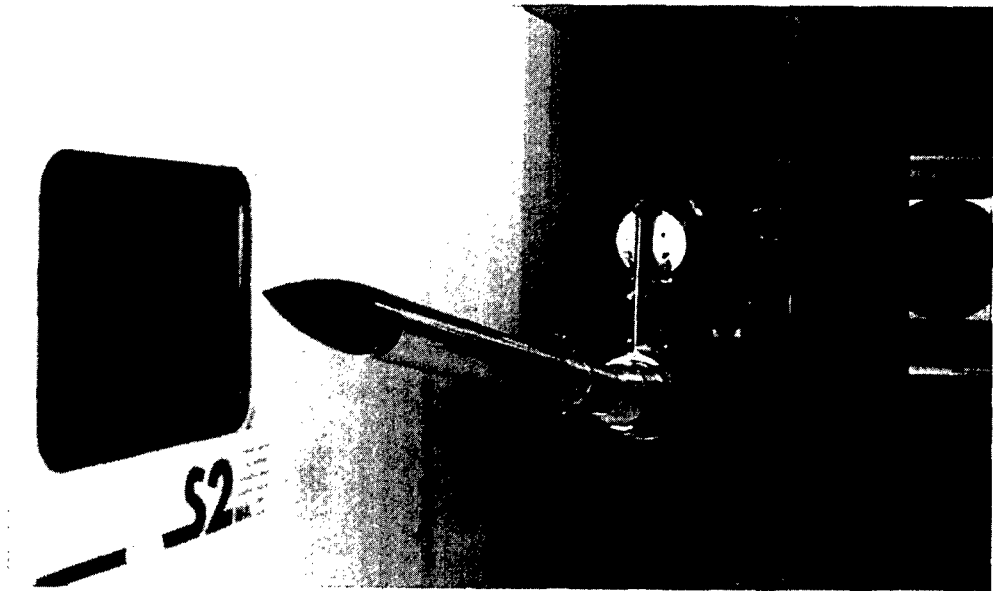


Figure 1. Maquette dans la soufflerie S2MA

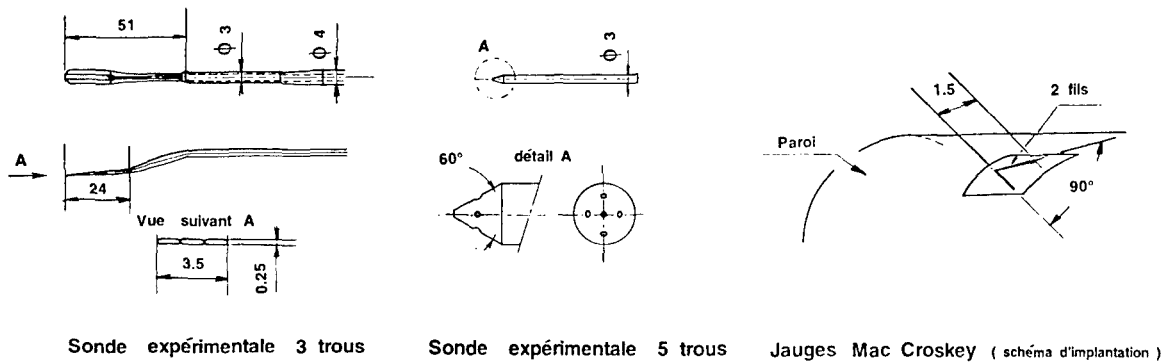


Figure 2. Instrumentation

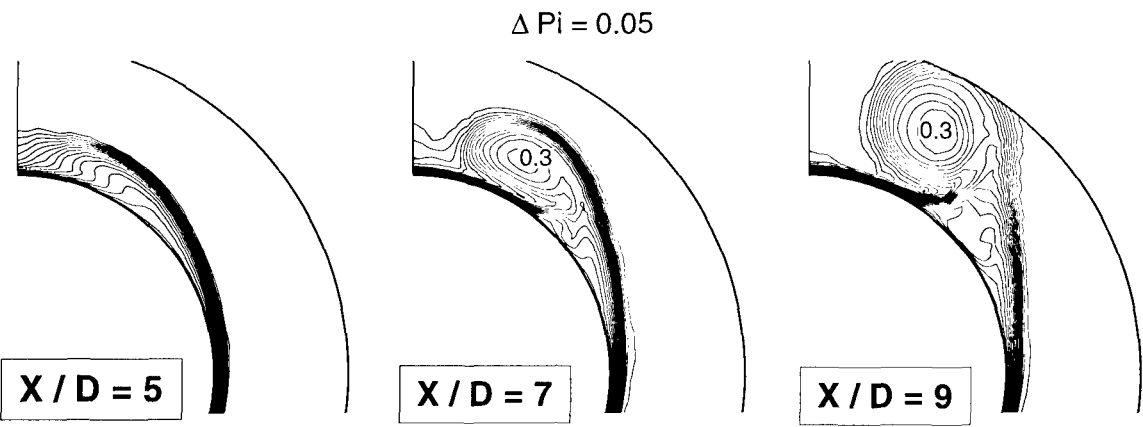


Figure 3. Champ de pression d'arrêt à Mach 2 et 10° d'incidence

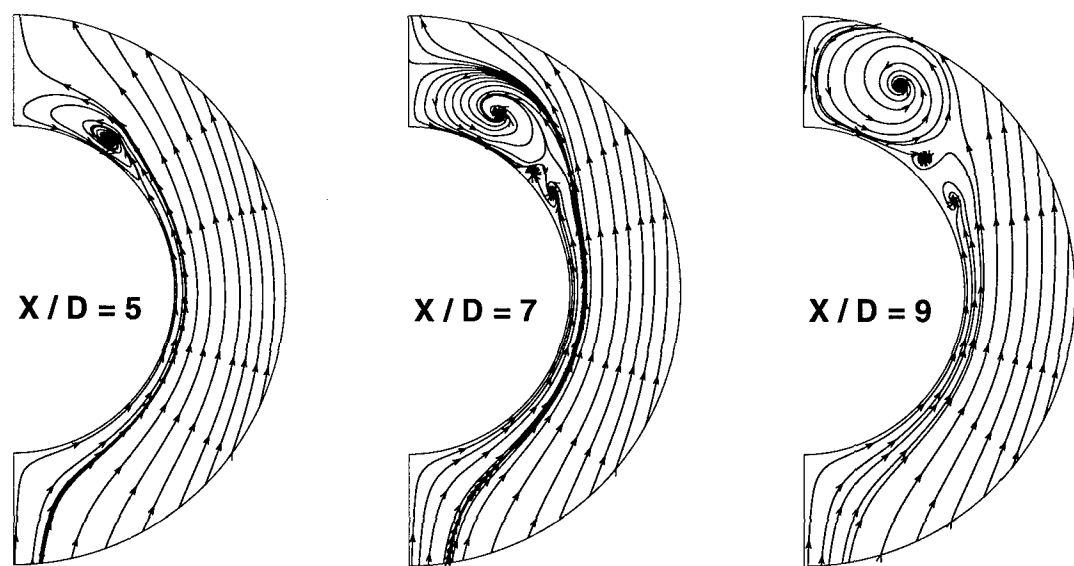


Figure 4. Pseudo lignes de courant - Mach 2 - $\alpha = 10^\circ$

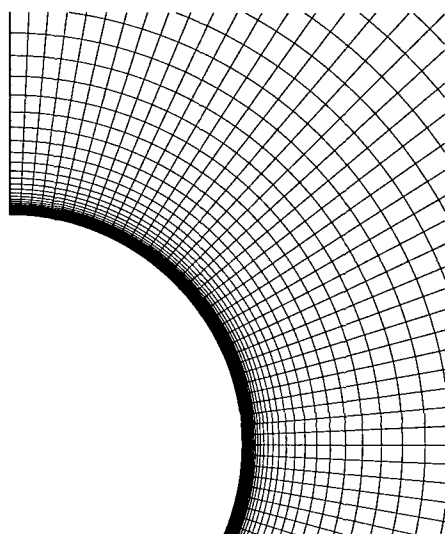


Figure 5. Maillage d'une section transversale

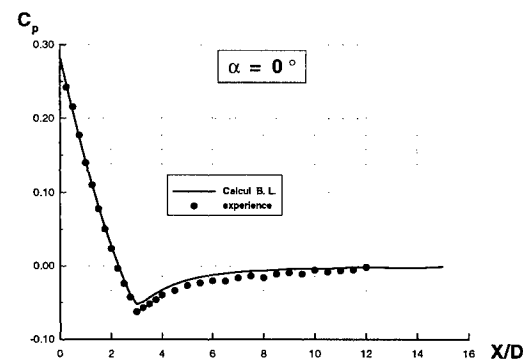


Figure 7. Evolution du coefficient de pression pariétale à Mach 2

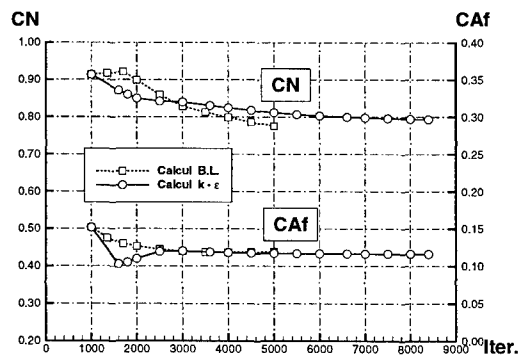


Figure 6. Convergence des coefficients aérodynamiques pour Mach 2 - $\alpha = 10^\circ$

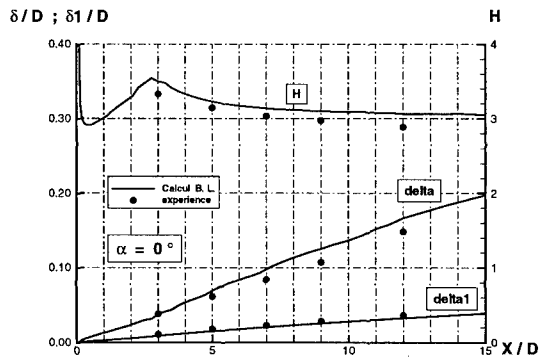


Figure 8. Evolution longitudinale des paramètres de la couche limite pour Mach 2 - $\alpha = 0^\circ$

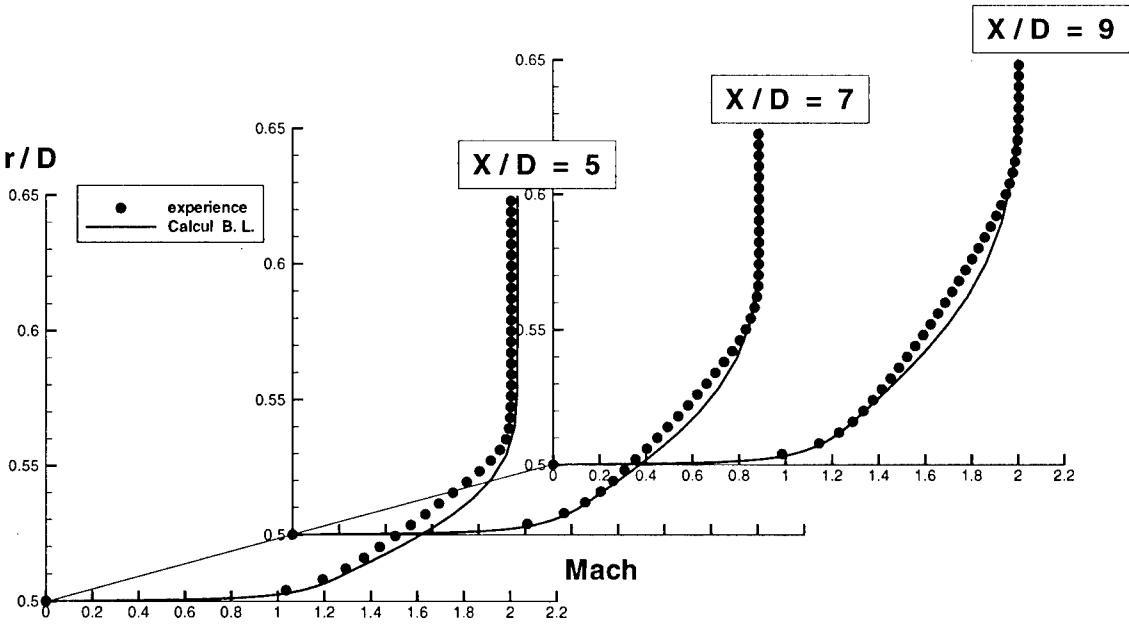


Figure 9. Profils de couche limite pour Mach 2 - $\alpha = 0^\circ$

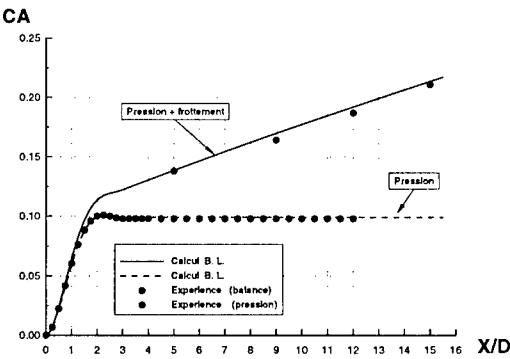


Figure 10. Coefficient de force axiale - Mach 2 - $\alpha = 0^\circ$

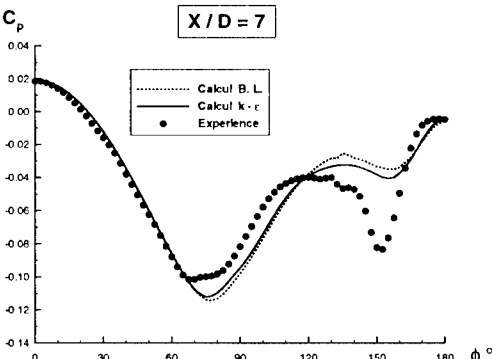


Figure 12. Coefficient de pression - Mach 2 - $\alpha = 10^\circ$

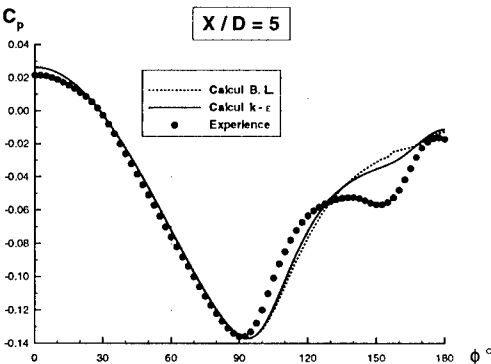


Figure 11. Coefficient de pression - Mach 2 - $\alpha = 10^\circ$

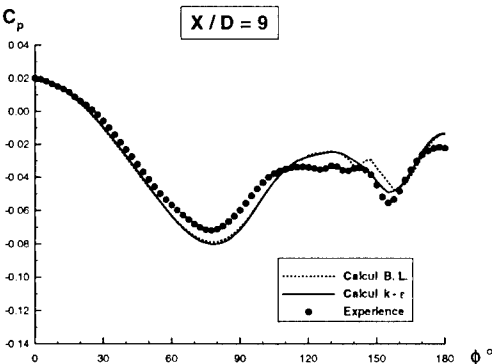


Figure 13. Coefficient de pression - Mach 2 - $\alpha = 10^\circ$

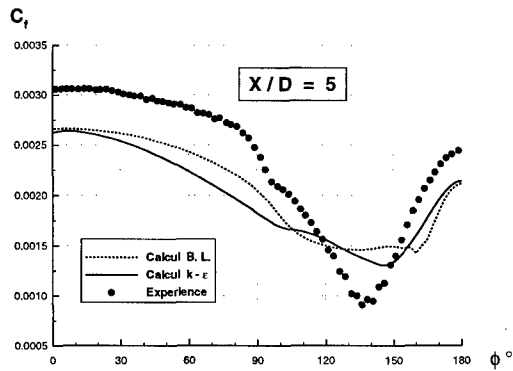


Figure 14. Coefficient de frottement pariétal
Mach 2 - $\alpha = 10^\circ$

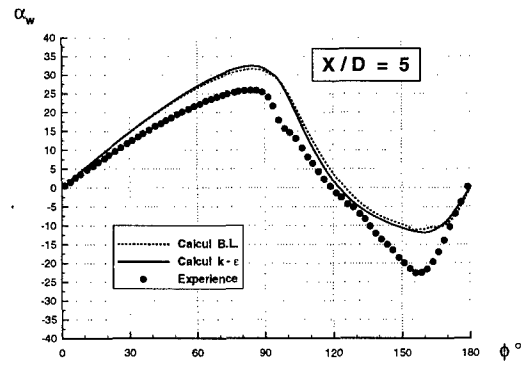


Figure 17. Direction du frottement pariétal
Mach 2 - $\alpha = 10^\circ$

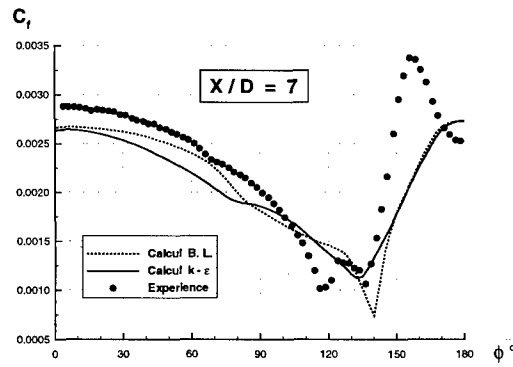


Figure 15. Coefficient de frottement pariétal
Mach 2 - $\alpha = 10^\circ$

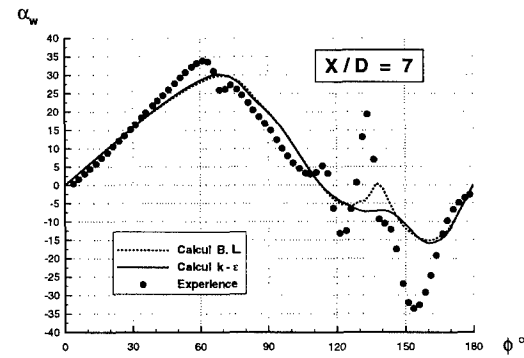


Figure 18. Direction du frottement pariétal
Mach 2 - $\alpha = 10^\circ$

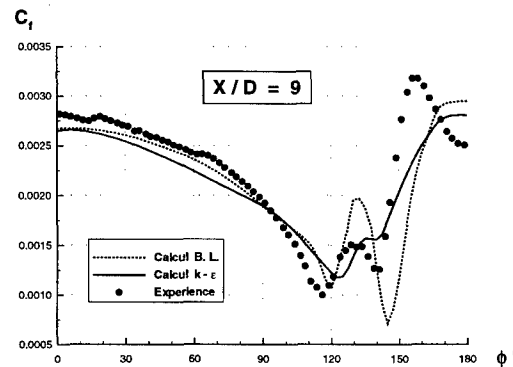


Figure 16. Coefficient de frottement pariétal
Mach 2 - $\alpha = 10^\circ$

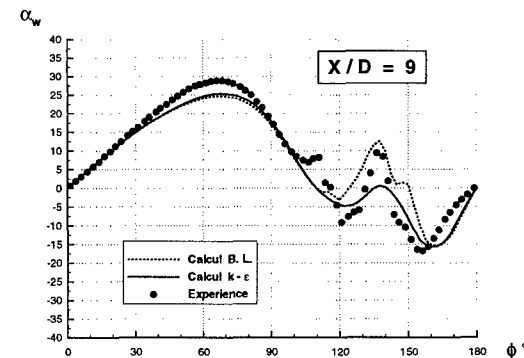


Figure 19. Direction du frottement pariétal
Mach 2 - $\alpha = 10^\circ$

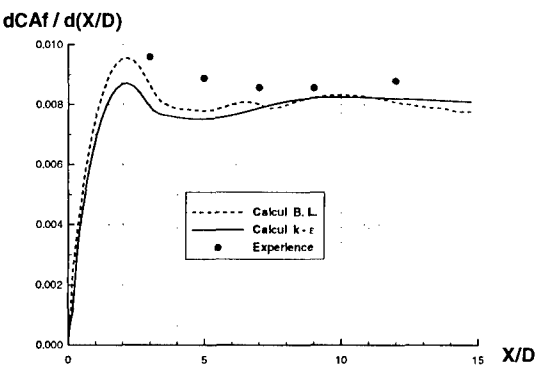


Figure 20. Distribution de traînée de frottement
Mach 2 - $\alpha = 10^\circ$

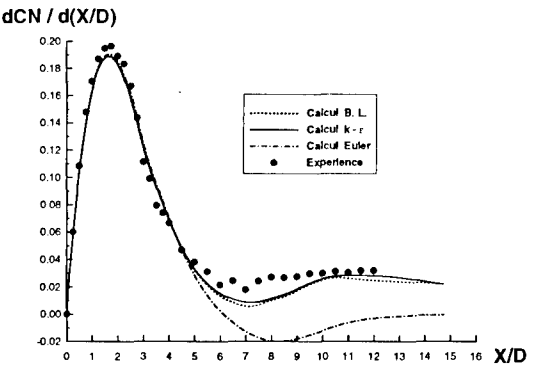


Figure 22. Distribution de force normale
Mach 2 - $\alpha = 10^\circ$

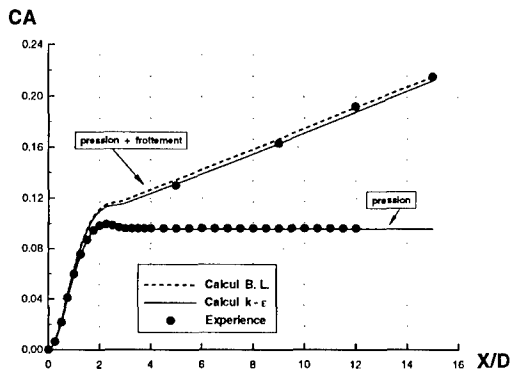


Figure 21. Coefficient de force axiale
Mach 2 - $\alpha = 10^\circ$

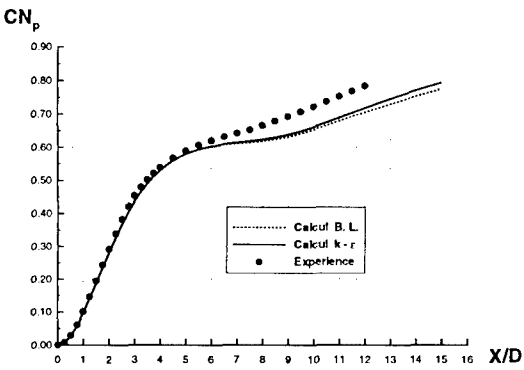


Figure 23. Coefficient de force normale
Mach 2 - $\alpha = 10^\circ$

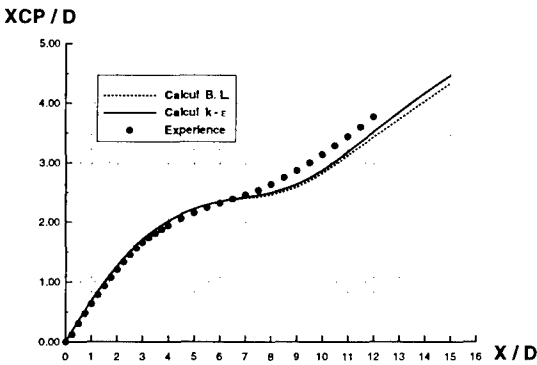


Figure 24. Centre de poussée
Mach 2 - $\alpha = 10^\circ$

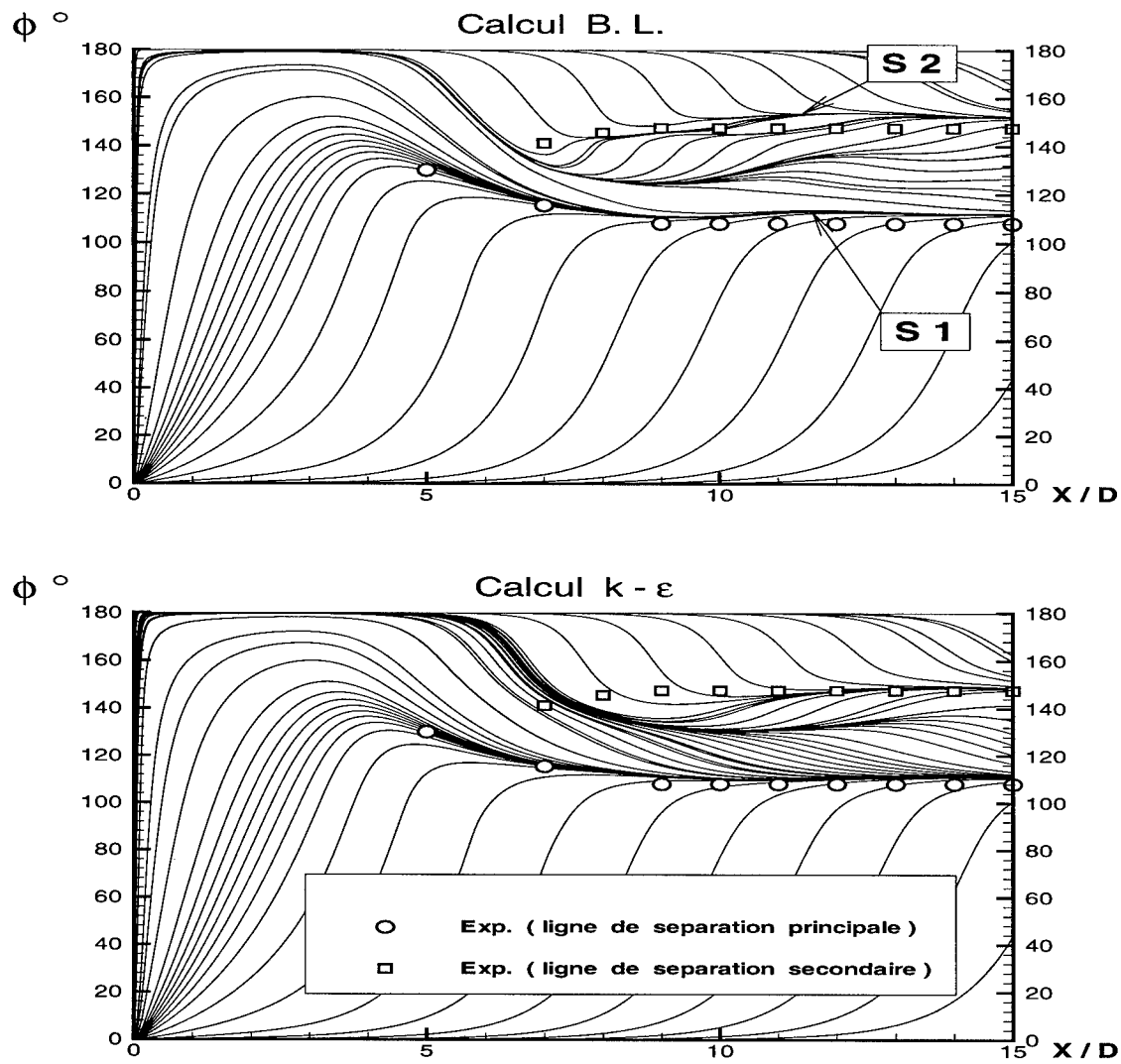


Figure 25. Ligne de frottement
Mach 2 - $\alpha = 10^\circ$

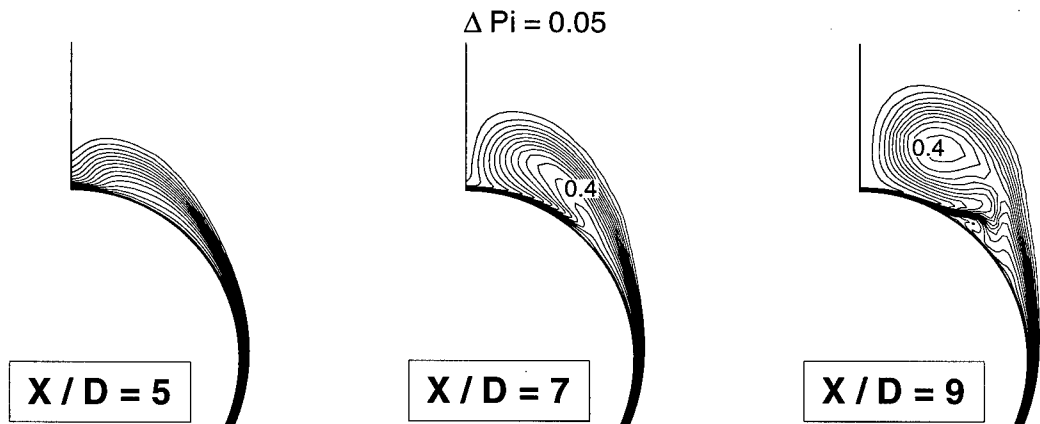


Figure 26. Champ de pression d'arrêt - Calcul Baldwin-Lomax
Mach 2 - $\alpha = 10^\circ$

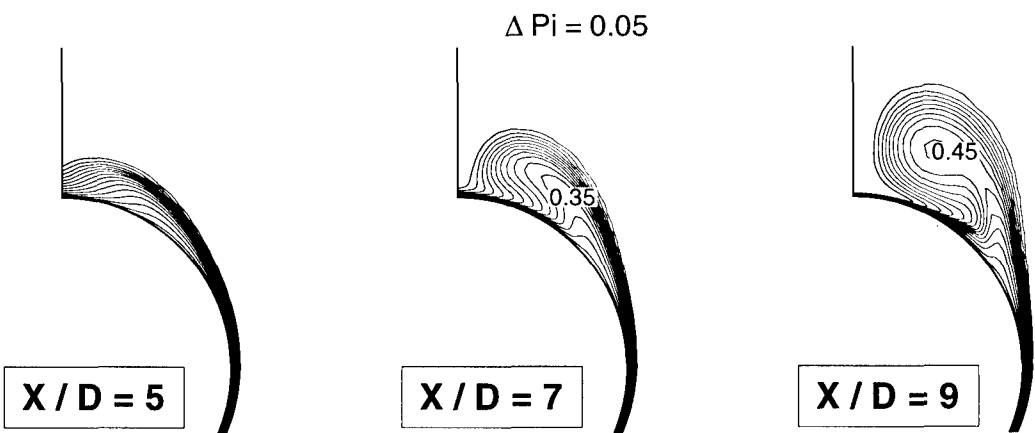


Figure 27. Champ de pression d'arrêt - Calcul K- ϵ
Mach 2 - $\alpha = 10^\circ$

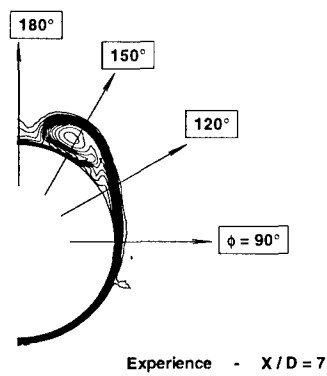


Figure 28. Définition des positions des profils de couche limite

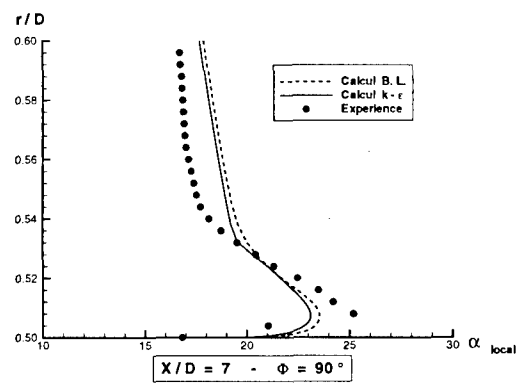


Figure 30. Profil d'incidence locale dans la couche limite - Mach 2 - $\alpha = 10^\circ$

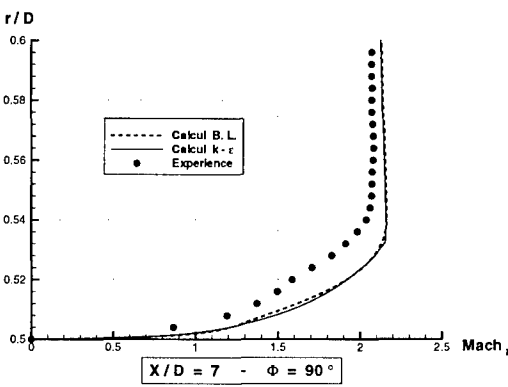


Figure 29. Profil de Mach dans la couche limite
Mach 2 - $\alpha = 10^\circ$

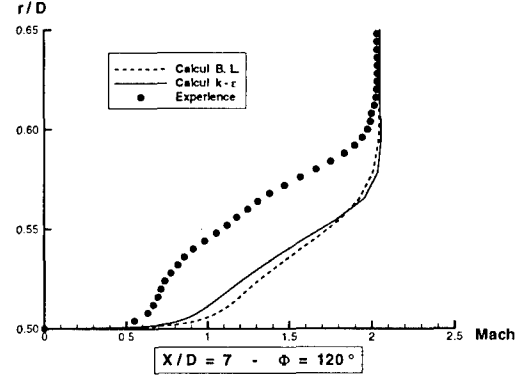


Figure 31. Profil de Mach dans la couche limite
Mach 2 - $\alpha = 10^\circ$

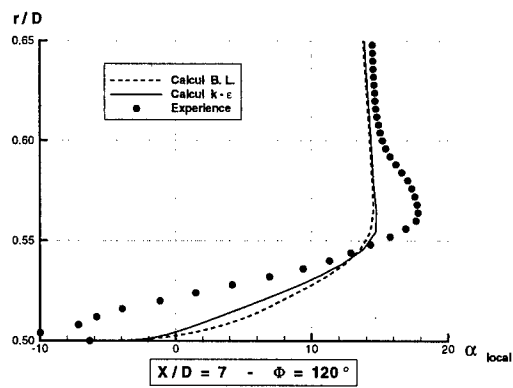


Figure 32. Profil d'incidence locale dans la couche limite - Mach 2 - $\alpha = 10^\circ$

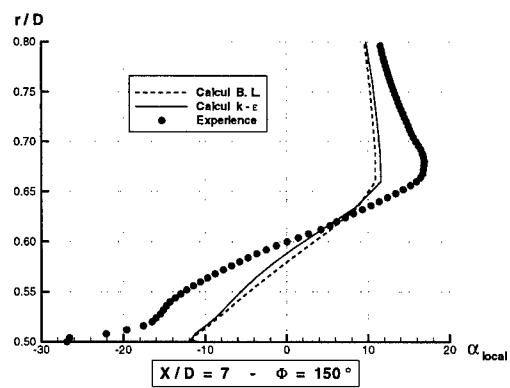


Figure 34. Profil d'incidence locale dans la couche limite - Mach 2 - $\alpha = 10^\circ$

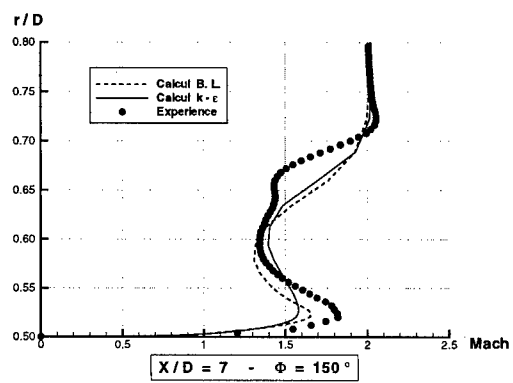


Figure 33. Profil de Mach dans la couche limite Mach 2 - $\alpha = 10^\circ$

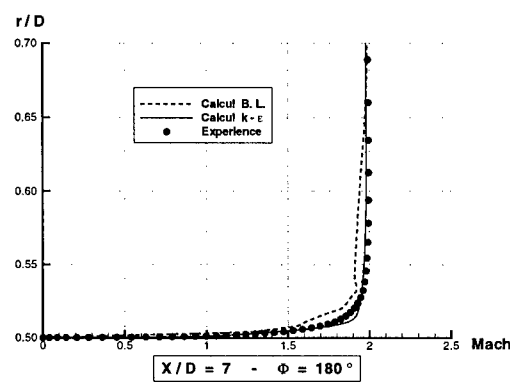


Figure 35. Profil de Mach dans la couche limite Mach 2 - $\alpha = 10^\circ$

Algebraic Turbulence Modelling for Vortical Flows around Slender Bodies

N. Qin and C. Jayatunga
College of Aeronautics, Cranfield University
Bedford MK43 0AL, UK.

Summary

In this paper, we present a study of algebraic turbulence modelling for vortical flows based on the Baldwin-Lomax two-layer formulation. Firstly, a recent modification of the wake function in the algebraic model by Panaras for swept shock boundary layer interaction problems has been extended for slender body vortical flows. Secondly, the reason for the failure of the Degani-Schiff model for some vortical flow problems has been analysed. Consequently, a new criterion for the determination of the modelling length scale, which is found crucial for a proper algebraic modelling for vortical flows, is proposed based on the curvature of the profile of the damped moment of vorticity. It has been demonstrated that, as compared with the popular Degani-Schiff model, both of the new algebraic models can produce much better results regarding the leeward side vortical structure for a complicated vortical flow problem around a slender body.

List of Symbols

C_p	Pressure coefficient
D	body diameter
E, F, G	transformed Navier-Stokes flux vectors
F	damped moment of vorticity, Eq.(14).
H	source term
i, j, k	grid indexes in streamwise, wall normal (radial) and circumferential directions respectively.
M	Mach number
Q	conservative flow variable vector
R	vector of the set of discretised PNS equations (residual vector)
Re	Reynolds number based on D
T	temperature
t	time
U	velocity magnitude
x, y, z	Cartesian co-ordinates in axial, sideways, upwards directions respectively
δ	boundary layer thickness
ϕ	circumferential angle in degrees
κ	curvature of F function, Eq.(21).
μ	viscosity
ρ	density

τ	pseudo time
ω	vorticity
ξ, η, ζ	transformed body fitted co-ordinates, representing streamwise, wall normal (radial) and circumferential directions respectively

Subscripts

i	inviscid
max	maximum
v	viscous
ref	reference value
t	turbulent

Introduction

Over recent years CFD has gained widespread acceptance as a tool to be used in the preliminary stages of missile design. Particularly useful for supersonic missile applications is the space marching parabolised Navier-Stokes approach.^[1-4] Its usefulness can be attributed to the following aspects: (i) its computational efficiency as compared with a fully three-dimensional time-marching Navier-Stokes solutions; (ii) its viscous capability suited for vortical flows around missile bodies at angles of attack. However the situation is still far from satisfactory because engineering design and analysis of candidate missiles shapes require a very fast response. Continuous efforts have been put on the acceleration of the PNS solution process. A recent development has been reported by Shaw and Qin^[5] to accelerate the PNS convergence. An implicit space-marching was combined with an implicit pseudo-time solver at each spatial station for an efficient solution of the PNS system.

Another unsatisfactory issue regarding current PNS methodologies is the accuracy for turbulent vortical flow simulation. A common failure is that the secondary vortex under the primary vortex is often washed out in the numerical prediction due to an excessive eddy-viscosity given by the turbulence model used. This leads to erroneous surface pressure prediction and misleading aerodynamic coefficients.

This paper addresses the capability of simple algebraic turbulence modelling for slender body vortical flows. The Degani-Schiff modification^[7] of

the Baldwin-Lomax algebraic model^[6] has been widely used for vortical flows, which, in many cases, results in significant improvement over the Baldwin-Lomax model by a better estimation of the turbulence viscosity in the separated vortical region. However the Degani-Schiff model can fail in some vortical flow situations. The failure of the model is analysed through an example and two ways to cure this problem are proposed. Firstly, a recent wake function model by Panaras has been extended and studied for slender body vortical problems. Secondly, a curvature-based model has been developed addressing some difficulties with the Degani-Schiff model. Both new models have improved the simulation of the leeward side vortical flow structure.

Numerical Method

Governing Equations

The steady Reynolds averaged Navier-Stokes equations express the conservation of mass, momentum and energy and may be written for a curvilinear co-ordinate system in the following manner,

$$E_{\xi} + F_{\eta} + G_{\zeta} = 0 \quad (1)$$

The parabolised Navier-Stokes equations are a simplified form of the full Navier-Stokes equations which are obtained under the assumptions that the flow is steady and that viscous terms in the streamwise direction are negligible in comparison to viscous terms in the cross flow directions. Under these assumptions the governing equations become,

$$(E_i) + (F_i - F_v) + (G_i - G_v) = 0 \quad (2)$$

Further assumptions for a space-marching approach to be valid are: (i) the flow outside of the boundary layer is supersonic in the streamwise direction; (ii) there is no streamwise separation. By applying Vigneron's approximation^[1], Equation (2) becomes parabolic in the streamwise (ξ) direction, which are named the parabolised Navier-Stokes equations.

Numerical Procedure

The numerical method employed for the solution of the governing equations, Equation (2), is based upon that developed for supersonic and hypersonic flows by Qin and Richards^[3] and Birch, *et al.*^[4] and Shaw and Qin^[5].

A high-resolution finite-volume scheme based upon Osher's flux difference splitting^[8] is employed for the spatial discretisation of the convective flux terms. In this procedure the numerical convective flux is

evaluated using an approximate Riemann solver, which can be written as,

$$\tilde{F}_{j+\frac{1}{2}} = \frac{1}{2} [F(Q_L) + F(Q_R)] - \frac{1}{2} \int_{Q_L}^{Q_R} \left| \frac{\partial F}{\partial Q} \right| dQ \quad (3)$$

where the integration in the last term is carried out using a natural ordering of the sub-paths parallel to the eigenvectors of the flux Jacobian. Higher order spatial accuracy is obtained using MUSCL interpolation together with a flux limiter. The viscous terms are discretised using second order accurate central differences through the use of the Gauss theorem.

After spatial discretisation of the crossflow terms a system of ordinary differential equations is obtained in the streamwise marching co-ordinate,

$$\left(\frac{\partial \bar{E}}{\partial \xi} \right)_{i,j,k} = -(\tilde{F}_{ij+\frac{1}{2},k} - \tilde{F}_{ij-\frac{1}{2},k} + \tilde{G}_{ij+\frac{1}{2},k} - \tilde{G}_{ij-\frac{1}{2},k}) \quad (4)$$

Here “ \sim ” indicates that the flux has been evaluated using Osher's approximate Riemann solver and includes the discretised viscous terms. Various discretisation methods can be adopted for the remaining streamwise flux derivative. In the present work a fully implicit method is employed using the backward Euler scheme. One implicit step of the method can be written as,

$$\begin{aligned} \bar{E}_{i,j,k} - \bar{E}_{i-1,j,k} = \\ -(\tilde{F}_{ij+\frac{1}{2},k} - \tilde{F}_{ij-\frac{1}{2},k} + \tilde{G}_{ij+\frac{1}{2},k} - \tilde{G}_{ij-\frac{1}{2},k}) \end{aligned} \quad (5)$$

The choice of an implicit streamwise marching strategy removes the need to consider stability restrictions when determining the size of the marching step. This approach is superior to the use of an explicit marching scheme that will generally require a much smaller marching step size than that determined from accuracy considerations alone.

In order to obtain an efficient solution of Equation (5) a pseudo-time term is introduced (this approach can be considered analogous to the dual time stepping methods employed in the solution of the unsteady Navier-Stokes equations) as follows,

$$\begin{aligned} \frac{\partial Q}{\partial \tau} = & -(\bar{E}_{i,j,k} - \bar{E}_{i-1,j,k} + \tilde{F}_{ij+\frac{1}{2},k} - \tilde{F}_{ij-\frac{1}{2},k} + \\ & \tilde{G}_{ij+\frac{1}{2},k} - \tilde{G}_{ij-\frac{1}{2},k}) = -R \end{aligned} \quad (6)$$

where τ denotes the pseudo-time. The pseudo-time term vanishes, provided that the flowfield is indeed steady, as $\tau \rightarrow \infty$, and the discretised form of the governing equations, Equation (5), are recovered. At each streamwise station the discretised equations are marched forward in pseudo-time until a converged steady state solution is obtained.

In the current implicit pseudo-time marching scheme, one implicit step of the time marching method can be written as,

$$\left(I + \Delta\tau \frac{\partial R^n}{\partial Q} \right) \Delta Q = -\Delta\tau R^n \quad (7)$$

in which R is the right hand side of Equation (6) and $\Delta Q = Q^{n+1} - Q^n$. The Jacobian term on the left-hand side of this equation is obtained from analytical expressions. Note that the Jacobian is the full Jacobian of the right-hand side R rather than the flux Jacobians used in many AF and ADI implicit schemes. This feature is one of the key features different from other implicit schemes, especially for high order discretisations.

The linear systems (7) is solved by a matrix-free AF preconditioned GMRES method. Further details of the methodology and numerical tests can be found in an AIAA Paper by Shaw and Qin^[5].

Turbulence Modelling for Vortical Flows

The Baldwin-Lomax Model

The Baldwin-Lomax model^[6] is one of the most well known models in the field of computational aerodynamics. It is the basis of the other three models to be presented later. We will give a brief description of the model and its formulations in this section for the sake of a clearer presentation of the later models.

The Baldwin-Lomax turbulence model is a two-layer, algebraic model based on the mixing length concept. It is patterned after the Cebeci-Smith model and introduces modifications that eliminate the need to search for the edge of the boundary layer to determine one of the length scales in the model. Its strength and weaknesses are well known in the CFD community; it gives reasonable accuracy for steady flows with little or no separation and performs poorly if there is large separation.

The eddy viscosity coefficient is given by

$$\mu_t = \begin{cases} (\mu_t)_{inner}, \eta \leq \eta_{crossover} \\ (\mu_t)_{outer}, \eta > \eta_{crossover} \end{cases} \quad (8)$$

where η is the local distance measured normal to the body surface and $\eta_{crossover}$ is the smallest value of η at which the turbulent viscosities calculated by both inner and outer formulas are equal. The values of μ_t in the inner layer, $(\mu_t)_{inner}$, and the outer layer, $(\mu_t)_{outer}$, are computed as follows.

The Prandtl mixing length hypothesis is used for the inner layer with a van Driest damping function, i.e.

$$(\mu_t)_{inner} = \rho l_{mix}^2 |\omega| \quad (9)$$

where the mixing length is given by

$$l_{mix} = k\eta(1 - e^{-\eta^+/A^+}) \quad (10)$$

and k is the von-Karman constant, and $|\omega|$ is the magnitude of the vorticity and the friction height is given by

$$\eta^+ = \frac{\rho_w u_\tau \eta}{\mu_w} = \eta \frac{\sqrt{\rho_w \tau_w}}{\mu_w} \quad (11)$$

Eddy viscosity in the outer layer is given by

$$(\mu_t)_{outer} = KC_{cp} \rho F_{wake} F_{Kleb} \quad (12)$$

where K is the Clauser constant, C_{cp} is an additional constant, and the wake function

$$F_{wake} = \min \left\{ \eta_{max} F_{max}, C_{wk} \eta_{max} U_{dif}^2 / F_{max} \right\} \quad (13)$$

The quantities η_{max} and F_{max} are determined from the function

$$F(\eta) = \eta |\omega| (1 - e^{-\eta^+/A^+}) \quad (14)$$

The quantity F_{max} is the maximum value of $F(\eta)$ that occurs in a profile and η_{max} is the value of η at which it occurs. The function $F(\eta)$ plays a key role in the turbulence modelling of vortical flows and represents the damped moment of vorticity, which will be briefly referred to as the moment of vorticity.

The eddy viscosity in the outer layer is multiplied by the Klebanoff intermittency factor given by

$$F_{Kleb}(\eta) = \left[1 + 5.5 \left(\frac{\eta}{\delta} \right)^6 \right]^{-1} \quad (15)$$

which provides a measure of the effect of intermittency, partly laminar and partly turbulent, in the outer layer. This will drive the eddy viscosity to zero in the flow further away from the boundary layer.

The boundary layer thickness in (15) is given by

$$\delta = \frac{\eta_{max}}{C_{Kleb}} \quad (16)$$

which has been well tested for supersonic attached boundary layers. The quantity U_{dif} in (13) is the difference between maximum and minimum velocity in the boundary layer profile.

As can be seen from the above, in the outer layer, the length scale η_{max} affects the viscosity through not only the wake function (13) but also the intermittency factor (15) via the definition of boundary layer thickness (16).

The constants appearing in the above relations are as follows:

$$\begin{aligned} k &= 0.41 & A^+ &= 26 & K &= 0.0168 \\ c_{cp} &= 1.6 & C_{wk} &= 0.25 & C_{Kleb} &= 0.3 \end{aligned} \quad (17)$$

The Degani-Schiff Model

The modification proposed by Degani and Schiff^[7] on the Baldwin-Lomax algebraic turbulence model^[6] for vortical flows has significantly improved the turbulent vortical flow simulation for many vortical flow test cases. It is based on the argument that the Baldwin-Lomax algebraic model is a reasonable model for attached turbulent boundary layers and the length scale used in it should be that representing the attached turbulent boundary layers. For slender body vortical flows, after the boundary layer has separated from the surface to form a vortical flow, there is an attached boundary layer underneath this vortex for which the Baldwin-Lomax model can be applied. The turbulence generation process is dominated by the attached boundary layers rather than the vortical flows, which are primarily governed by convective mechanism. It is therefore important to decide an appropriate length scale for these attached boundary layers. From analyses of the moment of vorticity distribution, multiple peaks were observed in the vortical flow region. It was suggested that the first peak away from the wall should be used in the model

to represent the attached boundary layer underlying the vortical structure.

A problem arises around the separation region. The peaks representing the attached boundary layer and the vortical sheet are very close together and the criterion used in the Degani-Schiff model, a certain percentage drop (typically 10%) in the profile, does not work properly. Degani and Schiff tried to compensate this by using the attached boundary layer length scale of the previous ray if a peak can be clearly identified within a cut-off distance from the wall defined at 150% of the peak position on the previous ray. This of course brings about uncertainties of the length scale in a region, which can have a crucial effect on the results.

From our numerical tests, we observed that the vortical peak position can be within the cut-off distance when the two peaks are merged. In this situation, the Degani-Schiff model will still pick up the wrong peak as that of the Baldwin-Lomax model, overestimating the turbulence viscosity near the crossflow separation. Even if the freezing is switched on, the length scale will be the one from the attached boundary layer upstream in the circumferential direction rather than the second normally thinner attached boundary layer underneath the separated boundary layer. Therefore it overestimates again the length scale.

Degani *et al.*^[9] recognised the weakness of the Degani-Schiff model in the vicinity of the crossflow separation and indicated that the accuracy of the model decreases as the region with a frozen length scale increases.

The Kcut Model

A later study by Panaras and Steger^[10] found that there may be another peak in the $F(\eta)$ profile in the sublayer in addition to the main peak in the boundary layer. It is much closer to the wall and is not the one that should be used in the turbulence model. However a computerised search may pick it up in the Degani-Schiff model. Therefore they suggested an empirical way called the Kcut method (they used K for the radial direction rather than J as in the present paper) to separate the outside vortical flow from the attached boundary layer so that an absolute maximum can be found between the wall and the Kcut position. In this way, both the vortex peak and the possible sublayer peak can be avoided in the search.

An obvious weakness of such an approach is the difficulty in determining the corresponding Kcut position beforehand for different streamwise stations and different flow conditions. It will be more difficult if the Kcut positions need to be found for both

primary and secondary vortices at the same station. It has the same problem as the Degani-Schiff model in region near the crossflow separation line when the boundary layer peak and the vortex peak cannot be separated.

The Panaras Models

Recently Panaras^[11] has observed, for swept shock/boundary layer interaction over a sharp-fin/flat-plate, the existence of a *low-turbulence tongue* under the primary vortex between the reattachment line and the secondary separation line. In a further paper^[12], he introduced two new algebraic models based the Baldwin-Lomax model considering the mixed flow nature. His study has been limited to swept shock-wave/turbulent boundary layer interactions for a sharp-fin/flat-plate geometry with a strongly conical vortical structure.

In the present research, we have evaluated these new algebraic models for vortical flows around slender bodies at supersonic speeds. Though the models have also been based on the Baldwin-Lomax model, a different path from the Degani-Schiff idea has been taken. Instead of finding the length scale for the attached turbulence boundary layers, the original length scale of the Baldwin-Lomax model, representing the primary separated boundary layer or the primary-vortex feeding sheet, has been used in his new models. The required modification to take the vortical flow into account comes from the modification in the calculation of the wake function in the outer part of the boundary layer. In the present paper, results from Panaras' second model are presented with necessary modification for vortical flows around slender bodies.

An integral part of the Panaras' model is the modification of the boundary layer thickness definition as related to F_{max} in the separated region. In his models, the following scheme for the calculation of the edge of the boundary layer has been used:

$$\left. \begin{aligned} \delta &= \eta_{max} + \left(\frac{1}{C_{Kleb}} - 1 \right) \eta_{ref}, \text{ if } \eta_{max} > \eta_{ref} \\ \delta &= \frac{\eta_{max}}{C_{Kleb}}, \text{ if } \eta_{max} < \eta_{ref} \end{aligned} \right\} \quad (18)$$

It relates to a reference point before the flow is separated. It was shown for his test cases that this modification provides a more realistic estimation of the edge of the viscous layer after separation, while the relation (16) in the basic model can overestimate the extent of the viscous region, covering a region above the separation vortex which actually is purely

inviscid. Note that for an attached boundary layer, there is no difference in the relationship between δ and η_{max} for the two models if the reference point is picked up just before separation.

The Panaras model was derived considering the low-turbulence tongue that exists underneath the conical separation vortex of a strong swept-shock/turbulent boundary layer interaction. This tongue creates a mixed-type separation bubble: turbulent in the region of the separation line and almost laminar between the secondary vortex and the reattachment line. This type of separation is not simulated accurately with the standard Baldwin-Lomax turbulence model.

The above led Panaras to conclude that a wake function is required which between the secondary vortex and the reattachment region will take very small values, but in the region of the separation point will have a variation comparable with that of the standard Baldwin-Lomax relations. Testing various options he found that a reasonable choice is the inverse of $\eta_{max} F_{max}$, properly scaled by $\eta_{ref} F_{ref}$. This new relation is applied a little downstream of this point as follows:

$$\left. \begin{aligned} F_{wake} &= \eta_{max} F_{max}, \text{ if } \eta_{max} < 1.03 \eta_{ref} \\ F_{wake} &= a (\eta_{ref} F_{ref})^2 / (\eta_{max} F_{max}), \text{ if } \eta_{max} > 1.03 \eta_{ref} \end{aligned} \right\} \quad (19)$$

A parametric analysis has led to the constant $a=3$. In Panaras' study for swept shock wave / boundary layer interaction, the flow outside the interaction region is undisturbed. Therefore a choice for the reference values is made using the conditions at the undisturbed boundary layer at the corresponding streamwise station.

However for the vortical flow around a slender body, the flow condition before the crossflow separation line is varying. The boundary layer develops not only in the streamwise direction but also in the circumferential direction. Initially, following Panaras' idea, we thought that the condition before the crossflow separation line could be a good choice for the reference condition. However disappointing results were produced using such a reference condition. Through numerical testing, it was found that the windward symmetric line seems to be a proper choice for the reference point and the Panaras model has been modified to

$$\left. \begin{aligned} F_{wake} &= \eta_{max} F_{max}, \text{ if } \eta_{max} < 1.5 \eta_{ref} \\ F_{wake} &= a (\eta_{ref} F_{ref})^2 / (\eta_{max} F_{max}), \text{ if } \eta_{max} > 1.5 \eta_{ref} \end{aligned} \right\} \quad (20)$$

We have changed the switching constant 1.03 in the original model to 1.5 for the current problem to make sure that the new model is only switched on after the crossflow separation line.

A Curvature-Based Model

After analysing the previous models, we propose a refined algebraic turbulence model for vortical flows around slender bodies. It is based on Degani and Schiff's idea^[7] of applying the eddy-viscosity model to the attached turbulent boundary layers underlying the leeward-side vortex structures. After the boundary layer is separated from the wall to form an axial vortical flow, the vortex structure is essentially inviscid and is governed primarily by the convection of vorticity generated within the attached boundary layers at the body surface.

To address the weak points of the Degani-Schiff model and the Kcut model, we need a criterion for the length scale representing the attached boundary layer that is clearer, more accurate and easily to be implemented for complicated vortical structures.

Reviewing the $F(\eta)$ profiles along the rays from the windward side to the leeward side, we can identify a clear point that represent the length scale required in the turbulence model. Instead of using the peaks in the $F(\eta)$ curve, we propose to use the curvature of the $F(\eta)$ curve, which can be readily calculated from:

$$\kappa = \frac{F''(\eta)}{[1 + (F'(\eta))^2]^{3/2}} \quad (21)$$

The curvature model of determining η_{max} is based on the fact that the function $F(\eta)$ has two convex regions in the boundary layer, one in the sublayer and one further away from the wall representing the boundary layer length scale. The first convex region in the sublayer can form a peak, i.e. a local maximum, in some situations as identified by Panaras and Steger^[10]. As mentioned before, a computerised search for the first maximum of the moment of vorticity, as suggested by Degani and Schiff, may select the sublayer value and not the one representing the attached boundary layer. This can be avoided by finding the minimum point in the curvature function in the second negative region. This point corresponds to the second maximum convex point representing the length scale for the attached boundary layer. In this manner the correct length scale can be found without ambiguity, resulting in a more accurate prediction of eddy viscosity coefficient.

The curvature-based model is derived based on the following assumption. No matter how many peaks

exit in the $F(\eta)$ distribution, the minimum in the second negative region in the curvature away from the wall should always represent the length scale for the attached boundary layer whether there is a vortical flow structure on top of it or not. This assumption is made based on the analysis of previous work of Degani and Schiff^[7] and Panaras and Steger^[10] and our own numerical experiments on boundary layer profiles in vortical flow regions.

In the above discussion, we have purposely used *convex* regions in $F(\eta)$ or *minimum* points in the curvature profiles of $F(\eta)$ rather than *peaks* or *maximum* points in $F(\eta)$. We believe that the *convex* property gives a more accurate description of the characteristics of the $F(\eta)$ curve in the boundary layer. None of the two convex regions necessarily form peaks in the attached boundary layer. The second convex region does not form a peak when the boundary layer edge and the vortex feeding sheet are close together after the primary or secondary crossflow separation point. These are the regions that caused problems for the Degani-Schiff model, which is illustrated later in our numerical tests.

In the implementation of the curvature method, the curvature of $F(\eta)$, κ , is obtained using (21) with the derivatives calculated by central differencing. A computerised search is then carried out for each ray in the η direction away from the wall for the second negative region in the κ profile. This region represents the second convex region in the $F(\eta)$ profile. The minimum point is found in this region and the corresponding η and $F(\eta)$ are defined as η_{max} and F_{max} in (13) for the wake function in the turbulence model. Note that although the subscript "max" has been kept here to be consistent with the original Baldwin-Lomax model, F_{max} does not necessarily represents a global maximum in $F(\eta)$ as in the Baldwin-Lomax model or a local maximum in $F(\eta)$ as in the Degani-Schiff model.

Numerical noises in the straight part of $F(\eta)$ could cause misjudgement in the above computerised search as κ could oscillates in a very small band around the 0 axis. This problem can be easily dealt with by setting up a *noise band* defined by:

$$|\kappa| \leq \varepsilon \quad (22)$$

where ε is a small number but greater than the numerical noises associated with the curvature. Within this noise band, the curvature κ is regarded as null in the program. In the current calculations, κ varies in a very large range up to $O(10^3)$. A reasonable choice was found to be $\varepsilon=1$. The

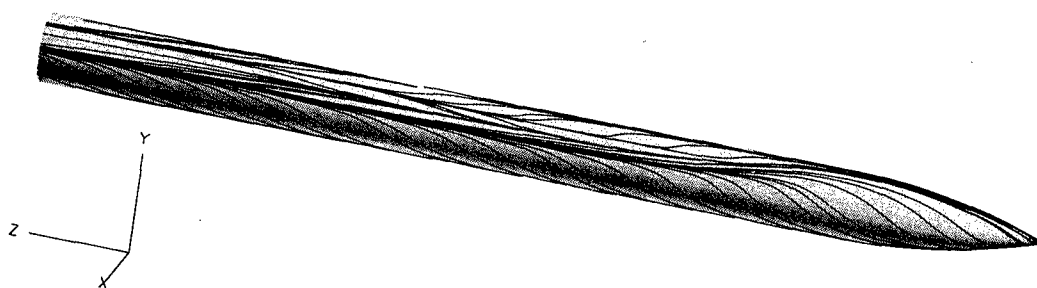


Figure 1. The ogive-cylinder geometry and surface skin friction lines

modelling method presented in this section will be referred to as the curvature model.

Results and Discussion

The Test Case

An ONERA ogive-cylinder test case^[13] has been used for the test of the turbulence models studied and proposed in the current paper. The reason for such a choice is the incapability of the popular Degani-Schiff model for such a vortical flow problem. It has produced disappointing results for the leeward side of the body and missed the secondary vortical structure. It is therefore interesting to find out whether the new models can improve the modelling capability of the vortical flows for such problems. The numerical tests were run at ten degrees of incidence at Mach number of 2.0 and at a Reynolds number of 1.2 million. The grid is a single block structured grid of $60 \times 85 \times 73$ in the streamwise, wall normal(radial) and circumferential directions respectively. It is a standard grid provided by a Garteur workshop and considered to be sufficiently clustered near the wall for the turbulence boundary layer resolution. The geometry and the wall skin friction lines obtained from the curvature model are shown in Figure 1.

Comparison of the Surface Pressure Distribution

In Figure 2, the surface pressure distributions are compared against the experimental data for the Degani-Schiff model, the Panaras model and the curvature model at streamwise stations at $x/D=5$, 7 and 9 respectively.

The two new models outperform the Degani-Schiff model consistently for all the three streamwise stations. The new models have picked up all the features in the experimental C_p distribution reasonably well. Remarkable improvements over the Degani-Schiff model can be found on the leeward side in the vortical flow region. Comparing the two new models, the curvature model seems to give a overall better results as judged by the experimental data.

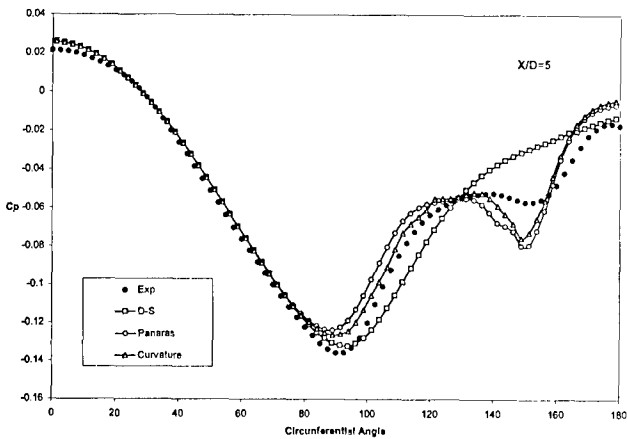
One can still observe the remaining discrepancies between the results from the new models and the experimental data. The second dip in the C_p distribution seems to have been exaggerated in the predictions at $x/D=5$ in the new models while the Degani-Schiff model misses this dip altogether. Apart from that, an almost constant small gap (about $\Delta C_p=0.005$) between the predicted C_p and the experimentally measured one can be seen even at the windward symmetry line, which may indicate a small systematic difference between the experiment and the computation.

Comparison of Flowfield

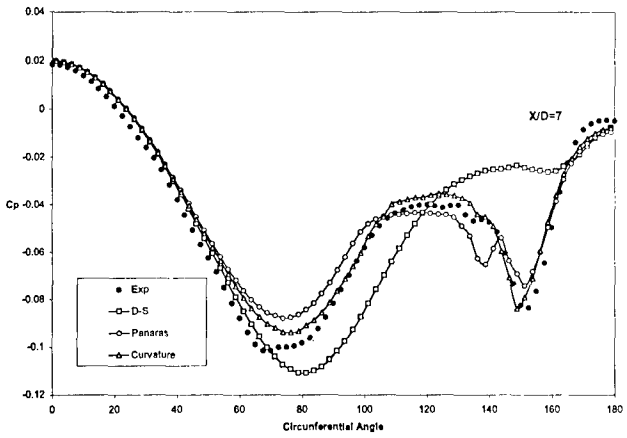
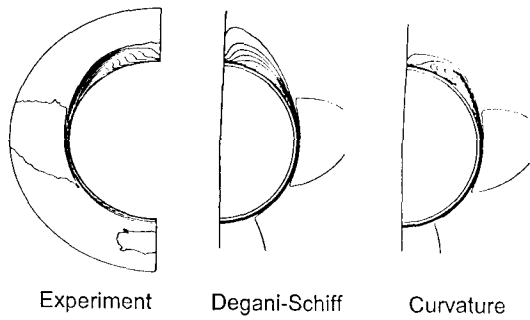
Figure 3 compares the Mach number contours from the experimental data and the computational results from the Dagani-Schiff model and the curvature model at $x/D=5$, 7 and 9. It confirms the capability of the curvature model in capturing flow features including the primary and secondary vortices and their core positions. The skin friction lines shown in Figure 1 illustrate clearly the primary and secondary separation lines (the convergent fish-bones) and the primary and secondary reattachment lines (the divergent fish-bones).

Difference in Model Length Scales

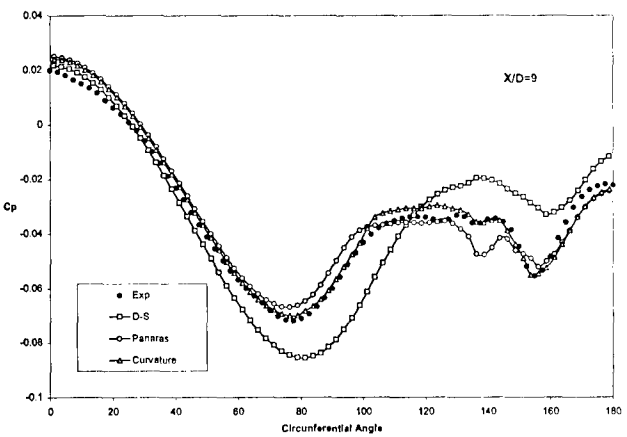
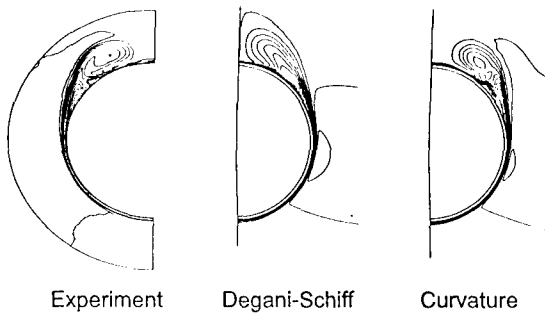
To illustrate how the length scale is picked up in the curvature model and its difference from that by the Degani-Schiff model, we plot the $F(\eta)$ distributions and their curvatures, κ , in Figure 5, for a selected number of rays in the vortical flow region at the $x/D=9$ streamwise location. These curves are based on the solution from the curvature model. As $F(\eta)$ reflects the moment of vorticity, a vorticity contour plot is shown in Figure 4 illustrating the selected rays. We have used a logarithm scale for the radial distance from wall, η , to have a better view of the behaviour of $F(\eta)$ in the attached boundary layers.



Mach Number Contours at $x/D=5$



Mach Number Contours at $x/D=7$



Mach Number Contours at $x/D=9$

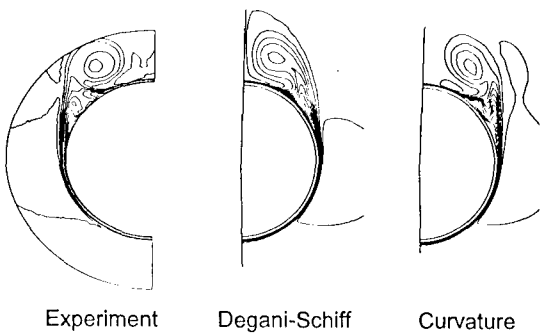


Figure 2. Wall pressure comparisons

Figure 3. Comparison of Mach number contours

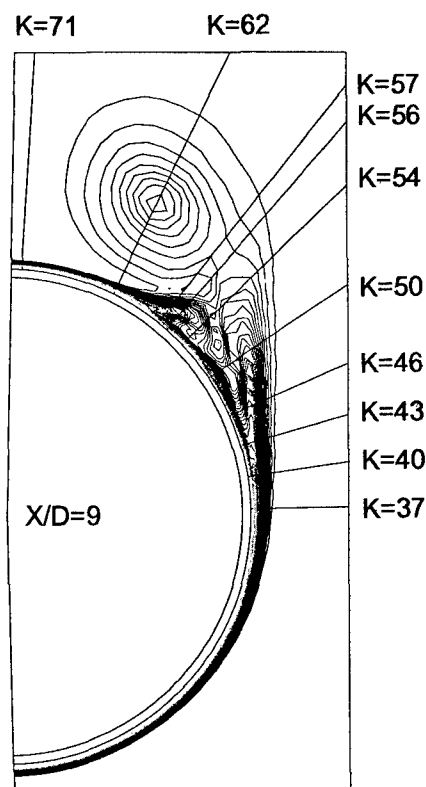


Figure 4. Vorticity contours and locations for F and κ profile plots

The vertical lines in both F and κ curves indicate the position picked by the curvature model for the length scale.

At $K=37$, the boundary layer from the windward side is attached. A typical distribution of the F function for an attached boundary layer without an overlaying vortical structure can be seen. There is no dispute on the length scale from any of the aforementioned models. The maximum F from the Baldwin-Lomax model, the first peak from the Degani-Schiff model and the minimum in the second negative region of the curvature coincide with each other.

At around $K=40$, the boundary layer coming from the windward side starts to separate. There should be a new boundary layer forming after the crossflow separation line coming from the leeward direction. This is reflected in the vorticity contour plot and in the second convex region and the second dip in the curvature. At this ray, the Degani-Schiff model would have picked up a length scale representing the separated boundary layer rather than the underlying attached boundary layer because the attached boundary layer does not give an identifiable peak.

This similar situation continues until around $K=50$ (covering $\sim 25^\circ$) when the Degani-Schiff model can identify the attached boundary layer as the first peak.

Before this point, huge differences exist between the length scales by the Degani-Schiff model and the curvature model. Practically in this region, there is no difference between the Degani-Schiff model and the Baldwin-Lomax model.

At $K=50$, the Degani-Schiff model will start to pick the right length scale as the curvature model while the Baldwin-Lomax model continues to pick the vortex-feeding sheet as the length scale.

However around the secondary separation $K=57$ and $K=56$, the Degani-Schiff model becomes problematic again. It will pick the secondary vortex feeding sheet rather than the underlying attached boundary layer.

Multiple peaks outside the boundary layer can be observed in the region where there are two overlaying vortices, both primary and secondary, as shown in $K=54$, 56 and 57 .

From $K=62$ onwards, the primary vortex and the underlying boundary layer are clearly separated and the Degani-Schiff model can pick the right length scale in this situation differentiating itself from the Baldwin-Lomax model.

Note that, in the Degani-Schiff model, the freezing of the η_{max} to the previous ray if no maximum in F can be found within the η_{cutoff} has little effects for the current case as the vortex-feeding sheet is within the η_{cutoff} distance. On the other hand, even the freezing is switched on, the attached boundary layer after the separation line tends to be much thinner than the boundary layer coming from the windward side and the frozen value for the length scale is still too large. This can be easily seen in Figures 4 and 5 for $K=37$ and $K=40$. Furthermore the freezing is difficult to be applied to the secondary separation region as the boundary layer comes from the reverse direction.

To summarise, the Degani-Schiff model picks higher values of η_{max} from the vortex-feeding sheet, i.e. the separated boundary layer, in the vicinity of the primary and secondary separation regions compared to those from the curvature model, which traces accurately the attached boundary layers. The problem with the Degani-Schiff model is caused by the fact that the attached boundary layer does not always give an identifiable peak. By looking for the *dip* in the curvature distribution, the curvature model overcomes this problem giving a meaningful length scale representing the attached boundary layer.

The Degani-Schiff model can be less problematic if the regions of unidentifiable boundary layer peak are

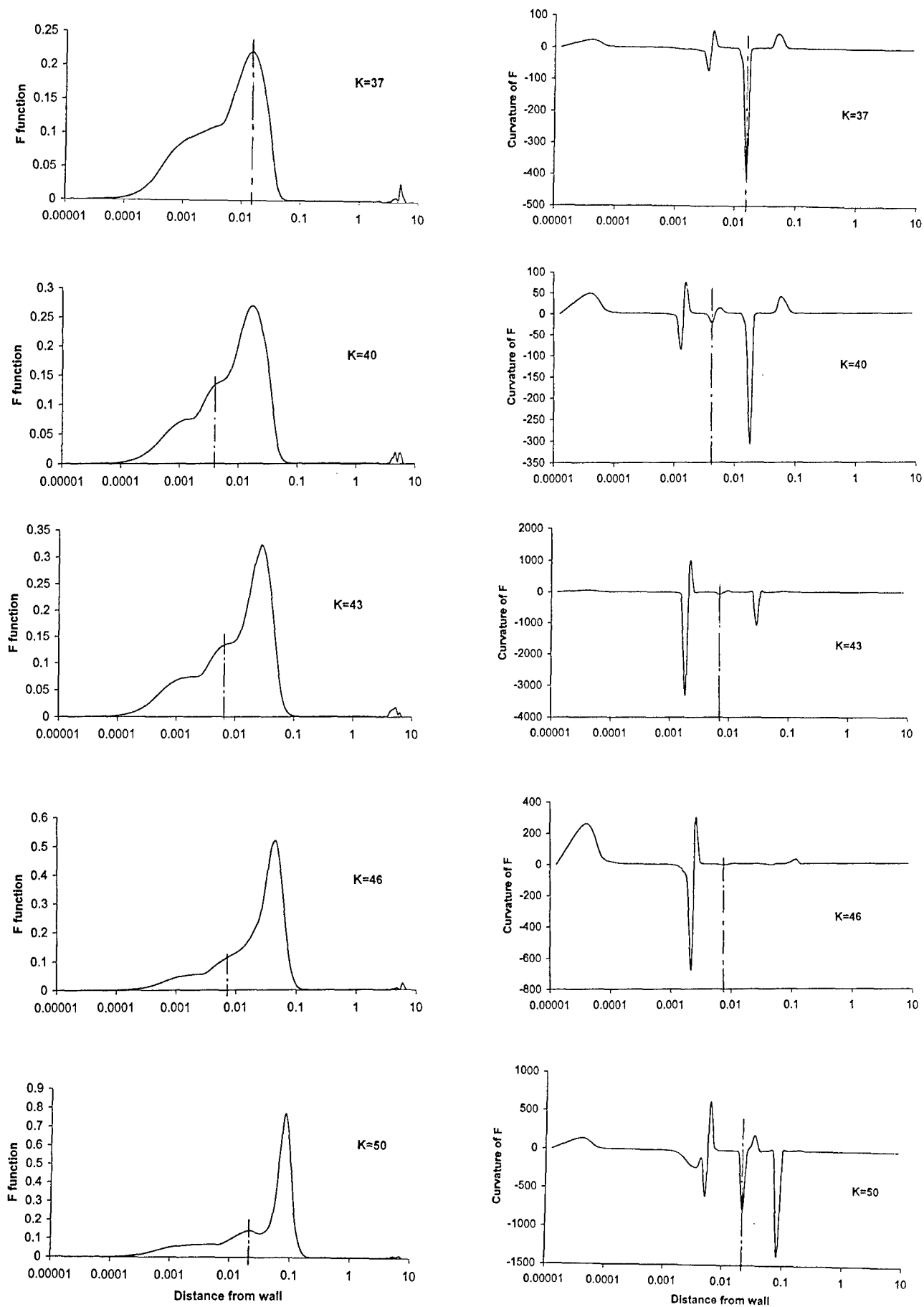


Figure 5. F functions and their curvature κ at selected rays.

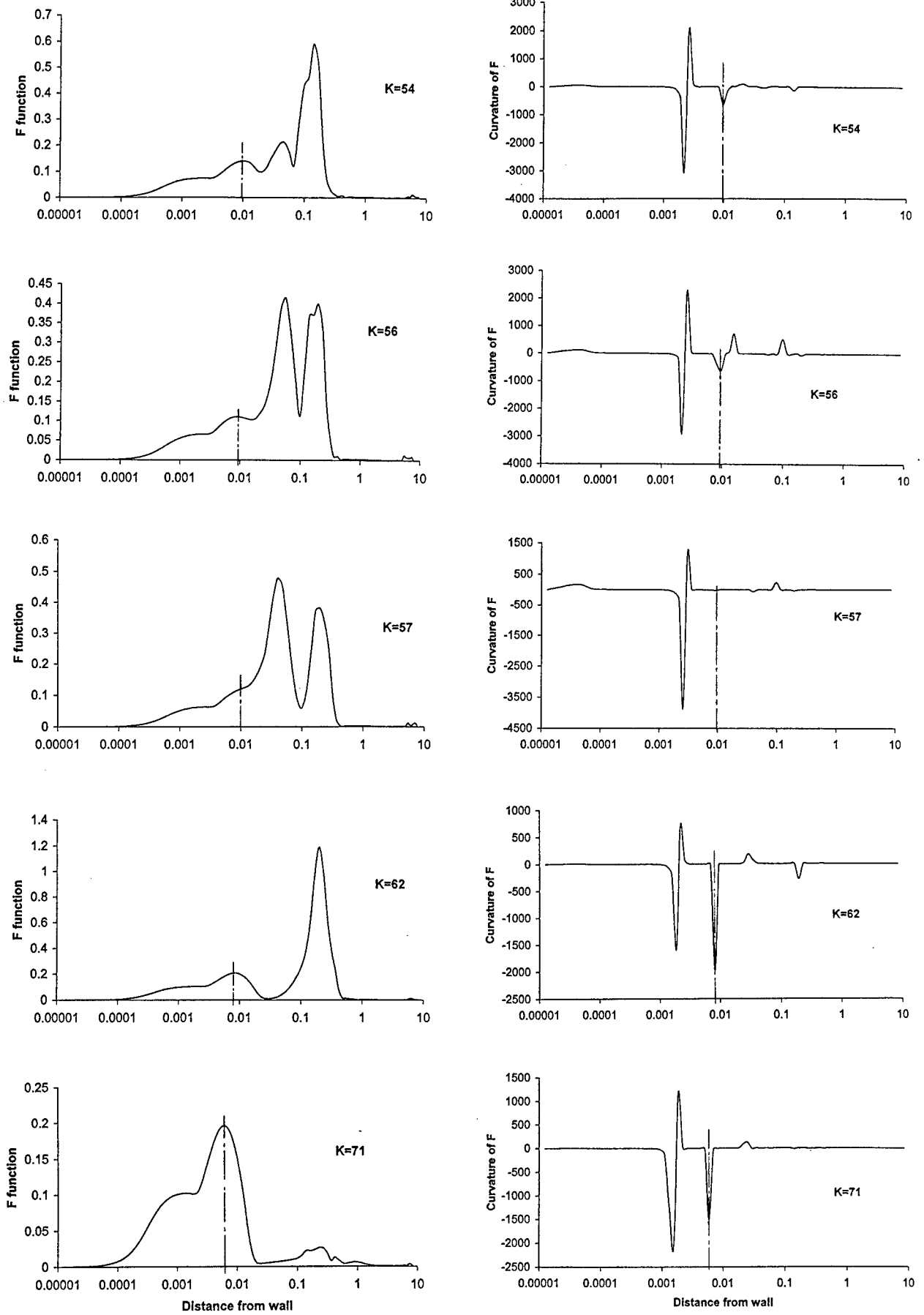


Figure 5. F functions and their curvature κ at selected rays (Cont.)

limited to very small areas. It is likely to be the case for higher angles of attack cases where the separated boundary layer tends to leave the surface more quickly and the attached boundary layer can form an identifiable peak earlier.

We remark that in the Panaras model the global maximum of $F(\eta)$ is used as in the original Baldwin-Lomax approach. The vortical flow structure is accounted for in the new wake function (20).

Conclusions

To address the weakness of the Degani-Schiff algebraic model for vortical flows, a curvature-based model has been proposed. It gives a clear and simple definition for the length scales of the attached boundary layers, including those under the primary, secondary or tertiary (if any) vortices. It therefore overcomes the uncertainties of the Degani-Schiff model in the crossflow separation line. For a complicated vortical flow test case involving multiple-vortex structures, the curvature model has produced much more reasonable results than those obtained from the Degani-Schiff model.

The Panaras model maintains the Baldwin-Lomax length scale for the separated boundary layer and modifies the wake function to get rid of the excessive turbulence in the vortical flow region. It has also improved the Degani-Schiff results providing reasonable results comparable with those from the curvature model. Some modifications are required for its application for vortical flows around slender bodies. However it was found that the choice of the reference point has a significant effect on the results and it is still an open question regarding to the choice of a proper reference conditions for such a model.

This research indicates that, if one is careful with the turbulence length scales in the algebraic model, reasonable results can be obtained for vortical flows around missiles without resorting to more expensive higher order turbulence models, which do not necessarily give better predictions.

Acknowledgements

The authors would like to thank Argyris Panaras, Trevor Birch and Scott Shaw for useful discussions during the research.

References

1. Vigneron, Y.C., Rakich, J.V. and Tannehill, J.C., "Calculation of supersonic viscous flows over delta wings with sharp subsonic leading edges", *AIAA Paper* 78-1137, July 1978.
2. Lawrence S.L. and Tannehill J.C., "Upwind algorithm for the parabolized Navier-Stokes equations" *AIAA Journal*, Vol. 27, No. 9, 1989, pp. 1175-1183.
3. Qin, N. and Richards, B.E., "Finite volume 3DNS and PNS solutions of hypersonic viscous flows around a delta wing using Oshers flux difference splitting", *Proceedings of a Workshop on Hypersonic Flows for Re-entry Problems*, Vol. 2, 1990, pp. 947-959.
4. Birch, T., Qin, N. and Jin, X., "Computation of supersonic viscous flows around a slender body at incidence", *AIAA Paper* 94-1938, 1994.
5. Shaw S. and Qin N., "A matrix-free preconditioned Krylov-subspace method for the PNS equations", *AIAA 36th Aerospace Sciences Meeting and Exhibit*, *AIAA Paper* 98-0111.
6. Baldwin B.S. and Lomax H., "Thin layer approximation and algebraic model for separated turbulent flows", *AIAA Paper* 78-0257.
7. Degani, D. and Schiff, L.B., "Computation of turbulent supersonic flows around pointed bodies having cross-flow separation", *J. Comp. Phys.*, V.66, 1986, pp173-196.
8. Osher, S. and Solomon, F., "Upwind difference schemes for hyperbolic systems of conservation laws", *Mathematics of computation*, Vol. 38 No. 158, 1982.
9. Degani D., Schiff B. and Levy Y. "Physical considerations governing computation of turbulent flows over bodies at large incidence", *AIAA Paper* 90-0096.
10. Panaras A.G. and Steger J.L. "A thin-layer solution of the flow about a prolate spheroid", *Z. Flugwiss.*, Vol. 12, 1988, pp. 173-180.
11. Panaras, A.G. "The effect of the structure of the swept shock-wave/turbulent boundary-layer interaction on turbulence modelling", *J. Fluid Mech.*, V.338, 1997, pp203-230.
12. Panaras, A.G., "Algebraic turbulence modelling for swept shock-wave/turbulent boundary-layer interactions", *AIAA J*, V.35, N.3, 1997, pp456-463.
13. Baudin, D., Champigny, P. and Pilon, J.A., "Boundary layer around a missile body at moderate angle of attack in supersonic flow: basic experiment and Navier-Stokes computations", *RTO Conference Proceedings on Missile Aerodynamics*, CP-608, Paper 19.

FILTERING ALGEBRAIC TURBULENCE MODELS FOR SUPERSONIC HIGH-INCIDENCE MISSILE FLOWS

M. Amato, G. Iaccarino

C.I.R.A., Centro Italiano Ricerche Aerospaziali, Via Maiorise - 81043 Capua (CE), Italy

Abstract

The application of algebraic turbulence models to the prediction of the vortical flows over missile configurations is presented in this paper. A review of available modifications of the Baldwin-Lomax model is presented; three new formulations are also discussed and tested. Two are based on a different link between the mean velocity gradients and the eddy viscosity; the third one uses some topological characteristics of the flow field to detect vortex tubes and to filter the eddy viscosity. The main advantage of these models with respect to other formulations presented in literature is the simplicity and the easy implementation even in industrial codes. The results obtained with the third model are in remarkable agreement with the experimental data.

1. Introduction

The prediction of supersonic flows at high incidence is a topic of considerable interest for the aerodynamic characterisation of missiles and military fighters⁽¹⁾. This flow regime includes streamwise and crossflow separations, shock/boundary-layer interactions, shock-to-shock interactions, etc. that are all inherently complex phenomena. A good knowledge of the

flow structure is determinant to correctly predict the aerodynamic forces; in fact, the computed forces and moments are highly sensitive to the strength, and position of the vortices due to the non-linearity of the phenomena involved. This is especially true for fighter aircraft where the extra lift coming from the vortices is exploited to improve maneuverability and agility.

The synergetic and integrated use of experimental and numerical techniques is mandatory to effectively design new configurations. In fact, CFD allows us to: individuate special flow field features before the wind tunnel testing, and concentrate measurements in specific areas; evaluate model loads; cross check with experimental results. Furthermore, CFD allows to overcome some restrictions typical of experiments: limited range of Reynolds number, limited amount of surface and field data, cost and complexity of the Wind Tunnel models, cost of operating Wind Tunnel. On the other hand, the use of CFD for practical applications requires massive use of super-computers and highly specialised engineers. Uncertainties on the reliability of CFD and specifically on the accuracy of Navier-Stokes solutions for certain flow regimes still exist. Main concerns are: the large amount of turn-around and computer time needed to perform an analysis; turbulence modeling; grid resolution; artificial dissipation effects.

Here, the focus is on turbulence modeling. In spite of the large effort put by the scientific community for developing new advanced turbulence models, simple algebraic turbulence models are still quite popular for practical applications^(2,3). This is due to different reasons: a) the implementation of new advanced models in large industrial codes is not straightforward and requires some time in order to get a validated reliable code; b) two equation models require a larger computational effort and, furthermore, they are generally less robust; c) the end-users show often a certain inertia in using newly developed codes; d) it is quite common to initialize the flow field for calculations with advanced turbulence models using solutions obtained with simple algebraic models; e) algebraic turbulence models are generally quite robust and relevant results are obtained for a large set of conditions for industrial applications. Moreover, the supersonic flow around a slender body at high angle of attack shows a typical two-layer boundary layer structure close the wall and, farther from it, a number of vortices that are essentially inviscid. This guarantees the applicability of model essentially derived for attached boundary-layer flows.

The standard algebraic model by Baldwin-Lomax⁽⁴⁾ and the modification by Degani-Schiff⁽⁵⁾ are successfully used to predict supersonic missile flows at low incidence. At higher incidence two-equation turbulence models seem much more appropriate,⁽⁶⁾ and recently some simulations of missile flows at high incidence have been carried out using a Low-Reynolds $k-\epsilon$ model⁽⁷⁾.

In this paper, a new way of *filtering* the Baldwin-Lomax turbulence model to better predict supersonic high incidence vortical flows is introduced. The key point is to evaluate the eddy viscosity using a filter based on the topological structures in the crossflow. The aim is to lower the dissipation introduced by the original turbulence model; in fact, a large value of the eddy viscosity is attained in the core of the primary vortex applying the standard formulation.

This new model is compared with: standard Baldwin-Lomax; Baldwin-Lomax with Degani-Schiff modification; Baldwin-Lomax with Marc Bredif⁽⁸⁾ modification, and a standard Low Reynolds $k-\epsilon$ model⁽⁶⁾. Two more models obtained from the Baldwin-Lomax by changing the turbulent velocity scale definition are introduced and tested even if the results are not reported because they are very similar to the standard model.

2. The Navier-Stokes Solver

The ZEN (Zonal Euler Navier-Stokes) flow solver is based on the multizone approach; three different sets of equations can be solved in each block: Euler, Thin-Layer Navier-Stokes (TLNS), Full Navier-Stokes (FNS) equations. In order to "close" the equations the perfect gas hypothesis is considered and, for turbulent flows, algebraic or two-equation models can be adopted. The discretisation of the flow equations is performed on a multiblock structured grid. The multiblock structure employed here has the peculiarity to be topologically unstructured (no requirement of one-block to one-block coupling). A finite volume cell centred scheme with explicit second and fourth order artificial dissipation is applied to build the discrete operator. The solution procedure is based on a time-like formulation, and a multistage explicit Runge-Kutta technique is used to march the solution in time toward the steady state. In order to accelerate convergence the local time stepping and implicit residual smoothing can be used together with a full multigrid approach. A large set of boundary conditions is available, including: adiabatic solid wall, solid wall with fixed temperature, solid wall with mass injection, slip solid wall, many free-stream conditions, inlet conditions for internal flows, propeller disk boundary conditions, inlet-outlet engine boundary conditions, etc. Different block-to-block coupling algorithms are available to take into account grid properties at the interfaces (smoothness, skewness, metric discontinu-

ity) and the governing equations employed in different blocks.

3. Turbulence Modeling

In the following a short description of the implemented turbulence models is given with particular care to the specific problems relative to the modeling of vortical flows and implementation difficulties.

Standard Baldwin-Lomax (BL)

The classical formulation of this model is well known from literature⁽⁴⁾; it is an isotropic, two-layer, algebraic eddy viscosity model. A profile of the eddy viscosity on a solid wall is a smooth blend of inner and outer formulations based on the definition of a length and velocity scales. The length scale (y_{max}) and velocity scale are determined searching, normally to the solid wall, for the (absolute) maximum of a function defined as:

$$\mathcal{F}(y, P) = y P (1 - \exp(-y^+/A))$$

where y^+ is the viscous wall distance and A is a constant⁽⁴⁾. The quantity P is obtained from the mean velocity field; in particular, it is assumed to be the vorticity magnitude:

$$P = ||\nabla \times \underline{V}||$$

where \underline{V} is the mean velocity vector. The problem of the standard model, when dealing with vortical flows, is that the function \mathcal{F} shows a first peak in the boundary layer and a second larger one in the vortex core; if the absolute maximum is picked incorrect turbulent scales are determined yielding to a very large eddy viscosity. Thus the computed flow field is smeared and important flow phenomena can be washed out from the numerical solution.

Degani-Schiff modification (DS)

In order to avoid spurious maxima of the function \mathcal{F} , Degani and Schiff proposed a filtering of the original model. The procedure is based on two successive steps. In the original

work by Degani and Schiff⁽⁵⁾: "a peak is considered to have been found when the value of \mathcal{F} drops to 90% of the local maximum value". When a single maximum is present (attached boundary layers at windward side) the procedure is straightforward. On the other hand, for separated vortical flows the presence of local maxima (together with spurious numerical wiggles) makes the choice of the proper one more complex. The second step is based on the application of a smoothing criterion to the computed length scale by the introduction of the so-called *cut-off* value, y_{co} . This smoothing is effective close to the separation lines; in fact, in these regions, the first local maximum of \mathcal{F} - within the boundary layer - is close (in the radial direction) to the second one - corresponding to the vortex core - thus leading to the failure of the maximum searching procedure described above. In this case, sweeping in the circumferential direction a jump (in the y_{max} location) would be found. The cut-off criterion assumes as correct length and velocity scales those detected at the previous station in the windward direction. Therefore the BL function \mathcal{F} is considered as:

$$\mathcal{F} = \mathcal{F}(y_{co}, P)$$

A disadvantage of this model is that it is not straightforward to be implemented in a general multiblock solver when the windward and leeward directions are not implicitly defined. Due to this problem, an alternative formulation of the DS model was implemented in the ZEN flow solver. The cut-off filtering was overcome by introducing a spline-biased smoothing of the \mathcal{F} function. By this way, local maxima due to numerical wiggles are eliminated, and, moreover, the failure of the original search procedure is avoided just picking the first maximum of the smoothed function \mathcal{F} .

Marc Bredif modification (MB)

An alternative way of filtering the Baldwin-Lomax model is to limit the search for the maximum of \mathcal{F} within a fixed distance from the wall that can be roughly evaluated in advance as the

boundary layer thickness⁽⁸⁾, δ . In particular, the BL function is defined as:

$$\mathcal{F} = \mathcal{F}(y_\delta, P)$$

where y_δ is the minimum distance between y and δ . Due to the uncertainties of this estimation, this approach can be regarded as an engineering approach to apply the Baldwin-Lomax model to vortex dominated flows. Nevertheless, it can be effective and easy to be coded even if it requires a user-defined parameter (δ) that has to be changed and optimized for every flow condition tested.

Crossflow Vorticity biased BL (CVBL)

The basic idea of this modification is to derive the function \mathcal{F} from a filtered vorticity field. In particular, it is assumed that the streamwise component of the vorticity, Ω_S , does not contribute to the eddy viscosity. This means that outside the boundary layer the cross components (radial and circumferential) of the vorticity approach to zero, whereas Ω_S attains its maximum value in the vortex core. In this case, the function \mathcal{F} depends on y and \tilde{P} :

$$\mathcal{F} = \mathcal{F}(y, \tilde{P})$$

where

$$\tilde{P} = \|(\nabla \times \underline{V}) - \underline{\Omega}_S\|$$

By this way no user-defined parameter (as the Degani-Schiff cut-off value) has been introduced, and the approach should be applicable to flow featuring crossflow separations straightforwardly.

Velocity Gradient biased BL (VGBL)

The rationale behind this model is the definition of a different turbulent velocity scale with respect to the one used in the standard Baldwin-Lomax model. In the BL model the mean velocity field affects the function \mathcal{F} and, therefore, the turbulent velocity scale, through the vorticity magnitude, P . In the present approach, the invariants of the mean velocity field are used instead of P .

Then, the new velocity scale is computed using the BL function \mathcal{F} defined as:

$$\mathcal{F} = \mathcal{F}(y, \bar{P})$$

where:

$$\bar{P} = \sqrt{(\nabla \underline{V})_{\circ}^S : (\nabla \underline{V})_{\circ}^S}$$

where the pedex \circ indicates the deviatoric component of the tensor whereas the apex S indicates its symmetric part. This term corresponds to the production of the turbulence kinetic energy due to the mean velocity gradients; moreover, this expression is used in the two-equation turbulence models as described in the dedicated subsection.

MG formulation

The aim is to handle separated vortical flows as well as attached flows without introducing any additional limiter or *cut-off* value as in the DS and MB modifications. Moreover, the driving principle is the simplicity of the implementation in a multiblock general-purpose flow solver. In order to achieve this objective, the original BL criterion for analyzing the \mathcal{F} function is retained (e.g. search for absolute maximum) without introducing any additional logic, such as test on the distance from the wall (MB) or checks on the absolute or relative maxima (DS). This new formulation detects the local flow feature, as boundary layer or vortical region, automatically.

Recently, large efforts are being spent by the research community to detect and analyze the structures of turbulent flows. In fact, in the open literature, many studies are presented on the following topics: fluid mechanics of coherent structures in near-wall flows⁽⁹⁾; turbulence modeling based on structures⁽¹⁰⁾; flow visualization of vortices in turbulent flows⁽¹¹⁾. The topological analysis of a vortical flow over a missile configuration was carried out by Delery⁽¹²⁾ and, afterwards by Grasso *et al.*⁽⁷⁾ with the aim of verifying the relationship between the topological critical points (nodes, saddle points, etc.) in experimental and numerical flow fields, respectively.

In the present work, the objective is to make use of topological information to correct (*filter*) the Baldwin-Lomax behavior in the regions dominated by the presence of intense vortices where a high level of eddy viscosity is introduced. This is due to the computation of spurious maxima generated by the large vorticity induced by a vortex.

The appropriate maximum must be selected inside the boundary layer and outside these vortical regions (*vortex tubes*). The identification of these tubes is performed following the work by Chong *et al.*⁽⁹⁾. The eigenvalues of the velocity gradient tensor (A_{ij}) characterize the topological structure of the flow field; therefore, the detection of a vortex tube is based on the evaluation of the discriminant of the characteristic equation of A_{ij} . In particular, we were not interested in characterizing the three-dimensional flow field structures but in identifying the crossflow topology only. Then, we compute the discriminant (Δ_c) of the crossflow velocity gradient and, according to its sign we filter the function \mathcal{F} of the standard Baldwin-Lomax model.

Formally, the turbulence scales are computed by defining the function

$$f = f(\mathcal{F}, \Delta_c)$$

where \mathcal{F} is the standard BL function. The filter f is such that the local maximum of \mathcal{F} is retained only if Δ_c is positive at the same location.

Low Reynolds k - ϵ (KE)

A two-equation model was successfully applied to supersonic vortical flows around an ogive-cylinder⁽⁷⁾. In this case the length and velocity scales are obtained using two differential equations for k and ϵ . The near wall turbulence is treated using a damping function approach based on the wall distance⁽¹³⁾. A higher accuracy should be reached with respect to the algebraic models because the velocity scale is not deduced directly from the mean velocity field. In particular, the velocity scale is computed by means of the turbulent kinetic energy, k and the

production of k is modeled using the invariants of the mean velocity gradient.

$$P_k = \mu_t (\nabla \underline{V})_o^s : (\nabla \underline{V})_o^s$$

It is worth noting that, for attached transonic boundary layers flows⁽¹⁴⁾, the production of the turbulent kinetic energy is usually modeled by using a simplified formulation:

$$P_k = \mu_t (||\nabla \times \underline{V}||)^2 = \mu_t P^2$$

4. Results

The numerical results are presented for the axisymmetric ogive-cylinder missile shown in Fig. 1. This configuration was experimentally tested by Delery *et al.*⁽¹²⁾ in supersonic regime at different angles of attack; the transition was triggered close to the body apex in the experiments. In the numerical calculations the assumed flow conditions are reported in Table 1 and the transition was fixed at the location indicated in Ref. 12. The computational grid was made up of ≈ 360000 cells with 7560 cells in each crossflow plane and 60 stations in the streamwise direction; in particular, in the circumferential direction 73 uniformly distributed grid points were used. This grid was generated by ONERA and obtained in the frame of the GARTEUR Action Group AG-24⁽¹⁵⁾.

The main objective of the numerical calculations is to test the new developed models (MG, CVBL, VGBL) and to compare the results to those obtained using the other turbulence models presented in section 3 for the case $\alpha = 10$ deg. The results for the models CVBL and VGBL are not presented because they are very similar to those obtained using the BL model. Therefore, the focus of the discussion will be on the MG formulation.

The first step of the present numerical analysis was devoted to an *a priori* test of the flow topology identification procedure discussed above. To this aim, we used a laminar solution to compute the discriminant Δ_c in some crossflow sections. In Fig. 2 we report the results

obtained at the station $x/D = 9$ for the cases $\alpha = 0$ deg and $\alpha = 10$ deg. The proposed *sensor* successfully detects the vortex tubes present in the flow field; in particular both primary and secondary vortices are captured. In Fig. 3, an additional verification of the proposed approach is reported; the BL and MG results are compared for the case $\alpha = 0$ deg in terms of the eddy viscosity distributions. As expected, no differences are appreciable and we can conclude that the MG model recovers the standard formulation when no vortices are present.

In Fig. 3, the crossflow distribution of the total pressure at $x/D = 8$ are presented for five turbulence models (BL, DS, MB, MG, KE) and compared to the experimental data. In this figure the total pressure scale ranges from 0 to 1. The corresponding eddy viscosity distributions are reported in Fig. 4.

As well known, the BL model washes out the superscript vortex due to the huge eddy viscosity introduced in the vortex core. The widely adopted DS modification corrects the misbehavior of the original formulation and compares very well with the experimental results. In fact, the primary vortex is accurately predicted in terms of position and pressure level. The results obtained applying the MB and the KE models present a highly developed vortical structure in the considered cross-section that has no equivalent in the measured data. This mismatch is due to the low levels of eddy viscosity attained with both models.

Finally, the MG model performs remarkably well with respect to the experiments; the comparison with the DS modification is satisfactory in terms of both total pressure and eddy viscosity. In particular, the MG and DS turbulent viscosities are in impressive agreement in spite of the very simple logic underlying the newly introduced model.

In Fig. 6 and in Fig. 7, a global view and a close-up of crossflow streamlines at $x/D = 8$ are reported, respectively. The experimental streamlines are obtained using only 20×20 data points and, therefore, their quality is not high.

However, the location of the primary vortex is clearly identified, whereas one or two secondary vortices seem to be present close to the body surface. The correct topological structure (three vortices) is resolved using the MB and KE models, but the position and the intensity of the primary recirculation and, consequently, of the secondary vortices, is not accurate. On the other hand, the DS and MG models predict the location of the main vortex very well; moreover, a secondary recirculation is correctly detected. The BL result shows a lower primary vortex strength with respect to the other results as can be inferred from the total pressure distributions in Fig. 4. In addition, no secondary separation are detected on the body due to the large dissipation introduced.

It is worth noting that the computational cost of the BL model and of the modifications presented and tested in this work is very similar; the main difference is the effort needed to code one or another model. From this point of view, starting from an implemented BL model, the MB and MG approaches are very easily introduced even in complex industrial solvers.

An additional analysis of the influence of the discretization formulas used for the velocity derivatives needed for the evaluation of the vorticity (in the BL \mathcal{F} function) and the crossflow discriminant was carried out. Two approaches were tested: in the first one, only the differences of the velocity along the grid lines in the normal-to-the-wall direction were retained (TLNS approximation) whereas, in the second one all the terms are considered (FNS approximation). The conclusion is that no differences are appreciable in the solution when the vorticity is evaluated in the approximated form, whilst for a correct analysis of the crossflow topology the discriminant computation must be performed using the FNS formulation.

5. Conclusion

In this work a modification of the algebraic turbulence model of Baldwin-Lomax is proposed

and tested for the calculation of the supersonic vortical flow over a missile body. The basic idea of this approach is to detect the flow features (i.e. vortices) using the discriminant of the crossflow velocity gradient tensor and, then, to filter the Baldwin-Lomax model. By this way, the large eddy viscosity introduced by the original model is limited. The results are compared to a set of experimental data; moreover, an overview of known formulation of algebraic and differential models for vortical flows is reported. The analysis of the results shows that the new model performs very well with respect to the experimental data and it is consistent to the well-known Degani-Schiff formulation. The considerable advantage is its simplicity to code in a complex industrial flow solver due to the use of local flow quantities instead of *crossflow history effects*. Moreover, no user-defined cut-off values are required.

References

1. N. M. Chaderjian, "Comparison of two Navier-Stokes Codes for Simulating High-Incidence Vortical Flow", *J. of Aircraft*, Vol. 30, No. 3, 1993
2. T. J. Birch, N. Qin, X. Jin, "Computation of Supersonic Viscous Flows Around a Slender Body at Incidence", AIAA 94-1938, 1994
3. P. Bellomi, M. Amato, *et al.*, "Computational Analysis for Predicting Aerodynamic Performances of the VEGA Lightsat Launcher", AIAA 97-2301, 1997
4. B. S. Baldwin, H. Lomax, "Thin Layer Approximation and Algebraic Model for Separated Turbulent Flows", AIAA 78-257, 1978
5. D. Degani, L. B. Schiff, "Computation of Turbulent Supersonic Flows around Pointed Bodies Having Crossflow Separation", *J. Of Computational Physics*, Vol. 66, pp. 173-196, 1986
6. H. Deniau, A. Lafon, "Progress in the Development and Validation of Turbulence Models for the Computation of 3D Supersonic Flows with Crossflow Separation", AIAA 95-0090, 1995
7. F. Grasso, G. Iaccarino, "On the Influence of Crossflow and Turbulence on the Missile Flow around a Supersonic Missile", *J. of Spacecraft and Rockets*, Vol. 35, No. 1, 1998
8. M. Bredif, *Private Communication*
9. M. S. Chong, *et al.*, "A Study of the Turbulent Structures of Wall-Bounded Shear Flows", *Proc. of 1996 CTR Summer Program*, pp. 383-404, 1996
10. S. C. Kassinos, W. C. Reynolds, "Advances in Structure-Based Turbulence Modeling", *1997 CTR Annual Research Briefs*, pp. 179-194, 1997
11. D. C. Banks, B. A. Singer, "Vortex Tubes in Turbulent Flows: Identification, Representation, Reconstruction", *Proc. Visualization 94*, Washington D.C., 1994
12. J. Delery, D. Pagan, P. Molton, "Basic Experiment on a Superscript Vortex Flow around a Missile Body", *J. of Spacecraft and Rockets*, Vol. 29, No. 3, 1992
13. H. Myong, N. Kasagi, "A New Approach to the Improvement of $k-\epsilon$ Turbulence Model for Wall Bounded Shear Flows", *JSME Intern. J.*, Serie 2, Vol. 33, No. 1, pp. 63-72, 1990
14. F. R. Menter, L. R. Rumsey, "Assessment of Two-equation Turbulence Models for Transonic Flows", AIAA 94-2343, 1994
15. GARTEUR AG-24, "Missile Aerodynamics: Navier-Stokes Calculations of the Supersonic Flow About Slender Configurations", Garteur Lim. Doc., 1996

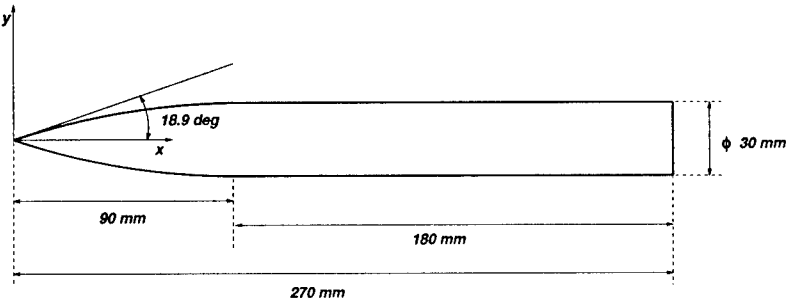


Figure 1 - Sketch of the Geometry

Table 1 - Flow Conditions

M_∞	2.0
Re_∞/m	5.33×10^6
T_∞°	330 K
p_∞°	50000 Pa
α	10 deg
D	0.03 m

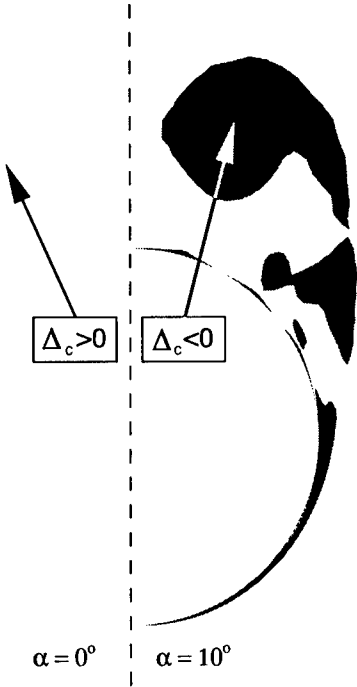


Figure 2 - Crossflow Discriminant (Δ_c) at $x/D=9$

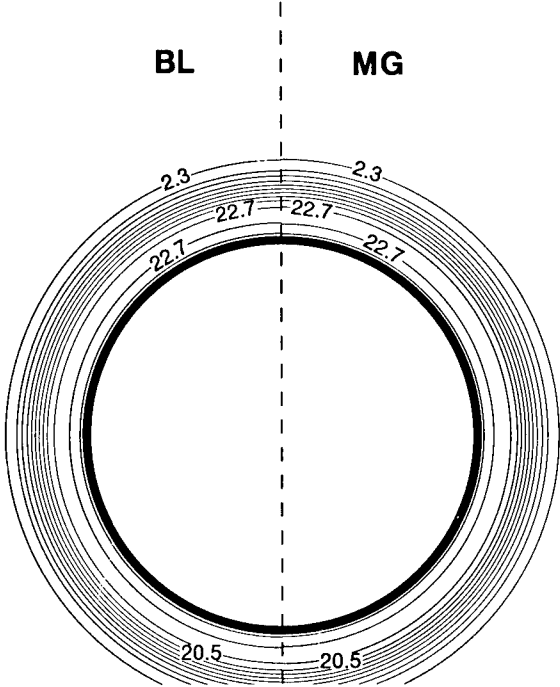
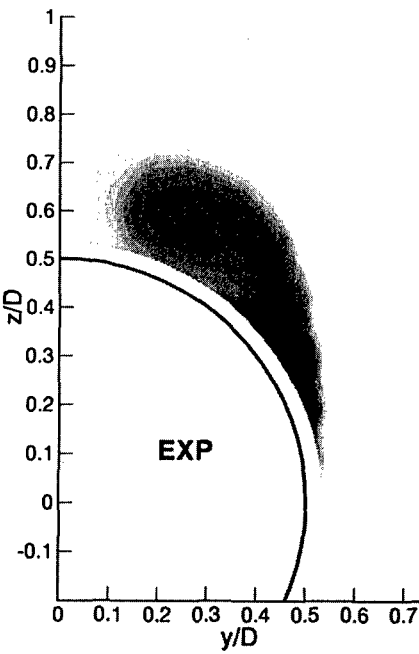
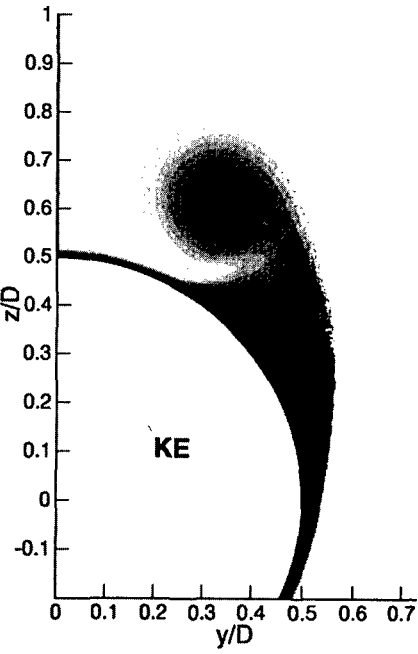
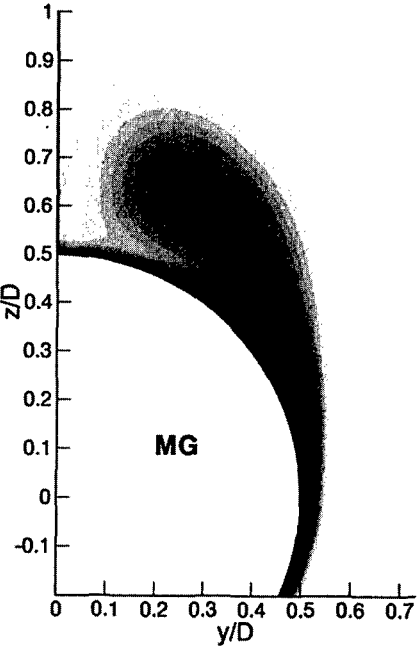
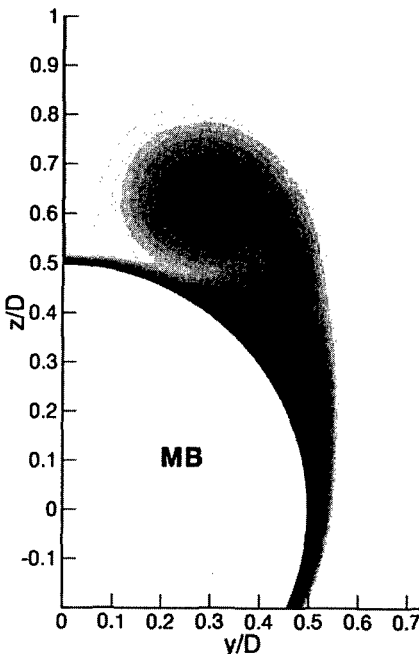
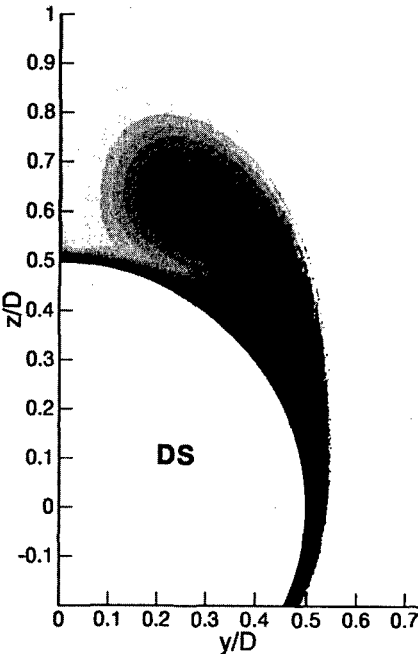
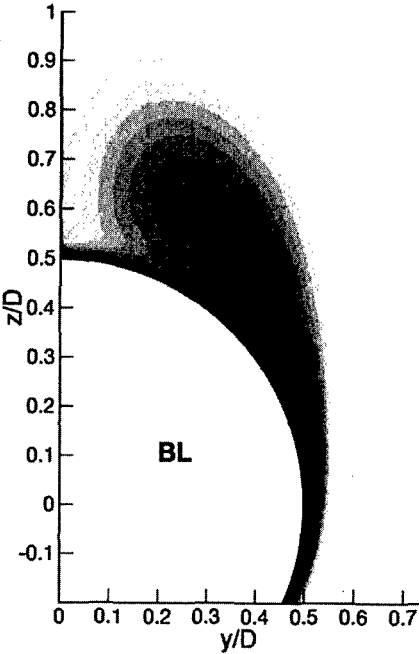
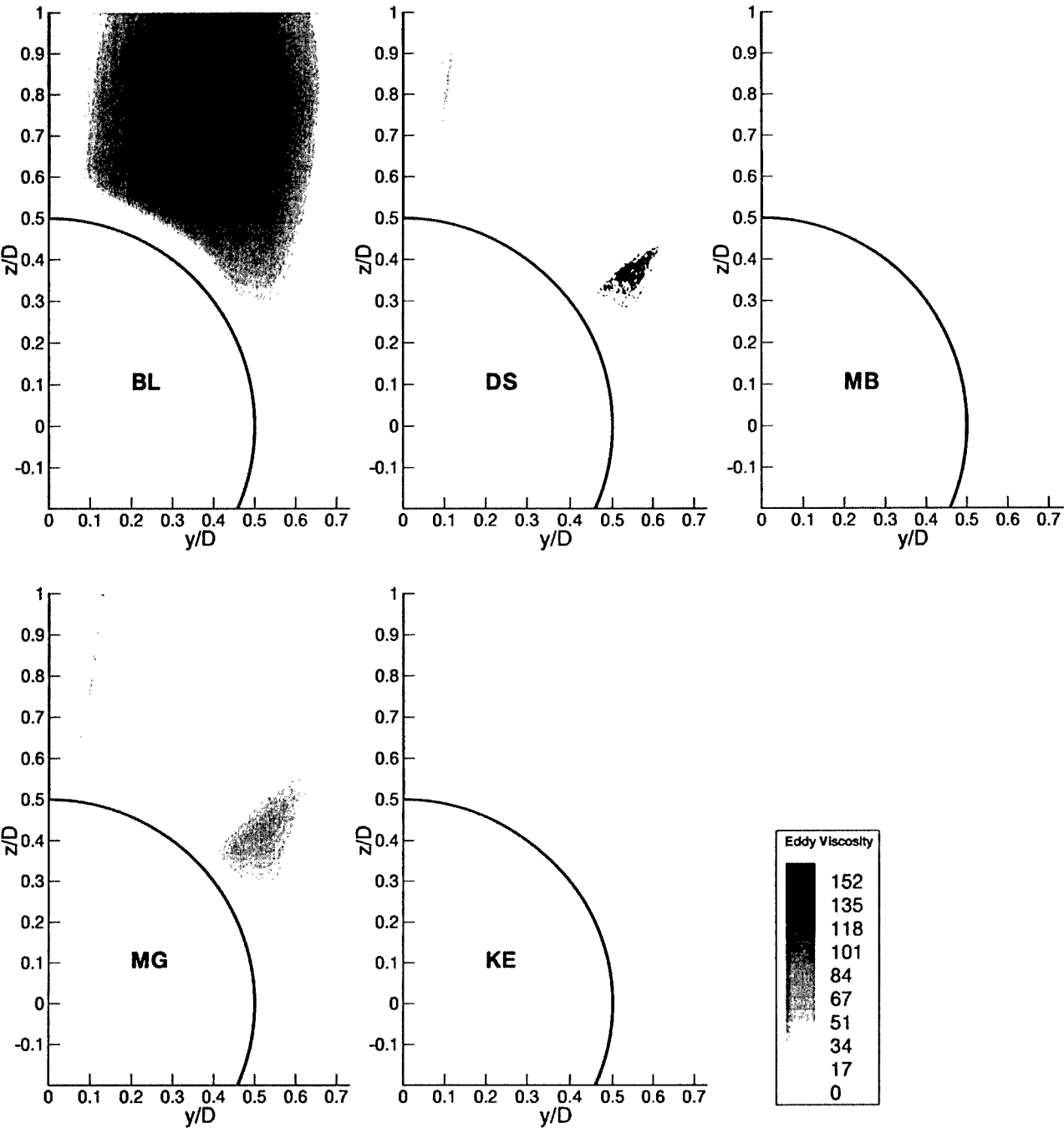


Figure 3 - Eddy Viscosity Distributions at $x/D=8$
 $\alpha = 0$





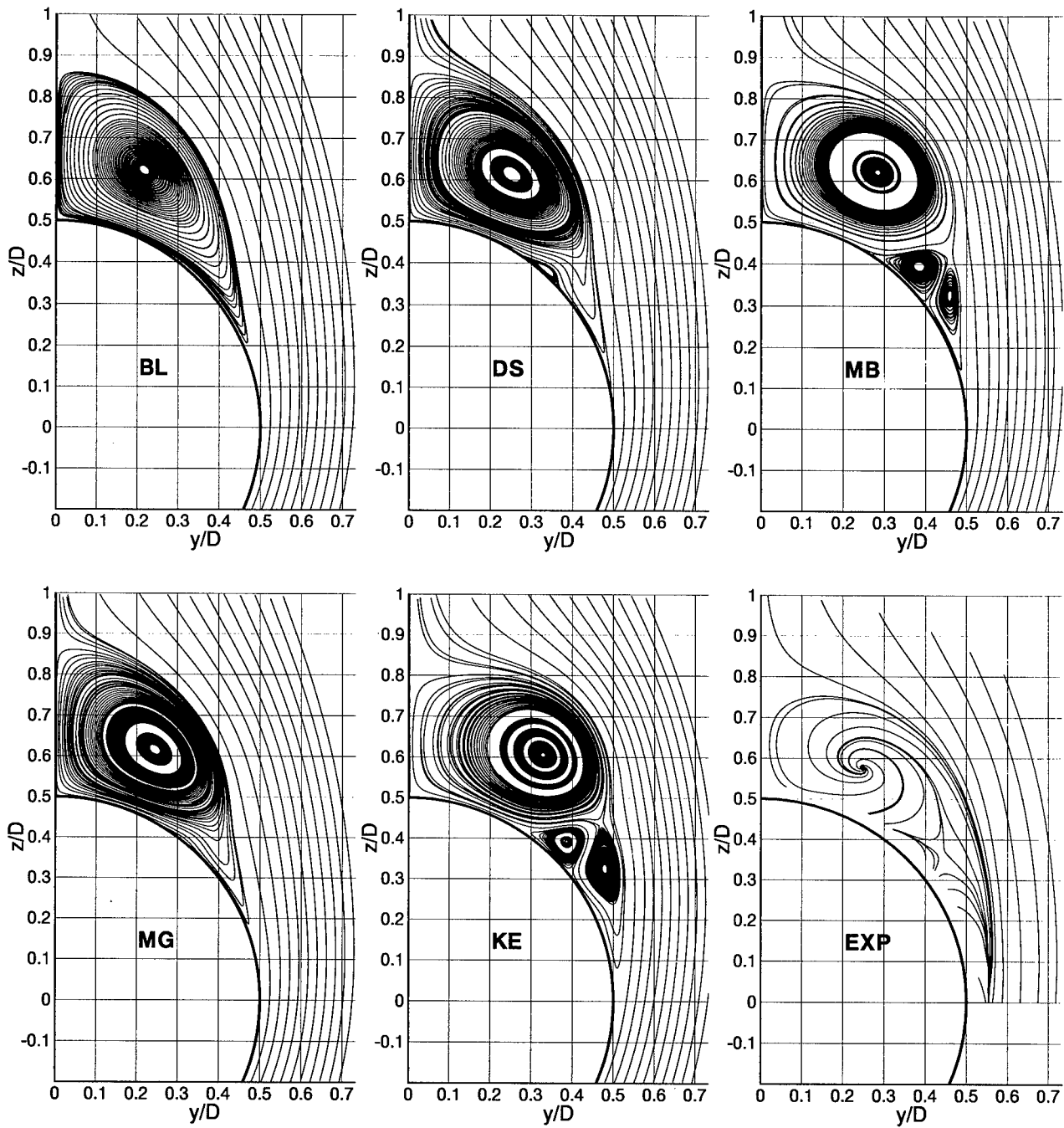


Figure 6 - Crossflow Streamlines at $x/D=8$

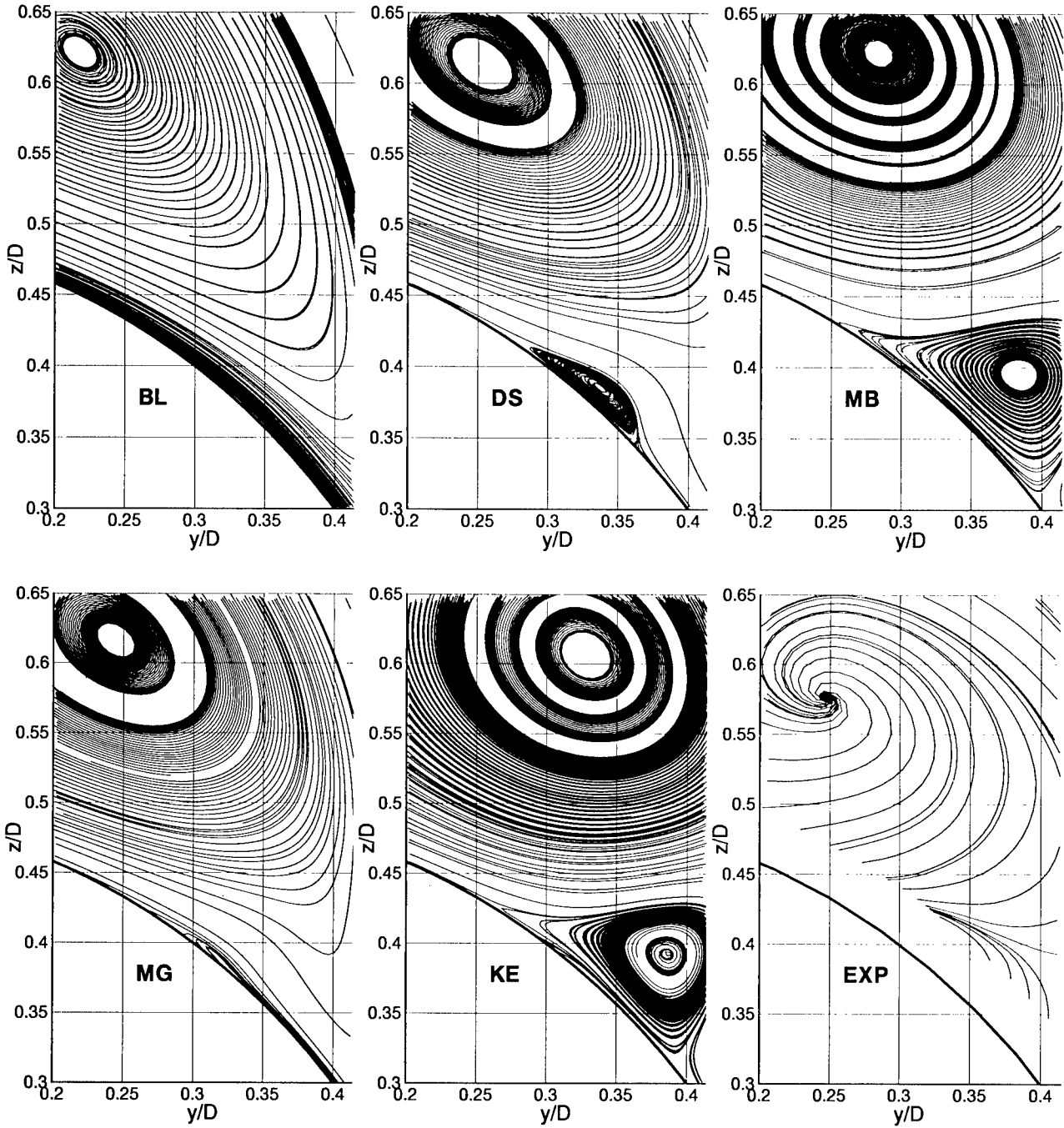


Figure 7 - Close up of Secondary Vortices at $x/D=8$

Simulation of laminar and turbulent flow over an ogive cylinder

E. van der Weide and H. Deconinck
von Karman Institute for Fluid Dynamics
Waterloose Steenweg 72
Sint-Genesius-Rode, Belgium

Abstract

The paper deals with the simulation of laminar and turbulent flow over an ogive cylinder, using an unstructured grid solver based on multidimensional upwind residual distribution schemes. For the turbulent computation use has been made of the two equation SST model of Menter, and implementation details are discussed. The solver uses a parallel implicit time integration on partitioned subdomains, where message passing and parallel linear systems solvers are based on the AZTEC library of Sandia laboratories. The first computation is laminar and turns out to be at the limit of unsteadiness, suggesting that the test conditions are transitional in reality. The second turbulent computation is steady and results for the pressure distribution compare well with the experimental data obtained at ONERA. Significant differences between the laminar and turbulent computation are found in the vortex pattern developing on the leaside.

1 INTRODUCTION

In this paper we report on the simulation of high Reynolds number viscous flows over an ogive cylinder at supersonic freestream conditions. The basic Navier-Stokes solver is an unstructured grid solver based on monotone multi-dimensional upwind residual distribution schemes:

- The *multidimensional flux balance* over a tetrahedral cell is decomposed into characteristic components, thus generalizing the 1D characteristic field decomposition (*flux difference splitting*) used in Godunov schemes.

- A *conservative linearization* ensures that the discretized characteristic components sum up to the conservative flux balance over the cell.

- Nonlinear monotone and second order *downwind distribution schemes* are used to update the vertices of the cell for each characteristic contribution, thus generalizing Lax-Wendrov type residual distribution schemes as proposed e.g. by Ni, or Morton and his collaborators.

The same discretization has proven to be robust and accurate for solving the turbulence transport equations. The parallel time integration on partitioned subdomains is based on an implicit Newton iterative method. The linear systems are solved with a preconditioned GMRES technique. For this purpose and also for the communication of boundary information, use is made of AZTEC, a parallel linear algebra library developed at Sandia laboratories. Due to the compactness of the stencil, communication overhead is minimal.

For the turbulence modelling, use has been made of the Menter SST model, which is a blending of the $k-\omega$ with the $k-\epsilon$ model, with the aim of obtaining the favorable properties of the $k-\omega$ model (compared to $k-\epsilon$) in the

wall region, while avoiding its freestream dependence by switching to $k-\epsilon$ at the boundary edge.

Two computations have been performed, one laminar and one fully turbulent, at the same freestream Mach number of 2, angle of attack of 10° and Reynolds number $Re_{\infty,D}/m = 5.33 \cdot 10^6/m$, for which experimental results are available from ONERA (J. Delery). Significant differences between the laminar and turbulent computation are found in the vortex pattern developing on the leaside. For the turbulent flow, the skin friction lines converge to a common three-dimensional separation line inducing the development of one vortex on each side of the ogive cylinder. For the laminar case two separation lines develop, and consequently two counterrotating vortices are found on each side. The laminar solution becomes asymmetric and unstable in the region of the afterbody, especially if the mesh is refined from 390965 to 850196 meshpoints. Both computations demonstrate the capabilities of the unstructured grid solver for high Reynolds number supersonic flows.

2 UPWIND DISCRETIZATION FOR THE INVISCID TERMS

The spatial discretization of the convective terms is based on a cell vertex approach on tetrahedral grids, with the unknowns located at the vertices of the tetrahedra. Upwind matrix distribution schemes have been developed on the compact stencil of nearest neighbours. These schemes allow sharp and monotonic shock capturing without extending the stencil [18]. Here, only a brief summary is given of the residual distribution schemes used in this work.

Consider first the unsteady hyperbolic system of Euler equations in quasilinear form, with U the conservative variables density, momentum and total energy:

$$\frac{\partial U}{\partial t} + A \frac{\partial U}{\partial x} + B \frac{\partial U}{\partial y} + C \frac{\partial U}{\partial z} = 0. \quad (1)$$

Assume further that this system has been linearized over a tetrahedral computational cell T (as discussed in section 2.3), such that the Jacobian matrices A , B and C are constant. The geometry of the cell is given in figure 1. Using Gauss' theorem the residual in integral form of equation (1) over cell T is

$$\begin{aligned} \Phi^T &= \iint_T \left(A \frac{\partial U}{\partial x} + B \frac{\partial U}{\partial y} + C \frac{\partial U}{\partial z} \right) d\Omega \quad (2) \\ &= - \oint_{\Gamma} (A n_{x_{int}} + B n_{y_{int}} + C n_{z_{int}}) U d\Gamma, \quad (3) \end{aligned}$$

where Φ^T is the vector containing the cell residuals, Γ is the boundary of the control volume T and $n_{x_{int}}$, $n_{y_{int}}$

and $n_{z,i}$ are the x , y and z component of the inward normal respectively. In the residual distribution approach, the contour integral is evaluated using the unknowns stored at the corners, and fractions of Φ^T are sent to the cell vertices. Assembling the contributions from all cells the nodal update is obtained. The semi-discretization in point i is then given by

$$\frac{dU_i}{dt} = -\frac{1}{V_i} \sum_T \beta_i^T \Phi^T. \quad (4)$$

Here, V_i is the volume of the median dual cell of node i and β_i^T is the distribution matrix of cell T to node i . For consistency one has $\sum_j \beta_j^T = I$, where the summation extends over all 4 vertices of a tetrahedron.

Assuming a linear variation of U , or equivalently using the trapezium integration rule, the cell residual Φ^T , equation (3), can be written as

$$\Phi^T = \sum_{i=1}^4 K_i U_i, \quad (5)$$

where U_i is the solution at vertex i and K_i the Jacobian based on the face normal \hat{n}_i :

$$K_i = \frac{1}{3} (A n_{x,i} + B n_{y,i} + C n_{z,i}), \quad (6)$$

with $n_{x,i}$, $n_{y,i}$ and $n_{z,i}$ the x , y and z component of the inward normal \hat{n}_i to the face opposed to vertex i , scaled with the area, see figure 1. The Jacobians K_i can be written as

$$K_i = R_i \Lambda_i L_i, \quad (7)$$

where the columns of R_i contain the right eigenvectors, Λ_i is a diagonal matrix of the eigenvalues and $L_i = R_i^{-1}$. As the system (1) is hyperbolic, the matrices R_i , Λ_i and L_i will be real. The matrices K_i^+ and K_i^- are given by

$$K_i^+ = R_i \Lambda_i^+ L_i, \quad K_i^- = R_i \Lambda_i^- L_i. \quad (8)$$

Here Λ_i^+ contains the positive and Λ_i^- the negative eigenvalues, $\Lambda_i^\pm = \frac{\Lambda_i \pm |\Lambda_i|}{2}$. The properties of the different schemes are determined by the way β_i^T is defined. Important properties are:

- **Positivity**

A monotonic scheme can be obtained by demanding positivity. Suppose that the numerical solution at mesh point i is U_i . Then the positivity property

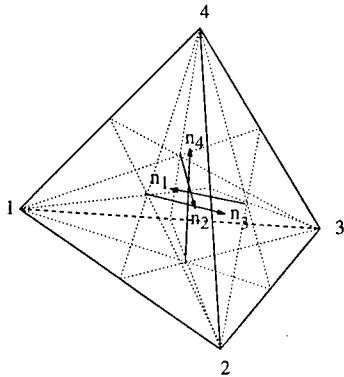


Fig. 1 : A generic tetrahedron with its inner scaled normals

requires that in the semi-discrete form of equation (1),

$$\frac{dU_i}{dt} V_i = - \sum_{k \neq i} C_{ki} (U_i - U_k), \quad (9)$$

the matrices C_{ki} are all positive semi-definite, which is a generalization of the scalar positivity also called Local Extremum Diminishing (LED) property. Condition (9) is called global positivity and is difficult to impose. Therefore a more restricted property, local positivity, see Roe [14] or Deconinck *et al.* [5], is introduced. This means that condition (9) is imposed for the contribution of every cell, which is very easy to check.

- **Linearity Preservation or Residual Property**

The ability to reproduce linear steady-state solutions exactly is obtained by demanding that no updates are sent to the vertices if the cell residual is zero. This is satisfied when the distribution matrices β_i^T are bounded, such that

$$\beta_i^T \Phi^T \rightarrow 0 \quad \text{when} \quad \Phi^T \rightarrow 0. \quad (10)$$

It can be proven that only nonlinear schemes can satisfy positivity and linearity preservation at the same time (Godunov's theorem). Therefore, linear Petrov-Galerkin finite-element schemes like the SUPG-scheme, cannot be monotonic, as they are linearity preserving, by construction.

2.1 The system first-order N-scheme

A first scheme we consider is the matrix generalization of the optimal first-order upwind scalar scheme for advection problems on triangular or tetrahedral grids, see Struijs *et al.* [17]. Using the Jacobians based on the face-normals, equations (6) and (8), the distribution to node i is defined as

$$\Phi_i^N = \beta_i^N \Phi^T = K_i^+ (U_i - U_{in}), \quad (11)$$

where the state U_{in} is given by

$$U_{in} = \left(\sum_j K_j^- \right)^{-1} \sum_j K_j^- U_j. \quad (12)$$

For a symmetrizable system such as the Euler system it is possible to verify that this scheme satisfies the positivity property (9). Energy stability, the only functional which possibly can be bounded for a multi-dimensional hyperbolic system by Barth, again with the assumption that the system can be transformed into a symmetric form.

2.2 The limited system N-scheme

The N-scheme is monotonic, but only first-order accurate in space, as it does not satisfy equation (10). A second-order scheme is obtained for the *scalar* case by limiting the distribution coefficients of the N-scheme as follows, see Deconinck *et al.* [3]

$$\beta_i^{limN} = \frac{\max(0, \beta_i^N)}{\sum_j \max(0, \beta_j^N)} \quad (13)$$

where

$$\beta_i^N = \frac{\Phi_i^N}{\Phi^T}. \quad (14)$$

The extension of equation (13) to systems is

$$\beta_i^{limN} = \left(\sum_j \beta_j^{N+} \right)^{-1} \beta_i^{N+}. \quad (15)$$

Here β_i^{N+} is the matrix based on the positive eigenvalues of the first-order distribution matrix β_i^N , implicitly defined by equation (11). In combination with the property of invariance for similarity transformations, this is enough to define β_i^{N+} uniquely for a commuting system:

$$\beta_i^N = R D_i L, \quad (16)$$

where D_i is a diagonal matrix with the k^{th} element d_i^k given by

$$d_i^k = \frac{l^k \cdot \Phi_i^N}{l^k \cdot \Phi^T}, \quad (17)$$

while L (with rows l^k) and R are the left and right eigenvector matrices of the K_i , which are independent of the normal. It is easy to check that this definition of the limited system N-scheme is equivalent to applying the scalar limited N-scheme to each of the decoupled characteristic equations and transforming the result back to the variable U . For a general non-commuting system these expressions have been generalized, see [19] for the details.

2.3 Conservative linearization

From the definition of the matrix schemes in the previous sections it is clear that they use the quasi-linear form of the equations with constant Jacobians per cell and especially the positivity property heavily relies on this fact. For solutions with discontinuities the conservative form must be solved to obtain the correct jump relations. The link between both formulations is given by the conservative linearization, briefly discussed here, for more details see Deconinck *et al.*[4]. Consider the conservation law

$$\frac{\partial U}{\partial t} + \vec{\nabla} \cdot \vec{F} = 0, \quad (18)$$

and its quasi-linear form

$$\frac{\partial U}{\partial t} + \frac{\partial \vec{F}}{\partial U} \cdot \vec{\nabla} U = 0. \quad (19)$$

The quasi-linear form (19) is conservative if for any cell T the relation

$$\oint_{\partial T} \vec{F} \cdot \vec{n} d\partial T \equiv \frac{\partial \vec{F}}{\partial Z}(\bar{Z}) \cdot \oint_{\partial T} Z \vec{n} d\partial T \quad (20)$$

is identically satisfied. Here, Z is an arbitrary set of independent variables, \bar{Z} a cell averaged state of these variables, ∂T the boundary of T and \vec{n} the normal of ∂T . On triangles in 2D and tetrahedra in 3D it has been shown [4], that the arithmetic average of the nodal values of the Roe parameter vector $Z = \sqrt{\rho}(1, u, v, w, H)^T$ satisfies (20), thus extending 1D Roe-averaging to two and three space dimensions.

3 THE NAVIER-STOKES EQUATIONS

Adding the visous terms, the conservation form of the compressible Navier-Stokes equations is obtained,

$$\frac{\partial U}{\partial t} + \frac{\partial F_j}{\partial x_j} = \frac{\partial F_j^v}{\partial x_j}, \quad (21)$$

where F_j are the inviscid flux vectors and F_j^v the viscous flux vectors defined as:

$$F_j^v = \begin{pmatrix} 0 \\ \tau_{ij} \\ u_k \tau_{jk} - q_j \end{pmatrix}. \quad (22)$$

Here, τ is the viscous stress tensor and q the heat flux vector. For a Newtonian fluid considered here, τ is a linear function of the velocity gradients:

$$\tau_{ij} = \mu \left(\frac{\partial u_i}{\partial x_j} + \frac{\partial u_j}{\partial x_i} - \frac{2}{3} \frac{\partial u_k}{\partial x_k} \delta_{ij} \right), \quad (23)$$

where μ is the molecular viscosity coefficient. In all computations, the semi-empirical formula of Sutherland [21] is used:

$$\frac{\mu}{\mu_0} = \left(\frac{T}{T_0} \right)^{\frac{3}{2}} \frac{T_0 + S}{T + S}. \quad (24)$$

The constants for air are:

$$\mu_0 = 1.716 \cdot 10^{-5} \text{ kg m}^{-1} \text{ s}^{-1}, \quad (25)$$

$$T_0 = 273.15 \text{ K}, \quad (26)$$

$$S = 110.55 \text{ K}. \quad (27)$$

The heat flux is modeled according to Fourier's law:

$$q_j = -\kappa \frac{\partial T}{\partial x_j}, \quad (28)$$

where the thermal conductivity coefficient κ is related to μ and the specific heat capacity at constant pressure, c_p , by the non-dimensional Prandtl number:

$$Pr = \frac{\mu c_p}{\kappa}. \quad (29)$$

For air, the Prandtl number is approximately constant for temperatures between 200 and 600 K and equal to 0.72. This approximation is used in all the computations presented in this work.

3.1 Space discretization for advective-diffusive systems

In [19] it has been shown that the above upwind discretization for the inviscid terms can be interpreted as a Petrov Galerkin approach based on linear finite elements. It is well known that for such a finite element approach, a consistent discretization of second order diffusion terms is obtained by the standard Galerkin finite element discretization, and this is the approach followed in this work. As a result, the compact stencil of nearest neighbours is also preserved for the Navier-Stokes equations. More specifically, the Galerkin discretization of node i of cell T for the diffusive part of the scalar advection-diffusion equation,

$$\frac{\partial u}{\partial t} + \vec{a} \cdot \vec{\nabla} u - \nu \left(\frac{\partial^2 u}{\partial x^2} + \frac{\partial^2 u}{\partial y^2} + \frac{\partial^2 u}{\partial z^2} \right) = 0, \quad (30)$$

becomes:

$$\Phi_i^{dif} = \frac{\vec{n}_i}{3} \cdot \nu \sum_{j=1}^4 u_j \frac{\vec{n}_j}{3V_T}, \quad (31)$$

where \vec{n}_i are the inward scaled normals, see figure 1, and V_T the volume of cell T . The discretization of the viscous fluxes of the Navier-Stokes equations is similar.

3.2 Turbulence models

Most aeronautical flows are turbulent and the only practical way to compute these high Reynolds number flows is to model the influence of the turbulence on the mean flow. The resulting set of Reynolds averaged Navier-Stokes (RANS) equations are identical to (21), except for the laminar viscous stress tensor τ in equation (22) which is replaced by the sum of τ and the turbulent or Reynolds stress tensor σ and similarly for the heat flux. The Reynolds stresses must be modeled by a so-called turbulence model. One can distinguish zero-equation or algebraic models such as the Baldwin-Lomax model [2], one-equation models which solve a single transport equation for the eddy-viscosity such as the Spalart-Allmaras [16] model, two-equation models which model the eddy-viscosity by two additional transport equations and finally second-order closure models which solve a transport equation for every element of the Reynolds stress tensor σ .

The zero-equation models are non-local in nature, typically information along a line in the boundary layer is needed, and therefore difficult to implement on unstructured grids. Moreover their results are not as good as the results of one- and two-equation models. The second-order closure models on the other hand are very much an area of ongoing research [20] and will therefore not be considered either.

Therefore, the turbulence models used in this work are one- and two-equation models, although in this paper the discussion is limited to the two-equation models. The generic form of these additional equations is:

$$\frac{\partial \phi}{\partial t} + u_i \frac{\partial \phi}{\partial x_i} = \frac{\partial}{\partial x_i} \left(\nu_\phi \frac{\partial \phi}{\partial x_i} \right) + \Sigma^+ + \Sigma^-. \quad (32)$$

Here ϕ stands for any of the turbulent quantities, ν_ϕ is a diffusion coefficient corresponding to ϕ , Σ^+ the production source term and Σ^- the destruction source term. Note that the turbulent variables are always advected along the streamlines. First it is explained how this type of equation is discretized. Then the models used in the computations are discussed.

3.2.1 Discretization of the turbulent transport equations

Equation (32) is an advection-diffusion equation with source terms. As it is essential that the turbulent quantity ϕ remains positive, the advective part is discretized with the positive N- or limited N-scheme scheme. The diffusive part is discretized using standard Galerkin finite elements as discussed before.

In principle the Petrov-Galerkin interpretation of the schemes, also leads to a straightforward discretization of the source terms Σ^+ and Σ^- : If these terms are assumed to be constant per control volume, the distribution to node l of cell T is:

$$R_{l,source} = \beta_l V_T (\Sigma^+ + \Sigma^-), \quad (33)$$

where V_T is the volume of the tetrahedron and β_l the distribution coefficient of the advection scheme. The distribution (33) shows that the source term must be upwinded to have a consistent discretization. Numerical experiments however showed that this approach was not very stable and a point wise discretization of the source terms has been used. This leads to the following semi-discrete version of equation (32) at node l :

$$V_l \frac{\partial \phi_l}{\partial t} + \sum_{T \in \Omega_l} (R_{l,inv} + R_{l,vis}) = V_l (\Sigma_l^+ + \Sigma_l^-). \quad (34)$$

Here, V_l is the volume of the median dual cell of node l , the summation extends over all control volumes which belong to the neighborhood Ω_l , and $R_{l,inv}$ and $R_{l,vis}$ are the result of the discretization of the advection and the diffusion term respectively. A study on a model equation has shown that the reduction in accuracy due to this inconsistency in the source term discretization is negligible. If Σ_l^+ or Σ_l^- contain gradients, these are reconstructed with the Galerkin scheme:

$$\nabla \vartheta_l = \frac{1}{V_l} \sum_{T \in \Omega_l} \frac{V_T}{4} \nabla \vartheta^T, \quad (35)$$

where $\nabla \vartheta_l$ is the gradient of a certain quantity ϑ in node l , and $\nabla \vartheta^T$ the constant gradient in cell T .

In general, the source terms Σ^+ and Σ^- are stiff, which makes explicit time integration impossible and some kind of implicit algorithm must be used. To increase stability, Patankar [12] proposed to treat only the destruction source term Σ^- in an implicit manner. Usually Σ^- does not contain derivatives and is only a function of the nodal state U_l . Consequently, an implicit treatment of Σ_l^- in combination with the explicit forward Euler time integrator for the other terms, leads to the following point-implicit method:

$$\left(\frac{1}{\Delta t_l} - \frac{\partial \Sigma_l^-}{\partial \phi_l} \right) (\phi_l^{n+1} - \phi_l^n) = R_l. \quad (36)$$

As $\frac{\partial \Sigma_l^-}{\partial \phi_l}$ is negative, the update is under-relaxed compared to the fully explicit algorithm. This makes the use of semi-explicit time integrators even less attractive for turbulent flows than for laminar ones and consequently implicit methods must be considered as discussed in section 4.

For the fully implicit backward Euler method, the Jacobian matrices of the entire residual R_l must be computed. As the turbulent quantities are advected along the streamline, there is a coupling with the Navier-Stokes equations. This coupling however is neglected for two reasons, (1): due to the explicit treatment of the production source term Σ_l^+ , Newton convergence cannot be expected anyway and therefore the relatively weak coupling with the Navier-Stokes equations does not have much influence, and (2): it was found, see also e.g. [9], that neglecting these terms was beneficial for stability. For two-equation models even the coupling between the two turbulent quantities is neglected. An extra advantage of this approach is a saving of a factor two in memory (for two-equation models), which especially in 3D is not negligible.

3.2.2 The $k - \omega$ model

Unlike many other two-equation models, the $k - \omega$ model [22] does not require damping functions in the viscous sublayer. It is therefore numerically easier to handle than for example the low-Reynolds version of the $k - \varepsilon$ model [8]. The two additional transport equations for k , the

turbulent kinetic energy, and ω , its specific dissipation rate, in non-dimensional (k is made dimensionless by U_∞^2 and ω by $\frac{U_\infty}{L}$) conservation form are:

$$\underbrace{\frac{\partial \rho k}{\partial t}}_I + \underbrace{\frac{\partial \rho k u_i}{\partial x_i}}_{II} = \underbrace{\frac{1}{Re_\infty} \frac{\partial}{\partial x_i} \left[(\mu + \sigma_{k1} \mu_t) \frac{\partial k}{\partial x_i} \right]}_{III} + \underbrace{\sigma_{ij} \frac{\partial u_i}{\partial x_j}}_{IV} - \underbrace{\beta^* \rho \omega k}_V \quad (37)$$

$$\underbrace{\frac{\partial \rho \omega}{\partial t}}_I + \underbrace{\frac{\partial \rho \omega u_i}{\partial x_i}}_{II} = \underbrace{\frac{1}{Re_\infty} \frac{\partial}{\partial x_i} \left[(\mu + \sigma_{\omega 1} \mu_t) \frac{\partial \omega}{\partial x_i} \right]}_{III} + \underbrace{Re_\infty \frac{\gamma_1 \rho}{\mu_t} \sigma_{ij} \frac{\partial u_i}{\partial x_j}}_{IV} - \underbrace{\beta_1 \rho \omega^2}_V \quad (38)$$

Here the terms I indicate the time-derivatives, II the advection parts, III the diffusion terms, IV the production terms and V the destruction terms. The definition of σ_{ij} for two-equation models is slightly changed:

$$\sigma_{ij} = \frac{1}{Re_\infty} \mu_t \left(\frac{\partial u_i}{\partial x_j} + \frac{\partial u_j}{\partial x_i} - \frac{2}{3} \frac{\partial u_k}{\partial x_k} \delta_{ij} \right) - \frac{2}{3} \rho k \delta_{ij}. \quad (39)$$

The last term is present to ensure that the turbulent normal stresses sum up to $-2\rho k$. In one-equation models there is no separate equation for k , and this effect is ignored. The modeling of the turbulent heat flux remains unchanged. The non-dimensional eddy viscosity is defined as:

$$\mu_t = Re_\infty \frac{\rho k}{\omega}. \quad (40)$$

The modeling constants are:

$$\begin{aligned} \sigma_{k1} &= 0.5, \quad \sigma_{\omega 1} = 0.5, \quad \beta_1 = 0.075 \\ \beta^* &= 0.09, \quad \kappa = 0.41, \quad \gamma_1 = \frac{\beta_1}{\beta^*} - \frac{\sigma_{\omega 1} \kappa^2}{\sqrt{\beta^*}}. \end{aligned} \quad (41)$$

Menter [10] recommends the following boundary conditions at the freestream:

$$\omega_\infty = (1 \rightarrow 10), \quad k_\infty = \frac{10^{-(2 \rightarrow 5)} \omega_\infty}{Re_\infty}, \quad (42)$$

and at the solid walls:

$$\omega = \frac{10}{Re_\infty} \frac{6\mu}{\rho \beta_1 (\Delta y_1)^2}, \quad k = 0,$$

where Δy_1 is the normal grid spacing at the wall.

Due to the introduction of the turbulent kinetic energy k , the definition of the total energy becomes:

$$\rho E = \frac{p}{\gamma - 1} + \frac{1}{2} \rho u_i u_i + \rho k, \quad (43)$$

i.e. the turbulence is taken into account in the conservation of energy, although this effect is of secondary importance.

Of more concern is the presence of the term $-\frac{2}{3}\rho k$ in the turbulent normal stresses, see equation (39). This term, when discretized with the Galerkin method, could lead to instabilities, because it appears in the Navier-Stokes equations as a first derivative. Therefore it is incorporated in the pressure by the introduction of an effective pressure p' ,

$$p' = p + \frac{2}{3} \rho k, \quad (44)$$

and discretized in an upwind manner. This and the contribution of k to the total energy changes the acoustic eigenvalues of the inviscid Jacobians. Instead of $u_i \pm a$ these are now given by $u_i \pm a'$, where

$$a' = \sqrt{(\gamma - 1) \left(H - \frac{1}{2} u_i u_i \right) + \left(1 - \frac{\gamma}{3} \right) k}. \quad (45)$$

Also this effect has been taken into account when the $k - \omega$ or any other two-equation turbulence model was used.

3.2.3 The BSL model

The main disadvantage of the $k - \omega$ model is its sensitivity to the rather arbitrary freestream values of k and ω , equation (42), in the outer part of the boundary layer. Menter's idea [10] was to combine the good properties of the $k - \omega$ model, i.e. no need for wall functions and accurate prediction in the near wall region of the boundary layer, with the good properties of the $k - \varepsilon$ model, mainly its freestream independence, and to avoid the bad properties of both models. The result is the Baseline (BSL) model, which is a blending between both previously mentioned models in $k - \omega$ formulation:

$$\begin{aligned} \frac{\partial \rho k}{\partial t} + \frac{\partial \rho k u_i}{\partial x_i} &= \frac{1}{Re_\infty} \frac{\partial}{\partial x_i} \left[(\mu + \sigma_k \mu_t) \frac{\partial k}{\partial x_i} \right] \\ &= \sigma_{ij} \frac{\partial u_i}{\partial x_j} - \beta^* \rho \omega k \end{aligned} \quad (46)$$

$$\begin{aligned} \frac{\partial \rho \omega}{\partial t} + \frac{\partial \rho \omega u_i}{\partial x_i} &= \frac{1}{Re_\infty} \frac{\partial}{\partial x_i} \left[(\mu + \sigma_\omega \mu_t) \frac{\partial \omega}{\partial x_i} \right] \\ &+ 2\rho(1 - F_1) \sigma_{\omega 2} \frac{1}{\omega} \frac{\partial k}{\partial x_i} \frac{\partial \omega}{\partial x_i} \\ &+ Re_\infty \frac{\gamma \rho}{\mu_t} \sigma_{ij} \frac{\partial u_i}{\partial x_j} - \beta \rho \omega^2, \end{aligned} \quad (47)$$

The blending function F_1 has been defined as:

$$F_1 = \tanh(\arg_1^4) \quad (48)$$

where

$$\arg_1 = \min \left[\max \left(\frac{\sqrt{k}}{0.09 \omega D}, \frac{1}{Re_\infty} \frac{500 \mu}{\rho D^2 \omega} \right), \frac{4 \rho \sigma_{\omega 2} k}{CD_{k\omega} D^2} \right]$$

with D is distance to the nearest wall and

$$CD_{k\omega} = \max \left(2\rho \sigma_{\omega 2} \frac{1}{\omega} \frac{\partial k}{\partial x_i} \frac{\partial \omega}{\partial x_i}, 10^{-20} \right) \quad (49)$$

The constants appearing in the BSL model are actually not constants any more, but a blending between the $k - \omega$ values, equation (41), and the $k - \varepsilon$ values:

$$\begin{aligned} \sigma_{k2} &= 1.0, \quad \sigma_{\omega 2} = 0.856, \quad \beta_2 = 0.0828 \\ \beta^* &= 0.09, \quad \kappa = 0.41, \quad \gamma_2 = \frac{\beta_2}{\beta^*} - \frac{\sigma_{\omega 2} \kappa^2}{\sqrt{\beta^*}}. \end{aligned} \quad (50)$$

If any of the $k - \omega$ constants are indicated by ϕ_1 and any of the $k - \varepsilon$ constants by ϕ_2 , then the "constants" of the BSL model, indicated by ϕ , are given by:

$$\phi = F_1 \phi_1 + (1 - F_1) \phi_2. \quad (51)$$

Here F_1 is defined in equation (48). The freestream and wall boundary conditions are identical to the $k - \omega$ model, see equation (42).

3.2.4 The SST model

The Shear-Stress Transport (SST) model [10] uses the same transport equations for k and ω and the same blending function F_1 as the BSL model, equations (46), (47) and (48), but the $k - \omega$ constants have been slightly changed:

$$\begin{aligned} \sigma_{k1} &= 0.85, \quad \sigma_{\omega1} = 0.5, \quad \beta_1 = 0.075 \\ \beta^* &= 0.09, \quad \kappa = 0.41, \quad \gamma_1 = \frac{\beta_1}{\beta^*} - \frac{\sigma_{\omega1}\kappa^2}{\sqrt{\beta^*}}. \end{aligned} \quad (52)$$

A second modification is the definition of the eddy-viscosity:

$$\mu_t = Re_\infty \frac{a_1 \rho k}{\max(a_1 \omega, |\Omega| F_2)} \quad (53)$$

$$F_2 = \tanh(arg_2^2) \quad (54)$$

$$arg_2 = \max\left(2 \frac{\sqrt{k}}{0.09 \omega D}, \frac{1}{Re_\infty} \frac{500 \mu}{\rho D^2 \omega}\right) \quad (55)$$

where $|\Omega|$ is again the magnitude of the vorticity vector. The constant a_1 is taken equal to 0.31. Comparison with the definition (40) of the BSL model shows that the eddy-viscosity of the SST-model is at most equal to, but usually less than, that of the BSL model. This limits the production of turbulence and improves the model's performance in adverse pressure gradient flows [10, 11, 15].

4 PARALLEL TEMPORAL DISCRETIZATION

In this section a parallel implicit algorithm is explained for the integration in time of the ordinary set of differential equations

$$\frac{dU}{dt} = RES(U), \quad (56)$$

which is the result of the spatial discretization. First the sequential algorithm is explained, followed by the parallelization technique.

As only steady-state problems are considered, time-accuracy is not important and the backward Euler method is used to integrate equation (56). This results in the nonlinear system for the state on time $t = t^{n+1}$

$$\frac{U^{n+1} - U^n}{\Delta t} = RES(U^{n+1}), \quad (57)$$

where Δt indicates the local time step. The right hand side of equation (57) is approximated using a Newton linearization, which leads to the following linear system for the update $\Delta U = U^{n+1} - U^n$:

$$\left[\frac{I}{\Delta t} - \frac{\partial RES(U^n)}{\partial U^n} \right] \Delta U = RES(U^n). \quad (58)$$

This loop is repeated in time until convergence. Analytical computation of the exact Jacobian matrix $\frac{\partial RES}{\partial U}$ becomes increasingly intractable and a numerical evaluation becomes attractive. Truncating the Taylor expansion of $RES_i(U_j + \epsilon_m 1_m)$ (the nodal residual at node i with the m^{th} component of U at node j perturbed by a small quantity ϵ_m) to the first-order terms, one has:

$$\left[\frac{\partial RES_i(U)}{\partial U_j} \right]_m \simeq \frac{RES_i(U_j + \epsilon_m 1_m) - RES_i(U_j)}{\epsilon_m}. \quad (59)$$

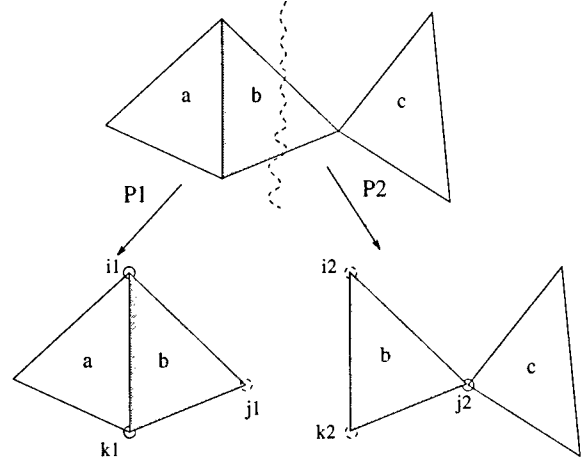


Fig. 2 : VOD, Close-up of the overlapping strip and respective mapping onto processors, internal (solid circles) and external (dashed circles) nodes.

Because of the compact stencil of the discretization, this numerical computation of the Jacobian requires a rather limited number of additional cell residual evaluations (12 and 20 for laminar flows in two and three dimensions respectively). The expression used for ϵ_m is

$$\epsilon_m = \epsilon \operatorname{sign}(U_m) \max(|U_m|, 10^{-3}), \quad (60)$$

where $\operatorname{sign}(U_m)$ is 1 for positive and -1 for negative U_m . The constant ϵ is a user specified value and is of the order 10^{-7} to 10^{-9} . Because of these small values of the disturbances it is important that all computations are done in double precision and the dimensionless Navier-Stokes equations are used to minimize errors due to the finite arithmetic.

Alternatively, approximate analytical Jacobians can be used, especially for turbulent problems and the nonlinear second-order discretization. These approximate Jacobians, when carefully designed, enhance stability in the early stages of the iteration process. The price paid is that no Newton convergence can be obtained, something which could not be achieved anyway in the above mentioned cases. Only the Picard Jacobian of the system N-scheme has been used. As the viscous terms are discretized with the Galerkin method, their Jacobians can be computed analytically without too many difficulties. For turbulent computations the eddy-viscosity is frozen and only the destruction term is linearized.

As the implicit solver is very memory intensive, the solver has been parallelized using the domain decomposition approach.

For the partitioning into the required number of subdomains (usually the number of processors), Metis has been used, see Karypis and Kumar [7]. For the message passing and for the parallel solution of the linear system (58), use has been made of the AZTEC library of SANDIA National Laboratories, see Hutchinson *et al.* [6]. This library completely hides the details of the parallelization for the user, whose only responsibility is to provide the matrix and right hand side in the suitable format. The domain decomposition method used by AZTEC is the vertex oriented decomposition (VOD) technique, see figure 2 for the 2D case; as a result, the separation between neighboring partitions occurs at the face-level and the vertices of the cut cells are duplicated on the two processors. Because of the compactness of the schemes, requiring only information from nearest neighbours, any computational task can be carried out in the same way as in the sequential code, provided that a single layer of nodes located on the outer boundaries of each subdomain have

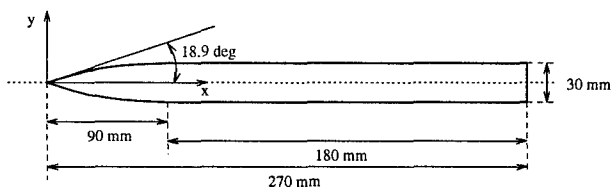


Fig. 3 : Geometry definition of the ogive cylinder.

M_∞	2.0
α	10°
T_∞	330 K
Wall	adiabatic
Re_∞/m	$5.33 \cdot 10^6/m$
P_t	50 kPa

Table 1 : Flow conditions for the ogive cylinder test case.

been properly updated. Hence, communication overhead is absolutely minimal.

The iterative solvers inside AZTEC are Krylov subspace methods, like GMRES, BiCGSTAB, etc., which in general must be preconditioned to achieve an acceptable performance. The only preconditioner inside the current AZTEC release, which performed good enough for our applications, was the Block Incomplete LU factorization without additional fill in, BILU(0). Unfortunately, this requires an additional storage of a full matrix, which is unacceptable in 3D. Therefore a modified version of this preconditioner, BMILU(0), which only requires the storage of an extra block diagonal, like Block Jacobi, has been added to the AZTEC library. In the future releases, this preconditioner will become standard available.

5 FLOW OVER AN OGIVE CYLINDER

In this section we discuss the results of the laminar and turbulent computation over an ogive cylinder. The geometry definition is shown in figure 3. It has been investigated experimentally by ONERA [1] for a whole set of incidence angles, but only $\alpha = 10^\circ$ has been computed here. The flow conditions are given in table 1.

Two cases may be distinguished: the case where the boundary layer undergoes natural transition and the case where the boundary layer has been tripped near the apex. For the numerical computation fully laminar and fully turbulent flow have been assumed respectively. All computations have been carried out on the Cray T3E of the

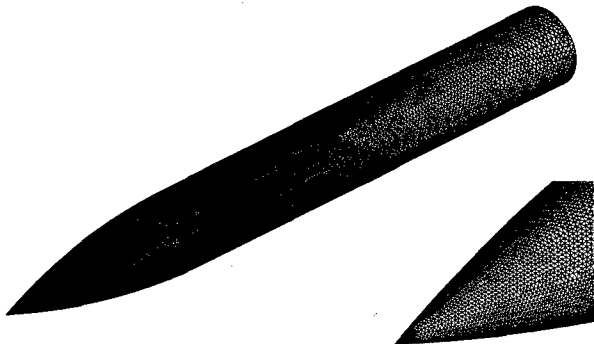


Fig. 4 : Surface grid of the ogive cylinder (17,893 nodes), entire and zoom near the apex.

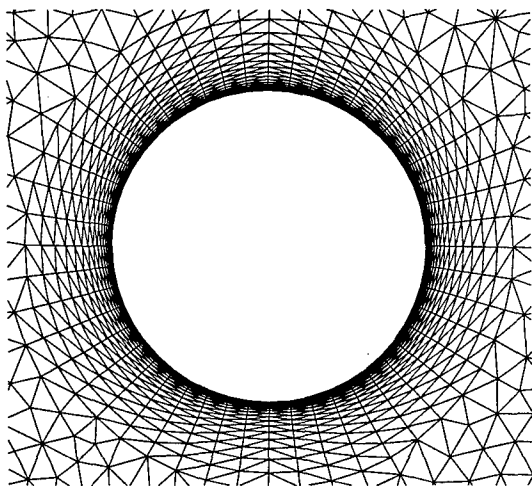
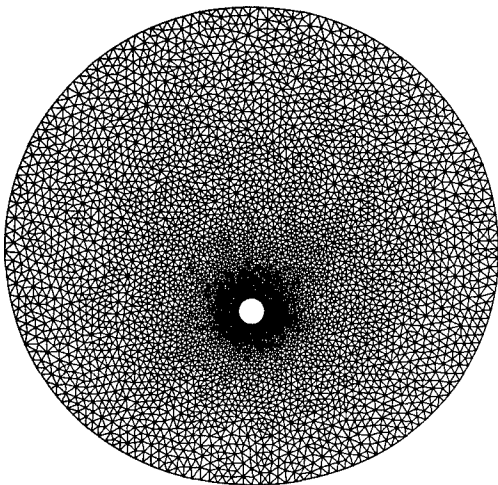


Fig. 5 : Surface grid of the outflow plane, entire (top) and zoom (bottom) (5480 nodes).

University of Delft. Each processor is equipped with 128 MB of RAM.

5.1 The laminar case

The mesh has been created with the grid generator of the University of Swansea [13] and consists of 390,965 nodes and 2,302,869 tetrahedra. Due to limitations of the software, a symmetry plane could not be used and the full problem had to be computed. The surface mesh of the ogive-cylinder and of the outflow plane are shown in figure 4 and 5 respectively. In the boundary layer 26 viscous layers are used with an initial normal spacing of 10^{-5} m and a stretching factor of 1.2. This guarantees a smooth transition to the isotropic part of the grid, as can be seen in figure 5.

To meet the memory requirements for the implicit solver the code has been run on 32 processors. As can be seen in the convergence history, figure 6, Newton convergence has been obtained for the first-order scheme in 15 iterations, in combination with numerical Jacobians. The starting CFL number was 1.0 and was multiplied every time step by 5.0, until a maximum of 10^6 . The second-order scheme, with approximate N-scheme Jacobians and CFL = 100, stalls after $2\frac{1}{2}$ orders relative from the restart. The total CPU time is roughly 5 hours, of

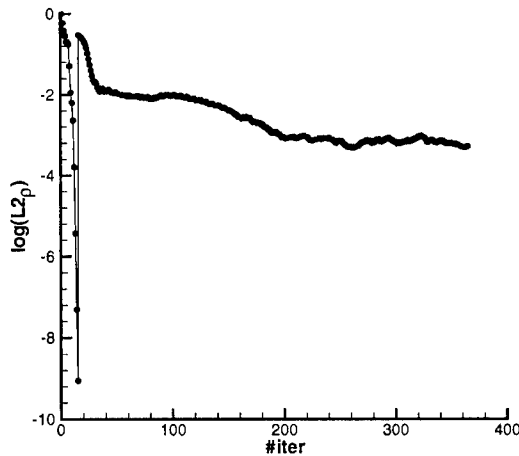


Fig. 6 : Convergence history for the laminar ogive cylinder, coarse grid.

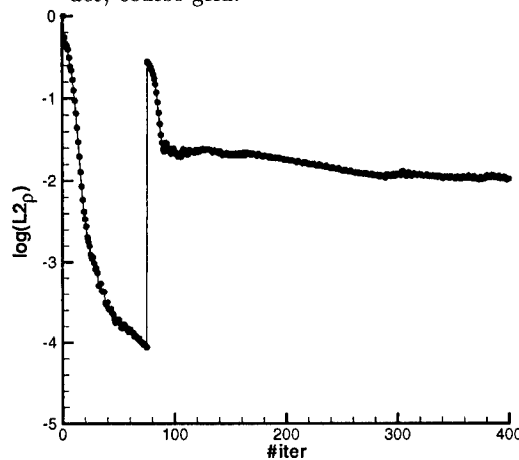


Fig. 7 : Convergence history for the laminar ogive cylinder, fine grid.

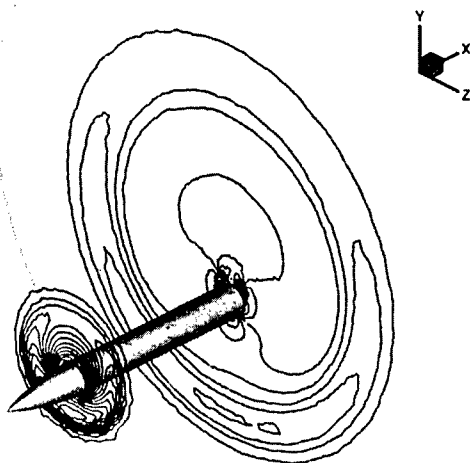


Fig. 8 : Mach number isolines for the laminar ogive cylinder, system limited N-scheme, min = 0.0, max = 2.1, step = 0.02.

which 90% is taken by the second-order scheme. Mach number isolines in the outflow plane ($x = 0.27$ m) and in the plane $x = 0.08$ m are shown in figure 8. In the outflow plane the main vortices are clearly visible and

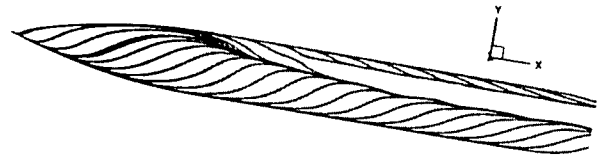


Fig. 9 : Computed skin friction lines for the laminar ogive cylinder, system limited N-scheme.

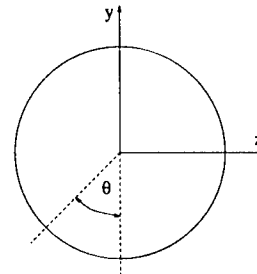


Fig. 10 : Definition of angle θ .

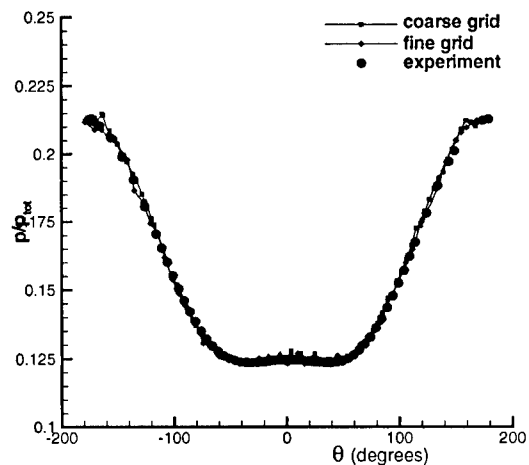


Fig. 11 : Surface pressure distribution, $x = 0.045$ m, laminar case.

also the bow shock can be identified. The skin friction lines (computed from the traction force) are depicted in figure 9. Two separation lines can be distinguished and consequently two counter-rotating vortices are present (on each side of the body). The main separation line shows a wavy behavior, an indication that this solution is not stable and most likely unsteady. As the grid is quite coarse, the laminar solution has also been computed on the grid for the turbulent case, which is described in the next paragraph. The convergence history is shown in figure 7. As the initial normal spacing of this grid is 10 times smaller than the coarse grid, the aspect ratios of the cells near the body are much larger (maximum value ± 1500). Consequently, the nonlinear problem is more difficult too solve and no Newton convergence could be obtained for the first-order scheme. Therefore, both the first and the second-order solution are computed in combination with analytical Jacobians and CFL = 100. On this fine grid, the second-order solution only converges one order of magnitude relative from the restart, figure 7, which is much less than the turbulent case, figure 16. Also this indicates that the laminar solution is probably unsteady. The total CPU-time on 64 processors of the Cray T3E is approximately 7 hours. Figures 11 to 15 compare the computed surface pressure

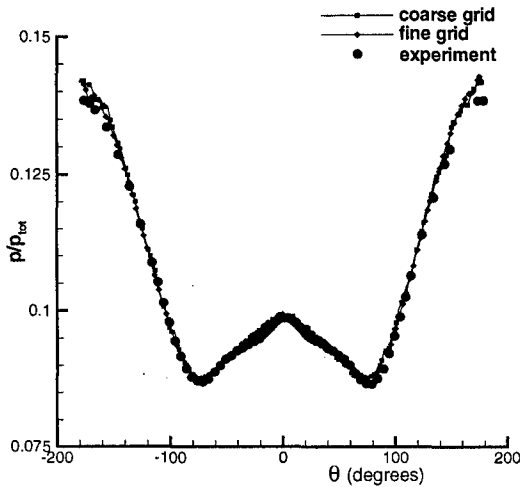


Fig. 12 : Surface pressure distribution, $x = 0.09$ m, laminar case.

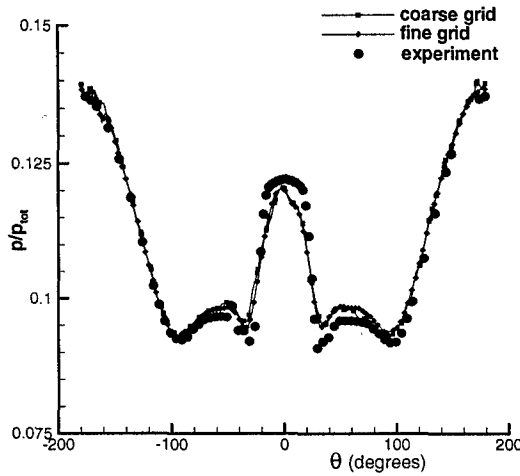


Fig. 13 : Surface pressure distribution, $x = 0.135$ m, laminar case.

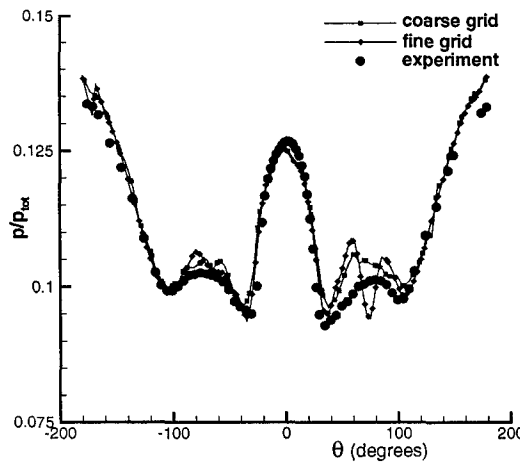


Fig. 14 : Surface pressure distribution, $x = 0.18$ m, laminar case.

distributions on the two grids with the experimental values in several crossflow planes. The angle θ is defined in figure 10. It is clear that the further downstream the comparison is made the worse the agreement becomes. In the plane $x = 0.135$ m, figure 13 the numerical solu-

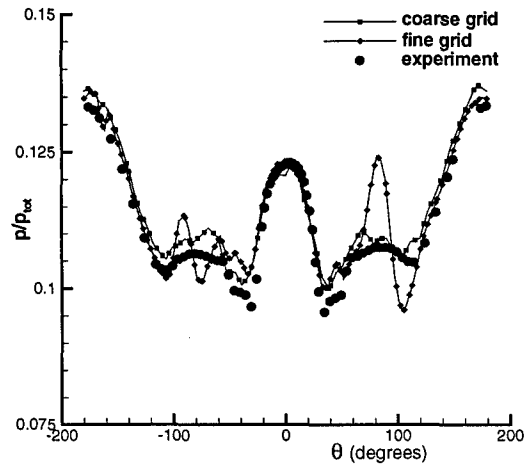


Fig. 15 : Surface pressure distribution, $x = 0.225$ m, laminar case.

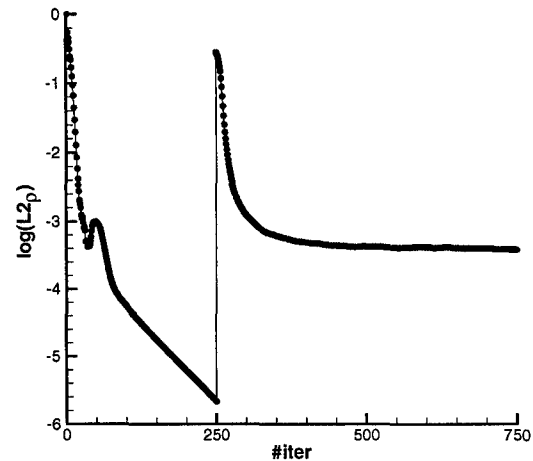


Fig. 16 : Convergence history for the turbulent ogive cylinder, SST-model.

tions start to deviate from the experimental values, but on both grids the pressure distribution is still symmetric. This is not the case anymore in figures 14 and 15. Especially on the fine grid, the solution is asymmetric and unsteady. The probable explanation for this is that the flow in the experiment is transitional, while in the computation laminar conditions have been assumed. Apparently the transition to turbulence stabilizes the flow field, such that the experimental flow field is steady. Note that the asymmetry is found, only because the full problem is computed. If a symmetry plane is used, and thus the flow is forced to be symmetric, it might be possible to obtain a steady, laminar solution.

5.2 The turbulent case

Also this mesh has been created with the grid generator from the University of Swansea [13] and, as explained earlier, has also been used as the fine grid for the laminar case. It consists of 850,196 nodes (5,048,481 tetrahedra), the initial normal spacing is 10^{-6} m and 38 viscous layers with a stretching factor of 1.2 have been used to guarantee a smooth transition from the viscous layers to the isotropic part of the grid. The surface grid is slightly finer than the laminar grid, 23,187 nodes on the ogive cylinder and 12,758 in the outflow plane.

The convergence history, analytical N-scheme Jacobians and $CFL = 100$ for both the N- and limited N-scheme, for the SST-model is shown in figure 16. To meet the memory requirements for the implicit solver, the computation must be done on 64 processors of the Cray T3E and it took approximately 36 CPU-hours. The first-order N-scheme is converging quite well and probably more orders of magnitude can be reached than the approximately 6 orders where it has been stopped. The limited N-scheme converges about 3 orders relative from the restart, which is much more than the laminar solution on this grid, see figure 7. As the maximum value of the eddy-viscosity

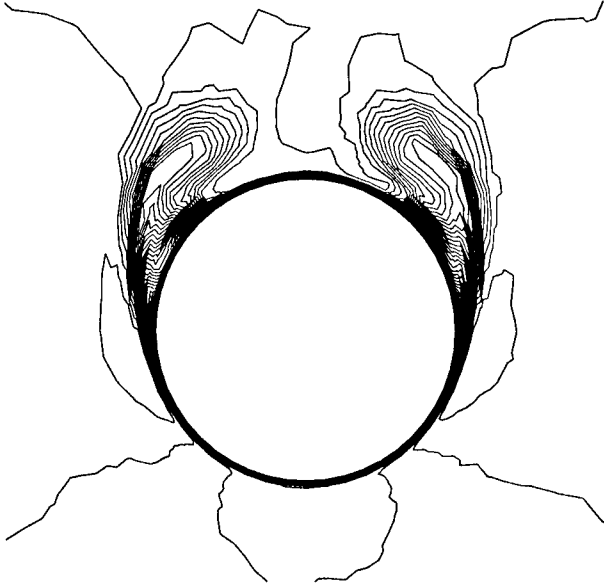


Fig. 17 : Mach number isolines in the outflow plane for the laminar solution, limited N-scheme, min = 0.0, max = 2.08, step = 0.04

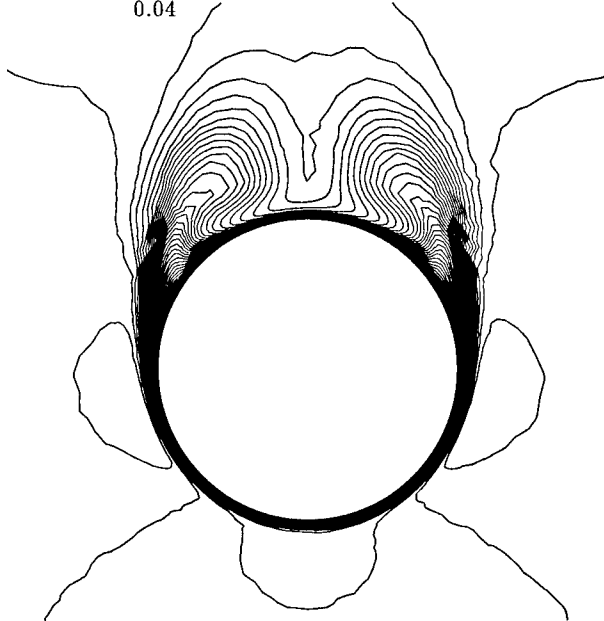


Fig. 18 : Mach number isolines in the outflow plane for the turbulent SST solution, limited N-scheme, min = 0.0, max = 2.09, step = 0.04

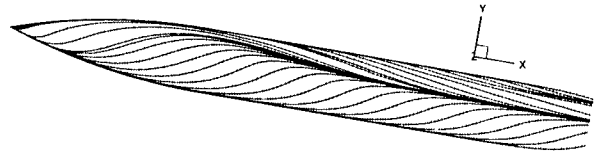


Fig. 19 : Computed oil-flow pattern for the turbulent ogive cylinder, system limited N-scheme, SST-model.

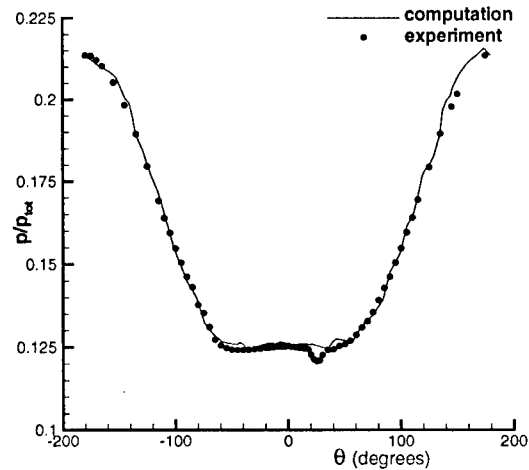


Fig. 20 : Surface pressure distribution, $x = 0.045$ m, turbulent case, SST-model.

did not change more than 0.1% between iteration 700 and 750, it has been assumed that the solution was converged. Consequently, the turbulent case is steady (in a Reynolds averaged sense).

Mach number isolines in the outflow plane for the laminar and turbulent solution are shown in figure 17 and 18 respectively. Clearly, for the turbulent solution the vortices are located more above the body than for the laminar computation. This is caused by the fact that, due to the stabilizing influence of the turbulence, the main separation line has been shifted in the leeward direction of the model. This is seen if figures 9 and 19 are compared. The main separation line is much straighter for the turbulent case, indicating that the solution is more stable than the laminar solution. Furthermore, the secondary separation, the formation of the second vortex, occurs much later for the turbulent problem.

Figures 20 to 25 show the computed and measured surface pressure distributions in several x cross-sections for the limited N-scheme solution in combination with the SST turbulence model. The agreement with the experimental data is very good. There are some slight deviations, especially when the vortex is present, see figures 23 and 24. This might be a grid effect and in principle computations on a finer grid and with other turbulence models should be performed to verify grid convergence and the effect of the turbulence model. However this has been omitted, because of the large computational effort (36 hours on 64 processors) to obtain a solution for this problem. In combination with the backward Euler time integration method, the algorithm is very stable, even for turbulent flows. Starting from a uniform flow field, also for the turbulent quantities, did not pose any problems for the flow solver.

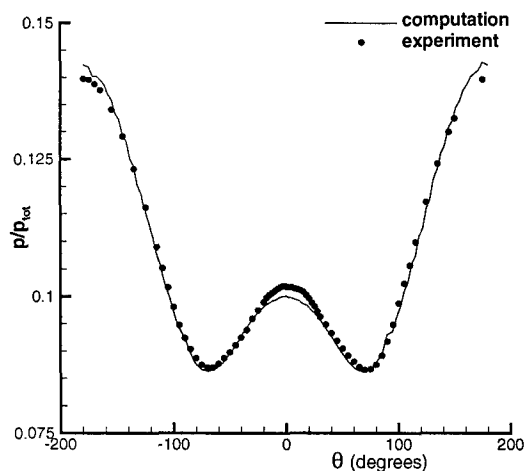


Fig. 21 : Surface pressure distribution, $x = 0.09$ m, turbulent case, SST-model.

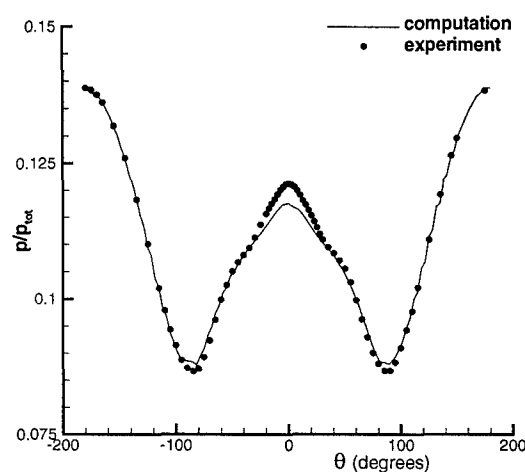


Fig. 22 : Surface pressure distribution, $x = 0.135$ m, turbulent case, SST-model.

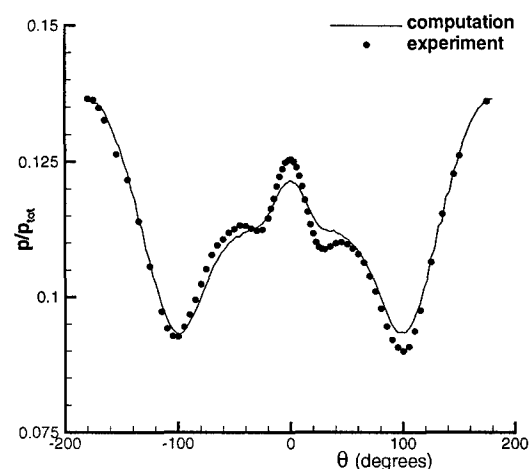


Fig. 23 : Surface pressure distribution, $x = 0.18$ m, turbulent case, SST-model.

CONCLUSIONS

A parallelized multidimensional upwind cell vertex solver on compact stencils has been applied to laminar and turbulent supersonic flow around an ogive cylinder. Arguments have been given for the unsteadiness of the laminar case. The solution of the turbulent problem shows

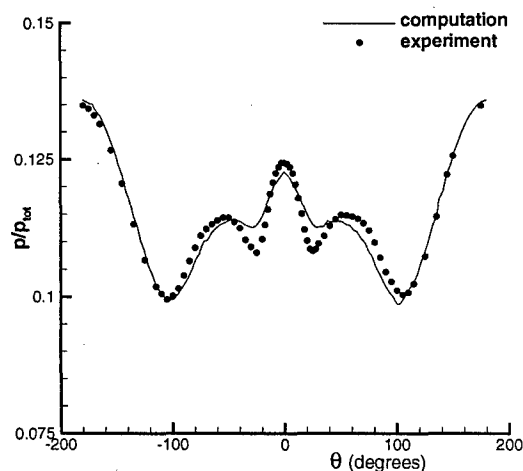


Fig. 24 : Surface pressure distribution, $x = 0.225$ m, turbulent case, SST-model.

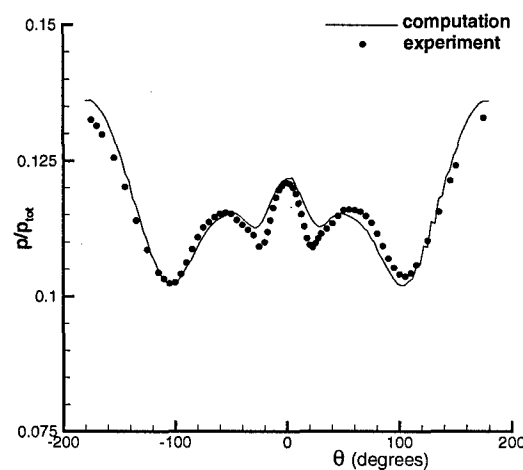


Fig. 25 : Surface pressure distribution, $x = 0.255$ m, turbulent case, SST-model.

good agreement with the experimental surface pressures. This test case shows that the multi-dimensional upwind discretization technique is able to solve 3D turbulent viscous flows. Although implicit time integration is advantageous for computing these high Reynolds number flows, the large memory needed is a severe drawback for its routine use.

REFERENCES

- [1] AGARD Advisory Report No 303. *A Selection of Experimental Test Cases for the Validation of CFD codes*. AGARD, 1994.
- [2] B.S. Baldwin and H. Lomax. Thin layer approximation and algebraic model for separated turbulent flows. 1978. AIAA paper 78-0275.
- [3] H. Deconinck, H. Paillère, R. Struijs, and P.L. Roe. Multidimensional upwind schemes based on fluctuation-splitting for systems of conservation laws. *Journal of Computational Mechanics*, 11(5/6):323-340, 1993.
- [4] H. Deconinck, P.L. Roe, and R. Struijs. A Multi-dimensional Generalization of Roe's Flux Difference

- Splitter for the Euler Equations. *Journal of Computers and Fluids*, 22:215–222, 1993.
- [5] H. Deconinck, R. Struijs, G. Bourgois, and P.L. Roe. Compact advection schemes on unstructured grids. In *VKI LS 1993-04, Computational Fluid Dynamics*, 1993.
- [6] S.A. Hutchinson, J.N. Shadid, and R.S. Tuminaro. Aztec User's Guide: Version 1.1. Technical Report SAND95-1559, Sandia National Laboratories, 1995.
- [7] G. Karypis and V. Kumar. Metis, Unstructured Graph Partitioning and Sparse Matrix Ordering System, v.2.0. Technical report, University of Minnesota, Department of Computer Science, 1995.
- [8] B.E. Launder and D.B. Spalding. The numerical computation of turbulent flows. *Computer Methods in Applied Mechanics and Engineering*, 3:269–289, 1974.
- [9] F. Menter, H. Grotjans, and F. Unger. Numerical Aspects of Turbulence Modelling for the Reynolds Averaged Navier-Stokes Equations. In *VKI LS 1997-02, Computational Fluid Dynamics*, 1997.
- [10] F.R. Menter. Two-Equation Eddy-Viscosity Turbulence Models for Engineering Applications. *AIAA-Journal*, 32(8):1598–1605, 1994.
- [11] F.R. Menter and C.L. Rumsey. Assessment of Two-Equation Turbulence Models for Transonic Flows. 1994. AIAA paper 94-2343.
- [12] S.V. Patankar. *Numerical Heat Transfer and Fluid Flow*. Hemisphere Publishing Corporation, 1980.
- [13] O. Hassan; K. Morgan; E.J. Probert; J. Peraire. Unstructured tetrahedral mesh generation for three-dimensional viscous flows. *International journal for numerical methods in engineering*, 39:549–567, 1996.
- [14] P.L. Roe. Linear advection schemes on triangular meshes. Technical report, Cranfield Institute of Technology, November 1987. CoA 8720.
- [15] C. Rumsey, T. Gatski, S. Ying, and A. Bertelrud. Prediction of high-lift flows using turbulence closure models. 1997. AIAA paper 97-2260.
- [16] P. R. Spalart and S. R. Allmaras. A one-equation turbulence model for aerodynamical flows. *La Recherche Aéronautique*, (1):5–21, 1994.
- [17] R. Struijs, H. Deconinck, and P.L. Roe. Fluctuation Splitting Schemes for the 2D Euler Equations. In *VKI LS 1991-01, Computational Fluid Dynamics*, 1991.
- [18] E. van der Weide and H. Deconinck. Positive Matrix Distribution Schemes for Hyperbolic Systems, with application to the Euler Equations. pages 747–753, Paris, France, 1996. Wiley.
- [19] E. van der Weide and H. Deconinck. Upwind Residual Distribution methods for compressible flow: An alternative to Finite Volume and Finite Element methods; Part II: System Schemes and Applications. In *VKI LS 1997-02, Computational Fluid Dynamics*, 1997.
- [20] D. Vandromme. Overview of Turbulence Models for CFD in Industry. In *VKI LS 1995-03, Industrial Computational Fluid Dynamics*, 1995.
- [21] W.G. Vincenti and Jr. C.H. Kruger. *Introduction to Physical Gas Dynamics*. John Wiley & Sons, 1965.
- [22] D.C. Wilcox. Reassessment of the Scale-Determining Equation for Advanced Turbulence Models. *AIAA-Journal*, 26(11):1299–1310, 1988.

Turbulence Modelling for Supersonic Missile Aerodynamics: From Mixing-Length to Reynolds-Stress Models

Frédéric Thivet¹, Hugues Deniau², Jean-Marc Moschetta³, Jean-Victor Hachemin⁴

¹ ONERA CERT, DMAE, B.P. 4025, 31055 Toulouse Cedex 4, France

² ENSMA, LEA, B.P. 109, 86960 Futuroscope Cedex, France

³ SUPAERO, Département d'Aérodynamique, B.P. 4032, 31055 Toulouse Cedex 4, France

⁴ AEROSPATIALE MISSILES, 91370 Verrières-Le-Buisson, France

1. SUMMARY

Turbulence modelling is a key-point for the prediction of missile aerodynamics. On the basis of Parabolized Navier-Stokes computations, a variety of two-equation and Reynolds-Stress-Equation models have been analysed to assess their ability to predict relevant aerodynamical parameters for the design of missile shapes. Practical details, which are essential to implement the models in a robust and reliable way, are also given. Six test-cases, featuring flows around missile bodies at various angles of attack and including a finned configuration, are examined. Practical tools are given for missile designers to select the appropriate turbulence model, depending on the desired properties, such as accuracy, reliability. . . Algebraic models are shown to be dramatically impractical to predict developed vortical flows. The different levels of improvements achieved by the use of two-equation models, compressibility corrections and then Reynolds-Stress-Equation models are clearly demonstrated.

2. INTRODUCTION

The design of modern tactical supersonic missiles is heavily dependent upon the prediction and understanding of the vortical structures which appear along the leeward side of missile bodies. Accurate prediction of the flowfield is all the more needed that the leeward vortices may strongly interact with wings or fins located downstream. Furthermore, total pressure losses in the core of the vortices must be precisely estimated to allow a correct design of air intakes. On the top of that complexity, high Reynolds number flight conditions and compressibility effects must be taken into account in modelling turbulence for supersonic tactical missile aerodynamics.

Owing to their numerical efficiency, Parabolized Navier-Stokes (PNS) codes have been widely used by supersonic missile designers to accurately compute crossflow separation as long as no significant subsonic pockets are present in the computational domain. The high cost usually associated with the numerical simulation of three-dimensional turbulent flows is dramatically reduced by a PNS non-iterative space-marching strategy. Consequently, a non-iterative PNS solver, named TORPEDO, has been first developed and validated for laminar flows [1, 2], and subsequently extended to deal with turbulent flows [3, 4].

The present paper is aimed at providing detailed side-by-side comparisons of a variety of algebraic, two-equation and Reynolds-Stress Equation (RSE) models in terms of accuracy and robustness for the prediction of supersonic turbulent flows around missiles when large crossflow separated zones are present.

3. TEST-CASES

The experimental study of Pagan and Molton [5] was selected because it simultaneously provides 1) detailed surface pressure distributions, 2) oil flow visualizations to determine skin-friction lines, and 3) accurate flowfield total pressure measurements. The model used is a nine-caliber ogive-cylinder equipped with a three-caliber circular ogive of diameter $D = 30$ mm. The freestream conditions are $M_\infty = 2.0$, $Re_D = 1.61 \times 10^5$, $T_\infty = 183$ K and the incidence is varied from 0 to 20°. Above an angle of attack of 10°, two main vortices take place on the leeward side of the ogive-cylinder. They tend to develop and move upward as the flow goes downstream. At 15° and 20°, the vortical structure is more complex with a larger separated region including a secondary vortex. More recently, further measurements including skin friction coefficients have been carried out using the same conditions, except for the Reynolds number ($Re_D = 1.2 \times 10^6$) [6].

In addition, the experimental study of Owen and Horstman [7] was selected because it provides skin friction and velocity profiles measurements. The model is a cone-ogive-cylinder at 0° angle of attack under the conditions: $M_\infty = 7.2$, $Re_D = 2.21 \times 10^6$.

The AEROSPATIALE MISSILES ASTER forebody was used to demonstrate the ability of the present method to adequately simulate supersonic turbulent flows about finned-missile configurations. The body consists of an ogive-cylinder with four symmetrical fins of zero leading edge sweep angle starting at 7.4 calibers from the apex. The total body length is 12.8 calibers and a roll angle of 45° was considered in the present study. When placed at 10° angle of attack, two leeward vortices develop along the unfinned portion of the missile body. These vortices are split by the fins while 4 wing-tip vortices strongly interact with the 2 leeward vortices. Although surface pressure distributions were measured, experimental results are classified and therefore, cannot be published here. It is nevertheless interesting to compare numerical results in order to illustrate the influence of turbulence modelling when fairly complex physics is being considered.

4. NUMERICAL METHOD

The present PNS solver, named TORPEDO [1, 2] has been developed by AEROSPATIALE MISSILES in collaboration with ONERA CERT and SUPAERO. It is a non-iterative upwind implicit space-marching solver, which is based on the adaptation of Roe's scheme to the steady three-dimensional Parabolized Navier-Stokes equations written in a body-fitted coordinate system. A standard assumption to derive the PNS equations is that only a portion ω of the streamwise pressure gradient is retained following the approach developed by Vigneron *et al.* [8]. The

implicit discretization of the PNS equations results in a block-pentadiagonal system of algebraic equations which is solved using an efficient double ADI-iterative method. The viscous fluxes are evaluated using conventional second order accurate central differencing, while inviscid fluxes are discretized using an adaptation of Roe's original method to the steady Riemann problem in each transverse direction. Here, as opposed to the method originally developed by Lawrence [9], Roe's scheme is applied throughout the whole flowfield including the subsonic part of the boundary layer. An approximate average value of ω is used to evaluate the inviscid numerical flux at the interface following Korte's analysis [10]. To upgrade the scheme accuracy, a corrective term is added to the above first-order upwind scheme following Chakravarthy-Osher's non-MUSCL technique [11]. Implicit boundary conditions were implemented for both the viscous and the inviscid terms. Finally, various turbulence models ranging from algebraic to two-equation and Reynolds-Stress models [3, 4] were included.

5. LIMITATIONS OF AN ALGEBRAIC MODEL

The Baldwin and Lomax's model [12] is one of the most commonly used turbulence models for industrial applications, mainly because it is a simple algebraic model which does not directly depend on a boundary layer thickness estimate. As every algebraic model, it was built to calculate turbulent boundary layers, and some modifications must be added to calculate other flowfields. For flows around slender bodies with crossflow separation, Degani and Schiff proposed to retain the first maximum of the Baldwin function along each ray of a cross-section, when several maxima occurs (BLDS [13]). For other applications, the second maximum may have to be retained.

On regular grids, the results strongly depend on two parameters of the first-maximum-finding method: the number of rays and a cut-off value. The influence of these parameters was studied on the ogive-cylinder test-case at 10° angle of attack. The study showed that the force coefficients were highly sensitive to the values of these parameters (the lift coefficient could vary by 20%). The analysis of the flowfields using two sets of parameters showed that the differences were located in the crossflow separation region, where both maxima of the Baldwin function are too close to each other to be accurately resolved by the method. In the ogive-cylinder cases, an additional procedure was used to ensure that the first maximum was actually found, and that the solution was mesh-independent. Only such a procedure, which success has to be checked on each configuration, can lead to meaningful results. It shows that the BLDS model is not reliable enough to be used for intensive industrial studies.

The BLDS results presented on the ogive-cylinder test-cases are free from perturbations coming from the first-maximum finding procedure. For the ogive-cylinder test-case at 10° angle of attack, the location of the primary separation line is in agreement with the experiment (Fig.2). The wall pressure coefficient attests the presence of the primary vortex, but the levels are not quite close to measurements, neither in the crossflow separation region nor under the primary vortex (Fig.1). The total pressure field shows that the vortex is a little too developed (Fig.3). At a higher angle of attack, the BLDS model is unable to predict the primary vortex shape (Fig.7, 8), the total pressure loss or the pressure coefficient (Fig.4).

Finally, the BLDS model is not suitable to calculate missile aerodynamics because: 1) a reliable implementation to handle various complex turbulent flows seems to be impossible; and 2) like every algebraic model, it cannot accurately predict flows where turbulence develops far from the walls; the last point is due to the fact that algebraic models are based on the assumption that the turbulence scale is related to the boundary layer thickness.

Consequently, transport-equation models seem to be far more advisable.

6. TWO-EQUATION MODELS

The aim of the study on two-equation models is to provide a classification for supersonic missile configurations, based on the difficulty to get: 1) a robust discretization (*i.e.* which allows to produce results on various problems), and 2) reliable (*i.e.* weakly mesh-dependent) and accurate results. In the following, we will refer to robustness and reliability in this sense.

6.1 Standard Two-Equation Models

Two-equation models consist of transport equations for the turbulent kinetic energy k and a second variable, which allows to define a local turbulence scale. The constants of the models are fitted to reproduce basic turbulence features, and damping functions are often introduced to mimic near-wall effects. The behaviour of a given model is mainly related to the second variable definition and to the variables which the damping functions depend on.

Launder and Sharma were among the first authors to propose a two-equation model (LSke [14]) based on the isotropic dissipation $\bar{\epsilon} = \epsilon - 2\nu(\partial\sqrt{k}/\partial x_l)(\partial\sqrt{k}/\partial x_l)$. The true dissipation ϵ was isotropized in order to simplify the wall conditions ($k_w = 0, \bar{\epsilon}_w = 0$). As the damping functions depend on the local turbulent Reynolds number $R_t = k^2/\nu\epsilon$ only, it seems possible to implement this model independently from the walls location. This is not true, because the damping functions are built to mimic the near-wall behaviour only, so that they must not vary elsewhere. Now, around slender bodies at incidence, these damping functions "wake up" in vortices developing from the apex, although these regions may be strongly turbulent and do not need any damping. When implementing any model containing wall-damping functions (even if they depend on R_t only), one has to take care of confining their influence in boundary layers. This introduces a dependence on the walls location. Nevertheless, the LSke model may be considered as an easy one to implement in a robust and reliable manner.

Two others $k - \bar{\epsilon}$ models are considered: Nagano and Hishida's (NHke [15]), and Chien's (Chke [16]), the damping functions of which depend on the non-dimensionalized distance from the wall y^+ .

More recently, improvements have been obtained with a variety of models based on the true dissipation ϵ . The main drawbacks of such models come from the conditions at the wall (see §6.3). Nagano and Tagawa's (NTke [17]) and Myong and Kasagi's (MKke [18]) are both $k - \epsilon$ models, the main differences of which lie in the expression of the wall-damping functions, which depend on y^+ .

Models by Shih, Rodi *et al.* as described in [19, 20], were considered. The damping functions depend on R_t or y^+ either, and are determined after Direct Numerical

Simulations (DNS). Since predictions worse than BLDS's were obtained in the ogive-cylinder test-case at 10° of incidence, no more result or comment are given afterwards.

So, Zhang and Speziale (SZke [21]) proposed an original approach to damp the sink term in the ε transport equation: the part of the damping function accounting for near-wall effects is written as $\tilde{\varepsilon}/\varepsilon$. Owing to the nature of the damping functions and wall conditions, this model requires a very careful discretization, and refinement at the wall is needed to avoid divergence of the calculation.

Wilcox and Menter BSL model (WMko [22]), which may be considered as a two-layer $k - \omega/k - \varepsilon$ model, ω being the specific dissipation, is considered here because the absence of damping functions is very interesting from a practical viewpoint. However, it is not easy to implement in a general way, because the asymptotic behaviour of ω as $1/y^2$ at the wall has to be imposed on a few points (3 to 5) above the walls, and weak numerical instabilities in Menter's function may lead to undesirable shifts between $k - \varepsilon$ and $k - \omega$ models along a single ray.

Finally, Smith's $k - \ell$ model (Smkl [23]) is considered for its simplicity. As ℓ behaves as y at the wall, no stiff behaviour is expected and the implementation is very easy.

6.2 Compressibility Corrections

Compressibility corrections originally designed for free-shear flows are considered in order to get possible improvements over standard $k - \varepsilon$ models in the vortices. The first correction is based on the work by Sarkar on dilatational dissipation and pressure-dilatation correlation [24, 25], with the constants proposed by Morrison [26] for high-Reynolds flows (SM correction). The second correction is a simplification of Zeman's proposal [27] due to Vandromme and Zeman [28] (VZ correction). This correction had to be damped at the wall by the factor $1 - \exp(y^+/26)$ in order to avoid undesirable effects close to the walls. This should also be done with the SM correction for slightly higher Mach numbers.

6.3 Numerical Treatment of Two-Equation Models

The transport equations of turbulent variables are loosely coupled with the mean flow equations and solved by applying the Osher scheme for scalar equations, upgraded to second order by the Chakravarthy-Osher [11] technique.

For $k - \varepsilon$ models, wall conditions are not straightforward, and unfortunately, they strongly influence the stability and accuracy of the calculations. Either the wall normal derivative of the dissipation is set to zero (although it has no physical basis, it enhances stability), or the dissipation is set to a value which balances the diffusion of k at the wall, according to the asymptotic behaviour of the k transport equation. Here, satisfactory results were obtained with the condition: $\varepsilon_w = 2\nu(\partial\sqrt{k}/\partial n)^2|_w$ discretized to first order. Because of a stiffer behaviour at the wall, $k - \varepsilon$ models are more sensitive to mesh refinement than $k - \tilde{\varepsilon}$ models. This sensitivity can be reduced by using the \tilde{k} formulation proposed in [4] and used here.

For all models containing wall-damping functions and extra source terms, one must take care that these functions only act in near-wall regions (see §6.1) and that the implicit scheme only takes into account the stabilizing part of the source terms derivatives [3].

It was proved that the most efficient way to use two-equation models consists in beginning the computation

with the BLDS algebraic model and switching to the two-equation model as soon as turbulence has reached a sufficient level. Criteria were developed to determine the switching location, as well as a procedure to define the turbulent variables from the known turbulent viscosity and mean flow variables [3]. The usefulness of such a procedure is illustrated in §8.3.1.

7. REYNOLDS-STRESS-EQUATION MODELS

The aim of studying RSE models is to show the improvement achieved over two-equation models and to demonstrate their ability to compute realistic configurations.

7.1 Free-Flow RSE Models

The evolution equation for the Reynolds stress $\overline{u_i u_j}$ can be written into a classical form:

$$\underbrace{\frac{\partial \rho U_i \overline{u_i u_j}}{\partial x_l}}_{\text{convection}} = \underbrace{P_{ij}}_{\text{production}} + \underbrace{\Phi_{ij}}_{\text{redistribution}} - \underbrace{\varepsilon_{ij}}_{\text{dissipation}} + \underbrace{D_{tij}}_{\text{turbulent diffusion}} + \underbrace{D_{vij}}_{\text{viscous diffusion}} \quad (1)$$

where Φ_{ij} , ε_{ij} and D_{tij} have to be modelled. Differences between RSE and two-equation models are due mainly to the pressure-strain correlation Φ_{ij} , which accounts for the fact that the energy associated with the different Reynolds stresses is not equally distributed. This term is split into slow and rapid parts $\Phi_{ij,1}$ and $\Phi_{ij,2}$. The rapid part is evaluated using an expansion with respect to the anisotropy tensor components $a_{ij} = \overline{u_i u_j}/k - \frac{2}{3}\delta_{ij}$ under the assumption that the flow is homogeneous and weakly anisotropic. According to the order of expansion, one obtains either linear models such as the Launder-Reece-Rodi (LRR [29]) and Speziale-Sarkar-Gatski (SSG [30]) models or nonlinear models such as the Fu-Launder-Tselepidakis (FLT [31]) and Shih-Lumley (ShL [32]) models. Model constants are determined in such a way that some mathematical properties are satisfied, or that numerical results match experiments.

7.2 Near-Wall Modelling for RSE Models

Full wall-bounded-flow RSE models are used here. It means that the Reynolds-Stress equations are integrated down to the wall. This method only allows to account for expected anisotropy effects in the near-wall layer. Moreover, this method is much more advisable than the classical one, which consists in coupling free-flow RSE models with wall-laws or wall-bounded-flow $k - \varepsilon$ models. In these classical two-layer models, RSE are solved down to the logarithmic layer only, where Reynolds stresses are specified through algebraic relations, assuming the existence of an equilibrium layer which is very doubtful in complex three-dimensional flows.

Various models are available in the literature, depending on the choice for the pressure-strain correlation model and for the wall-damping functions. In most wall-bounded-flow RSE models, the pressure-strain correlation is based on a linear model. The difference between the models lies in the feature of the wall proximity effects modelling, which either depends on turbulent viscosity only (often through R_t), as in the near-wall SSG model (SSRs [33]), or on the turbulence structure as well, as in the Launder-Shima (LSRs [34]) and Hanjalić-Jakirlić (HJRs [35]) models. The motivation for the second approach is twofold: 1) wall-effects are not confined in the viscous sublayer since they affect the boundary layer

up to $y^+ = 60$, and 2) wall-effects modify the normal Reynolds stress in a better way, since turbulence reaches a two-component limit at the wall. This selective behaviour cannot be reproduced by a simple function of R_t .

Linear models for the pressure-strain correlation are known to be rather inaccurate to predict anisotropy effects and the misalignment between turbulent and viscous shear stresses [36]. Therefore it is interesting to deal with nonlinear models. However, the modelling of wall proximity effects in nonlinear RSE models faces several difficulties: 1) the knowledge of energy-transfer processes between Reynolds stresses is very poor; 2) models obtained in homogeneous turbulent flows are not able to reproduce energy transfer in the vicinity of the wall, where the turbulence features are strongly anisotropic and inhomogeneous. Such wall-bounded-flow nonlinear RSE models are nevertheless built by a careful term-by-term fit to each component of Reynolds stress balance obtained by DNS. Unfortunately, these models [37, 38, 39] are unable to predict a high Reynolds number flow on a flat plate [4]. Consequently, they were not considered in this study.

An original two-layer approach is proposed instead. A free-flow nonlinear model (FLT) is used in the fully turbulent region of boundary layers (and above), while a wall-bounded-flow linear model is used in the viscous sublayer: LSrs, HJrs or SSrs. The resulting models are denoted by LSFL, HJFL and SSFL respectively [4].

7.3 Special Numerical Treatment

When using a nonlinear RSE model, stability is strongly improved if the transport equations for the Reynolds stresses are expressed in terms of the anisotropy tensor components. However, no simple wall conditions exist for these components, and the boundary layer had to be split into two parts: in the inner layer, the unknowns of the RSE are the Reynolds stresses while in the outer layer, the unknowns are the anisotropy tensor components. Results proved to be fairly independent on the location of the matching surface between both regions.

8. ANALYSIS OF THE RESULTS

For each configuration, results with different models are presented on the same mesh, which was defined to produce grid-converged solutions with all models. Figures concerning the results obtained with some of the models are omitted here for brevity (e.g. Smkl results, since they are very close to WMko). Comments relative to results illustrated by a figure are stressed with a *. Grades from -3 to 3 (see Tab.2) are given to the models according to the accuracy of their prediction of the wall pressure coefficients (C_p) at different locations, the total pressure contours (P_t) which give the shape of the primary vortex, the wall skin friction coefficients (C_f) and the boundary layer thicknesses (δ). These grades are gathered in Tab.1.

8.1 Wall Pressures and Vortical Structures

8.1.1 10° Ogive-Cylinder

Computed and measured results are compared in cross-section $x/D = 7$ (Fig.1, 3). Even in this simple case, the BLDS model* gives rather poor results (§5.).

Among two-equation models, best results are obtained with the SZke* and WMko* models. They are the only ones to accurately predict the pressure level near the crossflow separation ($\Phi \simeq 105^\circ$). Good results are obtained with LSke*, MKke* and Smkl models, except for

the pressure in the crossflow separation region and the vortex shape. Results obtained with Chke and NTke models, which are almost equivalent to NHke and MKke respectively, will not be presented in all following cases.

All RSE models* give noticeably similar results, at the level of the best two-equation models, the HJrs model* being the best one. Two-layer RSE models further improve the wall pressure under the primary vortex, but they slightly overestimate its intensity. A constant in one damping function of the original SSrs model had to be tuned in order to make the computation possible and to obtain results comparable to HJrs and LSrs. Therefore, this modification must be kept in mind to assess subsequent SSrs results.

8.1.2 15° Ogive-Cylinder

Computed and measured results are compared in cross-sections $x/D = 6$, where the primary vortex just begins to separate from the boundary layer, and $x/D = 8$, where it behaves as a free vortex. Wall pressure coefficients are plotted in Fig.4, 5, 6, while total pressure contours are sketched in Fig.7 and 8.

Very poor results are obtained with the BLDS algebraic model*. Among the standard two-equation models, the best pressure coefficients are obtained with NHke and then MKke* models: they only slightly underestimate the pressure coefficient near the primary separation line ($\phi \simeq 100^\circ$). However, a better sketch of the vortical structures is obtained at $x/D = 8$ with LSke*, which unfortunately gives very inaccurate pressure coefficient levels near the separation line. The WMko* and Smkl models give a fairly good primary vortex, but the secondary flow is too developed and leads to poor pressure level prediction in this region ($\phi = 20 - 40^\circ$). The SZke model*, which gives the best results at 10° angle of attack, produces the worst at 15° !

With the standard two-equation models, the vortex develops too late as compared to experiment (Fig.7 top) and pressure is too low near the separation line (Fig.4); these points are dramatically improved with the compressibility corrections (Fig.7 bottom and 5). But now, the SM correction applied to both the MKke* and SZke* models degrades the prediction of the pressure plateau under the vortical structures. These drawbacks are avoided with the VZ correction (MKVZ model*), which even further improves the vortex shape at $x/D = 8$. The compressibility corrections increase the dissipation in the vortex core, and subsequently decrease the turbulent kinetic energy level (Fig.9) and the turbulent viscosity.

Very good results are obtained with RSE models also, except in the crossflow separation region. The prediction of the shape of the vortices by HJFL* and SSFL* models, is even better than in the case of the MKVZ model. RSE models are also successful in predicting the pressure plateau under the vortical structures. The anisotropy introduced by RSE models lead to a decrease in the turbulent kinetic energy level in the core of the vortex (Fig.9). Although the mechanism is different, the effect is similar to that obtained with compressibility corrections.

8.1.3 20° Ogive-Cylinder

Total pressure contours at $x/D = 8$ for a 20° angle of attack are sketched on Fig.16, in order to show that the conclusions at 15° are still valid when incidence increases.

Model	Pagan [5], $\alpha = 10^\circ$					Pagan [5], $\alpha = 15^\circ$				Pagan [5], $\alpha = 20^\circ$				Σ_1	Owen [7]		Σ_2	R
	$C_p, \Phi(^{\circ}) =$			1st Vtx	Σ	$C_p, \Phi(^{\circ}) =$		1st Vtx	Σ	$C_p, \Phi(^{\circ}) =$		1st Vtx	Σ		C_f	δ		
	25	50	105			30	100			plat	100							
Two-Equation Models																		
LSke	1	1	1	2	5	2	-1	2	3	1	0	0	1	9	-3	-3	3	2
NHke	1	1	1	1	4	1	2	0	3					≤ 7				2
Chke	1	1	1	1	4									≤ 7	-2	-2	≤ 3	2
NTke	1	1	1	1	4									≈ 7	1	0	≈ 8	1
MKke	1	2	1	2	6	1	1	0	2	1	0	0	1	9			≈ 10	1
SZke	2	2	3	3	10	-1	0	0	-1	1	-1	0	0	9	2	1	11	0
WMko	2	2	2	3	9	-2	1	1	0	1	1	1	3	12	1	0	13	0
Smkl	1	1	1	3	6	-2	2	1	1	1	0	0	1	8	3	1	12	3
Two-Equation Models with Compressibility Corrections																		
SZSM	2	1	3	3	9	1	1	2	4	2	1	1	4	17				-1
MKSM	1	2	1	2	6	-1	2	1	2	2	1	1	4	12				0
MKVZ	1	2	1	2	6	2	3	2	7	2	2	2	6	19				1
Reynolds-Stress-Equation Models																		
LSrs	1	1	2	3	7										1	-1		-2
HJrs	1	2	3	3	9			2										-2
SSrs	1	1	3	3	8													-2
HJSL	3	1	2	2	8													-2
HJFL	3	1	2	2	8	2	-1			2	-1	2	3	≈ 15			≈ 19	-3
LSFL						3	-1	3	5					≈ 15	2	2	≈ 19	-3
SSFL	3	1	2	2	8	2	-1	2	3	3	0	2	5	16			≈ 20	-3

Table 1: Models Evaluation Grid (see Tab. 2 for the meaning of the grades) - Columns Σ give indicative sumtotals without any weighting of the composing grades - In column Σ_1 , the total grade concerns C_p and P_i predictions - In column Σ_2 , the total grade concerns C_f and δ predictions also - Column **R** is relative to robustness and reliability (§6.).

N	results vs measurements	robustness and reliability (R)
3	very close to experiment	very easy
2	good	easy
1	adequate	fairly easy
0	fair	average
-1	rather poor	rather difficult
-2	poor	difficult
-3	very far from experiment	tricky

Table 2: Meaning of the grades used in Tab. 1

Standard two-equation models fail to predict the pressure level near the primary separation line (the best is WMko, the worst is SZke), which is improved by using compressibility corrections (with VZ correction above all), but not with RSE models. Improvement in the pressure plateau is obtained with both corrected two-equation and RSE models. As compared to other standard two-equation models, such as MKke*, WMko* predicts a better shape of the vortices, which is improved by using compressibility corrections (see the MKVZ* result), although the vortical structures become slightly too intense; this drawback is avoided with RSE models.

8.2 Wall Shear Stresses

8.2.1 10, 15 and 20° Ogive-Cylinders

In Fig.2 are sketched the friction lines obtained with BLDS and WMko models, this last one being representative of transport-equation models here. The measured location of the primary separation line is plotted on these figures. The line begins at $x/D = 4$ in both the experiment and the WMko solution, while it begins at $x/D = 5$ with the BLDS algebraic model. The prediction of the separation line location is good with the two-equation model, and only fair with the BLDS model. The secondary flow is absent from the BLDS solution.

Model	$C_f \times 10^3, x(m) =$			$\delta (cm), x(m) =$		
	1.15	1.76	2.37	1.15	1.76	2.37
expe	0.90	0.85	0.80	1.70	2.50	3.30
LSke	0.50	0.55	0.60	0.80	1.16	2.10
Chke	0.70	0.80	0.75	0.90	1.90	2.45
NTke	0.85	0.80	0.77	1.60	2.00	2.53
SZke	0.87	0.82	0.80	1.60	2.20	2.70
WMko	0.95	0.89	0.83	1.60	2.07	2.53
Smkl	0.88	0.85	0.80	1.50	2.20	2.90
LSrs	0.85	0.80	0.75	1.50	1.90	2.50
LSFL	0.88	0.82	0.78	1.60	2.30	3.10

Table 3: Owen and Horstman's Measurements [7]

At 20° angle of attack, BLDS and two-equation models predict the beginning of the separation line at $x/D = 1.5$ as in the experiment; if the location of this line is well predicted by the MKVZ model (Fig.15) for instance, this is not the case with the BLDS model. Less good results are obtained with RSE models, which is linked to the failure in predicting the pressure level in this region.

Finally Fig.10 shows the dramatic improvement achieved by RSE models in the prediction of the skin friction of the 10° ogive-cylinder test-case (see §3.), as compared to typical results obtained with a two-equation model.

8.2.2 0° Cone-Ogive-Cylinder

In Tab.3 are given the measured and computed skin friction coefficients and boundary layer thicknesses at various cross-sections of the Owen and Horstman's model at 0° angle of attack (§3.). It shows that $k - \bar{\epsilon}$ models (LSke, Chke) give poor predictions, $k - \epsilon$ models give adequate (NTke, MKke) or even good results (SZke), and Smkl model is very good. The results obtained on this test-case are to be related to the ability of the models to predict the logarithmic law in compressible flows. The SM correction degrades the result, which is consistent

with the fact that it is not built to account for boundary layer compressibility effects. Very good results are obtained with the two-layer LSFL RSE model.

8.3 Computations of a Finned Configuration

8.3.1 Specific Numerical Treatments

In order to compute finned configurations, special care has to be taken to set the distance and the normal direction to the wall, which are required by most of the models. Here, the "distance to the wall" of a mesh point is set to the minimum value of the distances to each point lying on the walls, and the data associated with the corresponding wall point are used to compute the required variables (y^+ , the "normal direction to the wall"...).

The computation of the first marching plane of the finned portion of the ASTER configuration starts from the interpolation of the solution obtained in the last marching plane of the unfinned portion. The fins intersect flow regions where the turbulence level is either high, near the body and in the primary vortex core, or very low, such as near the wing tips. The computation with turbulence transport equations can be carried out only in regions where turbulence level is high enough (e.g. $R_t > 200$). Elsewhere, an algebraic model (BLDS here) is appropriate. The whole domain is computed with the transport-equation models after cross-section $x/D = 11$.

8.3.2 Results

Two-equation and RSE models agree on wall pressure coefficients, except near the leeward sides of the fins. Significant differences appear in the skin friction (Fig.14).

If two-equation models give similar total pressure fields and vortices intensities, RSE models lead to significantly different predictions (Fig.11). After the upper fin has intersected the primary vortex into two fully turbulent vortical structures, the main vortex slides above the fin up to its tip, and the second one slides along the body down to the lower fin (Fig.13). Since the HJrs model predicts lower turbulence levels in the core of these vortices than LSke (Fig.12), both vortices move faster towards the upper wing tip and the lower wing junction respectively. On the opposite, the other vortices, near the wings tips, develop slightly slower with the RSE than with the two-equation model. The reason is that these vortices come from the fresh boundary layers developing on the fins, and that the HJrs model predicts higher turbulence level than LSke in boundary layers.

9. CONCLUSION

A detailed analysis of turbulence models has been carried out and is summarized in Tab.1, which can be used to reach many conclusions, depending on the viewpoint adopted. The Baldwin and Lomax's algebraic model (BLDS) has been shown to be dramatically insufficient to predict developed vortical flows. Two-equation models which the damping functions are set after DNS, are not yet suitable to address high-Reynolds-number wall-bounded flows. Reliable results are fairly easy to obtain with models based on the isotropized dissipation as the Launder and Sharma's $k - \epsilon$ model (LSke), but their accuracy is only adequate, and can even be poor when skin friction is considered. Among $k - \epsilon$ models based on the true dissipation, the So, Zhang and Speziale's model (SZke) is rather irregular: it gives the best results up to 10° angle of attack, but the worst at 15° and above. The $k - \omega$ model (WMko) gives good results on the whole set of test-cases,

but its reliability is subjected to special treatment to cure its intrinsic sensitivity to boundary conditions. Finally, the best compromise between accuracy and reliability is achieved by the Myong and Kasagi's $k - \epsilon$ model (MKke, carefully discretized) and the Smith's $k - \ell$ model (Smkl), which is the less mesh-dependent model near the walls. The overall computing costs using different two-equation models are fairly comparable, and about 20% higher than when using an algebraic model.

Compressibility corrections bring significant improvements in predicting the crossflow separation at high angles of attack. The advisable choice is to take a good standard two-equation model (e.g. MKke) and to enhance it by adding the Vandromme and Zeman's compressibility correction (VZ). This correction, if properly damped in boundary layers, does not seem to modify the cost nor the reliability of the computation.

In the case of RSE models which damping functions depend on turbulence structural parameters, such as Hanjalic and Jakirlic's (HJrs) or Launder and Shima's (LSrs) models, improvement over two-equation models can be obtained without tuning any parameter. This improvement is clearly visible in the vortices evolution and the wall pressure underneath. When these models are associated with a free-flow nonlinear RSE model, even better results can be obtained. However, they cannot improve the results in the crossflow separation region. The increased cost is about 50% over two-equation models.

Further developments are needed to account for compressibility effects in the boundary layers and to use free-flow compressibility corrections with $k - \ell$ and RSE models. In order to increase the ability of the solver to address missile configurations, a conservative multi-domain approach is currently being developed [40].

10. ACKNOWLEDGEMENTS

The work was done during the preparation of second author's Ph.D. at ONERA CERT, under CIFRE Contract by AEROSPATIALE MISSILES, and during his postdoctoral year at ONERA CERT. The work was partly supported by DRET (French Ministry of Defence). The authors thank Dr.B.Aupoix for his constructive comments on the paper.

REFERENCES

1. Moschetta, J.-M., Lafon, A. and Deniau, H., "Numerical Investigation of Supersonic Vortical Flow About a Missile Body", J. Spacecraft Rockets, 32, 5, Sep.-Oct. 1995, pp 765-770.
2. Moschetta, J.-M., Thivet, F. and Deniau, H., "PNS Computation of the Supersonic Vortical Flow About an Ogive-Cylinder at Incidence", First Europe-US High Speed Flow Field Database Workshop, 12-14 Nov. 1997.
3. Deniau, H., Lafon, A. and Moschetta, J.-M., "Progress in the Development and Validation of Turbulence Models for the Computation of 3D Supersonic Flows with Crossflow Separation", Jan. 1995, AIAA Paper 95-0090.
4. Deniau, H., Thivet, F. and Moschetta, J.-M., "Prediction of 3D Supersonic Flows Including Crossflow Separation Using Low-Reynolds-Number Turbulence Models", 11th Symposium on Turbulent Shear Flows, 8-11 Sep. 1997.
5. Pagan, D., Molton, P. and Delery, J., "Basic Experiment on a Supersonic Vortex Flow Around a Missile

- Body", *J. Spacecraft Rockets*, 29, 3, May-June 1992, pp 373-378.
6. Baudin, D. and Pilon, J. A., "Ecoulement tourbillonnaire autour d'un fuselage de missile", Rep. n° 165/4277 AY, ONERA, Jan. 1995.
 7. Owen, F. K., Horstman, C. C. and Kussoy, M. I., "Mean and fluctuating flow measurements on a fully-developed, non-adiabatic, hypersonic boundary layer", *J. Fluid Mech.*, 70, 2, July 1975, pp 393-413.
 8. Vigneron, Y. C., Rakich, J. V. and Tannehill, J. C., "Calculation of Supersonic Viscous Flow Over Delta Wings with Sharp Subsonic Leading Edges", July 1978, AIAA Paper 78-1137.
 9. Lawrence, S. L., Tannehill, J. C. and Chaussee, D. S., "Upwind Algorithm for the Parabolized Navier-Stokes Equations", *AIAA J.*, 27, 9, Sep. 1989, pp 1175-1183.
 10. Korte, J. J. and Mc Rae, D. S., "Explicit Upwind Algorithm for the Parabolized Navier-Stokes Equations", Jan. 1988, AIAA Paper 88-0716.
 11. Chakravarthy, S. R. and Osher, S., "A New Class of High Accuracy TVD Schemes for Hyperbolic Conservation Laws", Jan. 1985, AIAA Paper 85-0363.
 12. Baldwin, B. S. and Lomax, H., "Thin Layer Approximation and Algebraic Model for Separated Turbulent Flows", Jan. 1978, AIAA Paper 78-257.
 13. Degani, D. and Schiff, L. B., "Computation of Turbulent Supersonic Flows around Pointed Bodies Having Crossflow Separation", *J. Comp. Phys.*, 66, 1, 1986, pp 173-196.
 14. Launder, B. E. and Sharma, B. I., "Application of the energy-dissipation model of turbulence to the calculation of flow near a spinning disc", *Let. Heat Mass Transfer*, 1, 2, Feb. 1974, pp 131-138.
 15. Nagano, Y. and Hishida, M., "Improved Form of the $k-\epsilon$ Model for Wall Turbulent Shear Flows", *J. Fluid Engng*, 109, June 1987, pp 156-160.
 16. Chien, K.-Y., "Predictions of Channel and Boundary-Layer Flows with a Low-Reynolds-Number Turbulence Model", *AIAA J.*, 20, 1, Jan. 1982, pp 33-38.
 17. Nagano, Y. and Tagawa, M., "An Improved $k-\epsilon$ Model for Boundary Layer Flows", *J. Fluid Engng*, 119, Mar. 1990, pp 33-39.
 18. Myong, H. K. and Kasagi, N., "Prediction of Anisotropy of the Near-Wall Turbulence With an Anisotropic Low-Reynolds-Number $k-\epsilon$ Turbulence Model", *J. Fluid Engng*, 112, Dec. 1990, pp 521-524.
 19. Shih, T.-H. and Hsu, A. T., "An Improved $k-\epsilon$ Model for Near-Wall Turbulence", Jan. 1991, AIAA Paper 91-0611.
 20. Rodi, W. and Mansour, N. N., "Low Reynolds number $k-\epsilon$ modelling with the aid of direct simulation data", *J. Fluid Mech.*, 250, May 1993, pp 509-529.
 21. So, R. M. C., Zhang, H. S. and Speziale, C. G., "Near-Wall Modeling of the Dissipation Rate Equation", *AIAA J.*, 29, 12, Dec. 1991, pp 2069-2076.
 22. Menter, F. R., "Zonal Two Equation $k-\omega$ Turbulence Models for Aerodynamic Flows", July 1993, AIAA Paper 93-2906.
 23. Smith, B. R., "A Near-Wall Model for the $k-\ell$ Two-Equation Turbulence Model", June 1994, AIAA Paper 94-2386.
 24. Sarkar, S., Erlebacher, G., Y. H. M. and Kreiss, H. O., "The Analysis and Modelling of Dilatational Terms in Compressible Turbulence", *J. Fluid Mech.*, 227, June 1991, pp 473-493.
 25. Sarkar, S., "The Pressure-Dilatation Correlation in Compressible Flows", *Phys. Fluids*, 4, 12, Dec. 1992, pp 2674-2682.
 26. Morrison, J. H., "A Compressible Navier-Stokes Solver With Two-Equation and Reynolds Stress Turbulence Closure Models", NASA CR 4440, May 1992.
 27. Zeman, O., "Dilatation Dissipation: The Concept and Application in Modeling Compressible Mixing Layers", *Phys. Fluids*, 2, 2, Feb. 1990, pp 178-188.
 28. Vandromme, D. and Zeman, O., "Response of a Supersonic Boundary Layer to a Compression Corner", in "Studying Turbulence Using Numerical Simulation Databases - IV", pp 247-258, Center for Turbulence Research, Nov. 1992.
 29. Launder, B. E., Reece, G. J. and Rodi, W., "Progress in the Development of a Reynolds-Stress Turbulence Closure", *J. Fluid Mech.*, 68, 3, Apr. 1975, pp 537-566.
 30. Speziale, C. G., Sarkar, S. and Gatski, T. B., "Modelling the Pressure-Strain Correlation of Turbulence: An Invariant Dynamical Systems Approach", *J. Fluid Mech.*, 227, June 1991, pp 245-272.
 31. Fu, S., Launder, B. E. and Tselepidakis, D. P., "Accommodating the Effects of High-Strain Rates in Modelling the Pressure-Strain Correlation", UMIST Technical Report TFD/87/5, 1987.
 32. Shih, T.-H. and Lumley, J. L., "Second-Order Modeling of Near-Wall Turbulence", *Phys. Fluids*, 29, 4, Apr. 1986, pp 971-975.
 33. So, R. M. C., Aksoy, H., Sommer, T. P. and Yuan, S. P., "Development of a Near-Wall Reynolds-Stress Closure Based on the SSG Model for the Pressure Strain", NASA CR 4618, Aug. 1994.
 34. Launder, B. E. and Shima, N., "Second-Moment Closure for the Near-Wall Sublayer: Development and Application", *AIAA J.*, 27, 10, Oct. 1989, pp 1319-1325.
 35. Hanjalic, K. and Jakirlic, S., "A Model of Stress Dissipation in Second-Moment Closures", in "Advances in Turbulence IV", Kluwer Academic Publishers, Dordrecht, June 1993.
 36. Malecki, P., Étude de modèles de turbulence pour les couches limites tridimensionnelles, (250 p.), Ph.D. Thesis, SUPAERO, No 150, Nov. 1994.
 37. Shih, T.-H. and Mansour, N. N., "Modelling of near-wall turbulence", in "Engineering Turbulence Modelling and Experiments", Elsevier Science Publishers, Amsterdam, 1990.
 38. Launder, B. E. and Tselepidakis, D. P., "Progress and Paradoxes in Modelling Near-Wall Turbulence", pp 29-1-1/6, Eighth Symposium on Turbulent Shear Flows, 9-11 Sep. 1991.
 39. Launder, B. E. and Li, S. P., "The Elimination of Wall-Topography Parameters from Second-Moment Closure", *Phys. Fluids*, 6, 2, Feb. 1994, pp 999-1006.
 40. Grondin, G. and Thivet, F., "Computation of Supersonic Flows Around a Missile Configuration with a Conservative Multi-Domain Technique for Steady PNS Equations", in "Computational Fluid Dynamics '98", John Wiley & Sons, 1998.

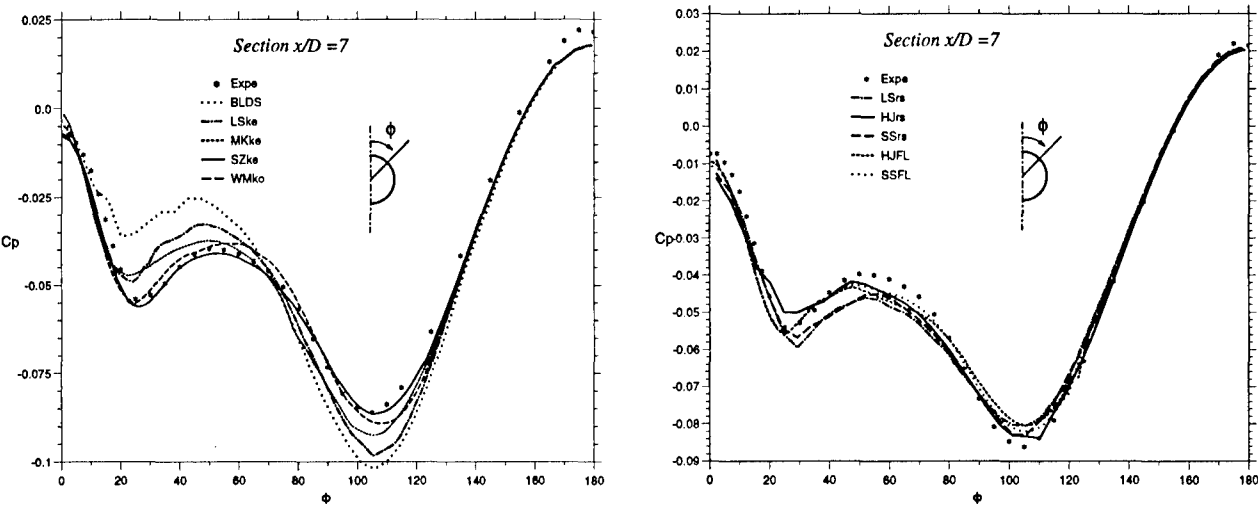


Figure 1: Ogive-cylinder, $M_\infty = 2.0$, $Re_D = 1.61 \times 10^5$, $\alpha = 10^\circ$ - Wall pressure coefficient in cross-section $x/D = 7$

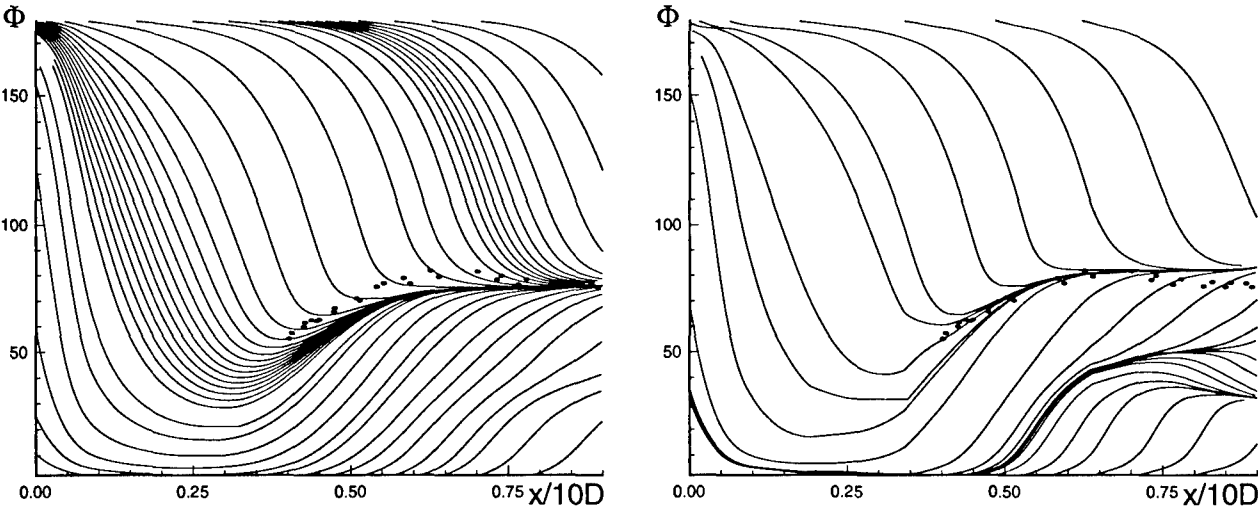


Figure 2: Ogive-cylinder, $M_\infty = 2.0$, $Re_D = 1.61 \times 10^5$, $\alpha = 10^\circ$ - Skin friction lines - Left: BLDS, Right: WMko

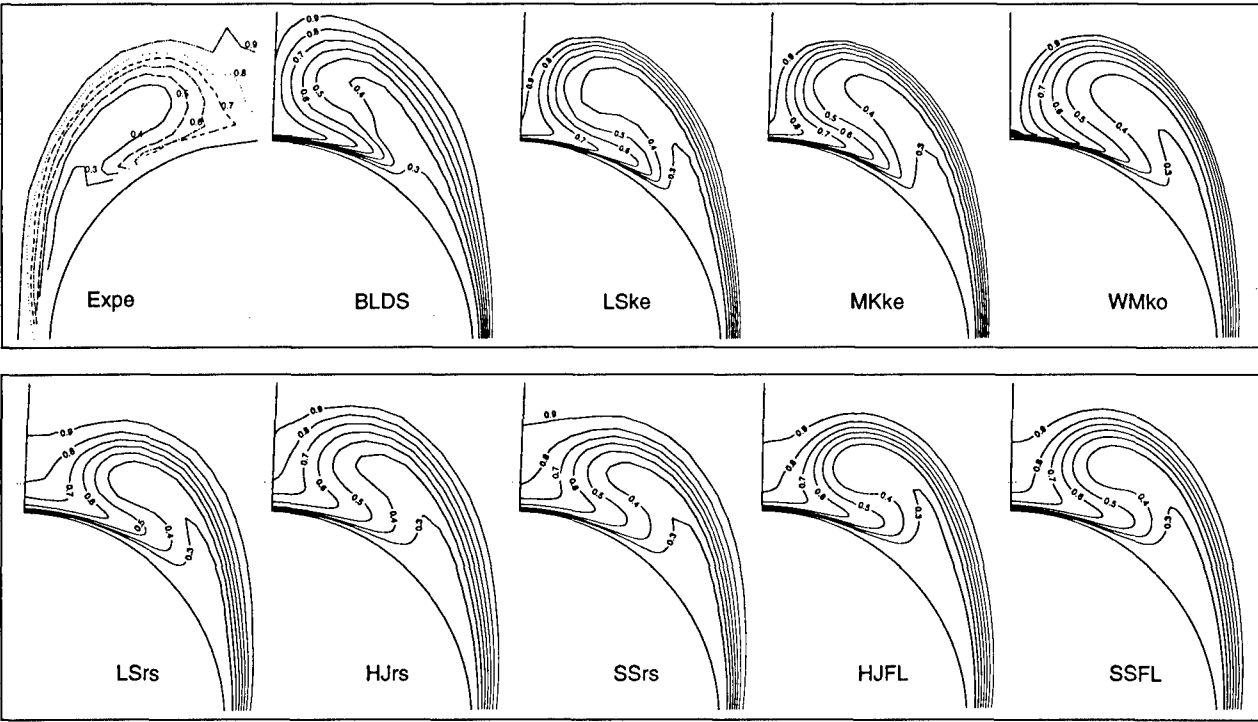


Figure 3: Ogive-cylinder, $M_\infty = 2.0$, $Re_D = 1.61 \times 10^5$, $\alpha = 10^\circ$ - Total pressure contours in cross-section $x/D = 7$

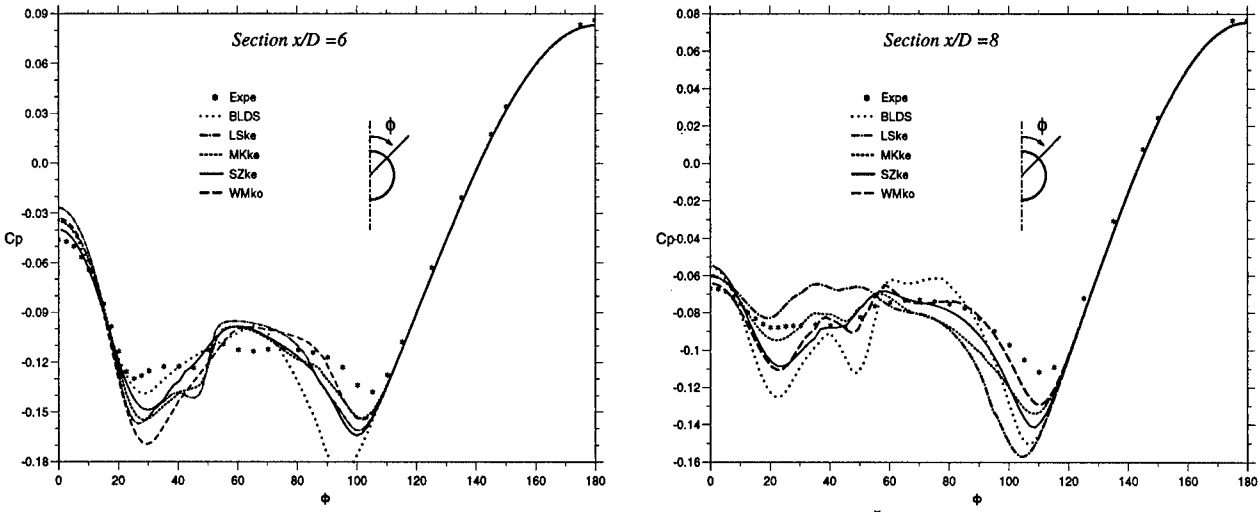


Figure 4: Ogive-cylinder, $M_\infty = 2.0$, $Re_D = 1.61 \times 10^5$, $\alpha = 15^\circ$
Wall pressure coefficient in cross-sections $x/D = 6$ and 8 - Algebraic and standard two-equation models

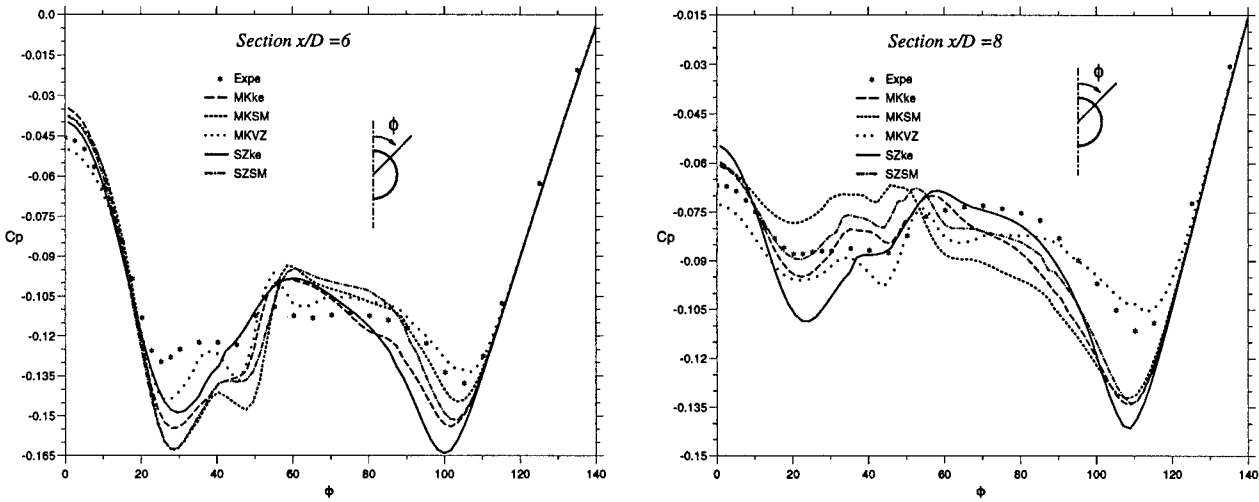


Figure 5: Ogive-cylinder, $M_\infty = 2.0$, $Re_D = 1.61 \times 10^5$, $\alpha = 15^\circ$
Wall pressure coefficient in cross-sections $x/D = 6$ and 8 - Two-equation models with compressibility corrections

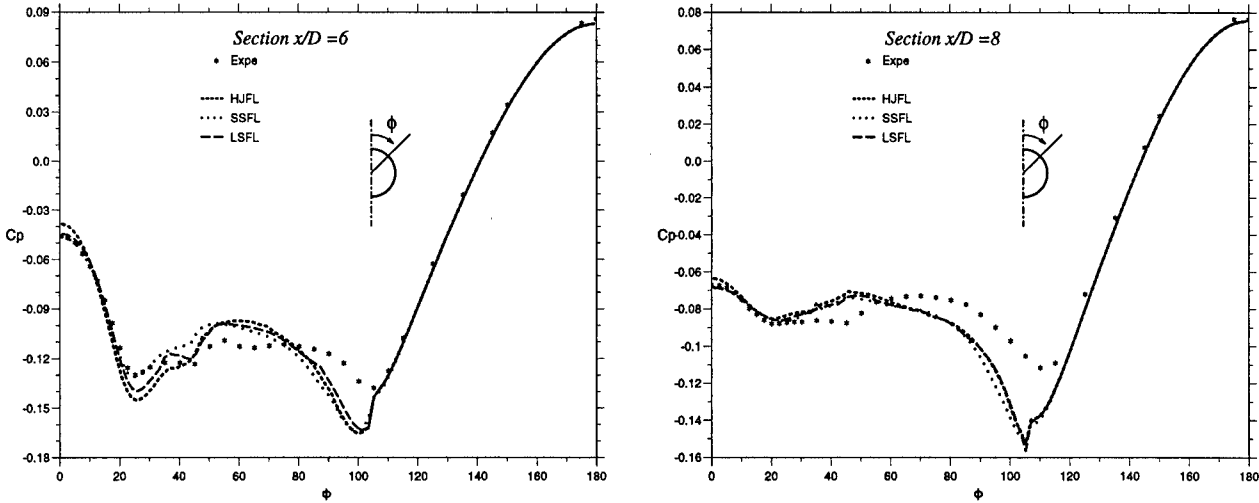


Figure 6: Ogive-cylinder, $M_\infty = 2.0$, $Re_D = 1.61 \times 10^5$, $\alpha = 15^\circ$
Wall pressure coefficient in cross-sections $x/D = 6$ and 8 - RSE models

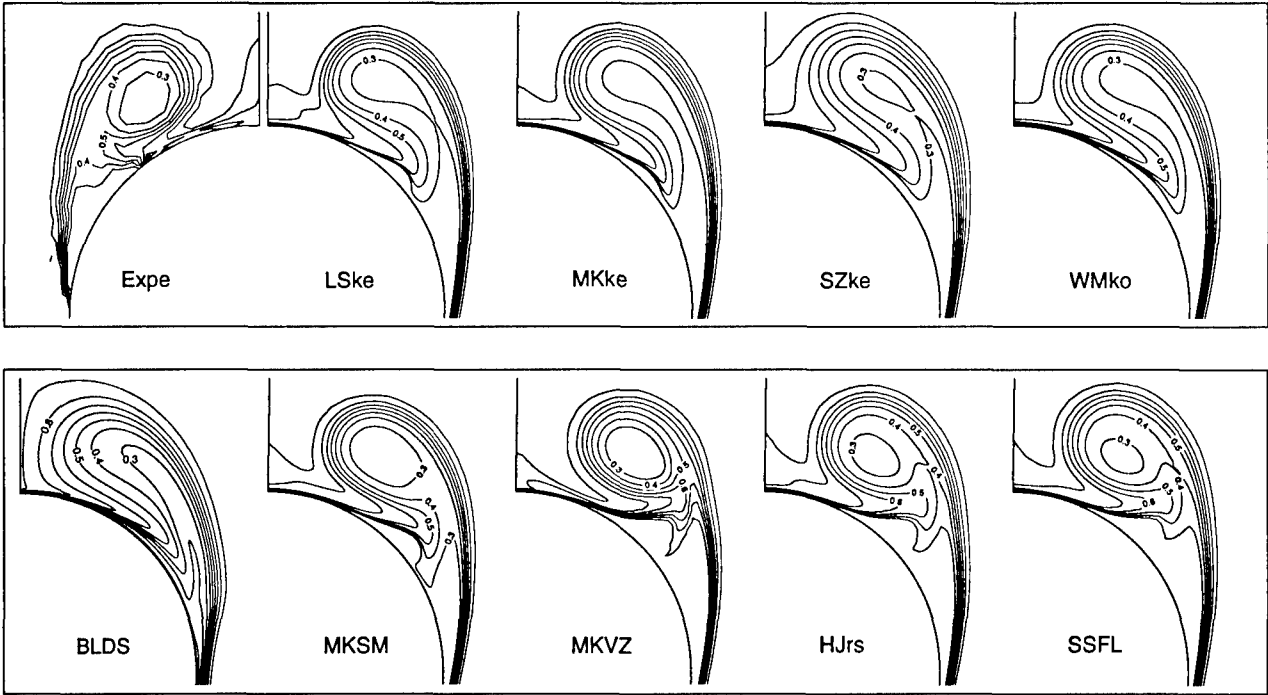


Figure 7: Ogive-cylinder, $M_\infty = 2.0$, $Re_D = 1.61 \times 10^5$, $\alpha = 15^\circ$ - Total pressure contours in cross-section $x/D = 6$

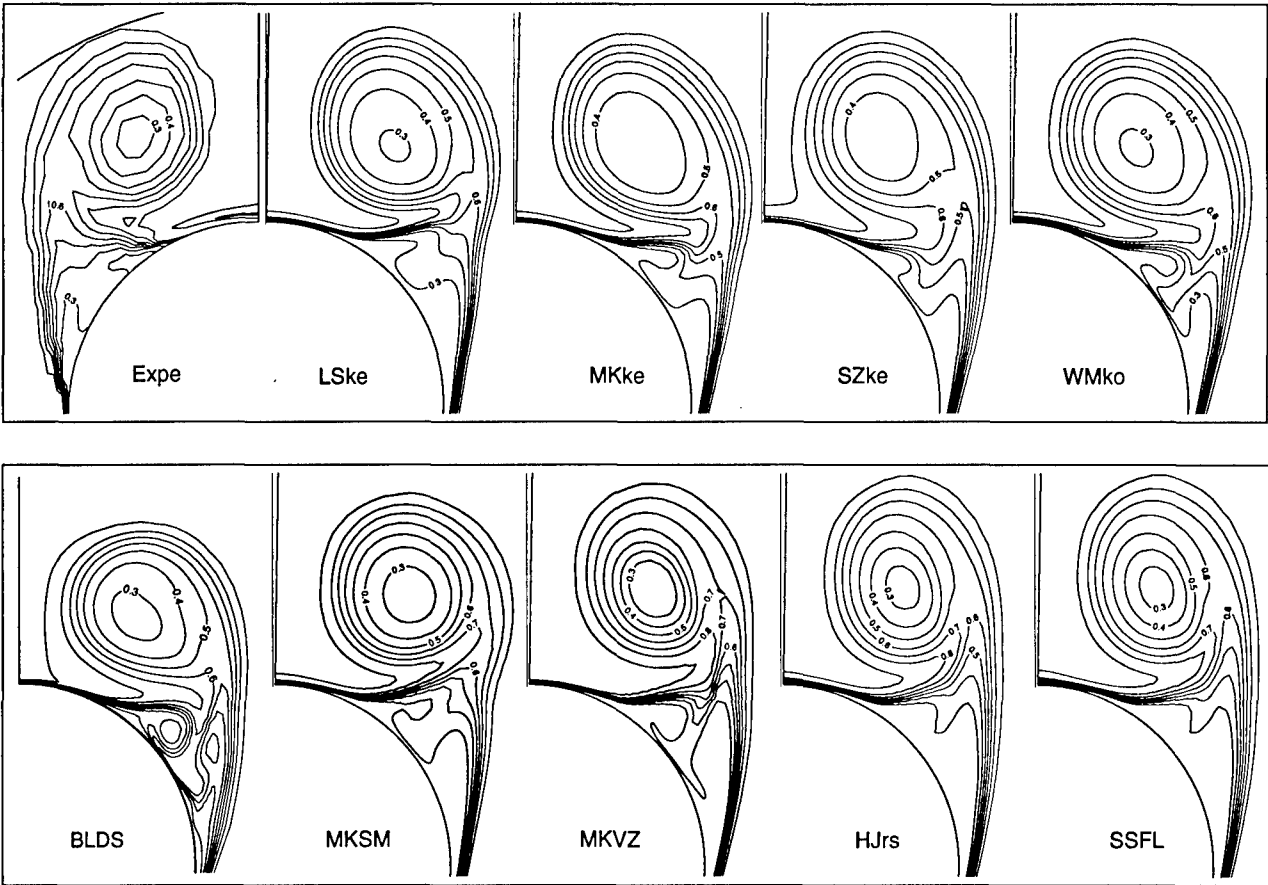


Figure 8: Ogive-cylinder, $M_\infty = 2.0$, $Re_D = 1.61 \times 10^5$, $\alpha = 15^\circ$ - Total pressure contours in cross-section $x/D = 8$

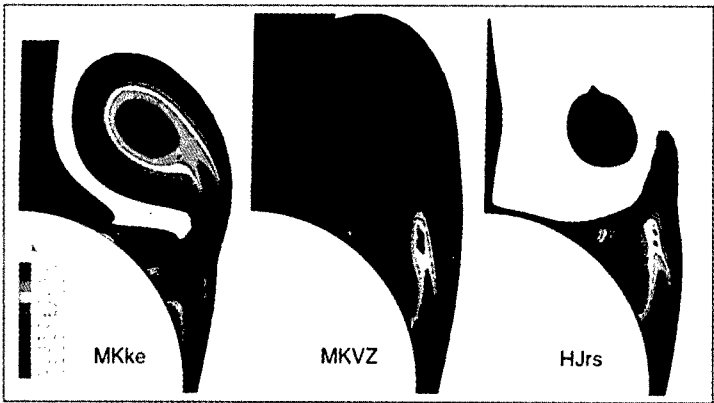


Figure 9: Ogive-cylinder,
 $M_\infty = 2.0, Re_D = 1.61 \times 10^5, \alpha = 15^\circ$
Turbulent kinetic energy contours in cross-section $x/D = 8$

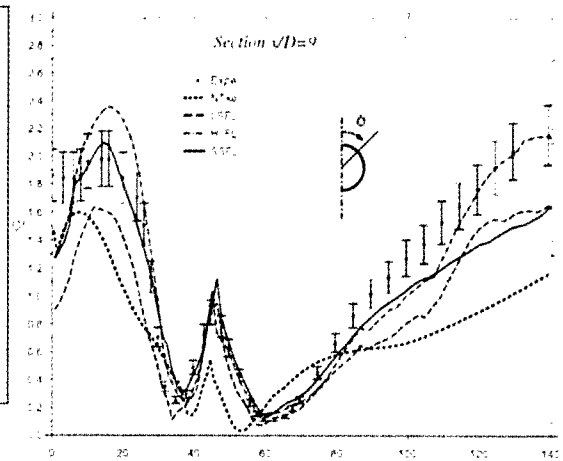


Figure 10: Ogive-cylinder,
 $M_\infty = 2.0, Re_D = 1.2 \times 10^6, \alpha = 10^\circ$
Skin friction coefficient in cross-section $x/D = 9$

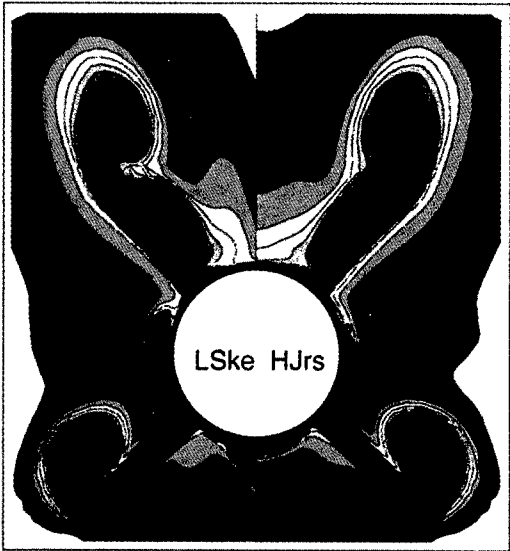


Figure 11: ASTER Forebody $\alpha = 10^\circ$
Total pressure contours in cross-section $x/D = 12.8$

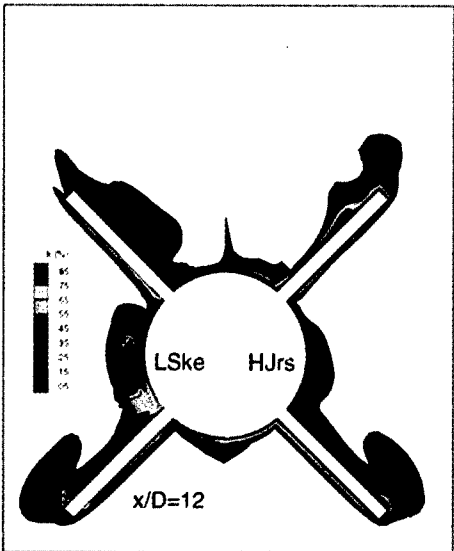
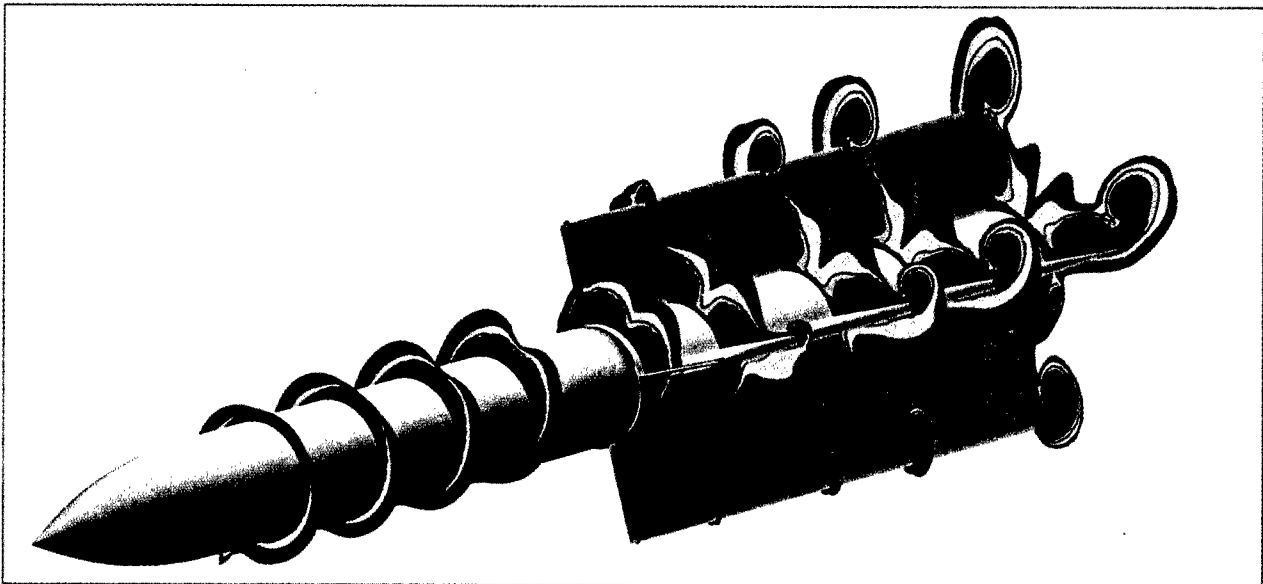


Figure 12: ASTER Forebody $\alpha = 10^\circ$
Turbulent kinetic energy contours in cross-section $x/D = 12$



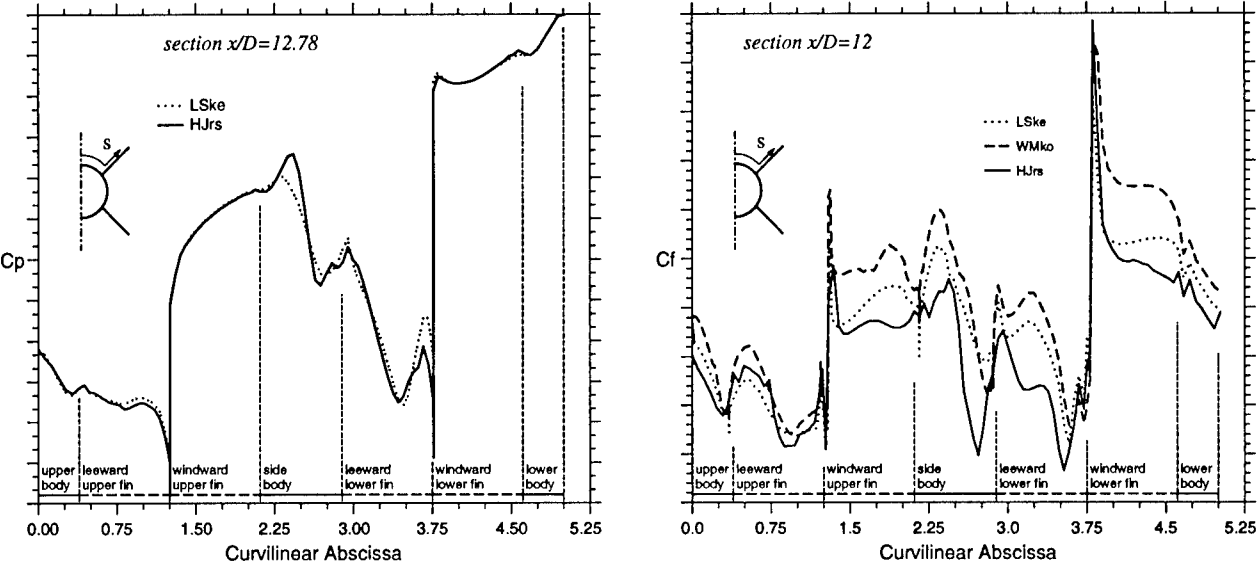


Figure 14: ASTER Forebody $\alpha = 10^\circ$
Wall pressure coefficient in cross-section $x/D = 12.8$ and Skin friction coefficient in cross-section $x/D = 12$

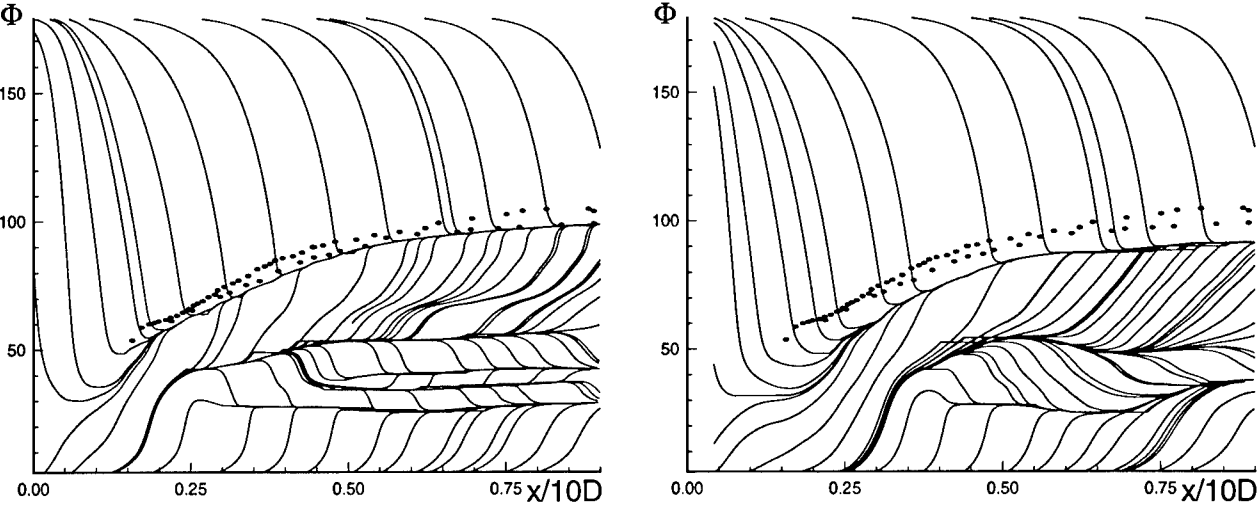


Figure 15: Ogive-cylinder, $M_\infty = 2.0$, $Re_D = 1.61 \times 10^5$, $\alpha = 20^\circ$ - Skin friction lines - Left: MKVZ, Right: HJrs

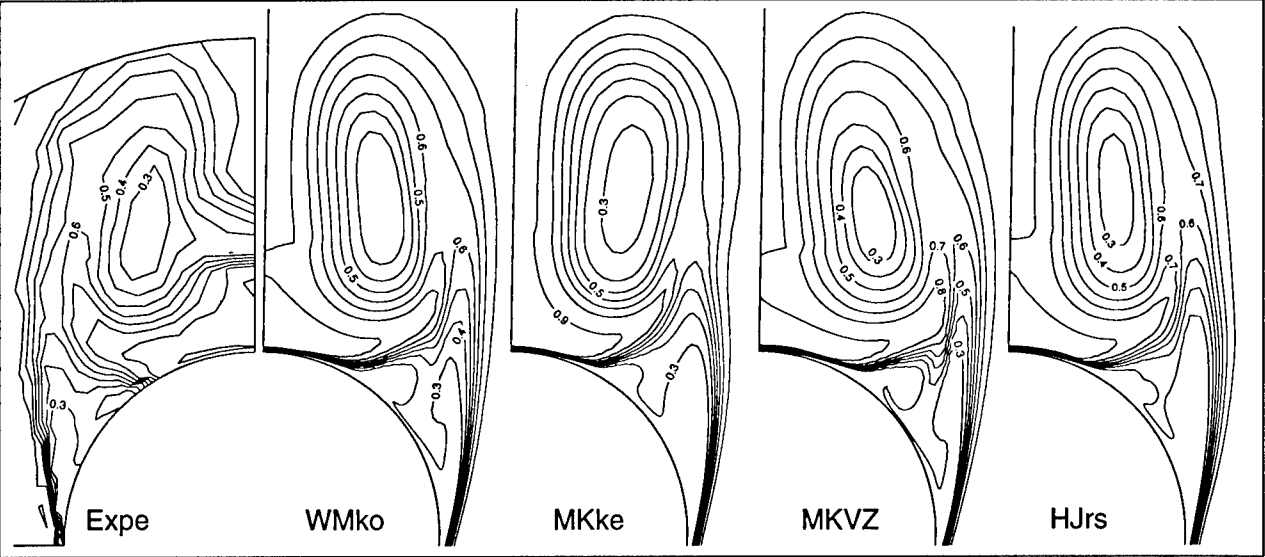


Figure 16: Ogive-cylinder, $M_\infty = 2.0$, $Re_D = 1.61 \times 10^5$, $\alpha = 20^\circ$ - Total pressure contours in cross-section $x/D = 8$

SIMULATION OF VISCOUS AND HIGH TEMPERATURE GAS EFFECTS ON STANDARD SHAPES IN HYPERSONIC FLOW

J.-M. Charbonnier, W. Dieudonné, S. Paris
von Kármán Institute for Fluid Dynamics
Aeronautics / Aerospace Department
Chaussée de Waterloo, 72
1640 Rhode Saint Genèse, Belgium

J. Muylaert, L. Walpot
ESA-European Space Research and Technology Center
Aerothermodynamics Section
Noordwijk, The Netherlands

SUMMARY

In the design process of a hypersonic vehicles, the ground testing facilities are not able to provide a full simulation of the actual flight conditions. Therefore the validation of the design tools used can only be supported by partial simulations, and extrapolation to flight conditions can only be validated by flight experiments. In the frame of the European Space Agency program entitled "Hypersonic Ground Testing Comprehension and Use for Design and Computational Fluid Dynamics Support", the von Karman Institute has extended the operating envelope of the Longshot free piston hypersonic wind tunnel to the use of CO₂ as test gas in addition to N₂. The analysis of the influence of the specific heat ratio and viscous interaction parameter on the flow over the ELECTRE and the Hyperboloid-Flare is presented both on the experimental and numerical stand points. Finally, high temperature gas effects on these geometries are also discussed based on measurements carried out in the ONERA-F4 and DLR-HEG high enthalpy facilities to support the interest in simulating these effects using classical "cold" facilities with various test gas.

1. INTRODUCTION

Due to the very high level of stagnation temperatures, the chemistry taking place downstream of the bow shock of a hypersonic vehicle may produce atomic oxygen and nitrogen and eventually ionize the atoms. If one would consider the mixture created as a combination of perfect gases, it is possible to determine an equivalent specific heat ratio which is lower than the value of air. Of course during their flow over the model, the chemical components may react together and consequently, the composition of the mixture will change. In order to simulate these phenomena, the natural tendency is to try to reproduce in wind tunnel the flight conditions. This implies that the reservoir temperature of the wind tunnel should be very high. The experimentalists are then facing the problem that the test gas will already react in the reservoir and will not recombine to a composition equivalent to the stagnant air of the atmosphere when it arrives onto the model. In such a case, the analysis of the data collected on the model is rather difficult to achieve because the gas which flows on the model is not always fully characterized.

In order to assess the influence of high temperature gas effects, a simpler approach consists in using a heavy test gas with a specific heat ratio γ lower than the value of air at ambient conditions. This simulation corresponds to the case of a frozen composition for the mixture of components created downstream of the shock which would pass around the body. The purpose of the work reported is to analyze the

effect of the specific heat ratio coupled with viscous effects on two generic configurations: the ELECTRE and the Hyperboloid-Flare. Tests are carried out in the VKI-Longshot hypersonic facility operated with nitrogen and with carbon dioxide as test gases and compared with numerical simulations.

In the next section, the newly defined flow conditions in the VKI-Longshot wind tunnel are presented and calibration data are compared to numerical simulations. Then, the measured wall heat transfer and pressure distributions on the ELECTRE and Hyperboloid-Flare are presented. The numerical rebuilding of the experiments is presented and the viscous and specific heat ratio influences on these two configurations are discussed.

2. THE VKI-LONGSHOT FACILITY

2.1 Introduction

The VKI-Longshot is a free piston wind tunnel which uses a piston to compress the test gas. It can provide very high pressure levels (up to 4000 bars) for moderate temperatures (up to 2500K). The facility is classified as a cold hypersonic facility because the test gas (usually N₂) can be considered as a perfect gas. Classically, the facility operates with N₂ using a contoured nozzle (Mach 14) [1]. In this study, new operating conditions using N₂ or CO₂ and a conical nozzle of 355 mm exit diameter were defined. It must be noticed that the contoured nozzle would not have been adapted for CO₂. As previously mentioned, the purpose of using two test gases with different specific heat ratios γ is to provide a partial simulation of the so-called high temperature gas effects. Carbon dioxide has been selected as the second test gas because it has a γ value of 1.3 and it is easier to handle than CF₄ ($\gamma=1.12$). Since the properties of N₂ and CO₂ are different, it is likely that the Mach number in the exit section will be different for the two gases. Therefore in order to compare the results obtained with the two gases, some similarity parameters other than Mach and Reynolds numbers have to be kept constant. The parameter, known as the viscous interaction parameter \bar{V}^* , allows to normalize pressure, heat transfer and force measurements from various wind tunnels for blunt bodies such as Hermes at angle of attack and for sharper configurations [2,3].

In the Longshot, the viscous interaction parameter \bar{V}^* based on infinite upstream conditions was selected as the similarity parameter and kept constant when changing the test gas.

$$\bar{V}^* = \frac{M_\infty}{\sqrt{\text{Re}_L}} \sqrt{C^*} \quad (1)$$

where $C^* = \frac{T_w \mu^*}{T^* \mu_w}$ and $L = 0.12m$ and the reference temperature T^* is defined by:

$$T^* = 0.468 \cdot T_w + 0.532 \cdot T_w + 0.195 \cdot \left(\frac{\gamma-1}{2} \right) \cdot M_w^2 \cdot T_w \quad (2)$$

The choice of 2 values of $\overline{V^*}$ is based on typical reentry data for the Shuttle Orbiter and for the Apollo capsule. The four new operating conditions (LSCN1 to 4, table 1) defined for the conical nozzle are calibrated and the nozzle flow field is simulated using a Navier-Stokes code with turbulence modeling.

2.2 Calibration techniques and data processing

The way to process the data in the Longshot as in many other short duration hypersonic wind tunnels is to measure quantities in the test section (Pitot pressure and heat transfer at stagnation point of an hemisphere), the total pressure in the test chamber and to infer the flow conditions using a model for the flow expansion in the nozzle. Because of the very high pressure in the reservoir of the Longshot (up to 250 MPa for these conditions), it is required to account for dense gas effects. For that, van der Waals equations of state are used to define the real reservoir conditions (P0real and T0real). Equivalent perfect gas conditions (P0perf. & T0perf) are defined by expressing the equality of the entropy and enthalpy based on the van der Waals and the perfect gas equations of state [4,5,6,7]. The test gas at these equivalent perfect gas conditions is then expanded in the nozzle. The free stream properties are obtained by an iterative procedure starting from the pressure measured in the reservoir (P0real) and a guessed reservoir temperature T0real. The equivalent perfect gas conditions are computed and the Mach number is directly obtained from the normal shock relation using the Pitot pressure (Pt2) and the perfect gas total pressure (P0perf). The stagnation heat flux on the hemisphere is computed using Fay-Riddell formulation and compared to the actual measurement. The total temperature (T0real) is modified and the process is repeated until the computed and measured heat fluxes are identical. When this condition is satisfied, the free stream flow properties can be computed. It is important to notice that this procedure is applied at each instant during the run time of the facility making an assumption of quasi-steady flow in the nozzle. Since the Longshot operation is based on the compression of a finite amount of gas in the reservoir, the pressure and the temperature are decaying during the run time (10 to 20 ms). This leads to a moderate decrease of the Reynolds number during the run time of the facility.

2.3 Analysis of the calibration results

As expected from the conical nature of the flow, it is observed that between the first section investigated at 0.02 m (Sect. I) from the nozzle exit and the second one at 0.4 m (Sect. II), the flow accelerates. The Mach number values on the nozzle centerline for the two investigated sections and the four test conditions are summarized in table 2.

First re-buildings of the flow in the nozzle using the VKI-MB code clearly indicated that the nozzle wall boundary layer is turbulent and that transition occurs upstream of the first wall heat transfer gauge (0.3 m from the throat). In the code, the boundary layer transition is replaced by a switch from a laminar to a turbulent computation. In order to determine the transition location, several computations were carried out for

condition LSCN1 varying the transition onset from the throat to 0.3 m downstream. Figure 1 shows the normalized Pitot pressure computed for three transition locations compared to the laminar case, illustrating the effect on the Pitot pressure and on the size of the jet potential core.

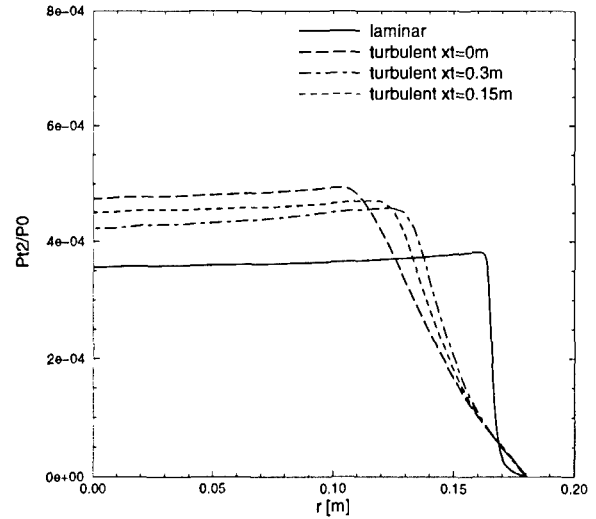


Figure 1: Laminar and turbulent computed Pitot profiles at nozzle exit for condition LSCN1

After comparison with the experiments (figures 2 & 3), the transition location in the computations was fixed at 0.15 m for all four flow conditions. This location enables a good comparison of the measured and computed pressure (figure 4) and heat transfer (figure 5) distributions along the nozzle wall. In the jet, still a fair agreement between the measured and computed Pitot pressure Pt2 (figure 6) and stagnation heat transfer Qt2 (figure 7) is observed in the downstream section (sect. II).

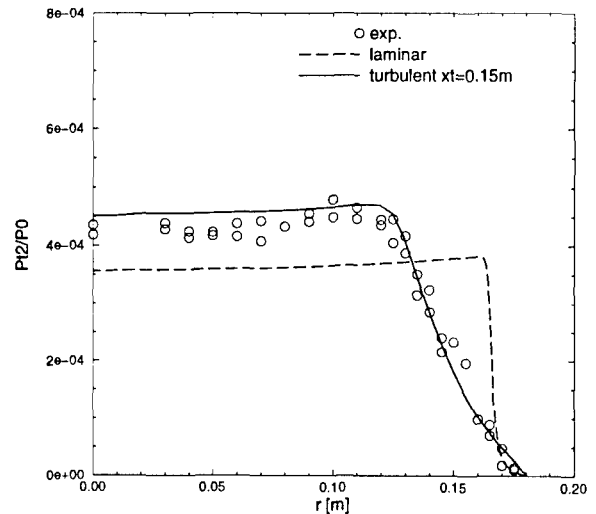


Figure 2: Measured and computed Pitot profiles at nozzle exit for condition LSCN1 (Sect. I)

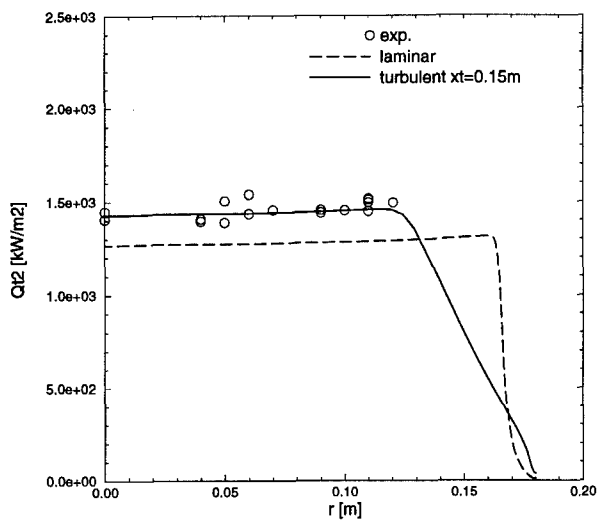


Figure 3: Measured and computed stagnation heat flux profiles at nozzle exit for condition LSCN1 (Sect. I)

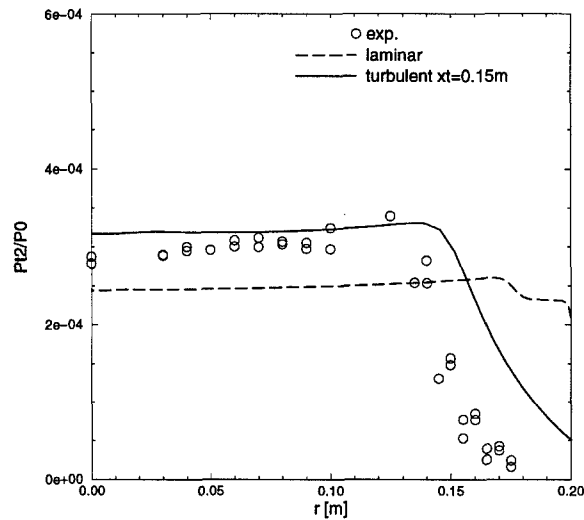


Figure 6: Measured and computed Pitot profiles at nozzle exit for condition LSCN1 (Sect. II)

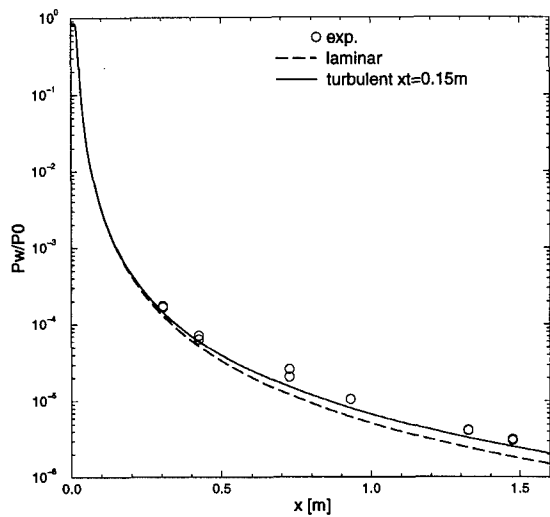


Figure 4: Measured and computed pressure distribution along the nozzle wall for condition LSCN1

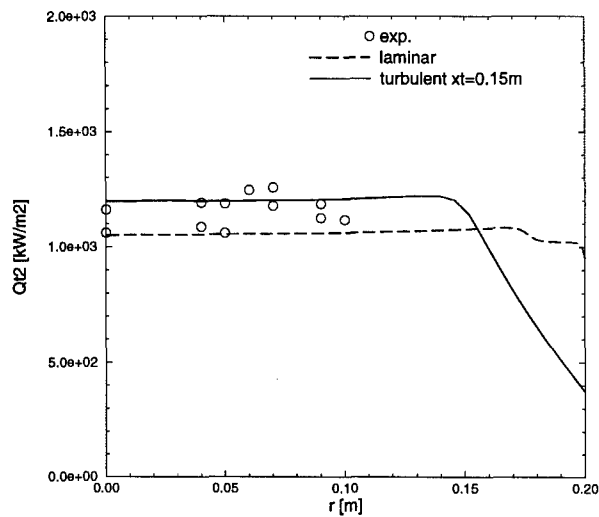


Figure 7: Measured and computed stagnation heat flux profiles at nozzle exit for condition LSCN1 (Sect. II)

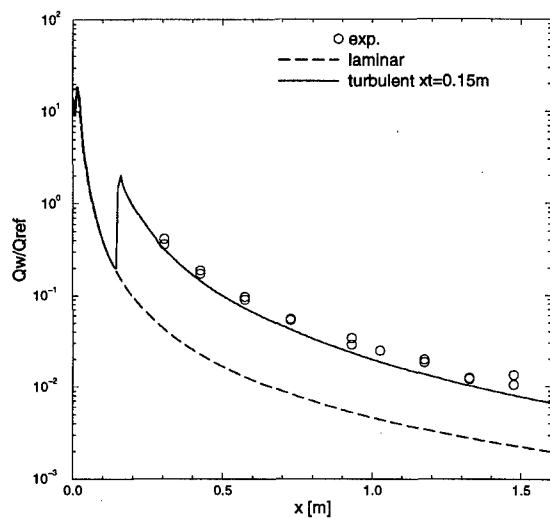


Figure 5: Measured and computed heat flux distribution along the nozzle wall for condition LSCN1

A similar analysis was carried out for the four test conditions. A good agreement was found between measured and computed data for LSCN1 & LSCN3 (N₂) whereas for LSCN2 & LSCN4 (CO₂), although the nozzle wall data were found in good agreement (figures 8 & 9), the measured Pitot pressures were offset with respect to the computed values (figures 10 & 11). This difference is believed to be associated with non-thermally perfect gas behavior associated with vibrational excitation of the test gas molecule. Although the reservoir temperature is high, there is no dissociation because of the high pressure. However, there is a large vibrational excitation which may be frozen during the first part of the expansion [8].

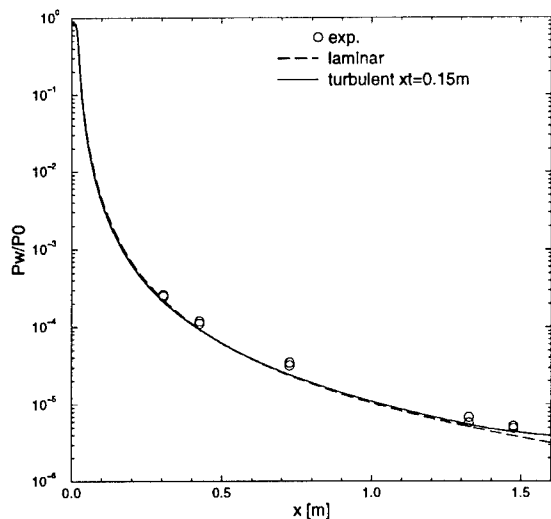


Figure 8: Measured and computed wall pressure along the nozzle for condition LSCN2

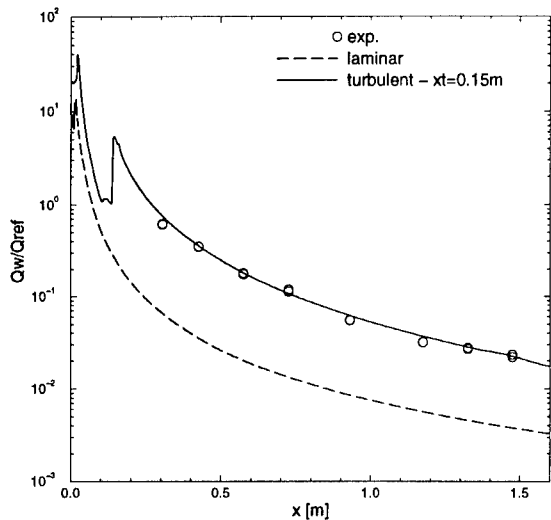


Figure 9: Measured and computed wall heat flux along the nozzle for condition LSCN2

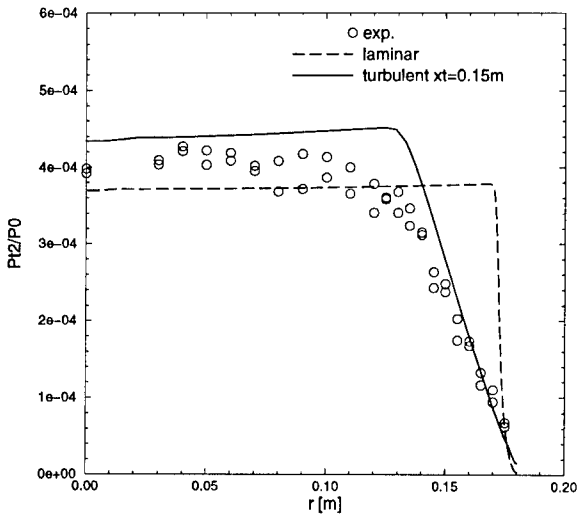


Figure 10: Measured and computed Pitot profiles at nozzle exit for condition LSCN2 (Sect. I)

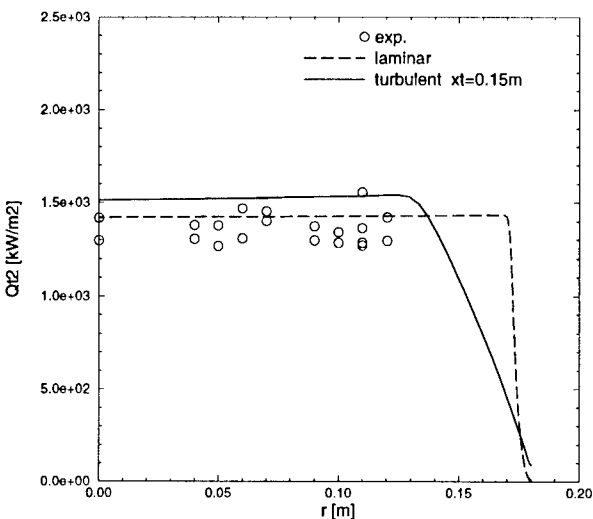


Figure 11: Measured and computed stagnation heat flux profiles at nozzle exit for condition LSCN2 (Sect. I)

In order to investigate the effect of non thermally perfect gas on the computed flow field, computations were performed with the chemically reacting flow code LORE [9] for condition LSCN1 (with N2). In the LORE code, the turbulence model implemented is the Baldwin-Lomax whereas in the VKI-MB, the Spalart-Allmaras model [10] was used. In order to distinguish the contribution of the turbulence model from the effect of the non-thermally perfect gas, perfect gas computations were also performed with LORE. In fact as illustrated in figure 12, for perfect gas computations, the turbulence model used influences the Mach number in the potential core. For the same transition location, the Baldwin Lomax model results in a thinner boundary layer and consequently in a slightly higher Mach number at the nozzle outlet.

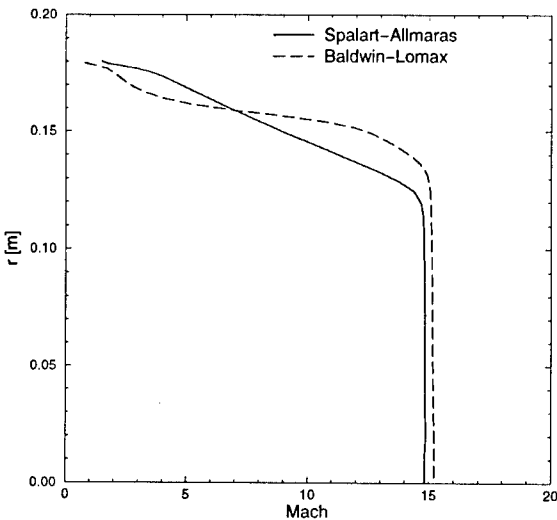


Figure 12: Computed Mach number profiles at nozzle exit for condition LSCN1 - perfect gas

The chemically reacting gas computation results are plotted in figure 13 in comparison with perfect gas computations with the two turbulence models. For this flow condition (LSCN1) with N2, there is only a small vibrational excitation effect taking place. However, there seems to be some identifiable effects on the Mach profile in the boundary layer which turns out to be the thickest of the three computations resulting in

smaller Mach number in the potential core compared to the perfect gas Spalart-Allmaras computation. The maximum difference between the Mach numbers obtained from these three computations (for fixed transition location) is of the order of 5%.

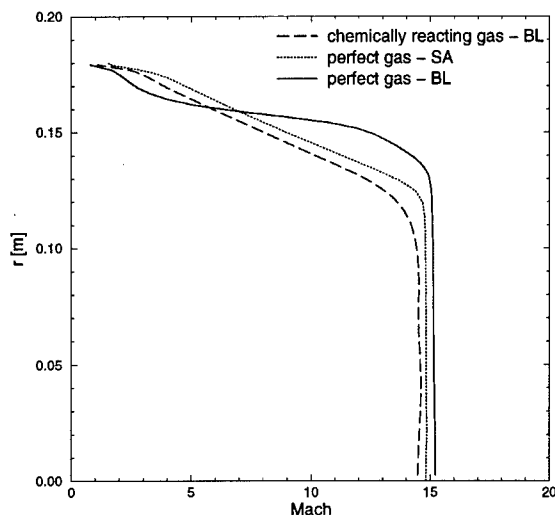


Figure 13: Computed Mach number profiles at nozzle exit for condition LSCN1

For the conditions LSCN2 & LSCN4 (with CO₂), reacting flow computations are under progress to investigate the vibrational excitation effects for the conditions with CO₂ as they are expected to be significant.

3. FLOW FIELD OVER THE ELECTRE

The ELECTRE model is a blunt cone illustrated in figure 14. equipped with pressure gauges and thermocouples.

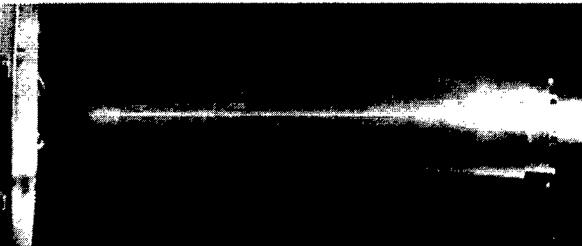


Figure 14: ELECTRE model in the Longshot test section

The influence of the rarefaction parameter and of the specific heat ratio on the wall pressure and heat transfer on ELECTRE was evaluated using perfect gas computations. As observed in figures 15 & 16, Cp and St are only slightly dependent on the specific heat ratio. The viscous interaction parameter has almost no influence on Cp whereas it clearly affects St on the conical part of the model.

Actually the influence of the specific heat ratio is clearly visible on the schlieren photograph presented in figure 17. The lower the value of γ , the closer the bow shock from the nose. The effect of γ on the shock standoff distance is indeed important since for conditions LSCN2 & LSCN4, the Mach number is lower than for the two other conditions with N₂ which effect is to increase the standoff distance. It means that the influence of the decrease in Mach number is more than compensated by the effect of the decrease in γ .

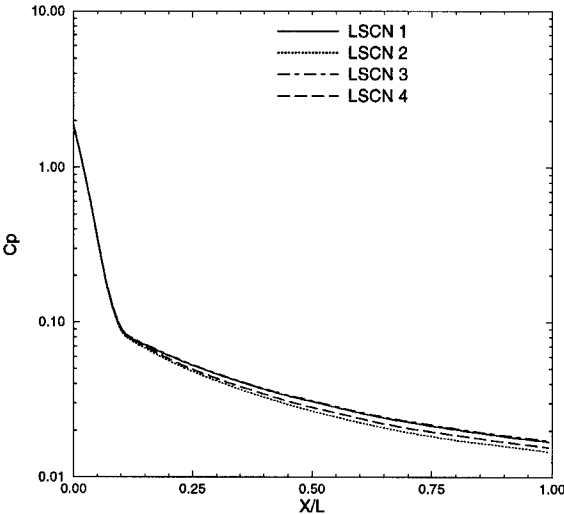


Figure 15: Computed Cp distribution on ELECTRE for the four flow conditions in the Longshot

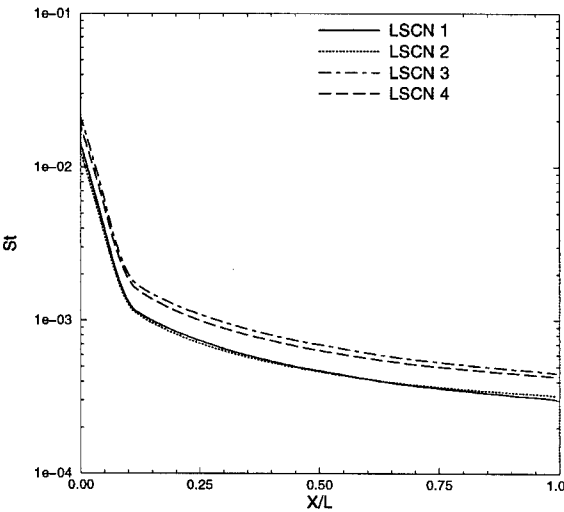


Figure 16: Computed St distribution on ELECTRE for the four flow conditions in the Longshot

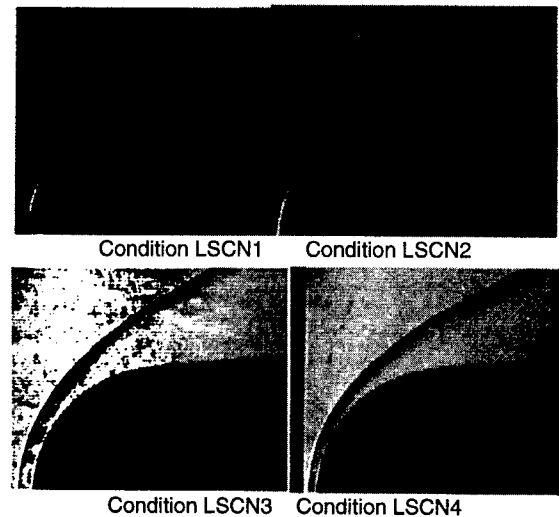


Figure 17: Schlieren photograph of the flow over the ELECTRE for the four flow conditions in the Longshot

Figure 18 shows the pressure coefficient Cp measured for the four operating conditions. As already mentioned, the effect of the change in flow condition could only be detected on the

conical part of the model. In fact due to a non appropriate pressure and heat transfer equipment of the ELECTRE model with respect to the flow conditions in the Longshot, the uncertainties in the measurements on the conical part are quite large. For purpose of clarity, the measurements on the rear part of the cone showing high levels of uncertainty have been removed from the plots presented in this section.

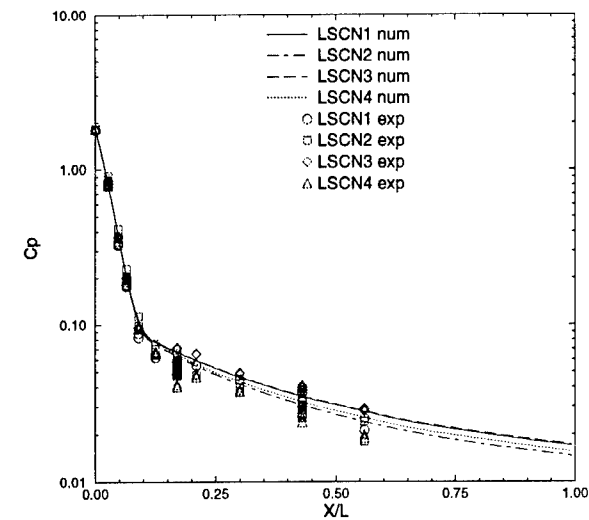


Figure 18: Measured and computed wall pressure coefficients on ELECTRE

As expected, for a given viscous interaction parameter, the measured Stanton number distributions are quite identical between the two corresponding conditions. Normalizing the Stanton number by the viscous interaction parameter leads to find almost a single curve for the four flow conditions in the Longshot as illustrated in figure 19.

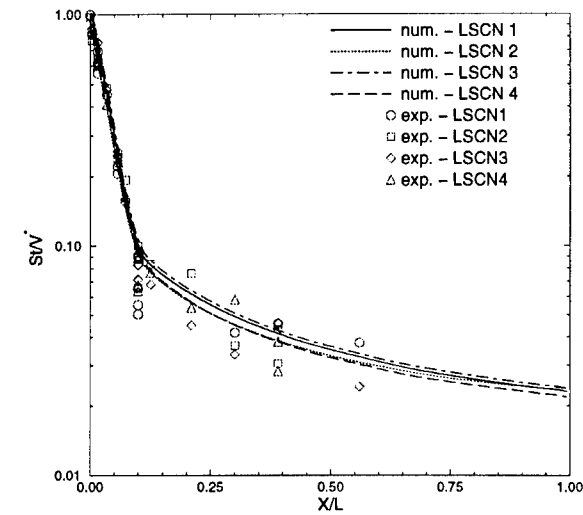


Figure 19: Normalized heat transfer coefficient measured and computed on ELECTRE for the four flow conditions

4. FLOW FIELD OVER THE HYPERBOLOID-FLARE

The Hyperboloid-Flare model equipped with pressure gauges and thermocouples is shown in figure 20. As for the ELECTRE model, the influence of γ and of the viscous interaction parameter was evaluated using perfect gas computations.

Figure 21 shows the pressure distribution computed on the Hyperboloid-Flare for the four operating conditions of the Longshot. Except in the separation region (which is not fully grid converged), the pressure on the Hyperboloid part is exactly the same for the four conditions.

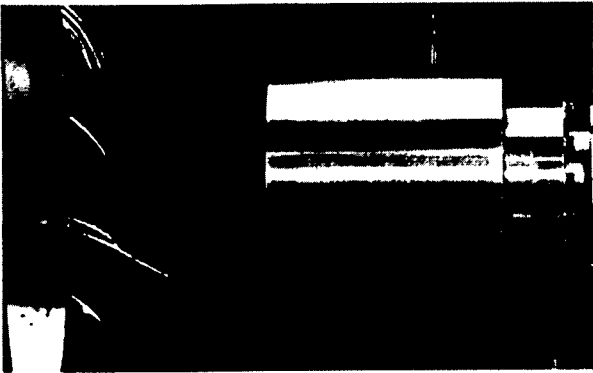


Figure 20: Hyperboloid-Flare model in the Longshot test section

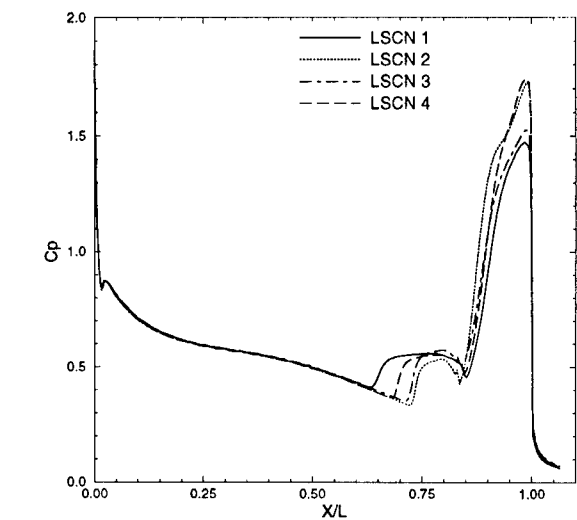


Figure 21: Computed pressure coefficient on the Hyperboloid-Flare model

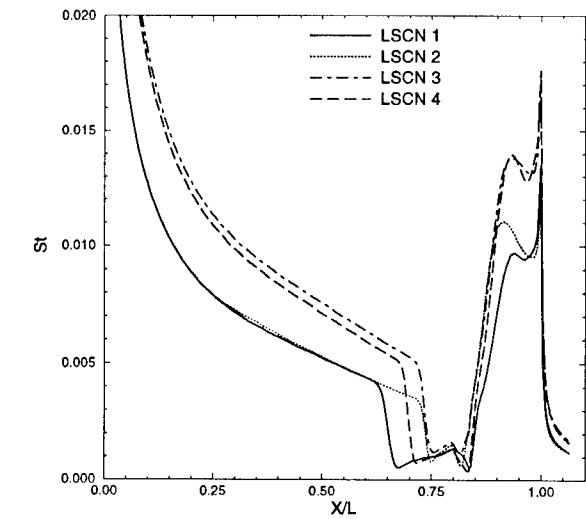


Figure 22: Computed Stanton number on the Hyperboloid-Flare model

A similar analysis for the Stanton number distribution (figure 22) shows the very low effect of γ , and on the contrary a

significant influence of the viscous parameter. In fact as done previously for the ELECTRE, the normalization of the Stanton number with the viscous interaction parameter allows to obtain a single curve on the Hyperboloid part for the four operating conditions.

Figure 23 shows the pressure coefficient C_p measured for the four flow conditions. As observed, the effects of the change in flow conditions are essentially located on the separated region and on the flare. However, there are differences associated with change in specific heat ratio observable on the Hyperboloid part that cannot be explained from the computations. For the heat transfer, as expected from the numerical simulations, the normalized Stanton number distributions measured for the four conditions (figure 24) match to a single curve on the Hyperboloid part. On the flare part, there are more important differences between the conditions with respect to what was expected from the laminar computations in figure 22.

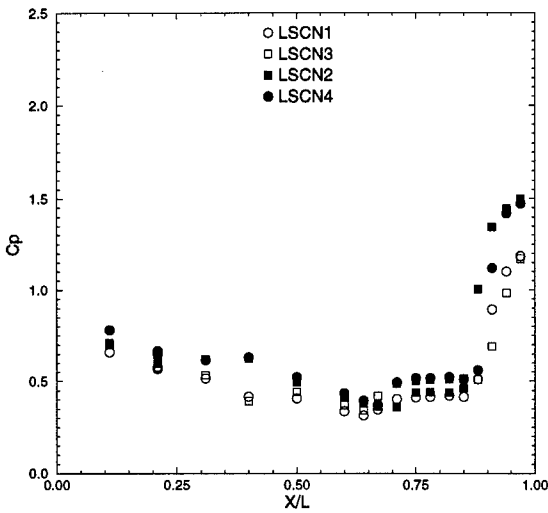


Figure 23: Measured wall pressure coefficient on the Hyperboloid-Flare model

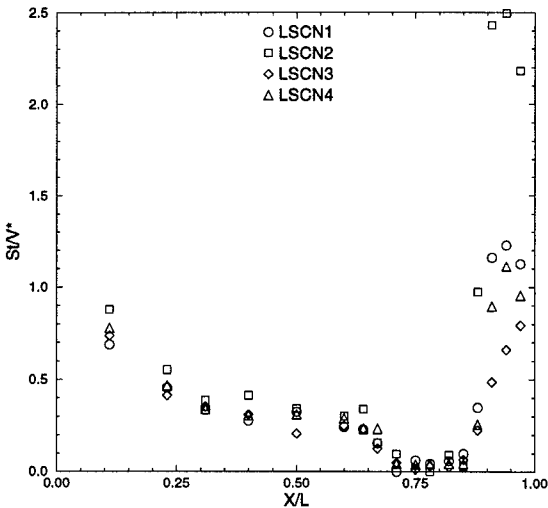


Figure 24: Normalized heat transfer coefficient measured on the Hyperboloid-Flare model

This is assumed to result from a transitional or turbulent re-attachment of the shear layer on the flare. In fact, the highest heat transfer level on the flare is observed for condition LSCN2 which corresponds to one of the two high Reynolds conditions (table 1). In figure 25, the transitional or turbulent

nature of the re-attachment can be seen for LSCN1 & LSCN2 whereas a clear laminar re-attaching boundary layer is visible for conditions LSCN3 & LSCN4.

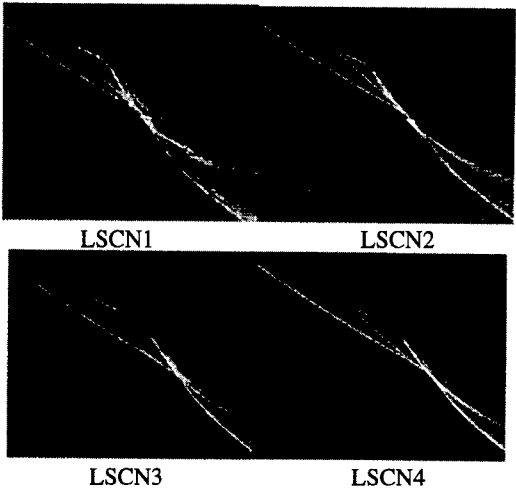


Figure 25: Details of schlieren visualizations on the Hyperboloid-Flare for the four conditions

During the shot, the Reynolds number decreases slowly. Table 3 gives the changes in Reynolds and Mach numbers and in viscous interaction parameter during the run time. Although modest, the variations observed during the run are sufficient to evolve from a transitional or turbulent re-attachment to a laminar one for the flow conditions with the highest Reynolds number (LSCN1 & LSCN2) as illustrated in figure 26 for condition LSCN2.

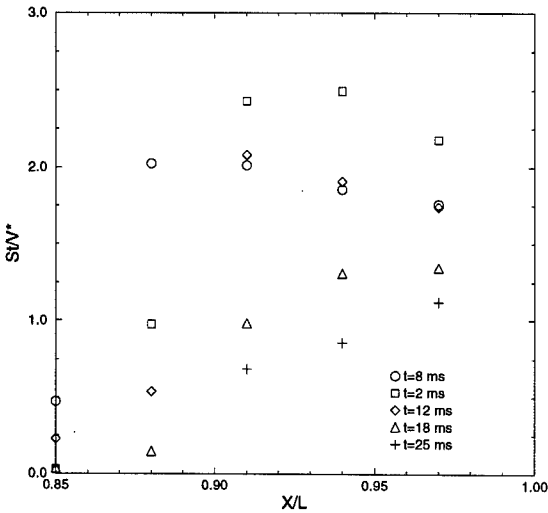


Figure 26: Normalized heat transfer coefficient measured at re-attachment on the flare during the run time for condition LSCN2

5. COMPARISON WITH MEASUREMENTS IN HIGH ENTHALPY FACILITIES

The data obtained in the Longshot tunnel varying the test gas specific heat ratio and the viscous interaction parameter are compared to measurements made in high enthalpy facilities (ONERA-F4 and DLR-HEG).

Pressure distribution measured in the ONERA-F4 hot shot tunnel for a reservoir pressure of 30 MPa and reduced enthalpy of 165 [11] and in the DLR-HEG for a reservoir

pressure of 38.6 MPa and reduced enthalpy of 268 [12] are plotted in figure 27 with the predicted C_p for the four Longshot conditions. The corresponding heat fluxes normalized by the stagnation heat flux on ELECTRE are plotted with the Longshot computed values in figure 28. One has to keep in mind that the data in figure 28 are normalized by the stagnation value which is different in HEG, in F4 and in the Longshot. From these comparisons, it can be concluded that for this geometry, the pressure distribution on the model is hardly influenced by the thermo-chemical state of the gas with respect to the uncertainty levels achieved on the pressure measurement on the rear cone. On the contrary, the heat flux on the conical part is not only affected by the viscous interaction parameter (see figure 16), but also by the thermo-chemical state of the gas and catalytic properties of the wall.

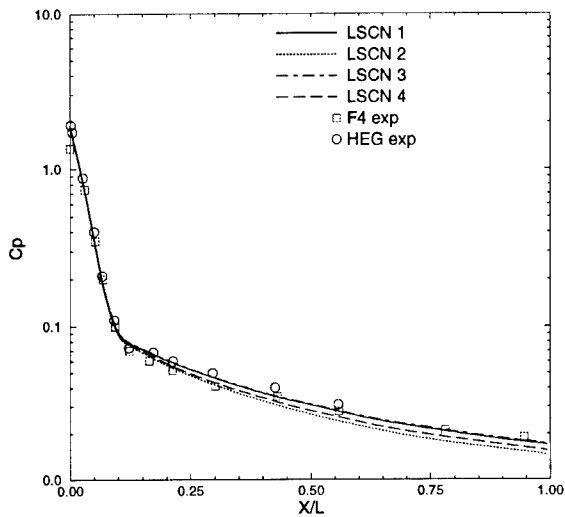


Figure 27: Pressure coefficient on ELECTRE for Longshot, F4 and HEG conditions

The HEG heat transfer data were found to agree well with full catalytic computations in [13] whereas non catalytic computations gave lower heat flux levels on the cone. The heat flux data in F4 are found significantly lower than almost all chemically reacting computations carried out in [14].

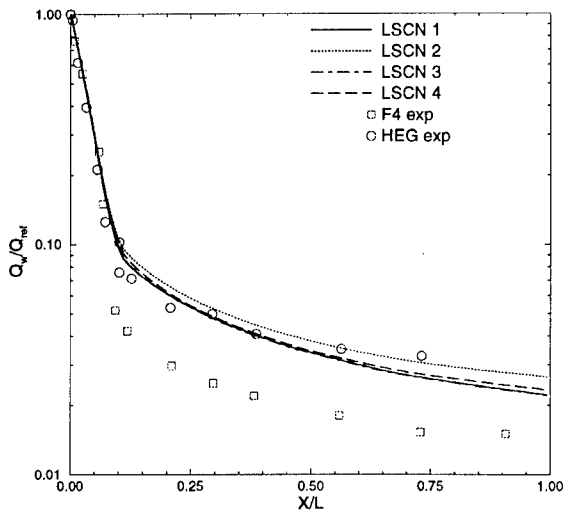


Figure 28: Normalized heat flux on ELECTRE for Longshot, F4 and HEG conditions

A possible explanation for the different behavior of normalized heat flux data in HEG and F4 could be associated

with the fact that the gas thermo-chemical state in the F4 case evolves significantly while expanding over the rear cone of ELECTRE and not in the case of HEG. This is supported by the observation that in the Longshot when the specific heat ratio or the viscous interaction parameter of the upstream flow is changed, there is no effect on the normalized heat flux distribution on ELECTRE. On the Hyperboloid part, as for ELECTRE, it is noticeable that the pressure distribution is very similar for the Longshot conditions and for the conditions in the ONERA-F4 [15] as illustrated in figure 29.

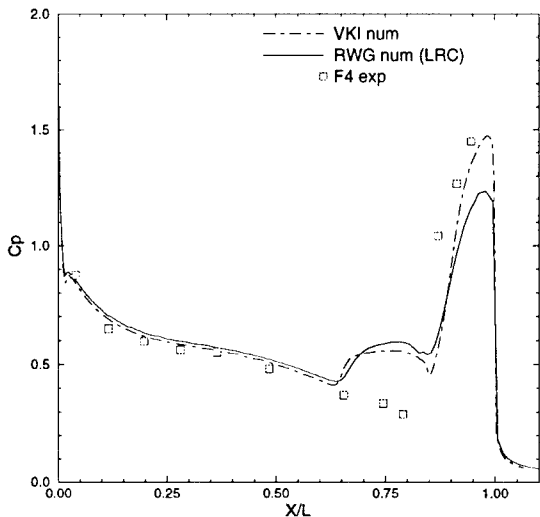


Figure 29: Pressure coefficient on the Hyperboloid-Flare in Longshot, DLR-RWG and ONERA-F4

The pressure distribution computed for the DLR-RWG conditions (cold hypersonic wind tunnel Mach 6.73) [16] is also plotted in this figure showing a fair agreement between all wall pressures on the Hyperboloid part. As expected, the change in flow conditions between these three wind tunnels modifies the pressure in the separated region and on the flare. The same conclusion is reached when analyzing the normalized Stanton number distributions on the Hyperboloid part for the Longshot and the RWG conditions in figure 30.

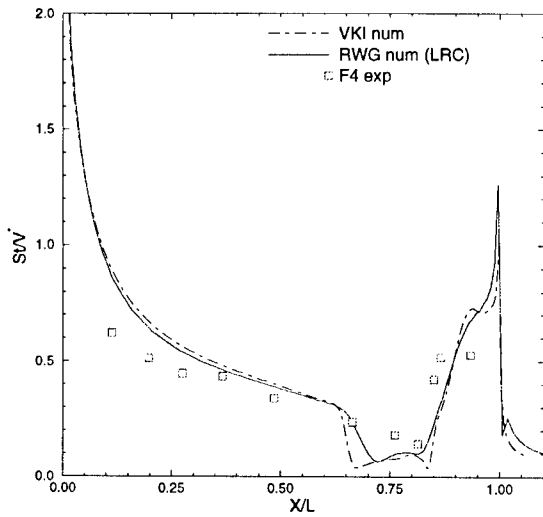


Figure 30: Normalized Stanton number distribution on the Hyperboloid-Flare in Longshot, DLR-RWG and ONERA-F4

On the contrary and as already noticed for the ELECTRE, the values measured in F4 conditions are lower than the computed values for the Longshot and for RWG. A good agreement was found with chemically reacting computations on a full catalytic wall in [17] which would here again indicate that there is a significant change of the gas properties over the Hyperboloid in F4 which cannot be duplicated by the simulations in the Longshot.

It is important to keep in mind that the heat flux on the ELECTRE and on the Hyperboloid part is very sensitive to the viscous interaction parameter as demonstrated by the Longshot experiments. Therefore it would be advisable to investigate the change in boundary layer edge properties (local viscous interaction parameter) between frozen and equilibrium computations in F4 and HEG conditions. With respect to the heat flux measurements carried out in F4, this analysis may help to point out any viscous effects induced by the chemically reacting nature of flow that could contribute to the differences illustrated before.

6. CONCLUDING REMARKS

The extension of the VKI-Longshot hypersonic gun tunnel for the simulation of high temperature gas and viscous effects in low enthalpy conditions has been presented. This simulation is obtained by using two gases (N₂ and CO₂) of different specific heat ratio and by an appropriate choice of the reservoir conditions so that the viscous interaction parameter can be kept constant while changing the specific heat ratio and vice versa. The calibration data of the flow in the nozzle are compared to numerical simulations indicating that the vibrational excitation of CO₂ has to be accounted for while it is negligible for N₂.

The ELECTRE and Hyperboloid-Flare standard models were tested in the Longshot. The analysis of the data shows that in general the pressure distribution is not very sensitive to the variation in specific heat ratio and viscous interaction parameter. On the contrary, the heat transfer levels on the ELECTRE and on the Hyperboloid are sensitive to the viscous interaction parameter which can be used to normalize the heat transfer coefficient.

Comparisons with appropriately normalized measurements carried out in high enthalpy facilities (F4 & HEG) show a good agreement for pressure. The lower normalized heat transfer levels measured in F4 for both models compared to Longshot and HEG results may be an indication of significant changes in the gas flowing over the model due to thermo-chemical effects for the F4 conditions. Further investigations analyzing chemically reacting computations would be required to confirm this explanation.

REFERENCES

[1]: Simeonides, G., The VKI Hypersonic Wind Tunnels and associated measurement techniques, von Karman Institute, Technical Memorandum 46, Nov. 1990.
 [2]: Bertin, J.J., Hypersonic Aerothermodynamics, AIAA Education Series, 1994.
 [3]: Olivier, H., Gronig, H., Hypersonic model testing in a shock tunnel, AIAA/DGLR 5th International Aerospace Planes and Hypersonic Technologies Conference, AIAA paper 93-5004, Dec. 1993.
 [4]: Culotta, S., Enkenhus, K.R., Analytical expressions for the thermodynamic properties of dense nitrogen, von Karman Institute, Technical Note 50, Sept. 1968.

[5]: Hirschfelder, J.O., Buehler, R.J., McGee, H.A., Sutton, J.R., Generalized equations of state for gases and liquids, Industrial and Engineering Chemistry, Vol. 50, N 3, March 1958, pp. 375-385.
 [6]: Culotta, S., Richards, B.E., Methods for determining conditions in real gas nitrogen expanding flows, von Karman Institute, Technical Note 58, Feb. 1970
 [7]: Hirschfelder, J.O., Curtiss, C.F., Bird, R.B., Molecular theories of gases and liquids, edition John Wiley & Sons, 1954
 [8]: Boudreau, A. H., Characterization of flow fields in hypersonic ground test facilities, Von Karman Institute Lecture Series 199-03 Methodology of Hypersonic Testing, Feb. 1993
 [9]: Walpot, L., Bakker, P. G., Development and validation of a 3 dimensional thermo-chemical non-equilibrium Navier-Stokes solver, Memorandum 815, Technical University Delft, NL, 1997
 [10]: Pacciorri, R., Dieudonné, W., Degrez, G., Charbonnier, J.-M., Deconinck, H., Validation of the Spalart-Allmaras turbulence model for application in hypersonic flows, 28th AIAA Fluid Dynamics Conference, 4th AIAA Shear Flow Control Conference, Snowmass Village, CO, USA, June 29-July 2, 1997
 [11]: Schwane, R., Test case 1b ELECTRE in F4 conditions, in Description of the testcases, MSTP Workshop 1996 on Reentry Aerothermodynamics and Ground-to-Flight Extrapolation, ESA-ESTEC Noordwijk, NL, March 1996
 [12]: Schwane, R., Test case 2b ELECTRE in HEG conditions, in Description of the testcases, MSTP Workshop 1996 on Reentry Aerothermodynamics and Ground-to-Flight Extrapolation, ESA-ESTEC Noordwijk, NL, March 1996
 [13]: Walpot, L., Kordulla, W., Synthesis of flow simulations for test case 2.b, ELECTRE model in the hypersonic impulse facility HEG, MSTP Workshop 1996 on Reentry Aerothermodynamics and Ground-to-Flight Extrapolation, ESA-ESTEC Noordwijk, NL, March 1996
 [14]: Sagnier, Ph., Borrelli, S., Synthesis of the contributions to the ELECTRE in F4 tests case 1.b, MSTP Workshop 1996 on Reentry Aerothermodynamics and Ground-to-Flight Extrapolation, ESA-ESTEC Noordwijk, NL, March 1996
 [15]: Schwane, R., Test case 1.c Hyperboloid-Flare in F4 conditions, in Description of the testcases, MSTP Workshop 1996 on Reentry Aerothermodynamics and Ground-to-Flight Extrapolation, ESA-ESTEC Noordwijk, NL, March 1996
 [16]: Dieudonné, W., Charbonnier, J.-M., Deconinck, H., Test case 3b Hyperboloid-Flare standard model at RWG reference calibration points, MSTP Workshop 1996 on Reentry Aerothermodynamics and Ground-to-Flight Extrapolation, ESA-ESTEC Noordwijk, NL, March 1996
 [17]: Devezeaux, D., Tribot, J.-P., Synthesis of contributions to the Hyperboloid-Flare in F4 test case 1.c, MSTP Workshop 1996 on Reentry Aerothermodynamics and Ground-to-Flight Extrapolation, ESA-ESTEC Noordwijk, NL, March 1996

TABLES

Cond. #	Test Gas	γ	Mach #	Reynolds #	Treservoir	Preservoir	$\overline{V^*}$
		[-]	[-]	[10 ⁶ /m]	[K]	[10 ⁵ Pa]	[-]
LSCN1	N2	1.4	15	7.5	2000	950	0.013
LSCN2	CO2	1.3	11.2	6.7	2000	1300	0.013
LSCN3	N2	1.4	14.8	4.2	1900	500	0.018
LSCN4	CO2	1.3	13.3	4.6	2250	2250	0.018

Table 1: Operating conditions for Longshot with conical nozzle

Section	LSCN1	LSCN2	LSCN3	LSCN4
I	15	11.2	14.8	13.3
II	16.4	12	16.2	14.2

Table 2: Measured Mach number on the centerline in sections I and II

Condition LSCN1				Condition LSCN3			
t m[s]	$\overline{V^*}$	10 ⁵ x Rey.	Mach	t m[s]	$\overline{V^*}$	10 ⁵ x Rey.	Mach
2	0.0112	12.57	15.39	2	0.0149	6.52	14.85
6	0.011	13.48	15.37	6	0.0158	6.03	14.83
8	0.0112	13.31	15.39	8	0.0159	6.24	14.91
11.5	0.0119	11.73	15.27	11	0.017	5.53	14.96
14	0.0121	11.67	15.35	13	0.0166	6.07	15.05

Condition LSCN2				Condition LSCN4			
t m[s]	$\overline{V^*}$	10 ⁵ x Rey.	Mach	t m[s]	$\overline{V^*}$	10 ⁵ x Rey.	Mach
2	0.0118	8.65	11.61	2	0.0167	6.63	13.86
8	0.0102	13.39	11.64	6	0.018	5.62	13.76
12	0.011	11.56	11.63	13	0.0167	6.9	13.7
18	0.0121	9.59	11.59	20	0.018	6.05	13.67
25	0.0119	10.11	11.36	30	0.0165	7.54	13.51

Table 3: Variation of the free stream properties in the test time window for the tests performed on Hyperboloid-Flare with the 4 operating conditions

A REVIEW OF SOME RECENT NEW AND IMPROVED SEMI-EMPIRICAL AEROPREDICTION METHODS

F. G. Moore
R. M. McInville
T. C. Hymer
Weapons Systems Department
Naval Surface Warfare Center
Dahlgren Division
Dahlgren, VA 22448 USA

SUMMARY

This paper reviews some new and improved semiempirical aeroprediction methods developed during the last five years. Some of these methods have been incorporated into the latest version of the aeroprediction code available to the public (AP95), and all methods will be a part of the next version of the code to be released later this year (AP98). The new and improved methods include: a) methods to compute nonlinear aerodynamics (normal force, axial force, and center of pressure) to high angle-of-attack (AOA); b) an approach to distribute these nonlinear loads on the body and lifting surfaces; and c) an improved method to compute aerodynamics of noncircular cross section configurations. Results of the new methods are compared to experimental data and in general, quite good agreement is obtained for a semiempirical prediction tool.

LIST OF SYMBOLS

AOA	Angle of Attack
APC	Aeroprediction Code
AP95, AP98	Aeroprediction Code, 1995 and 1998 versions respectively
AR	Aspect Ratio = b_1^2/A_w
a	semimajor axis of ellipse
A_{REF}	Reference area (maximum cross-sectional area of body, if a body is present, or planform area of wing, if wing alone)(ft ²)
A_w, S_w	Planform area of wing in crossflow plane (ft ²)
A_{WETTED}	Area of body or wing which flow touches
b	Semiminor axis of ellipse
b_1	Wing span (not including body)(ft)
C_A	Axial force coefficient
C_{A_0}	Axial force coefficient at zero AOA
C_{A_α}	Axial force coefficient due to AOA
C_{A_δ}	Axial force coefficient due to control deflection
C_M	Pitching moment coefficient (based on reference area and body diameter, if body present, or mean aerodynamic chord, if wing alone)
$(C_n/C_{n_0})_{SB}, (C_n/C_{n_0})_N$	Ratio of the local normal force coefficient of a body with a noncircular cross section to that with a circular cross section calculated by slender body and Newtonian theory respectively
C_N	Normal force coefficient
C_{N_B}	Normal force coefficient of body alone
$C_{N_{B(V)}}$	Negative afterbody normal-force coefficient due to canard or wing-shed vortices
$C_{N_{B(W)}}, C_{N_{B(T)}}$	Normal force coefficient on body in presence of wing or tail

$C_{N_{T(V)}}$	Negative normal-force coefficient component on tail due to wing or canard-shed vortex
C_{N_w}	Normal force coefficient of wing alone
$C_{N_{w(B)}}, C_{N_{T(B)}}$	Normal-force coefficient of wing or tail in presence of body
C_{N_α}	Normal-force coefficient derivative
C_r, C_t	Root and tip chord (ft), respectively
f_w, f_T	Lateral location of wing or tail vortex (measured in feet from body center line)
i	Tail interference factor
k	Parameter used to define corner radius for squares and triangles ($k = r_n/W_m$)
$K_{B(W)}, K_{B(T)}$	Ratio of additional body normal-force coefficient in presence of wing, or tail to wing, or tail alone normal-force coefficient at $\delta = 0$ deg
$k_{B(W)}, k_{B(T)}$	Ratio of additional body normal-force coefficient due to presence of wing or tail at a control deflection to that of wing or tail alone at $\alpha = 0$ deg
$k_{w(B)}, k_{T(B)}$	Ratio of wing or tail normal-force coefficient of body due to a control deflection to that of wing or tail alone at $\alpha = 0$ deg
M_∞	Freestream Mach number
NF	Newtonian correction factor
r	Radius of body (ft)
r_n	Corner radius of a rounded corner on square or triangle
r_w, r_T	Radius of body at wing or tail locations
s	Wing or tail semispan plus the body radius in wing-body lift methodology
W_m	Maximum diameter of a triangle or square as measured normal to the velocity vector
X_{CP}	Center of pressure (in feet or calibers from some reference point that can be specified) in x direction
α	Angle of attack (deg)
α_w, α_T	Local angle of attack of wing or tail ($\alpha + \delta_w$ or $\alpha + \delta_T$, respectively, in degrees)
δ_w, δ_T	Deflection of wing or tail surfaces (deg), positive leading edge up
Φ	Circumferential position around body where $\Phi = 0$ is leeward plane (deg) and represents fins in plus "+" roll orientation

SUBSCRIPTS

L	Linear
LT	Linear theory
NL	Nonlinear
SBT	Slender body theory

1 INTRODUCTION

The first author of this paper was invited to give lectures at the Missile Aerodynamics shortcourse held in Brussels, Belgium and Ankara, Turkey during the month of June 1994.¹ These lectures covered the field of semi-empirical aerodynamic prediction. Specifically, semi-empirical methods were defined relative to more accurate numerical techniques and the advantages and disadvantages of each were discussed. The major amount of time during the lectures was given to the various approximate methods the author has used or developed during the course of the aeroprediction codes history. This included the first version completed in 1972 (termed AP72) to the latest version completed at that time (AP93).

Since 1994, there has been an additional version of the aeroprediction code developed (AP95)² and by the end of 1998, the AP98 will be ready for transition to outside agencies. The purpose of this paper is, thus, to review the new and improved semiempirical aerodynamic prediction methods which have been developed since the AGARD lectures in 1994. Some of the new theoretical methods include extension of the nonlinear normal force and center of pressure above angle of attack (AOA) of 30 deg;^{3,4,5} extension of the nonlinear aerodynamics to the roll position of 45 deg (fins in "x" or cross fin arrangement;⁶ an improved method for predicting axial force at high AOA;⁷ methodology to distribute the nonlinear aerodynamic loads on the body and lifting surfaces.⁸ In addition, new methodology has just been developed for noncircular body cross section missile configurations. Both the AP95 and AP98 come with interactive personal computer pre- and post-processor software packages⁹ which make the code much more user-friendly than the AP93 and prior versions.

2 NEW AND IMPROVED METHODS DISCUSSION

The approach here to describe the new and improved methods will be brief because of limitations on the paper's length. Open literature references of the methods will be given for those interested in obtaining more details on the methods, including all the detailed equations, figures, and comparisons to data.

The general approach of the aeroprediction code is to use linear theory, slender body theory (SBT), or second-order perturbation theory to predict aerodynamics on general missile configurations at low AOA and over a broad Mach number range. Several large missile component wind tunnel data bases¹⁰⁻¹² are then used to predict the nonlinear aerodynamics at large AOA. These empirical terms are then fine-tuned based on comparison of the overall predictions to test data on missile configurations outside the Reference 10-12 data bases.

2.1 Axial Force Coefficient

The new methodology for computing axial force is documented in Reference 7. Basically, Reference 7 assumed

$$C_A = C_{A_0} + C_{A_\alpha} \quad (1)$$

where C_{A_0} represents the zero AOA axial force coefficient, and C_{A_α} , the change in axial force as AOA increases or decreases. C_{A_0} is estimated quite well using the low AOA methods discussed in References 1 and 2. However, the methodology for treating C_{A_α} in the AP95² could be refined considerably, particularly at subsonic Mach numbers where C_{A_α} can actually go negative. The other area where C_{A_α} of the AP95 required improvement was when α and δ were of opposite sign.

The new methodology of Reference 7 treated C_{A_α} as a fourth-order equation in AOA. That is

$$C_{A_\alpha} \equiv f(M, \alpha) = A\alpha + B\alpha^2 + C\alpha^3 + D\alpha^4 \quad (2)$$

The constants A, B, C, and D were evaluated using several wind tunnel data bases for body-alone and body-tail configurations. For wing-body-tail cases, the body-tail parameters were adjusted somewhat based on wind tunnel data on wing-body-tail cases in conjunction with the AP95.

To model the change in axial force with control deflection and AOA, the following equations are utilized:

$$C_{A_{b_w}} = (C_{N_{w(B)}} \sin \delta_w) f(M, \alpha_w) \quad (3)$$

$$C_{A_{b_T}} = (C_{N_{T(B)}} + C_{N_{T(V)}}) \sin \delta_T f(M, \alpha_T) \quad (4)$$

where

$$\begin{aligned} \alpha_w &= \alpha + \delta_w \\ \alpha_T &= \alpha + \delta_T \end{aligned} \quad (5)$$

It was found that when α and δ were of the same sign, $f(M, \alpha)$ was close to 1.0. However, when α and δ were of opposite signs, the axial force contributions due to control deflection were too high. As a result, empirical expressions were derived for $f(M, \alpha)$ at the two roll positions of $\Phi = 0$ and $\Phi = 45$ deg. These empirical results were derived by use of the AP98 in conjunction with wind tunnel data where the controls were deflected. Note that the only roll dependence of C_{A_α} comes from control deflection. If there are no control surfaces deflected, then C_{A_α} is approximately the same within the present prediction accuracy for $\Phi = 0$ deg and $\Phi = 45$ deg.

2.2 Normal Force Coefficient

2.2.1 Configuration Aerodynamics

The approach taken here to model the configuration normal force is to use the component buildup approach originally defined by Pitts et al.¹³ where the total normal force of the overall configuration is defined by

$$C_N = C_{N_B} + [(K_{W(B)} + K_{B(W)})\alpha + (k_{W(B)} + k_{B(W)})\delta_w] (C_{N\alpha})_W$$

$$+ [(K_{T(B)} + K_{B(T)})\alpha + (k_{T(B)} + k_{B(T)})\delta_T] (C_{N\alpha})_T + C_{N_{TV}} + C_{N_{B(V)}} \quad (6)$$

Reference 13 used linear aerodynamics to estimate each term in Equation (6). However, the approach used here is to take each term in Equation (6) and define a linear component based on conventional analytical techniques¹ and then a nonlinear component based on wind tunnel component data bases.¹⁰⁻¹² Once this nonlinear term has been defined empirically, simple mathematical expressions are derived to represent the empirical data as a function of the various physical parameters. This new mathematical model is then exercised on configurations within and outside the data base upon which it was developed. The mathematical model is then fine-tuned.

2.2.2 Missile Component Normal Force Coefficient

Referring to Equation (6), the body alone term is

$$C_{N_B} = (C_{N_L})_B + (C_{N_M})_B \quad (7)$$

The linear component of Equation (6) is determined by linear theory supersonically and empirically at subsonic and transonic Mach numbers. The nonlinear term is computed using a modified version of the Allen-Perkins¹⁴ crossflow theory with the modifications being in computing supercritical and subcritical flow.

The wing alone or tail alone lift terms of Equation (6) are computed using a fourth-order equation in AOA. That is,

$$C_{N_w} = a_1 \alpha_w + a_2 \alpha_w^2 + a_3 \alpha_w^3 + a_4 \alpha_w^4 \quad (8)$$

where $\alpha_w = \alpha + \delta_w$; a_1 is the slope of the C_{N_w} curve near $\alpha = 0$ deg and is computed using lifting surface theory or three-dimensional thin wing theory. The other constants a_2 , a_3 , and a_4 are evaluated empirically using large data bases.³

The interference terms of Equation (6) due to AOA at zero control deflection ($K_{W(B)}$, $K_{B(W)}$, $K_{T(B)}$, $K_{B(T)}$) are predicted by

$$K = K_{SBT} + \Delta K(\alpha, M, AR, \lambda, \Phi)_{LT} \quad (9)$$

The first term of Equation (9) is the SBT or linear theory (LT) value of the interference terms. The deviation of Equation (9) from SBT or LT, $\Delta K(\alpha, M, AR, \lambda, \Phi)$, is estimated by the large missile component data bases of References 10 and 12. These are included in the AP98¹⁴ in terms of tables of data.

The interference terms due to control deflection ($k_{W(B)}$, $k_{B(W)}$, $k_{T(B)}$, $k_{B(T)}$) of Equation (6) are estimated based on more simplified equations. These are of the form:

$$k_{W(B)} = C_1(M) [k_{W(B)}]_{SBT} + C_2(|\alpha_w|, M) \quad (10a)$$

$$k_{B(W)} = [k_{B(W)}]_{SBT} + C(\alpha_w) \quad (10b)$$

The constants C_1 , C_2 , and C of Equation (10) were determined based on the use of the aeroprediction code in comparison to total force and moments on configurations tested in the tunnel.

The last interference term considered is that of the wing-shed vortices on the tail surfaces. It is the next to last term of Equation (6). In general, the nonlinear form of $C_{N_{TV}}$ is defined by¹⁴

$$C_{N_{TV}} = \frac{A_w (C_{N_{\alpha}})_w (C_{N_{\alpha}})_T [K_{W(B)}\alpha + F k_{W(B)}\delta_w]}{2\pi (AR)_T (l_w - r_w) A_{ref}} \quad (11)$$

Equation (11) reverts back to SBT for low AOA. At higher AOA, $(C_{N_{\alpha}})_w$, $(C_{N_{\alpha}})_T$, $K_{W(B)}$, $k_{W(B)}$, F , i_1 , and i_4 all have nonlinearities. The terms i_1 and i_4 of Equation (11) represents the wing-tail interference factor for the windward and leeward planes respectively. At $\Phi = 0$ deg, only the i_1 factor is of interest, whereas at $\Phi = 45$ deg, both the leeward and windward planes are considered. The nonlinearity is introduced into i_1 and i_4 in the $\Phi = 45$ deg roll by defining loading factors for the windward and leeward plane fins.^{5,6}

The parameter F of Equation (11) is used as a control on the control deflection component of $C_{N_{TV}}$ and is determined empirically based on comparisons of theory to experiment. To put an additional nonlinear control on the first term of $C_{N_{TV}}$, Equation (11) was broken down into components due to α and δ . That is,

$$C_{N_{TV}} = [C_{N_{TV}}]_L + [C_{N_{TV}}]_B \quad (12)$$

The term due to α of Equation (12), was then defined as

$$[C_{N_{TV}}]_L = A + B\alpha + C\alpha^2 + D\alpha^3 \quad (13)$$

for $\Phi = 0$ deg, and as

$$[C_{N_{TV}}]_R = G_1 [C_{N_{TV}}]_{BBT} \quad (14)$$

for $\Phi = 45$ deg. A, B, C, D, and G were all constants determined empirically based on data. In addition, a maximum value constraint was placed on the overall value of $C_{N_{TV}}$ so as not to allow it to exceed the lift on the tail alone.

The last term of Equation (6), $C_{N_{BV}}$, was not predicted explicitly. That is because it is already included in the missile component data bases of References 10 and 12. It is thus a part of the $K_{B(W)}$ and $K_{B(T)}$ terms of Equation (6). It was believed that to try to estimate this term analytically, then subtract it out from the wind tunnel data base and add it back in analytically for another configuration, would incur as large or larger errors than simply leaving it in as part of the body-wing interference terms and neglecting the resulting length scale effect.

2.3 Center of Pressure and Pitching Moment

The body-alone center of pressure is computed based on a weighted average of the linear and nonlinear components of normal force. That is,

$$X_{CP} = \frac{C_{N_L}(X_{CP})_L + C_{N_{NL}}(X_{CP})_{NL}}{C_{N_L} + C_{N_{NL}}} \quad (15)$$

where the linear center of pressure is defined based on low AOA methods¹ and the nonlinear center of pressure is the centroid of the planform area. Two nonlinear phenomena occur on the body-alone center of pressure that Equation (15) does not fully account for. These phenomena are the asymmetric shedding of vortices at AOA greater than about 25 deg and $M_\infty < 2.0$ and the transonic effects of a shock standing on the body. As a result, a table of center of pressure shifts was defined empirically as a function of AOA and Mach number.

The center of pressure of the wing-alone and wing-body normal force is assumed to vary from its linear value at zero AOA to the centroid of the wing planform at 60 deg AOA. If A and B are the centers of pressure of the linear and nonlinear normal force terms (in percent of mean geometric chord), and $\alpha_w = \alpha + \delta$, then the center of pressure of the wing-body or wing-alone lift is

$$(X_{CP})_{WB} = (X_{CP})_W = A + \frac{1}{36} |\alpha_w| (B - A) + \frac{1}{5400} \alpha_w^2 (A - B) \quad (16)$$

Equation (16) is the methodology used for roll position of 0 deg.

When the fins are rolled to a non-zero roll orientation, the center of pressure Equation (16) will change because of the geometry of the wings and an asymmetric effect on the wing loading. To visualize this effect, imagine a missile rolled to $\Phi = 45$ deg and

increasing in AOA. As AOA increases, two things occur. First, the windward plane fins carry more and more of the load compared to the leeward plane fins. Second, the local Mach number in the windward plane is different, and typically lower, than the leeward plane. This has the effect of shifting the wing-alone center of pressure forward in the windward plane. Since the load and wing centers of pressure are different on the windward and leeward plane fins, this results in a net forward shift in the center of pressure for $\Phi = 45$ deg roll compared to the $\Phi = 0$ deg computation of Equation (16). This shift appears to occur for all Mach numbers, and is largest at moderate AOA, and goes to zero at AOA 0 and 90 deg. At 90 deg AOA, the windward plane fins carry almost all the load compared to the leeward plane fins, but geometrically, the fins are all aligned perpendicular to the AOA plane. This center of pressure shift was derived in Reference 14 and is, for $\alpha \leq 65$,

$$(\Delta X_{CP})_{WB} = - \left[r + \left(\frac{b}{C_r + C_l} \right) \left(\frac{C_r}{2} - \frac{C_l}{3} \right) \right] \cos(\Phi) \sin(2\alpha) \left(\frac{0.8\alpha}{65} \right)$$

or $\alpha > 65$,

$$(\Delta X_{CP})_{WB} = -0.8 \left[r + \left(\frac{b}{C_r + C_l} \right) \left(\frac{C_r}{2} - \frac{C_l}{3} \right) \right] \cos\Phi \sin(2\alpha) \quad (17)$$

Equation (17) is added to Equation (16) for the roll orientation of 45 deg.

The center of pressure of the body-wing carryover normal force contribution is at the centroid of the Mach box created by the Mach lines from the leading and trailing edges of the wings as they cross the body planar surface. For $\Phi = 45$ deg roll, the local Mach number, computed by Modified Newtonian Theory, is used to define the Mach box. This has the effect of shifting the center of pressure of this component of normal force slightly forward.

Knowing both normal force from Section 2.2 methods and center of pressure from Section 2.3, the pitching moment of a configuration component or of the entire configuration is then

$$C_M = - X_{CP} C_N \quad (18)$$

where nose up is considered positive.

2.4 Nonlinear Aerodynamic Loads Distribution

Section 2.2 discussed how the nonlinear normal force loads were computed for typical missile configurations. This nonlinear aerodynamic load is defined primarily in terms of total force, moment, and center of pressure. Some distribution information is provided for the nonlinear component of the body loads, but none is currently available for the lifting surface loads or for their interference effects of the body. This situation is not restrictive in terms of aerodynamic and performance

analysis. Structural engineers, however, need to know not only the magnitude of the aerodynamic forces, but also how they are distributed over the surface of a missile if they are to determine the shear and bending moments to which its components will be subjected. For this reason, the AP95 code was modified to allow the prediction of the distribution of the nonlinear, as well as the linear, aerodynamic loads over both the body and control surfaces.⁸ All interference effects were included in the analysis in addition to the individual component nonlinear aerodynamics. It is believed that the next version of the Aeroprediction Code (AP98) will be the first semiempirical code of its kind to offer this capability.

The body-alone load distribution is composed of a linear term, which is computed based on integration of the pressures computed along and around the body, and the local component of nonlinear load from the viscous crossflow methodology. Comparison of this approach to CFD results⁸ showed that the predicted load in the nose region was slightly too high at low AOA. As a result, some of the nonlinear load in the nose region was shifted to the afterbody below AOA of 30 deg. The total normal force and pitching moments were held constant before and after the load redistribution. A better match of approximate body loads with CFD was then obtained.

The body-wing and body-tail loads of Equation (6) are represented using the Mach lines from the leading and trailing edges of the wing or tail, in conjunction with the total normal force component load. The total normal force component load is used to determine the height of the trapezoidal load created in the vicinity of the root chord by the carryover of the induced wing effects onto the body. If these induced effects fall behind the end of the body, the height of the trapezoid is readjusted to make sure the total local integrated loads equals that of the aerodynamic component.

The load on the wing in conjunction with the body is assumed to vary proportionally to its linear distribution. The linear distribution is computed analytically along the chord and at

several chordwise locations on the wing span. In validating this assumption against CFD data, it was seen to be quite reasonable.

The wing-tail interference load (next to last term of Equation (6)) is assumed to be distributed in a " $1/r^2$ " manner from where the wing-shed vortex hits the tail surface. Also, some of the wing-tail load is distributed onto the body between the tail surfaces. The reader is referred to Reference 8 for the details of this methodology.

2.5 Robust Nonaxisymmetric Body Methodology

The desire to increase weapon range and maneuverability, to design weapons which are more optimum from an aircraft total drag and radar signature standpoint, or to provide optimum loadout of multiple missiles in a ship's vertical launcher has driven weapon designers to consider nonaxisymmetric body shapes. Some typical shapes are shown in Figure 1. While most missiles in the United States and foreign countries in existence today have axisymmetric body configurations, these conceptual design tradeoffs of various configurations other than axisymmetric require engineering estimates of aerodynamics. Current state-of-the-art methods for predicting aerodynamics of nonaxisymmetric body shapes with engineering accuracy are much more limited than for axisymmetric bodies. This is primarily driven by the fact that to get reasonable accuracy of the aerodynamics requires an accurate description of the body geometry. To describe the geometry of a complex body shape accurately can take days or weeks depending on the requirements of the aerodynamics code being used.

To reduce the geometry generation problem, the technique of Jorgensen^{15,16} was extended. This technique allows one to calculate the aerodynamics of a nonaxisymmetric body based on an equivalent axisymmetric body. Generally, it is easier to obtain the cross-sectional area of a noncircular cross section than it is the detailed three-dimensional coordinates. This also allows the aeroprediction code to be used directly, once the equivalent axisymmetric body has been determined from one of the configurations of Figure 1.

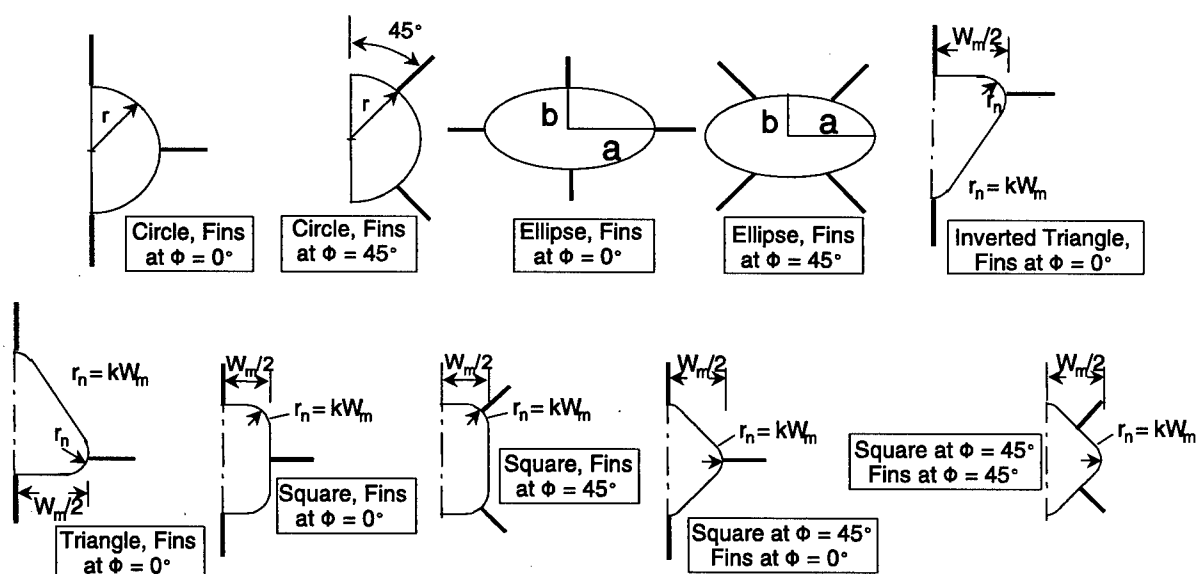


Figure 1. Some Noncircular Cross-section, Wing-Body Configurations for the Aeroprediction Code.

Basically, the method of Jorgensen¹⁶ defined the axial and normal force and pitching moment coefficients as

$$C_A = C_{A_0} \cos^2 \alpha \quad (19)$$

$$C_N = C_{N_L} \left(\frac{C_n}{C_{n_0}} \right)_{SB} + C_{N_{NL}} \left(\frac{C_n}{C_{n_0}} \right)_N NF \quad (20)$$

$$C_M = C_{M_L} \left(\frac{C_n}{C_{n_0}} \right)_{SB} + C_{M_{NL}} \left(\frac{C_n}{C_{n_0}} \right)_N NF \quad (21)$$

where the Newtonian Correction Factor, NF, was added by the present authors.¹⁷ The wing-body interference effects were based on extensions of Nelson¹⁸ and Est and Nelson¹⁹ at low AOA and the method of the present paper at high AOA.

Several new additions to the state-of-the-art were made in extending the methods of References 16, 18, and 19. First of all, additional equations were derived for $(C_n/C_{n_0})_N$ for shapes other than ellipses. Secondly, NF was derived for low crossflow Mach numbers where Newtonian theory was inaccurate. Jorgensen had no factor, NF, in his equations. Third, a critical Reynolds number was defined for noncircular shapes as a function of the circular value of R_{Nc} . Fourth, the AOA axial force was computed using the method of Section 2.1 versus Equation (19). Fifth, as already mentioned, wing-body interference factors at low AOA were based on extensions to the methodology of References 18 and 19 at low AOA and the method of Section 2.2 at high AOA. Thus, the body cross-sectional shape was allowed to influence the aerodynamics at low and moderate AOA, whereas at AOA greater than about 30 deg, it was not. Finally, slender body theory scaling factors were derived to allow one to compare aerodynamics computed based on an equivalent axisymmetric body or a body of constant width to wind tunnel data taken on a body of constant width or constant cross-sectional area. Once again, the reader is referred to Reference 17 for the details of this new methodology.

3 COMPARISON OF NEW METHODS TO EXPERIMENT

Several cases are selected to illustrate the new methods when compared to experimental data. The first case considers a wing-body-tail case (see Figure 2) with experimental data given in Reference 20. This configuration has a length of about 18 calibers with a tangent ogive nose of 2.25 calibers in length. It has wings and tails of fairly high aspect ratios of 2.8 and 2.6 respectively. Data were taken at Mach numbers 1.5 to 4.63, for AOAs to 45 deg and wing control deflections of 0 and 10 deg at M of 1.5 and 2.0 and 0 to 20 deg at M of 2.35 to 4.63. Tail control was also considered and control deflections of 0 to -20 deg for the same roll and freestream conditions as for the wing control were used in the wind tunnel measurements. The data were taken at a Reynolds number of $2.5 \times 10^6/\text{ft}$ and boundary layer trips were

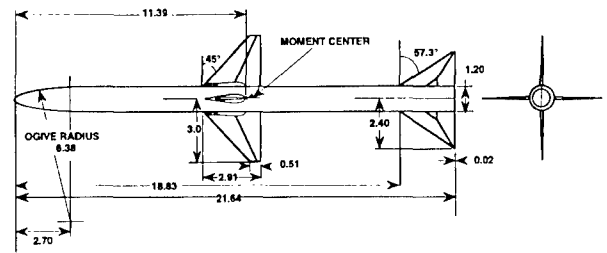


Figure 2. Air-to-air Missile Configuration Used in Validation²⁰ (All Dimensions in Inches).

also used. The model had a hollow chamber, and chamber axial force measurements were given separately in Reference 20. These were added to the data so total axial force comparisons of theory and experiment could be made.

Figures 3a, 3b and 3c show some typical comparisons of the AP98 compared to experiment. These figures are all for a single Mach number of 2.87. Other Mach numbers have been considered and results^{6,7} are comparable to those for Mach number 2.87 in terms of accuracy. Figure 3a presents the zero control deflection results for $\Phi = 0$ and 45 deg roll. Results are shown in terms of axial and normal force coefficients and pitching moment coefficients. Figure 3b presents the similar results for a wing control deflection of 20 deg and Figure 3c presents results when the tails are deflected -20 deg. Note that in all cases, the AP98 gives very acceptable agreement to data. Average accuracy levels of C_A and C_N are well within the goals of ± 10 percent. The pitching moment comparisons at first glance do not appear to be as good as desired. However, when viewed in terms of center of pressure, the worst case is for $\Phi = 0$ deg at AOA of 40 deg. Here the center of pressure error is 2.2 percent of the body length, well within the average accuracy goal of ± 4 percent of the body length.

Figure 4 illustrates the new nonlinear loads capability developed for structural analysis (see Reference 8 for the details of this new methodology). The Figure 2 configuration is used as an example where, here, experimental data is replaced by thin layer Navier Stokes computations since no experimental data were available for local loads. The Navier Stokes computations agreed within a few percent of experiment for the total loads. Hence, it is believed the local loads are also reasonably accurate. Again a Mach number of 2.87 is selected for comparison and at a roll orientation of 0 deg with an AOA of 40 deg. Body, wing and tail local load, shear and bending moments are given for the AP98 and CFD. The body information is given as a function of x/t , whereas the wing and tail information is with respect to the spanwise variable $y/b/2$. Here $x/t = 0$ is the nose tip and $y/b/2 = 0$ is the wing or tail root chord where it attaches to the body. Results for other Mach numbers, roll angles and AOA's are similar to these results and are shown in Reference 8. Note that very good agreement of the semiempirical load, shear, and bending moment compared to CFD computations is shown in Figure 4.

The last new technology to be illustrated is the robust nonaxisymmetric body methodology. Reference 17 gives the details of this new methodology. Two cases are considered.

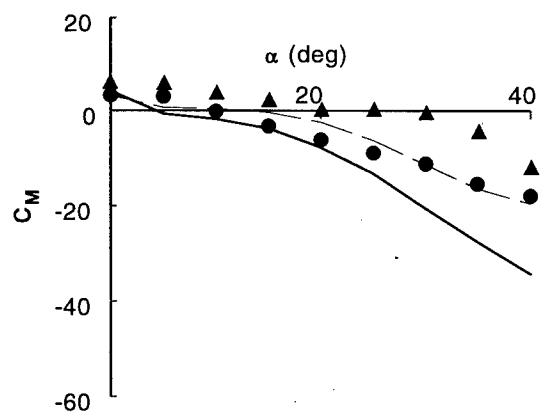
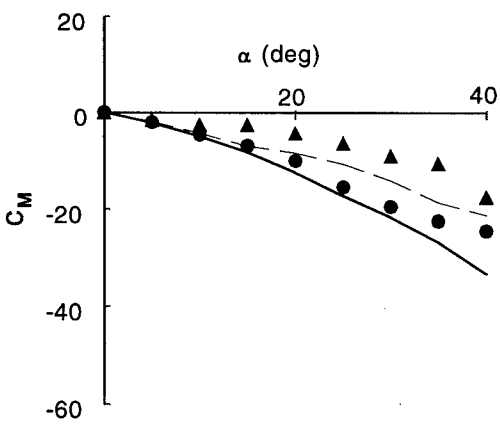
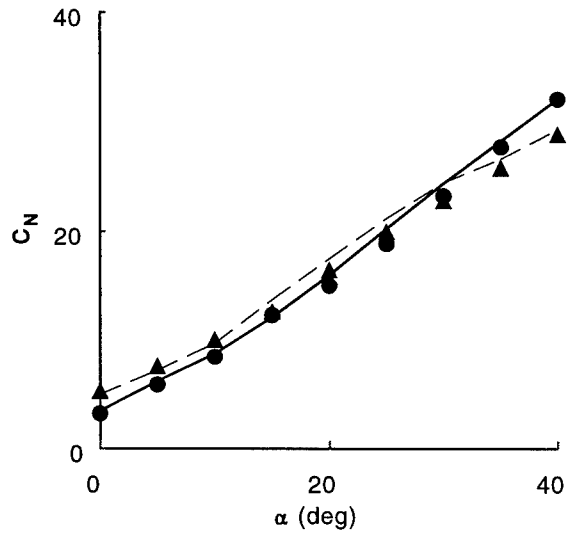
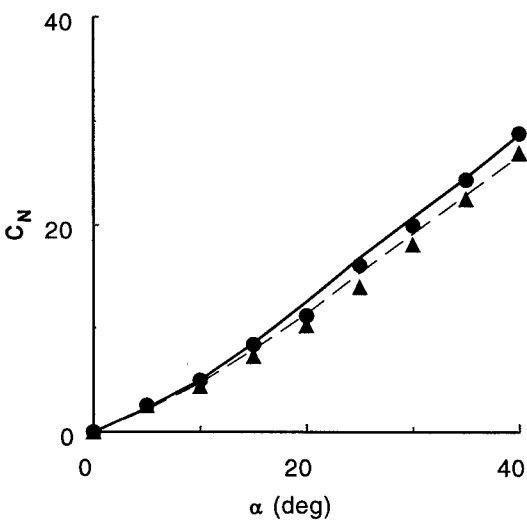
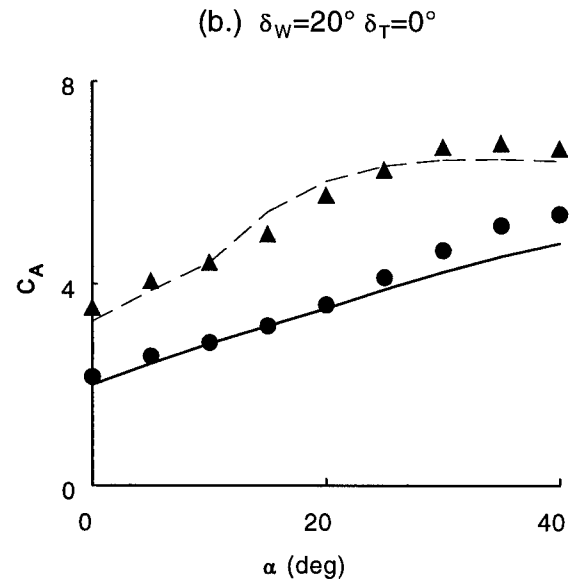
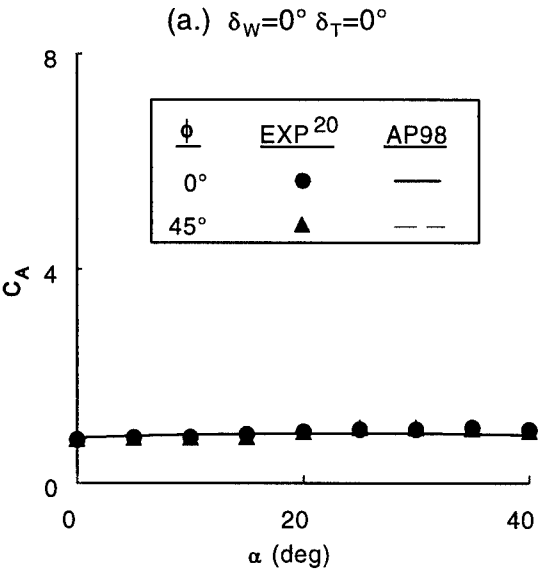


Figure 3. Axial, Normal, and Pitching Moment Coefficient Comparisons of Theory and Experiment ($M_\infty = 2.87$).

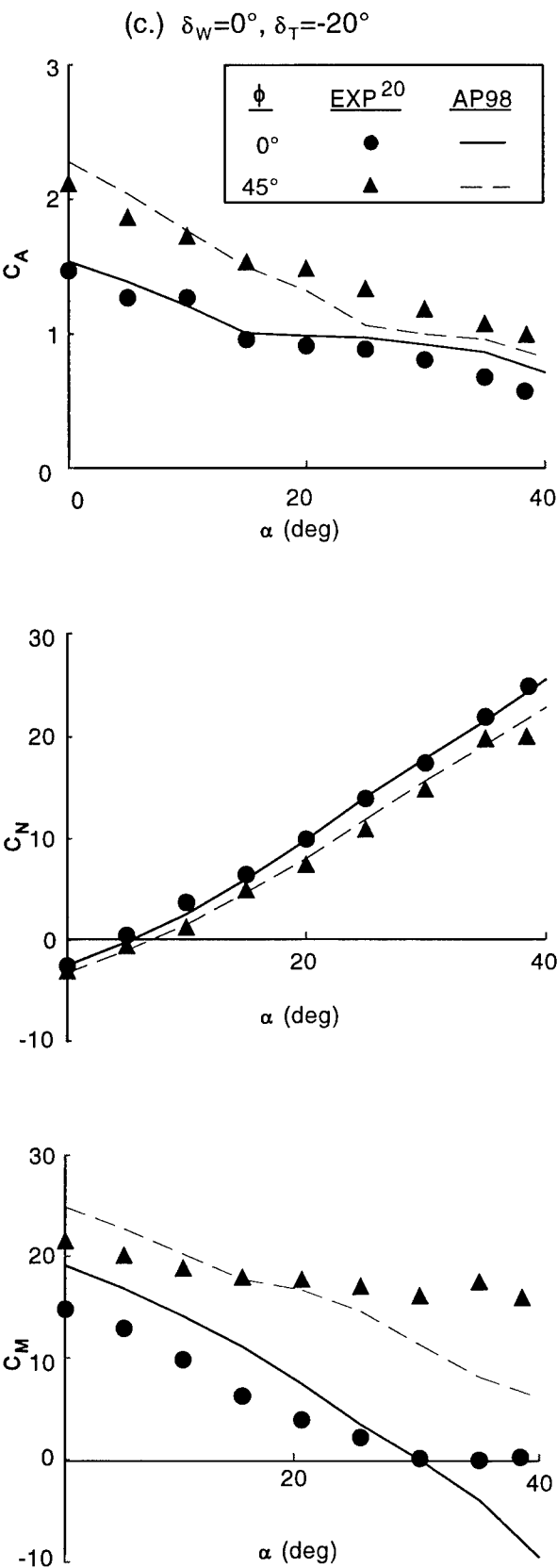


Figure 3. Axial, Normal, and Pitching Moment Coefficient Comparisons of Theory and Experiment ($M_\infty = 2.87$) (Continued).

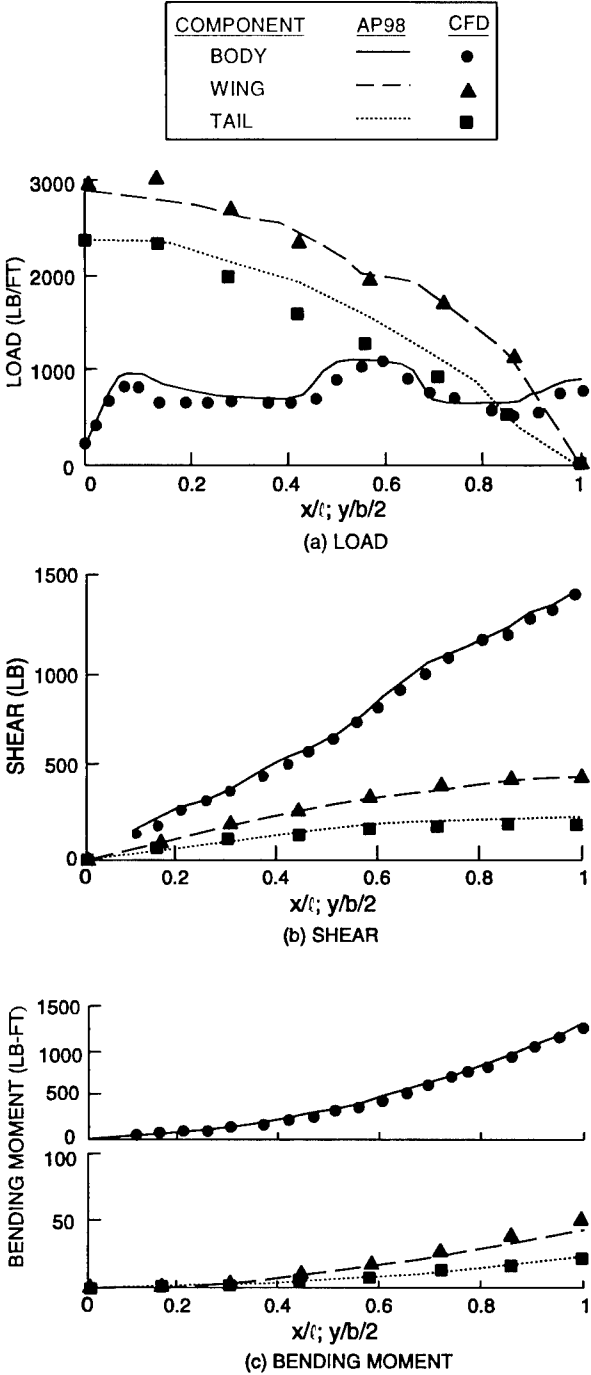


Figure 4. Load, Shear, and Bending Moment for Configuration of Figure 2 ($M_\infty = 2.87, \phi = 0^\circ, \alpha = 40^\circ$).

The first case closely resembles the configurations about which the methodology was developed, whereas the second case illustrates use of the new technology for a configuration which deviates significantly from the cross sectional shapes of Figure 1.

The first nonaxisymmetric body data base considered is for ellipses^{15,21} and squares and triangles.¹⁵ This configuration set is shown in Figure 5. This configuration was tested to 24 deg AOA at $M_\infty = 1.98$ and 3.88 in Reference 15. All bodies in Figure 5 have the same cross sectional area as the circle. The

corner radii of the squares and triangles were very small, so a value of $k = 0$ was assumed in the computations. The elliptical shape 10-caliber body of Figure 5 was tested later²¹ at Mach numbers 0.6 to 2.0 and to AOA 56 deg. The case shown here will thus be the elliptical 10-caliber-long body tests of Reference 21, which go to 56 deg AOA, and the square and triangular tests of Reference 15, which go only to 24 deg AOA. Not all results will be shown, as the References 15 and 21 data bases were fairly extensive. Most of these results are shown in Reference 17, however.

Figure 6 gives the elliptical body results for a Mach number of 2.0. Results shown are for ellipticity values of 0.5, 1.0 and 2.0 and are given in terms of normal and axial force coefficients and center of pressure. To get the ellipticity value of 0.5, configuration B_2 is simply rotated to the $\phi=90^\circ$ roll position as shown in Figure 5. Also, the axial force coefficient does not include a base drag component. In examining the Figure 6 comparisons of theory and experiment, it is seen the theory does a fairly good job of predicting the aerodynamics on the elliptical case. The normal force and center of pressure predictions are quite encouraging as they are well within the average accuracy levels of ± 10 percent and ± 4 percent of body length respectively. The axial force prediction comparisons are not as good as desired. However, this could be due to measurement accuracy where it is difficult to get accurate axial force measurements with a sting designed for measuring normal force at high AOA.

Theoretical and experimental results for the squares and triangles of Figure 5 are given in Figures 7 and 8 respectively. Only the 10-caliber-long configuration results at $M = 1.98$ are shown. Here the results are given in terms of lift coefficient,

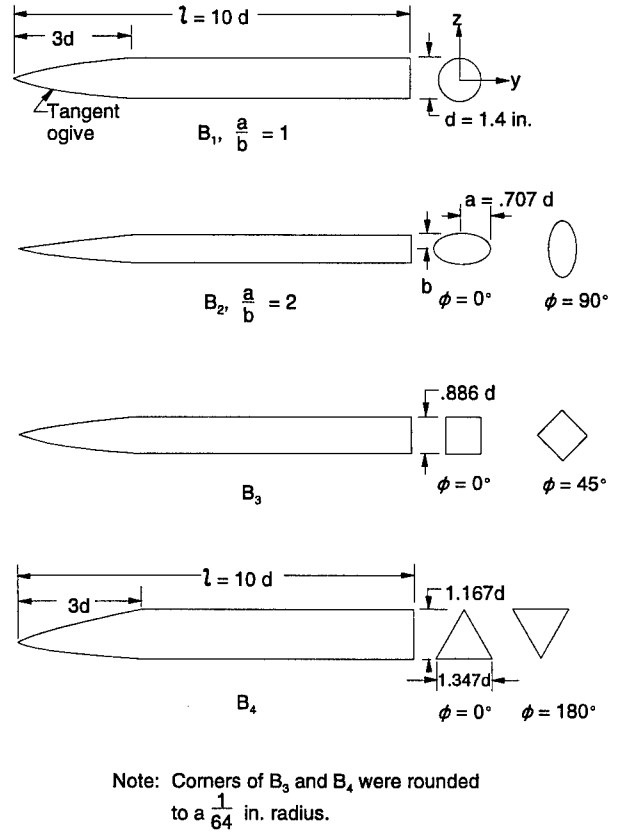


Figure 5. Body Alone Configurations With Elliptical, Square, Diamond, Triangular, and Inverted Triangular Shapes (Reference 15).

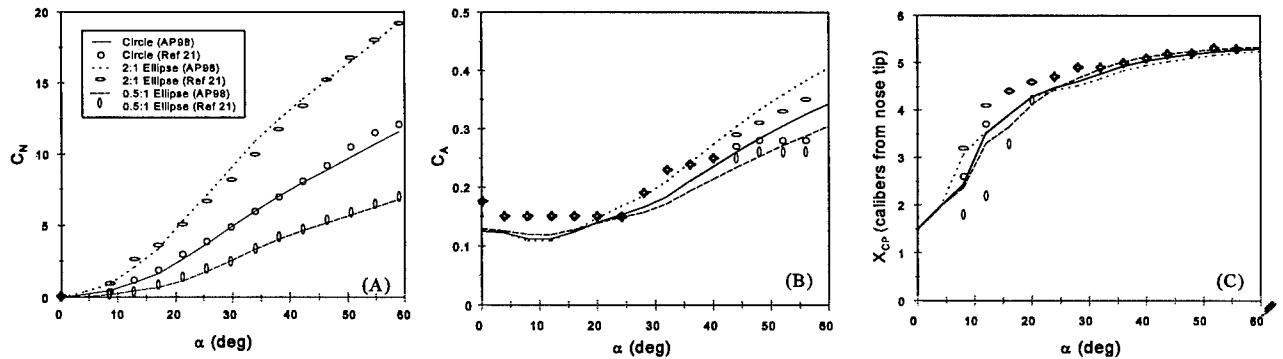


Figure 6. Aerodynamic Data for 2:1 and 0.5:1 Ellipses of Fig. 5 Compared to Circular Body at $M = 2.0$: (A) Normal Force Coefficient, (B) Axial Force Coefficient, (C) Center of Pressure.

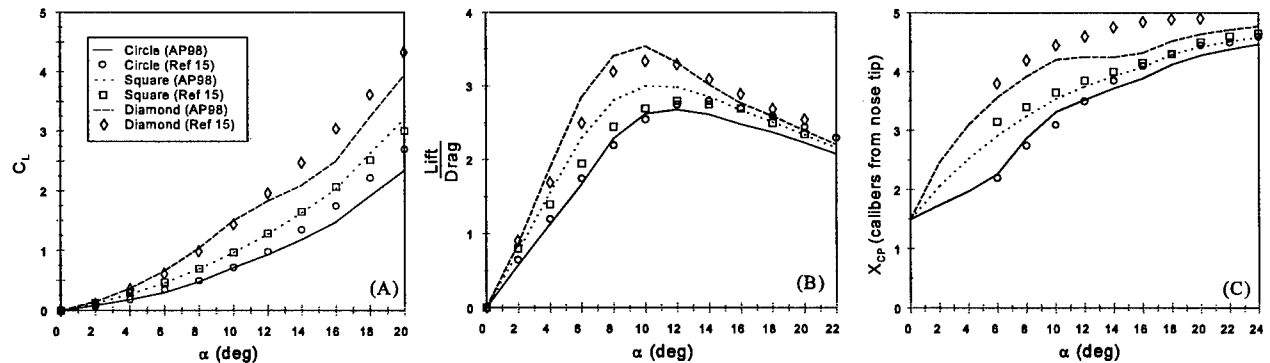


Figure 7. Aerodynamic Data of Squares ($k = 0.0$) and Diamonds ($k = 0.0$) of Fig. 5 Compared to Circular Body at $M = 1.98$ ($l/d = 10$): (A) Lift Coefficient, (B) Lift to Drag Ratio, (C) Center of Pressure.

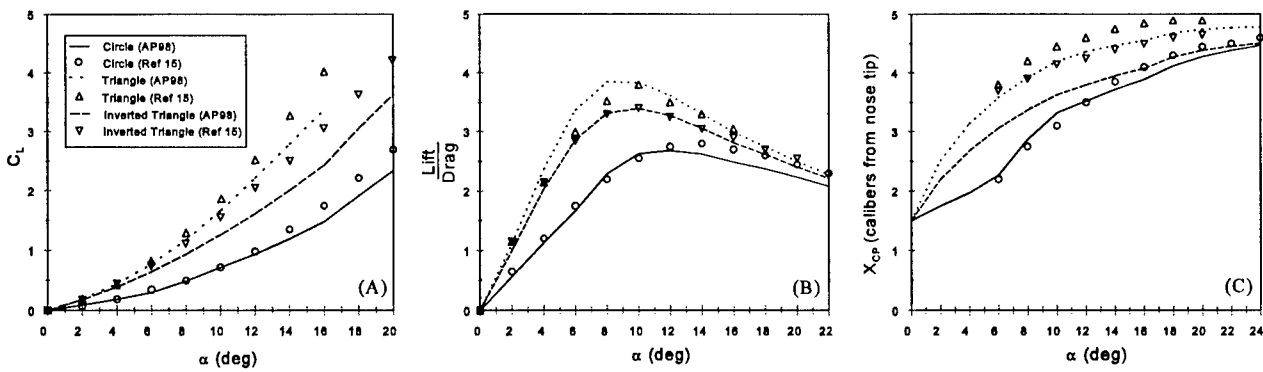


Figure 8. Aerodynamic Data of Triangles ($k = 0.0$) and Inverted Triangles ($k = 0.0$) of Fig. 5 Compared to Circular Body at $M = 1.98$ ($l/d = 10$): (A) Lift Coefficient, (B) Lift to Drag Ratio, (C) Center of Pressure.

lift-to-drag ratio and center of pressure. In general, comparison of theory and experiment for the squares and diamonds is quite encouraging, although not as good as the circular cross section shapes. The triangular shaped body predictions for lift coefficient tend to be somewhat low as AOA increases. However, this is to be expected since the values for the circular cylinder results are also low. Lift-to-drag ratio predictions are quite good, with the peak values being reasonably well predicted. Center of pressure prediction for the triangular shape is well within the ± 4 percent of body length used as a criteria for axisymmetric bodies. However, the inverted triangle center of pressure predictions slightly exceed this value.

The last configuration shown (see Figure 9) is a waverider configuration taken from Reference 22. Lift, drag, and pitching moment comparisons of theory and experiment at $M = 14.0$ to $\alpha = 25$ deg are shown in Figure 10. Results are quite encouraging, even though this configuration does not quite fit the triangular shape, which has 60 deg angles in all corners. Note that these results are based on a 375 in.² planform area.

No average accuracy assessment has been made as of yet for the nonaxisymmetric body configurations similar to that available for axisymmetric bodies. As more comparisons are made, this may become more feasible. At present, the average accuracy of the normal and axial force coefficients and center of pressure appears to be almost as good as the axisymmetric body, if the configurations are similar to those of Figure 1. However, when cases such as shown in Figure 9 are considered, the average accuracy levels are expected to be somewhat worse than when cases similar to Figure 1 are considered.

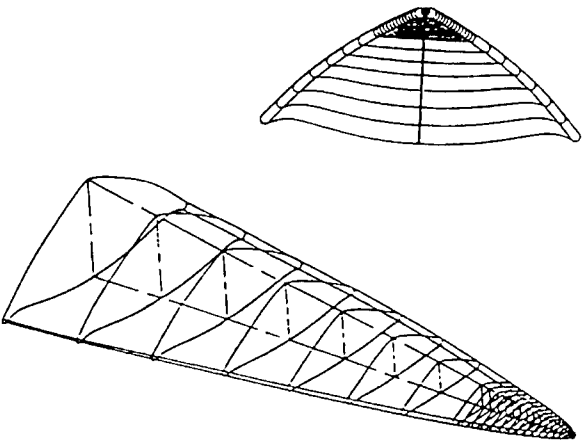


Figure 9. Wire-Frame Geometry of the Waverider (from Ref. 22).

REFERENCES

1. Moore, F. G., "Engineering Codes: State-of-the-Art and New Methods," Invited AGARD Paper No. 2 on Missile Aerodynamics, given at Brussels, Belgium and Ankara, Turkey, June 1994.
2. Moore, F. G.; McInville, R. M.; and Hymer, T., "The 1995 Version of the NSWC Aeroprediction Code: Part I - Summary of New Theoretical Methodology," NSWCDD/TR-94/379, February 1995.

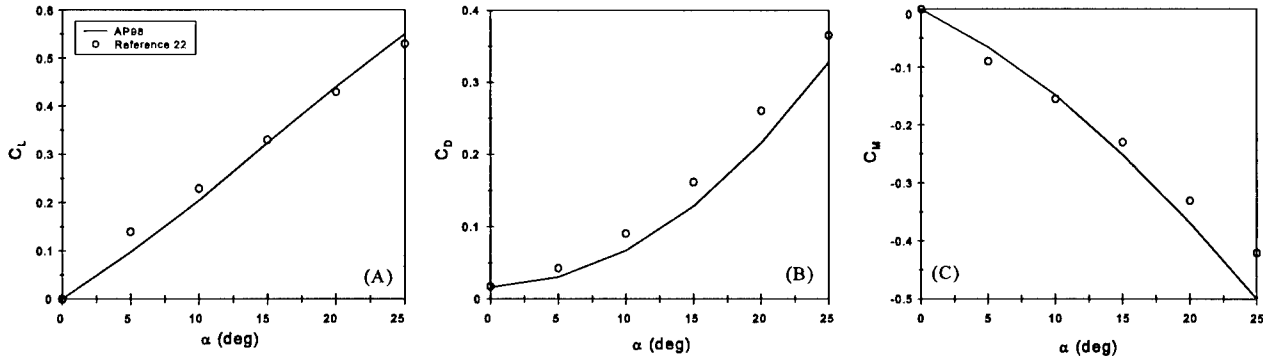


Figure 10. Aerodynamic Data for the Mach 14 Waverider of Fig. 9: (A) Lift Coefficient, (B) Axial Force Coefficient, (C) Moment Coefficient.

3. Moore, F. G. and McInville, R. M., "Calculation of Wing-Alone Aerodynamics to High Angles of Attack," JSR, January-February 1995, Vol. 32, No. 1, pp. 187-189.
4. Moore, F. G.; McInville, R. M.; and Hymer, T. C., "Aeroprediction Code for Angle of Attack Above 30 Degrees," JSR, Vol. 33, No. 3, May-June 1996, pp. 366-373.
5. Moore, F. G. and McInville, R. M., "New Semiempirical Model for Wing Tail Interference," JSR, Vol. 34, No. 1, January-February 1997, pp. 48-53.
6. Moore, F. G. and McInville, R. M., "Nonlinear Aeroprediction Methodology for Roll Position of 45 Degrees," JSR, Vol. 34, No. 1, January-February 1997, pp. 54-61.
7. Moore, F. G. and Hymer, T., "An Improved Method for Predicting Axial Force at High Angle of Attack," NSWCDD/TR-96/240, February 1997.
8. Moore, F. G.; McInville, R. M.; and Housh, C., "Methods for Distributing Semiempirical, Nonlinear, Aerodynamic Loads on Missile Components," AIAA Paper No. 97-1969, 28th AIAA Fluid Dynamics Conference, 30 June - 2 July 1997, Snowmass Village, Colorado.
9. Hymer, T.; Down, C.; and Moore, F. G., "Users Guide for an Interactive, Personal Computer Interface for the Aeroprediction Code," NSWCDD/TR-94/107, June 1994.
10. NASA Langley Research Center Tri-Service Missile Data Base, Transmitted from NASA/LFC Jerry M. Allen to NAVSWC on 5 November 1991 (formal documentation in process).
11. Stallings, R. L., Jr. and Lamb, M., "Wing-Alone Aerodynamics Characteristic for High Angles of Attack at Supersonic Speeds," NASA Technical Paper 1889, July 1981.
12. Baker, W. B., Jr., "Static Aerodynamics Characteristics of a Series of Generalized Slender Bodies With and Without Fins at Mach Numbers from 0.6 to 3.0 and Angles of Attack from 0 to 180°," AEDC TR 75-124, Vol. I and II, May 1976, Tullahoma, Tennessee.
13. Pitts, W. C.; Nielsen, J. N.; and Kaatari, G. E., "Lift and Center of Pressure of Wing-Body-Tail Combinations at Subsonic, Transonic, and Supersonic Speeds," NACA TR 1307, 1957.
14. Moore, F. G. and McInville, R. M., "Extension of the NSWCDD Aeroprediction code to the Roll Position of 45 Degrees," NSWCDD/TR-95/160, December 1995.
15. Jorgensen, L. H., "Inclined Bodies of Various Cross Sections at Supersonic Speeds," NASA Memo 10-3-58A, 1958.
16. Jorgensen, L. H., "A Method for Estimating Static Aerodynamic Characteristics for Slender Bodies of Circular and Noncircular Cross Section Alone and with Lifting Surfaces at Angles of Attack from 0° to 90°," NASA TN D-7228, 1973.
17. Moore, F. G.; McInville, R. M.; and Hymer, T., "An Improved Semiempirical Method for Calculating Aerodynamics of Missiles with Noncircular Bodies," NSWCDD/TR-97/20, September 1997.
18. Nelson, H. F., "Wing-Body Interference Lift for Supersonic Missiles with Elliptical Cross-Section Fuselages," JSR, Vol. 26, No. 5, September-October 1989, pp. 322-329.
19. Est, B. E. and Nelson, H. F., "Wing-Body Carryover and Fin Center of Pressure for Missiles with Noncircular Fuselage Cross Sections," AIAA 91-2856, Atmospheric Flight Mechanics Conference, New Orleans, LA, August 1991.
20. Monta, W. J., "Supersonic Aerodynamic Characteristics of a Sparrow III Type Missile Model with Wing Controls and Comparison with Existing Tail-Control Results," NASA TP 1078, November 1977.
21. Jorgensen, L. H. and Nelson, E. R., "Experimental Aerodynamic Characteristics for Bodies of Elliptic Cross Section at Angles of Attack from 0° to 58° and Mach Numbers from 0.6 to 2.0," NASA TM X-3129, 1975.
22. Gillum, M. J. and Lewis, M. J., "Analysis of Experimental Results on a Mach 14 Waverider with Blunt Leading Edges," AIAA 96-0812, 34th Aerospace Science Meeting and Exhibit, Reno, NV, January 1996.

ACKNOWLEDGMENT

The work described in this paper was supported through the Office of Naval Research (Mr. Dave Siegel) by the following programs: the Air Launched Weapons Program managed at the Naval Air Warfare Center, China Lake, CA, by Mr. Tom Loftus and Dr. Craig Porter, and the Surface Weapons Systems Technology Program managed at the Naval Surface Warfare Center, Dahlgren Division (NSWCDD) by Mr. Robin Staton and Mr. Gil Graff. Also, some support was provided by the Marine Corps Weaponry Technology Program managed at NSWCDD by Mr. Bob Stiegler. The authors express appreciation for support received in this work.

Le code de prévision aérodynamique de l'ONERA : "MISSILE"

P. Denis

Office National d'Etude et de Recherches Aérospatiales (ONERA)
92322 Châtillon Cedex - France

1. SOMMAIRE

Le code MISSILE a été développé pour estimer rapidement les caractéristiques aérodynamiques des missiles de Mach 0 à Mach 10, pour des incidences allant jusqu'à 40°, des angles de braquage des surfaces de contrôle de $\pm 30^\circ$ et pour des angles de roulis indifférents. La méthodologie utilisée dans ce code repose sur le concept de l'incidence équivalente avec intégration des effets tourbillonnaires, et combine des méthodes semi-empiriques, théoriques, et des corrélations issues de bases de données. Chaque modélisation figurant dans ce programme provient de résultats d'essai ou est validée par ceux-ci. Les potentialités de ce code sont présentées et de nombreuses comparaisons sont effectuées, démontrant ainsi la précision et l'utilité d'un tel outil pour la définition géométrique des engins lors des phases d'avant-projets.

2. LISTE DES SYMBOLES

CA	= coefficient de traînée
Cdc	= coefficient de traînée d'un cylindre de longueur infinie
Cl _p	= coefficient d'amortissement en roulis
Cm _q	= coefficient d'amortissement en tangage
CN	= coefficient de portance
CN α	= coefficient de gradient de portance ($=\partial CN/\partial \alpha$)
CN _A	= coefficient de portance de la voilure isolée
CN _{A(F)}	= coefficient de portance de la voilure montée sur fuselage
Cn _l	= coefficient d'amortissement en lacet
D	= diamètre du fuselage
K _{ϕ}	= coefficient d'interaction "incidence-dérapiage"
K _{β}	= coefficient d'interaction en dérapage
K _A	= coefficient d'interaction du fuselage sur l'aile
K _F	= coefficient d'interaction de l'aile sur le fuselage
L	= longueur du fuselage
M _o	= nombre de Mach
q _l	= pression dynamique locale
q _o	= pression dynamique de l'écoulement ∞ amont
Sp	= surface projetée concernée par l'écoulement tourbillonnaire
Sref	= surface de référence ($=\pi D^2/4$)
Xcp/c	= abscisse du centre de poussée de la voilure isolée par rapport à la corde à l'implanture
Xcp/D	= abscisse du centre de poussée de l'élément
Xf _o /D	= abscisse du foyer aérodynamique du missile
X _s /D	= abscisse de décollement des tourbillons d'ogive
X _r /D	= abscisse du point d'application de la force tourbillonnaire du fuselage

Ycp/h	= ordonnée du centre de poussée de la voilure isolée
α	= angle d'incidence du missile
δ	= angle de braquage des surfaces de contrôle
η	= rapport des coefficients de traînée entre un cylindre de longueur finie et un cylindre de longueur infinie
ϵ	= effilement de la voilure
λ	= allongement de la voilure
ϕ	= angle de roulis
β	= angle de dérapage
$\Delta\alpha_i, \Delta\beta_i$	= incidence et dérapage induits par l'écoulement tourbillonnaire
Λ_{ij}	= coefficients d'interférence des voilures adjacentes et opposées
α_i	= incidence locale vue par la voilure
β_i	= dérapage local vu par la voilure

3. INTRODUCTION

Les codes semi-empiriques de prévision des coefficients aérodynamiques sont et resteront pendant longtemps des outils indispensables pour les équipes d'avant-projet. De ce fait, l'ONERA développe depuis plusieurs années le code "MISSILE", utilisé par de nombreux industriels. Ce code estime tous les coefficients aérodynamiques d'un engin, à savoir les forces normale, latérale et axiale, les moments de tangage, lacet et roulis ainsi que les moments d'amortissement. La méthodologie employée combine des méthodes semi-empiriques, théoriques et des corrélations issues de bases de données. Grâce à de nombreux essais en soufflerie, des bases de données conséquentes relatives à des fuselages, des voilures isolées et montées sur fuselage, ont été obtenues et de nombreuses modélisations en sont déduites. Le concept de l'incidence équivalente est utilisé dans le code avec la particularité de prendre en compte les effets tourbillonnaires.

Le domaine d'application du code est directement lié à celui des bases de données établies lors d'essais en soufflerie et peut se résumer ainsi :

nombre de Mach :	$0 \leq M_o \leq 10$
angle d'incidence :	$\alpha \leq 40^\circ$
angle de roulis :	indifférent
angle de braquage :	$-30^\circ \leq \delta \leq 30^\circ$
élancement du fuselage :	$L/D \leq 40$

Le code MISSILE s'applique à des engins composés d'un fuselage axisymétrique muni d'une ogive parabolique, hémisphérique ou conique. A cela peuvent s'ajouter des prises d'air latérales, des canards, des ailes et des gouvernes (le nombre d'éléments composant l'ensemble de l'empennage étant compris entre 2 et 8), une jupe ou un

rétreint et une surcalibration du fuselage permettant de traiter les configurations avec accélérateur. Une synthèse de toutes ces configurations est résumée figure 1.

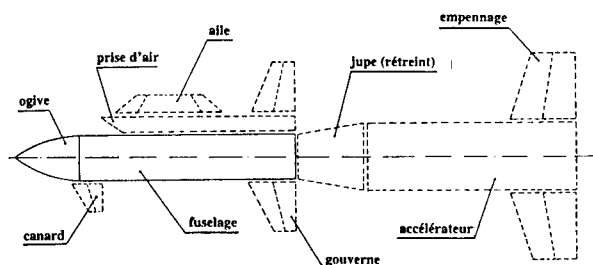


Fig.1 : Description des différentes configurations calculables par le code MISSILE

4. METHODOLOGIES

4.1 Fuselage seul

Le calcul des caractéristiques aérodynamiques du fuselage seul est basé sur la théorie de Allen et Perkins¹; les formulations en sont les suivantes :

$$CN_F = CN\alpha_F \cdot \left(\frac{\sin(2\alpha)}{2} \right) + \eta \cdot Cdc \cdot \left(\frac{Sp}{S_{ref}} \right) \cdot \sin^2 \alpha$$

$$\left(\frac{X_{cp}}{D} \right)_F = \frac{(CN\alpha_F \cdot \left(\frac{\sin(2\alpha)}{2} \right) \cdot \frac{X_F}{D} + \eta \cdot Cdc \cdot \left(\frac{Sp}{S_{ref}} \right) \cdot \sin^2 \alpha \cdot \frac{X_T}{D})}{CN_F}$$

L'effort de portance se décompose donc en un terme linéaire $CN\alpha_F \cdot \left(\frac{\sin(2\alpha)}{2} \right)$ et un terme non-linéaire

$\eta \cdot Cdc \cdot \left(\frac{Sp}{S_{ref}} \right) \cdot \sin^2 \alpha$, chacun d'entre eux faisant appel à une méthode ou une modélisation propre dans le code.

Ainsi, les caractéristiques linéaires du fuselage (gradient de portance, foyer aérodynamique) sont obtenues par interpolation dans les bases de données du DFVLR relatives au fuselage seul, et étendues aux fuselages de grand allongement et aux nombres de Mach élevés grâce à de nombreux essais complémentaires réalisés à l'ONERA.

Une très bonne prévision du gradient de portance et du foyer aérodynamique est ainsi obtenue sur toute la plage de Mach du code, comme le montre les résultats relatifs à un fuselage "classique" de missile, de 16 calibres de longueur et muni d'une ogive de 3 calibres (figure 2).

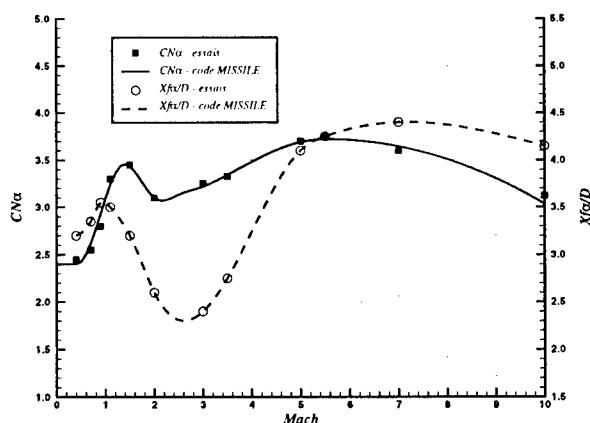


Fig.2 : Evolutions et comparaisons du gradient de portance et du foyer aérodynamique d'un fuselage de 16 calibres

Quant aux caractéristiques non-linéaires (portance tourbillonnaire et point d'application), les essais réalisés à l'ONERA ont permis d'étendre la modélisation habituelle du coefficient de traînée d'un cylindre de longueur infinie "Cdc" (figure 3) jusqu'à Mach 10 et de l'affiner pour les nombres de Mach inférieurs à 2,0. On constate alors que ce coefficient, pour les faibles nombres de Mach transversaux, dépend du nombre de Reynolds et donc du régime de l'écoulement (laminaire, turbulent ou transitionnel); pour les nombres de Mach transversaux plus importants, cette dépendance tend à disparaître du fait de l'apparition d'ondes de chocs dans l'écoulement transverse. On note enfin une évolution très différente de ce coefficient pour les forts nombres de Mach ($M > 3,0$).

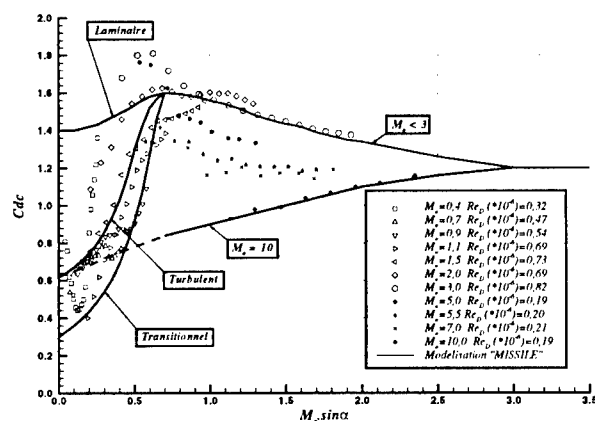


Fig.3 : Evolution du coefficient de traînée d'un cylindre de longueur infinie

De même, ces essais ont permis de localiser le point d'application de la force tourbillonnaire " X_p/D " avec comme surface projetée S_p , la surface frontale située entre l'abscisse du décollement tourbillonnaire " X_s/D " et le culot du fuselage. Les résultats d'essais ainsi que la modélisation qui en découle en fonction du nombre de Mach transversal sont présentés figure 4. On note alors que ce point d'application évolue entre 35 et 50 % de la longueur du fuselage concernée par l'écoulement tourbillonnaire.

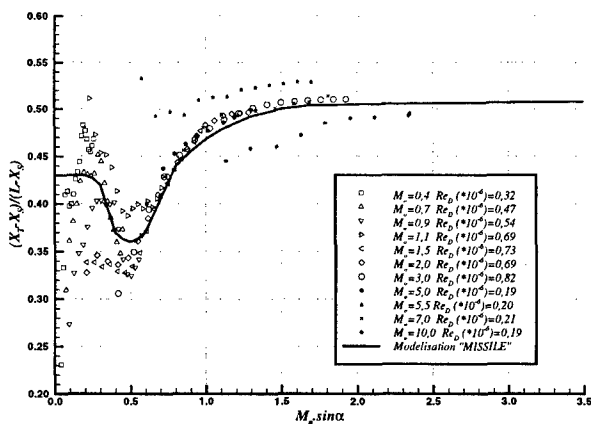


Fig. 4 : Evolution du point d'application de la force tourbillonnaire

A partir de résultats d'essais effectués au LRBA³, des modélisations semblables ont été réalisées pour les fuselages munis de prises d'air latérales. Ces prises d'air peuvent être de différents types, bidimensionnelles ou axisymétriques, et peuvent être au nombre de 2, 3 ou 4.

Pour des fuselages munis d'une jupe ou d'un rétreint, le code MISSILE utilise la théorie "choc-détente"³, recalée par des essais en soufflerie, pour calculer la contribution de cet élément. Cette méthode est aussi utilisée lors des calculs avec accélérateur (fuselage bicalibre) par décomposition en deux parties de fuselage cylindrique et d'une jupe.

Ainsi, la figure 5, où sont présentés les résultats à Mach 2,0 d'une configuration "fuselage / jupe" pour trois allongements de fuselage (16, 25 et 35 calibres), montre un très bon accord entre essais et calculs du coefficient de portance et du centre de poussée dans tout le domaine d'incidence et pour toutes les configurations. En particulier, les évolutions très différentes du centre de poussée en fonction de l'allongement du fuselage confirment la bonne prévision de la portance tourbillonnaire et de son point d'application pour les fuselages de grand allongement, comme rencontrés sur certains projectiles.

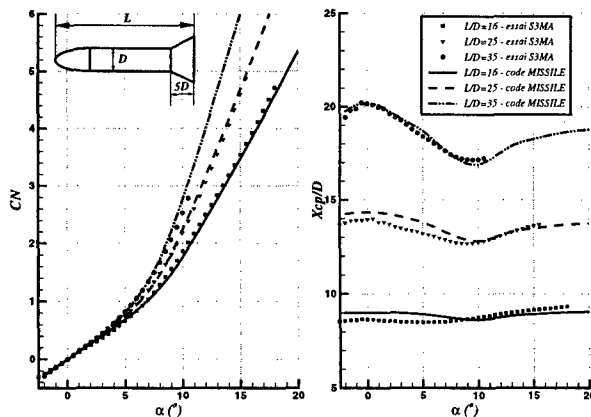


Fig. 5 : Evolutions et comparaisons du coefficient de portance et du centre de poussée de différentes configurations "fuselage / jupe" à Mach 3,0

4.2 Voilure isolée

La modélisation des caractéristiques aérodynamiques des voilures (portance et point d'application) repose sur une base de données conséquente. Des essais ont été réalisés dans la soufflerie S3MA de l'ONERA à l'aide d'un montage à la paroi et d'une balance 3 composantes, pour des incidences allant jusqu'à 90° et des nombres de Mach compris entre 0,4 et 5,5. Les voilures considérées et décrites figure 6 ont un allongement compris entre 0,25 et 3, un effilement de 0 à 1, des angles de flèche aux bords d'attaque et de fuite variés, voire même des flèches inverses.

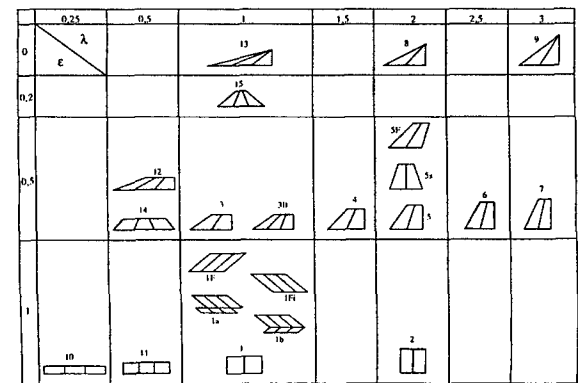


Fig. 6 : Base de données des voilures isolées

A partir de ces données expérimentales, un certain nombre de paramètres aérodynamiques, fonctions du nombre de Mach et des caractéristiques géométriques de la voilure (λ , ϵ), ont été sélectionnés afin de permettre la modélisation du coefficient de portance (CN_A) et du centre de poussée (X_{cp}/c , Y_{cp}/h) pour n'importe quelle voilure (figures 7 & 8). Au delà de Mach 5,5, les différents paramètres sont interpolés entre leur valeur à ce nombre de Mach et celle se déduisant des caractéristiques aérodynamiques des ailes en hypersonique.

De même, le montage en soufflerie modifiant les caractéristiques aérodynamiques de la voilure pour des incidences élevées ($\alpha > 50^\circ$) en supersonique, une approximation donnant le CN_A à $\alpha = 90^\circ$ a été utilisée.

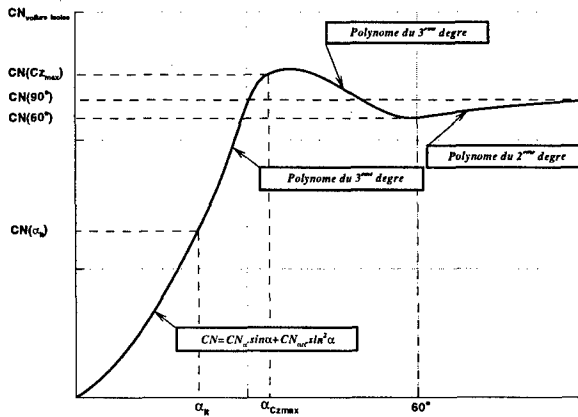


Fig. 7 : Modélisation du coefficient de portance de la voilure isolée

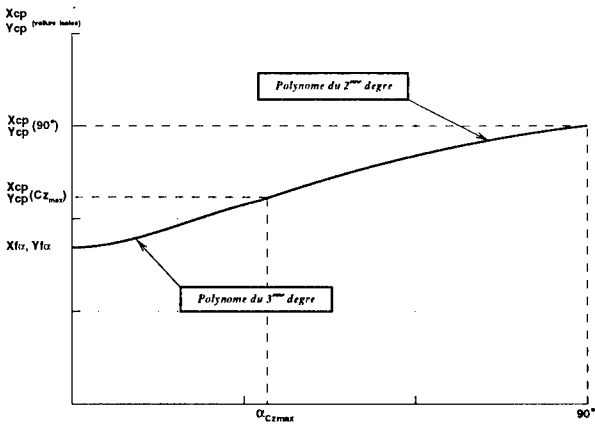


Fig. 8 : Modélisation du centre de poussée de la voilure isolée

Deux exemples de comparaisons "essai / calcul MISSILE" sont donnés en subsonique et supersonique pour deux géométries différentes de voilures (figures 9 et 10). Au vu de ces résultats, on remarque immédiatement la différence d'évolution du coefficient de portance en incidence en fonction du nombre de Mach, une différence parfaitement prise en compte par la modélisation introduite dans le code MISSILE. Par ailleurs, toutes les comparaisons effectuées sur les ailes figurant dans la base de données ont montré la validité de cette modélisation sur tout le domaine d'utilisation du code.

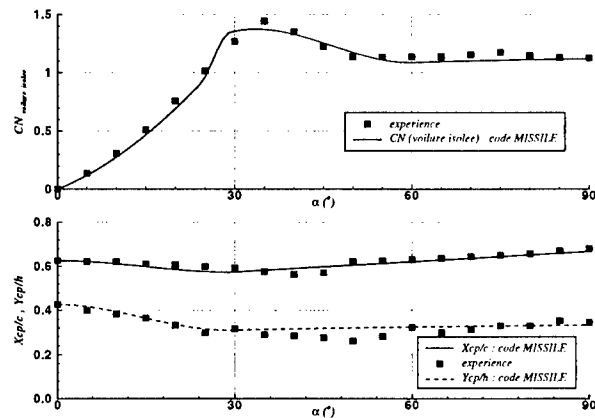


Fig. 9 : Comparaison des caractéristiques aérodynamiques de l'aile n°13 ($\epsilon=0$, $\lambda=1$) à Mach 0,4

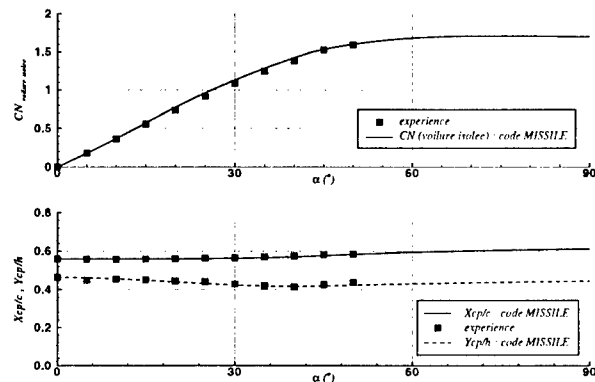


Fig. 10 : Comparaison des caractéristiques aérodynamiques de l'aile n°5 ($\epsilon=0,5$, $\lambda=2$) à Mach 2,0

Ce même montage en soufflerie, appliqué à des voilures d'allongement et d'effilement variés et faisant un angle ϕ avec l'horizontale, a permis de mettre en évidence la variation de portance des ailes en fonction des incidences et dérapages locaux vus par celles-ci. La figure 11 présente l'évolution, à Mach 2,0, du coefficient de portance de l'aile n°5 figurant dans la base de données en fonction de l'incidence locale $\alpha \cdot \cos(\phi)$. On note alors que pour une même incidence locale, de 24° par exemple, le coefficient de portance de l'aile isolée varie par rapport à sa valeur nominale ($\phi=0^\circ$) de -8% à $+29\%$ respectivement pour des angles de roulis de -45° et 45° , ce qui est non négligeable.

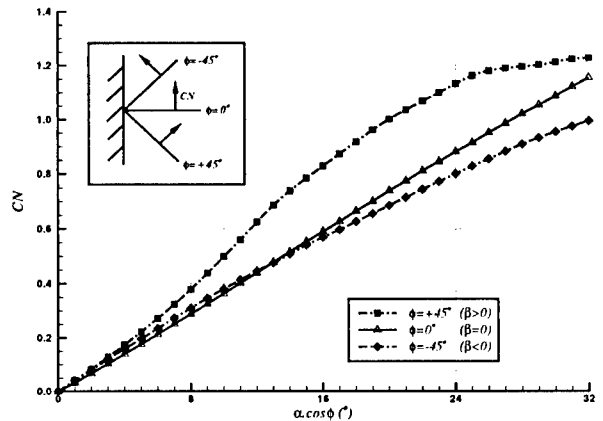


Fig. 11 : Evolution du coefficient de portance de l'aile isolée n° 5 en fonction de l'angle de roulis, à Mach 2,0.

Afin de prendre en compte cette variation dans le code MISSILE, un coefficient de couplage "incidence-dérapiage" K_ϕ a été déduit des valeurs expérimentales,

$$K_\phi(\alpha) = \left(\frac{CN(\phi \neq 0^\circ, \alpha \cdot \cos \phi)}{CN(\phi = 0^\circ, \alpha)} - 1 \right) \cdot \frac{1}{\alpha \cdot \sin \phi}$$

puis modélisé en fonction du nombre de Mach, de l'incidence locale et des caractéristiques géométriques de la voilure (λ , ϵ).

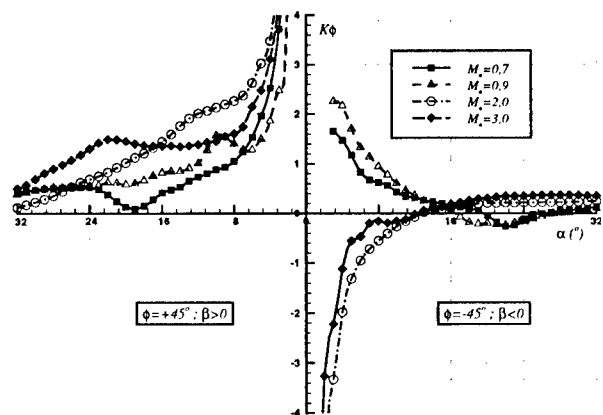


Fig. 12 : Evolution du coefficient de couplage "incidence-dérapiage" de l'aile n°5 en fonction du nombre de Mach

La figure 12, relative aux résultats de l'aile n°5, présente l'évolution de ce coefficient. L'analyse de ces essais semble indiquer que quels que soient la géométrie de la voilure et

le nombre de Mach, K_A , reste proche de zéro pour les dérapages négatifs mais tend vers des valeurs beaucoup plus importantes (jusqu'à 3) pour les dérapages positifs.

4.3 Voilure sur fuselage

La détermination des caractéristiques aérodynamiques de la voilure montée sur le fuselage repose sur l'utilisation du concept de l'incidence équivalente avec cependant quelques adaptations par rapport à la formulation proposée par Nielsen⁴. La méthodologie utilisée est la suivante :

a/ détermination des incidence et dérapage locaux vus par la voilure montée sur fuselage :

$$\tan(\alpha_l) = [K_A \cdot \tan\alpha \cdot \cos\phi + \tan(\Delta\alpha_T) + \Lambda_{44} \cdot \tan(\delta)]$$

$$\sin(\beta_l) = [K_\beta \cdot \sin\alpha \cdot \sin\phi + \sin(\Delta\beta_T)]$$

où $K_A \cdot \tan\alpha \cdot \cos\phi$ et $K_\beta \cdot \sin\alpha \cdot \sin\phi$ représentent l'incidence et le dérapage vus par l'aile montée sur un fuselage à l'incidence α et à roulis ϕ , $\Lambda_{44} \cdot \tan(\delta)$ l'incidence due à son braquage δ , $\tan(\Delta\alpha_T)$ et $\sin(\Delta\beta_T)$ l'incidence et le dérapage induits sur l'aile par les différents tourbillons ;

b/ détermination du coefficient de portance de la voilure montée sur le fuselage :

$$CN_{A(F)}(\alpha, \phi) = CN_A(\alpha_l) \cdot [1 + K_\phi \cdot \sin(\beta_l)]$$

où $CN_A(\alpha_l)$ représente la valeur du coefficient de portance de l'aile isolée à l'incidence α_l et $K_\phi \cdot \sin(\beta_l)$ l'influence du dérapage local ;

c/ correction due à l'influence des voilures environnantes :

$$CN_{A(F)} = CN_{A(F)} - \Lambda_{43} \cdot \Sigma CN_{A(F)}(adj) - \Lambda_{42} \cdot CN_{A(F)}(opp)$$

où Λ_{43} et Λ_{42} sont les coefficients d'interaction dus, respectivement à la présence des ailes adjacentes et opposée à la voilure calculée ;

d/ correction du coefficient de portance de la voilure montée sur fuselage en fonction de la pression dynamique locale :

$$CN_{A(F)}(\alpha, \phi, q_l) = CN_{A(F)}(\alpha, \phi) \cdot \left(\frac{q_l}{q_o} \right)$$

où $\left(\frac{q_l}{q_o} \right)$ est le rapport de la pression dynamique locale à celle à l'infini amont ;

e/ intégration du coefficient de portance de la voilure montée sur le fuselage dans l'ensemble de la configuration :

$$CN_{(aile/fuselage)} = CN(\alpha, \phi, q_l) \cdot \left(1 + \frac{K_F}{K_A} \right) \cdot \frac{S_A}{S_{ref}}$$

L'établissement de cette méthode nécessite de bien connaître les différents coefficients d'interaction. A cette fin, une base de données relative aux voilures montées sur fuselage a donc été établie grâce à plusieurs campagnes d'essais dans les souffleries S3MA et R2/R3Ch de l'ONERA.

Comme le montre la figure 13, quelques ailes déjà testées isolément, et dont les caractéristiques géométriques représentent au mieux l'ensemble du domaine, ont été choisies, montées braquées ou non à différentes positions longitudinales sur un fuselage puis étudiées de Mach 0,4 à Mach 10 sur un fuselage dont l'incidence pouvait atteindre 40°. Les pesées de la voilure et de l'ensemble complet ont alors été effectuées.

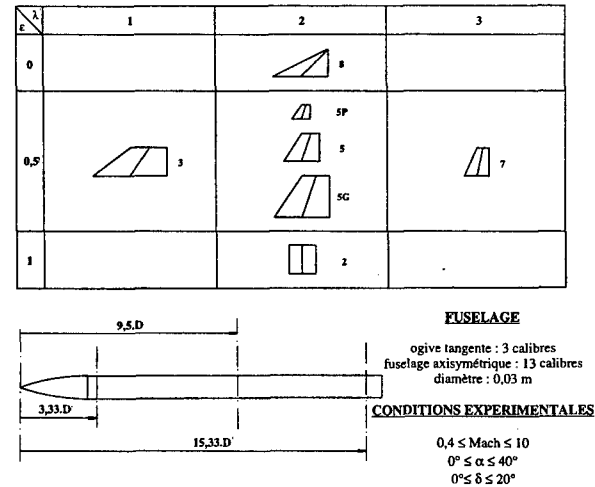


Fig. 13 : Base de données des voilures montées sur fuselage

Partant initialement de la théorie des corps élanés pour définir les valeurs nominales des coefficients d'interaction (K_A , K_F , Λ_{42} , Λ_{43} , Λ_{44} , K_β et K_ϕ), les résultats des essais des voilures isolées et montées sur fuselage ont permis certaines corrections, et plus particulièrement sur les coefficients K_A et K_F .

Ainsi, le coefficient d'interaction K_A est corrigé de la façon suivante :

$$K_A = (K_A)_{C.E.} + \Delta(K_A) \text{ avec}$$

$$\Delta(K_A) = f\left(\lambda, \frac{X}{D}, \text{Mach}, \alpha\right)$$

La correction la plus importante est liée à l'incidence et au nombre de Mach, comme le montre la figure 14.

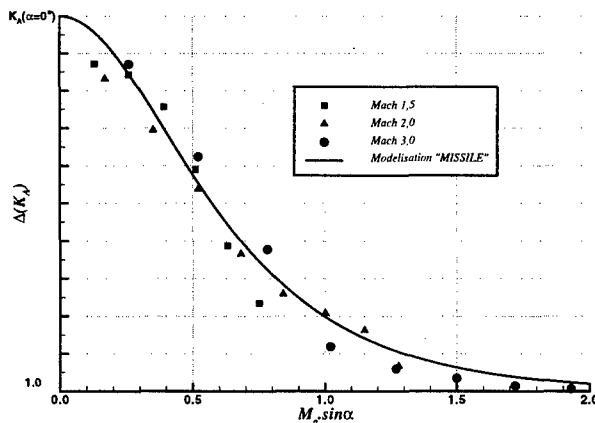


Fig. 14 : Correction du coefficient d'interaction "aile/fuselage" en fonction du nombre de Mach et de l'incidence

L'étude de l'influence des différents tourbillons sur la portance d'une voilure montée sur fuselage s'est faite à partir des sondages effectués à la soufflerie S2MA autour du fuselage seul puis autour du fuselage muni des précédentes voilures, pour des nombres de Mach variant de 0,4 à 3,0 et pour des incidences allant jusqu'à 40°. Les mesures ont été réalisées à l'aide d'un peigne composé de sondes 5 trous. Après analyse des cartographies de l'écoulement, figure 15, ces essais ont mis en évidence les trois types de tourbillons existants autour d'un engin, à savoir les tourbillons d'ogive, d'ailes et d'arrière-corps.

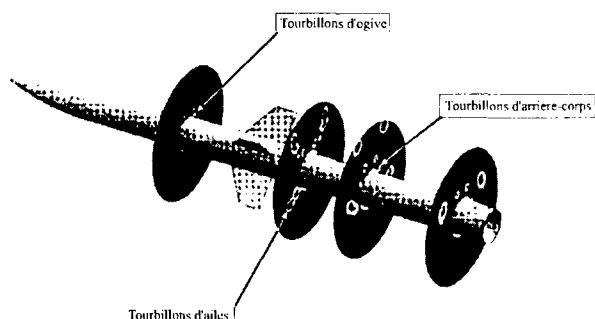


Fig. 15 : Description de l'écoulement tourbillonnaire autour d'un missile

La modélisation retenue dans le code MISSILE est basée sur des tourbillons filaments à noyau visqueux. Pour chaque tourbillon, une origine, une intensité, une position et un rayon visqueux sont définis en fonction des conditions de l'écoulement (Mach, incidence) et des caractéristiques géométriques de chaque élément composant le missile.

Ainsi, les tourbillons d'ogive modélisés dans le code sont au nombre de deux, contrarotatifs, avec des caractéristiques (intensité, position et rayon visqueux) fonction de la variable $(X-X_s) \cdot \sin \alpha$ où X_s est leur abscisse d'origine (fonction uniquement de α).

Les tourbillons d'ailes, de même nombre que celles-ci, ont une intensité proportionnelle à la portance de l'aile et leur position est liée aux dimensions du bord de fuite.

Quant aux tourbillons d'arrière-corps, ils sont semblables aux tourbillons d'ogive et n'apparaissent que si la longueur du fuselage en aval de la voilure est importante ou l'incidence du missile élevée.

Les trajectoires de ces tourbillons sont calculées les unes par rapport aux autres, pas à pas, par une méthode de Runge-Kutta d'ordre 2, en considérant les potentiels induits par ces tourbillons. De plus, le recours à des transformations conformes est nécessaire pour connaître l'évolution des trajectoires au niveau des ailes.

Les positions respectives de chaque tourbillon étant connues au niveau de la voilure considérée, une intégration par la formule de Biot-Savart permet d'estimer les incidence et dérapage induits par le système tourbillonnaire ($\Delta \alpha_i, \Delta \beta_i$).

La figure 16, comparant le coefficient de portance de la gouverne extradors en présence ou non de la voilure amont,

souligne l'importance de la prise en compte du système tourbillonnaire dans la détermination des efforts. En effet, on constate que la présence de la voilure amont et du sillage qu'elle génère entraîne une déportance considérable sur les gouvernes extradors au fur et à mesure que l'incidence augmente, effet bien représenté par le code "MISSILE".

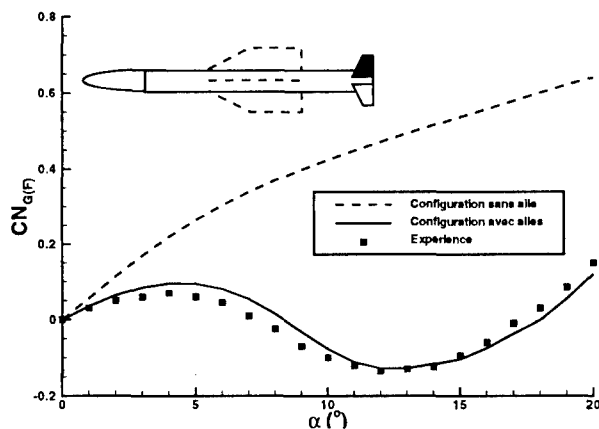


Fig. 16 : Coefficient de portance de la gouverne extradors en présence ou non de la voilure amont - $M_0=0,8$

Enfin, la variation de pression dynamique locale autour du fuselage, due à la présence des tourbillons, de l'écoulement transversal et du choc de nez pour les nombres de Mach supersonique et les incidences élevées, est modélisée dans ce code. Cette modélisation s'appuie sur les résultats expérimentaux de sondages d'écoulement et sur quelques résultats de calculs Euler pour préciser les caractéristiques du choc.

Une comparaison entre les résultats expérimentaux et ceux donnés par le code MISSILE est montrée figure 17, à Mach 0,4 et 2,0 et pour une voilure de hauteur égale à un calibre. On constate immédiatement des évolutions différentes de la pression dynamique suivant le régime de vitesse, ainsi qu'une variation importante en fonction de l'angle de roulis. La modélisation réalisée évalue au mieux ces variations dans l'ensemble du domaine d'utilisation.

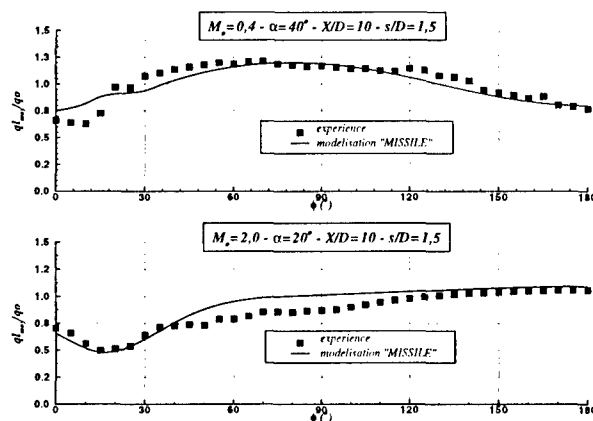


Fig. 17 : Comparaison de la pression dynamique locale à Mach 0,4 et 2,0

Deux exemples d'application à Mach 2,0 et relatifs à un fuselage muni de l'aile n°5, placée à 10 calibres de la pointe avant, sont présentés figures 18 et 19. Ils montrent

l'importance de ces effets (tourbillons et pression dynamique locale) pour la prévision de la portance d'une aile montée sur fuselage. La figure 18 met en évidence le déficit de portance de la voilure extradors (voilure n°1) dû à la présence proche des tourbillons d'ogive et une légère augmentation de la portance intrados (voilure n°4) pour les fortes incidences liée à l'effet de compression de l'intrados du fuselage. La figure 19, présentant l'évolution de la portance de la voilure en fonction de l'angle de roulis au même nombre de Mach et pour 20° d'incidence, met en avant l'influence de ces deux paramètres et confirme la bonne prise en compte de ces phénomènes par le code MISSILE.

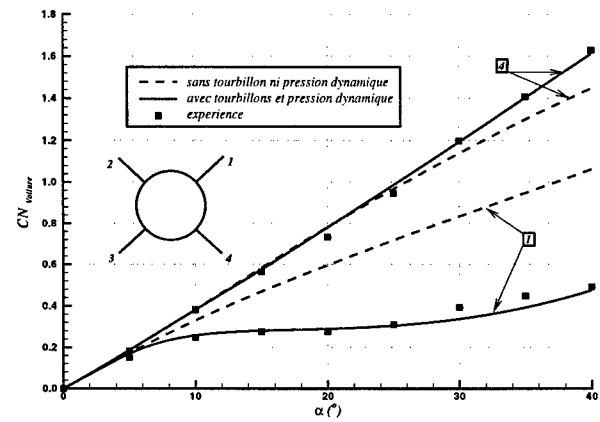


Fig. 18 : Influence de la pression dynamique et de l'écoulement tourbillonnaire sur la portance des ailes en incidence

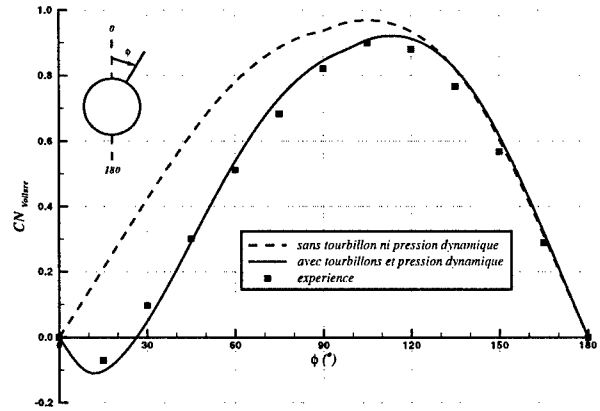


Fig. 19: Influence de la pression dynamique et de l'écoulement tourbillonnaire sur la portance des ailes en roulis

4.4 Modélisation de la traînée

Comme pour la détermination de tous les autres coefficients aérodynamiques, le coefficient de traînée est obtenu par décomposition de l'engin en éléments simples sur lesquels viennent s'appliquer les théories usuellement utilisées pour le calcul de la traînée. Le tableau ci-dessous répertorie les différentes méthodes figurant dans le code MISSILE en fonction du domaine de vol.

Mach	Subsonique	Supersonique	Hypersonique
frottement	Méthode intégrale (MICHEL) ⁵		
pression	Empirique	Théorie. linéaire + Newton modif.	Choc-détente + Newton modif.
culot	Empirique		

Après avoir estimé le coefficient de traînée à incidence nulle du missile, une variation autour de cette valeur en fonction de l'incidence (essentiellement pour le subsonique) et des braquages éventuels des surfaces portantes est effectuée à l'aide de la relation suivante : $CA = CA_0 + \Delta CA(\alpha) + \Delta CA(\alpha, \delta)$ avec $\Delta CA(\alpha, \delta) = a \cdot \delta^2 + b \cdot \alpha \delta$

La figure 20 présente une comparaison "essai / calcul" du coefficient de traînée d'une configuration générique d'engin (ogive parabolique pointue d'allongement 3, épaisseur relative des ailes et de gouvernes respectivement de 4% et 6%), à Mach 0,8 et 2,0 et pour des incidences modérées. La valeur du coefficient de traînée à incidence nulle est parfaitement déterminée pour ces deux nombres de Mach et les évolutions en incidence sont relativement bien décrites par le code.

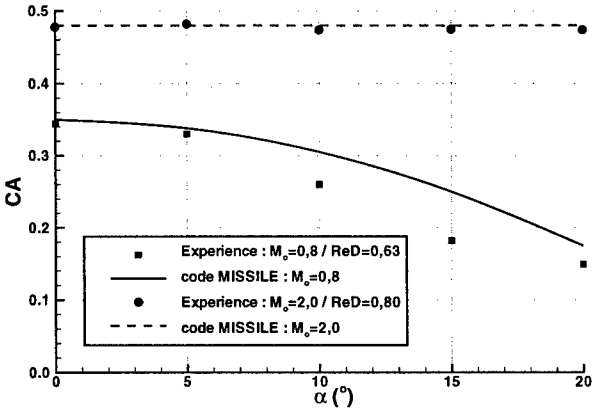


Fig. 20 : Evolution du coefficient de traînée en incidence et à Mach 0,8 et 2,0 d'une configuration générique de missile.

4.5 Modélisation des coefficients d'amortissement

Le code MISSILE ne calcule que les coefficients de moments d'amortissement en tangage Cm_q , en lacet Cn_r , et en roulis Cl_p . Les méthodes utilisées pour leur détermination étant nombreuses, la théorie des corps élancés appliquée sur chaque élément composant l'engin est retenue pour les moments de tangage et de lacet et un compromis entre plusieurs méthodes (théorie des corps élancés, DATCOM, Nielsen), suivant la configuration étudiée, est réalisé pour le moment de roulis.

L'erreur faite sur la prévision de ces coefficients d'amortissement reste importante et est fonction de la complexité géométrique de l'engin; elle varie de $\pm 10\%$ pour les configurations les plus simples à $\pm 30\%$ pour les plus complexes.

5. VALIDATIONS

Lors de la description du code, de nombreuses comparaisons entre les résultats d'essais et ceux donnés par le code MISSILE ont été présentées pour des configurations simples de type fuselage seul, fuselage de grand allongement avec jupe et fuselage muni d'une série de voilures. Afin de valider plus globalement les méthodes utilisées dans ce code semi-empirique, des comparaisons sur des configurations plus complexes sont présentées ci-après.

La première configuration choisie est constituée d'un fuselage de 16 calibres de longueur, muni d'une ogive parabolique pointue de trois calibres, de canards et de gouvernes cruciformes, alignées avec les canards (position ++); ces voilures, de forme identique, correspondent à l'aile n°5 précédemment citée.

Les résultats obtenus pour les coefficients de portance et de moments de tangage, à Mach 3, en incidence et pour deux angles de braquage des canards ($\delta=0^\circ$ et 20°) sont regroupés respectivement figures 21 et 22.

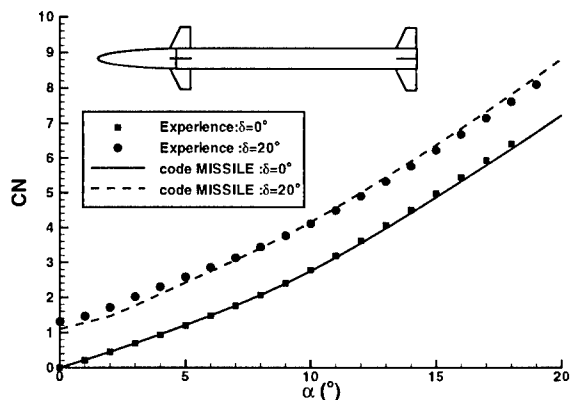


Fig. 21 : Coefficient de portance en fonction de l'incidence et de l'angle de braquage.

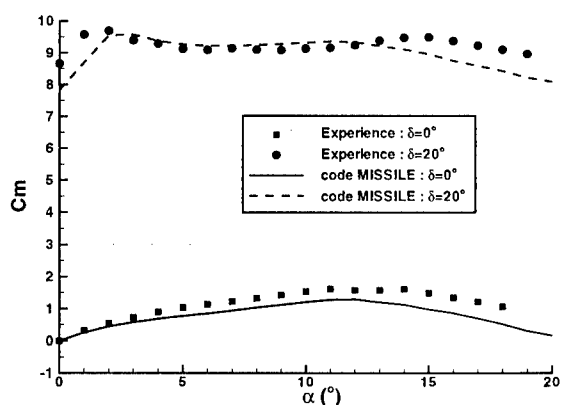


Fig. 22 : Coefficient de moment de tangage en fonction de l'incidence et de l'angle de braquage.

On constate, au travers de ces deux figures, le bon accord entre les valeurs de soufflerie et celles données par le code MISSILE. Ce résultat est essentiellement dû à la bonne estimation par le code des trajectoires tourbillonnaires, dont l'effet devient prépondérant lorsque les distances entre les voilures amont et aval sont importantes.

La deuxième configuration retenue se compose du même fuselage que précédemment, de deux séries de voilures cruciformes croisées ayant respectivement pour caractéristiques géométriques $\lambda=0,5$ et $\varepsilon=0,5$ pour l'aile et $\lambda=2$, $\varepsilon=0,5$ pour la gouverne.

La figure 16 ayant montré la bonne prédiction par le code MISSILE du coefficient de portance de la gouverne extradors pour une configuration analogue, il est alors intéressant de comparer l'évolution du moment de roulis calculé avec les résultats expérimentaux. Ceci est effectué à Mach 0,8 et $\phi=22,5^\circ$, pour des incidences allant jusqu'à 20° (figure 23).

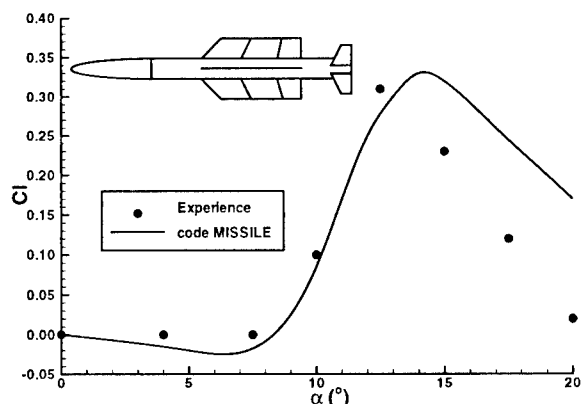


Fig. 23 : Evolution du coefficient de moment de roulis à Mach 0,8 et $\phi=22,5^\circ$

Au vu de cette figure, on remarque que l'allure du coefficient de moment de roulis est bien décrite par le code. Les interactions tourbillonnaires, principale cause de la mauvaise prédiction du moment de roulis par les codes semi-empiriques, sont ici parfaitement maîtrisées, comme par exemple l'apparition de l'interaction "aile intrados / gouverne extradors" qui est mise en évidence autour de 13° d'incidence. Toutefois, on note que les variations en amplitude sont légèrement surestimées, mais restent faibles et acceptables pour ce type de coefficient.

La troisième et dernière validation est effectuée sur une configuration ressemblant géométriquement à la précédente mais avec un empennage arrière constitué de 8 éléments équirépartis.

Les comparaisons relatives aux évolutions des coefficients de portance et de moment de tangage en incidence et à Mach 2, sont présentées figures 24 et 25.

Malgré le nombre conséquent de gouvernes, la prévision des coefficients globaux par le code MISSILE est excellente, en particulier la stabilité, l'erreur sur le centre de poussée de l'engin ne dépassant pas 0,1 calibre.

Au regard de ces résultats et de ceux présentés figure 5, on peut affirmer que le code MISSILE constitue un excellent outil pour l'étude des projectiles (fuselage de grand allongement et muni d'un nombre important de gouvernes).

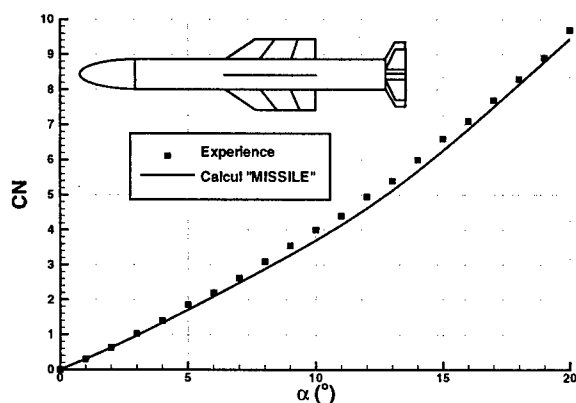


Fig. 24 : Evolution du coefficient de portance à Mach 2,0 en fonction de l'incidence

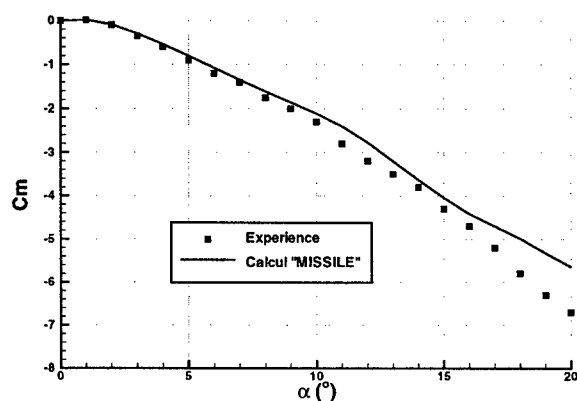


Fig. 25 : Evolution du coefficient de moment de tangage à Mach 2,0 en fonction de l'incidence

6. CONCLUSION

Un programme semi-empirique de calcul des coefficients aérodynamiques globaux des missiles a été développé à l'ONERA depuis environ 15 ans.

Initialement basé sur les théories générales relatives aux missiles, ce code n'a cessé d'évoluer grâce à de nombreux essais en soufflerie et à l'établissement de bases de données importantes. Les modélisations des divers coefficients ont ainsi pu être affinées, et en particulier le système tourbillonnaire engendré par les différents éléments du missile a pu être finement pris en compte, et a été intégré dans le concept d'incidence équivalente.

Au travers des multiples comparaisons présentées dans cet article, on a pu constater le bon accord existant entre les résultats expérimentaux et ceux donnés par le code MISSILE, et ceci sur tout son domaine d'utilisation, ce qui en fait un excellent outil d'avant-projet.

Le développement de ce code se poursuit actuellement à l'ONERA par l'extension du domaine de vol aux grandes incidences et par une validation approfondie sur de nombreuses géométries de missiles.

7. REFERENCES

1. Allen, J. H., and Perkins, E. W., "Characteristics of Flow Over Inclined Bodies of Revolution", NACA RM A 50L07, 1965.
2. Champigny, P., Baudin, D., et Gonidec, P., "Prévision des coefficients aérodynamiques de missiles munis de prises d'air", Symposium AGARD/FDP, Friedrichshafen, 23-26 avril 1990.
3. Engineering Design Handbook, "Design of Aerodynamically Stabilized Free Rockets", Headquarters, U.S. Army Material Command, July 1968.
4. Hemsch, M. J., and Nielsen, J. N., "The equivalent Angle-of-Attack Concept for Engineering Analysis" Tactical Missile Aerodynamics, edited by M. J. Hemsch and J. N. Nielsen, Progress in Astronautics and Aeronautics, Vol. 104, AIAA, New York, 1986, pp. 482-518.
5. Michel, R., "Couches limites, frottement et transfert de chaleur", Cours Sup'Aéro, 1972.

3D EULER AND THIN LAYER NAVIER STOKES SOLUTIONS FOR MISSILES AT SUPERSONIC SPEEDS AND HIGH ANGLES OF ATTACK

E. Oktay^{*}, N. Alemdaroğlu[†], E. Tarhan[‡]

ROKETSAN, Missiles Industries Inc., Elmadağ, 06780 Ankara, Turkey.

P. Champigny[§] and P. d'Espiney[¶]

ONERA, F-92322 Chatillon, Cedex, France.

SUMMARY

The purpose of this paper is to validate a 3D unstructured Euler flow solver, USER3D and a structured thin layer Navier-Stokes flow solver, TLNS, against the experimental data and to compare with the Euler and the Navier-Stokes solver, (FLU3M), of ONERA for two different missile geometries at a Mach number of $M=2$ and at various angles of attack, α , ($0 < \alpha < 20^\circ$). The first one is a conventional missile geometry with an ogive nose, a cylindrical body and four straight tail fins. The second one is an unconventional missile geometry with a lenticular body and no tail fins. The present results are found to be in good agreement with the available results and the differences observed between them are explained in detail. The unstructured Euler code, USER3D, proved to be accurate, fast and reliable for determining the overall aerodynamic characteristics of the missiles whereas the thin layer Navier-Stokes (TLNS) solutions are found to be effective in predicting the detailed viscous behaviour of the flow field over the conventional and unconventional missile geometries studied.

1. INTRODUCTION

Computational Fluid Dynamics (CFD) has become a very important and effective design tool in aerodynamics research. Besides reducing the time required for expensive wind tunnel testing, CFD can provide additional insight to the analysis and design of aerodynamic vehicles. Today CFD has become a standard and an inevitable design tool for the aerodynamicist. Although, the computational time increases with the geometrical complexity of the vehicle, it is still much less expensive to obtain solutions by CFD methods as compared to experimental work. One of the important applications of CFD is definitely the design of missiles.

An unstructured 3D Euler solver^{1,2}, USER3D is developed and used extensively by Roketsan as a design tool for predicting as well as for improving the performances of missiles. The reliability of any kind of flight simulation for missiles depends upon the accuracies with which the aerodynamic coefficients of the complex missile geometries are predicted. Hence, the results of CFD predictions must be carefully tuned and validated against available experimental data such that they can be applied without any ambiguity and questions. The starting point of this particular research was to validate the USER3D and TLNS codes against experimental data and other available CFD codes. This work is a product of the joint research initiated between Roketsan and ONERA and is supported by the AGARD Fluid Dynamics Panel.

Two different missile geometries are studied. The first one is a conventional missile geometry with an ogive nose, a cylindrical body and four straight tail fins. The second one is an unconventional missile geometry with a lenticular body shape and no tail fins. This geometry was previously investigated by d'Espiney³, using different computational methods such as a panel method, HISS, and a semi-empirical method, SHABP, as well as the ONERA's Euler code. This reference also details the experimental investigations performed on this geometry and compares the computational results with the experimental data. Further computations on the same geometry using the thin layer and space-marching Navier-Stokes solvers are performed and the results were compared with the Euler and experimental results⁴. Further studies on the same geometry using the 3D laminar and 2D turbulent computations with the Navier-Stokes solver, FLU3M, are also given by C. Jouet and P. d'Espiney⁵. The details of the experiments carried out at ONERA on this model are also reported⁶.

The results of the Euler computations that will be given in this paper are previously presented in detail². Although the main emphasis in this paper will be mostly on the computations performed by thin layer Navier-Stokes solver, the same Euler computations will also be presented here for the sake of completeness of the discussions. All of the Euler computations are performed at a free stream Mach number of $M_\infty=2.0$ and

^{*} Chief Engineer, Ph.D, Engineering Development Department.

[†] Consultant, Professor, Aeronautical Engineering Department, Middle East Technical University, Ankara, Turkey.

[‡] Engineer, Engineering Development Department.

[§] Chief, Hypersonic Missiles and Launchers, Applied Aerodynamics Department.

[¶] Senior Research Engineer, Applied Aerodynamics Department.

at different angles of attack, α , $0^\circ \leq \alpha \leq 20^\circ$. On the other hand, TLNS computations are presented only for some selected discrete cases: for the conventional missile geometry $M=2.0$, $\alpha=5^\circ, 10^\circ$, and for the lenticular body, $M=2.0$, $\alpha=10^\circ$, $Re=2 \times 10^6$ and for laminar flow only for both of the cases. The computational results obtained by Euler (USER3D) and TLNS for each of the test cases are compared with each other as well as with the computational results of ONERA, obtained by their Euler and Navier-Stokes code (FLU3M) and thin layer Navier-Stokes code^{3,4,5} (FLU3NS). All of these results are then compared with the experimental results of ONERA. In general, it is observed that the predictions of the unstructured Euler and the TLNS codes are in good agreement with both the numerical and the experimental results of ONERA.

2. THE FLOW SOLVER USER3D

The unstructured Euler flow solver, USER3D which is used in this study, is developed in ROKETSAN¹ and its details are given in reference 7. This code employs a fully-conservative cell centered finite volume method applied to the tetrahedral cells of the computational grid. Second order spatial discretization is based on Roe's flux difference splitting method⁷. For time integration, m-stage Runge-Kutta time-stepping scheme⁸ is used. Local time stepping and implicit residual smoothing accelerate its convergence to steady state.

Higher order interpolation and reconstruction schemes together with total variation diminishing (TVD) limiter scheme are incorporated into the code to enhance the numerical accuracy of the computations. In this way, a higher order accuracy in space is obtained even in highly stretched bad grids.

2.1. The Governing Equations

The time dependent Euler equations for an ideal compressible fluid in the absence of external forces are given in the integral form as

$$\frac{\partial}{\partial t} \iiint_{\Omega} Q dV + \iint_{\partial\Omega} F(Q) \cdot \mathbf{n} dS = 0$$

Here Ω represents the physical domain with a boundary $\partial\Omega$. Where

$$Q = \begin{Bmatrix} \rho \\ \rho u \\ \rho v \\ \rho w \\ e \end{Bmatrix} \quad F(Q) \cdot \mathbf{n} = (\mathbf{V} \cdot \mathbf{n}) \begin{Bmatrix} \rho \\ \rho u \\ \rho v \\ \rho w \\ e + p \end{Bmatrix} + p \begin{Bmatrix} 0 \\ n_x \\ n_y \\ n_z \\ 0 \end{Bmatrix}$$

Here n_x, n_y, n_z are the Cartesian components of the exterior surface unit normal \mathbf{n} on the boundary $\partial\Omega$. Pressure can be expressed as

$$p = (\gamma - 1) \left[e - \frac{1}{2} \rho (u^2 + v^2 + w^2) \right]$$

2.2. Boundary Conditions

Flow tangency condition was imposed on the walls and symmetry planes by setting the velocities on the boundary faces to their cell-center values and then subtracting the component normal to the solid surface. Density and pressure boundary conditions were simply set to the cell-centered values.

Characteristic boundary conditions were applied to the far-field boundary for each computation using the fixed and extrapolated Riemann invariants corresponding to the incoming and outgoing waves. The incoming Riemann invariants is determined from the freestream flow and outgoing invariant is extrapolated from the interior domain. The invariants are used to determine the locally normal velocity component and speed of sound. At an outflow boundary, the two tangential velocity components and the entropy were extrapolated from the interior, while at the inflow boundary they were specified as having the far-field values. These five quantities provide a complete definition of the flow in the far field.

3. THE FLOW SOLVER TLNS

The three dimensional structured thin layer Navier-Stokes (TLNS) solver which was used in this study is a multiblock flow solver adapted on the finite differencing with second order accuracy in space and time. This code uses an implicit approximate factorization algorithm of Beam and Warming⁹ and a diagonalization procedure with similarity transformation suggested by Pulliam and Chaussee¹⁰. In the matrix solution, LU-ADI technique (Alternating Direction Implicit method with Lower and Upper bidiagonalization) is applied. This flow solver is also capable of using variable time stepping for fast convergence to steady-state solutions. As for the dissipation models, fourth order explicit and second order implicit smoothing terms are adapted into the scheme.

3.1. The Governing Equations

In the thin layer Navier-Stokes equations, the viscous effects in the directions along the solid boundary are neglected compared with those in normal direction to the solid boundary. Due to this assumption, the thin layer Navier-Stokes equations can be expressed in the generalized curvilinear coordinates (ξ, η, ζ) as;

$$\frac{\partial Q}{\partial t} + \frac{\partial f}{\partial \xi} + \frac{\partial g}{\partial \eta} + \frac{\partial h}{\partial \zeta} = \frac{1}{Re_\infty} \frac{\partial s}{\partial \zeta}$$

where, f, g and h are the inviscid flux vectors in ξ, η and ζ directions respectively and s is the viscous flux vector in the ζ direction. The curvilinear components ξ and η are set along the solid boundary whereas ζ is normal to this boundary. The details of the formulation can be found in references^{11,12}.

3.2. Boundary Conditions

For the solid boundaries, adiabatic walls and no slip boundary conditions are imposed. Pressure is obtained from the normal momentum equation and the energy is updated by using the wall pressure. For supersonic inflow, the flow variables are taken from the freestream values and for supersonic outflow, they are extrapolated from the computational domain. A three point linear interpolation technique is used for matching the surface conditions in the multiblock cases.

4. GRID GENERATION

4.1. Grid Generation For Euler Computations

The unstructured grids used for the Euler computations are generated using the commercially available CAD tool, I-DEASTM. Although this tool is not very convenient for generating the appropriate grid suitable for our present studies, various control features of the code are used until an appropriate grid distribution is achieved. However, one of the basic advantages of using this tool for grid generation lies in the fact that the available geometry directly comes from this design package. Thus, any major modification made to the external geometry of the missile is passed directly to the CFD analysis. In order to get nearly the same grid distribution as in the ONERA studies, another in house developed grid generation code is used. Although this is a structured grid generation code, it has the capability of generating structured tetrahedral grids with appropriate grid interconnectivity feature suitable for interfacing with the USER3D code².

4.2. Grid Generation For TLNS Computations

The grids used for TLNS computations are provided by ONERA and therefore they are exactly the same grids as used in their computations^{4,5}.

5. RESULTS AND DISCUSSION

5.1. Conventional Missile

The geometry for the conventional missile is given in Figure 1. The missile has a tangent ogive nose section followed by a cylindrical body and four straight tail fins. The fins have a constant thickness ratio of $t/c=0.07$ along their span. The unstructured Euler grid generated for this geometry has 297164 cells with 54029 nodes and 603129 faces for half body and is given in Figure 2a. The structured grid used for the TLNS solutions is given in Figure 2b, which is the same grid used by ONERA. This is a multi-block grid which is composed of 6 blocks. The ogive-cylinder body is defined by two blocks each composed of $54 \times 73 \times 85$ grid points. The tail fins region is divided into 4 blocks, each having $40 \times 37 \times 85$ grid points. The complete flow field around the missile calculated by the Euler solver USER3D is presented in Figure 3 for $M=2.0$, $\alpha=20^\circ$ as iso-Mach contours. Figure 4, shows the variation of the normal force coefficient C_N with angle of attack α . The results of Euler computations are compared with those of experiments as well as with the results of FLU3M. The TLNS results for 10° and 20° are also plotted on the same figure. It is observed that all of the results are in very good agreement until 5° angle of attack after which the present results overestimate and the FLU3M results underestimate the experimental values. However, the present Euler and TLNS results are observed to be much closer to the experimental data. The increasing discrepancy between the computational and the experimental results can be attributed to viscous effects becoming dominant especially at high angles of attack. The perfect fit of FLU3M result with experimental data at 20° angle of attack is a pure coincidence which is not an expected behaviour for inviscid Euler solutions. The variation of the pitching moment coefficient about 8D axial position with respect to the angle of attack is given in Figure 5. Remarkable agreement between all of the methods used and the experimental values are observed up to 10° angle of attack after which both of the solutions are observed to deviate from the experimental data as expected due to the inherent behaviour of Euler solutions at high angles of attack as explained above. The distributions of pressure coefficient C_p with axial distance x/D , at 20° angle of attack, both on the wind-ward and on the lee-ward sides of the missile surface are given in Figure 6. up to a distance of $12D$ which is before the fin location. The comparison of the two Euler results (USER3D and

FLU3M) up to this location, shows good agreement between each other as well as with the experimental data. At this high angle of attack, the body vortices interact with the tail fins and the flow around the tail fins will be totally governed by these vortices. These complicated flow phenomena explain the differences observed between the Euler computations and the experiments at high angles of attack (20°) in Figures 4.-6. Variation of the center of pressure location in the axial direction at different angles of attack is given in Figure 7. Here, the present Euler code, USER3D, underpredicts and FLU3M overpredicts the X_{CP} locations up to 15° angle of attack, after which all the values coincide. This behaviour can be explained by the cancellations of the opposing predictions observed in C_m and C_N coefficients due to the definition of X_{CP} being proportional to the ratio of C_m to C_N .

As for the calculations of the individual fin aerodynamic characteristics, Figure 8. shows the predictions of C_N for fin No: 1. It is observed that the agreement between the two computational methods and the experimental data are very good for all of the angles of attack studied. The variation of the center of pressure location along the x direction, X_{CP} , for this fin is given in Figure 9. It is observed that both of the computational methods slightly over predict the experimental data. The maximum difference is around 6% of the base chord and decreases with increasing angle of attack. This behaviour is exactly opposite to the behaviour observed in Figure 10., which indicates the variation of Y_{CP} , with respect to the angle of attack. This time, both of the numerical methods' predictions lie below the experimental data. The maximum difference is around 3% of the base chord of the fin. It is to be noticed that the Y_{CP} is measured from the centerline of the missile where as the X_{CP} is measured from the tip of the root chord. The plan form area of the fin is taken as the reference area while calculating the center of pressure locations.

5.2. Unconventional Missile

The geometry of the unconventional missile is given in Figure 11. The unstructured grid used for Euler computations is given in Figure 12a. The structured Navier-Stokes grid generated for this unconventional lenticular body geometry is given in Figure 12b. This grid is provided by ONERA and is the same grid which was used in their Navier-Stokes calculations⁴ consisting of 91x85x40 grid points.

The overall normal force coefficient, C_N , variation with angle of attack, α , as calculated by the Euler and TLNS solvers is presented in Figure 13. The

results of Euler computations of ONERA as well as their experimental results are also plotted on the same figure. Navier-Stokes computations are performed for only one angle of attack, $\alpha = 10^\circ$. Contrary to our expectations and regardless of its deficiency in depicting the complete physical features of the flow field, the results of Euler computations are observed to be in good agreement with the experimental data. Same behaviour is observed in Figure 14. where the surface pressure coefficient, C_p calculated by the Euler methods are plotted for $\alpha=20^\circ$. Here, one can also see the close match between the Euler computations and the experiments on the windward and the leeward sides excluding the separated regions near and behind the sharp edges of the lenticular body.

The overall flow field around the lenticular body as calculated by the TLNS solver is given in Figure 15, as iso-Mach contour plots at an angle of attack of $\alpha=10^\circ$. This prediction is in very good agreement with those of Euler computations² and those of experimental data⁶. More interesting at this angle of attack is certainly the vortical flow structure on the leeward side of the body. The details of this vortical flow is given in Figure 16, as iso-stagnation pressure contour plots drawn at various cross planes along the flow direction. The complete and detailed evolution of the vortical flow pattern on the leeward surface is clearly depicted in Figure 17 as sequential x-plane images. It is observed that initially there is a single vortex closer to the vertical central plane (xz plane) of the body (inner vortex) which subsequently evolves into a double co-rotating vortex with the addition of a secondary outer vortex (the sharp edge vortex) at around $x/L = 0.571$. Further downstream, this later vortex outgrows the first vortex at a much faster rate and eventually merges with it at about $x/L=0.62$. The merger of these two vortices accelerates further the growth rate of this single unified vortex giving rise to a secondary small counter rotating vortex at about the same location of merger. Further downstream along the flow one can observe the pairing of these secondary counter rotating vortices at around $x/L= 0.756$.

Again related with this vortical flow structure, Figure 18a, and b show the experimental surface oil flow visualisation and computed surface skin friction lines along the leeward side of the lenticular body respectively. One can observe comparatively the close agreement of the separation and the reattachment lines along these experimental and computational figures. A possible interpretation for the reattachment and separation lines observed at $x/L=0.571$ can be given in conjunction with the cross flow vortical structure at this plane. The schematic representation of the flow is given in Figure 18c. The two co-rotating vortices designated as F_1 and F_3 are the inner and outer vortices as described previously. The flow separates from the sharp

edge of the body, separation line S_1 , reattaches at the center line as R_1 and follows the surface. Reattachment line R_2 and separation line S_2 are both related to the secondary counter rotating vortex, F_2 . Although the most inner line, line C, can be thought as another separation line, it is interpreted as concentrated surface skin friction lines⁴. The extend of line C given by the computations in Figure 18b. is shorter than what is observed experimentally in the oil flow visualization in figure 18a. The same discrepancy was also reported by Jouet C. and d'Espiney P.⁵ and the cause of which was attributed to the nature of the thin layer Navier-Stokes solutions. Full Navier-Stokes solutions of ONERA⁵ gave a larger extend for this C line which agreed better with the oil flow visualizations. Therefore, it is much likely the present result would be better if the computations were performed with an appropriate turbulence model. The comparison of calculated and experimental surface pressure coefficients are given in Figures 19a, 19b for $x/L=0.571$ and 0.915 respectively for 10° angle of attack case. Although the general behaviour of the pressure coefficients are well predicted with the TLNS computations, discrepancies are observed in particular on the lee-ward side of the missile. At $x/L=0.571$ the two co-rotating vortices on the leeward side are clearly evidenced by the two suction peaks. Although the measured suction peak corresponding to the outer vortex (sharp edge vortex) is more pronounced than the computed values, this behaviour is exactly reversed for the inner vortex, where the experimental values are lower than the computational predictions. At $x/L=0.915$, the C_p distribution is completely different and the wind ward pressure coefficient falls below that of the leeward value around the sharp edge, most probably due to the boattail effect and the separation of flow from the sharp edge. The discrepancies observed in this region may be attributed to the Reynolds number effect and to flow becoming totally turbulent. The laminar flow computations are no longer valid in this boattail region and therefore turbulent calculations must be performed with some appropriate turbulence modelling. The differences observed in the overall C_p values between the experiments and the calculations for the leeward and windward sides of the body can also be explained in terms of the Reynolds number effect. The experiments are performed at a much larger Reynolds number (18×10^6) than that of the computations (2×10^6). At this large Reynolds number it is much likely the flow is turbulent, whereas all the present calculations are performed for laminar flow case only.

Typical convergence histories for USER3D and TLNS solvers are given in Figure 20a. and 20b. For unconventional missile geometry, the USER3D solutions were obtained with approximately 3000 time iterations for a reduction of about 3.5 orders of magnitude in the total average residuals. Typical runtimes are about 17 hours of CPU time on a HP730 workstation, 8.5 hours on a HP-C110 workstation or 4 hours on a single processor of SGI ORIGIN2000 parallel machine. However, each TLNS run for the same geometry, takes about 144 hours on the single processor of ORIGIN2000 parallel machine at the end of 26000 time steps for $CFL = 0.1$ and 3.5 orders of magnitude of reduction in the total average residual.

6. CONCLUSIONS

The main emphasis in this paper has been on the thin layer Navier-Stokes computational results for the conventional and unconventional missile geometries for which Euler results have already been presented². The TLNS results are presented with the previous Euler results which are then compared with both the experimental data and the computations of ONERA, both by full and thin layer Navier Stokes solvers, (FLU3M and FLU3NS).

The aerodynamic characteristics for the conventional and the unconventional missile geometries calculated with TLNS code are found to agree well with the calculations of FLU3NS as well as with the experimental data. It is observed that the predictions of both the TLNS and the FLU3NS codes showed discrepancies with the experimental data in separated regions where viscous effects became dominant such as in the vortical flow regions on the leeward sides of the missiles at high angles of attack. The vortical flow structure is analysed and presented in detail for the case of the lenticular body. Several interesting features of this vortical flow are evidenced, such as the existence of two co-rotating vortices: the inner and the outer vortices, the domination of the sharp edge vortex (outer vortex) and their coalescing into a single vortex. It must be noticed that these computations are performed for laminar case only and no turbulence model was incorporated. The comparison of these vortical flow structures with the available experimental results of ONERA reveal good agreement. Although the thin layer assumptions are used through out these calculations, the physics of the vortical flow is surprisingly well predicted. Comparison of the computed surface skin friction lines with those of oil flow visualisations provides good insight to the explanation of the separation and reattachment lines on the leeward surface.

On the other hand, it is observed that the predictions of Euler computations for the overall coefficients are in good agreement with the TLNS solutions. Therefore,

when the overall coefficients are the main concern, it is sufficient to solve the Euler equations. However, when details of the flow field are requested, one must solve the full or the thin layer Navier Stokes equations.

7. ACKNOWLEDGEMENTS

This research was supported by the NATO, AGARD, Fluid Dynamics Panel (FDP), as a support project. The authors would like to acknowledge this support. Turkish participants would also like to express their appreciation to ONERA for providing the necessary support for the success of this research.

The authors would like to thank Mr. Serkan Şen for providing the TLNS solver and his guidance during running this code.

Thanks are also to Dr. Mahir Çakıroğlu, for providing the structured Euler grid used for the conventional missile.

8. REFERENCES

1. Oktay E., "USER3D, 3 Dimensional Unstructured Euler Solver", Roketsan Engineering Development Department, SAD Report, SA-RS-RP-R 009/442, Ankara, May 1994.
2. Oktay E., Alemdaroğlu N., Tarhan E., Champigny P., d'Espiney P., "Unstructured 3D-Euler Computations for Missile at Supersonic Speeds and High Angles of Attack", AIAA-98-0392, AIAA 36th Aerospace Sciences Meeting and Exhibit, Reno, NV, Jan. 12-15, 1998.
3. d'Espiney P., "Comparaison de Differentes Methodes de Calcul Appliquees a un Fuselage de Section Lenticulaire", AGARD/FDP symposium on Missiles Aerodynamics, Friedrichshafen (Germany), April 23-26, 1990.
4. Borrel M., d'Espiney P. and Jouet C., "Three Dimensional Thin Layer and Space Marching Navier-Stokes Computations Using an Implicit MUSCL Approach: Comparison with Experiments and Euler Computations". 9th GAMM Conference on Numerical Methods in Fluid Dynamics, Lausanne, Switzerland, September 25-117, 1991.
5. Jouet C., and d'Espiney P., "3D Laminar and 2D Turbulent Computations with the Navier-Stokes Solver FLU3M", 8th Int. Conf. On Numerical Methods in Laminar and Turbulent Flow, University of Swansea, (U.K.), July 18-23, 1993.
6. Champigny P., "Test Data on a Non-Circular Body for Subsonic, Transonic and Supersonic Mach Numbers", A Selection of Experimental Test Cases for the Validation of CFD Codes, AGARD Advisory Report No 303, AGARD-AR-303 vol II, August 1994, ppC6-1, C6-11.
7. Roe P., L., "Characteristic - Based Schemes for the Euler Equations", Annual Review of Fluid Mechanics, Vol. 18, 1986.
8. Jameson A. and Baker T. J., "Solution of the Euler Equations by Finite Volume Methods Using Runge-Kutta Time Stepping Schemes", AIAA Paper 81-1259, June 1981.
9. Beam, R. and Warming, R. F., " An Implicit Finite Difference for Hyperbolic System in Conservation-Law Form," Journal of Computational Physics, Vol 22, Sept 1976, pp.347-363.
10. Pulliam, T. H. and Chaussee, D. S., "A Diagonal Form of an Implicit Approximate-Factorization Algorithm," Journal of Computational Physics, Vol. 39, Feb. 1981, pp. 347-363.
11. Kaynak Ü., Flores J., " Advances in the Computation of Transonic Separated Flows over Finite Wings", AIAA Paper 87-1195.
12. Şen T. S., "Numerical Solution of Various Test Cases by Using A Thin Layer Navier-Stokes Code", MS Thesis, Submitted to the Graduate School of Natural and Applied Sciences of the Middle East Technical University, Ankara, September 1994.
13. Borrel M., d'Espiney P. and Jouet C., "Supersonic Vortical Flows Around an Ogive -Cylinder: Laminar and Turbulent Computations", First European Computational Fluid Dynamics Conference, Brussels, Belgium, September 7-11, 1992.

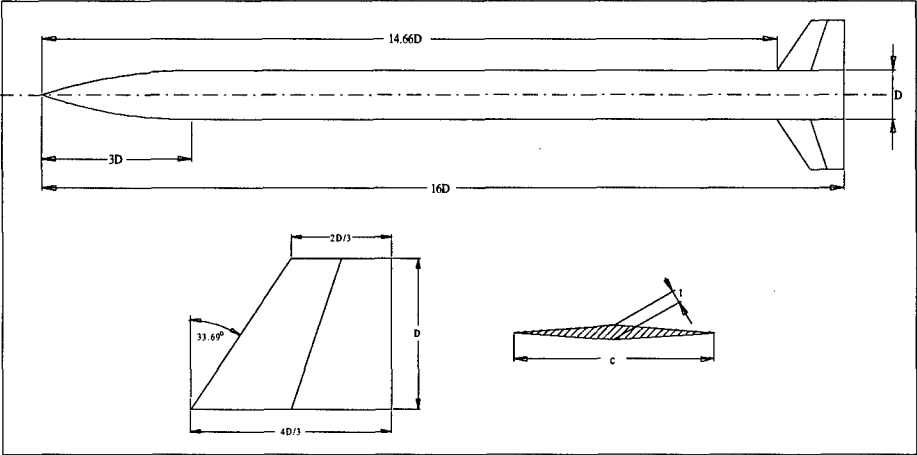


Figure 1. Conventional missile geometry with four tail fins.

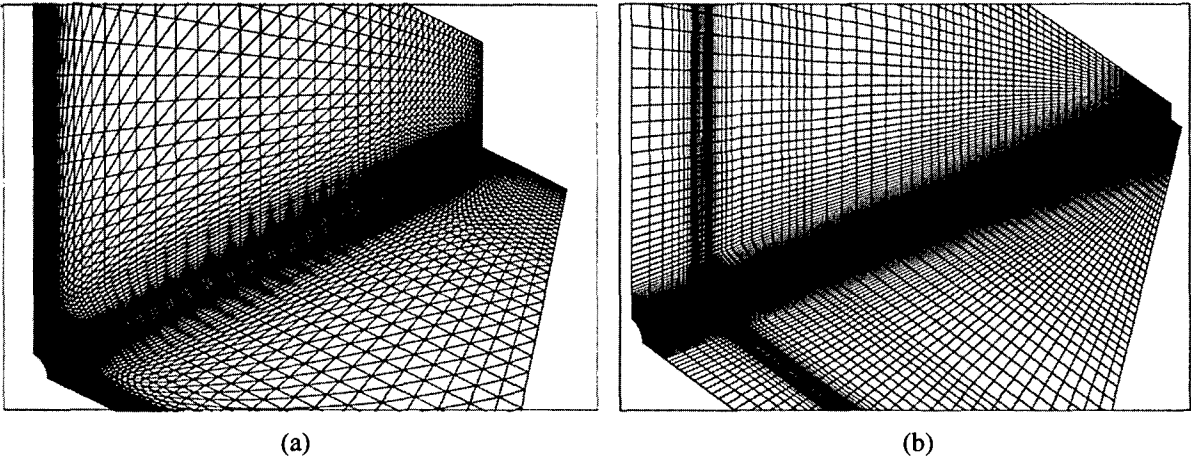


Figure 2(a) Unstructured and (2b) structured grid generated for the conventional missile.

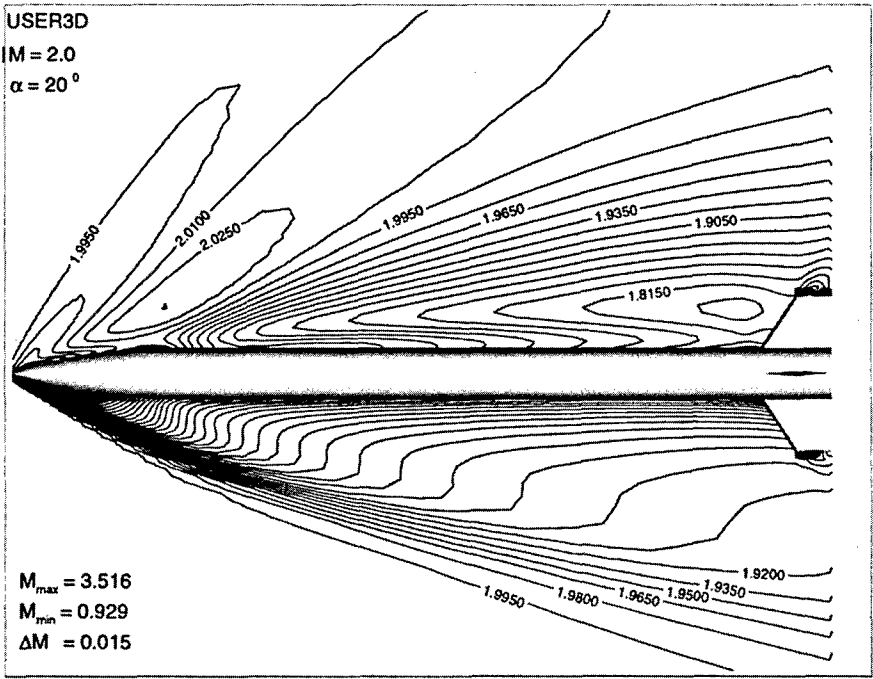


Figure 3. Mach contours (USER3D) at $M=2.0, \alpha=20^\circ$.

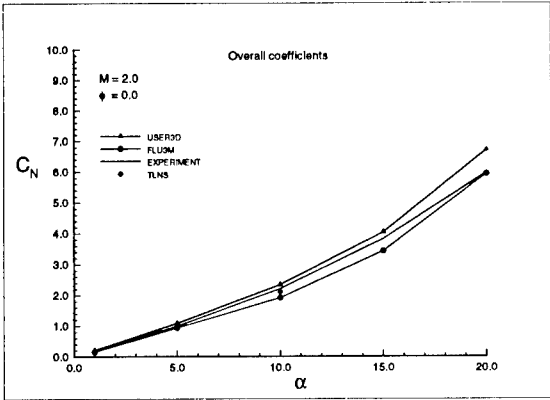


Figure 4. Variation of normal force coefficient with angle of attack.

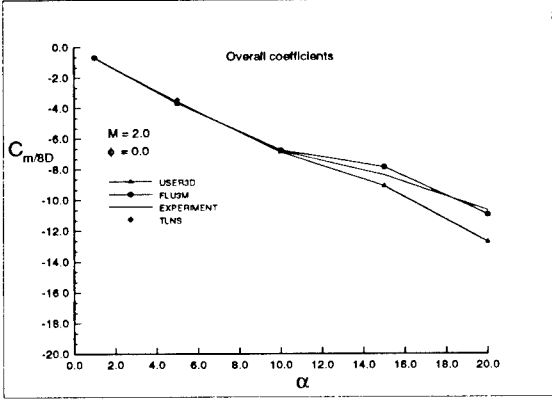


Figure 5. Variation of pitching moment coefficient about $X/D=8$ location.

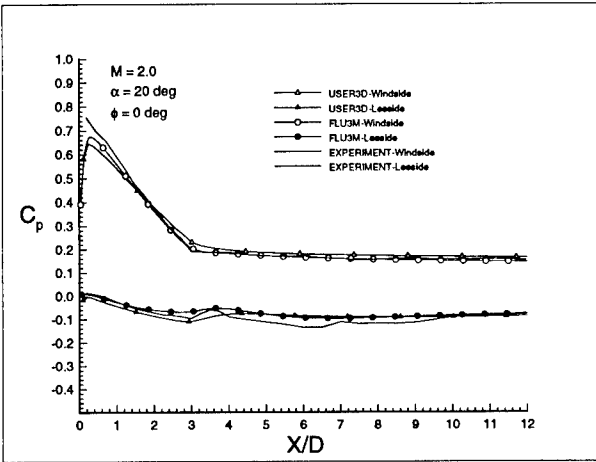


Figure 6. Variation of pressure coefficient, on the surface with axial distance.

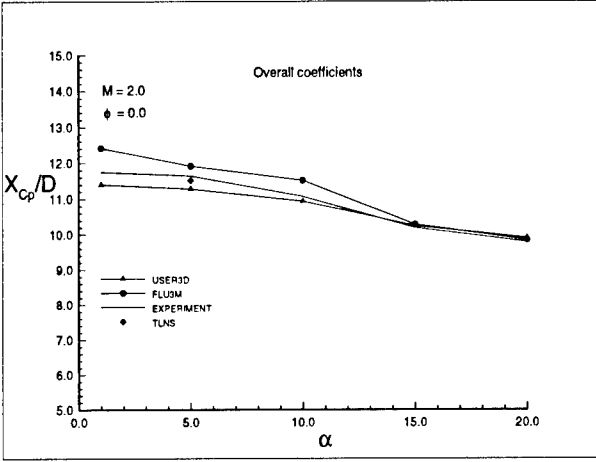


Figure 7. Variation of the axial location of center of pressure with angle of attack.

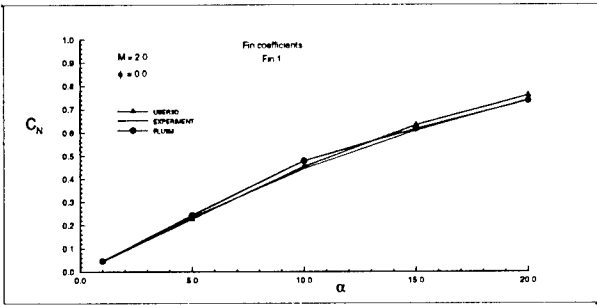


Figure 8. Variation of normal force coefficient for fin no.1 with angle of attack.

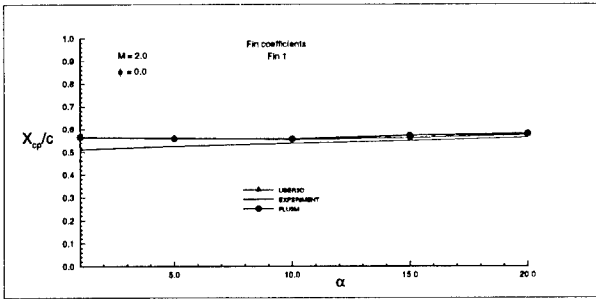


Figure 9. Variation of axial location of center of pressure for fin no.1 with angle of attack.

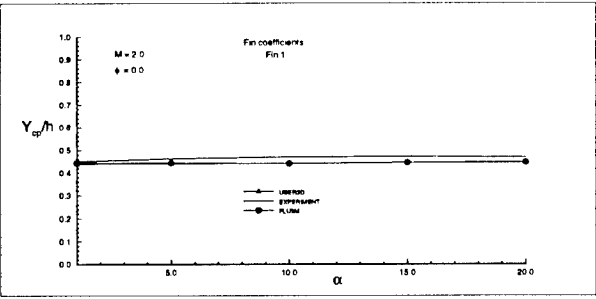


Figure 10. Variation of y location of center of pressure for fin no. 1 with angle of attack.

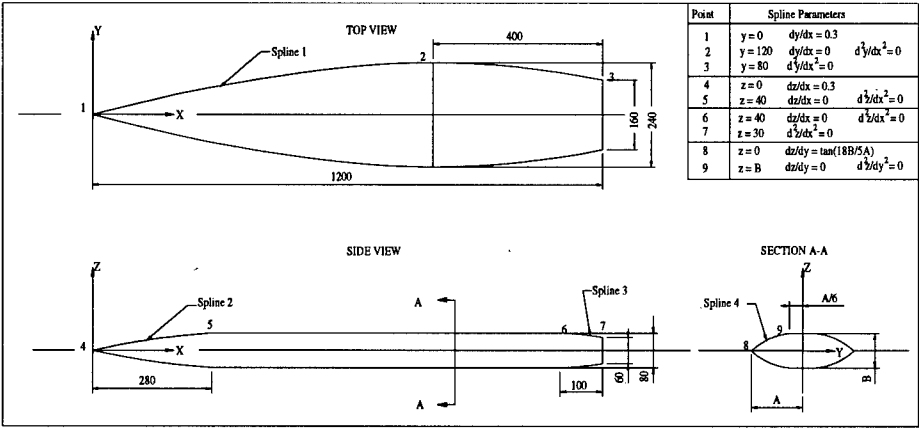


Figure 11. Unconventional missile geometry having lenticular cross-section.

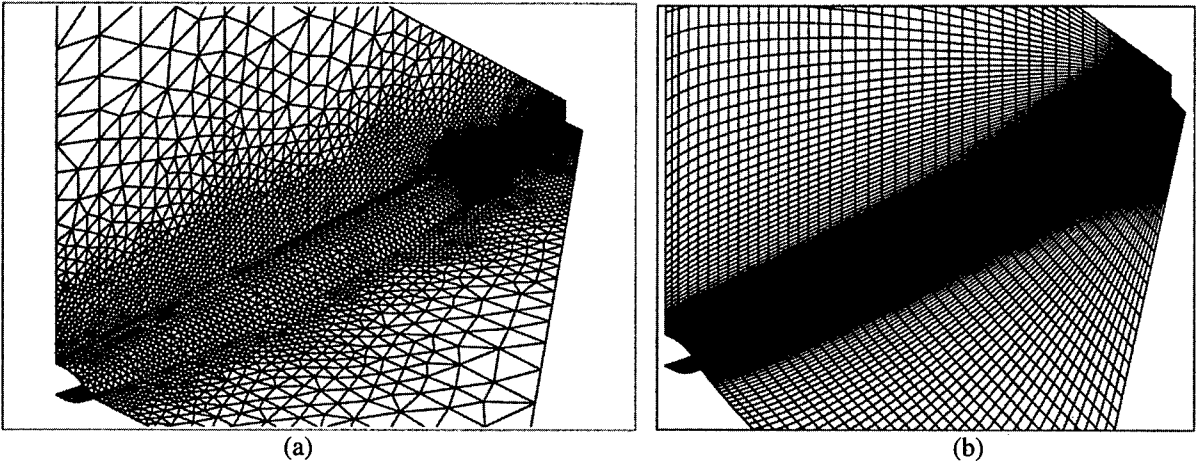


Figure 12. (a) Unstructured and (b) structured grid for the lenticular body.

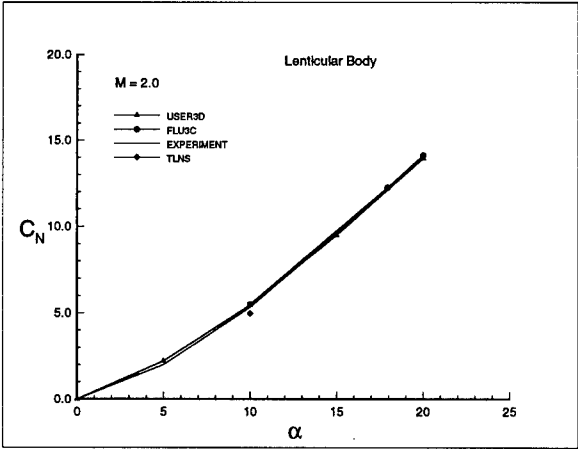


Figure 13. Variation of normal force coefficient for the lenticular body with angle of attack.

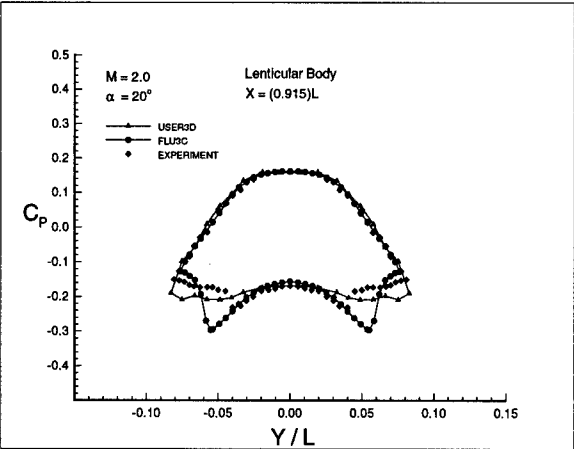


Figure 14. Pressure coefficient distribution on the surface at a cross plane located at $X/L=0.915$.

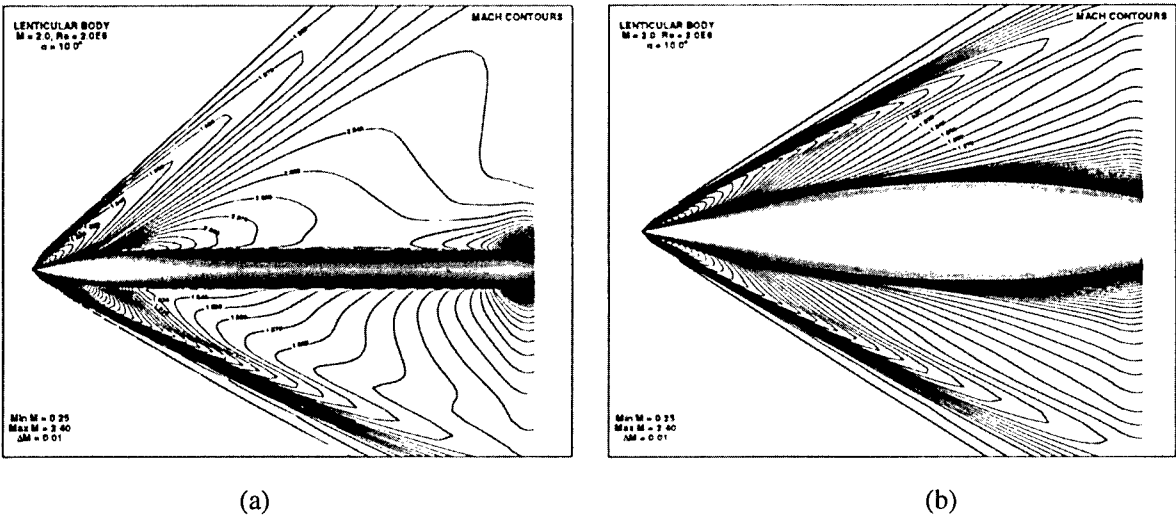


Figure 15. Iso-Mach lines around the lenticular body (obtained by TLNS), (a) side view, (b) top view.

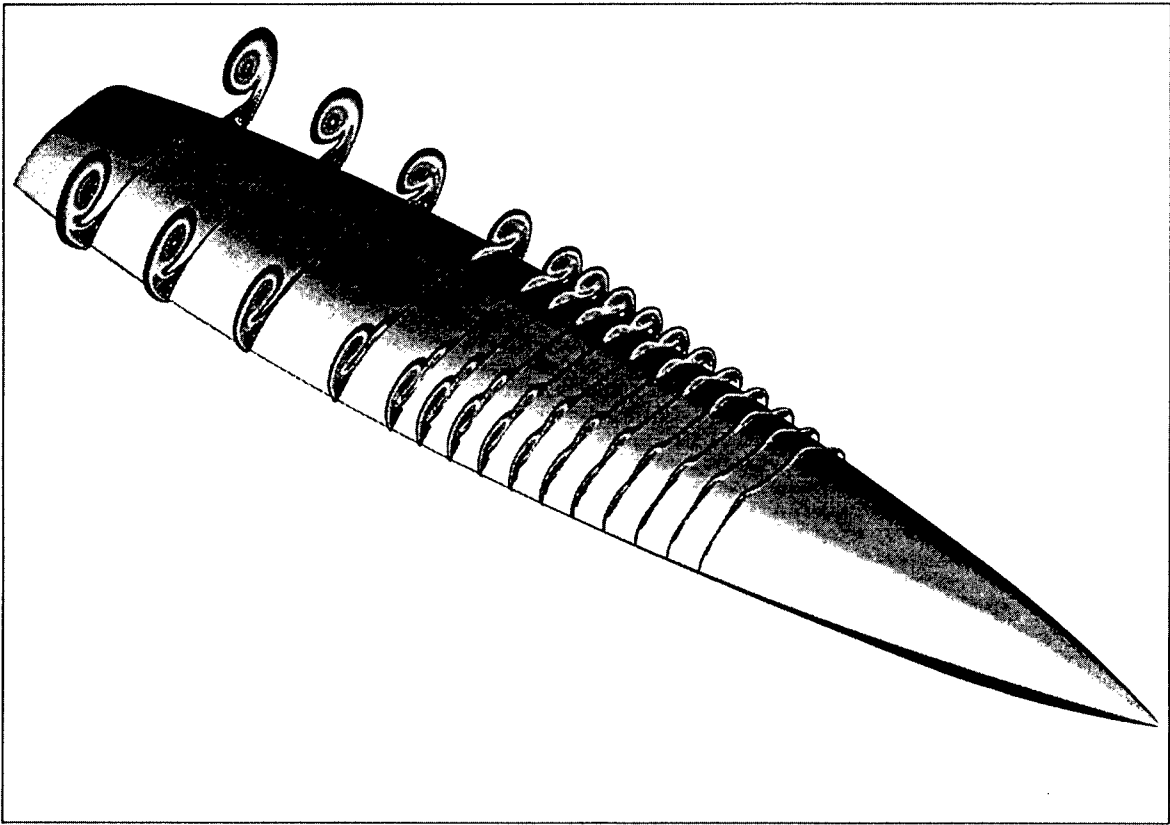


Figure 16. Iso-Stagnation pressure contours on the lenticular body (obtained by TLNS, $M = 2.0$, $\alpha = 10.0^\circ$, $Re = 2.0E6$).

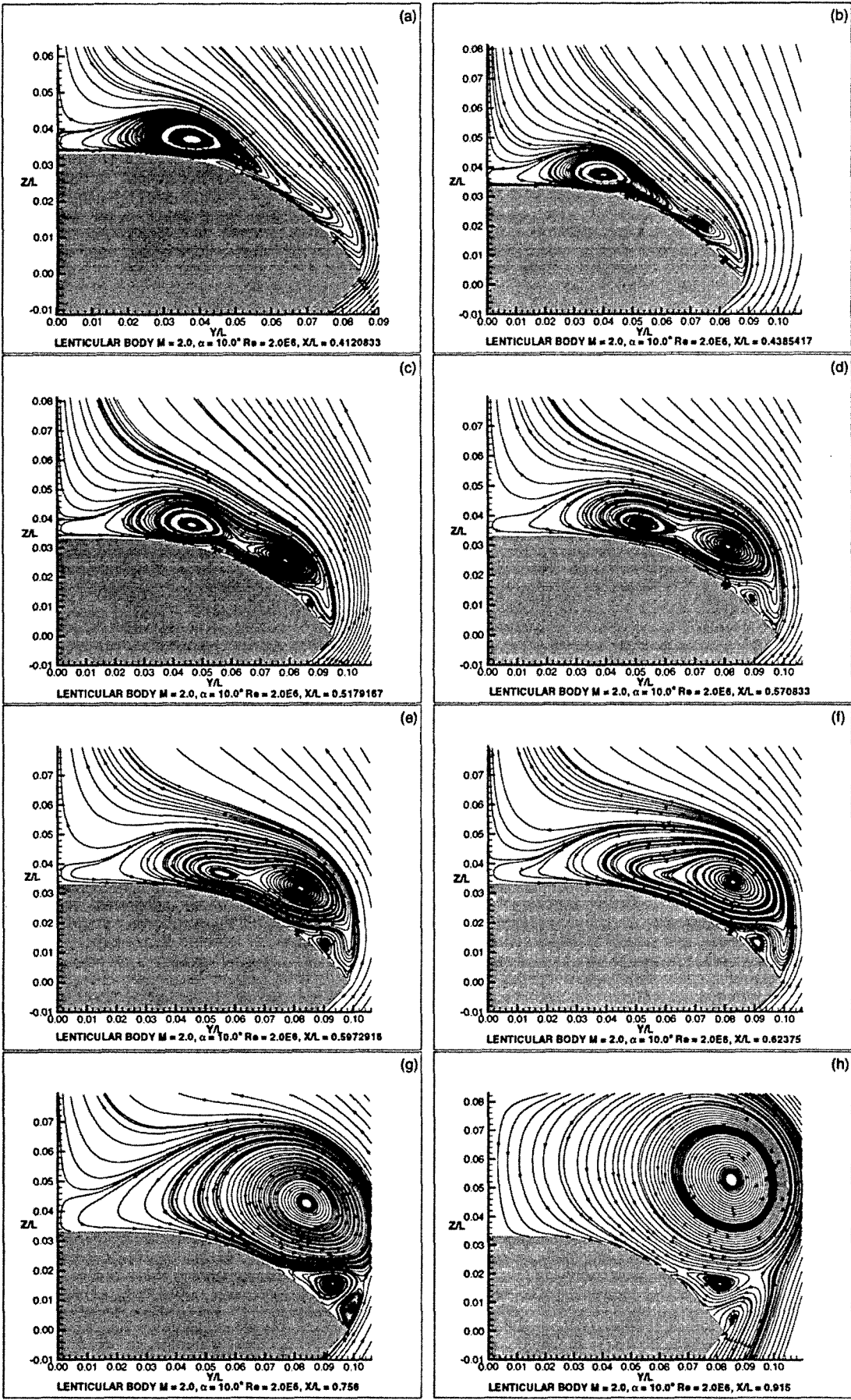


Figure 17. Crossflow streamlines at various planes.

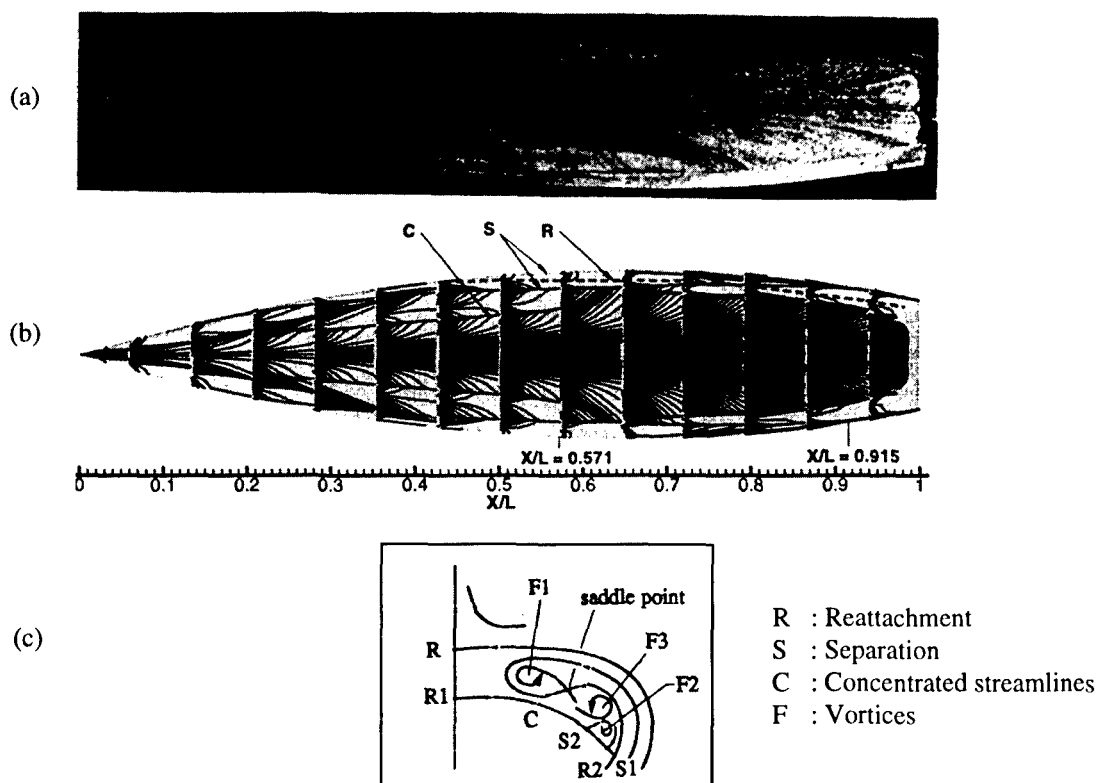


Figure 18. Surface skin friction lines, (a) Experiment, (b) TLNS solution, (c) crossflow organization.

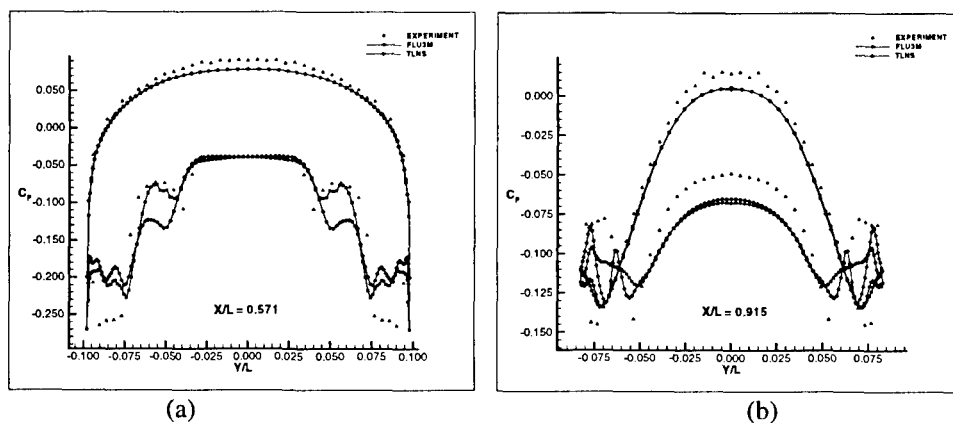


Figure 19. Pressure coefficient distribution on the surface, ($M=2.0$, $\alpha = 10.0^\circ$, $Re=2.0E6$), (a) $x/L = 0.571$, (b) $x/L = 0.915$.

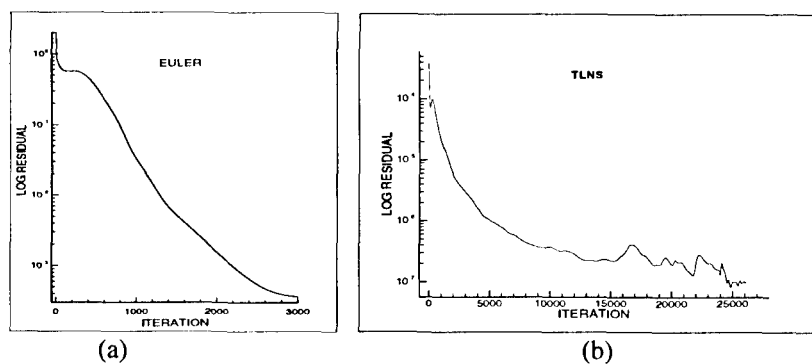


Figure 20. Convergence history for lenticular body, (a) USER3D, (b) TLNS.

COMPUTATIONAL INVESTIGATIONS OF SUBSONIC HIGH ANGLE OF ATTACK MISSILE FLOWS

Ismail H. Tuncer
Middle East Technical University
Turkey Inono Bulvari PK 6531
06531 Ankara, Turkey

Max F. Platzer
Naval Postgraduate School
Code AA / Tu, Monterey
CA 93943-5106, USA

Robert D. VanDyken
NAWC-WD
Code 473110D, China Lake
CA 93555, USA

ABSTRACT

In this paper recent computations of subsonic flow over a complete missile configuration and an ogive-cylinder using the Navier-Stokes solver OVERFLOW and the panel code PMARC are reviewed. Navier-Stokes solutions for the complete missile are presented for angles of attack up to sixty degrees. The agreement with available force and moment data is quite good up to thirty degrees, but starts to deviate for the higher incidences. It is also shown that the panel code solutions over the missile forebody provides an efficient solution and good agreement with the Navier-Stokes calculations for incidence angles up to ten degrees. Flow over an ogive-cylinder computations shows that this agreement can be extended to approximately twenty degrees if vortex wakes shed from the cylindrical body are incorporated into the panel code. The paper concludes with suggestions for future work.

INTRODUCTION

It is the objective of this paper to review the authors' recent computational investigations of subsonic flow over typical missile configurations at high angles of attack. Two numerical approaches are being explored, namely solutions based on the Reynolds-averaged compressible Navier-Stokes equations and solutions based on the inviscid incompressible flow equations, but with the inclusion of vortex wakes from the missile body to model high angle of attack effects. For the first approach, the NASA-Ames developed OVERFLOW code is used which is based on the Navier-Stokes equations, in the second approach vortex wakes are incorporated into the NASA-Ames developed panel code PMARC. The rationale for the development of the panel method is the advantage to be gained from a method which bridges the gap between a very rapid but mostly empirically based method, such as Moore's aeroprediction code AP-95, and the very time-consuming Navier-Stokes codes. Therefore, systematic comparisons between PMARC and Navier-Stokes solutions as well as between the two numerical approaches and the available

⁰There is no restriction on the presentation and publication of this paper.

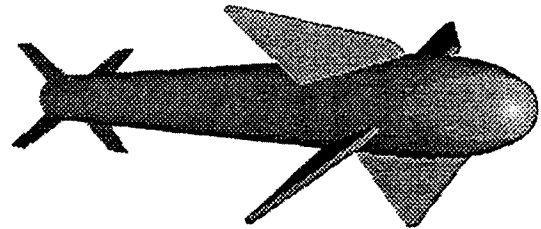


Fig. 1 Missile configuration at 10 deg canard deflection.

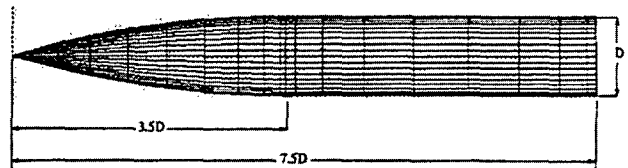


Fig. 2 Ogive-cylinder body

experimental data are presented so that the range of validity of the two approaches can be assessed.

We first computed subsonic flows over the missile configuration (Figure 1) using the OVERFLOW Navier-Stokes solver between 15° and 60° angle of attacks, and analyzed the flowfields in terms of particles traces and surface streamlines. We also compared the integrated aerodynamic loads against the experimental data. We next computed the flow over the forebody of the same missile using the OVERFLOW and the panel code PMARC at a low angle of attack range, between 0° and 14° for a comparison between the prediction of the two codes. Finally we employed the PMARC code for the simulation of separated flows over an ogive cylinder (Figure 2) at high incidences and to evaluate the suitability of panel codes for aerodynamic missile design work.

NUMERICAL METHODS

In this work, we have employed two NASA-Ames developed flow solvers: OVERFLOW version 1.6ap and PMARC version 12.22.

OVERFLOW Navier-Stokes Solver

OVERFLOW is a compressible, Reynolds-averaged Navier-Stokes solver[1, 2]. It accommodates computational domains discretized with overset grids, which are preprocessed with the PEGSUS code. This code has several discretization and time integration schemes for each subgrid. In our studies, in which one of the (i,j,k) grid directions aligns with the free-stream flow direction, the partial flux vector splitting algorithm was selected. Otherwise, the 3-factor diagonal scheme with central differencing was employed. The partial flux vector splitting algorithm uses Steger-Warming flux vector splitting for discretization of the convection terms in the stream-wise direction, and central differencing in the other two directions. For the flux splitting algorithm, the central differencing smoothing coefficient was gradually reduced to about 0.06 from the starting value of 0.10. For the central difference algorithm on the canard and tail surfaces the fourth-order smoothing coefficient was similarly reduced to 0.08 from 0.10. The flowfield was assumed to be fully turbulent and the Baldwin-Lomax algebraic eddy viscosity model with the Degani-Schiff cutoff was employed. Local time stepping was used for convergence to a steady-state solution. The convergence criterion was based on the L2 norm of the residuals and the time variation of the integrated aerodynamic loads. No-slip conditions were applied at the solid surface boundaries and, at the farfield boundaries, one-dimensional Riemann invariant extrapolation was used. The computational domain, which consists of the missile body, the sting, the canards and tails, and the flow field around them, was partitioned into zonal blocks. These blocks were discretized with structured subgrids, which were overset on each other. The flowfield was assumed to be symmetric with respect to the mid-plane so that only the computational domain over the half-missile configuration needed to be discretized.

PMARC Potential Flow Solver

The NASA-Ames developed panel code, PMARC, is a low-order potential flow solver for simulating flows over complex three-dimensional geometries[3]. The flowfield is assumed to be inviscid, irrotational and incompressible. PMARC solves the Laplace equation for the velocity potential over a closed body using doublets and source singularities placed on solid surfaces and wakes. The unknown doublet and source strengths are determined by imposing the proper flow tangency and trailing edge conditions. The resulting linear system of equations is then solved using an iterative matrix solver. Wakes can be shed from trailing edges of lifting surfaces or from prescribed separation lines along the panel distribution. The wakes are then convected downstream by marching in time. PMARC has an option for modeling symmetric flowfields. This allows

to panel only half of the configuration and symmetrical influence coefficients account for the other symmetrical half in the lateral direction.

RESULTS

Navier-Stokes calculations[4] for the complete missile configuration (Figure 1) are shown in Figures 3,4, and 5 at incidence angles of 25, 45, and 60 degrees, respectively. In this study we only considered the flows at 45 deg roll angle (X-configuration), and zero sideslip angle. The flowfield is therefore assumed to be symmetric with respect to the mid-plane, and only the computational domain over the half-missile configuration is discretized. The computational domain around the canards and the tails, the gaps between the canard and the body, and the zones over the missile body are discretized with structured subgrids. Thirteen subgrids with a total number of approximately 1 million grid points are employed. The canard, tail and gap grids, and the outer grids around them are relatively high resolution viscous grids with clustered grid distributions around the leading edges. The y^+ values were on the order of $O(1)$ for all the surface grids. The outer boundaries of the computational domain are located about 5 missile lengths away. Flowfields were assumed to be steady with $M_\infty = 0.3$, and $Re_D = 0.95 \cdot 10^6$, where the Reynolds number is based on the diameter of the missile body. The local time-stepping option in the OVERFLOW solver was employed to converge to a steady-state solution. All the computations were carried out on remote CRAY Y-MP and CRAY C90 supercomputers. A typical computation took about 6000-8000 timesteps and 30-40 CPU hours on a CRAY Y-MP.

The FAST flow visualization software from NASA-Ames was utilized for postprocessing the flowfield data. The computed flowfields were analyzed in terms of particle traces, helicity contours and surface streamlines. Helicity is defined as the dot product of velocity and vorticity vectors, which emphasizes the vorticity in the flow direction.

It is seen that the flow separation and the vortical structures shed from the canards and from the missile body become increasingly extensive and complex with increasing incidence and, as a result, the prediction of the normal force and of the pitching moment starts to deviate from the available experimental results[5] as shown in Figure 6. The delay in the predicted pitching moment stall suggests that the loss of suction on the canard surfaces and the missile forebody is underpredicted in the computations. The leveling-off of the moment coefficient at angles of attack greater than 40 deg, which is captured in the computations, is attributed to the massive flow separation and the stall over the canards, tails and the missile forebody. Cal-

culations for the same missile were given earlier by Hsieh et al [6] for fully laminar flow and by Ekaterinaris [7] for fully turbulent flow.

Figure 7 shows the OVERFLOW computed surface pressure contours on the forebody of the missile shown in Figure 1 as the angle of attack is increased from zero to fourteen degrees[8]. The total number of grid points used was approximately 875,000 and a typical run for a converged solution took between 4000 to 6000 time steps. Figures 8 and 9 shows a comparison between the OVERFLOW and the PMARC computed surface pressures on both the leeward and windward sides of the forebody[8]. In the PMARC computations, the missile body was modeled with approximately 5000 surface panels. The panels were clustered around the missile nose, canard-body junction, and leading and trailing edges of the canards. It is seen that up to six degrees incidence the flow stays attached over the forebody. At six degrees, the development of a vortex from the leading edge of the canards can be observed. At incidences of ten and fourteen degrees, the flow separates over the aft-body and the canard vortices become stronger. The flow between the canards becomes quite complex due to the development of corner flows around the canard-body junctions and the leading edge vortices. Clearly, starting from about ten degrees incidence, the viscous effects begin to dominate the flowfield with strong canard vortices, corner flows, and flow separation over the aft-body. Consistent with these observations, the OVERFLOW and PMARC computed pressure distributions are in excellent agreement up to six degrees incidence, whereas substantial discrepancies start to appear at ten and fourteen degrees on the top (leeward) side.

Evidently, PMARC calculations at still higher incidence angles are meaningful only if the flow separation from the missile body is included in the computations. Therefore the flow over the ogive-cylinder body shown on Figure 2 was computed by attaching two wakes, one shed from the cylinder base and the other shed along the cylindrical body[9]. The circumferential position of the wake separation line along the cylindrical body, Θ_w , was varied parametrically, but the axial starting location was selected based on the available experimental data. Figure 10 shows the computed windward side and circumferential pressure distributions with the wakes attached. Also, the normal force and pitching moment coefficients are predicted well, as shown in Figure 11. It is seen that the agreement with Lamont's experimental data[10] is quite good at incidences of 15 and 20 degrees, except in the fully separated wake region on the leeward side.

DISCUSSION

The results show that the OVERFLOW Navier-Stokes solutions yield detailed flow features and good agreement with the available measured force and moment data up to considerably higher incidences. However, at incidences greater than thirty degrees, especially for configurations involving strong vortex interactions, the Navier-Stokes solutions show substantial deviations from the available experiments. The sources for these disagreements can be traced to the following assumptions in the computations:

- a) The flow was assumed to be symmetric so that only solutions for the half-missile configuration were computed. Yet, it is well known that this assumption is unrealistic at high incidence angles.
- b) The extent of the vortical wakes shed from the missile body is dependent on the state of the boundary layer at separation. Hence the laminar/transitional/turbulent boundary layer development over the missile body needs to be computed. Therefore, the assumption of fully laminar or fully turbulent flow is likely to be a significant source of error
- c) A third source of error stems from the turbulence model used in the computations. Sturek et al [11] recently presented a comprehensive set of computations for transonic and supersonic flow over an ogive-cylinder configurations using various available Navier-Stokes solvers and turbulence models. They concluded that no best turbulence model could be identified in the comparisons to available experiments.

On the other hand, PMARC is a computationally efficient tool in the low incidence range up to ten degrees at low subsonic flight speeds and, after incorporation of vortex wakes shed from the missile body, PMARC offers the potential of providing computationally efficient predictions up to twenty degrees of incidence.

RECOMMENDATIONS FOR FUTURE WORK

Comparisons with integrated load data, such as normal force and moment coefficients, is insufficient to fully understand the flow physics which needs to be modeled. Therefore, a comprehensive experimental effort is required which enables the acquisition of detailed surface pressure and flowfield data. This data will be instrumental in guiding the thrust and extent of future computational work, such as computations of the flow over complete missiles instead of over half-body configurations, thereby allowing the development of flow asymmetry and unsteadiness at

high incidence angles and incorporation of boundary layer transition from laminar to turbulent flow.

ACKNOWLEDGMENT

The authors gratefully acknowledge the support of this work by the Office of Naval Research (Mr. David Siegel) and the Naval Air Warfare Center Weapons Division, China Lake (Dr. Craig Porter).

REFERENCES

1. Buning, P., et al., "OVERFLOW User's Manual, NASA Ames Research Center, June 1995
2. Degani, D. and Schiff, L.B., "Computation of Turbulent Supersonic Flows around Pointed Bodies Having Crossflow Separation", *Journal of Computational Physics*, Vol. 66, No. 1, pp. 173-196, 1986
3. Ashby, D.L., Dudley, M.R., Iguchi, S.K., Browne, L., Katz, J., "Potential Flow Theory and Operational Guide for the Panel Code PMARC-12," COSMIC Program ARC-13362, COSMIC, Athens, GA, Dec. 1992
4. Tuncer, I.H., Platzer, M.F., van Dyken, R.D., "A Computational Study of Subsonic Flowfields over a Missile Configuration", AIAA paper 97-0635
5. Smith, E.H., Hebbar, S.K., and Platzer, M.F., "Aerodynamic Characteristics of a Canard-Controlled Missile at High Angles of Attack, *Journal of Spacecraft and Rockets*, Vol. 31, No. 5, pp. 766-772, Sept.-Oct. 1994
6. Hsieh, T., Priolo, F.J., and Wardlaw, A.B., Jr., "Navier-Stokes Calculation of Flow over a Complete Missile to 60 Degree Incidence", AIAA paper 95-0760, 1995
7. Ekaterinaris, J.A., "Analysis of Flowfields over Missile Configurations at Subsonic Speeds", *Journal of Spacecraft and Rockets*, Vol. 32, No. 3, pp. 385-391, May-June 1995
8. Tuncer, I.H., Marvin, R., Platzer, M.F., "Numerical Investigation of Subsonic Flow over a Typical Missile Forebody", AIAA Paper 96-0189
9. Tuncer, I.H. and Platzer, M.F., "PMARC Potential Flow Solutions with Wakes over an Ogive Cylinder at High Incidence", AIAA Paper 97-1968
10. Lamont, P.J., "Pressure Around an Inclined Ogive Cylinder with Laminar, Transitional, or Turbulent Separation", *AIAA Journal*, Vol. 20, pp. 1482-1499, 1982
11. Sturek, W.B., Birch, T., Lauzon, M., Housh, C., Manter, J., Josyula, E., Soni, B., "The Application of CFD to the Prediction of Missile Body Vortices", AIAA Paper 97-0637

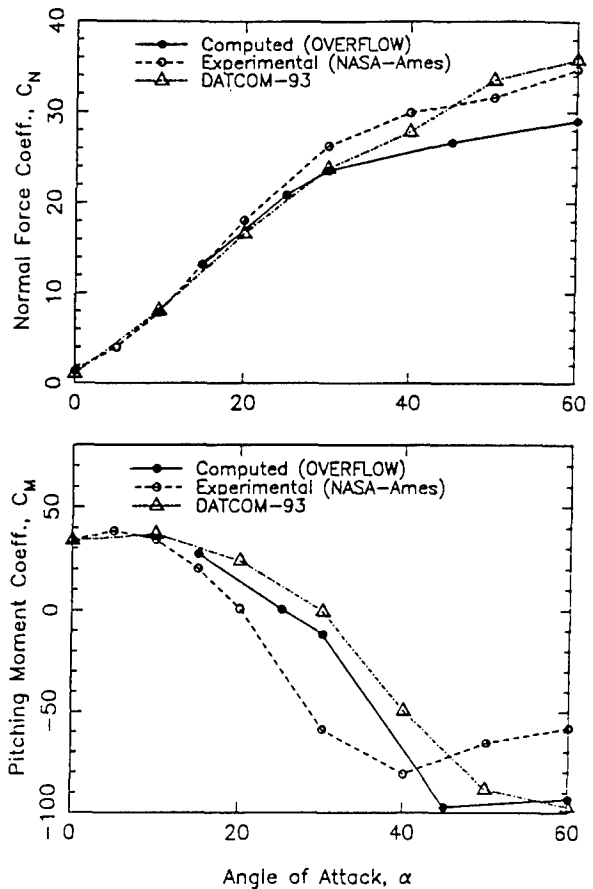


Fig. 6 Aerodynamic loads at $\delta = 10$ deg $M = 0.3$, $Re_D = 0.95 \cdot 10^6$

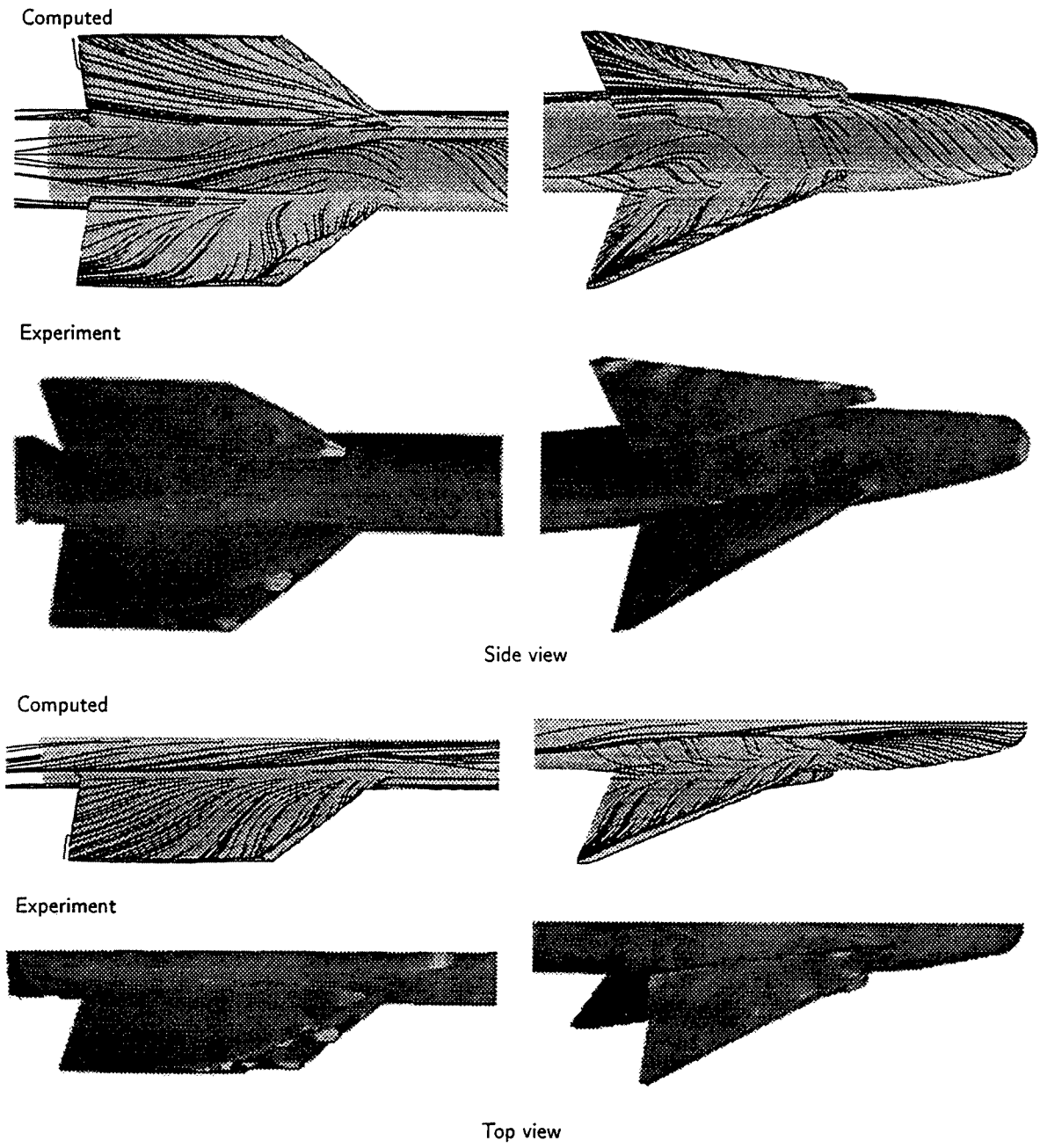


Fig. 3 Computed and experimental surface streamlines at the forebody and tail sections at $\alpha = 25$ deg.

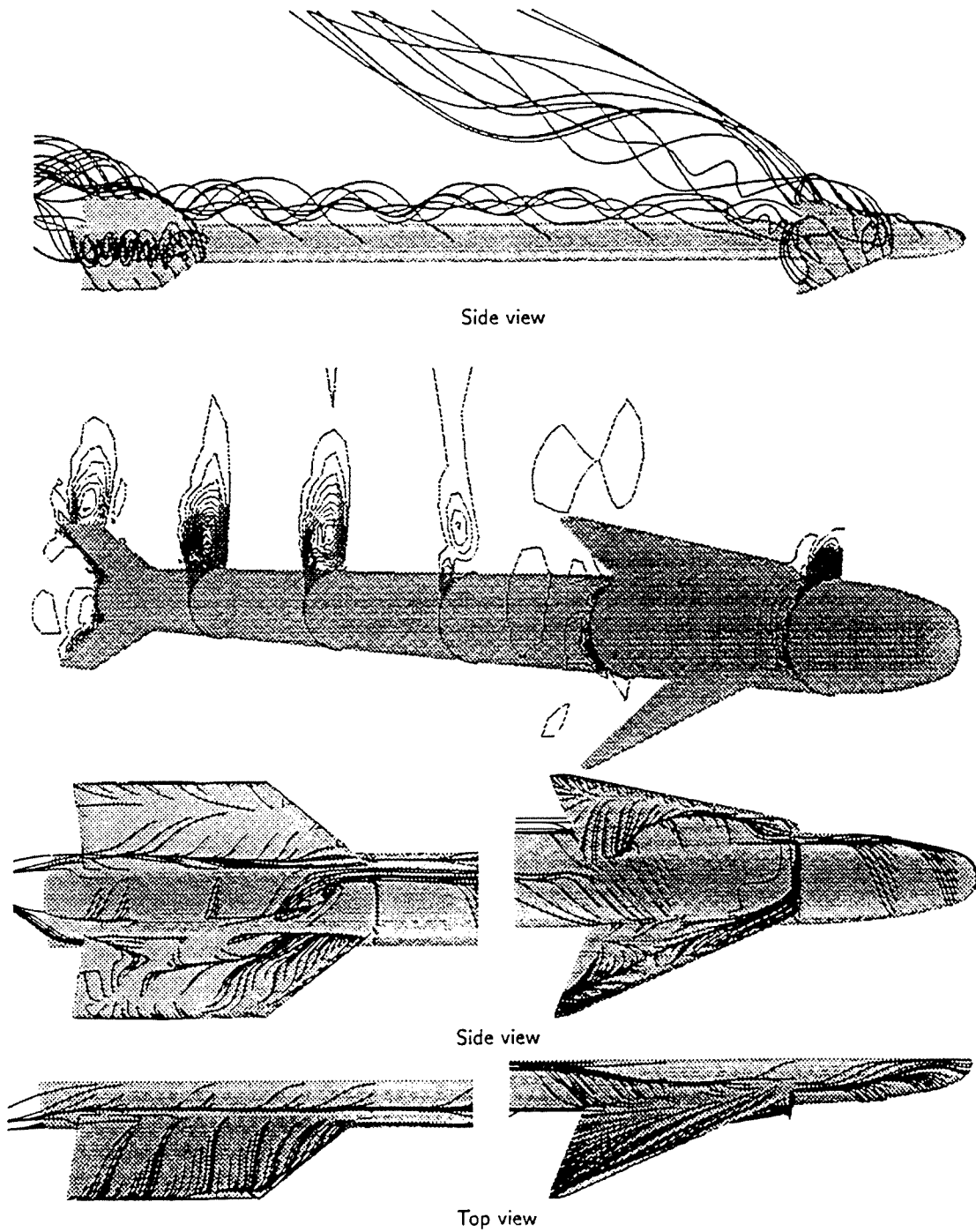


Fig. 4 Particle traces, helicity contours and surface streamlines at the forebody and tail sections at $\alpha = 45$ deg.

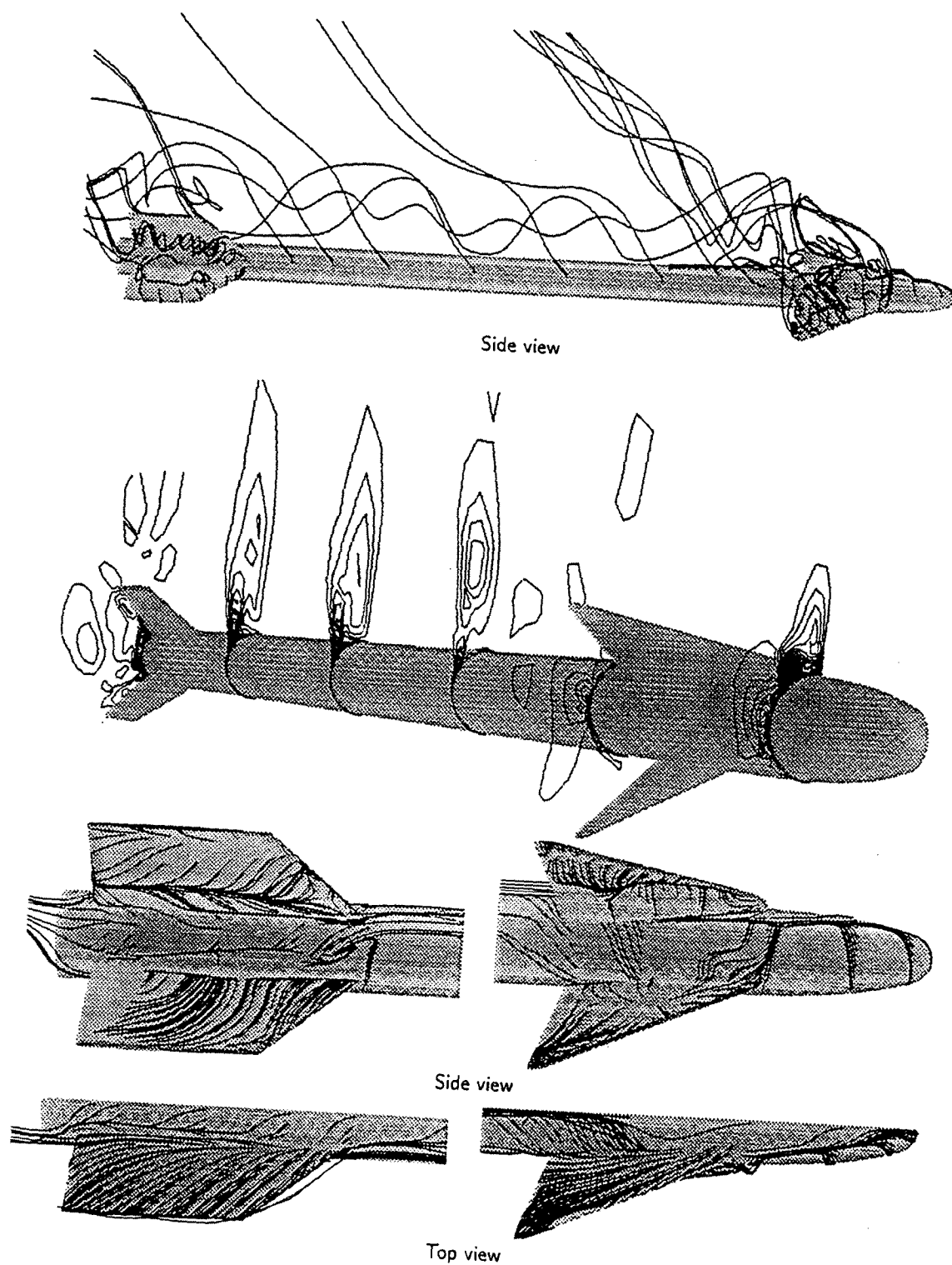


Fig. 5 Particle traces, helicity contours and surface streamlines at the forebody and tail sections at $\alpha = 60^\circ$.

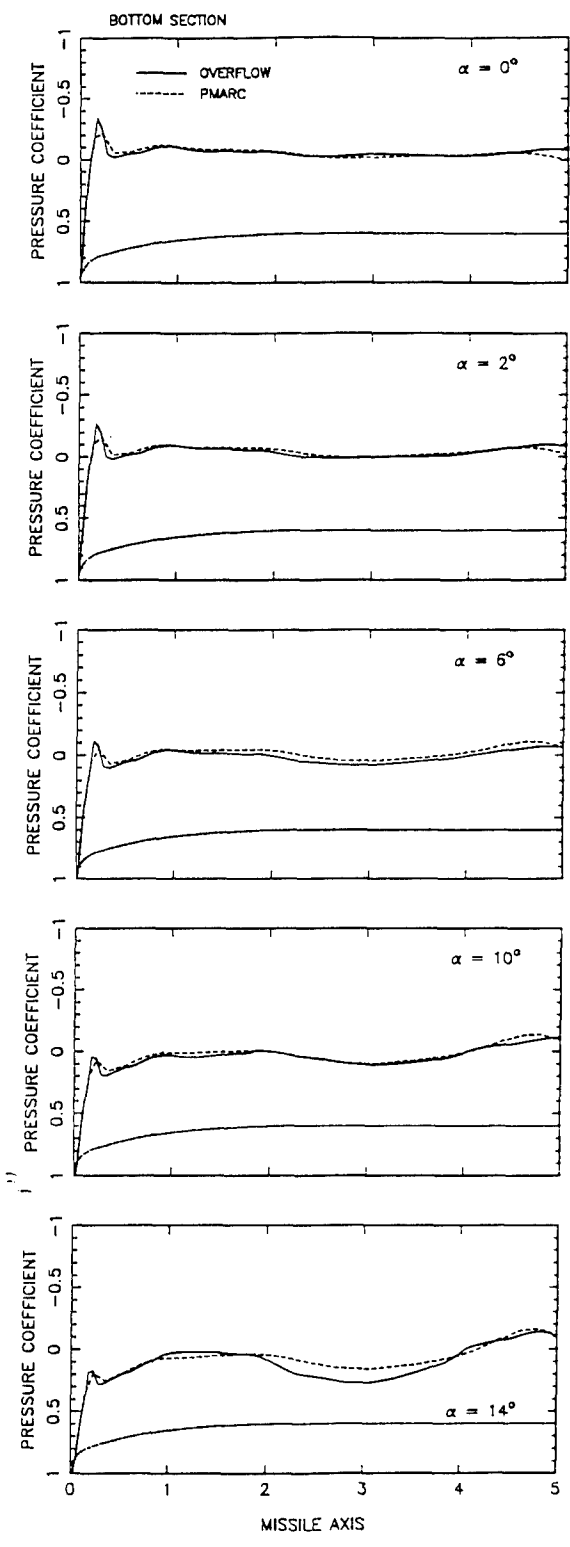


Fig. 8 Windward side surface pressure comparisons over a missile forebody at $M_\infty = 0.3$, $Re = 2 \cdot 10^6$.

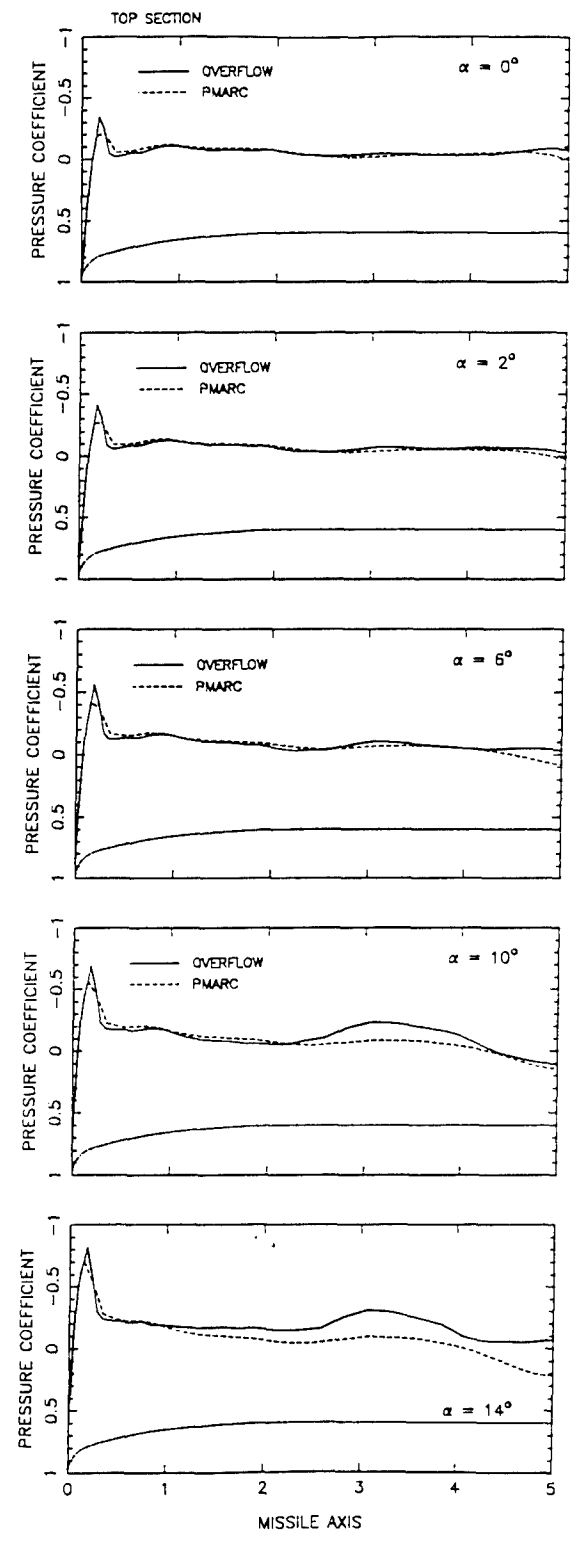


Fig. 9 Leeward side surface pressure comparisons over a missile forebody at $M_\infty = 0.3$, $Re = 2 \cdot 10^6$.

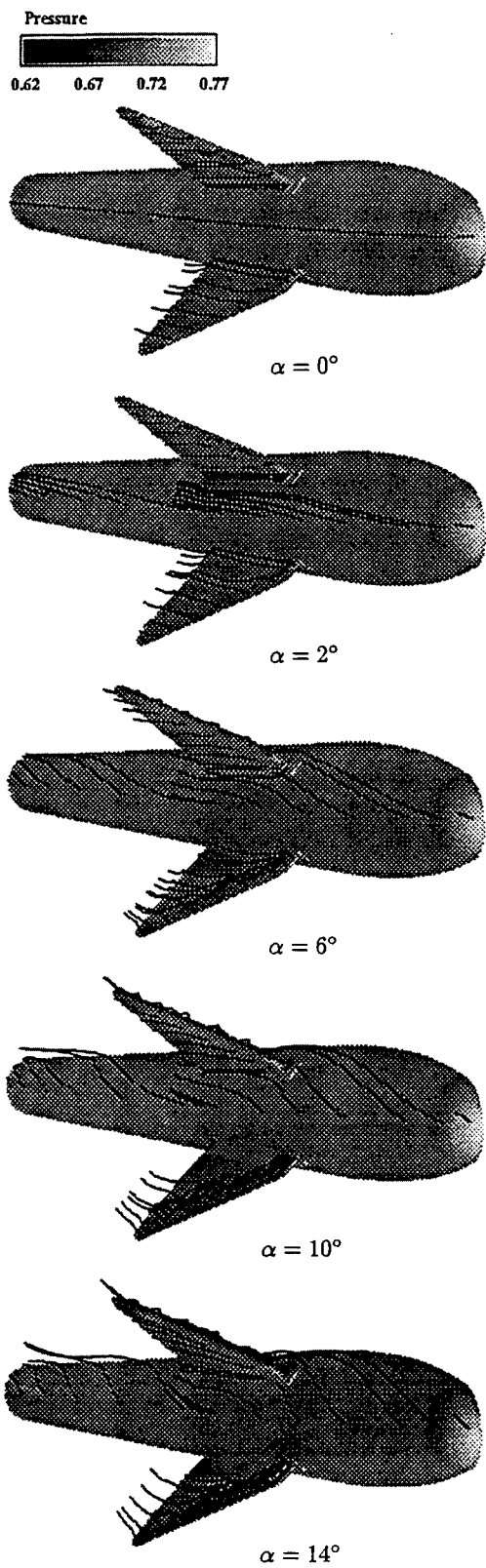


Fig. 7 Surface pressure contours and particle traces over a missile forebody at $M_\infty = 0.3$, $Re_D = 2 \cdot 10^6$.

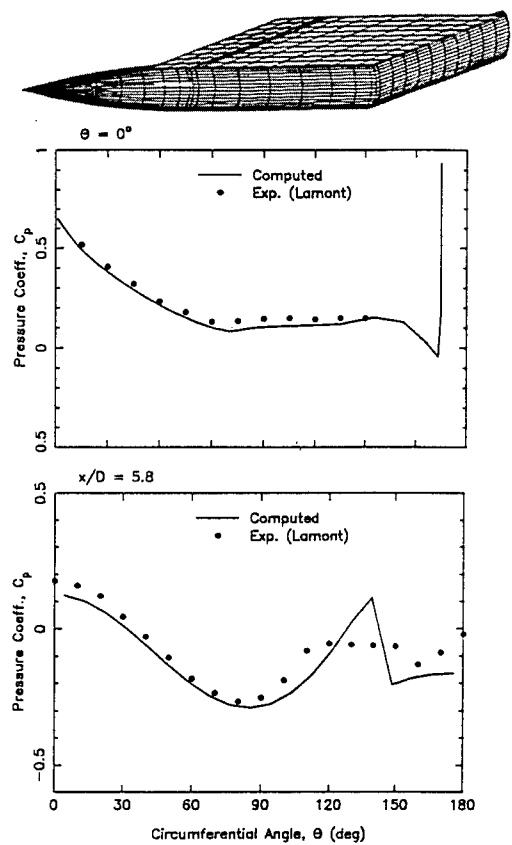


Fig. 10 Inviscid surface pressure distribution over an ogive cylinder at $\alpha = 15^\circ$, $\Theta_w = 144^\circ$

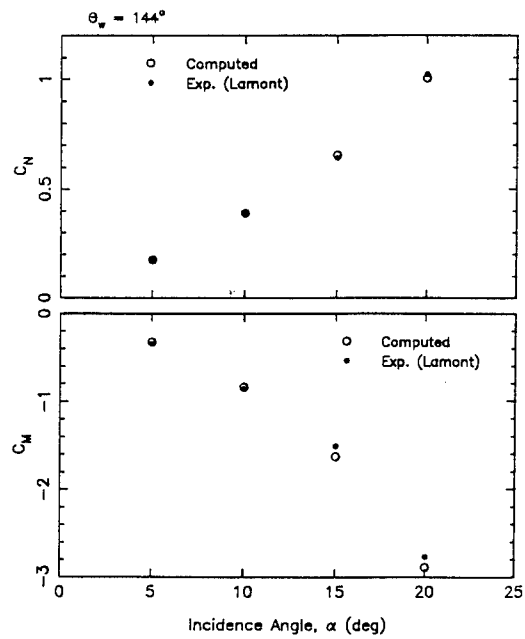


Fig. 11 Normal force and pitching moment coefficients

PREDICTION OF PITCH-DAMPING FOR SYMMETRIC MISSILES

Paul Weinacht
Aerodynamics Branch
U.S. Army Research Laboratory
Aberdeen Proving Ground, Maryland 21005-5066

1. SUMMARY

An approach for predicting the pitch-damping performance of symmetric missiles is presented. Several types of forced motions are utilized to excite the aerodynamic forces and moments that are normally associated with unsteady motion. A key feature of these motions is that steady flow fields are produced by the selected motions. Flow field predictions are accomplished using Navier-Stokes computational techniques that make use of a noninertial rotating coordinate frame resulting from the imposed motions. The aerodynamic forces and moments are then determined from the computed flow field. Applications of the method presented in this paper include predictions of the pitch-damping sum for axisymmetric projectiles at high subsonic, transonic, and supersonic velocities and prediction of the pitch-damping sum for finned projectiles at supersonic velocities. The method is also applied to determine the individual components of the pitch-damping sum for axisymmetric and finned flight bodies.

2. LIST OF SYMBOLS

a_∞	freestream speed of sound
C_m	pitching moment coefficient
C_{m_α}	slope of the pitching moment coefficient with angle of attack
$C_{m_q} + C_{m_{\dot{\alpha}}}$	pitch damping moment coefficient
C_n	side moment coefficient
C_{n_α}	slope of the side moment coefficient with angle of attack
$C_{n_{p\alpha}}$	Magnus moment coefficient
C_{N_α}	slope of the normal force coefficient with angle of attack
$C_{N_q} + C_{N_{\dot{\alpha}}}$	pitch damping force coefficient
D	projectile diameter
e	total energy per unit volume
$\hat{E}, \hat{F}, \hat{G}$	flux vectors in transformed coordinates
\hat{H}	source term in Navier-Stokes eqs.
J	jacobian
l	characteristic length, typically D
M_∞	freestream Mach number
p	pressure, as used in N-S eqs.
\dot{p}	spin rate, as used roll equations
Re	Reynolds number, $a_\infty \rho_\infty D / \mu_\infty$
s_{cg}	center of gravity shift, calibers
\hat{S}	viscous flux vector
S_{ref}	reference area of projectile, $\pi D^2 / 4$
t	time
u, v, w	velocity components in x,y,z directions
V	freestream velocity
x, y, z	Cartesian coordinates w.r.t. body

Note: Force coefficients are scaled, $F / \frac{1}{2} \rho_\infty a_\infty^2 M_\infty^2 S_{ref}$; Moment coefficients are scaled, $M / \frac{1}{2} \rho_\infty a_\infty^2 M_\infty^2 D S_{ref}$

Greek Symbols

α	angle of attack
γ	ratio of specific heats, in N-S eqs.
γ	cosine of the angle of attack, as used in aerodynamic force and moment eqs.
δ	sine of the angle of attack
μ, μ_t	laminar and turbulent viscosity
ξ, η, ζ	transformed coordinates in N-S eqs.
ξ	complex angle of attack
ρ	density
ρ_∞	freestream density
Ω	coning rate of projectile
$\frac{\Omega D}{V}$	nondimensional coning rate

Superscripts

$()'$	rate of change with respect to time
$()'$	rate of change with respect to space
$()$	referenced to non-rolling coordinate frame

3. INTRODUCTION

The aerodynamic performance of projectiles and missiles has a strong effect on their ultimate effectiveness. One important aerodynamic characteristic, pitch-damping performance, plays an important role in the overall flight behavior. If pitch-damping performance is compromised, the flight body may experience decreased effectiveness as evidenced by decreased range or degraded terminal lethality. The research developments described here utilize a multi-disciplinary approach, involving flight mechanics and computational fluid dynamics, for predicting the pitch-damping performance of projectiles and missiles.

The computationally based method represents a breakthrough on several counts. First, the technique utilizes steady motions to excite forces and moments normally associated with unsteady motions. This avoids brute force methods, based on unsteady flow techniques, which are computationally inefficient. Second, the technique is a general approach that is valid across the envelope of flight velocities normally considered for tactical weapons. Finally, the technique permits the determination of aerodynamic properties that can be difficult or expensive to determine experimentally.

To predict the aerodynamic forces and moments of interest, a sophisticated computational capability has been developed based on the thin-layer Navier-Stokes equations. The technique allows the three-dimensional viscous turbulent flow field acting on the body in re-

sponse to the applied motions to be determined. The aerodynamic forces and moments can then be computed from the integrated effects of the pressure and viscous stresses acting on the body. A key feature of the technique is the use of a body-fixed rotating coordinate frame that allows the flow field to be viewed from a steady frame. Because this is a noninertial coordinate frame, the governing equations have been modified to include the centrifugal and Coriolis body forces due the coordinate system rotation.

Two computational techniques have been implemented to cover the envelope of flight velocities. For high subsonic, transonic, or low supersonic flows, a time-marching thin-layer technique based on the implicit flux-splitting scheme has been applied. The steady-state flow field is obtained in a time-iterative manner. At supersonic velocities, a parabolized Navier-Stokes (PNS) technique is applied. The PNS technique takes advantage of flow characteristics at supersonic velocity that allow the steady-state flow field to be obtained from a single sweep through the computational grid. The technique is an order of magnitude more efficient than the time-marching approach.

This paper presents an overview of recent developments and applications in pitch-damping prediction.¹⁻⁶ In the next several sections, flight mechanics theory and computational technique are briefly described. Results are then presented for axisymmetric and finned symmetric missiles.

4. THEORETICAL BACKGROUND

4.1 The Force and Moment Expansion

It is common in many aerodynamics applications to use a body-fixed, non-rolling coordinate system to describe both the dynamics and the system of forces and moments that act on the flight vehicle.⁷ The non-rolling coordinate system allows the description of the vehicle dynamics to be simplified for certain classes of flight vehicles that possess particular types of geometric symmetry. Rotationally symmetric flight vehicles, which are the focus of the current research, represent one class of vehicles where the non-rolling frame has been effectively (and traditionally) used. For more complicated geometries, such as aircraft, the advantages of the non-rolling frame are reduced and other coordinate frames such as a completely body-fixed coordinate system are typically used.

In the current effort, the primary reason for initially describing the aerodynamic forces and moments using the non-rolling coordinate system is the fact that the description is well established for symmetric flight vehicles. The non-rolling coordinate frame is an orthogonal right-handed system ($\tilde{x}, \tilde{y}, \tilde{z}$) centered at the body center of gravity (CG). The \tilde{x} -axis is aligned along the projectile longitudinal axis with the positive direction oriented toward the projectile nose. The \tilde{z} -axis is "initially" oriented downward with the $\tilde{x} - \tilde{z}$ plane perpendicular to the ground. The angular motion of the non-rolling coordinate frame is such that, with respect to an inertial frame, the \tilde{x} -component of the coordinate frame's angular velocity is zero. Although the time-dependent orientation of the non-rolling frame may be difficult to visualize, the non-rolling frame is essentially

equivalent to the "fixed-plane" coordinate system for small amplitude motions. In the fixed-plane coordinate system, the $\tilde{x} - \tilde{z}$ plane remains perpendicular to the ground for all time. The total angular velocity of the flight vehicle can be described in terms of its angular velocity components (p, \tilde{q}, \tilde{r}) along the \tilde{x}, \tilde{y} and \tilde{z} axes, respectively. The angular velocity of the non-rolling frame can be described in terms of the transverse angular velocities \tilde{q} and \tilde{r} because the angular velocity of the non-rolling frame along the \tilde{x} -axis is always zero. The flight body may, however, have a non-zero spin rate, p , about its longitudinal axis. Further details about these coordinate frames are discussed in Ref. 7.

The moment expansion for a rotationally symmetric missile in the non-rolling coordinate frame is shown in Eq. (1). This moment expansion is similar to the moment proposed by Murphy.⁷ The moment formulation uses complex variables to separate the moment components, \tilde{C}_m and \tilde{C}_n , that are oriented along the \tilde{y} and \tilde{z} axes, respectively. The third moment component, the roll moment, can be handled separately and is not of consequence in this study.

$$\tilde{C}_m + i\tilde{C}_n = \left[\left(\frac{pl}{V}\right)C_{n_{pa}} + C_{n_a} - iC_{m_a}\right]\tilde{\xi} + C_{m_q}\tilde{\mu} - iC_{m_a}\tilde{\xi}' \quad (1)$$

In the moment expansion, the pitching moment coefficient slope, C_{m_a} , and the coefficient C_{m_q} represent moments that are proportional to the complex yaw, $\tilde{\xi}$, and yawing rate, $\tilde{\xi}'$, respectively. The side moment coefficient slope C_{n_a} produces a moment that is proportional to the complex yaw but acts perpendicular to the pitching moment coefficient in the transverse plane. The complex yaw and yawing rate are defined below. (In the analysis presented here, there is no need to distinguish between pitch and yaw and the terms may be interchanged. The usage follows that of Murphy.⁷)

$$\tilde{\xi} = \frac{\tilde{v} + i\tilde{w}}{V} \quad (2)$$

$$\tilde{\xi}' \equiv \frac{d\tilde{\xi}}{d\left(\frac{s}{l}\right)} \quad (3)$$

Here, \tilde{v} and \tilde{w} are the \tilde{y} and \tilde{z} components of the velocity vector, \tilde{V} , that describes the velocity of the body CG relative to the inertial frame. The magnitude of this vector is denoted as V . The angular rate is obtained by taking the derivative of the complex yaw with respect to the flight path coordinate, s , which is non-dimensionalized by some characteristic length, l , typically the body diameter.

The coefficient, C_{m_q} , represents a moment that is proportional to the complex transverse angular velocity of the vehicle, $\tilde{\mu}$, as defined below.

$$\tilde{\mu} = \frac{(\tilde{q} + i\tilde{r})l}{V} \quad (4)$$

Here, \tilde{q} and \tilde{r} are the \tilde{y} and \tilde{z} components of angular velocity of the vehicle in the non-rolling coordinate system. The remaining coefficient in the moment expansion, the Magnus moment coefficient, $C_{n_{pa}}$, accounts for a side moment due to flow asymmetries produced by the combination of spin and yaw.

It should be noted that the moment formulation neglects the variation of the moments with roll angle under the assumption that these variations are small. For axisymmetric vehicles, the variations with roll angle should not exist because the geometry will not change as the roll orientation changes. Roll variations in the aerodynamic coefficients for other types of rotationally symmetric vehicles are typically negligible for small amplitude motions. In general, roll variations may be difficult to detect in flight because the effect of roll orientation tends to be averaged-out over the course of a yaw cycle if the body is spinning.

4.2 Coning Motion

For many applications, the pitch-damping coefficient sum, rather than the individual damping coefficients, may be desired. In this case, steady coning motion can be utilized to obtain the pitch-damping coefficient sum from a single motion. In steady coning motion, the longitudinal axis of the flight body performs a rotation at a constant angular velocity about a line parallel to the freestream velocity vector and coincident with the body's center of gravity, while oriented at a constant angle with respect to the freestream velocity vector. This is shown schematically in Figure 1. In the context of this report, coning motion also requires the center of gravity to traverse a rectilinear path at constant velocity such that the freestream velocity vector has a fixed orientation with the inertial frame.

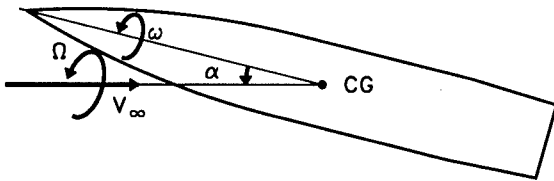


Figure 1. Schematic of coning motion

The net transverse aerodynamic moment in the non-rolling frame can be determined for each of the motions by substituting the appropriately determined angle of attack and angular rates, $\tilde{\xi}'$ and $\tilde{\mu}$, into Eq. (1).

$$\tilde{\xi} = i\delta e^{i\Omega\gamma t} \quad (5)$$

$$\delta = \sin \alpha \quad (6)$$

$$\gamma = \cos \alpha \quad (7)$$

$$\tilde{\xi}' = -\left(\frac{\Omega l}{V}\right)\gamma\delta e^{i\Omega\gamma t} \quad (8)$$

$$\tilde{\mu} = i\left(\frac{\Omega l}{V}\right)\delta e^{i\gamma\Omega t} \quad (9)$$

With these substitutions, the resulting expression for the transverse aerodynamic moment in the non-rolling frame will be periodic in time, which also indicates that the flowfield will be periodic in time when viewed from the non-rolling coordinate frame. However, a steady flowfield should be observed when examined from an orthogonal right-handed coordinate system that has its x -axis aligned with the longitudinal axis of the body with the x and z axes parallel to the pitch-plane. This coordinate frame is referred to as the coning frame. The transverse aerodynamic moments in the non-rolling frame can

be transformed to the coning coordinate frame where the steady flowfield exists, using the following relations:

$$C_m + iC_n = (\tilde{C}_m + i\tilde{C}_n)e^{-i\Omega\gamma t} \quad (10)$$

Using the transformation, the moments in the coning reference frame are written as follows:

$$C_m + iC_n = \left\{ i\left(\frac{pl}{V}\right)C_{n_{p\alpha}} + iC_{n_\alpha} + i\left(\frac{\Omega l}{V}\right)[C_{m_q} + \gamma C_{m_\dot{\alpha}}] + C_{m_\alpha} \right\} \delta \quad (11)$$

The moments in this reference frame do not show an explicit time-dependence, indicating that a steady flow field potentially exists. Note also that the expansion is not completely defined in this form because the angular velocity p is still arbitrary. In this paper, two particular forms of coning motion, *steady lunar coning motion* and *steady zero-spin motion*, are utilized. The two motions differ in their treatment of the angular velocity about the longitudinal axis.

In steady lunar coning motion, the angular velocity of the projectile results purely from the rotation of the projectile about the free-stream velocity vector. The angular velocity of the projectile includes a component along the projectile's longitudinal axis, which by definition is the spin rate of the projectile in the non-rolling coordinate system. The relation between spin rate, p , and coning rate, Ω , for the case of steady lunar coning motion is

$$p = \Omega \cos \alpha_t = \Omega \gamma \quad (12)$$

For steady lunar coning motion, the coning frame and the body rotate at the same angular velocity, and there is no rotation of the pitch plane with respect to the body. Because the boundary conditions in the coning frame do not introduce any time-dependency into the problem, when observed from the coning reference frame, the resulting flowfield is expected to be steady for small angles of attack and for small coning rates. It is important to realize that because the coning frame is rotating at a constant angular velocity and because the body does not rotate with respect to the coning frame of reference, there is no requirement for the body to have any special forms of geometric symmetry (i.e., axisymmetry) for steady flow to exist.

The resulting moment expansion has the following form for lunar coning motion.

$$C_m + iC_n = i\delta\left(\frac{\Omega l}{V}\right)\{\gamma C_{n_{p\alpha}} + [C_{m_q} + \gamma C_{m_\dot{\alpha}}]\} + iC_{n_\alpha}\delta + C_{m_\alpha}\delta \quad (13)$$

In steady zero-spin coning motion, the angular velocity of the projectile consists of the vector sum of two angular velocity vectors. The first vector produces a rotation of the projectile's longitudinal axis about the free-stream velocity vector (coning motion), $\vec{\Omega}$, and the second produces a rotation of the projectile about its longitudinal axis (spinning motion), $\vec{\omega}$. (See Figure 1.) In general, there is no requirement for the spin rate to be coupled to the coning rate. However, in the context

of this paper, zero-spin coning motion requires that $\vec{\omega}$ be equal in magnitude but opposite in sign to the component of $\vec{\Omega}$ along the longitudinal axis, $\omega = -\Omega \cos \alpha_t$. In this case, the total angular velocity of the body about the longitudinal axis is zero; hence, the spin rate in the non-rolling coordinate system is zero.

$$p = 0. \quad (14)$$

For the case of steady zero-spin coning motion, the body will rotate in the coning reference frame with a rate of rotation that is proportional to the coning rate ($\omega = -\Omega \cos \alpha_t$). This rotation does not produce a time-dependent boundary condition for axisymmetric bodies, and a steady flowfield can exist. However, for non-axisymmetric bodies, the rotation of the body in the coning reference frame will produce a time-dependent (periodic) boundary condition and flowfield. Thus, when zero-spin coning motion is utilized, a steady flowfield is only possible for axisymmetric bodies.

The zero spin rate eliminates the Magnus term from the moment expansion. (Since there is no side moment C_{n_α} for axisymmetric bodies, this term is also dropped from the moment expansion.)

$$C_m + iC_n = i\delta\left(\frac{\Omega l}{V}\right)\{\gamma C_{n_{p\alpha}} + [C_{m_q} + \gamma C_{m_\dot{\alpha}}]\} + C_{m_\alpha} \delta \quad (15)$$

4.3 Helical Motions

Forces and moments related to the individual rates $\tilde{\mu}$ and $\tilde{\xi}'$, can be excited independently using two types of motion where the CG of the flight vehicle traverses a helical flight path. The first motion requires the vehicle's longitudinal axis to be oriented in the same direction as the center of rotation of the helix but displaced by a constant distance. Figure 2 shows a three-dimensional view of the motion.

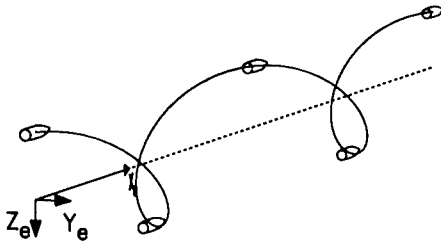


Figure 2. Helical motion with non-zero $\tilde{\alpha}$ and zero \tilde{q}

This particular motion produces no rotation of the non-rolling coordinate frame relative to an earth-fixed coordinate frame, and hence, the angular velocity $\tilde{\mu}$ is zero. The angle of attack and its angular rate vary continuously, producing moment components associated with the coefficients C_{m_α} and $C_{m_\dot{\alpha}}$, respectively. This motion is referred to as " $q = 0$ helical motion" because the angular rates associated with the damping coefficient C_{m_q} are zero.

For the second motion, the longitudinal axis of the flight vehicle remains tangent to the helical flight path at each point along the trajectory. Figure 3 shows

a three-dimensional view of this motion. The angle of attack of the incident airstream is zero since both the longitudinal axis of the body and the free-stream velocity vector are tangent to the flight path. The resulting yawing rate is also zero because the angle of attack is constant. The angular orientation of the flight body changes continuously with respect to an earth-fixed reference frame, producing a non-zero angular rate, $\tilde{\mu}$. As a result, moment components associated with the damping moment C_{m_q} are produced. This motion is referred to as " $\dot{\alpha} = 0$ helical motion" because the angular rates associated with the damping coefficient $C_{m_\dot{\alpha}}$ are zero. The $\dot{\alpha} = 0$ helical motion produces a steady flowfield when viewed from the appropriate coordinate system.

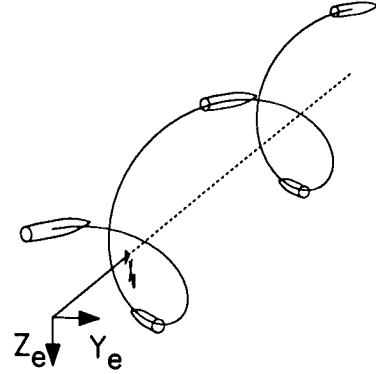


Figure 3. Helical motion with zero $\tilde{\alpha}$ and non-zero \tilde{q} .

The net transverse aerodynamic moment in the non-rolling frame can be determined for each of the motions by substituting the appropriately determined angle of attack and angular rates, $\tilde{\xi}'$ and $\tilde{\mu}$, into Eq. (1).

$q=0$ Helical Motion

$$\tilde{\xi} = -\delta e^{i\Omega t} \quad (16)$$

$$\delta = \frac{R_o \Omega}{\sqrt{U^2 + \Omega^2 R_o^2}} \quad (17)$$

$$\tilde{\xi}' = -i\left(\frac{\Omega l}{V}\right)\delta e^{i\Omega t} \quad (18)$$

$$\tilde{\mu} = 0 \quad (19)$$

$\dot{\alpha}=0$ Helical Motion

$$\tilde{\mu} = \frac{\Omega l}{V}(\sin \beta)e^{i\Omega t} \cos \beta \quad (20)$$

$$\cos \beta = \frac{U}{V} \quad (21)$$

$$\sin \beta = \frac{R_o \Omega}{V} \quad (22)$$

$$\tilde{\xi} = \tilde{\xi}' = 0 \quad (23)$$

Here, Ω is the angular velocity of the body about the helix axis, R_o is the perpendicular distance between the helix axis and the body CG, U is the component of velocity along the helix axis, and V is the total linear velocity of the CG.

For each of the helical motions, the transverse aerodynamic moment in the non-rolling frame will be periodic in time, which also indicates that the flowfield

will be periodic in time when viewed from the non-rolling coordinate frame. Similar to the approach used for coning motion, the time-dependency is removed by transforming to an orthogonal right-handed coordinate system that has its x -axis aligned with the longitudinal axis of the body and its z -axis along a line between the body CG and the axis of rotation of the helix. The transverse aerodynamic moments in the non-rolling frame can be transformed to the coordinate frame where the steady flowfield exists, using the following relations:

$q=0$ Helical Motion

$$C_m + iC_n = (\tilde{C}_m + i\tilde{C}_n)e^{-i\Omega t} \quad (24)$$

$\dot{\alpha}=0$ Helical Motion

$$C_m + iC_n = (\tilde{C}_m + i\tilde{C}_n)e^{-i\Omega t \cos \beta} \quad (25)$$

To completely define the moment expansion, the spin rate of the vehicle must be defined. Similar to coning motion, two forms of both types of helical motion are defined: lunar and zero-spin helical motion. In general, the zero-spin helical motion produces a steady flow field only for axisymmetric bodies. Similar to coning motion, the advantage of this motion is that it eliminates the Magnus moment from the moment expansion for the $q=0$ helical motion. The lunar forms of the helical motions produce steady flow fields even if the body is not axisymmetric, although the Magnus moment term remains in the moment expansion for the $q=0$ helical motion. Note that the Magnus term does not appear in either form of the $\dot{\alpha}=0$ helical motion because the angle of attack is zero. The resulting moment expansions are shown below.

Zero-Spin $q=0$ Helical Motion

$$C_m + iC_n = -C_{m\dot{\alpha}}\left(\frac{\Omega l}{V}\right)\frac{R_o\Omega}{V} + (C_{n\alpha} + iC_{m\alpha})\frac{R_o\Omega}{V} \quad (26)$$

Zero-Spin $\dot{\alpha}=0$ Helical Motion

$$C_m + iC_n = C_{m\dot{\alpha}}\left(\frac{\Omega l}{V}\right)\frac{R_o\Omega}{V} \quad (27)$$

Lunar $q=0$ Helical Motion

$$C_m + iC_n = -(C_{n_{p\alpha}} + C_{m\dot{\alpha}})\left(\frac{\Omega l}{V}\right)\frac{R_o\Omega}{V} + (C_{n\alpha} + iC_{m\alpha})\frac{R_o\Omega}{V} \quad (28)$$

Lunar $\dot{\alpha}=0$ Helical Motion

$$C_m + iC_n = C_{m\dot{\alpha}}\left(\frac{\Omega l}{V}\right)\frac{R_o\Omega}{V} \quad (29)$$

Similar expressions for the individual damping force coefficients can be developed using the same approach as applied for the moment coefficients.

5. COMPUTATIONAL TECHNIQUE

In the previous section, several types of steady motion were presented that produce aerodynamic forces and moments from which the various pitch-damping coefficients can be obtained. One unique feature of these motions is that they are steady motions. The advantage

of a steady motion over an unsteady motion is that a potentially time-independent flow field can be produced by a steady motion, permitting analysis using steady flow techniques. Such techniques can be computationally less expensive than time-dependent approaches. As shown in the previous section, the aerodynamic forces and moments were steady in particular coordinate systems that were aligned with the body axis. This implies that the flow field viewed from each of these coordinate frames is potentially steady and each of these coordinate frames may be a suitable coordinate frame for applying the computational approach. One feature of these coordinate frames is that they are rotating at a constant rate with respect to an inertial frame. Because of this, the governing equations of fluid motion must be modified to take into account the centrifugal and Coriolis force terms associated with the non-inertial rotating frame.

The time-dependent thin-layer Navier-Stokes equations are shown below.

$$\frac{\partial \hat{q}}{\partial t} + \frac{\partial \hat{E}}{\partial \xi} + \frac{\partial \hat{F}}{\partial \eta} + \frac{\partial \hat{G}}{\partial \zeta} + \hat{H} = \frac{1}{Re} \frac{\partial \hat{S}}{\partial \zeta} \quad (30)$$

The inviscid flux vectors, \hat{E} , \hat{F} , and \hat{G} , and the viscous term \hat{S} are functions of the dependent variable, $q^T = (\rho, \rho u, \rho v, \rho w, e)$. The important consideration for the current work is the addition of the source term, \hat{H} , which incorporates the effects of the centrifugal and Coriolis forces from the rotating coordinate frame produced by coning motion. The inviscid flux vectors and the source term are shown below. Details of the thin-layer viscous term are available in the literature.

$$\begin{aligned} \hat{E} &= \frac{1}{J} \begin{bmatrix} \rho U \\ \rho u U + \xi_x p \\ \rho v U + \xi_y p \\ \rho w U + \xi_z p \\ (e + p)U \end{bmatrix} & \hat{F} &= \frac{1}{J} \begin{bmatrix} \rho V \\ \rho u V + \eta_x p \\ \rho v V + \eta_y p \\ \rho w V + \eta_z p \\ (e + p)V \end{bmatrix} \\ \hat{G} &= \frac{1}{J} \begin{bmatrix} \rho W \\ \rho u W + \zeta_x p \\ \rho v W + \zeta_y p \\ \rho w W + \zeta_z p \\ (e + p)W \end{bmatrix} & \hat{H} &= \frac{1}{J} \begin{bmatrix} 0 \\ \rho f_x \\ \rho f_y \\ \rho f_z \\ (\rho u f_x + \rho v f_y + \rho w f_z) \end{bmatrix} \end{aligned} \quad (31)$$

The pressure, p , can be related to the dependent variables by applying the ideal gas law.

$$p = (\gamma - 1) \left[e - \frac{\rho}{2} (u^2 + v^2 + w^2) \right] \quad (32)$$

The turbulent viscosity, μ_t , which appears in the viscous matrices, was computed using the Baldwin-Lomax turbulence model.⁸

The Coriolis and centrifugal acceleration terms due to the rotating coordinate system, which are contained in the source term, \hat{H} , are shown below.

$$\vec{f} = 2\vec{\Omega} \times \vec{u} + \vec{\Omega} \times (\vec{\Omega} \times \vec{R}) \quad (33)$$

The Coriolis acceleration is a function of the angular velocity of the coordinate frame with respect to the inertial frame, $\vec{\Omega}$, and the fluid velocity vector, \vec{u} , which can

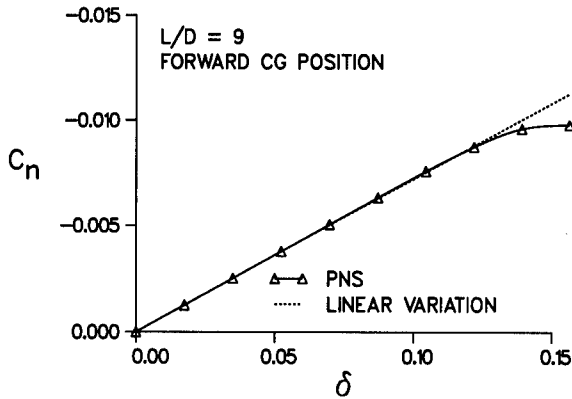


Figure 6. Variation of the side moment with sine of angle of attack, Army-Navy spinner rocket, $M_\infty = 2.5$, $\Omega D/V = 0.001$.

generated for the $L/D=5$ and $L/D=7$ bodies from the $L/D=9$ solution using a CG position located 4.0 calibers from the nosetip. This corresponds to the forward CG position of the $L/D=9$ body and the middle CG location of the $L/D=7$ body but is located aft of the three CG positions of the $L/D=5$ body. Using the CG translation relations, predictions of aerodynamic coefficients across the range of CG locations were made using the predicted aerodynamic coefficients obtained at the single CG location. The CG translation relation for the pitch-damping moment coefficient sum is shown below.

$$\hat{C}_{m_q} + \hat{C}_{m_{\dot{\alpha}}} = C_{m_q} + C_{m_{\dot{\alpha}}} - s_{cg}(C_{N_q} + C_{N_{\dot{\alpha}}}) + s_{cg}C_{m_{\alpha}} - s_{cg}^2 C_{N_{\alpha}}$$

The aerodynamic coefficients on the right-hand side represent the aerodynamic coefficients obtained from the baseline solution. The pitch-damping moment coefficient sum is a function of the center of gravity shift, s_{cg} . s_{cg} is in calibers and is positive for a CG shift toward the nose.

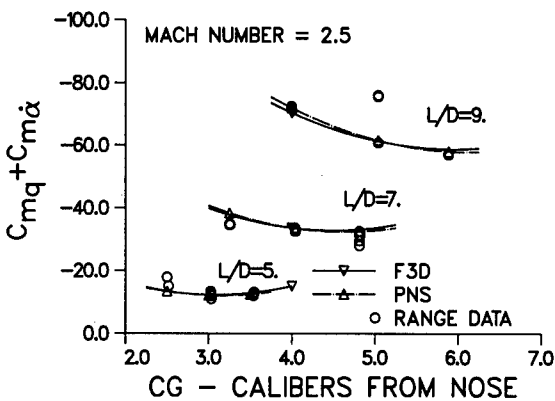


Figure 7. Pitch-damping moment coefficient sum versus CG location, $M_\infty = 2.5$.

Figure 7 shows the F3D and PNS predictions of the pitch-damping moment coefficient sum at Mach 2.5 for each of the three body lengths. Both the PNS and F3D predictions show excellent agreement with the range

data. The average difference between the F3D and PNS results at each of the three CG locations was less than 2% with a maximum difference of 4.3%. Similar agreement was found at Mach 1.8.

Predictions of the pitch-damping moment coefficient sum were also made at Mach 1.3 using the F3D code. The predicted variation of the damping moment with CG position, shown in Figure 8, is in good agreement with the range data for each of the three body lengths. The variations of the coefficients with body length and CG position are similar to the results at the higher Mach numbers. Because of the low Mach number, no PNS results could be obtained.

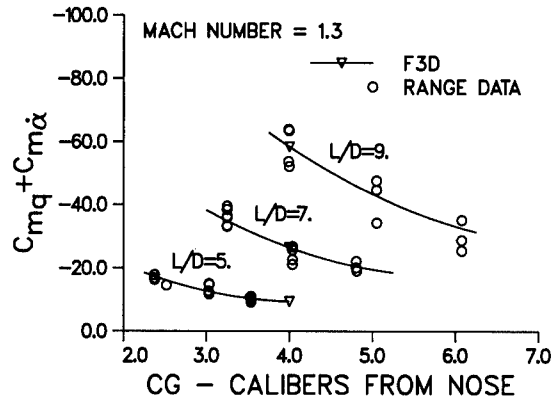


Figure 8. Pitch-damping moment coefficient sum versus CG location, $M_\infty = 1.3$.

The F3D predictions of the pitch-damping force coefficient sum at Mach 1.3, 1.8 and 2.5 is shown in Figure 9 as a function of body length. Also shown is the pitch-damping force coefficient sum obtained from the range firings using the variation of the pitch-damping moment coefficient sum with CG position. (The pitch-damping force coefficient sum contributes little to the in-flight motion and can only be determined from range tests in this manner.) The CG translation relations were again used to determine the value of the predicted pitch-damping force coefficient sum at the middle CG location for each body length. The predicted results are in good agreement with the range data. Both prediction and

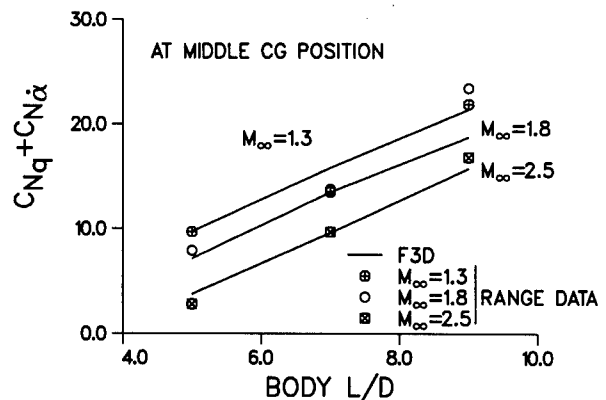


Figure 9. Pitch-damping force coefficient sum versus body length, middle CG location.

range data show an increasing trend of the pitch-damping force coefficient sum with decreasing Mach number and increasing body length. Though not shown, the PNS predictions at Mach 1.8 and 2.5 show a similar comparison with the experimental data.

Range results for the $L/D=7$ Army-Navy spinner rocket were used to validate the computational approach in the high subsonic through low supersonic regime. Predictions were made at 2° angle of attack and non-dimensional coning rates of $(\frac{\Omega D}{V}) = 0.010$. Although three different CG locations were tested in the range tests, the predicted results were obtained at the middle CG location of the $L/D=7$ body. The CG transformation relations were used to obtain predictions of the aerodynamic coefficients at the forward and rearward CG locations.

Figure 10 shows the predicted variation of the pitch-damping moment coefficient sum with Mach number as determined with the F3D code. Results are shown for forward (F), middle (M) and rearward (R) CG position located 3.25, 4.04 and 4.81 calibers from the nose. At high subsonic ($M_\infty = 0.8$) and low supersonic velocities, the predicted results are in good agreement with the range data. The predictions are somewhat higher than the range data near the sonic velocity. It is noted that the largest yaw flights were observed near Mach 1. Potentially, the high yaw condition resulted in non-linear aerodynamics that are not accounted for in the data reduction. The results show a generally decreasing trend with Mach number. The pitch-damping moment coefficient sum shows an increasing trend with forward movement of the CG location. This effect decreases with increasing velocity. The F3D and PNS predictions show a similar trend with Mach number at supersonic velocities for each of the three CG locations.

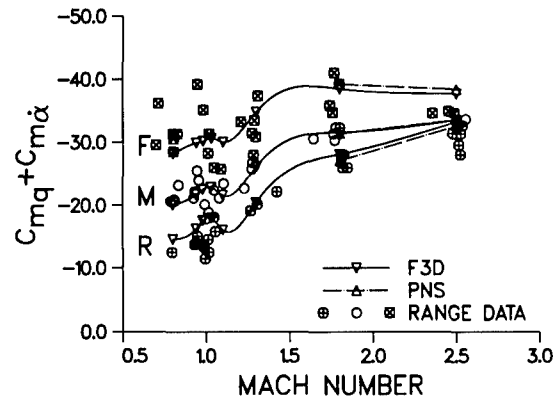


Figure 10. Variation of the pitch-damping moment coefficient sum with Mach number, $L/D=7$.

In addition to determining the total integrated force and moment coefficients for each body, the current method allows the distribution of the pitch-damping force and moment to be examined. Figure 11 shows the development of the pitch-damping moment coefficient sum over the $L/D=7$ body. The largest contributions to the pitch-damping moment are produced at the nose and rear of the body. The most significant variation with Mach number appears to occur on the cylindrical portion of the body just behind the nose. It is significant

to note that the predictions show a fairly consistent behavior from high subsonic to supersonic velocities for this body type. The distribution of the pitch-damping moment coefficient sum over the body is similar for the $L/D=5$ body.

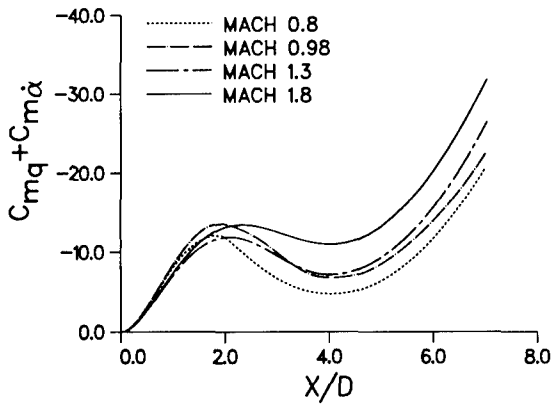


Figure 11. Development of the pitch-damping moment coefficient sum over the body, $L/D=7$, middle CG.

6.2 Individual Components of the Pitch-Damping Sum for Axisymmetric Projectiles

Using the helical motions, the individual components of the pitch-damping sum were also computed for the ANSR configuration. Figure 12 shows predictions of the pitch-damping moment coefficients, C_{mq} and $C_{m\dot{\alpha}}$, as a function of CG position for the $L/D=9$ body at Mach 2.5. Predictions obtained using the PNS computational approach are shown, along with results obtained with engineering design predictions made with slender body theory. The results show that the pitch-damping coefficient C_{mq} is larger than $C_{m\dot{\alpha}}$ for all the CG positions examined. The damping coefficient, $C_{m\dot{\alpha}}$, is nearly zero at the rearward CG for each of the body lengths. The trends shown by the slender body results are similar to the PNS results, although the slender body results are generally lower in magnitude.

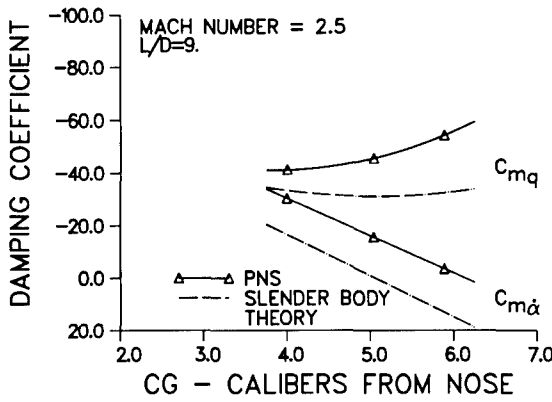


Figure 12. Variation of damping moment coefficients with CG location, $M = 2.5$, Army-Navy spinner rocket, $L/D=9$

The distribution of the pitch-damping moment coefficients over the ANSR $L/D=5$ body is shown in Figure 13. The force coefficient $C_{N\dot{\alpha}}$ is positive along the

body length with most of the force being generated at the aft end of the body. As a result, the moment coefficient $C_{m\dot{\alpha}}$ also shows its largest contributions from the tail. On the other hand, for the force coefficient, C_{Nq} , both the nose and cylindrical afterbody produce contributions to the force coefficient which are similar in magnitude but opposite in sign. This essentially imposes a couple on the body whose magnitude is reflected in the moment coefficient, C_{mq} .

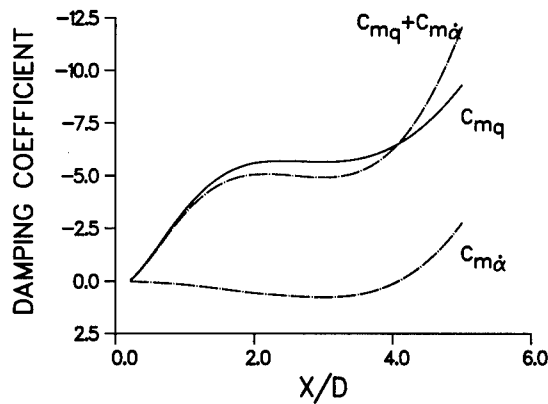


Figure 13. Development of pitch-damping moment coefficients over ANSR body, $M = 2.5$, $L/D=5$, middle CG position.

6.3 Pitch-Damping Sum for Finned Projectiles

Results have been obtained for a cone-cylinder forebody with aft-mounted fins. A schematic is shown in Figure 14. The fins on this flight body have roll-producing beveled surfaces at their trailing edges. Particular care has been taken to model the fin geometry accurately. Though not shown, the cylindrical portion of the body has a number of circumferential grooves that cover nearly two-thirds of the body. The effect of these grooves is not modeled in the current computations, though it is a subject of current research.

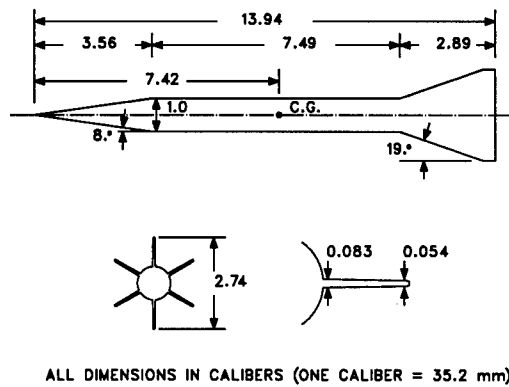


Figure 14. Schematic of the $L/D=14$ finned body.

As discussed previously, lunar coning motion is used to produce moments associated with the pitch-damping coefficients for non-axisymmetric bodies. Although Magnus force and moment coefficients cannot be separated from the pitch-damping coefficients in the

force and moment expansions, the Magnus coefficients are much smaller than the pitch-damping coefficients for these types of finned bodies and can be ignored.

The computations have been performed over a range of Mach numbers ($M_\infty = 3.0$ to 5.5), coning rates ($\Omega D/V = 0.0$ to 0.010), and angles of attack ($\alpha = 1^\circ$ to 5°) for free-flight, sea-level atmospheric conditions. The variation of the side force and moment with coning rate and angle of attack has been used to determine the pitch-damping coefficients for these finned flight bodies. Comparisons are made with data obtained from range firings.¹⁴

The computed variation of the side moment coefficient with coning rate at Mach 4 and 2° angle of attack is shown in Figure 15. The variation of the side moment coefficient with coning rate is seen to be linear across the range of coning rates examined here. This range of coning rates is representative of the pitching frequencies experienced by this body in flight. The results also show the existence of a small non-zero side moment coefficient at zero coning rate. This side moment is generated by flow asymmetries produced by the leeside body wake and the roll-producing fin bevels. The existence of this side moment at zero coning rate requires that computations be performed for at least two coning rates in order to evaluate the variation of the side moment coefficient with coning rate.

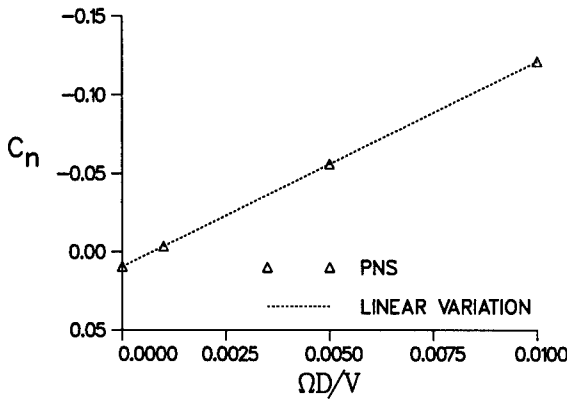


Figure 15. Variation of the side moment coefficient with coning rate, $L/D=14$ finned body, $M_\infty = 4$, $\alpha = 2^\circ$.

Predictions of the variation of the side moment with δ (the sine of the angle of attack) were also made. The computed results show that, at small angles of attack, the side moment varies linearly with δ but departs from a linear variation as the angle of attack approaches 5° . The pitch-damping force and moment coefficient sums were obtained by computing the side force and moment at 2° angle of attack and coning rates of $\frac{\Omega D}{V} = 0$ and $\frac{\Omega D}{V} = 0.010$. The variation of $C_{mq} + C_{mq\dot{\alpha}}$ with Mach number for the $L/D=14$ finned body is shown in Figure 16. The computed results are compared with range measurements of the pitch-damping coefficient. Though the range data shown here are considered well determined, some scatter is still evident because damping rates are typically difficult to measure. The experimental results do reflect the expected level of accuracy in determining this coefficient experimentally. The com-

parisons show that the computational results are within the accuracy of the experimental data and provide a measure of validation of the computational approach.

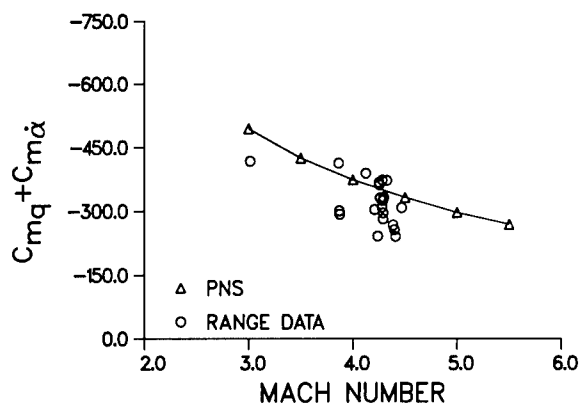


Figure 16. Variation of the pitch-damping moment coefficient sum with Mach number, $L/D=14$ finned body.

Figure 17 shows the development of the pitch-damping moment coefficient over the $L/D=14$ finned body at Mach 4 and 2° angle of attack. This figure shows that the fins contribute most of the pitch-damping moment coefficient sum with a smaller contribution from the nose.

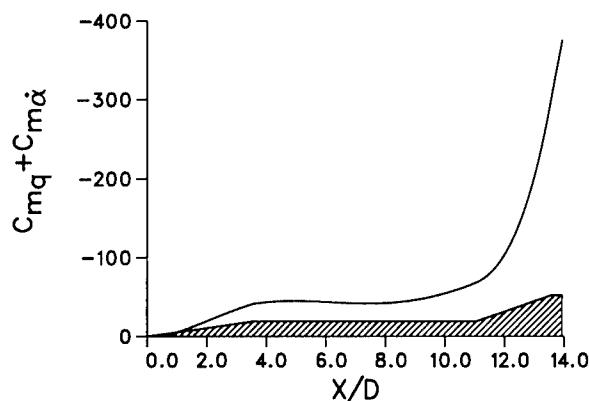
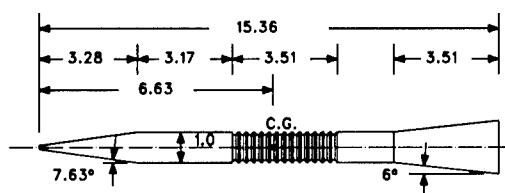


Figure 17. Development of the pitch-damping coefficient sum over $L/D=14$ finned body.

The pitch-damping characteristics of a family of flared flight bodies have also been predicted and comparisons made with aerodynamics range data.^{15, 16} A schematic of the baseline cone-cylinder-flare configuration is shown in Figure 18. Each of the flight bodies examined here has the same cone-cylinder forebody. The forebody has a slightly truncated conical nose. In the computations, the nose is modeled as a sharp tipped cone. The cylindrical portion of the body also has a number of sub-caliber grooves that permit the launch loads to be transferred from the sabot to the flight body during launch. These grooves are not modeled in the computations presented here.

Various afterbodies have been analyzed both experimentally and computationally. Schematics of the

afterbodies are shown in Figure 19. The configurations CS-V4-2 through CS-V4-5 have a one-caliber afterbody extension added to the baseline configuration, CS-V4-1. The angle of inclination of the conical extensions for configurations CS-V4-2 through CS-V4-5 are, respectively, 6° (simple extension of original flare), 0° (cylindrical skirt), 12° (steeper flare), and -6° (boattail). Configuration CS-V4-6 consists of 9.37° flare that has been machined to produce a square cross section over the last caliber of the body. Configuration CS-V4-7 is identical to the boattailed configuration CS-V4-5, except that four 12° fins have been added to the boattailed portion of the body. The fins are 0.153 calibers thick. The final configuration, CS-V4-8, is identical to the baseline configuration, except that four boundary layer strakes have been added to the flared portion of the body. The strakes are 0.153 calibers in height and width.



ALL DIMENSIONS IN CALIBERS (ONE CALIBER = 8.28 mm)

Figure 18. Schematic of the baseline flared flight body.

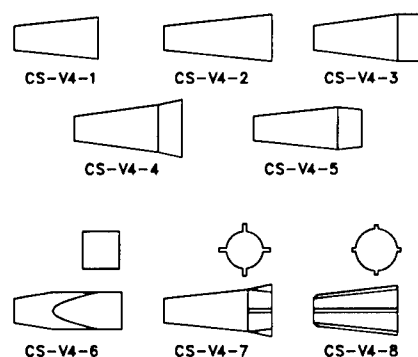


Figure 19. Afterbodies configurations for the flared flight body.

Lunar coning motion has been used to determine the pitch-damping coefficients. Because of the symmetry of the configurations, no side force or moment due to angle of attack exists ($C_{n\alpha} = 0$) for these configurations. For these bodies, experimental data (and, in the case of the axisymmetric bodies, computations) were used to demonstrate that the Magnus force and moment were small compared to the pitch-damping coefficients. From the variation of the side moment with coning rate and sine of the angle of attack, the pitch-damping coefficient sums were determined for each of the eight flared configurations. The predictions were obtained at 2° angle of attack and a non-dimensional coning rate of 0.010.

Figure 20 shows a comparison of the pitch-damping moment coefficient sums for each of the eight configurations at Mach 4. Both the PNS predictions and the range data are shown. Each of the bodies with the conical extensions, configurations CS-V4-2 through CS-

V4-5, has larger pitch-damping coefficient sums compared with the baseline configuration CS-V4-1. Computational predictions show a consistent increase in the pitch-damping for the bodies with the conical extensions with the boattailed configuration having the lowest pitch-damping coefficient and the steepest flare having the highest pitch-damping coefficient. These trends are, for the most part, reflected by the range data.

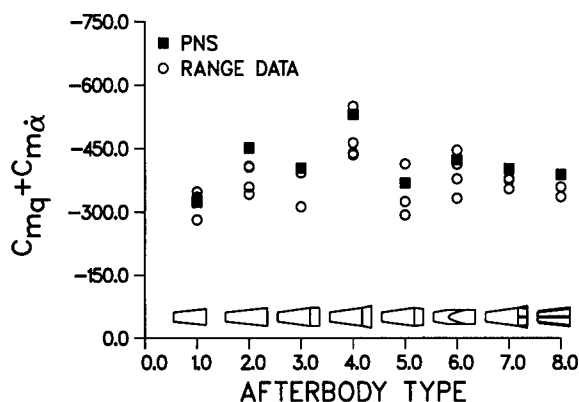


Figure 20. Pitch-damping moment coefficient sum versus afterbody geometry, $M_\infty = 4$.

The finned configuration, which is identical to the boattailed configuration except that four 12° swept fins have been added to the boattailed portion of the body, shows a modest increase in the damping over the boattailed configuration. The finned configuration, however, produces significantly less pitch-damping than the configuration with the 12° flare extension. Again, these trends are reflected by the range data. The configuration with the boundary layer strakes also produces a modest increase in the damping compared with the baseline configuration that has no strakes. The square base configuration (CS-V4-6), which has the same base area as the baseline configuration (CS-V4-1) and the configuration with the cylindrical skirt (CS-V4-3), produces more damping than the baseline configuration and slightly more damping than the cylindrical skirt.

6.4 Individual Components of the Pitch-Damping Sum for Finned Projectiles

Predictions of the individual components of the pitch-damping coefficient sum were also made for the $L/D=14$ finned body using $q = 0$ and $\dot{\alpha} = 0$ helical motions. The lunar forms of the helical motion must be used because of the non-axisymmetric body geometry. For the $\dot{\alpha} = 0$ helical motion, helical rotation rates of $\frac{\Omega D}{V} = 0.010$ and a rotational velocity ratio of $\frac{\Omega R_o}{V} = 0.0349$ were utilized to determine the damping coefficient C_{m_q} . For the $q = 0$ helical motion, two different helical rotation rates of $\frac{\Omega D}{V} = 0.010$ and $\frac{\Omega D}{V} = 0.001$ were utilized to separate the side moment C_{n_α} from the coefficient sum $C_{n_{p\alpha}} + C_{m_\alpha}$. A fixed rotational velocity ratio of $\frac{\Omega R_o}{V} = 0.0349$ was utilized to produce a total angle of attack of 2° .

Figure 21 shows the Mach number variation of both coefficients at supersonic velocities as predicted by the PNS code. As discussed above, the damping coefficient

C_{n_α} cannot be separated from the Magnus moment coefficient $C_{n_{p\alpha}}$. Thus, the coefficient sum $C_{m_\alpha} + C_{n_{p\alpha}}$ is shown in this figure. The computed magnitude of the coefficient sum $C_{m_\alpha} + C_{n_{p\alpha}}$, is not sufficiently large for the Magnus moment coefficient to be ignored in this case without more specific information regarding the Magnus moment. The predictions do indicate that the damping coefficient C_{m_q} is significantly larger than the damping coefficient C_{m_α} . The two sets of coefficient show a decreasing trend with Mach number.

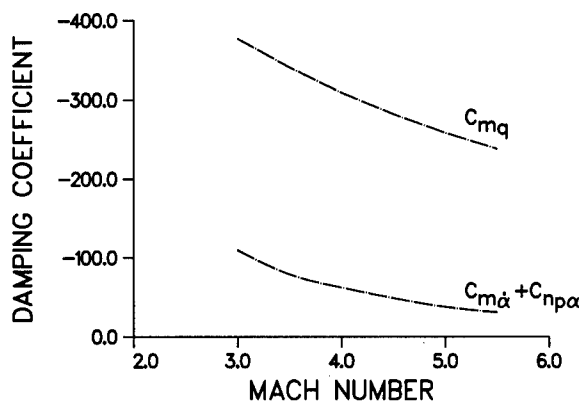


Figure 21. Variation of the pitch-damping coefficients with Mach number, $L/D=14$ finned body, PNS results.

The distribution of the damping coefficient C_{m_q} over the $L/D=14$ body at Mach 4 is shown in Figure 22. The PNS results for the finned body are compared with PNS results for a body-alone configuration and with slender body results for the $L/D=14$ finned body. The damping coefficient C_{m_q} shows a small contribution from the nose of the body with most of the damping coefficient being produced by the finned portion of the body. Without the fins, the PNS results show only a small increase over the last three calibers of body length. The slender body results show similar trends with the PNS results, but the contribution from the fins is over predicted by nearly a factor of two.

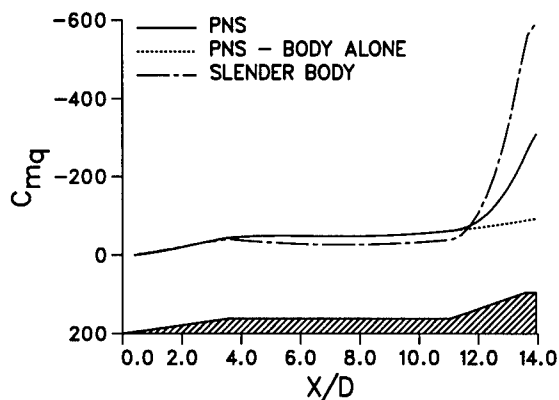


Figure 22. Development of the pitch-damping coefficient C_{m_q} over $L/D=14$ finned body, $M_\infty = 4$.

The distribution of the damping coefficient C_{m_α} is shown in Figure 23. PNS results for the finned body and

body-along configuration are shown along with slender body results. It is noted that the PNS results for the finned body are actually the coefficient sum $C_{m\dot{\alpha}} + C_{n_{p\alpha}}$ rather than the coefficient $C_{m\dot{\alpha}}$. The coefficient shows relatively little contribution from the nose and a modest contribution from the fins. The slender body theory again shows a trend similar to the PNS results although the magnitude of the variations is much larger.

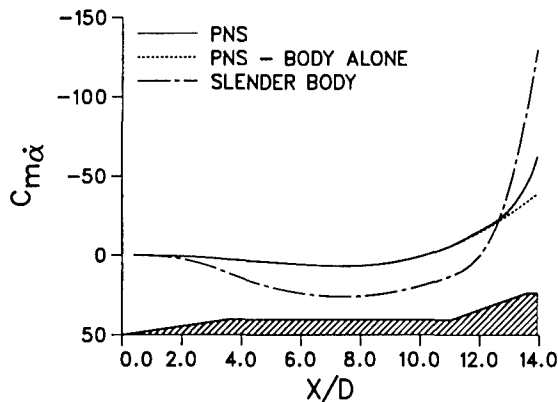


Figure 23. Development of the pitch-damping coefficient $C_{m\dot{\alpha}}$ over $L/D=14$ finned body, $M_\infty = 4$.

6. CONCLUSIONS

A method for predicting the pitch-damping characteristics of symmetric missiles using steady motions has been presented. Several types of steady motions are used to excite the aerodynamic forces and moments of interest. Two computational methods are applied to determine the pitch-damping coefficients at high subsonic, transonic, and supersonic flight velocities. The approach has been applied to compute the individual pitch-damping coefficients and the pitch-damping sum for axisymmetric and finned missile geometries. The predictions are validated with experimental data.

References

- Weinacht, P., and Sturek, W.B., "Navier-Stokes Predictions of Pitch Damping for Finned Projectiles Using Steady Coning Motion," AIAA Paper 90-3088, AIAA 8th Applied Aerodynamics Conference, Portland, OR, August 20-22, 1990.
- Weinacht, P., Sturek, W.B., and Schiff, L.B., "Navier-Stokes Predictions of Pitch-Damping for Axisymmetric Shell," *AIAA Journal of Spacecraft and Rockets*, Vol. 34, No. 6, pp. 753-761, Nov.-Dec. 1997.
- Weinacht, P., "Navier-Stokes Predictions of Pitch-Damping for a Family of Flared Projectiles," AIAA Paper 91-3339, 1991 AIAA 9th Applied Aerodynamics Conference, Baltimore, MD, September 1991.
- Weinacht, P., "Navier-Stokes Predictions of the Individual Components of the Pitch-Damping Coefficient Sum," AIAA Paper No. AIAA-95-3458, AIAA 1995 Atmospheric Flight Mechanics Meeting, Baltimore, MD, August 1995.
- Weinacht, P., "Prediction of Pitch-Damping Aerodynamics Derivatives Using Navier-Stokes Computational Techniques," Spring 1996, University of Delaware Ph.D. Dissertation, Newark, DE.
- Weinacht, P., "Prediction of Pitch-Damping of Projectiles at Low Supersonic and Transonic Velocities," AIAA Paper No. AIAA-98-0395, AIAA 36th Aerospace Sciences Meeting, Reno, NV, Jan. 1998.
- Murphy, C.H., "Free Flight Motion of Symmetric Missiles," U.S. Army Ballistic Research Laboratory, Aberdeen Proving Ground, Maryland, Report No. 1216, July 1963. (AD A442757)
- Baldwin, B.S., and Lomax, H., "Thin Layer Approximation and Algebraic Model for Separated Turbulent Flows," AIAA Paper 78-257, 16th Aerospace Sciences Meeting, January, 1978.
- Ying, S.X., Steger, J.L., Schiff, L.B., and Baganoff, D., "Numerical Simulation of Unsteady, Viscous, High-Angle-of-Attack Flows Using a Partially Flux-Split Algorithm," AIAA Paper 86-2179, August 1986.
- Sahu, J., and Steger, J.L., "Numerical Simulation of Three-Dimensional Transonic Flows," *International Journal for Numerical Methods in Fluids*, Vol. 10, 1990, pp. 855-873.
- Schiff, L.B., and Steger, J.L., "Numerical Simulation of Steady Supersonic Viscous Flow," *AIAA Journal*, Vol. 18, No. 12, December 1980, pp. 1421-1430.
- Murphy, C.H., and Schmidt, L.E., "The Effect of Length on the Aerodynamics Characteristics of Bodies of Revolution in Supersonic Flight," US Army Ballistic Research Laboratories, Report No. 876, Aberdeen Proving Ground, MD, August 1953.
- Schmidt, L.E., and Murphy, C.H., "The Aerodynamic Properties of the 7-Caliber Army-Navy Spinner Rocket in Transonic Flight," US Army Ballistic Research Laboratories, Memorandum Report No. 775, Aberdeen Proving Ground, MD, March 1954.
- Transonic Range Aerodynamic Database, U.S. Army Research Laboratory, Aberdeen Proving Ground, Maryland.
- Celmins, I., "Aerodynamic Characteristics of Fin and Flare-Stabilized 25mm XM910 Prototypes," US Army Ballistic Research Laboratory, Technical Report BRL-TR-2882, Aberdeen Proving Ground, MD, December 1987.
- Danberg, J.E., Sigal, A., and Celmins, I., "Aerodynamic Characteristics of a Family of Cone-Cylinder-Flare Projectiles," *Journal of Spacecraft and Rockets*, Vol. 27, No. 4, 1990, pp. 355-360.

COMPUTATIONAL FLUID DYNAMICS MODELING OF MULTIBODY MISSILE AERODYNAMIC INTERFERENCE

Jubaraj Sahu
Harris L. Edge
Karen R. Heavey
Earl N. Ferry

U.S. Army Research Laboratory
Aberdeen Proving Ground, MD 21005-5066, USA

ABSTRACT

Computational fluid dynamics (CFD) calculations have been performed for a multibody system consisting of a main missile and a number of submunitions. Numerical flow field computations have been made for various orientations and locations of submunitions using an unsteady, zonal Navier-Stokes code and the Chimera composite grid discretization technique at transonic speeds and zero degree angle of attack. Both steady-state and unsteady numerical results have been obtained and compared for a two-submunitions and missile system. Computed results show the details of the expected flow field features including the shock interactions. Computed results are compared with limited experimental data obtained for the same configuration and conditions and are generally found to be in good agreement with the data. Comparison of the unsteady and steady-state results do show an appreciable change in the aerodynamic forces and moments.

INTRODUCTION

Aerodynamic forces and moments are critical design parameters used in the design of shell and bodies flying in relative motion to each other. The advancement of computational fluid dynamics (CFD) has had a major impact on projectile design and development.¹⁻⁴ Improved computer technology and state-of-the-art numerical procedures enable solutions to complex, three-dimensional problems associated with projectile and missile aerodynamics. The research effort has focused on the development and application of a versatile overset grid numerical technique to solve multibody aerodynamic problems. This numerical capability

has been used successfully to determine the aerodynamics on a multibody problem of brilliant antiarmor (BAT) submunition dispersal from the Army tactical missile system (TACMS). Figure 1 shows a schematic diagram of this multibody system.

The complexity and uniqueness of this type of multibody problem result from the aerodynamic interference of the individual components, which include three-dimensional (3-D) shock-shock interactions, shock-boundary layer interactions, and highly viscous-dominated separated-flow regions. The overset grid technique, which is ideally suited to this problem, involves generating numerical grids about each body component and then oversetting them onto a base grid to form the complete model. With this composite overset grid approach, it is possible to determine the 3-D interacting flow field of the multibody system and the associated aerodynamic forces and moments at different positions and orientations without the need for costly regridding. The solution procedure of the developed technique is to compute the interference flow field at multiple locations until final converged solutions are obtained and then to integrate the pressure and viscous forces to obtain the total forces and moments. The complex physics and fluid dynamics structure of the 3-D aerodynamic interference for this multibody problem have been identified.

A description of the computational algorithm and the Chimera technique follow. The next section describes the model geometry and various computational grids used in the numerical computations. Results are shown for both steady-state computations for the missile with single and multiple BAT submunitions and a dynamic

computation with two submunitions at transonic speeds.

SOLUTION TECHNIQUE

Governing Equations. The complete set of 3-D, time-dependent, generalized-geometry, Reynolds-averaged, thin-layer Navier-Stokes equations is solved numerically to obtain a solution to this problem and can be written in general spatial coordinates ξ , η , and ζ as follows:⁵

$$\partial_\tau \hat{Q} + \partial_\xi \hat{F} + \partial_\eta \hat{G} + \partial_\zeta \hat{H} = Re^{-1} \partial_\zeta \hat{S}, \quad (1)$$

In Equation 1, \hat{Q} contains the dependent variables: density, three velocity components, and energy. The thin-layer approximation is used here, and the viscous terms involving velocity gradients in both the longitudinal and circumferential directions are neglected. The viscous terms are retained in the normal direction, ζ , and are collected into the vector \hat{S} . These viscous terms are used everywhere. In the wake or the base region, similar viscous terms¹ are also added in the streamwise direction, ξ . An implicit, approximately factored scheme is used to solve these equations.

Numerical Algorithm. The implicit, approximately factored scheme for the thin-layer Navier-Stokes equations using central differencing in the η and ζ directions and upwinding in ξ is written in the following form:⁶

$$\begin{aligned} & [I + i_b h \delta_\xi^b (\hat{A}^+)^n + i_b h \delta_\xi \hat{C}^n - i_b h Re^{-1} \delta_\zeta J^{-1} \hat{M}^n J \\ & - i_b D_i |_\zeta] \times [I + i_b h \delta_\xi^f (\hat{A}^-)^n + i_b h \delta_\eta \hat{B}^n \\ & - i_b D_i |_\eta] \Delta \hat{Q}^n = -i_b \Delta t \{ \delta_\xi^b [(\hat{F}^+)^n - \hat{F}_\infty^+] \\ & + \delta_\xi^f [(\hat{F}^-)^n - \hat{F}_\infty^-] + \delta_\eta (\hat{G}^n - \hat{G}_\infty) \\ & + \delta_\zeta (\hat{H}^n - \hat{H}_\infty) - Re^{-1} \delta_\zeta (\hat{S}^n - \hat{S}_\infty) \} \\ & - i_b D_e (\hat{Q}^n - \hat{Q}_\infty), \end{aligned} \quad (2)$$

where $h = \Delta t$ or $(\Delta t)/2$ and the free-stream base solution is used. Here, δ is typically a three-point second-order accurate central difference operator, $\tilde{\delta}$ is a midpoint operator used with the viscous terms, and the operators δ_ξ^b and δ_ξ^f are backward

and forward three-point difference operators. The flux \hat{F} has been eigensplit, and the matrices \hat{A} , \hat{B} , \hat{C} , and \hat{M} result from local linearization of the fluxes about the previous time level. Here, J denotes the Jacobian of the coordinate transformation. Dissipation operators D_e and D_i are used in the central space differencing directions.

Chimera Scheme. The Chimera overset grid technique⁷⁻⁹, which is ideally suited to multibody problems, involves generating independent grids about each body and then oversetting them onto a base grid to form the complete model. This procedure reduces a complex multibody problem into a number of simpler subproblems. An advantage of the overset grid technique is that it allows computational grids to be obtained for each body component separately and, thus, makes the grid generation process easier. Because each component grid is generated independently, portions of one grid may be found to lie within a solid boundary contained within another grid. Such points lie outside the computational domain and are excluded from the solution process. Equation 2 has been modified for Chimera overset grids by the introduction of the flag i_b to achieve just that. This i_b array accommodates the possibility of having arbitrary holes in the grid. The i_b array is defined such that $i_b = 1$ at normal grid points and $i_b = 0$ at hole points. Thus, when $i_b = 1$, Equation 2 becomes the standard scheme. But when $i_b = 0$, the algorithm reduces to $\Delta \hat{Q}^n = 0$ or $\hat{Q}^{n+1} = \hat{Q}^n$, leaving \hat{Q} unchanged at hole points. The set of grid points that form the border between the hole points and the normal field points are called intergrid boundary points. These points are updated by interpolating the solution from the overset grid that created the hole. Values of the i_b array and the interpolation coefficients needed for this update are provided by a separate algorithm.⁷ Figure 2 shows an example where the parent missile grid is a major grid and the BAT submunition grid is a minor grid. The submunition grid is completely overlapped by the missile grid, and thus its outer boundary can obtain information by interpolation from the missile grid. Similar data transfer or communication is needed from the submunition grid to the missile grid. However, a natural outer

boundary that overlaps the submunition grid does not exist for the missile grid. The overset grid technique creates an artificial boundary or a hole boundary within the missile grid that provides the required path for information transfer from the submunition grid to the missile grid. The resulting hole region is excluded from the flow field solution in the missile grid.

The Chimera method depends on three functions: domain connectivity, aerodynamics, and body dynamics. The aerodynamics code depends on the domain connectivity code¹⁰ to supply hole and interpolation information. The domain connectivity code, in turn, depends on the body dynamics code to supply the location and orientation of the moving bodies relative to the primary body. Finally, the body dynamics code depends on the aerodynamics code to provide the aerodynamic forces and moments acting on the moving bodies. For moving-body problems, all grids are allowed to move with 6 degrees of freedom (DOF) relative to an inertial reference frame. Accordingly, bodies can move with respect to others without the necessity of generating new grids. With this composite overset grid approach, it is thus possible to determine the aerodynamics associated with the bodies without the need for costly regridding. This also eliminates potential accuracy problems due to severe grid stretching used by many other techniques, such as the zonal blocked grid method commonly used in CFD.

MULTIBODY PROBLEM DESCRIPTION

The TACMS-BAT multibody problem involves the radial dispensing of several BAT submunitions (see Figure 1) at a transonic speed and, thus, was ideally suited for the numerical capability¹¹ described earlier. The 3-D radial dispensing of these submunitions depends on the initial ejection velocity. The flow field is complex and involves 3-D shock-boundary layer interactions, and TACMS-to-BAT as well as BAT-to-BAT interactions. Detailed experimental or theoretical data were not available to help evaluate the submunition dispensing phenomenon for the entire BAT system, and thus the numerical solution of this problem was initiated. The Chimera solution procedure was thus used to

determine the aerodynamic interference effects, and CFD was brought into the developmental phase of the BAT program to ensure successful dispensing of the submunitions.

The missile carries 13 submunitions; the first 10 outer BAT submunitions are radially dispensed, followed by the dispensing of 3 inner BAT submunitions from the TACMS. Once released from the missile bay, the self-guided BAT submunitions autonomously disperse over the hostile territory, use their sensors to detect targets, and deliver shaped charged warheads. The concern here is the flight dynamics and aerodynamics of the dispensing phenomenon. Application of the advanced CFD modeling technique to this multibody dispensing problem was to provide realistic simulation, detailed understanding of the underlying aerodynamic interference effects, and design information that can lead to successfully dispensing the BAT submunitions from the TACMS.

MODEL GEOMETRY AND GRIDS

An advantage of the Chimera technique is that it allows computational grids to be obtained for each body component separately and, thus, makes the grid generation process easier. Figure 3 shows a computational grid for the complete model, including the missile and the BAT submunitions. Also shown here are the sections of the three-dimensional BAT computational grids overset onto the missile grid. Figure 4 shows a computational grid for one BAT submunition. As part of the Chimera procedure, this BAT grid is partially cut by the missile body itself. Similarly, the presence of the BAT submunition cuts a hole in the missile grid (see Figure 5). The missile grid consists of three zones: one on the nose region ahead of the cavity, one in the cavity itself, and the third one aft of the cavity region. Each of these three zones is a rectangular grid. The grid around the submunition consists of two zones (one for the body and one for the base region) and was obtained using an C-topology and a rectangular topology, respectively. The submunition grids were individually generated and then overset as shown in Figure 3 to form the complete grid system. The computational grids shown here correspond to the pitch plane. The

missile grid serves as the main background grid for the computations. Figure 4 shows a computational grid for computations with the BAT submunition at a distance about a diameter away from the center line of symmetry of the missile. For steady-state or unsteady dynamic computations, the same submunition grids are used, and there was no need to regenerate new submunition grids. Typically, the missile grid consisted of 983,000 points. The entire grid system consisted of about 1.2 million points for the missile and one-BAT (with and without sting) case as well as for the two-BAT cases. Note that the grid setup allows computation of the base region flow field of the submunitions. Grid points are clustered near the missile and the BAT submunition surfaces to capture the viscous boundary layers. No attempt has been made to adapt the computational grids to gradients in the flow field variables.

The actual cavity surface of the missile bay where the BATs are stored in their original positions was used in the CFD computations. The flow field in the bay is viscously dominated, turbulent, and quite complex, with the BAT located in the near field. It is difficult to accurately determine the interference effects by theoretical or experimental means. This is especially true when the BAT is submerged in the bay. Limited wind-tunnel experimental data¹² are available for a reduced-scale model for the missile and BAT submunitions. However, such data can suffer from sting effects and for viscously dominated cavity flows may not scale to the real flight conditions.

RESULTS

Both steady-state and a dynamic unsteady numerical calculations have been performed to numerically simulate the missile and the BAT system. Computations have been run at $M_\infty = 1.2$ and 1.5. Computational modeling is restricted to the symmetric submunition dispersal. Here, the missile is at 0° angle of attack, and the BATs are dispensed symmetrically following the same radial trajectory away from the projectile. Appropriate symmetry is used for the one-BAT and multiple-BAT cases. For the multiple-BAT cases, the computational domain consists of a 36°

segment in the circumferential plane (see Figure 6). Also shown is the submunition grid, which is entirely contained in the background projectile grid. Because of symmetry, the requirements for grid sizes, computer resources such as computer memory, and run time are reduced.

The CFD modeling was initially used to compute transonic flow over the wind-tunnel model consisting of the missile and one sting-mounted BAT. Computations were also performed for the BAT without the sting for direct comparison (Figure 7). Computed Mach contours show some influence of the sting on the solution near the aft end of the cavity. Quantitatively, it affects the forces and moments acting on the BAT submunition and, to a lesser extent, on the missile itself. Computed surface pressures obtained from the flow field solution for the BAT submunition were compared with experimentally measured pressure on the BAT and were found to be in very good agreement for two different radial locations of the submunitions (Figure 8). Computed surface pressure on the missile cavity surface is shown in Figure 9 for the one-BAT case. Computed surface pressures again agree well with the experimental data. These comparisons lend confidence in the quality of the CFD results for the multibody system consisting of the missile and one BAT. The CFD modeling includes the wake and the base region of the BAT as they would be in real flight situations.

For the actual system, which consists of the TACMS and the 10 outer BAT submunitions, the present CFD capability was then used to compute the flow field for the flight conditions. This case now included not only BAT-to-TACMS interactions but also 3-D BAT-to-BAT interactions. Figure 10 shows the results of such a numerical simulation for the symmetric dispense of all 10 BAT submunitions from the TACMS. The computed Mach contours are shown at two selected positions along the BAT submunitions. The 3-D BAT-to-BAT interactions are clearly depicted in this figure. To get a better understanding of the aerodynamic interference associated with the TACMS-BAT system, numerical computations were performed with the BAT submunitions at various radial positions away from the missile. Figure 11 shows the

computed results for these cases for the actual transonic flight conditions from bottom to top. The first position corresponds to the BAT submunitions semi-chambered in the bay (cavity) of the missile. The next two positions are approximately 20.4 and 25.8 inches away from the center line of the missile. These pictures clearly show the complicated aerodynamic interference between the missile and the BAT submunitions in a longitudinal view. The flow inside the cavity is primarily subsonic and contains large regions of separated flow. The dramatic change in the interacting flow field can be observed as the BAT submunitions move farther and farther radially out from the semi-chambered position. The flow field over the submunitions is 3-D, and the computed results clearly show this feature in the wake or base region of the submunitions.

Computations were also performed for this multibody problem with five BATs at $M_\infty = 1.2$ and $\alpha = 0^\circ$. This case included modeling of half of the actual missile bay. Figure 12 shows the Mach number contours for this case. Qualitatively, it shows the expected shock structure and the flow field resulting from the submunition interactions. Figures 13 and 14 show the circumferential Mach number contours for the five-BAT case at two longitudinal stations, 2.5 and 3.2 calibers from the nose of the missile. Both locations are in the cavity of the missile. These figures show the BAT-to-BAT interactions and the effect of the cavity shape on the solutions. Figure 13 indicates a smaller region of low speed flow between the cavity surface and the bottom surfaces of the BATs and high speed flow near the top surfaces of the BATs. At a station downstream in the cavity, Figure 14 shows a large region of the low speed flow between the BATs and missile cavity surface as well as near and away from the top surfaces of the BATs. Aerodynamic forces and moments were obtained from the computed solutions. Figure 15 shows normal force coefficient, axial force coefficient, and pitching moment for the submunitions as a function of radius (measured from the center line of symmetry of the missile). These computed force and moment coefficients were compared with the experimental data and are found to be in good agreement with the data. The measured axial force coefficient does not include base drag

and computed axial force coefficient also excludes base drag of the submunitions for direct comparison.

A dynamic simulation was performed for the missile and the two-BAT case at $M_\infty = 1.5$ and $\alpha = 0^\circ$. The dynamic computations were started from a converged steady state solution with the submunitions located in the cavity chamber. The same computational grids (Figure 6) were used for the entire dynamic simulation event without the need of regridding. The Chimera procedure described earlier was also used for this computation. The forces and moments provided by the aerodynamics code were used by the body dynamics code to determine the location and orientation of the moving submunitions relative to the missile. This required domain connectivity (hole and interpolation information) at each time step. The domain connectivity information was then used in the aerodynamics code to provide the aerodynamic forces and moments. This procedure was repeated at each time step during the dynamic simulation. Figure 16 shows three snapshots of computed pressure contours in time. It shows the flow field changing significantly with the submunition being dispensed. The bottom picture corresponds to the initial position of the submunitions. The other two correspond to 16 and 45 msec in time. The submunitions were restricted to the pitch plane and were not allowed to yaw or roll. Figure 17 shows the force and moment history as a function of time. Shown here are the normal force, axial force, and pitching moment coefficients for the submunition. Since the computations include two-BAT submunitions, BAT-to-BAT interactions are included. These interactions are critical and have a strong effect on the aerodynamic forces and moments. The normal force and pitching moment coefficients indicate the unsteady nature of the interacting flow field. A case that corresponds to 16 msec in time during the dynamic simulation was selected and frozen to run a steady-state computation. This case corresponded to the submunition being at an angle -1° nose down (pitch angle). A static converged solution was then obtained for the missile and the submunitions in that orientation. Comparison of the static and dynamic results for this case is shown in Table 1. Again, all three force and moment coefficients are included. The axial force

coefficient (with or without base drag) does not change appreciably; however, normal force and pitching moment coefficients are seen to change significantly. These results indicate the importance of the dynamic numerical simulation, which may be needed to accurately predict the aerodynamics of the submunition dispersal.

CONCLUDING REMARKS

A computational study was undertaken to compute the 3-D flow fields for a multibody system consisting of a missile and multiple BAT submunitions. Flow computations were performed at transonic speeds ($M_\infty = 1.2, 1.5$) and $\alpha = 0.0^\circ$ using a 3-D unsteady Navier-Stokes code and Chimera composite grid discretization technique. Overset body conforming grids were used to individually model the missile and the BAT submunitions. Computed results have been obtained for different locations of the submunitions. Computed pressure and Mach contours show the details of the 3-D aerodynamic interference flow field for the missile and the submunitions. The computed flow field includes both the missile-to-BAT as well as BAT-to-BAT interactions. Both computed results for sting-mounted and no-sting models have been obtained for the one-BAT case, and the computed results do not show appreciable change in the surface pressures. Computed results for the multiple-BAT cases include BAT-to-BAT interactions and show their large effect on the computed forces and moments. Computed surface pressures as well as forces and moments have been compared with the experimental results for the same configuration and conditions and are generally found to be in good agreement with the data. Dynamic unsteady results were also obtained for a multiple-BAT case and compared with the static results for the same location and orientation of the submunitions. These comparisons show, in some cases, large changes in the aerodynamic force and moments between the static and dynamic computations. Future study will include modeling of asymmetric submunition dispersal, which will require full 3-D computations and large computing resources.

This work represents the application of a Chimera overlapping grids approach for accurate numerical calculation of aerodynamics involving multiple

bodies with and without relative motion. The predictive numerical capability has been used to provide the development community numerical data and basic flow field design information to more effectively guide the design of a multibody missile configuration. It allows accurate and realistic numerical prediction of interference effects and aerodynamics required for the improved design and modification to current and future multibody missile and projectile configurations.

REFERENCES

1. Sahu, J., "Numerical Simulations of Transonic Flows." *International Journal for Numerical Methods in Fluids*, vol. 10, no. 8, pp. 855-873, 1990.
2. Ferry, E. N., J. Sahu, and K. R. Heavey, "Navier-Stokes Computations of Sabot Discard using Chimera Scheme." Proceedings of the 16th International Symposium on Ballistics, September 1996.
3. Sahu, J., K. R. Heavey, and E. N. Ferry, "Computational Fluid Dynamics for Multiple Projectile Configurations." Proceedings of the 3rd Overset Composite Grid and Solution Technology Symposium, Los Alamos, NM, October 1996.
4. Sahu, J., K. R. Heavey, and C. J. Nietubicz, "Time-Dependent Navier-Stokes Computations for Submunitions in Relative Motion." Proceedings of the 6th International Symposium on Computational Fluid Dynamics, Lake Tahoe, NV, Sep. 1995.
5. Pulliam, T. H., and J. L. Steger, "On Implicit Finite-Difference Simulations of Three-Dimensional Flow," *AIAA Journal*, vol. 18, no. 2, Feb. 1982, pp. 159-167.
6. Steger, J. L., S. X. Ying, and L. B. Schiff, "A Partially Flux-Split Algorithm for Numerical Simulation of Compressible Inviscid and Viscous Flows." Proceedings of the Workshop on CFD, Institute of Nonlinear Sciences, University of California, Davis, CA, 1986.
7. Steger, J. L., F. C. Dougherty, and J. A. Benek,

"A Chimera Grid Scheme." *Advances in Grid Generation*, edited by K. N. Ghia and U. Ghia, ASME FED-5, June 1983.

8. Benek, J. A., T. L. Donegan, and N. E. Suhs, "Extended Chimera Grid Embedding Scheme With Application to Viscous Flows." AIAA Paper No. 87-1126-CP, 1987.

9. Meakin, R. L., "Computations of the Unsteady Flow About a Generic Wing/Pylon/Finned-Store Configuration." AIAA 92-4568-CP, August 1992.

10. Meakin, R. L., "A New Method for Establishing Inter-Grid Communication Among Systems of Overset Grids," AIAA 10th Computational Fluid Dynamics Conference, AIAA Paper No. 91-1586, June 1991.

11. Sahu, J., and C. J. Nietubicz, "Application of Chimera Technique to Projectiles in Relative Motion." ARL-TR-590, U.S. Army Research Laboratory, Aberdeen Proving Ground, MD, October 1994 (also see *AIAA Journal of Spacecraft and Rockets*, vol. 32, no. 5, Sep-Oct 1995).

12. Wooden, P. A., Brooks, W. B., Sahu, J., "Calibrating CFD predictions For Use In Multiple Store Separation Analysis," AIAA Paper No. 98-0754, January 1998.

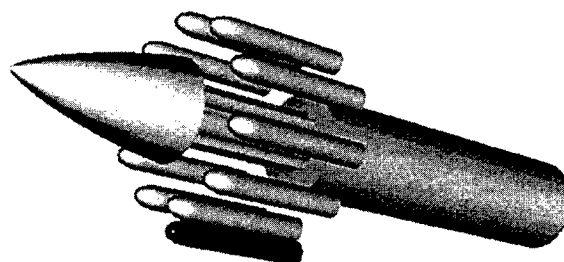


Figure 1. Schematic diagram of the multibody system

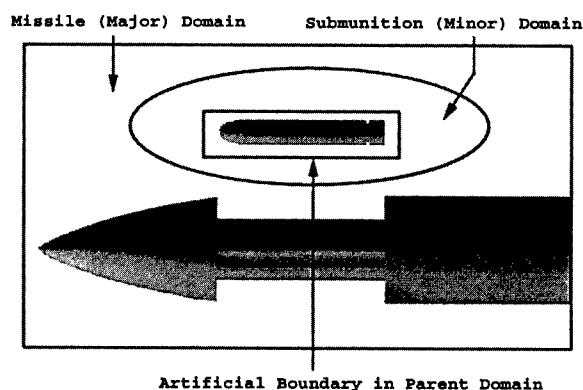


Figure 2. Intergrid communications

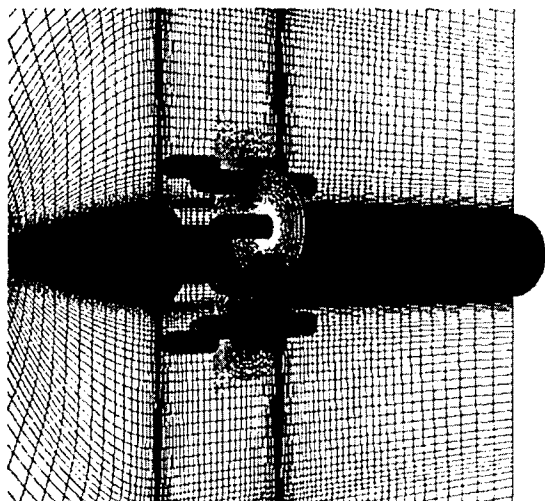


Figure 3. Grids for the BAT submunition dispensing from TACMS

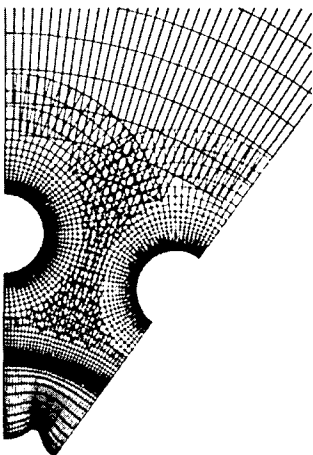


Figure 6. Circumferential cross-sectional grid

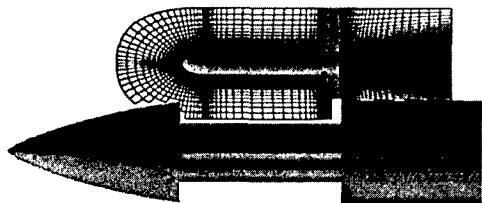


Figure 4. Computational grid for a submunition

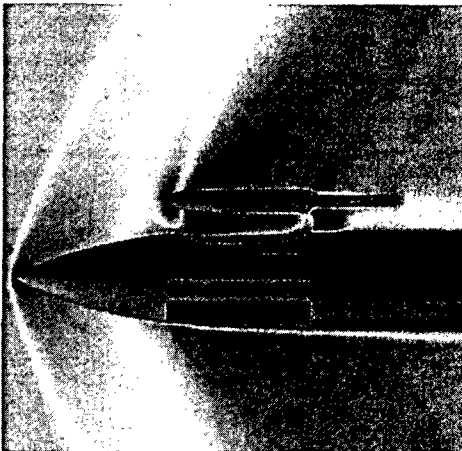
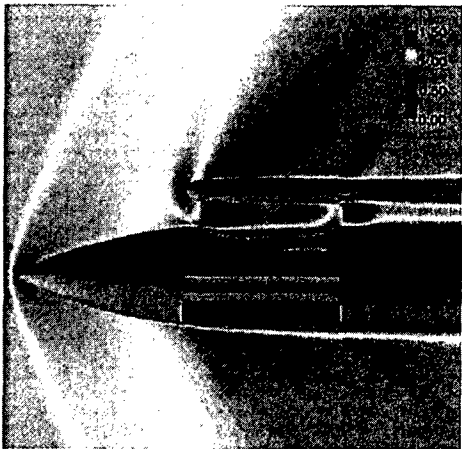


Figure 7. Computed Mach contours for single submunition with sting and no sting

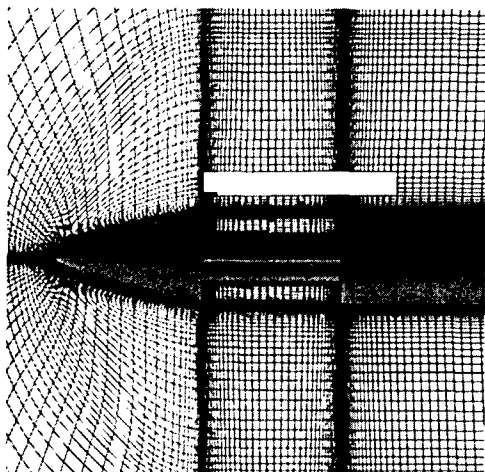


Figure 5. Computational grid for the missile

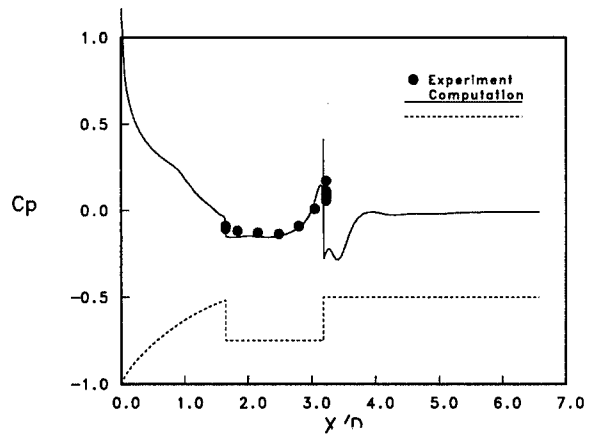
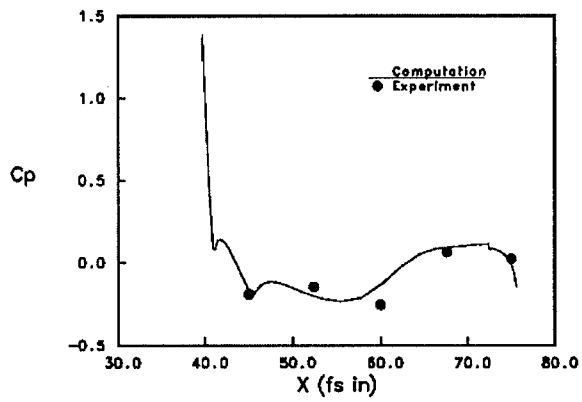


Figure 9. Computed surface pressure on the missile

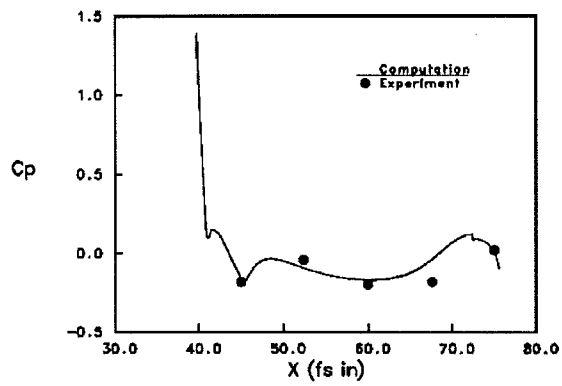


Figure 8. Computed surface pressures on the submunition at radius 20.35 (top) and 25.85 inch (bottom)

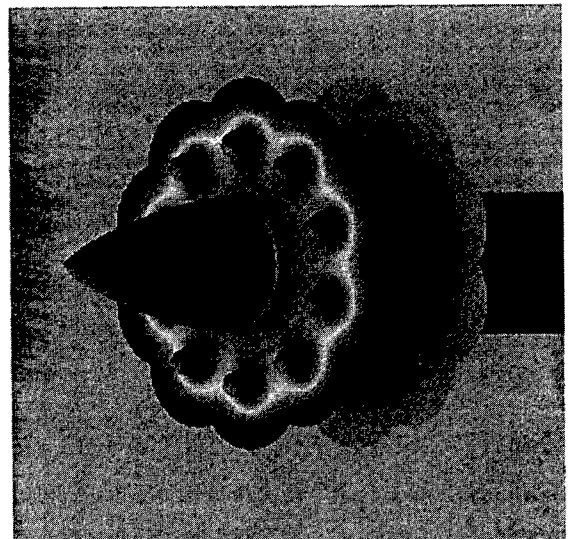


Figure 10. BAT-to-BAT interactions

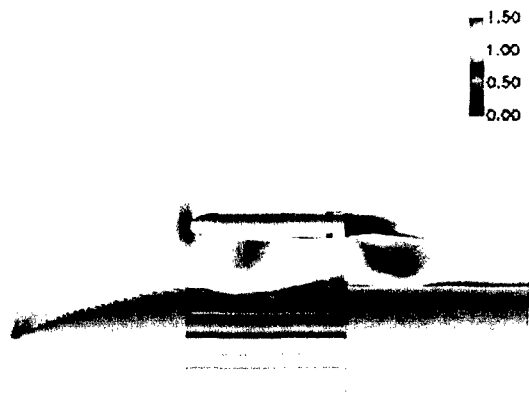


Figure 11. BAT-to-TACMS interactions for various submunition locations

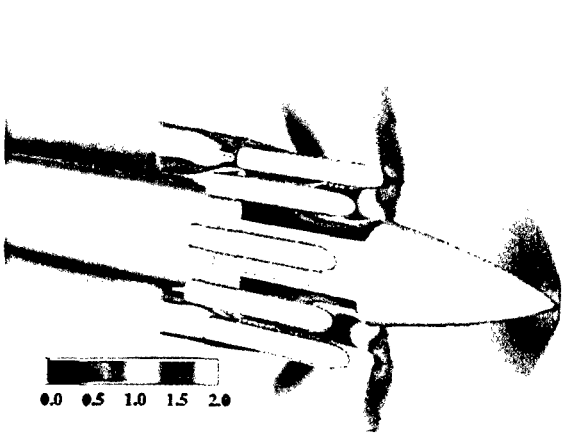


Figure 12. Mach contours for the 5-BAT case

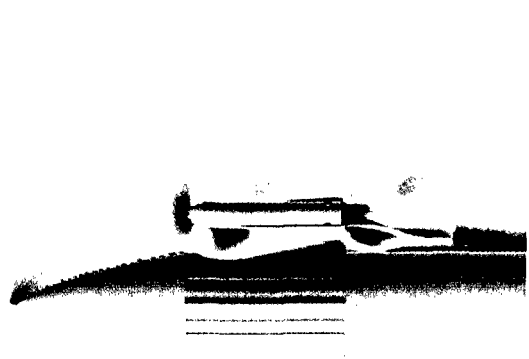


Figure 13. Mach contours at $X/D = 2.5$ calibers

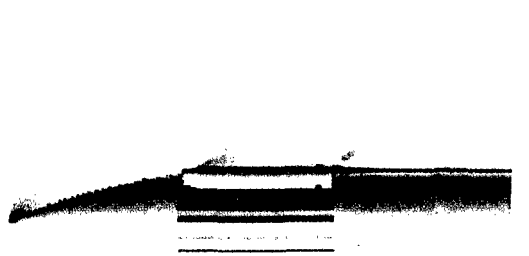


Figure 14. Mach contours at $X/D = 3.2$ calibers

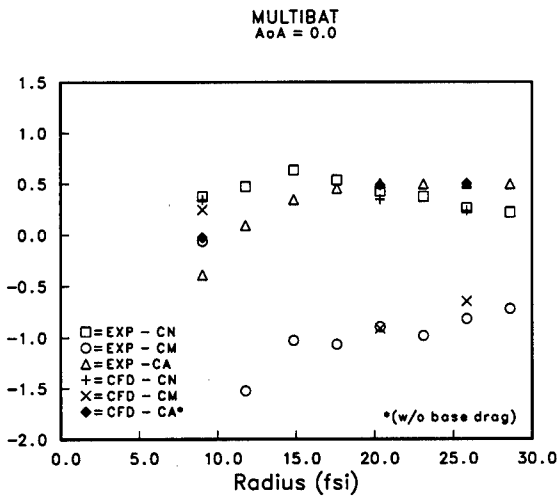


Figure 15. Force and moment coefficients

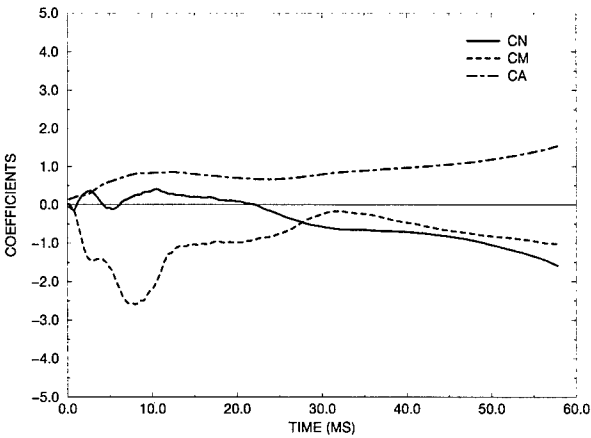


Figure 17. Time history of force and moment

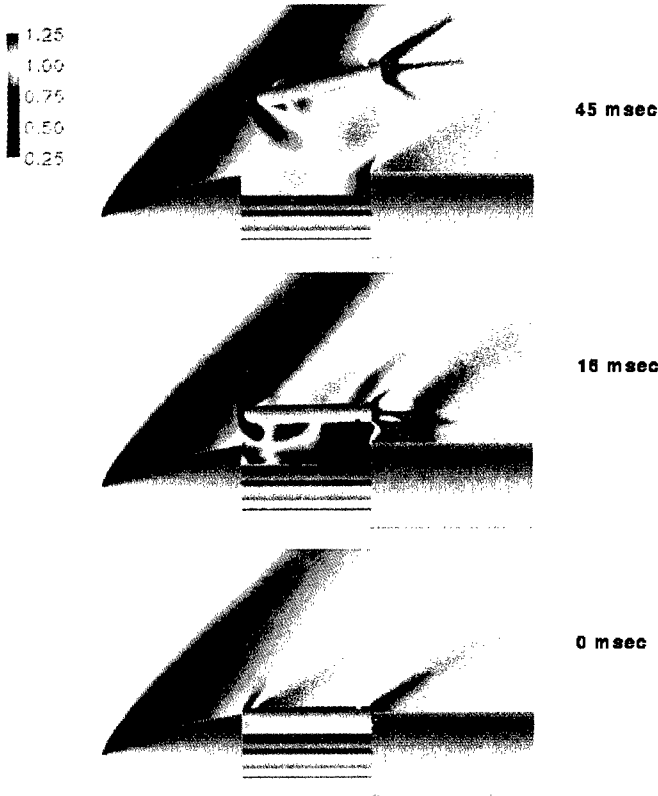


Figure 16. Mach contours for the dynamic case

Table 1. Static and dynamic force and moment comparison

	DYNAMIC	STATIC
	R= 20.23 fsi	R= 20.23 fsi
C _N	+ 0.18713	+ 0.39314
C _m	-1.02569	- 0.79019
C _A		
w/ base drag	+ 0.77647	+ 0.79422
w/o base drag	+ 0.56007	+ 0.58581

ADVANCES IN MISSILE AEROPROPULSIVE FLOWFIELD SIMULATION*

S. M. Dash
Combustion Research and Flow Technology, Inc.
174 North Main Street, P.O. Box 1150
Dublin, PA 18917 USA

B. J. Walker
U.S. Army Aviation and Missile Command
Attn: AMSAM-RD-SS-ST
Redstone Arsenal, AL 35898 USA

SUMMARY*

This paper summarizes advances made in Navier-Stokes predictive methodology for missile aeropropulsive flowfields implementing both structured and unstructured grid numerics. Future missile systems will be relying on varied forms of jet interaction control for enhanced maneuverability. The simulation of jet/aerodynamic interactions entails dealing with solid-propellant thermochemical and multi-phase flow issues as an integral part of the missile aerodynamic solution. Thrust amplification can be affected by both afterburning and by gas/particulate interactions. Turbulence modeling requires many advances not needed for conventional missile aerodynamic predictions. This paper will address the systematic upgrade and validation of structured and unstructured grid Navier-Stokes codes (CRAFT and CRUNCH) to deal with such aeropropulsive interactions. Another topic to be discussed is the treatment of cavity aeroacoustics and store dispense. Recent studies have highlighted the need to utilize a large eddy simulation (LES) framework to correctly predict the magnitude and spectral characteristics of cavity pressure-oscillations. Inclusion of varied grid-movement capabilities into a multiple-domain variant of the CRUNCH code permits it to analyze multi-body flows, with flux interfacing at domain boundaries providing improvements in accuracy over overset (Chimera) methods, particularly for closely spaced bodies where viscous effects strongly influence the aerodynamic coefficients. This new approach is being applied to submunition dispense, stage/booster separation, sensor window shroud removal, and related problems.

1.0 INTRODUCTION

1.1 Overview Of CRAFT Structured-Grid Code Features and Applications

The CRAFT Navier-Stokes code has been operational since 1990. Its development has entailed extension of implicit/upwind (Roe/TVD based) finite-volume numerics (formulated for hypersonic Space Plane applications under the NASP program) to varied combustive and aeropropulsive applications requiring advanced multi-phase capabilities for both liquid and solid propellant systems. At the previous NATO Missile Aerodynamics Symposium, Navier-Stokes capabilities described [1] utilized ADI-based central-difference numerics and contained basic thermochemical and turbulence model features. Such capabilities are supporting missile system design by industry, as typified by the applications of Srivastava [2].

The CRAFT code contains research grade nose-to-tail capabilities for both rocket [3,4] and airbreathing [5,6] missile systems with current research efforts focused on upgrades to the particulate and multi-phase combustive aspects for propulsive system and plume/aerodynamic interactive flowfield predictions, as will be discussed in a later section of this paper.

* Paper No. 31. Presented at Applied Vehicle Technology Panel Symposium and Meeting on "Missile Aerodynamics" NATO/RTO, Sorrento Palace Hotel Congress Center, Sorrento, Italy, 11-15 May 1998.

The present version of CRAFT contains rather generalized nonequilibrium capabilities for gas/particle interactions, utilizing either Eulerian or Lagrangian numerics for the dispersed phase, and including dense volumetric terms in the governing equation as well as a rather detailed representation of particulate/droplet combustion and/or vaporization [7,8].

Missile activities with CRAFT had earlier addressed signature-prediction simulation, highlighting the significant effects of aerodynamic interactions (in base/separated regions) on the structure of conventional (straight-back) plumes [9,10]. Other related work addressed the simulation of plume interactions in missile launchers [11]. Such problems involved complex 3D geometries and the need to adequately resolve varied (and often disparate) scales associated with nonequilibrium chemistry and particulate interactions. The practical solution of such flowfields required the utilization of parallel-architecture computers. A domain-decomposition approach was employed to parallelize the CRAFT code [12] with MPI implemented for interprocessor message passing. Adjacent domains can be interfaced with noncontiguous grids which can slide to permit relative motion in different grid frameworks (e.g. this would be used to interface missile fixed and launcher fixed grids in analyzing the flyout from a missile canister).

Present activities with CRAFT are focused on the evaluation and upgrade of turbulence and thermochemical/particulate modeling for missile aerodynamic applications. This work feeds directly into the upgrade of the unstructured-grid code, CRUNCH, as will be described in the next section. Turbulence modeling for flows with jet/plume interactions [13,14] requires going beyond a conventional (linear) two-equation (e.g. k- ϵ) framework, and entails dealing with high Mach number compressibility effects, with variations in turbulent Prandtl/Schmidt numbers, as well as with turbulent/chemical/particulate interactions. A section on turbulence modeling will highlight advances made in this area. Another area of recent emphasis is that of cavity aeroacoustics for which an LES framework is implemented [15]. This will also be discussed in the turbulence section. Present features of the CRAFT code are summarized below in Table I.

1.2 Overview Of CRUNCH Unstructured-Grid Code Features and Applications

CRUNCH code developmental activities initiated several years ago, with the starting point being the unstructured Euler code work of Barth, as contained his TRI3D code [16]. TRI3D implemented an edge-based cell-vertex structure, reducing memory requirements and flux construction operations from that of codes utilizing a cell-centered data structure. The upwind (Roe/TVD-based) finite-volume numerics in TRI3D were analogous to CRAFT's. A four-step Runge-Kutta integration procedure was implemented. The CRUNCH code is a full Navier-Stokes solver with generalized thermochemical and turbulence modeling capabilities. The research and development in going from TRI3D to CRUNCH has been quite substantive, with the path greatly expedited by the availability of many capabilities in the CRAFT code. A number of routines and procedures could be extracted from CRAFT and incorporated into CRUNCH with minimal extra manipulation.

Table I. Present Features of the CRAFT Three-Phase Navier-Stokes Code

NUMERICS	<ul style="list-style-type: none"> • 1D/2D/AXI/3D Finite-Volume Discretization • Implicit, Higher-Order Upwind (Roe/TVD) Formulation • Fully Implicit Source Terms/Boundary Conditions • Domain-Decomposition Parallel Architecture with MPI • Preconditioning Extensions
GRID FEATURES	<ul style="list-style-type: none"> • Grid Dynamics to Account for Moving Boundaries • Grid Patching/Blanking for Complex Geometries • Solution-Adaptive Gridding and Grid Embedding • Noncontiguous Grid Interfacing with Flux Preservation Across Domains
THERMO-CHEMISTRY	<ul style="list-style-type: none"> • Real Gas Mixtures (Calorically and Thermally Imperfect/JANNAF Thermo Tables/Virial EOS) • Finite-Rate Chemistry/Arbitrary Number of Species and Reactions • Fully Implicit Source Term Linearization
MULTIPHASE FLOW	<ul style="list-style-type: none"> • Nonequilibrium Particle/Droplet Solvers (Eulerian and Lagrangian Formulations) • Gas/Liquid Formulations with Volumetric Contributions • Grain/Ablative Coupling with Coupled Surface Recession • Fluidized Bed Combustion
HEAT/MASS TRANSFER	<ul style="list-style-type: none"> • Coupling with 3D Transient Heat Conduction Solution • Generalized Mass Transfer Boundary Conditions and Phase-Change
TURBULENCE	<ul style="list-style-type: none"> • $k-\epsilon$ /EASM Formulations with Compressibility/Vortical Upgrades and Several Low Re Near-Wall Formulations, Compressible Wall Function Methodology • LES Subgrid Scale Models • Particle Dispersion Formulations

Earliest work entailed the transitioning from Euler to viscous, and the inclusion of generalized multi-component gaseous species and chemical kinetics. The inclusion of combustion capabilities was not simplistic and entailed revisions to the flux limiters to permit capturing thin flamed zones [17,18]. Figure 1 shows a CRUNCH code prediction of shock-induced H₂/Air combustion in a duct using a tetrahedral mesh, while Figure 2 compares CRUNCH code and CRAFT code predictions for this problem. Further details and comparisons for blunt-body shock-induced combustion with the data of Lehr are described in Refs. 17 and 18.

Subsequent upgrades to CRUNCH entailed the inclusion of multiple-volume grid element capabilities (tets, hexes, pyramids, prisms, ...) and extensions to operate on parallel hardware platforms using domain-decomposition with MPI, as was done for CRAFT [19,20]. This step permitted utilization of hybrid grids and hence, wall normal meshes adjacent to solid surfaces which could be interfaced with outer region tetrahedral grids. Turbulence modeling extensions to date, have entailed the inclusion of a high Reynolds number, $k-\epsilon$ two-equation model with the near wall analyzed using a compressible wall function. The inclusion of two-equation turbulence modeling into an unstructured framework has not been straightforward and has also entailed specialized logic with flux limiters to permit obtaining solutions with tetrahedral grids that are comparable to those obtainable with a structured (or hex-based unstructured) grid. A number of unit problem comparative studies were performed to ensure proper operation of the turbulence modeling in CRUNCH for wall-bounded and free shear flows [19,20]. Figure 3 shows turbulent kinetic energy comparisons for a hot axisymmetric jet problem, comparing CRUNCH(tet-grid) and CRAFT code predictions. Figure 4 shows comparisons of a Mach 2.5 missile flowfield problem at a 10° angle-of-attack where CRUNCH used the $k\epsilon$ model with wall function [19]. Extensions to operate with implicit numerics using GMRES

matrix inversion is discussed in Ref. 20. The present features available in the CRUNCH code are summarized below in Table II. A discussion of multi-body flow extensions is presented in a later section.

2.0 TURBULENCE MODELING OVERVIEW

Turbulence modeling for missile aerodynamic predictions that are influenced by plume interactions requires going well beyond simple algebraic or basic two-equation (e.g. $k-\epsilon$) models. Free shear flows (including separation streamline shear layers) require incorporating compressibility effects to properly predict the observed reduction in mixing rates. Flows with vortical interactions require utilization of nonlinear stress-strain relations, as contained in full or reduced Reynolds-Stress models. Thermal/species turbulent diffusion may not be well represented by use of constant Prandtl and Schmidt numbers. Turbulent/chemistry/particle interactions cannot be neglected in many situations and models must be available to properly represent such effects.

Exploratory studies with an advanced turbulence modeling framework (Table III) are now in progress with some of the more recent work described in Refs. 6 and 21. Use of the Gatski-Speziale EASM model in combination with Sarkar compressibility-corrections (CC) has led to excellent comparisons of the Gruber-Dutton high speed shear layer data ($M_1=2.36/T_1=132k$; $M_2=0.27/T_2=285k$ – balanced-pressure) for which all three normal stress values are measured. The basic $k\epsilon$ model (see Ref. 13) over-predicts the spread rate and all turbulent stresses, with normal stresses being isotropic due to the linear stress-strain relation. The EASM model [23] predicts the non-isotropy and when supplemented by the latest Sarkar compressibility extensions (see Ref. 21), correctly predicts turbulent shear and normal stresses as shown in Figure 5.

Table II. Present Features of the CRUNCH Unstructured Navier-Stokes Code

NUMERICS	• Finite-Volume Roe/TVD Flux Construction, Vertex Storage
INTEGRATION	• Explicit Four-Step Runge-Kutta, Implicit GMRES
GRID ELEMENTS	• Tets, Hexes, Pyramids, ...
MULTI-BLOCK CAPABILITIES	• Domain Decomposition MPI, Independent Grids with Noncontiguous Interfacing
DYNAMIC GRID CAPABILITIES	• Node Movement Solver (Explicit Spring Analogy, Implicit — Linear Elasticity), Automated Embedding, Sliding Interfaces
GRID ADAPTION	• Gradient Based Embedding for Tets (3DTAG) and Hexes (Research Code)
THERMOCHEMISTRY	• Multi-component Gaseous Mixtures, Finite-Rate Kinetics
TURBULENCE	• $k\epsilon$ for RANS Applications with Compressible Wall Function, Smagorinsky LES for Dynamic Applications
MULTIPHASE FLOW	• Lagrangian Particulate Solver, Loosely Coupled
APPLICATIONS	• Advanced Missile Systems • Automotive Engine In-Cylinder Combustion • Store Separation • Cavity Aeroacoustics • Aircraft and Rotorcraft Plume/Wake Interactions

Table III. Advanced Turbulence Modeling Framework

Baseline Model	– Nonlinear extension of $k\epsilon$ Gatski/Speziale explicit algebraic stress model (EASM)
Compressibility	– Compressible-dissipation and pressure-dilatation models of Sarkar (CC)
Vortex-Stretching	– Compressible variation of Pope correction
Near-Wall	– Wall function, two-layer and low Re models
Variable Prandtl and Schmidt Numbers	– From solution of scalar fluctuation* and dissipation rate equations (k_g, ϵ_g) based on extensions of Nagano model

* Scalar fluctuation equations are also used for turbulent/chemistry PDF modeling work and for aero-optic/RCS signal propagation modeling which requires rms values of density/electron fluctuations.

Marked improvements are also obtained in analyzing jet-induced separation, performed for sonic N_2 normal slot injection into a Mach 2.7 approach flow for a static pressure ratio of 20/1. Mach number contours for this case are shown in Figure 5 (EASM/CC prediction) while pressure comparisons with data are shown in Figure 6. Two layer near-wall modeling is implemented since low Re models perform erratically for "real" (hot/combusting) jets whose analysis entails considerations of substantive near-wall density variations. Calculations are now in progress for this case using adaptive gridding (which should further improve solution quality) and for comparable cases with He injection, and with H_2 injection and combustion.

3.0 MULTIPHASE MODELING OVERVIEW

Multiphase flow capabilities in the CRAFT code have been derived from applications to varied problems, as summarized in Table IV. The methodology for inclusion of such capabilities into a Navier-Stokes framework is so specialized and problem-specific, that we maintain different versions for different applications.

Lagrangian methodology permits a detailed representation of ignition/vaporization/combustion and the numerical framework is grid independent permitting its utilization in both structured and unstructured gas-phase solvers. However, it can be computationally intensive and is cumbersome to implement with RANS turbulence modeling frameworks since the eddy scales must be tracked by the particles. Our implementation of Lagrangian methodology has primarily focused on transient flows and on LES simulations. Figure 7 exhibits an LES simulation of a supersonic jet laden with dilute particles of varied sizes showing the enhanced dispersion of mid-sized particles.

Eulerian methodology has been applied to steady rocket propulsive flows where the initial size distribution (at the nozzle entrance) is subdivided into several size bins. Figure 8 exhibits a three-size bin solution of a nozzle with Al_2O_3 particles subdivided into 1, 3.5, and $10\mu m$ bins. The solutions shows the striations associated with subdividing a continuous size distribution into a small number of bins — finer subdivision entails solving more PDE's and becomes impractical for greater than 5–10 size bins. Lagrangian solutions of this problem [8] require addressing smoothing techniques associated with letting 1 particle represent n particles ($n=10, 100, 1000, \dots$) — the larger the n , the less particles to carry but the more smoothing issues to deal with since the sampling in each cell may be inadequate.

Eulerian methodology also has limitations with regard to dealing with size changes associated with vaporization/combustion and/or collisions (shattering/agglomeration). Using a Sauter-mean diameter framework, the "averaged" size within each cell can be represented with size change effects. This approach works well where the particle source has a rather tight size distribution. It has been implemented for heterogeneous carbon combustion in rocket exhausts [7].

Under development is a new Eulerian PDF framework [24] that tracks the continuous size distribution and relates variations in velocity and temperature within each grid cell to this distribution. This work is proceeding systematically via a sequence of unit problem studies and upgrades to the framework. Figures 9a and 9b compare the PDF size distribution at a mid-point in the nozzle and at three positions at the exit plane (axis, central, nearwall) with size-binned solutions using a very fine size distribution (subdivided into 50 size bins).

Table IV. Summary of Multiphase Flow Advances

Rocket Propulsion	Gun Propulsion	Fuel/Air Explosives
<ul style="list-style-type: none">• Finite-volume/upwind particle solver• Drag/heat transfer correlations for high lag, M_p, Re_p• PDF Formulations	<ul style="list-style-type: none">• Gas/liquid framework• Lagrangian solver with dense volumetric contributions• Particle/droplet/propellant ignition and burn<ul style="list-style-type: none">– surface regression correlations	<ul style="list-style-type: none">• Metallic particle ignition and heterogeneous combustion• Sauder-mean diameter Eulerian framework• Nonspherical particle extensions
Chemical/Biological Lethality	Novel Effects	Jet Impingement/Thermal Sprays
<ul style="list-style-type: none">• Droplet vaporization• Neutralization reactions• Aero breakup (under development)• Non-Newtonian extensions (under development)	<ul style="list-style-type: none">• Blast mitigation by dynamic liquid interactions• Jet noise control by tuned vaporization (in progress)	<ul style="list-style-type: none">• Particle/turbulent interactions in LES framework• Complex phase-change interactions• Surface layer effects

The solution at the nozzle mid-point has a size distribution which is similar to that at the inflow station (coming from the combustor). At the exit plane, the distributions indicate the presence of only smaller size particles in the upper portion of the nozzle (since larger particles separate from the wall in the throat turn). Comparisons between PDF and binned size distributions are quite good.

Particle turbulence modeling using both Eulerian and Lagrangian methodology is currently being upgraded to account for "eddy-tossing" effects, as shown in Figure 7. Large eddy simulations are being utilized to support model calibration. Particulate interactions associated with lateral thrusters can modify aerodynamic coefficients and alter the structure of plume-induced separation. In addition, particle radiation to sensor windows or erosive effects of separation extending to window regions must be considered in missile system design.

4.0 MISSILE AERODYNAMIC STUDIES

Varied studies have been performed for generic supersonic missiles at angle-of-attack to establish sensitivities:

- (1) to using PNS or thin-layer approximations vs. full NS solutions;
- (2) to using wall function, two-layer, or low Re near-wall turbulence models; and,
- (3) to using advanced EASM/CC models rather than a basic (linear) $k\epsilon$ framework.

From the viewpoint of predicting aerodynamic coefficients in the absence of transverse jet interactions, the sensitivities are rather modest and the simplest approach (e.g. PNS with $k\epsilon$ /wall function) might suffice. This is exemplified by the CRAFT code comparisons for a Mach 2.5 missile at $\alpha=10^\circ$ comparing NS vs. PNS (Fig. 10) and Chien low Re vs. wall function (Fig. 11) stagnation pressure contours.

In these $k\epsilon$ -based comparisons, the gross turbulence structure is comparable and turbulent viscosity levels in the vortex core are much too large — a known problem with the $k\epsilon$ model for which varied ad hoc limiters have been implemented (see, e.g. the recent study of Josyula [25]). Preliminary work in analyzing the same case Josyula studied (Mach 2.5/ $\alpha=14^\circ$ from a collaborative US-UK-Canada study) has indicated that the EASM model with no modification yields the correct turbulence behavior, reducing peak levels in the vortex by a factor of nearly four. Figure 12 compares baseline $k\epsilon$ and EASM/CC turbulence model predictions showing peak levels of μ_t of 950 for the $k\epsilon$ prediction (Josyula predicted 990) and peak levels of about 250 with the EASM/CC prediction. Stagnation pressure contours appear comparable. More detailed comparative studies for this case are in progress. For analyzing control jet interactions with vortical structures it is imperative that viscosity levels be realistic and use of EASM/CC methodology or other nonlinear methodology appears mandatory.

For missiles with large lateral thrusters, combustion plays a major role in the jet interaction process, and hence, substantially affects thrust amplification. Figure 13 exhibits predictions of the pressure field associated with thruster plume interactions (exhausting from rectangular slot) under high-speed conditions with (a) afterburning off, and (b) afterburning on. The blockage effect of the plume with combustion-on is much greater as evidenced by the pressure interaction "footprint" on the missile surface.

5.0 DYNAMIC MULTI-BODY FLOWS

Recent activities have focused on the inclusion of varied grid movement capabilities into CRUNCH to deal with multi-body and/or complex boundary motion [26]. Both CRAFT and CRUNCH contain dynamic volumetric terms which account for cell acceleration. With structured grids, cell motion is limited to uni-directional stretching. With unstructured tetrahedral grids, cell motion can be generalized and controlled by grid motion equations based on spring analogies or upon linear elasticity formulations, as described in Ref. 26. The overall amount of motion is limited by grid quality constraints, and for substantive motion, must be supplemented by cell enrichment (or depletion) logic. The simplest enrichment technique is that of cell layering whereby layers of cells are added (or deleted) as near boundary cells become stretched(or squashed) beyond prescribed tolerances. For generalized multi-body interactions, the use of linear elasticity grid motion equations in combination with layering and creative domain-decomposition strategies permits the analysis of very complex dynamic problems. Figure 14 illustrates the grid motion associated with the separation of solid boosters from a high kinetic energy missile using only grid motion methodology. Using this same approach for a submunition dispense problem, for a substantive segment of the motion (Figure 15), leads to poor grid quality in the cavity zone (grids there become highly stretched). This is remedied by utilizing a multiple-domain grid with layering (Figure 16) for which a point-trajectory solution is shown in Figure 17. Recent applications to automotive in-cylinder flowfields including both valve and piston motion are described in Ref. 27.

6.0 CAVITY AEROACOUSTICS

A missile weapon bay, exposed to flow, can experience an intense aeroacoustic environment in and around the bay. The resultant turbulent flowfield in the weapons bay is complex with strong vortical gradients and potentially damaging pressure oscillations. The flowfield characteristics are strongly dependent on the length-to-depth (L/D) ratio of the weapon bay/cavity, the freestream conditions, approach boundary layer, and the characteristics of embedded submunition and other cavity components. Ejection of submunitions into this dynamic flowfield is difficult under the best of circumstances, and smooth separation from the weapons bay is not guaranteed.

In a recent study [15], the influence of the turbulence modeling approach taken on the analysis of a weapons bay was examined in detail and the resultant aeroacoustic implications were also addressed. With a view towards identifying the characteristics of the coupling between acoustics and turbulence, attention was restricted to "open" cavity configurations which are notable for strong aeroacoustic phenomena (pressure oscillations). It was demonstrated that engineering-oriented very large eddy simulation (VLES) with modest grids, provided a good representation of the interactions between narrow-band, acoustic tones and broad-band, vortical turbulent structures. VLES methodology provided a credible description of the narrow-band acoustic tones (and over-tones) as well as static and dynamic loads, with agreement observed between predicted and measured trends. Figure 18 exhibits the predicted sound pressure level (SPL) spectra while Figure 19 exhibits pressure oscillations at the afthead wall of an $L/D=4.5$ cavity with Mach 2 approach flow ($Re/L \sim 3 \times 10^6$). Comparable studies with algebraic and two-equation-based turbulence models pointed out the inadequacies of RANS modeling for flowfields characterized by such aeroacoustic phenomena. Figure 20 exhibits that LES time-averaged solutions differ from RANS solutions, showing 2 distinct recirculation zones rather than 1. All RANS solutions (different codes/different turbulence models) are similar and deficient.

7.0 CONCLUDING REMARKS

Advanced missile systems are relying increasingly upon varied forms of jet control for maneuvers. Aerodynamic simulations require upgrades to conventional turbulence modeling and inclusion of thermochemical/multiphase effects to account for plume interactions. Upgrades to structured (CRAFT) and unstructured (CRUNCH) Navier-Stokes codes to permit such interactive simulations have been described. Operation on parallel platforms, using domain-decomposition methodology, permits obtaining complex 3D solutions in a reasonable time. Unstructured numerics has advantages in gridding complex geometries and in adapting the grid to the flow structure using embedding techniques. It also permits dealing with complex, multi-body problems in an efficient manner. Flows with acoustic/turbulence interactions, such as weapons bay cavities, require utilization of an LES turbulence modeling framework which has been demonstrated to provide good comparisons with static and dynamic pressure loads in comparisons with recent experiments.

8.0 ACKNOWLEDGMENTS

The authors acknowledge the contributions of N. Sinha, B. York, A. Hosangadi, R. Lee, D. Kenzakowski, P. Cavallo, N. Tonello, E. Perrell, and N. Chidambaram, of Combustion Research and Flow Technology, Inc., and K. Kennedy of U.S. Army Aviation and Missile Command, who performed the varied simulations described in this paper and were instrumental in developing portions of the CRAFT and CRUNCH codes. Thanks to Ms. Paula Schachter for her expert preparation of this manuscript.

9.0 REFERENCES

- [1] Dash, S.M., Sinha, N., and York, B.J., "Computational Models with Advanced Thermochemistry for the Analysis of Missile/Plume Flowfield Interactions," AGARD Symposium on Missile Aerodynamics, AGARD CP-493, April 1990, pp. 31.1-31.30.
- [2] Srivastava, B., "Lateral Jet Control of a Supersonic Missile: CFD Predictions and Comparison to Force and Moment Measurements," AIAA Paper 97-0639, January 1997.
- [3] Dash, S.M., Lee, R.A., Sinha, N., and York, B.J., "Three-Dimensional End-to-End Simulation of Missile Plume/Aerodynamic Flowfields: Part 1 - Methodology & Base Region Studies," JANNAF 21st Exhaust Plume Tech. Mtg., LMSC, Sunnyvale, CA, Oct. 17-21, 1994.
- [4] Dash, S.M., York, B.J., Lee, R.A., and Sinha, N. "Advanced Computational Simulation of 3D Missile Flowfields," 22nd JANNAF Exhaust Plume Tech. Mtg., NASA/MSFC, Huntsville, AL, Oct. 23-27, 1995.
- [5] Kenzakowski, D. C., York, B.J. and Dash, S.M., "Analysis of Ducted Rocket Flowfields," 1996 JANNAF CS & PSHS Joint Meeting, NPGS, Monterey, CA., 4-8 November 1996.
- [6] Dash, S.M., Sinha, N., Tonello, N.A., Hosangadi, A., and Perrell, E.R., "Progress in the Computational Simulation of Turbulence and Multiphase Combustive Processes for Airbreathing Missiles," 1997 JANNAF Combustion Technology Subcommittee Meeting, West Palm Beach, FL, October 27-31, 1997.
- [7] Sinha, N., Dash, S.M., and Tonello, N.A., "Particulate Combustion Extensions to CRAFT Code with Rocket Exhaust Applications," 1997 JANNAF EPTS & SPIRITS Users Group Joint Meeting, Lockheed Martin Corp., Sunnyvale, CA, 7-11 April 1997.
- [8] Tonello, N.A., York, B.J., and Dash, S.M., "Eulerian and Lagrangian Nonequilibrium Particulate Methodology and Practical Applications," AIAA-97-2552, 32nd AIAA Thermophysics Conf., Atlanta, GA, June 23-25, 1997.
- [9] Dash, S.M., York, B.J., and Kenzakowski, D.C., "Simulation of Complete Tactical Missile Nozzle/Plume/Hardbody Flowfields for Signature Predictions," 1st JANNAF SPIRITS Users Group Meeting, U.S. Army Missile Command, Huntsville, AL, 17-18 June, 1992.
- [10] Dash, S.M., "Recent Progress in Rocket Exhaust Plume Flowfield Simulation Methodology," 1997 JANNAF EPTS & SPIRITS Users Group Joint Meeting, Lockheed Martin Corp., Sunnyvale, CA, 7-11 April 1997.
- [11] York, B.J., Kenzakowski, D.C., Lee, R.A., and Dash, S.M., "Upgrades to CRAFT Code for Simulation of Ducted Launcher/Plume Interactions," 1997 JANNAF EPTS & SPIRITS Users Group Joint Meeting, Lockheed Martin Corp., Sunnyvale, CA, 7-11 April 1997.
- [12] Hosangadi, A. Lee, R.A., Sinha, N., and Dash, S.M., "Parallel Multi-Block Extensions to CRAFT for Complex IB Applications," 1997 JANNAF Combustion Technology Subcommittee Mtg., West Palm Beach, FL, Oct. 27-31, 1997.
- [13] Dash, S.M. and Kenzakowski, D.C., "Future Direction in Turbulence Modeling in Jet Flowfield Simulation," AIAA-96-1775, 2nd AIAA/CEAS Aeroacoustics Conf. (17th AIAA Aeroacoustics Conf.), Penn State, State College, PA, May 6-8, 1996.
- [14] Dash, S.M., Kenzakowski, D.C., and Sinha, N., "Turbulent Aspects of Plume Aerodynamic Interactions," AIAA-95-2373, 31st AIAA Joint Propulsion Conference, San Diego, CA, July 10-12, 1995.
- [15] Sinha, N., York, B.J., Dash, S.M., Chidambaram, N., and Findlay, D., "A Perspective on the Simulation of Cavity Aeroacoustics," AIAA Paper 98-0286, 36th AIAA Aerospace Sciences Meeting, Reno, NV, January 12-15, 1998.
- [16] Barth, T.J., "A 3D Upwind Euler Solver for Unstructured Meshes," AIAA Paper 91-1548, June 1991.
- [17] Hosangadi, A., Lee, R.A., York, B.J., Sinha, N., and Dash, S.M., "A Three-Dimensional Unstructured Flow Solver for Reacting Multiphase Propulsive Flows," AIAA-95-0258, 33rd AIAA Aerospace Sciences Mtg., Reno, NV, January 9-12, 1995.
- [18] Hosangadi, A., Lee, R.A., York, B.J., Sinha, N. and Dash, S.M., "Upwind Unstructured Scheme for Three-Dimensional Combusting Flows," *Journal of Propulsion and Power*, Vol. 12, No. 3, May-June 1996, pp. 494-503.
- [19] Lee, R.A., Hosangadi, A., Dash, S.M., Cavallo, P.A., and Sinha, N., "Unstructured Grid Navier-Stokes Solver for Turbulent Reacting Flows with Dynamic Domains," AIAA-97-2000, to 28th AIAA Fluid Dynamics Conf., Snowmass, CO, June 29-July 2, 1997.
- [20] Hosangadi, A. and Sinha, N., "Hybrid, Viscous, Unstructured Mesh Solver for Propulsive Applications," AIAA Paper 98-3153, AIAA 34th JPC, July 13-15, 1998.
- [21] Dash, et al., "Turbulence Modeling Framework for Analysis of Subsonic/Supersonic Jet Noise Reduction Concepts," Phase I SBIR Final Technical Report for NASA LaRC, Combustion Research and Flow Technology, Inc., Report No.: CRAFT-9/97.010, September 1997.

- [22] Gruber, M.R. and Dutton, J.C., "Three-Dimensional Velocity Measurements in a Turbulent, Compressible Mixing Layer," UILU-ENG 92-4001, Univ. of Illinois, Urbana, January 1992.
- [23] Gatski, T.B. and Speziale, C.G., "On Explicit Algebraic Stress Models for Complex Turbulent Flows," ICASE Report No. 92-58, Nov. 1992 (also JFM, Vol. 254, 1993, pp. 59-78).
- [24] Perrell, E.R. and Dash, S.M., "PDF Methodology for Eulerian Solution of Particle Cloud Equations," submitted for presentation at 1998 ASME Fluid Engineering Division Summer Meeting, Washington, DC, June 21-25, 1999.
- [25] Josyula, E., "Computational Study of High-Angle-Of-Attack Missile flows Using Two-Equation Turbulence Models," AIAA Paper 98-0525, January 1998.
- [26] Cavallo, P.A., Hosangadi, A., Lee, R.A., and Dash, S.M., "Dynamic Unstructured Grid Methodology with Application to Aero/Propulsive Flowfields," AIAA-97-2310, 15th AIAA Applied Aerodynamics Conf., Atlanta, GA, June 23-25, 1997.
- [27] Sinha, N., Hosangadi, A., Lee, R.A., York, B.J., Cavallo, P.A., and Dash, S.M. "Applications of Upwind Combustive/Multiphase Numerics to Automotive In-cylinder and Fuel-Fill Flowfields," Paper No. FEDSM97-3027, 1997 ASME Fluids Engineering Division Summer Meeting, Vancouver, British Columbia, Canada, June 22-26, 1997.

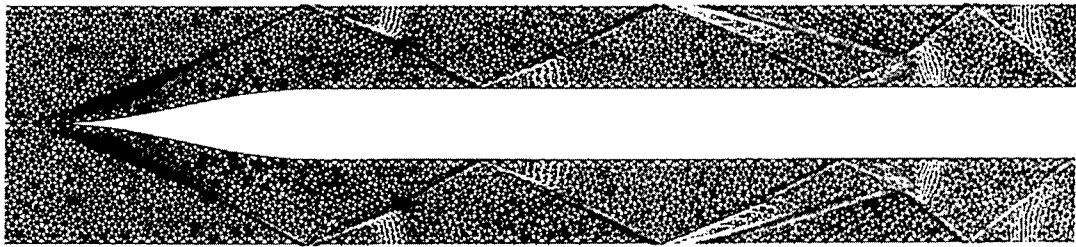


Figure 1. Density contours for CRUNCH analysis of shock-induced combustion in duct for premixed Hydrogen-Air.

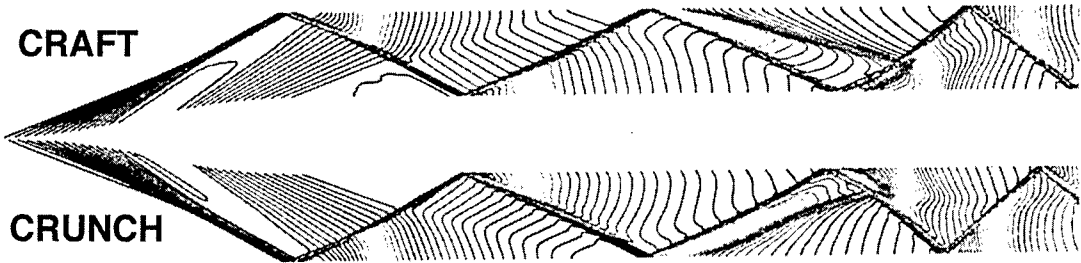


Figure 2. Comparison of CRAFT and CRUNCH solutions for shock-induced combustion problem.

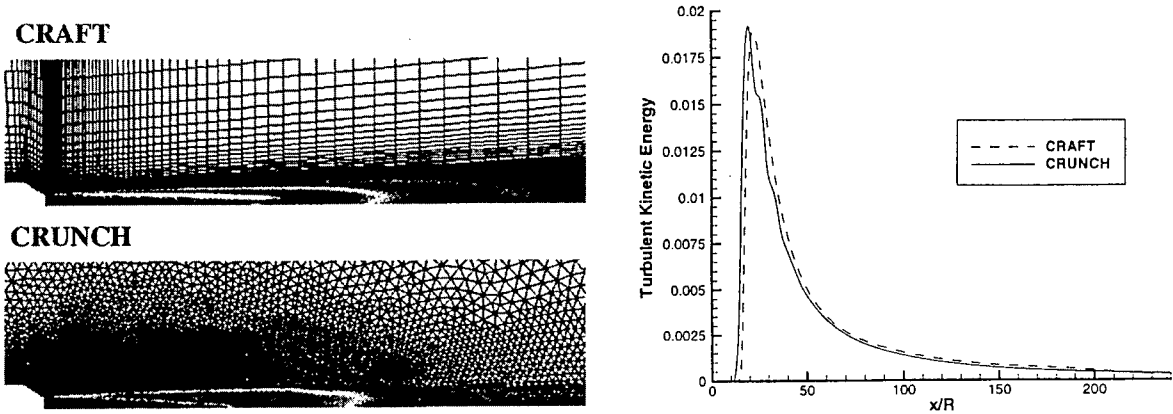


Figure 3. Comparison of CRAFT and CRUNCH solutions of hot subsonic jet turbulent structure using $k\epsilon$ model.

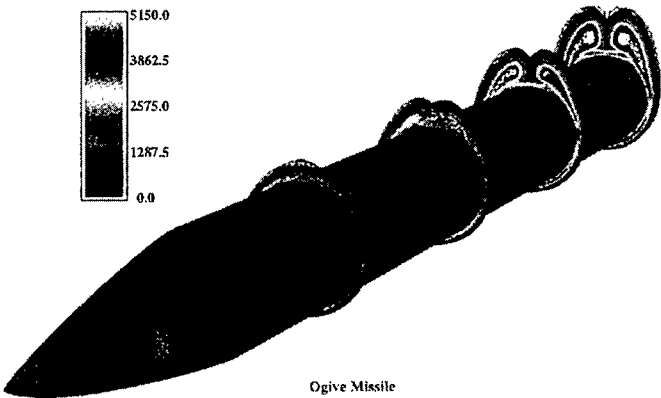


Figure 4. CRUNCH solution of Mach 2.5 missile flowfield at 10° angle-of-attack using $k\epsilon$ with wall function.

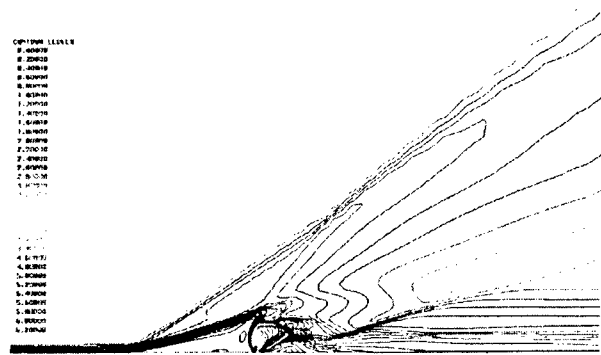


Figure 5. Mach number contours for sonic normal injection into Mach 2.7 approach flow (planar/slot injection).

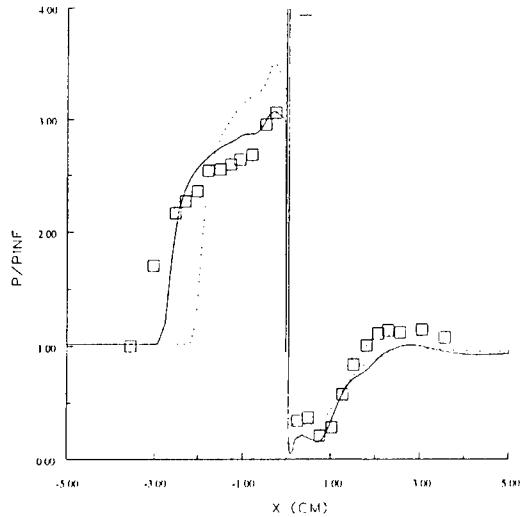


Figure 6. Comparison of surface pressure distributions for sonic jet injection case. (□□□□ Data of Kraemer & Tiwari, ——— EASM/CC, — — — ke).

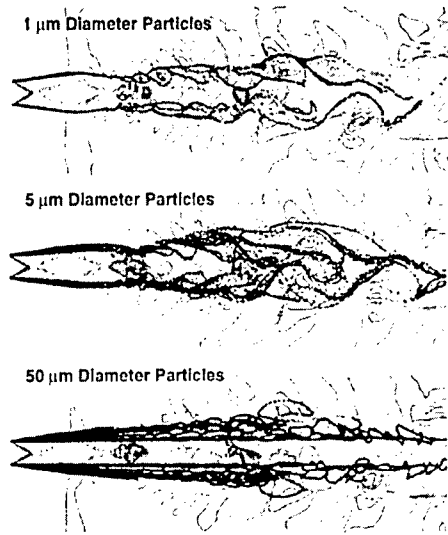


Figure 7. Instantaneous velocity contours of Mach jet with particle trajectories for 1, 5, and 50 μm.

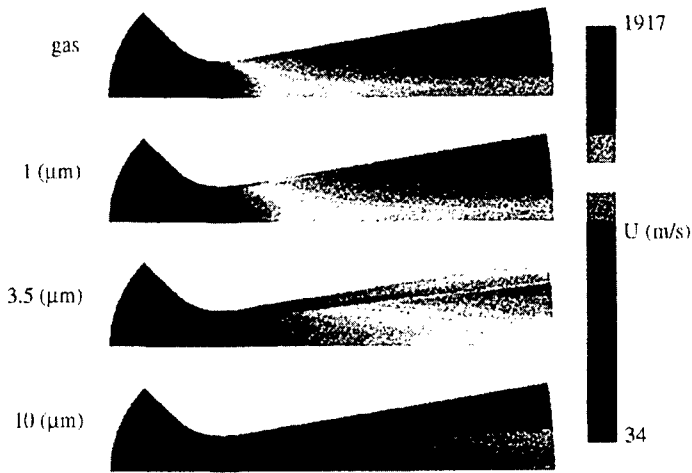


Figure 8. Velocity contours of nozzle flow with 30% mass loading of Al_2O_3 . Two-way coupling, three groups, $d_p = 1.0, 3.5, 10.0 \mu m$, 10% mass loading each group.

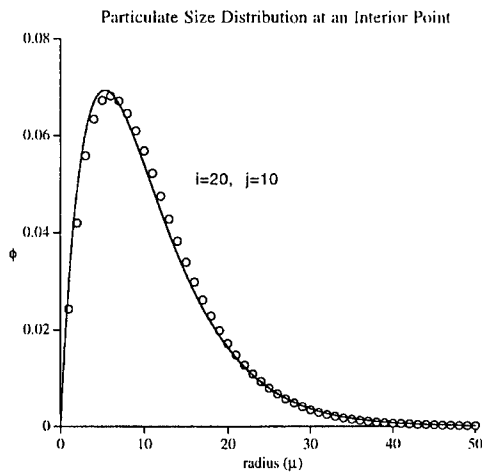


Fig. 9a.

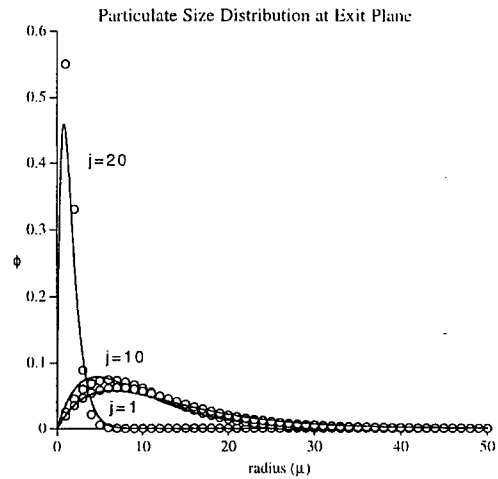


Fig. 9b.

Figure 9. Comparison of size-bin and PDF solutions for particle size distribution at (9a) a central point in the supersonic portion of the nozzle, and (9b) at several positions along the exit plane.

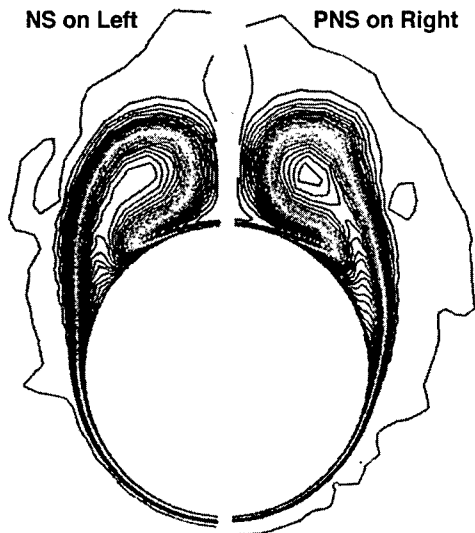


Figure 10. Comparison of stagnation pressures for Mach 2.5/ $a=10^\circ$ simulation using NS and PNS methodology.

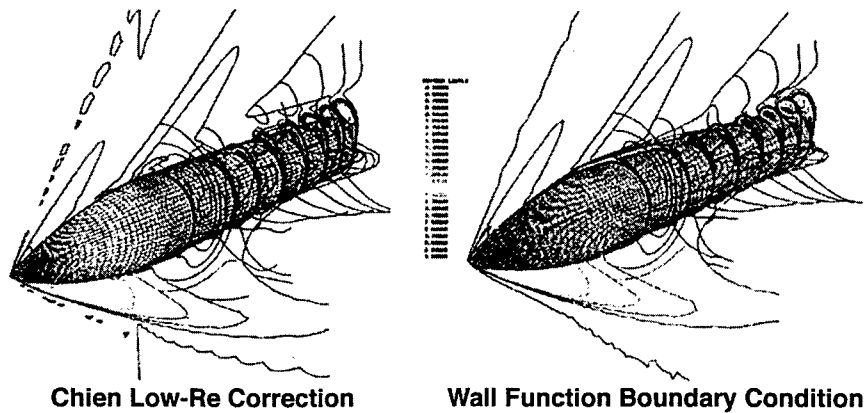


Figure 11. Comparison of stagnation pressures for Mach 2.5/ $a=10^\circ$ simulation using Chien low Re correction and wall function near-wall models.

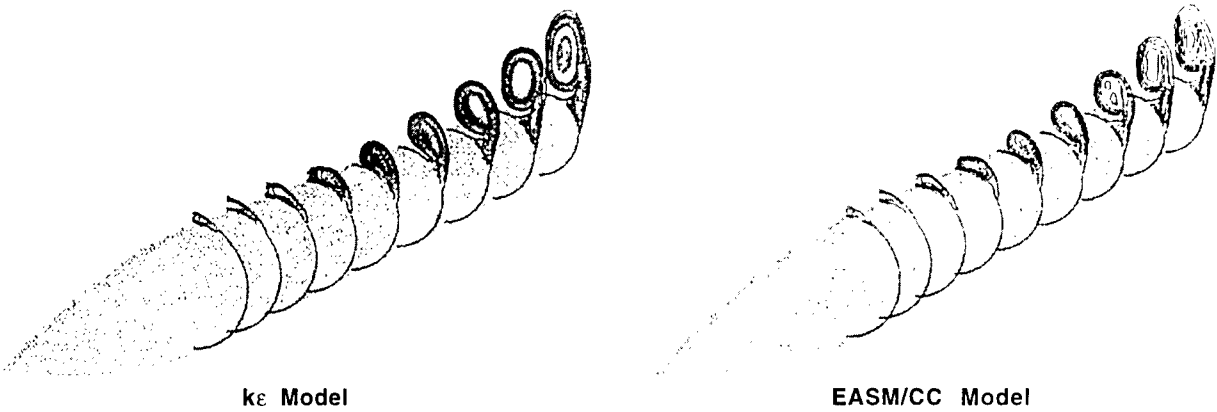


Figure 12. Comparison of turbulence viscosity contours using $k\epsilon$ and EASM/CC models for Mach 2.5/ $\alpha=14^\circ$ missile simulation.

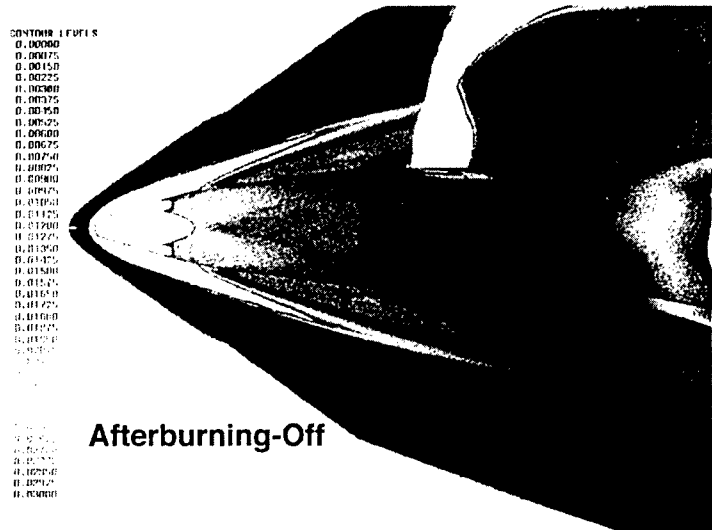


Figure 13a. Lateral thruster plume/aerodynamic interactions with afterburning off.

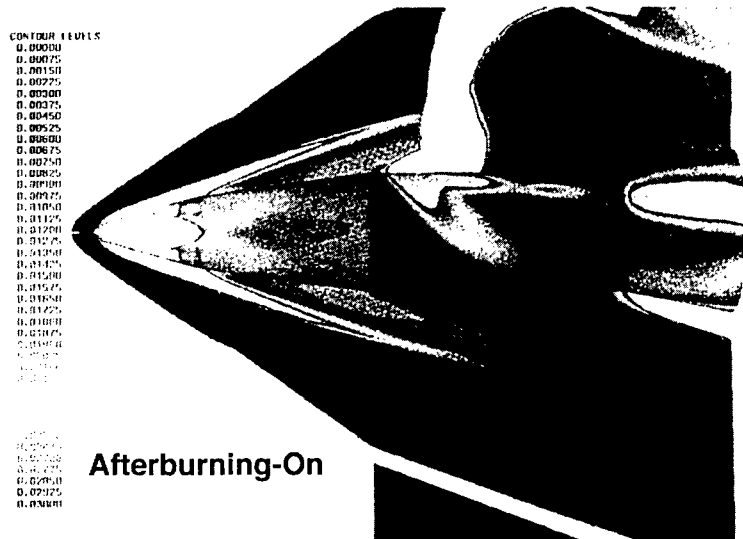


Figure 13b. Lateral thruster plume/aerodynamic interactions with afterburning on.

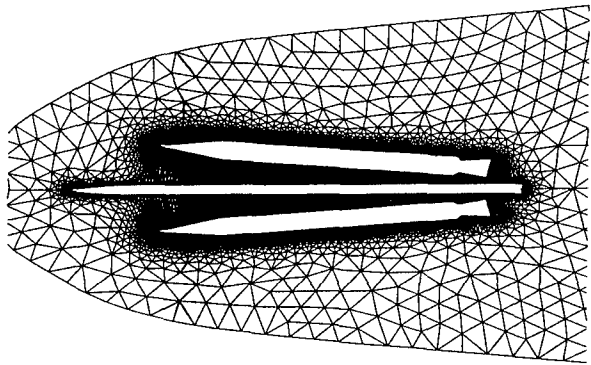


Figure 14. Unstructured mesh motion for booster separation.

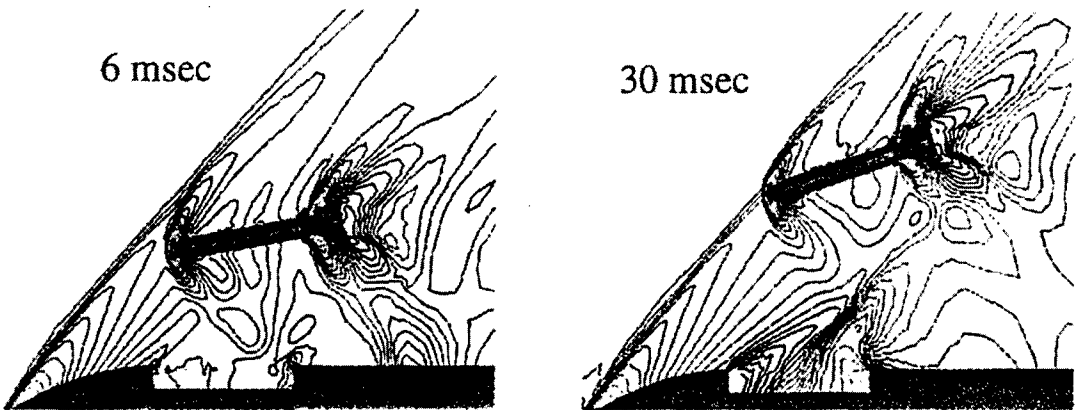


Figure 15. Time-accurate simulation of submunition flyout using single unstructured grid with linear elasticity grid motion solver.

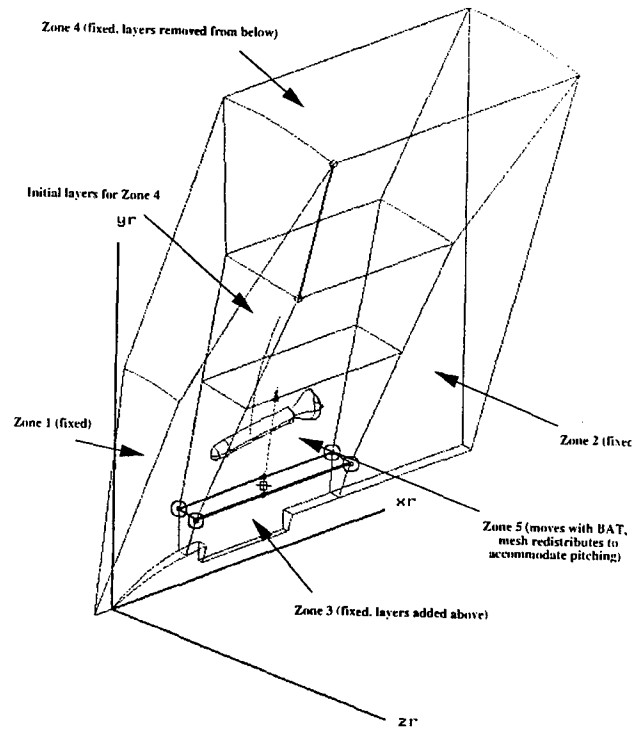


Figure 16. Multi-zone strategy for submunition dispense problem.

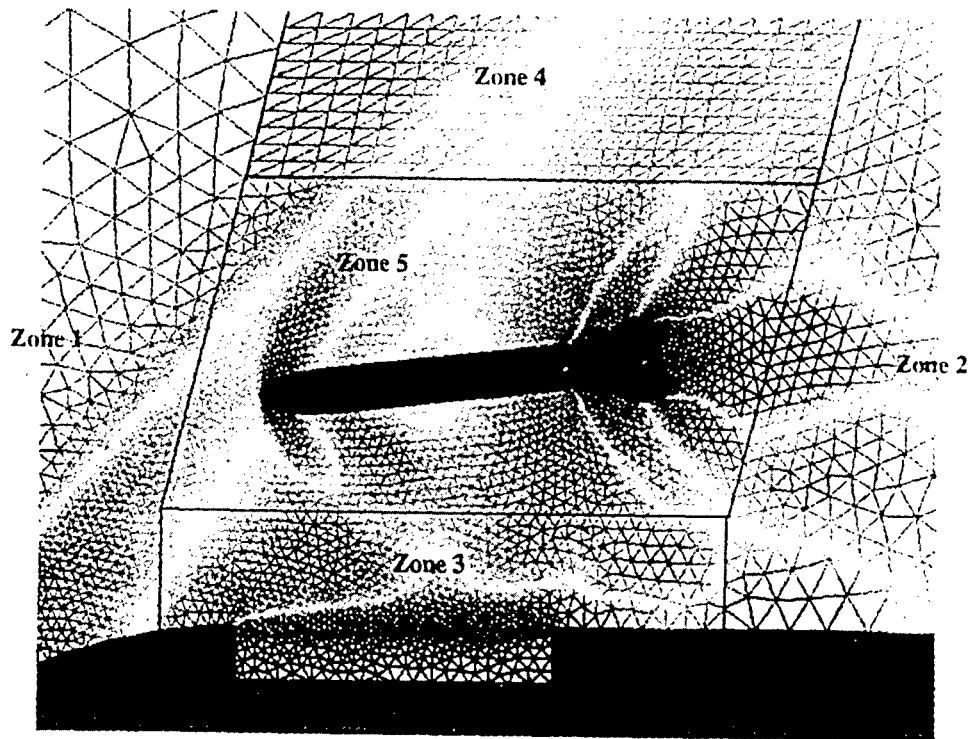


Figure 17. Snapshot of solution in cavity region using multi-zone formulation.

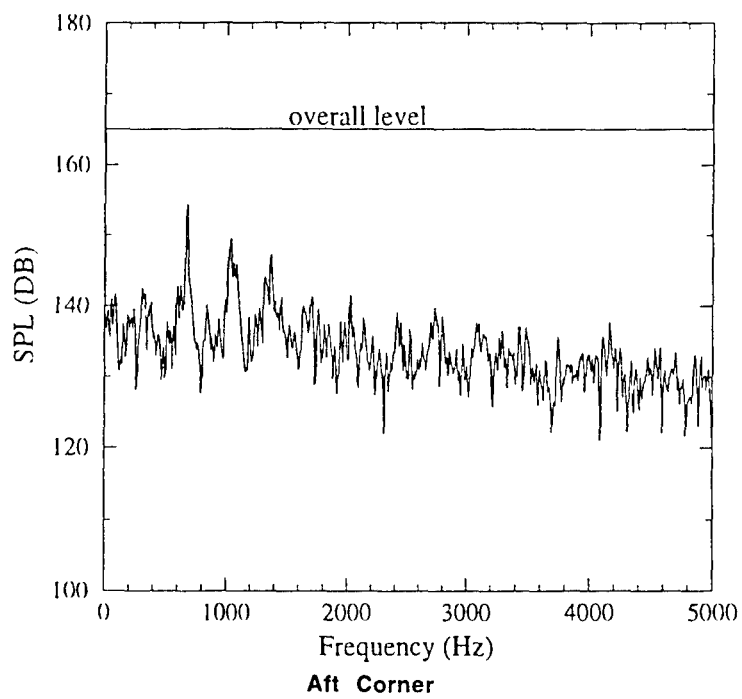


Figure 18. Sound pressure level (SPL) spectra on cavity floor.

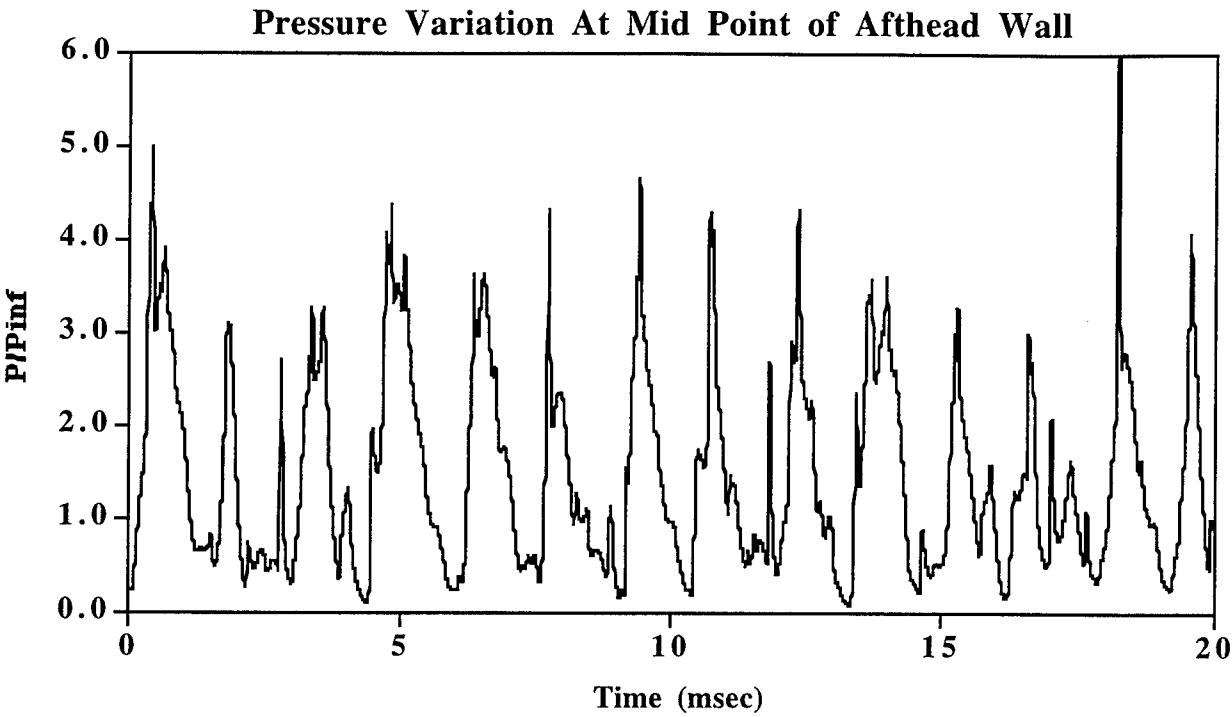


Figure 19. Pressure variation at mid-point of aft-head wall.

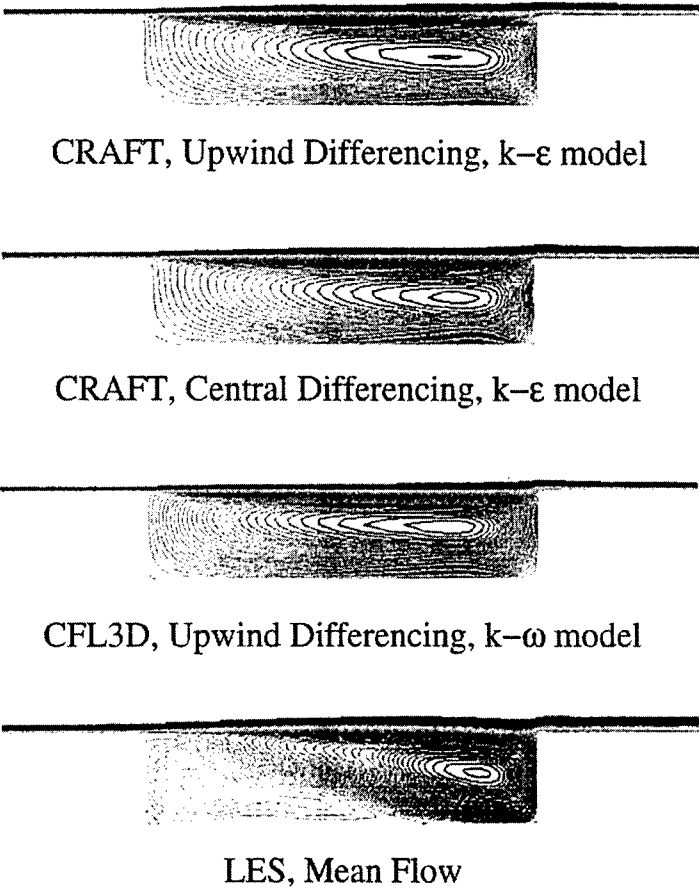


Figure 20. Mach 2.0 cavity flow simulation: comparison of streamline contours.

INDUSTRIAL USE OF CFD FOR MISSILE STUDIES : NEW TRENDS AT MATRA BAe DYNAMICS FRANCE

Marc Brédif, Florence Chapin, Christian Borel, Philippe Simon

MATRA BAe DYNAMICS France
Flight Dynamics Department
37, Avenue Louis Bréguet
Vélizy, 78146 FRANCE

SUMMARY

This paper describes the industrial use of CFD tools at MATRA BAe DYNAMICS France. Recent applications are presented that show the versatility and the potentiality of the AEROLOG software ; they concern the simulation of multi-species flows and complex flows. The complementarity between CFD and experiments is illustrated by examples dealing with jet flows, high pressure internal flows, non uniform flow aerodynamics, and missile release trajectory predictions. Work in progress about aeroelastic computations is depicted ; the interest of code parallelisation is emphasized. Finally, our point of view is given about the Navier-Stokes approach for missile computations.

1. INTRODUCTION

Since the beginning of the eighties, CFD tools are in extensive use for the aerodynamic studies of missiles at Matra BAe Dynamics France. The EULER model lying on the assumption of inviscid flow has been routinely used during this period at different steps of missile projects, mostly concerning external aerodynamic studies. Ten years ago, a majority of the CFD community thought that, before the year 2000, the Navier-Stokes model would gradually replace the Euler assumption for standard use. This is actually not the case at Matra BAe Dynamics, due to at least three factors : the still prohibitive cost of repeated Navier-Stokes computations, the lack of maturity of turbulent models tailored for missile applications, and the too long period of time spent in preprocessing activities (preparation of CAD database, mesh generation and control).

The evolution concerning CFD tools in our company has been quite different than the one expected : new trends have appeared in order to broaden the use of the EULER model. This has been made possible thanks to the modular approach described in the next paragraph ; illustrations will then be given about new kinds of applications of the CFD tools.

2. SIMULATION TOOL

The standard software used at MATRA BAe Dynamics is the AEROLOG proprietary code [1-2]. The modular approach has been retained, consisting of four different libraries of subroutines : preprocessing, numerical solver, physical model and

post-processing.

2.1 Preprocessing

The preprocessing library includes different tools : the CAT-MESH module allows mesh generation (for simple geometries) or mesh modification, enhancement and repair ; in the latter case, the basic mesh has been previously generated by a CAD-interfaced tool (ICEM software from Control Data for instance). The CHIMOS module, developed in collaboration with Aerospatiale and ONERA, is an automatic preprocessing tool which allows the use of arbitrary overlapping multiblock grids thanks to the Chimera approach [3] (see figure 21) ; its primary use concerns release studies of missiles under combat aircrafts [6].

2.2 Numerical solver

The numerical solver handles an arbitrary set of Partial Differential Equations of the form :

$$\frac{\partial U}{\partial t} + \text{div}(\vec{V}_r U) = \text{div}(F(W, \nabla W, S)) + H(W)$$

Where U is the array of Conservative Variables, W is the array of Primitive Variables, S is the array of auxiliary variables, F is the flux vector and H describes the source terms ; V_r is the velocity of the fluid relative to the frame of reference. This general approach allows the computation on moving meshes (aeroelastic computations for example) : in this case the grid velocity which varies in space and time according to the mesh deformation is added to the fluid velocity V_r . Moreover, the frame of reference in which equations are written is completely arbitrary, the six components (translational and rotational velocity) describing the movement of the relative frame relative to an inertial frame being user specified.

The grid system is a set of multi-block (I,J,K)-structured meshes with possible overlapping. The basic time-space discretisation is the Lax-Wendroff one-step explicit cell vertex finite volume scheme proposed by Ni [4] ; an implicit residual smoothing step is added according to the ideas of Lerat [5], thus allowing CFL numbers up to 5 with a local time-stepping technique ; moreover, the Ni multigrid scheme is also available. Reasons for this choice is the simplicity of programming allowing a straightforward decoupling between numerics and physics, together with a low number of

operations to be performed per point and per iteration. For example, less than 1000 floating point operations have to be performed per point and per iteration for an implicit EULER simulation, leading to a CPU time less than 5 hours on a typical workstation (rated 50 Mflops) for 2000 iterations on a 400.000 nodes mesh. The memory requirements are also limited, 256 Mbytes being sufficient for a 1.000.000 nodes mesh (32 bits accuracy).

2.3 Physical models

There are 4 physical models available in the 1997 version of AEROLOG : Euler mono-species with constant total enthalpy assumption, Euler mono-species, Euler multi-species with specific heats eventually depending on temperature, and Navier-Stokes mono-species with eventually the Baldwin-Lomax turbulent model. Other versions are under development : Euler mono-species with real gaz and Navier-Stokes mono-species with the standard (k,ϵ) turbulent model including low Reynolds numbers modelling (Jones-Launder version).

Each physical model corresponds to a set of approximately ten subroutines, called by the numerical solver, which describe :

- The link between conservative variables U and primitive variables W .
- The expression of auxiliary variables S .
- The expression of fluid relative velocity V_r function of U .
- The expression of fluxes F and source terms H .
- The expression of boundary conditions, either concerning the primitive variables W or the fluxes F .
- The expression of local time step Δt for a CFL number equal to 1.

For example, in the Navier-Stokes model, Conservative variables are $U=(\rho, \rho u_a, \rho v_a, \rho w_a, \rho E_a)$, Primitive variables are $W=(u_r, v_r, w_r, p, T)$, where (u_r, v_r, w_r) are the components of relative velocity V_r and (u_a, v_a, w_a) are the components of the absolute velocity V_a ; $E_a = e + V_a^2/2$ is the total energy, with the internal energy e function of temperature T . Auxiliary variables S are the laminar viscosity μ_l function of T and the turbulent viscosity μ_t computed by using the Baldwin-Lomax model.

2.4 Post-processing tools

The use of simulation tools demands more and more complex post-processing in order to satisfy the questions asked by the project people. For an increasing number of cases, the knowledge of the aerodynamic efforts is only a very small part of the information given by the simulation. During the last years, a number of possibilities has been added to our tools, which has allowed to broaden the use of CFD :

- Computation of derived fields, like local velocity angles.
- Automatic computation of distributed loads.
- Projection of solid surface fields onto structural meshes for the computation of structural loads.
- Interpolation of fields on 3-D cartesian grids for the evaluation of disturbance velocity fields around aircrafts.
- Computation of beam trajectories inside the flow taking into account the variation of the local optical index n .

New algorithms have been developed, partly based on the algorithms used for the Chimera pre-processor. Some illustrations of these new possibilities will be given in the forthcoming examples.

3. SIMULATION OF MULTI-SPECIES FLOWS

3.1 Jet computations

The presence of propulsion jets can have an influence on the aerodynamic characteristics of the missile, especially when the jet is underexpanded. The computational tool is adapted to the study of this problem, because it is in general very difficult to measure in wind tunnel the missile aerodynamics with jet on. Considering that thermodynamic constants of propulsive jets differ from the thermodynamic constants of the air, it is mandatory for these simulations to activate the multi-species option of the CFD code.

An example of such a use concerns the effect of the jet on the rear part of a missile in the transonic regime. Calling p_j the total jet pressure and p_0 the freestream air pressure, the quantity p_j/p_0 can vary during the propulsive phase either due to altitude changes or combustion modifications. Figure 1 shows the mesh used for the computations ; figure 2 illustrates the effect of pressure variation on the compression shock ahead of the afterbody at Mach 1.18 .

A parametric study has been performed using AEROLOG, allowing to predict the jet shape as a function of Mach number and pressure ratio (figure 3). Wind tunnel experiments have been carried out after that study with missile models mounted on different stings, with sting shapes designed after the previous computational results : the effect of jet propulsion on the aerodynamics has been predicted thanks to the combined use of CFD and experiments.

3.2 Simulation of pneumatic systems

For some applications, the perfect gaz assumption is no more valid : this is in particular true for pneumatic systems used for missile release under aircrafts. The initial momentum is given to the missile by a complex mechanical system whose energy is provided by a small size bottle containing high pressure nitrogen (hundreds of bars) ; after the opening of the bottle, the gaz expands in a pipe and acts on a piston which provokes the desired movement of the missile (see figure 4).

The pressure exerted by the gaz on the piston, and therefore its velocity, is a function of the circuit geometry. The design of such a system can highly benefit from the use of simulation tools, with the condition that the code can take into account real gaz effects.

A preliminary physical model in AEROLOG allows the modeling of real gaz with an arbitrary equation of state. This option has been used for the simulation of the previously described pneumatic system, with a mesh extent varying in time according to the piston position. It is clear on figures 5 and 6 that the real gaz simulation improves the quality of the prediction when compared with experiments : in particular, the piston velocity is accurately described by the model.

This study is an example of the advantage of the modular approach of AEROLOG which allows easy substitution or improvement of a physical model while keeping unchanged all the well tested numerical parts.

4. SIMULATION OF COMPLEX FLOWS

4.1 Non uniform flow aerodynamics

The CFD tools can provide help to improve a missile design, optimize some characteristics, analyse at reduced cost possible alternatives, or prepare wind tunnel experiments ;

nevertheless, in all cases, the aerodynamic model of a missile in uniform flow is based mainly on detailed wind tunnel experiments. Figures 7 and 8 show the computational mesh and a surface pressure result for the MICA air-to-air missile ; the predicted lift force and pitching moment coefficient CL and Cm are generally in good agreement with the experiments. The knowledge of the aerodynamic characteristics of missiles in non uniform flow is an important aspect of prediction methods concerning missile release trajectories under aircrafts. Such an approach is routinely used at MATRA BAe Dynamics France (see [6]) under the name «EULER+local angle of attack method» («EULER-incidences locales» in french). The building of a NUFA (Non Uniform Flow Aerodynamics) model is generally an extension of the basic model based on semi-empirical considerations ; the CFD approach can here calibrate and validate such a model in a powerful way.

For instance, as illustrated on figure 9, computations are made at a given Mach number and incidence (here $M=1.5$ and $\alpha=10^\circ$) in two different frames of reference attached to the missile : the first one is inertial, whereas the second one is animated by a pitch movement around the Center of Gravity at constant rate q . For the latter case, the missile sees the upstream flowfield with an angle of attack linearly varying from nose to tail. The analysis of vertical load distributions for both cases (figure 10) provides the guidelines for the calibration of the different constants appearing in the NUFA model.

4.2 Prediction of missile release trajectory under aircraft

A more sophisticated approach consists in coupling the CFD code with a 6 DOF model, thus avoiding necessary simplifications or approximations made in the previous technique, at the cost of increased computational time.

The feasibility of this approach has been studied at MATRA BAe DYNAMICS by combining the CHIMOS pre-processing tool based on chimera meshes, AEROLOG and a 6 DOF model. In order to avoid excessive CPU time, computations have been realised every 0.1 second around the configuration composed of the DASSAULT MIRAGE 2000 fighter aircraft and the MATRA BAe APACHE stand-off missile ; the position of missile relative to the aircraft has been obtained by a numerical integration of forces and moments on the missile at each position giving the aerodynamic right hand side of the flight mechanics equations solved by 6 DOF routines. In order to compare with a flight test, the initial conditions concerning the aircraft and the missile have been taken from this test ; after ten computations, the missile trajectory during the first second has been fully determined (figure 11), and the agreement between the predicted and the real missile position has been considered satisfactory (figure 12).

These promising results open the possibility to use simulation tools for the prediction of very complex flows, when the power of computers for a given cost will have decreased by one or two orders of magnitude.

5. AEROELASTIC COMPUTATIONS

5.1 Structural static loads

CFD simulations give access to the local loads distribution on

every part of the missile. Figure 13 shows the pressure coefficient field on the rear part of a missile together with the vertical load distribution $\Delta CL/\Delta x$ applied on different parts : control surfaces, ventral fins, rear cover. This last diagram is automatically generated by the post-processing tool, thus saving time during the exploitation phase of the CFD study.

For some applications, it is often necessary to perform a detailed structural analysis based on finite element codes such as NASTRAN. For this purpose, the surface on which aerodynamic loads are applied is triangulated, and the resulting mesh differs from the original CFD mesh. Therefore a projection tool is needed in order to prescribe the boundary conditions on the finite element mesh. This projection tool has to deal with two important issues : first, the two underlying geometries can differ, due to simplifications made either for flow simulation or for structural computations ; second, there can be holes in the original CFD mesh due to the presence of fins or control surfaces which no more exist in the structural mesh. Figure 14 is an example of such a case.

Starting from the algorithms developed for Chimera applications, a very robust projection method has been implemented in our post-processing software which handles any kind of situation, giving as output the values of the projected field on the finite element mesh together with the projection distance for each finite element node. Figure 15 illustrates the efficiency of this post-processing option on the same example as before.

Reciprocally, if necessary, the displacement field computed by the structural code can be interpolated back to the CFD mesh for a new computation taking into account the effect of the geometry deformation.

5.2 Dynamic loads

In some situations, the dynamic coupling between the aerodynamic loads and the structural response cannot be neglected, for example for high aspect ratio wings ; the well known «flutter» phenomenon often leads to the ruin of the missile and therefore has to be avoided. Up to now, a set of methods is used to predict the appearance of flutter, essentially empirical rules completed with simplified computations made with aeroelastic modules of finite element softwares. The numerical approach, in the latter case, is based on panel methods which assume a linear response of the flow with respect to the geometric displacements of the lifting surfaces.

Unfortunately, this linear behaviour is no more valid in the transonic regime ; a more complex approach has to be undertaken, based on a nonlinear flow code such as an EULER finite volume method. In order to explore this possibility, and thanks to the versatility of the AEROLOG software, a preliminary study has been undertaken, consisting in computing the flow field around a cyclically oscillating airfoil with two different techniques. The airfoil, equipped with a NACA0012 profile, has a chord C equal to 1m and a span length equal to 11C ; its harmonic movement combines torsion and bending with the following law (x is along the chord, y is the spanwise direction and z is orthogonal to the wing planform, the origin being the leading edge of the root chord) :

$$\Delta z = (0.04381 \cdot (0.25 - x) + 0.1606 \cdot (y/11)^3) \sin(\Omega^* T^*)$$

T^* is the adimensionalised time TV_0/C with V_0 the upstream uniform velocity ; in the following example, the Mach number

has been taken equal to 0.755, V_0 equal to 256.7 m/s, and the reduced pulsation $\Omega^* T^*$ equal to 0.162. An overview of the problem is shown on figure 16.

The first strategy has consisted in using the moving mesh option of the AEROLOG code ; in practice, the initial mesh ($T=0$) and the mesh corresponding to the maximal deformation ($\Omega^* T^*=90^\circ$) are given as inputs ; during the computations the mesh nodes are displaced according to the harmonic law and mesh displacement velocities are taken into account in flux computations. The pressure distribution is presented on figure XX for the phase angle $\Omega^* T^* = \Phi$ equal to 0° and 90° (figure 17).

The second strategy is based on the simplified assumption that the mesh variation is very weak ; the mesh remains fixed and only wall boundary conditions are modified : the fluid normal velocity in the flux computations is replaced by the velocity of the wing orthogonal to the surface (these conditions are hereafter called «blowing» conditions).

Figures 18 and 19 illustrate the variations of the wing global efforts during the periodic movement. The two strategies give similar results, apart from the pitching moment variation due to very small values ($C_m = \pm 0.015$).

Consequently, an important step has been reached towards the prediction of flutter phenomena in the transonic regime ; it remains to replace the imposed wing displacement by the actual displacement predicted by the structural code.

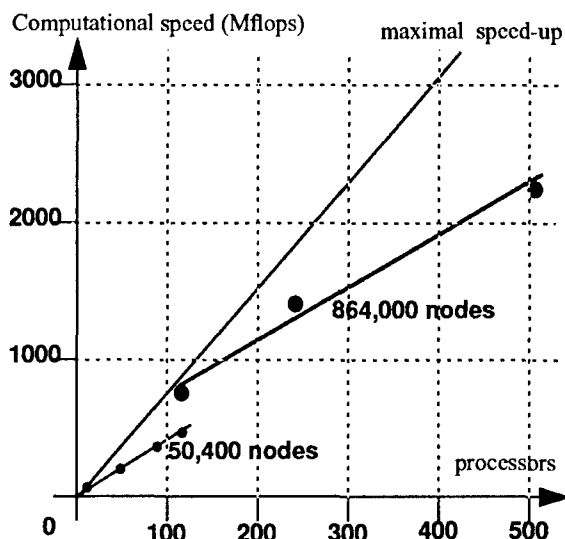
6. PARALLEL SIMULATIONS

6.1 AEROLOG parallel solver using message passing

A flexible massively parallel implementation of the AEROLOG code has been obtained through a second level of mesh decomposition which is performed at runtime by each processing task. Given the initial mesh topology and the number of processing tasks, each subdomain is decomposed into mesh blocks, through a regular splitting along mesh plans in the three mesh directions, taking into account load balancing and interface minimization constraints [7]. This second level of mesh decomposition is illustrated on figure 20 with the mesh around the APACHE missile designed with 5 subdomains and automatically splitted into 32 blocks.

After the subdomain decomposition, the mesh blocks are then distributed one to one among the processing tasks and the matching conditions on the block interfaces are handled through message passing. The portability of the message passing code is obtained thanks to intermediate libraries which translate vendors libraries into home-defined message passing routines [8]. PVM, MPI, NX and other intermediate libraries have already been linked to the AEROLOG parallel code.

This approach has proved to be efficient and scalable on various shared and distributed parallel architectures. We give in the following curves performance results obtained with the INTEL-PARAGON machine up to 500 processors : we can observe the increasing parallel overhead with the number of processors when dealing with a constant problem size, while a nearly perfect scalability is achieved with proportional problem sizes.



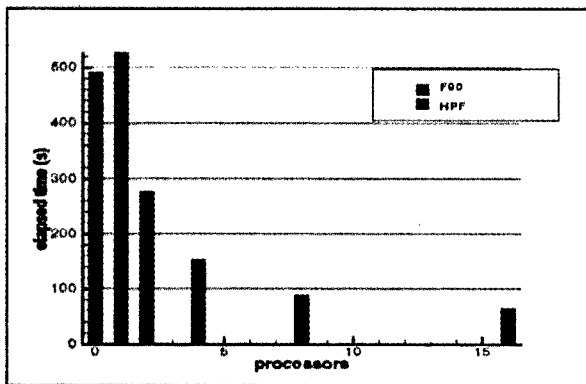
This performance result confirms an obvious remark : even with a good implementation of the parallel code, the size of the computing network needs to be fitted with the problem size. Therefore, medium size parallel machines with a few tenth of processors are well suited to today's Euler applications while Navier-stokes simulations will require Massively Parallel Systems which are more considered as demonstrators at the moment.

6.2 AEROLOG parallel solver using HPF

Aiming at a unique (ie. sequential and parallel) and portable (ie. shared and distributed memory) code, MATRA BAe DYNAMICS has participated to the PHAROS ESPRIT-4 project of the European Community, which ended December 97. The objective of the project was the porting of four industrial applications to HPF with the support of HPF experts, using reengineering tools and compilers from software vendors.

The AEROLOG coarse grain parallelism strategy based on domain decomposition has been adapted to HPF paradigm. This choice involves less changes of the F77 initial code (most of the subroutines remain unchanged, except for the F90 declarations) and it exploits the natural locality of data attached to the same subdomain.

Even if the porting effort was founded heavier than expected, due to an important restructuring of the code data structures required for an efficient F90 + HPF implementation, the result of this work in terms of parallel efficiency is very encouraging taking into account the recent introduction of the HPF standard. Considering a realistic test-case of supersonic flow around a blunt body with a 150000 point mesh, the following computing times were obtained on a SP2 machine :



Nevertheless, the parallel efficiency with HPF decreases rapidly when the number of parallel tasks becomes higher than 16, whereas the message passing version still works fine. This is due to remaining non parallel sections in the HPF code, which should be further enhanced, and to an insufficient maturity of F90+HPF compilers/optimizers.

7. NAVIER-STOKES SIMULATIONS

All the numerical results shown before have been obtained with models based on the EULER equations ; viscous effects have been neglected mainly for cost reasons. For a certain number of problems, the EULER assumption is valid : external flows around missiles at moderate angles of attack for instance. When flow separation occurs on smooth surfaces, the EULER assumption is no more valid and important discrepancies can be found between the EULER numerical results and wind tunnel experiments. This situation arises, for instance, in the case of Body-Tail configurations characterized by forebody vortices which interact with the vortices generated by the control surfaces.

The prediction of the rolling moment C_l on B.T. configurations demands the use of the NAVIER-STOKES model : an example is given on figures 22.a and 22.b concerning a supersonic missile at Mach 3, $\alpha=10^\circ$ and a non-symmetric roll position.

The EULER model (fig. 22.a) predicts a nearly zero rolling moment, whereas the experiments give the value of 0.023 ; the AEROLOG code used with the NAVIER-STOKES + Baldwin-Lomax turbulence model (fig. 22.b) improves the quality of the prediction by giving a value of 0.013, at the expense of a simulation time multiplied by more than 20.

It is clear that much progress remains to be done in the future for a routine use of NAVIER-STOKES models : turbulent models have to be improved and adapted to the type of flows encountered around missiles ; mesh adaption to boundary layer and highly vortical regions has to be undertaken. The decrease of elapsed computational time will be obtained thanks to the use of parallel computers executing programs using the message passing paradigm, or eventually a HPF-like approach.

8. CONCLUDING REMARKS

The main goal of the CFD team of MATRA BAe DYNAMICS France during the recent years has been to broaden the use of CFD-based methods for missile aerodynamics. The purpose was not to develop tools that **compete** with wind tunnel experiments ; the aim is to propose to the missile designer experimental tools and numerical methods that **complement** one another. Actually, more and more prediction methods combine both techniques : examples given in this paper concerning jet propulsion effects and characterization of Non Uniform Flow Aerodynamics illustrate this point.

Nevertheless, in domains where experiments are either expensive or difficult to use, the CFD approach can replace - or will replace - the experimentally based techniques ; the prediction of structural loads and aeroelastic phenomena is, from our point of view, a good illustration of that aspect.

The needs to improve accuracy of the numerical tools is clear : the Navier-Stokes approach is the good answer to that requirement. Much remains to be done in this area, even if the feasibility of N.S. simulations has been demonstrated.

To end with an optimistic remark, one must be confident concerning the improvement of computing power for a given cost : parallelisation techniques have already proven their efficiency and the forthcoming generations of processors - and computer architectures - will still widen the use of CFD for missile aerodynamics.

ACKNOWLEDGEMENTS

The AEROLOG software has been developed with support of the french DGA (DRET and SPMT) ; work on HPF programming has been funded by the European Community through the PHAROS ESPRIT-4 project ; developments and validations concerning the chimera technique applied to missile separation studies have been funded by the DGA (SPAe) through collaborations with ONERA and AEROSPATIALE missiles.

REFERENCES

- [1] *Simulation d'un Système de Déviation de Jet à l'Aide des Equations d'Euler*
M. Brédif, J. J. Chattot, C. Koeck & P. Werlé
AGARD CP 412, pp. 13.1-13.11, 1986.
- [2] *Parallelized implicit Euler solver for the analysis of unsteady aerodynamic flows*
C. Borel & M. Brédif
Proceedings of the First European Computational Fluid Dynamics Conference, pp. 1069-1072, 1992.
- [3] *Two new Chimera Methods : application to missile separation*
J.P. Gillyboeuf, P. Mansuy & S. Pavsic
AIAA paper n° 95-0353, 1995.
- [4] *A Multiple Grid Scheme for Solving the Euler Equations*
R.H. Ni

AIAA Journal, Vol. 20, pp. 343-349, 1982.

[5]

An Implicit Finite-Volume Method For Solving The Euler Equations

A. Lerat, J. Sidès & V. Daru

Lecture Notes in Physics 170, pp. 343-349, 1982.

[6]

Méthodes pour la prédiction de séparation de charges : Etat de l'art à MATRA DEFENSE

C. Jeune, P. Mansuy, E. Ribadeau-Dumas & M. Brédif

AGARD FDP Symposium on «Aerodynamics of Store Integration and Separation», AGARD-CP-570, 1996.

[7]

Implementation of an Industrial CFD Code on a Massively Parallel Computer with Distributed Memory

F. Choukroun, F.X. Roux, C. Borel & M. Brédif

Parallel CFD'93 : New Algorithms and Applications, pp. 271-276, Elsevier Science, 1995.

[8]

Portable Implementation of a non Conform Industrial CFD Code on MIMD MPP Systems

C. Borel & B. Culty

Parallel CFD'94 : New Algorithms and Applications, pp. 169-176, Elsevier Science, 1995.

Figure 1

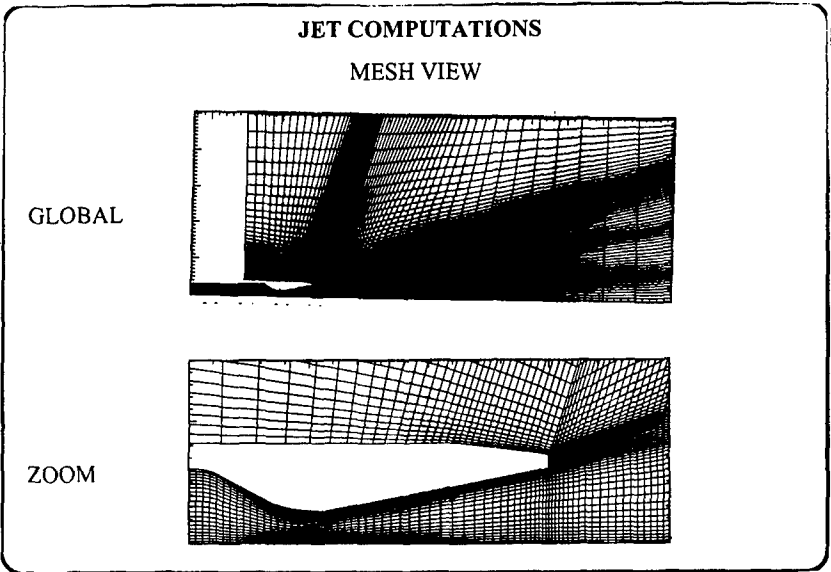


Figure 2

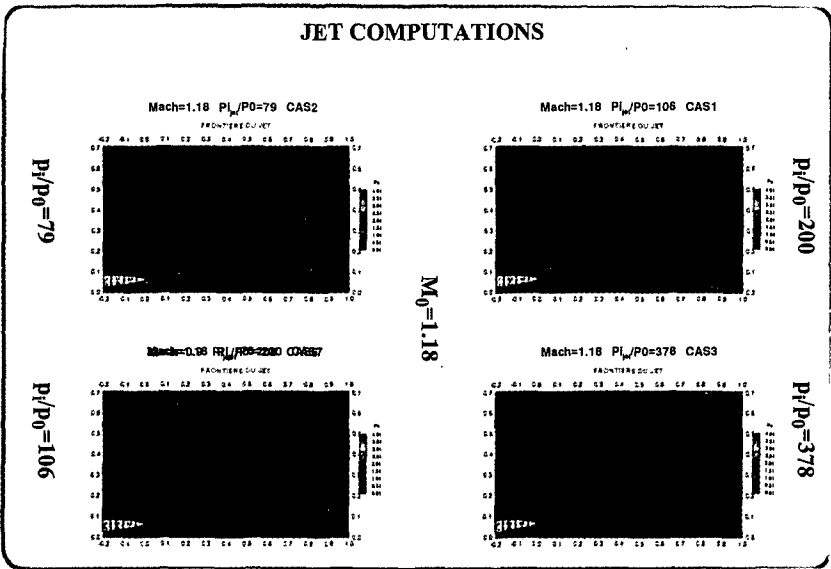


Figure 3

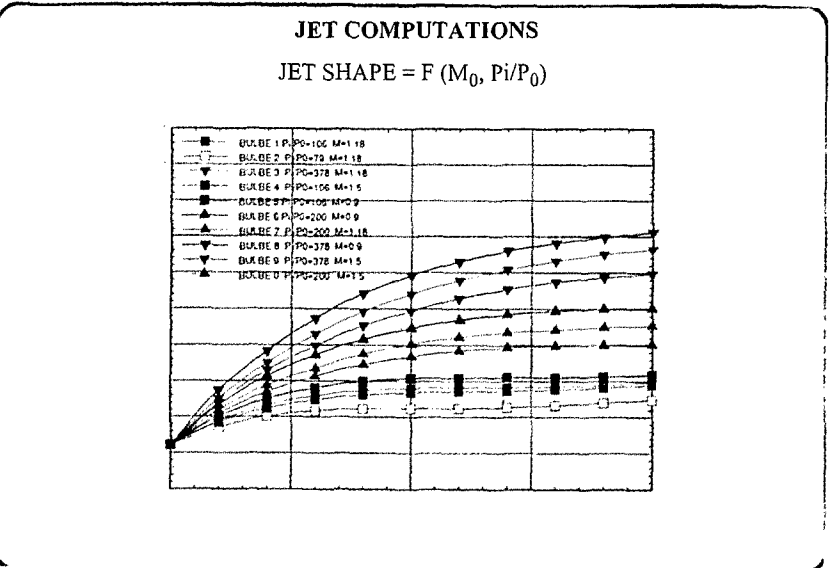


Figure 4

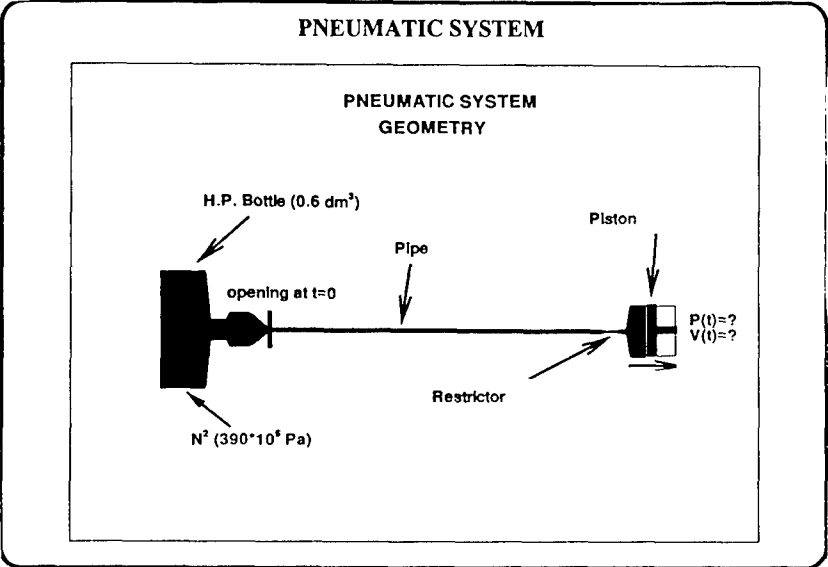


Figure 5

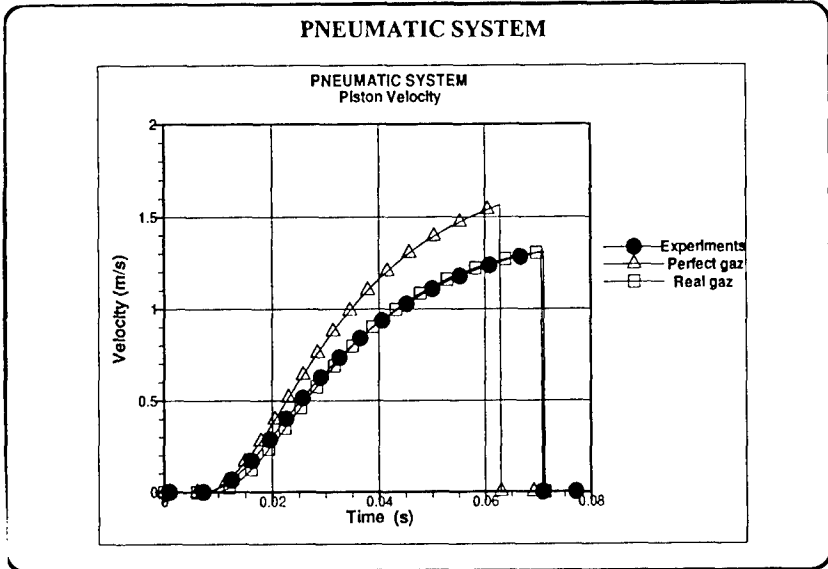


Figure 6

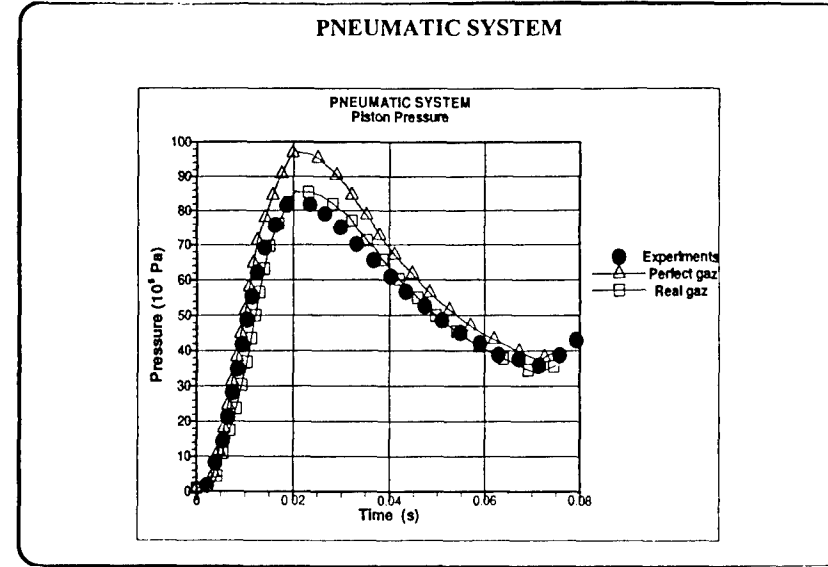


Figure 7

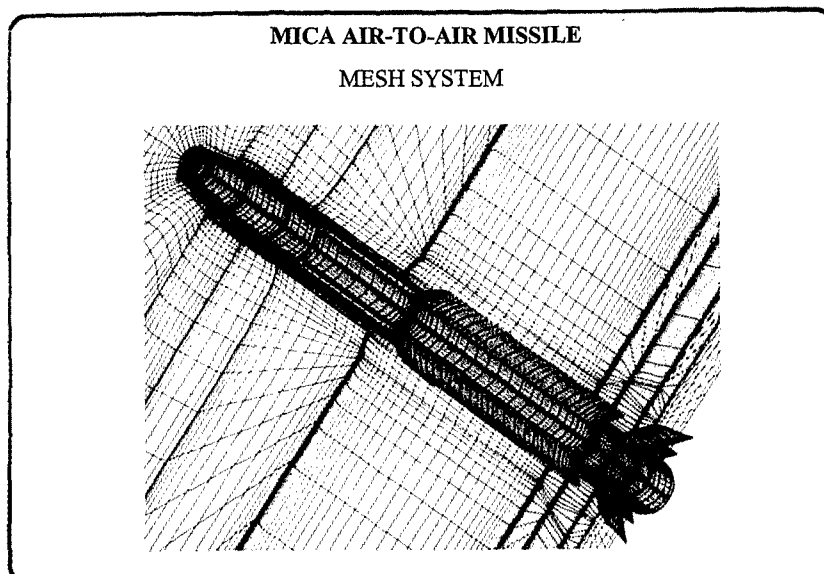


Figure 8



Figure 9

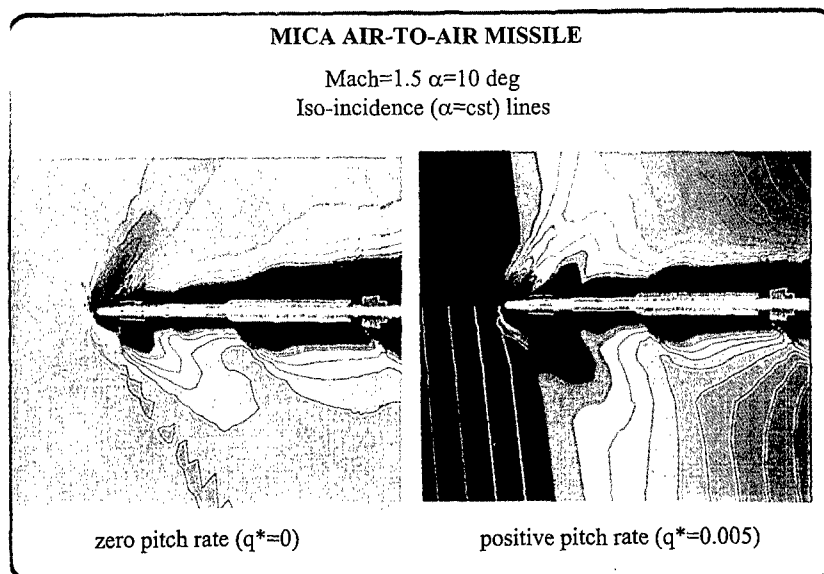


Figure 10

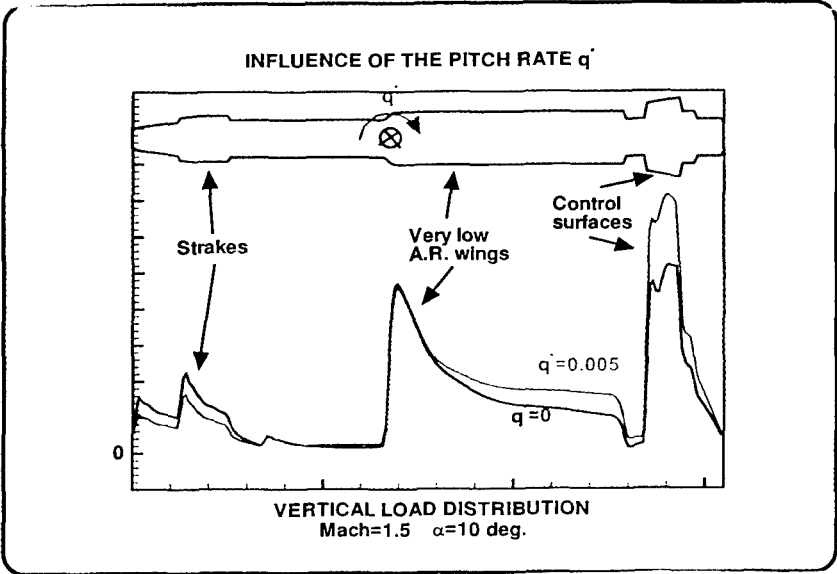


Figure 11

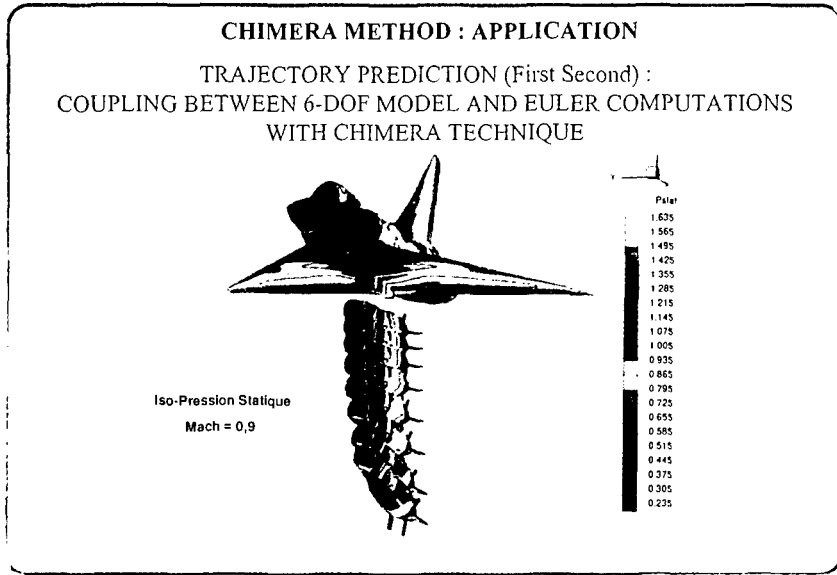


Figure 12

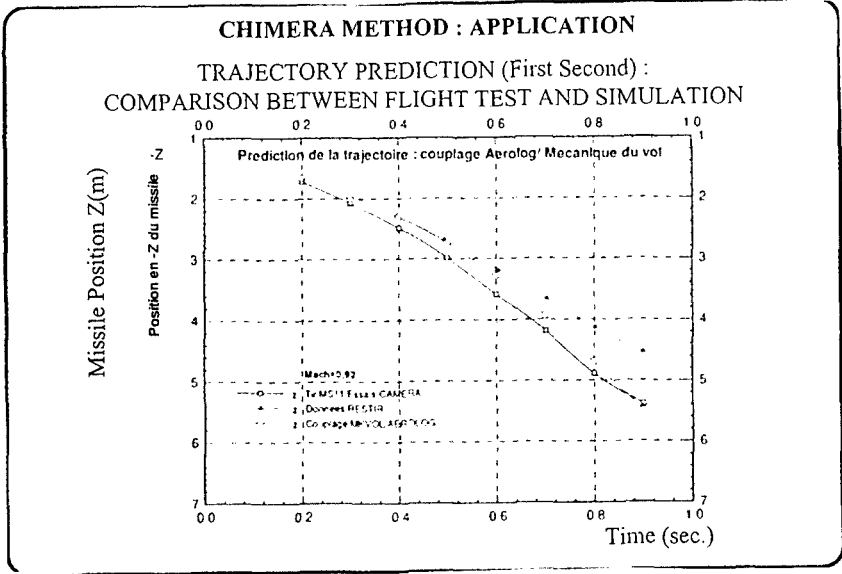


Figure 13

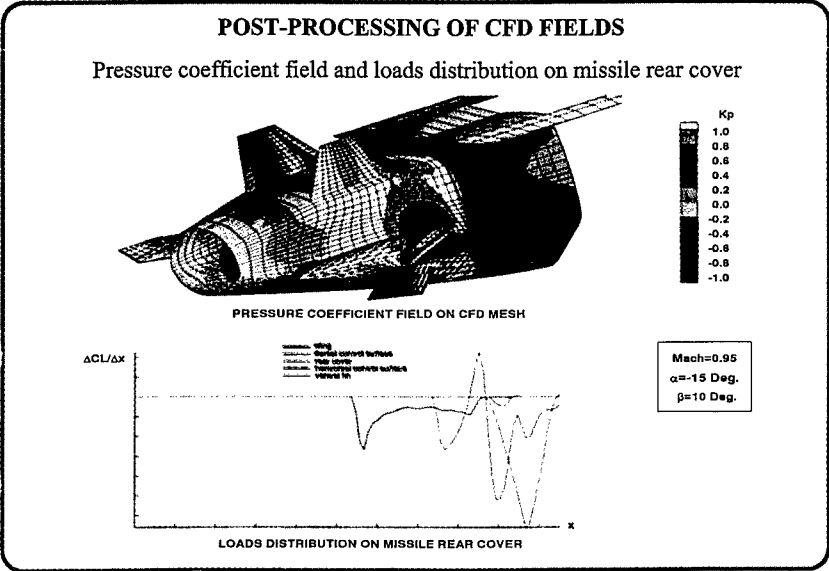


Figure 14

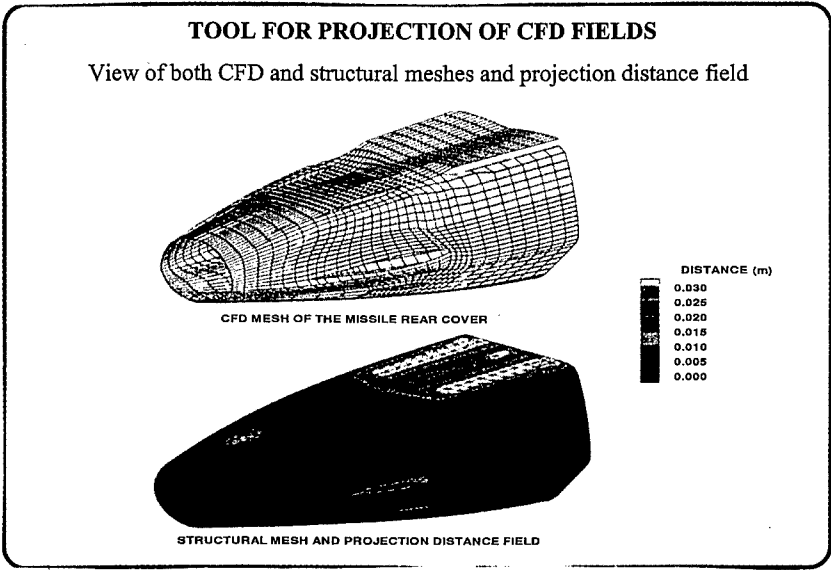


Figure 15

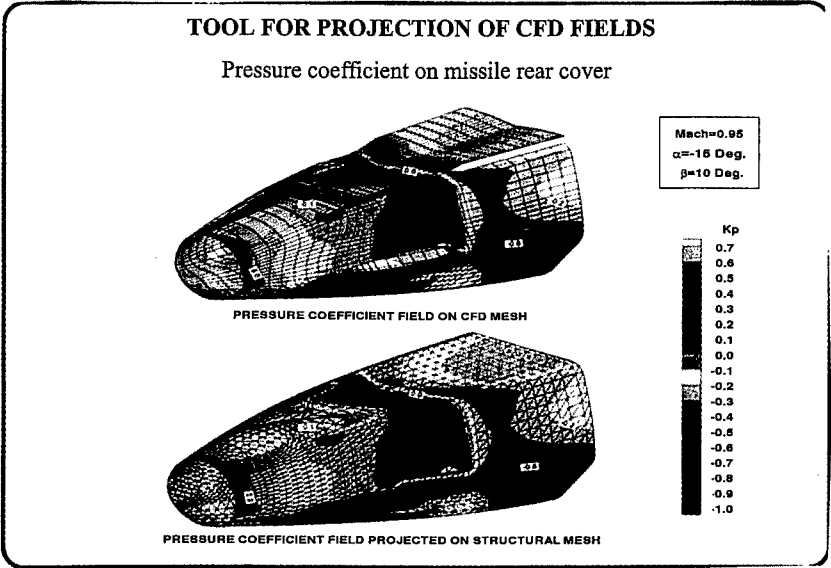


Figure 16

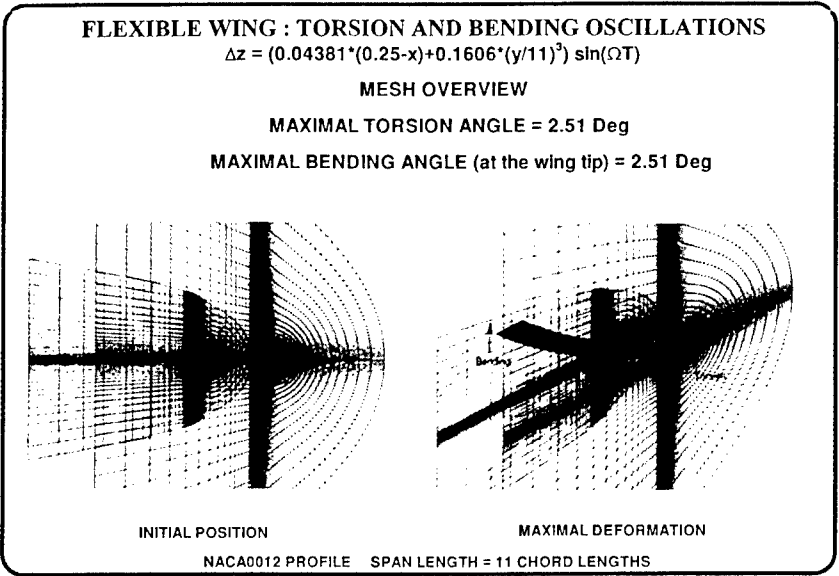


Figure 17

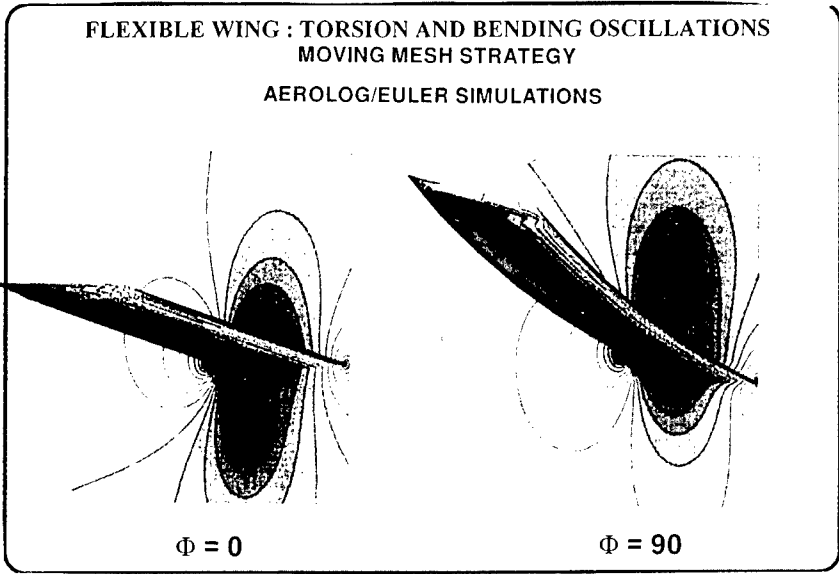
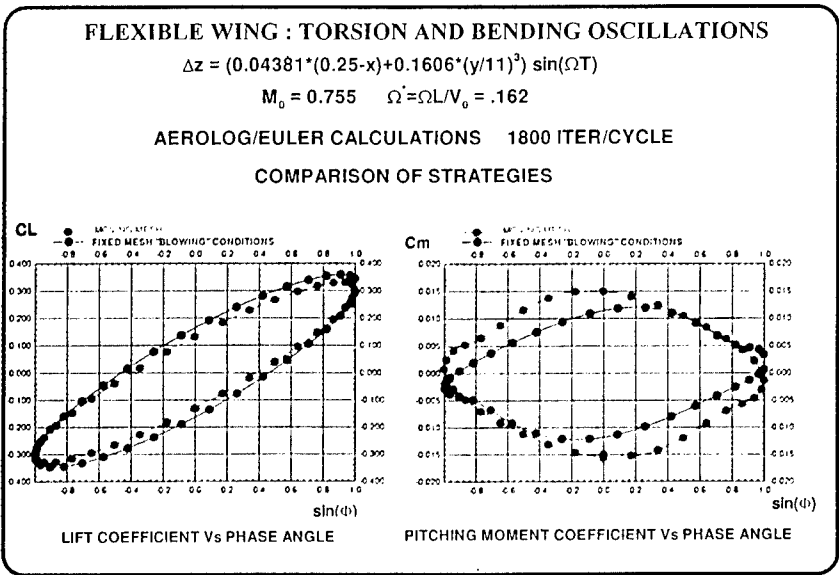


Figure 18



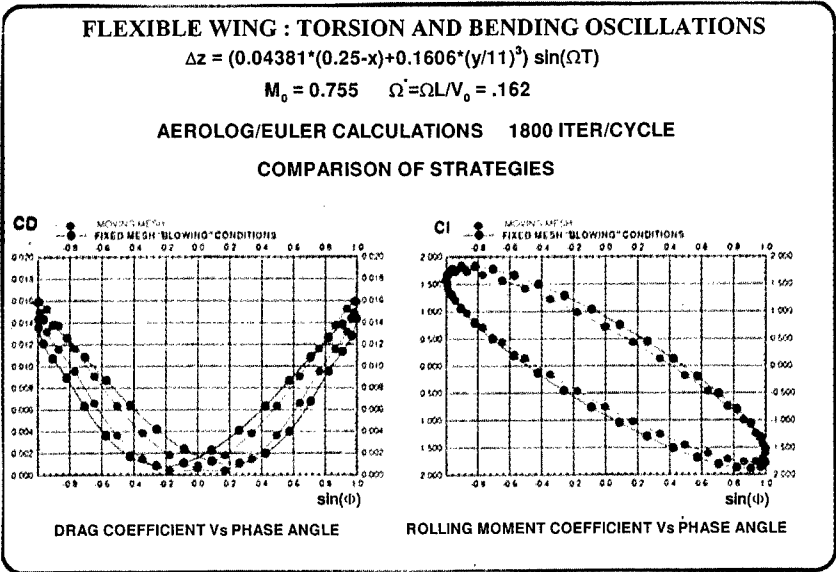


Figure 19

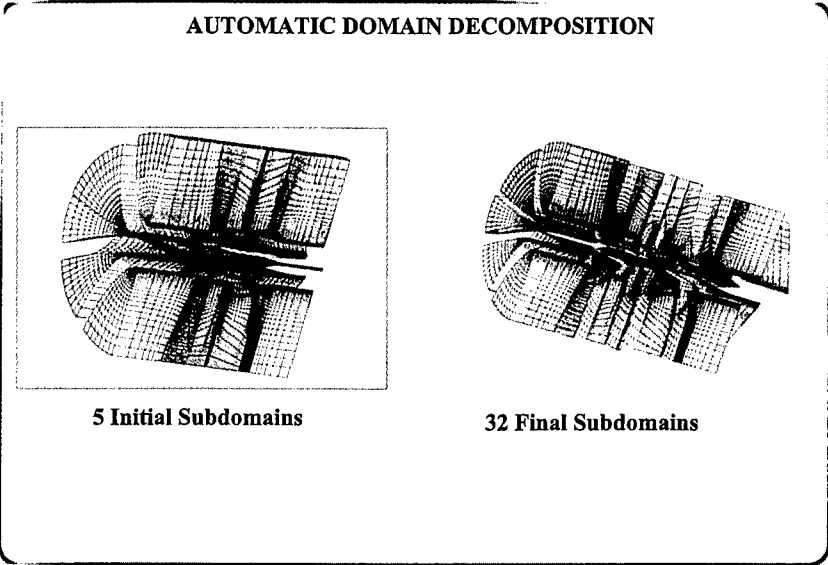


Figure 20

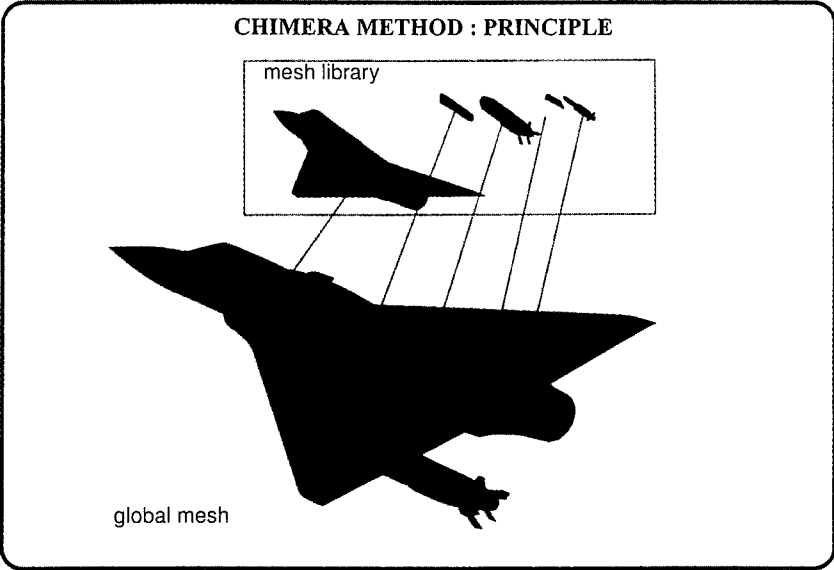


Figure 21

NAVIER-STOKES COMPUTATIONS
SUPERSONIC MISSILE Mach=3 $\alpha=10^0$ $\phi=65^0$

EULER

CPU TIME = 5 hours
Rolling Moment = 0.0013

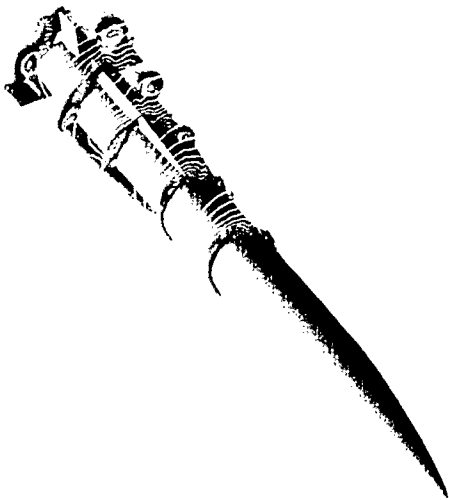


Figure 22.a

Experimental Rolling Moment = 0.021

NAVIER-STOKES/B.LOMAX

CPU TIME = 111 hours
Rolling moment = 0.013

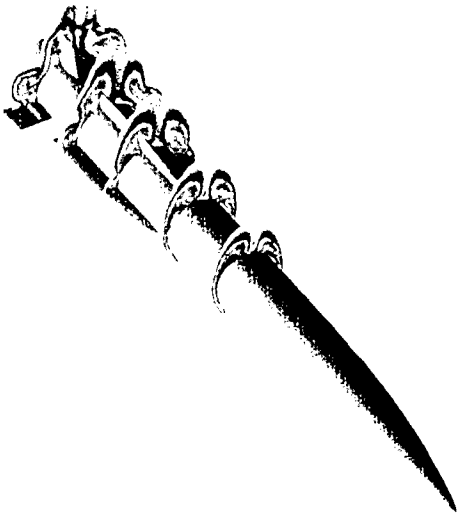


Figure 22.b

ROLE OF CFD IN MISSILE AERODYNAMIC DESIGN: A REVIEW OF RECENT EFFORTS AT RAYTHEON

B. Srivastava, J. Furtek, A. Shelton, R. Paduano
Raytheon Systems Company
Systems Design Laboratory
Tewksbury, MA 01876
USA

1. SUMMARY

Computational Fluid Dynamics (CFD) predictions for several supersonic missile models with wings, tails, divert jets, wire covers and strakes at several angles-of-attack and tail fin deflections of 10 and 20 deg are compared with the model wind tunnel tests. The results show excellent comparisons of all forces and moments with the measured data. Additional several example studies are discussed to show that these predictive capabilities provide a powerful design and analysis tool that can be judiciously combined with the wind tunnel tests to reduce the overall system development cost and to enhance the system reliability for the current and future generation missiles.

2. INTRODUCTION

Computational Fluid Dynamics (CFD) is playing an ever increasing role in aerodynamic design for advanced flight vehicles either for performance improvement of the existing system for a new missions or for new concept development for future missions. A cost effective design process is to judiciously combine the wind tunnel tests and CFD studies that exploit the inherent strengths of each of these. This can only be achieved through a focused program that provides the necessary support and infrastructure needed for the task. At Raytheon's System Design Laboratory, a CFD program that was initiated a few years ago, is impacting the missile aerodynamic design process from efficiency and cost considerations. The subject matter of this paper deals with a brief overview of the effort in this area. It discusses the CFD aspects of software and hardware capabilities, validation results for generic missile systems with wings, tails and other relevant appendages, divert jet for missile control, and fin deflections. Missile related design applications are then discussed to outline the missile load distribution methodology, multibody interactions (such as a/c mounted missile with pylon) and plume effects. Relevant conclusions as well as our future efforts are briefly enumerated.

A coupled wind tunnel and CFD based progressive design flowchart is shown in Fig. (1) which highlights the specific role of the CFD during missile design process. The right branches of the flowchart are traditional past efforts that are being currently augmented with the left branches based on the CFD technology. As shown in this chart, contributions from *validated CFD* in the areas of missile load distribution, free-flight scaling, heat transfer effects, sensor optical quality and captive loads are typical since the corresponding repeat wind tunnel tests for achieving design iterations or

modifications are prohibitively expensive. An alternate approach is to utilize the like data base for CFD validation studies with subsequent design trade-off studies. Postflight analysis using CFD are additional ways to supplement the quest of flight observed anomalies. However, emphasis must be placed on the cautious utilization of CFD within the realm of appropriate validation which highlights the modeling issues, boundary approaches and grid effects for a given application. Numerous considerations such as those depicted through Fig. (2) are the necessary ingredients of a CFD validation process. A design team must build these over a substantial time period to make the needed impact on the design and development environment.

3. COMPUTATIONAL CAPABILITIES

For most missile applications, a server with parallel compute capability is a requirement to meet the needed challenge in a design environment. Relevant pre and post-processing software/workstations as well as parallel CFD solvers, complete the minimum requirement for a thriving CFD design activity. The work reported here was done on a DIGITAL 8400 with six processors, GRIDGEN (Ref. 1) as a preprocessor and TECPLOT (Ref. 2) as a postprocessor. Most of the computations were performed with 1-2 Million grid points with a turn-around time of approximately 6-10 hours with dedicated 4-6 processors. Specific examples contain the relevant details. Most of the computations reported here were performed using the flow solver PARCH for which additional details are available in Refs. (3-5). Details of many of the results presented here are also available through several other past presentations of the current authors. These references are cited along with the relevant example cases. All reported CFD results are based on appropriate convergence studies, grid accuracy effects, boundary effects and the type of flow solver (Euler versus Navier-Stokes, laminar versus turbulent) needed. In majority of the cases studied, it was determined that an Euler solver is adequate to provide a good estimate of the force and moment coefficients. Utilization of more complex flow models with turbulence did not yield any appreciable change in the predicted force and moment coefficients.

4. EXAMPLE STUDIES

4.1 Supersonic Missile with Wings and Tails

4.1.1 Symmetric Cases

Extensive comparisons of wind tunnel data and CFD computations at angles-of-attack from 0 to 35 deg for

symmetric supersonic flight configurations have been made to demonstrate the validation aspects of our CFD methodology. A sample of 16 such cases at Mach Nos. of 2, 3, 4, and 5 with angles-of-attack going up to 30 deg with both "x" and "+" configurations of the missile is shown in Fig. (3) for a wind tunnel missile model "A". Additional cases of CFD comparisons that go up to 40 deg angle-of-attack are shown in Fig. (4) where results are presented for Mach Nos. of 3, 4 and angles-of-attack 20, 30 and 40 deg for "x" and "+" missile configuration using a missile model "B". These validations show the capability of CFD model to predict the overall force and moments of a missile in supersonic flows. The right side of Fig. (4) also shows the procedure that was utilized in the design process for computing the missile airframe load distribution. Essentially, the CFD based pressure distribution is used to compute the overall axial load distribution and any differences between the wind tunnel values and CFD are adjusted through a linear correction term. Notice from this figure that the corrected distribution is only marginally different from the CFD derived distribution. Varying forms of this methodology is used to derive the component load distribution. All design load distributions are currently channeled through controlled CFD/tunnel data bases.

4.1.2 Asymmetric Cases

All asymmetric cases in this category are presented with the divert jet case that are presented below.

4.2 Supersonic Missile with Wings and Tails with Divert Jets

4.2.1 Symmetric Cases

Divert jets promise missile agility. However, the aerodynamics of jet and free-stream interaction is very complex. We have developed a good understanding of the jet interaction through utilization of CFD models. Extensive comparisons of wind tunnel data and CFD computations at angles-of-attack from 0 to 25 deg for symmetric flight configurations with divert jets of thrust ratio ($T/q.s$, where T is thrust, q is free-stream dynamic head and s is the missile cross-sectional area) of 0 (no jet), 1 and 4 are presented in Fig. (5). Notice the excellent comparative agreements. This figure also shows the cross-plane Mach number contours along the missile with a jet thrust ratio of 4, showing dominant supersonic flows. Details of these test cases are available in Ref. (3).

4.2.2 Asymmetric Cases

Figs. (6, 7) show the computed results and their comparison with the wind tunnel data for missile model "A" in asymmetric configuration at a nominal Mach number of 4 and angles-of-attack going up to 20 deg with jet thrust ratio of 0, 1 and 4. Notice the excellent predictive capability of CFD for all five force and moment coefficients when compared to the wind tunnel data for a wide range of cases. These figures show the deviation of the CFD predicted

coefficients from the wind tunnel data along with the 45 deg line that represents the ideal line for an exact match. Symbols falling on this line show an exact match with the wind tunnel data. The bar in these figures indicate the ± 5 percent local deviation from the ideal line. There are some predictions that compare better with the data than others. The specific ones that do not compare well are enumerated in these figures. There is no specific trend in the enumerated cases for the observed deviations from the wind tunnel data. Also, notice from the roll moment comparisons in Fig. (7) that there is good amount of data scatter near zero indicating the possibility of wind tunnel balance measurement errors for numerically small moment coefficients. Further details of these results can be obtained from Ref. (6).

4.3 Supersonic Missile with Wings and Deflected Tails

Missile with fin deflections are fairly challenging to simulate with CFD methods due to the stringent grid requirements. We have made a significant progress in this area using novel grid topologies. Extensive comparisons of the wind tunnel data and CFD computations at angles-of-attack from 0 to 50 deg for symmetric and asymmetric flight configurations with fin deflection of 10 and 20 deg have been recently performed. Some examples of these cases are shown in Figs. (8, 9). Fig. (8) shows the CFD computation for a missile model "A" with 10 deg pitch fin deflection at a flight Mach number of 5.5 and at an angle-of-attack of 20 deg. Notice that the coefficients compare very well with the wind tunnel data. Fig. (9) shows the results for a fin deflection of 20 deg for the same missile in both the symmetric "x" and "+" configurations with angles-of-attack going up to 50 deg. The results are now presented for normal force coefficient and the center of pressure location to eliminate the arbitrary choice of a moment reference location associated with the longitudinal moments.

4.4 Supersonic Missile with Appendages

External wire covers are common appendages for missiles. Design of these appendages require aerodynamic load distribution along its length for attachment (pin) design. Wind tunnel tests have been used previously to reduce the associated drag effects and provide the overall total force and moments carried by these components. Uncertainty, however, prevails over the distributive load that can optimize the design process and thus reduce the overall missile weight. Validations are needed for the overall CFD predictions as well as for the load carried by these components. An example of this level of computation is shown in Fig. (10) for a missile model "C" at a flight Mach number of 5.5 and angle-of-attack of 20 and 24 deg. The overall CFD and wind tunnel force and moment coefficient comparisons are excellent as shown in this figure. Fig. (11) shows the loads on the windward wire cover. Measured experimental data typically utilize a trapezoidal load variation, which have been compared with the CFD load distribution for three flight conditions. Notice that the peak near the leading

edge for critical design is significantly higher than estimated by wind tunnel measurement. It was possible to modify the design using the CFD/wind tunnel coupled studies, in this instance.

4.5 Concept Development

CFD methodology also provides a means for early concept development without much associated cost. An example of this class of applications is the low force amplification factor associated with a windward jet. Several conceptual studies suggested that this low amplification factor cannot be enhanced to one or more without making a major change in the missile design (Refs. 3, 6). Additional studies were then conducted using CFD to demonstrate that wing tip mounted divert jets can alleviate this performance limitation (Ref. 7).

4.6 Plume Effects

Effects of plume on missile airframe aerodynamics for supersonic flows is discussed here very briefly. At certain altitudes, missile exhaust plume can interfere with the control surfaces to warrant specific studies. Typically expensive wind tunnel tests are needed to address airframe-plume interactions even with cold exhaust tests. Model mounting, exhaust gas simulation and balance mounting in the wind tunnel tests create many difficult issues. At times, a solid plume shape has been utilized to quantify these effects. We have recently performed several studies to quantify these effects utilizing CFD studies. An example is shown in Fig. (12). The exhaust nozzle flow was simulated by specifying the nozzle exit conditions (velocity distribution etc.) with a single component hot gas. Afterburning and subsequent chemistry effects were not included in the present computations. A full Navier-Stokes analysis was performed at a lower and a higher altitude of interest to assess the total changes in the force and moment coefficients. For this case, the results show very marginal changes in the overall force and moment coefficients. Similar studies were conducted to assess the influence of the plume on the control effectiveness.

4.7 Complex Missile Geometry

Most of the results presented above show a typical missile geometry with ogive cylinder forebody. This kind of geometry requires a grid topology that is fairly easily constructed. Complexity in missile geometry can complicate the grid construction process. It is critical that in such cases appropriate effort is devoted to create a quality grid consistent with the flow solver. An example is a missile which has a complex forebody, as well as a complex tail mounting in the rear of the missile as shown in Fig. (13). This missile consists of a flat nose-window, a roll-control nose strake, puffed-up side cheeks, a step down in diameter and later a fin assembly mounting at the rear end. Missile surface pressure distribution obtained from the CFD computations for a flight Mach number of 2.7, an angle-of-attack

of 26 deg with windward window is shown in this figure. All flow details are properly resolved. Fig. (14) shows the axial load distribution on every component of the missile as well as a comparison of the overall force and moment coefficient with the wind tunnel data. Notice that the comparison is good.

4.8 Multibody Effects

Captive loads determination is an important design criteria for air-to-air missiles. Current analytic/empirical methods are inadequate to provide needed design data. Wind tunnel tests can provide the needed interference effects. Cost constraints, however, preclude these kind of tests in the early design phase. CFD can provide an adequate means to bridge the gap. For the missile discussed above, wind tunnel tests were conducted to determine the torque required to rotate the nose for target observation at numerous flight conditions. However, during captive flight, nose-to-nose interference can alter the projected torque requirements. CFD methodology was used to estimate these effects for two missiles mounted on a simulated aircraft (only wing interference) with pylons. CFD validation studies were first conducted to predict the single model wind tunnel measured nose torque which established a basis for further design trade-off studies. Further studies related to two missiles with wing and pylons as shown in Fig. (15). Captive flight conditions were at an angle-of-attack of 10 deg, a flight Mach number of 1.2 and a side slip angle of 45 deg. The overall results of the CFD computation is shown in Fig. (15) with surface pressure distribution and a cross-plane pressure distribution. Using these types of studies, it was possible to estimate the interference effects for design applications.

5. SUMMARY AND CONCLUSIONS

CFD technology has a vast potential to contribute in a design environment that can result in substantial program cost savings as well as enhanced product reliability. These are only a few of the vast arena of CFD applicability. The examples cited in this paper have resulted in a better quantification of the design parameters through a judicious amalgamation of CFD and wind tunnel technology. A close coupling of the wind tunnel test programs and CFD projects are, thus, essential to exploit the most out of the two technology areas. For CFD to meet its challenges, an up-front focused technical effort is required in terms of resources, infrastructure and personnel. It has been shown that when that happens, the CFD technology can meet the desired challenges of the design environment.

6. REFERENCES

- (1) "GRIDGEN", Software Licensed by Pointwise Inc., P.O. Box 210698, Bedford, Texas 76095-7698, USA
- (2) "TECPLOT", Software Licensed by Amtec Engineering Inc., P.O. Box 3633, Bellevue, WA 98009-3633, USA

- (3) Srivastava, B. N., "Lateral Jet Control of Supersonic Missile: CFD Predictions and Comparisons to Force and Moment Measurement", AIAA Paper No. 97-0639, 35th Aerospace Sciences Meeting, Reno, Nevada, January 6-10, 1997
- (4) Srivastava, B. N., "CFD Analysis and Validation for Lateral Jet Control of a Missile", AIAA Paper No. 96-0288, 34th Aerospace Sciences Meeting, Reno, Nevada, January, 1996. Also, *Journal of Spacecrafts and Rockets*, Vol. 34, No. 5, pp 584-592, September, 1997
- (5) Dash, S. M., York, B. J., Sinha, N., Lee, R. A., Hosangadi, A., and Kenzakowski, D. C., "Recent Developments in the Simulation of Steady and Transient Transverse Jet Interactions for Missile, Rotorcraft and Propulsive Applications", AGARD Meeting on Computational and Experimental Assessments of Jets in a Cross Flow, 1993, pp 29-1, 29-21
- (6) Srivastava, B. N., "Computation and Validation of Asymmetric Force and Moment Coefficients for Lateral Jet Controlled Supersonic Missile", AIAA Paper No. 98-2410-CP, 16th Applied Aerodynamics Conference (AIAA), Albuquerque, NM, June, 1998
- (7) Srivastava, B. N., "Lateral Jet Control of a Supersonic Missile: Computational Studies with Forward, Rear Body and Wing Tip Mounted Jets", AIAA Paper No. 97-2247, 15th Applied Aerodynamics Conference, Atlanta, June 23-25, 1997

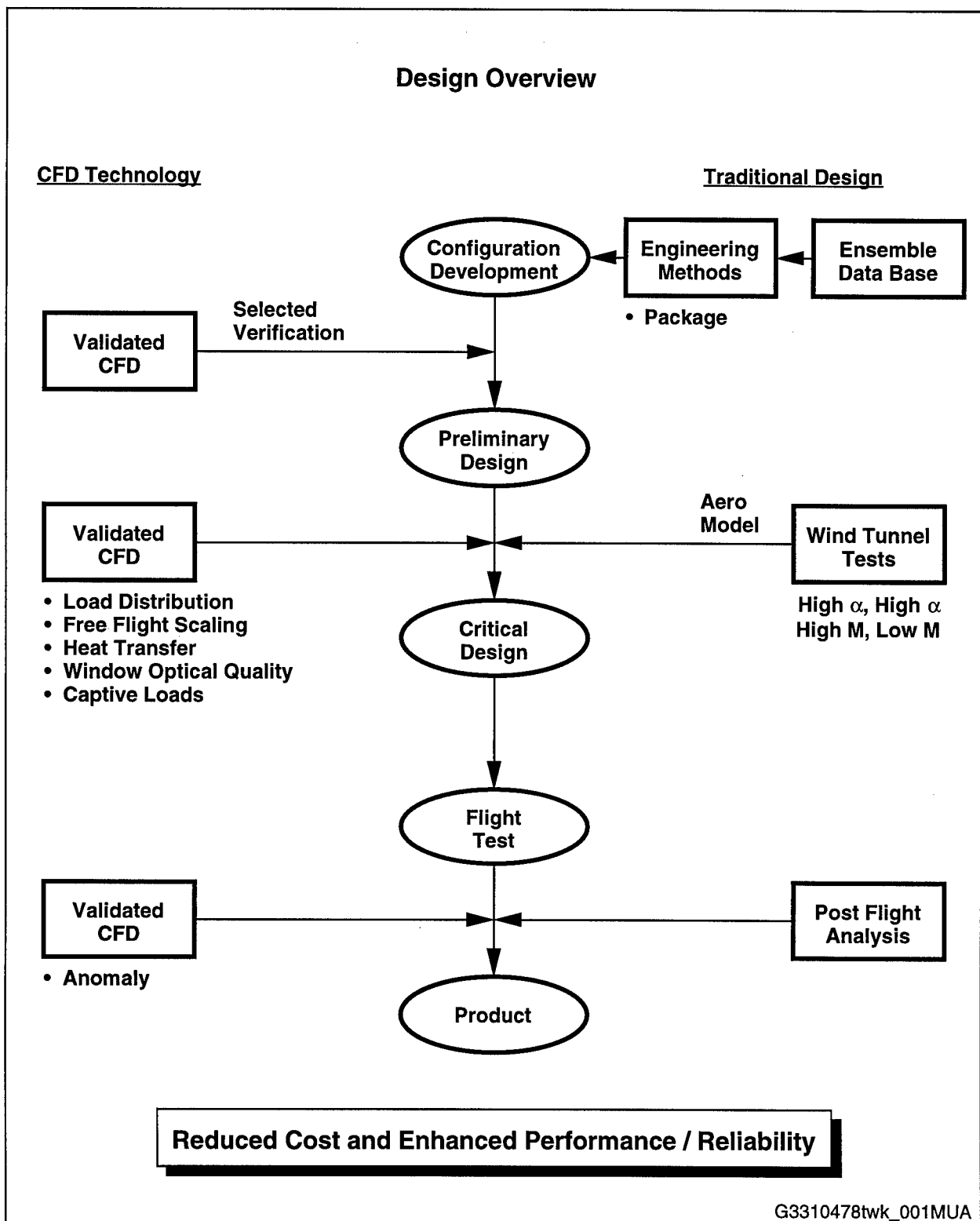


Fig. (1). Role of CFD in Missile Design

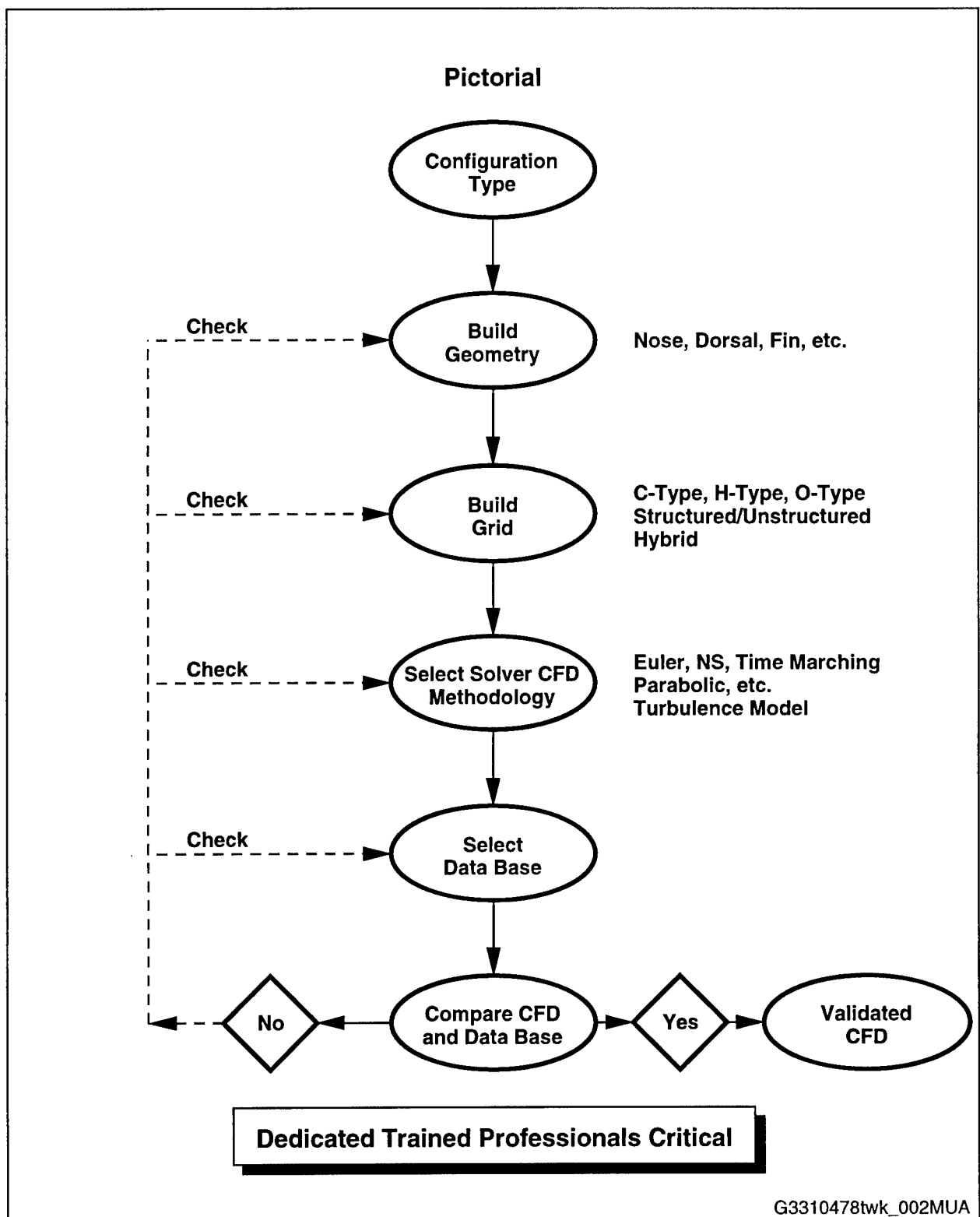


Fig. (2). CFD Validation Methodology

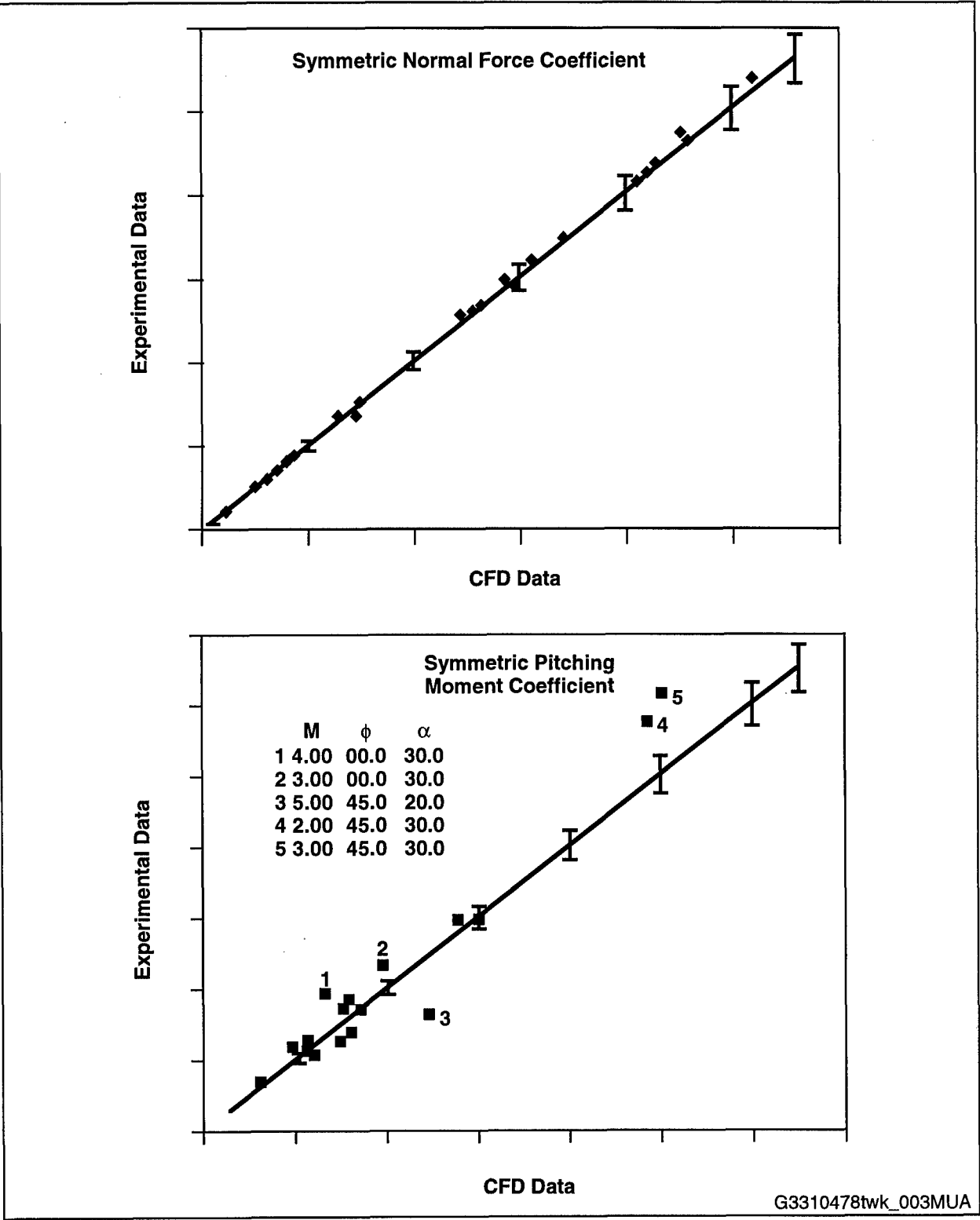


Fig. (3). CFD Validation for Missile Model A (Symmetric Configuration)
[M = 2, 3, 4, 5, 0 ≤ α < 35 deg, T/q.s = 0.0, 16 Cases]

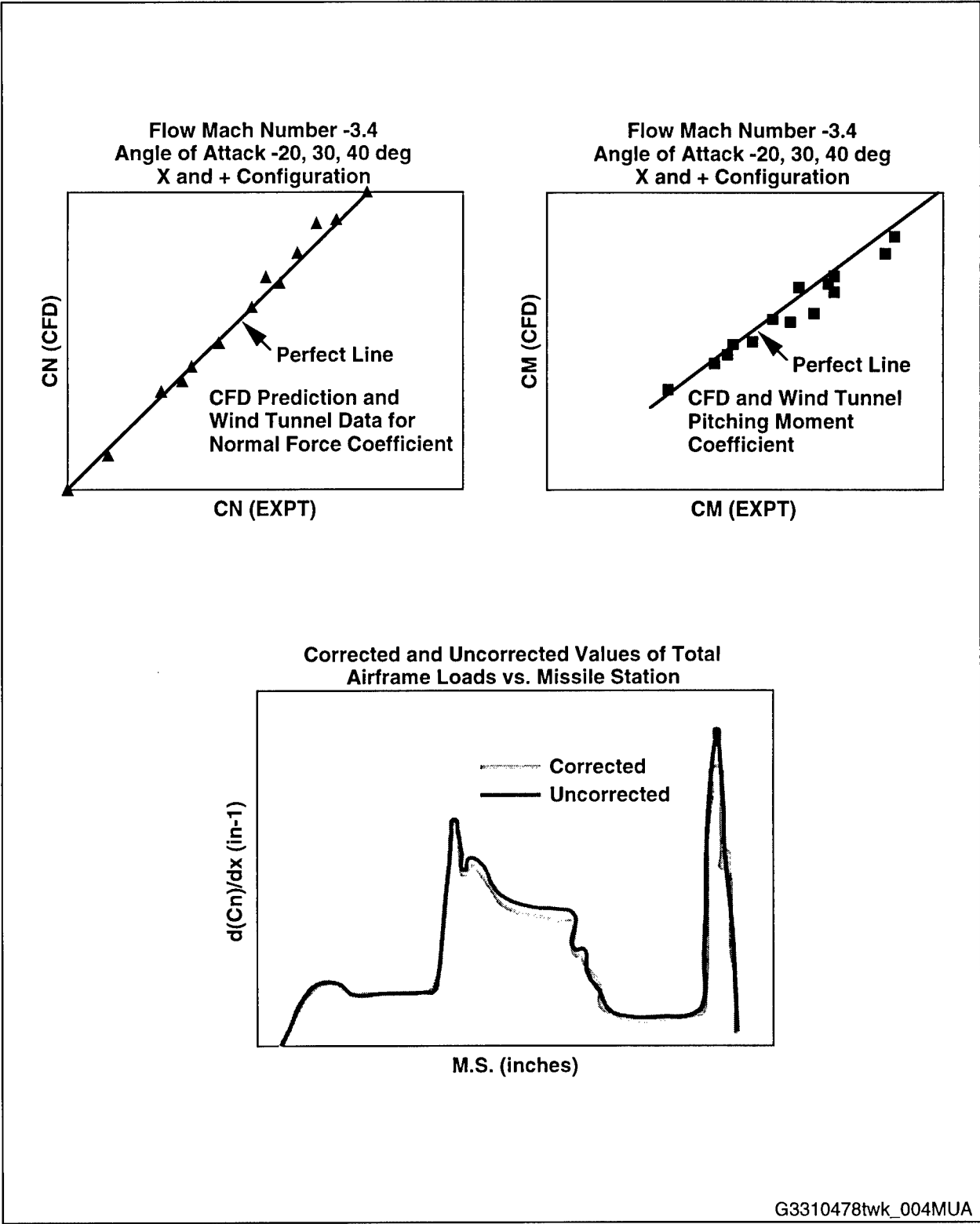


Fig. (4). CFD Validation for Missile Model B (Symmetric Configuration)
[M = 2, 4, α = 20, 30, 40 deg, T/q.s = 0.0, 13 Cases]

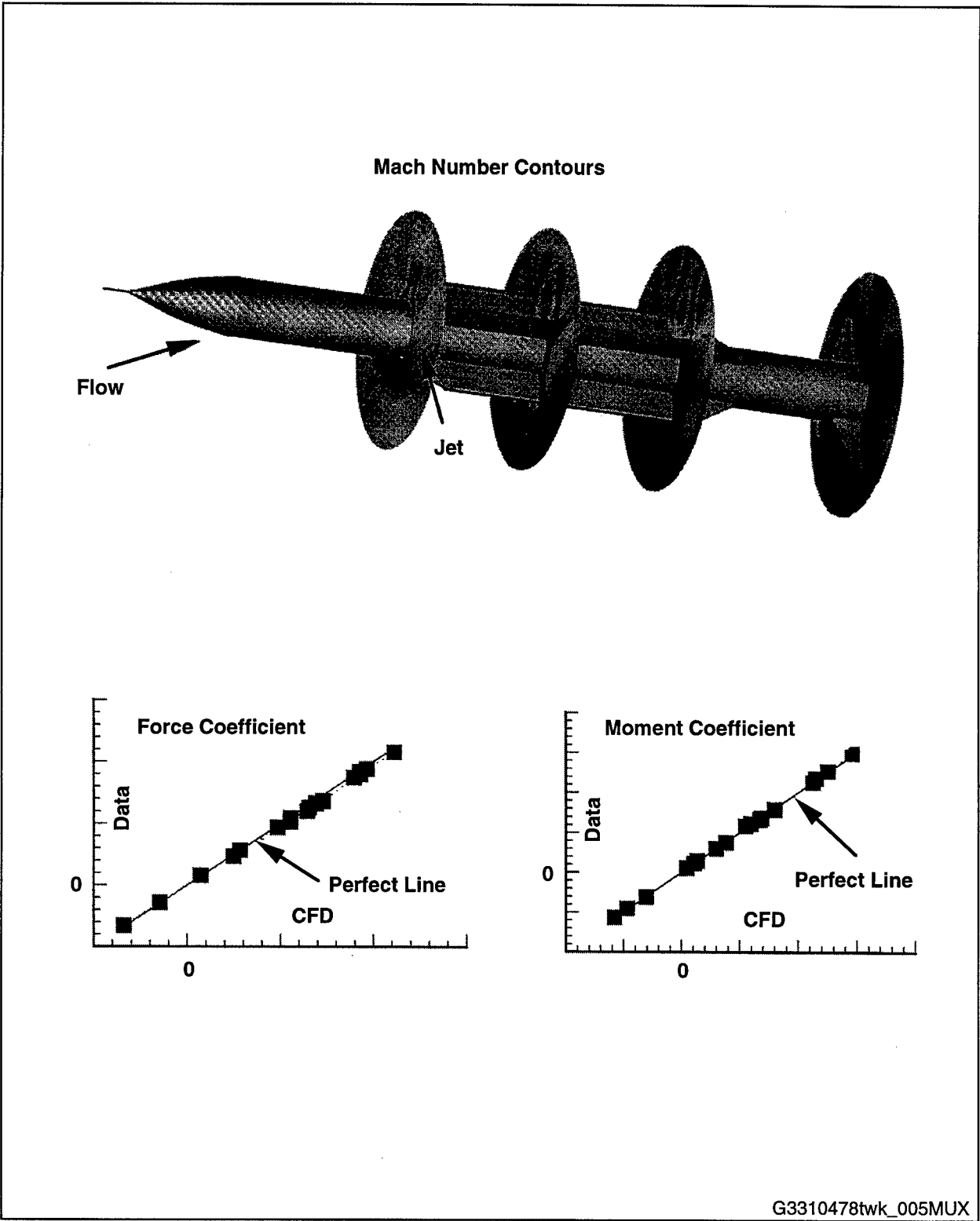


Fig. (5). CFD Validation for Missile Model A (Symmetric Configuration)
[$M = 4.0$, $0.0 \leq \alpha \leq 25$ deg, $|T/q.s| = 0, 1, 4$, Leeward/Windward, 17 Cases]

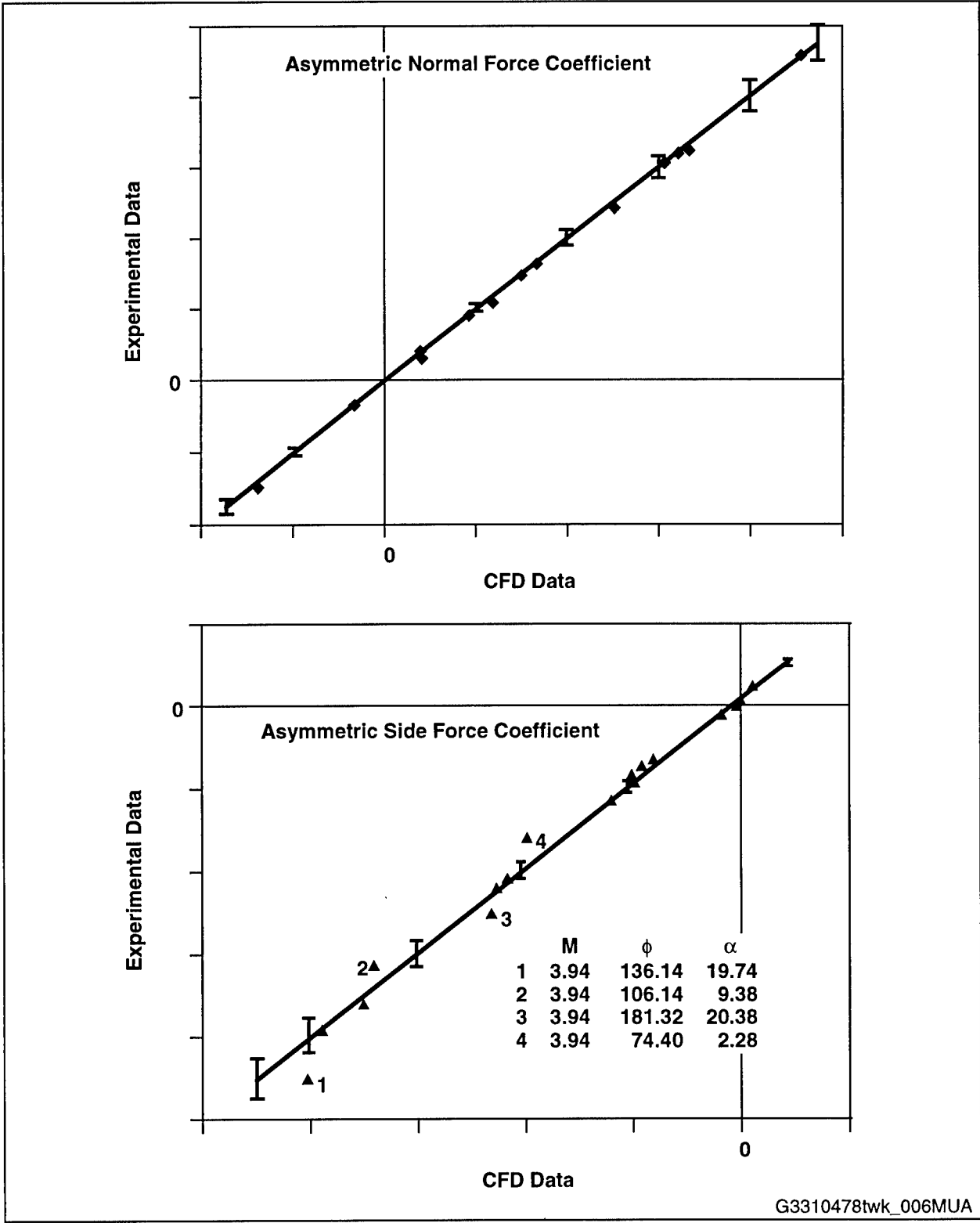


Fig. (6). CFD Validation for Missile Model A (Asymmetric Configuration)
($M = 4.0, 0 \leq \alpha \leq 20 \text{ deg}, |T/q.s| = 0, 1, 4, 17 \text{ Cases}$)

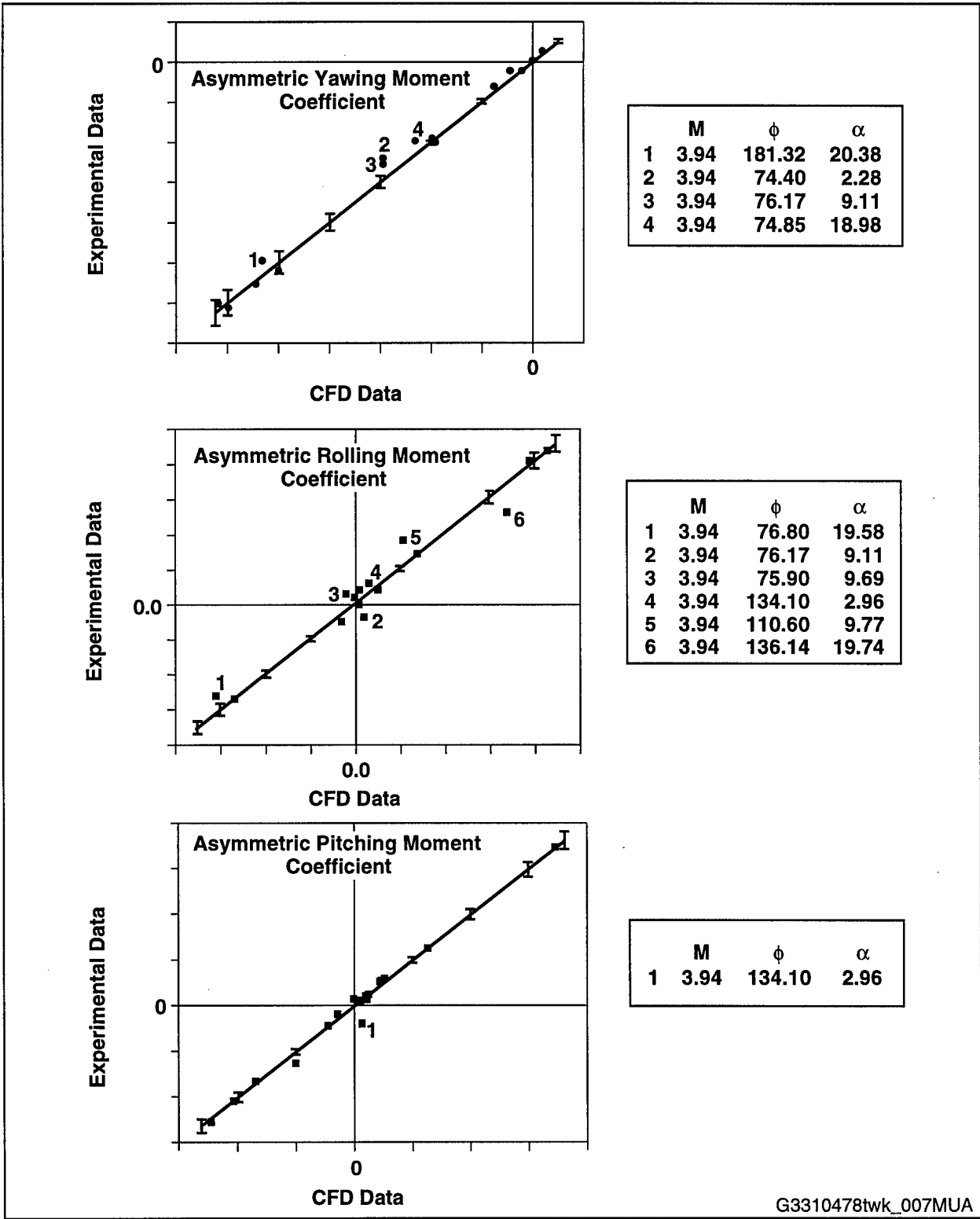


Fig. (7). CFD Validation for Missile Model A (Asymmetric Configuration)
[M = 4.0, 0 ≤ α ≤ 20 deg, |T/q.s| = 0, 1, 4]

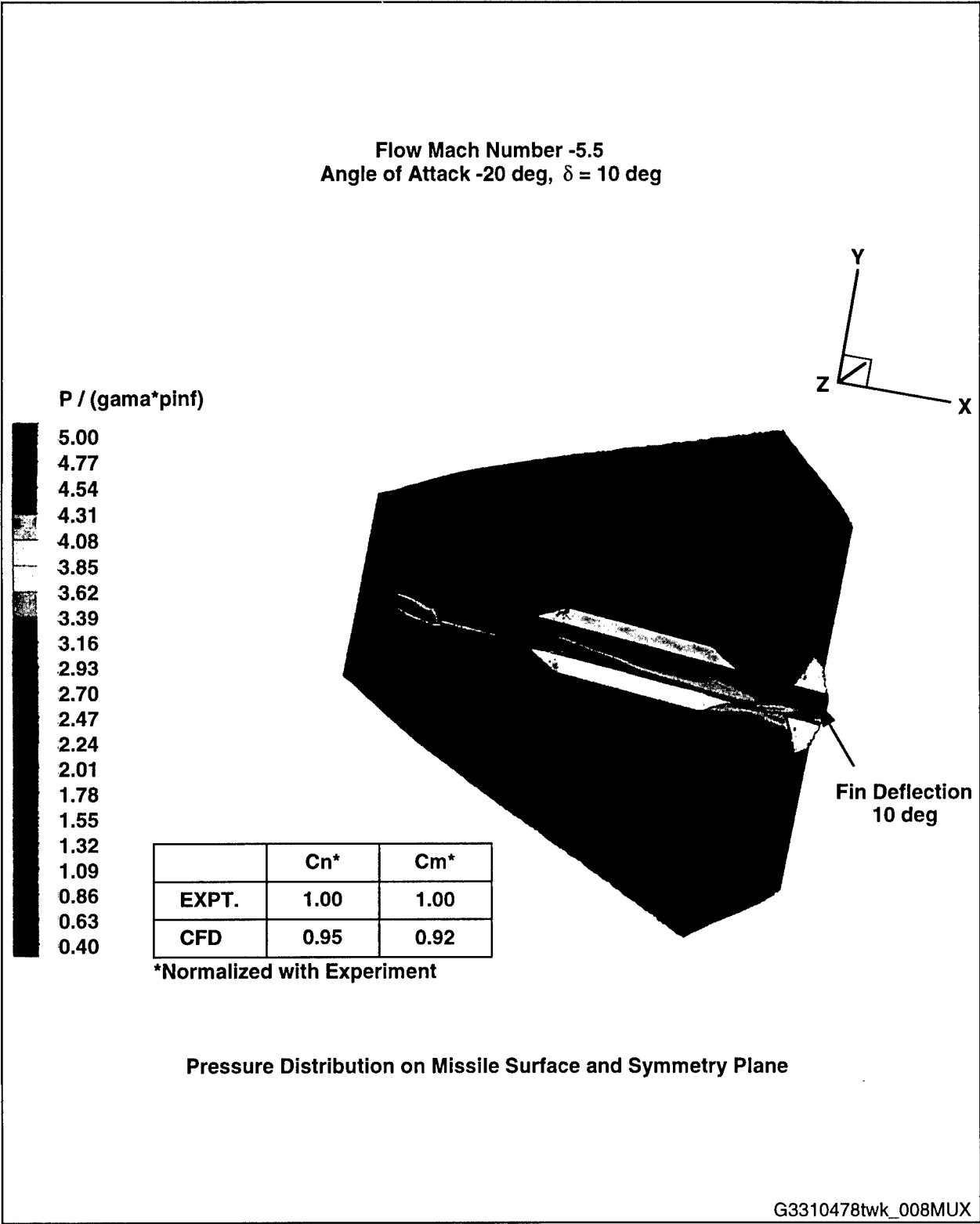


Fig. (8). CFD Simulation of a Missile Model A with Fin Deflection
(Flow Mach Number -5.5, Angle-of-Attack -20 deg, $\delta = 10$ deg)

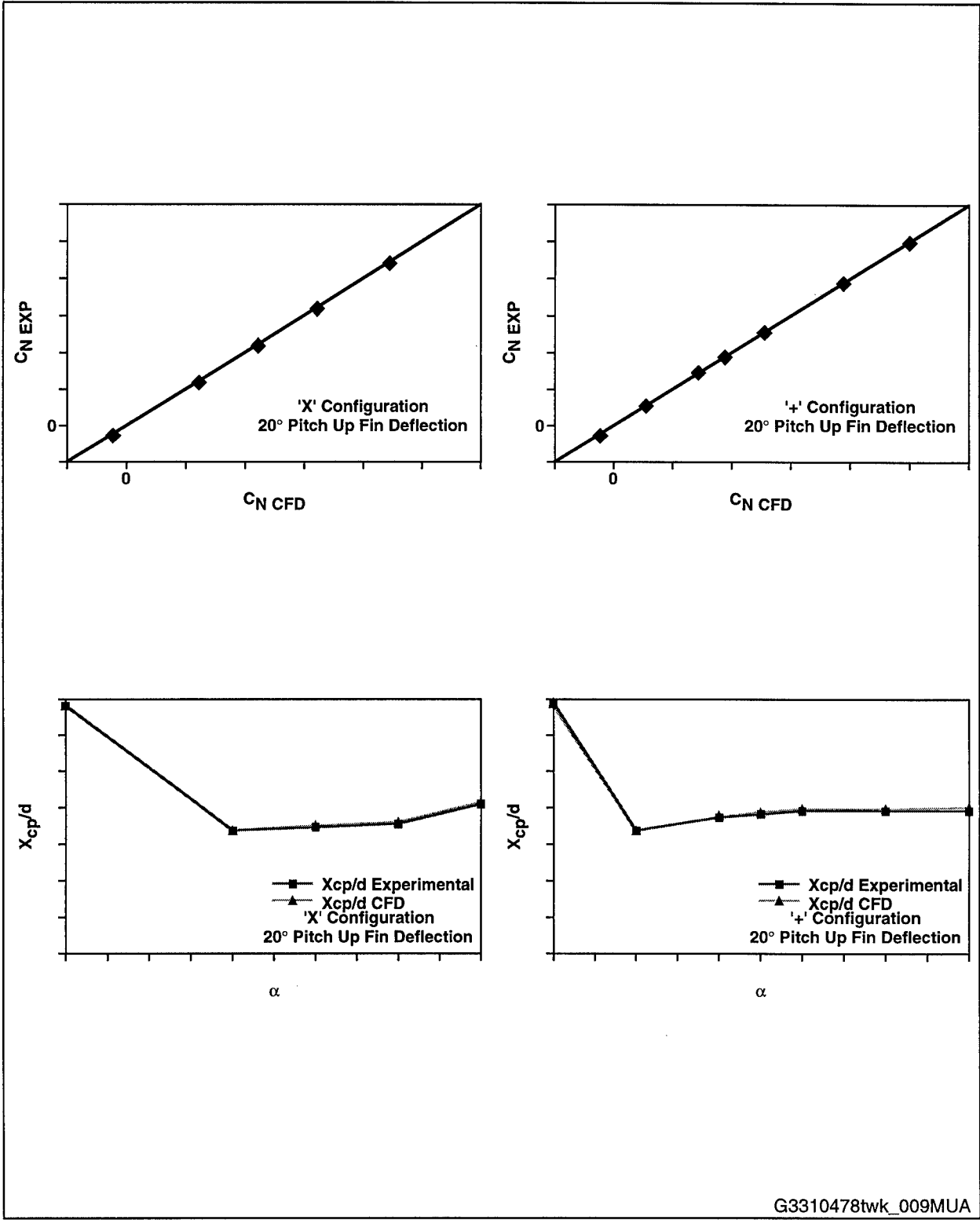
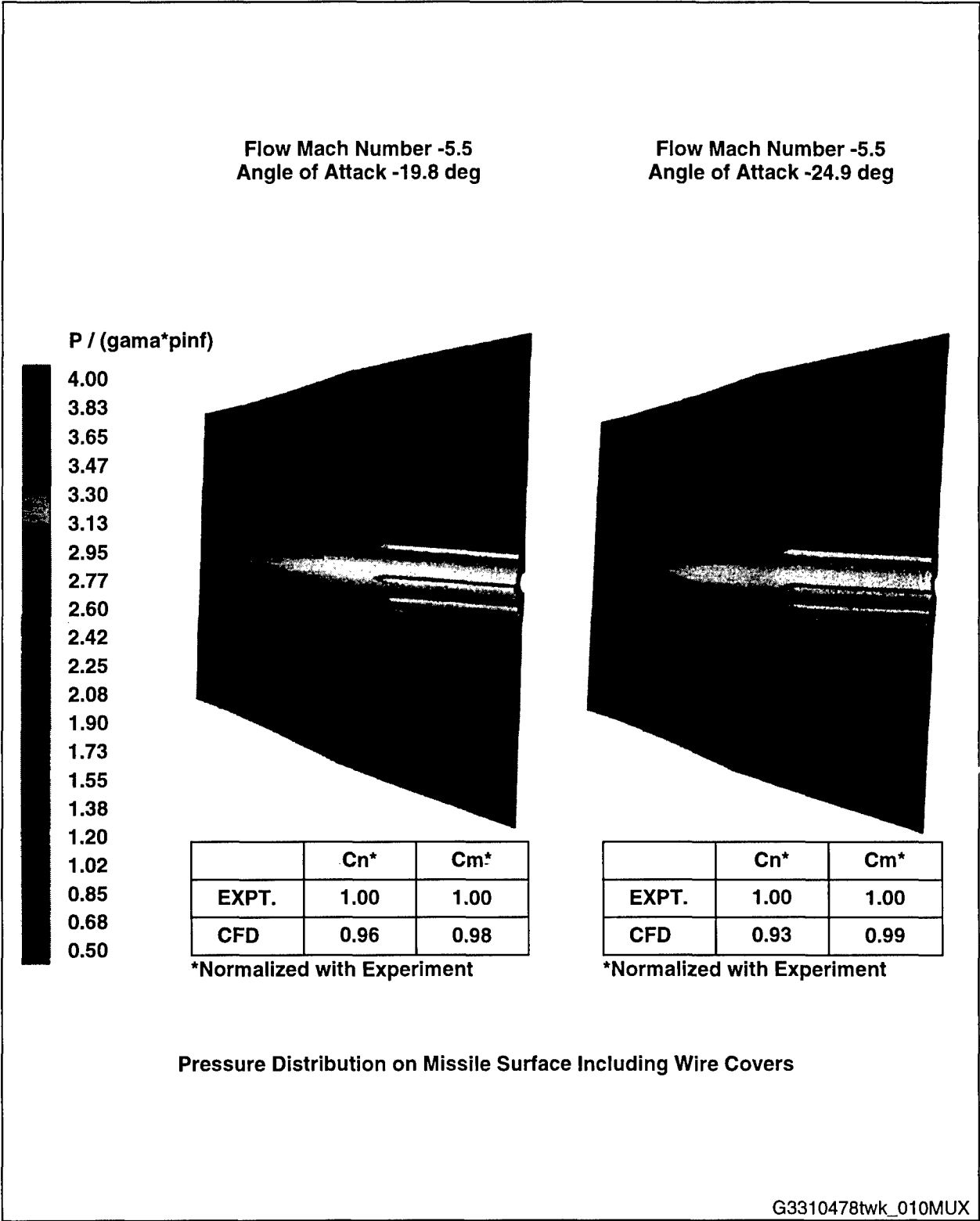


Fig. (9). CFD Validation with Fin Deflection for Missile Model A
[$M = 4.0$, $\delta = 20^\circ$, $0 \leq \alpha \leq 50^\circ$]



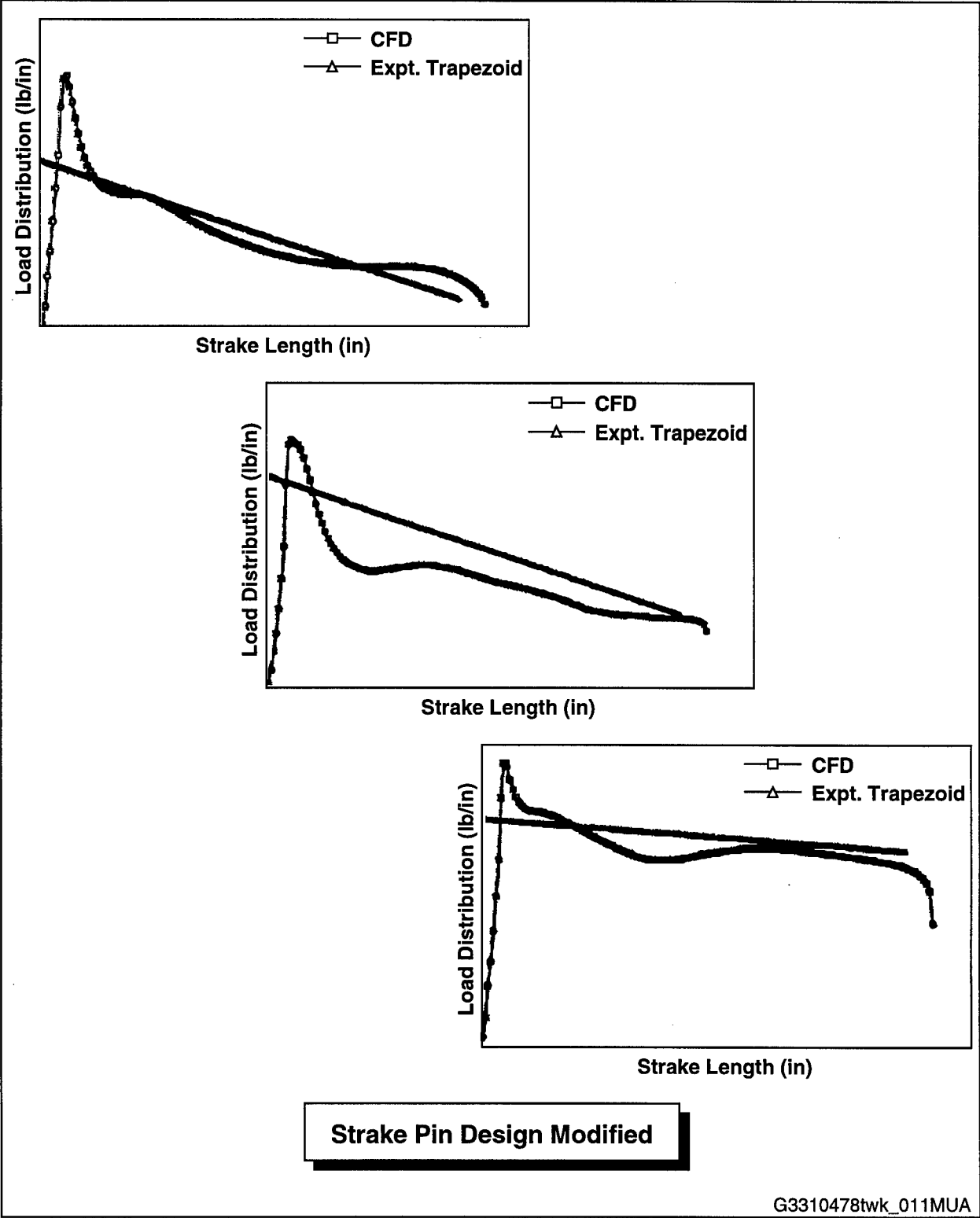


Fig. (11). Comparison of CFD and Wind Tunnel Measurements Stake Load Distribution
[M = 5.5, varying angle-of-attack]

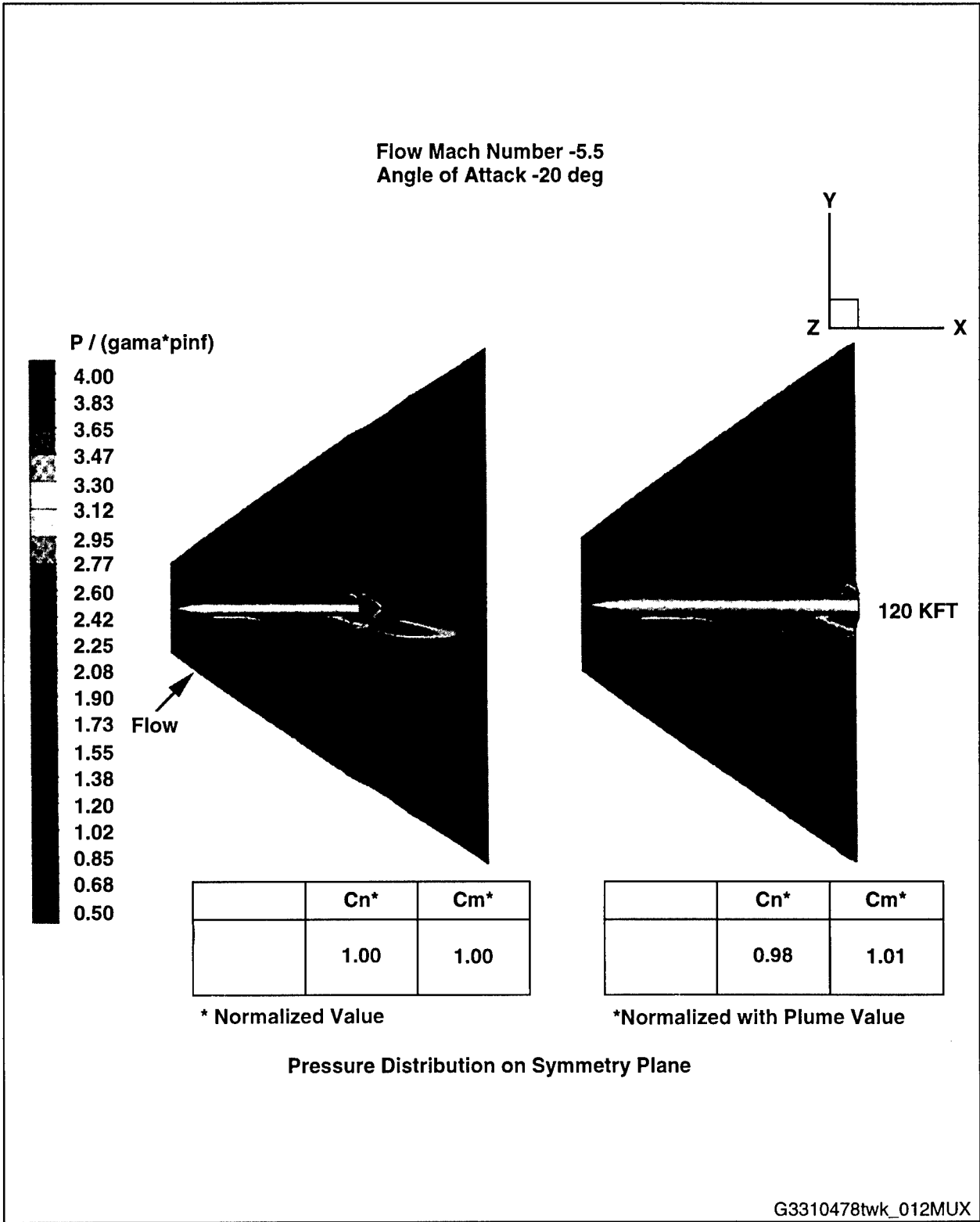


Fig. (12). CFD Simulation of a Missile With and Without Plume

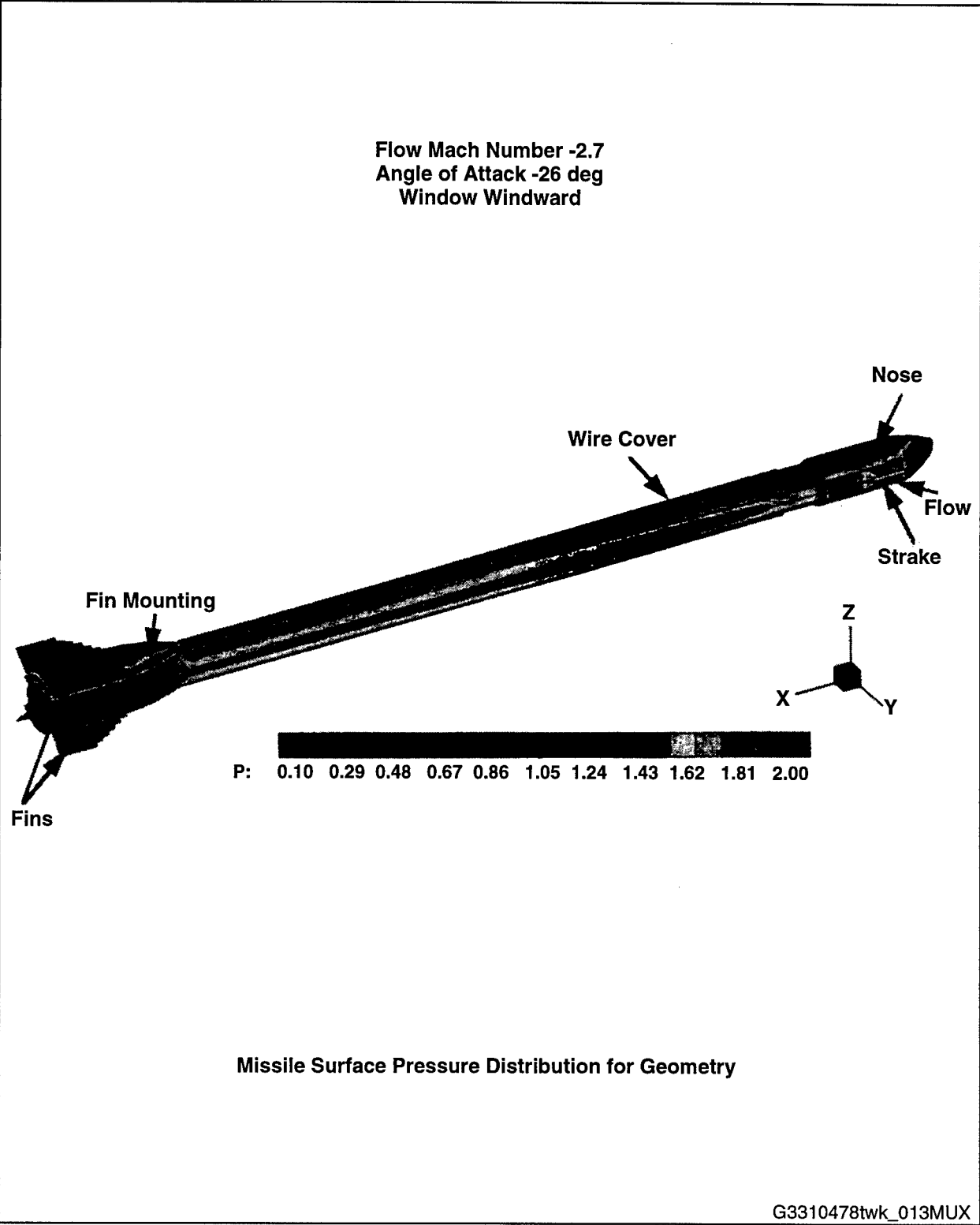


Fig. (13). CFD Simulation of a Rotate-To-View Nose Missile
($M = 2.7$, $\alpha = 26$ deg)

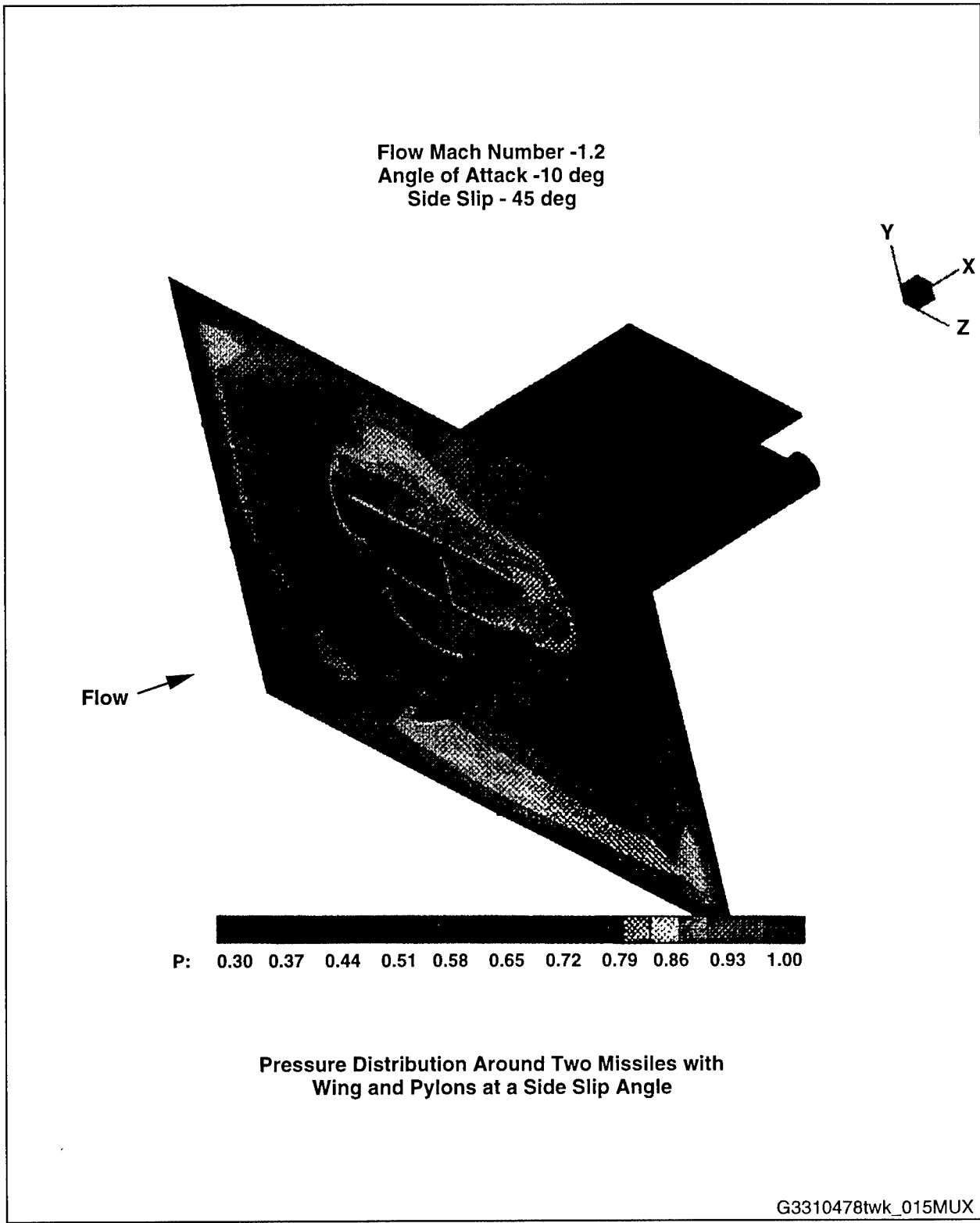


Fig. (14). CFD Load Distribution for a Rotate-To-View (RTV) Missile

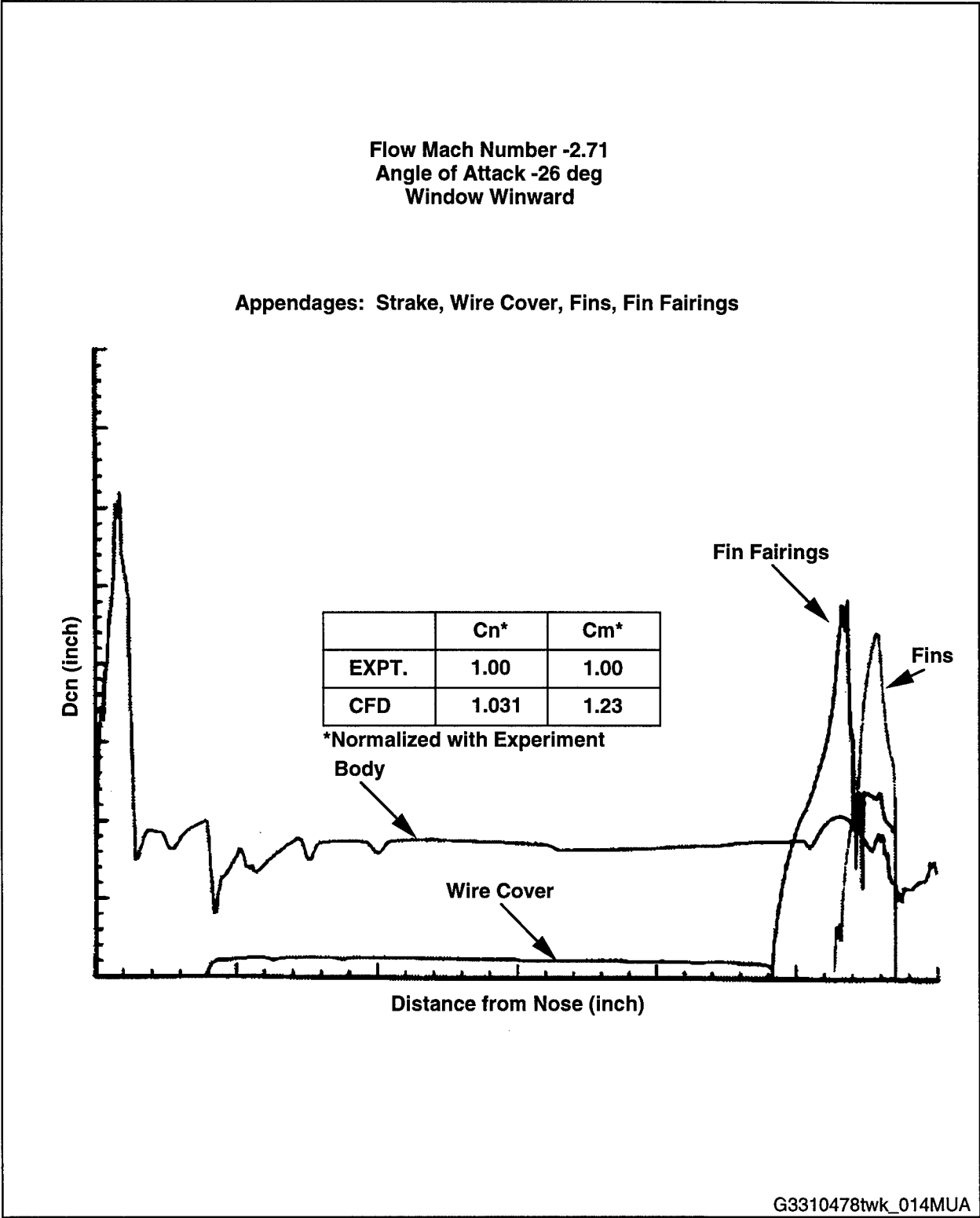


Fig. (15). CFD Simulation of RTV Missiles with Wing and Pylon

MISSILE AERODYNAMIC TESTING AT THE ARNOLD ENGINEERING DEVELOPMENT CENTER (AEDC)*

Edward J. Marquart, William R. Lawrence, and F. Clark Lawrence
 Sverdrup Technology, Inc., AEDC Group
 Arnold Engineering Development Center
 Arnold Air Force Base, TN 37389

ABSTRACT

With the need for missiles to become more maneuverable and at the same time cost less to develop, the ground testing methodology for the development of modern missiles is being redesigned at the Arnold Engineering Development Center (AEDC). The AEDC, located in middle Tennessee, USA, is one of the major ground test complexes in the world and has continuous-flow wind tunnel facilities to evaluate test articles at speeds from Mach number 0.1 to Mach number 10. Modern missiles are flying at increasingly higher angles of attack using fins and/or jets (both pulsating and continuous flow) for control and maneuverability. Dynamic and transient missile aerodynamic ground test measurements are becoming increasingly important for modern missile autopilot development. The recent advances and planned improvements at the AEDC in missile ground test measurement technology that allow the development of advanced missile autopilots and control systems at a reduced cost are discussed. Test hardware and testing methodology for missiles both with and without jet control that acquire and verify all static, dynamic, and transient aerodynamic information for modern missile autopilot development in three separate wind tunnel tests are detailed.

NOMENCLATURE

α	Angle of attack, deg
c	Damping coefficient
Cl_p	Roll-damping moment coefficient, per rad
Cn_p	Magnus moment coefficient, per rad
Cy_p	Magnus force coefficient, per rad
D	Model diameter, ft
FN	Normal force, lb
I_x	Model roll moment of inertia, slug-ft ²
k	Spring constant, lb/ft
l_p	Damping moment parameter, ft-lb-sec
m	Mass of article, slugs
ML	Rolling moment, in.-lb
p	Test article roll rate, rad/sec
Q	Dynamic pressure, lb/ft ²
RFP	Reduced frequency parameter, $pD/2V$
S	Reference and test article base area, ft ²
t	Time, sec
V	Free-stream velocity, ft/sec

z Position of mass relative to equilibrium spring position, ft

ζ Damping ratio

INTRODUCTION

At the Arnold Engineering Development Center (AEDC) shown in Fig. 1, autopilot and missile control system development testing have previously been based primarily upon static wind tunnel test and evaluation methodologies with little regard for dynamic and transient effects. There is a general lack of dynamic wind tunnel test techniques that could be used to evaluate transient flow phenomena. Problems associated with transient flow fields, such as vortex shedding and bursting resulting from high angle-of-attack maneuvering and transient jet interaction from pulsating control jets, are often not discovered until flight tests are performed late in the acquisition process. Ground testing methodologies using dynamic test techniques are being developed and used to identify problems prior to flight testing. Methodologies are used during the system development process to obtain information to help achieve system capability beyond what is predicted from static wind tunnel tests by taking advantage of transient phenomena like the additional lift force associated with dynamic stall. Missile autopilot control systems could allow enhanced maneuvering (both offensive and evasive) beyond what is predicted from static tests. More maneuvering performance may be available to flight control systems by including other transient phenomena in the system design.

The dynamic test and evaluation process includes three phases. In the exploration phase, conditions of dynamic and transient flow fields are simulated in a wind tunnel environment. Two wind tunnel tests can simulate the static, dynamic, and transient flow fields of modern missiles. During the first test, static force and moment data are acquired and the roll degree of freedom is investigated. The second test acquires,



Fig. 1. Arnold Engineering Development Center (AEDC).

* The research reported herein was performed by the Arnold Engineering Development Center (AEDC), Air Force Materiel Command. Work and analysis for this research were performed by personnel of Sverdrup Technology, Inc., AEDC Group, technical services contractor for AEDC. Further reproduction is authorized to satisfy needs of the U. S. Government. **Approved for public release; distribution unlimited.**

static force and moment data and investigates the pitch/yaw degree of freedom. High-frequency response measurement techniques are employed with the balances of both tests to quantify transient flow-field phenomena. Understanding changes of dynamic and transient flow phenomena resulting from modification of flow fields using flow control techniques is an important goal of the exploratory phase of the dynamic test and evaluation process.

The second phase of the process is the control system enhancement process. Autopilots and control systems can be improved with an understanding of dynamic and transient flow phenomena. Architecture design changes including nonlinear control algorithms of fully coupled flight control systems will optimize flight vehicle performance in transient flight conditions. New flight vehicle designs can be optimized for transient flight conditions.

The third test and evaluation phase is the autopilot and control system validation phase where system performance is evaluated in wind tunnel test facilities at simulated flight conditions. The testing methodology of flight simulation in a wind tunnel test environment is known as Virtual Flight Testing (VFT). The flight test simulation in a wind tunnel may use a free rotational motion mechanism such as a spherical bearing or a high-speed attitude positioning system. This test demonstrates and validates the control system and allows all three rotational degrees of freedom to be evaluated.

TEST 1: STATIC STABILITY, DRAG, AND ROLL DEGREE OF FREEDOM

Roll-damping and Magnus effects are important when determining delivery accuracy of spinning missiles, artillery rounds, and re-entry vehicles; however, these parameters have often been estimated rather than measured in the past because of limited budgets and the higher priority needs to acquire static stability and drag performance data. AEDC has re-engineered the spin-damping and Magnus measurement technique¹ to adapt it to today's environment of reduced resources available for testing and reduced development time for new systems. The newly engineered spin damping dynamic test technique is designed to provide the ability to simultaneously obtain roll-damping coefficients, Magnus force and moment coefficients, and all six static force and moment measurements during a single wind tunnel test at reduced cost.

The new hardware improvements involve replacing the traditional 4-component Magnus balance (no drag and no roll) that was specially built to make highly accurate Magnus measurements² with a standard 6-component static force and moment balance. In concert with the re-engineered testing methodology, data productivity increases by a factor of 4 on average, and reduces run times from 4 to 5 minutes per run to 1 to 2 minutes per run. The historical trend of pretest work (preparation, installation, and checkout) of various spin damping tests for the last 15 years is presented in Fig. 2. The representative level for early 1980s work that included the evaluation of the test mechanism bearing friction damping and other non-value-added efforts is almost 6,000 man-hours, whereas the representative pretest work for the late 1990s using the re-engineered testing methodology is less than 2,000 man-hours. The current level is approximately one-third of the previous level because of the re-engineered methodology and other improvements developed over the past decade.

Cost reduction advantages sometimes reduce data quality. Tests were recently performed on a representative interceptor flight vehicle in Aerodynamic Wind Tunnel 4T at the AEDC using the new methodology hardware. The data acquired during these tests were statistically analyzed to quantify the estimated uncertainty. Typical comparison of Mach number 0.75 static data obtained while the model was spinning and while the model was stationary are presented in Figs. 3a-c for normal-

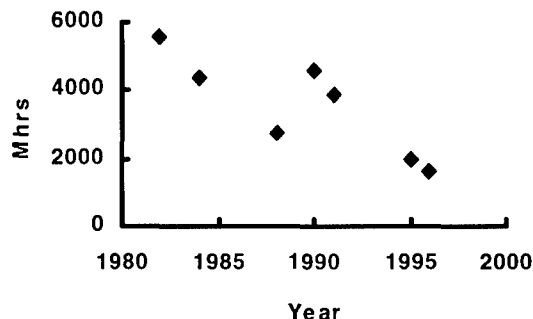
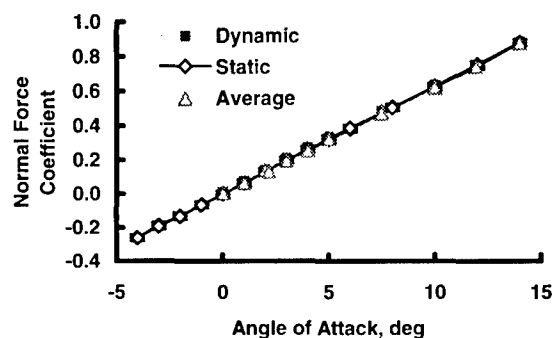
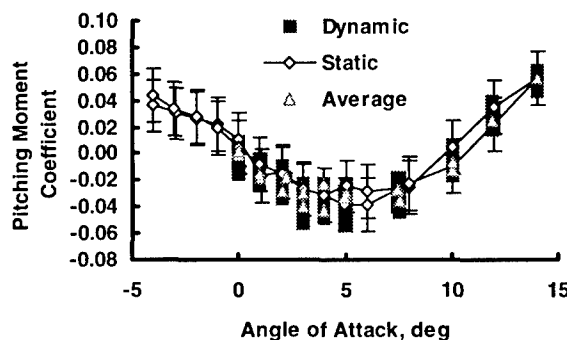


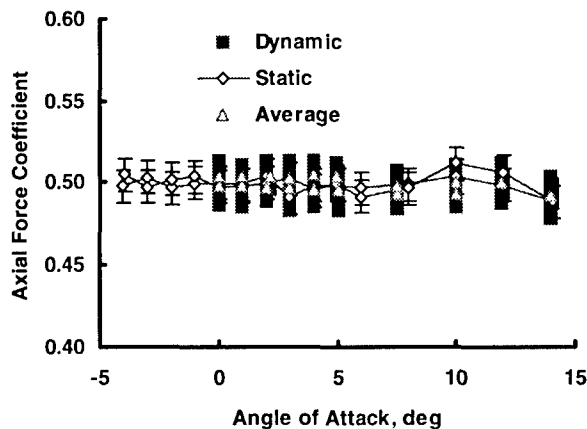
Fig. 2. Pre-test manhours for Magnus and spin damping tests.



a. Normal force coefficient



b. Pitching moment coefficient



c. Axial force coefficient

Fig. 3. Comparison of data for spinning and stationary model.

force coefficient, pitching-moment coefficient, and forebody axial-force coefficient, respectively. The uncertainty bands of the static data obtained while the model was stationary are also indicated in the figures. Averages of measurements of the normal-force coefficients, pitching-moment coefficients, and forebody axial-force coefficients obtained while the model is spinning are in excellent agreement with data obtained with the model stationary. Therefore, static stability and drag performance data may be obtained simultaneously with spin damping and Magnus data to combine what would normally be two tests into one single, efficient test.

The aerodynamic roll-damping moment coefficient Cl_p is determined from the measured exponential roll-rate decay of the model during a run, the tare damping (bearing friction) of the test mechanism, and the model moment of inertia. The equation used to calculate roll-damping moment coefficient is:

$$Cl_p = (I_{p_{total}} - I_{p_{tare}})2V/QSD^2 \quad (1)$$

The roll rate $p(t)$ is represented by an exponential equation to obtain the ratio of the total roll damping moment $l_{p_{total}}$ and roll inertia I_x as follows:

$$p(t) = (p_{initial} - p_{steady\ state})e^{\left(\frac{I_{p_{total}}}{I_x}\right)t} + p_{steady\ state} \quad (2)$$

The model roll moment of inertia is determined in a lab prior to the test and the measurement uncertainty contributes to the uncertainty of the roll-damping moment coefficient. The repeatability of the model moment of inertia measurement technique is presented in Fig. 4. The standard deviation of the inertia measurements shown is 0.00002 slug-ft² or 0.1 percent. The uncertainty of the model roll moment of inertia measurements has an insignificant impact on the uncertainty of roll damping moment.

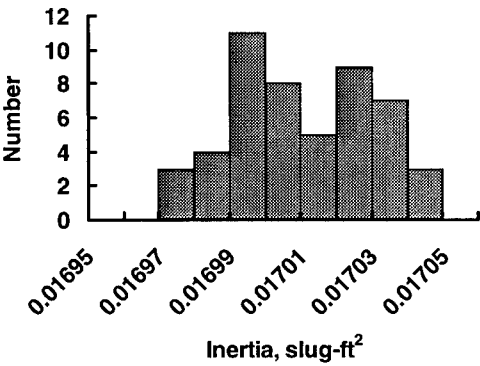


Fig. 4. Repeatability of model inertia measurements.

The model roll-rate decay during a run is determined by both the balance tare (bearing friction) damping of the test mechanism and the aerodynamic damping of the spinning model. The balance tare damping must be determined separately and subtracted from the total damping as displayed in Eq. (1) to obtain the desired aerodynamic damping value. The evaluation of the bearing friction tare damping is eliminated from the new pretest laboratory preparation work since it is measured directly in the tunnel by the rolling-moment component of the standard 6-component balance. A typical example of roll component measurements during a low spin rate run (400 rpm) is

presented in Fig. 5. Even though the typical goodness of fit for the relatively low spin rate runs is poor, Fig. 6 shows the distribution of tare levels acquired throughout the test is bell shaped with a standard deviation of 0.000012 ft-lb sec. The statistically obtained uncertainty and the repeatability of the roll-damping coefficient (Cl_p) measurements for the high spin rate (20,000 rpm) tests is ± 0.002 . The results from the statistical analysis indicate that the roll-damping uncertainty at high spin rates is approximately twice the uncertainty for other tests with similar roll rates that were obtained using the conventional methodology requiring additional lab work and more cost.

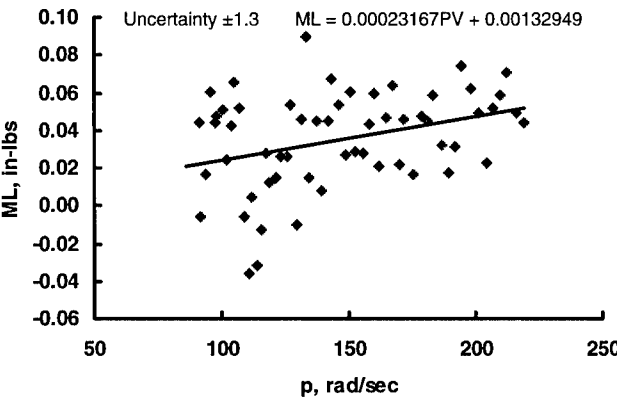


Fig. 5. Typical bearing friction torque measurement.

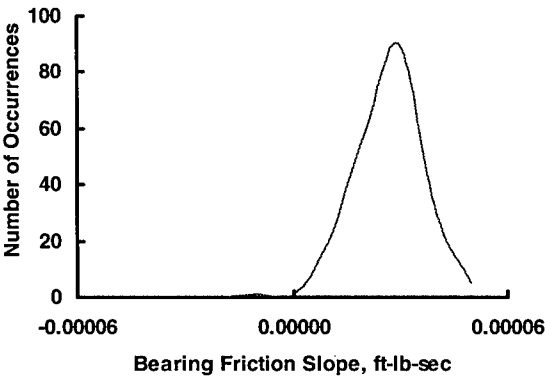
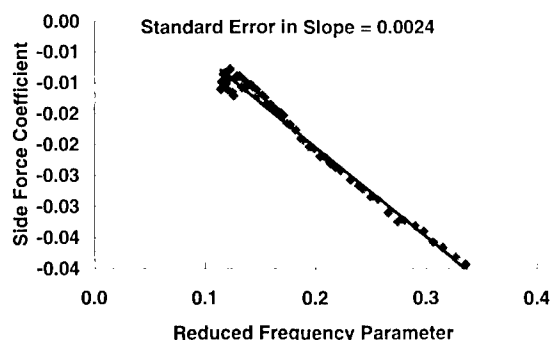
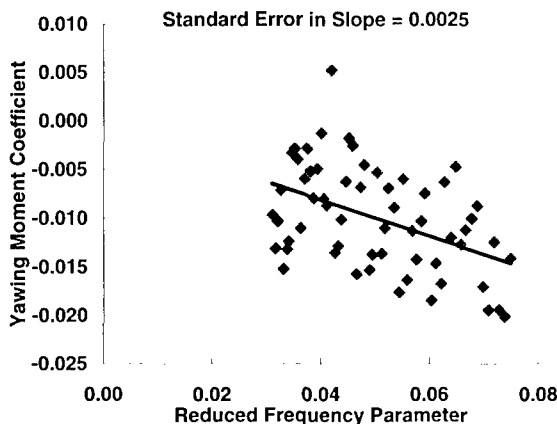


Fig. 6. Histogram of low spin rate test bearing friction slopes.

A similar statistical analysis is performed on typical Magnus data obtained during the tests. The Magnus force and moment coefficients are the values of the slopes of the side-force coefficient and yawing-moment coefficients charted against the reduced frequency parameter (RFP). The reduced frequency parameter is a nondimensional parameter that is proportional to spin rate. Typical examples of the Magnus force and moment coefficient data charted against the reduced frequency parameter, the slopes, and the uncertainty of the slopes are presented in Figs. 7a - 7b, respectively. Typical statistical uncertainties of Magnus force coefficient and Magnus moment coefficient for high spin rate tests are ± 0.004 and ± 0.004 , respectively. Typical repeatability of Magnus force coefficient and Magnus moment coefficient measurements for high spin rate tests using the new hardware are ± 0.003 and ± 0.01 , respectively. The measurement accuracy of Magnus force coefficient and Magnus moment coefficient using the new hardware is similar to the measurement accuracy of the conventional hardware.



a. Side force coefficient



b. Yawing moment coefficient

Fig. 7. Side force and yawing moment coefficients versus reduced frequency parameter at 10 deg angle of attack.

The following table summarizes the uncertainty of the parameters discussed:

Parameter	Uncertainty	Statistical	Repeatability
Hardware	Conventional	New	New
C_{l_p}	± 0.001	± 0.002	± 0.002
C_{y_p}	± 0.01	± 0.004	± 0.003
C_{n_p}	± 0.01	± 0.004	± 0.01

The newly re-engineered spin damping and Magnus measurement process is twice as productive and requires two-thirds fewer manhours than the conventional process with comparable measurement uncertainty.

TEST 2: STATIC STABILITY, PITCH/YAW DAMPING, AND IMPULSE MEASUREMENTS

A wind tunnel test mechanism is being developed at the AEDC that can provide mass flow to the test article and also able to obtain static stability, dynamic stability, and impulse data at a reasonable cost. The mechanism can obtain the following information during the test entry:

1. Five-component (no drag) static force and moment data both with and without mass flow
2. Five-component impulse data
3. Pitch damping and yaw damping data (rotary and plunging combined)
4. Cross and cross-coupling derivative data.

This mechanism is ideally suited to obtain the necessary information required for the development of autopilots for missiles with pulsating jet control.

The approach selected for developing a mechanism to measure short-duration forces and moments in continuous flow tunnels is based on the method developed for making force and moment measurements in short-duration (shock) tunnels (Ref. 3). The method for making short-duration static force and moment measurements in wind tunnels combines accelerometers with standard static force and moment strain-gage balances to produce an instrument that has both the frequency response of accelerometers and the operational efficiency of standard wind tunnel balances.

The theory presented here for a one-component measurement is generally expandable to several components of measurement. For a single-degree-of-freedom system, the following differential equation combines acceleration, damping, and spring terms and illustrates the type of data reduction to calculate the impressed load:

$$m\ddot{z} + c\dot{z} + kz = FN(t) \quad (3)$$

The short-duration normal force $FN(t)$ is calculated by adding together the information from an accelerometer, rate transducer, and balance. The acceleration term (\ddot{z}) is obtained from an accelerometer, the damping term (\dot{z}) is obtained from either a rate transducer or the integration of the accelerometer measurements, and the spring term (z) is obtained from the balance. The impulse is the integration of the short duration force $FN(t)$ with respect to time over the time of the pulse duration. Therefore the impulse of a pulsed jet used to control intercept missiles is calculated from readings from accelerometers, rate transducers, and a balance.

A cross-flexure balance similar to the one displayed in Fig. 8 was chosen for the laboratory development⁴ since the pivot point of the cross flexure can be known in advance from static calibration of the impulse experiment. A concept drawing of the laboratory setup to validate the measurement technique is presented in Fig. 9. A cylindrical calibration body to simulate a test article is attached to the cross-flexure balance. The cross-flexure balance is mounted to the end of a sting that is mounted to a large bulkhead of the test facility.

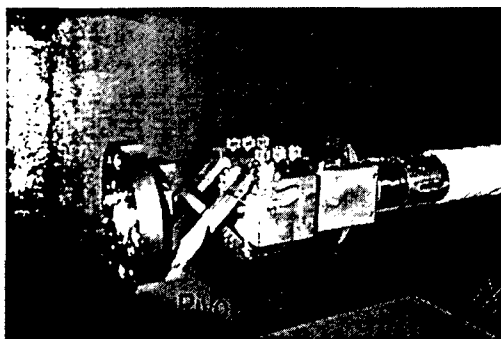


Fig. 8. Cross flexure balance.

The impulse measurement mechanism is modeled to facilitate understanding of the results of the laboratory experiment. The system equations of motion are solved with a computer program to model the experimental hardware dynamics. The program translates, compiles, and executes a Fortran code to

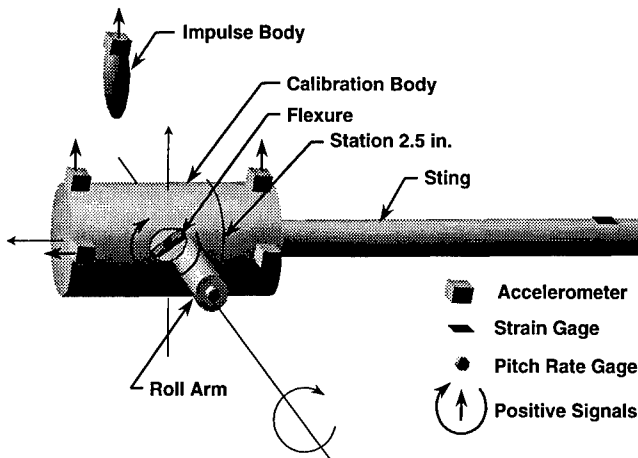


Fig. 9. Concept drawing of impulse measurement hardware.

solve the differential equations, and outputs the variables for the various test cases. Realistic mass, moment of inertia, spring stiffness, and impulse loads are used in the computer model. The equations of motion also include the aerodynamics of a representative configuration in a wind tunnel environment. The equations used to model the measurement capability also include electrical noise and filtering effects of the transducers.

A short-duration externally impressed force and moment is included with the modeling equations, and the system's response to the impressed load is used to examine certain properties of the system. The 40-msec external force and moment included in the simulation is presented in Fig. 10. The load increases linearly from zero for the first 10 msec, is constant for the next 20 msec, and then decreases linearly to zero over the final 10 msec. The system's representative response to the load is also presented in Fig. 10. Only the accelerometers respond to provide the primary information during the first 10 msec of the representative impulse. After the first 10 msec the sting responds by flexing, resistance to motion caused by the flexing motion causes the decrease in the measured acceleration during the next 20 msec of a constant impressed load. For this case, both the acceleration term and the spring term are needed for reasonable accuracy for a load with a duration longer than 10 msec.

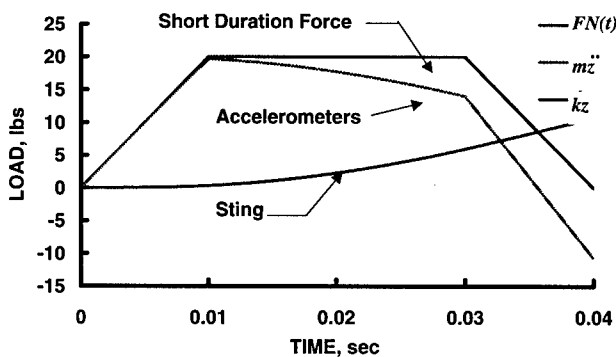


Fig. 10. Math model results.

The math model is a tool used to evaluate different assumptions of the measurement technique to guide the development. The technology to make direct measurements of acceleration for the first term in Eq. (3) is mature and well understood. Similarly, the strain gages used to measure the spring term for the third term in Eq. (3) are also well understood. However, the second term in Eq. (3) is the damping term and is proportional to

velocity. Methods to obtain rate information are to either differentiate position information from the strain gages, or to integrate acceleration information from the accelerometers. Either option is computationally cumbersome and requires the knowledge of the past to calculate the present state. Therefore, comparisons are made using the math model of two calculations of the short-duration force and moment measurements; one calculation includes the damping term (second term) in Eq. (3), and the other does not include the damping term. The two calculations for damping levels of zeta (ζ) of 5 percent are presented in Figs. 11 and 12 for force and moment, respectively. No significant errors between the two calculations are observed for the first 10 msec. However, errors of approximately 5 to 10 percent during the second half of the 40 msec pulse are shown in Figs. 11 and 12 for force and moment, respectively. Inclusion of the damping term is necessary for large values of damping (ζ of 5 percent), and may be neglected for small levels of damping (ζ of 0.5 percent). The necessary inclusion of the damping term complicates the data reduction. Posttest evaluation of total pitch damping from the test data may be required before making final calculations of short-duration force or moment measurements to include the damping terms.

A laboratory experiment was performed to demonstrate the concept of a two-component (pitching moment and normal force) measurement system. The laboratory setup is shown in Fig. 13. A 5-msec impulse load was impressed on the test mechanism with an impulse hammer. The mechanism's response to

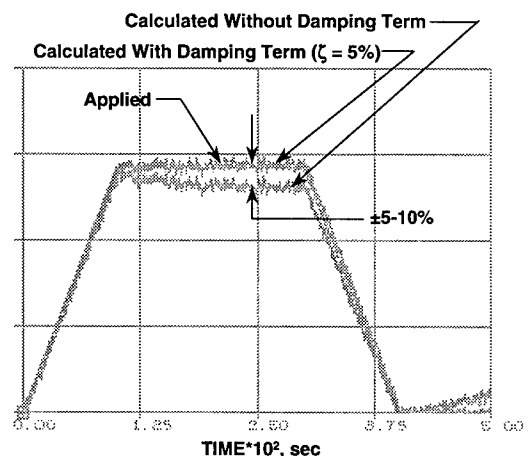


Fig. 11. Short duration applied force.

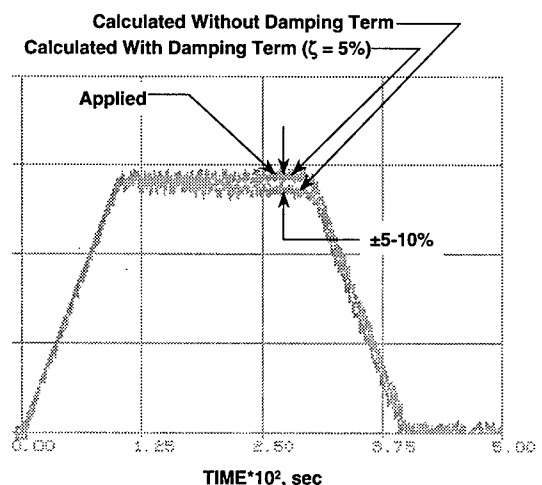


Fig. 12. Short duration applied moment.

the 5-msec impulse load is presented in Fig. 14. As presented in Fig. 14, the difference in the calculation of force from the response of the mechanism and the 5-msec impulse load measured by the impulse hammer is ± 2 percent.

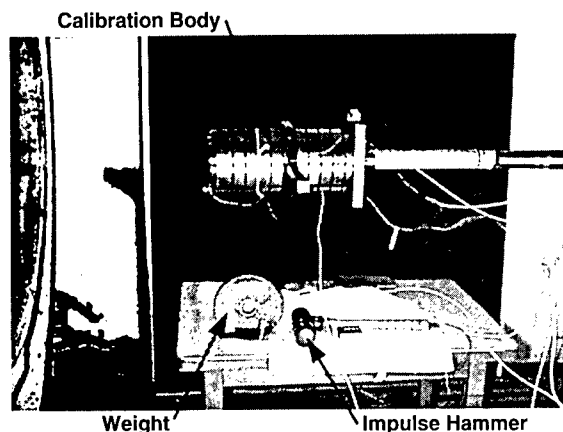


Fig. 13. Laboratory setup of impulse measurement hardware.

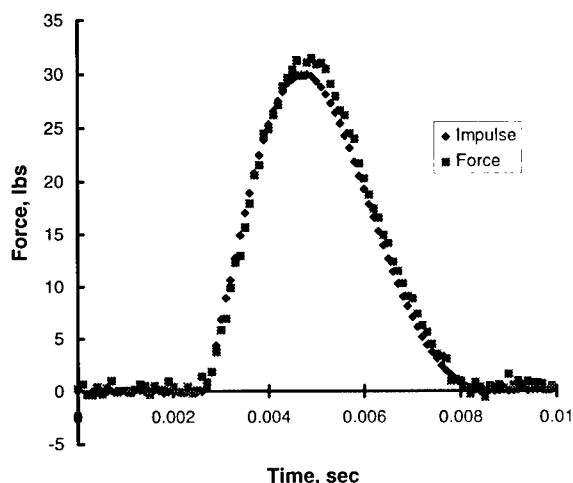


Fig. 14. Comparison of impulse hammer and balance measurements.

A 50-msec impulse was impressed on the test mechanism using a heavy weight that was attached to the calibration body by a very thin wire. An accelerometer was attached to the heavy weight and the weight was tied with some slack in the thin wire to the calibration body. The weight was dropped from a location directly beneath the calibration body. The slack in the wire was taken out as the weight dropped and the wire stretched and eventually snapped. The stretching process took approximately 50 msec and the acceleration was measured during the stretching process. The magnitude of the load was not well known; however, the location of the load was very well known. The response of the test mechanism to the 50-msec impulse is presented in Fig. 15. The load location was correctly measured to ± 0.05 in. There was excellent agreement (± 0.05 in.) between the impressed 50-msec impulse load and the resulting calculations using data from the measurement system. The above-described measurement technique is valid for impulse measurements.

After the impulse data are acquired, the cross-flexure balance continues to oscillate until the motion dampens out. A notional drawing of the representative balance signal is presented in Fig. 16. Pitch-damping measurements of the test article are obtained during the exponential decay of the oscillations

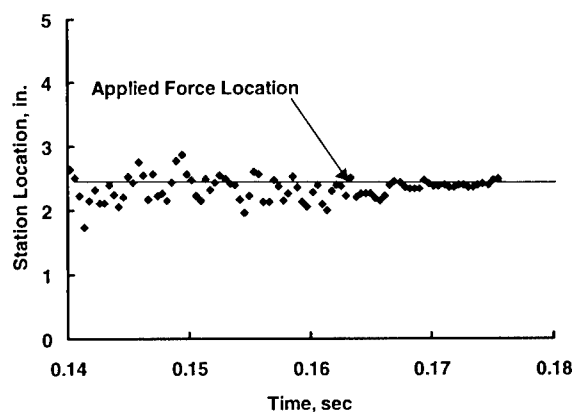


Fig. 15. Impulse center-of-force location.

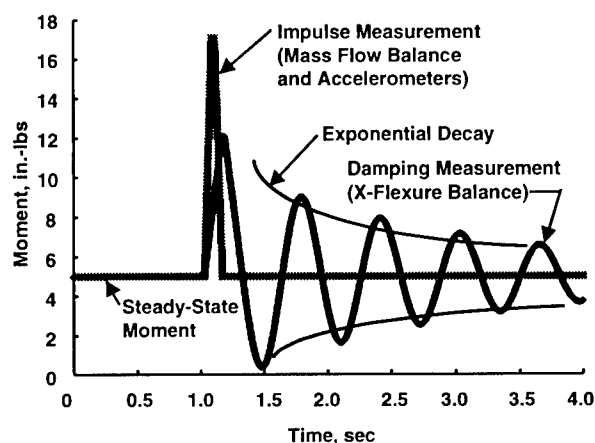


Fig. 16. Notional drawing of representative cross-flexure balance signals.

after the impulse. If the test mechanism also includes side load measurement capability, then the measurement of cross and cross-coupling measurements can also be made.

TEST 3: VIRTUAL FLIGHT TESTING

Heretofore, control systems of interceptor missiles have been developed using static aerodynamic force and moment data obtained in wind tunnels with stationary flow conditions. Math models have been developed from these data and used to approximate the vehicle aerodynamics in hardware-in-the-loop simulations of control system functions. This method has worked well for vehicles that encounter mostly steady flight, small angles of attack, and relatively benign maneuvers. The new generation of interceptor missiles will incorporate new control devices like microelectrical-mechanical systems (MEMS) or pulsating control jets. When these devices deploy, they cause very complicated aerodynamic interactions which, coupled with the resulting violent motion of the vehicle, can affect vehicle's motion in unexpected and undesirable ways.

To account for unexpected motion, large uncertainties are built into the math models used in the simulations. With a capability to measure and understand unsteady phenomena, uncertainties can be reduced and the control system can be designed to account for the motion that will actually occur. Development of control systems that perform near the edge of the operating envelope can be greatly enhanced by including a test and evaluation capability that allows the software designer to manage dynamic conditions rather than simply tolerating them.

There is currently not a good way to evaluate airframe and control system performance under unsteady conditions prior to flight. The vehicle designers are left to identify problems during flight test, modify the vehicle and control system design, and flight test again until the desired response is achieved. This process is very costly because it requires several expensive flight tests, assets are not recoverable, and lengthy turnaround times are experienced. During a flight test, only limited information can be measured over a short period of time.

A new experimental methodology, referred to as Virtual Flight Testing (VFT), will allow acquisition of flight-like test data in a ground test facility. VFT is an approximate simulation of flight testing by closed-loop integration of ground test facilities to verify autopilot performance prior to actual flight. Some features of VFT are similar to hardware-in-the-loop (HWIL) testing, except that VFT allows the missile to perform at simulated flight conditions in the wind tunnel. This type of testing more realistically simulates the aerodynamic and dynamic environments that the flight vehicle will encounter they can be modeled from static force and moment wind tunnel data. The test concept is similar to the one demonstrated by Balakrishna⁵ for one degree of rotational freedom, except a VFT may have up to 3 degrees of rotational freedom.⁶

A schematic of a VFT is presented in Fig. 17 where the test article is mounted in the wind tunnel on a bearing, an actuated sting mount, or a combination of both. Control commands from the autopilot are transmitted to the test article via telemetry. The control commands (either a control surface movement or a jet blowing) are executed and the model responds. The forces and angular information from the test mechanism are transmitted or transferred to a data acquisition computer where the data are recorded and used to calculate the trajectory of the flight vehicle. The trajectory calculations are transmitted to the autopilot for the autopilot to determine the next set of control commands. The next set of control commands are issued to the intercept missile, and the process is repeated.

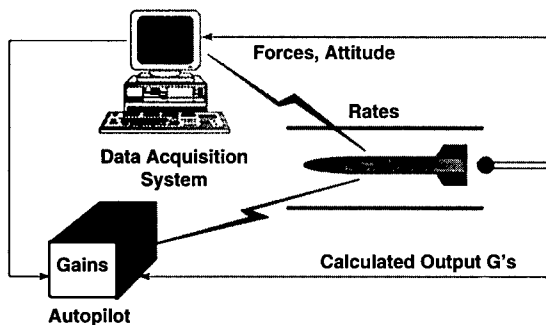


Fig. 17. Virtual flight test schematic drawing.

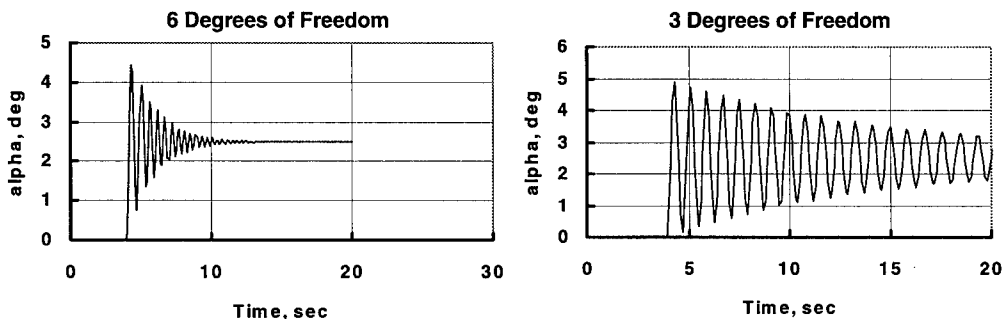


Fig. 18. Responses to step inputs.

There are three options for mounting the test article in the wind tunnel. The first option is a spherical bearing that provides 3 degrees of freedom (3-DOF) of near-frictionless rotational motion of the test article. The advantages of using a spherical bearing are that the rotations are in response to actual aerodynamic loads and the technology is readily available. The disadvantage is that the absence of the translational degrees of freedom does not allow the component of angle of attack from plunging motion. Because there is no translation of the model in the wind tunnel and the wind velocity vector direction is constant with respect to the wind tunnel, the flight path angle is zero and the angle of attack is the same as the pitch angle.

To quantify the difference between the response of a vehicle in flight and that of a wind tunnel model mounted on a spherical bearing, a six degree-of-freedom (6-DOF) trajectory simulation was used to predict the path of a flight vehicle and the motion of a model in the wind tunnel. For the wind tunnel simulation, the programmed equations of motion were modified to constrain the translation of the model, while allowing it to freely rotate about its center of gravity. This effectively made the simulation a three-degree-of-freedom (yaw, pitch, roll) model of the motion in the wind tunnel.

The 6-DOF and 3-DOF programs were used to compute the open-loop response to a step control surface deflection input for a vehicle in flight and for a wind tunnel model, respectively. The angle-of-attack response is shown in Fig. 18. It is clear that by not allowing the wind tunnel model to translate, the aerodynamic damping is reduced significantly, and the model will take longer to reach the steady-state condition. Therefore, a control system that is successfully demonstrated in a wind tunnel with the more severe 3-DOF case should perform adequately in flight.

A simple pitch flight control system was used to control the vertical acceleration of a missile. The control system employed pitch rate feedback to damp the short period oscillations. The acceleration commands were provided to the control system by a proportional navigation guidance system. The missile transfer function was replaced with 6-DOF calculations that took control surface deflection inputs and computed the missile rates and positions to be fed back to the control system and the navigation system.

The missile was then "flown" along a path to intercept a moving target to show that the system was stable and that control could be maintained throughout the intercept mission. Once the controllability was established with the 6-DOF implementation, the 3-DOF equations of motion were used to simulate the motion of the missile in the wind tunnel as the model responded to control system commands. Again, the intercept mission was

"flown" with the 3-DOF simulation and the target was intercepted successfully. Interception of the target demonstrated, that the system was stable and that control could be maintained throughout the intercept mission.

The 6-DOF simulation was used to compute the amplitude ratio and phase angle as a function of frequency for the flight control system. The Bode plots shown in Fig. 19 were constructed, and the gain and phase margins were computed for the system. This information provides a measure of the relative stability of the system. The same information was then generated using the 3-DOF equations to simulate the response in the wind tunnel. The results are compared with the flight case in Fig. 19. As can be seen, the comparison between the flight and tunnel simulations is very good.

The second option for mounting the test article in the wind tunnel is to use an actuated sting/balance combination. An actuated sting/balance combination consists of a high-speed pitching mechanism and a high-frequency response balance. The high-speed pitch mechanism can place the test article at the proper angle of attack in real time. Therefore, the actuated sting mounting option does not have the disadvantages of the spherical bearing. Force measurements from the high-frequency response balance are included in the calculations to compute angle of attack that is used to command the high-speed pitching mechanism. The 6-DOF calculations are included in the loop with the control system. In this scenario, other external forces, such as thrust forces, jet damping forces or varying mass and inertia could be simulated. Information could be extracted from the 6-DOF calculations during the test from which the relative stability of the control system could be evaluated.

The third option for mounting the test article in the wind tunnel is a combination of the first two. A cylindrical bearing attached to the front end of the actuated sting/balance combination will allow free rotation about the roll axis. Because of the nature of the equations of motion, the free-rolling test article will replicate in-plane free-flight motion. The elimination of the forced roll positioning mechanism will simplify the design of the high-speed pitching mechanism.

SUMMARY AND CONCLUSIONS

Typical missile development methodology does not involve completely modeling dynamic motion of airframes. At present, static wind tunnel data are collected on representative airframes, an aerodynamic model is constructed from the static data, and the aerodynamic model (with some semi-empirical estimates of the dynamic aerodynamic loading) is incorporated in flight simulations for prediction of missile performance. This procedure

lacks fidelity in the prediction of the dynamic loading and response of airframes, especially in highly dynamic environments such as rapid pitching, yawing, and rolling.

Three wind tunnel tests that fully describe the aerodynamics of highly maneuvering missiles and demonstrate of the autopilots and control systems have been discussed. The first test is a static stability, drag, and roll degree of freedom test. Development of a newly engineered methodology allows the simultaneous acquisition of six-component static force and moment data and roll damping and Magnus data. The methodology decreases the man-hours to one-third of the amount required a decade ago, and data productivity increases by a factor of four. The data uncertainty of the newly engineered methodology is comparable to the uncertainty of traditional methodology.

The second test is a static stability and pitch or yaw damping degree of freedom test. The testing methodology allows the simultaneous acquisition of five-component static force and moment data both with and without mass flow, along with impulse data and pitch or yaw damping. Cross and cross coupling derivatives may also be obtained when the proper test hardware is used. The impulse measurement capability allows the assessment of the effects of pulsating jets and of vortex shedding and vortex bursting on vehicle control and maneuverability.

After the completion of the first two wind tunnel tests, the static, dynamic, and transient aerodynamics will become better understood. Autopilots and control systems may be designed not just to tolerate the dynamic phenomena, but to exploit the phenomena for beneficial use towards the mission objectives. It is proposed to utilize wind tunnels to determine the motion of missile systems in highly dynamic environments.

Currently, missiles transition from simulations based on static aerodynamics to flight testing. Flight testing is extremely expensive and time consuming. The third test in the series, referred to as Virtual Flight Testing (VFT), is a testing methodology that demonstrates advanced autopilots in a wind tunnel environment. The airframe is mounted on a dynamic sting so that the airframe can move rapidly to the appropriate position corresponding to a flight trajectory. The mounting system is either a low-friction bearing or actuated sting for rapid maneuvers to match flight situations. VFT is an approximate simulation of flight testing; it allows the closed-loop demonstration of autopilots and control systems. It is hoped that VFT methodology can bridge the gap between ground testing and flight testing. In doing so, VFT could reduce the number of flight tests and result in program cost savings.

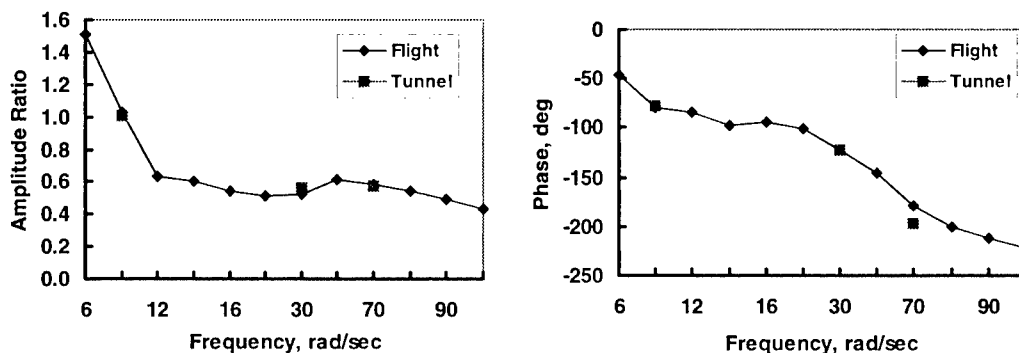


Fig. 19. Amplitude ratio and phase angle versus frequency.

The use of the three test approaches described herein to develop highly maneuvering missiles will minimize development time and reduce both program costs and risks. The three-test series is designed as a package to incorporate modern technology into the process to develop superior missile weapon systems at a reduced cost.

REFERENCES

1. Marquart, E. J. and Heim, E. R. "Re-Engineering of the Spin-Damping and Magnus Measurement Technique at the Arnold Engineering Development Center (AEDC)" AIAA 98-0611, 36th Aerospace Sciences Meeting, January 1998.
2. Uselton, J. C. and Carman, J. B. "Wind Tunnel Test on the Apache Sounding Rocket with Various Spin Rates at Supersonic Speeds," AEDC-TR-69-57, May 1969.
3. Bernstein, L. "Force Measurements in Short-duration Hypersonic Facilities," AGARDograph No. 214, November 1975.
4. Marquart, E. J. and Coulter, S. M. "Impulse Measurement Technology Development at the Arnold Engineering Development Center (AEDC)" AIAA 98-0203, 36th Aerospace Sciences Meeting, January 1998.
5. Balakrishna, S. and Niranjana, T. "Wind Tunnel Dynamic Flying Study of the Pitching Moment Derivatives of the Standard Dynamics Model in Active Control," AIAA 87-2626, August 1987.
6. Marquart, E. J. and Ratliff, C. R. "An Assessment of a Potential Test Technique: Virtual Flight Testing (VFT)," AIAA 95-3415, Flight Simulations Technologies Conference; August 1995.

An Experimental and Numerical Study of a Supersonic Spinning Missile.

S.T. McIlwain, P.C.G. Mallon, R.J. Fleming, G. McConnell
Shorts Missile Systems Ltd,
Alanbrooke Road,
Castlereagh,
Belfast. BT6 9HB
Northern Ireland.

Summary

A series of Wind Tunnel tests have been performed to determine the aerodynamic characteristics of a spinning canard controlled missile. Comparisons are made between results obtained on a spinning missile wind tunnel model, a static wind tunnel model and computational results. The test article consisted of a free rolling missile body with a decoupled nose section. The body had four equally canted fins at the rear to provide roll whilst the decoupled nose section was fitted with two differentially set canards and attached directly to the wind tunnel balance around which the rear body was allowed to free spin. Force and moment measurements were made on the model using the wind tunnel balance system which could then be compared directly to the results of the static wind tunnel test and also to the CFD results which modelled the static case. Analysis of the dynamic data and static data averaged over the interdigtation angular range showed a close correlation with the CFD results in the major force and moment components. However, there were significant differences observed in cross plane force and moment measurements between the static and dynamic cases and also between the static experimental result and the computational result. In the latter case the correlation was improved by including a separation model in the computational model. Further, when the experimental nose rolling moment coefficient was analysed, significant differences were observed between the static, dynamic and computational results.

List of Symbols

CA	Axial Force Coefficient
Cn	Yawing Moment Coefficient
Cm	Pitching Moment Coefficient
Cl	Rolling Moment Coefficient
Cl _t	Rolling Moment Coefficient (tails)
Cl _{pn}	Roll Damping Coefficient
λ	Aerodynamic Roll Orientation
σ	Total Incidence
M	Mach Number
BT	Body-Tail
BCT	Body-Control-Tail

1.0 Introduction

A missile that is canard controlled is normally subject to interference effects caused by the interaction of the canard vortices with the tails. One particular method of resolving this problem is to decouple the nose section from the spinning rear body or employ a free spinning tail unit. The designer is then faced with the problem of avoiding the generation of Magnus effects on a spinning finned cylindrical body. Despite the large amount of work devoted to the study of Magnus effects on, particularly, missile type bodies¹⁻³, the source, magnitude and remedy for problematic cases is still treated on an individual basis. The term Magnus effect when used to describe out-of-plane forces and moments on supersonic missiles is generally

an umbrella term, which covers a range of different effects and their origin. Some of these out-of-plane forces and moments are closer to the true sense of the Magnus phenomenon than others as they depend to a large extent on a high body roll rate before any effect is witnessed. Other types of Magnus effect have their origin in the relative location and deflection of wings, canards or tails on the body and roll rate becomes secondary in importance. Even the direction of the force and corresponding moment due to classical Magnus is known in some cases to change sign for these different origins of the Magnus effect.

The classical Magnus force is generated on a slender body at incidence spinning about its longitudinal axis and is due to a circulation superimposed on the freestream velocity. The tangible evidence of this is a distortion of the boundary layer by the 'moving wall' effect effectively altering the shape of the body and presenting an asymmetric slender body to the oncoming freestream. As boundary layer separation occurs with increasing incidence, the unequal separation pattern (due to unequal boundary layer development) imparts a net vorticity into the wake implying a circulation remaining on the body. However, for transonic and supersonic cross flow Mach numbers, where the influence of the body spin rate is restricted, any Magnus force that develops must be due to pressure changes on the body resulting from other sources. For instance the asymmetric vortex pattern shed into the wake, which in itself can lead to a source of out-of-plane forces, can also, in combination with a downstream tail or wing unit, be amplified to generate even larger forces. It should be noted that because of the dependence of the classical Magnus force on the boundary layer properties, the state of the boundary layer over the slender body will also be important in determining the magnitude and in some cases the direction of the Magnus force.

Some other sources of Magnus effect may be termed Pseudo Magnus effects as they are a result of fin deflection angles, incidence and roll rate rather than the latter two terms alone as described above. The best known of these types of Pseudo Magnus effect is that due to the blanketing of the fins rolling through the lee of the missile. This alters the lift force on the lee-side fin resulting in an out of balance force. It should be noted that this situation will present itself in a static test on a body with canted fins, with a greater magnitude than that found in a dynamic case where the body has established an equilibrium roll rate. Another source of the Pseudo Magnus effect is due to the inclination of the lift vector on a canted fin establishing an axial force component, which differs on each fin depending on their relative incidence. Further to this, the base pressure on each canted fin can also be thought of as a possible source of Magnus effect.

As noted above, the source, magnitude and even the direction of any Magnus effect is typically heavily dependent on the geometrical features of the body. In the work reported here, a rolling missile with a decoupled nose section was used as a basis to determine the source and magnitude of any Magnus

forces acting on the body and to examine and compare the effects of testing a spinning missile model as compared to a static article. Comparisons were made between static tests and computational tests, which aided understanding of the flow characteristics involved. Various experiments were performed, both rolling and non-rolling and with the option of including forward control surfaces on the static decoupled nose section. The work provides a simple reminder of the importance of Magnus effects in missile aerodynamics and shows the important effect of the body vortex system on the aerodynamic characteristics of a rolling tail missile.

2.0 Experiments

The model for this series of tests consisted of a 3" diameter cylindrical body with a 3:1 tangent ogive nose with a total length of 18 calibres. The nose of the body was rigidly fixed internally to the sting and six component balance assembly around which the decoupled rear body was allowed to free spin on bearings under the action of four canted rear fins. Two different fin cant settings were used as the method for altering the spin rate of the rear body. An electrically operated braking system was fitted between the fixed nose section and the rear body and was used to stop model rotation if required. The model spin rate was indicated by a sensor fixed to the sting at the rear of the model that detected the passing of dark and light bands on the model base. The nose section could also be fitted with fixed control surfaces set at 12° (starboard) and 8° (port). Details of the model are shown in fig.1.

Experiments were carried out in the DERA Bedford Supersonic Pressurised continuous closed circuit Wind Tunnel. The working section of the tunnel is 1.23m x 0.92m (3' x 4') and the Mach range is from 2.5 to 5.0 with stagnation pressures ranging from 10 to 1200kPa resulting in a maximum Reynolds number of 42 million/metre. The sting and balance assembly is motorised in pitch and roll for rapid incidence changes. Flow visualisation for the experiments was based mainly on continuous schlieren and video monitoring which was also used to capture some Laser Vapour screen images. A sting incorporating a 2.25" balance assembly supported the model. Static data had been obtained by fixing the rear body at a series of precise interdigitation angles with respect to the nose section and carrying out pitch and roll sweeps over the flight envelope. The static results were averaged over the full interdigitation range for comparison directly with the dynamic results.

Test Conditions and Procedure

The test conditions for this series of experiments is presented below:

Mach No.	Reynolds No.	Tail Angles°	σ° Range
2.5	23.3x10 ⁶	0.5°/1.0°	-2° to 26°
3.0	28.1x10 ⁶	0.5°/1.0°	-2° to 26°
3.5	32.9x10 ⁶	0.5°/1.0°	-2° to 26°

After securing the tunnel and establishing test conditions, the missile was set to zero incidence, the brake on the model was released and the model allowed to free spin to the equilibrium roll rate. Once the roll rate had reached equilibrium conditions, the data acquisition process was initiated. Measurements were also taken specifically during model spin up (to observe the growth or decay of any Magnus effect) and after equilibrium roll rate had been achieved and consisted of the six components of Normal and Side force, Pitching and Yawing Moments, Rolling Moment and Axial force. Initial

tests set the model pitch angle for the run after which the nose section was rotated through -180° to +180° (for tests with control surfaces in place). Other experiments were performed at fixed nose roll orientations and pitch was continuously varied from -2° to +26°.

3.0 Computational Analysis

The computational results were obtained using two commercially available codes: NEARZEUS from Near Inc. and Rampant from Fluent Europe although the majority of the work reported here was completed using the NEARZEUS code. This code is a development of the Zonal Euler Solver (ZEUS) code originally developed by Wardlaw et al⁴ and combines a semi-automatic multiple zone gridding technique with a second order Godunov method. The code was specifically developed to determine the aerodynamic characteristics of supersonic missiles and takes advantage of the parabolic nature of the governing equations in using a space marching predictor corrector technique as the core of the algorithm. This, along with the inviscid constitution of the equations ensured a relatively quick solution time for flow around the Missile body at supersonic Mach numbers. The main limitation of the code is the condition of the axial flow remaining supersonic which effectively limits the flow conditions on the missile to Mach numbers greater than 1.5 at low angles of incidence or Mach numbers greater than 2.0 at higher incidences. The code produces output at every new grid section established by the space marching algorithm so assisting in the interpretation of the source of the various forces and moments along the body.

4.0 Results and Discussion

Results for the various wind tunnel tests on different configurations and computational results are compared in this section. Figure 2 shows the variation of pitching moment on the full configuration (Body, Tails and Canards) as sigma is increased (λ=0°). For the model with canards deflected at 12° and 8° a normal pitching moment curve was expected with a positive trim incidence. All three methods indicated the correct trend for the pitching moment and it was clear that the spinning rear body had little effect on this coefficient when compared with the averaged interdigitated result for the static case. The computational result also compared quite favourably with the two experimental methods at incidences below the trim point at σ=8.0°; above this value cross-flow separation and vortex development had a considerable effect on the experimental pitching moment which was not modelled in the computational result.

Although the physics of the flow at incidences beyond 8.0° were not accurately modelled in the code, results for nose rolling moment were considered quite valid due to their relatively far upstream location free from large scale body vortex and cross flow separation interference. Fig. 3 shows the nose rolling moment variation with roll orientation at trim conditions for the three different methods. Due to a starboard cant angle of 12° and a port cant angle of 8°, a negative rolling moment was expected at λ=0°. Also, as nose roll angle varied and one canard became more fully exposed to the windward flow whilst the other was partially shielded, the nose rolling moment would reflect this variation with nose roll angle. This trend for rolling moment was predicted by all three techniques, however, there was some discrepancy in the magnitude of the mean rolling moment. A comparison with a flight result using telemetry data (not shown) indicated that the theoretical result was closest to the true rolling moment coefficient. The large discrepancy between the dynamic

rolling moment measurement and the other two methods was attributed to a combination of rolling friction on the sting and resonance effects over part of the roll angle range as the canard vortices slowed the body roll rate to match a resonant frequency of the system.

As stated previously, one of the aims of the research exercise was to determine the size and direction of any Magnus effects on the configuration by comparing static and dynamic results for out-of-plane side forces and yawing moments using results for different configurations i.e. body, body-tail and full configurations. The Fin-Pseudo Magnus effect was clearly illustrated by comparing the results of the static and dynamic tests for the Full Configuration, fig. 4 at Mach 3.5. The figure shows the expected large increase in cross-plane yawing moment for the static case (averaged interdigitated result) as incidence increases for a roll angle of $\lambda=0^\circ$. This was attributed to a combination of the increased effectiveness of the windward fins as incidence increased and also to the shielding of the upper fin by the body wake leaving the panel normal force on the lower fin to provide the indicated yawing moment. As mentioned previously, for a free spinning model rotating in equilibrium under the action of the canted fins, it was expected that as incidence increased the resultant yawing moment would be reduced in comparison to that on the static case. This is clearly indicated in fig. 4, which shows an increase in yawing moment with incidence for the dynamic cases only at higher incidences. It can also be said that any body Magnus effect present on the configuration was of a low magnitude in comparison with the static result. The results for the dynamic case are more fully examined below.

The delay in the increase in yawing moment for the dynamic case was examined using results obtained for the dynamic case using a further two different measurement techniques. The first method held the nose roll position constant while the pitch angle was increased; data was continuously monitored throughout the pitch sweep. The second method examined the development of forces and moments on the missile as the roll rate increased from zero up to the equilibrium value at that particular incidence. The data was continuously recorded until well after equilibrium conditions had been achieved. In both tests, the nose roll position was held at $\lambda=0^\circ$. Both these tests provided checks of the data with the standard roll sweep tests presented earlier. Fig. 5 shows the development of yawing moment on the full configuration at Mach 3.5. It was clear that the same trend of increasing yawing moment was present in these tests as was recorded using the roll sweep tests and shown previously in fig. 4. It was also clear that there was a non-linear variation in yawing moment occurring around an incidence of 10° which correlated in all three measurement methods and matched an unexplained phenomena noted in the work of Usleton and Carman¹. Beyond an incidence of around 16° , there was an increase in yawing moment with increasing incidence although the precise angle at which this increase occurred was different for each of the tests. These discrepancies had been noted for both the full configuration and the Body-Tail configuration indicating that there was little effect of the canard vortex system on the results. Therefore, to gain a better understanding of the underlying aerodynamic phenomena that may be present, the spin rate of the body-tail configuration was plotted as a function of incidence for the pitch sweep case and compared to a prediction of the expected rear body spin rate derived from the summation of the static rear body rolling moment coefficient and the damping coefficient obtained from the dynamic spin up tests at $\sigma=0^\circ$. Results are shown in fig. 6. Up to an incidence of around 12° there was a generally good correlation between the trends in the dynamic test spin rate and the predicted spin rate from

static measurements. However beyond this incidence the rear body spin rate reduced steadily with increasing incidence whilst the predicted result using the static rolling moment coefficient increased slightly with incidence. The approximately constant trend up to around 12° was also observed in tests by Usleton and Carman¹ where the spin rate on that model remained constant with increasing incidence up to around 16° . Usleton and Carman¹ also reported that the development of side force on the missile was due to the increased effectiveness of the windward fin and not attributable to blanketing effects on the lee side fin. For this reason it was expected that the roll moment coefficient would increase with incidence for the static case and correspondingly the spin rate for the rear body would also increase with incidence. Reasons for the discrepancy between the static rolling moment coefficient and the dynamic roll rate on the rear body are examined below. Initially it was thought that the reduction in rear body spin rate was due to bearing friction on the rear body that would increase with load as incidence increased. An analysis of equilibrium roll rates for tests on a body-tail configuration with tail fin settings of 0.5° compared to tests with tail fin settings of 1.0° gave an estimate of the bearing friction. Despite some friction effects being revealed, this did not account for all the differences observed between the static prediction and the dynamic result. The reduction in roll rate was therefore partly attributed to the only other difference between the static and dynamic tests i.e. the distribution of driving torque relative to the roll damping moment on the spinning tail fins. Analysis of spin up data on the rear body, fig. 7, revealed that the damping coefficient is reduced at 10° in comparison with the zero incidence value; beyond 10° , the damping coefficient increases again to a value at 20° of incidence which was greater than the zero incidence case. In summary, a reduction in damping moment coefficient was observed at low incidences before increasing again at higher incidences. The derivation of this term is independent of any friction effects and is therefore considered accurate. Similarly, a plot of the roll driving coefficient also showed a reduction with incidence, fig. 8 for both the full configuration and the Body-Canard configuration. It was accepted that the derivation of the roll driving coefficient could be corrupted by friction effects, however the estimate of friction previously derived would indicate that friction does not account for all of the reduction in driving moment for the full configuration case. Summarising, it can be stated that by comparing the trends of the roll driving and roll damping coefficients, an overall reduction in spin rate was indicated. Further evidence of the mechanism(s) that might be responsible for altering the distribution of the roll driving and damping coefficients on the rear body, particularly over the incidence range 6° to around 12° was sought by examining schlieren images of the Body-Tail tests. Observations showed the body vortex system moving up through the tail region with increasing incidence until at an incidence of 10° the vortices were at the tips of the tail fins; with further increase in incidence, the vortices moved further away from the tails.

These observations can be related to the development of cross-plane yawing moment with incidence. As stated previously, the yawing moment variation with incidence in the dynamic case was highly non-linear above incidences of $\sigma=10^\circ$. It was now clear that as the body vortex system moved away from the tail fins at around 10° , a positive side force and large negative yawing moment was measured. The yawing moment then increased positively with incidence.

The physical reason behind the reduction in roll driving and damping coefficient at intermediate incidences and the non-

linear variation of yawing moment was attributed to the effect of an asymmetric body vortex system moving through the tail region and it is believed there were two mechanisms associated with these variations in coefficients. At incidences below 10° , the body vortex lies close to the rear of the body and it was believed induced a cross flow, which had the effect of simultaneously reducing the roll driving and damping coefficients. This was confirmed as a possible flow mechanism by studying cross flow patterns from the computational analysis. As incidence increased beyond 10° and the body vortex system developed away from the body, the roll driving coefficient would increase back toward interference free levels whilst the roll damping coefficient would increase due to the induced cross flow on the tail region. The large increase in negative yawing moment on the body was attributed to an asymmetric vortex pattern, which led to a body vortex element lying adjacent to missile starboard. This directly influenced the tail panels at 10° incidence through the low pressure induced beneath the core on each rotating panel. The sum of the overall effect was a large negative yawing moment whilst the vortex core remained in close proximity to the tails. As the vortex core moved away from the tail panels, the increased effectiveness of the windward tail panels increased the positive yawing moment, similar to the static case.

It was also interesting to note that at an incidence of around 22° , the body vortex system was seen to alter its characteristic in the schlieren images, becoming more diffuse and difficult to detect as a discrete aerodynamic phenomenon. At this incidence, the damping coefficient was at a level expected i.e. the reduction in damping coefficient was no longer present. The slope of the spin rate curve for the rear body was also observed to alter and there were large oscillations in the yawing moment at this incidence. This evidence suggested that the 'stabilising' effect of the body vortex system was no longer present.

It was also worth noting the similarity at very low incidences ($\sigma < 4^\circ$) between the rear body spin rate for the full configuration and the predicted spin rate calculated from the static rolling moment coefficient values (and the dynamic clpn variation with σ), shown in fig. 9. This shows three predicted spin rates for a nose roll position of 5° , 0° and -5° in comparison with the single dynamic case at a nose roll position of $\lambda = 0^\circ$. It was clear that the dynamic spin rate closely matched the static result for $\lambda = 5^\circ$. This suggested that the vortex system from the canards was being shifted to an effective roll position of $\lambda = 5^\circ$ by the effect of the spinning rear body.

Further evidence of the body vortex effect can be seen in the variation of rear body roll moment coefficient, fig. 10, for the static body-tail case. It was noted that the large sinusoidal variation in the rolling moment coefficient was only apparent as incidence increased beyond 4° i.e. as the body vortex system developed over the model. The amplitude of the variation increased with incidence until 10° . Beyond this incidence, the amplitude of the rolling moment coefficient began to decrease again. Figs. 11a and 11b show the rolling moment characteristics of the Body-Canard-Tail configurations for static and dynamic models. It should be noted that the static result was obtained by subtracting the Body Canard results for rolling moment from the full configuration results to obtain the rear body rolling moment in the presence of the canards and so provide a direct comparison with the dynamic case. By comparison with the trends shown in fig. 3 and fig. 10, it was apparent that the canard vortices had modulated the tail rolling moment variation by inducing a

downwash velocity in the vicinity of the tails. The effect was most clearly seen at lower incidence when the canard vortices would be in the immediate vicinity of the tails. As incidence increased, the effect of the canard vortices was mitigated and the slope of the rolling moment curve through the $\lambda = 0^\circ$ location was reversed. It was also interesting to note in fig. 11 that the dynamic measurements replicated the trend of the static results in almost all regions of the nose roll range even at the higher incidences. In both the static and dynamic cases shown in these figures it was clear that the magnitude of the downwash velocity varied as the location and strength of the vortices varied with nose roll position relative to the tail region causing the variation in rolling moment with incidence. Evidence of the proximity effect of the body vortex system can be also be seen in figs. 12 and 13 which show the variation of yawing moment and side force around the $\lambda = 0^\circ$ position for incidence angles of $\sigma = 8.0^\circ$ and $\sigma = 18.0^\circ$. Whilst the side force remained linear for $\sigma = 8.0^\circ$ over the small angular lambda range, the corresponding yawing moment varied non-linearly. At $\sigma = 18.0^\circ$ the yawing moment showed a linear variation with lambda. This was indicative of the large effects of the body vortex system passing through the tail region at the lower incidence and altering the pressure distribution on the rear of the missile.

One of the main reasons for a decoupled nose and tail section is to reduce the effect of the canard or control surface vortices on the overall rolling moment on the missile. Although the avoidance of roll reversal on the configuration may be achieved simply due to the decoupled nose section, the canard vortices can still cause large aerodynamic effects on the overall configuration. One of the most revealing results to come out of the study was the large effect of the canard vortices on the rotation rate of the rear body. This effect had been predicted from the static rear body tests that showed very low total rolling moment for particular values of nose roll angle, fig. 14 for the full configuration. In the dynamic tests, the vorticity shed from the canards at particular values of sigma and lambda in combination with a small amount of friction was of sufficient strength to cause the spinning rear body roll rate to reduce until the rear body had stopped spinning altogether. Spinning re-commenced whenever the canard vortices had reduced in strength or moved far enough away from the tail surfaces.

It was clear from all of the work described above that body vortex system played a major role in accounting for some of the non-linearities observed in the aerodynamic characteristics of the configuration. However, results from the laser vapour screen flow visualisation were inconclusive in providing definitive proof of any asymmetric body vortex shedding due to body spin rate on any of the configurations except where there was a large amount of interference from the canard vortices. As a first step to modelling the asymmetric vortex effect, a forced separation option that modelled the cross flow separation was incorporated into the NEARZEUS solver to study the body vortex effect on the yawing moment. The forced separation model in NEARZEUS is based on that developed by Kwong et al⁵, where the axial and circumferential separation can be defined by the user along with the velocity angles at incidence. A number of separation lines (including approximated non-linear patterns) can be defined in this way which allows the user to define separation patterns similar to either those reported in the literature, see for instance Hodges et al⁶ or Mendenhall and Neilsen⁷, or those observed in experimental work. The danger of simply using an inviscid solver to examine cross-plane yaw effects on a body-tail configuration which are affected to a large extent by the shielding of the individual tail panels as they rotate into

the lee-side of the body is illustrated in figs. 15 and 16 for an incidence of $\sigma=6.0^\circ$. Fig. 15 shows the true cross plane yawing moment in the body axis system and the comparison with the numerical result. Clearly there was a good degree of correlation between the experimental and the numerical result over the 90° roll angle range. At this point it should be remembered that in the body axis system at $\lambda=90^\circ$ the yawing moment becomes the primary moment due to the body incidence and so discrepancies between the experimental result and the numerical result can appear small. This is more clearly seen by examining cross-plane yawing moment about an axis which remains fixed in space or more generally referred to as the tunnel axis system, fig. 16. The figure shows the effect of the tail configuration rolling through the 90° roll angle range for the experiment compared with the NEARZEUS result transformed into the same tunnel axis system. It is clear that the numerical result does not follow the trend of the experimental result at all with only some degree of correlation at the orthogonal points. (The reason for the match at these points is the relatively low total incidence of the upper and lower vertical fins). As roll angle varies from $\lambda=0^\circ$, the lower fin will be subjected to an increasing incidence with full exposure to the oncoming freestream flow, whilst the upper fin also increasing in incidence is shielded from the freestream flow by the effect of the body and the vortex system.

By including a separated flow pattern in the NEARZEUS model, as described above, a more realistic flow separation pattern was achieved. This was clearly seen in velocity vector plots and again in cross-plane yawing moment results in both the rolling body axis and the tunnel axis system, figs. 17, 18 and 19. The line that defined the separation varied from a circumferential location of between 45° at the upstream location to 90° at the downstream location and over a body length ranging from a point 3 calibres aft of the nose to 8 calibres aft of the nose. It was interesting also to compare the results for this separated flow model in terms of the tail rolling moment at the same total incidence angle and over a 90° roll orientation with both the experimental results and results using the standard (non-separated flow) NEARZEUS. Results for the three methods are shown in fig. 20. It was clear that the separated flow model had provided a close comparison with the experimental results for the tail rolling moment in both magnitude and variation over the 90° roll angle range. The standard version of the code had predicted the mean rolling moment with a high degree of accuracy but omitted to predict the large variation of rolling moment with roll angle.

These results for tail rolling moment can be contrasted with the results for the nose rolling moment discussed earlier where a separation model was not required for the code to provide a high degree of accuracy in the prediction of nose rolling moment. The physical explanation for this appeared to lie in the cross flow development at the respective locations on the missile. At the nose location there was little shielding of the upper fin by the body vortex system on the experimental model whereas at the rear of the missile a large body vortex system would be present. Also, in comparison with the tail panels which were larger and cruciform in arrangement, the panel-panel interference on the control surfaces would be reduced and since the deflection angles on the canards were also large resulting in high loadings on the windward fin, this further reduced the margin of error in the prediction. Whether the separated flow system was effective in introducing a modulation to the rear body rolling moment purely as a result of its presence alone or by augmenting the panel-panel interference effects on the tail fins was not clear.

5.0 Conclusions

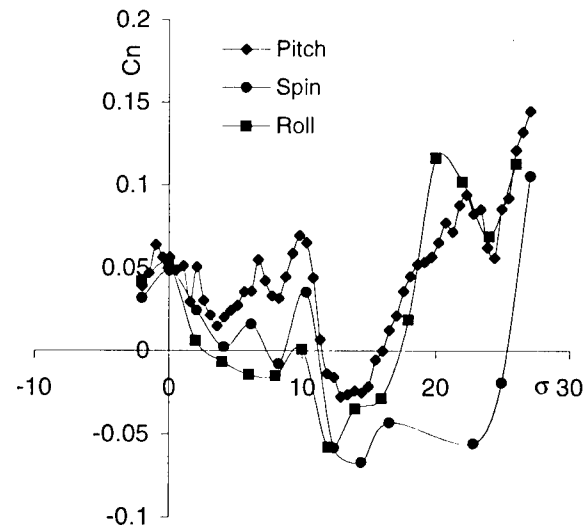
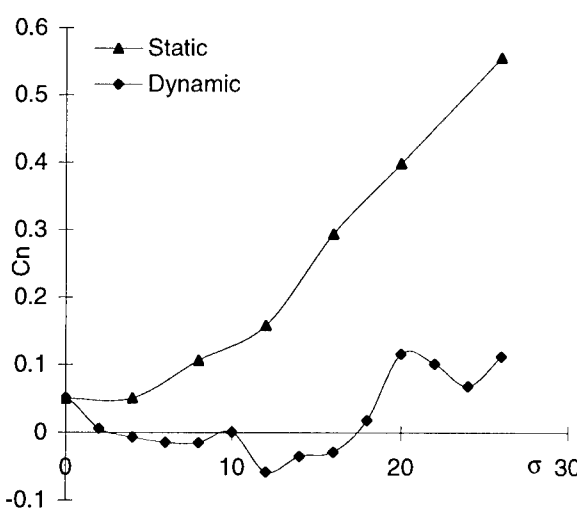
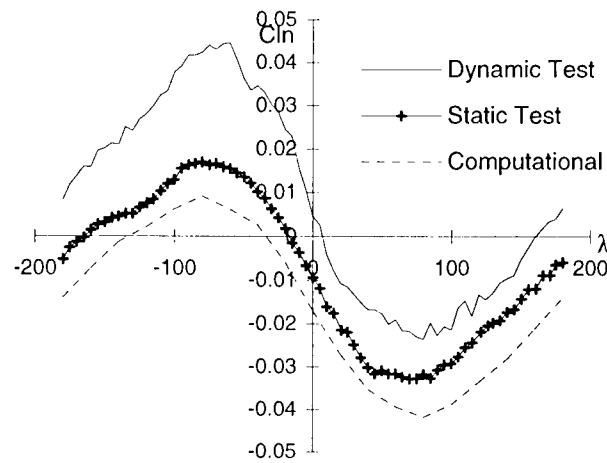
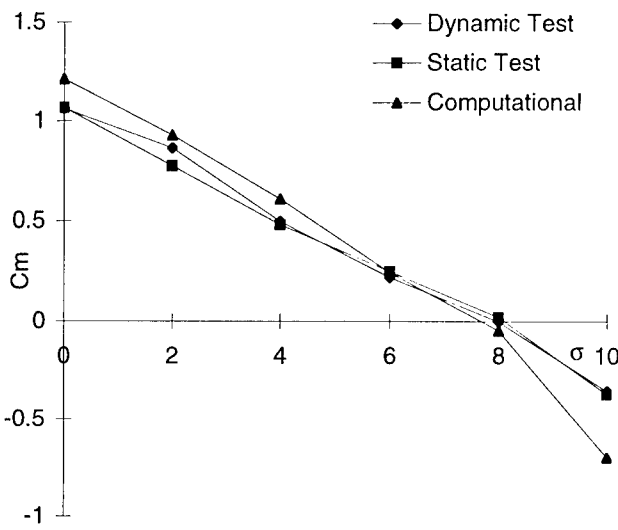
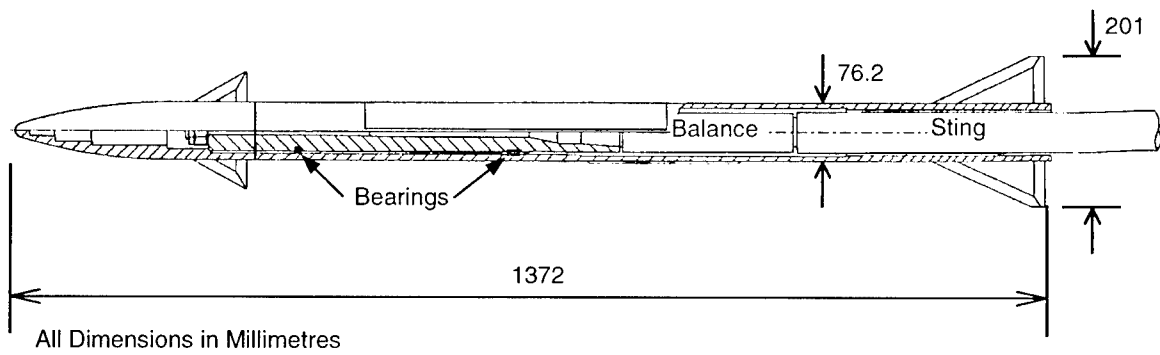
The research presented in this paper was part of an overall examination of the effects of a rolling airframe as compared to a static airframe tested at similar averaged conditions to the rolling case. The work has compared rolling moments, normal and side forces and pitch and yaw moments on the dynamic model, the static model and a computational model of the static experiment. The main conclusion of the work was that despite the decoupled nose section, which remained stationary with respect to the spinning rear body, there was still a high degree of vortex interference on the spinning tails. This resulted primarily in a modulation of the rolling moment on the tail fins, which was large enough to arrest the spin of the rear body at certain incidences and roll orientations. There was some evidence of the fin-Magnus effects on different configurations primarily seen by a delay in the increase in yawing moment as compared to the static case, however these results were compromised to a certain degree by bearing friction. Computational analysis was also able to confirm many of the aerodynamic coefficients observed on the static case. It was necessary to augment the predicted cross flow in the computational work to provide a better comparison with the aerodynamic characteristics of the tails. In general the work provides a reminder of the importance of body-vortex interference and Magnus effects on a finned missile.

6.0 Acknowledgements

The authors wish to thank Shorts Missile Systems Ltd for their permission to publish this work and also acknowledge the assistance of Roy Black and Erl Johnston.

7.0 References

1. Uselton, J.C. and Carman, J.B., 'A study of the Magnus effects on a sounding rocket at supersonic speeds', AIAA Paper No. 70-207, Jan. 1970
2. Platou, A.S., 'Magnus Characteristics of Finned and Nonfinned Projectiles', AIAA Journal, Vol. 3, No. 1, Jan. 1965.
3. Benton, E.R., 'Supersonic Magnus Effects on a Finned Missile', AIAA Journal, Vol. 2, No. 1, Jan. 1964.
4. Wardlaw, A.B., Jr. and Davis, S.F., 'A Second Order Godunov Method for Tactical Missiles', in AGARD 58th Meeting of the Fluid Dynamic Symposium on Applications of Computational Fluid Dynamics in Aeronautics, April 1986.
5. Kwong, C.M. and Myring, D.F., 'Fusiform Body Separation Flowfield Calculations using Euler and Boundary Layer Methods', in Raes Conference on Prediction and Exploitation of Separated Flows, Paper No. 27, 1989.
6. Hodges, J., Ward, L.C. and Birch, T.J., 'Pressure Measurements on Slender Bodies at Supersonic Speeds and Development of Flow Separation Criteria for Euler Codes', in AGARD Missile Aerodynamics, Conference Procs., CP493.
7. Mendenhall, M.R. and Neilsen, J.N., 'Effect of Symmetrical Vortex Shedding on the Longitudinal Aerodynamic Characteristics of Wing Body Tail Combinations', NASA CR-2473, Jan. 1975.



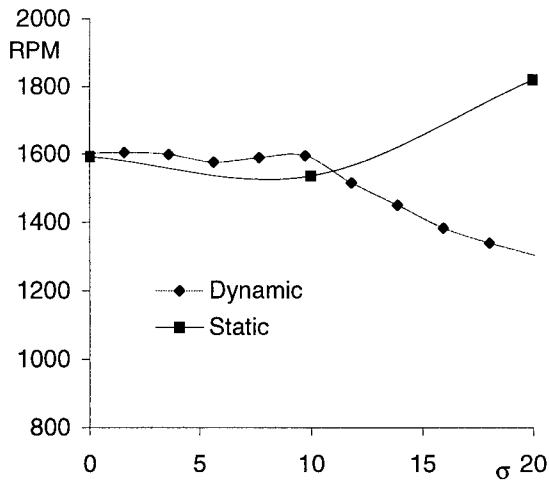


Fig. 6 Comparison of BT roll rate for dynamic case and static CI predictions.

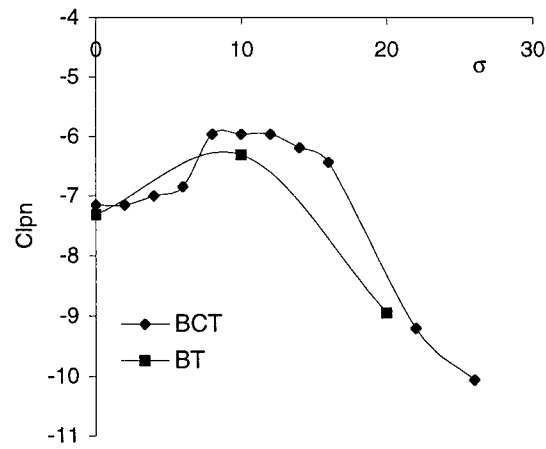


Fig. 7 Variation of tail roll damping coefficient for BT and BCT configurations, Mach 3.5

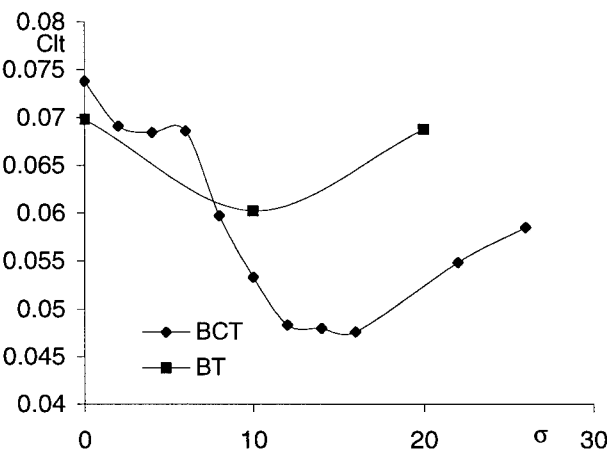


Fig. 8 Variation of Tail Roll Driving Coefficient, Mach 3.5. (Zero friction assumed).

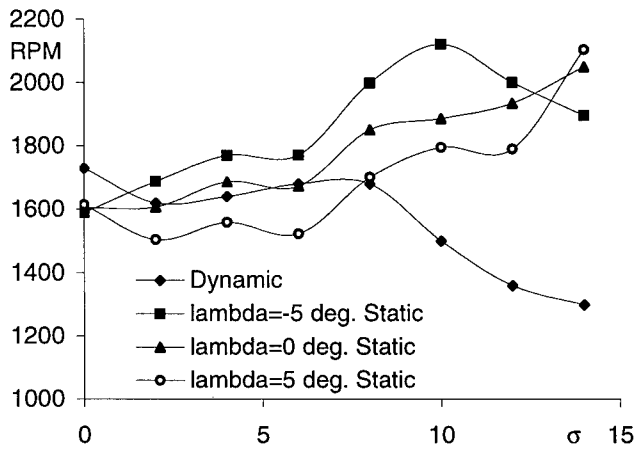


Fig. 9 Roll Rate Comparison for dynamic case (BCT) and derived static results Mach 3.5.

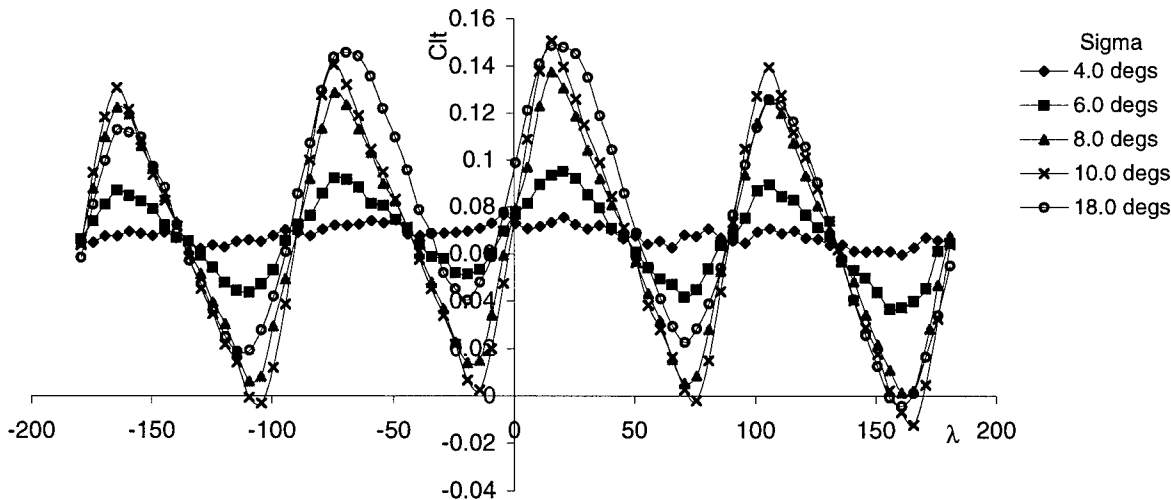


Fig. 10 Variation of Rolling Moment for BT configuration with increasing incidence (sigma).

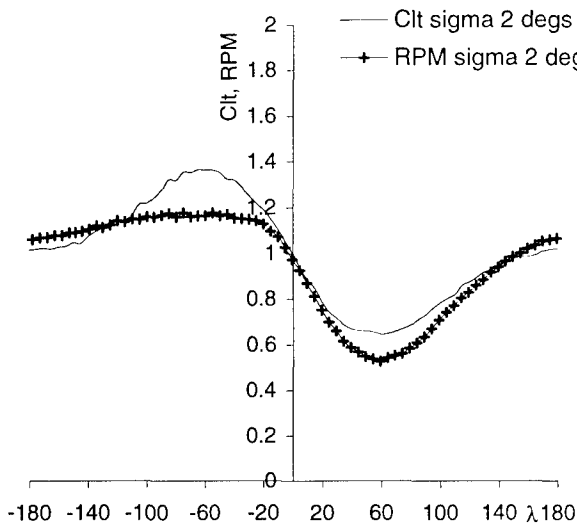


Fig. 11a Comparison of Static Body Torque with Dynamic Roll Rate (normalised), Mach 3.5.

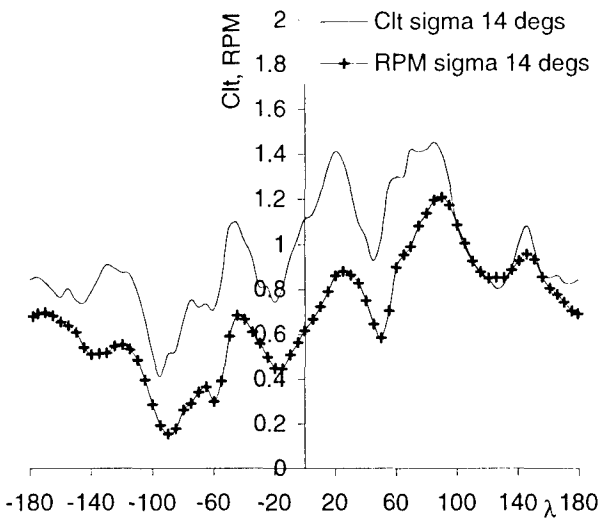


Fig. 11b Comparison of Static Body Torque with Dynamic Roll Rate (normalised), Mach 3.5.

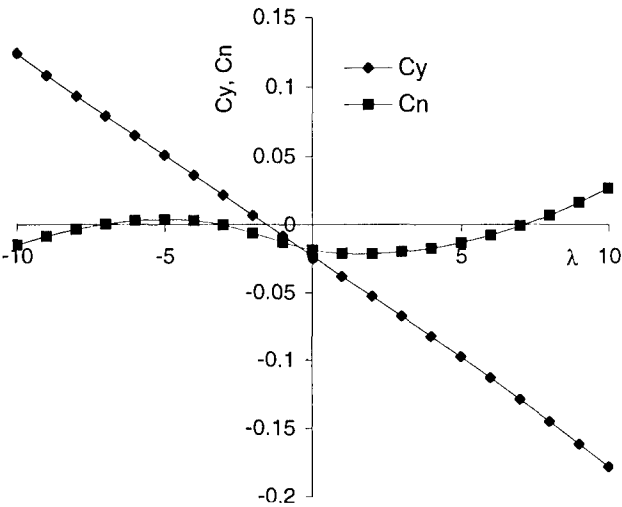


Fig. 12 Variation of Side Force and Yawing Moment, sigma 8.0 degs, Mach 3.5, BCT.

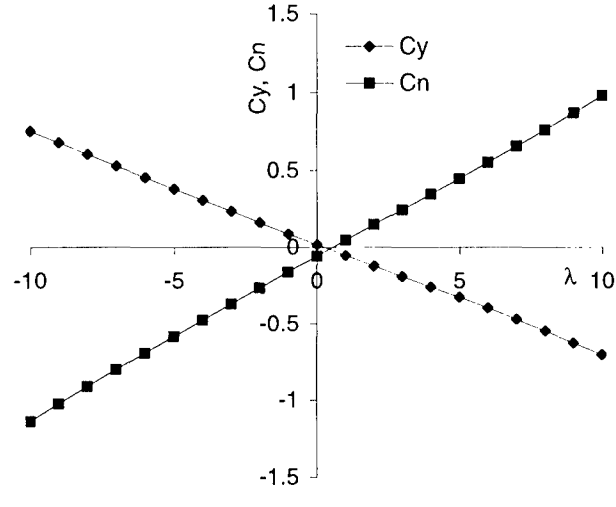


Fig. 13 Variation of Side Force and Yawing Moment, sigma 18.0 degs, Mach 3.5 BCT.

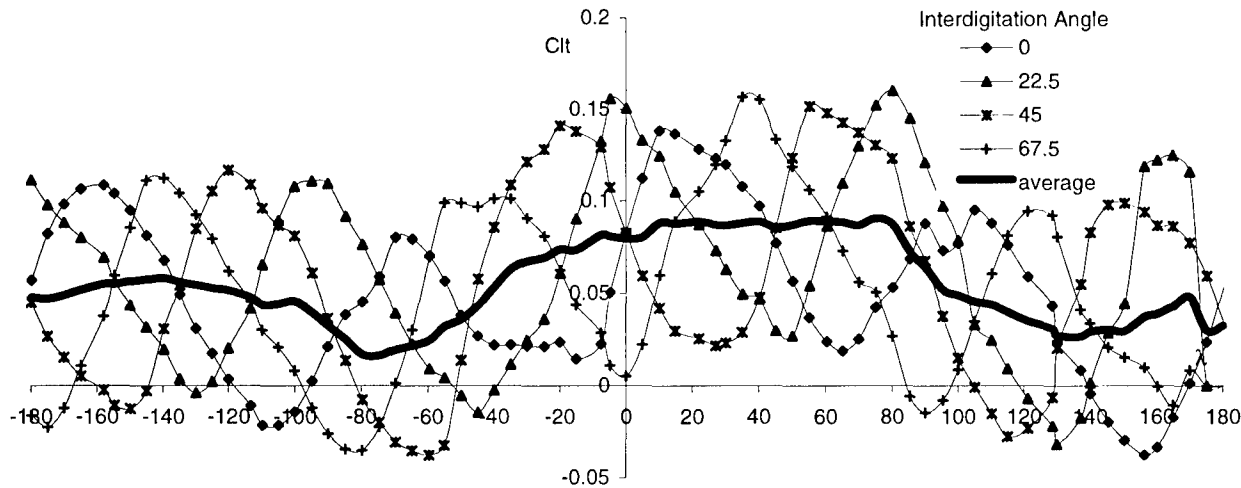


Fig. 14 Variation of Tail Rolling Moment Coefficient in Presence of Canards (BCT-BC) for various tail interdigitation angles, Mach 3.5 $\sigma = 12.0$ degs.

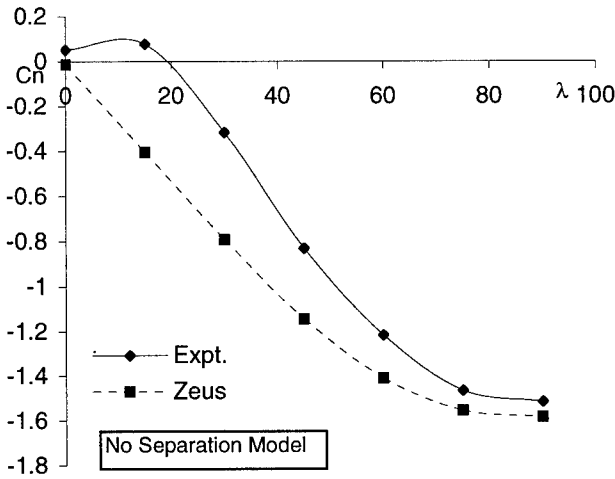


Fig. 15 Variation of Yawing Moment for BT config. (rolling Body Axis), $M= 3.5$, $\sigma=6.0$ deg

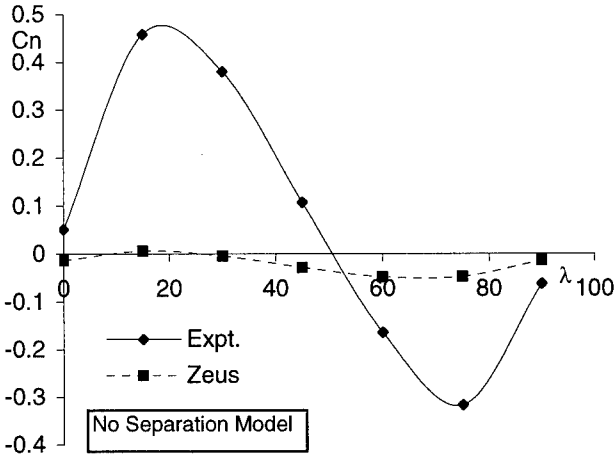


Fig. 16 Variation of Yawing Moment for BT config. (Tunnel Axis), $M= 3.5$, $\sigma= 6.0$ deg

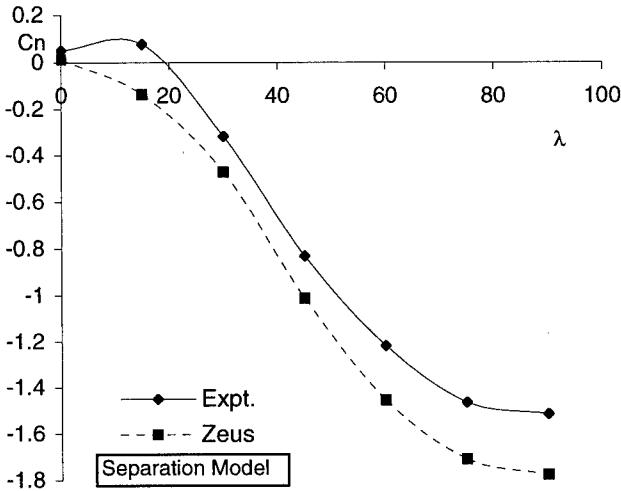


Fig. 17 Variation of Yawing Moment for BT config. (Rolling Body Axis), $M=3.5$, $\sigma=6.0$ deg

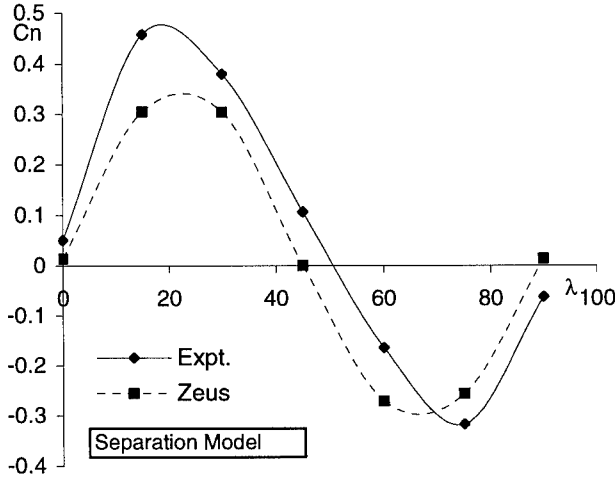


Fig. 18 Variation of Yawing Moment for BT config. (Tunnel Axis), $M= 3.5$, $\sigma=6.0$ deg

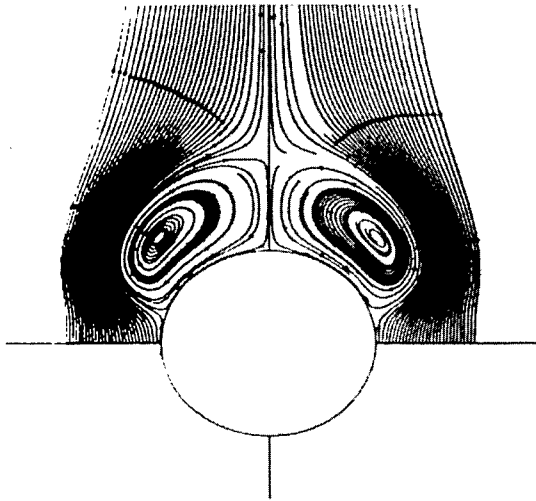


Fig. 19 Vortex pattern on rear body generated by NEARZEUS with separation model, $M=3.5$ $\sigma=6.0$ deg

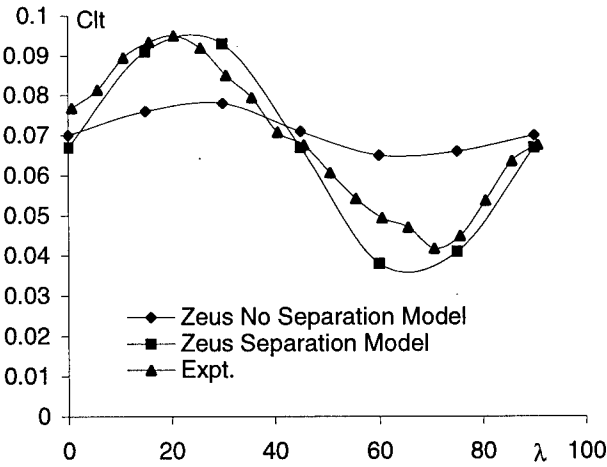


Fig. 20 Variation of Tail Rolling Moment with λ , Mach 3.5, $\sigma=6.0$ degs.

Air Intake Studies : Experimental measurements and computational modelling

P. E. H. Abrahamsen[†] B. A. Pettersson Reif[†] L. Sætran[†] J. B. Fossdal[†]

[†]Kongsberg Defence & Aerospace AS
N-3601 Kongsberg, Norway

[‡]Norwegian University of Science and Technology
Division of Applied Mechanics, Fluid Dynamics and Thermodynamics
N-7034 Trondheim, Norway

1. SUMMARY

The flow in an S-shaped air intake has been studied, using experimental and computational methods. The results have been compared with available experimental data. In the computational study a non-linear eddy viscosity model has been compared with a linear counterpart. In the experimental study, measurements of an Isentropic Light Piston Tunnel has been carried out. The results of the study show that the described methodology can be used for air intake design.

2. LIST OF SYMBOLS

DC ₆₀	Static distortion parameter, $\frac{p_{t60} - p_{tef}}{q_{ef}}$
DH	Static distortion parameter, $\frac{p_{tmax} - p_{tmin}}{p_{tef}}$
E_t	Total energy
k	Turbulence energy, $\frac{1}{2} \overline{u_i u_i}$
P_{ij}	Production of Reynolds stress components
PR	Pressure recovery factor, $\frac{p_{tef}}{p_{t0}}$
p	Static pressure
p_t	Total pressure
p_{t0}	Total pressure in freestream
p_{tef}	Mean total pressure at engine face (e.f.)
p_{t60}	Mean tot. pr. in worst 60° sector at e.f.
p_{tmax}	Maximum total pressure at e.f.
p_{tmin}	Minimum total pressure at e.f.
q_{ef}	Mean dynamic pressure at engine face
S_{ij}	Mean rate of strain tensor, $\partial_j U_i + \partial_i U_j$
T	Temperature
\vec{U}	Velocity vector, $(U, V, W) = (U_1, U_2, U_3)$
\vec{x}	Spatial vector, $(x, y, z) = (x_1, x_2, x_3)$
δ_{ij}	Kronecker delta
ϵ	Turbulent dissipation rate
μ	Molecular viscosity
μ_T	Eddy viscosity
ρ	Density
τ_{ij}	Stress tensor
Ω_{ij}	Mean vorticity tensor, $\partial_j U_i - \partial_i U_j$
Ω_i	Vorticity vector, $\epsilon_{ijk} \partial_j U_k$
ϵ_{ijk}	Permutation tensor
$\rho \overline{u_i u_j}$	Reynolds stress tensor

3. INTRODUCTION

Kongsberg Defence & Aerospace AS (KDA) is engaged by the Royal Norwegian Navy Materiel Command to develop a new anti-ship missile (NSM) for the Royal Norwegian Navy. While the present series of Penguin Missiles made by KDA have rocket cruise engines, the new missile in development will be powered by a turbojet engine with a pitot air intake. NSM is subjected to strict requirements of both high engine net thrust and small dimensions and a crucial component to these requirements is the air intake. Apart from external disturbances, a significant source of intake flow distortion is associated with the flow inside the intake duct (S-duct) itself. The combination of a highly turning S-duct and a significant divergence of the cross-sectional area makes the flow susceptible to separation which leads to low total pressure recovery and thereby reduced engine performance. A highly distorted flow field at the engine face might also lead to compressor stall and a subsequent engine surge which even may cause engine flameout.

The need for an optimal solution to this problem made it necessary to find a design method that is both reliable and cost effective. There is a lot of ongoing work world wide to increase the accuracy and efficiency of both computational fluid dynamics simulations (CFD) and optimisation methods such as inverse design. CFD analysis is becoming an increasingly important tool in the design cycle in the industry today since it offers a more cost effective procedure than traditional wind tunnel testing. However, CFD analysis is merely applied as a conceptual design tool since it can not entirely replace physical wind tunnel measurements. A crucial ingredient of a reliable CFD analysis is that the simulation results have been verified against accurate data for similar flow configurations, typically obtained by experimental measurements in engineering applications.

KDA adopted a conceptual design procedure for the NSM air intake where initial effort was put on the isolated S-duct, optimising the internal flow by CFD methods and verifying the results by experiments. The next step is then to integrate the optimised S-duct in

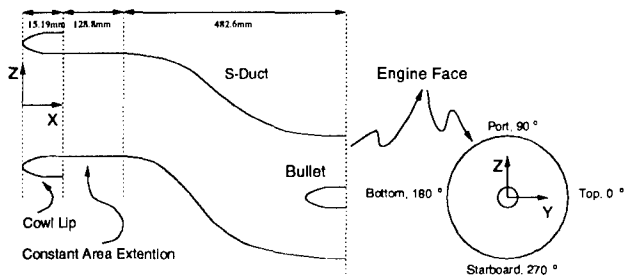


Figure 1: Definition of Air intake geometry

a complete missile model (both for CFD analysis and wind tunnel tests) to account for the effect of a disturbed inlet flow field. The objective of the present work is twofold: (i) to improve the predictive capabilities of the CFD code 'CFD-norway' [1] for internal flows and (ii) to verify the capabilities of the Isentropic Light Piston Tunnel (ILPT) [2] at the Norwegian University of Science and Technology to faithfully reproduce the flow field inside a S-duct. Both numerical simulations and experimental results are compared with AGARD Working Group 13s measurements of the RAE M2129 S-duct (corresponding to the low mass flow test case 3.2) [3], see figure 1 for air intake definitions. It should however be pointed out that the results presented in this paper are the outcome of a preliminary study conducted at KDA.

4. DESCRIPTION OF METHODOLOGY

4.1 Computational Modelling

CFD analysis has become an increasingly important tool in the design cycle of modern industry. The applications of CFD are covering a wide range of flows which basically can be divided into two types: (i) aeronautical and (ii) industrial flows. The first type includes aerospace applications such as external aerodynamics whereas the latter typically covers low speed internal flows. Both types are influenced by turbulence but the former can be considered to involve moderately complex physics whereas the latter type is characterized by very complex physics. CFD codes are traditionally based on the Reynolds Averaged Navier Stokes equations which require a model for the unknown single point correlation of fluctuating velocities, i.e. the so called Reynolds stresses. Recognizing the fact that the level of sophistication of turbulence models successfully can be linked to these two types of flow families, makes it possible to optimize the computational effort required for a given problem.

A viable approach to air intake design is to apply less sophisticated turbulence models to the external flow calculations which then provide inlet conditions for internal flow simulations, thus taking into account effects of fuselage boundary layers, etc. The internal flow computations, which inevitably require more complex turbulence closures, can then be applied to a smaller computational domain so that the computational cost is significantly reduced. The flow inside the

air intake is mainly characterized by three-dimensional turbulent boundary layers, affected by an adverse pressure gradient, and a potential core flow. In addition laminar-turbulent transition and a mean swirling motion are also most likely present. Furthermore, the imposed streamline curvature in a turning intake affects not only the mean flow field but also the intensity and structure of the turbulence. It is therefore unfortunate that the majority of commonly used CFD tools today adopt turbulence closures based on Boussinesq's linear stress-strain relationship. An inherent shortcoming of these closures (e.g. the standard $k - \epsilon$ model) is that they are unable to capture direct effects of body forces on the turbulence.

Marquis & Ong [4], [5] recently adopted a number of different closures, ranging from linear eddy-viscosity models to full Reynolds stress transport models (RSTM), to compute the flow inside a semicircular to circular S-duct. They pointed out the existence of non-equilibrium turbulence which implies that the commonly used wall-function approach should be abandoned. Although the physically more appealing low-Reynolds number near-wall treatment implies a highly dense computational grid close to solid boundaries and therefore often is abandoned, it is believed to be of crucial importance to resolve this area of the flow in order to improve model predictions in the future. Marquis & Ong [4], [5] furthermore concluded that turbulence transport played a significant role in their S-duct configuration and subsequently concluded that a low Reynolds number RSTM may be the best approach in the future. However, the application of near-wall RSTMs are not tractable at present mostly due to numerical stability issues which lead to very high computational costs.

However, there is an ongoing research effort towards more reliable turbulence closures which are able to more accurately predict complex flow fields without compromising the computational cost to any significant extent. Notably closures that are able to account for anisotropic turbulence. The linear Boussinesq relation is in the present study replaced by a nonlinear constitutive relation between the turbulent stresses and mean strains; a somewhat modified form of the low-Reynolds number nonlinear eddy-viscosity model due to Craft et al. [6] is adopted.

Although this approach is based on a significantly weaker fundamental foundation than RSTM closures, it offers a viable alternative since it retains some of the numerical advantages of the linear effective viscosity approach. The present study also employs the linear $k - \epsilon$ model due to Chien [7] which has been extensively applied in many engineering applications, for comparative purposes.

4.1.1 Governing equations

The complete set of governing equations for compressible flow consist of the continuity equation, three mean momentum equations and the energy equation. The

effect of turbulence is accounted for by variations of the commonly used $k - \epsilon$ model. In the following, all equations will be written using cartesian tensor notation with spatial vector \vec{x} and the mean velocity vector \vec{U} . The usual summation rule for repeated indices is applied.

The turbulent quantities k and ϵ are solved in two separate transport equations, where k denotes the turbulence energy and ϵ is the scalar dissipation rate of turbulence. For numerical reasons it is convenient to split the dissipation rate $\epsilon = \tilde{\epsilon} + D$ and then solve for the quantity $\tilde{\epsilon}$, which attain a constant wall value. The function D is computed explicitly.

The transport equations governing the flow field can be written as :

$$\partial_t \mathbf{U} + \partial_x \mathbf{F} + \partial_y \mathbf{G} + \partial_z \mathbf{H} = \mathbf{I} \quad (1)$$

where ∂_i denotes the spatial derivative with respect to i , and:

$$\mathbf{U}^T = [\rho \quad \rho U \quad \rho V \quad \rho W \quad E_t \quad \rho k \quad \rho \tilde{\epsilon}] \quad (2a)$$

$$\mathbf{F} = \begin{bmatrix} \rho U \\ \rho U^2 + p + \tau_{xx} \\ \rho UV + \tau_{xy} \\ \rho UW + \tau_{xz} \\ (E_t + p)U + \tau_{xx}U + \tau_{xy}V + \tau_{xz}W - k_t \partial_x T \\ \rho U k - (\mu + \mu_T / \sigma_k) \partial_x k \\ \rho U \tilde{\epsilon} - (\mu + \mu_T / \sigma_\epsilon) \partial_x \tilde{\epsilon} \end{bmatrix} \quad (2b)$$

$$\mathbf{G} = \begin{bmatrix} \rho V \\ \rho UV + \tau_{xy} \\ \rho V^2 + p + \tau_{yy} \\ \rho VW + \tau_{yz} \\ (E_t + p)V + \tau_{xy}U + \tau_{yy}V + \tau_{yz}W - k_t \partial_y T \\ \rho V k - (\mu + \mu_T / \sigma_k) \partial_y k \\ \rho V \tilde{\epsilon} - (\mu + \mu_T / \sigma_\epsilon) \partial_y \tilde{\epsilon} \end{bmatrix} \quad (2c)$$

$$\mathbf{H} = \begin{bmatrix} \rho W \\ \rho UW + \tau_{xz} \\ \rho VW + \tau_{yz} \\ \rho W^2 + p + \tau_{zz} \\ (E_t + p)W + \tau_{xz}U + \tau_{yz}V + \tau_{zz}W - k_t \partial_z T \\ \rho W k - (\mu + \mu_T / \sigma_k) \partial_z k \\ \rho W \tilde{\epsilon} - (\mu + \mu_T / \sigma_\epsilon) \partial_z \tilde{\epsilon} \end{bmatrix} \quad (2d)$$

$$\mathbf{I} = \begin{bmatrix} 0 \\ 0 \\ 0 \\ 0 \\ 0 \\ P_k - \rho(\tilde{\epsilon} + D) \\ c_{\epsilon 1} f_1 \frac{\tilde{\epsilon}}{k} P_k - c_{\epsilon 2} \rho f_2 \frac{\tilde{\epsilon}^2}{k} + \rho E \end{bmatrix} \quad (2e)$$

where the stresses are defined as :

$$\begin{aligned} \tau_{xx} &= -\mu(4/3 \partial_x U - 2/3(\partial_y V + \partial_z W)) + \overline{\rho u^2} \\ \tau_{yy} &= -\mu(4/3 \partial_y V - 2/3(\partial_x U + \partial_z W)) + \overline{\rho v^2} \\ \tau_{zz} &= -\mu(4/3 \partial_z W - 2/3(\partial_x U + \partial_y V)) + \overline{\rho w^2} \\ \tau_{yz} &= \tau_{zy} = -\mu(\partial_z V + \partial_y W) + \overline{\rho v w} \\ \tau_{xy} &= \tau_{yx} = -\mu(\partial_y U + \partial_x V) + \overline{\rho u v} \\ \tau_{xz} &= \tau_{zx} = -\mu(\partial_z U + \partial_x W) + \overline{\rho u w} \end{aligned} \quad (3)$$

It should be noted that equation (2e) represents the turbulence model source terms. For details cf. [6] and [7].

4.1.2 Turbulence Modelling

Among the factors that have made the $k - \epsilon$ models popular, are their simplicity and computational robustness, of major importance. Compared to the RSTMs, $k - \epsilon$ models give comparable accuracy in simple turbulent shear flows. All $k - \epsilon$ models are based on the assumption that turbulence can be described by a scalar turbulence viscosity in analogy with molecular viscosity, a so called *eddy viscosity* (μ_T). The form may vary but it can in general be expressed as:

$$\mu_T = c_\mu \rho f_\mu \frac{k^2}{\tilde{\epsilon}} \quad (4)$$

where c_μ is a constant and f_μ is a damping function employed to compensate for near wall effects.

Commonly used $k - \epsilon$ models, such as the model due to Chien [7], employ the Boussinesq assumption that the Reynolds stresses is a linear function of the mean rate-of-strain S_{ij} , i.e. :

$$-\overline{\rho u_i u_j} = \mu_T (S_{ij} - 1/3 \delta_{ij} S_{kk}) - 2/3 \delta_{ij} \rho k \quad (5)$$

This linear assumption has proven to be fundamentally wrong for complex flows e.g. rotating flows and flows affected by streamline curvature. This fact limits the usefulness of models based on this assumption.

To extend the capabilities of the $k - \epsilon$ model Craft et.al. [6] proposed a model based on a constitutive relation, in which the Reynolds-stresses are functions including up to third order elements of both the mean rate of strain S_{ij} and mean intrinsic vorticity tensor Ω_{ij} . The model is thereby sensitized to the anisotropy of the turbulence, which plays an important role in flows affected by body forces e.g. streamline curvature. The cubic model can be expressed for compressible flow as :

$$\begin{aligned} -\overline{\rho u_i u_j} &= \mu_T (S_{ij} - 1/3 \delta_{ij} S_{kk}) - 2/3 \delta_{ij} \rho k \\ &\quad - C_1 b (S_{ik} S_{kj} - 1/3 \delta_{ij} S_{kl} S_{kl}) \\ &\quad - C_2 b (\Omega_{ik} S_{kj} + \Omega_{jk} S_{ki}) \\ &\quad - C_3 b (\Omega_{ik} \Omega_{jk} - 1/3 \delta_{ij} \Omega_{km} \Omega_{km}) \\ &\quad - C_4 d (S_{ki} \Omega_{lj} + S_{kj} \Omega_{li}) \\ &\quad - 2/3 \delta_{ij} S_{km} \Omega_{lm} S_{kl} \\ &\quad - C_5 d (S_{ij} - 1/3 \delta_{ij} S_{kk}) S_{lm} S_{lm} \\ &\quad - C_6 d (S_{ij} - 1/3 \delta_{ij} S_{kk}) \Omega_{lm} \Omega_{lm} \end{aligned} \quad (6)$$

See Craft et al. [6] for details on model coefficients.

An important feature of engineering flows in general is the three dimensionality of the mean velocity field. Although this statement might seem excessive, the majority of industrial CFD computations simply adopt turbulence closures devised for two dimensional (2D) flows. An important difference between the turbulence in a three dimensional (3D) boundary layer, as compared to a 2D boundary layer, is that the Reynolds stresses are not colinear with the mean shear in the 3D case. This implies that the linear eddy viscosity hypothesis becomes inconsistent. To more closely study this effect, Moin et al. [8] conducted direct numerical simulations of a 3D turbulent channel flow and concluded that the turbulent energy level was reduced compared to its 2D counterpart. Durbin [9] subsequently suggested that the observed effect could be represented in single-point closures by an increase of the rate of turbulent energy dissipation ϵ . Durbin [9] proposed the following expression as an additional source term to the dissipation rate transport equation :

$$S_{\epsilon 1} = 2.0 \frac{\Omega_i P_{ik} P_{kj} \Omega_j}{\epsilon T_k \Omega_n \Omega_n} \quad (7)$$

where $T_k = \sqrt{\mu/\rho\epsilon}$ denotes the Kolmogorov time scale. P_{ij} is the rate of production of the Reynolds stress components due to mean shear and Ω_i is the vorticity vector.

4.1.3 Numerical Approach

The three-dimensional Reynolds-averaged Navier-Stokes equations are solved by a time stepping finite volume method (cf. [1], [10], [11] and [12]). The time derivatives are used as a numerical method to reach a steady state solution only. Time stepping is performed by a second order three-stage Runge-Kutta method, and the method applies cell centred fluxes for spatial discretisation, stabilised by a fourth order damping term.

The computational domain is, due to the complexity of the S-duct geometry, discretised using a boundary fitted mesh. Assuming symmetry in the flowfield, only half of the air intake is computed. The grid used for the two numerical calculations consist of 67920 cell volumes, arranged in three different cell blocks. The boundary mesh is shown in figure 2, and the mesh in the symmetry plane is shown in figure 3.

In order to solve the equations given in section 4.1.1, the equations are transformed from the cartesian coordinate system (x, y, z) , to a computational domain (η, ξ, ζ) where all spatial distances are of length unity. The bounds of the computational domain are the transformed physical boundaries. To simplify the implemented numerical scheme the thin-layer approximation is used on the transformed equations. The approximation implies that only derivatives normal to physical boundaries are of importance, with the tangential terms negligible.

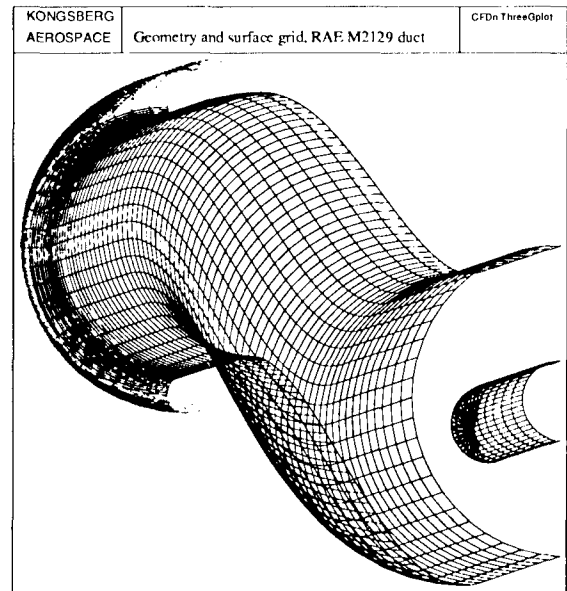


Figure 2: Surface mesh for the air intake.

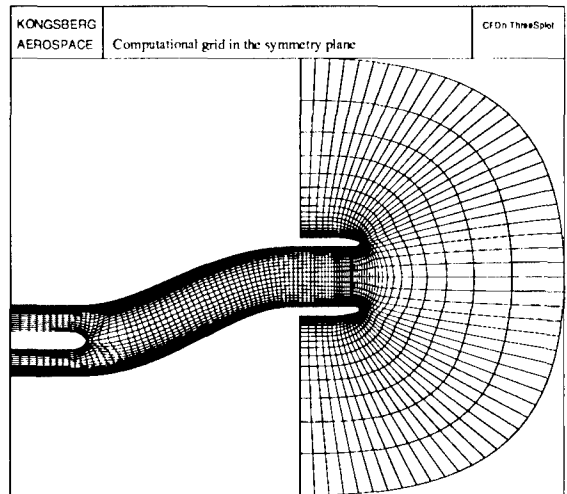


Figure 3: Computational mesh in symmetry plane.

No-slip conditions are enforced on solid walls (except on the engine bullet where slip conditions are employed) and non-reflective conditions are applied at the far field inflow boundary. Constant streamwise gradients of the primitive variables are assumed at the outflow boundary inside the duct, applied one outlet diameter downstream from the engine face.

4.2 Experimental Method

The experiments were performed using an Isentropic Light Piston Tunnel facility. The principle of the device may be outlined with reference to figure 4. The test gas is contained in a tube and is compressed isentropically by a piston which is propelled by gas entering the tube from a high pressure reservoir. When the test gas, in this case air, has been compressed to a certain pressure it is allowed to flow through the working section and the pressure within the tube may be maintained constant as long as the volumetric flow

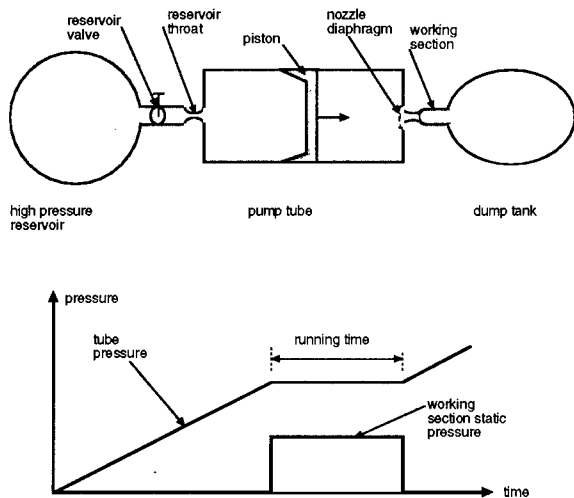


Figure 4: Experimental setup for ILPT facility.

rate of gas into the tube from the high pressure reservoir is the same as that leaving through the working section. The sketch of the ILPT seen in figure 4 consists of a high pressure reservoir connected via a throat and a valve to the pump tube which vents through the working section nozzle into the dump tank. A smooth piston runs in the tube, starting its travel at the high pressure reservoir end, and is driven down the tube by the gas entering from the reservoir, thereby compressing the gas initially within the tube.

A bursting diaphragm isolates the pump tube from the working section nozzle and this is arranged to open when the test gas has been compressed to a specified pressure. When this occurs the test gas flows out through the nozzle and if the volumetric flow rate out of the tube equals that flowing into the tube from the reservoir, the test gas conditions will remain constant until the piston reaches the nozzle entrance. This mode is provided, for the subsonic experiment reported here, using sonic nozzles downstream the working section.

When the gas flows through the working section under this kind of 'matched' conditions, the work done by the gas within the tube on the gas leaving through the nozzle equals the work done by the reservoir and the condition within the test gas remain constant. The ideal form of the pressure history in the tube and the working section are sketched in figure 4.

The volume of the high pressure reservoir is 3 cubic meters and is, for the experiments reported here, kept at a pressure of 7 bars. The 600 mm inner diameter pump tube is 4.5 m long and the 7 kg piston is made of Kevlarfiber reinforced epoxy. Circular aluminium plates are used for bursting diaphragms, in which partial cuts are milled in order to obtain good experimental repeatability. The test model geometry is at scale 1:3. The facility effective running time is about 1 second, and all measurements are made with fast pressure transducers situated along the 'starboard' side of the S-duct for static pressure measurements, and at total-head probes at the 'engine-face' cross-section.

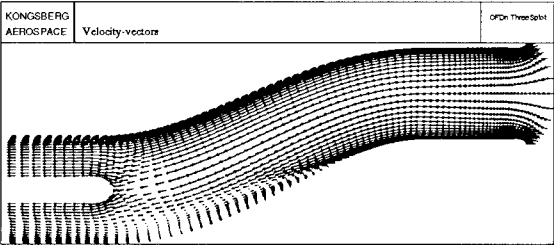


Figure 5: Velocity vectors in symmery plane.

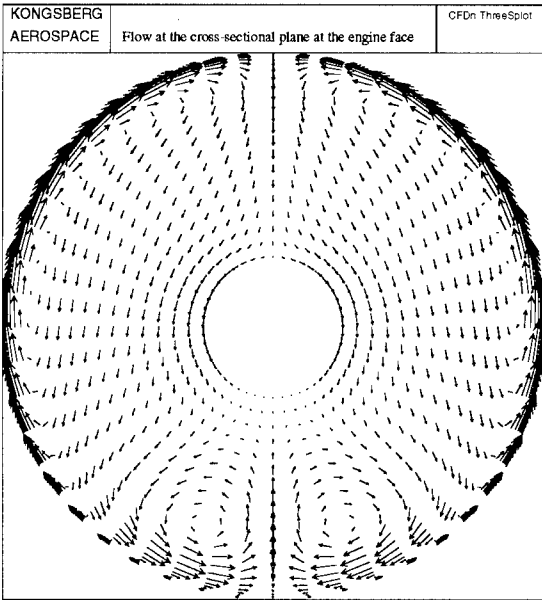


Figure 6: Vortex formation at the engine face.

	AGARD	ILPT	Craft et al.	Chien
PR	0.9897	0.9873	0.9919	0.9772
DC ₆₀	-0.226	-	-0.180	-0.545
DH	0.041	0.064	-	-

Table 1: Predicted pressure recovery (PR) and static distortion parameters (DC₆₀) and (DH).

5. RESULTS & DISCUSSION

To assess the quality of the numerical computations and experimental measurements in the present study, the results are compared with AGARD Working Group measurements [3], which serve as a set of reference data. The general flow characteristics inside the S-duct predicted by the non-linear model are displayed in figures 5 and 6. The flowfield exhibits a separation along the starboard side (see figure 5). Furthermore, the imbalance between radial pressure gradient and centrifugal force sets up two counterrotating stream-wise vorticies, clearly visible in figure 6. Another pair of vorticies can also be observed close to the top and bottom side of the air intake.

At the engine face, the deviation from ideal conditions can be quantified by the area weighted pressure recovery PR and the two static distortion parameters DC₆₀ and DH, displayed in table 1. It can be seen that both computations and experiments predict the pressure recovery in a satisfactory way. From the computations,

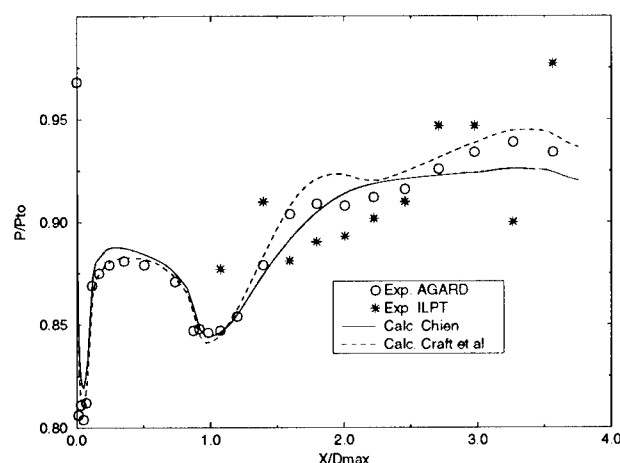


Figure 7: Static pressure distribution along starboard side of air intake duct.

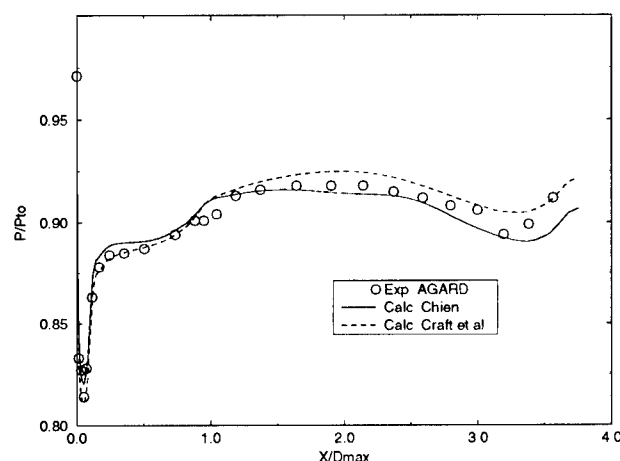


Figure 8: Static pressure distribution along port side of air intake duct.

the nonlinear model show a better distortion parameter DC_{60} than the linear model.

The normalized static pressure distribution along the starboard and port side of the air intake are shown in figures 7 and 8. The spatial distance is nondimensionalized with the outer diameter of the cowl lip, $D_{max} = 168.7\text{mm}$.

It is difficult to point at large differences in the results. Both numerical models exhibit approximately the same static pressure distribution. However, the non-linear closure is able to predict a flow separation along the starboard side, in contrast to the linear model. The ILPT data also give the an impression of the pressure distribution, although there is considerable noise in the measured values. It should be pointed out that the ILPT static pressure measurements are not very reliable due to problems with the data sampling system. These problems were unfortunately discovered after the test campaign were ended, and could not therefore be accounted for.

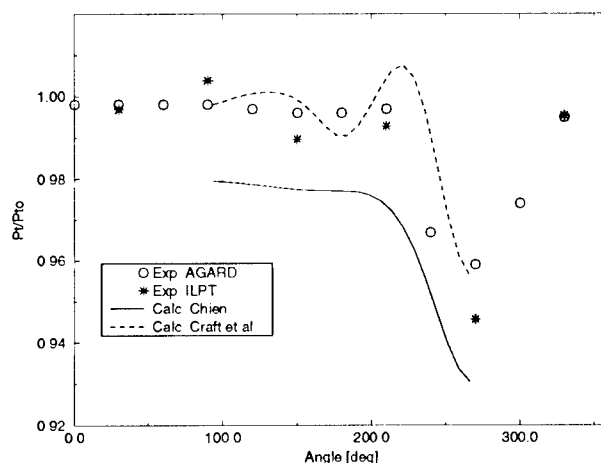


Figure 9: Total pressure in annulus 2 at the engine face.

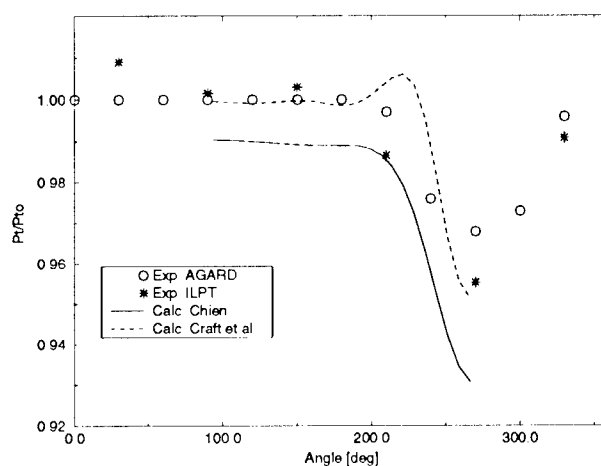


Figure 10: Total Pressure in annulus 3 at the engine face.

The figures 9 and 10 show the total pressure in two annuli at the engine face. The diameter of annulus 2 and 3 are $D_2 = 133.6\text{mm}$ and $D_3 = 119.4\text{mm}$, respectively. The linear model predicts a tendency very similar to the AGARD measurements, but the magnitude is underpredicted. An apparent problem with the non-linear model is revealed; the oscillatory behaviour of the total pressure variation is coupled to an unsteadiness of the computations. Although several attempts were made to quench the transient behaviour of the solution, it was concluded that further work is needed in order to resolve this matter. The ILPT measurements resembles the AGARD results closely.

6. CONCLUDING REMARKS

This first preliminary development study of a conceptual air intake design approach considered at KDA has revealed an encouraging potential. The combination of an improved CFD method and low cost experimental

measurements seem to be a viable approach. However, further work is still needed in order to establish complete confidence in the method.

The adopted non-linear numerical modelling approach seems to improve the predictive capability of the CFD tool used at KDA.

Although the computational cost of the numerical computations has been increased (approx. by a factor 1.8 as compared to the linear eddyviscosity approach), this more elaborate modelling strategy has proven to be a viable alternative to industrial applications.

REFERENCES

- [1] Øye, I.J., Dr.Ing. Thesis 1996-118, The Norwegian University of Science and Technology, 1996.
- [2] Jones, T. V., Schultz, D. L. & Hendley A. D., "On the Flow in an Isentropic Light Piston Tunnel", Dept. Engineering Science, University of Oxford, 1973.
- [3] "Air Intakes for High Speed Vehicles", AGARD ADVISORY REPORT 270, Fluid Dynamics Panel Working Group 13, 1991.
- [4] Marquis, A. J. & Ong, L.Y., "The Use of Linear and Non-Linear Low Reynolds Number Models in the calculations of flow in a RAE M2129 S-Duct", Proc. 11th Symp. Turbulent Shear Flows, Grenoble, September 1997, Paper 3.
- [5] Marquis, A. J. & Ong, L.Y., "Computation of Incompressible Flow in a RAE M2129 SemiCircular to Circular Diffusing Duct", in "Computational Fluid Dynamics Conference", ECCOMAS, 1996, Paris France.
- [6] Craft, T.J., Launder, B. E. & Suga, K., "Extending the applicability of eddyviscosity models through the use of deformation invariants and non-linear elements", in "5th Int. Symp. Refined Flow Modelling and Turbulence Measurements", IAHR Conference, Paris, 125, 1993.
- [7] Chien, K. Y., "Predictions of Channel and Boundary-Layer Flows with a Low-Reynoldsnumber Turbulence Model", AIAA Journal, Vol.20, pp. 33-38, 1982.
- [8] Moin, P., Shih, T. -H., Driver, D. & Mansour, N., "Direct numerical simulation of a three-dimensional turbulent boundary layer", Phys. Fluids A 2, 1846, 1990.
- [9] Durbin, P. A., "On modelling three-dimensional turbulent wall layers", Phys. Fluids A 5, 1231, 1993.
- [10] Eriksson, L.-E., FFA TN 1985-20, The Aeronautical Institute of Sweden, Stockholm, 1985.
- [11] Eriksson, L.-E., HOG Report 1987:102 (A), Division of Hydro- and Gas Dynamics, The Norwegian Institute of Technology, 1987.
- [12] Jameson, A., Schmidt, W. & Turkel, E., AIAA Paper 81-1259, 1981.

Optimal Missile Inlet Design by means of Automated Numerical Optimization

Michael Blaize* Doyle Knight†
Department of Mechanical and Aerospace Engineering

Khaled Rasheed‡
Department of Computer Science

Rutgers University - The State University of New Jersey
98 Brett Road · Piscataway
New Jersey 08854-8058 · U.S.A.

Yan Kergaravat*
Numerical Simulation Department
AEROSPATIALE-MISSILES
2 Rue Béranger · B.P. 84
92323 Châtillon CEDEX · France

Abstract

This paper presents a numerical method developed to optimize two-dimensional supersonic ramjet missile inlets in an automated way. The objective is to maximize the propulsive performances of the inlet, not only for one flight condition, but over an entire mission. This innovative computational process has been applied to the redesign of existing inlets and to the design of new ones. It combines an optimization algorithm which generates and selects inlet geometries, with a flow solver which calculates the inlet performances, within an automated iterative loop. The design strategy yields great improvements of the baseline inlet in a very short period of time. Successful results are presented for the optimization of a generic inlet for a typical mission. The validity of the increase in total pressure recovery achieved by the automated optimization loop is verified using Navier-Stokes computations. The application and the possible benefits of such a tool for the aerospace industry are presented through the example of AEROSPATIALE-MISSILES.

* AEROSPATIALE-MISSILES Engineer.

† Professor, AIAA Associate Fellow.

‡ Research Associate.

1 INTRODUCTION

Over the years, the design of high-performing supersonic missile inlets has become an intricate exercise. Actually, in addition to the design complexity, the aerospace industry has to deal with constantly revised and shortened design cycle. As a result, new design techniques have emerged taking advantage of the combined progress in computer technology, high-end simulation tools and artificial intelligence schemes. This paper describes one of these new design processes, which has been implemented with a view to achieve optimal performing supersonic inlets in a short period of time. This innovative design methodology is based upon the coupling of an efficient and robust optimization algorithm and a fast semi-empirical simulation tool. The purpose of the automated optimization loop is to maximize the aerodynamic performance of the inlet from one single flight condition to an entire mission which brings together several flight conditions. The propulsive performances of a supersonic inlet can be assessed by means of three coefficients: the total pressure recovery coefficient η , the air capture ratio ϵ and the drag coefficient C_D . The total pressure recovery indicates the energy losses through the compression process. It

is the main performance characteristic which should be maximized at any given flow condition. The two other coefficients have to meet constraints defined by the mission to be performed and the engine to be used.

The first part of this paper describes the automated design methodology in terms of software implementation and objective treatments. Then, the efficiency of the optimization process is demonstrated through the design of an optimal ramjet missile inlet for a particular mission. The results are analyzed thoroughly while compared to a formal baseline inlet. The improvements achieved are verified using a Navier-Stokes code. The third part is devoted to the actual implementation of this new design capability at AEROSPATIALE-MISSILES. Typical applications are presented. The current limitations of the methodology are discussed and future developments are described.

2 AUTOMATED DESIGN METHODOLOGY

The numerical method consists of an optimization algorithm and a flow solver coupled within an automated loop. The optimizer is the Genetic Algorithm GADO¹ developed at Rutgers University, U.S.A. by K. Rasheed *et al* [1]. The flow solver is OCEAS [2], which has been developed at AEROSPATIALE-MISSILES, France. The different codes and the optimization loop are presented in more detail below.

2.1 Optimization Algorithm

Within recent years, optimization methods have evolved very fast, and currently several kinds of algorithm are available. They are divided into two main categories : *global* and *local* methods. The local methods search the design space by means of gradient computations and therefore are confined to a local region. The global methods use stochastic schemes in order to take into account the whole design space. As a matter of fact, the second category is more likely to find the global optimum. Moreover, they are still effective on discontinuous design spaces because they do not require any gradient calculations.

Among the global optimizers, Genetic Algorithms,

¹GADO is an acronym for: Genetic Algorithm for Design Optimization

commonly denoted GAs, have demonstrated their effectiveness in very diversified engineering problems [3, 4, 5, 6, 7]. Genetic Algorithms are search algorithms that mimic the behavior of natural selection to solve given problems [8]. These algorithms first generate a random collection (population) of potential solutions (individuals or candidates). Using mutations and recombinations (crossover operations), they evolve the population towards better solutions, as individuals become adapted to the problem faced. The GA that will be used belongs to the same theory; nevertheless, it has several improvements that make it more efficient and reliable. GADO is the name of this special GA. A preliminary version of GADO has been used in this research, and did not include all the modules described in [7]. Compared to classical GAs, GADO has several improvements that have proved to increase the accuracy, speed and reliability of the search process. Further information on the special implementation of this GA can be found in [1, 4, 5, 7].

2.2 Simulation Tool

To compute the aerodynamic performances of candidate inlets, a flow solver is needed. The most accurate tools available are Navier-Stokes flow solvers. However, today they are too CPU time demanding to be included in an automated search that requires thousands of flow field computations. Therefore, a simple, fast and reasonably accurate flow solver called OCEAS is used within the automated optimization loop, while a Navier-Stokes analysis code is used to verify the final results. OCEAS employs simple but accurate physical models that require little CPU time. Any single computation requires 2 CPU seconds only, using a DEC ALPHA 2100 work station. OCEAS is used to compute the critical values of the total pressure recovery and the air capture ratio as well as the off-design drag coefficient.

2.3 Implementation of the Loop

Figure 1 shows the implementation of the automated optimization process. One can see that the process forms a loop in which the GA guides the search by choosing a new candidate design whose fitness is evaluated, based on the objective and penalty functions.

In the event of a single-objective optimization (i.e., when the performances of the inlet have to be optimized for only one flight condition), the purpose of the automated process is simply to find the confi-

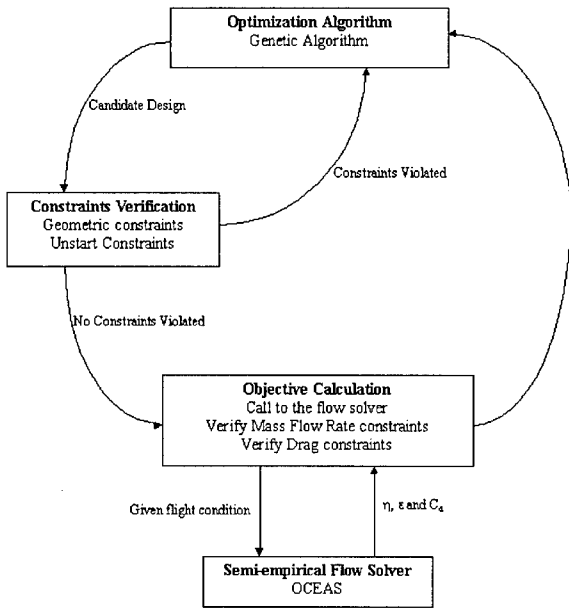


Figure 1: Automated optimization loop

guration that will maximize the total pressure recovery while satisfying constraints on the air capture ratio and the drag coefficient. With a view to optimize inlets for an entire mission, the optimization becomes multi-objective and a new strategy has to be defined. This strategy is based upon the mission definition but also the characteristics of the motor used to perform the flight.

3 MISSION OPTIMIZATION STRATEGY

To perform effectively the optimization over an entire mission, the constraints, objectives and requirements throughout the mission have to be investigated.

3.1 Definition of the Mission

A mission for a supersonic ramjet-powered missile can generally be divided into several stages. Figure 2 presents a typical mission overview. The first stage is called *acceleration*. The booster phase is ignored and it is assumed that the mission starts at a Mach number greater than the unstart limit which is a design parameter. Immediately after, the missile must accelerate and climb to its cruise altitude and speed. During this stage, the missile must have a sufficient thrust in order to accelerate. To satisfy this constraint, the mass flow rate must be greater

than the engine specific value. At this stage, the total pressure recovery is generally high because of the lower Mach numbers. The next step is the *cruise* stage. During this period, the objective is to cover the greatest distance as possible. Therefore, the total pressure recovery must be maximized while the mass flow rate must be at least equal to an acceptable threshold. This acceptable value has to be defined with a view to satisfy motor constraints. As the missile is getting closer to its target, it enters the *maneuver* stage. At this point the dominating parameter is again the total pressure recovery. Its value must be maximized while the mass flow rate must be greater than an other acceptable minimum.

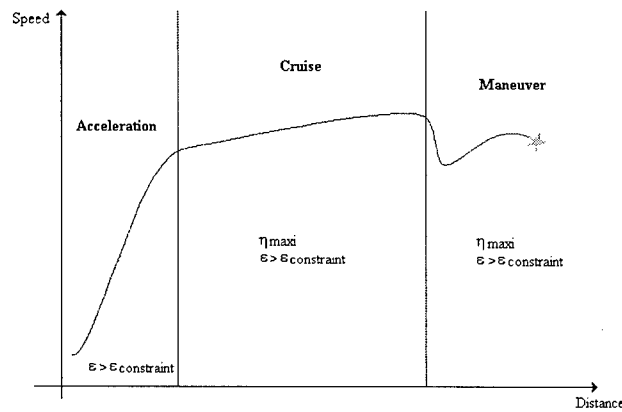


Figure 2: Mission profile overview

To sum up, the total pressure recovery has to be maximized for all mission stages while the mass flow rate must be kept greater than acceptable values. As it has been previously investigated in [3], it is not possible to maximize the total pressure recovery for the entire mission without making some compromise between all mission points. Thereby, regarding the particular mission requirements and given engine performances, a *target curve* has to be defined with a view to guide the optimization process.

3.2 Optimization Strategy

The target curve will give, for all the mission stages (i.e., for all flow conditions encountered by the missile), the values of the total pressure recovery that best fit the given motor and mission profile. However, the target value will be slightly overestimated to keep all optimized values below it. This curve is noted $\eta_{tgt} = f(Mach)$. In addition to this target curve, constraints on the air capture ratio values have to be met throughout the stages, creating another curve called the *constraint curve* and noted

$\epsilon_{cons} = g(Mach)$. The goal of the automated optimization loop is to minimize the gap between the performance curve of the currently analyzed inlet and the target curve while taking into consideration the mass flow rate constraints. OCEAS will be used during the optimization process, while a Navier-Stokes flow solver will be used to verify the optimal design.

4 APPLICATION

4.1 Generic Mission Description

The missile is launched from a fighter aircraft during a penetration raid. The aircraft is flying at low altitude and is being attacked by other military planes flying at higher altitudes. The missile is fired from the attacked aircraft in direction of its opponents. During the acceleration stage, the missile reaches a medium altitude and its speed typically increases from Mach 2.0 to Mach 3.5. During the cruise stage, the missile continues to fly at medium altitude and keeps its speed at Mach 3.5. When the missile approaches its target, it enters the maneuver stage and begins to climb in direction of the enemy which tries to escape in altitude. The Mach number is then raising up to 4.0 and the angle of attack changes. Figure 3 depicts the change in altitude and speed during the mission. For the purpose of the optimization, this mission is discretized in 6 flow conditions which correspond to essential phases of the flight. Typical conditions are summarized in Table 1, where M_∞ is the upstream Mach number, Z is the altitude, α the angle of attack and FC is an acronym for Flight Condition.

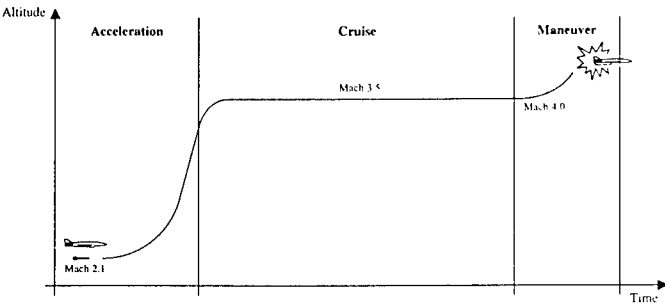


Figure 3: Altitude and Mach number evolution throughout the mission

The target curve for the total pressure recovery η and the constraint curve for the capture area ratio c have been defined carefully upon the mission specifications and the ramjet engine expected to be used on board the missile. The target values for η have

been slightly overestimated with a view to give an unreachable goal to the optimizer. Figures 5 and 6 show the specified curves. The performances of the inlet are calculated for the six different flow conditions given in Table 1.

Table 1: Flight conditions throughout the mission

Quantity	FC1	FC2	FC3	FC4	FC5	FC6
M_∞	2.0	2.5	3.0	3.5	3.5	4.0
$Z(km)$	0.1	5	10.	10.	10.	15.
$\alpha(deg.)$	0	0	0	0	4	0

4.2 Generic Inlet Model

The optimization methodology has been applied to the redesign of an existing *generic inlet*. The design process has been performed using 9 degrees of freedom. Figure 4 shows the inlet sketch with the design parameters. The inlet has a fixed length, width and height so that the overall missile volume constraint is satisfied. The optimization focuses on finding the best performing supersonic diffuser and throat section. Therefore, the angle and length of each ramp segment are being optimized as well as the apex location of the cowl and its internal shape. The inlet model considered in this study does not incorporate any boundary layer bleed.

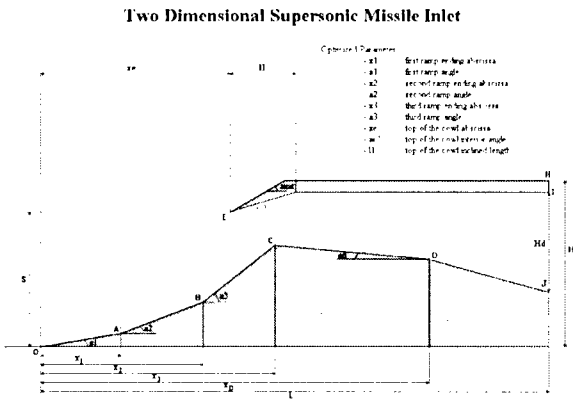


Figure 4: Inlet sketch

4.3 Optimization Results

The optimization requires 30,000 iterations of the genetic algorithm. The objective function is computed

only for feasible candidates which satisfy the geometric and aerodynamic constraints. A total of 9,000 feasible designs were encountered, which means that the flow solver was called 54,000 times (6 flow conditions). The whole process takes about 40 CPU hours on a DEC ALPHA 2100 workstation. Significant improvements have been achieved by the automated optimization loop. As one can see on Figure 5, the capture area ratio of the optimized inlet matches the constraint curve at every Mach number. Figure 6 presents the comparison between the target, the baseline and the optimized performances. The total pressure recovery of the optimized inlet is 10% to 15% higher than the baseline generic inlet. The improvements depend on the Mach number during the mission, but the largest improvements (in percentage of the baseline values) occur at high Mach numbers.

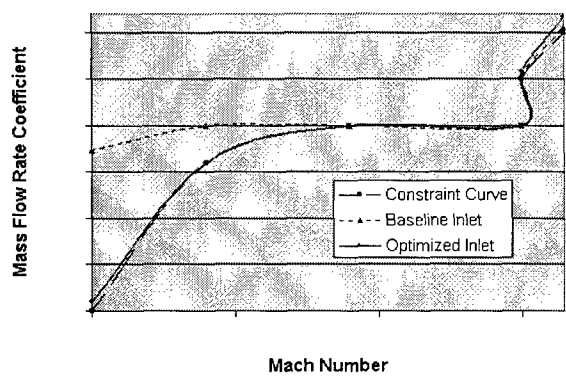


Figure 5: Air capture ratio comparison between original and optimized inlets

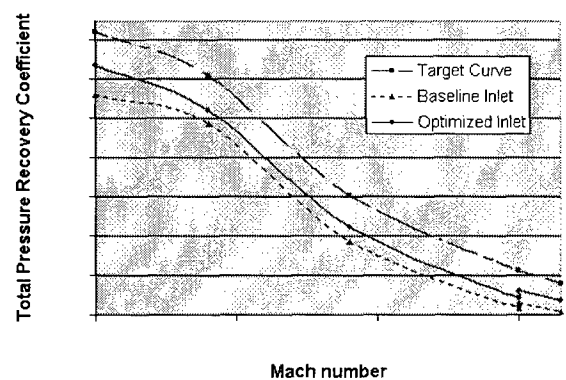


Figure 6: Total pressure recovery comparison between original and optimized inlets

4.4 Verification

The significant improvements achieved by the automated optimization process have been verified using a high-end Navier-Stokes flow solver. The simulations have been performed in 2-D with the commercial code GASP developed by AeroSoft Inc. The two-dimensional computational mesh is composed of two blocks. The total mesh size is 176 points by 64 points. The two-equation Chien $k-\epsilon$ turbulence model is used. The inviscid fluxes are calculated using the Van Leer split flux with min-mod limiter. The integration is performed by an implicit two factor AF scheme with relaxation sweeping in the streamwise direction. To assess the performances of the missile inlet, the critical conditions must be achieved by positioning the terminal shock at the throat location in the inlet duct. At this regime, the back pressure at the exit of the diffuser is unknown and has to be determined using a root search. Therefore, several simulations have to be performed in order to reach the desired condition. One flow field computation typically requires 4 CPU hours on a DEC ALPHA 2100 workstation for a grid of the size mentioned above. Reaching the critical regime takes 5 to 7 computations, leading to an overall computational time of about 30 CPU hours. One can see the huge difference between the times required by the Navier-Stokes simulation and the semi-empirical flow solver OCEAS. Two Mach numbers are investigated for verification: Mach 2.5 and Mach 3.5 with no angle of attack.

Table 2: OCEAS and GASP computations of baseline and optimized inlets for Mach 2.5

Var.	Code	Baseline	Optimum	Δ_{BO}
η	OCEAS	0.704	0.750	6.5%
	GASP	0.624	0.687	10.1%
	Δ_{OG}	12.8%	9.2%	
ϵ	OCEAS	0.994	0.960	
	GASP	0.999	0.982	
	Δ_{OG}	0.5%	2.2%	

The performances of the optimized inlet, as well as the baseline inlet, have been assessed using the Navier-Stokes simulation for the two Mach numbers considered here. Tables 2 and 3 present the comparison between the OCEAS predictions and the GASP simulations for the total pressure recovery η and the capture area ratio ϵ for Mach 2.5 and 3.5 respectively. These tables also present the improvements

Table 3: OCEAS and GASP computations of baseline and optimized inlets for Mach 3.5

Var.	Code	Baseline	Optimum	Δ_{BO}
η	OCEAS	0.248	0.274	10.4%
	GASP	0.232	0.256	10.3%
	Δ_{OG}	6.9%	7.0%	
ϵ	OCEAS	1.000	1.000	
	GASP	0.974	0.980	
	Δ_{OG}	2.7%	2.0%	

Δ_{BO} indicated by both codes between the baseline and the optimized inlet. Δ_{OG} represents the discrepancy between the OCEAS and the GASP results. Although there is a difference of 7% to 13% in the predicted values of η between the OCEAS and GASP simulations, *it is essential to note that the improvement in η obtained by the automated optimization using OCEAS is verified by GASP in every case.* Thus, the use of OCEAS in the automated optimization loop leads to performance improvements that are confirmed by the Navier-Stokes flow solver. The final improvements at Mach 2.5 and Mach 3.5 are respectively of 10.1% and 10.3% based on the GASP simulations. Those increases in total pressure recovery represent a significant improvement of the aerodynamic performance of the missile inlet. Figures 7 and 8 compare the Mach number contours for the baseline and the optimized inlets for Mach 2.5.

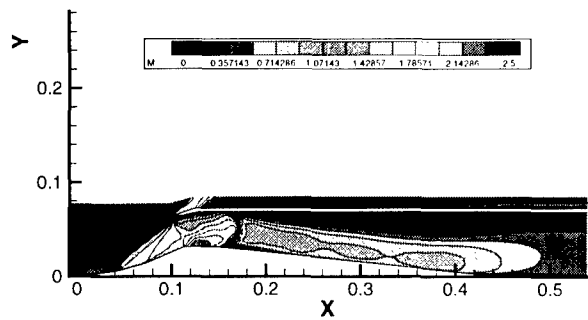


Figure 7: Mach number contours for GASP computation of baseline inlet at Mach 2.5

4.5 Conclusion

The efficiency and the reliability of the automated optimization process have been demonstrated throughout this test case of mission optimization applied to a conventional two-dimensional ramjet mis-

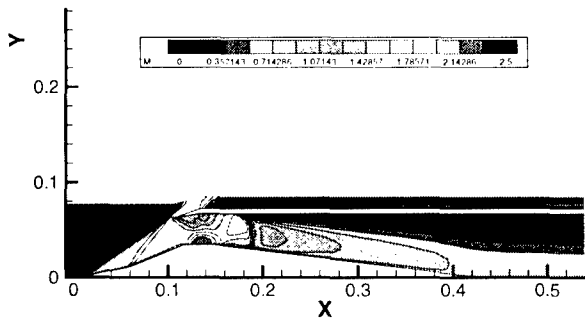


Figure 8: Mach number contours for GASP computation of optimized inlet at Mach 2.5

sile inlet. In addition to the significant improvement in the aerodynamic performance of the air intake, the final geometry has been designed in a very short period of time compared to classical design techniques. This design process has been incorporated into the aerospace industry to help engineers to achieve near optimal inlet designs for their specific problems. The following section describes the actual use of this new design technique at AEROSPATIALE-MISSILES.

5 AN INDUSTRIAL VIEW

The current specifications for the next generation of supersonic air breathing missiles require to extend their range and increase their maneuverability [11]. These two requirements have very strong implications on the design of the air induction system, even more so in the case of ramjet-powered missiles. In fact, the maximum thrust and the minimum fuel consumption are directly determined from the inlet/ramjet throat association [10]. Increasing the range generally means reducing the engine fuel consumption during acceleration/climb and cruise which in turn necessitates a high total pressure recovery for the inlet. Improving the maneuverability translates into increasing the maximum possible thrust and load factor which also implies a high inlet total pressure recovery for flight conditions which can be very different from cruise conditions.

Because missile inlets traditionally have fixed geometries (for reasons of cost), the design of the supersonic diffuser is the result of a compromise between several choices and constraints, some of them being the unstart and design Mach numbers, the critical capture area ratio and total pressure recovery during cruise and maneuvers. Even for basic 2-D geome-

5.2 Typical Applications and Impact

A simple yet important verification of the numerical method has been made prior to any other test. It has been checked that the resulting inlet of a single flight condition optimization operates “on design” at this particular Mach number, and that the optimal total pressure recovery is better than any other “human made” design. Successful results have been obtained for this verification.

Then, the method has been applied to the redesign of 2-D rectangular supersonic inlets. The particular case of missiles with bank-to-turn steering mode has been chosen so that the 2-D approximation is acceptable over the mission. If the overall objective of the inlet optimization is to improve the missile range for a given mission profile, a given engine and a given inlet capture area, then the optimization problem must be formulated in the following way. Because gains will be obtained for conditions for which the operation of the engine is limited by the baseline inlet maximum performance, the optimization must concentrate on these points. This typically corresponds to the acceleration/climb phase of the flight. If the baseline inlet is characterized by the unstart Mach number M_{uns} , and performances during acceleration ϵ_{acc} , η_{acc} and cruise ϵ_{cru} , η_{cru} , the set of constraints should be: verify unstart at M_{uns} , treat ϵ_{acc} , ϵ_{cru} and η_{cru} as constraints, and maximize the total pressure recovery for the limiting points. Preliminary computations have shown that an improvement of 9% is foreseeable.

As a reminder, an improvement of 10% in critical total pressure recovery can lead up to a 30% improvement in thrust coefficient if the engine limits are not reached. This would permit a higher rate of climb and possibly a range increase depending on the trajectory strategy.

The numerical optimization method is very well suited to the needs of design engineers. It is fast, flexible, robust and allows to perform trade studies with a lot of parameters, both geometrical and operational.

5.3 Limitations and Perspectives

The main drawback of the current numerical optimization method lies in its 2-D limitation. Even for 2-D geometries, it is well known that the flow in the vicinity of the missile body becomes strongly three-dimensional as soon as there is angle of attack and/or side slip angle. Other weaknesses are

related to the flow solver. Most of the discrepancies between the OCEAS results and the GASP results (Tables 2 and 3) come from the inappropriate modeling of the viscous losses in the subsonic diffuser. Also, most of the “real world” inlets have a boundary layer bleed which can not be accounted for precisely with OCEAS.

Thus, two directions of improvement are followed today. The first one is the implementation of a 3-D geometrical description of the inlet. This corresponds to a significant increase in the complexity of the design problem for two reasons. First, the third dimension implies new parameters and consequently more degrees of freedom for the optimization search. Second, because there is no simple 3-D calculation method available, the solver has to be replaced by an Euler code which in turn requires the implementation of an automated mesh generator in the optimization loop. The second research direction is the development or rather the finalization of a numerical code tailored for fast and accurate performance prediction. Current efforts involve the coupling of an Euler solver for the supersonic diffuser with improved semi-empirical methods for the subsonic diffuser.

A very promising and challenging perspective of the application of artificial intelligence techniques and computational physics is the multidisciplinary design of air breathing missiles with automated numerical methods.

6 CONCLUSIONS

An automated optimization loop for two-dimensional supersonic inlets over an entire mission has been developed and is currently used within the aerospace industry at AEROSPATIALE-MISSILES. This powerful and innovative tool helps to design inlets either for a specific flight condition or for an entire mission in far less time and more efficiently than any conventional method. Successful results have been obtained and significant improvements have been verified with a Navier-Stokes flow solver. The automated optimization loop presented in this paper can only address two-dimensional inlet shapes because of the limitations of its simple flow solver. Current efforts are focused on the development of a three-dimensional optimization process.

7 ACKNOWLEDGMENTS

Technical and financial support for this research was provided by AEROSPATIALE-MISSILES, France and the HPCD (Hypercomputing and Design) Project supported by the Advanced Research Projects Agency of the Department of Defense, U.S.A. through contract ARPA-DABT 63-93-C-0064. The content of the information herein does not necessarily reflect the position of the government and official endorsement should not be inferred. We would like to thank Keith Miyake, Vijay Shukla, Donald Smith and Ge-Cheng Zha for their invaluable assistance in this research.

References

- [1] K. Rasheed, H. Hirsh, A. Gelsey, "A genetic algorithm for continuous design space search", *Artificial Intelligence Engineering*, Vol 11 N 3, July 1997.
- [2] R.G. Lacau, P. Garnero, F. Gaible, "Computation of Supersonic Intakes", *AGARD Special Course on Missile Aerodynamics*, AGARD Report 804, 1994.
- [3] M. Blaize, D. Knight, K. Rasheed, "Automated Optimization of Two Dimensional High Speed Missile Inlets", *AIAA Paper*, Paper No. 98-0950, 1998.
- [4] K. Rasheed, H. Hirsh, "Using case based learning to improve genetic algorithm based design optimization", *Proceedings of the Seventh International Conference on Genetic Algorithms*.
- [5] K. Rasheed, H. Hirsh, "Guided Crossover: A new operator for Genetic Algorithm based optimization", *Technical Report HPCD-TR-50*, Department of Computer Science, Rutgers University, New Brunswick, NJ, 1997.
- [6] G.-C. Zha, D. Smith, K. Rasheed, A. Gelsey, D. Knight, M. Schwabacher, "High performance supersonic missile inlet design using automated optimization", *6th AIAA/NASA/ISSMO Symposium on Multidisciplinary Analysis and Optimization*, AIAA 96-4142, p1355, Sept. 4-6, 1996.
- [7] K. Rasheed, "GADO : A Genetic Algorithm For Continuous Design Optimization", *Ph.D. Thesis*, Department of Computer Science, Rutgers University, January 1998.
- [8] D. Whitley, "A Genetic Algorithm Tutorial", *Technical Report CS-93-103*, Department of Computer Science, Colorado State University, November 10, 1993.
- [9] X. Montazel, Y. Kergaravat, M. Blaize, "Navier-Stokes Simulation Methodology for Supersonic Missile Inlets", *13th International Symposium on Air Breathing Engines*, ISABE 97-7029, 1997.
- [10] J.-M. Laurent, P. Garnero, "Propulsion par Statoréacteur pour Missiles dans le domaine Mach 3 à 4.5", *AGARD Conference Proceedings 526*, Symposium on Airbreathing Propulsion for Missiles and Projectiles, 1992.
- [11] M. S. Ivey, R. K. Oldham, "Potential Missile Flight Performance Gains from Improvements to the Propulsion System", *AGARD Conference Proceedings 526*, Symposium on Airbreathing Propulsion for Missiles and Projectiles, 1992.

Coupled Aerokinetic Heating of Missile Structures at High Velocities

Stefan R. Körber*

BGT Bodenseewerk Gerätetechnik GmbH
P.O. Box 10 11 55
88641 Überlingen
Germany

SUMMARY

This paper presents a numerical tool to calculate the aerokinetic heating of missile structures flying at high velocities. It is intended to support wind tunnel tests and enable engineers to do design variations in a cheaper and a more time saving manner compared to experiments. The numerical method consists of two programs, one to calculate the flow around the missile configuration via a super / hypersonic computational fluid dynamics (CFD) code (solved for the Navier-Stokes-equations) and another to simulate the temperature (and stress) evolution within the bulk material via a multi-dimensional heat transfer code. Both programs are coupled using a surface energy-balance method which accounts for the permanent physical interactions at the missile's surface. In order to save CPU-time without loosing neither accuracy nor numerical stability or consistency a so-called *loose coupling* of both modules is presented. This method is applied to several test cases. Since the aerokinetic heating mostly effects those components located in the vicinity of the nose region of the missile, a blunt-body nose and a flat IR-window integrated in the nose were investigated. For some test cases experimental data from either wind tunnel tests and/or free flight experiments are available and are compared to the numerical results.

1. INTRODUCTION

When designing missiles to operate for some period of time at high supersonic or hypersonic velocities one has to deal not only with the conventional problems such as aerodynamic design, material selection or IR/RF seeker design. Along with these general features there is another most important design aspect arising only when flying at high velocities: the aerokinetic heating of the missile structure. Those components of the missile which are mostly affected by the aerokinetic heating are the ones in the vicinity of the nose region, which is usually the hottest spot of the missile. The most critical components in this area are the IR-seeker windows and the RF-radomes. This is because their functional capability depends highly on the temperature level and the thermal induced stresses within the bulk material. Usually, when temperature and/or stress exceeds a certain level, a performance degradation of these

seeker devices up to their complete failure may occur. Since the operational success of the missile mission depends on the seekers working during the entire mission, especially during the final end game, the effects of the aerokinetic heating have to be accounted for.

Unfortunately, those seeker components highly affected by the aerokinetic heating, i.e. the IR-windows, claim for design features which are contrary to the aerodynamic and aerothermodynamic demands. From the optical point of view a flat or hemispherical IR-window located in the vicinity of the missile's nose section, exposed to the free stream at a high angle of incidence, is favoured. Usually, this constellation will lead to high temperatures and stresses within the bulk material. On the other hand, in order to reduce aerokinetic heating and drag, the aero(thermo)-dynamic considerations demand a drag optimized configuration, with a low angle of incidence of the IR-window. The achievement of a final missile design to satisfy all demands concerning the aero(thermo)dynamic and the optical aspects can normally only be reached through several iterations during the entire design process. Usually, on both sides compromises have to be made. Since experimental investigations are too expensive and costly and not flexible enough, the development of a numerical tool for design optimization is desired which is able to account for both the aero(thermo)dynamic and optical design features as well as the phenomena of aerokinetic heating within the bulk.

In the following the general features of aerokinetic heating are shown and a tool for the numerical simulation is presented. This tool consists of two programs, one for the CFD (Computational Fluid Dynamics) calculations of the surrounding fluid flow and another one for calculating the thermal/mechanical quantities within the bulk material. Both programs are coupled in a loose way in order to model the physical interactions at the material's surface.

2. AEROKINETIC HEATING OF MISSILE STRUCTURES

2.1 Aerokinetic Heating in System Design

When designing missiles one has usually to deal with several features to fulfil the operational demands. The most important ones are the aerodynamic design and the selection of specific materials to meet the structural and optical (IR &

*Research Engineer, System Design, Missiles Division, Phone: +49-7551-89-6194, fax: +49-7551-89-2351, e-mail: koerber@fk.bgt.de

RF) demands (Fig.1). The aerodynamic design copes with features such as flight profile, flight performance or the missile shape. The material selection depends mainly on their IR/RF-properties and their capability of withstanding certain environmental conditions. At lower supersonic speed these two design features can be faced independantly. At higher velocities, however, due the effects of aerokinetic heating, those two features are correlated. Depending on the flight velocity and the shape of the missile configuration the recovery temperature within the boundary will reach a high level. Consequently, there is a high amount of heat transfered to the missile structure which causes also an enormous temperature rise within the bulk material. Along with this high thermal induced stresses are generated. Both effects may lead to a final device failure, i.e. high temperatures may causes a change of physical properties (such as IR/RF-transmission, reflexion or refraction) to worse or the material may even break due to high internal stresses. Hence, all of the aspects must be considered all together with their mutual influence and the restrictions arising from the aerokinetic heating, i.e. temperature and thermal induced stresses (see Fig.1). The necessary compromises within the final missile design are often restricted to the IR-window design: The optical viewpoint (i.e. high optical performance) favours a flat IR-window at a high angle of attack, the aerodynamic priority is a drag optimized window which has a small angle of incidence and hence reduces the aerokinetic heating.

2.2 Critical Features of Aerokinetic Heating

When accelerated to high velocities or when flying at high speed for a longer period of time the high temperature rise and the final high temperature level within the surrounding boundary layer causes the missile bulk material to heat up (see Fig.2). During its entire mission, this process of aerokinetic heating strikes the missile structure in two quite different ways.

Usually, a typical flight profile can be divided into two consecutive phases, the boost phase and the following sustain and/or ballistic phase. During the boost phase the boundary layer and hence the missile structure are extremely heated up. Consequently, high temporal and spacial temperature gradients are generated within the bulk material, a phenomena usually related to as *thermal shock*. The following sustain or ballistic phase is characterised by a continuous gradual heating of the bulk material, at most up to the radiation adiabatic wall temperature of the corresponding flight conditions. In many cases the temperature level within the missile structure tends to *exceed the critical temperature* of the bulk material and thus causes unavoidable performance degradations, i.e. crucial material properties usually become worse.

2.2.1 Thermal Shock

The high acceleration during the boost phase causes a high temperature increase within the boundary layer. In the vicinity of the stagnation point the temperature level is considerable higher than at positions downstream of the missile's nose. Due to the initially low environmental temperature of the bulk a high temperature gradient within the boundary layer is generated. Hence, a high heat transfer to the bulk is generated, mainly in the nose region where usually the sensitive IR-windows are located.

Since the bulk's thermal reaction is much more sluggish than the one of air, especially during the first moments after launch, only the bulk's outer part facing the air is heated extremely. Therefore, not only a high temperature gradient perpendicular to the material's surface is generated, but also high stresses are generated within the bulk due to the different thermal expansion of the individual bulk layers. Usually, the thermal induced stresses in the normal direction of the surface are much higher than those in the direction parallel to the surface. The highest stresses in the parallel direction occur usually in the transition region where the boundary-layer flow changes from laminar to turbulent behavior (see section 3 below).

Depending on the acceleration profile and the material properties, the inherent stress limit of the material can easily be exceeded followed by a material failure, i.e. a crack or break.

2.2.2 Exceeding of Critical Temperature

During a longer exposure time at a certain velocity level (sustain phase), the bulk material will gradually heat up. The maximum temperature at infinite exposure time is given by the local radiation adiabatic wall temperature, which indicates the equilibrium when finally heat transfer has vanished. While heating up the temperature level within the bulk may exceed the material's critical temperature, above which the properties of the material begin to change significantly. Most of all they tend to become worse in a nonacceptable way. Concerning the IR-windows the most important properties affected are the emission and transmission and of the IR-radiance and the variation of the refraction index.

3. AERODYNAMIC HEAT TRANSFER

3.1 Heat Transfer Boundary-Layer - Bulk Surface

The behavior of the flow within the boundary layer has a significant influence on the amount of heat transfered to the bulk. Generally known is the fact that the heat transfer of a turbulent flow is up to five times higher (depending on the missile's shape) than the one of a laminar flow.

A favoured location of the critical components (e.g. IR-windows) of the missile would therefore be the laminar zone, but, unfortunately, the length of this zone is usually not large enough to cover the entire component, i.e. parts of this component will be covered by the transition zone and/or the fully turbulent zone. Even worse is the fact that within the transition zone there is a large increase in heat transfer from the lower laminar quantity up to the high level of the fully turbulent flow (see Fig.3). Since the transitional region is beyond a complete theoretical understanding, it is nowadays hard to give a reliable prediction of the location and extension of this zone. Even so a lot of factors, e.g. motor vibrations, variations of velocity or angle of attack, may cause an upstream shift of the transition zone, one usually has to take all three zones into account when considering the flow behavior covering the component in question.

The background for the numerical calculation of the aerokinetic heat transfer is independent of the actual flow behavior and can be done in the following way.

For any spatial point on the surface of the missile structure the energy balance equation holds. Assuming that radiation effects are not negligible, energy balance can be written as

$$\dot{q}_w = \dot{q}_{\text{conv}} - \dot{q}_{\text{rad}}$$

where \dot{q}_{conv} is the contribution of the convective heat flux from the boundary layer flow to the material's surface, \dot{q}_{rad} is the amount of heat flux reflected via radiation and \dot{q}_w is the actual part of the heat flux transferred into the bulk (see also Fig. 4 for illustration)

The convective heat flux is calculated by

$$\dot{q}_{\text{conv}} = \rho_e \cdot u_e \cdot c_{p,\text{Air}} \cdot \text{St}_e \cdot (T_{\text{aw}} - T_w)$$

assuming air as a caloric perfect gas. The index e indicates the quantities at the outer edge of the boundary layer, whereas St_e is the Stanton number and T_{aw} the adiabatic wall temperature defined by

$$T_{\text{aw}} = T_e \cdot (1 + 0.5 \cdot r \cdot (\kappa - 1) \text{Ma}_e^2)$$

κ is the specific heat ratio of air, Ma_e is the local Mach number and r is the recovery factor, which is usually set to 0.85 for laminar flow and 0.88 for turbulent flow.

The radiative heat flux is given by Stefan Boltzmann's law

$$\dot{q}_{\text{rad}} = \varepsilon_{\text{rad}} \cdot \sigma_B \cdot (T_w^4 - T_{\text{env}}^4)$$

with T_{env} being the environmental temperature, ε_{rad} the surface emission coefficient and σ_B the Boltzmann constant. Finally, the heat flux transferred into the bulk is given by

$$\dot{q}_w = \alpha \cdot (T_{\text{raw}} - T_w)$$

α is the heat transfer coefficient and T_{raw} is the radiation adiabatic wall temperature. It should be noticed that T_{raw} is always less or equal T_{aw} . Only if radiation is absent (i.e. $\dot{q}_{\text{rad}} = 0$) both temperatures are equal.

3.2 Hypersonic Transition

Transition from laminar to turbulent flow behavior occurs when the amplification of the boundary layer instabilities cause the laminar flow to break down. Such instabilities originate from flow disturbances, which are transformed into instabilities due to external influences. Various parameters such as pressure gradient, compressibility, surface curvature or surface roughness lead to different kinds of instabilities, such as Tollmien-Schlichting-, Goertler- or cross-flow instabilities.

The beginning of the laminar flow breakdown defines the starting point of transition (Fig.3). The region downstream this point until finally the turbulent flow is fully developed is referred to as the transition zone. Up to now, no theoretical knowledge is at hand to give a full understanding of transition or mark precisely the beginning or the end of the transition zone. This is particularly true for hypersonic flow, where the extension of the transition zone may be as long as the laminar zone itself. For reasons of simplification one often defines a specific point (transition point) to mark transition. The running length x_T of this point is defined via the transition Reynolds number Re_T

$$\text{Re}_T = \rho_e \cdot u_e \cdot x_T / \mu_e$$

ρ_e , u_e and μ_e indicate the density, velocity and viscosity taken at the boundary layer edge, respectively. For hypersonic speed Re_T depends mainly on the free stream Mach number, the wall temperature, surface radiation and nose bluntness. Typical values for Re_T range between 10^5 and 10^8 . Due to lack of theoretical knowledge the prediction of Re_T for any special kind of application usually requires the fallback on approximation methods or experimental data.

Fig.4 shows the heat transfer distribution versus the running length. Apart from transition begin and end the *transition-onset* and the *transition peak* are shown. Transition onset defines the point where the actual heat transfer differs for the first time plainly from the fully laminar considerations. Within the transition region an almost linear increase in heat transfer is registered, which slightly overshoots the fully turbulent value (transition peak) just after transition has ended. Both the onset and the peak depend on the configuration shape and vanish in case of a cone.

Furthermore, the considerations concerning the heat transfer distribution give way to an easy theoretical investigation of transition and heat transfer. Doing both fully laminar and turbulent numerical calculations of the corresponding heat transfer, the actual heat flux distribution, given transition begin and end, is constructed via the following method. Upstream the transition begin and downstream the transition end, both the fully laminar and fully turbulent courses are adopted, whereas in the region in between a linear interpolation between the laminar heat flux value taken at transition begin and the turbulent heat flux value taken at transition end is made to fill this gap.

With this method at hand it is easy to investigate the influence of transition as well as to define the boundary points of transition once experimental data are available.

4. NUMERICAL SIMULATION

4.1 Numerical Tools

The numerical method to calculate the aerokinetic heating of missile structures at high velocities consists of two different codes. One code is used to calculate the fluid flow around the missile structure (CFD) and another one is used for temperature and stress calculations within the bulk material.

The CFD calculations are done using the commercial code RAMPANT™ by FLUENT INC. This code uses a finite volume Navier-Stokes solver of second order in time and space for the flow equations. Optionally turbulence effects can be accounted for via the k - ε or RNG k - ε turbulence model.

The thermal and mechanical analysis within the bulk material is done using the program TEPROSIM, developed by BGT. This program solves for the three-dimensional inhomogeneous heat equation using an explicit time marching method. Recently, this program was replaced by another commercial program, the code ANSYS® by CADFEM.

Since both programs are developed for their special purpose of calculating either fluid flow problems or thermal / mechanical problems, they have to be coupled in an adequate way to be used for simulations of aerokinetic heating. The interface of both programs is defined by the surface of the missile structure. At this interface a physical model caring for the mutual interactions between the fluid flow and the bulk's surface has to be implemented.

In the following two different ways of modelling the occurrences at the interface are described. Beforehand, an analysis of characteristic times will help to define a necessary global time step to ensure numerical convergence and consistency of the entire program.

4.2 Time Analysis

In order to do a reliable analysis of problems concerning the aerokinetic heating, the coupling of both programs has to be done such that a global numerical consistency and stability is guaranteed. In numerics the coupling of both programs can only be done at discrete temporal points (anchor points) of the flight profile. The distance between two point is determined via a characteristic time analysis.

Characteristic times of physical processes define a period of time where significant changes within the entire process occur. In fluid dynamic problems characteristic times are defined by the convective changes within the flow. In case of heat conduction the characteristic time is determined by temperature changes due to heat fluxes.

Even so the characteristic times within the boundary-layer due to effects of friction and turbulence are usually much smaller than those related to convection, they only play a subordinated role since their influence on the global flow behavior is negligible. Referring to a velocity of about Ma 3 to Ma 6 and a length scale of about 0.1m (missile diameter) the fluidal characteristic time is about 10^{-5} to 10^{-4} seconds (see Fig.5).

For the heat conduction within the bulk material the characteristic times are referred to a length scale of about 1-10 mm (bulk thickness) and hence have a magnitude of about 0.1 to 1 second. The driving forces concerning the heat conduction are the physical properties of the heat capacity c_p and heat transfer ratio λ .

A comparison of both values shows that the fluid flow is the crucial process defining a global physical characteristic time step. For the numerical characteristic time, assuming an identical numerical cell width of about 0.1mm in both programs, the difference in orders of magnitude remains the same (Fig.5). An interpretation of these characteristic times would mean that given a numerical time step referred to the thermal process one would have to integrate over 10^3 up to 10^4 fluidal time steps. Since one time step of integrating the fluid flow equations is much more costly than a thermal time step integration, a direct coupling of both programs at every fluidal time step lies far beyond reasonable CPU-times.

As a result of this time analysis a so-called *loose-coupling* is implemented which combines both programs in a CPU-time saving mannner without loosing much of numerical accuracy.

4.3 Numerical Coupling

In this study the flow environment code and the thermal response code are loosely coupled in such a manner that both codes can share the correct surface conditions. The flow computations use the surface temperatures obtained from the thermal response code, and the thermal response code uses the energy-balance conditions and the convective heat-transfer rates obtained from the flow solver. The final solution is obtained through iterations between both codes. The characteristic times for the fluid flow and the heat conduction differ by a few orders of magnitude. Hence, the iteration strategy for solving flight trajectory based transient aerokinetic heat problems is such that the both modules are coupled at selected times in the flight path trajectory. These times (anchor points) are set apart based on the characteristic time of the heat transfer. Between these anchor points, the heat transfer is assumed to vary linearly. The heat equation is integrated over the corresponding time interval with the amount of heat transferred considered as a heat source. Fig. 6 shows an illustration of this method.

4.3.1 Energy-Balance Method

In this method the energy-balance-equation is assumed to hold at every point of the intersection surface. Depending on the temperature the radiation term in the energy-balance equation is optionally accounted for.

To start the global iteration process an equilibrium condition is assumed and the flow field is computed using a constant wall temperature given by the structure temperature. This results in a heat flux at time zero. Then, an initial guess for the wall temperature is generated for the first anchor point by solving the flowfield. The resultant convective heat transfer is assumed to vary linearly in time and is substituted into a subiterative heat conduction equation which is integrated in time up to the first anchor point. The solution yields the wall temperature and the conductive heat flux satisfying the surface energy balance. The wall temperature distribution is fed back into the CFD code as a constant wall temperature condition upon which the flow field is recomputed to obtain improved heat fluxes. This iteration is repeated with updated values until convergence is obtained. Then integration to the next anchor point follows.

4.3.2 Coupling Without Feedback

Furtheron, another much simpler method of computing aerokinetic heating processes was applied. This method has less accuracy, but since it is easier to handle and less CPU-time consuming, it may often be used for approximative calculations.

The main feature of this method is the missing feedback of the actual physical conditions at the bulk's surface back on the fluid flow, i.e. there is only a one way influence from the boundary layer flow onto the bulk's surface. At every anchor point the boundary conditions for the flow solver are set to a constant global temperature distribution along the entire missile surface. According to these conditions the corresponding heat fluxes are calculated in terms of the dimensionless Stanton number. These values are used as a source input for the heat conduction calculations. Again the variation of the Stanton number between two anchor points is assumed to be linear.

5. APPLICATIONS

5.1 Survey

The problem of aerokinetic heating is mainly restricted to missiles flying at high velocities. The most critical part affected by aerokinetic heating is in general the nose section, which is usually the hottest spot of the missile. For several operational reasons the seeker components (IR/RF) should be arranged within the nose region and are therefore affected extremely by aerokinetic heating. Unfortunately, the materials to be used for the seekers are endurable only within a certain range of temperature and thermal / mechanical stresses. Especially for these seeker applications the knowledge of the aerokinetic heating is a crucial parameter for their final design.

On the basis of this background information two design configurations (Fig.7) were chosen for application of aerokinetic heating calculations using the methods described above. The two design configurations under investigation are a blunt-body nose and a nose containing a flat IR-window. For both configurations experimental data are or will soon be available, partly from wind tunnel tests or free flight experiments. The numerical calculations were done according to the experimental conditions in order to make comparisons easy and to validate the numerical code. For the blunt-body configuration additionally a comparison between both available numerical codes and the corresponding experimental data from a free flight test program has been made.

5.2 Aerokinetic Heating of an IR-Window Exposed to Steady-State Flow Conditions

In this case the investigated configuration consists of an circular sapphire window integrated in the nose region of a conical missile structure (Fig.8). This configuration is exposed in a steady state free stream of air. According to the flow conditions generated by the wind tunnel, the free stream conditions for the accompanied numerical simulations are set to:

Mach number	$Ma_{\infty} = 3.50$
Temperature of free stream	$T_{\infty} = 350 \text{ K}$
Altitude (free stream pressure)	$Alt = 675 \text{ m}$

Fig.8 shows a sketch of the experimental hardware. Highlighted is the part of the structure modelled in the numerical calculation. Since the entire configuration is 2d-rotational symmetric only the upper half is considered. The implanted circular sapphire window is clued with its backward part to the surrounding steel airframe. The part facing the free stream is separated from the airframe by a small slit of air. Before exposed to the wind tunnel's free stream the initial temperature of the entire configuration equals the environmental temperature. The data of the sapphire window are as follows.

Thickness	= 9 mm
Diameter	= 35 mm
T_{initial}	= 15 °C

Since the wind tunnel conditions are supposed to generate a large amount of turbulence the flow behavior within the boundary layer is set to fully turbulent in the numerical calculation.

Fig. 9 shows the static temperature distribution around the missile nose for the defined free stream conditions. Apart from the changes within the boundary layer this distribution will remain nearly constant throughout the exposition. Inside the bulk material the evolution of temperature is highly unsteady. For different exposure times (1sec, 5sec, 20 sec), Fig.11 shows the temperature distribution within the bulk material.

Already after 1 second of exposure time the effect of the different material properties can clearly be seen. Since the thermal conductivity of steel is within a lower temperature range considerably higher than the one of sapphire and additionally the heat capacity of steel is generally higher than that of sapphire, the heat convection within steel is higher. This causes the temperature gradient (normal to the surface) within the steel airframe to be slightly higher than in the sapphire window. This effect is amplified while exposure time goes on (see Fig.11 after 5 sec). Since the thermal conductivity of sapphire decreases and the one of steel increases while temperature rises the temperature gradient is reversed while time proceeds. At about a temperature of 300°C to 350°C the thermal conductivity of steel exceeds the corresponding magnitude for sapphire. Thus, the temperature distribution after 20 seconds shows that the temperature gradient within steel has become smaller than within sapphire. On the whole the temperature within the bulk tends to smooth. The adhesive between the sapphire window and the steel airframe has an isolating effect, whereas the air slit has only a small effect on the temperature evolution at the adjacent surfaces.

5.3 Aerokinetic Heating of an IR-Window Under Realistic Flight Conditions

The same configuration as in the previous section is now considered under a realistic flight path trajectory as shown in Fig.10. This one is a typical flight profile for a short range missile with an all boost motor. After a short time of boosting where the missile is accelerated to its maximum speed the missile starts to loose speed due to the high air drag during the following gliding/coast phase.

The corresponding temperature evolution within the bulk material (IR-window and steel airframe) usually shows a very high rise in temperature at the outer surface. The maximum temperature at this surface will be achieved with a small time delay after the velocity maximum. This is due to the fact that after booster burnout the surrounding temperature of the boundary layer is still higher than the temperature at the bulk's surface. The missile structure will be heated as long as the fluid-sided temperature will exceed the surface temperature. Hereafter the temperature will decrease. Inside the bulk material there will be only a gradual increase in temperature leading to a far lesser peak at the inner surface, which is achieved just a few seconds after the velocity maximum.

In Fig.12 a momentary view of the temperature distribution within the bulk is shown at two different times. The first distribution at about 1.75 sec (when the global temperature maximum exists), shows again the sluggish thermal behavior of sapphire and steel. Even so the surface is heated up to a higher temperature level the middle and inner part remain nearly unaffected. At a later time, when the missile has lost a lot of its kinetic energy and hence the heat fluxes

are again at a lower level, the temperature at the outer surfaces has fallen down again, whereas the middle and inner part of the material still tend to increase, although at a far less degree.

Looking at the temporal evolution of the temperature at the outer and inner surface of the IR-window configuration (Fig. 13 & 14), not only the effect of the different thermal properties and reactions of sapphire and steel can be seen, but also the sluggish heat transport inside the bulk. At the outer surface the steel airframe heats up more quickly during the few moments after launch than the sapphire window due to its different thermal properties. Since the relation of these thermal properties is inverted at higher temperatures, the reaction time for heat conduction is inverted too. At higher temperature levels the sapphire window gains more temperature than the steel airframe. The temperature evolution at the inner surface shows a nearly radial homogenous heating up. The air slit heats up more quickly than the bulk, but has only little effect on the adjacent surfaces, whereas the adhesive between the steel airframe and the sapphire window has an extreme isolating effect.

5.3 Realistic Flight Conditions -

Comparison of Different Methods

In this application the aerokinetic heating of a blunt-body configuration is calculated via two different numerical methods and the results are compared with experimental data, which are taken from measurements during a test flight. The flight profile resembles the one shown in the previous section.

The blunt body as shown in Fig.15 is made of steel with four temperature measurement points integrated at the outer surface at different angles from the longitudinal axis. Even so experimental data are only available for about 1.5 sec, the most important features are extractable.

The diagrams of temperature versus time at the different measurement points (Fig.16 & 17) show that at a distance farther off the rotational axis the temperature rises to a higher level than in the vicinity of the axis. At the outer part of the blunt-body where the curvature is highest the temperature reaches its maximum. Fig.16 & 17 show both the experimental data in comparison with those results obtained with the two different numerical methods, the energy-balance method and the non-feedback method, respectively. As can easily be seen, the energy-balance method shows globally a far better correspondance with the experimental data than the non-feedback method. The differences which occur in the non-feedback method are due to the fixation of the wall temperature (in the CFD-calculations) at every anchor point to a constant value. Even so experience would help to predict the actual temperature at the wall in a more accurate way, it will still be impossible to account for the mutual interaction between the boundary layer flow and the material heating.

6. CONCLUSION

This paper presented a method to perform numerical calculations of the aerokinetic heating of missile structures during their operational mission. With growing velocities it was shown that the missile design is more and more

dependant on the temperature evolution within the missile's bulk material and hence a reliable numerical prediction method is desirable. The entire simulation program described in this paper consists of two different codes, one for the surrounding fluid flow calculations (RAMPANTTM) and another one for the heat and stress calculations within the bulk (TEPROSIM, recently replaced by ANSYS[®]). Both programs were loosely coupled, in order to save CPU-time without losing accuracy in the whole. Two methods were presented, one which accounted for the mutual interaction between the boundary layer flow and the bulk at the intersection surface (energy-balance-method) and one which only considered the heat flux from the boundary layer to the bulk without caring for the actual temperature distribution within the bulk. Both methods were applied to a blunt-body configuration, where also experimental data from a flight test program were available. A comparison of both methods showed a far better agreement of the energy-balance method with the experimental data than the non feedback-method. Using the energy balance method two more calculations were done, related to experiments planned in the nearby future. In both cases the configuration consists of a flat sapphire window integrated in the nose cone of a missile. This configuration will be exposed in a wind tunnel under constant free stream conditions and will be tested under realistic flight conditions. For both cases numerical calculations will help to support the experimental design in advance and will help afterwards to verify the numerical code.

REFERENCES

- Imlay, S.T., Soetrisno, M., Roberts, D.W., Coupled Flow and Heat Transfer Analysis using Structured-Unstructured Grids, AIAA-96-0622, January 1996
- Molvik, G.A., Milos, F.S., Chen, Y.-K., and Squire, T.H., Computation of High-Speed Flow Fields with Multi-dimensional Solid Heat Conduction, AIAA-95-2116, June 1995
- Milos, F.S., and Rasky, D.J., Review of Numerical Procedures for Computational Surface Thermochemistry, Journal of Thermophysics and Heat Transfer, Vol. 8, No. 1, 1994, pp 24-34
- Milos, F.S., Chen, Y.-K., Solution Strategy for Thermal Response of Nonablating Thermal Protection Systems at Hypersonic Speeds, AIAA-96-0615, January 1996
- Kontinos, D., Coupled Thermal Analysis Method with Application to Metallic Thermal Protection Panels, J. Thermophysics and Heat Transfer, Vol. 11, No. 2, April-June 1997
- Chen, Y.-K., Henline, W.D., Analysis of Hypersonic Arcjet Flow Fields and Surface Heating of Blunt Bodies, AIAA Paper 93-0272, Jan. 1993
- Thornton, E.A. and Dechaumphai, P., Coupled Flow, Thermal and Structural Analysis of Aerodynamically Heated Panels, Journal of Aircraft, Vol. 25, No. 11, 1988, pp. 1052-1059
- Olsen, G.C. and Smith, R.E., Analysis of Aerothermal

Loads on Spherical Dome Pertuberances, AIAA Jounal, Vol. 23, No. 5, 1985, pp. 650-656

Olsen, G.C. and Smith, R.E., Aerothermal Loads Analysis for High Speed Flow over a Quilted Surface Configuration, AIAA Paper 84-1630, June 1984

Yamamoto, Y., and Yoshioka, M., CFD and FEM Coupling Analysis of Orex Aerothermodynamic Flight Data, AIAA Paper 95-2087, June 1995

Gülhan, A.. Interaction of Thermal Protection Material with the High-Enthalpy Flow of the Arc-Heated Wind Tunnel LBK, J. Shock Waves, Springer 1995

Anderson, J.D. Jr. Hypersonic and High Temperature Gas Dynamics, McGraw-Hill, New York

Anderson, J.D. Jr. Modern Compressible Flow, McGraw-Hill, New York

Müller, L., Henckels A.. Visualisierung der Grenzschichttransition im Hochgeschwindigkeitsbereich mittels FPA-Infrarot-Meßtechnik, IB DLR Köln-Porz

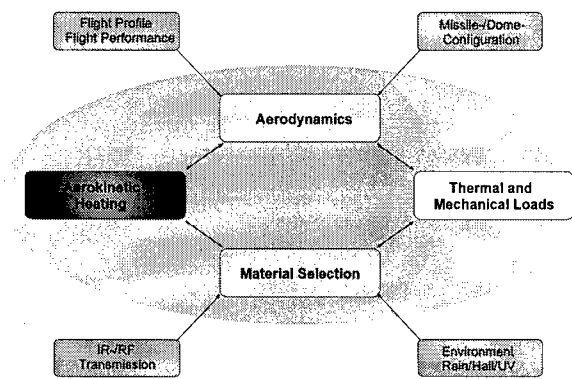


Figure 1: Critical Features in Super-/Hypersonic Missile Design

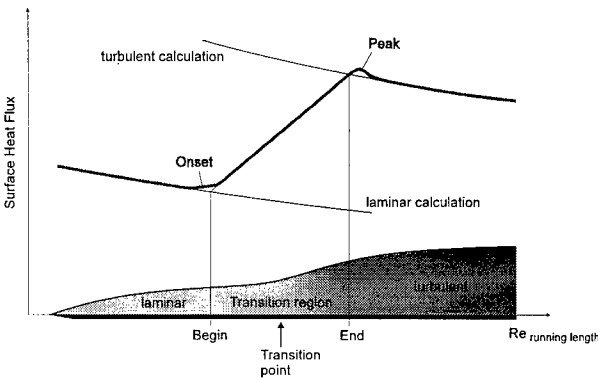


Figure 3: Heat Transfer within Boundary Layer

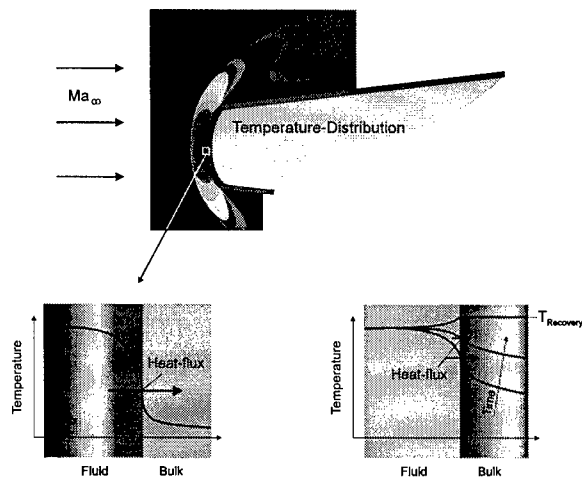


Figure 2: Aerokinetic Heating of Missile Structures

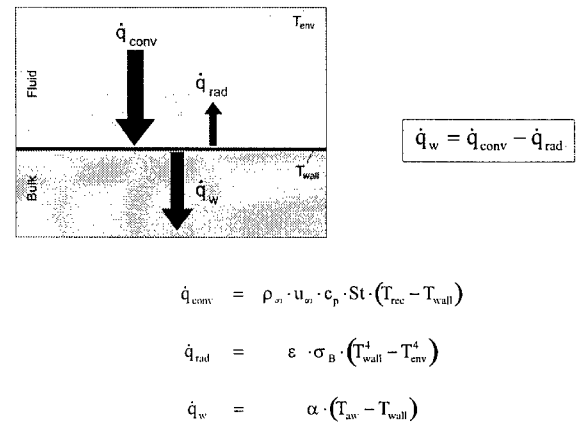
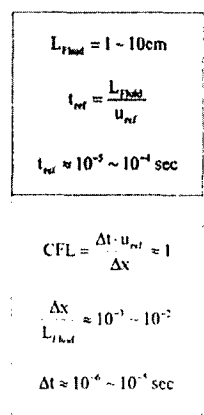
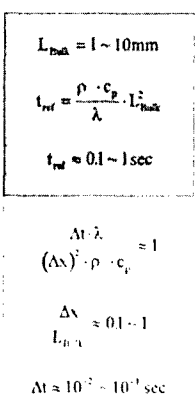


Figure 4: Surface Energy Balance

Convection in Fluid Flow

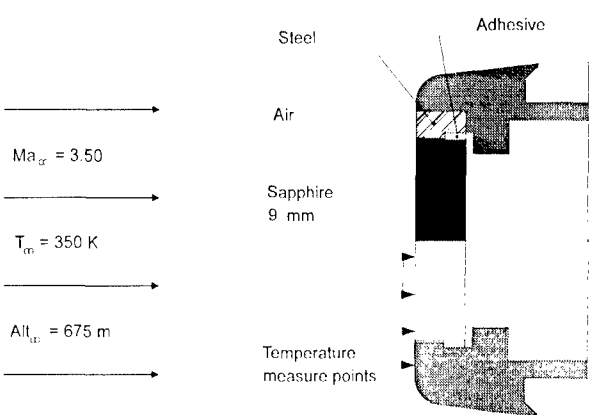


Material Heating



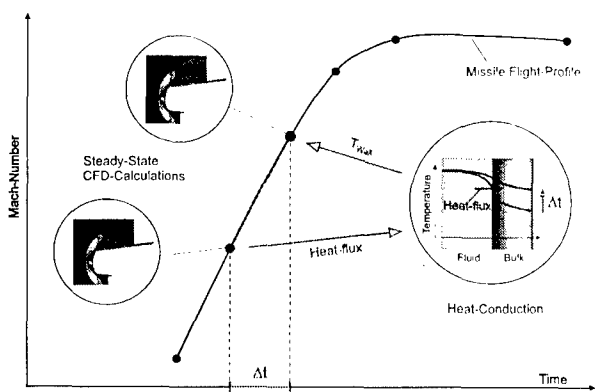
physics

numerics

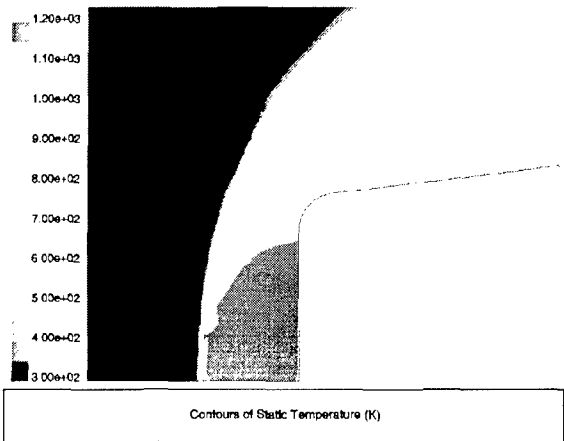


Figur 5: Characteristic Time Scales

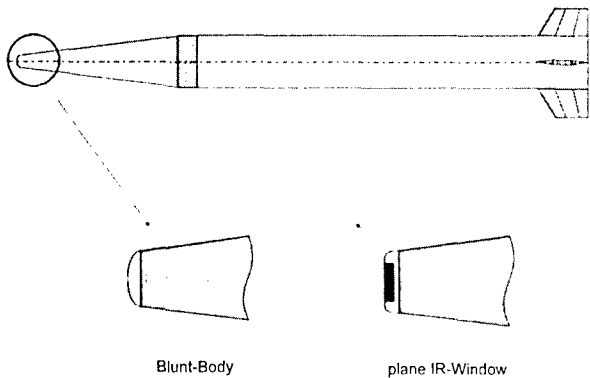
Figur 8: Nose Configuration with IR-Window



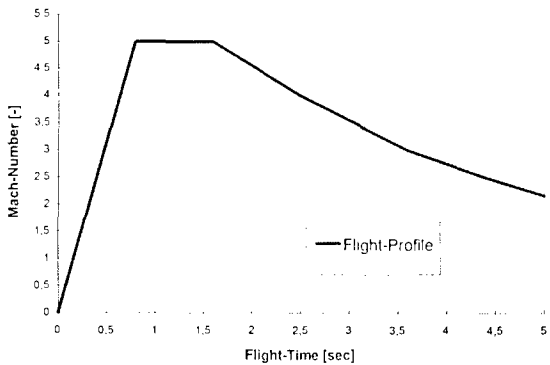
Figur 6: Schematics of Fluid-Structure-Coupling



Figur 9: Static Temperature Distribution Around the Missile Nose



Figur 7: Different Nose Configurations



Figur 10: Typical Flight Profile for Surface-to-Air Missiles

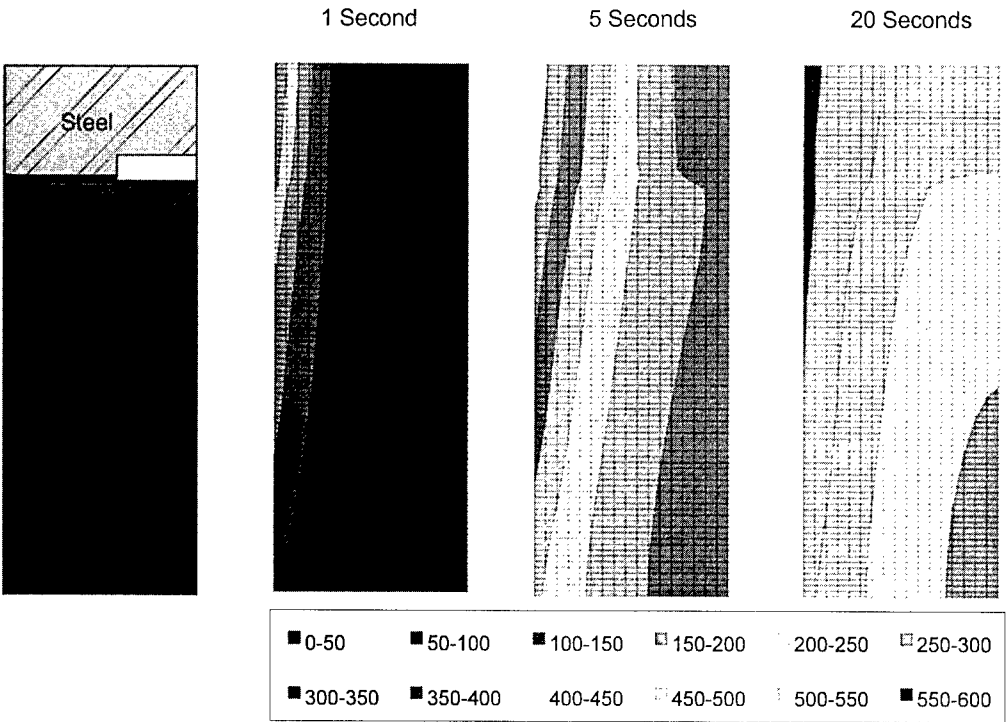


Figure 11: Temperature Distribution Inside the Bulk Material [°C]
Exposition to Free-Stream in Wind Tunnel

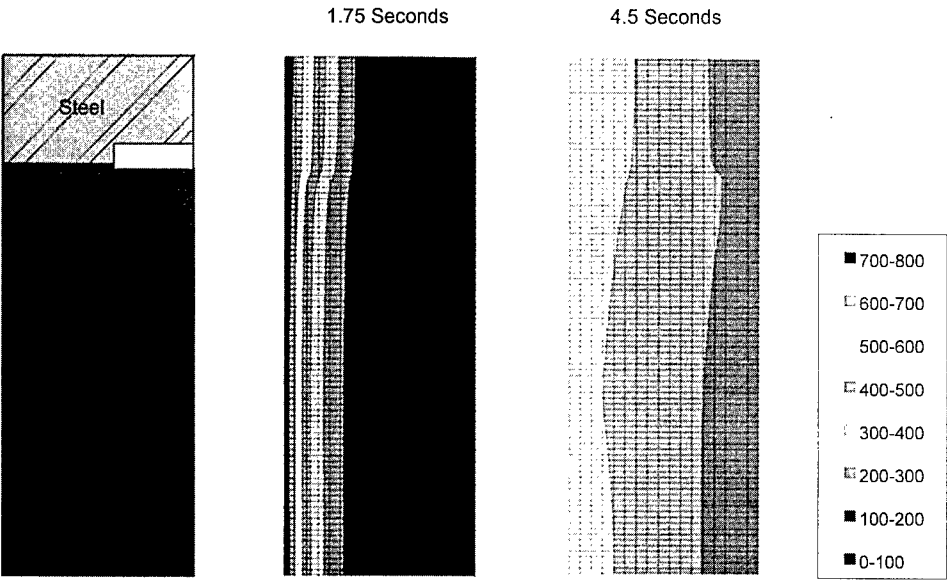


Figure 12: Temperature-Distribution Inside the Bulk Material [°C]
Free Flight Experiment

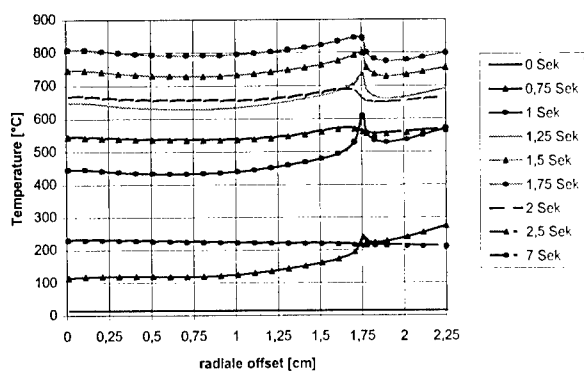


Figure 13: Temperature Distribution at the Outer Surface at Various Times - Real Flight Profile

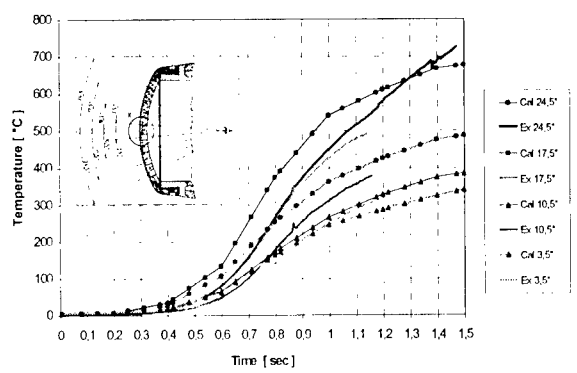


Figure 16: Comparison Experiment - Numerics Non-Feedback Coupling (Ex = Experiment / Cal = Calculated Data)

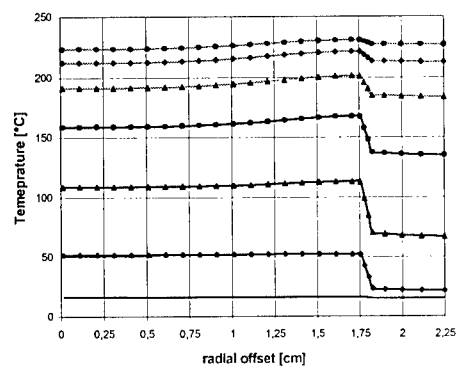


Figure 14: Temperature Distribution at the Inner Surface at Various Times - Real Flight Profile

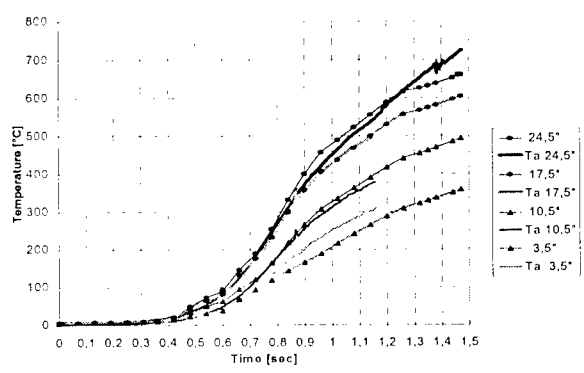


Figure 17: Comparison Experiment - Numerics Energy-Balance-Method (Ta = Experiment)

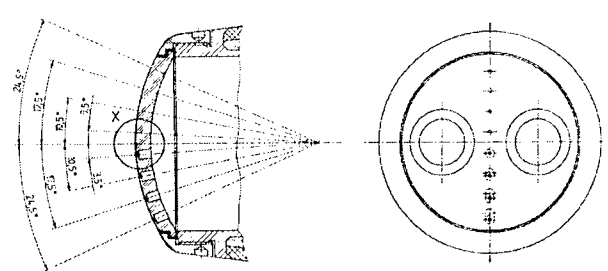


Figure 15: Blunt-Body Nose Configuration with Temperature Measurement Points

Aero-optic and Aerothermal Performance of Externally Cooled Infrared Window at Hypersonic Flight Conditions

George W. Sutton

ANSER

1215 J. Davis Hwy Suite 800
Arlington, VA 22202, USA

John E. Pond

Analysis and Applications Associates, Inc.

2614 Arties St., #31
Huntsville, AL 35805, USA

1. SUMMARY

The results of aero-optics calculations and experiments are presented and compared, for a generic 3D shape of missile forecone with external optical window cooling. The flow field and turbulent flow over the window cause a line-of-sight error and blurring of an image of an imaging optical sensor (IOS). A description of the equations and methodology are presented for predicting these effects. Both time average and instantaneous blur circles are presented. The results compare favorably with experiments.

2. INTRODUCTION

Imaging optical sensors (IOS) are being introduced into hypersonic rockets and missiles, whose high speed provides greater range. While aerospikes in front of optical domes have been suggested in the past, the current emphasis is on side-mounted cooled optical windows for the IOS, see Fig.1. To protect the optical window from hypersonic aerodynamic heating, external or internal cooling of the window is required but the IOS image may be aberrated by aero-optic effects of the shock-heated air flowfield and window coolant, because they have different indices of refraction. In addition, the interface between the shock-heated airflow and the external coolant is a turbulent shear layer, which increases the size of the blur circle.

This paper deals with the aero-optical aberrations for a side-mounted window with coolant gas flow injected parallel to the window on its exterior as a wall jet and the effects on the IOS. The stored coolant nominally is near room temperature. The optimum design dictates a coolant rate sufficient to protect the window from encroachment by the external shock-heated hot air flow. This sets the height of the coolant exit slot nozzle. The pressure of the coolant after expansion through its nozzle should

match the external aerodynamic pressure on the window. The minimum coolant usage occurs at a coolant nozzle exit Mach number of unity; but for convenience slightly supersonic nozzle exit conditions are usually used. As the external flow mixes with the coolant, a highly turbulent shear layer is formed and is the major source of aero-optic aberration.

We have developed a rigorous treatment for calculating the aero-optics aberrations. It has been applied to a two-dimensional wedge geometry and validated with experimental optical measurements¹. It was further refined to provide instantaneous blur circles². The superiority of helium coolant gas over nitrogen, due to the closer match of the index of refraction of helium to the shock heated air was also confirmed².

The present work presents a brief review of the theory and its application to a representative three dimensional shape of a hypersonic optical interceptor, namely a tetracone with the window on one face, see Fig. 2. The results of the theoretical predictions are compared to the results of experimental measurements in the Aero Optics Experimental Center's (AOEC) LENS shock tunnel which duplicates hypersonic flight conditions¹¹.

3. THEORY

3.1 Computational Fluid Mechanics

A three-dimensional computational fluid dynamics, (CFD) solution of the mean flow over the seeker head, window near field and coolant shear layer was performed using a full Navier-Stokes solver utilizing a two equation $k-\epsilon$ turbulence model with compressibility correction; which calculates the mean flow quantities, turbulent kinetic energy, and turbulent dissipation from the solution. The

Presented at the NATO/RTA Symposium of Applied Vehicle Technology Panel on Missile Aerodynamics, May 11-14, 1998

aerodynamic computer code FDNS³ was used for this study. This code is pressure-based, with a non-staggered grid, chemically reacting, Navier-Stokes solver. An adaptive upwinding differencing scheme is used for the spatial discretization. The code has equilibrium and finite rate algorithms for computing species concentrations, thermodynamic, and transport properties. A noniterative time-marching scheme was used; however, subiterations can be used if necessary. To provide smooth shock solutions, adaptive dissipation terms were added to the pressure correction equation. Once the pressure correction equation is satisfied, the velocity field is updated, and the density field is updated through the equation of state. To ensure the updated velocity, density, and pressure fields satisfy the continuity equation, the pressure correction solution is repeated several times before marching to the next step. This represents a multi-corrector solution procedure. The calculated density flow field around the AOEC 3D tare model is shown in Fig. 3.

A turbulent eddy viscosity is used to model the turbulent flow regions. The turbulent eddy viscosity component of the effective viscosity was determined from a two-equation $k-\epsilon$ model. A compressibility correction term, $E_k = M_t^2 \langle \rho \rangle \epsilon$ was added to the turbulent kinetic energy equation¹, where M_t is the turbulent Mach number $= k^{1/2}/a$; it produced the correct spreading rate as seen in Schlieren photographs. The optical effects of turbulence depends on two quantities; the distribution of the turbulence scale size l' and the index-of-refraction fluctuations $\langle n'^2 \rangle$. The former is found from the turbulence equilibrium condition:

$$l' = k^{3/2} / \epsilon \quad (1)$$

and the latter was modeled through the "g" transport equation⁴:

$$\begin{aligned} \rho u \frac{\partial g}{\partial x} + \rho v \frac{\partial g}{\partial y} &= \frac{\partial}{\partial y} \left(\frac{\mu_t + \mu_l}{\sigma} \right) + \\ &+ C_1 \left(\frac{\partial n}{\partial y} \right)^2 - C_2 \frac{\rho \epsilon g}{k} \end{aligned} \quad (2)$$

Fig. 4 shows the profiles along the line of sight of 40° from the axis of symmetry of the model. Figs. 5a shows the mean index of refraction; 5b shows the fluctuations of the index of refraction; and 5c shows the length scale, for helium coolant. These are along the line-of-sight of the experiment.

3.2 Aero-Optic Formulation

Aero-optic effects are generally caused by fluid flow over a window, dome, or cavity aperture. Aero-optics theory predicts the blurring of im-ages and boresight error due to fluid disturbances which causes density, hence index of refraction variations along the optical path.

It is first necessary to obtain the optical aberrations from the mean flow field. The optical path difference is given by:

$$OPD(X, Y) = \int_0^L \sum_i \rho_i(x, y, z) b_i dz \quad (3)$$

where r_i is the partial density and b_i is the Gladstone-Dale constant for the i th species and z is the direction of propagation. The process is carried out by passing each ray through the cells defined by the CFD grid points. The value of the mean index of refraction is found on the face where the ray pierces into the cell by using the following interpolation formula, see Fig. 5:

$$n = \frac{1}{4} \left[(1 - \xi)(1 - \eta)n_i + (1 + \xi)(1 - \eta)n_j + (1 + \xi)(1 + \eta)n_m + (1 - \xi)(1 + \eta)n_k \right] \quad (4)$$

Equation (4) maps the aerodynamic grid into the optical grid. It interpolates over the quadrilateral with $n_i - n_k$, the index of refraction at the nodes and η, ξ , the intrinsic coordinates found from an iterative solution of a nonlinear equation once the Cartesian coordinates of the pierce point are known. Integration through the cell is carried out using the trapezoidal rule. No further contribution to the OPD is taken once the outer surface of the window is reached.

The various contributions to the wave front aberration are illustrated in Fig. 6. Fig. 6a shows the raw results of the calculation. The mean value of the wave front distortion has no effect on the optical aberrations; hence it is subtracted, as is shown in Fig. 6b. The next

step was to find the boresight error, which in optical terms, is the tilt of the optical wavefront. By using the expression $bx + dy$, the tip d and tilt b are found by minimizing the rms error between the OPD and $bx + dy$. The result is shown in Fig. 6c. The concentric circles of index of refraction indicate that the wavefront is spherical, which changes the focal length and leads to blurring. If sensor had a refocus capability, it could be subtracted which would lead to the wavefront shown in Fig. 6d. The resulting modulation transfer function due to the mean flow field is shown in Fig. 7.

For the turbulent shear layer we use a rigorous approach using the correlation function of the index of refraction fluctuations⁵. It is summarized below from a more detailed derivation⁶. It starts with the scalar wave equation for the electric field u given by:

$$\nabla^2 u = -\frac{1}{c^2} \frac{\partial^2 u}{\partial t^2} \quad (5)$$

where c is the mean speed of light and t is time. In spherical spatial coordinates, and a temporally sinusoidal point source of circular frequency ω there is a simple solution of Eq. (5), given by:

$$u(r) = -\frac{i}{\lambda r} u_0 e^{ikr} \quad (6)$$

where $k = \omega/c = 2\pi/\lambda$ and λ is the optical wavelength. r is the distance from the source to the measurement point and u_0 is the initial amplitude taken at the pupil. Eq. (6) is integrated over the pupil area. Nonuniformities of the index of refraction n , this causes a wave front distortion in the direction of propagation (chosen as the z direction), given by Eq.(1):

$$\Delta z = \int n \, dz \quad (7)$$

where the integration is over the distorted path between the object and the aperture. The resulting phase distortion is $ik\Delta z$ which is added to the exponential in Eq. (6). Next, r is expanded in terms of the distance z from the focal plane to the aperture and the transverse coordinates x, y of the image at the focal plane is such that $x, y \ll z$. With u_0 constant across the aperture which is typical of a point source object, the result is the focal point intensity distribution given by:

$$u(\theta_x, \theta_y) = -\frac{i}{\lambda F} u_0 \int_A e^{ik \int_0^z \Delta n(x, y, z) dz} e^{-ik(x\theta_x + y\theta_y)} dx dy \quad (8)$$

Here, x, y are coordinates in the aperture plane and θ_x, θ_y are the angles to portions of the image as measured from the optical center line, from the center of the aperture. Also, the mean value of z between the aperture and the object is the focal length F , indicated in the denominator of Eq. (8). Note the dependence on the wavelength λ . For different wavelengths, the optical distortion at the focal plane will be different. In general, the longer the wavelength, the less the blurring at the IOS focal plane caused by the flow field or turbulence.

Equation (8) is used for the steady non turbulent but distorted portions of the flow field. When squared, it forms the image blur due to those distortions; its Fourier transform forms the modulation transfer function (MTF)

τ_{ff} . A measure of optical distortion is the Strehl ratio, the ratio of the central intensity of the point spread function (PSF) image of an un-resolved source to the diffraction-limited PSF.

For turbulent flows, the time-average intensity is formed by multiplying Eq. (8) by its complex conjugate $u^*(x', y')$ and taking the ensemble average of the product. For a Gaussian distribution of fluctuations (not to be confused with a Gaussian correlation function), the averaging yields:

$$I(\theta_x, \theta_y) = \frac{I_0}{\lambda^2 F^2} \iiint e^{ik(\theta_x \xi + \theta_y \eta)} e^{-2k^2 \int \Delta n^2 (\Lambda - \int C d\zeta) dz} d\xi d\eta dx dy \quad (9)$$

where ξ, η are $x'-x$ and $y'-y$, respectively; that is the correlation function is a function only of the separation distances between two points around the point x, y, z . Λ is the integral scale size of the turbulence, discussed below.

It is known that the correlation function in turbulent shear flows is an ellipsoid^{7,8} with its major axis at an angle to the flow vector. The line of sight can be upstream at various angles, so it is expected that the anisotropy of the turbulence will have an effect. Since that effects requires further quantification, it is not used in the present study. Thus, with the assumed symmetry we use $\rho = (\xi^2 + \eta^2)^{1/2}$.

At this point, the turbulence parameters are still a function of the position x, y of the aperture. The effect of spatial variations of the turbulence parameters was been investigated for a case where they varied greatly in the streamwise direction⁹. The result was that integration along the central (chief) ray gave the same result as integration over the entire aperture to within 10%. Next, in the ξ, η plane the coordinates are converted to cylindrical coordinates ρ, ϕ and result is integrated over ϕ , allowed by the assumed symmetry of the correlation function. Using the central ray as representative, integration over the aperture x, y results in the familiar overlap circle given by:

$$t_D = (2/\lambda) [D^2 \cos^{-1}(r/D) - r(D^2 - r^2)^{1/2}] \quad (10)$$

The result is:

$$I(\theta) = \frac{\pi I_0}{2\lambda^2 F^2} \int_0^D \rho d\rho J_0(k\rho\theta) \tau_D \cdot e^{-2k^2 \int_0^{\Delta n^2} [\Lambda - J_0(\sqrt{\rho^2 + \zeta^2} d\zeta)] dz} \quad (11)$$

where J_0 is the Bessel function of zero order.

Note that $\Lambda = \int_0^\infty C(\zeta) d\zeta$. Care should be taken

when the scale size of the turbulence is a large fraction of the thickness of the shear layer¹⁰. Although the use of a Gaussian correlation function allows calculation of the blur circle in a closed algebraic form and generates an asymptotic size of the blur circle as $\lambda \rightarrow 0^5$, it is unphysical and not used herein. The correlation function for the shear layer is more realistically represented as an exponential, consistent with measurements in shear layers. However, the physics of turbulence requires

that $\lim_{z \rightarrow 0} dC(z)/dz = 0$. The exponential form does not permit the determination of the size of the blur circle as $\lambda \rightarrow 0$. This has no practical consequence for this analysis. The integral inside the exponential of Eq. (11) becomes:

$$\int_0^\infty e^{-\sqrt{\frac{\rho^2}{\Lambda^2} + \frac{\zeta^2}{\Lambda^2}}} d\zeta = \rho K_1\left(\frac{\rho}{\Lambda}\right) \quad (12)$$

where K_1 is the modified Bessel function of order 1 which was represented by an algebraic expression in the computer program. The kernel in Eq. (11) is the turbulence MTF, τ_T . The performance of two coolants was evaluated for a the seeker window on the 3D tare tetra-cone. Nitrogen coolant was found to cause a large amount of optical aberration due to large index-of-refraction fluctuations generated in the shear layer which was caused by the mismatch in mean density between the cold coolant layer and hot shock layer external flow. The large density gradient in the mixing layer was the dominant factor in turbulence production. To lessen the density gradient in the shear layer, helium gas coolant was investigated. It was found that the mean density of the helium gas coolant more closely matched the hot shock layer density due to its low molecular weight, thus minimizing production of index-of-refraction fluctuations in the shear layer. The rms wave front distortion for a helium cooled window at a typical endoatmospheric condition was found to be four to five times less than with nitrogen coolant. The MTF for the helium coolant/shock layer air turbulent shear layer is shown in Fig. 8. The blur circle point spread function and encircled energy curves are shown in Fig. 9, in comparison with predictions for no aero-optical distortions, e.g., diffraction-limited.

The Fourier transform of the product of $\tau_{ff} \bullet \tau_D \bullet \tau_T$ is used to calculate the total time-averaged blur circle. This is shown in Fig. 10.

3.3 Instantaneous Blur Circles

For many optical experiments involving flow, pulsed laser holography is used. Because the pulse time is so small, the resulting blur circle

is not time averaged, but instead is instantaneous. These have been calculated previously², using the following method. The term in the second exponential of Eq. (9) is the time average phase correlation function $\overline{\Phi}(x,y)$ in the plane of the pupil or aperture; its power spectral density is given by:

$$P(k_x, k_y) = \int_{-\infty}^{\infty} \int_{-\infty}^{\infty} \Phi(x,y) e^{-i(k_x x + k_y y)} dx dy \quad (13)$$

An instantaneous phase map in the pupil plane is generated from:

$$\Phi_i(x,y) = \int_{-\infty}^{\infty} \int_{-\infty}^{\infty} P(k_x, k_y) \left| z(k_x, k_y) \right|^{1/2} e^{i(k_x x + k_y y)} dk_x dk_y \quad (14)$$

where z is a random number with a Gaussian distribution. A typical realization of the phase map is shown in Fig. 11. The Fourier transform of it gives the intensity at the focal plane of an unresolved object; see Fig. 12.

4. EXPERIMENTAL RESULTS

Favorable comparison of the theory and experiments were previously reported for comparisons with the AOEC 2D wedge model¹. The experimental results for the AOEC 3D tetracone model¹¹ and comparisons with our calculations are shown in Table 1 below. The test conditions were a velocity of 2.73 km/s, free stream temperature and density of 198°K and 0.055 Kg/m³ respectively. It can be seen that the agreement is very good. The rms wavefront distortion obtained from the holographic image is smaller than predicted for the time average, while the Strehl ratio for the instantaneous blur circle calculated from the former is larger than that of the long time image prediction. The holographic method does not include image centroid jitter. Thus, the long time, averaged blur circle will usually have a reduced Strehl ratio compared to that calculated from the holographic phase map. The long time Strehl ratio for N² was measured both in the visible and the IR. Extrapolation of the IR results to the visible causes excellent agreement with the predictions. The cause of the discrepancy with the visible light imager is unknown. In general, the calculation techniques presented herein are validated by the comparison with experiment.

5. SUMMARY

The aero-optic phenomena around externally cooled windows for imaging optical sensors on endoatmospheric hypersonic vehicles has been described. The effects were evaluated with a 3D full Navier-Stokes code with a two equation turbulence model with compressibility correction. These results were then incorporated into the aero-optics codes for both the index-of-refraction disturbances. The effect on the blur circle and boresight error were evaluated, and compared favorably to recent experiments.

6. REFERENCES

- 1 Sutton, G.W., Pond, J.E., Snow, R., and Hwang, Y., "Hypersonic Interceptor Aero-Optics Performance Predictions," *J. Spacecraft & Rockets*, 31,4, July-Aug. 1994, pp592-599.
- 2 Sutton, G.W., Pond, J.E., and Hwang, Y., "Phase-Aberrated Instantaneous Target Realizations Due to the Coolant Over and Optical Window in Hypersonic Flight," *Proc. 3rd Annual AIAA/BMDO Interceptor Technology Conference*, July 11-14, 1994; available from DTIC.
- 3 Wang, T., and Chen, Y.S., "A unified Navier-Stokes Flowfield and Performance Analysis of Liquid Rocket Engines," *AIAA Paper 909-2994*, 1990.
- 4 Launder, B.E., and Spaulding, D.B., *Mathematical Models of Turbulence*, Academic Press, N.Y., 1972, pp. 126-127.
- 5 Sutton, G.W., "Effects of Turbulent Fluctuations in an Optically Active Fluid Medium," *AIAA Journal*, 7,9, Sept. 1969, pp. 1737-1743.
- 6 Sutton, G.W., "Aero-Optical Foundations and Applications," *AIAA Journal*, 23,10, Oct. 1985, pp1525-1537 (appendix)
- 7 Smith, M.W., and Smits, A.J., "Visualization of the structure of supersonic turbulent boundary layers," *Experiments in Fluids* (Springer-Verlag), 18, 1995, pp 288-302, Fig. 15.
- 8 Truman, C.R., and Lee, M.J., "Effects of organized turbulence structures on the phase distortions in a coherent optical beam propagation through a turbulent shear flow," *Phys. Fluids A*, 2, May 1990, pp. 851-857.
- 9 Sutton, G.W., "The Effect of Inhomogeneous Turbulence on Imaging Through Turbulence Layers," *Appl. Opt.*, 33, 18, June 1994, pp 3972-3.
- 10 Havener, G., "Optical Wave Front Variance: A Study of Analytic Methods in Use Today," *AIAA Paper 92-0654*, 30th Aerospace Science Meeting, Reno, Jan. 1992.
- 11 Holden, M., Parker, R., and Walker, B., "Interceptor Testing in the LENS Aerothermal/Aero-Optical Test Facility," *Proc. 6th AIAA/BMDO Technology Readiness Conference*, Aug. 18-22, 1997; available from the Defense Technical Information Center.

Table 1
Comparison with Experiments

Nitrogen Window Coolant	Holographic rms wavefront distortion @ 0.69μm	Instantaneous Strehl ratio from rms wave front @ .69μm	Long time average image Strehl ratio @ 0.63 μm	Boresight error, μrad
Experiment	0.337 waves	0.045	0.031,0.0060*	not reported
Calculation	0.456 waves		0.002	28.6

Helium Window Coolant	Holographic rms wavefront distortion @ 0.69μm	Instantaneous Strehl ratio from rms wave front @ .69μm	Long time average image Strehl ratio @ 0.63 μm	Boresight error, μrad
Experiment	0.051 waves	0.923	not reported	14±12**
Calculation	0.082 waves		0.802	19.6

* extrapolated from infrared images
** after correcting for free stream density

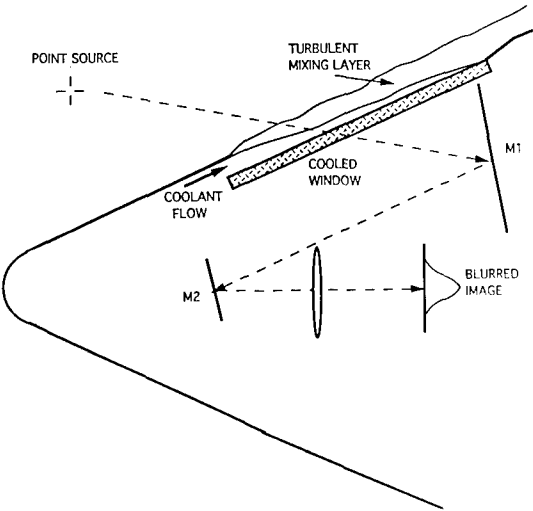


Fig. 1. Sketch of aero-optic environment around a hypersonic window.

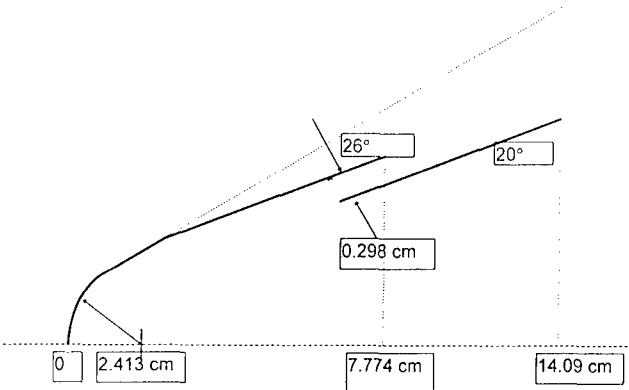


Fig. 2. Cross section of test model.

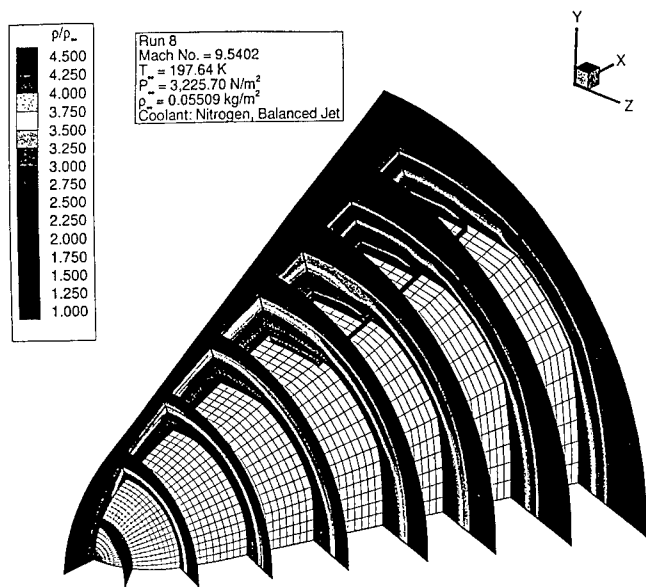


Fig. 3. CFD results for the 3D tare model, showing density field.

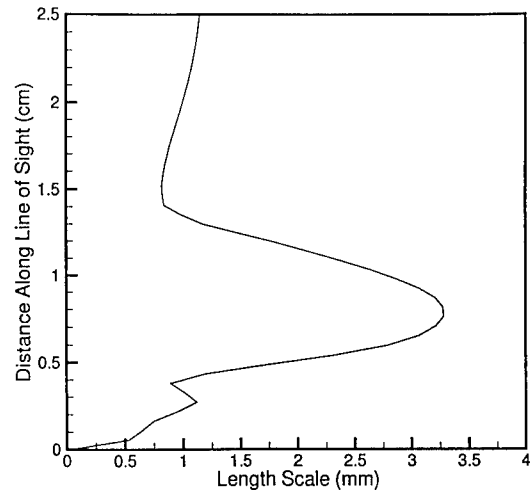
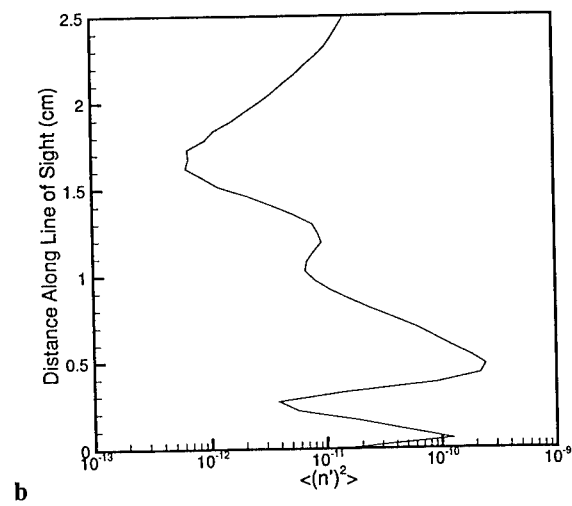
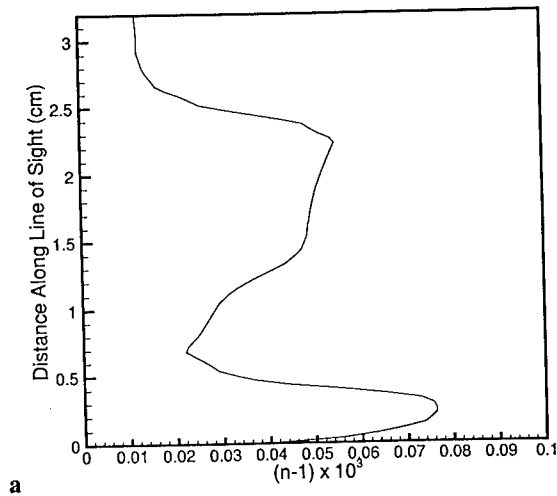
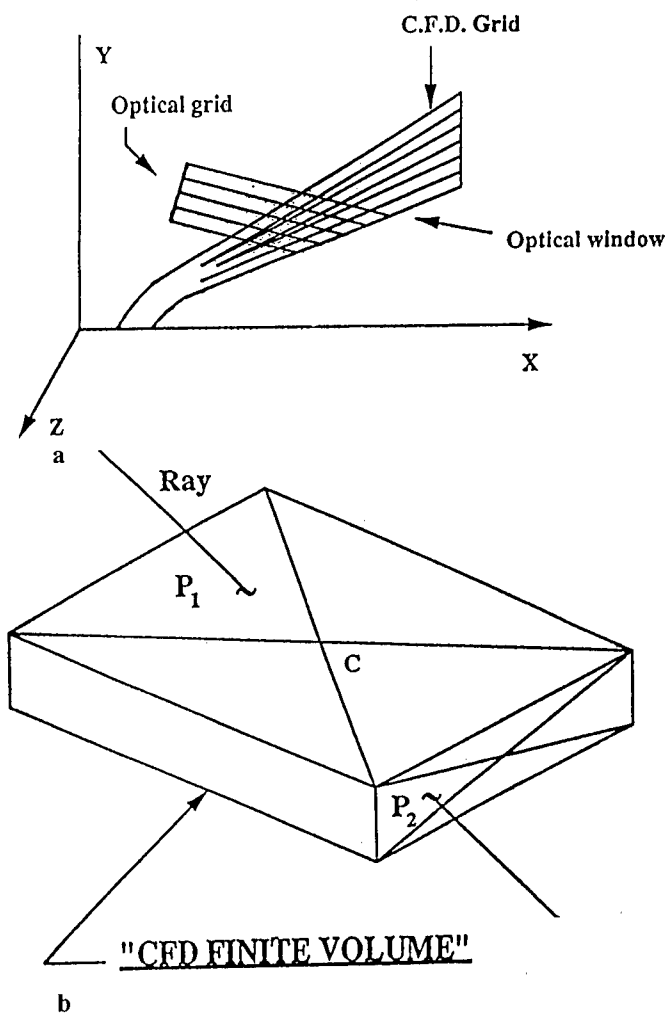
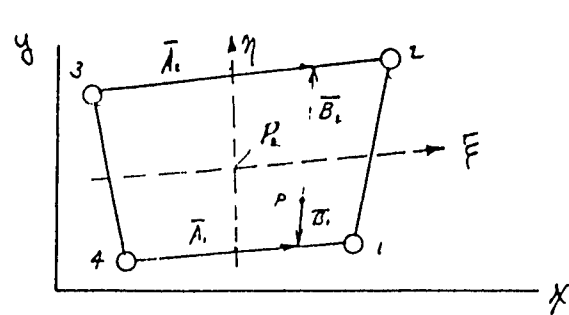
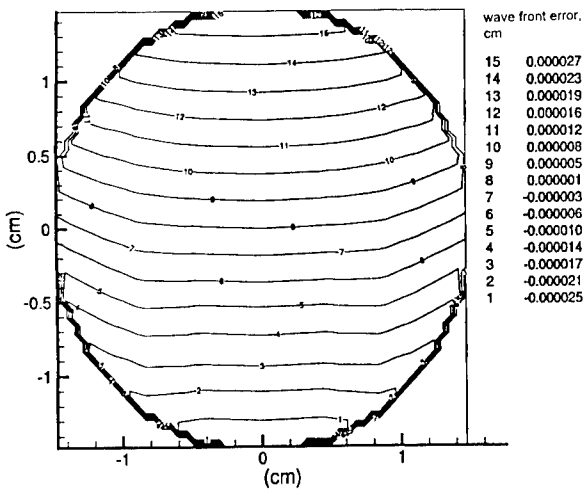


Fig. 4. Profiles along the line of sight of 40° from the axis of the model, for helium coolant. a: mean index of refraction; b: fluctuations of the index of refraction; and c: turbulence length scale.

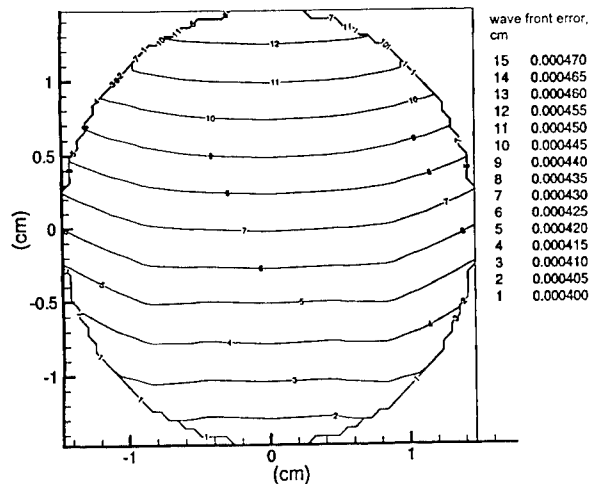




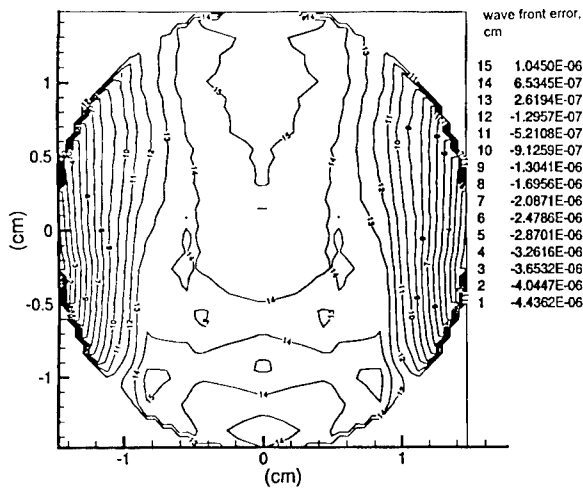
c
Fig. 5. a. CFD and optical grids. b. Method of obtaining index of refraction and path length through a CFD cell. c. Interpolation technique to implement b.



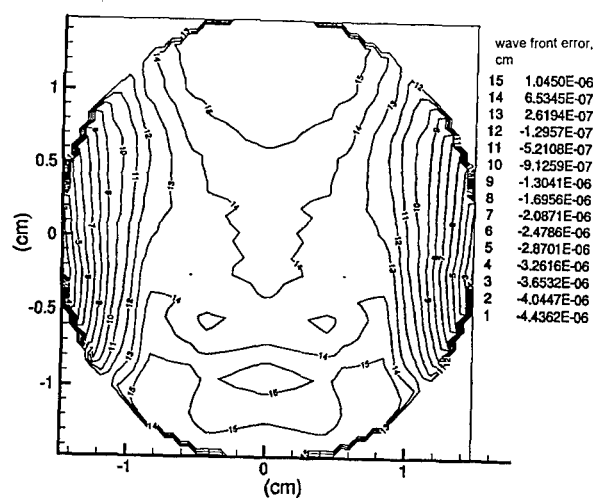
b



a



c



d

Fig. 6. Wave front optical path differences. a: Raw results. b: After subtraction of mean. c: After subtraction of tilt. d: After subtraction of focus.

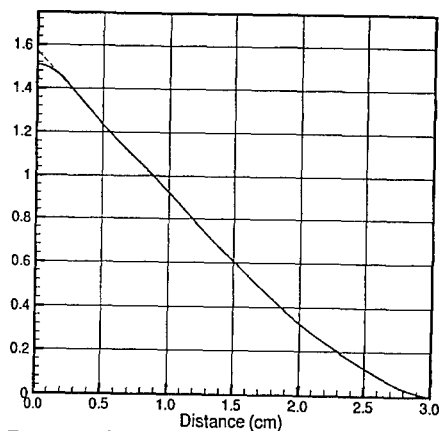


Fig. 7. Modulation transfer function due to wave front error shown in Fig. 6d. Wave-length = $0.69 \mu\text{m}$; pupil size = 3 cm.

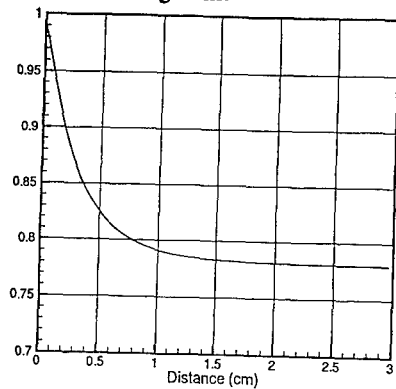


Fig. 8. Modulation transfer function due to turbulent shear layer between helium coolant and shock-heated air flowfield. Wavelength = $0.69 \mu\text{m}$; pupil size = 3 cm.

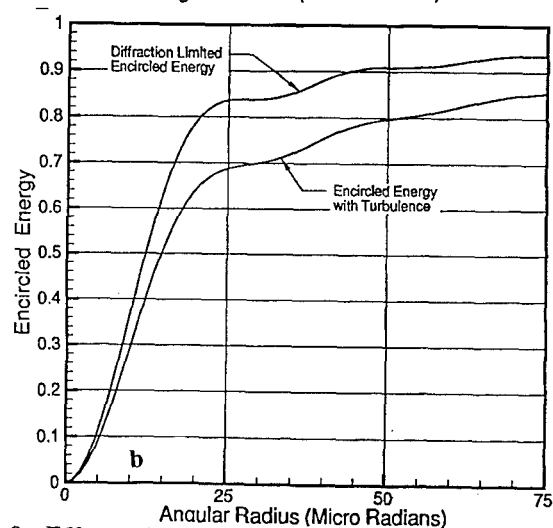
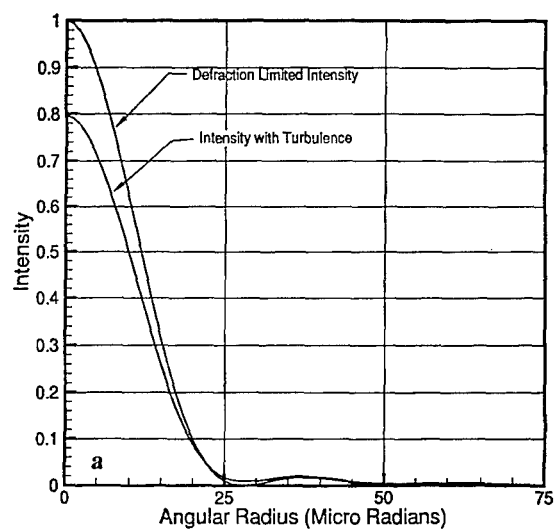
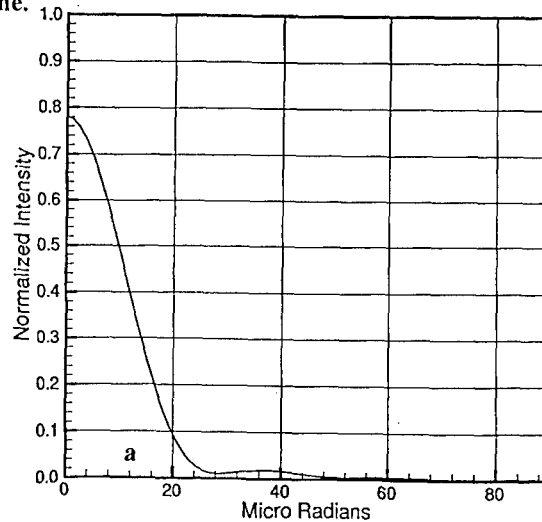


Fig. 9. Effect of only turbulence on blur circle. Wavelength = $0.69 \mu\text{m}$; pupil size = 3 cm. a: Radial profile of optical energy at focal plane (point spread function). b: Encircled energy at focal plane.



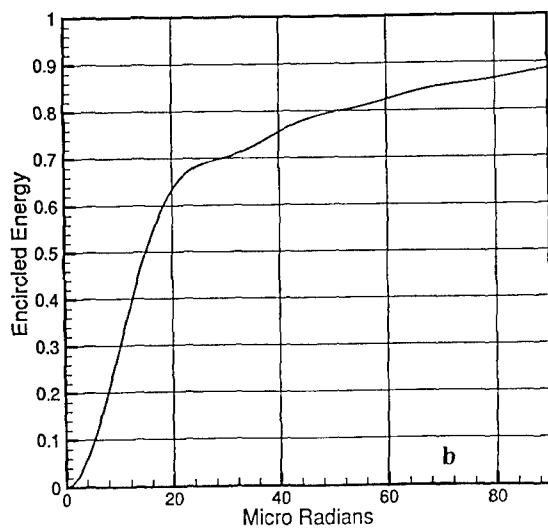


Fig. 10. Combined effects of mean flow field and turbulent shear layer. Wavelength = $0.69 \mu\text{m}$; pupil size = 3 cm. a: point spread function; b: encircled energy.

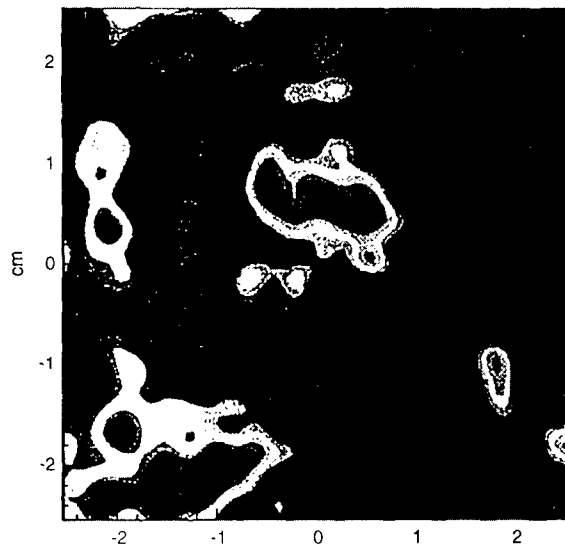
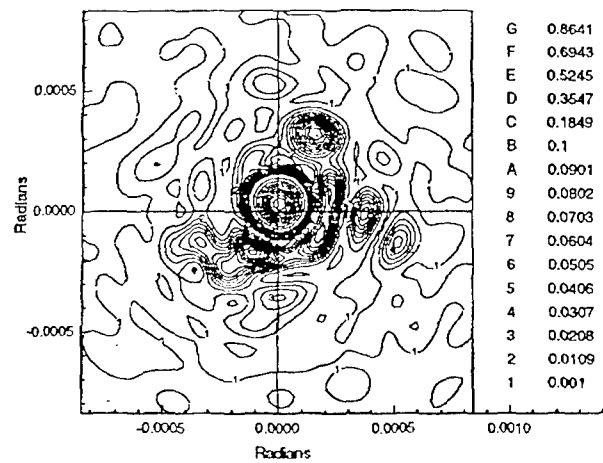
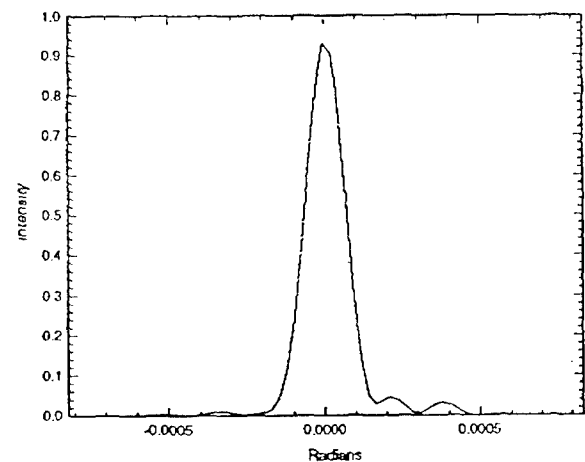


Fig. 11 Coolant shear layer turbulence instantaneous phase map at pupil.



a



b

Fig. 12. Intensity contours at focal plane and point spread function for instantaneous phase map of Fig. 10.

Time-averaged and unsteady loads on a missile at launch from an internal weapons bay.

J. A. Ross, J. Odedra

High Speed and Weapon Aerodynamics, Mechanical Sciences Sector,
Defence Evaluation and Research Agency, Bedford, United Kingdom, MK41 6AE.

SUMMARY

This paper describes an experimental programme which has investigated the component loads acting on a typical missile (AMRAAM) when located within weapons bays of different geometry. Measurements have been made of wing panel loads, fin panel loads and body pressure distributions. Both time-averaged (steady-state) and unsteady pressures have been measured. The effects of weapon bay doors on the pressures and panel loads acting on the missile have also been measured.

It is shown that the measured results can be used to understand the differing total loads measured on the missile in earlier tests, and thus provide an insight into developing appropriate ways of minimising carriage and release problems identified in earlier experimental programmes.

LIST OF SYMBOLS.

CHm	Wing or fin hinge moment coefficient, deflecting wing or fin. Direction as defined in fig 7.
CMB	Pitching Moment coefficient. Positive with store nose towards cavity ceiling. In missile body axes.
CNB	Normal force coefficient, ($=C_Z$). Positive towards ceiling of cavity. In missile body axes.
CP	Static pressure coefficient, (Referenced to free-stream).
CNF	Wing or fin normal force coefficient. Normal to plane of panel. Direction as defined in fig 7.
D	Cavity depth.
HM	Wing or fin hinge moment. Direction defined in fig 7.
L	Cavity length.
M	Mach number.
NF	Wing or fin normal force. Direction defined in fig 7.
rms	Root-mean-square.
SPL	Sound pressure level, (dB).
T	Time.
U	Free stream velocity, (Feet per second).
X	Longitudinal co-ordinate. Positive in aft direction. Origin at front edge of cavity.
Z	Normal co-ordinate. Positive moving out of cavity. Origin in plane of cavity exit.
d	Store diameter.
f	Frequency, (Hz).
l	AMRAAM missile length
m	Small integer number, (1, 2, 3,).
x	AMRAAM missile longitudinal co-ordinate. Positive in aft direction. Origin at missile nose.
γ	Constant (after Rossiter, ref 10).
ϕ_m	AMRAAM missile roll angle. Defined in fig 6.

1 INTRODUCTION

Earlier studies^{1 to 4}, and similar studies in the USA^{5 to 8}, have identified a number of problems with the carriage and release of stores in internal weapons bays. Depending on length-to-depth ratio, weapons cavities can be classified as aerodynamically shallow or deep (closed or open). Although the precise boundaries do change

with Mach number, cavities with length-to-depth ratios of less than seven are found to be aerodynamically deep⁵, while those with length-to-depth ratios greater than twelve⁵ are aerodynamically shallow. In the region between these limits the flow is a combination of both types of regime and the cavity is called transitional.

Shallow and deep cavities are characterised by different types of flow. In the former, the approaching flow penetrates into the cavity, reaches and flows along the ceiling before separating and turning quite rapidly to exit near the rear wall. For deep cavities, flow penetration into the cavity is minimal, with only a small deviation of the approaching flow and the generation of weak circulating regions within the cavity. These different types of cavities are identified by characteristic and distinct forms of pressure distribution measured within the cavity. When stores are carried within weapon bays, shallow and deep geometries lead to quite different types of problem from a carriage and release standpoint, both of which are directly related to the type of flowfield present.

In the shallow case, stores can be subjected to large loads and moments, and in particular very large pitching moments have been measured. These loads and moments pose problems in the design of carriage equipment and launch devices. In addition, the large pitching moments make store release difficult, and give rise to the problem of the stores rising back into the cavity and colliding with the aircraft. Within shallow cavities, when the bay doors are open, the stores and the aircraft structure will be subjected to high levels of fluctuating pressure of a broadband nature. rms levels of 160 dB have been measured.

In deep cavities store forces and moments are much more modest making structural strength and release less problematic. However, when the cavity is open, extreme levels of fluctuating pressures are found and rms levels of up to 174 dB have been measured. In addition, most of the energy of the fluctuating pressures is concentrated into a small number of very distinct frequencies. These acoustic levels are capable of damaging components of the on-board stores and aircraft structure.

Examples of the normal force and pitching moments experienced by a missile emerging from aerodynamically shallow and deep weapons cavities are shown in fig 1, and corresponding simulated weapon release trajectories in fig 2. Fig 3 compares the unsteady pressure environments, shown in terms of rms amplitude against frequency, found within deep and shallow weapons bays.

This paper details work from a research programme, which has investigated the components leading to the total loads measured on a typical air-to-air missile when carried within an internal weapons bay. Measurements have been made of wing panel loads, fin panel loads and body pressure distributions. Both time-averaged (steady-state) and unsteady pressures have been measured. The effects of weapon bay doors on the pressures and panel loads acting on the missile have also been measured.

It is shown that the results can be used to understand the differing total loads measured on the missile in earlier tests and thus provide an insight into developing appropriate ways of minimising carriage and release problems identified in earlier experimental programmes.

2 EXPERIMENTAL CONFIGURATIONS.

The experimental programme is based around a generic model, fig 4, which is designed to carry stores of up to one-tenth scale. This model permits the measurement of loads and moments acting on the stores as they are traversed through weapon cavities of different geometry. It also provides for detailed measurement of the steady-state and unsteady environments to which weapons will be subjected. The measured forces and moments, provide vital information required in the design process and allow weapon release characteristics to be assessed.

Having identified potential problems^{1 to 4} with the carriage and release of stores arising from the loads and environments created by cavity flowfields, further tests have been made to examine the detailed source of the measured loads and the variation of the unsteady environment throughout the volume of the weapons bay.

For this test series a special version at one tenth scale of an AMRAAM missile model was manufactured to facilitate the measurement of both time-averaged and unsteady pressures over the missile as it traverses through the weapon cavity, and at the same time measure the three-component fin and wing panel loads by means of panel strain-gauge balances. Due to the large amount of instrumentation built into the small scale model, it was not possible to use the normal five-component internal strain gauge balance within the missile, and this test series was dedicated to the measurement of missile pressures and panel forces.

Details of the pressure plotting installed on the one tenth scale AMRAAM missile are shown in fig 5. Two rows of 10 high frequency response 25 PSI absolute pressure transducers are installed longitudinally at stations 90° apart (designated STN 180 and STN 90). In use, the signals from these transducers are split, with one part monitored by DC coupled instrumentation to measure time-averaged or 'steady-state' pressures, while the second part is fed, AC coupled, to an unsteady pressure analysis system. Unsteady pressure data was recorded in the form of five second records sampled at a rate of 6000 Hz.

Fig 6 provides details of the strain-gauged missile wing and fin. The panel balances on both wing and fin are arranged to measure three components of panel load :

- normal force, normal to the plane of the panel
- hinge moment, the moment trying to deflect the panel
- root bending moment, the moment bending the panel about its root chord.

The pressure plotted AMRAAM missile incorporates an integral sting mounting which connects to the remote drive mechanism allowing the store to be traversed throughout the depth of the cavity and into the free-stream outside the weapon cavity. Full details of this mechanism are given in ref 1. The mounting of the integral sting to the missile drive mechanism allows the missile to be mounted at different roll orientations within the cavity. This is illustrated in fig 7 where the missile is shown installed within a weapon bay at roll orientations of 0° and 180°. In the tests each model build was tested twice with the missile in roll positions of 0° and 180° which increased pressure measurements to cover four longitudinal stations (with a total of 40 pressure measuring points) as shown in fig 7. As all tests were performed with a symmetric configuration of a single missile on the cavity centre-line, the tests at 0° and 180° place the strain-gauged wing and fin in both inner and outer locations relative to the cavity exit, and thus provide complete coverage of wing and fin loads.

The tests were performed with a cavity measuring 20 inches (0.508m) long and 4 inches (0.102m) wide. Cavity depths of 2

inches (0.051m) and 4 inch (0.102m) were used giving examples of geometries with length to depth ratios of 10 and 5, where behaviour typical of aerodynamically shallow and aerodynamically deep cavities are exhibited respectively. In addition, for both the shallow and deep cavity options, configurations featuring 90° (vertical) bay doors¹ were tested.

Tests Mach numbers were 0.6, 0.85, 0.98, 1.19 and 1.35. In the case of the shallow cavity without bay doors, the metric missile was set at incidences of -10°, 0° and +10°, and for the other configurations the incidence of the metric missile was set to zero. In each case, missile time-averaged pressures, missile unsteady pressures and wing and fin panel loads were measured on the metric missile as it was traversed from its innermost location within the cavity, to the maximum distance outside the cavity of seven store diameters. All tests were carried out in the Aircraft Research Association Ltd 9 ft x 8 ft (2.75 m x 2.4 m) transonic wind tunnel⁹.

3 RESULTS : STORE FORCES AND MOMENTS.

3.1 Store loads: basis of analysis.

The objective of the tests was to use measured panel loads and time-averaged pressures on the store to identify the sources of the overall forces and moments measured in earlier tests^{1 to 4}, in order to identify which features of missile design lead to high loadings and thus to point to ways of minimising problems.

Forty time-averaged pressures are distributed over the missile in four longitudinal rows with longitudinal positions ranging from $X/L=0.035$ to $X/L=0.905$. Combining the pressure measurements from the tests with the missile set at 0° and 180° gives pressure measurements at azimuthal locations of 0°, 90°, 180° and 270°. Although forty pressures in four rows is an insufficient number to provide an accurate integration of the missile body loading distribution, such an integration (together with interpolation of pressures at 5° between the measurement stations) does provide a guide to the proportion of the measured overall forces generated on the missile body, and over which areas these are generated. In addition the wing and fin strain gauges provide the individual contributions from the wings and fins. Measured panel hinge moments allow the exact location of the panel loads to be determined and their contribution to overall moment to be determined. In this way the overall loads on the missile can be built up from the different components and compared with the earlier overall loads measured by internal strain gauge balance.

3.2 Measured store loads: shallow cavity ($L/D=10.0$).

An example of the normal force and pitching moments measured on the AMRAAM missile when traversed through the cavity is shown in fig 8 for the shallower of the cavities examined ($L/D=10.0$). Results are for a low supersonic Mach number ($M=1.19$), but are typical of all Mach numbers and also configurations without bay doors. The high levels of 'nose-into-cavity' pitching moments can lead to potential carriage problems and make the store difficult to release.

Fig 9 shows typical missile pressure distributions at subsonic speed for the case without bay doors. Pressures at the 90° and 270° roll positions are similar as might be expected for the symmetrical configuration. Generally the missile experiences suction over the forward third of its length followed by positive pressure increasing with longitudinal position over the aft section. Comparison of the pressure distributions at the 0° and 180° roll positions indicates that the missile experiences an inward force over the forward 60% of its length followed by an outward force over the rear 40%. Pressure distributions found for the low supersonic speed case with bay doors, not illustrated here, are in general similar, but at some vertical positions show complex longitudinal pressure variations

over the forward part of the missile due to interaction with the oblique terminal shock generated inside the cavity where flow becomes subsonic. Full details of all measured pressures are given in the test report⁹.

Missile longitudinal body loading distributions from integration of the measured pressures are shown in fig 10 for the shallow cavity configuration with no bay doors at subsonic speeds and for the bay door configuration at low supersonic speeds. It is clear that over the forward portions of the missile an inward (positive) normal force is experienced, and over the aft portions of the missile an outward normal force is generated, with maximum values at the rearmost section of the missile body. These variations are consistent with inward flow penetration over the forward regions of the cavity followed by a rapid outflow near the rear of the cavity as has been postulated in earlier reports^{1,2}. The observed body load variation will also significantly contribute to the high 'nose-into-cavity' pitching moment, as the inward acting normal force acts largely forward of the moment reference point and the outward acting normal force is aft of the moment reference. In the supersonic case the irregular nature of the loading distribution due to shock wave interactions is clear.

Fin loads together with the appropriate hinge moments are shown in fig 11 for the bay door case at low supersonic speed. Taking account of the sign convention defined in fig 7 for the panel load balances, these figures show that as the missile emerges from the cavity significant levels of outward force are generated on the fins (both lower and upper) and this again suggests the presence of a region of outflow towards the rear of the cavity. With the aft location of the rear fins, it is clear that the fin load will contribute significantly to the overall moment due to the large moment arm.

Corresponding wing loads are shown in figs 12 and 13 for bay door (supersonic) and no bay door (subsonic) cases. These loads are very small for the configuration with bay doors. For the subsonic configuration without bay doors wing loads are greater but still more modest than those experienced by the fins, and are generally less than half of the corresponding fin loads and act in an inward direction. Wing loads are at maximum values near the cavity exit plane for the inner wings, decaying to near zero inside the cavity and as the store moves further out of the cavity. The pattern is different for the outer wings with maximum values being found well within the cavity and decaying to near zero at short distances outside the cavity. As the AMRAAM wings lie near the mid-body length and near to the moment reference point the contribution to measured moment is relatively small and wing loads contribute little to overall measured pitching moment.

Fig 14 compares measured overall normal force and pitching moment with those derived by summing contributions from integrated body pressures, measured fin loads and measured wing loads which are also shown. The figure shows results for the configuration with bay doors at low supersonic speed. Trends in pitching moment and normal force are well predicted. Differences in magnitude are evident, and these are most likely to originate in the integrated body components, because, as discussed earlier, the forty pressures distributed over the missile in four rows of ten is insufficient to derive accurate loadings through integration. Nevertheless the measured overall forces and moments are in sufficient agreement with those derived from the separate components to be confident that the individual components correctly identify the sources leading to the measured overall values.

As can be seen in figs 14 the high pitching moments generated on the AMRAAM missile in the case of a shallow cavity arise almost

wholly from the contributions of the rear fins and the missile body. The wings situated approximately mid-way along the missile and also mid-way along the cavity length contribute little to pitching moment. When the missile is wholly within the cavity the body and the fins contribute approximately 50% each to the pitching moment. As the missile emerges from the cavity and moves into the free-stream the rear fin contribution increases relative to the body contribution.

Both the body and fin contributions to pitching moment are in keeping with a flow penetrating deep into the cavity in the forward regions and turning out sharply near the rear of the cavity, a flow pattern typical of cavities which are aerodynamically shallow^{7,12}. Within the cavity where pitching moment due to missile fins is lowest and comparable with the body generated pitching moment the fins are shielded from the full extent of the outflow, and as they move out of the cavity they experience the full extent of the outflow leading to the larger pitching moment contribution.

Body pitching moment is also in keeping with the inflow and outflow associated with this cavity geometry. The variation of body normal force along the cavity, fig 10, shows the highest inward normal force contributions over the forward portion of the missile, while over the rearmost portion the body experiences a high outward normal force due to the outflow. These opposing normal force contributions lead to the contribution to pitching moment of the missile body. The generation of this pitching moment is solely due to local incidences generated by the flow within the cavity as the missile is mounted at zero degrees of incidence within the cavity.

The build-up of the total normal force from the various components is also clear from fig 14. Again the correct trends are predicted. For the case shown in fig 14, the body and rear fin contributions are each approximately 50% with the wings making only a small contribution, indicating at near mid-cavity the wings are situated in a flow near to zero incidence. The body and fin normal force contributions are both negative or 'out-of-cavity'. In the case of the fin contribution this is due to the rear outflow, while for the body contribution the high outward force generated by the outflow at the rear dominates the inward normal force over the forward portions of the missile body. In the case of the basic cavity, without bay doors, in subsonic flow, not shown here, the total normal force derived from components agrees less well with that measured directly although the correct trend is predicted.

3.3 Measured store loads: deep cavity ($L/D=5.0$).

Fig 15 shows typical measured missile pressure distributions. Only results for the 0° and 180° pressure plotting stations are shown, and these are presented for four different locations of the missile both within and outside the cavity. When the AMRAAM missile is within the cavity (Z/d negative) pressure variation is very mild along the length of the missile and there are no signs of the existence of any suction peak over the nose region. On an ogival nosed body in uniform flow a suction region would be expected where flow accelerates round the shoulder region, thus, the absence of this peak indicates a lack of flow over the missile nose region. As the missile emerges from the cavity into the free stream it is evident that the expected suction peaks do appear as the nose experiences the free-stream flow. For the case of $Z/d=0.0$, where the missile nose is in the cavity exit plane there is evidence of nose suction on the 0° (outermost) pressure distribution but none on the 180° (innermost) distribution.

Measured fin and wing loads for the deep cavity are shown in figs 16 and 17. Wing loading, fig 17, remains close to zero throughout the traverse and fin loads are much reduced compared to those

found for the shallow cavity, fig 11, indicating the absence of any great outflow near the rear of the cavity.

A component load analysis identical to those for the shallow weapon bays has been carried out for the deep cavity. The variation of local normal force level integrated from the body pressures is shown in fig 18 where this is seen to remain at a low value showing a gradual increase towards the rear of the cavity. A comparison of the missile total pitching moment and normal force derived from the individual components with the values measured directly is presented in fig 19. The trends in both pitching moment and normal force are again correctly identified. In the case of normal force the main contribution arises from the missile body component and in the case of pitching moment both the body and rear fins contribute roughly equally, where although fin normal force is at all times small, the large moment arm provided by the fins being so far aft makes this contribute significantly to the modest total pitching moment.

These results for the deep cavity are in keeping with the flowfield found within an aerodynamically deep cavity^{1,2,5} where free-stream flow passes largely over the cavity without penetrating inside to any great extent, and an unsteady circulatory region is established within the cavity.

3.4 Value of results in design of missiles/weapons bays.

The data acquired provides a database which will be of great benefit in the design of a practical internal carriage weapons scheme involving missiles, and provides guidelines which can be used to minimise troublesome store loadings such as high pitching moment, which can lead to store release problems. The identification of the loads which will be experienced by each component part of the configuration provides information which is necessary to ensure the viability of missile structure.

Results for aerodynamically shallow weapon bays show that a large proportion of the very high pitching moment generated arises from the interaction of the cavity outflow on the rear fins. This suggests that pitching moment can be reduced by removing the rear fins from the rearmost section of the cavity. This is done naturally for missiles where fins are situated further forward on the missile body, and ref 1 shows that lower pitching moments were measured on an ALARM missile in a similar shallow cavity geometry. Another simple option would be to simply locate the missile within the cavity as far forward as possible, so that separation of the rear fins and the rear cavity wall was maximised, although this solution risks requiring the cavity length to be greater than would otherwise be. Yet another option would be to install the missile with deflected fins, but this demands that missile control be active during the release process. The final obvious option, albeit requiring investment in missile design, would be to employ compressed carriage which has received some consideration, where when in-carriage missile fins are folded or wrapped around the body to be deployed after release.

4 UNSTEADY PRESSURES ON MISSILE.

4.1 Previous studies.

A number of earlier studies^{1 to 6}, have shown that within a weapons bay a harsh unsteady pressure or acoustic environment is generated which in certain cases could affect store structural integrity. Different types of unsteady environment are found depending on cavity geometry. For cavities which are aerodynamically deep¹ very high levels of acoustic disturbance is found. rms (root-mean-square) values of up to 174dB have been measured. In addition most of the acoustic energy is concentrated into a small number (three to four) discrete tones. For cavities which are aerodynamically shallow¹ high acoustic levels are still measured

(up to 160 dB has been measured) but the level is not as extreme as for deep cavities and the spectrum is broadband in nature with amplitude decaying steadily with increasing frequency.

Theories have been put forward by Rossiter¹⁰, and Tam and Block¹¹ on the mechanism of the observed tones for deep cavities. The former assumes a coupling of reflected acoustic disturbances with vortices shed from the front face, whilst the latter cites the effect of reflected acoustic disturbances on an unstable shear layer separating the cavity from the free stream. Both theories propose ways to calculate the frequencies at which such tones will occur, the former on the basis of empiricism, and the latter on the mathematical treatment of sound waves interacting with a shear layer. The two prediction techniques have been shown to give reasonable agreement with the observed frequencies in some cases. To date however, although attempts have been made, no method has been found to estimate the level of acoustic disturbances generated within a wide range of cavities, or how these levels may be modified by palliative devices.

Earlier work^{1 to 4} has analysed unsteady pressure data measured by means of high frequency response pressure transducers installed on the ceiling and walls of weapons bay cavities. For deep cavities it has been shown that the discrete tones can be reasonably well predicted (usually to within 5%) by the empirical formula developed by Rossiter¹⁰. In the current investigation the twenty unsteady pressure transducers in two longitudinal rows of ten, as shown in fig 4, allow the unsteady pressures acting on the missile to be measured, and for these to be compared with the measurements made on the cavity ceiling and walls.

4.2 Missile unsteady pressure : deep cavity (L/D=5.0).

Typical results from the unsteady pressure measurements on the missile within a deep cavity, (L/D=5.0) are shown in fig 20 with the missile at a position within the cavity of Z/d=0.5. The traces give the signal power spectral density plotted in terms of rms pressure amplitude. Results are plotted for pressure transducers at two different locations along the missile, x/l=0.138 and x/l=0.905. The results shown are with the missile at a roll orientation of 0°, and are located on the side of the missile nearest the cavity exit plane. Only results for M=0.85 are shown and discussed, as these are typical of all results at Mach numbers up to high subsonic, and those at low supersonic Mach numbers.

Results are similar to those measured on the ceiling of the same cavity in previous tests² and repeated in the current tests. The presence of several discrete frequency tones is evident, and most of the sound energy is concentrated into these tones. Extremely high levels of overall sound pressure level (SPL), varying at the locations shown from 157.5 dB to 167.8 dB are observed.

The frequencies of the discrete tones have been compared with predictions made by the empirical formula derived by Rossiter¹⁰. The empirical formula is:

$$f = \frac{U}{L} \frac{(m - \gamma)}{M / (1 + 0.2 M^2)^{1/2} + 1.75}$$

where f is frequency, U is free stream velocity, L is cavity length, m is a mode number taking values 1,2,3,....., and γ is a constant which depends on cavity L/D. Rossiter¹⁰ ref 10, determined the values of γ experimentally for cavities up to L/D=10, and this has been subsequently extended to L/D=13¹.

The frequencies calculated from Rossiter's formula for the deeper cavity are compared with those measured in fig. 20. Four of the

measured frequencies are predicted well, and to within 5%. One frequency not predicted by the Rossiter correlation, at 765 Hz is also evident. This frequency would appear to be a higher harmonic of the frequency at 382 Hz, which is indicated by the Rossiter correlation. All the measured frequencies of fig 20 are identical to those measured on the ceiling of the cavity.

Total rms sound pressure level (SPL) is found to increase from front to rear along the missile, with maximum values being found at the aft end as shown in fig 21. In this figure the variation of total rms sound pressure level with cavity longitudinal position (X/L) is shown for the unsteady pressures measured by the transducers located at the zero degree roll position, fig 7. This variation is similar to that found on the cavity ceiling, and the local minima found around 25% and 75% of cavity length² are evident. It is clear from fig 21 that unsteady pressure levels measured on the cavity ceiling or the cavity walls, as has been the case in earlier tests, does not necessarily define the maximum levels to which the missile will be subjected. Unsteady rms pressures are shown for two different depths within the cavity, one location outside the cavity and as measured on the cavity ceiling. As the missile moves through the cavity starting from its maximum depth within the cavity, unsteady pressure level increases. At a position with the missile axis 0.5 store diameters within the cavity unsteady pressure level approaches a maximum which is some 50% greater than the level measured on the ceiling. As the missile leaves the cavity unsteady pressure level is seen to decay fairly rapidly. It is not claimed that the precise location of the plane where maximum levels of sound pressure level occur has been identified, only that this is in the region near to the missile exit plane. Further analysis of existing data will allow the location of highest unsteady pressure to be determined more precisely.

4.3 Missile unsteady pressures : shallow cavity ($L/D=10.0$).

For shallower cavities, where L/D is large enough to ensure closed or at least transitional closed flow¹, essentially when the free-stream flow achieves substantial penetration into the cavity, the unsteady pressure environment is less severe than for deeper cavities, and generally does not exhibit discrete tones, although in some cases weak tones can be detected.

As shown in fig. 22, for the $L/D=10$ cavity at a Mach number of 0.85, the unsteady pressure signal is random in character, displaying a broad band of frequencies, whose amplitude decays gradually as frequency increases. Total rms sound pressure level is much lower than that found for the deep ($L/D=5.0$) cavity shown in fig 20. The unsteady pressure signal measured at a single point at a longitudinal station of $x/l=0.905$ on the missile is compared in fig 22 with that measured at an adjacent point on the cavity ceiling. It is evident that the two traces are almost identical in character, but that the rms sound pressure level measured at this point on the missile is some 10% higher than that measured on the cavity ceiling. This suggests that unsteady pressure measurements made on the cavity ceiling or walls provides a good measure of the type of environment to which the missile will be subjected, but that amplitude may well be different on the missile.

As for the deep cavity, overall sound pressure level (SPL), fig 23, increases as the missile moves outwards from its innermost position in the cavity, reaching a maximum about half a missile diameter inside the cavity. As the missile moves out of the cavity overall rms SPL decays significantly.

5 CONCLUSIONS.

This phase of the DERA research programme on the internal carriage of stores has investigated the different sources contributing to the overall forces and moments acting on a missile when located

in or near open weapon bays. It has also provided detailed time-averaged and unsteady pressure measurements over a missile together with wing and fin loads as the missile is traversed through weapon bays of different geometry.

The results show that the trends observed in the measured forces and moments on an AMRAAM missile within a weapons bay can be correctly predicted by summing the contributions from missile body, missile fins and missile wings. This allows the relative magnitudes of the different components to be identified.

The identification of the loads experienced by each component part of the configuration provides design information which is necessary to ensure the viability of missile structure.

The data acquired provides a database which will be of great benefit in the design of a practical internal carriage weapons scheme involving missiles, and provides design guidelines which can be used to minimise troublesome store loadings, such as high pitching moment leading to store release problems.

Results for aerodynamically shallow weapons bays show that a large proportion of the very high pitching moment generated arises from the interaction of the cavity outflow on the rear fins. This suggests that pitching moment can be reduced by removing the rear fins from the rearmost section of the cavity.

This is done naturally for missiles where fins are situated further forward on the missile body. Another simple option would be to locate the missile within the cavity as far forward as possible so that separation of the rear fins and the rear cavity wall was maximised. This solution risks requiring the cavity length to be greater than would otherwise be. Yet another option would be to install the missile with deflected fins, but this demands that missile control be active during the release process. The final option, albeit requiring investment in missile design, would be to employ compressed carriage, which is being elsewhere, where, when in-carriage, missile fins are folded or wrapped around the body to be deployed after release.

Unsteady pressures measured on the missile body are shown to have the same character as those measured on the cavity ceiling or cavity walls. In both deep and shallow cavities the missile is subjected to high levels of unsteady pressure. For deep cavities the acoustic environment is particularly harsh with most of the energy being concentrated into a small number of discrete tones. For shallow cavities the missile is subjected to a broadband frequency spectrum with amplitude decaying with increasing frequency.

Unsteady pressures measured on the cavity structure do not necessarily provide a correct measure of the amplitude to which the missile is exposed. As the missile emerges from within a weapons cavity, rms sound pressure level increases to a maximum with the missile near the cavity exit plane, and decays rapidly as the missile moves clear of the cavity.

6 ACKNOWLEDGEMENT.

The contribution to the work described in this paper by Mr R Sale and Mr J Carberry and other staff at Aircraft Research Association, Bedford, where much of the test programme has been carried out is gratefully acknowledged.

7 REFERENCES.

- 1 J. A. Ross, J. W. Peto, "Internal stores carriage research at RAE", RAE Tech Memo Aero 2233 Jan 1992.
- 2 J. A. Ross, J. W. Peto, M. A. Waskett "Internal stores carriage: the aerodynamic effects of weapon bay flowfields

on the internal carriage and release of stores", DRA/AS/AP/CR 93002/1 Aug 1993.

3 M. Waskett, J. A. Ross, "Internal carriage of stores : the effects of weapons bay doors", DRA/AS/HWA/ CR94292, Dec 1994.

4 J. A. Ross, M. B. Wood, J. W. Peto, "Internal carriage of stores :the effects of asymmetric carriage and multiple stores", DRA/AS/HWA/CR94139/1 July 1994.

5 F. J. Wilcox, "Experimental measurements of infernal store separation characteristics at supersonic speeds", Royal Aeronautical Society Conference Proceedings, Bath UK, 4th-6th April 1990, Paper No 5, April 1990.

6 R. L. Stallings: "Store separation from cavities at supersonic flight speeds." J Spacecraft, Vol. 20, pp 129-132, Apr. 1983.

7 R. E. Dix : "On simulation techniques for the separation of stores from internal installations." SAE Technical Paper Series 871799, Oct. 1988

8 A. B. Blair and R L Stallings: "Cavity door effects on Aerodynamic loads of stores separating from cavities." J. Aircraft, Vol 26, no. 7, pp615-620, July 1989.

9 R. Sale, "Details of tests in the ARA 2.74m x 2.74m transonic wind tunnel measuring the release disturbance of weapons carried in cavities. Sixth test series - October 1994. Pressure plotted missile and initial cavity bleed studies", ARA Contractor Report M219/18, Nov 1994.

10 J. E. Rossiter "Wind tunnel experiments on the flow over rectangular cavities at subsonic and transonic speeds", RAE Technical Report 64037, 1964.

11 C. K. W. Tam, P. J. Block "On the tones and pressure oscillations induced by flow over rectangular cavities", J. Fluid Mech, Vol 89, Part 2, pp 373-399, Nov 1978.

© British Crown Copyright 1998 /DERA.
Published with the permission of the Controller of Her Britannic Majesty's Stationary Office.

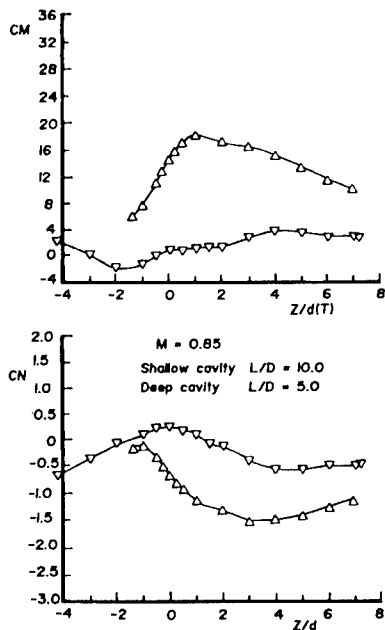


Fig. 1 Comparison of normal force and pitching moment on missile in shallow and deep cavities

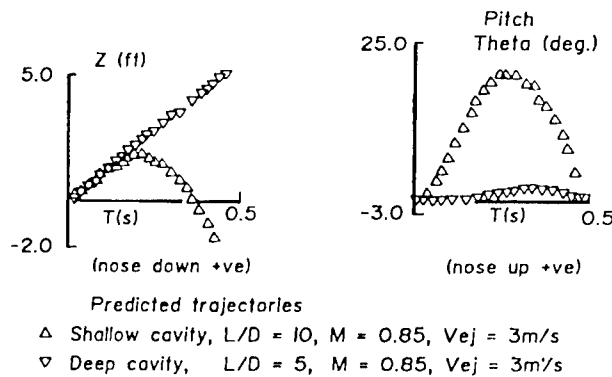


Fig. 2 Simulated missile release trajectories from shallow and deep cavities

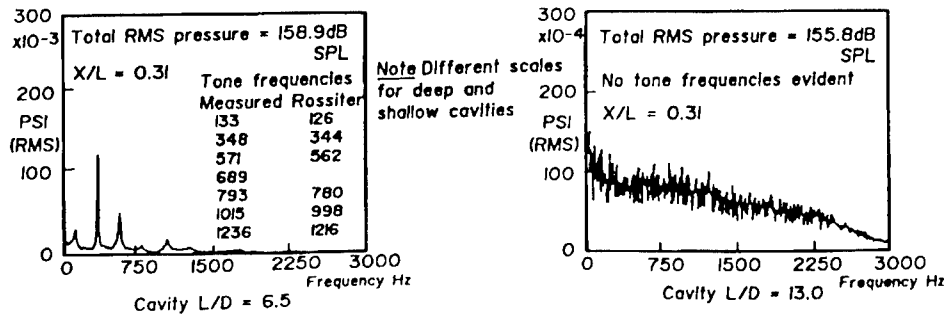


Fig. 3 Unsteady pressures in deep and shallow cavities

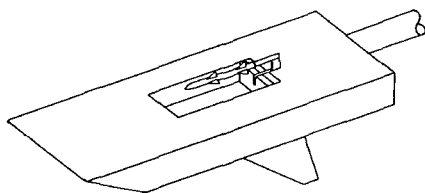


Fig. 4 Cavity with aft packing blocks simulating rearward movement of missiles

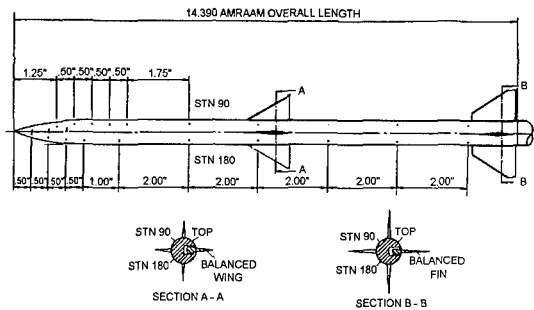


Fig. 5 Details of pressure plotting on AMRAAM missile

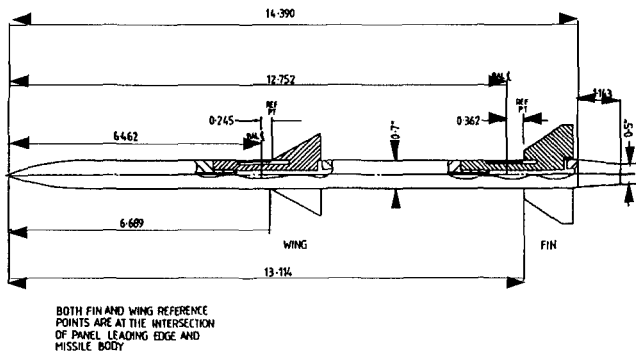


Fig. 6 Details of missile wing and fin panel balances

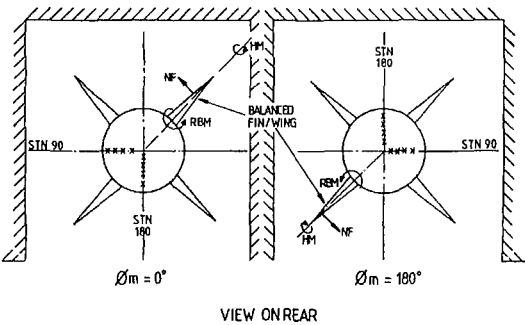


Fig. 7 Panel balance sign conventions and missile orientations

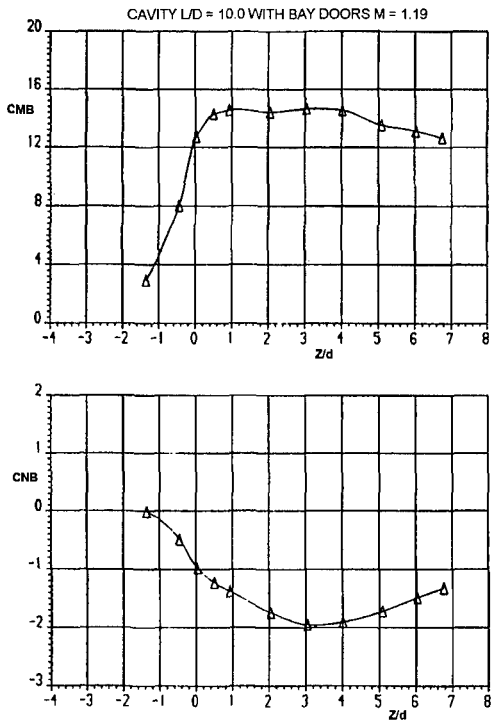


Fig. 8 Measured total pitching moment and normal force on AMRAAM missile in shallow cavity $L/D = 10.0$, with bay doors, $M = 1.19$

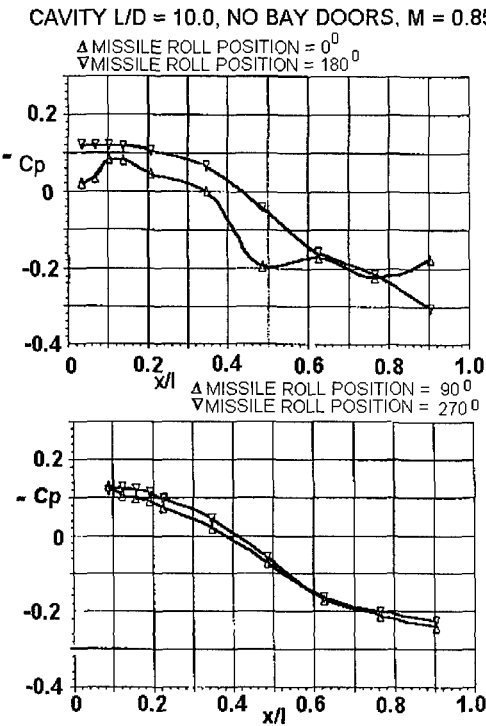


Fig. 9 Longitudinal pressure distribution along AMRAAM missile in shallow cavity $L/D = 10.0$, no bay doors, $M = 0.85$, $Z/d = 0.5$

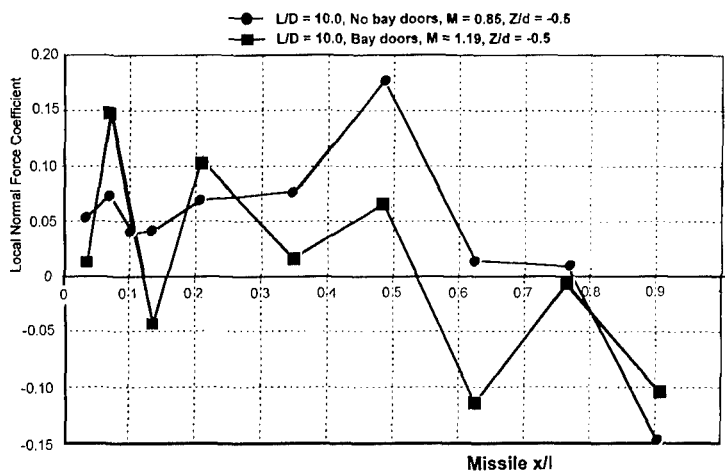


Fig. 10 Variation of local body normal force coefficient along missile body in shallow cavity $L/D = 10.0$

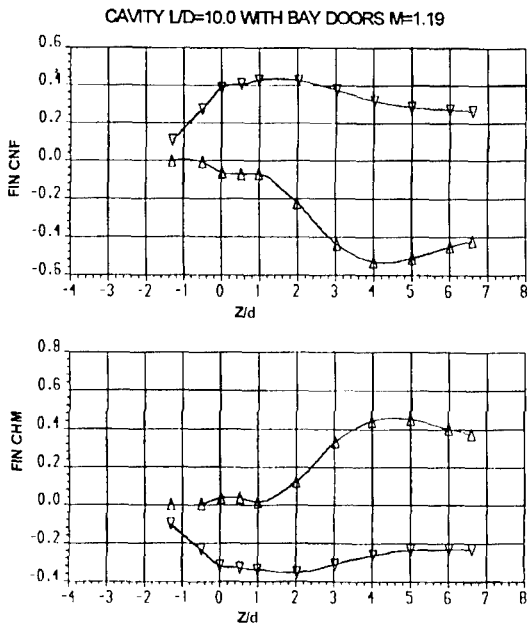


Fig. 11 Measured fin normal force and hinge moment on AMRAAM missile in shallow cavity $L/D = 10.0$, with bay doors, $M = 1.19$

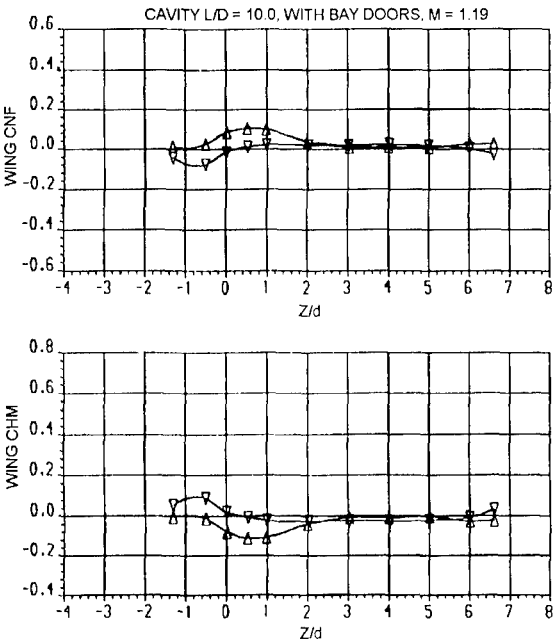


Fig. 12 Measured wing normal force and hinge moment on AMRAAM missile in shallow cavity $L/D = 10.0$, with bay doors, $M = 1.19$

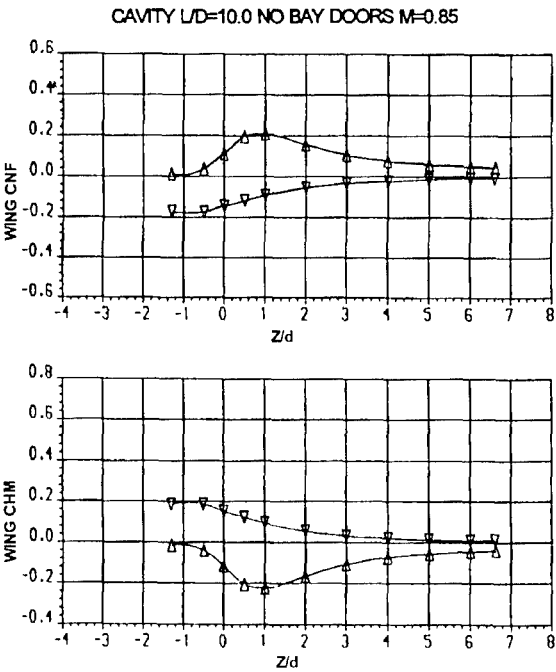


Fig. 13 Measured wing normal force and hinge moment on AMRAAM missile in shallow cavity $L/D = 10.0$, no bay doors, $M = 0.85$

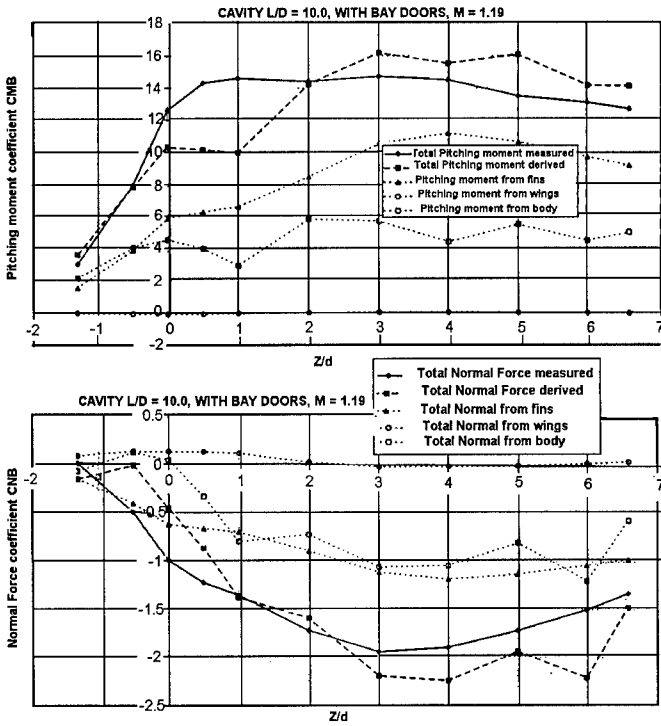


Fig. 14 Comparison of measured missile pitching moment and normal force and pitching moment and normal force derived from fin, wing and body components in shallow cavity $L/D = 10.0$, with bay doors, $M = 1.19$

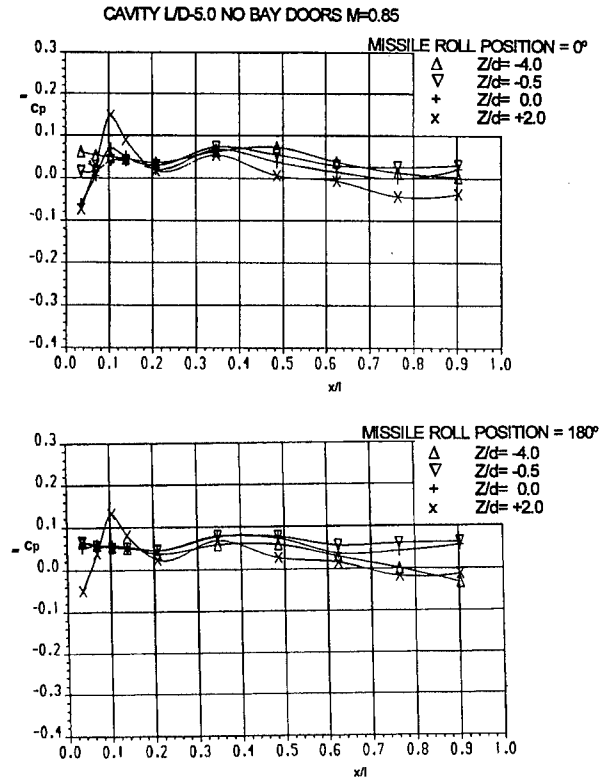


Fig. 15 Longitudinal pressure distribution along AMRAAM missile in deep cavity $L/D = 5.0$, no bay doors, $M = 0.85$, $Z/d = -4.0, -0.5, 0$ and 2.0

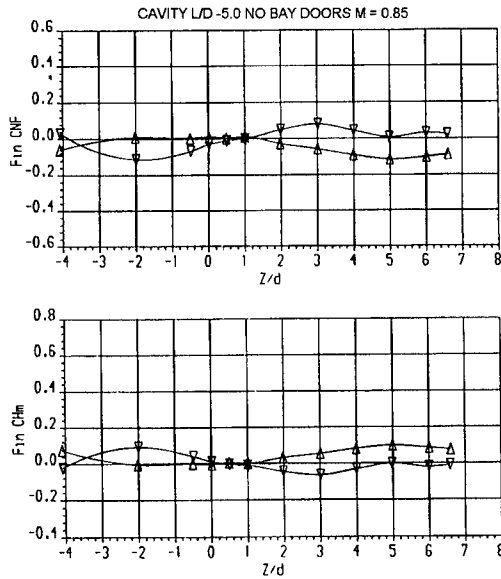


Fig. 16 Measured fin normal force and hinge moment on AMRAAM missile in deep cavity $L/D = 5.0$, no bay doors, $M = 0.85$

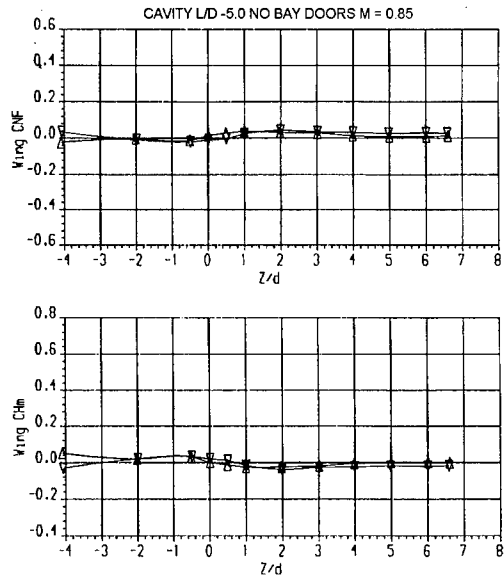


Fig. 17 Measured wing normal force and hinge moment on AMRAAM missile in deep cavity $L/D = 5.0$, no bay doors, $M = 0.85$

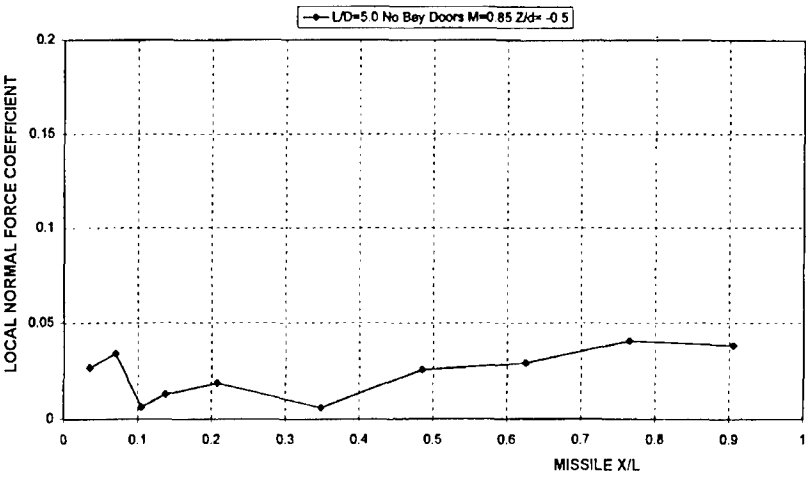


Fig. 18 Variation of local body normal force coefficient along missile body in deep cavity $L/D = 5.0$

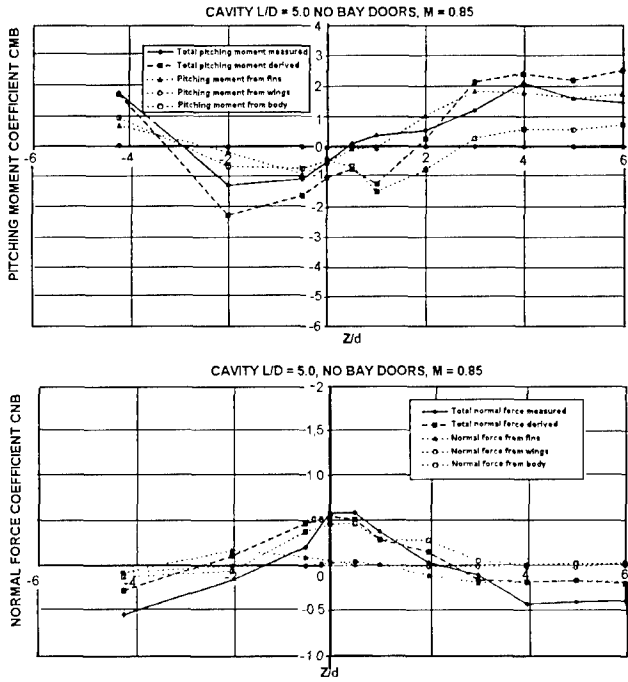


Fig. 19 Comparison of measured missile pitching moment and normal force and pitching moment and normal force derived from fin, wing and body components in deep cavity $L/D = 5.0$, no bay doors, $M = 0.85$

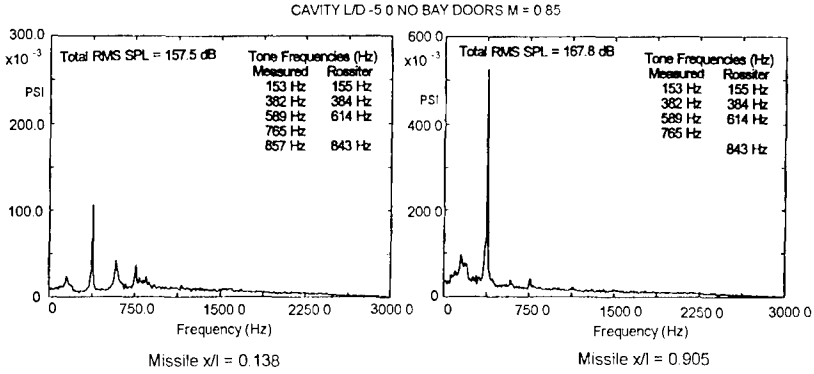


Fig. 20 Spectrum of unsteady pressure at two locations on missile body in deep cavity $L/D = 5.0$, $M = 0.85$, $Z/d = -0.5$

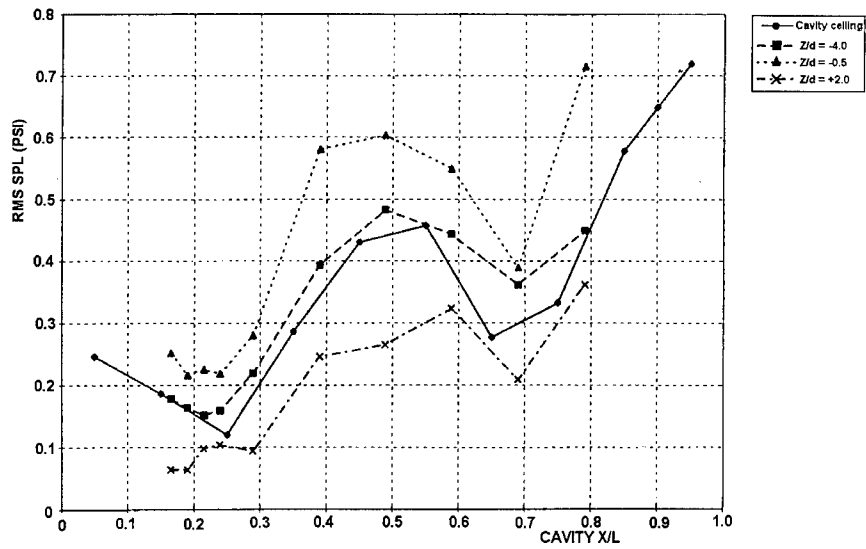


Fig. 21 Variation of total RMS unsteady pressure along cavity ceiling and AMRAAM missile at different Z/d positions in deep cavity $L/D = 5.0$, $M = 0.85$

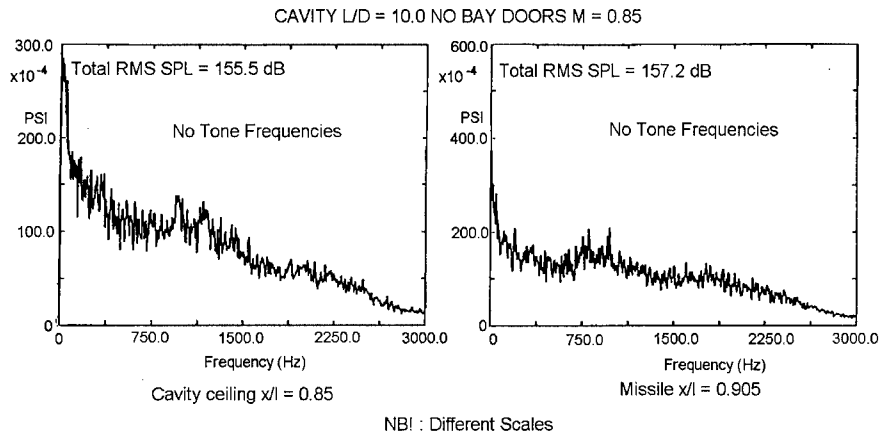


Fig. 22 Spectrum of unsteady pressure on cavity ceiling and at one location on missile body in shallow cavity $L/D = 10.0$, $M = 0.85$

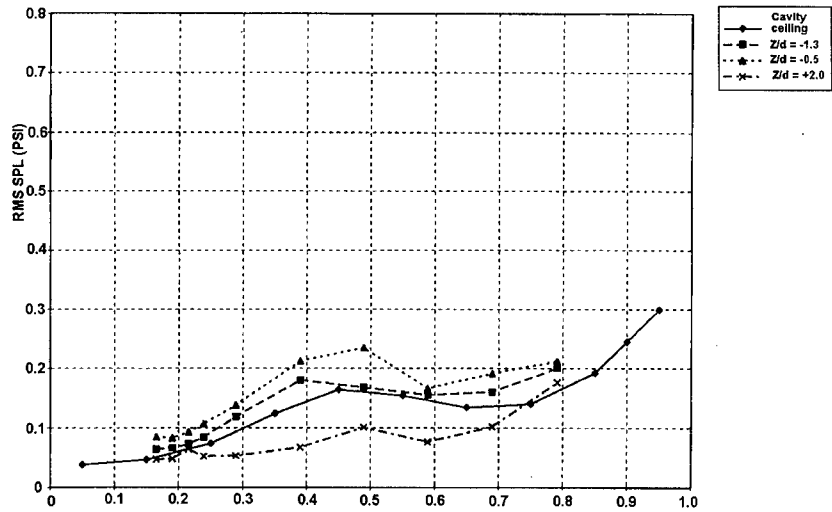


Fig. 23 Variation of total RMS unsteady pressure along cavity ceiling and AMRAAM missile at different Z/d positions in shallow cavity $L/D = 10.0$, $M = 0.85$

GENERAL DISCUSSION

R. Lacau, Aerospatiale, France

First we start with the Technical Evaluation, secondly, the General Discussion and finally, the closing remarks. The Technical Evaluation will be given by Dr. Paul Hennig. He is from Daimler-Benz Aerospace.

Dr. P. Hennig, Daimler-Benz

See Table of Contents for Technical Evaluation Report

M. Lacau

Thank you for this evaluation and relevant remarks which I think are good introduction for the general discussion which now is going to take place. Who will start?

N. Malmuth, Rockwell International, USA

I am in tune with a lot of what was said by the reviewer. Several thoughts came to mind as he was talking. I was thinking about some crosslinks regarding some of the subjects that he had down there, and some of the areas that have not been really discussed in this conference. I think that they would be good ones for future conferences. One of them is terminal ballistics, like high penetration, heavy missiles that can be used to penetrate targets. This is one area of interest. Another that is very closely related to the store separation problem is hypersonic vehicle staging. There is actually a general connection between missiles and ballistics that I think can be explored in a conference. So an even more general kind of conference can be considered, pardon the risqué title "Bodies in Relative Motion". You have discussed some interesting work. Let me quickly turn now to the breakdown that you made with respect to the different ways to approach the problem. You had a box that had to do with empirical methods. Another dealt with experimental methods. Yet another was called numerical methods. However, one box, which I think has not really been emphasized, and is an extremely important one, is 'theory'. Russians are very good at blending these things because their computers are not as powerful as ours yet. I think they understand this very well. When I talk about theory, I want to make it very clear what I mean. Normally, when we do CFD we have equation sets, such as linear theory and small perturbation theory. The latter could contain some non-linearities. Then we go to Euler and then Navier Stokes. For each class of problems, there are intermediate equation-sets that can be exploited for various problems. From the vantage of modern CFD, this is a highly neglected subject that we have to come back to. Some of the points you raised about doing work on speeding up is relevant to our 1999 Symposium, relevant to development and exploitation of fast turn-around techniques for optimization. In theory, we can do various things, we can make asymptotic approximations, which we can refine systematically. Today a neglected aspect has to do with similarity techniques such as the classical work of Sedov, for which there are many examples. I would like to see that field return and complement the CFD to achieve a symbiotic relationship between CFD, experiment, empirism and theory.

P. Hennig

It is true what you say. I thought that I included it here in the semi-empirical, and as I mentioned what I think is very, very important and what I missed in some presentations is the general insight into physics and what you say of theory, really means thinking of physics.

N. Malmuth

There is a process that you had on your hand written vu-graph. We are trying to get the first-order physics. The next thing is to get a mathematical equation set, a framework to express that. One of the presenters talked about an angle-of-attack 90 degree point. That is a very interesting case. How do I treat one 90 degree case? The first thing that comes to mind is that it looks like a crossflow over a cylinder. Is that an incompressible problem with vortex shedding? I can model that in certain time scales and length scales that are close or irrelevant to reveal the essential first-order of physics. I think it is the link between the physics and making this an approximate sound theoretical model. When I talk about empirical stuff there is a data-base, and I am hanging everything on the data-base, but this is different than theory.

P. Hennig

That is different. It is more like modeling and then analytical formulation.

G. Sutton, Anser Corp. USA

First of all, you had validation in quotation marks. I like what Paul Ruppert calls it. He calls it "reconciliation" between the CFD or the computer code results with the wind tunnel data. Second of all, the practicality is very important. I just don't see the aerodynamicists talking enough with materials and seeker people. I put together a very simple computer program for fly outs of interceptors. It includes everything: the thermal stress in the window, the window heating, the signal to noise, etc. It runs in 10 seconds per fly out, and I think I can reduce that to 1 second. Finally, and it has not

been discussed here, I think the onboard computer people have oversold themselves with respect to modern missiles. They have not delivered on the computational capabilities that the project office was counting on to steer the missile. Therefore, there have been many misses because of that. Part of that problem is the standards for the software, meaning how do you do the quality assurance of the software? That has not worked in many occasions. The failure has been in the computer and software. I would like to see more of the missiles be less dependent upon very sophisticated computer software and computer hardware because of this issue.

F.G. Moore, Naval Surface Warfare Center, USA

I would like to comment on one of your bullets about the semi-empirical models for side jets. I agree with that wholeheartedly and have been trying to market that now for over two years to our Ballistic Missile Defense Office. The basic fundamental problem, at least in terms of making a fast code, is that one needs a good data base. We have all these good data bases without jets for missiles and component buildup techniques. That has been the key in my judgment in making these fairly accurate semi-empirical models that do a reasonable job of modeling the physics of the non-linearities. In order for us to do the same thing with these side jets, we have to have a data base that has these jets going off at different places along the body with fins located at various relationships to the jets. It is a fairly expensive thing, and so far we haven't been able to be successful in getting that funded. We are still working on it, but it is an expensive process.

P. Hennig

It certainly is an expensive process. I mentioned especially in the case of those many-parameter problems, at least in Europe, we won't get the funding for it, so we have to select, and we have to select very, very, very carefully what we really want to measure, what we really want to calculate. That is connected very much inside the physics of the flow because we cannot afford to do another experiment with the same physical boundary conditions just a similar geometry, a little bit different geometry. We really have to concentrate on what is really different and select those things and try to fill our big multi-dimensional parameter space.

M. Dillenius, Nielsen Engineering & Research, USA

First of all, in answer to Frank Moore's comments, don't forget there is a data base called SIDJET put together in 1981 for the Navy - limited, but that is the beginning. Look at it sometime, it is not that bad. I could tell you more about it.

At Nielsen Engineering I have been involved in analytical prediction methods. It makes you kind of narrow minded. Then you talk with a missile airframe maker. I don't care what you say, it is the design cycle time that is important. Guidance and control guys say that they can do anything. Missile airframe designers believe wind tunnel tests, and they can be accomplished faster. I think this is the reality. However, this may change. Why? New Requirements. New missiles are going to maneuver, they are going to turn very fast. This is a challenge to the aerodynamic prediction people. CFD guys better learn how to do unsteady aero, meaning the vortex lag problem. That is the primary unsteady phenomena for a missile, that the missile actually moves under its own vortex cloud, if you want to call it that. That affects its aerodynamics. One thing we didn't hear about is the unsteady aero associated with the peculiar requirements of a sea-skimmer. Now if you look at the sea-skimmer, it sees the waves underneath which can cause unsteady aero. If it is long, it starts to flex. The simulation guys, and here again G and C people say that they have got it in hand, do not worry too much. Then they won't listen to the aerodynamicists until there is a problem. The seeker thinks it is at some altitude from the wave top and then sends that information to the controller, and in the meanwhile the missile is in a different position entirely. Some people know about that. Anyhow, I thought I'd bring up the sea-skimmer for the unsteady aerodynamics. I do mean REAL unsteady aerodynamics; I don't mean quasi-unsteady aerodynamics. We talked about submunition simulations. That is a missile problem and a nasty one. We have only seen the most simple setup. You can do that with simpler methods too, and get a first good estimate. For cases where the dispenser is at non-zero angle of attack, you have asymmetry in the problem and you better see how the trajectories go for each one of the submunitions. That is why the trajectories sometimes get so messy. So, when I started this little personal opinion, I was going to tell you that at the meetings that I have been to, the guidance and control people think that the aerodynamics are at best something that you worry about later. But I am hoping that because of the new requirements, and do bear in mind the new requirement of high maneuverability, the reduced frequencies might finally reach the level where vortex lag effects and maybe other REAL unsteady aerocffects become important. The CFD specialists better think about that. You have got your turbulence modeling problems, but the new requirements add a whole new challenge to missile aerodynamics prediction.

P. Hennig

I want to add something. Sea-skimmer is a problem like many other unsteady problems. There is also a problem in launch itself. High speed launch or launch of many missiles with short time in between them. There is a problem of

those interacting fields and especially in store separation, you did not mention now the airplanes being maneuvering while you have a store release. That is one of the biggest problems. The self-defense missiles of an airplane are sitting usually in very ugly areas of the airplane, in some edges or corners or something, and if you have high g maneuver of the airplane, and angle of attack, and you have to have the store separation of that, that is a real tricky problem.

M. Khalid, IAR/NRC, Canada

I think we expect too much in the way of excellence in performance from numerical methods, which may be based on semi-empirical formulations of classical methods or even modern CFD. Especially, when we know that in certain flow regimes numerical methods will not be able to cope. We should also place equal emphasis on quality of results from experimental data. We may want to conduct an uncertainty analysis of the possibility of errors in various measurement techniques and also appropriately address sting and tunnel wall interference effects in the entire range for which the experimental data is presented. It would not be such a bad idea to associate error bars whenever presenting experimental data against which numerical results are to be validated.

P. Hennig

You are certainly correct and I must add that. I mentioned the possibility of validating experimental data by some calculations.

K. Runne, DASA-LFK, Germany

I would like to suggest to add to the topics which have to be considered more deeply, which are mostly not very well understood, the topics of thermodynamics, especially we consider that in the future the ramjet missile will play certainly an important role, problems of thermodynamics of ideal and real gases have to be better understood. This is also valid for vertical thrusters for control. There are already a lot of theoretical possibilities, also a lot of programs, which can be used in connection with CFD. Of course, also on the semi-experimental field, many more things can be done than are done now. We had this time, two presentations on intake problems, but what was told is just the beginning. Much more has to be done and will be done in the future, and I think this topic of thermodynamics or aerothermodynamics should be integrated.

K. Naumann, ISL, France

I agree with the former comment. Certainly, every time will come up new methods which are very highly interactive and interdisciplinary. This also will surely encompass propulsion. For example, there was no pulsed detonation propulsion at this conference. But it is really hot stuff. With the detonation it is a special thing. There may also be other kinds of combustion. You are a ramjet man, but the scramjet will be also interesting for missiles. At ISL we are working experimentally, for example, also on the external combustion which might provide a very easy means of guiding very high-velocity projectiles, but it is very intrinsic and very tricky, so surely it is nothing which will be applied in the next decade, but the topic of missile aerodynamics surely is open to every time very new and very advanced developments.

P. Hennig

Yes, I think that we have the same opinion of this interdisciplinary point that was mentioned before concerning warhead and the penetration problem. There are a lot of these points. I don't know, probably I have not written down everything, but you can see a lot of fields which are connected with aerodynamics and which you have to consider in the future.

R. Lacau, Aerospatiale, France

I would like to make a comment about this last remark. Paul mentions what he called the interaction with other subjects or disciplines. My comment is not concerning techniques. My comment concerns organization. One year ago, there was a Fluid Dynamic Panel, Propulsion Panel, a Structure Panel and between these panels there was a wall, even though we had information, now this is finished. We move together FDP, PEP and SMP. You know in several companies now this has also been done for several years, usually in a private company we go quicker than in the research lab. If I look at this picture, there are different colors, I don't know if it is for the technique or if it is organization. It is physical fields? O.K. I will say, for example, at Aerospatiale Missile, today we group together structures, propulsion, aerodynamics, signature, in one group which were before three or more and now we put them together. It is the same, I believe, at MATRA. They put together what is now called Flight Dynamics. They put together aerodynamics, propulsion, signature. So we are on the good way to have a better interaction between all these kinds of physical disciplines. Just a last word. It is the way to go to multi-disciplinary optimization. Multi-disciplinary optimization can only go if people work together, but when you have an organization with walls, it is very difficult. Now they are all together, and it is a good organization, will go quicker in design and to reduce the cost of design, and to go to optimal design also.

R. Lacau

If there are no more comments, we will conclude this general discussion. It is time to close this Symposium. Let me just remind you that we have 115 persons who attended. There were 41 presentations. I hope you have been satisfied by these presentations which have covered numerous topics, I will not repeat what Paul has mentioned. We have seen

progress since the last meeting, and we have also shown progress on the work which still remains to be done. Now I invite Prof. Ciray for the formal closing.

C. Ciray, Middle East Technical University, Turkey

Thank you Dr. Lacau.

Ladies and Gentlemen. We come to the end of another activity of the past FDP, now RTO-AVT, the Symposium on Missile Aerodynamics. I think you would agree with me that we can consider it a successful Symposium. It is time to say *arrivederci*, but before saying this, we have to do something else. Let me go back two years. In a meeting of another Symposium like this of FDP, we had proposals prepared for our future FDP activities. There was a suggestion that we should make a symposium on missile aerodynamics. It was considered to be ripe. The idea essentially came from Dr. Lacau. This idea was discussed in the Panel, and it was accepted and endorsed. Then it was approved by the NDB. So it has been formally on the Agenda. Then we formed a Program Committee to organize this. I am going to mention the names of its members, and if they are present, I want them to stand up. Prof. Decuyper, Jean Muylaert, Dr. Lou Chan, Dr. Lacau, Mr. Sacher, from Greece Capt. Smyrlis, Prof. Golia, Prof. Russo, Mr. Elsenaar, Mr. Grandum from Norway, Dr. Luis Calavera, Capt. Akcay, Mr. Herring, and Mr. Dave Selegan. These gentlemen have worked for two years to organize. Please join me to thank them.

This was the technical part, but we had also a lot of things to be done for the organization. First of all, the local organization committee has decided on this nice surrounding of Sorrento. They have organized a wonderful reception on the first night, the buffet dinner on Monday night, and also the very nice treatment for the coffee breaks. The one behind this was our local coordinator and FDP man, Prof. Golia. Thank you, Prof. Golia. We thank also CIRA for the support and the sponsorship of the whole event. We have to thank for the technical tour to CIRA, which I think was a wonderful experience. Also to the General Director of CIRA, Mr. Mario Sala. Prof. Golia, please convey our thanks to him.

A technical meeting like this owes a great deal to the authors of the papers. The papers were really good. We thank the authors of the papers and mostly we thank those people who came to present their papers. We owe them an ovation. We have had a deep and highly learned evaluation of this meeting. The Technical Evaluator, Mr. Hennig from Daimler-Benz/LFK has done a good job, almost an academic lecture. It was very good. We thank you very much and also we thank those who have contributed to the discussion.

The sessions were administered well, and the papers almost always finished at the right time and almost always we had good discussions and a good deal of comments about the papers. Join me to thank the Chairmen of the Sessions. Whether the papers were presented in English or French, you always had the possibility to understand what was said. We owe thanks to the interpreters who were sitting behind these windows. I would like to mention their names, and ask you to show your appreciation. They are: Mme Lamon, M. Sheray, M. Delipia. Sometimes you were not very happy with the electronic gadgets, and some people referred to mechanical ones they had. But I think all-in-all the system was run very well and the presentation of these nice *vu-graphs* and so on have been shown in an expert way. We thank the technicians from SHAPE in Napoli, they are Sgts. McCrerey, Ladbroke, and a few young persons who were bringing the microphones and they are the students of Prof. Golia. We thank them all for their help. Now I am coming to the mastermind behind all this. There are two people behind: one of them is Jack, and if I call him Dr. Molloy, he is angry, but nevertheless, he can not say anything at this moment, later I do not know what he is going to do to me, Jack Molloy and Miss Danielle Pelat, we thank you very much for everything you have done.

No meeting is a successful one without a good, lively audience. I think the audience was wonderful, whether they were commenting or listening or whether they were discussing, they have contributed to the success of this meeting. Thank you ladies and gentlemen.

We come to some more serious matters. As it is our custom, we speak about our future activities. First, 1998 fall meeting, we are going to have two Symposia. You may realize that 1998 and 1999 are kind of transition periods from AGARD to RTO, 1998 is much more in the sense of AGARD, whereas 1999 is going to be more in the sense of RTO and starting with 2000 it is going to be all RTO. In October in Amsterdam, the old FDP is going to have the Fluid Dynamics Problems of Vehicles Operating Near or in the Air-Sea Interface. I recommend you attend this meeting. This is going to be a very, very interesting one. We have decided to have about 35 or 36 papers. Out of the 36 papers, if I remember right, about 15 or so are coming from Russia and the Ukraine. You will see very different type of creatures imagined to move close to the sea. Whether you personally are interested, or your company or your country is somehow interested, do something so that somebody attends this meeting. Don't be afraid whether you will understand Russian or not, we are going to have very good translations from Russian to English and to French. The papers will appear in English. That is going to be a good meeting. It was very difficult to make a selection, there were so many good papers. But it is exciting for the future. The other one is "Gas Turbine Engine Combustion Emission and Alternative Fuel". This is also going to be a good meeting. It will take place in Lisbon. Then we will have two workshops running at the same place, almost at

the same time. This is Corfu. The first one is the "Qualification of Life-extension Schemes for Engine Components" and the other one is "Structural Fatigue in the Presence of Corrosion". I think is very good to be studied at Corfu. This is our 1998 Program. I am going to say one or two things more about 1998, but it is going to appear in the last vu-graph. Now we come to 1999. This is much more on the RTO side. As it was suggested before, three groups of people from the old FDP, SMP, PEP are coming together; so we are going to have a big meeting. We are going to have one symposium, one specialist meeting and one workshop which are concurrent at the same place. This Symposium is on "Small Rocket Motors for Land, Sea and Air Launched Weapons Systems". You know that any member of AVT is responsible for his activities nine times more than in the past; because an FDP member in the past was responsible for only aerospace problems in fluid dynamics, but now a member of AVT is responsible for land, sea and air space. At the same time, for structures, fluid dynamics and propulsion. There will also be one special meeting on "Application of Damage Tolerance Principles for Improved Rotorcraft" and a workshop on "New Metallic Materials for Aging Aircraft". So, this is in the Spring of 1999 in Greece. Then in the Fall, we are going to have two Symposia, one Specialists Meeting and one Workshop in the same week. The first one is "Gas Turbine Operation and Technology for Land, Sea and Air Propulsion and Power Systems". This is a PEP type of thing. The second one is "Aerodynamic Design Optimization of Flight Vehicles in Multi-disciplinary Environment". And finally a Specialists meeting on "Design for Low Cost Operation and Support", and then a workshop on "Structural Aspects of Flexible Aircraft Control". My last vu-graph is on the Lecture Series. In 1998, you will have one on "Integrated Multi-Disciplinary Design of High Performance Multi-Stage Compression System" which is going to take place in Lyon, then Cologne. Then a special course at VKI on "Fluid Dynamics Research on Supersonic Aircraft" and again a special course which will be conducted in September at VKI and perhaps later at NASA Ames, "Higher Order Discretization Methods in CFD". In 1999, we have Lecture Series 217 on "Advanced Laser Measurement Techniques on Propulsion Systems" and two special courses, the first one "Development and Operation of UAV's for Civil and Military Applications" and the second one on "Measurement Techniques for High-enthalpy and Plasma Flows". These are our future activities, and we hope that they will please you.

Either you come yourself or recommend some other people to attend, tomorrow we are going to have the Technical Advancement Exchange Forum that will take place in this room from 9 o'clock to 11 o'clock. If we are going to have interesting exchanges, then we can push it until 12. Please attend and express your views, as for example topics that you want to see as an RTO activity. You have seen that our activities can be a Symposium, a Specialists' meeting, or a Workshop, or it can be a Working Group, or a Lecture Series, or it can be an AGARDograph. As I have done on the first day, I read the few lines in the Symposium Program. "Open to all AVT Panel Members, former AGARD and DRG Members and others upon invitation from any of the above"; I invite you all to the Forum.

Ladies and Gentlemen, this is really the end, so we will say arrivederci. Some of you will depart and some of you will stay until tomorrow morning. I am grateful for your contribution and presence.

Before closing this meeting I wish you all a safe return back home. I hope you have liked this meeting, and we hope to see you in another AVT activity in the future. Thank you.

REPORT DOCUMENTATION PAGE

1. Recipient's Reference	2. Originator's References RTO-MP-5 AC/323(AVT)TP/3	3. Further Reference ISBN 92-837-0002-3	4. Security Classification of Document UNCLASSIFIED/ UNLIMITED																		
5. Originator Research and Technology Organization North Atlantic Treaty Organization BP 25, 7 rue Ancelle, F-92201 Neuilly-sur-Seine Cedex, France																					
6. Title Missile Aerodynamics																					
7. Presented at/sponsored by The Applied Vehicle Technology Panel Symposium held in Sorrento, Italy, 11-14 May 1998.																					
8. Author(s)/Editor(s) Multiple			9. Date November 1998																		
10. Author's/Editor's Address Multiple			11. Pages 526																		
12. Distribution Statement There are no restrictions on the distribution of this document. Information about the availability of this and other RTO unclassified publications is given on the back cover.																					
13. Keywords/Descriptors <table><tr><td>Aerodynamics</td><td>Aerodynamic configurations</td></tr><tr><td>Missiles</td><td>Turbulence</td></tr><tr><td>Design</td><td>Turbulent flow</td></tr><tr><td>Computational fluid dynamics</td><td>Navier-Stokes equations</td></tr><tr><td>Fins</td><td>Computerized simulation</td></tr><tr><td>Aeroelasticity</td><td>Mathematical models</td></tr><tr><td>Control surfaces</td><td>Jet flow</td></tr><tr><td>Wind tunnel tests</td><td>Jet effects</td></tr><tr><td>Flight tests</td><td></td></tr></table>				Aerodynamics	Aerodynamic configurations	Missiles	Turbulence	Design	Turbulent flow	Computational fluid dynamics	Navier-Stokes equations	Fins	Computerized simulation	Aeroelasticity	Mathematical models	Control surfaces	Jet flow	Wind tunnel tests	Jet effects	Flight tests	
Aerodynamics	Aerodynamic configurations																				
Missiles	Turbulence																				
Design	Turbulent flow																				
Computational fluid dynamics	Navier-Stokes equations																				
Fins	Computerized simulation																				
Aeroelasticity	Mathematical models																				
Control surfaces	Jet flow																				
Wind tunnel tests	Jet effects																				
Flight tests																					
14. Abstract <p>Contains the papers prepared for the Symposium on 'Missile Aerodynamics' organised by the RTO Applied Vehicle Technology Panel (AVT), which was held 11-14 May 1998 in Sorrento, Italy. In addition, a Technical Evaluation Report aimed at assessing the success of the Symposium in meeting its objectives, and an edited transcript of the General Discussion held at the end of the Symposium are also included.</p> <p>This Symposium was dedicated to the memory of Dr. Jack Nielsen and a keynote paper addressed his contributions to Missile Aerodynamics. An additional keynote paper was presented on Future Missile System Trends and their Impact on Aerodynamics. In addition to the keynote presentations, 38 Papers were presented during sessions on the following subjects:</p> <ul style="list-style-type: none">- Aerodynamic Design- Unconventional Configurations- Jet Effects- Flows Physics and Turbulence Modeling- Prediction Methodology																					



RESEARCH AND TECHNOLOGY ORGANIZATION

BP 25 • 7 RUE ANCELLE

F-92201 NEUILLY-SUR-SEINE CEDEX • FRANCE

Télécopie 0(1)55.61.22.99 • Téléc 610 176

DIFFUSION DES PUBLICATIONS

RTO NON CLASSIFIEES

L'Organisation pour la recherche et la technologie de l'OTAN (RTO), détient un stock limité de certaines de ses publications récentes, ainsi que de celles de l'ancien AGARD (Groupe consultatif pour la recherche et les réalisations aérospatiales de l'OTAN). Celles-ci pourront éventuellement être obtenues sous forme de copie papier. Pour de plus amples renseignements concernant l'achat de ces ouvrages, adressez-vous par lettre ou par télécopie à l'adresse indiquée ci-dessus. Veuillez ne pas téléphoner.

Des exemplaires supplémentaires peuvent parfois être obtenus auprès des centres nationaux de distribution indiqués ci-dessous. Si vous souhaitez recevoir toutes les publications de la RTO, ou simplement celles qui concernent certains Panels, vous pouvez demander d'être inclus sur la liste d'envoi de l'un de ces centres.

Les publications de la RTO et de l'AGARD sont en vente auprès des agences de vente indiquées ci-dessous, sous forme de photocopie ou de microfiche. Certains originaux peuvent également être obtenus auprès de CASI.

CENTRES DE DIFFUSION NATIONAUX

ALLEMAGNE

Fachinformationszentrum Karlsruhe
D-76344 Eggenstein-Leopoldshafen 2

BELGIQUE

Coordinateur RTO - VSL/RTO
Etat-Major de la Force Aérienne
Quartier Reine Elisabeth
Rue d'Evere, B-1140 Bruxelles

CANADA

Directeur - Gestion de l'information
(Recherche et développement) - DRDGI 3
Ministère de la Défense nationale
Ottawa, Ontario K1A 0K2

DANEMARK

Danish Defence Research Establishment
Ryvangs Allé 1
P.O. Box 2715
DK-2100 Copenhagen Ø

ESPAGNE

INTA (RTO/AGARD Publications)
Carretera de Torrejón a Ajalvir, Pk.4
28850 Torrejón de Ardoz - Madrid

ETATS-UNIS

NASA Center for AeroSpace Information (CASI)
Parkway Center, 7121 Standard Drive
Hanover, MD 21076

FRANCE

O.N.E.R.A. (Direction)
29, Avenue de la Division Leclerc
92322 Châtillon Cedex

GRECE

Hellenic Air Force
Air War College
Scientific and Technical Library
Dekelia Air Force Base
Dekelia, Athens TGA 1010

ISLANDE

Director of Aviation
c/o Flugrad
Reykjavik

ITALIE

Aeronautica Militare
Ufficio Stralcio RTO/AGARD
Aeroporto Pratica di Mare
00040 Pomezia (Roma)

LUXEMBOURG

Voir Belgique

NORVEGE

Norwegian Defence Research Establishment
Attn: Biblioteket
P.O. Box 25
N-2007 Kjeller

PAYS-BAS

RTO Coordination Office
National Aerospace Laboratory NLR
P.O. Box 90502
1006 BM Amsterdam

PORTUGAL

Estado Maior da Força Aérea
SDFA - Centro de Documentação
Alfragide
P-2720 Amadora

ROYAUME-UNI

Defence Research Information Centre
Kentigern House
65 Brown Street
Glasgow G2 8EX

TURQUIE

Millî Savunma Başkanlığı (MSB)
ARGE Dairesi Başkanlığı (MSB)
06650 Bakanlıklar - Ankara

AGENCES DE VENTE

NASA Center for AeroSpace Information (CASI)

Parkway Center
7121 Standard Drive
Hanover, MD 21076

Etats-Unis

The British Library Document Supply Centre

Boston Spa, Wetherby
West Yorkshire LS23 7BQ

Royaume-Uni

Canada Institute for Scientific and Technical Information (CISTI)

National Research Council
Document Delivery,
Montreal Road, Building M-55
Ottawa K1A 0S2
Canada

Les demandes de documents RTO ou AGARD doivent comporter la dénomination "RTO" ou "AGARD" selon le cas, suivie du numéro de série (par exemple AGARD-AG-315). Des informations analogues, telles que le titre et la date de publication sont souhaitables. Des références bibliographiques complètes ainsi que des résumés des publications RTO et AGARD figurent dans les journaux suivants:

Scientific and Technical Aerospace Reports (STAR)

STAR peut être consulté en ligne au localisateur de ressources uniformes (URL) suivant:

<http://www.sti.nasa.gov/Pubs/star/Star.html>

STAR est édité par CASI dans le cadre du programme NASA d'information scientifique et technique (STI)
STI Program Office, MS 157A
NASA Langley Research Center
Hampton, Virginia 23681-0001
Etats-Unis

Government Reports Announcements & Index (GRA&I)

publié par le National Technical Information Service
Springfield

Virginia 2216

Etats-Unis

(accessible également en mode interactif dans la base de données bibliographiques en ligne du NTIS, et sur CD-ROM)



Imprimé par le Groupe Communication Canada Inc.

(membre de la Corporation St-Joseph)

45, boul. Sacré-Cœur, Hull (Québec), Canada K1A 0S7



RESEARCH AND TECHNOLOGY ORGANIZATION

BP 25 • 7 RUE ANGELLE

F-92201 NEUILLY-SUR-SEINE CEDEX • FRANCE

Telefax 0(1)55.61.22.99 • Telex 610 176

DISTRIBUTION OF UNCLASSIFIED
RTO PUBLICATIONS

NATO's Research and Technology Organization (RTO) holds limited quantities of some of its recent publications and those of the former AGARD (Advisory Group for Aerospace Research & Development of NATO), and these may be available for purchase in hard copy form. For more information, write or send a telefax to the address given above. **Please do not telephone.**

Further copies are sometimes available from the National Distribution Centres listed below. If you wish to receive all RTO publications, or just those relating to one or more specific RTO Panels, they may be willing to include you (or your organisation) in their distribution.

RTO and AGARD publications may be purchased from the Sales Agencies listed below, in photocopy or microfiche form. Original copies of some publications may be available from CASI.

NATIONAL DISTRIBUTION CENTRES

BELGIUM

Coordonateur RTO - VSL/RTO
Etat-Major de la Force Aérienne
Quartier Reine Elisabeth
Rue d'Evere, B-1140 Bruxelles

CANADA

Director Research & Development
Information Management - DRDIM 3
Dept of National Defence
Ottawa, Ontario K1A 0K2

DENMARK

Danish Defence Research Establishment
Ryvangs Allé 1
P.O. Box 2715
DK-2100 Copenhagen Ø

FRANCE

O.N.E.R.A. (Direction)
29 Avenue de la Division Leclerc
92322 Châtillon Cedex

GERMANY

Fachinformationszentrum Karlsruhe
D-76344 Eggenstein-Leopoldshafen 2

GREECE

Hellenic Air Force
Air War College
Scientific and Technical Library
Dekelia Air Force Base
Dekelia, Athens TGA 1010

ICELAND

Director of Aviation
c/o Flugrad
Reykjavik

ITALY

Aeronautica Militare
Ufficio Stralcio RTO/AGARD
Aeroporto Pratica di Mare
00040 Pomezia (Roma)

LUXEMBOURG

See Belgium

NETHERLANDS

RTO Coordination Office
National Aerospace Laboratory, NLR
P.O. Box 90502
1006 BM Amsterdam

NORWAY

Norwegian Defence Research Establishment
Attn: Biblioteket
P.O. Box 25
N-2007 Kjeller

PORTUGAL

Estado Maior da Força Aérea
SDFA - Centro de Documentação
Alfragide
P-2720 Amadora

SPAIN

INTA (RTO/AGARD Publications)
Carretera de Torrejón a Ajalvir, Pk.4
28850 Torrejón de Ardoz - Madrid

TURKEY

Milli Savunma Başkanlığı (MSB)
ARGE Dairesi Başkanlığı (MSB)
06650 Bakanlıklar - Ankara

UNITED KINGDOM

Defence Research Information Centre
Kentigern House
65 Brown Street
Glasgow G2 8EX

UNITED STATES

NASA Center for AeroSpace Information (CASI)
Parkway Center, 7121 Standard Drive
Hanover, MD 21076

SALES AGENCIES

NASA Center for AeroSpace
Information (CASI)

Parkway Center
7121 Standard Drive
Hanover, MD 21076
United States

The British Library Document
Supply Centre

Boston Spa, Wetherby
West Yorkshire LS23 7BQ
United Kingdom

Canada Institute for Scientific and
Technical Information (CISTI)

National Research Council
Document Delivery,
Montreal Road, Building M-55
Ottawa K1A 0S2
Canada

Requests for RTO or AGARD documents should include the word 'RTO' or 'AGARD', as appropriate, followed by the serial number (for example AGARD-AG-315). Collateral information such as title and publication date is desirable. Full bibliographical references and abstracts of RTO and AGARD publications are given in the following journals:

Scientific and Technical Aerospace Reports (STAR)

STAR is available on-line at the following uniform resource locator:

<http://www.sti.nasa.gov/Pubs/star/Star.html>

STAR is published by CASI for the NASA Scientific and Technical Information (STI) Program

STI Program Office, MS 157A
NASA Langley Research Center
Hampton, Virginia 23681-0001
United States

Government Reports Announcements & Index (GRA&I)

published by the National Technical Information Service
Springfield
Virginia 22161
United States
(also available online in the NTIS Bibliographic Database or on CD-ROM)



Printed by Canada Communication Group Inc.
(A St. Joseph Corporation Company)
45 Sacré-Cœur Blvd., Hull (Québec), Canada K1A 0S7